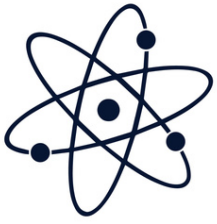


NELSON MANDELA  
UNIVERSITY



**100 years**  
of Physics in Africa  
Past, Present and  
Future

**Date:**  
**4-8 July 2022**

**Gqeberha**  
formerly Port Elizabeth

*Conference Proceedings*

**ANNUAL CONFERENCE OF THE SOUTH  
AFRICAN INSTITUTE OF PHYSICS (SAIP 2022)**

*Edited by Prof Aletta Prinsloo*

**PROCEEDINGS EDITOR-IN-CHIEF:**

Prof Aletta Prinsloo, University of Johannesburg

**PUBLISHER:**

The South African Institute of Physics (SAIP)

**COPYRIGHT NOTICE:**

© 2022 by the South African Institute of Physics

All rights reserved.

The conference was hosted virtually by the Nelson Mandela University on 4–8 July 2022. The Proceedings of SAIP 2022, the 66<sup>th</sup> Annual Conference of the South African Institute of Physics, will be available electronically only on the SAIP website: [www.saip.org.za](http://www.saip.org.za).

Permission to make digital or hard copies of part or all of this work for personal or classroom use is granted without fee provided that copies are not made or distributed for profit or commercial advantage and that copies bear this notice and the full citation on the first page. Abstracting with credit is permitted. To copy otherwise, to republish, to post on servers, or to distribute to lists, requires specific permissions and/or a fee. Request permissions from the SAIP Office:

phone: +27 (0)12 841 2655 / 2627

email: [info@saip.org.za](mailto:info@saip.org.za)

ISBN: 978-0-6397-4426-1

South African Institute of Physics  
CSIR Main Campus, Building 33  
Meiring Naude Rd, Pretoria.

# CONTENTS

<b>Editorial</b>	<b>9</b>
<b>Message from the Organisers</b>	<b>11</b>
• Local Organising Committee . . . . .	12
<b>Divisions, Editorial Team, and Reviewers</b>	<b>13</b>
• Division Chairs . . . . .	13
• Editorial Team . . . . .	14
• List of Reviewers . . . . .	16
• Group Photo of Delegates . . . . .	20
<b>A Physics of Condensed Matter and Materials</b>	<b>23</b>
• Atomistic simulation studies of binary $\text{Rh}_9\text{S}_8$ and ternary $\text{Ru}_4\text{Pd}_5\text{S}_8$ Pentlandite-like systems . . . . .	24
• Structural stability of some gold (Au) and silver (Ag) nanoparticles . . . . .	30
• Preparation and characterization of erbium-activated yttrium orthovanadate-phosphate by chemical bath deposition . . . . .	36
• Electronic, elastic, and transport properties of alpha-type copper sulphide . . . . .	43
• Development of machine learning models for predicting energies of sodium-ion battery materials . . . . .	49
• Structural and magnetic study of $\text{NdCrTiO}_5$ nanoparticles . . . . .	55
• Effects of deposition temperature on the properties of CdTe thin films prepared by electrodeposition method for solar energy applications . . . . .	62
• Structural stability of Cubic $\text{Ti}_2\text{AlV}$ and Tetragonal $\text{TiAl}_2\text{V}$ using First Principle Calculations . . . . .	68
• Tin (IV) oxide-coated gold nanocomposite materials for solar thermal energy collection and harvesting . . . . .	73
• The phase stability, mechanical and electronic properties of CsCl-type intermetallic: $\text{Ti}_{50}\text{TM}_{50}$ (TM = Ni, Ru and Pd), a first-principles approach . . . . .	81
• Effect of $\text{Ce}^{3+}$ substitution at B site on magnetic phase transitions in $\text{CoCr}_2\text{O}_4$ nanoparticles . . . . .	88

• Computational analyses of graphene quantum dots for anode material in lithium-ion batteries . . . . .	97
• Impact of Cr substitution on magnetic properties of cobalt-doped ZnO nanoparticles	103
• Structure, optical and magnetic properties of combustion synthesized Ni-Cr doped ZnO . . . . .	111
• Synthesis, Characterization and Simulation of Graphene Oxide Nanomaterial for Application in Hybrid Supercapacitors . . . . .	118
• Investigating the effects of Carbon and Boron atoms on the $\tau$ -MnAl alloy properties employing the first principle approach . . . . .	123
• Electronic, Magnetic and Mechanical Properties of Nd <sub>2</sub> Fe <sub>14</sub> B Permanent Magnets: Ab Initio Study . . . . .	127
• Synthesis of copper nanowires for application as flexible transparent conducting electrodes . . . . .	133
• Study of magnetic properties in doped intermediate valent Ce <sub>2</sub> Rh <sub>2</sub> Ga . . . . .	139
• Mechanical properties of Ti <sub>50-x</sub> Hf <sub>x</sub> Pt <sub>50</sub> , ( $0 < x < 50$ ) for high shape memory alloys applications . . . . .	145
<b>B Nuclear, Particle, and Radiation Physics</b>	<b>153</b>
• Design and development of the ALICE common readout unit user logic firmware for the Muon Identifier readout chain . . . . .	154
• Search for dark sector showering in ATLAS using semi-visible jets . . . . .	161
• Studying the Production of a Singlet Scalar at Future $e^+e^-$ Colliders with Deep Neural Networks . . . . .	168
• Evaluation and Optimisation of a Generative-Classification Hybrid Variational Autoencoder in the Search for Resonances at the LHC . . . . .	175
• Time stability of the response of gap and crack scintillators of the Tile Calorimeter of the ATLAS detector to isolated muons from $W \rightarrow \mu\nu_\mu$ events . . . . .	182
• Study of systematic uncertainties and spurious signals of resonant $H \rightarrow Z\gamma$ production at ATLAS Experiment . . . . .	189
• Compatibility of the CMS dilepton spectra with the Neutral Scalar with Mass around 151 GeV . . . . .	195
• A study of top quark pair production in association with a high energy photon at the LHC . . . . .	200
• Kernel Density Estimation-based simulation of Monte-Carlo events at LHC . . . . .	206
• Search for resonant production of strongly-coupled dark matter in proton-proton collisions . . . . .	212
• A search for $tWZ$ production with the ATLAS detector using the three and four lepton final states in proton-proton collisions at $\sqrt{s} = 13$ TeV . . . . .	218
• Characterisation of a new LSO block detector for Positron Emission Particle Tracking	224
• Search for new spin-1 boson using ATLAS detector data . . . . .	230
• Geant4 Analysis of Secondary Neutrons in Proton Therapy . . . . .	236
• Investigating the effect of neutrons on cadmium zinc telluride Compton camera . . . . .	242
• Higgs boson decays to four leptons and missing transverse momentum via dark vector bosons . . . . .	248
• A frequentist study of the false signals generated in the training of semi-supervised neural network classifiers using a Wasserstein Generative Adversarial Network as a data generator . . . . .	254
• Simulation of neutron and electron damage in Al <sub>2</sub> O <sub>3</sub> and MgO using the FLUKA code . . . . .	261

<b>C Photonics</b>	<b>267</b>
• Towards two-mode mode averaging with Orbital Angular Momentum modes . . . . .	268
• Effects of nanoparticle geometry on photon statistics . . . . .	274
• <i>In vitro</i> effects of aluminium (iii) phthalocyanine chloride tetra sulphonic acid-mediated photodynamic therapy on oesophageal cancer . . . . .	279
• Recombinant antibody-conjugated silver nanoparticles for improved drug delivery in photodynamic therapy for metastatic melanoma . . . . .	286
• <i>In vitro</i> antiproliferative effects of berberine in phthalocyanine-mediated photodynamic therapy on MCF-7 breast cancer cells with overexpressed P-Glycoprotein	293
• Investigating the morphology of an optically trapped particle using Mie scattering .	299
• Photobiomodulation at 830 nm modulates proliferation and migration of wounded fibroblast cells . . . . .	305
• Simulation of a malaria nanoplasmonic biosensor based on extraordinary optical transmission . . . . .	311
• Wavelength calibration of a monochromator system . . . . .	317
• Photonic quantum entanglement . . . . .	323
• Photobiomodulation at 830 nm influences diabetic wound healing <i>in vitro</i> through modulation of inflammatory cytokines . . . . .	328
<b>D Astrophysics and Space Science</b>	<b>335</b>
• Interacting viscous dark cosmology . . . . .	336
• Probing dark matter in 2HDM+S with MGCLS . . . . .	345
• A Closer Look at Potential Exoplanets Targets from the Nooitgedacht Observatory	351
• Primordial Black Holes and the SZ effect . . . . .	357
• Studying gas flows in the SUNBIRD starburst galaxies and LIRGs: Gas flows in NGC 6000 . . . . .	362
• From setting up a new telescope to optimizing astrometric solutions . . . . .	369
• Investigating HI size-mass relation in TNG50 and MIGHTEE-HI . . . . .	375
• Spectral and temporal analysis of short gamma-raybursts detected by the Fermi space telescope with known redshift . . . . .	382
• Spatially-resolved stellar kinematics of the CLoGS brightest group early-type galaxies	389
• MeerChoirs: Preliminary neutral gas kinematics of interacting galaxies in the J1250-20 group . . . . .	395
• Tracing Water Masers at their Smallest Scale with VLBI . . . . .	402
• Simulating the radio emission of dark matter for new high-resolution observations with MeerKAT . . . . .	408
• MeerKAT's view on galaxy clusters: Diffuse radio emission in MeerKAT Galaxy Cluster Legacy Survey . . . . .	414
• Collimation of Ion Density Distribution of Vacuum Arc Thrusters with Axial Magnetic Fields . . . . .	419
• Compact stars: Numerical solutions to the structure equations using Python . . . . .	425
<b>E Physics for Development, Education, and Outreach</b>	<b>433</b>
• The inclusion of nature of science in grade 12 high-stakes physics assessments in South Africa . . . . .	434
• Exploring the impact of teacher education programme on the development of pre-service science teachers' TPACK . . . . .	438
• Correlations between matriculation marks and mechanics misconceptions . . . . .	444
• Language in learning. Does teaching Physics in isiZulu aid students' understanding?	450

---

• The impact of simulation experiments on the understanding of the concepts of acceleration and energy . . . . .	456
• Students' understanding of physical components of electrical circuits . . . . .	463
• The effects of monitored peer teaching and learning on the understanding of basic Physics concepts . . . . .	470
• Teach electronics to applied Physics students: Prototyping, design and research on a printed circuit board . . . . .	477
• High School learners' difficulties with kinematics graphs . . . . .	482
• Using a Mobile Kibble Balance to explain Physics principles in Education . . . . .	490
<b>F Applied Physics</b>	<b>497</b>
• Synthesis and characterization of adsorbent biopolymer composite pellets and their potential application for VOCs removal from pharmaceutical effluents . . . . .	498
• Sol-gel derived and electrospun mesoporous TiO <sub>2</sub> : Effects of calcining temperature on the structure, morphology and surface area . . . . .	505
• A Nonlinear Logistic Regression Model for the Measurement of Drug Potency in Photodynamic Therapy . . . . .	511
• Implementation of the LED Integrator panel for the Prometeo system in the ATLAS Tile Calorimeter . . . . .	517
• Upgrade of ATLAS Tile Calorimeter TTC system for Phase-II test-beam campaigns	523
• Threading a Laser Through the Eye of a Needle: Multimode Fibre Coupling in Turbulence . . . . .	528
• Ion fraction measurements of vacuum arc thrusters . . . . .	535
• Comparison between the empirical and machine techniques to predict global solar irradiance for Mutale area in Limpopo Province, South Africa . . . . .	541
• Investigating the effects of turbulence-induced tilt and lateral displacement on OAM modes . . . . .	547
• Environmental Monitoring in the ATLAS ITk Detector . . . . .	553
• The investigation between covariability of energy fluxes and CO <sub>2</sub> flux exchanges at Skukuza Kruger National Park by Eddy Covariance technique . . . . .	559
• Characterisation of bulk materials using fast neutron transmission analysis . . . . .	565
• Validation of the Monte Carlo Detector Effects Model for the UCT Polaris Compton Camera . . . . .	570
• Setting up an environment that continuously analyse The ATLAS Tile Calorimeter temperature data . . . . .	576
• A modified Zinc oxide gas sensor approach to detect oxidizing gases . . . . .	582
• MicroPEPT: A step towards hybrid PEPT detectors . . . . .	588
• Developing an infectiousness model for droplet transmission . . . . .	594
• Measurement of fast neutron removal cross sections for the elemental analysis of concrete . . . . .	600
• Communication distance and security improvement in satellite based quantum key distribution via photon polarization pseudo-random bases encoding . . . . .	606
• Direct-coupled photovoltaic water pumping system sizing using borehole hydraulic parameters . . . . .	620
<b>G Theoretical and Computational Physics</b>	<b>627</b>
• Black holes and nilmanifolds: quasinormal mode calculations . . . . .	628
• The 5D MSSM at two loops . . . . .	634
• Matters of the $R_h = ct$ universe . . . . .	640
• The QCD Equation of State in Small Systems . . . . .	648

---

- 
- Energies of the Anharmonic Oscillator using the Metropolis Algorithm and Matrix Methods . . . . . 654
  - Quantum Network Coding on a Superconducting Processor . . . . . 660
  - Cavity QED based Open Quantum Walks . . . . . 666
  - Analytic Continuation of the Generalized Epstein zeta function for calculating finite system corrections in  $\phi^4$  theory . . . . . 672
  - Structural, thermodynamics, mechanical and thermal properties of monazite-type  $\text{LnPO}_4$  (Ln=La, Ce): A first principles study . . . . . 677
  - Particle rapidity distributions in Pb+Pb and Au+Au high-energy collisions from the Ultra-relativistic Quantum Molecular Dynamics (UrQMD 3.3p2) model at  $E_{elb} = 200$  AGeV. . . . . 683
  - Modeling the infectiousness of droplets when exposed to ultra-violet germicidal system: A computational fluid dynamics approach . . . . . 689
  - An Introduction to Statistical Thermal Models for Particle Production in Heavy-Ion Collisions . . . . . 695



# EDITORIAL

Nelson Mandela University (NMU) hosted the annual South African Institute of Physics (SAIP) conference virtually during 2022. Despite the fact that many of the Covid-19 pandemic limitations were lifted, there were still many uncertainties and with interested parties hesitant to travel, NMU decided to rather run the 66<sup>th</sup> conference in the series of SAIP as a virtual event. This was done with great success and the delegates commented on the professional running of the online event. Some papers from this online meeting are collected in this peer-reviewed volume. Submissions for the proceedings of SAIP2022 were handled by an Editorial Board headed by an Editor-in-Chief and Associate Editors responsible for submissions in different subject tracks.

The Editorial Board of the SAIP2022 Proceedings received 120 manuscripts for consideration by the advertised deadline. A total of 106 of these manuscripts met the relevant criteria and were submitted to a full peer-review process involving many individual reviewers. The list of the reviewer names are reflected elsewhere in the document and it is noted that certain reviewers took responsibility for more than one manuscript. The style of these proceedings is that of the (British) Institute of Physics Conference Series, similar to the styling used in previous SAIP Proceedings. Authors were requested to ensure that the defined layout were adhered to in their submitted pdf documents. In the past the review process was initiated with a layout review, followed by a content review. This year the Associate Editors conducted the layout review on each manuscript parallel with the content review. It was noted that there were small deviations between the layout templates available in MSWord and Latex – both of these formats were accepted by the Associate Editors. Manuscripts that deviated considerably from the specified layout specifications, while still broadly appropriate in their composition, were referred back to the authors for layout corrections. This was done in one step, together with the content reviews prepared by knowledgeable experts in each field. This year the Editorial Board aimed to reduce the time between the submissions and publication, with the authors being informed of the outcome of their submissions before the closure for the December holiday and the publication of the document online shortly after that.

The publication of the SAIP Proceedings are highly dependent on the efficiency of the Associate Editors and the goodwill of reviewers from the scientific community in South Africa. The Editor-in-Chief wishes to acknowledge the hard work of the Associate Editors who spent much

time considering the papers and reviewer reports in order to ensure that acceptable academic standards were met during peer-review for the proceedings to be credible. The majority of the content reviews received were done with great care and diligence and to the highest standards. The Editorial Board wishes to voice their sincere thanks to the participating Reviewers for their pro bono work, specifically to those Reviewers that read more than one paper. The meticulous reviewing process described above has ensured that these proceedings contain thoroughly peer-reviewed manuscripts of a high professional standard, which report on novel work that has not been published elsewhere.

This year the Editorial Board included a Technical Associate Editor, Dr Bruno Letarte from NWU. He took responsibility for finalising the complete document and ensured that it was of a high technical standard. The Editor-in-Chief wish to recognise Dr Letarte's enormous contribution in preparing the neat final document. The Editorial Board appreciate all the hours you dedicated into producing this exceptional document.

The Editor-in-Chief also wishes to recognise and thank Prof Strauss from NWU, Mr Mokhine from the SAIP office and Mr Jano Jonker from MNU for their support and help in preparing these proceedings.

Finally, the Editorial Board wishes to thank all of the authors for submitting their research work to this proceedings to undergo the rigorous review process. It is our sincere hope that the final product offered here constitutes a due outcome of their hard work.

# MESSAGE FROM THE ORGANISERS

The year 2022 is of great significance to the global physics community, being both the centenary of the International Union of Pure and Applied Physics (IUPAP 100) and also the International Year of Basic Sciences for Sustainable Development (IYBSSD 2022). As such, the 66<sup>th</sup> South African Institute of Physics Annual Conference aptly focused on “100 Years of Physics in Africa: Past, Present and Future”. As the LOC (from Nelson Mandela University), we are privileged and proud to have been part of this historical event.

We would like to thank all participants, sponsors, editors and reviewers, without whom this conference would not have been possible. A special word of thanks to the plenary speakers for their willingness to give us their excellent lectures. Despite this conference being virtual (the last as such!), we as the LOC hope that it nevertheless contributed to the sense of community amongst physicists locally, and that it inspired the younger generation of physics students to persevere in their studies by showcasing the important role that physics plays in building a better and brighter future for all!



From left to right at the back: Prof Ernest van Dyk, Prof Japie Engelbrecht, Prof André Venter, Mr Jano Jonker, Prof JR Botha, Mr Collin Bacela, Prof Tim Gibbon. Front row, from left to right: Dr Lindsay Westraadt, Ms Chanie Neveling, Dr Gretta Hashe.

## Local Organising Committee

- **Lindsay Westraadt** – Chair Person
- **Chanie Neveling** – Secretariat
- **JR Botha and Japie Engelbrecht** – Scientific Programme
- **André Venter** – Sponsorship
- **Ernest van Dyk** – Budget and Finances
- **Tim Gibbon and Nobom Hashe** – School and Public Programme
- **Collin Bacela** – Teachers Programme
- **Jano Jonker** – Proceedings
- **Brian Masara** – SAIP Representative

# DIVISIONS, EDITORIAL TEAM, AND REVIEWERS

## Division Chairs

- **Physics of Condensed Matter and Materials**
  - Rudolph Erasmus, University of the Witwatersrand
- **Nuclear, Particle, and Radiation Physics**
  - Bruce Mellado, University of the Witwatersrand
  - Rudolph Nchodu, NRF/ iThemba LABS
- **Photonics**
  - Pieter Neethling, Stellenbosch University
- **Astrophysics and Space Science**
  - Zama Katanzi, SANSA
- **Physics for Development, Education, and Outreach**
  - Sam Ramaila, University of Johannesburg
- **Applied Physics**
  - Phil Ferrer, University of the Witwatersrand
  - Tjaart Krüger, University of Pretoria
- **Theoretical and Computational Physics**
  - Alan Cornell, University of Johannesburg

---

## Editorial Team

### Editor-in-chief:

– **Aletta Prinsloo** is a Professor of Physics in the Department of Physics at the University of Johannesburg. She is an NRF rated research physicist in the field of experimental solid state physics. Her research is focused on the magnetism of chromium-based bulk alloys, thin films and nanomaterials.

### Associate Editors:

- **Physics of Condensed Matter and Materials**

- **Charles Sheppard** is an Associate Professor and a member of the Cr Research Group in the Physics Department at the University of Johannesburg. His current research interest focuses on the various physical properties observed in bulk Cr alloys, Cr thin films, and chrome oxide magnetic nano-materials.

- **Nuclear, Particle, and Radiation Physics**

- **Mukesh Kumar** is a Lecturer of Physics in the School of Physics at the University of the Witwatersrand. He is an NRF Y- rated research physicist in the field of high energy particle physics. His research is focused on Higgs boson, top quark, and dark matter physics at the Large Hadron Collider (CERN) including the future  $e^-p$  and  $e^+e^-$  colliders. He is a member of TileCal Speaker committee for ATLAS detector at CERN.

- **Photonics**

- **Pieter Neethling** is a Senior Lecturer in the Physics Department at Stellenbosch University. He is currently the Director of the Laser Research Institute at Stellenbosch University and the Chairman of the Photonics Division of the SAIP. His research focus is applied laser spectroscopy with applications in chemical and biological systems.

- **Astrophysics and Space Science**

- **Eugene Engelbrecht** is a Professor of Physics at North-West University, whose research covers topics relevant to the transport of charged particles in turbulent astrophysical plasmas, including both theoretical and observational aspects pertaining to cosmic ray modulation, non-linear diffusion theories, and plasma turbulence.

- **Physics for Development, Education, and Outreach**

- **Grace Phalwane** is a Dental Doctor and Health Professions Educationalist in the Department of Community Dentistry at the Sefako Makgatho Health Sciences University. Her research interest is focused on the Service Learning (SL), Problem-Based Learning (PBL) and Inter-Professional Education (IPE).

- **Applied Physics**

- **Thulani Hlatshwayo** is an associate Professor in the Department of Physics in the Faculty of Natural & Agricultural Sciences. His research is focussed on the understanding of the release of radioactive fission products from fuel in the modern nuclear reactors, where chemical vapour deposited (CVD)-SiC is the main barrier to fission products, and on finding alternative materials for nuclear waste storage. Professor Hlatshwayo recently received the Exceptional Young Researchers Award by the University of Pretoria. He is a PIs coordinator for SA-JINR projects in material research and nanoscience and is C2 NRF rated.

- **Kittessa Roro** is the Principal Researcher & Research Group Leader for Energy Supply & Demand (ESD) Research Group (RG) within the Energy Centre at the Smart Places Cluster of the CSIR. He is C2 NRF rated researcher in the field of Energy, Renewable Energy, nanotechnology and solid-state Physics. The ESD RG underpins the Energy Centre work in solar, on- and off-shore wind, renewable energy production/supply forecasting, energy efficiency / demand response, and thermal energy optimisation inclusive of thermal energy efficiency, recovery, and storage. The group also research on techno-economic viability of emerging and existing approaches to energy supply and end-use efficiency to provide impartial advocacy to industry and consumers.
- **Theoretical and Computational Physics**
  - **W. A. Horowitz** is an Associate Professor of Physics at the University of Cape Town. Among other honours, Prof Horowitz has received the Claude Leon Merit Award for Early-Career Researchers and the Meiring Naudé Medal for Outstanding Early Career Contributions to Science from the Royal Society of South Africa. Prof Horowitz' research explores the non-trivial emergent many-body properties of the strong force using the methods of perturbative quantum field theory and the AdS/CFT correspondence.
- **Technical**
  - **Bruno Letarte** is a Senior Lecturer at the Centre for Space Research of the North-West University. He specialises in observational astronomy, photometry as well as spectroscopy, with his main interest in stellar astrophysics. He manages the optical telescope at the Nooitgedacht observatory, used to train undergraduate and postgraduate students. He is also the physics subject group leader, what other universities call head of department, on the Potchefstroom campus.

## Proceedings Online Administration:

- **Tebogo Mokhine**, South African Institute of Physics

---

## List of Reviewers

- **Prof Amare Abebe** – North-West University, RSA
- **Dr Shimaa Abuzeid** – Ain Shams University -Cairo, Egypt
- **Dr Olaleru Akin** – Yaba College of Technology, Nigeria
- **Dr Odochukwu B Akuru** – Tshwane University of Technology, RSA
- **Prof Akintunde Ayodeji Alonge** – University of Johannesburg, RSA
- **Dr Ruth Aluko** – University of the Witwatersrand, RSA
- **Prof Pieta J Ankiewicz** – University of Johannesburg, RSA
- **Dr Abraham Aava** – TRIUMF Canada’s particle accelerator centre, Canada
- **Mr Mphathi Collin Bacela** – Nelson Mandela University, RSA
- **Dr Mokae Bambo** – Mintek, RSA
- **Dr Teboho Belle** – CSIR, RSA
- **Dr Muaaz Bhamjee** – University of Johannesburg, RSA
- **Dr Saphina Biira** – Busitema University, Uganda
- **Dr Marguerite Blignaut** – Stellenbosch University, RSA
- **Dr Gurthwin Bosman** – Stellenbosch University, RSA
- **Prof Andy Buffler** – University of Cape Town, RSA
- **Prof Zinhle Buthelezi** – NRF/ iThemba LABS; WITS School of Physics, RSA
- **Prof Emanuela Carleschi** – University of Johannesburg, RSA
- **Dr Chun-Hung Chen** – Naresuan University, Thailand
- **Dr Andrew Chen** – University of the Witwatersrand, RSA
- **Prof Nithaya Chetty** – University of Pretoria, RSA
- **Prof James Chibueze** – North-West University, RSA
- **Dr Hing-Tong Cho** – Tamkang University, Taiwan
- **Prof Pierre J Cilliers** – SANSA, RSA
- **Prof Elizabeth Coetsee-Hugo** – University of Free State, RSA
- **Prof Simon Connell** – University of Johannesburg, RSA
- **Prof Alan Cornell** – University of Johannesburg, RSA
- **Dr Mitchell Cox** – University of the Witwatersrand, RSA

- **Dr Álvaro de la Cruz-Dombriz** – University of Cape Town, RSA
- **Dr Thomas Dietel** – University of Cape Town, RSA
- **Prof Cesareo Dominguez** – University of Cape Town, RSA
- **Prof Bryan Doyle** – University of Johannesburg, RSA
- **Dr Angela Dudley** – University of the Witwatersrand, RSA
- **Dr Adams Duniya** – BIUST, Botswana
- **Prof Eugene Engelbrecht** – North-West University, RSA
- **Prof Chris Engelbrecht** – Retired, RSA
- **Mr Oluwatoyin Olabisi Ewuola** – University of Johannesburg, RSA
- **Dr Derek Fish** – Unizulu Science Centre, RSA
- **Dr Juvet Fru** – University of Pretoria, RSA
- **Prof Benjamin Fuks** – Sorbonne Université, France
- **Prof Igle Gledhill** – University of the Witwatersrand, RSA
- **Prof Diane Grayson** – University of the Witwatersrand, RSA
- **Dr Lokesha Handalagere Shankarappa** – University of Johannesburg, RSA
- **Prof Richard Harris** – University of the Free State, RSA
- **Prof Thulani Hlatshwayo** – University of Pretoria, RSA
- **Prof W. A. Horowitz** – University of Cape Town, RSA
- **Dr Yanping Huang** – IHEP, China
- **Dr Yaseera Ismael** – University of KwaZulu-Natal, RSA
- **Dr Susan Jacobs** – University of Johannesburg, RSA
- **Prof Daniel Jobert** – University of the Witwatersrand, RSA
- **Mr Jano Jonker** – Nelson Mandela University, RSA
- **Prof Deepak Kar** – University of the Witwatersrand, RSA
- **Dr James Keaveney** – University of Cape Town, RSA
- **Prof Mesfin Kebede** – University of South Africa, RSA
- **Dr Garreth Kemp** – University of Johannesburg, RSA
- **Dr Najimuddin Khan** – HRI, India
- **Dr Bonginkosi Khoza** – University of Johannesburg, RSA
- **Dr Korir Kiptiemoi** – Moi University, Kenya

- 
- **Dr Isobel Kolbé** – Universidade de Santiago de Compostela, Spain
  - **Prof Nukri Komin** – University of the Witwatersrand, RSA
  - **Dr Chester Kotsedi** – NRF/ iThemba LABS, RSA
  - **Dr Hannes Kriel** – Stellenbosch University, RSA
  - **Prof Tjaart Kruger** – University of Pretoria, RSA
  - **Dr Satendra Kumar** – IIT; UNA, India
  - **Dr Mukesh Kumar** – University of the Witwatersrand, RSA
  - **Dr Pannan Kyesmen** – University of Pretoria, RSA
  - **Prof Lerothodi Leeuw** – University of the Western Cape, RSA
  - **Dr Bruno Letarte** – North-West University, RSA
  - **Prof Ben Loos** – Stellenbosch University, RSA
  - **Prof Ilani Loubser** – North-West University, RSA
  - **Dr Mawande Lushozi** – University of Cape Town, RSA
  - **Dr Kelebogile Maabong-Tau** – University of Botswana, Botswana
  - **Dr Chemist Mabena** – CSIR, RSA
  - **Dr Siyabonga Majola** – University of Johannesburg, RSA
  - **Dr Nicholas Makau** – University of Eldoret, Kenya
  - **Dr Peane Maleka** – NRF/ iThemba LABS, RSA
  - **Dr Edwin Mapasha** – University of Pretoria, RSA
  - **Dr Deon Marais** – NECSA, RSA
  - **Dr Paulo Marchegiani** – University of the Witwatersrand, RSA
  - **Dr Marco Mariola** – University of KwaZulu-Natal, RSA
  - **Dr Bathisile Masina** – CSIR, RSA
  - **Dr Loyiso Maweza** – CSIR, RSA
  - **Prof Bruce May** – University of the Western Cape, RSA
  - **Dr Rachid Mazini** – CERN, Switzerland
  - **Dr Vanessa McBride** – NRF South African Astronomical Observatory, RSA
  - **Dr Linda Mdletshe** – University of Zululand, RSA
  - **Prof Phumlani Mdluli** – Mintek, RSA
  - **Dr Bruce Mellado** – University of the Witwatersrand, RSA

- **Dr Rebecca Mhlongo** – Sefako Makgatho Health Sciences University, RSA
- **Prof Matlab Mirzayev** – Joint Institute for Nuclear research -Dubna, Russia
- **Prof Simiso Mkhonta** – University of Eswatini, Swaziland
- **Dr Michaela Mlynarikova** – CERN, Switzerland
- **Prof Sabata Moloi** – University of South Africa, RSA
- **Dr Taswald Moodley** – Mintek, RSA
- **Dr Blessed Muchono** – University of Eswatini, Swaziland
- **Prof Azwinndini Muroga** – Nelson Mandela University, RSA
- **Dr Darryl Naidoo** – CSIR, RSA
- **Prof Deena Naidoo** – University of the Witwatersrand, RSA
- **Dr Pieter Neethling** – Stellenbosch University, RSA
- **Dr Edward Nkadimeng** – CERN, Switzerland
- **Dr Steven Nkosi** – University of Limpopo, RSA
- **Dr Volkmar Nolting** – Vaal University of Technology, RSA
- **Prof Sifiso Ntshangase** – University of Zululand, RSA
- **Dr Nangamso Nyangiwe** – Tshwane University of Technology, RSA
- **Dr Saturnin Ombinda-Lemboumba** – CSIR, RSA
- **Dr Ezekiel Omotoso** – Obafemi Awolowo University, Nigeria
- **Dr Masimba Paradza** – Cape Peninsula University of Technology, RSA
- **Dr Alexander Paradzah** – Chinhoyi University of Technology, Zimbabwe
- **Dr Motlalepula Grace Phalwane** – Sefako Makgatho Health Sciences University, RSA
- **Dr Shashi Prabhakar** – Physical Research Laboratory, India
- **Prof Aletta Prinsloo** – University of Johannesburg, RSA
- **Dr Tshepo Ramarumo** – Sefako Makgatho Health Sciences University, RSA
- **Prof Erich Rohwer** – Stellenbosch University, RSA
- **Dr Kittessa Roro** – CSIR, RSA
- **Dr Arnoux Rossow** – Joint Institute for Nuclear research -Dubna, Russia
- **Prof Solly Seeletse** – Sefako Makgatho Health Sciences University, RSA
- **Dr Moagisi Edwin Seleka** – Sefako Makgatho Health Sciences University, RSA
- **Dr Lebogang Sesale** – Sefako Makgatho Health Sciences University, RSA

- **Dr Bertie Seyffert** – North-West University, RSA
- **Prof Charles Sheppard** – University of Johannesburg, RSA
- **Prof Ilya Sinayskiy** – University of KwaZulu-Natal, RSA
- **Dr Makuhane Sithole** – University of Zululand, RSA
- **Prof Vladimir Skuratov** – Joint Institute for Nuclear Research, Russia
- **Prof Buyi Sondezi** – University of Johannesburg, RSA
- **Dr Lynndle Square** – North-West University, RSA
- **Dr Christine Steenkamp** – Stellenbosch University, RSA
- **Dr Ruhann Steyn** – North-West University, RSA
- **Prof Du Toit Strauss** – North-West University, RSA
- **Prof Mark Tame** – Stellenbosch University, RSA
- **Dr Henerica Tazvinga** – SAWS, RSA
- **Prof Moise Tchokonte Tchoala** – University of Western Cape, RSA
- **Dr Thabisile Thabethe** – University of Pretoria, RSA
- **Prof Iyabo Usman** – University of the Witwatersrand, RSA
- **Prof Johan van der Walt** – North-West University, RSA
- **Dr Brian van Soelen** – University of the Free State, RSA
- **Prof Christo Venter** – North-West University, RSA
- **Dr Robert Warmbier** – University of Johannesburg, RSA
- **Dr Heneric Wilkens** – CERN, Switzerland
- **Prof Hartmut Winkler** – University of Johannesburg, RSA
- **Dr Dawit Worku** – Cape Peninsula University of Technology, RSA
- **Dr Maosen Zhou** – IHEP; UCAS, China

## Group Photo of Delegates





DIVISION

A

PHYSICS OF CONDENSED MATTER AND  
MATERIALS

# Atomistic simulation studies of binary $\text{Rh}_9\text{S}_8$ and ternary $\text{Ru}_4\text{Pd}_5\text{S}_8$ Pentlandite-like systems

**KB Molala, MA Mehlape, PP Mkhonto and PE Ngoepe**

Materials Modelling Centre, University of Limpopo, Private Bag x1106, Sovenga, 0727, South Africa

E-mail: [barnardkgwajana@gmail.com](mailto:barnardkgwajana@gmail.com)

**Abstract.** Pentlandite (Pn) is an iron nickel sulphite with chemical formula of  $(\text{Fe,Ni})_9\text{S}_8$  and is contained mainly in the Merensky Reef (~30%) of the Bushveld complex. Pn systems are known to host precious metals in solid solutions or as intergrowths. However, the effect of temperature and pressure on  $\text{Rh}_9\text{S}_8$  and  $\text{Ru}_4\text{Pd}_5\text{S}_8$  Pn-like structures has not been established. Pentlandite structures have been studied mostly experimentally but computational studies have been scarce. In this study, we derived interatomic potentials for binary  $\text{Rh}_9\text{S}_8$  and ternary  $\text{Ru}_4\text{Pd}_5\text{S}_8$  Pentlandite-like systems, which produced the elastic constants that are in good agreement with *ab-initio* density functional theory (DFT) results. Classical atomistic simulation suggest that the melting temperature for binary  $\text{Rh}_9\text{S}_8$  and ternary  $\text{Ru}_4\text{Pd}_5\text{S}_8$  Pn-like systems are near 1000K and 600K respectively.

## 1. Introduction

Metal sulphides are important in many fields of science such as in metallurgy, materials science, geochemistry, physics, geology and chemistry. They serve as a source of the world's precious metal-bearing minerals that are economically and industrially significant [1]. Sulphide minerals are the most, diverse and richest in terms of physical, chemical and structural properties [2]. Pentlandite minerals are well known to host platinum group elements (PGEs), either as solid solutions or as intergrowths [3]. Palladium and rhodium are the PGEs contained mostly in pentlandite [4]. Thus the PGEs may exist in the pentlandite structure forming PGEs-Pentlandite-like (PGEs-Pn-like) systems. Owing to their high concentration in the Bushveld Complex, it draws much attention to identify these new phases and their stabilities that will establish new knowledge in searching for new minerals. Investigation of such phases presents a number of geological search and experimental tests that are time consuming and expensive. Computational modelling methods is an option that may be used to search and test new phases using minimal time and resources prior to beginning full laboratory testing. Furthermore, computational modelling methods have established thermodynamic and electronic signatures for stabilities of  $\text{Co}_9\text{S}_8$ , and the naturally occurring  $(\text{Fe,Ni})_9\text{S}_8$  pentlandite, which were found to be consistent with experimental results [5][6]The initial work on the stability of pentlandite-like structures, i.e.  $\text{M}_9\text{S}_8$  ( $\text{M} = \text{Ru, Pd, Os, Pt, Ir, Rh}$ ),  $(\text{Ru, Pd})_9\text{S}_8$  and  $(\text{Os, Pt})_9\text{S}_8$  was investigated using Density Functional Theory (DFT) [7]. However, DFT method was for the calculation of elastic constants to be used as the observables for the derivation of interatomic potentials for atomistic simulation study.

The derived interatomic potentials of  $\text{Rh}_9\text{S}_8$  and  $\text{Ru}_4\text{Pd}_5\text{S}_8$  were validated by the accurate determination of structure and elastic constants. Atomistic simulation method, i.e. Molecular dynamics (MD) was used to investigate the structural and dynamical properties of pentlandite-like structures ( $\text{Rh}_9\text{S}_8$  and  $\text{Ru}_4\text{Pd}_5\text{S}_8$ ).

### 1.1. Crystal Structure

The description of the pentlandite-like structures used in this work were based on geometry of pentlandite structure with space group of  $Fm\bar{3}m$  (225) [8]. The study focused on the 68 atoms conventional unit cell of the pentlandite structures with the formula  $(M,M)_{36}S_{32}$ . There are four  $M_9S_8$  units in the conventional cubic unit cell, with the sulphur atoms forming an almost cubic close-packed framework. The corresponding unrelaxed distances between the octahedral metal  $M(O)$  and face-capping sulphur  $S(f)$  were  $M(O)-S(f) = 2.5978 \text{ \AA}$ . The distances between tetrahedral metal  $M(T)$  and face-capping  $S(f)$  and linked sulphurs  $S(l)$  were,  $M(T)-S(f) = 2.460 \text{ \AA}$  and  $M(T)-S(l) = 2.295 \text{ \AA}$ . The crystal structure of the Pn-like systems used in this study in Figure 1.

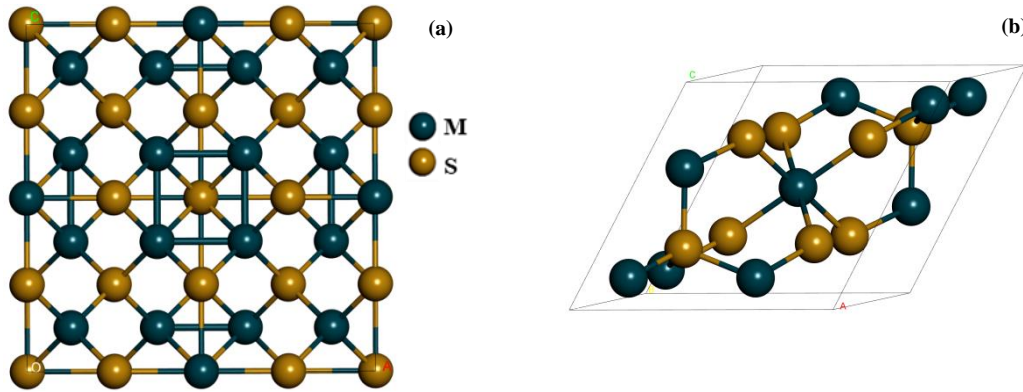


**Figure 1.** Binary pentlandite-like models of  $M_9S_8$ : (a) conventional 68 atoms unit cell and (b) primitive 17 atoms unit cell.

## 2. Computational Method

The atomistic simulation method in the present study was conducted using General Utility Lattice Program (GULP) code [9], which requires the use of interatomic potential functions. In this study GULP code as implemented in BIOVIA Materials Studio was used to derive the interatomic potentials of Pn-like system. The Potential parameters were adjusted to reproduce the elastic constants and lattice parameter from *ab-initio* and available experimental data. The calculations were based on the Born ionic model of a solid [10] and parameters were derived for short range interactions represented by the Buckingham potential, Morse potential and three body terms.

### 2.1. Buckingham Potential

In the Buckingham potential, the repulsive term is represented by an exponential term and the potential takes the form

$$U(r_{ij}) = A_{ij} \times \exp\left(\frac{-r_{ij}}{\rho_{ij}}\right) - \frac{C_{ij}}{r_{ij}^6} \quad (1)$$

where  $A_{ij}$  and  $\rho_{ij}$  are parameters that represent the ion size and hardness, respectively, while the  $C_{ij}$  describe the attractive interaction and  $r_{ij}$  is the distance between ion  $i$  and ion  $j$ .

### 2.1. Morse Potential

The Morse potential is used to model the interactions between covalently bonded atoms and has the form

$$U(r_{ij}) = D_{ij} \left(1 - \exp(-B_{ij} \times (r_{ij} - r_0))\right)^2 - D_{ij} \quad (2)$$

where  $D_{ij}$  is the bond dissociation energy,  $r_0$  is the equilibrium bond distance, and  $B_{ij}$  is a function of the slope of the potential energy well.

**Table 1.** Interatomic potential parameters for the Rh<sub>9</sub>S<sub>8</sub> as derived in the present study.

Potentials			
Buckingham Potentials	A (eV)	$\rho$ (Å)	C (eV.Å <sup>-6</sup> )
S core – S core	1130.533064	0.184528	0.000
Morse Potential	D (eV)	$\rho$ (Å)	$r_0$ (Å)
Rh core – S core	3.0	1.633754	2.600
Three-body potential	K (eV/rad <sup>-2</sup> )		$\theta_0$ (°)
S core Rh core S core	0.82		109.503
Rh core S core Rh	2.89		109.503

### 2.2 Three-Body Potential

A further component of the interactions of covalent species is the bond-bending term, which is added to take into account the energy penalty for deviations from the equilibrium value. Hence, this potential describes the directionality of the bonds and has a simple harmonic form:

$$U(\Theta_{ijk}) = \frac{1}{2} k_{ijk} (\Theta_{ijk} - \Theta_0)^2 \quad (3)$$

where  $k_{ijk}$  is the three-body force constant,  $\Theta_0$  is equilibrium angle and  $\Theta_{ijk}$  is the angle between two interatomic vectors  $i - j$  and  $j - k$ .

The potential parameters of Rh<sub>9</sub>S<sub>8</sub> are given in Table 1, and Table 2 gives the potentials of Ru<sub>4</sub>Pd<sub>5</sub>S<sub>8</sub> used in this study.

**Table 2.** Interatomic potential parameters for the Ru<sub>4</sub>Pd<sub>5</sub>S<sub>8</sub> as derived in the present study.

Potentials			
Buckingham Potentials	A (eV)	$\rho$ (Å)	C (eV.Å <sup>-6</sup> )
S core – S core	1130.533064	0.184528	0.000
Morse Potential	D (eV)	$\rho$ (Å)	$r_0$ (Å)
Ru core – S core	3.5	1.20	2.21
Morse Potential	D (eV)	$\rho$ (Å)	$r_0$ (Å)
Pd core – S core	3.90	1.20	2.18
Three-body potential	K (eV.rad <sup>-2</sup> )		$\theta_0$ (°)
S core Ru core Ru core	3.601		109.503
Ru core S core S core	2.82		109.503
S core Pd core Pd core	0.89		109.503
Pd core S core S core	0.89		109.503

## 3. Results and Discussion

In this section we consider the validation of our derived interatomic potential model for both binary Rh<sub>9</sub>S<sub>8</sub> and ternary Ru<sub>4</sub>Pd<sub>5</sub>S<sub>8</sub> Pn-like Systems. The potential models are developed to simplify the complexity of the quantum mechanical computations. The elastic constants, calculated by ab initio DFT method using VASP code [11], were used as input data for the development of potentials models.

**Table 3.** Calculated elastic constant and lattice parameters obtained from GULP and VASP code.

Structures	Elastic constants			Lattice parameter $a$ (Å)
	$C_{11}$	$C_{12}$	$C_{44}$	
Rh <sub>9</sub> S <sub>8</sub>	210.03 (211.15)[7]	123.07 (87.68) [7]	50.17 (42.37) [7]	9.80 (10.47) [7] (9.12)[12]
Ru <sub>4</sub> Pd <sub>5</sub> S <sub>8</sub>	176.13 (178.00)[7]	69.34 (67.30) [7]	38.41 (36.01) [7]	

To validate our potential models we start by showing the properties that were obtained from our derived potentials i.e., Table 3 shows the calculated lattice parameters and elastic constants obtained from different methods, GULP and VASP code. Interestingly lattice parameter of  $\text{Rh}_9\text{S}_8$  obtained from GULP code was in good agreement with both VASP code and experimental. Moreover the elastic constants of  $\text{Ru}_4\text{Pd}_5\text{S}_8$  obtained from GULP compared very well with the elastic constants from VASP code (ab initio DFT method).

### 3.1. Molecular Dynamics

To study the temperature effect on  $\text{Rh}_9\text{S}_8$  and  $\text{Ru}_4\text{Pd}_5\text{S}_8$  Pn-like systems, we used molecular dynamics (MD) method as embedded in GULP code using NVT ensemble.  $3 \times 3 \times 3$  supercell were used when performing MD. Figure 2 (a) shows the total radial distribution functions (RDFs) of  $\text{Rh}_9\text{S}_8$  supercell at various temperatures. The RDFs of  $\text{Rh}_9\text{S}_8$  showed the sharp peaks at 300K suggesting that the system was still in a solid phase and we further observed that the  $\text{Rh}_9\text{S}_8$  crystal structure was still ordered. At 1000K the peaks started to be smooth showing that the structure changed phase and as the temperature increases the peaks fades away at 1500 K the RDF showed  $\text{Rh}_9\text{S}_8$  was in another phase and the system was completely disordered. Figure 2 (b) the total RDFs of  $\text{Ru}_4\text{Pd}_5\text{S}_8$  at various temperatures, we observed sharp peaks at 300 K and at 600 K the peaks started to be smooth suggesting phase change. At 1000K the peaks fades away and  $\text{Ru}_4\text{Pd}_5\text{S}_8$  structure lost crystallinity. Figure 3 and figure 4 clearly shows the structural changes of  $\text{Rh}_9\text{S}_8$  and  $\text{Ru}_4\text{Pd}_5\text{S}_8$  structure after MD simulations at various temperatures respectively which agrees very well with the RDFs.

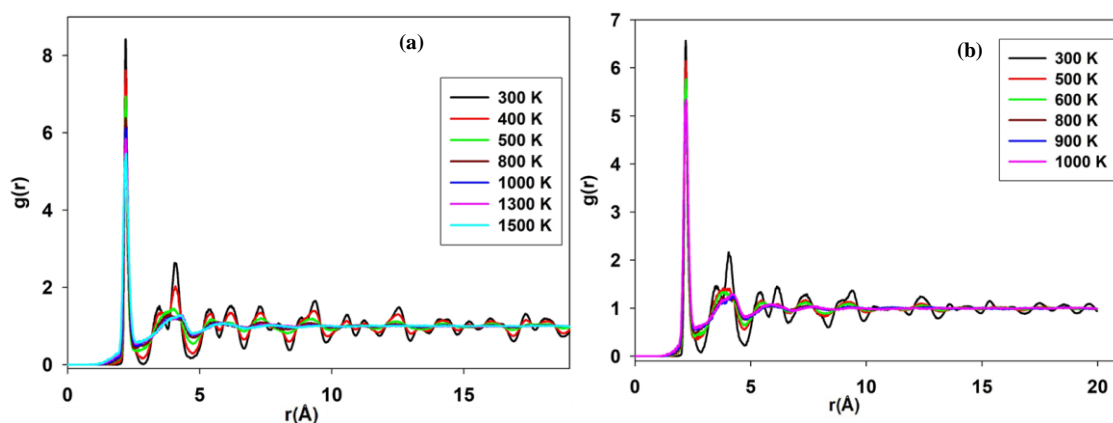


**Figure 2.** Total RDFs of (a)  $\text{Rh}_9\text{S}_8$  and (b)  $\text{Ru}_4\text{Pd}_5\text{S}_8$  supercell at various temperatures.

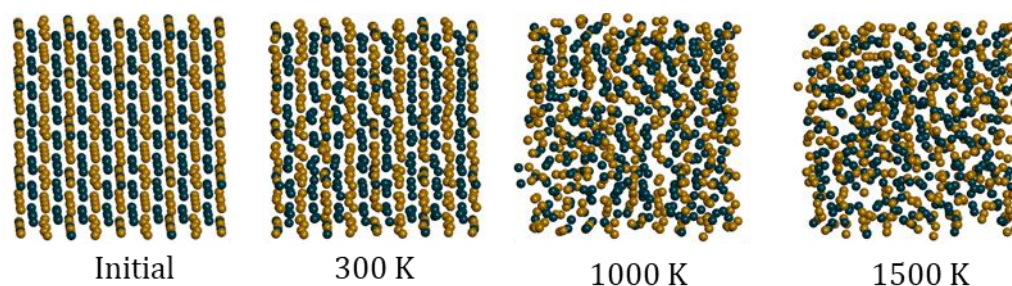


**Figure 3.** Structural changes of  $\text{Rh}_9\text{S}_8$  structure after MD simulations at various temperatures.

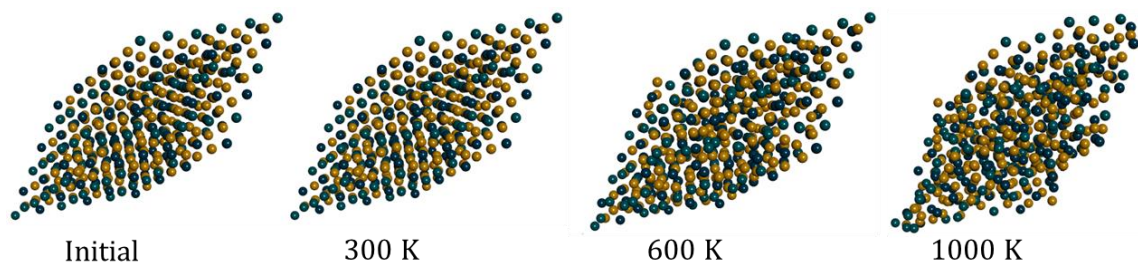


**Figure 4.** Structural changes of  $\text{Ru}_4\text{Pd}_5\text{S}_8$  structure after MD simulations at various temperatures.

The average mean squared displacement (MSD) is one of the method to investigate the atom mobility. MSD refers to the square of the average displacement of particles in a certain period of time [13]. Figure 5 shows the total MSD as a function of time at different temperatures for (a)  $\text{Rh}_9\text{S}_8$  and (b)  $\text{Ru}_4\text{Pd}_5\text{S}_8$ . From the MSD of  $\text{Rh}_9\text{S}_8$  we observed less atomic mobility between 300 K and 800 K temperatures and as the temperatures increases from 1000 K to 1800 K we observed increases at atomic mobility within  $\text{Rh}_9\text{S}_8$  system. The MSD of  $\text{Ru}_4\text{Pd}_5\text{S}_8$  showed that there was less atom mobility between 300K and 500K temperatures and as the temperatures increases from 600 K to 900 K we observed increases at atomic mobility within  $\text{Ru}_4\text{Pd}_5\text{S}_8$  system. For both  $\text{Rh}_9\text{S}_8$  and  $\text{Ru}_4\text{Pd}_5\text{S}_8$ , the same temperature range were observed through the RDFs in Figure 2 demonstrate that after initial diffusion for a period of time, the ions quickly reached the stable stage and then maintained a relatively stable diffusion level. A linear relationship is observed between MSD and simulation time.

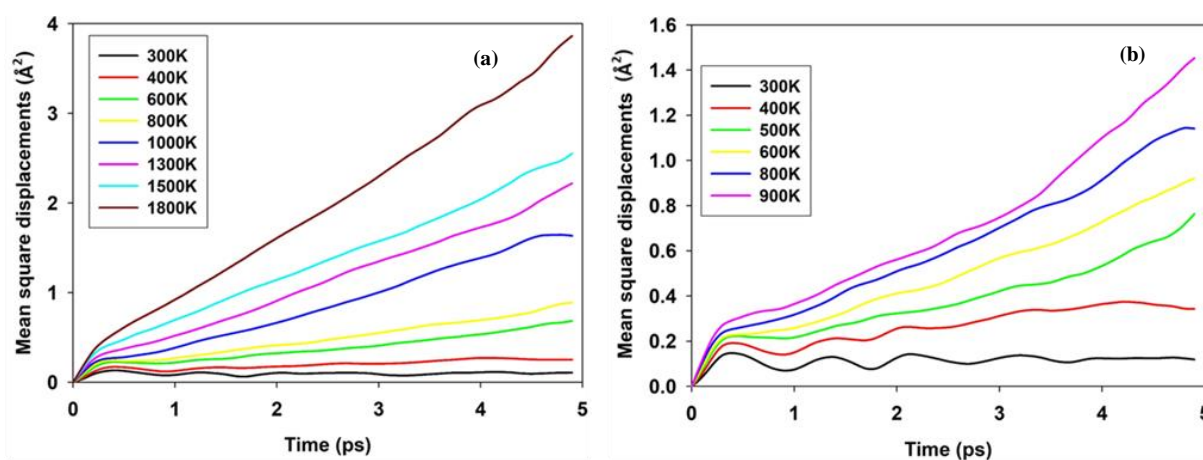


**Figure 5.** The variation of MSD of (a)  $\text{Rh}_9\text{S}_8$  and (b)  $\text{Ru}_4\text{Pd}_5\text{S}_8$  with time at various temperatures.

#### 4. Conclusion

The phase temperature effect on binary  $\text{Rh}_9\text{S}_8$  and ternary  $\text{Ru}_4\text{Pd}_5\text{S}_8$  system were investigated using atomistic simulation. Interatomic potentials were derived using GULP code and elastic constants from GULP were comparable with ab initio's. The lattice parameter of  $\text{Rh}_9\text{S}_8$  was in good agreement with experimental. RDFs shows and  $\text{Rh}_9\text{S}_8$  and  $\text{Ru}_4\text{Pd}_5\text{S}_8$  loses crystallinity near 1000K and 600K respectively, the MSD further showed that the atomic mobility increases with increasing temperature. Thus the refitted potentials gave reasonable results and may further be helpful to future studies regarding the structural and elastic properties, and other related properties of pentlandite-like systems.

#### Acknowledgements

The calculations were performed at the Materials Modelling Centre (MMC), University of Limpopo, and at the Centre for High Performance Computing (CHPC), in Cape Town. We wish to acknowledge

National Research Foundation (NRF), Department of Science and Innovation (DSI) and the DSI-NRF South African Research Chair Initiative (SARChI) for funding this work.

### References

- [1] Waldner P and Sitte W 2008 *J. Phys. Chem. Solids.* **69** 923
- [2] Johan Z, Ohnenstetter M, Slansky E, Barron L M and Suppel D 1989 *Mineral. Petrol.* **40** 289
- [3] Wang Q and Heiskanen K 1990 *Int. J. Miner. Process.* **29** 99
- [4] Godel B, Barnes S and Maier W D 2007 *J. Petrol.* **48** 1569
- [5] Chauke H R, Nguyen-Manh D, Ngoepe P E, Pettifor D G, and Fries S G 2002 *Phys. Rev.* **66** 155100
- [6] Mehlae M A 2013 PhD Thesis. University of Limpopo
- [7] Molala K B 2021 MSc Dissertation. University of Limpopo
- [8] Geller S 1962 *Acta Crystallogr.* **15** 1195
- [9] Gale J D and Rohl A L 2003 *Mol. Simul.* **5** 341
- [10] Born M and Huang K 1954 *Dynamical Theory of Crystal Lattices 1st edition.* Oxford: University Press
- [11] Kresse G, Furthmüller J and Hafner J 1994 *Phys. Rev. B.* **50** 13181
- [12] Kjekshus A 1960 *Acta Chem. Scand.* **14** 1623
- [13] Wang G, Cui Y, Li X, Yang S, Zhao J, Tang H and Li X 2020 *Minerals* **10** 14

## Structural stability of some gold (Au) and silver (Ag) nanoparticles

MW Makgoba<sup>1</sup>, TE Mosuang<sup>1</sup>, MA Mahladi<sup>1</sup>, MG Matshaba<sup>1</sup>, RR Maphanga<sup>2</sup>, N Mhlana<sup>3</sup>, T Mokheba<sup>3</sup>.

<sup>1</sup>Department of Physics, University of Limpopo, Private Bag x1106, Sovenga, 0727, South Africa.

<sup>2</sup>Council for Scientific industrial research/CSIR, Pretoria, South Africa,

<sup>3</sup>Advanced Materials Division/MINTEK, Private Bag X3015, Randburg 2125, Gauteng Province, South Africa.

E-mail: makgoba.walter@gmail.com

**Abstract.** Classical molecular dynamics was used to study the structural stability of Au and Ag nanoparticles. The structures were modelled at various temperatures in an NVT Evans ensemble. The many-body Sutton-Chen potential was employed to describe the interactions between atoms in both nanoparticles. Change in entropy was calculated from the variation of total energy against temperature for both Au and Ag nanoparticles. Radial distribution functions were utilised to predict the most probable Au and Ag nanoparticle structures. To probe the mobility of Au and Ag atoms in their systems, the mean square displacements (MSDs) were plotted, in which diffusion constants were calculated to be 0.58 and 1.87 Å<sup>2</sup>.ps<sup>-1</sup> for Au and Ag atoms respectively at 300 K.

### 1. Introduction

Nanoparticles (NPs) of gold (Au) and silver (Ag) have stirred up considerable scientific interest, because of their high potential for clinical applications in different areas such as biological sensing, biomedical imaging and drug delivery [1, 2]. These nanoparticles have unique physical-chemical properties such as chemical surface functionalization, optical and electronic characteristics that allows the nanoparticles to easily interact with biological molecules when introduced in the biological environment during clinical applications [1]. The fascinating properties of these nanomaterials are attributed to the electronic distribution on the metal along the nanoparticle surface, which depends mostly on its size and shape that can be controlled during the synthesis procedure [1, 3]. Gold and silver can be built into various nanomaterials which include nanospheres [3, 4], nanocubes [5, 6], nanorods [7], etc, with different and enhanced properties for different clinical applications.

Both gold and silver nanomaterials (AuNMs and AgNMs) can be synthesized using different methods which involve physical, chemical and biological procedures. The biologically prepared synthesis of NPs has been favoured due to its cost effectiveness and environment friendliness which uses biological systems such as plant extracts and small biomolecules for the synthesis of AgNMs [8]. Gurunathan *et al.* [2] and Kalishwaralal *et al.* [9] commented that physically and chemically produced AgNMs are hazardous and quite expensive to fabricate. On the AuNMs front, Au nanorods are favoured

in various applications due to their unique properties, such as their ability to be synthesized in high quality via seeded crystallisation from solution, their adjustability of the plasmon resonance by varying the aspect ratio, excellent tunability as well as biocompatibility- these listed properties make Au nanorods potential candidates for biological, biomedical and bio-sensing applications [10]. Quantitatively, according to Faraday *et al.* [11] and Davey [12], at nanoscale both the gold and silver samples adopt the face-centred cubic (FCC) phase. In this FCC phase, thermodynamic properties of the two nanomaterials can be studied well by variation of energy, temperature, and pressure. Consequently, in this paper, the most probable Au and Ag nanospheres are being explored with the aid of the molecular dynamics approach.

## 2. Methodology

The classical molecular dynamics (MD) method, using leapfrog verlet (LF) algorithm to integrate the equations of motion was carried out in this study. This method is one of the popular computational that studies the physical movement of atoms and molecules [13]. It has already been established that the molecular dynamics method can simulate nanoparticles in sheets or aggregates and reveal many details such as optical, electrical, and sensing capabilities that may not be accessible experimentally [13]. The DL\_POLY [14] software was utilized to execute the MD simulations because of its effectiveness in handling the potentials and structures preferred for this work. Gold and silver bulk supercells with 4000 atoms each were explored at 0 K in an NVT Evans ensemble, where N represents the number of particles, V is volume of the system at temperature T. The equilibrium structures of the supercells were attained at 48.943 and 60.121 Å for Au and Ag respectively. The nanospheres were then extracted from the equilibrated bulk supercells for ultimate stability analysis. The many-body Sutton-Chen potentials [15] were employed to model the interactions between atoms in the nanospheres. Variation of total energy as a function of temperature was then investigated for both Au and Ag nanospheres. The radial distribution functions (RDFs) were utilized to predict the most probable Au and Ag-nanospheres structures while mean square displacements (MSDs) were considered to study the mobility of Au and Ag atoms in their structures.

## 3. Results and discussion

### 3.1. Modelled bulk Au and Ag crystals at 0 K.

Both Au and Ag precious metals can be obtained in bulk and nanomaterial forms. In this section, the stability of the bulk forms on these two are being discussed. The ultimate idea is to extract nanospheres from the bulk and properties such as the lattice parameter and cohesive energy need to be known. The bulk forms of Au and Ag supercells each with 4000 atoms were modelled at 0 K using the NVT ensemble. In the process, the total energy of the supercells were observed with the changing supercell lattice constants. Figure 1 presents the behavior of the energy at various supercell lattice constants for the acquired equilibrium structures of both the Au and Ag supercells. The bulk equilibrium structures of Au and Ag were attained at the simulated lattice constant of 48.943 Å and 60.121 Å respectively. The Au supercell lattice constant of 48.943 Å and Ag supercell lattice constant of 60.121 Å are noted in Table 1. The cohesive energy was calculated during simulations and found to be 3.673 eV.atom<sup>-1</sup> and 2.810 eV.atom<sup>-1</sup> for Au and Ag supercells respectively. Moreover, the computed values agree well with experimental measurements in Table 1 [16].

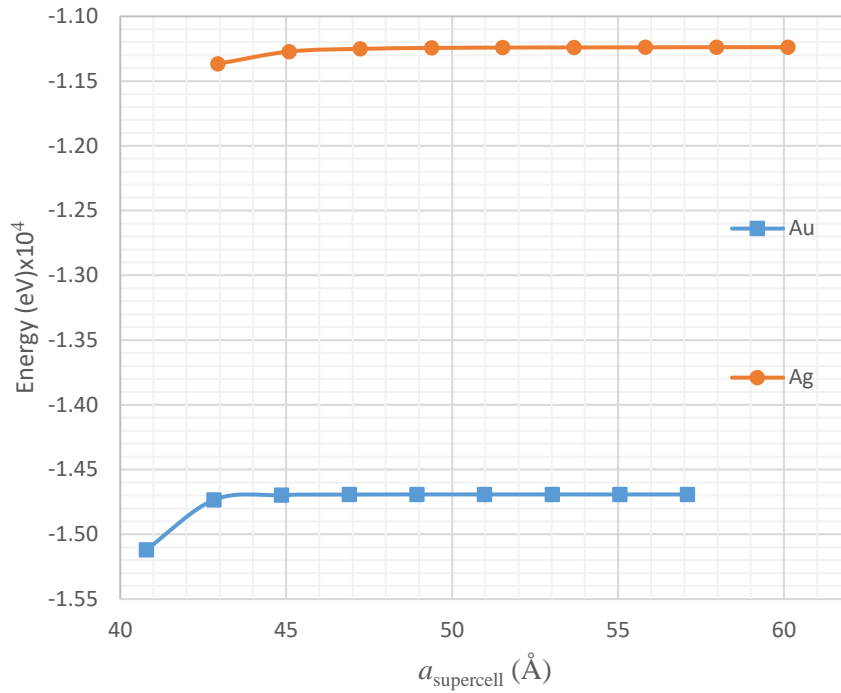


**Figure 1.** The energy is plotted as a function of the lattice constant ( $a_{\text{supercell}}$ ) for the bulk Au and Ag structures with 4000 atoms at 0 K.

**Table 1.** The supercell lattice constant ( $a_{\text{supercell}}$ ), the total energy, the cohesive energy and its experimental reference all at 0 K for both Au and Ag bulk structures. The experimental values for the cohesive energy are from ref [16].

	$a_{\text{supercell}} (\text{Å})$	$E_{\text{total}} \times 10^4 (\text{eV})$	Cohesive energy ( $\text{eV} \cdot \text{atom}^{-1}$ )	Cohesive energy ( $\text{eV} \cdot \text{atom}^{-1}$ ) (experimental)
Au	48.943	-1.469	3.673	3.810
Ag	60.121	-1.124	2.810	2.950

### 3.2. Au-nanospheres and Ag-nanospheres

**3.2.1. Energy-temperature relations.** The Au-nanospheres (Au-nss) and Ag-nanospheres (Ag-nss) are extracted directly from the bulk Au and Ag supercells discussed above in section 3.1. Subsequently, the Au-nss and Ag-nss are made of 2067 atoms each with lattice constants ( $a_{\text{nanosphere}}$ ) of 48.943 and 60.121 Å at the original 0 K. Figure 2 shows the graph of energy as a function of temperature for Au and Ag nanospheres. The energy increases linearly with increasing temperature. A disjoint or discontinuity can be observed in the plots between temperatures 700 – 800 K for Au-nss while in Ag-nss the discontinuity is noticed between 900 – 1000 K. Such behavior suggests the probable transition in the structures from a solid crystal to liquid. The structures become amorphous in the disjoint region. Similar behavior of energy-temperature variation was reported by Wang *et al.* [17] on icosahedral Au nanoparticles. Interestingly, Gafner *et al.* [18] reported a similar behavior for Cu and Ni nanoparticles. Comparable energy-temperature transitions were also reported on clusters and nanoalloys [19, 20]. A change in entropy, calculated from the slope of the graphs is found to be  $7 \times 10^{-4}$  and  $8 \times 10^{-4} \text{ eV} \cdot \text{K}^{-1}$  for Au-nss and Ag-nss respectively, as displayed in Table 2. A greater change in entropy occurs on the Ag-nss than the Au-nss.

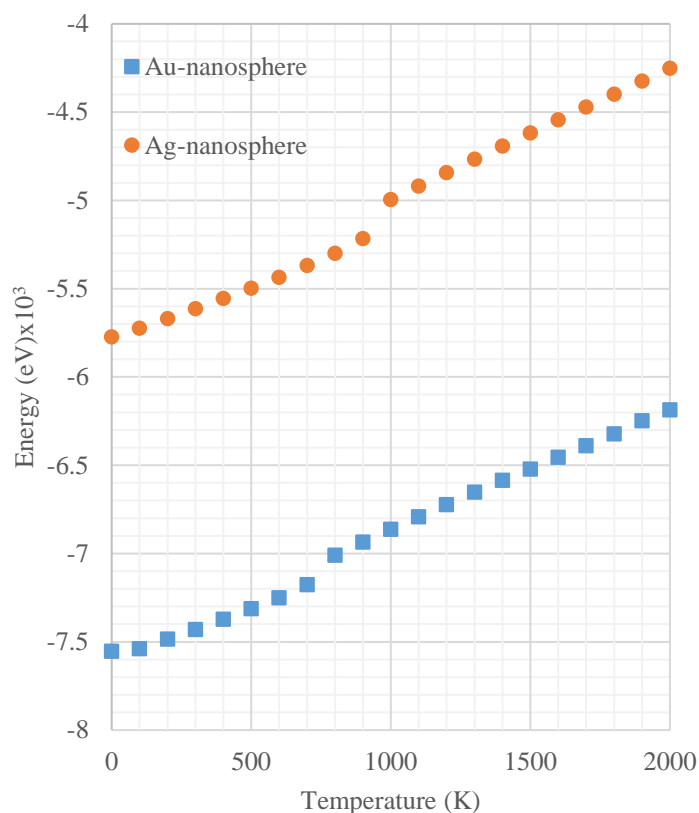


**Figure 2.** The variation of energy with temperature for Ag- and Au-nanospheres.

**Table 2.** Change in entropy for both Au- and Ag-nanospheres.

	Au-nanosphere	Ag-nanosphere
Entropy (eV.K <sup>-1</sup> ) x 10 <sup>-4</sup>	7.000	8.000

**3.2.2. Radial distribution functions.** The radial distribution functions (RDFs) are necessary when analysing the structure of fluids and solids [21]. Researchers including Pathania et al. [21] have used RDFs for the analysis of fluid structures. For this reason, the RDFs have been utilized in identifying a possible phase change of Au-nss and Ag-nss over a prescribed temperature range. In Figure 3(a) and (b), the RDFs at 300, 600, 700, and 800 K for the Au-nss and Ag-nss respectively are presented. In the plots, it can be seen that the peak heights ( $g(r)$ ) decrease with the increasing temperature, as well as diminishing with the increasing radial distance ( $r$ ). The trend suggests a possible phase transition from solid to fluid state. Consequently, on the Au-nss at 800 K, only the first and second nearest neighbor Au – Au displacements can be described with reliable values (Figure 3(a)) on the abscissa as the RDF peaks are vanishing with increasing  $r$ . This observation seems to support the energy – temperature relation observed in Figure 2 for Au-nss with the transition of energy-temperature at 700 K to 800 K where the structure at 800 K becomes highly deformed. The Ag-nss depicts the phase transition temperature in the region of 900 – 1000 K.

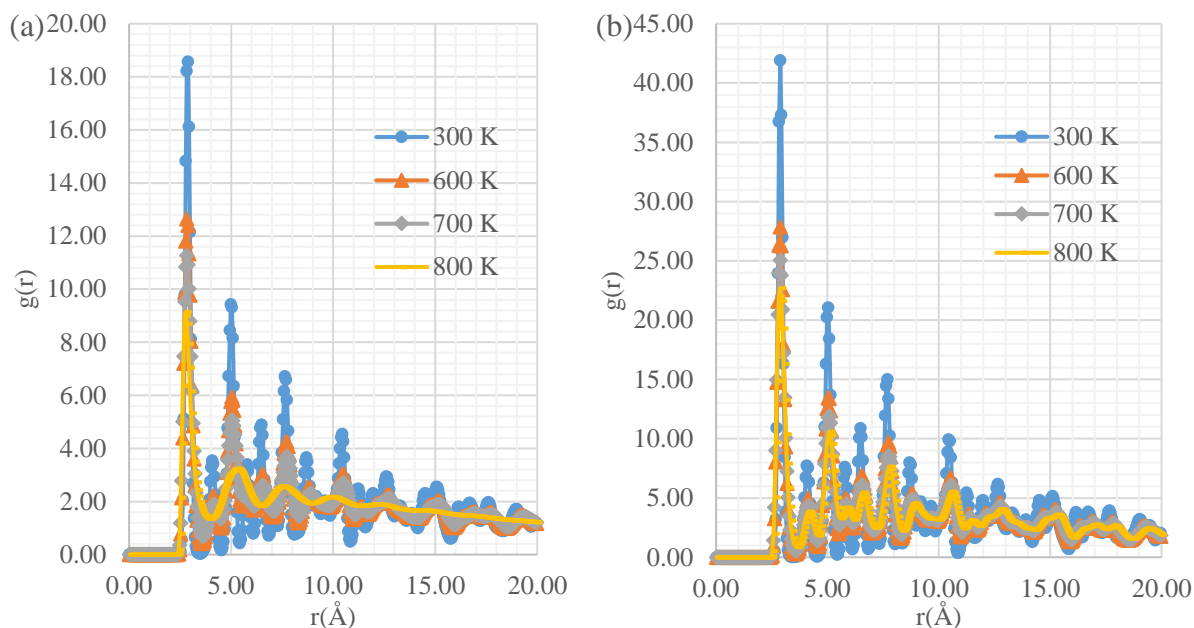


**Figure 3.** The radial distribution functions (RDFs) for Au- (a) and Ag-nanospheres (b) respectively plotted at 300, 600, 700, and 800 K.

**3.2.3 Mean square displacements.** Mean square displacements (MSDs) have been utilised to describe the movement of atoms in solids, liquids as well as gases [22]. Therefore, it has been reported that the MSDs will increase linearly with relation to time when diffusion takes place [22]. As such, to probe the mobility of the Au and Ag ions in their Au-nanospheres (Au-nss) and Ag-nanospheres (Ag-nss) systems respectively, the mean square displacements (MSDs) plots were constructed. The respective ion diffusion constants  $D$  were calculated as the slope of the MSDs plots. Figures 4 (a) – (b) illustrate the MSDs graphs of Au-nss and Ag-nss respectively at 300, 600, and 700 K. The values of the calculated diffusion constants are displayed in Table 3. The Au ions have the diffusion constants that increase with increasing temperature. The Au-nss show liquid features in the RDFs at 800 K. However, in the case of Ag-nanospheres (Ag-nss), the diffusion constants seem to decrease with increasing temperature. The low values of  $D$  is because of the atomic mobility in the Ag-nss is generally slow and this was noticed in the RDFs where the structure remains very much a solid crystal at a higher temperature of 800 K. The RDFs for silver remains with many peaks indicating strong interactions between atoms which will signify less mobility in the atoms.

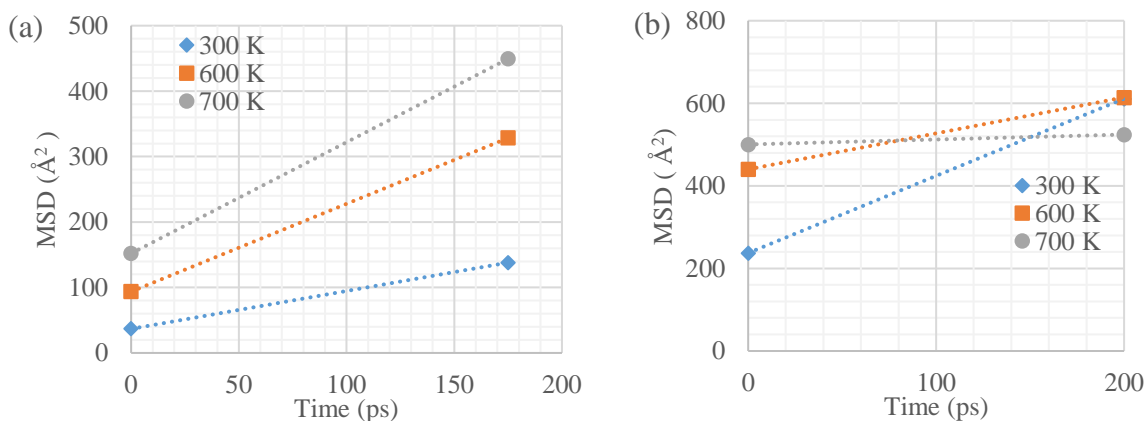


**Figure 4.** Mean square displacements for Au- (a) and Ag-nanospheres (b) respectively at 300, 600, and 700 K.

**Table 3.** Calculated diffusion constants (D) for Au- and Ag-nanospheres at 300, 600, and 700 K.

Temperature (K)	300	600	700
D for Au-nanospheres ( $\text{\AA}^2.\text{ps}^{-1}$ )	0.58	1.46	1.70
D for Ag-nanospheres ( $\text{\AA}^2.\text{ps}^{-1}$ )	1.87	0.87	0.12

#### 4. Conclusion

Classical molecular dynamics simulations have been successfully applied to follow the trend from a bulk crystal structure to a nanocluster in gold and silver metals. The Sutton-Chen potential correctly predicts the energies and lattice constants of the bulk materials. The cohesive energy for the bulk supercells fairly agrees with the experimental data. The transition of the structure in the nanospheres was followed with the assistance of the RDFs which shows that Au-nss reaches amorphous phase quicker than Ag-nss. The energy-temperature plots confirm the earlier transition with the discontinuity occurring at 700 K for Au-nss and at 900 K for the Ag-nss. The MSDs indicate more atomic mobility in the Au-nss as compared to Ag-nss where the structure retains solid features even at 800 K.

#### References

- [1] Elahi N and Kamali M, *a review Talanta*, **184** (2018), pp. 537-556.
- [2] Gurunathan S, Park J H, Han J W and Kim J H, *Int. J. Nanomed.* **10** (2015), pp. 4203-4222.
- [3] Link S and El-Sayed M A, *J. Phys. Chem. B*, **103** (1999), pp. 4213-4214.
- [4] Liang *et al.*, *J. Phys. Chem. C*, **114** (2010), 2010 pp.7427-7431.
- [5] Sun Y and Xia Y, *J. American Chem. Soc.*, **126** (2004), pp. 3892-3901.
- [6] Wu X., Ming T., Wang X., Wang P., Wang J., Chen J. *ACS Nano*. **4** (2010), pp.113-120.
- [7] Cepak V M and Martin C R, *J. Phys. Chem. B*, **102** (1998), pp. 9985-9990.
- [8] Zannatul F and Abderrahim N. *Int. J. Mol. Sci.* **21** (2020), pp. 4-5.
- [9] Kalishwaralal K, Gurunathan S, Vaidyanathan R, Venkataraman D, Pandian S R, Muniyandi J, Hariharan N and Eom S H, *Colloids Surf. B Biointerfaces*. **74** (2009), pp. 328-335.
- [10] Shajari *et al.*, *Opt. Mater.*, **64** (2017), pp. 376-383.
- [11] Faraday M, *Philos. Trans. R. Soc. Lond.* **147** (1857), pp. 145-181.
- [12] Davey W P, *Phys. Rev.* **25** (1925), pp. 753-761.
- [13] Frenkel D and Smit B, *Understanding Molecular Simulation*. 2nd ed., Academic, San Diego (2002).
- [14] Smith W, Forester T R and Todorov I T, *The DL\_POLY 2 User Manual*, STFC Daresbury Laboratory, Daresbury, Warrington WA4 4AD Cheshire, UK (2009).
- [15] Sutton A P and Chen J, *Phil. Mag. Lett.* **61** (1990) pp. 139-146.
- [16] Kimura Y, Qi Y, Cagin, T and Goddard W A III, Caltech ASCI Technical Report (1998).
- [17] Wang Y, Teitel S and Dellago C, *Chem Phys Lett.* **394** (2004), pp. 257-261.
- [18] Gafner S L, Redel L V, and Gafner Yu Ya, *J. Comput. Theor. Nanosci.* **6** (2009), pp. 820-827.
- [19] Baletto F, Mottet C and Ferrando R, *Chem Phys Lett.* **354** (2002), pp.82-87.
- [20] Pavan L, Baletto F and Novakovic R, *Phys. Chem. Phys.* **17** (2015), pp. 28364-28371.
- [21] Pathania Y and Ahluwalia P K, *J. Phys.*, **65** (2005), pp. 457-468.
- [22] Gao F and Qu J, *Mater. Lett.* **73** (2012), pp. 92-94.

## Preparation and characterization of erbium-activated yttrium orthovanadate-phosphate by chemical bath deposition

M Mokoena<sup>1</sup>, KG Tshabalala<sup>1</sup>, HC Swart<sup>1</sup>, BF Dejene<sup>2</sup>, MR Mhlongo<sup>3</sup>, and S.J Motloung<sup>1</sup>

<sup>1</sup>Department of Physics, University of the Free State, P.O. Box 339, Bloemfontein/QwaQwa campus, 9300, South Africa

<sup>2</sup>Department of Chemical and Physical Science, Walter Sisulu University (Mthatha Campus), Private Bag X 1, Mthatha, 5117

<sup>3</sup>Department of Physics, Sefako Makgatho Health Science University, Medunsa 0204, South Africa

E-mail: [tlousj@gmail.com](mailto:tlousj@gmail.com)

**Abstract.** Erbium ( $\text{Er}^{3+}$ ) activated yttrium orthovanadate-phosphate ( $\text{YV}_{0.5}\text{P}_{0.5}\text{O}_4$ ) nanomaterials were prepared by chemical bath deposition. The concentration of  $\text{Er}^{3+}$  varied between 1 and 10 mol%. The structure, surface morphology, elemental composition, and optical analysis were carried out by X-ray diffraction (XRD), scanning electron microscopy (SEM), energy-dispersive X-ray spectroscopy (EDS), and ultraviolet–visible (UV) spectroscopy. XRD results showed that all the samples have a tetragonal zircon structure. SEM shows that the particles were in the nano-range and portrayed nanosphere shapes. The presence of all the elements forming  $\text{YV}_{0.5}\text{P}_{0.5}\text{O}_4$ :  $\text{Er}^{3+}$  was verified by EDS. Diffuse reflectance spectra (DRS) revealed a broad absorption band in the UV region which is attributed to the absorption of  $\text{VO}_4^{3-}$ . The  $f \rightarrow f$  transitions of  $\text{Er}^{3+}$  were also observed at 380, 407, 451, 489, 523, 546, and 654 nm and were attributed to  ${}^4\text{I}_{15/2} - {}^4\text{G}_{11/2}$ ,  ${}^4\text{I}_{15/2} - {}^4\text{F}_j$  ( $J = 3/2, 5/2, 7/2, 9/2$ ),  ${}^4\text{I}_{15/2} - {}^2\text{H}_{9/2}$ ,  ${}^2\text{H}_{11/2} - {}^4\text{I}_{15/2}$ , and  ${}^4\text{S}_{3/2} - {}^4\text{I}_{15/2}$  electronic transitions of  $\text{Er}^{3+}$ . Lastly, the estimated band gaps were found to be between 3.76 and 3.82 eV.

### 1. Introduction

In recent years, lanthanide ( $\text{Ln}^{3+}$ )-activated up-conversion (UC) materials have become a topic of intense research due to their superior chemical and characteristic optical properties, such as their low optical background, excellent photostability, ease of manufacture, low toxicity, and high UC luminescence [1]. Our world faces a serious energy issue. Fossil fuels are presently the main energy source, but they present challenges such as environmental pollution and the depletion of such fuels; hence there is a need for alternative renewable energy sources. Therefore, in this study, our focus was on synthesizing a UC luminescent material that can act as a UC layer when exposed to infrared light. Currently, rare-earth (RE) doped nanophosphors are considered superior optical materials to produce light-emitting materials. RE ions exhibit narrow emission and excitation bands due to an electronic transition from  $f-f$ , which is why they are widely used to generate luminescence. A wide range of applications can be achieved with rare-earth luminescence materials, including phosphors, display monitors, X-ray imaging, scintillators, lasers, and optical amplifiers [2]. A number of trivalent lanthanide ions, including  $\text{Er}^{3+}$ ,  $\text{Tm}^{3+}$ ,  $\text{Ho}^{3+}$ , and  $\text{Pr}^{3+}$ , act as activators for UC processes due to their high energy levels. There have already been various UC

phosphors developed, such as  $\text{Ln}^{3+}$  doped rare earth oxides, rare earth fluorides, alkaline earth metal fluorides, etc. [3]. Several studies have been performed on the UC process for disordered matrices doped with the  $4f^{11}$  lanthanide ion  $\text{Er}^{3+}$ .  $\text{Er}^{3+}$  is one of the rare-earth ions that is usually used as an important activator in luminescent materials because it provides intermediate levels ( $^4\text{I}_{1/2}$  and  $^4\text{I}_{3/2}$ ) with equally spaced and longer lifetime excited states, and this enables the conversion of infrared light to visible light [4]. The  $\text{Er}^{3+}$  ions may be excited either under down conversion or up conversion excitations to display green and white emission applications [5].

The most suitable host must have low phonon energy in order to engage non-radiative processes at a lower probability and then optimize the desired application performance. One of the newest developed phosphors are RE orthovanadates and orthophosphates with the general formula  $\text{MNO}_4$ , where  $\text{M} = \text{Sc}, \text{Y}, \text{La}, \text{Gd}$  or  $\text{Lu}$  and  $\text{N} = \text{V}$  or  $\text{P}$ . Among these orthovanadates or orthophosphates, yttrium orthovanadates ( $\text{YVO}_4$ ) and orthophosphate ( $\text{YPO}_4$ ) have been studied for a long time because they possess interesting properties, such as excellent thermal, mechanical, optical properties and chemical stability [6, 7]. Vanadate and phosphates can be combined to form orthovanadate-phosphate hosts, this orthovanadate-phosphate host can be achieved by partially replacing the  $\text{V}^{5+}$  ions with  $\text{P}^{5+}$  ions (or vice versa) in the  $\text{YVO}_4$  (or  $\text{YPO}_4$ ) system, usually resulting in a tetragonal structure [8]. Motloung *et al.* [9] have illustrated that the stability and high-temperature luminescent properties of  $\text{YVO}_4$  and  $\text{YPO}_4$  can be enhanced by the orthovanadate-phosphate system.

In this study,  $\text{Er}^{3+}$  doped  $\text{YV}_{0.5}\text{P}_{0.5}\text{O}_4$  powder materials were prepared by the chemical bath deposition (CBD) method. There are published reports on the synthesis of  $\text{Er}^{3+}$  doped  $\text{YV}_{0.5}\text{P}_{0.5}\text{O}_4$  using various synthesis methods [7]. However, to the best of our knowledge, there are no reports on the synthesis of  $\text{Er}^{3+}$  doped  $\text{YV}_{0.5}\text{P}_{0.5}\text{O}_4$  by CBD. The method, which is cheap and simple, is a low-temperature technique that uses a solution that produces a crystal size that is often very small and homogeneous. The phase structures, morphologies, elemental, and optical properties of the  $\text{YV}_{0.5}\text{P}_{0.5}\text{O}_4$ :  $x\%$   $\text{Er}^{3+}$  samples were investigated in detail.

## 2. Experiment

Yttrium nitrate hexahydrate ( $\text{Y}(\text{NO}_3)_3 \cdot (\text{H}_2\text{O})_6$ ) (99.8% trace metal bases), ammonium metavanadate ( $\text{NH}_4\text{VO}_4$ ) (P = 99%), ammonia (25%  $\text{NH}_3$ ), erbium (III) acetate hydrate  $\text{C}_6\text{H}_9\text{ErO}_6 \cdot \text{H}_2\text{O}$  (99.8% trace metal bases), ammonium dihydrogen phosphate ( $\text{NH}_4\text{H}_2\text{PO}_4$ ) and deionized water were used throughout the experiment. All solvents and chemicals used were of analytical grade and purchased from Sigma Aldrich.  $\text{YV}_{0.5}\text{P}_{0.5}\text{O}_4$ :  $x\%$   $\text{Er}^{3+}$  (where  $x = 1, 3, 5, 7,$  and  $10$ ) phosphor-powders doped with  $\text{Er}^{3+}$  ( $x$  mol%) were prepared by chemical bath deposition at  $80^\circ\text{C}$ . In a typical preparation, 0.05M of  $\text{Y}(\text{NO}_3)_3 \cdot (\text{H}_2\text{O})_6$ , 0.025M of  $\text{NH}_4\text{VO}_4$ , and 0.025 M  $\text{NH}_4\text{H}_2\text{PO}_4$  solutions were prepared using deionized water under magnetic stirring. The solutions were stirred to allow homogenous mixing. The volume ratios (1:0.5:0.5) were then considered for each solution in the following order: 50 ml of  $\text{Y}(\text{NO}_3)_3 \cdot (\text{H}_2\text{O})_6$  was first added to the test tube placed in the water bath, followed by the addition of 50 ml of  $\text{NH}_4\text{VO}_4$  solution and 50ml of  $\text{NH}_4\text{H}_2\text{PO}_4$  solution, and lastly, 50 ml of (25%  $\text{NH}_3$ ) solution was added dropwise. The samples were prepared at five different concentrations of  $\text{Er}^{3+}$  (1, 3, 5, 7, and 10%). A white precipitate formed after the mixture was continuously stirred for several seconds. The reaction took place until 50ml of (25%  $\text{NH}_3$ ) was used. The product was then allowed to stabilize and cool down overnight. Finally, the precipitates were collected, washed several times with ethanol and deionized water to remove the residue, and desiccated at room temperature for a maximum of three days to ensure that powders were dried prior to characterization.

The structure and phase purity of the samples were investigated by using XRD (Bruker D8 Advanced Powder Diffractometer). The morphology, elemental mapping, and elemental composition of these materials were obtained using Tescan Vega 3 scanning electron microscopy (SEM) fitted with Oxford X-Max<sup>N</sup> energy-dispersive X-ray spectroscopy (EDS). Reflectance spectra were measured using UV-vis spectrophotometer Lambda 950 (PerkinElmer).

### 3. Results and discussion

#### 3.1 X-ray diffraction

XRD patterns of the  $YV_{0.5}P_{0.5}O_4$  nano phosphors doped with  $Er^{3+}$  at different concentrations are presented in Figure 1. The XRD spectra show that the diffraction peaks matched well with the tetragonal zircon phase of  $YVO_4$  (JCPDS file no. 17 – 0341). Figure 1 shows that the gradual increase of  $Er^{3+}$  from 1 to 10% mole did not influence the crystal structure. As the concentration of the dopant was increased, the XRD peak shows a slight shift to a higher diffraction degree (Figure 2(a)). This implies that the dopant ions are successfully and uniformly incorporated into the  $YV_{0.5}P_{0.5}O_4$  host lattice [10]. This shift could be because of strains that are caused by the differences in ionic radii between vanadium ( $\sim 0.54 \text{ \AA}$ ), phosphorus ( $\sim 0.35 \text{ \AA}$ ), and the  $Er^{3+}$  ( $0.89 \text{ \AA}$ ) [9]. To replace the trivalent yttrium ions with atomic radii of  $0.9 \text{ \AA}$  with, the trivalent  $Er^{3+}$  ions with atomic radii of  $0.89 \text{ \AA}$  are introduced in the  $YV_{0.5}P_{0.5}O_4: Er^{3+}$  system. Since both  $Y^{3+}$  and  $Er^{3+}$  ions have the same valency,  $Er^{3+}$  ion substitutions at the  $Y^{3+}$  site in  $YV_{0.5}P_{0.5}O_4$  can lead to charge compensation issues [11]. According to the results, the phosphor powders were crystalline, and the diffraction peaks were found to be generally broad, and this could be due to the small crystalline size of the material [6, 12]. No peaks are detected for any other impurities, demonstrating that pure phase products can be obtained when using the CBD synthesis method, and  $Er^{3+}$  can successfully replace  $Y^{3+}$ .

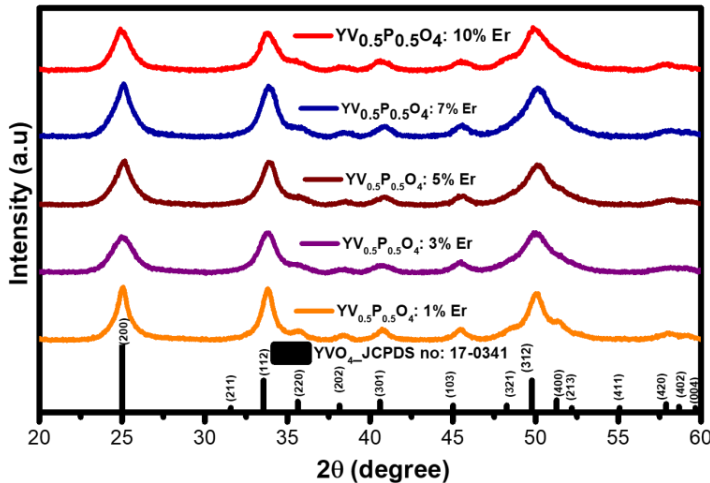
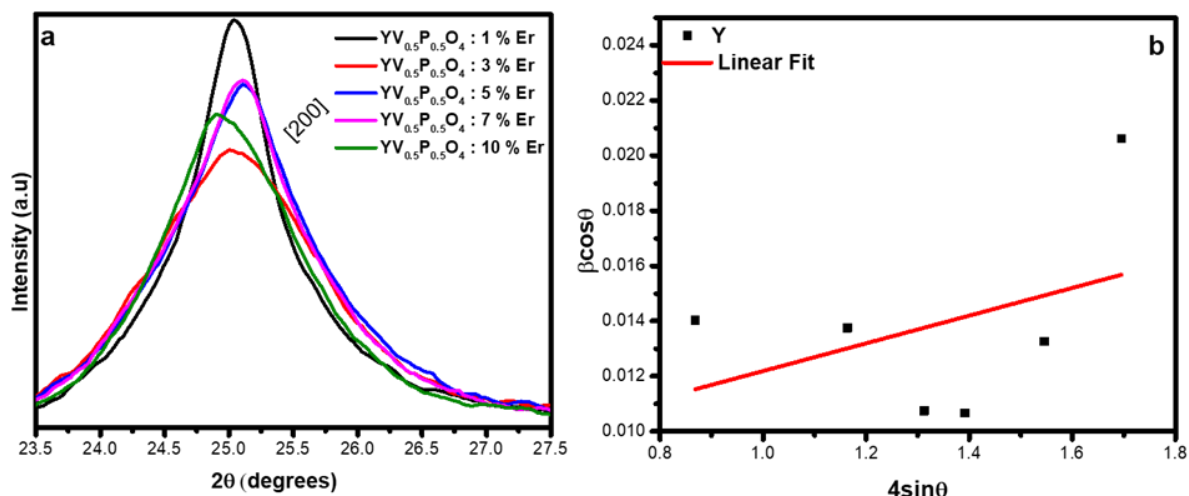


Figure 1. XRD pattern of  $YV_{0.5}P_{0.5}O_4:x\% Er^{3+}$  and JCPDS file.

Figure 2(a) shows an expanded view of the (200) diffraction peak for the samples synthesized at the different  $Er^{3+}$  concentrations. Williamson-Hall formula (equation 1) [13] was used to estimate the crystallite sizes and lattice strains:

$$B_{hkl} \cos\theta = 4\epsilon \sin\theta + \frac{0.9 \lambda}{D}, \quad (1)$$

where  $D$  is the crystallite size,  $\epsilon$  is the lattice strain,  $\lambda$  is the wavelength of the x-ray radiation ( $1.5406 \text{ \AA}$ ),  $\beta$  is the full width at half maximum (FWHM) intensity, and  $\theta$  is the diffraction angle at the peak position. The term  $(\beta \cos\theta)$  was plotted with respect to  $(4 \sin\theta)$  for the preferred orientation peaks of  $YV_{0.5}P_{0.5}O_4:1\%Er^{3+}$  in figure 2(a). The same procedure was used for different concentrations of  $Er^{3+}$ . The results were found to be in a range of 17 to 19 nm and 0.00973 to 0.00502 for the crystallite sizes and lattice strains, respectively. The crystalline sizes were found to be fluctuating as  $Er^{3+}$  increased.



**Figure 2.** (a) Diffraction patterns of (200) for  $YV_{0.5}P_{0.5}O_4$  doped with various  $Er^{3+}$  concentration, (b) A plot of  $\beta \cos \theta$  as a function of  $4 \sin \theta$  of  $YV_{0.5}P_{0.5}O_4:1\% Er^{3+}$ .

### 3.2 Scanning electron microscopy

The morphology of the prepared powder samples at various  $Er^{3+}$  mole concentrations is shown in figure 3. The samples mainly consist of small primarily nanospheres structures, which show some conglomeration phenomena. Figure 3(f and g) shows low magnification, and it is observed that the product presents a bulk morphology conglomerating with an irregular quadrilateral shape with a uniform size. These results agree with XRD, which says that particles are tetragonal in shape. The mole concentration of  $Er^{3+}$  did not have influence on the morphology of the nanoparticles at low magnification. These irregular quadrilateral shape-like structures might be due to several nanospheres agglomeration. It is also noticed that low doping concentrations of  $Er^{3+}$  did not significantly affect morphology and the particle size did not change much as  $Er^{3+}$  concentration was increased.

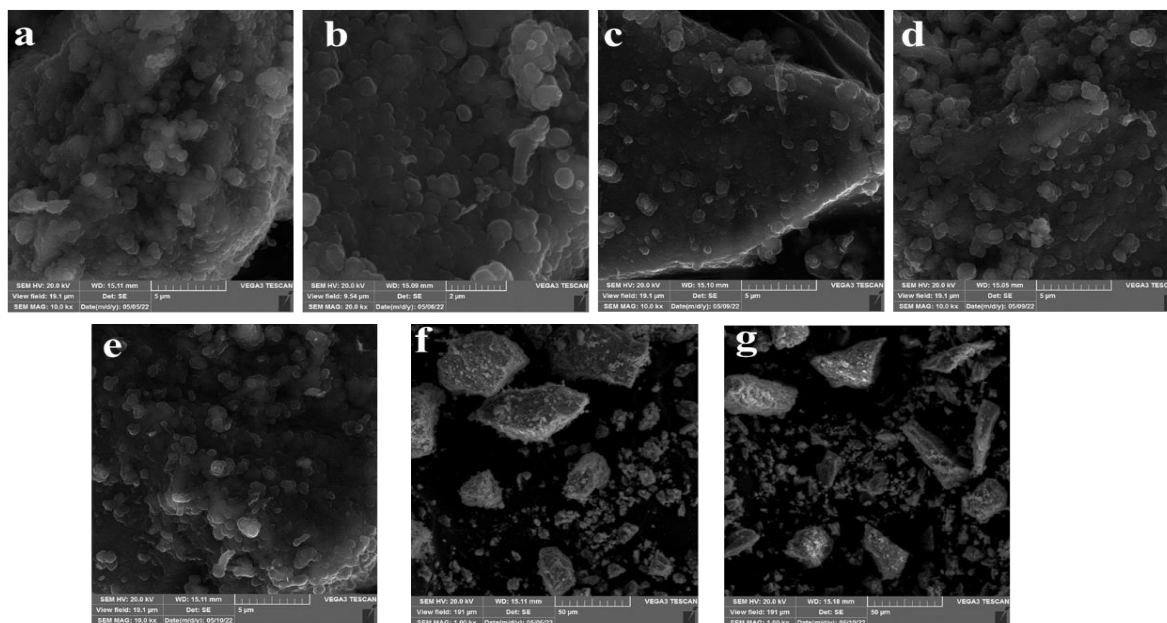


**Figure 3.** SEM images of (a, f)  $YV_{0.5}P_{0.5}O_4:1\%Er^{3+}$ , (b)  $YV_{0.5}P_{0.5}O_4:3\% Er^{3+}$ , (c)  $YV_{0.5}P_{0.5}O_4:5\% Er^{3+}$ , (d)  $YV_{0.5}P_{0.5}O_4:7\% Er^{3+}$ , (e, g)  $YV_{0.5}P_{0.5}O_4:10\% Er^{3+}$ .

### 3.3 Energy-dispersive X-ray spectroscopy

Electron diffraction X-ray spectroscopy (EDS) was used to analyze the composition of transition metals that are used to prepare  $YV_{0.5}P_{0.5}O_4:x\% Er^{3+}$ .

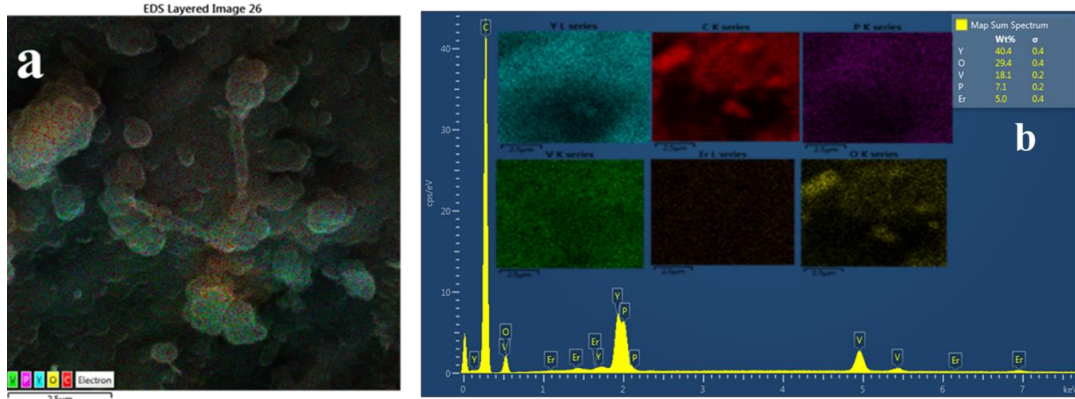


**Figure 4.** (a) The EDS elemental map and (b) the EDS spectrum of  $YV_{0.5}P_{0.5}O_4:5\% Er^{3+}$ .

Elemental mapping of  $YV_{0.5}P_{0.5}O_4:5\% Er^{3+}$  nanophosphor was observed through SEM to identify the composition of yttrium (Y), vanadium (V), phosphorus (P), oxygen (O), and erbium (Er) (Figure 4(a)) and the insert (Figure 4(b)). The EDS spectrum (Figure 4(b)) confirms the presence of the anticipated elements Y, V, P, O and Er in the  $YV_{0.5}P_{0.5}O_4:5\% Er^{3+}$  samples. A carbon (C) peak was observed due to carbon tape being mounted to the sample when it was prepared for EDS measurements. In this study, the dopant was used at a low concentration thus, it was detected to be very small. No impurities were detected, which is in agreement with the XRD results. The same results were obtained for  $YV_{0.5}P_{0.5}O_4:1\% Er^{3+}$ ,  $YV_{0.5}P_{0.5}O_4:3\% Er^{3+}$ ,  $YV_{0.5}P_{0.5}O_4:7\% Er^{3+}$ , and  $YV_{0.5}P_{0.5}O_4:10\% Er^{3+}$  samples.

### 3.4 UV-Vis reflectance spectroscopy

$YV_{0.5}P_{0.5}O_4$  nanopowder was subjected to a UV-vis spectrometer to collect diffused reflectance spectrum and examine rare earth dopants' influence on its optical properties. The reflectance spectrum of  $YV_{0.5}P_{0.5}O_4$  nano phosphors recorded as the function of wavelength in the wavelength range 200–800 nm prepared at various  $Er^{3+}$  molar concentrations is shown in figure 5(a). It is evident that all the nanophosphors exhibited a reflectance edge at about  $\sim 317$  nm and this edge is attributed to the oxygen-to-vanadium atom charge transfer in the  $VO_4^{3-}$  units [9, 14]. In addition to the vanadate reflectance, the intrinsic f-f transitions of the  $Er^{3+}$  ion are noticed and are located at 380, 407, 451, 489, 523, 546, and 654 nm. These observed peaks can be attributed to the absorption of the  $Er^{3+}$  ion in the visible range and correspond to the electronic transition from  $^4I_{15/2} - ^4G_{11/2}$ ,  $^4I_{15/2} - ^4F_J$  ( $J = 3/2, 5/2, 7/2, 9/2$ ),  $^4I_{15/2} - ^2H_{9/2}$ ,  $^2H_{11/2} - ^4I_{15/2}$ , and  $^4S_{3/2} - ^4I_{15/2}$  respectively [8, 14, 15]. Figure 5(a) shows that the reflectance intensity decreased as the molar concentration of  $Er^{3+}$  ions increased.

The transformed Kubelka-Munk reflectance given in equation 2 [16] was used to obtain approximate band gap energies for the prepared powder samples:

$$\frac{K}{S} = \frac{(1-R)^2}{2R}, \quad (2)$$

where  $R$  is a reflectance value, and  $K$  and  $S$  are the absorption and scattering coefficients. The bandgap,  $E_g$ , was calculated using the absorption edge wavelength for the interband transition in accordance with the equation below [17]:

$$\alpha h\nu = A(h\nu - E_g)^2, \quad (3)$$

where  $\alpha$ ,  $h\nu$ ,  $A$ , and  $E_g$  represent the light absorption coefficient, photon energy, proportional constant, and the bandgap value, respectively.

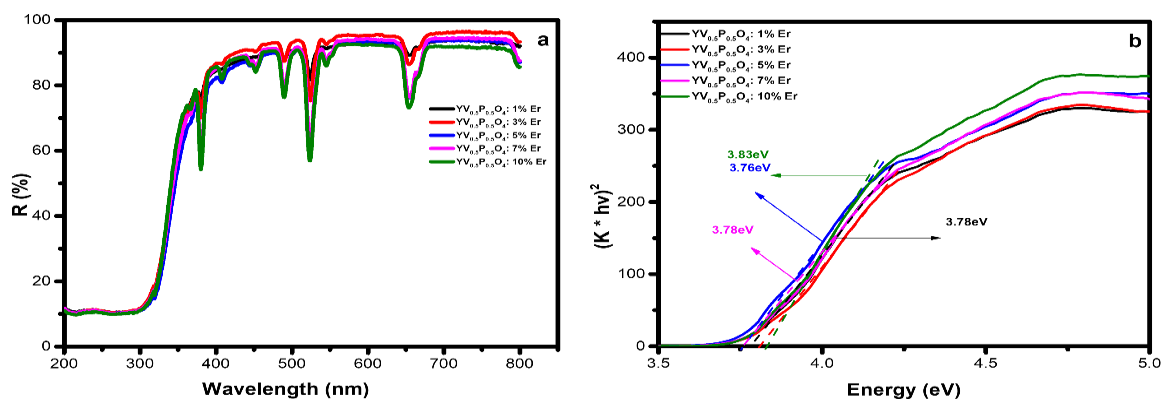


**Figure 5.** (a) The diffuse reflectance spectra of YV<sub>0.5</sub>P<sub>0.5</sub>O<sub>4</sub>:x%Er<sup>3+</sup>, (b) Transformed Kubelka–Munk reflectance of YV<sub>0.5</sub>P<sub>0.5</sub>O<sub>4</sub>:x%Er<sup>3+</sup>.

These were represented in a transformed Kubelka-Munk reflectance plot represented in figure 5(b). The band gap was estimated by extrapolating a straight line from the band edge to the intersection with  $h\nu$  is the x-axis. From figure 5(b), the band gaps of YV<sub>0.5</sub>P<sub>0.5</sub>O<sub>4</sub>:1% Er<sup>3+</sup>, YV<sub>0.5</sub>P<sub>0.5</sub>O<sub>4</sub>:3% Er<sup>3+</sup>, YV<sub>0.5</sub>P<sub>0.5</sub>O<sub>4</sub>:5% Er<sup>3+</sup>, YV<sub>0.5</sub>P<sub>0.5</sub>O<sub>4</sub>:7% Er<sup>3+</sup> and YV<sub>0.5</sub>P<sub>0.5</sub>O<sub>4</sub>:10% Er<sup>3+</sup> were extrapolated and found to be in the range of 3.78 to 3.82 eV. The optical band gap energy of the doped YV<sub>0.5</sub>P<sub>0.5</sub>O<sub>4</sub> fluctuated as the molar concentrations of Er<sup>3+</sup> was increased. This result is in accordance with the crystalline size, which fluctuated as the molar concentration of Er<sup>3+</sup> increased, as confirmed by XRD analyses.

#### 4. Conclusion

In conclusion, Er<sup>3+</sup> doped YV<sub>0.5</sub>P<sub>0.5</sub>O<sub>4</sub> phosphor powder have been synthesized by the CBD method for different concentrations of Er<sup>3+</sup> ions and are characterized by XRD, SEM, EDS and UV. A successful introduction of Er<sup>3+</sup> ions into the YV<sub>0.5</sub>P<sub>0.5</sub>O<sub>4</sub> lattice has been confirmed by XRD, SEM, and EDS measurements. As evidenced by XRD, the preparation of nanoparticles appeared to present a single phase of tetragonal zircon structure. The as-formed hybrid precursor materials present uniform small, primarily nanospheres like morphologies. The UV–vis reflectance spectra showed an intense Er<sup>3+</sup> green peaks due to <sup>2</sup>H<sub>11/2</sub> – <sup>4</sup>I<sub>15/2</sub>, and <sup>4</sup>S<sub>3/2</sub> – <sup>4</sup>I<sub>15/2</sub> transitions and other f→f transitions of Er<sup>3+</sup> were also observed and were attributed <sup>4</sup>I<sub>15/2</sub> – <sup>4</sup>G<sub>11/2</sub>, <sup>4</sup>I<sub>15/2</sub> – <sup>4</sup>F<sub>J</sub> (J= 3/2, 5/2, 7/2, 9/2), <sup>4</sup>I<sub>15/2</sub> – <sup>2</sup>H<sub>9/2</sub>, electronic transitions of Er<sup>3+</sup>. The band gap energies were calculated using a transformed reflectance Kubelka-Munk plot.

#### Acknowledgment

The authors gratefully thank the NRF, the Research Fund of the University of the Free State, and the Department of Science and Technology (DST) of South Africa. This work is based on the research supported by the South African Research Chairs Initiative of the Department of Science and Technology and the National Research Foundation of South Africa.

#### References

- [1] Fan W, Zhao F, Dou J, and Guo X, *Chem Eng Sci*, **242** 116734.
- [2] Sun Y, Liu H, Wang X, Kong X, and Zhang H 2006 *Chem. Mater.* **18** 2726-2732
- [3] Zhang C, Ma P, Li C, Li G, Huang S, Yang D, Shang M, Kang X and Lin J 2011 *J. Mater. Chem.* **21** 717-723
- [4] Liang Y, Chui P, Sun X, Zhao Y Cheng F, and Sun K 2013 *J. Alloys Comp.* **552** 289–293
- [5] Beltaif M, Koubaa T, Kallel T, Dammak M, Guidara K, and Khirouni K 2019 *Solid State Sci.* **90** 21–28
- [6] Motloung S J, Tshabalala K G, and Ntwaeaborwa O M 2017 *Adv. Mater. Lett.* **8** 735–740
- [7] Miao J, Wen Y, Wang W, Su J, Xu J, Zhong P and Rao W 2015 *J. Mater. Sci. - Mater. Electron.* **26** 6178-6181
- [8] Ayachi F, Saidi K, Chaabani W, and Dammak M 2021 *J. Lumin.* **240** 1184511
- [9] Motloung S J, Lephoti M A, Tshabalala K G, and Ntwaeaborwa O M 2018 *Physica B.* **535** 211–215
- [10] Gavrilović T V, Jovanović D J, Lojpur V, and Dramićanin M D 2014 *Sci. Rep.* **4** :4209 DOI:10.1038/srep04209

- [11] Thakur S and Gathania A K 2016 *J. Mater. Sci. - Mater. Electron.* **27** 1988–1993
- [12] Ansari A A and Labis J P 2012 *Mater. Lett.* **88** 152–155
- [13] Mote V D, Purushotham Y, and Dole B N 2012 *J. Theoret. Appl. Phys.* **6** 2251- 7235
- [14] Obregón S and Colón G 2015 *Chem. Eng. J.* **262** 29–33
- [15] Lee D Y, Lee M H, and Cho 2012 *Curr. Appl. Phys.* **12** 1229–1233.
- [16] Motloun S V, Kumari P, Koao L F, Motaung T E, Hlatshwayo T T, and Mochane M. J 2018 *Mater. Today Commun.* **14** 294–301
- [17] Borja-Urby R, Diaz-Torres L A, Salas P, Angeles-Chavez C, and Meza O 2011 *Mater. Sci. Eng., B.* **176** 1388–1392

# Electronic, elastic, and transport properties of alpha-type copper sulphide

**M Ramoshaba and TE Mosuang**

Department of Physics, University of Limpopo, Private Bag x1106, Sovenga, 0727, South Africa

E-mail: [moshibudi.ramoshaba@ul.ac.za](mailto:moshibudi.ramoshaba@ul.ac.za), [thuto.mosuang@ul.ac.za](mailto:thuto.mosuang@ul.ac.za)

**Abstract.** A full potential all-electron density functional method within generalised gradient approximation is used to investigate the electronic, elastic and transport structure of alpha-type copper sulphide. The electronic structure suggests a semimetallic material with a zero band gap. Elastic calculations suggest a hard material with the bulk to shear modulus ratio of 0.381. The transport properties were estimated using the Boltzmann transport approach. Electrical conductivity, Seebeck coefficient, and thermal conductivity suggest p-type conductivity.

## 1. Introduction

Cu<sub>2</sub>S is one of the copper sulphide forms referred to as chalcocite [1]. Yet studies by Zimmer *et al.* and other researchers indicate that Cu<sub>2-x</sub>S exists in different crystallographic modifications, which are monoclinic, hexagonal, cubic and orthorhombic phase [1-4]. A monoclinic  $\alpha$ -chalcocite Cu<sub>2</sub>S phase is created from the base hexagonal closed packed sulphur atoms (S) lattice [1]. In this arrangement, a trigonal and tetrahedral coordination of copper with central sulphur atoms alternate within the root hexagonal closed packed sulphur matrix. Depending on the value of  $x$  in the composition Cu<sub>2-x</sub>S, at 90 – 104 °C, a sub-level steady state chalcocite can be obtained [2]. When  $x = 0$ , in the temperature range 90 – 435 °C, the hexagonal phase of high-level chalcocite exists. A digenite cubic phase can also be existent in the temperature range 72 – 1130 °C [2, 3]. This configuration is based on anti-fluorite structure where copper (Cu) ions occupy the face centred cubic (fcc) lattice, whilst the sulphur ions occupy the sub-cubic closed packed cell within the fcc lattice [3].

Further literature studies show that even the cubic formation of Cu<sub>x</sub>S manifest in different forms which are specified by numerous locations of Cu atoms in the S atoms framework [4]. Moreover, lattice locations of the Cu atoms in this arrangement vary with the value of  $x$  within  $2 < x < 1$ . Like in the Cu<sub>2-x</sub>S setup, a probable transition from one phase to another depends highly on the local environment kinetic factors [4]. A range of metal sulphides demonstrates good transport properties, but the Cu<sub>x</sub>S family is being favoured because they are non-toxic, cost effective, and are made from earth-abundant elements [4, 5]. In this study, a copper rich cubic  $\alpha$ -chalcocite (Cu<sub>2</sub>S) has been modelled to understand its electrical and thermal transport properties.

## 2. Computational Method

The calculations are based on the density functional theory (DFT). In this approach, the ground state total energy calculations depend entirely on the k-points mesh on a given system and the size of the basis set of the applied wave functions. The generalized gradient approximation (GGA) exchange-

correlation energy as proposed by Perdew, Burke, and Ernzerhof (PBE) has also been utilised throughout the calculations [6-7]. The Exciting Code which make use of all-electrons in a given system in order obtain the full-potential when solving the Kohn-Sham equations has been used [8]. In order to simplify the calculations, real crystals are transformed in the k-space to Brillouin zones using the Monkhorst and Pack approximation scheme [9]. Initial calculations on the band structure, densities of states, and elastic constants require reliable optimized k-point mesh grid and sufficient expansion of the basis-set wave functions [8].

The thermo-electric transport properties are obtained by calculating the electronic transport coefficients from the Boltzmann theory [10, 11]. Such calculations apply time relaxations and rigid body approximations in order to correctly handle the semi-classical solutions of the Boltzmann equation [11, 12]. Specifically, the electronic transport coefficients of interest are electrical conductivity  $\sigma$ , thermal conductivity  $\kappa$ , Seebeck coefficient  $S$ , and the figure of merit  $ZT$ . These coefficients will be calculated with respect to the chemical potential at temperature 300 K. The relaxation time of 10 fs will be applied throughout the calculations. When calculating the transport coefficients, only the k-points with eigenenergies near the Fermi level are relevant [12]. In order to achieve this, a single self-consistent calculation is performed from the original ground state total energy calculations. The optimized lattice constants of cubic alpha  $\text{Cu}_2\text{S}$  used in this model calculations are  $a = b = c = 5.739 \text{ \AA}$ .

### 3. Results and Discussion

The electronic, elastic and transport properties of alpha  $\text{Cu}_2\text{S}$  were performed under at temperature. The electronic properties describe the state and behaviour of electrons in the material. For example, the electronic band structure and the density of state, describe the state of the electrons in terms of their energy,  $E$ . Elastic properties determine the mechanical properties of the material. The transport properties assist with the understanding of various interactions in electronic systems such as the Seebeck coefficient, electrical conductivity, thermal conductivity and the power factor.

#### 3.1. Electronic Properties

The electronic structure of any material is important in order to understand the sub-atomic properties. This information is obtained from the calculated density of states (DOS) and band structure through the materials electron density. Figures 1 and 2, shows the calculated band structure and the total density of state of the cubic alpha  $\text{Cu}_2\text{S}$  respectively. The band structure (Figure 1) indicates that the material has a zero band gap which suggest a metallic behaviour. The top of valence band and the bottom of the conduction band touch one another from L to  $\Gamma$  points along the Fermi level. In figure 2, above the Fermi level, the DOS displays a mixture of deep level states possibly originating from the Cu and S electrons. At the Fermi level the overlap of orbitals maybe due to the Cu  $3d$ -states mixing with S  $4p$ -states. Below the Fermi level, existence of  $s$  states for both Cu and S electrons are suggested. Also, the DOS shows that the nature of the valence band maximum (VBM) is widely Cu  $d$ -like. The results are in agreement with other theoretical calculations like those of Mazin [13] under DFT formalism within local-density approximations (LDA) approximation.

#### 3.2. Elastic Properties

Systematically, the elastic properties of alpha  $\text{Cu}_2\text{S}$  were also computed. The calculations assist in understanding the stability, stiffness, ductility and anisotropy of the material. Young's modulus measures the stiffness of the materials, bulk modulus refers to the resistance to shape deformation, shear modulus reflects the resistance against the shear deformation and Poisson's ratio will measure the ductility of the material [14]. There are three independent elastic constants in the cubic crystal structure, which are  $C_{11}$ ;  $C_{12}$ , and  $C_{44}$ . These elastic constants were calculated using the ElaStic@exciting [15] interface, which can be used to obtain full elastic constants of any crystal systems.

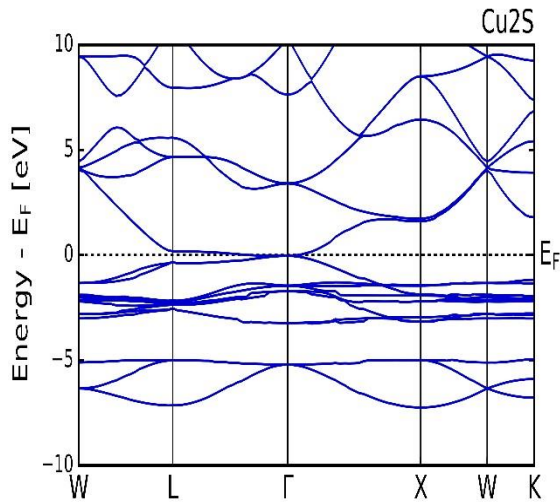


**Figure 1** Band structure of  $\text{Cu}_2\text{S}$ .

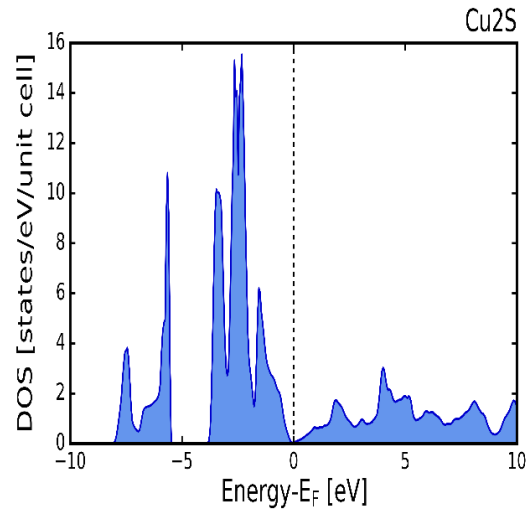


**Figure 2** Density of states of  $\text{Cu}_2\text{S}$ .

The elastic constants  $C_{11}$ ,  $C_{12}$  and  $C_{44}$  assist in describing the mechanical hardness of the material with respect to deformation. The first two constants describe the crystal response to tension, while  $C_{44}$  describes the response to shear strain. Alpha  $\text{Cu}_2\text{S}$  is cubic; as such, the deformation stability needs to satisfy the following trend:  $C_{11} > 0$ ;  $C_{12} > 0$ ;  $C_{11} - |C_{12}| > 0$  and  $C_{44} > 0$  [16]. Most of the stability conditions are satisfied by our results except one condition which is  $C_{11} - |C_{12}| > 0$ . In this study,  $C_{11} - |C_{12}| < 0$  which does not satisfy the deformation stability of cubic. Because of this condition, it can be concluded that, the material alpha- $\text{Cu}_2\text{S}$  is mechanically unstable and demonstrate some inhomogeneous character [16]. The Poisson's ratio ( $\nu$ ) which was calculated using  $C_{12}$  and  $C_{14}$  was found to be a positive value of 0.381 which is between 0 and 0.5. This positive value of  $\nu$  shows that when the  $\text{Cu}_2\text{S}$  compound stretched in one direction, it tends to expand in the other two directions perpendicular to the direction of compression [16]. Mott *et al.* [17], explained that for incompressible material, the bulk modulus ( $B$ ) is typically large compared to the shear modulus ( $G$ ) and Poisson's ratio has to be close to 0.5. From this, it can be concluded that the material  $\text{Cu}_2\text{S}$  is incompressible [17]. The Young's modulus value suggests some form of inelasticity [18].

**Table 1:** Elastic constants ( $C_{11}$ ;  $C_{12}$ ;  $C_{44}$ ), bulk modulus ( $B$ ), Young's modulus ( $Y$ ) and shear modulus ( $G$ ), all in GPa and Poisson's ratio ( $\nu$ ).

$\alpha\text{-Cu}_2\text{S}$	$C_{11}$	$C_{12}$	$C_{44}$	$B$	$Y$	$G$	$\nu$
This work (GPa)	64.349	75.477	23.442	71.767	63.421	23.442	0.381
Literature (GPa)				77.980(10)	65.413(11)	23.692 (10)	0.360 (11)

### 3.3. Transport Properties

In figures 3 to 6, only 300 K temperature thermo-electrical transport properties are considered. The behaviour of the Seebeck coefficient against the chemical potential is displayed in figure 3, and shows two notable maximum peaks of  $150 \mu\text{V.K}^{-1}$  at  $\mu = -0.05 \text{ eV}$  and  $-100 \mu\text{V.K}^{-1}$  at  $\mu = 0.05 \text{ eV}$ . It must also be clarified that on the chemical potential abscissa in figure 3, the positive and negative values suggest the electrons (n-type) and holes (p-type) dopants respectively [12].

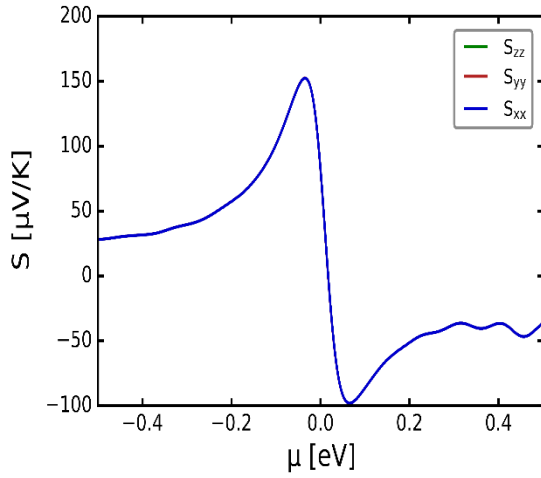


**Figure 3** Seebeck coefficient vs chemical potential of  $\text{Cu}_2\text{S}$  at 300 K.

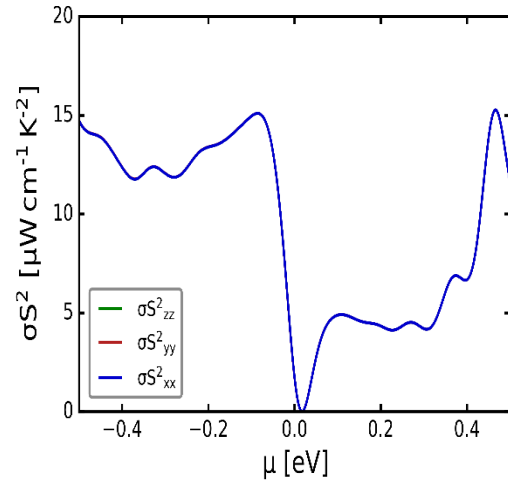


**Figure 4** Power factor vs chemical potential of  $\text{Cu}_2\text{S}$  at 300 K.

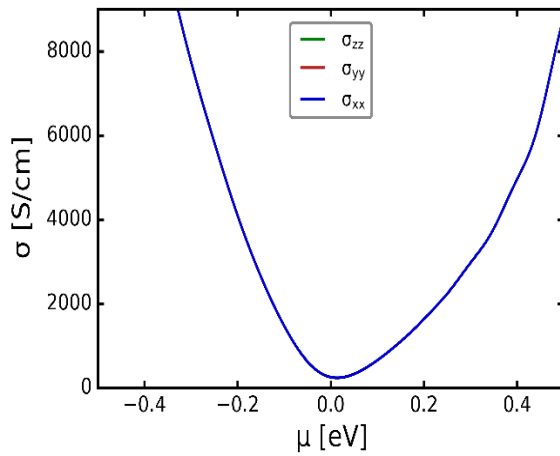


**Figure 5** Electrical conductivity vs chemical potential of  $\text{Cu}_2\text{S}$  at 300 K.

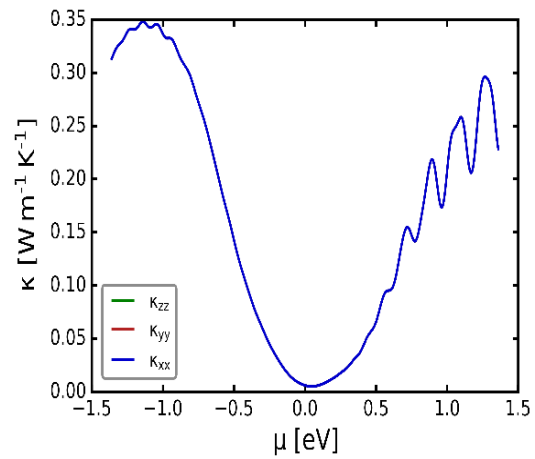


**Figure 6** Thermal conductivity vs chemical potential of  $\text{Cu}_2\text{S}$  at 300 K.

As such, the maximum value of  $S$  lies on the p-type doping zone and the minimum value lies on the n-type doping zone. The power factor ( $\sigma S^2$ ) quantity describes how efficient a given thermo-electric material is [12]. In figure 4, a maximum power factor of about  $15 \mu\text{W}\cdot\text{cm}^{-1}\cdot\text{K}^{-1}$  is observed in the negative zone of the chemical potential and a minimum value of about  $0 \mu\text{W}\cdot\text{cm}^{-1}\cdot\text{K}^{-1}$  in the positive zone. As noted with the Seebeck coefficient, the values further suggest power factor that the cubic alpha  $\text{Cu}_2\text{S}$  is more inclined to the p-type conductivity.

The electrical and thermal conductivity plots vs  $\mu$  are displayed in figures 5 and 6 respectively. Both curves display a similar behaviour relative to the changing chemical potential ( $\mu$ ) and their turning points are at the fermi level. Around the fermi level, the electrical conductivity suggests the metallic behaviour as the curve does not entirely touch the zero level of the  $\sigma$ . On the other hand, the thermal conductivity does touch zero level of the  $\kappa$  suggest poor thermal conductivity at this point. Mahan and Sofo [10] expressed that a good thermo-electric material is expected have a large Seebeck coefficient, high electrical conductivity and a low thermal conductivity in order to acquire an enhanced figure of merit [4, 10-12]. In this instance,  $S$  is having a high value of  $150 \mu\text{V}\cdot\text{K}^{-1}$  and  $\kappa$  maximum value of  $0.35 \text{ W}\cdot\text{cm}^{-1}\cdot\text{K}^{-1}$  which is considered small. A conclusion will be that the alpha  $\text{Cu}_2\text{S}$  satisfy the properties of being a thermo-electric material.

Figures 7 and 8 show the graphs of Seebeck coefficient and power factor against temperature respectively. Moreover, all values have a positive Seebeck coefficient indicating that the  $\text{Cu}_2\text{S}$  compound is a p-type semiconductor. According to Narjis *et al.* [5], the positive values of Seebeck coefficient suggest that transport properties are dominated by holes, which are found in p-type materials. The highest measured Seebeck coefficient is about  $59 \mu\text{V.K}^{-1}$  at 1000 K, and the smallest is about  $22 \mu\text{V.K}^{-1}$  at 300 K. Both graphs increase with the increasing temperature [19]. Figures 9 and 10 graphs present electrical and thermal conductivity against temperature respectively. The electrical conductivity increase linearly with the increasing temperature. A maximum electrical conductivity of about  $3.6 \Omega.\text{cm.s}^{-1}$  at 1000 K is achieved. In the same manner, the thermal conductivity increases exponentially with the increasing temperature. In this case, a thermal conductivity of about  $1.8 \text{W}(\text{cmKs})^{-1}$  at 1000 K is obtained. In addition, figure 10 illustrates that the thermal conductivity of alpha  $\text{Cu}_2\text{S}$  is still very low to the value of about  $0.2 \text{W}.\text{cm}^{-1}.\text{K}^{-1}$ . Such property further confirm the thermal property of the materials in line some previous studies [20, 21].

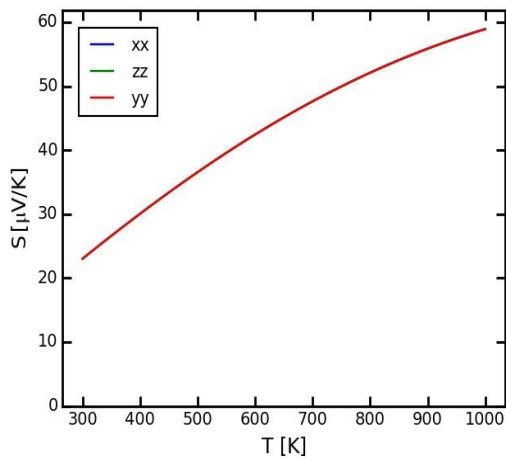


Figure 7 Seebeck coefficient vs temperature

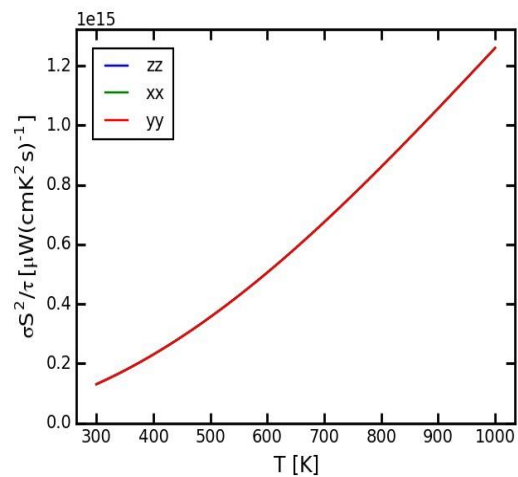


Figure 8 Power factor vs temperature.

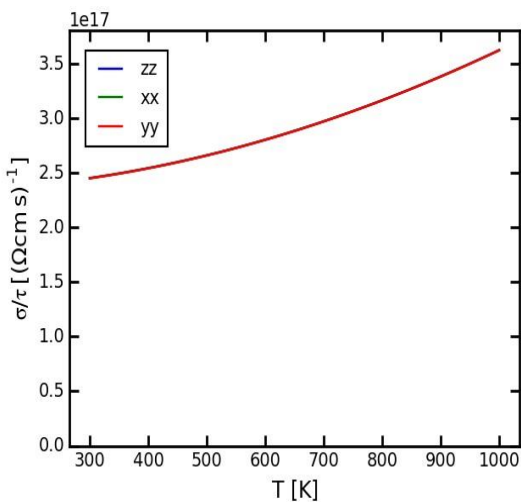


Figure 9. Electrical conductivity vs temperature

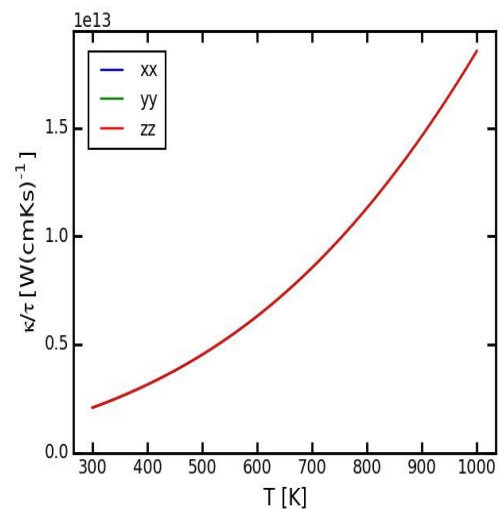


Figure 10. Thermal conductivity vs temperature.

#### 4. Conclusion

The electronic properties results are in agreement with previous studies, which shows that the cubic alpha copper sulphide is a semi-metallic material with zero band gap. This zero band gap is attributed to the band structure geometry between the symmetry points L and  $\Gamma$ . Elastic constants show that the material is mechanically stable and it has a low shear modulus and high bulk modulus which are in agreement with previous studies. Thermo-electric transport properties of the material suggest a p-type conductivity. The high positive Seebeck coefficient, the high electrical conductivity, and the low thermal conductivity values suggest alpha Cu<sub>2</sub>S as a good thermo-electric transport material. This is further corroborated by the little change of the electrical conductivity with increasing temperature. Very small, suppressed thermal conductivity values with increasing temperature further support the findings. Such low shear and high bulk modulus materials have potential in thermo-electric transport applications.

#### 5. Acknowledgments

Special thanks to my supervisor Prof TE Mosuang. UL is thanked for their financial support. CHPC is highly indebted for the computational facilities.

#### References

- [1] Zimmer D, Ruiz-Fuertes J, et al. 2018 *Phys. Rev B* **97**, 134111
- [2] Kumar S.A et al. 2014, *J Chem Eng.* **1**(1): 1002.
- [3] Pósfai M and Buseck P.R., 1994 *Am. Mineral.* **79**, 308,
- [4] Jiang Q, Yan H, Khaliq J, Shen Y, Simpson K, Reece MJ 2014 *J. Mater. Chem. A* **2**, 9486
- [5] Narjis A, Outzourhit A, Aberkouks A, El Hasnaoui A, Nkhaili L 2018 *J. Semiconductor* **39** 122001-1
- [6] Perdew J.P, Burke K and Ernzerhof M, 1996 *Phys. Rev. Lett* **77** 3865
- [7] Kresse G and Joubert D, 1999 *Phys. Rev. B* **59** 1758
- [8] Gulans A, Kontur S, Meisenbichler C, Nabok D, Pavone P, Rigamonti S, Sagmeister S, Werner U, Draxl C, 2014 *J. Phys.: Condens Matter* **26** 363202
- [9] Monkhorst H.J and J.D Pack J.D, 1976 *Phys. Rev. B* **13** 5188
- [10] Mahan GD, Sofo JO 1996 *Proc. Natl. Acad. Sci.* **93** 7436
- [11] Madsen GK and Singh DJ 2006 *Comput. Phys. Commun.* **174** 67
- [12] Scheidemantel TJ, Ambrosch-Draxl C, Thonhauser T, Badding JV, Sofo JO 2003 *Phys. Rev. B* **68** 125210
- [13] Mazin I.I, 2012 *Phys. Rev. B* **85** 115133
- [14] Yao H, Ouyang L, Ching W-Y 2007 *J. Am. Ceram. Soc.* **90** 3194
- [15] Golesorkhtabar R, Pavone P, Spitaler J, Puschnig P, Draxl C 2013 *Comp. Phys. Comm.* **184** 1861
- [16] Jamal M, Asadabadi S.J, Ahmad I, Aliabad HAR 2014 *Comp. Mater. Sci.* **95** 592
- [17] Mott PH, Dorgan JR, Roland GM 2008 *J. Sound and Vibrations* **312** 572
- [18] Cygan T, Wozniak J, Petrus M, Lachowski A, Pawlak W, Adamczyk-Cieślak B, Jastrzębska A, Rozmysłowska-Wojciechowska A, Wojciechowski T, Ziemkowska W, Olszyna A 2021 *Materials* **14** 829
- [19] Mulla R, Rabinal MK 2016 *App. Surface Sci.* 397
- [20] Liu H.L, Shi X, Xu F, Zhang L, Zhang W, Chen L, Li Q, Uher C, Day T, Snyder GJ 2012 *Nat. Mater.* **11** 422  
Yang D, Su X, Yan Y, He J, Uher C, Tang X 2016 *APL Mater.* **4** 116110-1

# Development of machine learning models for predicting energies of sodium-ion battery materials

KM Monareng<sup>1</sup>, RR Maphanga<sup>2,3</sup>, and PS Ntoahae<sup>1</sup>

<sup>1</sup>Department of Physics, University of Limpopo, Private Bag X 1106, Sovenga, 0727

<sup>2</sup>Next Generation Enterprises and Institutions, Council for Scientific and Industrial Research, P.O. Box 395, Pretoria, 0001

<sup>3</sup>National Institute for Theoretical and Computational Sciences, NITheCS, Gauteng, 2000

E-mail: [mabelkmonareng@gmail.com](mailto:mabelkmonareng@gmail.com)

**Abstract.** Machine learning methods have recently found applications in many areas of physics, chemistry, biology, and materials science, where large datasets are available. In this paper, machine learning regression techniques are applied to a large amount of density functional theory calculated data to develop machine learning models capable of accurately predicting the formation and total energy of sodium-ion battery cathode materials. Amongst various algorithms that are evaluated, the Bayesian ridge model is found to be the best model in predicting the formation energy with an accuracy of 0.99 and 0.01 eV coefficient of determination and mean square error, respectively, and final energy with 0.98 and 0.03 eV accuracy for the coefficient of determination and mean square error, respectively. The results show that the descriptors used to predict the energies have a predictive capacity with a high accuracy.

## 1. Introduction

The development of energy storage and conversion devices is essential to reduce the discontinuities and instability of renewable energy generation [1]. New eco-friendly energy sources are necessary in the current era, as they are expected to reduce greenhouse gas emissions and ultimately benefit human health. Over the past two decades, lithium-ion batteries (LIBs) have dominated the portable electronics industry and solid-state electrochemical research [2]. Due to the use of LIBs in portable electronics such as laptops, electric vehicles, and cell phones, lithium-ion batteries have received a lot of attention [3]. Among the most favourable characteristics of Li-ion batteries are their longer lifetime, higher energy, high efficiencies, and power densities. Despite their success, lithium-ion batteries are expensive to produce due to limited lithium resources in the Earth's crust and, in addition, large-scale energy storage is not possible with this technology.

Despite concerted efforts to develop novel materials for energy storage technologies, there is a continuous need for technologies that can push the limits on material properties [4]. Alkaline-ion batteries have developed rapidly in recent decades due to their high energy density and environmentally friendly properties [1]. These batteries have gained a good reputation as alternatives to LIBs due to the high abundance of Na- and K-ions in the environment. Sodium-ion battery (SIB) technology has gained the privilege of enabling new and more demanding applications for large-scale energy storage systems than LIBs; this is due to the high abundance of sodium-ion resources present in the Earth's crust and seawater [5, 6]. Quantum mechanical methods have been shown to be successful in predicting and finding functional new materials, such as SIB materials, to replace LIB materials; however, the calculations are computationally expensive and time-consuming. The lack of suitable electrodes and

electrolyte materials has limited the development of sodium-ion batteries. In this context, the data-driven machine learning (ML) approach has recently found ways to address material discovery at a faster rate and with limited use of computational resources.

Previous studies have shown that a combination of density functional theory (DFT) and machine learning (ML) methods can accelerate the prediction of material properties and the discovery of novel materials [7, 8]. Machine learning models and algorithms are increasingly applied in battery materials research, with superior time efficiency and high accuracy in property prediction. Some examples include successful application to predict the properties of battery material properties [9-11] and discovery of new battery materials [12, 13]. In this paper, we develop machine learning models capable of accurately predicting the formation and total energy of sodium-ion battery cathode materials.

## 2. Methodology

Machine learning algorithms are typically expressed as a computer program that can learn from experience (E) with respect to some class of tasks (T) and the performance measure (P) [1]. Thus, ML is simply denoted as  $\langle P, T, E \rangle$ . The main interpretation is that a computer program is said to learn from experience E with respect to some class of tasks T and a performance measure P if its performance on tasks in T, as measured by P, improves with experience E. It is not the purpose of this paper to discuss details on the theoretical background of machine learning methods, models, and their applications in materials science; however, more details can be found elsewhere in the literature [14]. With regard to materials science, the ML process consists of the three key steps summarized in the following subsections.

### 2.1. Sample construction

In this step, there are two important activities, namely data curation and feature engineering. The data are cleaned, pre-processed, while features are engineered to help improve the accuracy of property prediction. Pymatgen Materials Genomes was used to extract materials data from the Materials Project Database [15], which contains 7397 different sodium containing materials with different properties calculated using DFT. Chemical descriptors were used to construct machine learning features based on fundamental atomic properties, such as the chemical formula and atomic number. Feature vectors were then generated from details of the chemical formula. The features extracted from the Materials Project include: formation energy per atom, final energy per atom, energy, Fermi energy, energy above hull, density, and bandgap. To obtain the chemical name (X) of a material, an algorithm was developed to generate a set of chemical and physical descriptive attributes in which the energies (Y) were predicted. Descriptor attributes were used to predict formation and final energy in this study.

### 2.2. Model development

Model development is a black box that links the input data to the output data employing a set of functions, which can be either linear or non-linear based on the input data. The models were developed using a Scikit library machine learning module and a Python code. The data was divided into 70% train set and 30% test set. The tested models include the Bayesian ridge (BR), gradient boosting regressor (GBR), light gradient boosting machine (LGBM), extra trees regressor (ETR), orthogonal matching pursuit (OMP), and random forest regressor (RFR) among others. Detailed descriptions of all these models [16-18] and their application in materials science can be found elsewhere [14, 19].

### 2.3. Model evaluation

The model evaluation step involves evaluating and validating the performance accuracy of the developed models. A model was evaluated using different evaluation metrics to measure its performance. In this case, to evaluate the accuracy of the model, we compared the calculated DFT properties with the values predicted by the ML model employing K-fold cross validation. For the light gradient boosting machine, the hyperparameters used include the number of trees = 1000, the maximum depth = 3 and the regularization of L2 = 1 without cross validation and the number of trees = 350, maximum depth = 10 and L2 regularization = 10 with cross validation. The hyperparameter used for the

Bayesian ridge model iteration = 350 without cross validation and iteration = 50 with cross validation. The following precision measures were used to evaluate the performance of the model: coefficient of determination ( $R^2$ ) and mean square error (MSE).

Coefficient of determination is computed using the formula:

$$R^2 = 1 - \frac{\sum_i (y_i - \hat{y}_i)^2}{\sum_i (y_i - \bar{y})^2} \quad (1)$$

where  $y_i$ , are the observed true DFT values,  $\hat{y}_i$  are the ML predicted values, and  $\bar{y}$  is the mean value of the  $i$ -th sample and the sample size of the testing set. It is recommended that an  $R^2$  reading of 0.8 or higher is adequate for a good reading, indicating that the model is fitting well. The MSE provides an indication of the quality of the model and is defined as:

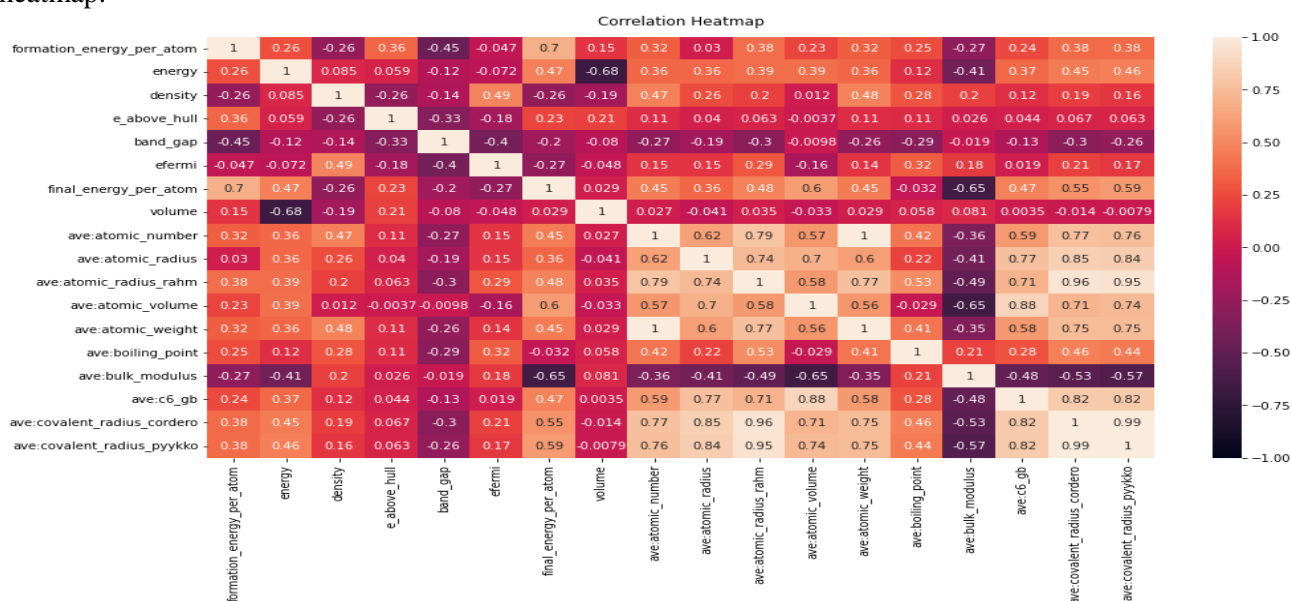
$$MSE = \frac{1}{n} \sum_{i=1}^n (y_i - \hat{y}_i)^2 \quad (2)$$

where  $n$  is the number of data points. Zero mean square error shows that the model predicted 100% correct actual values; hence the model must achieve MSE closer to zero.

### 3. Results and discussion

#### 3.1. Feature engineering

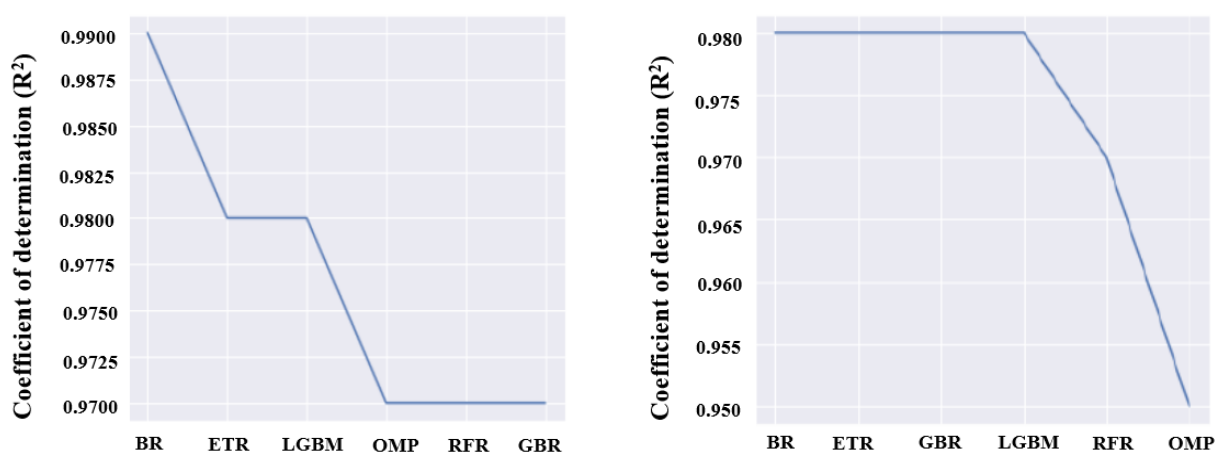
Figure 1 shows 18 x 18 matrix correlation heatmap ranging from -1 to 1 with squares representing the relationship between variables to predict both the formation and total energy of sodium containing materials. When the correlation is close to 1 or -1, it implies that the variables have a strong relationship. In addition, a value closer to zero indicates that the two variables are not linearly related. Since all the diagonals are -1 (black) or 1 (fawn), there is a perfect correlation. A larger number and darker or lighter colour indicates a stronger correlation between the two variables. In this study, 18 descriptors were considered and evaluated in order to determine the important descriptors in predicting the energies. The average covalent radius and average single bond covalent radius were found to be the most important features, with feature correlation ranging between 0.82 and 0.99, respectively, as can be seen on the heatmap.



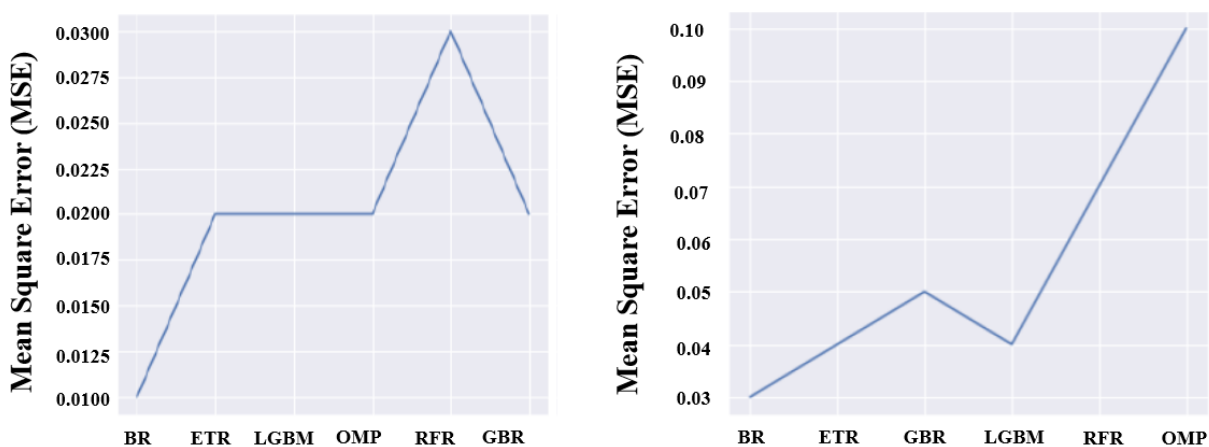
**Figure 1.** Correlation heatmap for predicting the formation energy and total energy.

### 3.2. Model selection

The best model is selected on its capability to predict the target property, in this case formation and total energy. Figure 2 illustrates the measures of the predicted coefficient of determination for the formation (left) and final energy (right) as determined by various models while Figure 3 shows the measures of the predicted formation energy MSE (left) and final energy MSE (right) as determined by various models. During model tuning, data was pre-processed using statistical normalization, then hyperparameters were optimized using cross-validation score. The tuned algorithm was fitted to the training data, which comprised 70%, and the learned model was then applied to the test data, which comprised 30%. Various models were evaluated by resampling on data collected outside the sample (or, more precisely, the development process of the model). Amongst the developed models, the Bayesian ridge was found to be the best model based on its accuracy in predicting the energies.



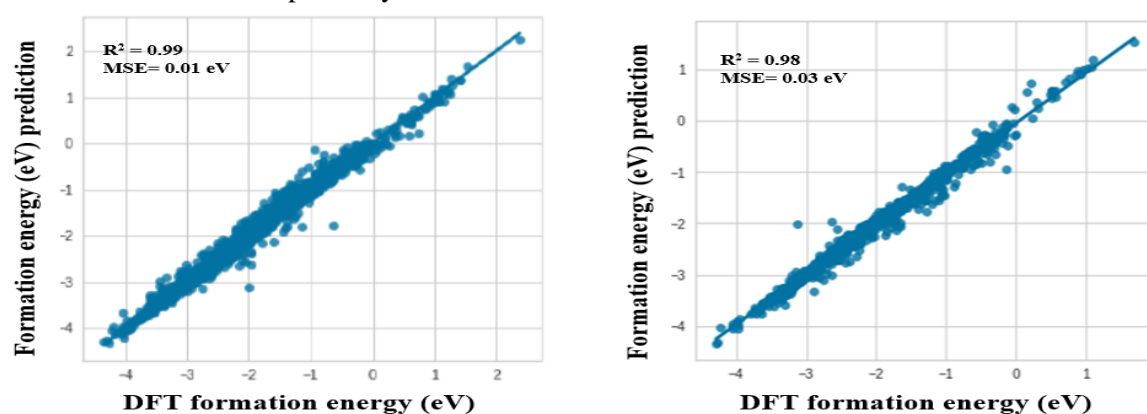
**Figure 2.** Measures of predicted formation energy coefficient of determination (left) and final energy coefficient of determination (right) as determined by various models.



**Figure 3.** Measures of predicted formation energy mean square error (left) and final energy mean square error (right) as determined by various models.

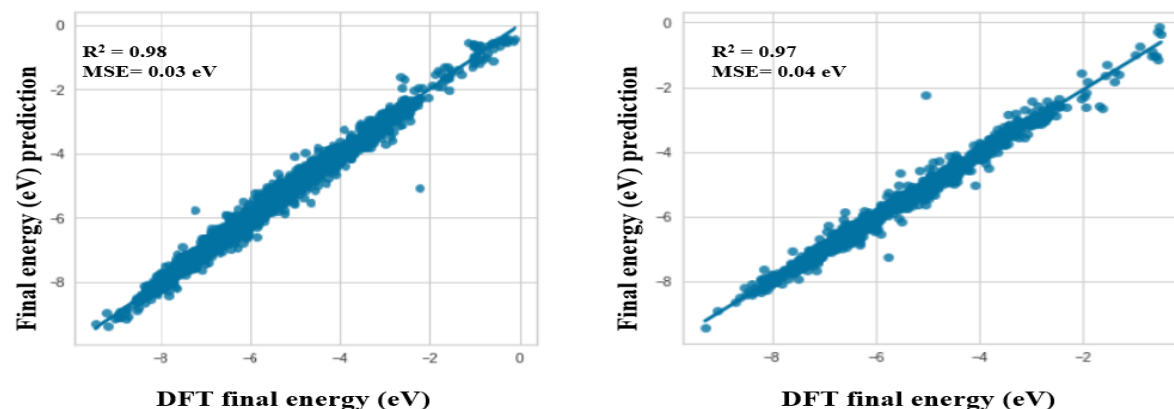
### 3.3. Model validation

Figure 4 shows graphical representations of model performance in the training set (left) and the test set (right), containing data points that reflect the predicted formation energy as a function of the DFT calculated formation energy obtained using Bayesian ridge regressor. Bayesian ridge regression was found to be the best performing model with the predicted formation energy achieving a coefficient of determination  $R^2$  of 0.99 and an MSE of 0.01 eV. LGBM predicted formation energy poorly with a coefficient of determination of 0.59 and a mean square error of 1.40 eV for the training set and 0.55 and 1.51 eV, respectively, for the testing set. Due to this poor performance of LGBM, features that did not add value to the prediction of the formation energy were removed in order to determine the role that feature vectors play on model performance. The models were trained again with few feature vectors (density and band gap were removed) and found to have improved the performance up to 0.69 and 0.01 eV for  $R^2$  and MSE, respectively.



**Figure 4.** Parity plot of Bayesian ridge model predicted formation energy versus DFT formation energy model performance in train set (left) and test set (right).

Figure 5 shows a graphical representation of the model performance in training set (left) and test set (right), containing data points that reflect the predicted final energy as a function of DFT calculated final energy obtained from the Materials Project database. Based on the small difference between the train and test-model performance results, it is evident that the models were not overfitted. Bayesian ridge regression with elemental descriptors predicted the final energy, achieving a coefficient of determination  $R^2$  of 0.97 and an MSE of 0.04 eV. Later, the performance of the optimized algorithm gave an  $R^2$  of 0.98 and an MSE of 0.03 eV through model tuning. For the best advantage, all the points should pass through the diagonal regressed line, and the model Bayesian ridge resulted in a high regression score.



**Figure 5.** Parity plot of Bayesian ridge predicted final energy versus DFT final energy model performance in train set (left) and testing set (right).

#### 4. Conclusion

The machine learning models were successfully developed, from which the formation and final energies of various sodium-ion battery materials were predicted. The average covalent radius and the average single-bond covalent radius were the most important features for predicting the formation and final energy of these materials. Several models were evaluated, and the best model was selected based on its accuracy in predicting the afore-mentioned energies. Amongst the various algorithms that were evaluated, Bayesian ridge model was found to be the best model with the following accuracy measures: coefficient of determination  $R^2$  of 0.99 and 0.98 for formation and final energy respectively, mean square error of 0.01 and 0.03 eV for formation energy and final energy respectively. The machine learning models were further validated, from which the DFT calculated properties were compared with their corresponding predicted machine learning values. There is good agreement between the model on the train and the test set. Machine learning models can yield accurate material properties faster, making them useful in materials-properties prediction.

#### 5. Acknowledgments

The study is funded by the Department of Science and Innovation-Inter-bursary Support (IBS) Programme of the Council for Scientific and Industrial Research, and the funding support is duly acknowledged.

#### References

- [1] Kauwe S, Rhone T and Sparks T 2019 Crystal (Basel). **9** 1-9
- [2] Peng L, Zhu Y, Chen D, Ruoff R and Yu G 2016 Adv. Energy Mater. **6** 1-21
- [3] Takagishi Y, Yamanaka T and Yamaue T 2019 Batteries. **5** 1-14
- [4] Chayambuka K, Mulder G, Danilov D and Notten P 2018 Adv. Energy Mater. **8** 1-49
- [5] Kim S, Seo D, Ma X, Ceder G and Kang K 2012 Adv. Energy Mater. **2** 710-21
- [6] Hwang J, Myung S and Sun S 2017 Chem. Soc. Rev. **46** 3529-614
- [7] Hautier G, Fischer C, Jain A, Mueller T, Ceder G 2010 Chem. Mater. **22** 3762-67
- [8] Hautier B, Agrawal A, Kirklin S, Saal J, Doak J, Thompson A, Zhang K, Choudhary A and Wolverton C 2014 Phys. Rev. B. **89** 1-7
- [9] Maphanga R, Mokoena T and Ratsoma R 2021 Mater. Today: Proceedings. **38** 773-8
- [10] Joshi R, Eickholt J, Li L, Fornari M, Barone V and Peralta J 2019 ACS Appl. Mater. & Interfaces. **11** 18494-503
- [11] Liu Y, Guo B, Zhou X, Li Y and Shi S 2020 Energy Stor. Mater. **31** 434-50
- [12] Moses I, Joshi R, Ozdemir B, Kumar N, Eickholt J and Barone V 2021 ACS Appl. Mater. & Interfaces. **13** 53355-62
- [13] Liu Y, Niu C, Wang Z, Gan Y, Zhu Y, Sun S and Shen T 2020 J. Mater. Sci. **57** 113-22
- [14] Mueller T, Kusne A and Ramprasad R 2019 Rev. Comput. Chem. **29** 186-273
- [15] <https://materialsproject.org>
- [16] Fan J, Ma X, Wu L, Zhang F, Yu X and Zeng W 2019 Agric. Water Manag. **225** 105758
- [17] Polamuri R, Srinivas K and Mohan A 2019 IJRTE. **8** 2277-3878
- [18] MacKay D 1992 CNS. **4** 415-47
- [19] Schmidt J, Marques M, Botti S and Marques M 2019 npj Comput Mater. **5** 1-36

## Structural and magnetic study of NdCrTiO<sub>5</sub> nanoparticles

B Bharati<sup>1,2</sup>, P Mohanty<sup>2</sup>, ARE Prinsloo<sup>2</sup> and CJ Sheppard<sup>2</sup>

<sup>1</sup>Spectrum Analytical Facility, Faculty of Science, University of Johannesburg, P.O. Box 524, Auckland Park, Johannesburg 2006, South Africa

<sup>2</sup>Cr Research Group, Department of Physics, University of Johannesburg, P.O. Box 524, Auckland Park, Johannesburg 2006, South Africa

E-mail: [bharatib@uj.ac.za](mailto:bharatib@uj.ac.za)

**Abstract.** *RCrTiO<sub>5</sub>* compounds shows interesting magnetic behaviour because of the presence of two magnetic sublattices,  $R^{3+}$  and  $Cr^{3+}$ . This contribution focuses on the synthesis, structure, morphology and magnetic properties of nano *NdCrTiO<sub>5</sub>*, that belongs to this group. The orthorhombic crystal structure with lattice parameters,  $a$ ,  $b$ ,  $c$  is  $7.5715 \pm 0.0007$ ,  $8.7270 \pm 0.0008$  and  $5.7916 \pm 0.0006$  Å, respectively, was confirmed through x-ray diffraction. The average particle size obtained from the transmission electron microscopy is  $33 \pm 1$  nm, selected area diffraction pattern confirms the crystalline nature of the sample and energy dispersive x-ray spectroscopy confirms the elemental composition. From the temperature-dependent magnetization measurement on the nanoparticles the Néel temperature, temperature,  $T_N$ , could not be obtained. This is in contrast with the previously observed  $T_N$  in bulk samples at 18 and 21 K and might be due to the reduced size of the material. Further, the ferromagnetic nature of the material was observed from the magnetization as the function of field measurement with coercivity  $0.018 \pm 0.001$  T,  $0.019 \pm 0.001$  T and exchange bias  $-0.004 \pm 0.001$  T,  $-0.003 \pm 0.001$  T, at 2 K and 10 K, respectively. The observed anomalous properties are discussed considering the size effect.

### 1. Introduction

In order to improve the device technologies new and advanced magnetic materials are in search of materials which exhibit properties such as, exchange bias (EB), magnetization reversal (MR), spin switching (SS), spin reorientation (SR) and significant magnetocaloric effect (MCE) [1-2]. In a multiferroic material, multiple ferroic states co-exist [1-2], and it is visualized that the co-dependence of the order parameters might contribute to spintronics, as well as to novel memory devices [3-5]. In general, remarkable and exciting physics are probable wherever two or more type of spin sublattices contribute to the material's observed magnetism [6-8]. *RMn<sub>2</sub>O<sub>5</sub>* ( $R$  = rare-earth ions), are the group of compounds, multiferroic in nature, which are attracting the attention of various researchers because of the two contributing magnetic sublattices in the compound [8-10]. These *RMn<sub>2</sub>O<sub>5</sub>* compounds crystallize in an orthorhombic structure, having a space group *Pbam* [8-9]. In these compounds, the sublattice of rare-earth ion is magnetized moderately through the Mn ions [8].

The *RCrTiO<sub>5</sub>* family also has an orthorhombic crystal structure similar to that of *RMn<sub>2</sub>O<sub>5</sub>* [11-12]. In this series of compounds, one can expect to find exceptional and fascinating magnetic behavior because of the co-existence of two magnetic sublattices;  $Cr^{3+}$  and  $R^{3+}$ . However, currently there are only a few reports on these materials and most of them are in bulk form [1, 4-7]. Hwang et al. [4] synthesised the *NdCrTiO<sub>5</sub>* and estimated its dielectric constant and pyroelectric current. Das et al. [13],

showed magnetic properties such as SR and compensation in bulk DyCrTiO<sub>5</sub>, as well as in HoCrTiO<sub>5</sub> and also observed EB effect. Recently, the reports published on nano DyCrTiO<sub>5</sub> and GdCrTiO<sub>5</sub>, are showing structural and magnetic behavior of the material [14-15]. Exchange coupling among different atoms of an oxide compound having a rare-earth constituent depicts interesting magnetic behavior [1, 4, 13]. A shift in the hysteresis loop across the applied field axis originates in FM-AFM systems because of this exchange coupling. The magnitude of this shifting is known as exchange bias field ( $H_{ex}$ ) [16]. This exchange bias effect is attributed to the coupling between two magnetic sublattices in the perovskites [17-18]. Zheng et al. [19] also observed an exchange bias effect in YMnO<sub>3</sub>, which is ascribed to the uncompensated surface spins of the nanoparticles. Nowadays, the world is looking towards the nanostructured materials because of their improved properties, which comes from their enhanced surface-to-volume ratio, as well as uncompensated surface spins [20]. The uncompensated surface spins present can significantly modify the magnetic properties, as well as other physical properties [20-21]. The change in the structural properties subsequently brings about concomitant changes in the magnetic nature of these materials [22-23].

Nano NdCrTiO<sub>5</sub> is one of the promising materials from the RCrTiO<sub>5</sub> group yet to be explored. Various magnetic transitions are expected and interpreting the underlying physics responsible for the observed properties of NdCrTiO<sub>5</sub> in the nano form will be most interesting. Therefore, this contribution reports on the properties of NdCrTiO<sub>5</sub> particles synthesized using the sol-gel technique [20-21], considering x-ray diffraction (XRD), transmission electron microscopy (TEM), magnetization ( $M$ ) as function of temperature ( $T$ ) as well as with magnetic field ( $\mu_0 H$ ) results. In addition the modification of magnetic properties on reducing the particle size to nano dimensions will also be discussed in this work.

## 2. Experimental details

Synthesis of the NdCrTiO<sub>5</sub> sample was carried out by the sol-gel method [20-21]. The calculated stoichiometric amounts of Nd(NO<sub>3</sub>)<sub>3</sub>, Cr(NO<sub>3</sub>)<sub>3</sub> and Ti(OC<sub>3</sub>H<sub>7</sub>)<sub>4</sub> were mixed with ethanol. The solution of the precursors were stirred using a magnetic stirrer [20-21]. Ten milliliters (10 ml) of distilled water was added into the solution while constantly stirring. The solution was continuously stirred for another half an hour, where after the solution was aged for 24 h. A solid sample was obtained after drying the aged solution and crushed to powder. The powdered sample was then calcined at 800 °C for three hours in a box furnace. The prepared sample was used for characterization, using x-ray diffraction (XRD) technique with Cu-K $\alpha$  radiation ( $\lambda = 1.5406 \text{ \AA}$ ), transmission electron microscope (TEM) and vibrating sample magnetometer (VSM) using a Cryogenic Cryogen Free Physical Properties Measurement System, with a vibrating sample magnetometer insert.

## 3. Results and discussion

### 3.1. Structural properties of NdCrTiO<sub>5</sub>

Firstly, the NdCrTiO<sub>5</sub> sample was characterized using XRD techniques to determine the structural properties of the material. The XRD pattern obtained is shown in Figure 1 and it was analyzed using FULLPROF software [24]. The data for the sample shows it having orthorhombic crystal structure with a  $Pbam$  space group, similarly as was observed in bulk sample prepared by solid state route [4]. The unit cell parameters  $a$ ,  $b$  and  $c$  has found to be  $7.5715 \pm 0.0007$ ,  $8.7270 \pm 0.0008$  and  $5.7916 \pm 0.0006 \text{ \AA}$ , respectively, while the cell volume found from the refinement parameters is  $382.69 \pm 0.06 \text{ \AA}^3$ . In previous reported data on a polycrystalline bulk NdCrTiO<sub>5</sub> sample [4] the reported cell parameters  $a$ ,  $b$  and  $c$ , are  $7.5812 \pm 0.0002$ ,  $8.6803 \pm 0.0002$  and  $5.8123 \pm 0.0003 \text{ \AA}$ , respectively. The XRD patterns could be well resolved with the ( $hkl$ ) reflections of the orthorhombic structure and the distinct diffraction peaks signify the crystallinity of the particles. No other peaks corresponding to any other impurities have appeared. Minor shifting has been observed in few peak positions because of internal stresses in nano material in line with previously reported results [25]. Along with peak shifting, peak broadening is observed due to nano size of the material (confirmed from the TEM) [26].

In the orthorhombic phase a large number of peaks are observed, but for the sample in the nano form a few peaks are merged [14-15]. In this case the difference between the experimental and calculated data is obtained due to shifting and merging of peaks [25-26]. Further, the crystallite size of the sample has been calculated using Scherrer's formula and found to be  $39.0 \pm 0.6$  nm [14-15].

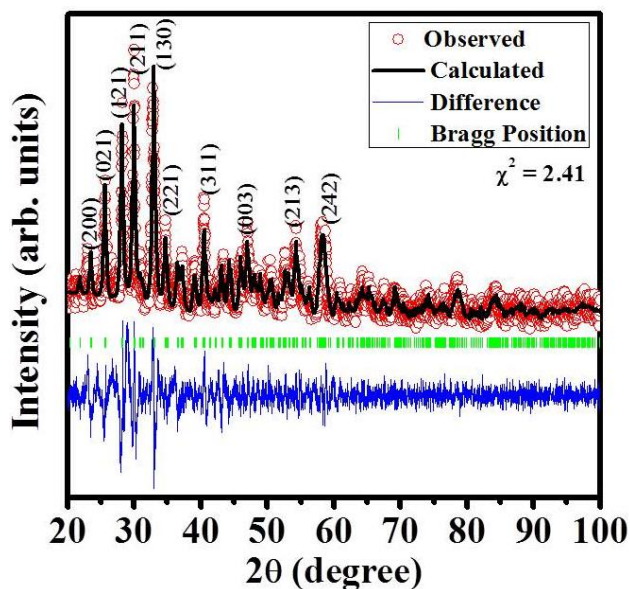


**Figure 1.** The fitted XRD pattern of the NdCrTiO<sub>5</sub> nanoparticles using the FULLPROF program [29].

The TEM image of synthesised NdCrTiO<sub>5</sub> is shown in Figure 2(a) and the particle size distribution is shown in Figure 2(b). The sample consists particles of various sizes and shapes. The particle size distribution histogram is fitted using log-normal fit [21]. The average particle size for the synthesized sample was found to be  $33 \pm 1$  nm, with particle size distribution ranging from 20 to 70 nm. Using the sol-gel technique, the NdCrTiO<sub>5</sub> nanoparticles are synthesised in a shortened time of only three hours and the calcination temperature is also low compared to solid state synthesis [4]. In the case of bulk NdCrTiO<sub>5</sub> the heating time was more than 24 h and temperature is 1300 °C [4]. Comparing with the earlier synthesis process of NdCrTiO<sub>5</sub>, the present sol-gel synthesis method is therefore relatively easy and consumes less time. Figure 2(c) shows the TEM image of the selected area electron diffraction (SAED) pattern. From the dotted SAED pattern it was predicted that sample was of crystalline nature [20]. In general, energy-dispersive x-ray spectroscopy (EDS) is used to determine the elements composition, here the EDS is shown in Figure 2(d). The obtained result of elemental composition from EDS was Nd, Cr, Ti, O, C and Cu. The Nd, Cr, Ti and O are from the synthesised material, whereas C and Cu are from the TEM grids. Previous reports on bulk NdCrTiO<sub>5</sub> samples [4-5] showed interesting dielectric and magnetoelectric properties. Thus, as a starting point, in the present study the magnetic properties of the nano NdCrTiO<sub>5</sub> are investigated.

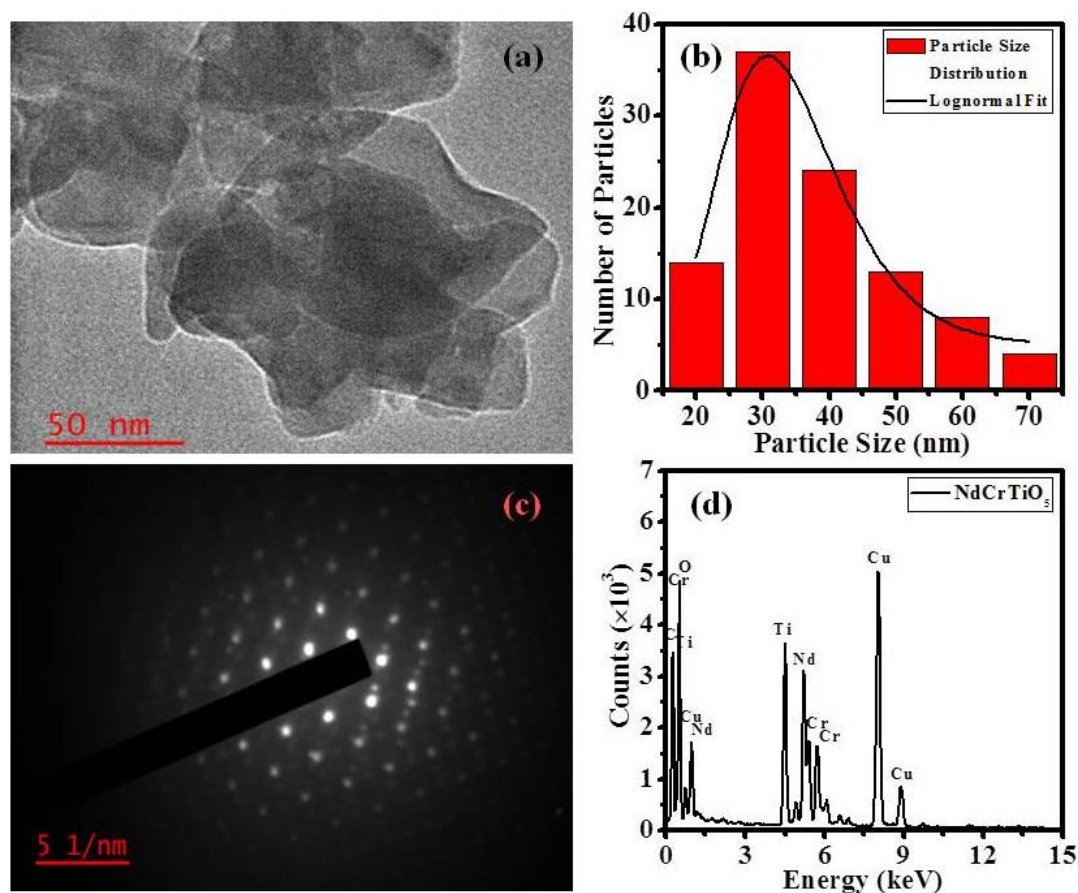


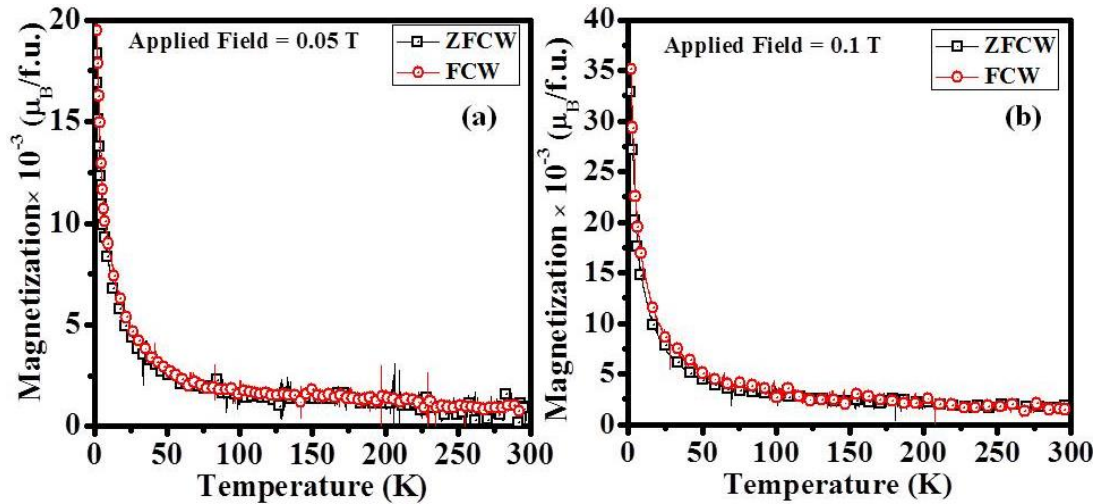
**Figure 2.** (a) TEM image, (b) particle size distribution using log-normal fit, (c) SAED pattern and (d) energy dispersive x-ray spectroscopy of the NdCrTiO<sub>5</sub> nanoparticles.

### 3.2. Magnetic properties of NdCrTiO<sub>5</sub>

The dc-magnetization as a function of temperature was carried out for NdCrTiO<sub>5</sub> nanoparticles under zero-field-cooling-warming (ZFCW), field-cool-warming (FCW) protocols [14-15]. In ZFCW cycle, the sample was made to cool down to the base temperature of 2 K without any applied magnetic field. Then a magnetic field was applied and magnetization measured from 2 to 300 K. Thereafter, the same applied field was applied and the sample was cooled at the same rate as in ZFCW cycle. After reaching at 2 K, the magnetization ( $M$ ) as a function of temperature ( $T$ ) was measured from 2 to 300 K in a FCW measurement [14-15].

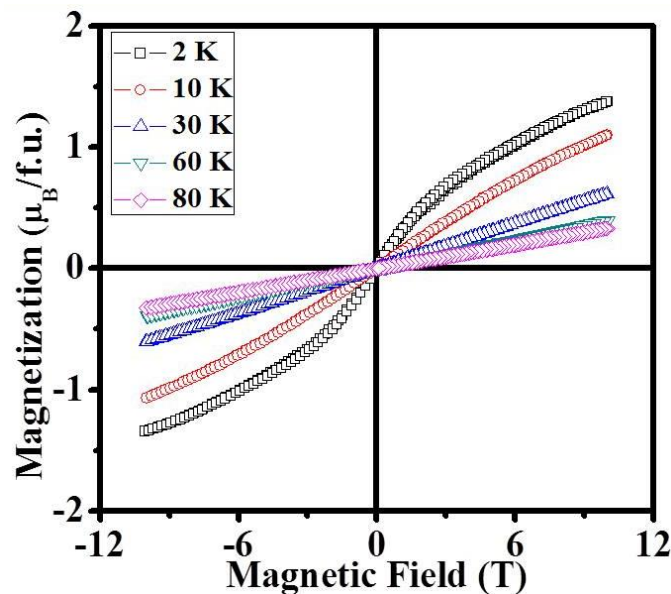
The  $M(T)$  curves for NdCrTiO<sub>5</sub> are shown in Figure 3(a) and (b). Figure 3(a) indicates the measurement carried out at an applied field 0.05 T and Figure 3(b) is for the measurement cycles carried out at applied field 0.1 T. In bulk samples the Néel temperature,  $T_N$ , was observed around 18 to 21 K, but in this case no such transition was observed in the mentioned temperature range. This might be due to changes in magnetic properties because of nano-sized nature of the material [4-5] studied here. According to literature, it has been found that with changing the size of oxide materials, the various properties can be significantly influenced and changed [21-22]. In Mn doped TiO<sub>2</sub>, when the particle size is 12 nm the obtained structure was anatase but when the particle size was 15 nm both anatase and rutile structure are existing [21]. Another, report shows anatase to brookite phase transformation with increasing the particle size from 22.6 nm to 84.5 nm [22]. Based on the previous reports [14-15, 21-22], it can be considered that the change in dimensions can bring about novel

properties in the material, as noticed in the present work. As examples, consider earlier reports on bulk  $\text{DyCrTiO}_5$  [13] indicated SR (spin reorientation), not observed in nanoparticles of the same material [14]. However, in bulk  $\text{GdCrTiO}_5$  [1] SR was not observed, but in nano  $\text{GdCrTiO}_5$  [15] SR was observed.



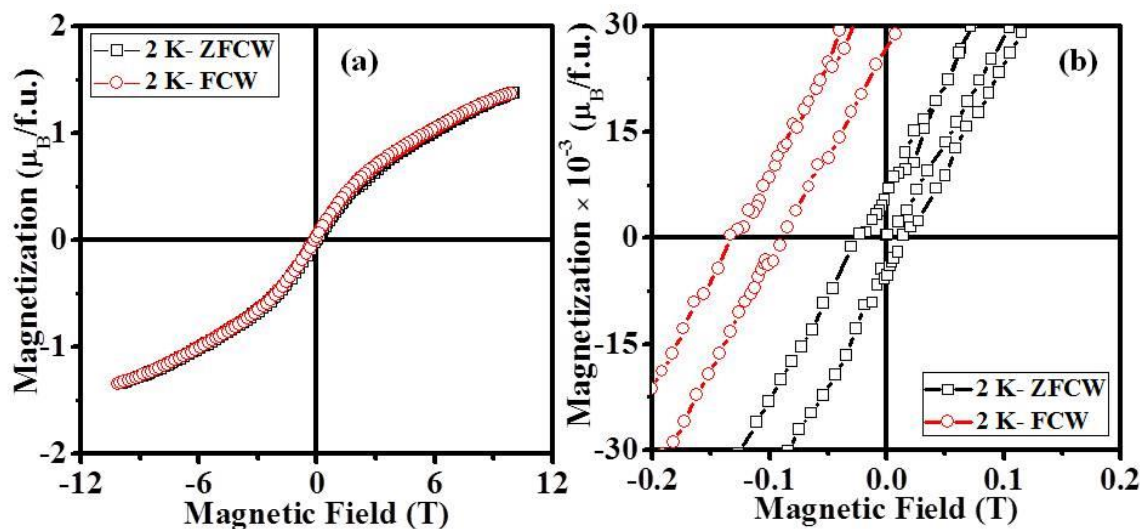
**Figure 3.**  $M(T)$  data for  $\text{NdCrTiO}_5$  nanoparticles with probing fields of (a) 0.05 T and (b) 0.1 T.

Figure 4 shows the  $M(\mu_0 H)$  loops of the  $\text{NdCrTiO}_5$  nanoparticles, recorded at 2, 10, 30, 60, 80 K with ZFCW protocol. The curve indicates paramagnetic behavior of the material with increase in temperature. From the curves obtained at 2 and 10 K, the exchange bias ( $H_{\text{ex}}$ ) and coercivity ( $H_c$ ) was evaluated, using following equations,  $H_{\text{ex}} = [H_1 + H_2]/2$ ,  $H_c = [H_1 - H_2]/2$ , respectively, where  $H_1$  and  $H_2$  are the positive and negative crossing of the  $M(\mu_0 H)$  curves on the applied field axis [17, 27-28]. The obtained value of coercivity,  $0.018 \pm 0.001$ ,  $0.019 \pm 0.001$  T and exchange bias,  $-0.004 \pm 0.001$ ,  $-0.003 \pm 0.001$  T, at 2 and 10 K, respectively. The finite values of coercivity indicate the soft ferromagnetic nature of the material [29]. The recorded  $M(\mu_0 H)$  curves indicate the weak FM nature of the material.



**Figure 4.** Magnetization as a function of applied field at 2, 10, 30, 60, 80 K.

Further,  $M(\mu_0 H)$  measurements carried out at 2 K under FCW condition to confirm the exchange bias effect in the material as depicted in Figure 5(a). In Figure 5(b) the zoomed view of the measured curves of both ZFCW and FCW are asymmetric in nature with shifting of hysteresis loop. The ZFCW showing positive exchange bias, whereas FCW condition gives negative exchange bias, that clearly demonstrate the exchange bias effect of the synthesized sample. Deepak et al. [17], demonstrates that the EB obtained in the single phase, La<sub>0.5</sub>Pr<sub>0.5</sub>CrO<sub>3</sub>, is because of the exchange coupling between Pr<sup>3+</sup> and Cr<sup>3+</sup>. EB have been observed in SmCrO<sub>3</sub> due to the interaction between Sm<sup>3+</sup> moment and Cr<sup>3+</sup> moment [27]. Similarly, TmCrO<sub>3</sub> exhibiting EB effect, which obtained due to the interaction of Tm<sup>3+</sup> and Cr<sup>3+</sup> [30]. In one of the earlier report, Hong et al. [31] showing EB in a single-phase NdMnO<sub>3</sub> system due to the coupling between Nd<sup>3+</sup> and Mn<sup>3+</sup>. EB was for the first time observed in YMnO<sub>3</sub> nanoparticles, which is attributed to the exchange coupling between uncompensated spins found on the surface of the nanoparticles [19]. In a recently reported nano DyCrTiO<sub>5</sub> system EB is ascribed to complex magnetic interaction of surface uncompensated spins between each other [14]. Similar to the reported results, in the present case EB is attributed to the surface uncompensated spins and their magnetic interaction.



**Figure 5.** Magnetization as a function of applied field for the NdCrTiO<sub>5</sub> nanoparticles (a) at 2 K ZFCW and FCW, (b) zoomed view of the loops.

#### 4. Conclusions

NdCrTiO<sub>5</sub> nanoparticles were synthesized using a simple sol-gel technique to explore the role of size on structural and magnetic properties. The synthesized NdCrTiO<sub>5</sub> nanoparticles were calcined at 800 °C for three hours. The orthorhombic crystal structure was confirmed from the XRD pattern having lattice parameters,  $a$ ,  $b$ ,  $c$  of  $7.5715 \pm 0.0007$ ,  $8.7270 \pm 0.0008$  and  $5.7916 \pm 0.0006$  Å, respectively. The nanosize ( $33 \pm 1$  nm) of the particles as well as elemental composition of the material was confirmed from the TEM results. Due to nanosize of the material  $T_N$  is not observed from the temperature-dependent magnetization measurement, which was observed in bulk samples. Field dependent magnetization study showed the exchange bias effect which is consequence of uncompensated spins on the surface of the material. These observed anomalous properties might be due to the size effect.

**Acknowledgments:**

Financial aid from the SANRF (Grant No. 120856), as well as the University of Johannesburg (UJ) URC and FRC (Grant Nos. 282810, 083135) is acknowledged. The use of the NEP Cryogenic Physical Properties Measurement System at UJ, obtained with the financial support from the SANRF (Grant No. 88080) and UJ, RSA, is acknowledged. The use of the Spectrum facility in the FoS at UJ is acknowledged.

**References**

- [1] Das M, Roy S, Khan N and Mandal P 2018 *Phys. Rev. B* **98** 104420
- [2] Perzanowski M, Zarzycki A, Gregor-Pawlowski J and, Marszalek M 2020 *ACS Appl. Mater. Interfaces* **12** 39926
- [3] Blachowicz T and Ehrmann A 2021 *Coatings* **11** 122
- [4] Hwang J, Choi ES, Zhou HD, Lu J and Schlottmann P 2012 *Phys. Rev. B.* **85** 024415
- [5] Saha J, Sharma G and Patnaik S 2014 *J. Magn. Magn. Mater.* **360** 34
- [6] Basu T, Adroja DT, Kolb F, von Nidda HA, Ruff A, Hemmida M, Hillier AD, Telling M, Sampathkumaran EV, Loidl A and Krohns S 2017 *Phys. Rev. B* **96** 184431
- [7] Guedes EB, Martins HP, Abbate M, Masunaga SH, Ramirez FE, Jardim RF and Mossaneck RJ 2017 *J. Alloy and Compounds* **724** 67
- [8] Noda Y, Kimura H, Fukunaga M, Kobayashi S, Kagomiya I and Kohn K 2008 *J. Phys.: Condens. Matter.* **20** 434206
- [9] Blake GR, Chapon LC, Radaelli PG, Park S, Hur N, Cheong SW and Rodriguez-Carvajal 2005 *Phys. Rev. B.* **71** 214402
- [10] Balli M, Mansouri S, Jandl S, Fournier P and Dimitrov DZ 2017 *Magnetochemistry* **3** 36
- [11] Basu T, Singh K, Gohil S, Ghosh S and Sampathkumaran EV 2015 *J. Appl. Phys.* **118** 234103
- [12] Greenblatt M, Hornreich RM and Sharon B 1974 *J Solid State Chemistry* **10** 371
- [13] Das M, Roy S, Mahalingam K, Ganesan V and Mandal P 2019 *J. Phys.: Condens. Matter.* **32** 035802
- [14] Bharati B, Mohanty P, Sheppard CJ and Prinsloo AR 2022 *J. Magn. Magn. Mater.* **546** 168862.
- [15] Bharati B, Mohanty P, Sheppard CJ and Prinsloo AR 2022 *AIP Advances* **12** 035245
- [16] Morales R, Basaran AC, Villegas JE, Navas D, Soriano N, Mora B, Redondo C, Batlle X and Schuller IK 2015 *Phys. Rev. Lett.* **114** 097202
- [17] Deepak, Kumar A and Yusuf SM 2020 *J. Appl. Phys.* **127** 213903
- [18] Tang YK, Sun Y and Cheng ZH 2006 *Phys. Rev. B* **73** 174419
- [19] Zheng HW, Liu YF, Zhang WY, Liu SJ, Zhang HR and Wang KF 2010 *J. Appl. Phys.* **107** 053901
- [20] Bharati B, Sonkar AK, Singh N, Dash D and Rath C 2017 *Mater. Res. Express* **4** 085503
- [21] Bharati B, Mishra NC, Sinha AS and Rath C 2020 *Mater. Res. Bulletin* **123** 110710
- [22] Bharati B, Mishra NC, Kanjilal D and Rath C 2018 *Applied Surface Science* **428** 723
- [23] Mohanty P, Singh VP, Mishra NC, Ojha S, Kanjilal D and Rath C 2014 *J. Phys. D: Appl. Phys.* **47** 315001
- [24] Rodríguez-Carvajal J 1993 *Physica B: Condensed Matter.* **192** 55
- [25] Sen S, Halder SK and Gupta SS 1973 *J. Phys. D: Appl. Phys.* **6** 1978
- [26] Kumar L, Kumar P, Narayan A and Kar M 2013 *International Nano Letters* **83** 8
- [27] Huang S, Zerihun G, Tian Z, Yuan S, Gong G, Yin C and Wang L 2014 *Ceramics International* **40** 13937
- [28] Wang L, Rao GH, Zhang X, Zhang LL, Wang SW and Yao QR 2016 *Ceramics International* **42** 10171
- [29] Miao XF, Mitsui Y, Dugulan AI, Caron L, Thang NV, Manuel P, Koyama K, Takahashi K, Van Dijk NH and Brück E 2016 *Phys. Rev. B.* **94** 094426
- [30] Lakhani A, Dash S, Banerjee A, Chaddah P, Chen X and Ramanujan RV 2011 *Applied Physics Letters* Dec 12;99(24):242503.
- [31] Hong F, Cheng Z, Wang J, Wang X and S. Dou 2012 *Appl. Phys. Letter* **101** 102411

# Effects of deposition temperature on the properties of CdTe thin films prepared by electrodeposition method for solar energy applications

AU. Yimamu<sup>1,2</sup>, BF. Dejene<sup>3</sup>, JJ. Terblans<sup>1</sup>, HC. Swart<sup>1</sup> and SJ. Motlounj<sup>1</sup>

<sup>1</sup> Department of Physics, University of the Free State, P.O. Box 339, Bloemfontein/QwaQwa campus, 9300, South Africa

<sup>2</sup> Department of Physics, Adama Science and Technology University, Adama, Ethiopia

<sup>3</sup> Department of Physics, Walter Sisulu University (Mthatha), Mthatha, South Africa

E-mail: [ahemed.dilla2010@gmail.com](mailto:ahemed.dilla2010@gmail.com), [tlousj@gmail.com](mailto:tlousj@gmail.com)

**Abstract.** Cadmium telluride (CdTe) thin films were synthesized using a low-cost two electrode electrodeposition method in an acidic aqueous solution. The solution contained 1.M of cadmium acetate dihydrate ( $\text{Cd}(\text{CH}_3\text{OO})_2 \cdot 2\text{H}_2\text{O}$ ) as Cd precursor and 1 ml of tellurium dioxide ( $\text{TeO}_2$ ) as Te precursor. The thin films were deposited on a coated glass fluorin doped tin oxide (FTO) substrates. During deposition the solution temperature was varied at 50, 60, 70, and 85 °C. The structure and phase purity, optical properties, surface morphology and elemental composition of the films were investigated by X-ray diffraction (XRD), ultraviolet-visible (UV-Vis) spectrophotometry, scanning electron microscopy (SEM), and energy-dispersive X-ray spectroscopy (EDS). The XRD results showed that the CdTe thin films have a polycrystalline cubic zinc blend and a hexagonal structure. The results confirmed that the preferential orientation (111) XRD peak intensity increased with the deposition temperature and the crystallite size also increased from 20 to 29 nm. UV-Vis spectroscopy measurements indicated that the optical band gap decreased with an increase in deposition temperature. The SEM images showed that the surface morphology changed with an increase in deposition temperature. EDS confirmed the presence of all the elements in the desired compound and its analysis showed that the composition of Cd and Te varies with temperature.

## 1. Introduction

Semiconductor materials play an important role in energy conversion processes. In particular, chalcogenide group (II-IV) compound semiconductor are used for solar cell applications [1]. Cadmium telluride (CdTe) thin film is one of the best known absorber layer owing to its novel physical and chemical properties, such as a high absorption coefficient, direct band gap, and energy band gap, which is near the ideal energy band gap of the absorber material, environmental stability, variable conductivity and growth by low cost method. Due to these, CdTe is used for different applications such as imaging detectors [2], LEDs [3], and solar cells [4]. Different physical and chemical growth techniques are used for the deposition of CdTe thin films. Each deposition technique has its advantages and disadvantages. The two-electrode electrodeposition method is selected because of its advantages such as scalability, manufacturability, self-purification, low cost, waste reduction, simplicity and production of both *n*- and *p*-type conductivity by varying the deposition voltage [5].

CdTe thin films have been deposited by electrodeposition method from different cadmium precursors, such as  $\text{Cd}(\text{NO}_3)_2$  [6],  $\text{CdSO}_4$  [7], and  $\text{CdCl}_2$  [8] as reported by different research groups, and the results showed that the quality and properties of the film varied with the precursor. The quality of the CdTe thin film depends on the deposition parameters, such as the deposition time period, concentration of ions in the electrolyte bath, pH of the electrolytic solution, stirring rate, growth voltage and electrolysis bath temperature. Optimization of these parameters on CdTe thin films allows growth for desired applications [9].

It is known that the properties of the absorber layer depend on its thickness. The thickness of the film in the electron deposition method depends on various growth parameters such as current density,

the temperature of the solution, the concentration of Te in the solution, pH of the solution, and the cleaning process of the FTO glass substrate before preparation. The objective of the present work is to optimize growth temperature to synthesize the CdTe thin films by electrodeposition while keeping other growth parameters unchanged in order to understand the growth temperature effects from a cadmium acetate precursor. The growth temperature affects the rate of CdTe thin film growth and is mostly dependent on the rate of release of  $\text{Cd}^{2+}$  and  $\text{Te}^{2+}$  ions from the complex state which condenses on an ion-by-ion basis on the substrate. This in turn determines the thickness of the CdTe thin film.

When the temperature increases, the motion of the ions in the electrolyte bath increases and the solubility of the solvents increases [10]. When the current density is high the deposition rate increases, and the crystallinity of the film increases. Therefore, it is important to study the effect of deposition temperature in detail.

There are reports about electrodeposition of CdTe thin films using Cd sources such as cadmium chloride, cadmium nitrate and cadmium sulphate in the literature. However, there are very scarce, if any, literature about two-electrode electrodeposition of CdTe thin films using cadmium acetate as a precursor. Moreover, the reports about electrodeposition of CdTe thin films using two-electrode method are limited in the literature since most researchers report on the three electrode electrodeposition method. The main aim of this study was to investigate the effect of the deposition temperature on the properties of CdTe thin films grown by two electrode electrodeposition method for possible application in photovoltaic industry. The two electrode is adopted in this work to reduce the cost of production of these films.

## 2. Materials and Method

Electrochemical deposition of CdTe thin films was performed using an electrolyte solution containing 1.0 M cadmium acetate dihydrate [ $\text{Cd}(\text{CH}_3\text{COO})_2 \cdot 2\text{H}_2\text{O}$ ], with 98% purity, as the cadmium precursor and 1 ml tellurium dioxide  $\text{TeO}_2$  with 99% purity as the tellurium precursor. Both chemicals were laboratory reagent grade  $\text{Cd}(\text{CH}_3\text{COO})_2 \cdot 2\text{H}_2\text{O}$  purchased from Emsure, Germany and  $\text{TeO}_2$  purchased from Sigma Aldrich and used as the electrolyte solution. Prior to electrodeposition takes place the four glass substrates/FTO were cut into small size 2.5 x 2.5cm and washed ultrasonically in laboratory soap solution in deionized (DI) water for 30 min. Finally, the substrates were washed with ethanol, acetone and methanol, respectively and rinsed with deionized water between washing and drying in air.

The deposition voltage was adjusted to 1250 mV and, the pH of the electrolyte was  $2.00 \pm 0.02$  using either dilute HCl or ammonium hydroxide ( $\text{NH}_4\text{OH}$ ) at room temperature. The temperature of the electrolyte solution bath was adjusted to 50, 60, 70, 85°C with moderate stirring during the deposition using a magnetic stirrer. The source of the electrolyte solution as electrical power used for the 2-electrode system was a computerized Gill AC potentiostat (ACM Instruments, United Kingdom). Insulating polytetrafluoroethylene (PTFE) was used to attach the glass/FTO substrate to a high purity graphite rod, which served as the working electrode (cathode). Before CdTe thin film deposition, the cadmium acetate solution in 400 ml was electro purified for 48 h with a deposition voltage less than the Cd element deposited, which was determined by cyclic voltammetry. Te containing solution was prepared by dissolving 2g of  $\text{TeO}_2$  in 30 ml diluted HCl solution and stirred for 2 h since  $\text{TeO}_2$  is insoluble in water and soluble in acidic media. 1 ml of the  $\text{TeO}_2$  solution was added to the Cd containing solution and stirred for 300 min to maintain uniformity in the solution.

## 3. Results and discussion

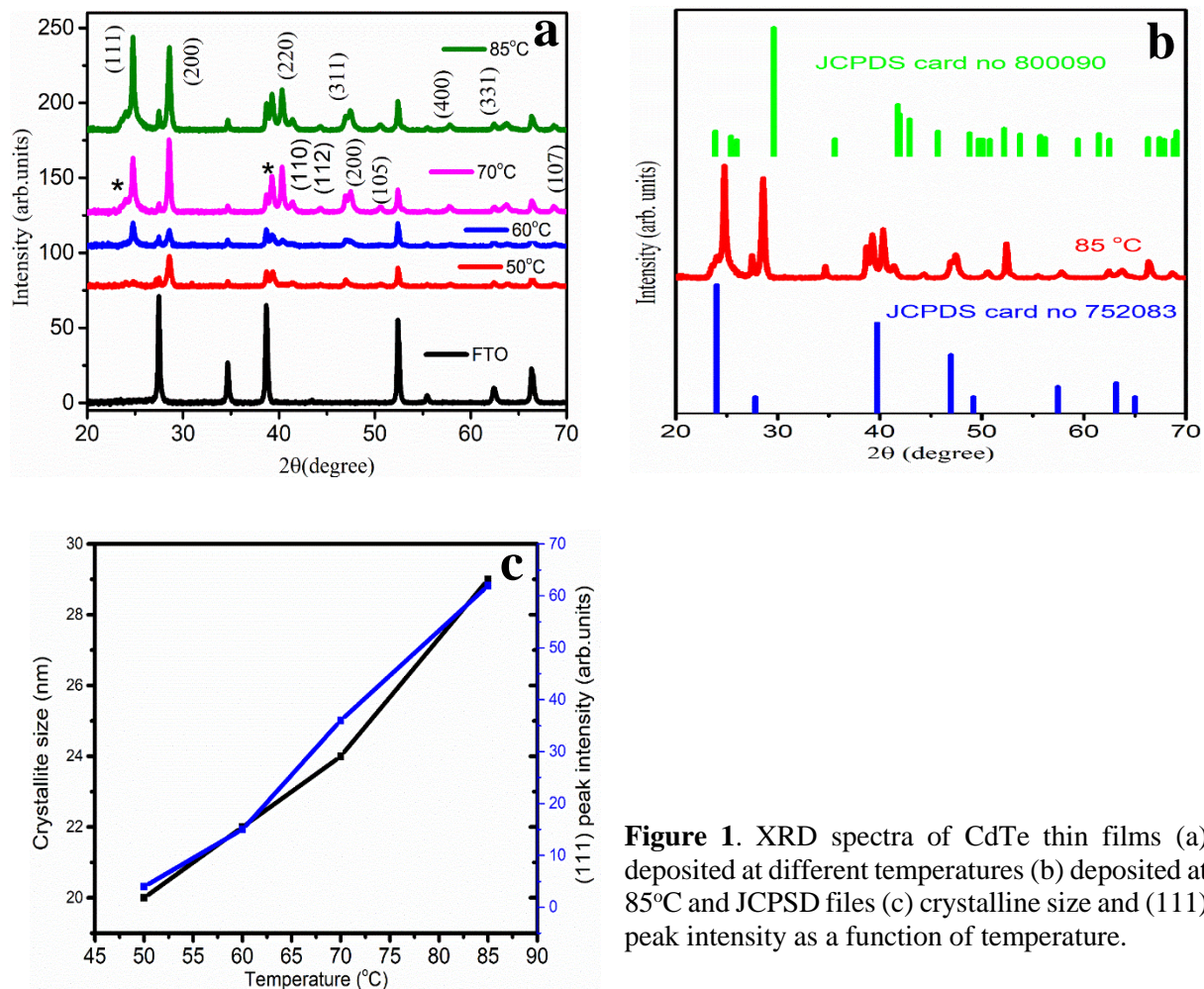
### 3.1 Structural properties

The structural properties of the CdTe thin films were investigated using a Bruker D8 Advance X-ray diffractometer (XRD) measurement with a monochromatic wavelength of 1.5416 Å. The X-ray generator voltage and current were maintained at 40 kV and 40 mA, respectively. The XRD measurements were carried out by setting the incident angle from 20 to 70° to identify the degree of crystallinity and the crystal structure of the CdTe layers grown on the glass/FTO. Figure 1 (a) shows the XRD spectra of CdTe thin films grown by the electrodeposition method. Overall, it was observed that

the prepared CdTe thin films had both cubic and hexagonal polycrystalline structures. Figure 1(b) shows that the results agree with the JCPDS data 752083 for a cubic zinc blend structure and 800090 for the hexagonal structure. The peak (111) is located at an angle of 24.7 and the other peaks at 28.23, 40.32, 47.3, 57.76 and 63.7 with phase of (200), (220), (311), (400) and (331), respectively. The hexagonal structure having 41.3, 44.6 and 68.8 with (110) and (112) and (107) respectively. Therefore, CdTe was found in a mixed polycrystalline phase which is in agreement with other reported results. The peaks labelled \* are  $Cd_xTeO_y$  related [8]. The crystallite size can be calculated using the Scherrer formula, as shown in equation 1 [6].

$$D = \frac{0.9\lambda}{\beta \cos\theta}, \quad (1)$$

where the parameter  $D$  is the crystallite size,  $\beta$  is the full width at half maximum (FWHM) in radian,  $\lambda$  is the wavelength of the X-rays (0.15406 nm for Cu  $K\alpha$ ), and  $\theta$  is the Bragg's diffraction angle in degree.



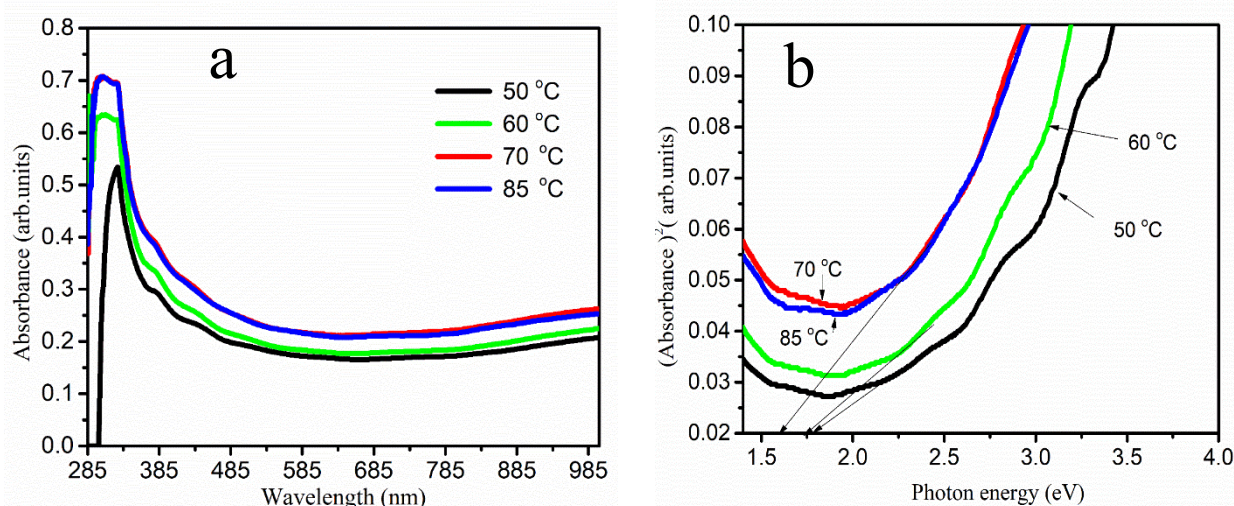
**Figure 1.** XRD spectra of CdTe thin films (a) deposited at different temperatures (b) deposited at 85°C and JCPDS files (c) crystalline size and (111) peak intensity as a function of temperature.

Figure 1(c) shows the graph of (111) peak intensity and crystallite size as a function of deposition temperature. It is clearly observed that the intensity of (111) peak increases with an increase in the deposition temperature from 50 to 85 °C, while the crystallite size increased from 20 to 29 nm. It was observed that the maximum crystallite size was obtained when the deposition temperature was 85°C. During electrodeposition in aqueous solution, deposition temperatures are restricted to 90°C due to the

boiling point of water of 100°C. If the deposition temperature is increased to near or above 100°C, water will evaporate.

### 3.2 Optical properties

Optical absorption measurements of the CdTe layers were carried out using a Carry 50 Scan using ultraviolet- visible (UV-VIS) spectroscopy to estimate the band gap of the films. Figure 2 (a) shows the absorbance as a function of wavelength. The results show that the absorbance ( $A$ ) increased with an increase in the deposition temperature. The maximum absorbance was recorded for the sample that was deposited at the temperature of 85 °C. Figure 2 (b) shows the absorbance square as a function of photon energy ( $h\nu$ ). The band gap energies were calculated by plotting the absorbance square as a function of  $h\nu$  and using the extrapolation of the ( $A^2 = 0$ ) tangent line through  $h\nu$  axis. From the results, the energy band gaps were 1.83, 1.75, 1.62 and 1.62 eV for deposition temperatures of 50, 60, 70, and 85 °C respectively. When the deposition temperature was 50 °C the energy band gap was 1.83 eV which indicates that the CdTe thin film contained more Te and pinholes since Te have positive redox potential compared to Cd that is why it was deposited at low deposition voltage and at low temperature. Due to this reason Te is active in the solution and it is deposited first on the substrate. At low temperatures the thin film is Te rich, meaning there is excess of Te and less Cd elements in the CdTe thin film [11]. When the temperature was increased the band gap decreased and when the deposition temperature was 85 °C the band gap became 1.62 eV. The band gap energy varied with the deposition temperature.



**Figure 2.** CdTe a) absorbance as a function of wavelength (nm) and b)  $A^2$  a function of energy (eV)

### 3.3 Morphological property

SEM images were obtained to study the surface morphology, grain size and uniform coverage of the substrate by the film. The results confirmed that the glass (FTO) was covered by the CdTe thin film and as shown in figure 3 (a), at a low temperature of 50 °C the grain sizes were small and not uniform. As the deposition temperature increases to 85°C (figure 3 (b)) there is an increase in grain size. In both cases, it can be observed that the particles are agglomerated and composed of various shapes, including irregular, spherical and rods like structures with different lengths and sizes. CdTe thin film with larger grain size, uniform surface morphology was observed when the sample was deposited at a temperature of 85 °C and this is in good agreement with the XRD results. The thickness of the thin film increased from 1.5 $\mu\text{m}$  to 3.2  $\mu\text{m}$  as the deposition temperature was increased from 50 to 85 °C. The insert in figure 3(b) shows the SEM image of the sample prepared at 60°C.

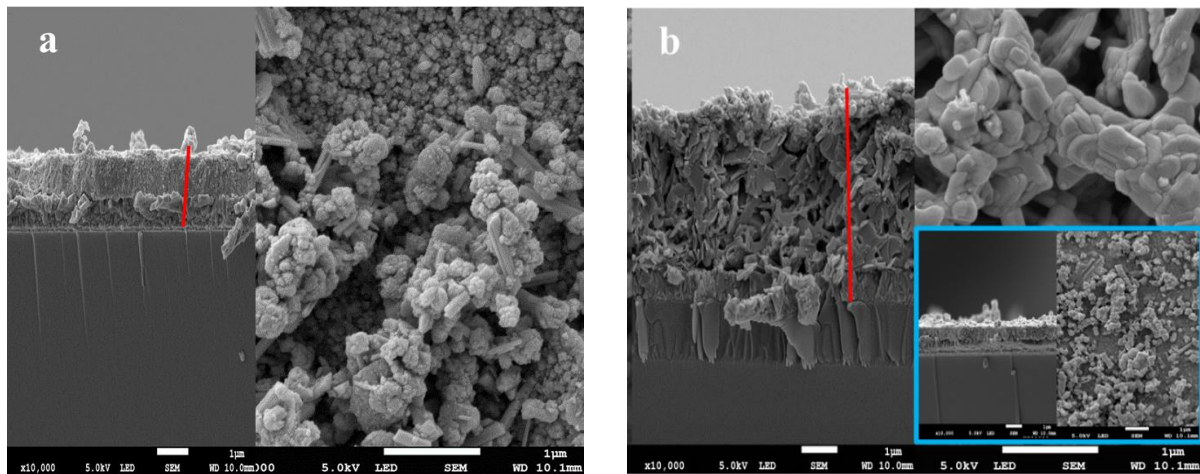


**Figure 3.** SEM images of CdTe thin films as deposited at (a) 50 °C, and (b) 85 °C

### 3.4 Compositional properties

EDS measurements were used to investigate the elemental composition of CdTe thin films grown at different deposition temperatures.

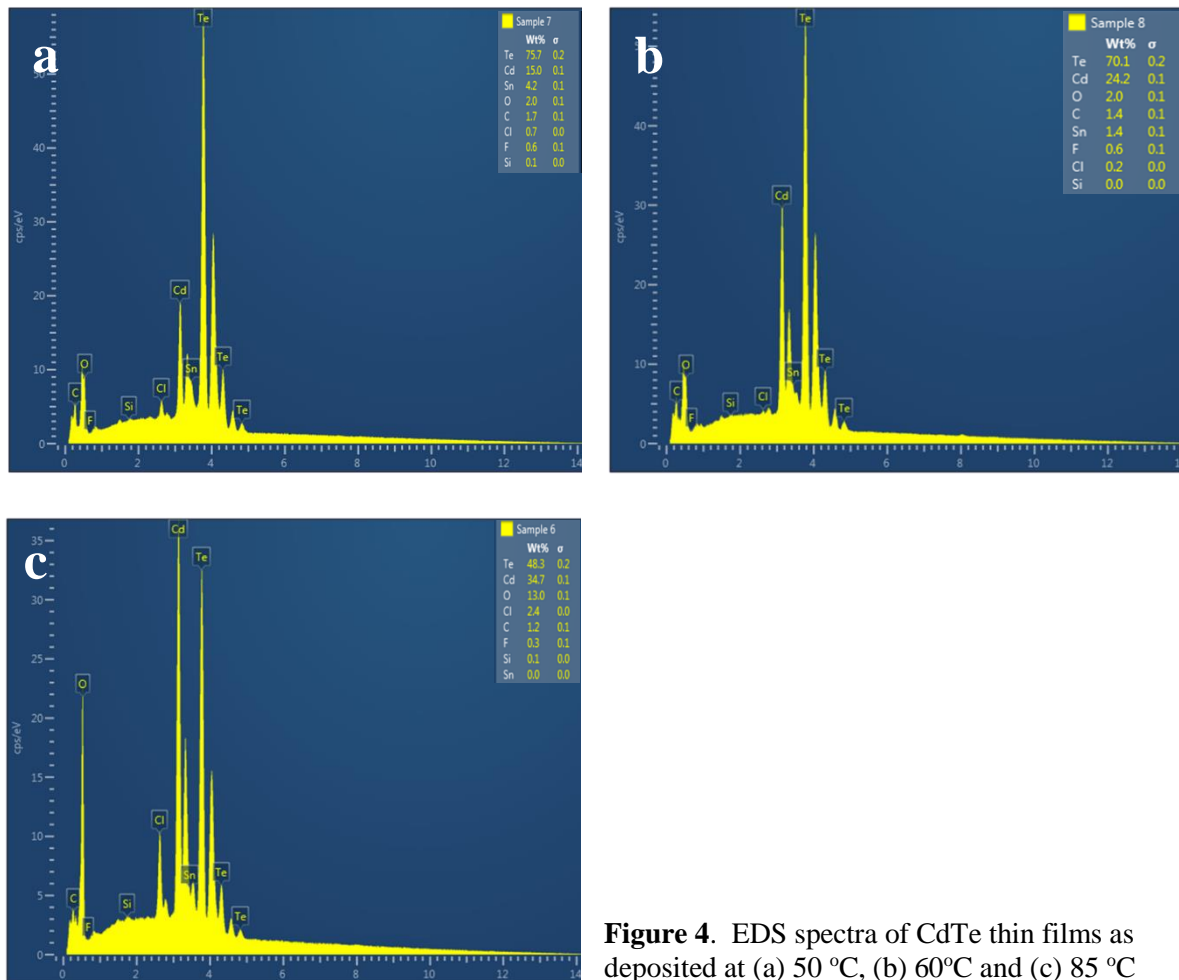


**Figure 4.** EDS spectra of CdTe thin films as deposited at (a) 50 °C, (b) 60°C and (c) 85 °C

The results showed that for the required compound (i.e., CdTe) both Cd and Te were present as shown in figure 4. It is observed from the results that Cd increases with an increase in deposition temperature. In contrast, Te decreases with an increase in temperature. The calculated atomic percentage of Te was found to be 81.6, 78.0 and 55.0 while that of Cd was 18.4, 22.0 and 45.0 for the deposition temperatures of 50, 60 and 85 °C. Generally, acidic media remove Cd, and the film becomes Te rich while basic media remove Te and the film becomes Cd rich. It can be observed that the concentration of Te is greater than that of Cd for all the samples. To get equal amounts of Cd and Te, usually, post deposition treatment like dipping the film into CdCl<sub>2</sub> solution, drying it in air, and annealing at 400°C for 15 min is required [12]. However, this is not the purpose of our current study, and the samples were used as prepared without post deposition treatment. For this work, the better composition of CdTe thin film was obtained when the deposition temperature was 85 °C which is in good agreement with other previous report [13].

#### 4. Conclusion

CdTe thin films were successfully grown by the electrodeposition method using a cadmium acetate and tellurium dioxide as Cd and Te sources, respectively. The thin films were deposited at different temperatures. The XRD results indicated that the crystallinity of the films and the crystal sizes increased as the temperature increased. Furthermore, CdTe thin films were found to be polycrystalline in both cubic and hexagonal structure. The UV-VIS measurements indicated that the energy band gap decreased as the temperature increased. The SEM results showed that the morphology of the thin films improved as the temperature was increased. The EDS results revealed that as the temperature increased the concentration of Cd increased while that of Te decreased. Further analysis confirmed that the quality of the films increased with temperature. When the film was deposited at 85°C, the atomic percentage of Cd and Te are 45 and 55 respectively. Therefore, it is important to study the effect of temperature for thin film growth for the desired applications.

#### Acknowledgments

The authors gratefully thank the NRF, the Research Fund of the University of the Free State and the Department of Science and Technology (DST) of South Africa. This work is based on the research supported by the South African Research Chairs Initiative of the Department of Science and Technology and the National Research Foundation of South Africa.

#### References

- [1] I. M. Dharmad, 2011, *9th Photovolt. Sci. Appl. Technol. Conf. C95*.
- [2] A. M. D. Ede, E. J. Morton, and P. Deantonis, 2001, *Nucl. Instruments Methods Phys. Res. Sect. A Accel. Spectrometers, Detect. Assoc. Equip.*, vol. **458**, no. 1, 7.
- [3] Nagaura, T., Phan, H., Malgras, V., Pham, T., Lim, H., Ashok, A., Kim, J., You, J., Nguyen, N., Na, J., Yamauchi, Y., 2021. *Angew. Chemie* **133**, 9746.
- [4] O. K. Echendu, K. B. Okeoma, C. I. Oriaku, and I. M. Dharmadasa 2016, *Adv.Mater.Sci.Eng.* vol. **2016**,10.
- [5] I. M. Dharmadasa and J. Haigh, 2006, *J. Electrochem. Soc.*, vol. **153**, no. 1, G47.
- [6] A. A. Ojo, I. M. Dharmadasa, E. Materials, and S. Group, 2019. April, 1.
- [7] A. E. Alam, O. I. Olusola, D. A. L. Loch, K. Shukla, W. M. Cranton, and I. M. Dharmadasa, 2020, *Sci. Rep.*, no. **0123456789**, 1.
- [8] H. I. Salim, V. Patel, A. Abbas, J. M. Walls, and I. M. Dharmadasa, 2015, *J. Mater. Sci. Mater. Electron.*, vol. **26**, no. 5, 3119.
- [9] S. Saha, M. Johnson, F. Altayaran, Y. Wang, D. Wang, and Q. Zhang, 2020, *Electrochem*, vol. **1**, 286.
- [10] M. Soliman, A. B. Kashyout, M. Shabana, and M. Elgamal, 2001, *Renew. Energy*, vol. **23**, no. 3, 471.
- [11] Dharmadasa, I.M., Echendu, O.K., Fauzi, F.B., Abdul-manaf, N.A., 2015, *J. Mater. Sci. Mater. Electron.*, vol. **26**, no. 7, 4571.
- [12] Dharmadasa, I.M., Echendu, O.K., Fauzi, F., Abdul-Manaf, N.A., Olusola, O.I., Salim, H.I., Madugu, M.L., Ojo, A.A., 2017. *J. Mater. Sci. Mater. Electron.* **28**, 2343.
- [13] A. A. Ojo and I. M. Dharmadasa, 2019, *Coatings*, vol. **9**, no. 6, 1.

# Structural stability of Cubic Ti<sub>2</sub>AlV and Tetragonal TiAl<sub>2</sub>V using First Principle Calculations

DM Tshwane<sup>1,2\*</sup> and R Modiba<sup>1</sup>

<sup>1</sup>Future Production: Manufacturing, Advanced Materials Engineering, CSIR, PO Box 395, Pretoria, 0001, South Africa

<sup>2</sup>National Institute for Theoretical and Computational Sciences (NITheCS), Gauteng 2000, South Africa

E-mail: DTshwane@csir.co.za

**Abstract.** TiAlV intermetallic alloys are used as key functional materials in various industries due to their superior properties. However, our understanding of their structural phase stabilities is still limited and remains confined. In this work density functional theory approach was employed to investigate the structural and electronic stability of cubic Ti<sub>2</sub>AlV and tetragonal TiAl<sub>2</sub>V phases. The stabilities of these structures were determined by calculating the heats of formation and electronic properties. The calculated heats of formation values revealed that both phases are thermodynamically stable since  $\Delta H_f < 0$ . Moreover, it was found that the TiAl<sub>2</sub>V structure is energetically more stable than Ti<sub>2</sub>AlV. Also, the partial density of states was studied to investigate the electronic properties.

## 1. Introduction

Ti-Al-V-based alloys are widely employed in biomedical, aerospace, automotive, space, and other important industries. This is due to their low density, high strength, and good corrosion resistance requirements [1, 2]. Many investigations have shown that heat treatment would promote microstructures of Ti-Al-V alloys, allowing for superior mechanical properties. A better understanding of the structure and morphology of precipitates can further improve the strength of alloys [3]. These alloys are available in binary AB and ternary A<sub>2</sub>BC stoichiometric compositions. Deviations from the stoichiometric composition are accommodated by vacancies on the various sublattice sites and/or antisites [4].

The effect of structural qualities, however, varies. As a result, it is vital to investigate the intrinsic properties of each phase as well as their impact. Banerjee *et al.* [5] investigated the chemical compositions and microstructures measured across the Ti<sub>8</sub>Al<sub>x</sub>V grade. They reported that the volume fraction of the alpha phase decreased with an increase in the V content, and the volume fraction of the beta phase increased. Furthermore, the microstructure and mechanical properties of Ti-Al-V powder have been investigated. It has been reported that the microstructure of equiaxed to columnar grains varies. Moreover, as the mass content of Al increases, the beta grain size decreases [6].

First principle calculation was used to study the site occupancy of the B2 phase in Ti<sub>2</sub>AlX (X= V, Cr, Fe, Mo, Ta, Nb, Zr, Hf and Re) intermetallic [7]. According to their findings, all the alloys were found to be thermodynamically stable, and the formation energy results indicated that the B2 phase is the most stable. Wan *et al.* [8] studied the structural and electronic properties of second phases and solid solutions in Ti-xAl-yV alloys using First principle approach. The formation enthalpy for the alpha and beta phases was found to be -0.295 and 62.786 eV. atom<sup>-1</sup>, respectively. Therefore, it was stated that the alpha phase has greater structural and formation stability than the beta phase due to its lower formation

enthalpy. This indicated that the Ti-Al-V  $\alpha$  phase has the strongest alloying ability and structural stability. The structural phase is one of the most important measures for controlling the properties of a material and causing a significant change in performance. As a result, it is necessary to investigate the properties of various phases.

In the present study, the structural and electronic properties of the cubic ( $\text{Ti}_2\text{AlV}$ ) and tetragonal ( $\text{TiAl}_2\text{V}$ ) crystals were investigated using density functional theory calculations. To characterize the structures, the heats of formation and electronic properties of the two phases were calculated. The current findings will provide theoretical insight into the thermodynamic comparison of the  $\text{Ti}_2\text{AlV}$  and  $\text{TiAl}_2\text{V}$  compositions.

## 2. Computational Setup

Cambridge Series Total Energy Package (CASTEP) code [9], as implemented in Material Studio software, was used for all density functional theory calculations [10, 11]. To calculate the geometry optimization, a generalized gradient approximation with the Perdew-Burke-Ernzerhof (PBE) exchange-correction functional was used [12]. Geometry optimization calculations were employed using the Broyden-Fletcher-Goldfarb-Shanno (BFGS) algorithm. The Monkhorst-Pack scheme [13] was used to integrate the k-points. Cut-off energy was set to 600 eV with k-points of  $6 \times 6 \times 6$  and  $6 \times 6 \times 5$  for both cubic and tetragonal structures. The maximum force tolerance and displacement were set at 0.03 eV and  $10^{-3}$ , eV. atom<sup>-1</sup>, respectively. Heats of formation ( $\Delta H_f$ ) of  $\text{TiAl}_2\text{V}$  and  $\text{Ti}_2\text{AlV}$  structures were calculated as follows:

$$\Delta H_f = E_{\text{tot}} - \sum_i n_i E_i \quad (1)$$

whereby,  $E_{\text{tot}}$  and  $E_i$  are the total energies of crystal structures ( $\text{Ti}_2\text{AlV}$  and  $\text{TiAl}_2\text{V}$ ) and individual atoms (Ti, Al and V). The  $n_i$  represents the number of an atomic configuration of the element.

## 3. Results and Discussion

### 3.1. Crystal structures and Heats of formation

The intermetallic alloy of  $\text{TiAlV}$  mostly consists of two crystal structures which are face-centred tetragonal (L10) and face-centred cubic. It is noted that the face-centred tetragonal is an Al-rich crystal with chemical formula  $\text{TiAl}_2\text{V}$  and cubic structure is defined as Ti-rich phase  $\text{Ti}_2\text{AlV}$ , crystallizes in P4/mmm and F-43M space group, respectively. Figure 1 illustrate the atomic crystal structures of these phases,  $\text{TiAl}_2\text{V}$  and  $\text{Ti}_2\text{AlV}$ . The bulk properties of these two crystals were calculated and the results are presented in Table 1. The equilibrium lattice parameter of  $\text{Ti}_2\text{AlV}$  is  $a = 6.337 \text{ \AA}$  and  $\text{TiAl}_2\text{V}$   $a = 5.469 \text{ \AA}$  and  $c/a = 1.45 \text{ \AA}$ . The obtained parameter for  $\text{Ti}_2\text{AlV}$  is in good agreement with the value previous results [14]. If the  $c/a$  ratio is 1/2, the pseudo-cubic tetragonal phase is formed, as referred to in the literature [15]. The equivalent  $c/a$  ratio value of 1.45 was obtained in the current study.

Structural stability of  $\text{TiAl}_2\text{V}$  and  $\text{Ti}_2\text{AlV}$  were analyzed using heats of formation ( $\Delta H_f$ ), which is defined as the energy required to form the phase crystal from single atoms. A lower formation energy of the crystal structure implies more structural stability. Heats of formation per atom for the two phases were calculated using Eqn. 1 and the results are shown in Table 1. The calculated  $\Delta H_f$  of  $\text{Ti}_2\text{AlV}$  and  $\text{TiAl}_2\text{V}$  structure is  $-0.121 \text{ eV. atom}^{-1}$  and  $-0.412 \text{ eV. atom}^{-1}$ , respectively. A negative  $\Delta H_f$  value for both structures indicates the possibility of these two phases forming spontaneously, implying thermodynamic stability. Our current findings on heats of formation value for  $\text{Ti}_2\text{AlV}$  structure agree well with the previously reported values ( $-0.112 \text{ eV. atom}^{-1}$ ) [7]. However, the  $\text{TiAl}_2\text{V}$  structure was found to have the lowest  $\Delta H_f$ , indicating that the tetragonal phase shows higher structural stability than cubic. As a result, it is possible to deduce that  $\text{TiAl}_2\text{V}$  crystal has stronger stability and forming capacity than  $\text{Ti}_2\text{AlV}$ . This is in line with the fact that the alpha phase of Ti-Al-V solid solution has a greater capacity to form than the beta phase [8].

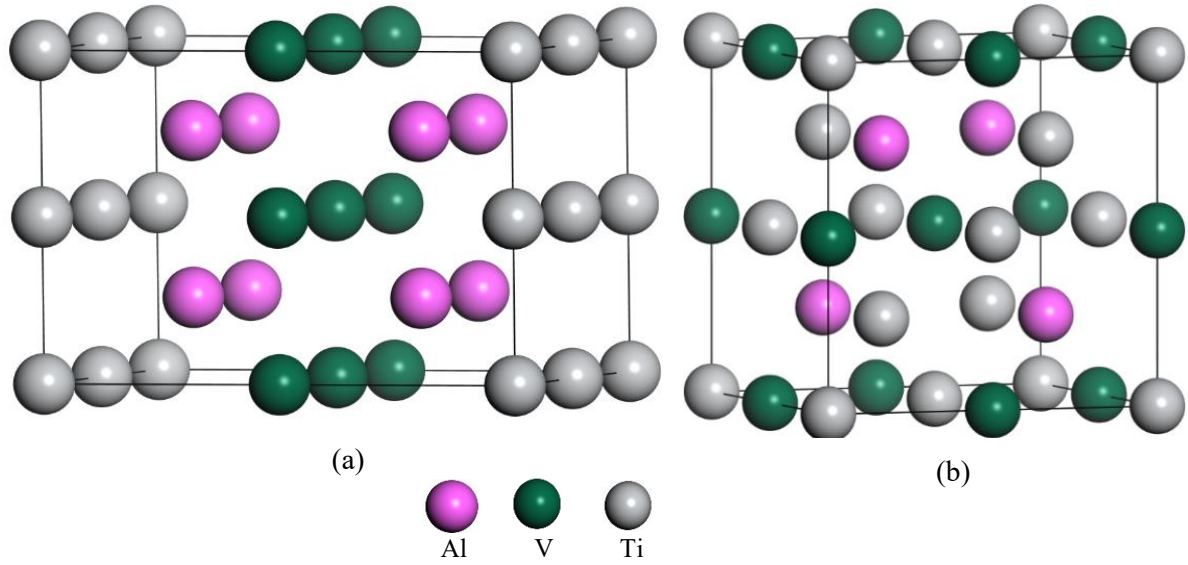


**Figure 1.** Optimized crystal structure of (a) tetragonal ( $t\text{-TiAl}_2\text{V}$ ) and (b) cubic ( $c\text{-Ti}_2\text{AlV}$ ) phase.

**Table 1.** The calculated heats of formation ( $\Delta H_f$ ), present and previous lattice parameters for cubic and tetragonal structures.

structures	methods	$a$ ( $\text{\AA}$ )	$c/a$	$V(\text{\AA}^3)$	$\Delta H_f$ (eV. atom $^{-1}$ )
$c\text{-Ti}_2\text{AlV}$	present	6.337	-	254.4	-0.121
	previous	6.337 [14]	-	-	-0.112 [7]
$t\text{-TiAl}_2\text{V}$	present	5.469	1.45	244.2	-0.412

### 3.2. Density of states

To further understand the electronic properties and interaction for both cubic and tetragonal structures, partial and total density of states (PDOS) are investigated. PDOS and TDOS curves are presented in Figure 2 and Figure 3, respectively. This DOS plot highlights the contribution of different atoms and orbitals. We noted that all in all structures, the main peak at the Fermi level is most contributed from the  $-d$  orbital from the 3d orbital of Ti and V atoms, while less contribution was noted from the  $-p$  orbital. This observation indicated that both structures have metallic behaviour. Moreover, the conductive region/side mostly consists of 3d (Ti and V) hybridize with the  $-2p$  Al atom. This shows the bonding character displayed by Ti-Al, Ti-V and Al-V from the hybridization between the lone pair in the  $-2p$  and  $-3d$  individual atoms. Both DOSs of these compounds display a deep pseudo-gap right above the Fermi level, this is due to a strong covalent interaction between the atoms. In addition, Figure 3 presents the TDOS curves for the two compounds, it was observed that the TDOS curve for  $\text{TiAl}_2\text{V}$  lies lower at the Fermi level ( $E_F$ ) whereas the  $E_F$  for  $\text{Ti}_2\text{AlV}$  is higher on the TDOS curve. This suggests that the FCT  $\text{TiAl}_2\text{V}$  crystal is more stable than the FCC  $\text{Ti}_2\text{AlV}$  crystal which supports the stability trend observed in the heats of formation values. The cubic system's Fermi level is typically located in the middle of the DOS peak. The high TDOS near  $E_F$ , on the other hand, causes high energy, which leads to poor structural stability in the cubic state [16].

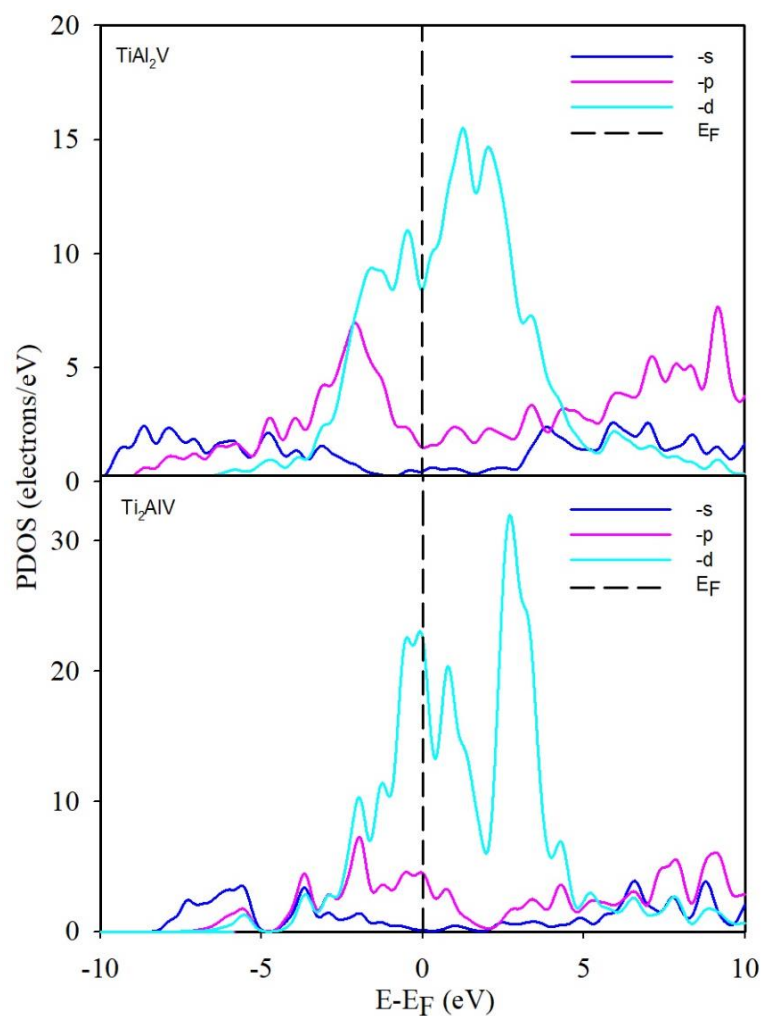


**Figure 2.** Partial density of states (PDOS) calculated for tetragonal ( $\text{TiAl}_2\text{V}$ ) and cubic ( $\text{Ti}_2\text{AlV}$ ) structures.

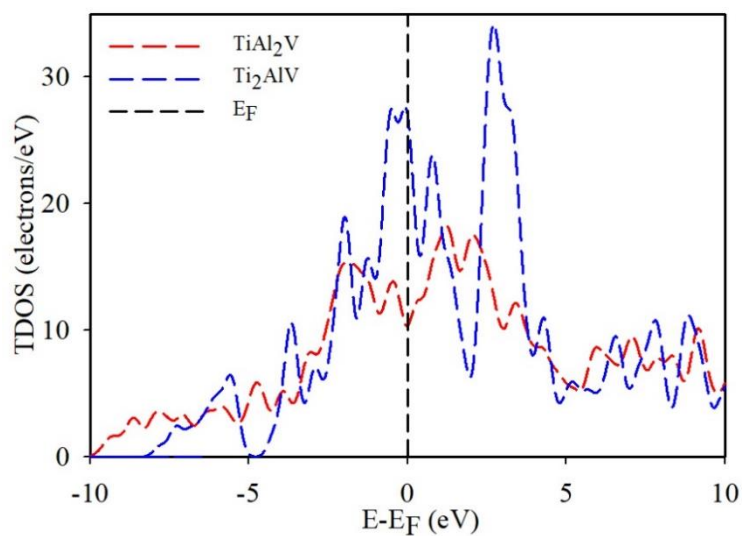


**Figure 3.** Total density of states (TDOS) plot for cubic ( $\text{Ti}_2\text{AlV}$ ) and tetragonal ( $\text{TiAl}_2\text{V}$ ) structures.

#### 4. Conclusion

In summary, density functional theory calculations were successfully utilized to investigate the structural stability of  $Ti_2AlV$  and  $TiAl_2V$  compounds. Both structures were discovered to be thermodynamically stable, having negative values for heats of formation. The calculated heats of formation values indicated that  $TiAl_2V$  had a strongest structural stability than  $Ti_2AlV$ . According to electronic calculation, it was observed that the TDOS curve for  $TiAl_2V$  lies lower at the Fermi level than the  $Ti_2AlV$  compound. This implies that the tetragonal phase ( $TiAl_2V$ ) is structurally more stable than the cubic phase ( $Ti_2AlV$ ).

#### Acknowledgement

The authors acknowledge the Department of Science and Innovation (DSI) and Council for Scientific and Industrial Research for financial support. Center for High-Performance Computing for computing resources.

#### Reference

- [1] Boyer R R 2010 *J. Miner. Met. Mater. Soc.* **62** 21-24
- [2] Hou Y P, Guo S, Qiao X L, Tian T, Meng Q K, Cheng X N and Zhao X Q 2016 *J. Mech. Behav. Biomed. Mater.* **59** 220-225
- [3] Bolz S, Oehring M, Lindemann J, Pyczak F, Paul J, Stark A, Lippmann T, Schrüfer S, Roth-Fagaraseanu D and Schreyer A 2015 *Intermetallics* **58** 71-83
- [4] Bradley A J and Taylor A 1973 *Proc. R. Soc. Lond. A.* **159** 56
- [5] Banerjee R, Bhattacharyya D, Viswanathan G B and Fraser H L 2004, *Acta Mater.* **52** 377-385
- [6] Tan H, Zhang F, Chen J, Lin X and Huang W 2011 *Chinese. Opt. Lett.* **9** 051403
- [7] Pathak A, 2019 *Chinese J. Phys.* **60** 339-334
- [8] Wan Y, Zeng Y, Qian X, Yang Q, Sun K, Zhang Y, Shang X, Quan G and Jiang B 2020 *J. Phys. B: Condens. Matter*, **59**1 412241
- [9] Segall M D, Lindan P J D, Probert M J, Pickard C J, Hasnip P J, Clark S J and Payne M C 2002 *J. Phys. Condens. Matter.* **14** 2717-2744
- [10] Hohenberg P and Kohn W 1964 *Phys. Rev.* **136** B864-B871
- [11] Kohn W and Sham L J 1965 *Phys. Rev.* **140** A1133
- [12] Perdew P, Burke K and Enzerhof M 1996 *Phys. Rev. Lett.* **77** 3865-3868
- [13] Monkhorst H J and Pack J D 1976 *Phys. Rev. B* **13** 5188
- [14] Zheng N and Jin Y 2012 *J. Magn. Magn. Mater.* **324** 3099-3104
- [15] Zeba I, Bashir N, Ahmad R, Shakil M, Rizwan M, Rafique M and S.S.A. Gillani S S A 2020 *Bull. Mater. Sci.* **43** 1-9
- [16] Faleev S V, Ferrante Y, Jeong J, Samant M G, Jones B and Parkin S S 2017 *Phys. Rev. Appl.* 034022

# Tin (IV) oxide-coated gold nanocomposite materials for solar thermal energy collection and harvesting

T Makgale, P Kyesmen and M Diale<sup>1</sup>

<sup>1</sup>SARCHI: Clean and Green energy, University of Pretoria, Department of Physics, Hatfield, 0028, South Africa

E-mail: [u14007739@tuks.co.za](mailto:u14007739@tuks.co.za), [panna.kyesmen@up.ac.za](mailto:panna.kyesmen@up.ac.za),  
[mmantsae.diale@up.ac.za](mailto:mmantsae.diale@up.ac.za)

**Abstract.** The synthesis of various stable metallic nanoparticles is increasingly becoming the source of interest to researchers, this is due to their key features such as surface plasmonic activity, catalytic activity, and stability, amongst others. These therefore indicate their potential uses in several promising applications. This study describes the synthesis of SnO<sub>2</sub>-coated gold nanostructures, including nanospheres, nanoprisms, nano-octahedrals, and nano-octahedrals, with the aim to demonstrate the stabilizing effect of SnO<sub>2</sub> on the various gold nanostructures. Herein we also study the various resulting metal-semiconductor systems which might have general relevance in broadening our understanding of metal oxide semiconductor stabilization and interaction at the surface of a metal. The wet chemistry approach used in this study was previously used to synthesize gold nanospheres stabilized with SiO<sub>2</sub>, herein SnO<sub>2</sub> is investigated as an alternative to SiO<sub>2</sub>. Additionally, we demonstrate the potential uses of the stable colloids of Au@SnO<sub>2</sub> (pronounced tin (iv) oxide coated gold) nanocomposite materials as heat transfer fluid additives, owing to the outstanding heat storage capabilities of the SnO<sub>2</sub> coating material and the impeccable surface plasmonic resonance activities of the core Au metal structures. The surface plasmonic resonance (SPR) activities and structural stabilities of the resulting Au@SnO<sub>2</sub> colloids were determined and monitored using ultraviolet-visible (UV-Vis) spectroscopy. The UV-Vis spectra demonstrated a clear stabilization and absorption enhancement due the coating material. Furthermore, morphological analysis of the metal nanomaterials before and after coating were carried out using transmission electron microscopy (TEM), showed strong evidence of the stabilization resulting from the metal-semiconductor interaction. While the reaction mechanisms initiated at the metal-semiconductor interface is complicated by many factors including spatial non-uniformities, the morphological analysis of the Au@SnO<sub>2</sub> also aided our description of the proposed reaction mechanisms.

## 1. Introduction

In recent years, the synthesis of various stable metallic nanostructures with controlled sizes, shapes, architecture, composition, and properties, has increasingly become the source of interest to researcher seeking to develop materials suitable for such promising applications as solar thermal energy collection and transportation. The aim has been to acquire the nanostructures of gold, silver, gadolinium, and platinum. This is primarily because these structures, with key features such as surface plasmonic activity, catalytic activity, and stability, have proven to be the ideal building blocks in various applications including localized heat generation [1], energy harvesting [2], biosensing, optoelectronics,

and catalysis [3, 4]. However, many of these metallic nanostructures, specifically Gold (Au), suffer significant drawbacks related to the agglomeration of particles or the formation of complex particle linkages, which tend to limit their applicability lifespan. From an applications perspective, the useful special properties of nanomaterials are those that stem from the single isolated particles, and these properties are in general negatively affected, or lost in the case of particle interactions [5]. As such, significant considerations concerning our ability to isolate these nanoparticles from each other is warranted, since two or more particle interactions may cause significant changes in the material properties. Nanocomposite materials of the core/shell architectural type offer a simple solution to this limitation. These are multi-phase materials, in which at least one primary phase has the desired properties of interest to be harnessed, and an additional distance-holder secondary phase to assist in stabilizing the initial primary phase. To improve the applicability of Au, Tin (IV) oxide ( $\text{SnO}_2$ ) is used as a secondary distance-holder phase in the synthesis of Au@ $\text{SnO}_2$  (pronounced Tin (IV) oxide coated – Gold) nanocomposite materials. Thus, this study describes the synthesis of  $\text{SnO}_2$  stabilized Au nanostructures which include nanospheres, nanoprisms, and nanorods. The resulting stable Au@ $\text{SnO}_2$  nanocomposite materials were further evaluated as potential colloid additives for solar thermal energy collection and transportation [6, 7]. Additionally, valuable information about  $\text{SnO}_2$  stabilization and interaction at the surfaces of the resulting various (Au -  $\text{SnO}_2$ ) systems is noted.

## 2. Experimental

General Considerations: Commercial samples of Hydrochloric acid (HCl) and Sodium hydroxide (NaOH), Sodium stannate trihydrate ( $\text{Na}_2\text{SnO}_3 \cdot 3\text{H}_2\text{O}$ ), Chloroauric acid ( $\text{HAuCl}_4 \cdot 3\text{H}_2\text{O}$ ), Cetyltrimethylammonium- bromide (CTAB), L-ascorbic acid, and Silver Nitrate ( $\text{AgNO}_3$ ), and Sodium borohydride ( $\text{NaBH}_4$ ) were used as received. All manipulations were performed in air. Deionized water was used in the synthetic preparations and stability studies. The synthetic methodologies for the CTAB-stabilized, and  $\text{SnO}_2$ -coated Au nanostructures were based on published procedures and are summarized below [8-12].

### 2.1. Synthetic preparations of tin (IV) oxide coated gold (Au@ $\text{SnO}_2$ ) nanostructures

Figure 1 shows the experimental work undertaken in the synthesis and characterization of the nanocomposite materials of Au@ $\text{SnO}_2$ . The Au@ $\text{SnO}_2$  nanocomposite materials are synthesized via a three-step process. The initial Au seeds synthesis step involves the reduction reaction of the  $\text{HAuCl}_4$  salt with  $\text{NaBH}_4$  as the reducing agent, in the presence of sodium citrate utilised as a capping agent. The resulting seeds are then used as-prepared in the seed-mediated growth of the Au- nanospheres, nanorods, and nanoprisms in the second step. The third step is the hydrothermal spontaneous encapsulation process of the various Au structures with  $\text{SnO}_2$  nanoparticles, and it is undertaken under basic reaction conditions using NaOH and  $\text{Na}_2\text{SnO}_3 \cdot 3\text{H}_2\text{O}$ , as the sources of  $\text{OH}^-$  and  $\text{SnO}_2$  respectively. To re-concentrate the particles and remove unreacted reagents, such as CTAB, we centrifuged (30 min at 3500 rpm) the samples between each of the major steps above.

### 2.2. Characterization

The sizes and morphologies of the Au nanostructures before and after  $\text{SnO}_2$  coating were determined using a JEOL FEGTEM-2100 FX transmission electron microscope (TEM) operated at a bias voltage of 200 kV. The samples for TEM analyses were prepared by dipping the carbon-coated copper TEM grids into the various colloidal sample solutions of Au@ $\text{SnO}_2$  structures and then allowed to dry in air. This process was repeated (10 times or more) to obtain a quantity of sample suitable for analysis. The UV-Vis spectra were obtained in the range 300–1000 nm using a Cary 50 Scan UV-Vis spectrometer. The samples for UV-Vis analyses were prepared by placing 1 ml of the as-prepared aqueous solutions into the quartz cuvettes and diluting to the mark with deionized water. The colloidal stabilities of these various Au@ $\text{SnO}_2$  samples were determined from their UV-Vis spectra collected for each solution over an extended period of three months and compared with the spectra of the parent solutions.



**Figure 1:** Synthetic experimental setup for synthesis of Au@SnO<sub>2</sub> nanocomposite structures. In the Figure, (A) Au seed synthesis, (B) Seed mediated growth of the nanostructures, (C) hydrothermal spontaneous encapsulation process of the Au nanostructures, and (D) the segmentation of the samples

### 3. Results and Discussion

#### 3.1. Synthesis results and discussion

As mentioned in Section 2, Tin (IV) oxide coated gold (Au@SnO<sub>2</sub>) nanocomposite materials can be prepared via three steps, and the synthetic procedures are adapted from the indicated literature references. Scheme 1 in Figure 2 below, illustrates the synthetic procedures used in the synthesis of SnO<sub>2</sub>-coated Au nanospheres [4], nanorods [4], and nanoprisms [16].

First, gold nanospheres (40 nm average particle diameter) were synthesised using a common CTAB stabilised NaBH<sub>4</sub> reduction reaction method. These nanospheres served as seeds in the subsequent steps for the syntheses of nanorods and nanoprisms. The seed-mediated growth of these structures required a careful selection of reagents to aid in the site-selective growth of the seeds by controlling their sizes and the shapes. The aspect-ratio of the gold nanorods was controlled by the addition of AgNO<sub>3</sub>, whilst their growth rate was lowered by the addition of HCl. For gold nanoprisms, the necessary reagents proved to be NaOH and NaI, which respectively aided in controlling the direction of deposition of the depositing atoms and in improving the flat-anisotropic (planar) growth of the prisms. In each case, it was necessary to control the sizes of the depositing atoms since depositing atoms of the same size as the seed particles would result in complex structures, and this was accomplished using L-ascorbic acid.

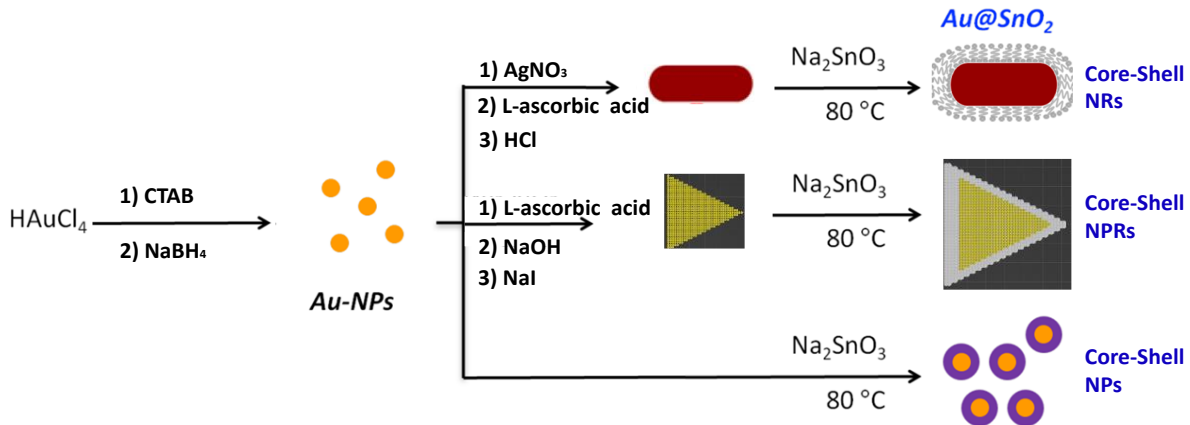


**Figure 2:** Scheme 1. Synthesis of SnO<sub>2</sub>-coated Au nanospheres, nanorods, and nanoprisms.

The preparation of the SnO<sub>2</sub>-coated Au nanospheres, nanorods, and nanoprisms involved the spontaneous encapsulation of these Au nanostructures within the shell of SnO<sub>2</sub> nanocrystalline particles, upon the addition of sodium stannate trihydrate (Na<sub>2</sub>SnO<sub>3</sub>·3H<sub>2</sub>O) via a simple hydrothermal process in the presence of NaOH. SnO<sub>2</sub> is an inorganic semiconductor compound (Band gap of 3.6 eV at room temperature [12]) with high chemical and thermal stability. And a nanocrystalline layer of SnO<sub>2</sub> nanoparticles around the Au nanostructures occurs following the hydrolysis of stannate at a temperature of above 60°C through the reaction equations in Figure 3.



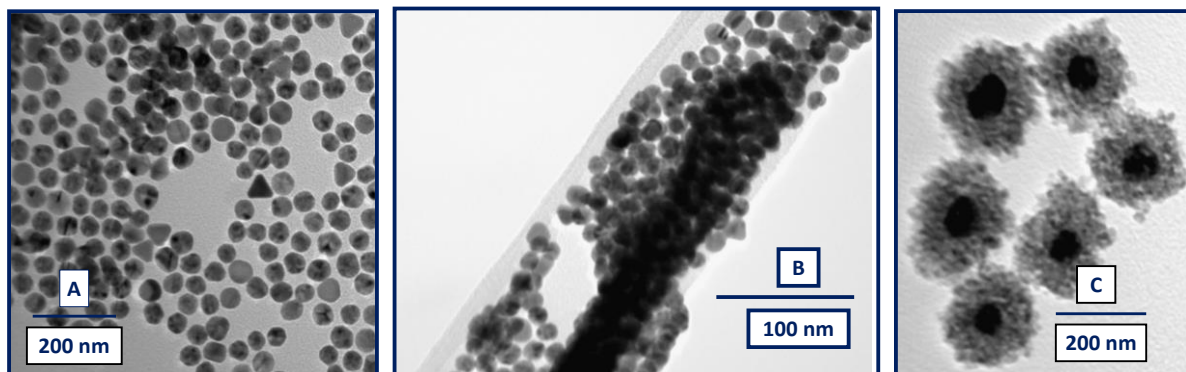
**Figure 3:** Stannate hydrolysis process [13].

The SnO<sub>2</sub> nanocrystalline particles resulting from equation 4 in Figure 3 spontaneously encapsulate themselves around the Au-nanostructures in a non-uniform fashion resulting in a mesoporous layer. As expected, after coating the Au nanostructures with SnO<sub>2</sub>, their sizes (diameters and lengths) increased this is due to the formation of the Au@SnO<sub>2</sub> nanocomposite materials. The Au@SnO<sub>2</sub> composite materials of the nanospheres increased to an average particle diameter of 65 nm, and the average particle lengths of the Au@SnO<sub>2</sub> nanocomposite materials of the nanorods and nanoprisms increased to 132 and 300 nm, respectively.

### 3.2. Morphological analysis

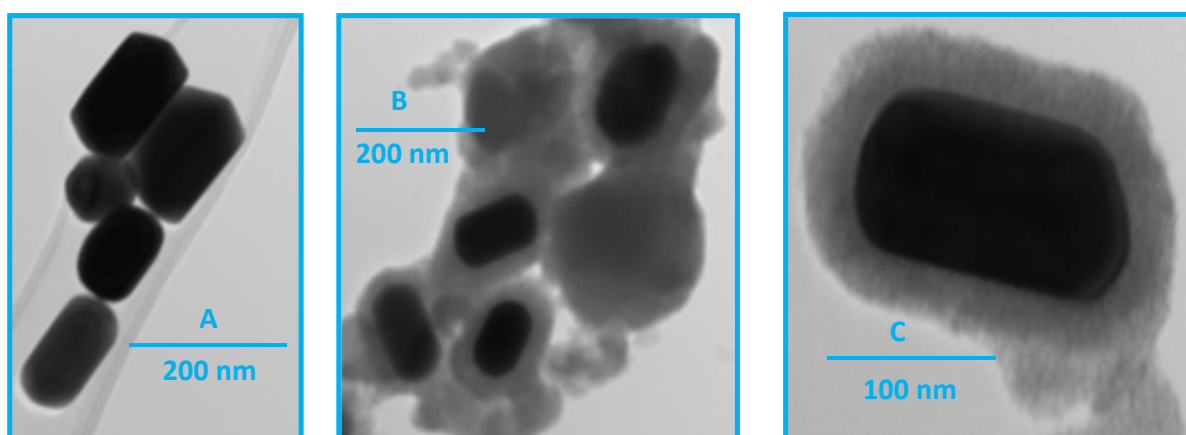
Figure 4 shows TEM micrographs of the Au nanospheres. From the TEM micrographs, the nano-spherical structures can be classified as zero-dimensional nanomaterials, having sizes that are less than a 100 nm in all dimensions. The particle size measurements of the samples were collected over a period of three months to monitor and evaluate their structural stability. The Au nanospheres displayed an average particle diameter of about 60 nm. This particle size was maintained throughout the assessment period, however a degree of particle agglomeration of the uncoated Au nanospheres started emerging. After imparting a SnO<sub>2</sub> coating of thickness of approximately 150 nm, the composite particle sizes increased to average particle diameters of approximately 208 nm, and these coated Au nanospheres remained kernelled inside the SnO<sub>2</sub> coatings, which aided them in maintaining their structural stability

over the three months period. The TEM micrographs also showed that the SnO<sub>2</sub> coated Au nanospherical particles have excellent uniformity and excellent Au to SnO<sub>2</sub> distribution.



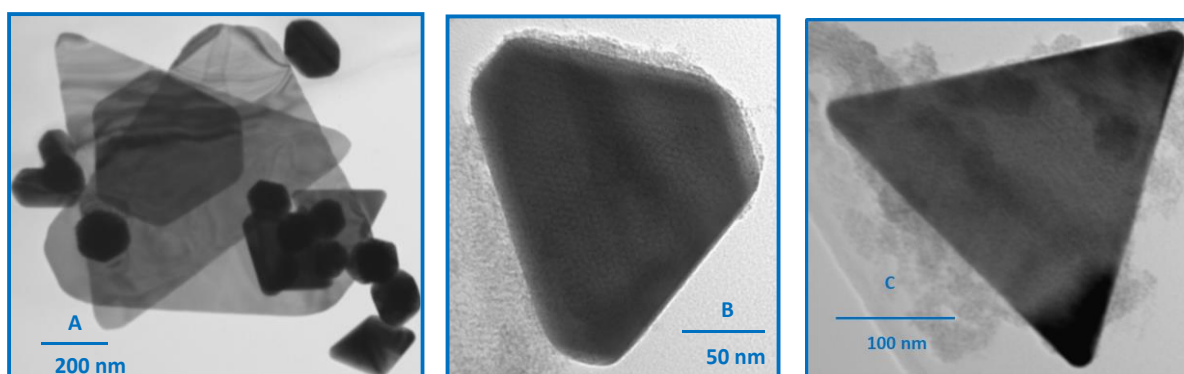
**Figure 4:** TEM micrographs of Au nanospheres before (A – B) and after (C) SnO<sub>2</sub> coating, images are taken over a period of 3 months.

Figure 5 shows the TEM micrographs of the Au nanorods. From the TEM micrographs, the nanorod structures can be classified as one-dimensional nanomaterials, having sizes that are less than a 100 nm in exactly two dimensions. The Au nanorods displayed an average particle diameter of about 70 nm, and an average length of about 130 nm before SnO<sub>2</sub> coating was imparted. After imparting a SnO<sub>2</sub> coating of thickness of approximately 40 nm, the composite particle lengths increased to an average of approximately 202 nm. The TEM micrographs of the SnO<sub>2</sub> coated Au nanorods showed the distribution of SnO<sub>2</sub> nanoparticles around the Au nanorods, which indicated a degree of non-uniform distribution typically observed in meso-porous layers of nanomaterials. A uniform distribution of the Au nanomaterials to the SnO<sub>2</sub> nanocrystalline particles was also observed.



**Figure 5:** TEM micrographs of Au nanorods before and after SnO<sub>2</sub> coating.

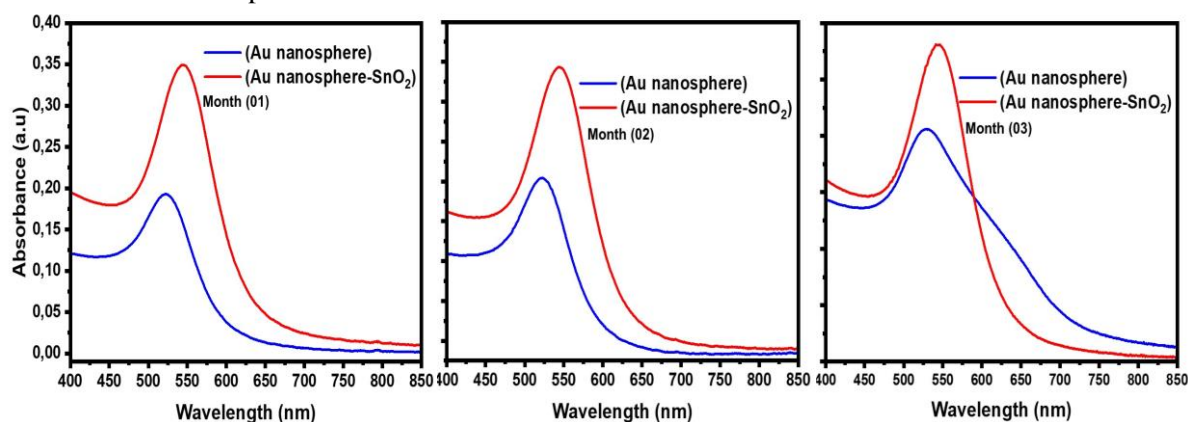
Figure 6 shows the TEM micrographs of the Au nanoprisms. From the TEM micrographs, the Au nanoprism structures can be classified as two-dimensional nanomaterials, having sizes that are greater than a 100 nm in exactly two dimensions. These are therefore referred to as thin film nanomaterials characterized by having a thickness of a few atoms. The Au nanoprisms displayed average areas of about 15574 nm<sup>2</sup> and 18199 nm<sup>2</sup>, before and after imparting a SnO<sub>2</sub> coating of approximately 10 nm. The TEM micrographs of the SnO<sub>2</sub> coated nanoprisms showed the distribution of SnO<sub>2</sub> nanoparticles around the Au nanoprisms, which indicated a degree of non-uniform distribution like that observed in the coated nanorods, which implies that a meso-porous layer of SnO<sub>2</sub> nanomaterials has encapsulated the Au core structures. The TEM micrographs for the also indicated that there is poor Au to SnO<sub>2</sub> distribution.



**Figure 6:** TEM micrographs of Au nanoprisms before and after SnO<sub>2</sub> coating.

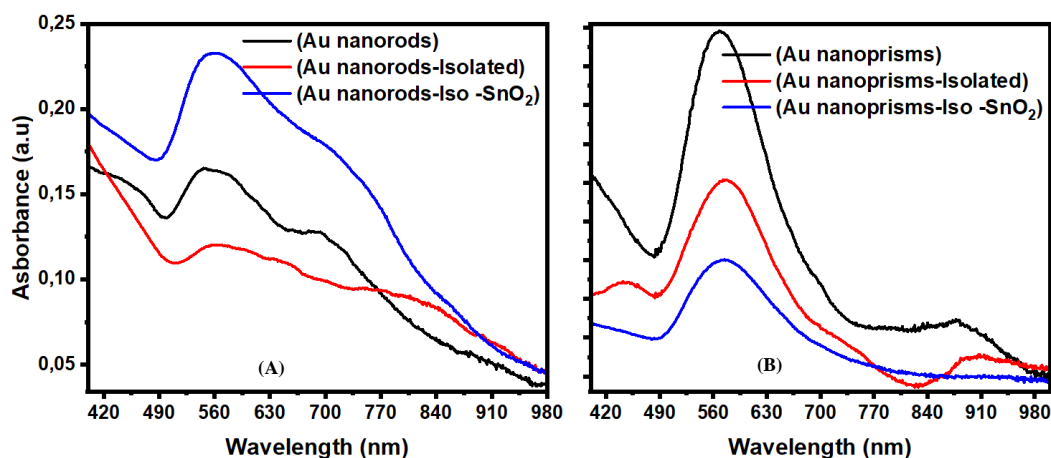
### 3.3. Spectroscopic analysis

Figure 7 shows the absorption spectra of the colloidal sample solutions of the uncoated and coated Au nanostructures. The surface plasmon resonance (SPR) bands observed for the uncoated and SnO<sub>2</sub>-stabilized/coated Au nanospheres had maxima at 522 nm, and 552 nm, respectively, which are consistent with previously reported values [14]. As mentioned, the stability of the Au nanospheres was monitored over a period of three months, and from the UV-Vis spectra it can be observed that the coated Au nanospheres were excellently stabilized by the SnO<sub>2</sub> coating nanocrystalline materials, as opposed to their uncoated counterparts.



**Figure 7:** The UV-Vis spectra of the Au-nanospheres, collected over a three-month period.

Figure 8 (a): Au nanorods shows the SPR bands (Transverse and Longitudinal) for the uncoated and SnO<sub>2</sub>-stabilized/coated Au nanorods which had maxima (560 and 702 nm), and (562 and 710 nm), respectively. which are consistent with previously reported values [17, 28]. Figure 8 (b): Au nanoprisms shows the SPR bands (only Transverse, since their longitudinal bands were out of range of the UV-Vis instrument) for the uncoated and SnO<sub>2</sub>-stabilized/coated Au nanoprisms which had maxima at 562 and 564 nm, respectively.



**Figure 8:** The UV-Vis spectra of the (A) Au-nanorods and (B) Au-nanoprisms.

The red shifts of the SPR bands for the  $\text{SnO}_2$ -stabilized/coated Au nanostructures (nanospheres, nanorods, and nanoprisms) are due to the high refractive indexes of 2.2 due to the  $\text{SnO}_2$  [15] coatings. Notably, the SPR band of the  $\text{SnO}_2$ -coated particles was observed to undergo a red shift with increasing thickness of the  $\text{SnO}_2$  layer.

#### 4. Conclusion

In summary, three different Tin (IV) oxide coated Gold ( $\text{Au@SnO}_2$ ) nanocomposite materials of the core-shell architectural type were synthesised. These materials consisted of Au nanospheres, nanoprisms, and nanorods as the primary phases, which assumed the core/kernel positions. Whilst the  $\text{SnO}_2$  nanocrystalline layers served as the secondary distance-holder phase, thus assuming the shell position. We investigated the stabilities of these nanocomposite materials. The morphological analysis of these materials demonstrated convincing evidence of structural stability. That is, the kernelled Au nanostructures remained perfectly and uniformly dispersed from each other and completely kernelled inside the shells, thus preserving the colloidal structural stability. The  $\text{Au@SnO}_2$  nanospheres proved to be more durable as opposed to their uncoated counterparts. Furthermore, TEM micrographs of the Au nanoprisms revealed the nature/arrangement of the  $\text{SnO}_2$  nanoparticles around the Au metal surfaces, this proved to be a mesoporous structural layer with open pores which exposed parts of the surface. As such, any future application that might seek to use the metal surface can do so through the partial pores of the coating layer. In addition to improving the stability of the Au nanostructures,  $\text{SnO}_2$  has also demonstrated an enhancing capability to the optical properties of these Au structures. That is, we observed significant enhanced absorption as well as band shift for the  $\text{Au@SnO}_2$  nanocomposite materials. The enhancement is due to the high refractive index of  $\text{SnO}_2$ , while the redshift is due to the partial increase in size of the Au nanostructures.

#### Acknowledgements

The University of Pretoria and the SARCHI: Clean and Green energy research group led by Prof Mmantsae Diale supported this research. We thank Ms Charity Maepa for assistance with the TEM micrographs, Dr Juvet N Fru for assistance with the UV-Vis spectra, and Dr Panna Kyesmen for endless assistance and co-supervision with the research. The work is based on research supported in part by the National Research Foundation of South Africa (Grant MND210426597512).

#### 5. References

- [1] Yuan N, Caixia K, Qi G, Jingjing W, Haiying Z and Changshun W, 2015, Heat generation and stability of a plasmonic, *Journal of Physics D: Applied Physics*, vol. **49**, no. 055302, pp. 1-10.

- [2] Mohammadnia A, Rezaia A, Ziaour B M, Sedaghati F and Rosendahl L, 2020, Hybrid energy harvesting to maximize power generation from solar energy, *Energy Conservation Management*, vol. **112352**, p. 205.
- [3] Myeongju K and Younghun K, 2020, Au-coated Fe<sub>3</sub>O<sub>4</sub>@SiO<sub>2</sub> core-shell particles with photothermal activity, *Elsevier*, vol. **600**, no. 124957, pp. 1-7.
- [4] Zhou N, Polavarapu L, Wong Q and Xu Q H, 2015, Mesoporous SnO<sub>2</sub>-coated metal Nanoparticles with Enhanced Catalytic Efficiency, *ACS: Applied Materials and Interfaces*, vol. **7**, p. 4844–4850.
- [5] Vollath D, 2013, Nanomaterials and nanocomposites, in *Nanomaterials: An introduction to synthesis, properties and applications.*, p. 5.
- [6] Choi U Sand Eastman J A, 1995, Enhancing thermal conductivity of fluids with nanoparticles, developments and applications of non-newtonian flows., *The American Society of Mechanical Engineers*, vol. **66**, no. 231, pp. 99-105.
- [7] Choi U S and Eastman J A, 2001, Enhanced heat transfer using nanofluids. United States of America Patent US6221275B1.
- [8] Su L, Hu S, Zhang L and Wang Z, 2017, A Fast and Efficient Replacement of CTAB with MUA on the surface of Gold Nanorods Assisted by a water-Immiscible Liquid., *Advanced Science NEWS (SMALL)*, pp. 1-9.
- [9] Lee S H, Rusakova I and Hoffman D Z, 2013, Monodisperse SnO<sub>2</sub>-Coated Gold Nanoparticles Are Markedly More Stable than Analogous SiO<sub>2</sub>-Coated Gold Nanoparticles, *ACS: Applied materials and interfaces*, vol. **5**, p. 2479–2484.
- [10] Sun M, Ran G, Fu Q and Xu W, 2015, The effect of Iodide on the synthesis of gold nanoprisms, *Journal of Experimental Nanoscience*, vol. **10**, no. 17, pp. 1309-1318.
- [11] Lee H S, Rusakova I, Hoffman D, Jacobson A and Lee R, 2013, Monodisperse SnO<sub>2</sub>-coated Gold Nanoparticles Are Markedly more stable than analogous SiO<sub>2</sub>-coated gold nanoparticles., *ACS: Applied Materials and Interfaces*, vol. **5**, pp. 2479-2484.
- [12] Zhou W, Liu Y, Yang Y and Wu P, 2014, Band gap engineering of SnO<sub>2</sub> by Epitaxial Stain: Experimental and Theoretical investigations, *The journal of Physical Chemistry*, vol. **12**, no. 118, pp. 6448-6453.
- [13] Korczyk A B, Mackiewicz E, Soliwoda K R, Grobelny J and Celichowski G, 2020, Facile synthesis of SnO<sub>2</sub> shell followed bby microwave treatment for high environmental stability of Ag nanoparticles, *The Royal Society of Chemistry*, vol. **10**, pp. 38424-38436.
- [14] Oldfield G, Ung Tand Mulvaney P, 2000, Au@SnO<sub>2</sub> core-shell nanocapacitors, *Advanced AMaterials*, vol. **12**, no. 20, pp. 1519-1522.
- [15] Kim W Tand Lee D U, 2000, Microstructural, electrical, and optical properties of SnO<sub>2</sub> nanocrystalline thin films grown on InP (100) substrates for applications as gas sensor devices, *Journal of Applied Physics*, vol. **88**, p. 3759.
- [16] Huang Y, Ferhan A R, Gao Y, Dandapat A, Kim D H, 2014, High-yield synthesis of triangular gold nanoplates with improved shape uniformity, tunable edge length and thickness, *The Royal Society of Chemistry*, vol. **637457**, p. 1-3.

# The phase stability, mechanical and electronic properties of CsCl-type intermetallic: $\text{Ti}_{50}\text{TM}_{50}$ (TM = Ni, Ru and Pd), a first-principles approach

BS Ngobe<sup>1,2</sup>, MJ Phasha<sup>1</sup>, RG Diale<sup>1</sup> and MP Molepo<sup>2</sup>

<sup>1</sup> Advanced Materials Division, MINTEK, Randburg, South Africa

<sup>2</sup> School of Physics, University of the Witwatersrand, Johannesburg, South Africa

E-mail: [Bonganing@mintek.co.za](mailto:Bonganing@mintek.co.za) and [2623288@students.wits.ac.za](mailto:2623288@students.wits.ac.za)

**Abstract.** Most Ti-based CsCl-type compounds solidify to an ordered B2 phase at high temperature and upon cooling they transform martensitically to lower-temperature phases. In this work, phase stability, mechanical and electronic properties of three CsCl-type intermetallics  $\text{Ti}_{50}\text{TM}_{50}$  (TM=Ni, Ru and Pd) computed using density functional theory (DFT) based on the first-principles technique are reported. The obtained lattice parameters are in good agreement with experimental results, an indication that the computational parameters used can be reliable to calculate other physical properties. Enthalpy of formations ( $\Delta H_f$ ) and density of states (DOS), which are used to evaluate the thermodynamic stability of the compound, were calculated from the geometrically optimized crystal structures. High negative heat of formation (-0.75 eV/atom) was obtained for  $\text{Ti}_{50}\text{Ru}_{50}$  phase, and its Fermi level was found to coincide with the centre of the pseudogap, demonstrating high stability and resistance to phase transition amongst the investigated compounds. The primary elastic constants ( $C_{11}$ ,  $C_{12}$  and  $C_{44}$ ) and shear elastic coefficient ( $C'$ ) for cubic crystals were calculated.  $\text{Ti}_{50}\text{Ru}_{50}$  and  $\text{Ti}_{50}\text{Ni}_{50}$  complied with the mechanical stability while  $\text{Ti}_{50}\text{Pd}_{50}$  did not comply. Furthermore,  $\text{Ti}_{50}\text{Ru}_{50}$  was found to exhibit only positive frequencies indicative of the absence of phase transition, while  $\text{Ti}_{50}\text{Pd}_{50}$  and  $\text{Ti}_{50}\text{Ni}_{50}$  exhibit both positive and negative frequencies signifying possible phase transition to lower temperature phases.

## 1. Introduction

Nitinol is a commercial name given to equiatomic TiNi intermetallic compounds [1-2]. It is part of intermetallic compounds that form instantly from a molten liquid containing atoms of Group IVB (Ti, Zr and Hf) plus that of Group VIII B - IB metals of the periodic table [3]. On cooling, it crystallizes to an ordered B2 of Cesium Chloride (CsCl) type near the equiatomic compositional range [1, 4-5]. B2 is a high-symmetry austenite phase that exists at high temperatures, and upon further cooling, it undergoes a diffusionless solid-to-solid structural change to a low-symmetry martensitic phase [1-2, 6-7]. Structural alloys that conform to this phenomenon are called shape memory alloys (SMA) [1, 4-5]. These are a unique class of materials with an ability to remember previous crystal arrangement and properties, and currently enjoy a wide range of structural applications in medical and engineering materials [1-2].

Apart from its excellent shape memory effect and pseudo-elasticity, Nitinol has its drawbacks such as its low-temperature application that hinders it as an SMA for high-temperature (HTSMA) applications that exceed  $100^{\circ}\text{C}$  [1-2]. On the other hand, Platinum group metals (PGMs) which are located in Group VIII B of the periodic table of elements, form the B2 phase with Group VIB metals near 50:50 atomic percentage [3, 8]. Their nobleness and high-temperature stability enable PGMs as the candidate of choice for high-temperature applications [9]. Ti-PGMs based such as  $\text{Ti}_{50}\text{Pt}_{50}$  and  $\text{Ti}_{50}\text{Pd}_{50}$  are currently explored as potential candidates for high-temperature applications, such as aerospace engines [4-5, 10]. Previous studies demonstrated and reported that some of the Ti-PGMs based compounds such as  $\text{Ti}_{50}\text{Ru}_{50}$  and  $\text{Ti}_{50}\text{Os}_{50}$  do not have shape memory effect (SME); their B2 phase remains ordered and stable down to room temperature [11].

In this study, we report work carried out using first-principles calculations based on density functional theory to compute the phase stability, mechanical and electronic properties of the three investigated  $\text{Ti}_{50}\text{TM}_{50}$  (TM = Ni, Ru and Pd) compounds.

## 2. Computational methods

The calculations reported here were carried out using first-principles density functional theory as implemented in Cambridge Serial Total Energy Package (CASTEP) code [12, 13]. The ultra-soft pseudopotentials (USSPs) were used to model the electron-ion interactions [14]. The electron-exchange correlation was described by the Perdew-Burke-Ernzerhof (PBE) functional of the generalized gradient approximation (GGA) [15, 16]. The energy cut-off of 500 eV and the k-points of  $13 \times 13 \times 13$  were used and found to be sufficient enough to converge the total energy of the investigated B2 compounds.

All the equilibrium B2 crystal structures were obtained through geometry optimization in the Brayden-Fletcher-Goldfarb-Shanno (BFGS) minimization scheme [17]. The convergence criterion of less than  $1 \times 10^{-5}$  eV/atom, the maximum residual forces of  $0.03$  eV/Å, the maximum residual bulk stress of  $0.05$  GPa and the maximum atomic displacement of  $1 \times 10^{-3}$  Å were utilised to achieve maximum accuracy.

Figure 1 shows the schematic representation of the crystal structure used to carry the structural and thermodynamic, electronic and vibrational stability of the CsCl-type compounds reported in this research work. The lattice dynamics were computed via the finite displacement method as implemented in the CASTEP code.

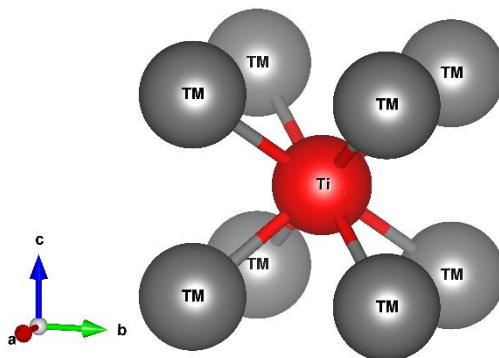


**Figure 1.** Schematic representation of B2 crystal geometry of  $\text{Ti}_{50}\text{TM}_{50}$  (TM = Ni, Ru and Pd) used in this study work

## 3. Results and discussion

### 3.1. Structural and thermodynamic properties

Table 1 present the calculated lattice parameters and the formation enthalpies that were determined from the relaxed crystal geometries of the three investigated B2 compounds. The obtained lattice parameters

of the investigated B2 compounds were found to be comparable to those reported by other authors [3, 18-20].

**Table 1-** Structural parameters of the investigated B2 crystal geometry.

Crystal structure	Lattice parameters, a (Å)		Formation enthalpies, ( $\Delta H_F$ ) eV.atom <sup>-1</sup>	
	This work	Literature	This word	Literature
<b>Ti<sub>50</sub>Ni<sub>50</sub></b>	3.01	3.02 <sup>[18]</sup>	-0.382	-0.357 <sup>[23]</sup> , 0.352 <sup>[24]</sup> -
<b>Ti<sub>50</sub>Pd<sub>50</sub></b>	3.17	3.17 <sup>[20]</sup>	-0.508	-0.530 <sup>[9]</sup> , 0.511 <sup>[23]</sup> -
<b>Ti<sub>50</sub>Ru<sub>50</sub></b>	3.08	3.09 <sup>[3, 19]</sup>	-0.750	-0.743 <sup>[8]</sup> , 0.770 <sup>[9]</sup> -

Moreover, the phase stability of any compound can be deduced from the formation enthalpies as expressed in Equation 1 [8, 21], and it is used to indicate the thermodynamic ability of a compound to chemically form. A phase is said to be thermodynamically stable if  $\Delta H_F$  is found to be negative, else the phase becomes less stable if less negative or unstable if found to be positive at 0 K [22]:

$$\Delta H_F = \frac{1}{2} (E_{Bin}^{Tot} - E_{Element}^{Ti} - E_{Element}^{TM}), \quad (1)$$

where,  $E_{Bin}^{Tot}$  represent the total energy of the B2 compound,  $E_{Element}^{Ti}$  and  $E_{Element}^{TM}$  represent the elemental total energies of Ti and TM in their ground-state crystal structures. As presented in Table 1, all the investigated B2 compounds were found to be thermodynamically stable ( $\Delta H_F < 0$ ), with Ti<sub>50</sub>Ru<sub>50</sub> and Ti<sub>50</sub>Ni<sub>50</sub>, found to be the most and least thermodynamically stable compounds respectively. Again, the results reported here were found to be in accordance with results reported by other researchers [8-9, 23-24].

### 3.2. Mechanical stability

Elastic constants ( $C_{ij}$ ) are part of the primary output parameters of first-principles calculations, as they provide a link between the mechanical and dynamic behaviour of crystals [25-26]. Key properties of materials such as physical and mechanical can be deduced from the elastic constants. B2 compounds consist of a simplest cubic form of a stiffness matrix, where the number of the independent elastic constants are reduced to three ( $C_{11}$ ,  $C_{12}$  and  $C_{44}$ ) in the Voigt notation, and the shear elastic coefficient  $C'$  for assessing the compound's prospect to undergo a phase transition (to ascertain stability or instability) at lower temperatures can be expressed as shown in Equation 2:

$$C' = \left( \frac{C_{11} - C_{12}}{2} \right). \quad (2)$$

According to Born-Huang's dynamical theory [27-28], the mechanical stability criteria for B2 compounds can be determined by holistically satisfying the criteria given by a set of expressions in Equation 3:

$$C_{11} > 0, C_{44} > 0, C_{11} - C_{12} > 0, C_{11} + 2C_{12} > 0. \quad (3)$$

The crystal's mechanical stability decreases when closer to phase transition [29], where the tetragonal shear modulus ( $C'$ ) becomes smaller than the monoclinic shear constant ( $C_{44}$ ), which represents the stiffness of the crystal against shear. Table 2 present the elastic parameters of the investigated B2 compounds. Both  $\text{Ti}_{50}\text{Ru}_{50}$  and  $\text{Ti}_{50}\text{Ni}_{50}$  satisfied all the mechanical stability criteria as detailed in Equation 3, while  $\text{Ti}_{50}\text{Pd}_{50}$  did not comply ( $C_{11} < C_{12}$ ) with the above-mentioned criteria. This is an indication that this B2 ( $\text{Ti}_{50}\text{Pd}_{50}$ ) compound is prone to undergo a phase transition at much higher temperatures.

**Table 2.** Elastic constants as well as their calculated modulus of elasticity for the investigated B2 compounds.

B2 crystal	Elastic constants (GPa)			
	$C_{11}$	$C_{12}$	$C_{44}$	$C'$
$\text{Ti}_{50}\text{Ni}_{50}$	206.7	138.7	47.1	34.0
$\text{Ti}_{50}\text{Pd}_{50}$	148.5	164.0	51.5	-7.8
$\text{Ti}_{50}\text{Ru}_{50}$	396.1	122.5	82.7	136.8

### 3.3. Electronic and vibrational stability

A compound is considered stable at 0K if there are no soft modes along high symmetry directions in the Brillouin zone (BZ) [30]. And the presence of soft modes or negative frequencies indicates the instability of the crystal, an indication of the likelihood to undergo a phase transition, accompanied by lattice deformation [30-31].

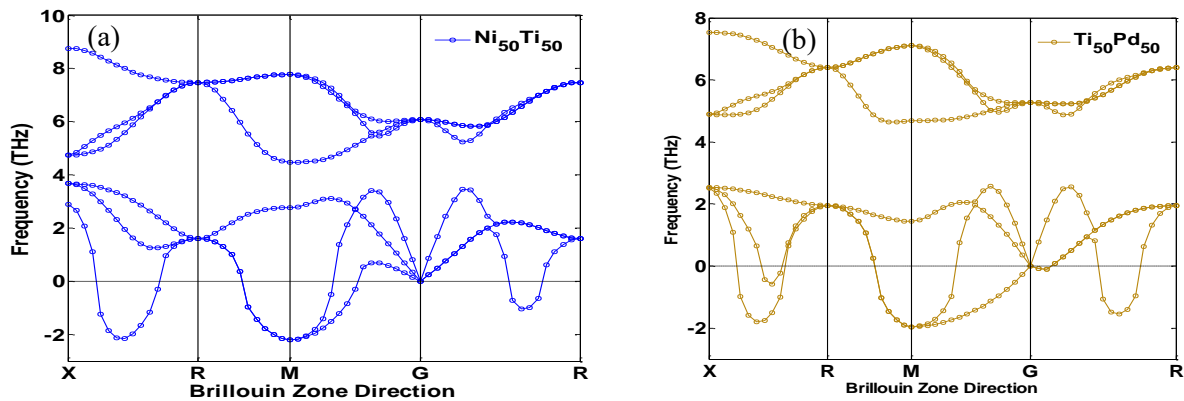


**Figure 2.** Phonon dispersion curves of the investigated B2 compounds, (a)  $\text{Ti}_{50}\text{Ni}_{50}$  and (b)  $\text{Ti}_{50}\text{Pd}_{50}$  plotted along selected Brillouin zone.

Figures 2 and 3 represent the electronic properties of the investigated compounds, the phonon dispersion curves plotted along selected Brillouin zone as well as their corresponding total density of states computed at 0K. As can be seen, Figures 2 (a) and (b) show the phonon dispersion curves for  $\text{Ti}_{50}\text{Ni}_{50}$  and  $\text{Ti}_{50}\text{Pd}_{50}$  respectively, and both were found to consist of both positive (real) and negative (imaginary) vibrational frequencies. The imaginary frequencies are located between **X-R**, **G-R** and **M**

symmetry points, thereby making these compound phases dynamically unstable at 0K, an indication of possible phase transition to lower temperature phases. Figure 3 represents the phonon vibrational frequencies for  $\text{Ti}_{50}\text{Ru}_{50}$  that were found to be real (positive) in all Brillouin directions, and this is a clear demonstration that this B2 phase is dynamically stable, with no prospect of phase transition to a lower temperature phase.

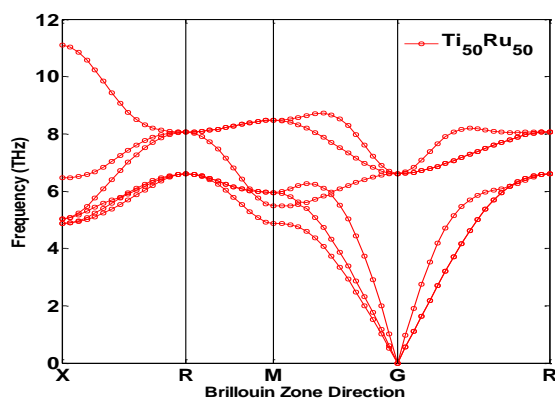


**Figure 3.** Phonon dispersion curves of B2  $\text{Ti}_{50}\text{Ru}_{50}$  compound plotted along selected Brillouin zone.

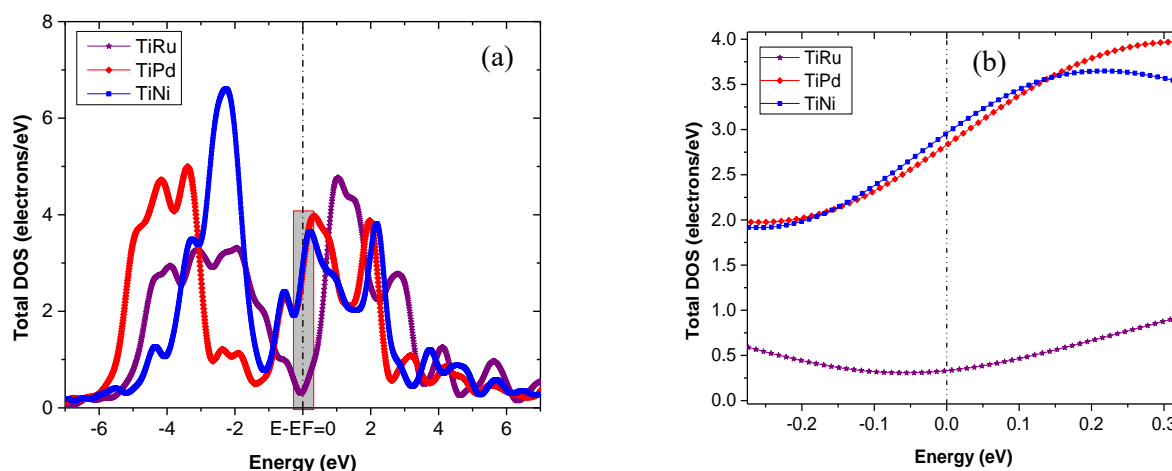


**Figure 4.** Total density of states (TDOS) of the three investigated B2 compounds (a), as well as the zoom-out section (b) for clear visibility.

Figure 4 shows the total density of states of the three investigated CsCl compounds reported in this study work. TDOS represented in Figure 4 show that B2  $\text{Ti}_{50}\text{Ru}_{50}$  remain stable down to ambient temperature with no possibility of phase transformation. This is indicated by its Fermi level ( $E-E_F=0$ ) that cuts the deep valley (pseudogap) at the centre. In the very same Figure 4, one can also observe that both B2  $\text{Ti}_{50}\text{Ni}_{50}$  and  $\text{Ti}_{50}\text{Pd}_{50}$  were found to be unstable at lower temperatures, their Fermi level was found to have shifted towards the bonding region and cuts the pseudogap on the rising shoulder. The aforementioned demonstrate that the high symmetry B2 phases of  $\text{Ti}_{50}\text{Ni}_{50}$  and  $\text{Ti}_{50}\text{Pd}_{50}$  cannot maintain their high symmetry at low temperature (0K), suggesting a likelihood to undergo martensitic phase transition which is one of the characteristics of shape memory effect.

#### 4. Conclusions

The DFT model used to study the phase, mechanical and electronic stability of the investigated CsCl compounds show great reliability of the approach carried out. This was indicated by the lattice

parameters and heats of formation results found to be in good agreement with the available theoretical and experimental data. Using the calculated heats of formation, all the B2 compounds considered were found to be thermodynamically stable. This study further found B2 Ti<sub>50</sub>Ni<sub>50</sub> and Ti<sub>50</sub>Ru<sub>50</sub> to satisfy the mechanical stability criteria for cubic crystals ( $C_{11} > C_{12}$ ). However, B2 Ti<sub>50</sub>Pd<sub>50</sub> phase did not adhere to these criteria, which is an indication of phase transition at high temperatures, thus rendering it a potential material for the development of high-temperature shape memory alloys. The TDOS results obtained show that Ti<sub>50</sub>Ru<sub>50</sub> is stable as its Fermi level coincides with the centre of the pseudogap, while that of Ti<sub>50</sub>Pd<sub>50</sub> was found to have shifted towards the bonding state, signifying the stability and instability of the B2 phases at 0K, respectively. Furthermore, the phase stability of the B2 compounds was validated and verified through phonon vibrational frequencies.

B2 Ti<sub>50</sub>Ru<sub>50</sub> phase was found to be stable with only the positive vibrational frequency, while B2 Ti<sub>50</sub>Ni<sub>50</sub> and Ti<sub>50</sub>Pd<sub>50</sub> presented both positive and negative frequencies, an indication of dynamic instability of the B2 phase at low temperatures which signifies possible phase transition to lower temperature phases.

### Acknowledgements

This paper is published with the permission of MINTEK and The University of the Witwatersrand. The authors would like to thank the Advanced Metals Initiative (AMI) of the Department of Science and Innovation (DSI) for financial support. Finally, the gratitude is also extended to the Centre for High-Performance Computing (CHPC) in Cape Town for allowing us to carry out the calculations using their remote computing resources.

### References

- [1] Wadood A 2018 Higher Education Commission. 144
- [2] Wadood A 2016 *Adv. Mate. Sci. Eng.* **2016** 9
- [3] Bao W, Liu D, Duan Y and Peng M 2019 *Philos. Mag.* **99** 22
- [4] Kulkova, SE and Valujsky DV 2001 *J. Phys. IV* **11** 58
- [5] Kulkova SE, Valujsky DV, Kim JS, Lee G and Koo YM 2001 *Solid State Commun.* **119** 623
- [6] Khachin V 1989 *Rev. Phys. Appl.* **24** 739
- [7] Donkersloot H and Vucht JV 1970 *J. Less-Common. Met.* **20** 91
- [8] Xing WW, Chen XQ, Li DZ, Li LY, and Fu CL 2012 *Intermetallics.* **28** 24
- [9] Semenova E 1997 *Powder. Metall. MCeram.* **36** 404
- [10] Kong ZZ, Duan YH, Peng MJ, Qu DY and Bao LK 2019 *Physica. B: Cond. Matter.* **573** 21
- [11] John R and Ruben H 2011 *Mater. Sci. Appl.* **2** 1366
- [12] Segall MD, Philip JDL, Probert MJ, Pickard CJ, Hasnip PJ, Clark SJ and Payne MC 2002 *J. Phys. D: Condens. Matter.* **14** 2744
- [13] Clark SJ, Segall MD, Pickard CJ, Hasnip PJ, Probert MI, Refson K and Payne MC 2005 *Z. Kristallogr.* **220** 570
- [14] Vanderbilt D 1990 *Phys. Rev. B* **41** 7895
- [15] Perdew JP and Wang Y 1992 *Phys. Rev. B* **45** 13249
- [16] Perdew JP, Burke K and Ernzerhof M 1996 *Phys. Rev. Lett.* **77** 3865
- [17] Fischer T and Almlof J 1992 *J. Phys. Chem.* **96** 9774
- [18] Yu F, Liu Y 2019 *Computations.* **7** (57) 14
- [19] Jain E, Pagare G, Chouhan SS and Sanyal SP 2014 *Intermetallics* **54** 184
- [20] Chen XQ, Fu CL and Morris JR 2010 *Intermetallics* **18** 1006
- [21] Jaradat R, Abu-Jafar M, Abdelraziq I, Mousa A, Ouahrani T and Khenata R 2018 *AIP Adv.* **8** 20
- [22] Yang J, Huang JH, Ye Z, Fan DY, Chen SH and Zhao Y 2017 *Ceram. Int.* **43** 7761
- [23] Jung J, Ghosh G and Olson G 2003 *Acta Mater.* **51** 6357
- [24] Gachon JG, Selhaoui N, Aba B and Hertz J 1992 *J. Phase Equilibria* **13** 511

- [25] Liu S, Tang C and Zhan Y 2016 *Metall. Mater. Trans. A* **47** 1459
- [26] Wu SC, Fecher GH, Naghavi SS and Felser C 2019 *J. Appl. Phys.* **128** (8) 18
- [27] Gomisa O, Manjónb FJ, Rodríguez-Hernándezc P and Muñozc A 2019 *J. Phys. Chem. Solids*, **124** 120
- [28] Wagner M and Windl W 2008 *J. Acta Mater.* **56** 6245
- [29] Sedlák P, Janovská M, Bodnárová L, Heczko O and Seiner H 2020 *Metals* **10** (1383) 13
- [30] Si L, Jiang Z-Y, Zhou B, and Chen W-Z 2012 *Phys. B* **407** 351
- [31] Togo A and Tanaka I 2015 *Scri. Mater.* **108** 5

# Effect of $\text{Ce}^{3+}$ substitution at $B$ site on magnetic phase transitions in $\text{CoCr}_2\text{O}_4$ nanoparticles

P Mohanty, TJ Nkosi, ARE Prinsloo and CJ Sheppard

Cr Research Group, Department of Physics, University of Johannesburg, PO Box 524, Auckland Park 2006, Johannesburg, South Africa

E-mail: [pankajm@uj.ac.za](mailto:pankajm@uj.ac.za)

**Abstract.** The present work investigates the role of  $\text{Ce}^{3+}$  substitution at the  $\text{Cr}^{3+}$  site on spiral ordering and other magnetic transitions in  $\text{Co}(\text{Cr}_{0.95}\text{Ce}_{0.05})_2\text{O}_4$  nanoparticles. X-ray diffraction (XRD) studies of the sample calcined at  $600^\circ\text{C}$  revealed phase purity along with broadened diffraction peaks which are a signature of the size effect. The crystallite size ( $D$ ) estimated from the XRD was  $6.3 \pm 0.6$  nm. The average particle size calculated from the transmission electron microscopy (TEM) data was found to be  $D_{\text{TEM}} = 8.4 \pm 0.5$  nm, corroborating the XRD results. Electron diffraction patterns confirmed the crystalline nature of the nanoparticles having a bi-pyramidal shape. Magnetization measured as a function of the applied field showed an increase in coercivity as the temperature decreased below the Curie temperature,  $T_C$ . When magnetization was measured as a function of temperature, that indicated the ferrimagnetic behaviour, with  $T_C = 92.5 \pm 0.5$  K (using the “knee-point method”). However, the lock-in temperature observed for the  $\text{Co}(\text{Cr}_{0.95}\text{Ce}_{0.05})_2\text{O}_4$  nanoparticles,  $T_L = 15 \pm 2$  K, is in agreement with that previously reported for pure  $\text{CoCr}_2\text{O}_4$ . Interestingly the spiral ordering was smeared by substituting  $\text{Ce}^{3+}$  at the  $\text{Cr}^{3+}$  site. The present work describes the impact of rare-earth  $\text{Ce}^{3+}$  ion substitution at the  $B$  site that can alter the exchange interaction in such a way that causes the suppression of the spin spiral modulation.

## 1. Introduction

Broken inversion symmetry of the spin behaviour is observed in compounds that have a spiral ordering which leads to ferroelectricity [1].  $\text{CoCr}_2\text{O}_4$  is such a compound that has a complex conical-spiral spin ordering of ferrimagnetic nature that has a spontaneous magnetization [2]. This observed spiral ordering has been found to induce ferroelectric polarization [3]. The crystal structure of  $\text{CoCr}_2\text{O}_4$  is cubic spinel, where tetrahedral  $A$  sites are occupied by  $\text{Co}^{2+}$  and the octahedral  $B$  sites by  $\text{Cr}^{3+}$  [2, 3]. Isotropic antiferromagnetic  $A$ - $B$  and  $B$ - $B$  exchange interactions ( $J_{AB}$  and  $J_{BB}$ ) among the nearest neighbours with  $J_{BB}/J_{AB} > 2/3$ , gives the solution for the ferrimagnetic spiral ground state having the spins located on the conical surfaces [4, 5]. The properties of a ferrimagnetic (FiM) material can be understood by the combination ferromagnetic (FM) and antiferromagnetic (AFM) orderings [6]. The basic ordering of spins in the compound is AFM with unequal magnitudes that lead to a net FM order in the case of ferrimagnetic materials [6]. For  $\text{CoCr}_2\text{O}_4$ , the onset of ferrimagnetic transition occurs at  $T_C = 93$  K, and subsequent lowering of the temperature leads to a cross-over to the conical spin state with a uniform and transverse spiral spin state possessing an incommensurate propagation vector at  $T_S = 26$  K [3,7]. The lock-in transition occurs at  $T_L$  at a temperature of about 15 K, indicating the incommensurate to commensurate phase transition [8]. In a single crystal of  $\text{CoCr}_2\text{O}_4$ , the occurrence of ferroelectricity is concomitant with the conical spin modulation, which is also responsible for spontaneous magnetization [3]. Yamasaki et al. [3] confirmed the robust clamping between the ferromagnetic and ferroelectric domains leading to the multiferroic properties. Choi et al. [2] experimentally demonstrated the abrupt

jump in polarization and change in the sign at  $T_L$  with variation in temperature or change in isothermal magnetization without altering its direction at  $T_L$  and keeping the sign of the spiral wave vector unaltered.

To further understand the observed low-temperature transitions, works have been reported on polycrystalline [9], nanoparticle [10-13] and thin film [14, 15] based  $\text{CoCr}_2\text{O}_4$  samples. As the magnetic interaction strongly depends on the  $J_{AB}$  and  $J_{BB}$ , the effect of substituting either *A*-or *B*-site cations was found to be effective on the magnetic transitions at  $T_C$ ,  $T_S$  and  $T_L$  when different cations were substituted either at Co or Cr sites. The role of Ni [15-17], Cu [18], Mn [19], Mg [20], Ge [21] substitution at Co site, and Fe substitution [22, 23] at Cr sites have been explored by several groups. However, the substitution of a rare earth cation in  $\text{CoCr}_2\text{O}_4$  has not been investigated. In ferrites, with the formula  $M(\text{Fe}_2\text{O}_4)$  where *M* is a metal that can form divalent bonds, it has been found that the addition of a small amount of rare-earth ions significantly modifies the structural, magnetic and electric properties, depending on the rare-earth dopant used and its concentration [24]. Rare-earth ions possess unpaired *4f* electrons and strong spin-orbit coupling of angular momentum. The substitution of rare earth ions (*R*) into the  $\text{CoCr}_2\text{O}_4$  at Cr site can result in *R*-Cr interaction (*3d-4f* coupling) that may lead to modification of magnetic properties similar to that observed in rare-earth doped ferrites [25]. Cerium is the most abundant rare-earth element belonging to the lanthanide series having an atomic number of 58, which exhibits catalytic properties because of the shielding of *5p* and *4d* electrons in the *4f* orbital [26]. Cerium oxides demonstrate both 3+ and 4+ state that enables oxides of the form of  $\text{CeO}_2$  and  $\text{CeO}_{2-x}$  [26]. Thus, substitution using rare-earth  $\text{Ce}^{3+}$  substitution in  $\text{CoCr}_2\text{O}_4$  should be interesting to investigate that can manipulate the *R*- $\text{Cr}^{3+}$  interaction. The present work, therefore, discusses the role of  $\text{Ce}^{3+}$  substitution at the  $\text{Cr}^{3+}$  site on the structure and magnetic properties of  $\text{CoCr}_2\text{O}_4$ .

## 2. Experimental

Powder samples of  $\text{Co}(\text{Cr}_{0.95}\text{Ce}_{0.05})_2\text{O}_4$  were synthesized by sol-gel techniques [18]. In this process, stock solutions of 0.5 M cobalt nitrate ( $\text{Co}(\text{NO}_3)_2 \cdot 6\text{H}_2\text{O}$ ), chromium nitrate ( $\text{Cr}(\text{NO}_3)_3 \cdot 9\text{H}_2\text{O}$ ) and cerium chloride ( $\text{CeCl}_3 \cdot 7\text{H}_2\text{O}$ ) were prepared. The desired amount of the aforementioned solutions was taken in a beaker and stirred for one hour in order to obtain a homogeneous mixture. After an hour, 40 ml of ethylene glycol was added and the solution was stirred for another hour using a magnetic stirrer, whereafter, the solution was allowed to rest for 24 hours. The solution was then heated to evaporate the liquid. The remaining residue in the beaker was dried on a hot plate to obtain the powder. The residue was crushed to a fine powder and subsequently calcined at 600 °C in a box furnace for one hour.

The crystal structure of the samples was analyzed using a PAN Analytical X-ray Diffractometer (XRD) with *Cu-K $\alpha$*  radiation ( $\lambda = 1.54056 \text{ \AA}$ ). The microstructure of the calcined powder samples was studied using a JEM-2100 transmission electron microscope (TEM). Selected area electron diffraction (SAED) and energy-dispersive x-ray spectroscopy (EDS) of the samples were done using the same instrument. A 14 T Cryogen Free Physical and Magnetic Measurement System (CRYOGENIC Ltd., UK) with a vibrating sample magnetometer (VSM) insert was employed to carry out temperature and probing field-dependent magnetization measurements.

## 3. Results and discussion

Figure 1 (a) depicts the Rietveld refinement of the x-ray diffraction (XRD) pattern for the  $\text{Co}(\text{Cr}_{0.95}\text{Ce}_{0.05})_2\text{O}_4$  sample using the GSAS II software package [27]. The broadening of the peaks and the low intensity related to the background are ascribed to the size effect [28]. However, the diffraction peaks related to the major (111), (220), (311), (222), (400), (422), (511), (440) and (533) reflections of the  $\text{CoCr}_2\text{O}_4$  phase are distinct and could be labeled, as shown in Figure 1 (a). The lattice parameters and position coordinates obtained from the refinement are tabulated in Table 1. The ionic radius of  $\text{Ce}^{3+}$  in octahedral coordination is 1.101 Å compared to the  $\text{Cr}^{3+}$  ionic radii of 0.615 Å [29]. Even the large

ionic radii of  $\text{Ce}^{3+}$  compared to  $\text{Co}^{2+}$  (0.58 Å) forces it to occupy the *B* sites. Because of the large ionic radii of  $\text{Ce}^{3+}$ , the solubility of it in a matrix having ions of smaller ionic radii will decrease [30]. The obtained lattice parameter of 8.321 Å (Table 1) is similar in value to the reported lattice parameter of  $\text{CoCr}_2\text{O}_4$  of 8.326 Å [31]. In addition, the effect of larger ionic radii of  $\text{Ce}^{3+}$  has been found to restrict crystal growth, and as a consequence, a reduction in the mean particle size was observed [30].

In order to estimate the average particle size and micro-strain, the Williamson-Hall (W-H) equation [32] was used:

$$\beta \cos\theta = \frac{K\lambda}{D} + 4\varepsilon \sin\theta, \quad (1)$$

where  $\beta$  the FWHM (full width at half maxima),  $K$  is the shape factor (taken as 0.6 considering spherical particles),  $\lambda$  is the x-ray wavelength and  $D$  is the average crystallite size and  $\varepsilon$  is the micro-strain induced in powders due to crystal imperfection and distortion [32]. Plotting ( $\beta \cos\theta$ ) as a function of ( $4\sin\theta$ ) as shown in Figure 1 (b) one can estimate  $\varepsilon$  and  $D$  from the slope and intercept, respectively. The calculated value of  $D$  is  $6.3 \pm 0.6$  nm, and the negative slope of the plot gives the value  $\varepsilon = -0.002 \pm 0.001$ . Negative values of  $\varepsilon$  ( $-9.86 \times 10^{-4}$ ) were previously reported by Choudhary et al. [33] for  $\text{CoCr}_2\text{O}_4$  nanoparticles. In the present case, adding  $\text{Ce}^{3+}$  is found to increase the strain. The occurrence of micro-strain also manifests a large surface-to-volume ratio and crystal field stabilization energy (CFSE) for the synthesized nanoparticles [33]. Nanoparticles which possess higher surface to volume ratio have a direct relationship between the average crystallite size and induced micro-strain [33]. The negative value of the strain is an indicative of compressive strain in the crystallites and nanoparticles [34]. Thus, it can be affirmed that 600 °C is sufficient for the particles' phase formation.

In order to obtain the particle size and determine the crystallinity of the particles, transmission electron microscopy (TEM) with selected area diffraction (SAED) and high-resolution electron microscopy (HREM) were used. Figure 2 (a) shows the TEM image of the nanoparticles. The particles are well dispersed but non-uniform in size, with sizes ranging between 5 nm to 45 nm. In Figure 3 (a) the particle size histogram is given, together with a log-normal fit [35]. The average particle size was obtained from the TEM images at various locations and is found to be  $8.4 \pm 0.5$  nm. The average particle size corroborates the particle size obtained from the XRD results.

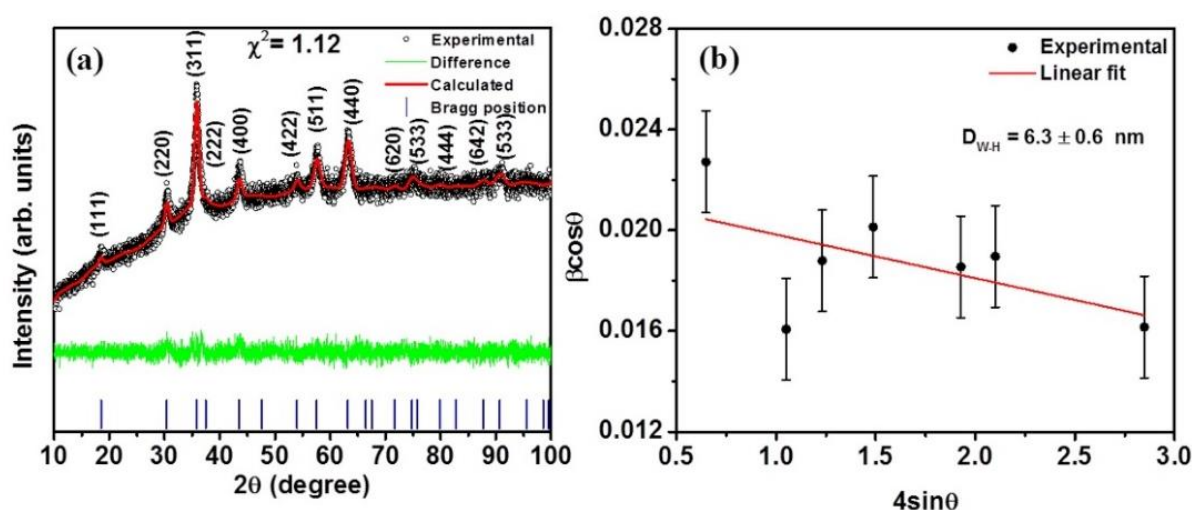


**Figure 1.** (a) Rietveld refinement of the XRD pattern of  $\text{Co}(\text{Cr}_{0.95}\text{Ce}_{0.05})_2\text{O}_4$  nanoparticles, where the black symbols are the measured data and red the Rietveld refined fit. (b) Williamson-Hall (W-H) plot for the sample.

**Table 1.** Position coordinates obtained from the Rietveld refinement ( $a = b = c = 8.32127$  (Å),  $\alpha = \beta = \gamma = 90$ ,  $wR = 2.38$  %,  $\chi^2 = 1.12$  and  $GOF = 1.06$ )

	x-coordinate (Å)	y- coordinate (Å)	z- coordinate (Å)
Co	0.12500	0.12500	0.12500
Cr	0.50000	0.50000	0.50000
O	0.25176	0.25176	0.25176
Ce	0.50000	0.50000	0.50000

Distinct spots are observed in the SAED image, shown as an inset to Figure 2 (a), taken from particles in the image of Figure 2 (a), confirming the crystallinity of the particles. HREM image given in Figure 2 (b) clearly shows the lattice fringes and bi-pyramidal shape. The lattice fringes are labeled as (111) planes of the cubic lattice (see Figure 2 (b)), which agrees with the crystallite size. The presence of elements, especially the rare-earth  $Ce^{3+}$ , was confirmed by energy-dispersive x-ray spectroscopy (EDS), as shown in Figure 3 (b). The peaks related to Cu and C arise from the carbon-coated Cu-grid used for the imaging.

To explore the magnetic transitions, magnetization (zero field cooled ( $M_{ZFC}$ ) and field cooled ( $M_{FC}$ )) as a function of temperature was measured using an encapsulated sample with a probing field of 0.01 T; results are shown in Figure 4 (a). The irreversible temperature where  $M_{ZFC}$  and  $M_{FC}$  bifurcate, was found to be at  $102 \pm 2$  K. The overall temperature behaviour of the Ce doped sample resembles that of  $CoCr_2O_4$  [30]. A minimum in magnetization at  $T = 15 \pm 2$  K in  $M_{FC}$  can be attributed to the  $T_L$  in the case of  $CoCr_2O_4$ . The feature related to spiral ordering which is observed at 26 K [3, 7] in  $CoCr_2O_4$ , is not observed in the present case. Zákutná et al. [13] found a critical size equal to 4.4 (1) nm above which spin-spiral can exist. A minimum spin-spiral period that can be accommodated in the nanoparticle of the size of 6.4 (1) nm has been reported by the same author [13]. In the present case, even though the particle size is above the critical size value, the absence of spiral ordering suggests the possible role of  $Ce^{3+}$  addition. W-H results already indicated a larger value of  $\epsilon$  in the present case compared to the

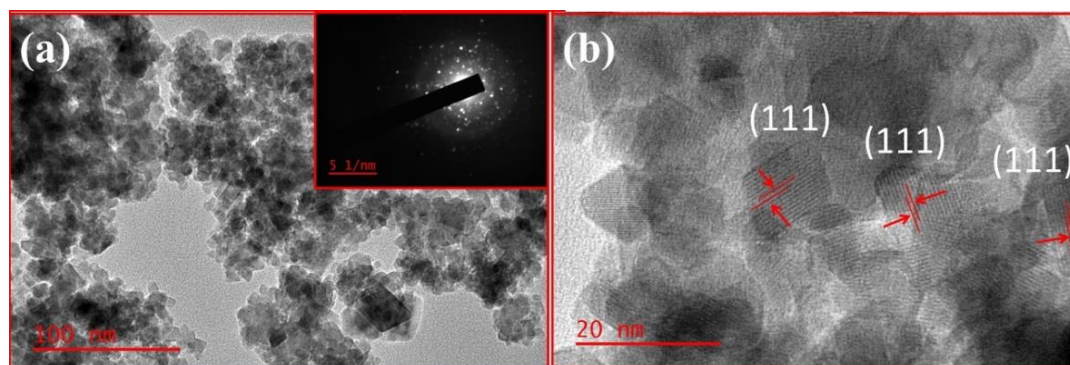


**Figure 2.** (a) TEM image of  $Co(Cr_{0.95}Ce_{0.05})_2O_4$  nanoparticles (inset shows the SAED pattern) and (b) HR-TEM image of  $Co(Cr_{0.95}Ce_{0.05})_2O_4$  nanoparticles showing lattice fringes related to (111).

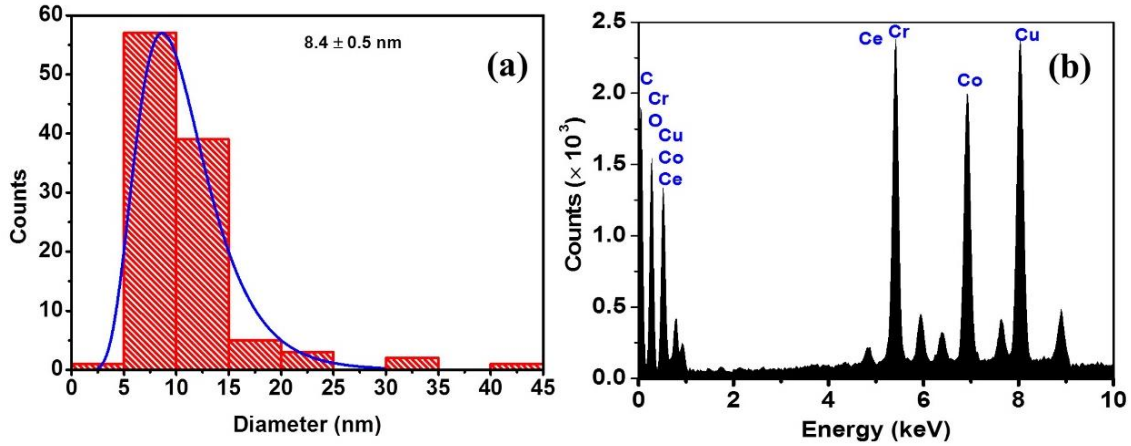


**Figure 3.** (a) Particle size histogram for  $\text{Co}(\text{Cr}_{0.95}\text{Ce}_{0.05})_2\text{O}_4$  nanoparticles resulted from TEM imaging and (b) EDS results for  $\text{Co}(\text{Cr}_{0.95}\text{Ce}_{0.05})_2\text{O}_4$  nanoparticles.

$\text{CoCr}_2\text{O}_4$  nanoparticles [33]. The disappearance of  $T_S$  was also noticed in epitaxial  $\text{CoCr}_2\text{O}_4$  thin films, where the role of strain was significant [15]. In  $\text{CoCr}_2\text{O}_4$  polycrystalline samples, applying external hydrostatic pressure up to 10 kbar using silicon oil as the pressure medium could only shift the  $T_S$  at a rate of about 0.1 K per kbar to high temperatures as a consequence of geometric frustration [36]. Hence, in the present case, the role of chemical pressure, created by doping an element chemically during the crystal formation, is found to be more dominant in alternating magnetic transitions.

Figure 4 (b) shows  $dM/dT$  plotted as function of temperature. The plot yields a minimum at  $86.6 \pm 0.3$  K indicating the  $T_C$  (Figure 4 (b)). On the other hand, using the “knee-point method” as used earlier [17], the value of  $T_C$  is estimated to be  $92.5 \pm 0.5$  (Figure 4 (c)). However, previous studies hinted that various methods to obtain  $T_C$  might be misleading, as in both methods, an external magnetic field was applied [31]. So far, the best method to find  $T_C$  is by neutron diffraction method, which is measured without any external magnetic field [31] that can be done in the future. Further, to understand deeper the  $\Delta M = |M_{FC} - M_{ZFC}|$  as a function of temperature has been plotted in Figure 4 (d). This clearly shows the double slope of the difference in the magnetization curve just below the Curie temperature. This type of double slope feature in  $\Delta M$  as a function of temperature was not observed in the case of Ni substituted  $\text{CoCr}_2\text{O}_4$  [31]. It is important to note that rare-earth Ce metal has a magnetic ordering below 12.5 K along with a magnetic moment of  $2.4 \mu_B$  [37]. The absence of any transition around that temperature indicates the absence of Ce in metallic form in the present nanoparticles.

The magnetization as a function of magnetic field ( $M(\mu_0 H)$ ) at constant temperature was performed at 3 K, 50 K, 75 K, 85 K, 95 K and 150 K. Figure 5 (a) shows the hysteresis loop measured at 3 K. The hysteresis loop reveals two observable kinks at field  $\mu_0 H = \pm 2.3$  T. Figure 5 (b) shows the hysteresis loops measured at 50 K, 75 K and 85 K. The coercivity significantly decreased compared to the hysteresis loop measured at 3 K. The hysteresis loop suggests the presence of uncompensated spins at the surface that behave like a paramagnet giving rise to a linear increase in magnetization once the loop closes with increasing the applied field [11]. Figure 5 (c) shows the hysteresis loop measured at 95 K and 150 K. Persistence of hysteresis up to 95 K suggests the  $T_C$  value to be higher than that, contrary to the observed  $T_C$  obtained by the “knee-point method”.

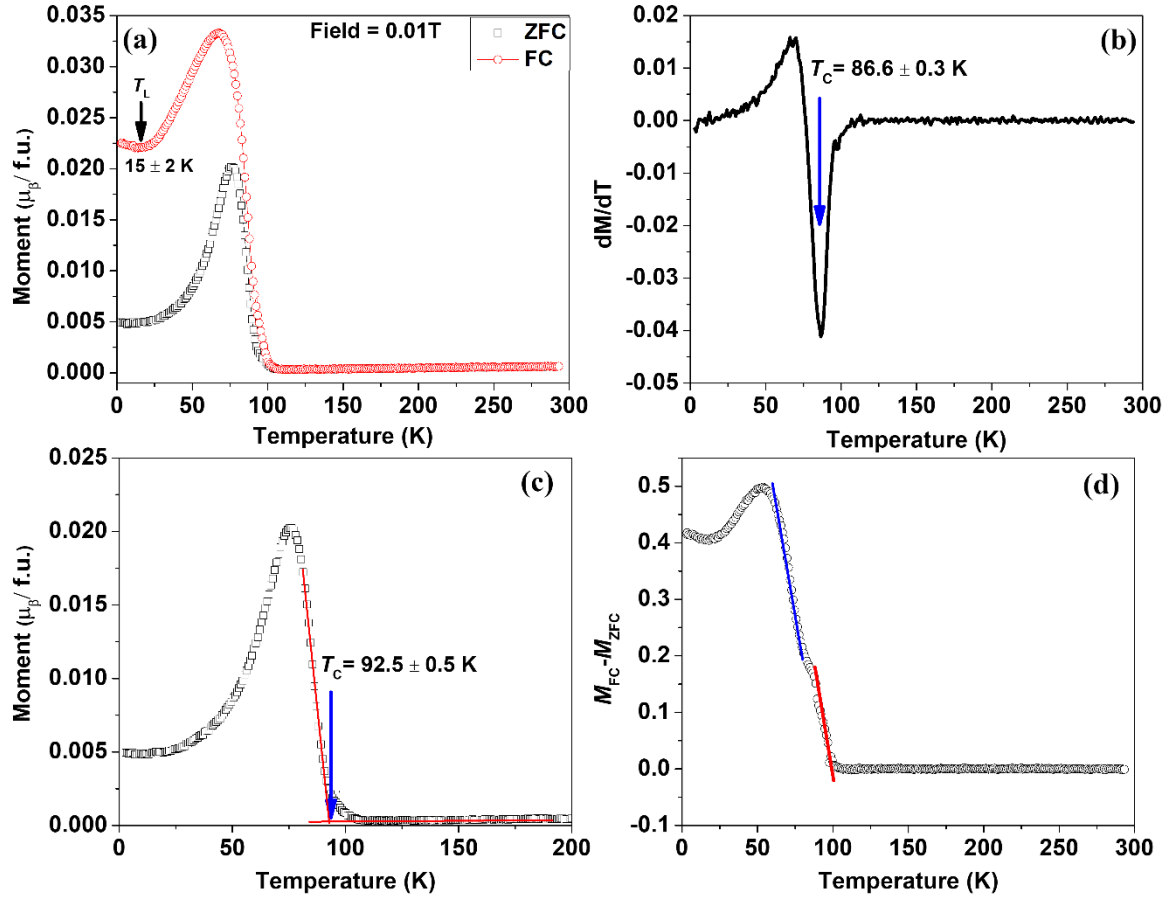


**Figure 4.** (a) Temperature-dependent magnetization measured with ZFC and FC protocols for  $\text{Co}(\text{Cr}_{0.95}\text{Ce}_{0.05})_2\text{O}_4$  nanoparticles, (b) First order derivative of the ZFC magnetization data as function of temperature for  $\text{Co}(\text{Cr}_{0.95}\text{Ce}_{0.05})_2\text{O}_4$  nanoparticles, (c) Estimation of  $T_C$  using knee-point method and (d)  $\Delta M = |M_{FC} - M_{ZFC}|$  values as function of temperature for  $\text{Co}(\text{Cr}_{0.95}\text{Ce}_{0.05})_2\text{O}_4$  nanoparticles.

However, at 150 K, the magnetization traces a linear curve indicative of paramagnetic nature, which is in accordance with the  $M$ - $T$  results. In Figure 5 (d), the hysteresis loops are shown for measurements done at 50 K, 75 K and 85 K. The hysteresis loops appeared to be opened up above and below the zero applied field regime. The feature is most distinct for the loop measured at 75 K and 85 K (see Figure 5 (d)). Similar constricted hysteresis loop can be attributed to the various exchange interaction among the magnetic cations at different atomic sites [18]. Upon careful observation of the virgin curve (see Figure 5 (d)), an increase in magnetization with an applied magnetic field shows that the magnetization increases going from 50 K to 75 K and then reduces in the case of 85 K. Such anomalous behaviour can be linked to the temperature dependent magnetization as reflected in Figure 5 (a). Locating the magnetization values at 50 K, 75 K and 85 K in the  $M_{ZFC}$  plot can explain the abnormal increases and then decrease in magnetization in the hysteresis loops measured from 50 K to 85 K.

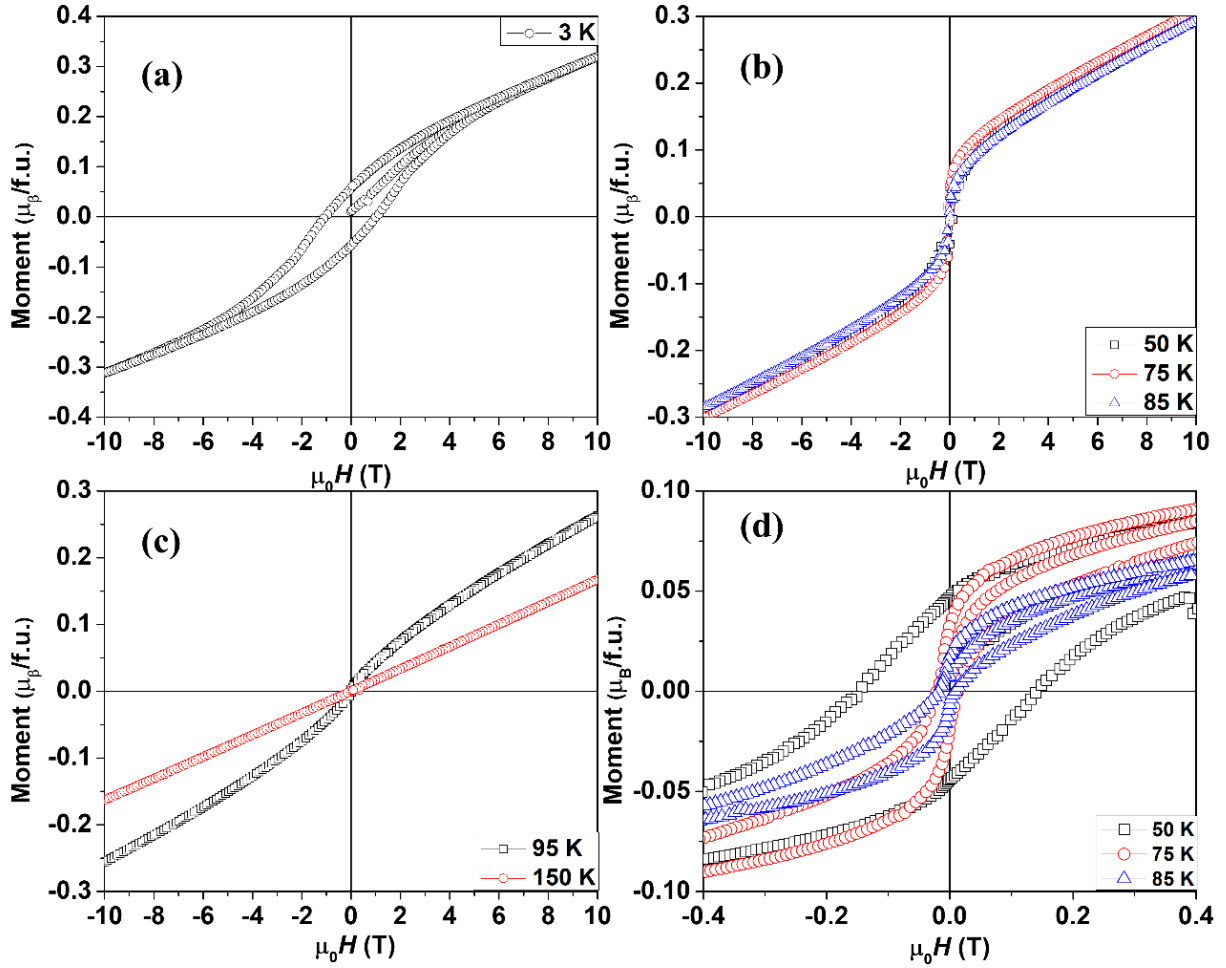


**Figure 5.** Magnetic field dependent magnetization measurement,  $M(\mu_0H)$ , for  $\text{Co}(\text{Cr}_{0.95}\text{Ce}_{0.05})_2\text{O}_4$  nanoparticles at (a) 3 K, (b) 50 K, 75 K and 85 K, (c) 95 K and 150 K, (d) Zoomed view around zero field regime for 50 K, 75 K and 85 K.

The fundamental magnetic parameters such as saturation magnetization ( $M_s$ ), remanence ( $M_r$ ) and coercivity ( $\mu_0H_c$ ) obtained from the hysteresis loops are tabulated in Table 2. The squareness of the hysteresis loops can be estimated by the parameter  $M_r/M_s$ , which is also tabulated in Table 2. The obtained ratios are less than 0.5 (except for 3 K) indicating magnetic multi-domains [38].

**Table 2.** Magnetic parameters obtained from temperature dependent hysteresis loops.

Temperature K	$M_s$ ( $\mu_B/\text{f.u.}$ )	$M_r$ ( $\mu_B/\text{f.u.}$ )	$\mu_0H_c$ (T)	Squareness ( $M_r/M_s$ )
3	0.31	0.57	1.038	1.84
50	0.30	0.05	0.995	0.17
75	0.31	0.03	0.017	0.10
85	0.29	0.02	0.015	0.07
95	0.26	0.004	0.030	0.015

#### 4. Conclusion

$\text{Co}(\text{Cr}_{0.95}\text{Ce}_{0.05})_2\text{O}_4$  nanoparticles were synthesized by a cost-effective sol-gel technique. The phase formation was achieved by calcining the powder samples at 600 °C. XRD confirms the phase purity, and the average crystallite was determined to be  $6.3 \pm 0.6$  nm. Careful analysis of the TEM results indicated a non-uniform distribution of particles with a mean particle size of  $8.4 \pm 0.5$  nm, obtained from the log-normal distribution of many bi-pyramidal particles.  $M_{\text{ZFC}}(T)$  and  $M_{\text{FC}}(T)$  measurements at low temperatures showed significant irreversibility and disappearance of spiral ordering, which is characteristic of the  $\text{CoCr}_2\text{O}_4$  phase. The low temperature hysteresis loops measured 50, 75 and 85 K showed the anomalous constricted nature around zero applied fields. Retention of the hysteretic behaviour up to 95 K clearly indicates the value of  $T_C$  beyond this value. The present work shows the potential impact of rare-earth  $\text{Ce}^{3+}$  ion substitution at the  $B$  site that can alter the exchange interaction in such a way that causes suppression of the spin modulation.

#### Acknowledgements

Financial aid from the SANRF (Grant No: 120856) and the UJ URC and FRC are acknowledged. The use of the NEP Cryogenic Physical Properties Measurement System at UJ, obtained with financial support from the SANRF (Grant No: 88080) and UJ, RSA, is acknowledged. The use of the Spectrum Analytical Facility in the FoS at UJ is conceded.

#### References

- [1] Khomskii D I 2006 *J. Magn. Magn. Mater.* **306** 1-8
- [2] Choi Y J, Okamoto J, Huang D J, Chao K S, Lin H J, Chen C T, Van Veenendaal M, Kaplan T A and Cheong S W. 2009 *Phys. Rev. Lett.* **102** 067601
- [3] Yamasaki Y, Miyasaka S, Kaneko Y, He J P, Arima T and Tokura Y 2006 *Phys. Rev. Lett.* **96** 207204
- [4] Lyons D H, Kaplan T A, Dwight K and Menyuk N 1962 *Phys. Rev.* **126** 540
- [5] Menyuk N. Magnetism. In Modern Aspects of Solid State Chemistry 1970 (pp. 159-217). Springer, Boston, MA
- [6] Majumdar K and Mahanti S D 2021 *J. Phys.: Condens. Matter* **33** 125801
- [7] Dzyaloshinsky I 1958 *J. Phys. Chem. Solids* **4** 241-55
- [8] Funahashi S, Morii Y and Child H R 1987 *J. App. Phys.* **61** 4114-6
- [9] Lawes G, Melot B, Page K, Ederer C, Hayward M A, Proffen T and Seshadri R 2006 *Phys. Rev. B* **74** 024413.
- [10] Dutta D P, Manjanna J and Tyagi A K 2009 *J. Appl. Phys.* **106** 043915
- [11] Kumar L, Mohanty P, Shripathi T and Rath C 2009 *Nanosci. Nanotech. Lett.* **1** 199-203
- [12] Zákutná D, Vlček J, Fítl P, Nemkovski K, Honecker D, Nižňanský D and Disch S 2018 *Phys. Rev. B* **98** 064407
- [13] Zákutná D, Alemayehu A, Vlček J, Nemkovski K, Grams C P, Nižňanský D, Honecker D and Disch S 2019 *Phys. Rev. B.* **100** 184427
- [14] Windsor Y W et al 2017 *Phys. Rev. B* **95** 224413
- [15] Mohanty P et al 2020 *Nanotechnology* **31** 285708
- [16] Bush A A, Shkuratov V Y, Kamentsev K E, Prokhorov A S, Zhukova E S, Gorshunov B P and Torgashev V I. 2012 *Phys. Rev. B* **85** 214112
- [17] Mohanty P, Sheppard C J, Prinsloo A R, Roos W D, Olivi L and Aquilanti G 2018 *J. Magn. Magn. Mater.* **451** 20-8
- [18] Mohanty P, Sheppard C J, Doyle B P, Carleschi E and Prinsloo A R 2021 *AIP Advances* **11** 025113
- [19] Nadeem K, Rehman H U, Zeb F, Ali E, Kamran M, Noshahi N A and Abbas H 2020 *J. Alloys. Comp.* **832** 155031
- [20] Rahman S, Saqib H, Zhang J, Errandonea D, Menéndez C, Cazorla C, Samanta S, Li X, Lu J and Wang L.

- 2018 *Phys. Rev. B* **97** 174102
- [21] Hernández N O et al 2021 *Phys. Rev. B* **103** 085123
- [22] Mohanty P, Prinsloo A R, Sheppard C J and Roos W D 2018 *Acta Phys. Pol. A.* **133** 574-7
- [23] Li C L, Yan T Y, Barasa G O, Li Y H, Zhang R, Fu Q S, Chen X H and Yuan S L 2018 *Ceram. Intern.* **44** 15446-52
- [24] Rahimi-Nasrabadi M, Behpour M, Sobhani-Nasab A and Jeddy M R 2016 *J. Mater. Sci: Mater Electron* **27** 11691-7
- [25] Hashim M, Raghasudha M, Meena S S, Shah J, Shirsath S E, Kumar S, Ravinder D, Bhatt P, Kumar R and Kotnala R K 2018 *J. Magn. Magn. Mater.* **449** 319-27
- [26] Singh K R, Nayak V, Sarkar T and Singh R P 2020 *RSC Adv* **10** 27194–27214
- [27] Toby B H and Von Dreele R B 2013 *J. Appl. Cryst.* **46** 544-9
- [28] Rath C, Mohanty P, Pandey A C and Mishra N C 2009 *J. Phys. D: Appl. Phys.* **42** 205101
- [29] Shannon R D 1976 *Acta Crystallographica Section A* **32** 751-67
- [30] Ghosh M P and Mukherjee S 2020 *J. Mater. Sci: Mater Electron* **31** 6207-16
- [31] Mohanty P, Venter A M, Sheppard C J and Prinsloo A R 2020 *J. Magn. Magn. Mater.* **498** 166217
- [32] Mote V D, Purushotham Y and Dole B N 2012 *J. Theor. Appl. Phys.* **6** 1-8
- [33] Choudhary P, Saxena P, Yadav A, Sinha A K, Rai V N, Varshney M D and Mishra A 2019 *J. Sup. Conduct. Nov. Magn.* **32** 2639-45
- [34] Tripathi A K, Mathpal M C, Kumar P, Singh M K, Soler M A and Agarwal A 2015 *J. Alloy. Comp.* **622** 37-47
- [35] Zákutná D, Repko A, Matulková I, Nižňanský D, Ardu A, Cannas C, Mantlíková A and Vejpravová 2014 *J. Nanopart. Res.* **16** 1-4
- [36] Chen X, Yang Z, Xie Y, Huang Z, Ling L, Zhang S, Pi L, Sun Y and Zhang Y 2013 *J. Appl. Phys.* **113** 17E129
- [37] Lock J M 1957 *Proc. Phys. Soc. B* **70** 566
- [38] Alshahrani B, ElSaeedy H I, Korna A H, Yakout H A, Maksoud M I, Fahim R A, Gobara M and Ashour AH 2021 *J. Mater. Sci: Mater Electron* **32** 780-97

# Computational analyses of graphene quantum dots for anode material in lithium-ion batteries

TM Mlotshwa<sup>1</sup>, L Jhamba<sup>1</sup>, NE Maluta<sup>1,2</sup>, JK Kirui<sup>1,2</sup>

<sup>1</sup>Department of Physics, University of Venda, P/Bag X 5050, Thohoyandou, 0950, South Africa

<sup>2</sup>National Institute for theoretical and Computational Sciences (NITheCS), Gauteng 2000, South Africa

E-mail: [thokozaanimxolisi@gmail.com](mailto:thokozaanimxolisi@gmail.com)

**Abstract.** Many renewable energy technologies are underperforming due to lack of optimal energy collection and storage. Renewable energy generation is not available all the time, it happens when the wind blows or the sun shines, storage is an essential part. Alongside, lithium-ion (LI) batteries are dominating the market as storage devices with recent advances towards the electric vehicles and renewable energy storage. Exploiting high capacity anode materials is one of the most effective ways to construct high energy density LI batteries. Energy, power, charge-discharge rate, cost, cycle life, safety and environmental impact are some of the parameters that need to be considered in adopting optimal LI batteries. As the recent development of batteries is mostly towards solid state batteries, small and high energy density materials are required. Graphene quantum dots (GQDs) have broad prospects in energy storage and conversion. First principle calculations are used to analyze optical properties of GQDs. The UV-vis spectra shows the maximum absorption peak at 750 nm within the edge of the visible region of the solar spectrum, thus favorable for renewable energy storage. Computational analyses strongly suggest the future development trend of GQDs research and its opportunities in energy storage devices.

## 1. Introduction

Lithium-ion (LI) batteries are one of the most used energy storage devices in many electronics to date. From small electronics, cellphones, laptops and toys to bigger machines such as electric vehicles, LI batteries play a huge role in making this machines work. LI batteries are also entering the renewable energy storage space with more pressure on the reduction of fossil fuel based energy production. This will help many countries reduce the cost of energy and can supply energy to everyone by harnessing clean natural energy from wind and solar. Renewable energy sources such as wind and solar are frequently fluctuating due to the ever-changing atmospheric conditions resulting in insufficient wind or sunshine. LI batteries have the potential to be fully utilized in various applications such as electric vehicles, renewable energy storage and electronics due to their countless advantages such as, longer life, high charge discharge rate, light weight, temperature tolerant, higher voltage and high power and energy density [1]. Currently used lithium-ion batteries contain mostly graphite as anode material.

The more reliable LI batteries still need more attention of the electrodes, in particular the graphite anode, some of whose downside experiences are, lower purity and more side reactions, instability of the layered structure, which can easily collapse after a long charging and high irreversible loss due to large surface areas, which consume available lithium ions and therefore reduce the battery energy density. LI batteries are considered because they have high energy density (120 - 150 Wh/kg<sub>cell</sub>), long cyclic stability

which is beneficial for most portable electronics including mobile phones and laptop computers, rapid response and relatively low self-discharge rate [2]. Lithium is also the lightest of all metals as indicated by its position on the periodic table and the most electropositive element which is a measure of how easily it can produce energy.

Graphite is one of the most used materials for the manufacturing of electronics useable for their low electrical resistivity, low thermal expansion and thermal conductivity and resistant to thermal shock [3]. A relatively new carbon-based material, graphene quantum dots (GQDs) has many advantages due to its unique properties that arise from their nanoscale small size [4]. GQDs emerged as novel materials in the recent decade, and have demonstrated superiority in numerous privileged properties. GQDs are considered superior due to facile preparation methodologies, low toxicity, high luminescent properties and high photo-stability against photobleaching and blinking, which have attracted substantial attention [5]. Several studies have evaluated different material for the anode material and yet graphite still gives a better performing energy storage device. The major anode materials used are graphite, nanostructured carbonaceous materials, metal oxides, metal nitrides, metal sulphides, metal phosphide, silicon, germanium, tin, phosphorous antimony, indium etc. [6]. Recent advancements in LI batteries include the solid-state batteries, which promotes the development of small and efficient storage devices.

Desired properties of anode material include porosity of the material, excellent conductivity, voltage match with coupled cathode material, high durability and it must be clean from impurities. Its constituent materials must be cheap and easily available. It must be light in weight and have very low current densities.

The working principle of LI batteries is shown in figure 1, the anode material used is graphite. It operates on the principle of Faradaic reactions in the bulk of the active material. The positive electrode receives electrons from the external circuit. The cathode stores Lithium and releases lithium ions when the battery is charging. A corresponding anode material is required to house the LI and electron pairs during the charging process. The electrolyte is a liquid that acts as a transporter of LI. The porous separator allows for LI to flow freely from the anode to the cathode and vice versa. The anode stores lithium and releases lithium-ions when the battery is discharging [7]. The negative electrode receives electrons from the external circuit during charging of the battery from the positive current collector. In this study, we use computational methods to analyze GQDs for application in renewable energy storage devices particularly the LI batteries. A semi-empirical molecular orbital package known as VAMP was used to carry out the calculations.

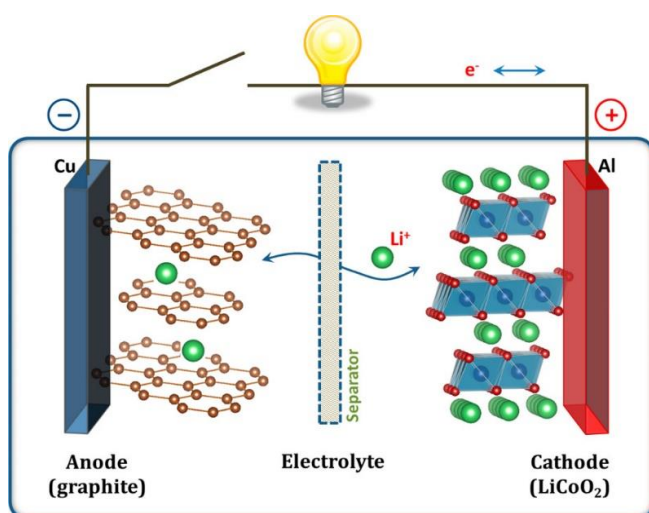


**Figure 1.** Working principle of LI batteries [8]. The anode material used is graphite.

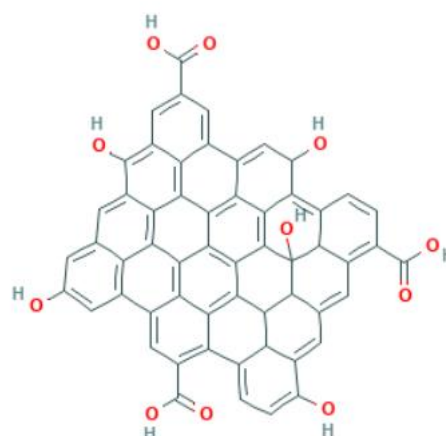


**Figure 2.** Chemical structure of GQDs obtained from PubChem database.

## 2. Computational methodology

GQDs are considered among the recent research interest in carbon based nanomaterials. Very few studies have been done with most being done experimentally [3]. Computational calculations are done using VAMP, a semi-empirical molecular orbital program that has been optimized to be highly numerically stable and fast. It contains many enhancements in comparison with normal geometry optimization methods so that it even optimizes problematic systems successfully. Other features of VAMP are transition state optimization, solvent models, and the calculation of many electronic properties. VAMP is used to determine the UV-vis spectrum and the HOMO (highest occupied molecular orbital) and LUMO (lowest unoccupied molecular orbital) energy orbitals of GQDs.

Since the chemical structure of GQDs is non-periodic, we had to use another computational package that accommodates calculation of density of states (DOS) and partial density of states (PDOS). The DOS and PDOS are determined by the density functional tight binding module (DFTB+) of material studio simulation package. DFTB+ is a semi-empirical tight binding method based on a two-centered approach to density functional theory (DFT), it uses approximations for large and complex structures to make calculations faster [9].

## 3. Results and discussion

### 3.1. Density of states

The density of states is determined by using a unique function, DFTB+ as implemented in the material studio package. Figure 3 shows the contribution of atoms of the GQDs in the Fermi region, the highest occupied and semi occupied orbitals are shown. The dominant states as expected come from the contribution of carbon atoms denoted by the 2p orbital. The highest peak is located at -4 eV of energy followed by a shoulder peak at -3.24 eV and 0 eV. The O-H groups take a small portion with oxygen having the highest peak at -3 eV, which is 17.5 electrons/eV less than the maximum peak of carbon atoms. Between energy regions of -2 to 9 eV, no contributions from hydrogen are observed. The Fermi region is therefore dominated with carbon atoms. The dominant carbon based peak at the centre of the DOS spectrum was also observed by Ortega *et.al* and their study suggested that just like graphene, the DOS vanishes at Fermi level [10]. This is observed through the contribution of the states from the hydrogen atom. The oxygen based states also exhibit this behaviour in the conduction band region, with very small peaks rising very close to the Fermi region.

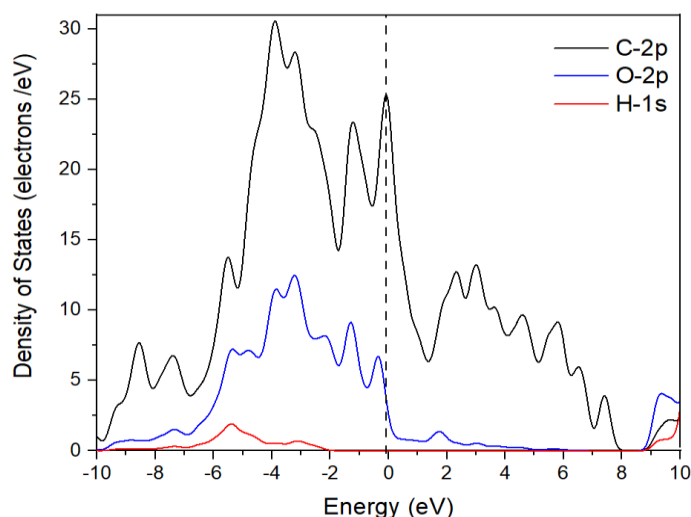


**Figure 3.** Density of states for GQDs calculated from material studios DFTB+ Energy module.

### 3.2. UV-vis spectrum

Figure 4 shows the UV-vis spectrum of GQDs. The UV-vis clearly shows the optical and electronic response of the material with longer wavelengths indicating less energy than shorter wavelengths. The absorption peak is located at 750 nm which lies at the edge of the visible spectrum hence motivating further investigation of the material. There are very few computational works to compare with this study but a very reasonable number of experimental works such as calculation of electronic absorption spectra by Timofeeva *et.al* [11]. In the study by Changzang *et.al*, there are no peaks observed on the spectrum in the visible region with the highest located at 200 nm, however, the photoluminescence give rise to peaks within the visible region of the solar spectrum [12]. Jauja-Ccana *et.al*, in their molecular dynamics study observes absorption band between 200 and 250 nm caused by electronic transition of the C=C bonds and between 300 and 400 nm corresponding to the electronic transition related to the C=O bonds [13]. These electronic transitions are characteristic of a graphemic materials. The isodensity surfaces of the quantum dot suggests a good absorbing material applicable to battery anode materials. Many studies of GQDs for applications in various fields are recent and thus lack conclusive findings and methodologies as studies are still carried out in this material.

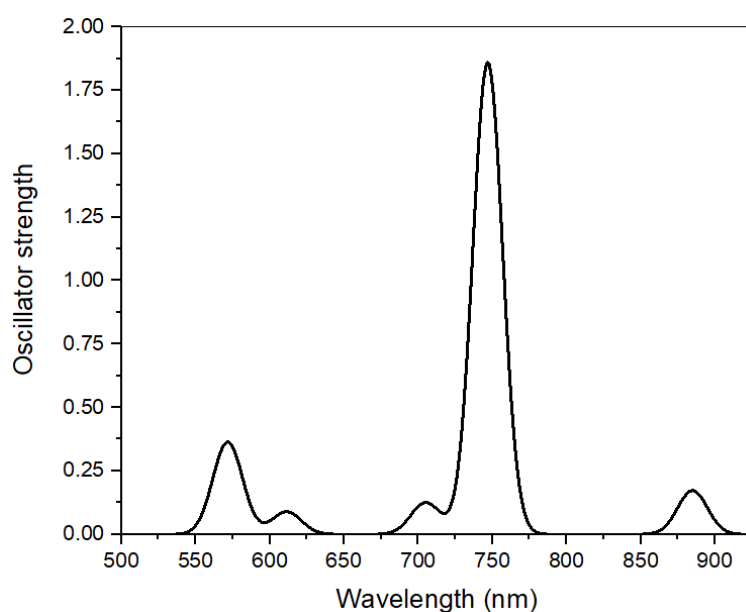


**Figure 4.** UV-vis spectrum of GQDs.

### 3.3. HOMO and LUMO energy orbitals

To analyse the stability of GQDs, molecular orbitals are determined. Figure 5 and 6 shows the HOMO and LUMO energy levels respectively. The HOMO and LUMO densities clearly shows the strength and stability of the material, with clusters of orbitals appearing on the top part and very few around the center. One key component of LI batteries improvement is the stability of its internal components. Clusters of orbitals appear to be attached to the carbon atoms, signaling very strong possibilities of containing only one type of atoms thus further studies can lead to GQDs that are clean from impurities. The HOMO eigenvalue is -7.349 eV while we have energy of -4.641 eV for the LUMO. In determining the HOMO and LUMO energy states of single layered quantum dots (SLGQDs), Bayat *et.al* obtained -7.15 eV and -4.25 eV for the HOMO and LUMO orbitals respectively [14]. The difference between the HOMO and LUMO gives an energy gap of 2.708 eV suggesting properties of semiconductor that can be tuneable to enhance its optical and electronic properties.

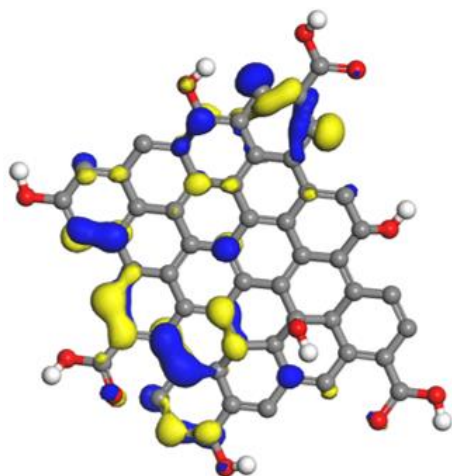


Figure 5. HOMO energy levels.

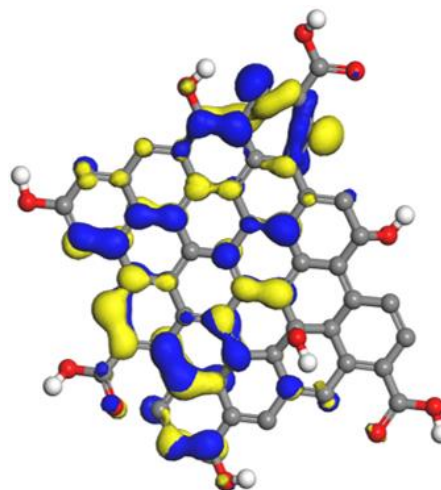


Figure 6. LUMO energy levels.

#### 4. Conclusion

The result shows strong probability of graphene quantum dots to be applied in storage devices. The results generally show good optical, excitation and spectral properties. GQDs have broad prospects in energy storage and conversion. First principle calculations are used to analyze optical properties of GQDs. The UV-vis spectra shows the maximum absorption peak at 750 nm within the edge of the visible region of the solar spectrum with one visible peak in the visible region at 575 nm, thus favorable for renewable energy storage. The HOMO and LUMO energy levels suggests an energy gap of 2.98 eV and hints at the stability of the structure with properties that can be tuneable to obtain GQDs that are clean form impurities. The density of states shows the possibilities of obtaining a pure GQDs structure through proper methods. The highest states around the Fermi region are due to the dominant carbon atoms in the structure. For GQDs to be applicable in LI batteries, one needs to consider a wide range of properties some not presented in this paper. Our results show the existence of tuneable properties to improve optical response of GQDs through the UV-vis spectrum in conjunction with the HOMO and LUMO orbitals, the DOS informs on the stability of the material. Computational analyses strongly suggest the future development trend of GQDs research and its opportunities in energy storage devices. This is due to GQDs satisfying several desired characteristics for anode materials.

#### 5. Acknowledgements

We would like to acknowledge the University of Venda for granting us the opportunity to carry out this research work and the Centre for High Performance Computing (CHPC) for allowing us to use their facilities.

#### References

- [1] T. Kim, W. Song, D.-Y. Son, L. K. Ono and Y. Qi, "Lithium-ion batteries: outlook on present, future, and hybridized technologies," *Journal of Materials Chemistry A*, vol. 7, pp. 2942-2964, 2019.
- [2] H. Fang, "Challenges with the ultimate energy density with lithium-ion batteries," *IOP Conference Series: Earth and Environmental Science*, vol. 781, pp. 1-7, 2021.
- [3] S. Campuzano, P. Yanez-Sedeno and J. M. Pingarron, "Carbon Dots and Graphene Quantum Dots in Electrochemical Biosensing," *Nanomaterials*, vol. 9, no. 634, pp. 1-18, 2019.
- [4] S. Bak, D. King and H. Lee, "Graphene quantum dots and their possible energy applications: A review," *Current Applied Physics*, vol. 16, pp. 1192-1201, 2016.
- [5] J. Diao, T. Wang and L. Li, "Graphene quantum dots as nanoprobes for fluorescent detection of propofol in emulsions," *Royal Society of Open Science*, vol. 6, pp. 1-9, 2019.
- [6] N. Pradeep, E. Sivasenthil, B. Janarthanam and S. Sharmila, "A Review of Anode Material for Lithium Ion Batteries," *Journal of Physics: Conference Series*, vol. 1362, pp. 1-16, 2019.

- [7] Y. Chen, Y. Kang, Y. Zhao, L. Wang, J. liu, y. Li, Z. Liang, X. He, X. Li, N. Tavajohi and B. Li, "A review of lithium-ion battery safety concerns: The issues, strategies and testing standards," *Journal of Energy Chemistry*, vol. 59, no. 2021, pp. 83-99, 2020.
- [8] J. B. Goodenough and k.-S. Park, "The Li-Ion Rechargeable Battery: A Perspective," *Journal of the American Chemical Society*, vol. 135, no. 4, pp. 1167-1176, 2013.
- [9] T. V. Mourik, M. Buhl and M.-P. Gaigeot, "Density functional theory across chemistry, physics and biology," *Philosophical Transactions of the Royal Society*, vol. 372, pp. 1-5, 2014.
- [10] O. Espinosa, I. A. Lukyanchuk and Y. G. Rubo, "Density of states in randomly shaped graphene quantum dots," *Superlattice and Microstructures*, vol. 49, pp. 283-287, 2011.
- [11] T. E. Timofeeva, M. N. Egorova and A. E. Tomskaya, "Calculations of electronic absorption spectra of polycyclic aromatic hydrocarbon models of graphene quantum dots," *AIP Conference Proceedings*, vol. 050022, pp. 1-4, 2021.
- [12] C. Zhao, X. Song, Y. Liu, Y. Fu, L. Ye, N. Wang, F. Wang, L. Li, M. Mohammadniaei, M. Zhang, Q. Zhang and J. Liu, "synthesis of graphene quantum dots and their applications in drug delivery," *Journal of Nanobiotechnology*, vol. 142, no. 18, pp. 1-32, 2020.
- [13] C. Jauja, H. A. V. Cordova, G. T. Feliciano and A. L. Gomez, "Experimental and molecular dynamics study of graphene oxide quantum dots interaction with solvents and its aggregation mechanism," *Journal of Molecular Liquids*, vol. 335, pp. 1-11, 2021.
- [14] A. Bayat and I. E. Saievar, "Sunthesis of green-photoluminescent single layer graphene quantum dots: Determination of HOMO and LUMO," *Journal of Luminescence*, vol. 192, pp. 180-183, 2017.

# Impact of Cr substitution on magnetic properties of cobalt-doped ZnO nanoparticles

H. S. Lokesh<sup>1\*</sup>, A. R. E. Prinsloo<sup>1</sup>, P. Mohanty<sup>1</sup> and C. J. Sheppard<sup>1</sup>

<sup>1</sup>Cr Research Group, Department of Physics, University of Johannesburg, PO Box 524, Auckland Park, Johannesburg, South Africa

E-mail: lokeshahs@uj.ac.za, hslokesh88@gmail.com

**Abstract.** This study focuses on the magnetic properties of  $\text{Zn}_{1-x}\text{Co}_x\text{O}$ , with  $x = 0.01, 0.03$ , and  $\text{Zn}_{0.96}\text{Co}_{0.01}\text{Cr}_{0.03}\text{O}$ , synthesized by solution combustion method. X-ray diffraction (XRD) revealed all the samples are in a hexagonal wurtzite structure. Rietveld refinement gives lattice parameters,  $a = b = 3.246 \text{ \AA}$ , and  $c = 5.201 \text{ \AA}$ , for  $\text{Zn}_{0.99}\text{Co}_{0.01}\text{O}$ ; matching standard data (PDF#36-1451), and marginally increased in  $\text{Zn}_{0.96}\text{Co}_{0.01}\text{Cr}_{0.03}\text{O}$ . The particle size determined using transmission electron microscope images was found to be  $39 \pm 1$ , and  $42 \pm 2 \text{ nm}$  for  $\text{Zn}_{1-x}\text{Co}_x\text{O}$  ( $x = 0.01, 0.03$ ), respectively, and  $14 \pm 2 \text{ nm}$  for  $\text{Zn}_{0.96}\text{Co}_{0.01}\text{Cr}_{0.03}\text{O}$ . Diffuse reflectance spectra show the absorption bands in all the samples at  $569 \text{ nm}$  ( ${}^4A_2(F) \rightarrow {}^4A_1(G)$ ),  $610 \text{ nm}$  ( ${}^4A_2(F) \rightarrow {}^4T_1(P)$ ) and  $660 \text{ nm}$  ( ${}^4A_2(F) \rightarrow {}^2E(G)$ ) are transitions of  $\text{Co}^{2+}$  ions replacing  $\text{Zn}^{2+}$  sites. In Co-Cr doped ZnO, the absorption bands at  $584 \text{ nm}$  ( ${}^4A_{2g}(F) \rightarrow {}^4T_{2g}(F)$ ) and  $715 \text{ nm}$  ( ${}^4A_{2g}(F) \rightarrow {}^2E_g(G)$ ) reflects the transition of  $\text{Cr}^{3+}$  ions in the lattice. Band-gap values found are  $3.306 \pm 0.003$ , and  $3.289 \pm 0.004 \text{ eV}$  for  $\text{Zn}_{1-x}\text{Co}_x\text{O}$  ( $x = 0.01, 0.03$ , respectively) and  $3.285 \pm 0.003 \text{ eV}$  for  $\text{Zn}_{0.96}\text{Co}_{0.01}\text{Cr}_{0.03}\text{O}$ . Magnetic measurements was carried out using a vibrating sample magnetometer. The  $\text{Zn}_{0.96}\text{Co}_{0.01}\text{Cr}_{0.03}\text{O}$  and  $\text{Zn}_{0.97}\text{Co}_{0.03}\text{O}$  samples show hysteretic behaviour in magnetization as function of applied field measurements, signifying RT ferromagnetism (FM). Cobalt-doped ZnO shows diamagnetism for  $x = 0.01$ , while RTFM is seen for the  $x = 0.03$  sample. The observed RTFM are explained based on bound magnetic polaron (BMP) mechanism. The number of BMPs created in  $\text{Zn}_{0.97}\text{Co}_{0.03}\text{O}$  was found to be  $2.5 \times 10^{14} \text{ cm}^{-3}$ . It is suggested that the exchange interaction of  $\text{Co}^{2+}$  and/or  $\text{Cr}^{3+}$  dopants mediated BMPs is ordering RTFM.

## 1. Introduction

Transition metal (TM) doped and co-doped ZnO nanoparticles have been attracting the attention of the scientific community for a few decades due to their promising magnetic properties at above room temperature and applications in spintronics [1,2]. Literature reports state the transition metal [TM: Fe, Mn, Ni, Co, Cr] doped ZnO showed ferromagnetism (FM) behaviour at room temperature, due to the presence intrinsic defects [3,4] or impurity phases [5,6] or ferromagnetic precipitates [7]. In particular, the  $\text{Zn}_{1-x}\text{Co}_x\text{O}$  with  $x \leq 0.05$ , nanoparticles exhibit a paramagnetic behaviour due to the lack of magnetic couplings [8,9]. Some reports showed weak room temperature ferromagnetism (RTFM) with the co-existence of superparamagnetic or paramagnetic behaviour for  $\text{Zn}_{1-x}\text{Co}_x\text{O}$  powder [5,6], this also depends on the synthesis method [4,6,10]. On other hand, the co-doping of the  $\text{Zn}_{1-x}\text{Co}_x\text{O}$  system with TM ions exhibits not only the enhancement of RTFM, but carrier-mediated magnetism can also be achieved through its suitable co-doping, as is reported for ZnO co-doped with the combination of Fe-Co [11], Cr-Co [12,13], Mn-Co [14], Cu-Co [15] and Al-Co [16] ions. TM ions co-doping play a key

role in altering the magnetic properties, from paramagnetic to antiferromagnetic or ferromagnetic behaviour at RT for  $Zn_{1-x}Co_xO$  system. However, the structure and magnetic properties of Cr-Co co-doped ZnO have been probed to a lesser extent. For this reason in this contribution explores the structure, optical and magnetic properties of Cr-Co co-doped ZnO samples synthesized by solution combustion method. In this work, the structure and morphology of the as-synthesized samples were examined using x-ray diffraction (XRD) and transmission electron microscopy (TEM). The optical and magnetic properties were probed using diffuse reflectance spectroscopy (DRS) and vibrating sample magnetometer (VSM), respectively. The role of Cr co-doping in  $Zn_{1-x}Co_xO$  to in initiating RTFM ordering and its effect on the optical properties are discussed.

## 2. Experimental details

$Zn_{1-x}Co_xO$ , with  $x = 0.01$  and  $0.03$ , and  $Zn_{0.96}Co_{0.01}Cr_{0.03}O$  samples were synthesized using the solution combustion method [17]. Sigma-Aldrich products of  $Zn(NO_3)_2 \cdot 6H_2O$  (98% c),  $NH_2CH_2COOH$  (99%),  $Co(NO_3)_2 \cdot 6H_2O$  and  $Cr(NO_3)_3 \cdot 9H_2O$  (99%) were used as initial materials. In a typical experiment, oxidizer to fuel ratio is unity. The stoichiometric amount of nitrates were dissolved in 30 ml double distilled water. The mixture was stirred, using a magnetic stirrer, until it became transparent. The solution is then placed into a pre-heated (at  $350 \pm 10$  °C) muffle furnace. Initially, the solution boils, then ignites and burns. The product was ground into a fine powder using an agate mortar and pestle. The as-prepared samples were initially characterized using the x-ray diffraction technique to test the phase purity using a Phillips PAN analytical X-pert Pro x-ray diffractometer (Cu-K $\alpha$  with  $\lambda = 1.54056$  Å). The particle size of the samples was estimated using transmission electron microscope (TEM) micrographs (Model: JEM-2100). The diffuse reflectance spectra (DRS) were recorded using an optical fiber spectrometer in the wavelength range of 250 to 750 nm. Typical information about the instrument was reported elsewhere [18]. The magnetization versus magnetic field measurements was carried out at room temperature using 14 T Cryogenic Physical Properties Measurement System with a vibrating sample magnetometer (VSM) insert.

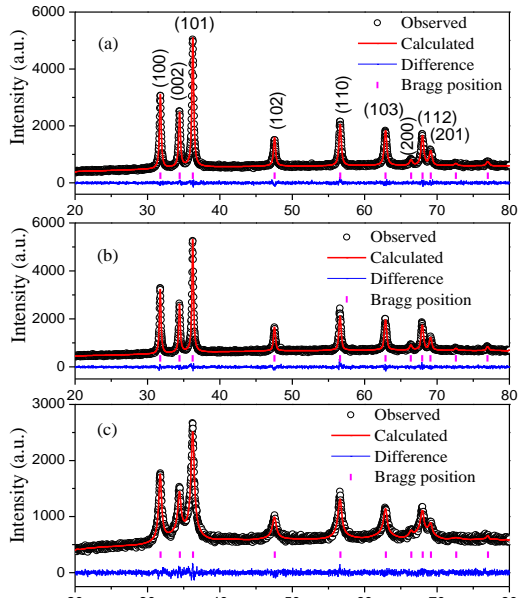
## 3. Results and discussion

Figure 1 shows Rietveld refinement of x-ray diffraction (XRD) patterns of as-prepared  $Zn_{0.99}Co_{0.01}O$ ,  $Zn_{0.97}Co_{0.03}O$  and  $Zn_{0.96}Co_{0.01}Cr_{0.03}O$  samples. It is observed that all the samples are polycrystalline and all diffraction peaks belong to a hexagonal wurtzite structure of ZnO with space group P63mc (PDF#36-1451). There are no secondary phases (no peaks corresponding to  $Co_2O_3$ ,  $Co_3O_4$ , or  $ZnCrO_4$  phase) observed in the samples. The peak shift in ( $2\theta$ ) position is indiscernible, due to the tetrahedral coordinated  $Co^{2+}$  (0.58 Å) and  $Cr^{3+}$  (0.61 Å) replaced  $Zn^{2+}$  (0.60 Å) sites [19–21]. Further, it is observed that full width half maximum (FWHM) of (100), (002) and (101) peaks slightly decreased in  $Zn_{0.97}Co_{0.03}O$  and enhanced in  $Zn_{0.96}Co_{0.01}Cr_{0.03}O$  when compared with  $Zn_{0.99}Co_{0.01}O$  sample. This implies that the crystallite size increases with the increase of Co content and decreased for Cr co-doped sample. XRD results confirm that a lower concentration of Co doping, as well as co-doping of Co and Cr ions, successfully substituted into the Zn site without modifying the ZnO structure. The FWHM of the peaks ( $\beta_{hkl}$ ) and interplanar spacing ( $d_{hkl}$ ), where ( $h, k, l$ ) refer to the Miller indices of the relevant plane, obtained from the Rietveld refinement analysis were used to determine the crystallite size ( $D$ ) and strain ( $\varepsilon$ ) using the size-strain plot (SSP) method [22,23]. The SSP equation [22,23] can be expressed as

$$\left(\frac{d_{hkl}\beta_{hkl}\cos\theta}{\lambda}\right)^2 = \frac{k\lambda}{D}\left(\frac{d_{hkl}^2\beta_{hkl}\cos\theta}{\lambda^2}\right) + \left(\frac{\varepsilon}{2\lambda}\right)^2.$$

Here  $k$  is the Scherrer constant (taken as 0.9, particles are nearly spherical) and  $\lambda$  is the wavelength of x-ray. The plots of  $\left(\frac{d_{hkl}\beta_{hkl}\cos\theta}{\lambda}\right)^2$  as a function of  $\left(\frac{d_{hkl}^2\beta_{hkl}\cos\theta}{\lambda^2}\right)$  are shown in figure 2. The  $D$  and  $\varepsilon$  were determined from slope and intercept of the linear fit of the plot, respectively. Further, the crystallite size ( $D$ ) and strain ( $\varepsilon$ ) were calculated using refinement parameters obtained from GSAS using the relation [24]  $D = \frac{18000k\lambda}{\pi L_x}$  and  $\varepsilon = \frac{\pi}{18000}L_y$ , respectively. Here  $L_x$  and  $L_y$  are GSAS fits of crystallite and strain

broadening with Lorentzian profile term, respectively. Unit cell parameters, such as lattice parameters and cell volume, were obtained from Rietveld refinement of XRD using the GSAS II software program [25]. The calculated structural and fitted parameters are tabulated in Table 1. There is a slight difference in crystallite size and lattice strain values calculated from the SSP and GSAS methods, as peaks with lower intensities are not considered for calculation in SSP method. The value of chi-square ( $\chi^2 \leq 1.4$ ), indicates good profile fitting between theoretical and experimental data. The average crystallite size increased for slightly increased in  $\text{Zn}_{0.97}\text{Co}_{0.03}\text{O}$  when compared with  $\text{Zn}_{0.99}\text{Co}_{0.01}\text{O}$  sample and it decreased in comparison for the Co–Cr co-doped ZnO.



**Figure 1.** Rietveld refinement of XRD patterns of (a)  $\text{Zn}_{0.99}\text{Co}_{0.01}\text{O}$ , (b)  $\text{Zn}_{0.97}\text{Co}_{0.03}\text{O}$  and (c)  $\text{Zn}_{0.96}\text{Co}_{0.01}\text{Cr}_{0.03}\text{O}$  analyzed using GSAS II program. The black open circle represent the experimental XRD data compared with the calculated profile (red line), the small purple vertical lines below the curve are the expected Bragg positions of wurtzite structure of ZnO and the residual of the refinement shown as blue solid line.

The lattice parameters  $a$ , and  $c$ , and cell volume are slightly enhanced in  $\text{Zn}_{0.97}\text{Co}_{0.03}\text{O}$  and  $\text{Zn}_{0.96}\text{Co}_{0.01}\text{Cr}_{0.03}\text{O}$  samples, as compared to  $\text{Zn}_{0.99}\text{Co}_{0.01}\text{O}$ . The changes in lattice parameters and cell volume are attributed to lattice distortion and defects created around dopant sites due to the differences in the ionic radii of the various cations (Zn, Co and Cr) [11,26]. The ratio of lattice parameters  $c/a$  was found to be  $1.6021 \pm 0.0001$  for all the samples. This obtained value is smaller than that of the stoichiometric wurtzite ZnO (1.633) and this is attributed to the presence of oxygen vacancies and other defects [11].

TEM micrographs of  $\text{Zn}_{0.99}\text{Co}_{0.01}\text{O}$ ,  $\text{Zn}_{0.97}\text{Co}_{0.03}\text{O}$  and  $\text{Zn}_{0.96}\text{Co}_{0.01}\text{Cr}_{0.03}\text{O}$  are shown in Figure 3 (a) to (c), respectively. It is observed that the particles are nearly spherical, but non-uniform in size. Furthermore, the co-doping of Cr strongly influences the particle size and the particles agglomeration (see Figure 3(c)). The particle distribution of the samples is shown in Figure 3 (d) to (f), and the size distribution bar graphs are well fitted with log-normal function. The average particle size is found to be  $39 \pm 1$  nm,  $42 \pm 2$  nm and  $14 \pm 2$  nm for  $\text{Zn}_{0.99}\text{Co}_{0.01}\text{O}$ ,  $\text{Zn}_{0.97}\text{Co}_{0.03}\text{O}$  and  $\text{Zn}_{0.96}\text{Co}_{0.01}\text{Cr}_{0.03}\text{O}$ , respectively.

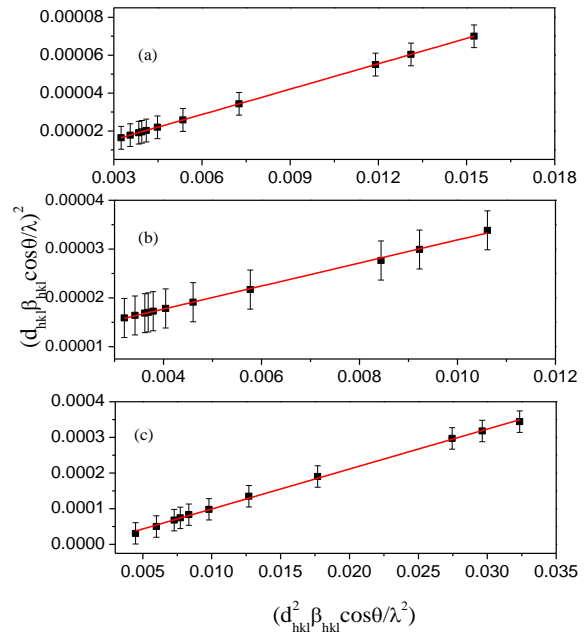


**Figure 2.** Plot of  $(d_{hkl}\beta_{hkl}\cos\theta/\lambda)^2$  as function of  $(d_{hkl}^2\beta_{hkl}\cos\theta/\lambda^2)$  for (a)  $\text{Zn}_{0.99}\text{Co}_{0.01}\text{O}$ , (b)  $\text{Zn}_{0.97}\text{Co}_{0.03}\text{O}$  and (c)  $\text{Zn}_{0.96}\text{Co}_{0.01}\text{Cr}_{0.03}\text{O}$  samples.

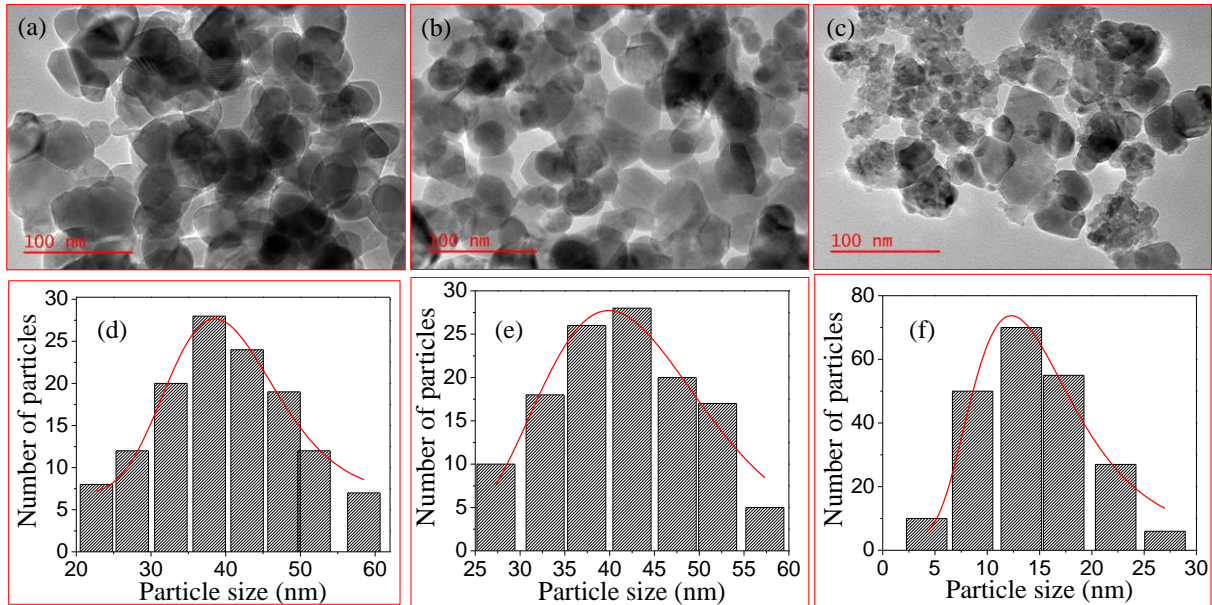


**Figure 3.** TEM images of (a)  $\text{Zn}_{0.99}\text{Co}_{0.01}\text{O}$ , (b)  $\text{Zn}_{0.97}\text{Co}_{0.03}\text{O}$  and (c)  $\text{Zn}_{0.96}\text{Co}_{0.01}\text{Cr}_{0.03}\text{O}$  samples and their corresponding particle size distribution of the samples are shown figure 3 (d) to (f), respectively.

**Table 1.** Structural parameters of  $\text{Zn}_{0.99}\text{Co}_{0.01}\text{O}$ ,  $\text{Zn}_{0.97}\text{Co}_{0.03}\text{O}$  and  $\text{Zn}_{0.96}\text{Co}_{0.01}\text{Cr}_{0.03}\text{O}$  samples estimated from Rietveld refinement of XRD using GSAS II program. The fitted parameters chi-square ( $\chi^2$ ), Weighted Profile ( $R_{\text{wp}}$ ) and scale F factor ( $R_{\text{F}}$ ) are given in Table 1.

Refined parameters	$\text{Zn}_{0.99}\text{Co}_{0.01}\text{O}$	$\text{Zn}_{0.97}\text{Co}_{0.03}\text{O}$	$\text{Zn}_{0.96}\text{Co}_{0.01}\text{Cr}_{0.03}\text{O}$
Crystallite size (nm)			
from SSP method	$31 \pm 1$	$40 \pm 1$	$12 \pm 1$
and GSAS	$34 \pm 1$	$42 \pm 1$	$12 \pm 1$
Strain (%) from SSP	$0.27 \pm 0.02$	$0.57 \pm 0.02$	$0.70 \pm 0.03$
GSAS	$0.20 \pm 0.02$	$0.24 \pm 0.02$	$0.34 \pm 0.02$
Particle size from TEM (nm)	$39 \pm 1$	$42 \pm 2$	$14 \pm 2$
Lattice parameters ( $\text{\AA}$ ) (Error: $\pm 0.0001$ )	$a = b = 3.2438$ $c = 5.1969$	3.2445 5.1968	3.2492 5.2057
Cell volume ( $\text{\AA}^3$ )	$47.359 \pm 0.002$	$47.379 \pm 0.002$	$47.596 \pm 0.003$
$\chi^2$	1.12	1.51	1.48
$R_{\text{wp}}$ (%)	4.01	4.46	4.53
$R_{\text{F}}$ (%)	3.14	5.28	4.06
Band-gap (eV)	$3.308 \pm 0.002$	$3.283 \pm 0.002$	$3.287 \pm 0.003$
Zn ( $x, y, z$ )	(0.333, 0.666, -0.006)	(0.333, 0.666, -0.009)	(0.333, 0.666, -0.005)
O ( $x, y, z$ )	(0.333, 0.666, 0.379)	(0.333, 0.666, 0.364)	(0.333, 0.666, 1.334)
Co ( $x, y, z$ )	(0.333, 0.666, 0.081)	(0.333, 0.660, -0.012)	(0.333, 0.666, 0.398)
Cr ( $x, y, z$ )	--	--	0.333, 0.660, 0.341)

The DRS spectra of  $\text{Zn}_{0.99}\text{Co}_{0.01}\text{O}$ ,  $\text{Zn}_{0.97}\text{Co}_{0.03}\text{O}$  and  $\text{Zn}_{0.96}\text{Co}_{0.01}\text{Cr}_{0.03}\text{O}$  samples are shown in Figure 4 (a). Three sub band-gap absorption peaks are observed in all the samples at 569 nm ( ${}^4A_2(F) \rightarrow {}^4A_1(G)$ ), 610 nm ( ${}^4A_2(F) \rightarrow {}^4T_1(P)$ ) and 660 nm ( ${}^4A_2(F) \rightarrow {}^2E(G)$ ) are transitions of Co ions with a tetrahedral

crystal field in the +2 state and replacing  $\text{Zn}^{2+}$  sites [27–29]. Furthermore, the weak sub band-gap absorption peaks that have appeared at 584 nm ( ${}^4A_{2g}(F) \rightarrow {}^4T_{2g}(F)$ ) and 715 nm ( ${}^4A_{2g}(F) \rightarrow {}^2E_g(G)$ ) are the transitions of  $\text{Cr}^{3+}$  ions [28,30] in the host ZnO lattice. The cobalt environment remains the same in both Co doped and Co–Cr co-doped ZnO samples. To determine the band-gap of the samples, the obtained diffuse reflectance spectra were converted to Kubelka–Munk function [31] using the relation:  $F(R) = \frac{(1-R)^2}{2R} = \frac{k}{s}$ , where  $R$  is the reflectance,  $k$  is the absorption co-efficient and  $s$  is the scattering co-efficient. Here,  $F(R)$  is proportional to absorption co-efficient, thus  $\alpha$  in the Tauc equation [31] [ $\alpha h\nu = C(h\nu - E_g)^{\frac{1}{2}}$ ] can be replaced with  $F(R)$ . For direct allowed transition [31], the Tauc relation becomes;  $[F(R)h\nu]^2 = A(h\nu - E_g)^2$ . The plots of  $[F(R)h\nu]^2$  against the  $h\nu$  for the various samples are shown in inset Figure 4(b) and the band-gap values of the samples were obtained by extrapolating from the linear region of  $[F(R)h\nu]^2$  to zero. The calculated band-gap values are presented in Table 1, showing that the band-gap values decreased in both  $\text{Zn}_{0.97}\text{Co}_{0.03}\text{O}$  and  $\text{Zn}_{0.96}\text{Co}_{0.01}\text{Cr}_{0.03}\text{O}$  samples, as compared to  $\text{Zn}_{0.99}\text{Co}_{0.01}\text{O}$ . The band-gap narrowing observed in the samples is due to the strong  $sp$ – $d$  spin exchange interaction between the ZnO band electrons and localized  $d$  electrons of the Co and/ or Cr ions substituting for  $\text{Zn}^{2+}$  ions [23].

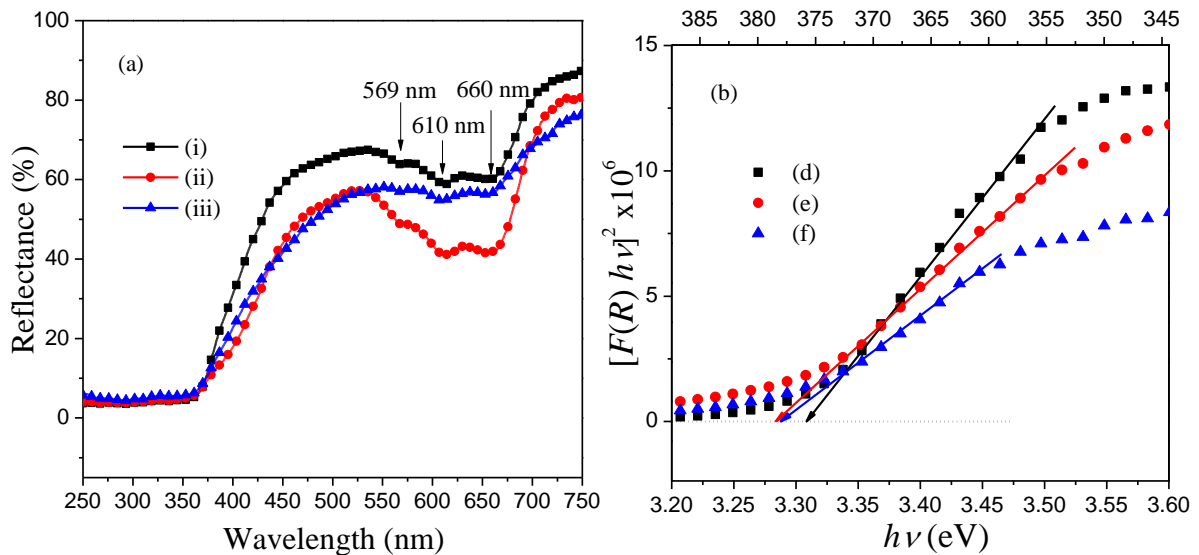


**Figure 4.** (a) DRS spectra of (i)  $\text{Zn}_{0.99}\text{Co}_{0.01}\text{O}$ , (ii)  $\text{Zn}_{0.97}\text{Co}_{0.03}\text{O}$  and (iii)  $\text{Zn}_{0.96}\text{Co}_{0.01}\text{Cr}_{0.03}\text{O}$  samples and the corresponding plots of  $[F(R)h\nu]^2$  as function of  $(h\nu)$  are shown in Figure 4 (b), referred to as (iv), (v) and (vi), respectively.

Our results confirm the tetrahedrally coordinated  $\text{Co}^{2+}$  ions replaced  $\text{Zn}^{2+}$  sites, the exchange interactions between the ZnO band electrons and localized  $d$  electrons of  $\text{Co}^{2+}$  ions are stronger than the interactions between the  $d$  electrons of the Cr ions [28]. Hence, the band-gap of  $\text{Zn}_{0.96}\text{Co}_{0.01}\text{Cr}_{0.03}\text{O}$  is slightly higher than  $\text{Zn}_{0.97}\text{Co}_{0.03}\text{O}$  sample.

The magnetic behaviour of the as-synthesized samples was measured at room temperature. The magnetization as function of applied magnetic field curves,  $M(\mu_0H)$ , of the  $\text{Zn}_{0.99}\text{Co}_{0.01}\text{O}$ ,  $\text{Zn}_{0.97}\text{Co}_{0.03}\text{O}$  and  $\text{Zn}_{0.96}\text{Co}_{0.01}\text{Cr}_{0.03}\text{O}$  are shown in Figure 5 (a) to (c), respectively. It is observed that the  $\text{Zn}_{0.97}\text{Co}_{0.03}\text{O}$  and  $\text{Zn}_{0.96}\text{Co}_{0.01}\text{Cr}_{0.03}\text{O}$  samples show ferromagnetic behaviour that is superimposed on the diamagnetic background. Therefore, the diamagnetic contribution was subtracted using relation [3];  $M_c = M_T - \chi_d H$ , where  $M_c$  is the corrected magnetization after removing the additional magnetic component,  $M_T$  is the total magnetization,  $\chi_d = dM/dH$  is the diamagnetic susceptibility and  $H$  is applied field. According to the literature, the  $M(\mu_0H)$  curve of  $\text{Zn}_{0.99}\text{Co}_{0.01}\text{O}$  measured at 300 K are

expected to show paramagnetic behaviour [3,32], however, it appears like antiferromagnetic that superimposed by diamagnetic background. Shi et al. [9] reported Co doped ZnO exhibits paramagnetism at lower Co concentration because of a lack of oxygen vacancies. El-Hilo and Hao et al. [3,32] reported that post-annealing of the Co doped ZnO samples under different atmospheric conditions (such as for example: O<sub>2</sub>, Ar, and H<sub>2</sub>) altered magnetic properties from paramagnetic to ferromagnetic or antiferromagnetic behaviour [3,32].

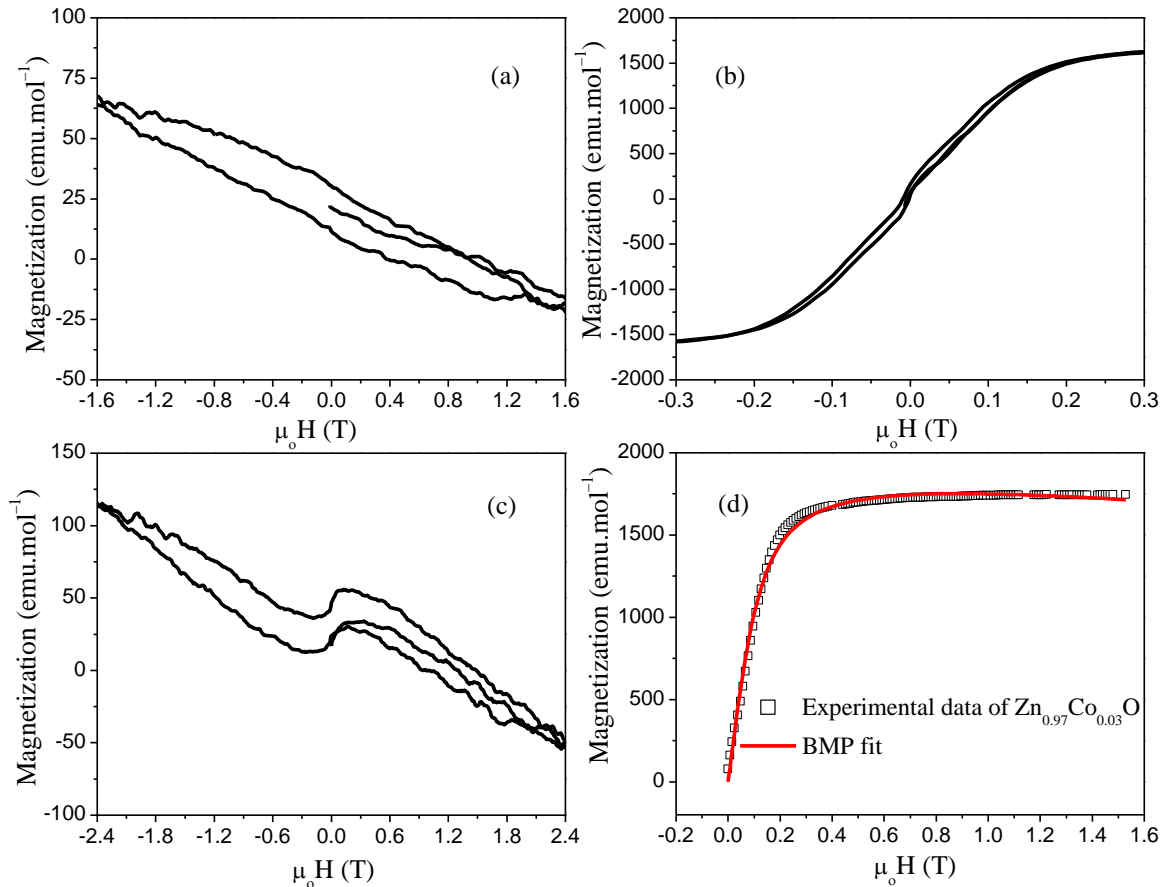


**Figure 5.** Magnetization as function of magnetic field of (a) Zn<sub>0.99</sub>Co<sub>0.01</sub>O, (b) Zn<sub>0.97</sub>Co<sub>0.03</sub>O and (c) Zn<sub>0.96</sub>Co<sub>0.01</sub>Cr<sub>0.03</sub>O samples measured at room temperature. (d) The symbol represent experimental data of  $M(\mu_0H)$  curve of Zn<sub>0.97</sub>Co<sub>0.03</sub>O and red line the fits to the experimental data using the BMP model.

The Zn<sub>0.97</sub>Co<sub>0.03</sub>O shows a hysteresis curve with the coercive field ( $H_c$ ) of  $3.5 \pm 0.2$  mT, indicating ferromagnetism at 300 K. The saturation magnetization ( $M_s$ ) is  $1715 \pm 5$  emu.mol<sup>-1</sup>. Some of the reports show the existence of RTFM in Co doped ZnO, which is attributed to the super-exchange interaction of Co<sup>2+</sup> ions [10], presence of defects [3,4,23,33,34] and Co cluster of secondary phase [5,6]. In the present work, the existence of secondary phase is ruled out, thus, the observed RTFM is considered intrinsic. To understand the intrinsic magnetic ordering, the experimental  $M(\mu_0H)$  curve of Zn<sub>0.97</sub>Co<sub>0.03</sub>O was fitted with bound magnetic polaron (BMP) model [35,36], as shown in Figure 5 (d). The number of BMPs formed in Zn<sub>0.97</sub>Co<sub>0.03</sub>O was found to be  $2.5 \times 10^{14}$  cm<sup>-3</sup>, which is less than the threshold ( $10^{18}$  cm<sup>-3</sup>) to mediate ferromagnetic ordering. Therefore, direct interaction of BMPs to order the system ferromagnetically cannot be simply applied here. DRS results confirm that the band-gap decrease with an increase in the Co dopant concentration, and this is also related to the changes of oxygen vacancies/defects concentration [11]. The present XRD results also confirm the presence of defects in the synthesized samples. These results support the BMP model as the coupling interaction of Co<sup>2+</sup> ions

within the volume (due to the presence of structural defects occupying a volume) [10] and oxygen vacancies/defects mediate the exchange coupling between  $\text{Co}^{2+}$  ions [3,4,8], resulting in the RTFM ordering in  $\text{Zn}_{0.97}\text{Co}_{0.03}\text{O}$  sample.

The weak RTFM is observed in  $\text{Zn}_{0.96}\text{Co}_{0.01}\text{Cr}_{0.03}\text{O}$ , as shown in Figure 4 (c). The  $H_c$  and  $M_s$  for this sample are found to be  $90 \pm 1$  mT and  $116 \pm 2$  emu.mol<sup>-1</sup>, respectively. Here, Cr co-doping plays a crucial role in mediating the distribution of Co ions in ZnO lattice and decreases the probability of antiferromagnetic coupling between the neighboring  $\text{Co}^{2+}$  ions [12,13]. The hybridization between the Co 3d states with the Cr-ion is induced donor band [12], possible role of the charge transfer from the donor band to the Co 3d states might be to modify the electrostatic interactions between  $\text{Co}^{2+}$  ions. Hence, Cr co-doping altered the magnetic properties from PM to FM behaviour.

#### 4. Conclusions

In summary, the combustion synthesized  $\text{Zn}_{1-x}\text{Co}_x\text{O}$ , with  $x = 0.01, 0.03$ , and  $\text{Zn}_{0.96}\text{Co}_{0.01}\text{Cr}_{0.03}\text{O}$  samples were found to be single phase of the wurtzite structure. The structural parameters were investigated using Rietveld refinement of the XRD results. TEM of the as synthesized powders showed nanoparticles with sizes  $39 \pm 1$ ,  $42 \pm 2$  and  $14 \pm 2$  nm for  $\text{Zn}_{0.99}\text{Co}_{0.01}\text{O}$ ,  $\text{Zn}_{0.97}\text{Co}_{0.03}\text{O}$  and  $\text{Zn}_{0.96}\text{Co}_{0.01}\text{Cr}_{0.03}\text{O}$ , respectively. The co-doping of Cr ions reduces the particle size and particles are agglomerated. DRS measurement showed three sub band-gap absorption peaks at 569, 610 and 660 nm are transitions of  $\text{Co}^{2+}$  ions. In Cr-Co co-doped sample an additional sub band-gap absorption peak appeared at 715 nm is the transition of  $\text{Cr}^{3+}$  ions. The band-gap is decreased with increase of Co concentration and Cr co-doped ZnO sample. The magnetic measurements of  $\text{Zn}_{0.99}\text{Co}_{0.01}\text{O}$  and  $\text{Zn}_{0.97}\text{Co}_{0.03}\text{O}$  exhibit PM and FM behaviour, respectively. The observed FM in  $\text{Zn}_{0.97}\text{Co}_{0.03}\text{O}$  is attributed to oxygen vacancies/defects associated with BMPs. In  $\text{Zn}_{0.96}\text{Co}_{0.01}\text{Cr}_{0.03}\text{O}$  sample, the Cr ions induce the hybridization between the Co 3d states and the charge transfer from the donor band to the Co 3d states turns to ferromagnetic interactions.

#### Acknowledgement

Financial aid from the South African National Research Foundation (Grant No's: 120856 and 88080) and the Faculty of Science, University of Johannesburg (UJ) URC and FRC is acknowledged. The use of the NEP Cryogenic Physical Properties Measurement System at UJ, obtained with financial support from the SANRF (Grant No: 88080) and UJ, RSA, is acknowledged.

#### References

- [1] Singh P, Kumar R and Singh R K 2019 *Ind. Eng. Chem. Res.* **58** 17130–63
- [2] Ozgur U, Alivov Y I, Liu C, Teke A, Reshchikov M A, Dogan S, Avrutin V, Cho S J and Morkoc H 2005 *J. Appl. Phys.* **98** 1–103
- [3] El-Hilo M, Dakhel A A and Yacoob Z J 2019 *J. Magn. Magn. Mater.* **482** 125–34
- [4] Singhal A, Achary S N, Manjanna J, Chatterjee S, Ayyub P and Tyagi A K 2010 *J. Phys. Chem. C* **114** 3422–30
- [5] Chanda A, Gupta S, Vasundhara M, Joshi S R, Mutta G R and Singh J 2017 *RSC Adv.* **7** 50527–36
- [6] Tiwari N, Doke S, Lohar A, Mahamuni S, Kamal C, Chakrabarti A, Choudhary R J, Mondal P, Jha S N and Bhattacharyya D 2016 *J. Phys. Chem. Solids* **90** 100–13
- [7] Opel M, Nielsen K W, Bauer S, Goennenwein S T B, Cezar J C, Schmeisser D, Simon J, Mader W and Gross R 2008 *Eur. Phys. J. B* **63** 437–44
- [8] Sivagamasundari A, Pugaze R, Chandrasekar S, Rajagopan S and Kannan R 2013 *Appl. Nanosci.* **3** 383–8
- [9] Shi T, Zhu S, Sun Z, Wei S and Liu W 2007 *Appl. Phys. Lett.* **90** 2005–8
- [10] Yao T, Yan W, Sun Z, Pan Z, Xie Y, Jiang Y, Ye J, Hu F and Wei S 2009 *J. Phys. Chem. C* **113** 14114–8

- [11] Beltrán J J, Osorio J A, Barrero C A, Hanna C B and Punnoose A 2013 *J. Appl. Phys.* **113** 1–4
- [12] Yan W, Sun Z, Liu Q, Yao T, Jiang Q, Hu F, Li Y, He J, Peng Y and Wei S 2010 *Appl. Phys. Lett.* **97** 90–3
- [13] Aljawfi R N, Rahman F and Batoo K M 2013 *J. Magn. Magn. Mater.* **332** 130–6
- [14] Kataoka T, Yamazaki Y, Sakamoto Y, Fujimori A, Chang F and Lin H 2010 *Appl. Phys. Lett.* **96** 252502
- [15] Assadi M H N, Zhang Y B and Li S 2010 *J. Phys. Condens. Matter* **22** 296004
- [16] Park J H, Lee S, Kim B S, Kim W K, Cho Y C, Oh M W, Cho C R and Jeong S Y 2014 *Appl. Phys. Lett.* **104** 1–5
- [17] Lokesha H S, Nagabhushana K R and Singh F 2017 *J. Lumin.* **192** 173–9
- [18] Satyanarayana Reddy S, Lokesha H S and Nagabhushana K R 2021 *Rev. Sci. Instrum.* **92** 093104
- [19] Kumar S, Tiwari N, Jha S N, Chatterjee S, Bhattacharyya D and Ghosh A K 2016 *RSC Adv.* **6** 107816–28
- [20] Jin C G, Yang Y, Wu Z F, Zhuge L J, Han Q, Wu X M, Li Y Y and Feng Z C 2014 *J. Mater. Chem. C* **2** 2992–7
- [21] Srineta G, Varshney P, Kumar R, Sajal V, Kulriya P K, Knobelc M and S.K. Sharma 2013 *Ceram. Int.* **39** 6077–6085
- [22] Kumar S, Asokan K, Singh R K, Chatterjee S, Kanjilal D and Ghosh A K 2014 *RSC Adv.* **4** 62123–31
- [23] Sharma D and Jha R 2017 *Ceram. Int.* **43** 8488–96
- [24] Bajpai G, Srivastava T, Patra N, Moirangthem I, Jha S N, Bhattacharyya D, Riyajuddin S, Ghosh K, Basaula D R, Khan M, Liu S W, Biring S and Sen S 2018 *RSC Adv.* **8** 24355–69
- [25] Toby B H and Von Dreele R B 2013 *J. Appl. Crystallogr.* **46** 544–9
- [26] Ashokkumar M and Muthukumaran S 2015 *Phys. E Low-Dimensional Syst. Nanostructures* **69** 354–9
- [27] Srinatha N, Nair K G M and Angadi B 2015 *Phys. B Condens. Matter* **474** 97–104
- [28] Beltrán J J, Barrero C A and Punnoose A 2016 *J. Phys. Chem. C* **120** 8969–78
- [29] Franco A and Pessoni H V S 2015 *Phys. B Condens. Matter* **476** 12–8
- [30] Babu B, Manjari V P, Aswani T, Rao G T, Stella R J and Ravikumar R V S S N 2014 *Indian J. Phys.* **88** 683–90
- [31] Morales A E, Mora E S and Pal U 2007 *Rev. Mex. Fis. S* **53** 18–22
- [32] Hao W, Li J, Xu H, Wang J and Wang T 2010 *ACS Appl. Mater. Interfaces* **2** 2053–9
- [33] Robkhob P, Tang I M and Thongmee S 2019 *J. Supercond. Nov. Magn.* **32** 3637–45
- [34] Shi T, Xiao Z, Yin Z, Li X, Wang Y, He H, Wang J, Yan W and Wei S 2010 *Appl. Phys. Lett.* **96** 1–4
- [35] Ali N, Singh B, Khan Z A, Vijaya A R, Tarafder K and Ghosh S 2019 *Sci. Rep.* **9** 3–9
- [36] Ali N, Singh B, A R V, Lal S, Yadav C S, Tarafder K and Ghosh S 2021 *J. Phys. Chem. C* **125** 7734–45

# Structure, optical and magnetic properties of combustion synthesized Ni-Cr doped ZnO

H. S. Lokesh<sup>1\*</sup>, C. J. Sheppard<sup>1</sup>, P. Mohanty<sup>1</sup> and A. R. E. Prinsloo<sup>1</sup>

<sup>1</sup>Cr Research Group, Department of Physics, University of Johannesburg, PO Box 524, Auckland Park, Johannesburg, South Africa

E-mail: [hslokesh88@gmail.com](mailto:hslokesh88@gmail.com), [lokeshahs@uj.ac.za](mailto:lokeshahs@uj.ac.za)

**Abstract.** Structural, optical and magnetic properties of combustion synthesized  $\text{Zn}_{0.96}\text{Ni}_{0.01}\text{Cr}_{0.03}\text{O}$  and  $\text{Zn}_{0.90}\text{Ni}_{0.05}\text{Cr}_{0.05}\text{O}$  have been investigated. X-ray diffraction (XRD) analyses confirm that samples are in the hexagonal wurtzite structure. No impurity peaks were detected in  $\text{Zn}_{0.96}\text{Ni}_{0.01}\text{Cr}_{0.03}\text{O}$ , while a weak secondary spike  $\text{ZnCr}_2\text{O}_4$  phase ( $2\theta = 43^\circ$ ) was identified in  $\text{Zn}_{0.90}\text{Ni}_{0.05}\text{Cr}_{0.05}\text{O}$ . Lattice parameters, obtained from Rietveld refinement, were found to be  $a = b = 3.2535 \pm 0.0002 \text{ \AA}$  for both the samples, while  $c = 5.2132 \pm 0.0003 \text{ \AA}$  for  $\text{Zn}_{0.96}\text{Ni}_{0.01}\text{Cr}_{0.03}\text{O}$  decreasing to  $5.2129 \pm 0.0002 \text{ \AA}$  for  $\text{Zn}_{0.90}\text{Ni}_{0.05}\text{Cr}_{0.05}\text{O}$ . These values are comparable with the standard data (PDF#36-1451). The particle size of the as-prepared samples is  $20 \pm 2$  and  $22 \pm 2$  nm for  $\text{Zn}_{0.96}\text{Ni}_{0.01}\text{Cr}_{0.03}\text{O}$  and  $\text{Zn}_{0.90}\text{Ni}_{0.05}\text{Cr}_{0.05}\text{O}$ , respectively. Diffuse reflectance spectra show a weak absorption band at 657 nm, characteristic of tetrahedral  $\text{Ni}^{2+}$  ions in the ZnO lattice. Band-gap values were  $3.293 \pm 0.003$  and  $3.273 \pm 0.003$  eV for  $\text{Zn}_{0.96}\text{Ni}_{0.01}\text{Cr}_{0.03}\text{O}$  and  $\text{Zn}_{0.90}\text{Ni}_{0.05}\text{Cr}_{0.05}\text{O}$ , respectively. Magnetization as a function of field measurements,  $M(\mu_0H)$ , were performed at room temperature using a vibrating sample magnetometer. The  $\text{Zn}_{0.96}\text{Ni}_{0.01}\text{Cr}_{0.03}\text{O}$  and  $\text{Zn}_{0.90}\text{Ni}_{0.05}\text{Cr}_{0.05}\text{O}$  samples show ferromagnetic (FM) and antiferromagnetic (AFM) behaviour, respectively. Point defects are the source for the obtained FM in  $\text{Zn}_{0.96}\text{Ni}_{0.01}\text{Cr}_{0.03}\text{O}$ . The exchange interaction between  $\text{Ni}^{2+}$  and  $\text{Cr}^{3+}$  dopants and the formation of a  $\text{ZnCr}_2\text{O}_4$  phase is responsible for AFM behaviour in  $\text{Zn}_{0.90}\text{Ni}_{0.05}\text{Cr}_{0.05}\text{O}$ . This study reveals that the  $\text{Ni}^{2+}$  and  $\text{Cr}^{3+}$  ions were successfully substituted into  $\text{Zn}^{2+}$  sites at lower concentrations of  $\text{Cr}^{3+}$  ions. At higher Cr concentrations, some of the Cr ions are in an octahedral rather than tetrahedral coordination causing the formation of a secondary phase. Interestingly, in Ni-Cr doped ZnO, the weak FM behaviour is transformed to AFM behaviour depending on the Ni and Cr content.

## 1. Introduction

Zinc oxide (ZnO) based materials have inspired great in the field of memory, detectors, light-emitting sources and the possibility of usage in next-generation spintronic devices [1,2]. Doping and co-doping with transition metals (TM) is an effective method to adjust ZnO's energy level surface states, which can enhance the optical and magnetic properties [1,3,4]. The literature report states doping and co-doping of Ni, Mn, Cr, and Co-doped ZnO receives much attention. It is investigated extensively for potential applications in novel memory and optical devices [5,6]. The ionic radius of  $\text{Ni}^{2+}$  (0.69 Å) and  $\text{Cr}^{3+}$  (0.63 Å) are comparable to that of  $\text{Zn}^{2+}$  ions (0.74 Å), and these are easily incorporated into the wurtzite structure of ZnO. Ni-doped ZnO shows room temperature ferromagnetism at a lower concentration of Ni ions ( $\leq 2\%$ ) and paramagnetism above it. Also, Ni-doped ZnO exhibits ferromagnetic behaviour from 2 to 355 K [1,7]. The Cr metal is antiferromagnetic below 311 K and

paramagnetic at high temperatures; only CrO<sub>2</sub> is ferromagnetic with a Curie Temperature of  $T_c = 386$  K [1]. Most of the available literature is focused either on Cr-doped Ni-doped ZnO [7]. There is a lack of studies of Ni-Cr co-doped ZnO nanoparticles in the literature. The present work focuses on the structure, optical and magnetic properties of Zn<sub>0.96</sub>Ni<sub>0.01</sub>Cr<sub>0.03</sub>O and Zn<sub>0.90</sub>Ni<sub>0.05</sub>Cr<sub>0.05</sub>O synthesized by the solution combustion method. Structural and morphological studies of the as-synthesized samples were done using x-ray diffraction (XRD) and transmission electron microscopy (TEM), respectively. The optical and magnetic measurements are carried out using diffuse reflectance spectroscopy (DRS) and a vibrating sample magnetometer (VSM).

## 2. Experimental details

Zn<sub>0.96</sub>Ni<sub>0.01</sub>Cr<sub>0.03</sub>O and Zn<sub>0.90</sub>Ni<sub>0.05</sub>Cr<sub>0.05</sub>O samples were synthesized using the solution combustion process with Zn(NO<sub>3</sub>)<sub>2</sub>·6H<sub>2</sub>O (98%), NH<sub>2</sub>CH<sub>2</sub>COOH (99%), and Ni(NO<sub>3</sub>)<sub>2</sub>·6H<sub>2</sub>O (99%) and Cr(NO<sub>3</sub>)<sub>3</sub>·9H<sub>2</sub>O (99%) as reactants procured from Sigma-Aldrich company. The procedure adopted during synthesis were reported elsewhere [8]. The as-synthesized samples were characterized using the x-ray diffraction technique to test the phase purity using a Phillips PAN analytical X-pert Pro x-ray diffractometer (Cu-K $\alpha$  with  $\lambda = 1.54056$  Å). Particle sizes of the samples were calculated using the micrographs obtained from a transmission electron microscope (TEM) (Model: JEM-2100). The diffuse reflectance spectra (DRS) were recorded using a laboratory spectrometer instrument [9]. The magnetic measurement was carried out using a Cryogenic Physical Properties Measurement System with a vibrating sample magnetometer (VSM) insert.

## 3. Results and discussion.

Rietveld refinement of x-ray diffraction (XRD) patterns of as-prepared Zn<sub>0.96</sub>Ni<sub>0.01</sub>Cr<sub>0.03</sub>O and Zn<sub>0.90</sub>Ni<sub>0.05</sub>Cr<sub>0.05</sub>O are shown in Figure 1. The diffraction peaks observed within the measurement of  $2\theta$  range 20° to 80° were compared with the standard file (PDF#36-1451). For Zn<sub>0.96</sub>Ni<sub>0.01</sub>Cr<sub>0.03</sub>O, all the peaks correspond to the hexagonal wurtzite structure of ZnO with space group P63mc. However, for the Zn<sub>0.90</sub>Ni<sub>0.05</sub>Cr<sub>0.05</sub>O, a secondary phase peak was observed at  $2\theta = 43^\circ$  which belongs to ZnCr<sub>2</sub>O<sub>4</sub> structure (PDF#22-1107). The observance of the secondary phase peak indicates that the Ni ions and Cr ions would not only substitute the Zn place but also exist as interstitial ions or enter into vacancies [10]. The full-width half maximum of the peaks ( $\beta_{hkl}$ ) and interplanar spacing for ( $h, k, \text{ and } l$ ) plane ( $d_{hkl}$ ) obtained from the Rietveld refinement of GSAS II software program [11] were used to determine the crystallite size ( $D$ ) and strain ( $\varepsilon$ ) using the size-strain plot (SSP) as given in equation (1) [12,13]:

$$\left(\frac{d_{hkl}\beta_{hkl}\cos\theta}{\lambda}\right)^2 = \frac{k\lambda}{D}\left(\frac{d_{hkl}^2\beta_{hkl}\cos\theta}{\lambda^2}\right) + \left(\frac{\varepsilon}{2\lambda}\right)^2 \quad \text{-----} \quad (1)$$

Where  $\lambda$  is the wavelength of the x-rays used, and  $k$  is the Scherrer constant (taken as 0.9, assuming spherical particles). The plot of  $\left(\frac{d_{hkl}\beta_{hkl}\cos\theta}{\lambda}\right)^2$  as a function of  $\left(\frac{d_{hkl}^2\beta_{hkl}\cos\theta}{\lambda^2}\right)$  is shown in Figure 2. The crystallite size and strain were determined from the slope and intercept of the linear fit of the plot, respectively. In addition, the crystallite size and strain calculated using refinement parameters obtained from GSAS using equation (2) and (3), respectively [14]:

$$D = \frac{18000k\lambda}{\pi L_x}, \quad \text{-----} \quad (2)$$

and:

$$\varepsilon = \frac{\pi}{18000} L_y, \quad \text{-----} \quad (3)$$

where  $L_x$  and  $L_y$  are GSAS fits of crystallite and strain broadening with Lorentzian profile term, respectively. Obtained unit cell parameters and fitted parameters are tabulated in Table 1. The value of chi-square ( $\chi^2 \leq 1.2$ ) indicated a good profile fit between theoretical and experimental data.

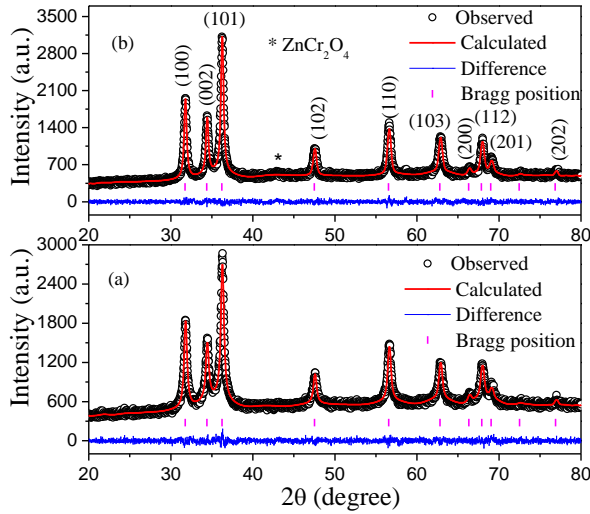


**Figure 1.** Rietveld refinement of XRD patterns of (a)  $\text{Zn}_{0.96}\text{Ni}_{0.01}\text{Cr}_{0.03}\text{O}$  and (b)  $\text{Zn}_{0.90}\text{Ni}_{0.05}\text{Cr}_{0.05}\text{O}$  analyzed using the GSAS II program. The black open circle represent the experimental XRD data compared with the calculated profile (red line), the small purple vertical lines below the curve are the expected Bragg positions of the wurtzite structure of ZnO and the residual of the refinement is shown as a solid blue line.

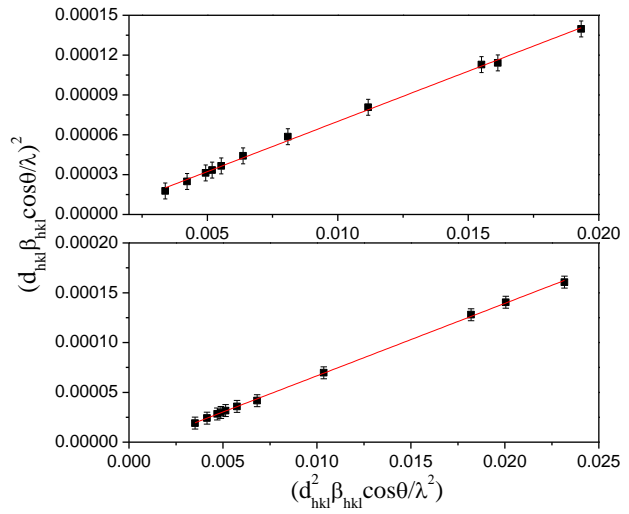


**Figure 2.** Plot of  $(d_{hkl}\beta_{hkl}\cos\theta/\lambda)^2$  as function of  $(d_{hkl}^2\beta_{hkl}\cos\theta/\lambda^2)$  for (a)  $\text{Zn}_{0.96}\text{Ni}_{0.01}\text{Cr}_{0.03}\text{O}$  and (b)  $\text{Zn}_{0.90}\text{Ni}_{0.05}\text{Cr}_{0.05}\text{O}$  samples.

**Table 1.** Structural parameters of  $\text{Zn}_{0.96}\text{Ni}_{0.01}\text{Cr}_{0.03}\text{O}$  and  $\text{Zn}_{0.90}\text{Ni}_{0.05}\text{Cr}_{0.05}\text{O}$  samples estimated from Rietveld refinement of XRD using the GSAS II program. The fitted parameters chi-square ( $\chi^2$ ), Weighted Profile ( $R_{wp}$ ) and scale F factor ( $R_F$ ) are given in Table 1.

Refined parameters	$\text{Zn}_{0.96}\text{Ni}_{0.01}\text{Cr}_{0.03}\text{O}$	$\text{Zn}_{0.90}\text{Ni}_{0.05}\text{Cr}_{0.05}\text{O}$
Crystallite size (nm) from SSP method and GSAS	$17 \pm 2$ $18 \pm 2$	$18 \pm 2$ $20 \pm 2$
Strain (%) from SSP	$0.72 \pm 0.02$	$0.76 \pm 0.02$
GSAS	$0.68 \pm 0.02$	$0.71 \pm 0.02$
Particle size from TEM (nm)	$20 \pm 2$	$22 \pm 2$
Lattice parameters ( $\text{\AA}$ ) (Error: $\pm 0.0001$ )	$a = b = 3.2535$ $c = 5.2132$	$3.2536$ $5.2129$
Cell volume ( $\text{\AA}^3$ )	$47.792 \pm 0.002$	$47.791 \pm 0.004$
$\chi^2$	1.10	1.14
$R_{wp}$ (%)	4.18	4.25
$R_F$ (%)	6.72	6.25
Band-gap (eV)	$3.293 \pm 0.002$	$3.273 \pm 0.002$
Zn ( $x, y, z$ )	(0.666, 0.333, 0.354)	(0.666, 0.333, 0.355)
O ( $x, y, z$ )	(0.666, 0.333, 0.666)	(0.666, 0.333, 0.666)
Co ( $x, y, z$ )	(0.666, 0.333, 0.324)	(0.666, 0.333, 0.325)
Ni ( $x, y, z$ )	(0.666, 0.333, 0.427)	(0.666, 0.333, 0.426)

The average crystallite size increased slightly in the lattice parameters  $a$ , and  $c$ , and cell volume is somewhat enhanced with an increase of Ni and Cr concentration. The changes in lattice parameters and cell volume are attributed to lattice distortion and defects created around dopants sites due to the difference in ionic radii of cations (Zn, Ni and Cr) [15,16]. The ratio of lattice parameters  $c/a$  was found to be  $1.6023 \pm 0.0001$  for all the samples. The estimated value is smaller than the stoichiometric wurtzite ZnO (1.633) and this is attributed to the presence of oxygen vacancies and other defects [16].

TEM micrographs of  $\text{Zn}_{0.96}\text{Ni}_{0.01}\text{Cr}_{0.03}\text{O}$  and  $\text{Zn}_{0.90}\text{Ni}_{0.05}\text{Cr}_{0.05}\text{O}$  are shown in Figure 3 (a) and (b), respectively. It is observed that the particles are nearly spherical but non-uniform in size. Energy dispersive x-ray spectroscopy (EDX), shown in Figure 3 (c) and (d) results, provides information about the chemical compositions in the samples, and there are no additional elements in the samples for  $\text{Zn}_{0.96}\text{Ni}_{0.01}\text{Cr}_{0.03}\text{O}$  and  $\text{Zn}_{0.90}\text{Ni}_{0.05}\text{Cr}_{0.05}\text{O}$ , respectively. The particle size distribution of the samples are shown in Figure 3 (e) and (f), respectively, and the sizes  $20 \pm 2$  nm and  $22 \pm 2$  nm for  $\text{Zn}_{0.96}\text{Ni}_{0.01}\text{Cr}_{0.03}\text{O}$  and  $\text{Zn}_{0.90}\text{Ni}_{0.05}\text{Cr}_{0.05}\text{O}$ , respectively.

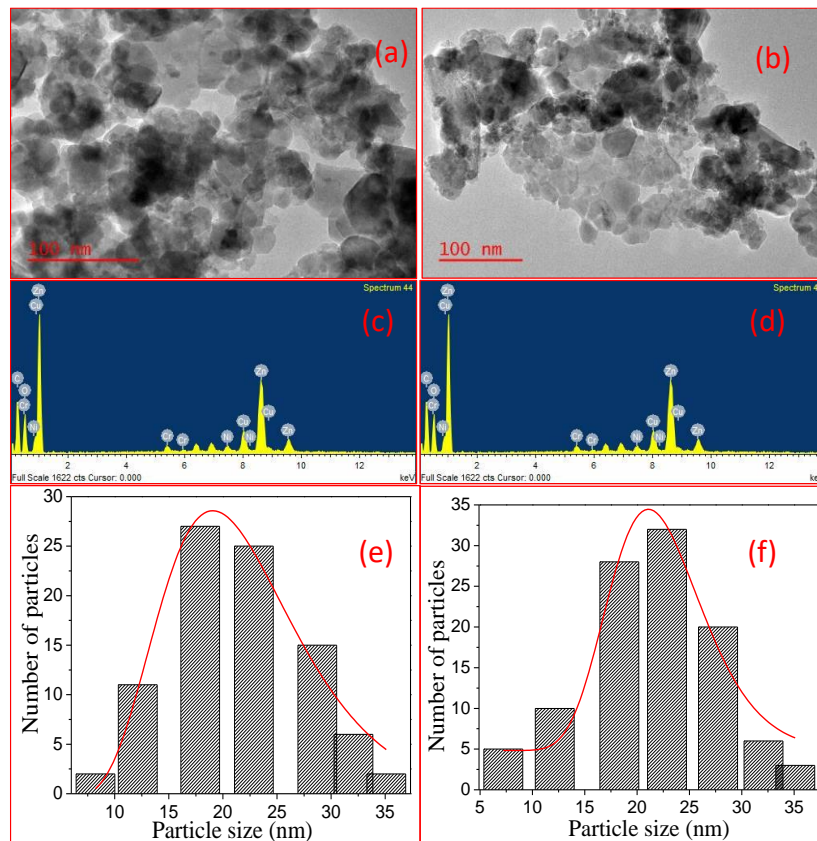


**Figure 3.** TEM images of (a)  $\text{Zn}_{0.96}\text{Ni}_{0.01}\text{Cr}_{0.03}\text{O}$  and (b)  $\text{Zn}_{0.90}\text{Ni}_{0.05}\text{Cr}_{0.05}\text{O}$  samples and their corresponding EDX image and particle size distribution of the samples are shown in figure 3 (c) to (f), respectively.

The DRS spectra of  $\text{Zn}_{0.96}\text{Ni}_{0.01}\text{Cr}_{0.03}\text{O}$  and  $\text{Zn}_{0.90}\text{Ni}_{0.05}\text{Cr}_{0.05}\text{O}$  samples are shown in Figure 4 (a). It is observed that the reflectance intensity decreased in the visible light region with an increase in Ni and Cr concentration. Both the samples show the mid-band-gap states appearing at 657 nm, which are assigned to the d–d transition bands, characteristic of  $\text{Ni}^{2+}$  with tetrahedral symmetry [17]. The absorption band at 657 nm corresponds to the  ${}^3T_1(F) \rightarrow {}^3T_1(P)$  transition of  $\text{Ni}^{2+}$  with tetrahedral symmetry. Furthermore, the weak sub band-gap absorption peaks are appeared between 710 and 730 nm ( ${}^4A_{2g}(F) \rightarrow {}^2E_g(G)$ ) are

the transitions of  $\text{Cr}^{3+}$  ions [17,18] in the host ZnO lattice. The absorption band appeared at 609 nm ( ${}^4A_{2g}(F) \rightarrow {}^4T_{2g}(F)$ ) is transitions of  $\text{Cr}^{3+}$  ions, indicating that some  $\text{Cr}^{3+}$  ions are at octahedral environment in the host ZnO lattice [17]. In order to determine the band-gap of the samples, the obtained diffuse reflectance spectra were converted to the Kubelka–Munk function [19] using the relation:  $F(R) = \frac{(1-R)^2}{2R} = \frac{k}{s}$ , where  $R$  is the reflectance,  $k$  is the absorption co-efficient and  $s$  is the scattering co-efficient. Here,  $F(R)$  is proportional to absorption co-efficient, thus  $\alpha$  in the Tauc equation [19] [ $\alpha h\nu = C(h\nu - E_g)^{\frac{1}{2}}$ ] can be replaced with  $F(R)$ . For direct allowed transition [19], the Tauc relation becomes;  $[F(R)h\nu]^2 = A(h\nu - E_g)^2$ . The plots of  $[F(R)h\nu]^2$  as function of  $h\nu$ , and shown in inset Figure 4(b). The band-gap values of the samples were obtained by extrapolating the linear region of  $[F(R)h\nu]^2 = 0$ . The calculated band-gap value is tabulated in Table 1. The band-gap value decreased with an increase of Ni and Cr concentration is due to the strong  $sp-d$  spin exchange interaction between the ZnO band electrons and localized  $d$  electrons of the Co and/or Cr ions substituting for  $\text{Zn}^{2+}$  ions than the exchange interactions of the  $d$  electrons of Ni and Cr ions [13].

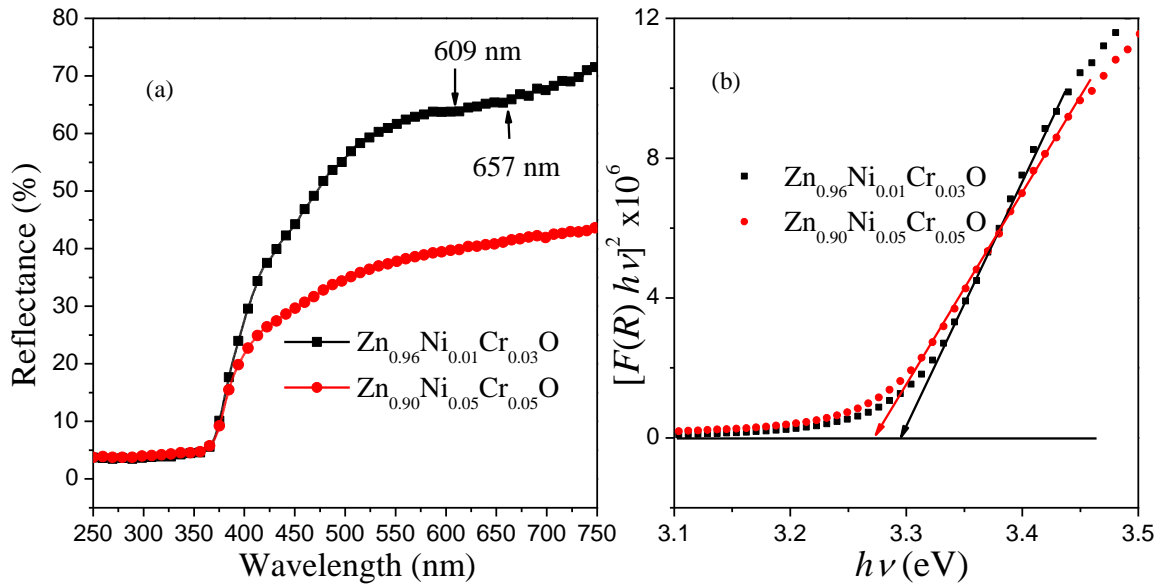


**Figure 4.** (a) DRS spectra of  $\text{Zn}_{0.96}\text{Ni}_{0.01}\text{Cr}_{0.03}\text{O}$  and  $\text{Zn}_{0.90}\text{Ni}_{0.05}\text{Cr}_{0.05}\text{O}$  samples and their corresponding plot of  $[F(R)h\nu]^2$  as function of  $(h\nu)$  are shown in Figure 4 (b), respectively.

The magnetic behaviour of the as-synthesized  $\text{Zn}_{0.96}\text{Ni}_{0.01}\text{Cr}_{0.03}\text{O}$  and  $\text{Zn}_{0.90}\text{Ni}_{0.05}\text{Cr}_{0.05}\text{O}$  samples was measured at room temperature. The magnetization as a function of applied magnetic field  $M(\mu_0H)$  curves is shown in Figure 5. The  $\text{Zn}_{0.96}\text{Ni}_{0.01}\text{Cr}_{0.03}\text{O}$  sample exhibit RTFM behaviour as evidenced by the clear and well-defined open hysteresis loops that are superimposed on the diamagnetic background. There are three possible reasons to observe the ferromagnetic behaviour in synthesized samples, viz. (i) formation of Ni and/ or Cr-related secondary phase, (ii) presence of magnetic impurities and (iii) extended defect because of the doping. In the present study, a magnetic cluster or secondary phase is ruled out, as confirmed by XRD and EDX. The XRD and diffuse reflectance spectroscopy results confirm the substitution of Ni and Cr ions at Zn sites of ZnO. The defects, especially single ionized oxygen vacancy, play a significant role in observed FM. This result suggests the origin of RTFM is related to intrinsic exchange interactions due to oxygen-related defects, which assisted bound magnetic polarons (BMPs) [20,21].

The  $\text{Zn}_{0.90}\text{Ni}_{0.05}\text{Cr}_{0.05}\text{O}$  sample shows antiferromagnetic behaviour at room temperature, as shown in Figure 5. Previous reports state that higher concentrations of Ni and Cr ions doped ZnO exhibit antiferromagnetic behaviour at room temperature [7,22]. The exchange interaction between  $\text{Ni}^{2+}$  and/or  $\text{Cr}^{3+}$  dopants and the formation of a  $\text{ZnCr}_2\text{O}_4$  phase is responsible for AFM behaviour in  $\text{Zn}_{0.90}\text{Ni}_{0.05}\text{Cr}_{0.05}\text{O}$ . This study reveals that with an increase in Cr concentration, more Cr ions are octahedrally coordinated rather than tetrahedral coordination, which causes the formation of the secondary phase.

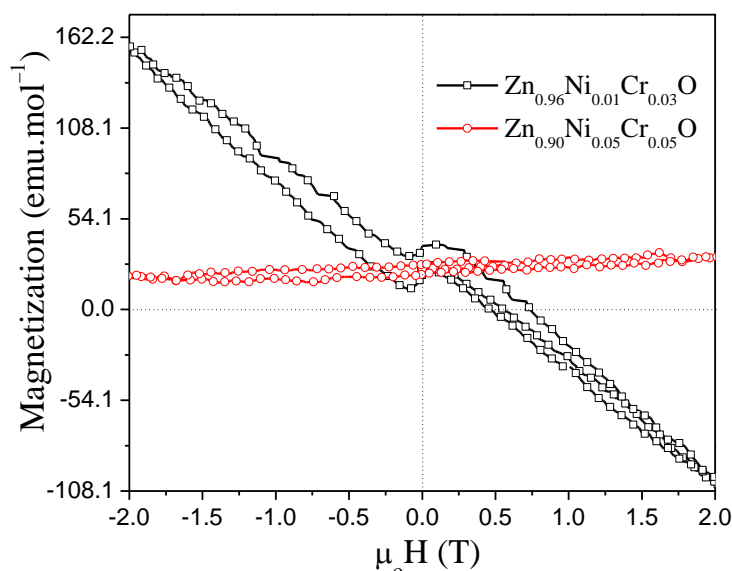


**Figure 5.** Magnetization as a function of the magnetic field of  $\text{Zn}_{0.96}\text{Ni}_{0.01}\text{Cr}_{0.03}\text{O}$  and  $\text{Zn}_{0.90}\text{Ni}_{0.05}\text{Cr}_{0.05}\text{O}$  samples measured at room temperature.

#### 4. Conclusions

The  $\text{Zn}_{0.96}\text{Ni}_{0.01}\text{Cr}_{0.03}\text{O}$  and  $\text{Zn}_{0.90}\text{Ni}_{0.05}\text{Cr}_{0.05}\text{O}$  nanoparticles were synthesized by the combustion method. The structural parameters were investigated using Rietveld refinement of the XRD results. Both the samples are in the hexagonal wurtzite structure and secondary phase ( $\text{ZnCr}_2\text{O}_4$  phase) present in  $\text{Zn}_{0.90}\text{Ni}_{0.05}\text{Cr}_{0.05}\text{O}$  sample. TEM results of the as-synthesized powders showed nanoparticles with sizes  $20 \pm 2$  nm and  $22 \pm 2$  nm for  $\text{Zn}_{0.96}\text{Ni}_{0.01}\text{Cr}_{0.03}\text{O}$  and  $\text{Zn}_{0.90}\text{Ni}_{0.05}\text{Cr}_{0.05}\text{O}$ , respectively. DRS measurement showed three subband-gap absorption peaks at 657, and 713 nm which are transitions of  $\text{Ni}^{2+}$  and  $\text{Cr}^{3+}$  ions, respectively. The band-gap is decreased with the increase of Ni and Cr concentration. The magnetic measurements of  $\text{Zn}_{0.96}\text{Ni}_{0.01}\text{Cr}_{0.03}\text{O}$  and  $\text{Zn}_{0.90}\text{Ni}_{0.05}\text{Cr}_{0.05}\text{O}$  exhibit FM and AFM behaviour, respectively. The observed FM in  $\text{Zn}_{0.96}\text{Ni}_{0.01}\text{Cr}_{0.03}\text{O}$  is attributed to oxygen vacancies/defects associated with BMPs. In  $\text{Zn}_{0.90}\text{Ni}_{0.05}\text{Cr}_{0.05}\text{O}$ , the exchange interaction between  $\text{Ni}^{2+}$  and/or  $\text{Cr}^{3+}$  dopants and forming a  $\text{ZnCr}_2\text{O}_4$  phase is responsible for AFM behaviour.

#### Acknowledgement

Financial aid from the South African National Research Foundation (Grant No's: 120856 and 88080) and the Faculty of Science, University of Johannesburg (UJ) URC and FRC is acknowledged. The use of the NEP Cryogenic Physical Properties Measurement System at UJ, obtained with financial support from the SANRF (Grant No: 88080) and UJ, RSA, is acknowledged.

#### References

- [1] Singh P, Kumar R and Singh R K 2019 *Ind. Eng. Chem. Res.* **58** 17130–63
- [2] Ozgur U, Alivov Y I, Liu C, Teke A, Reshchikov M A, Dogan S, Avrutin V, Cho S J and Morkoc H 2005 *J. Appl. Phys.* **98** 1–103
- [3] Yuan H, Xu M, Dong C, Ma J and Wang X 2019 *Appl. Surf. Sci.* **496** 143511

- 
- [4] Safeen A, Safeen K, Shafique M, Iqbal Y, Ahmed N, Rauf Khan M A, Asghar G, Althubeiti K, Al Otaibi S, Ali G, Shah W H and Khan R 2022 *RSC Adv.* **12** 11923–32
- [5] El-Hilo M, Dakhel A A and Yacoob Z J 2019 *J. Magn. Mater.* **482** 125–34
- [6] Singhal A, Achary S N, Manjanna J, Chatterjee S, Ayyub P and Tyagi A K 2010 *J. Phys. Chem. C* **114** 3422–30
- [7] Ekicibil A, Bulun G, Çetin S K, Dikmen Z, Orhun Ö, Firat T and Kiymaç K 2012 *J. Supercond. Nov. Magn.* **25** 435–40
- [8] Lokesha H S, Nagabhushana K R and Singh F 2017 *J. Lumin.* **192** 173–9
- [9] Satyanarayanareddy S, Lokesha H S and Nagabhushana K R 2021 *Rev. Sci. Instrum.*
- [10] Yang J, Fei L, Liu H, Liu Y, Gao M, Zhang Y and Yang L 2011 *J. Alloys Compd.* **509** 3672–6
- [11] Toby B H and Von Dreele R B 2013 *J. Appl. Crystallogr.* **46** 544–9
- [12] Kumar S, Asokan K, Singh R K, Chatterjee S, Kanjilal D and Ghosh A K 2014 *RSC Adv.* **4** 62123–31
- [13] Sharma D and Jha R 2017 *Ceram. Int.* **43** 8488–96
- [14] Bajpai G, Srivastava T, Patra N, Moirangthem I, Jha S N, Bhattacharyya D, Riyajuddin S, Ghosh K, Basaula D R, Khan M, Liu S W, Biring S and Sen S 2018 *RSC Adv.* **8** 24355–69
- [15] Ashokkumar M and Muthukumaran S 2015 *Phys. E Low-Dimensional Syst. Nanostructures* **69** 354–9
- [16] Beltrán J J, Osorio J A, Barrero C A, Hanna C B and Punnoose A 2013 *J. Appl. Phys.* **113** 1–4
- [17] Beltrán J J, Barrero C A and Punnoose A 2016 *J. Phys. Chem. C* **120** 8969–78
- [18] Babu B, Manjari V P, Aswani T, Rao G T, Stella R J and Ravikumar R V S S N 2014 *Indian J. Phys.* **88** 683–90
- [19] Morales A E, Mora E S and Pal U 2007 *Rev. Mex. Fis. S* **53** 18–22
- [20] Rana A K, Kumar Y, Rajput P, Jha S N, Bhattacharyya D and Shirage P M 2017 *ACS Appl. Mater. Interfaces* **9** 7691–700
- [21] Tawale J S, Kumar A, Swati G, Haranath D, Dhoble S J and Srivastava A K 2018 *Mater. Chem. Phys.* **205** 9–15
- [22] Kaur P, Kumar S, Negi N S and Rao S M 2015 *Appl. Nanosci.* **5** 367–72

# Synthesis, Characterization and Simulation of Graphene Oxide Nanomaterial for Application in Hybrid Supercapacitors

M T Nemukongwe<sup>1</sup>, J K Kirui<sup>1</sup>, N E Maluta<sup>1,2</sup> and R R Maphanga<sup>2,3</sup>

<sup>1</sup>Department of Physics, University of Venda, Private Bag X 5050, Thohoyandou, 0950

<sup>2</sup>National Institute for Theoretical and Computational Sciences, Gauteng, South Africa

<sup>3</sup>Council for Science and Industrial Research, P.O. Box 395, Pretoria, 0001

Email: [maanotry@gmail.com](mailto:maanotry@gmail.com)

**Abstract.** Energy storage is a major challenge in the development of many electronic devices. Graphene oxide (GO) has been suggested as a promising material for improved energy density in storage devices. In this study, GO was prepared by modified Hummer's method using graphite,  $\text{KMnO}_4$ ,  $\text{H}_2\text{SO}_4$  and  $\text{H}_3\text{PO}_4$ . From Fourier transformed infrared spectroscopy analysis, the transmittance broad band of carbonyl and hydroxyl were observed indicating the successful oxidation of graphite. Furthermore, ultraviolet-visible spectrum has the highest absorption peak at 905 nm which is in the infrared region. The highest occupied molecular orbital and lowest occupied molecular orbital structures show a band gap of -2.327eV and further confirm that GO can be a very good material for supercapacitors.

## 1. Introduction

Nanotechnology provides essential improvement potential for the development of efficient renewable energy storage [1-2]. Application of nanotechnology for renewable energy storage, involves designing and developing new innovative materials on the nanoscale dimension to enhance efficiency of storage [3]. The most commonly used energy storage devices are batteries. However, their reliability does not seem to stand the ever-growing demands of technological applications [4]. On the other hand, supercapacitors seem to be a perfect alternative to batteries for energy storage applications.

The physical and chemical properties of nanomaterials differ from one nanomaterial to another, and this can subsequently affect their efficiency in renewable energy storage. As a result, the search for new nanomaterials with relatively better electrochemical properties has spiked in recent years. In addition, researchers are exploring ways to modify various properties of nanomaterials for enhanced performance such as high-power density, energy density, and cycle stability. This has resulted in the focus on carbon-based nanomaterials for energy applications [5-12].

Carbon materials are becoming popular for use as electrodes for supercapacitors because of their ready availability, structural diversity, cost-effectiveness, and large active surface area [13, 14]. In addition, the flexibility of these materials permits modification and characterization to meet specific requirements for different applications [15].

The aim of this study was to experimentally synthesize and characterize graphene oxide and then simulate using theoretical methods. In particular, the density functional theory (DFT) method was used to investigate the optical properties whereas experimental methods were utilized to investigate the oxygen functional groups of the synthesized material.

## 2. Methods and materials

### 2.1. Experimental method

The preparation process of GO involved two steps: oxidation and exfoliation which are described in detail below:

#### Step 1: Oxidation

To synthesize GO we used 1 g of graphite powder and 9 g of potassium permanganate ( $\text{KMnO}_4$ ), mixed with 180 ml of sulphuric acid ( $\text{H}_2\text{SO}_4$ ) together with 20 ml of orthophosphoric acid ( $\text{H}_3\text{PO}_4$ ) and stirred using a magnetic stirrer for about 19 hours at a temperature of 40 °C. When the colour of the mixture turned greenish, 500 ml of distilled water was added to stop the reaction. Thereafter, 20 ml of hydrogen peroxide ( $\text{H}_2\text{O}_2$ ) was added to reduce manganese ions in the mixture until its colour changed to bright yellow, which is an indication of a complete oxidation process [16].

The oxidized mixture was then kept at room temperature to cool down. After cooling, it was filtered and washed by centrifugation for 3 hours using a mixture of 100 ml of distilled water and 15,6 ml of hydrochloric acid (HCl). Thereafter it was washed using distilled water for 1 hour, again with the aid of a centrifuge.

#### Step 2: Exfoliation

The GO product which was obtained after centrifugation was dispersed into 100 ml of distilled water for the formation of single-layer GO, and then it was heated while stirring with a magnetic stirrer for 19 hours at 60 °C. The resulting black paste was collected by centrifugation and dried at 70 °C for 24 hours.

### 2.2. Computational software

DFT is a computational quantum-mechanical modelling method aimed at quantitative understanding of material properties from the fundamental laws of quantum mechanics [17]. The theoretical study of GO was done using Materials Studio computing software. Materials Studio is a software for simulation and modelling of materials, such as ceramics, metals, polymers etc. Inside Materials Studio there is a package code called Vienna ab initio molecular dynamics package (VAMP). The structure of GO was built using Materials Studio whereas VAMP was used for the calculation of the optical properties in the form of the ultraviolet-visible (UV-Vis) spectrum.

### 2.3. Characterization techniques

#### 2.3.1. Fourier Transformed Infrared Spectroscopy:

Fourier transform infrared spectroscopy (FTIR) measures how much light a sample absorbs at each wavelength. This is achieved when the emitted radiation from an IR source passes through an interferometer composed of a beam splitter, a fixed mirror, and a moving mirror. The interferometer measures the wavelength of emitted light via interference patterns that help to increase accuracy. IR spectra are obtained by applying IR radiation to a sample and measuring the intensity of the passing radiation at a specific wavenumber. Consequently, IR radiation of certain molecular groups can be detected at specific wavenumbers [18]. FTIR is generally used to identify and compare the oxygen functional groups of carbon-based electrode materials [19-21].

### 2.3.2. Ultraviolet-Visible Spectroscopy:

Ultraviolet-visible spectroscopy/spectrophotometry (UV-Vis) is an optical spectroscopy that is based on the absorption of ultraviolet and visible light by a sample and also corresponds to electron excitation between the energy levels which provides the molecular orbitals, highest occupied molecular (HOMO) and lowest occupied molecular (LUMO). The absorption or reflectance in the visible spectral range directly affects the perceived colour of the chemical components involved. A UV-Vis measures the intensity of light passing through a sample solution in a cuvette and compares it to the intensity of the light before it passes through the sample. UV-Vis can be used to examine the optical features, electronic structures of materials and to monitor the degree of oxidation of carbon nanomaterials [19].

## 3. Results and discussion

### 3.1. FTIR results

Figure 1 and Figure 2 show FTIR spectra of graphite powder and GO, respectively. From Figure 2 it may be observed that there is a transmittance broad band between 3100 to 3300  $\text{cm}^{-1}$  due to hydroxyl group (O-H) and spectral troughs at 1730  $\text{cm}^{-1}$  and 1018  $\text{cm}^{-1}$  which are attributable to carbonyl group (C=O) and indicating the successful oxidation of graphene single layer of graphite after being exfoliated

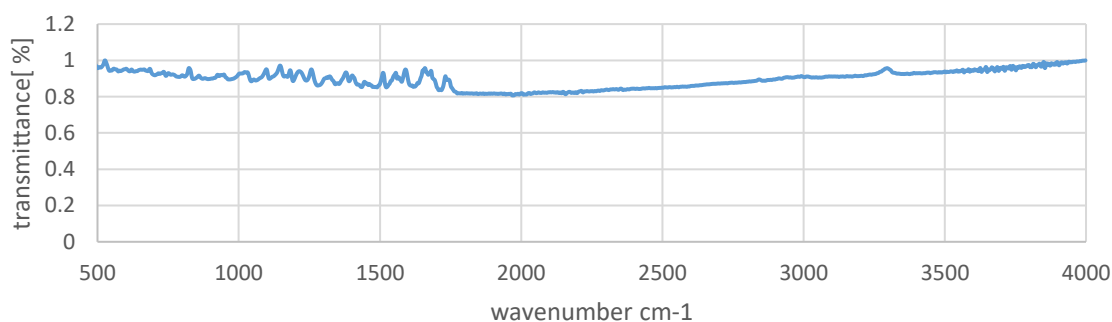


**Figure 1:** FTIR of graphite powder

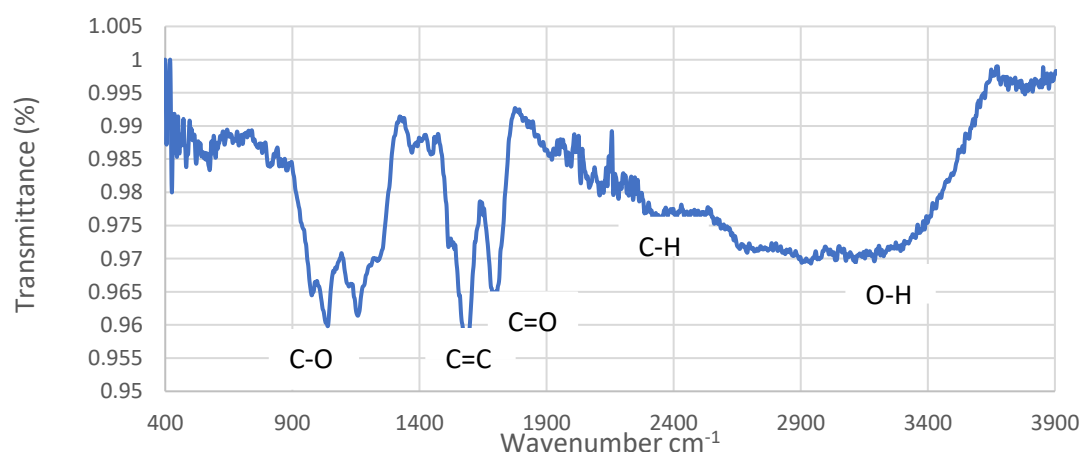


**Figure 2:** FTIR of graphene oxide

### 3.2. Optical properties

3.2.1. *UV-Vis spectrum:* VAMP calculations yielded, UV-Vis spectra shown in Figure 3. The highest absorption peak is located at 905 nm and the visible light absorption ranges from 700 nm to 1500 nm.

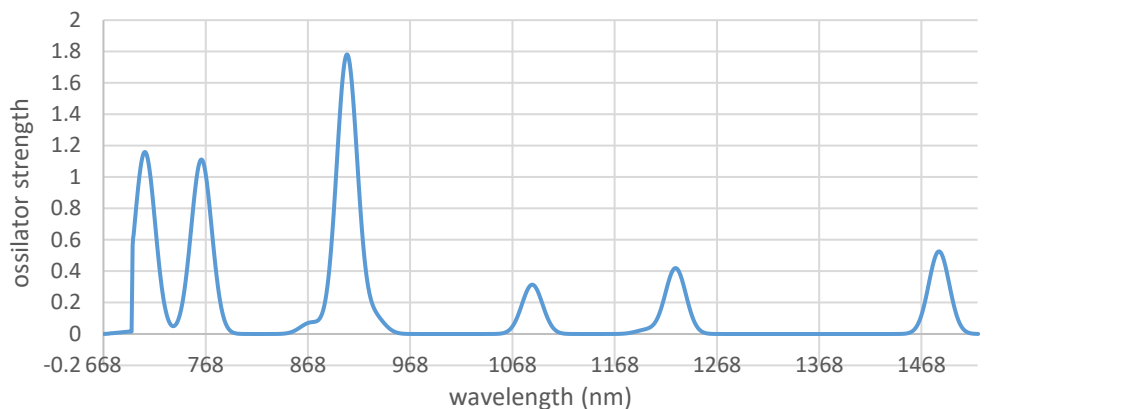
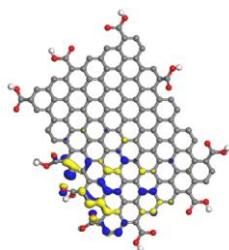
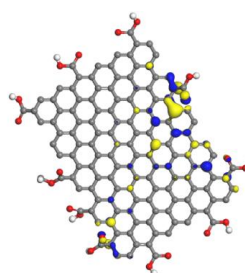


**Figure 3:** UV- Vis spectrum of GO.



(-4.89 eV)

**Figure 4:** LUMO structure of GO



(-7,217 eV)

**Figure 5:** HOMO structure of GO

## 4. Conclusion

Graphene oxide (GO) shows the presence of many oxygen-containing surface functional groups of carbonyl and hydroxyl in FTIR. However, the energies of HOMO and LUMO of GO are, -7.217 eV and -4.89 eV, respectively with a band gap of -2.327 eV which represents a semiconductor material that can behave as a conductor or an insulator. There is absorption in the range of 700 nm to 1500 nm but with less intensities at the higher wavelengths. No absorption was observed in the ultraviolet region. These results imply that GO has very good potential for supercapacitor application.

## Acknowledgement

Sincere gratitude goes to all my supervisors who guided and provided me with supervision throughout the course of my research. I give special thanks to Sipoyo D and Mlotshwa T M for their experimental and computational assistance

## References

- [1] Zhang Q, Uchaker E, Candelaria S L And Cao G 2013 Nanomaterials for energy conversion and storage. *Chem Soc Rev.* **42** 3127-3171
- [2] Pomerantseva E, Banaccorso F, Feng X, Cui Y and Gogotsi Y 2016 Energy storage: The future enabled by nanomaterials. *Science.* **366** 1-12
- [3] Manaktala S and Singh K M 2016 Nanotechnology for energy applications. *ISST Journal of Electrical & Electronics Engineering.* **7** p 63-69
- [4] Oyeniran O K. Synthesis and characterization of carbon-based nanostructured material electrodes for designing novel hybrid supercapacitors [dissertation] Faculty of Natural and Agricultural Sciences University of Pretoria. Pretoria South Africa 2018.

- [5] Avouris P and Dimitrakopoulos C 2012 Graphene: Synthesis and applications *Materials Today* **15** 86-97
- [6] Ghorbani M, Abdizadeh H And Golobostanfard M R 2015 Reduction of graphene oxide via modified hydrothermal method. *Procedia Materials Science*. **11** 326-330
- [7] Raja M, Kumar A B V K, Arora N and Subha J 2015 Studies on Electrochemical Properties of ZnO/rGO Nanocomposites as Electrode Materials for Supercapacitors. *Fullerenes Nanotubes carbon Nanostructures*. **23** 691-694
- [8] Wang H and Dai H 2013 Strongly coupled inorganic-nano-carbon hybrid materials for energy storage. *Chemical Society Reviews*. **47** 3088-3113.
- [9] Antink W H, Choi Y, Seong K, Kim J M and Piao Y 2018 Recent progress in porous graphene and reduced graphene oxide-based nanomaterials for electrochemical energy storage devices. *Advanced Materials Interfaces*. **5** 1-19.
- [10] Jayachandiran J, Yesuraj J, Arivanandhan M, Raja A, Suthanthiraraj S A, Jayavel R and Nedumaran, D 2018 Synthesis and Electrochemical Studies of rGO/ZnO Nanocomposite for Supercapacitor Application. *Journal of Inorganic and Organometallic Polymers and Materials*. **28** 2046-2055
- [11] Chaudhary S, James L S, Kumar A B V K, Ramana CH V V, Thomas S and Daewon K 2019 Reduced Graphene Oxide/ZnO Nanorods Nanocomposite: Structural, Electrical and Electrochemical Properties. *Journal of Inorganic and Organometallic Polymers and Materials* **29** 2282–2290
- [12] Li F, Jiang X, Zhao J And Zhang S 2015 Graphene oxide: A promising nanomaterial for energy and environmental applications. *Nano Energy* **16** 488-515.
- [13] Paul R and Dai L 2018 Interfacial aspects of carbon composites. *Composite Interfaces*. **25** 539-605
- [14] Jana A, Paul R and Roy A K 2019 Architectural design and promises of carbon materials for energy conversion and storage: in laboratory and industry. *Carbon Based Nanomaterials for Advanced Thermal and Electrochemical Energy Storage and Conversion* 25-61.
- [15] Paul R, Du R, Dai L, Ding Y, Wang Z L and Wei F 2019 3D Heteroatom-Doped Carbon Nanomaterials as Multifunctional Metal-Free Catalysts for Integrated Energy Devices. *Advanced Materials* **1805598** 1-6
- [16] Arthi G, Paulchamy B and Lignesh B D 2015 A sample approach to stepwise synthesis of graphene oxide nanomaterial. *Nanomedicine & Nanotechnology* **6** 1
- [17] Kurth S, Marques M A L and Gross E K U 2005 Density-Functional Theory. *Encyclopedia of Condensed Matter Physics* 395-402
- [18] Faghihzadeh F, Anaya N M, Schiffman L A and Oyanedel-Craver V 2016. Fourier transform infrared spectroscopy to assess molecular-level changes in microorganisms exposed to nanoparticles. *Nanotechnology for Environmental Engineering* 1-16.
- [19] Cheng Y And Liu J 2013 Carbon nanomaterials for flexible energy storage. *Material Research Letters* **1** 175-192.
- [20] Cao N and Zhang Y 2014 Study of Reduced Graphene Oxide Preparation by Hummers' Method and Related Characterization. *Journal of Nanomaterials* **2015** 1-5.
- [21] Hidayah N M S, Liu W, Lai C, Noriman N Z, Khe C S, Hashim U and Lee H C 2017. Comparison on graphite, graphene oxide and reduced graphene oxide: Synthesis and characterization. *AIP Conference Proceedings* **1892** 1-8.

# Investigating the effects of Carbon and Boron atoms on the $\tau$ -MnAl alloy properties employing the first principle approach

ID Sebe<sup>1\*</sup>, ME Sithole<sup>1</sup> and R Modiba<sup>2</sup>

<sup>1</sup>Department of Physics, Sefako Makgatho Health Science University, P.O. Box 94, Medunsa, 0204, South Africa.

<sup>2</sup>Materials Science and Manufacturing, CSIR, P.O. Box 395, Pretoria, 0001, South Africa.

\*E-mail: [itumelengsebe16@gmail.com](mailto:itumelengsebe16@gmail.com)

**Abstract.** Permanent magnet-based technologies are focusing on the use of  $\tau$ -phase magnetic alloys. The  $\tau$ -MnAl permanent magnetic alloys are interesting candidates to fill the performance gap between the expensive rare-earth-based magnets and the low performance ferrites. The purpose of the study was to investigate the effects of carbon and boron on the structural, electronic and magnetic properties of  $\tau$ -MnAl using the first principle method. The first principle calculations were performed using the density functional theory (DFT) within the generalized gradient approximation (GGA), with the perdue-burke-eruzer (PBE) function for exchange-correlation potential employed in CASTEP to study the electronic, and magnetic properties of  $\tau$ -MnAl magnets. The study revealed that  $\tau$ -MnAl have a total magnetic moment of  $3.04\mu_B$ , where Mn and Al have  $2.69\mu_B$  and  $0.35\mu_B$  respectively. A decrease in magnetic moment of Mn from  $2.69\mu_B$  to  $1.51\mu_B$  was obtained adding B atoms. The DOS of  $\tau$ -MnAl was observed to have a lower peak at the fermi level. The magnetic moment obtained for Mn was  $0.46\mu_B$  after C atoms were added. The DOS of  $\tau$ -Mn<sub>3</sub>AlC shifted to the right with the highest peak at the fermi level. The results obtained revealed that the DOS of  $\tau$ -Mn<sub>2</sub>AlB<sub>2</sub> and  $\tau$ -Mn<sub>3</sub>AlC have their highest peaks at the fermi level. This was due to the decrease in magnetic moment of Mn after adding C and B to  $\tau$ -MnAl.

## 1. Introduction

Permanent magnets are an essential component of modern life, where their use in technology is still expanding. They are the basic building blocks of various electromechanical and electrical devices. Based on the requirements for the various applications of permanent magnets, such as the strength of the magnet for a given size, the ability of the magnet to maintain its field in the presence of a reverse field, high temperatures, and hostile environments, as well as its cost [1]. Various energy-efficient appliances, direct-drive wind turbines, hybrid and electric motors, and wind turbines all contain significant amounts of permanent magnets. Due to their outstanding magnetic properties, rare earth magnets like Dy-substituted Nd<sub>2</sub>Fe<sub>14</sub>B, SmCo<sub>5</sub>, and Sm<sub>2</sub>Fe<sub>17</sub>N have been employed in all these devices. Nd, Sm and Dy, however, are becoming more expensive. As a result, creating powerful permanent magnets without rare earth elements is a growing concern [2].

Due to their significant advantages, such as high saturation magnetization, large theoretical  $(BH)_{max}$ , decent Curie temperature and extremely low cost. The tetragonal phase ( $\tau$ -phase) MnAl permanent magnetic alloys are an interesting candidate to close the performance gap between the expensive rare-earth-based magnets and the low performance ferrites [3]. The  $\tau$ -phase (tetragonal L1<sub>0</sub> superstructure, space group of P4/mmm) is the sole ferromagnetic phase in the MnAl binary system and

it is thermodynamically metastable [3]. This study aims to investigate the structural, magnetic, and electronic properties of  $\tau$ -MnAl alloys employing the first principle method.

## 2. Methodology

The Cambridge Sequence Total Energy Package (CASTEP) code and the Generalized Gradient Approximation in the Perdew-Burke-Eruzer (PBE) scheme were used in this study. The structural, electronic, and magnetic properties of the  $\tau$ -MnAl unit cell were calculated. We performed geometry optimization before calculations of  $\tau$ -MnAl properties and in all calculations spin-polarization was considered [4]. The convergence criterion for structure optimization and energy calculations was set to a fine quality. The experimental MnAl lattice parameter ( $a=3.93$  and  $c=3.56$ ) with the atomic radii ( $1.43\text{\AA}$  for Al and  $1.26\text{\AA}$  for Mn) and energy convergence of  $10^{-6}$  were utilized in all calculations. The tolerance for the stress concentration factor (SCF), energy, maximum force, and maximum displacement was set to eV/atom, eV/atom, 0.03, and 0.001 respectively for all calculations. The Brillouin-zone (BZ) integration Pack has been used with a 700eV energy cut-off and  $9\times 9\times 7$  Monkhorst-Pack  $k$ -point grids [5].

## 3. Results and discussion

### 3.1. Structural and Magnetic Properties of $\tau$ -MnAl

Fig 1 shows simulated crystal structure of  $\tau$ -MnAl. This is a metastable  $\tau$ -phase MnAl tetragonal  $L1_0$  superstructure, with a space group of  $P4/mmm$ . The  $\tau$ -MnAl structure is composed of 5 atoms (1 Mn and 4 Al atoms). The structure went through full geometry optimization. When the energy was at its lowest after optimization the cell was at its most stable states [4].

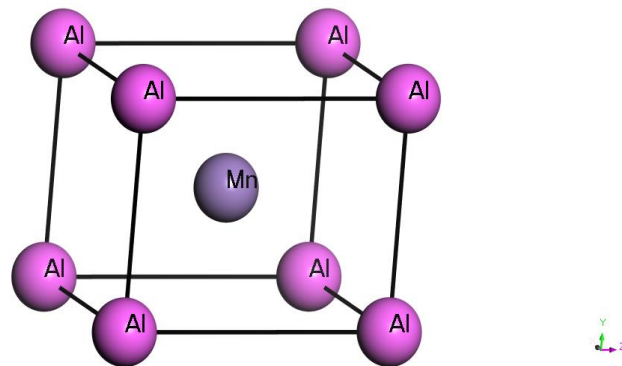


**Figure 1.** The crystal structure of  $\tau$ -MnAl.

Table 1, shows the calculated lattice parameters of the  $\tau$ -MnAl structure. The calculated  $c/a$  ratio with respect to pure  $\tau$ -MnAl doped with C and B were  $1.271\text{\AA}$ ,  $1\text{\AA}$  and  $0.495\text{\AA}$  which is close to that obtained in previous study [6]. When B and C atoms were added in  $\tau$ -MnAl, the increase in lattice parameters was observed.

**Table 1.** Lattice parameters of  $\tau$ -MnAl Structures.

Structures	a ( $\text{\AA}$ )	b ( $\text{\AA}$ )	c ( $\text{\AA}$ )	c/a ( $\text{\AA}$ )
$\tau$ -MnAl	2.753	2.753	3.500	1.271
$\tau$ -Mn <sub>2</sub> AlB <sub>2</sub>	5.727	5.727	2.834	0.495
$\tau$ -Mn <sub>3</sub> AlC	3.807	3.807	3.807	1.0

Table 2. shows the calculated total magnetic moments of  $\tau$ -MnAl structures. The magnetic moments of Mn and Al together equal  $3.04\mu_B$ , while Mn and Al alone had  $2.69\mu_B$  and  $0.35\mu_B$ , respectively. After B and C atoms were added, the magnetic moment of Mn decreases to  $1.5\mu_B$  and  $0.46\mu_B$  respectively. The positive and negative moments of Mn and Al atoms after adding C and B indicate antiferromagnetic coupling between their sublattice.

**Table 2.** The total magnetic moments of structures.

STRUCTURES	Mn( $\mu_B$ )	Al( $\mu_B$ )	B( $\mu_B$ )	C( $\mu_B$ )	Total( $\mu_B$ )
$\tau$ -MnAl	2.69	0.35	-	-	3.04
$\tau$ -Mn <sub>2</sub> AlB <sub>2</sub>	1.51	-0.24	-0.17	-	1.1
$\tau$ -Mn <sub>3</sub> AlC	0.46	-0.03	-	-0.04	0.39

### 3.2 Electronic Properties

#### 3.2.1 Density of states

The density of states (DOS) of doped (C and B) and undoped  $\tau$ -MnAl structures is shown in Fig 2. The instability of the structure is related to the Fermi level ( $E_f$ ), represented by the vertical line in Fig 2. Structures with the highest DOS at  $E_f$  are considered the least stable, whereas the lowest are the most stable [7]. The DOS of  $\tau$ -MnAl has its highest peak just before it reaches the Fermi level and is at its lowest peak when is at the fermi level which is antiferromagnetic. This is due to the high magnetic moment of Mn  $2.69\mu_B$ . The addition of carbon lowers the magnetic moment of Mn from  $2.69\mu_B$  to  $0.46\mu_B$ . The DOS of  $\tau$ -Mn<sub>3</sub>AlC is at its highest peak just as it approaches the Fermi level and a bit low but above that of  $\tau$ -MnAl at the Fermi level. The  $\tau$ -Mn<sub>2</sub>AlB<sub>2</sub> DOS is above both  $\tau$ -MnAl and  $\tau$ -Mn<sub>3</sub>AlC DOS from the range  $-15\text{eV}$  to  $18\text{eV}$ , except that it has a lower  $\tau$ -Mn<sub>3</sub>AlC peak when approaching the Fermi level.

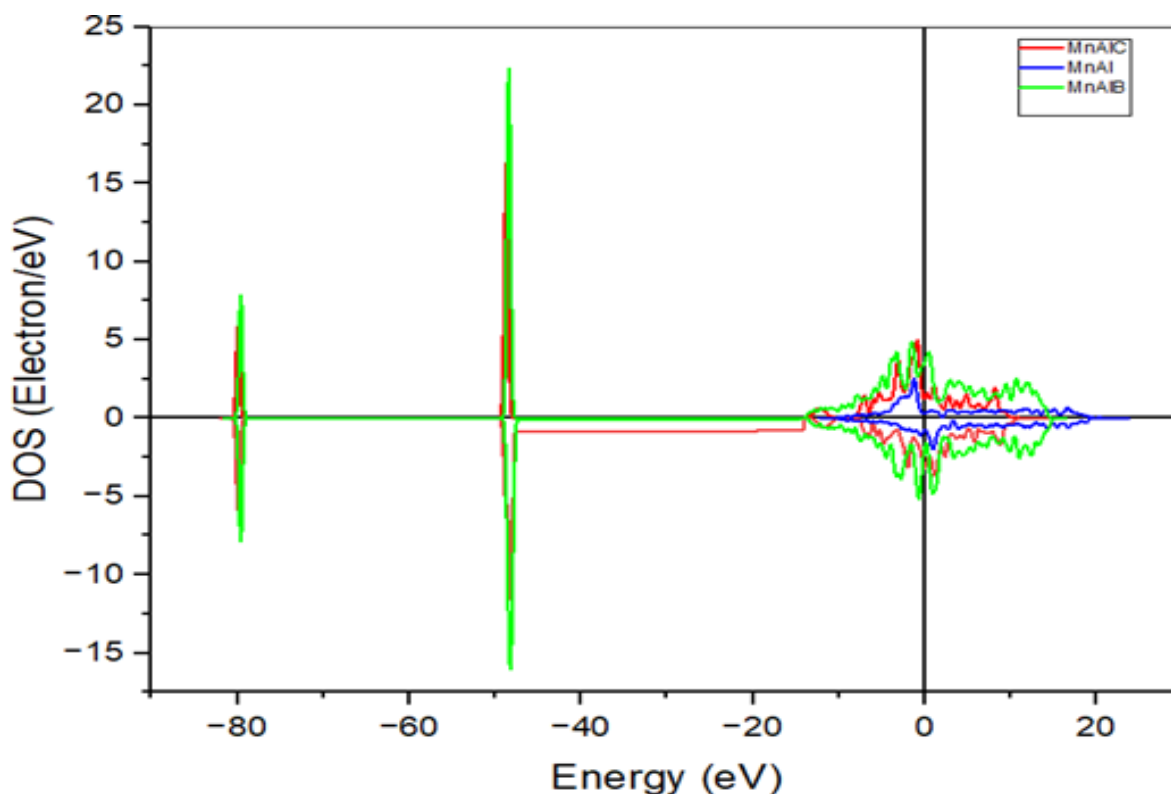


**Figure 2.** Comparison of the total density of states (DOS) for  $\tau$ -MnAl doped with C and B structures.  $E_F = E = 0$ .

#### 4. Conclusion

In conclusion, the  $\tau$ -MnAl structure was optimized using first principles PBE-GGA calculations. The electronic and magnetic properties, including lattice constants, densities of states, and magnetic moment, were examined. Due to the expansion of the crystal lattice caused by the inclusion of the carbon and boron atoms, the  $c/a$  ratio decreased. The  $\tau$ -MnAl doped with carbon seem to be the most stable since it has the lowest DOS at the Fermi level ( $E_f = 0$ ). Boron doped structure is the least stable since its DOS is the highest at Fermi level.

#### Acknowledgements

The authors thank Sefako Makgatho Health Science University and NRF for their financial support. The support from the CSIR is highly recognised. The calculations were performed using the computers of the high-performance computing centre (CHPC) in Cape Town.

#### References

- [1] McCallum R W, Lewis L, Skomski R, Kramer M J and Anderson I E 2014 Practical aspects of modern and future permanent magnets *Annu. Rev. Mater. Res.* **44** 451-77
- [2] Park J H, Hong Y K, Bae S, Lee J J, Jalli J, Abo G S, Neveu N, Kim S G, Choi C J and Lee J G 2010 Saturation magnetization and crystalline anisotropy calculations for MnAl permanent magnet *J. Appl. Phys.* **107** 1-5.
- [3] Zhao S, Wu Y, Wang J, Jia Y, Zhang T and Jiang C 2019 Realization of large coercivity in MnAl permanent magnet alloys by introducing nanoprecipitates *J. Magn. Mater.* **483** 164-68.
- [4] Yang J, Xiao Z, Wen Q and Yang F 2014 First principle study on the structural, electronic and magnetic properties of Ni<sub>4</sub>C *Compu. Conde. Matt.* **1** 51-57.
- [5] Miya L E and Sithole M E 2022 Investigating the electronic and magnetic properties of Dy, Y and La by site substitution on Nd<sub>2</sub>Fe<sub>14</sub>B permanent magnet employing the first-principle approach *Conf. SA Advan. Mater. Init.* **40** 224-227.
- [6] Kontos S, Fang H, Li J, Delczeg-Czirjak E K, Shafeie S, Svedlindh P, Sahlberg M and Gunnarsson K 2019 Measured and calculated properties of B-doped  $\tau$ -phase MnAl *J. Magn. Mater.* **474** 591-598.
- [7] Mahlangu R, Phasha M J, Chauke H R, Ngoepe P E 2013 Structural, elastic, and electronic properties of equiatomic PtTi as potential high-temperature shape memory alloy *Intermetallics.* **33** 27-32.

# Electronic, Magnetic and Mechanical Properties of Nd<sub>2</sub>Fe<sub>14</sub>B Permanent Magnets: Ab Initio Study

M.E Baloyi<sup>1\*</sup>, P.E Ngoepe<sup>1</sup> and H.R Chauke<sup>1</sup>

Materials Modelling Centre, University of Limpopo, Private Bag X1106, 0727, Sovenga, South Africa

E-mail: [mphame1a.baloyi@gmail.com](mailto:mphame1a.baloyi@gmail.com)

**Abstract.** Neodymium-based permanent magnets (Nd<sub>2</sub>Fe<sub>14</sub>B) are the potential permanent magnets for use in various applications due to their high magnetic field strength and resistance to demagnetisation. These magnets have various applications in wind turbines and electric vehicles due to their exceptional magnetic properties. However, they suffer from low operating temperatures below 585 K. In this study, we investigate the electronic, magnetic, and mechanical properties of neodymium magnets using the first-principle density functional theory approach. Nd<sub>2</sub>Fe<sub>14</sub>B was found to be thermodynamically stable since the heats of formation were negative. However, it was found that Nd<sub>2</sub>Fe<sub>14</sub>B is mechanically unstable. Moreover, the density of states was calculated to predict the electronic stability of the permanent magnets which is in agreement with the calculated heats of formation. The phonon dispersion curves were also calculated and Nd<sub>2</sub>Fe<sub>14</sub>B is found to be vibrationally unstable due to the presence of soft modes. The calculated magnetic moment compares well to the experimental findings. The substitution of Nd with available rare earth elements is suggested to enhance the stability and magnetic properties of the magnets.

## 1. Introduction

Permanent magnet (PM) is a material that retains its magnetic properties because of its intrinsic structure [1]. PM includes a variety of magnets including alnico, ferrite, ceramic, and rare-earth magnets. They are used in a variety of applications including motors, generators, sensors, transducers, mechanical devices, latches and imaging systems [2]. Rare earth magnets (RE) are strong permanent magnets made from rare earth elements. However, REs are extremely brittle and very susceptible to corrosion; they are usually plated or coated to prevent corrosion [3].

There are two types of well-known rare earth magnets namely samarium cobalt (SmCo<sub>5</sub>) magnets and neodymium (NdFeB) magnets, with SmCo<sub>5</sub> magnets being less common due to their higher cost and lower magnetic field [4]. The strongest rare earth magnets are sintered NdFeB magnets, which have the highest energy product of any commercial PM material [5, 6]. These magnets are used in cutting-edge technological applications. In addition, experimental studies show that the highest magnetic properties were obtained at the highest milling time, suggesting that milling time increases the value of the magnetic properties [7]. Neodymium magnets have been reported to have high magnetic field strength and resistance to demagnetization. However, they suffer from extremely low operating temperatures, known as the Curie temperature (T<sub>c</sub>) below 585 K [3] and poor mechanical properties. In addition, the anisotropy field suffers a significant decrease with increasing temperature [3, 8].

In this work, we study the thermodynamic, mechanical and vibrational stability of Nd<sub>2</sub>Fe<sub>14</sub>B magnets using density functional theory (DFT) techniques. Heats of formation, densities of states, elastic constants and phonon dispersion curves of Nd<sub>2</sub>Fe<sub>14</sub>B structures were investigated. The calculations indicate that Nd<sub>2</sub>Fe<sub>14</sub>B is vibrationally unstable. However, it was found that Nd<sub>2</sub>Fe<sub>14</sub>B does not meet the

tetragonal stability criteria, which is attributed to the mechanical instability of the material. In addition, the density of states was also calculated to predict the electronic stability of the permanent magnets.

## 2. Methodology

The calculations were carried out using *ab initio* density functional theory (DFT) [9] formalism as implemented in the Vienna *ab initio* simulation package (VASP) [10] with the projector augmented wave (PAW) [11]. An energy cut-off of 400 eV was used, as it was sufficient to converge the total energy of the tetragonal Nd<sub>2</sub>Fe<sub>14</sub>B magnets. For the exchange-correlation functional, the generalized gradient approximation of Perdew, Burke and Ernzerhof (GGA-PBE)sol [12] was chosen. The suitable k-points mesh according to Monkhorst and Pack [13] of 6x6x3 was used. A tetragonal Nd<sub>2</sub>Fe<sub>14</sub>B structure with 68 atoms was used (Figure 1). The phonon dispersion spectra were evaluated using PHONON code [14] as implemented in MedeA software.

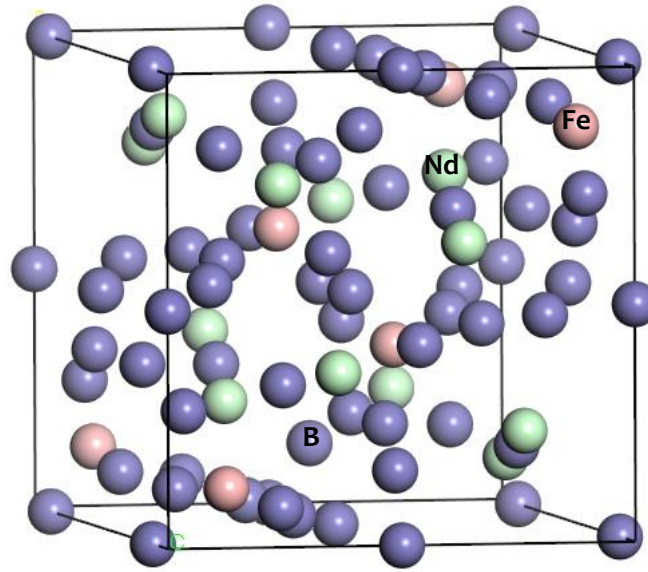


**Figure 1.** The atomic arrangement unit cell of the Nd<sub>2</sub>Fe<sub>14</sub>B system with a space group P4<sub>2</sub>/mmm.

## 3. Results and discussion

### 3.1. Structural and Thermodynamic Properties

In Table 1, the lattice parameters and heats of formation for the tetragonal Nd<sub>2</sub>Fe<sub>14</sub>B magnets are discussed. The magnet is a tetragonal structure consisting of a 68-atom unit cell and a space group of P4<sub>2</sub>/mmm, with atoms arranged in an eight-layer structure, 56-Fe, 8-Nd and 4-B atoms. The calculated *a* parameter of Nd<sub>2</sub>Fe<sub>14</sub>B was 8.249 Å whereas the *c* parameter was 12.12 Å. The results of the equilibrium lattice parameters agree with available experimental values (*a* = 8.82 Å and *c* = 12.25 Å) to within 6%. In addition, the heats of formation were calculated to determine the thermodynamic stability of the structure. The equation for determining the heats of formation ( $\Delta H_f$ ) is given by [23]:

$$\Delta H_f = E_c - \sum_i x_i E_i \quad (1)$$

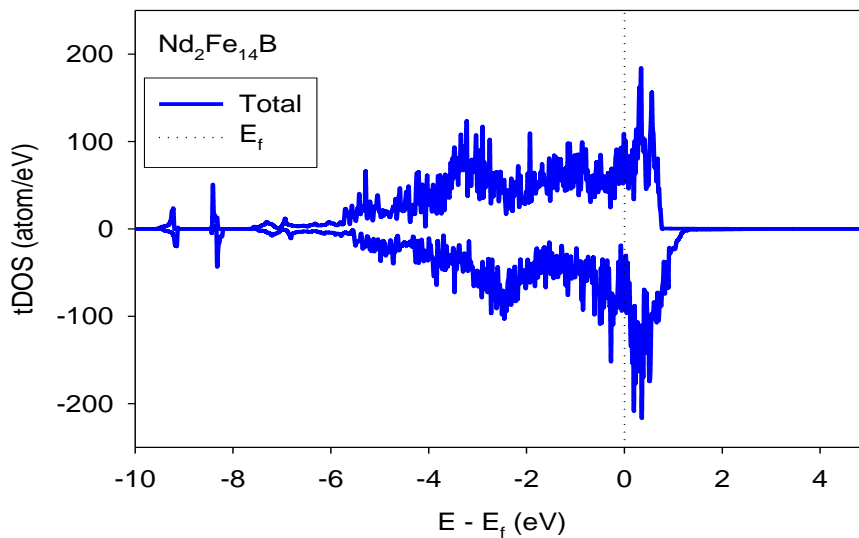
where  $E_c$  is the calculated total energy of the compound,  $E_i$  is the calculated total energy of element *i* in the compound. For a structure to be stable, the heat of formation must be negative; otherwise, a positive value indicates instability. The heats of formation were calculated to investigate the thermodynamic stability of Nd<sub>2</sub>Fe<sub>14</sub>B magnets as shown in Table 1. The heats of formation for the Nd<sub>2</sub>Fe<sub>14</sub>B permanent magnet were found to be -6.499 eV/atom, indicating the thermodynamic stability of the magnet.

**Table 1.** Lattice parameters and Heats of formation ( $\Delta H_f$ ) of the  $\text{Nd}_2\text{Fe}_{14}\text{B}$  magnets.

Structure	Lattice parameter (Å)		$\Delta H_f$ (eV/atoms)
	Calculated	Experimental [3]	
$\text{Nd}_2\text{Fe}_{14}\text{B}$	$a = 8.25$	$a = 8.82$	-6.499
	$b = 8.25$	$b = 8.82$	
	$c = 12.12$	$c = 12.25$	

### 3.2. Density of states

To further understand the difference in electronic structures of the  $\text{Nd}_2\text{Fe}_{14}\text{B}$  magnets, the partial density of states (DOS) are determined and the plots are shown in Figure 2 below. The partial density of states (PDOS) was calculated to determine the contribution of Nd, Fe, and B atomic orbitals. We note that the lower energy side is dominated by sets of peaks originating primarily from the d states of Fe, p states, and s states of B. On the lower energy side, the Fe 3d orbitals dominate from the Fermi level (0 eV) to -6 eV, while the B s-orbital is responsible for the peaks at -8 eV and -9 eV. The peaks of Fe 3d-states are clustered from -5 eV to 1 eV whereas B peaks around -5 eV to 0 eV, -8 eV and -9 eV. The highly localized Nd peaks are found to be located clustered around the  $E_f$  as shown in Figure 2. The f states of Nd are responsible for the higher energy peaks. We observe that f states of Nd and d states of Fe contribute to the observed peaks in the conduction band, with f states of Nd dominating. Boron does not influence the conduction band. Both Fe d-orbitals and Nd f-orbitals are responsible for the peaks at the  $E_f$ . The s and p orbitals of both Nd and Fe contribute less to the  $E_f$  peaks. The total DOS for  $\text{Nd}_2\text{Fe}_{14}\text{B}$  is dominated by the Fe 3d states as shown in Figure 2. In the  $E_f$ , the extremely localized peaks are observed to be clustered. Moreover, the  $E_f$  hits the DOS at the pseudogap which suggests that the structure is stable. As has been seen in the heats of formation, our total density of states calculations confirms that the  $\text{Nd}_2\text{Fe}_{14}\text{B}$  structure is electronically stable. This study compares to a previous report on the tDOS of  $\text{Nd}_2\text{Fe}_{14}\text{B}$  [15].

**Figure 2.** The total density of states for the  $\text{Nd}_2\text{Fe}_{14}\text{B}$  permanent magnets.

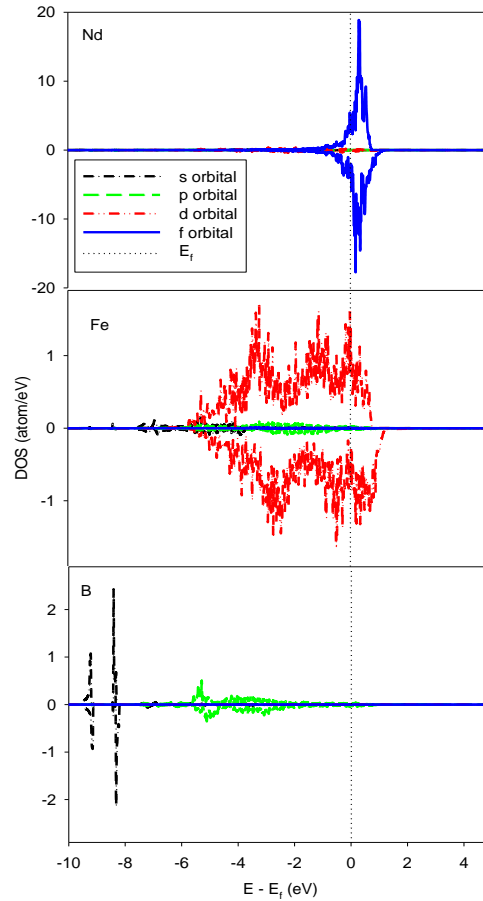


**Figure 3.** The partial density of states for the Nd<sub>2</sub>Fe<sub>14</sub>B permanent magnets.

### 3.3. Elastic Constants

The elastic constants, bulk, shear, Young moduli, Pugh, Poisson, and anisotropic ratios of Nd<sub>2</sub>Fe<sub>14</sub>B magnets are listed in Table 2. The following is the condition of tetragonal crystal stability [16]:

$$C_{44} > 0, C_{66} > 0, C_{11} > |C_{12}| \text{ and } C_{11} + C_{12} - \frac{2C_{13}^2}{C_{33}} > 0. \quad (2)$$

Our results show that the  $C_{11}$  is found to be greater than the absolute of  $C_{12}$  whereas the  $C_{44}$  and  $C_{66}$  are greater than zero. Moreover, two elastic constants are negative, namely  $C_{13}$  and  $C_{33}$  with values of -1412.67 and -2594.39, respectively. The calculated elastic shear modulus was found to be positive ( $C' = 110.96$ ). This suggests that the computed elastic constants of Nd<sub>2</sub>Fe<sub>14</sub>B satisfy tetragonal mechanical stability criteria (eq. 1). To deduce the mechanical strength of materials the elastic anisotropy (A) factor is used [17]. If the value of A is 1, the material is considered to be elastically isotropic (fewer microcracks within the material) and the degree of anisotropy is measured if the material is less than or greater than 1 [18]. Elastic anisotropy for non-cubic is indicated by  $A_1$ ,  $A_2$  and  $A_3$ . The calculated  $A_1$ ,  $A_2$  and  $A_3$  of Nd<sub>2</sub>Fe<sub>14</sub>B magnets all show anisotropic behaviour with values of 0.56, 0.31 and 1.79, respectively. In addition, we calculated the bulk to shear modulus (B/G) ratio, known as Pugh's ratio to investigate the fracture range or the ductility in these structures. Pugh proposed that material is ductile if Pugh's ratio is greater than 1.75 ( $B/G > 1.75$ ) otherwise brittle [19]. It is found that the B/G of the Nd<sub>2</sub>Fe<sub>14</sub>B phase is -14.42, which is smaller than 1.75, so Nd<sub>2</sub>Fe<sub>14</sub>B is a brittle phase. The magnetic moment of the Nd<sub>2</sub>Fe<sub>14</sub>B structure was calculated as shown in Table 2 below. The calculated magnetic moment was 35.63  $\mu_B$ , which agrees well with the experimental values of 35.0 B/f.u or 37.1 B/f.u [20, 3].

**Table 2.** Elastic constants (GPa), anisotropy, Pugh's ratio and magnetic moment ( $\mu\text{B}$ ) of  $\text{Nd}_2\text{Fe}_{14}\text{B}$  permanent magnets.

Properties	Calculated
$C_{11}$	472.47
$C_{12}$	250.56
$C_{13}$	-1412.67
$C_{16}$	449.37
$C_{33}$	-2594.39
$C_{44}$	110.36
$C_{66}$	61.82
$C'$	110.96
$A_1 = 2C_{66}/(C_{11}-C_{12})$	0.56
$A_2 = 2C_{66}/(C_{11}-C_{12})$	0.31
$A_3 = 2C_{44}/(C_{11} + C_{33} - 2C_{13})$	1.79
B/G	-14.42
Magnetic Moment	35.63

### 3.4. Phonon dispersions curves

Phonon dispersion curves and phonon density of states (DOS) for the  $\text{Nd}_2\text{Fe}_{14}\text{B}$  magnets are presented in Figure 4. The phonon dispersion is used to investigate the vibrational stability of these magnets, where the presence of soft modes in the negative frequency suggests the instability of the material otherwise stability. As it has been seen in the elastic properties, our phonon dispersion calculations (Figure 4) confirm that the  $\text{Nd}_2\text{Fe}_{14}\text{B}$  structure is vibrational unstable since there are soft modes observed in the phonon calculations. The soft modes are observed along X, M, Z, A, R and  $\Gamma$  directions. There are vibrations observed at -27 THz in the negative frequency along the  $\Gamma$  directions which indicate the instability of the material.

There is a small sharp peak along -7 THz which indicates the contribution of Nd, which is also ascribed to the DOS peak at 0 THz and 10 THz. Moreover, Fe is ascribed to the DOS peak around 15 THz and it is also responsible for vibrations in the negative frequency. B atom has a negligible effect or contribution towards the negative frequency, however, it is ascribed to the DOS peak at 18 THz. This suggests that Nd and Fe vibrations are responsible for the instability of the  $\text{Nd}_2\text{Fe}_{14}\text{B}$  structure.

## 4. Conclusions

The equilibrium lattice parameter, heats of formation, elastic properties, vibrational properties and electronic properties of  $\text{Nd}_2\text{Fe}_{14}\text{B}$  magnets were calculated using ab initio. It was found that the lattice parameter for  $\text{Nd}_2\text{Fe}_{14}\text{B}$  structures is in good agreement with the experimental findings.  $\text{Nd}_2\text{Fe}_{14}\text{B}$  is found to be thermodynamically stable with negative heats of formation, which is in good agreement with the calculated density of states. In addition, all of the elastic constants satisfy tetragonal stability criteria. The phonon dispersion curves show that the neodymium system is vibrationally unstable due to soft modes observed in the negative frequency. In conclusion,  $\text{Nd}_2\text{Fe}_{14}\text{B}$  magnets are found to show poor mechanical properties and the partial substitution of Nd with RE is suggested to enhance the stability and magnetic properties of magnets.

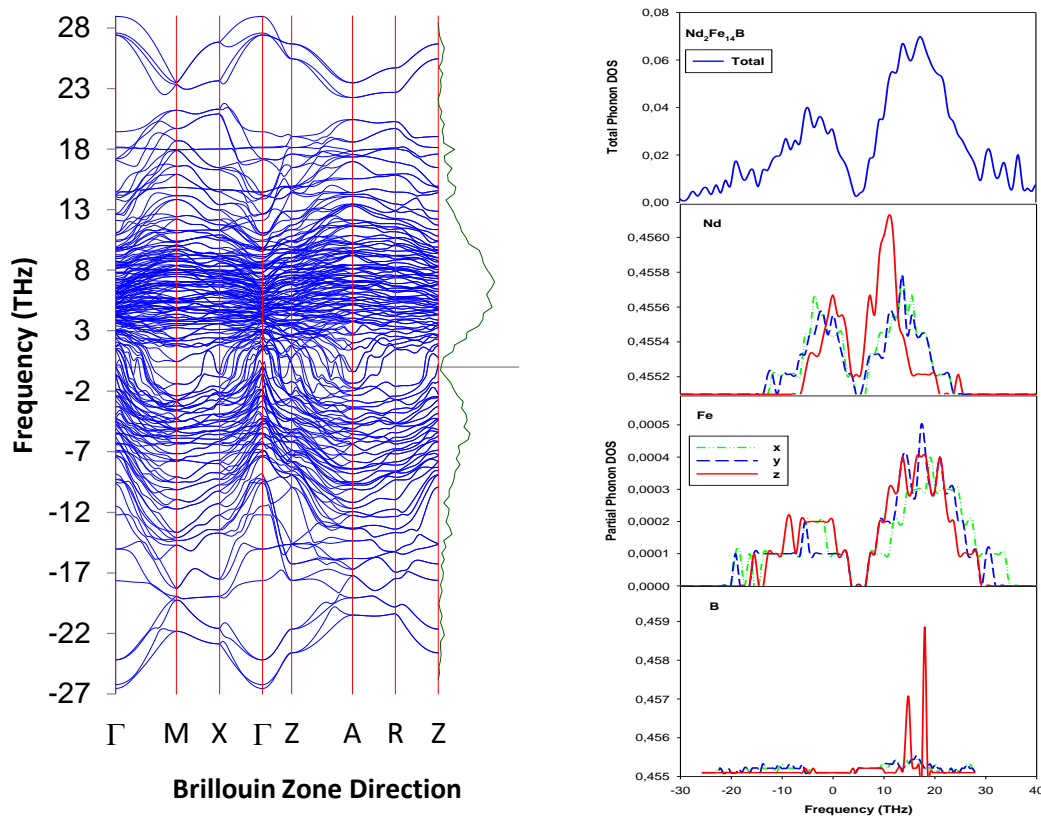


**Figure 4.** Phonon dispersions and phonon density of states for Nd<sub>2</sub>Fe<sub>14</sub>B permanent magnets.

### Acknowledgements

The authors would like to thank the National Research Foundation (NRF) and Titanium centre of competence (TiCoC) for their financial support. The Department of Science and Innovation (DSI) is widely acknowledged. The calculations were carried out on computers at the University of Limpopo's Materials Modelling Centre (MMC) and the Centre for High-Performance Computing (CHPC) in Cape Town.

### References

- [1] Coey J M D 2012 *Scripta Mater.*, **67**, 524-529
- [2] Gong Q, Yi M, Evans R F L, Gutfleisch O and Xu B 2020 *Mater. Research Lett.*, **8**, 89-96
- [3] Sagawa M, Fujimura S, Yamamoto H and Matsuura Y 1984 *IEEE Transactions on Magnetics*, **20**, 1584-1589
- [4] Yin X, Yue M, Lu Q, Wang F, Qiu Y, Liu W, Zuo T, Zha S, Li X and Yi X 2020 *Eng.*, **6**, 165-172
- [5] Coey J M D 2011 *IEEE Transactions on Magnetics*, **47**, 4671-4681
- [6] Yang J, Han J, Tian H, Zha L, Zhang X, Kim C S, Liang D, Yang W, Liu S and Wang C 2020 *Eng.*, **6**, 132-140
- [7] Ramlan P, Sardjono F, Gulo and Setiabudidaya D J 2016 *Phys.: Conf. Series*, **776**, 1-6
- [8] Tian Q, Zha L, Yang W and Qiao Q 2018 *AIP advances*, **8**, 1-6
- [9] Kohn W and Sham L J 1965 *Phys. Rev. B*, **140**, 1133-1138
- [10] Kresse G and Pack J H 1994 *Phys. Rev. B*, **49**, 251-269
- [11] Kresse G and Pack D J 1999 *Phys. Rev. B*, **59**, 1758-1775
- [12] Perdew P, Burke Kand Enzerhof M 1996 *Phys. Rev. Lett.*, **77**, 3865-3868
- [13] Monkhorst H J and Pack J D 1976 *Phys. Rev. B*, **13**, 5188-5192
- [14] Parlinski K, Li Z Q and Kawazoe Y 1997 *Phys. Rev. Lett.*, **78**, 4063-4066
- [15] Aly A E 2009 *Int. J. Pure and Appl. Phys.*, **5**, 215-229
- [16] Phasha M J, Ngoepe P E, Chauke H R, Pettifor D G and Nguyen-Mann D 2010 *Intermetallics*, **18**, 2083-2089
- [17] Sekkal A, Sahlaoui M and Benzair A 2018 *Intermetallic Comp.*, **73189**, 193-202
- [18] Mahlangu R, Chauke H R, Ngoepe P E and Phasha M J, 2013 *Intermetallics*, **33**, 27-32
- [19] S. F. Pugh 1954 *J. Sci.*, **45**, 823-843
- [20] Burzo E 1998 *Reports on Progress in Phys.*, **61**, 1099-1105
- [21] Sin'ko G V and Smirnov N A 2002 *J. Physics: Condensed Matter*, **14**, 6989-7005
- [22] Hennig R G, Carlsson A E, Kelton K F and Henley C L 2005 *Phys. Rev. B*, **71**, 144103
- [23] Tvergaard V and Hutchinson J W 1988 *J. Am. Ceram. Soc.*, **71**, 157-163
- [24] Fu H, Li D, Peng F, Gao T and Cheng X 2008 *Comput. Mater. Sci.*, **44**, 774-778

# Synthesis of copper nanowires for application as flexible transparent conducting electrodes

NW Hoy\* and PS Mbule

Department of Physics, CSET, University of South Africa, Johannesburg, 1710, South Africa

E-mail: 59842997@mylife.unisa.ac.za

**Abstract:** Copper nanowires (CuNWs) are a promising material for flexible transparent conductive electrodes due to their outstanding transparency and conductivity properties. Long and smooth CuNWs were successfully synthesized via a hydrothermal method and cleaned by n-hexane and water separation routine. The synthesized CuNWs were then deposited on a polycarbonate substrate to make flexible transparent conducting films as electrodes. X-ray diffraction, scanning electron spectroscopy, energy dispersive X-ray spectroscopy, atomic force microscopy, and a tensile microtester technique were used to characterize the prepared films/electrodes. Furthermore, aluminium (2 mol%) doped zinc oxide (AZO) layer was coated onto CuNWs to prevent a possible oxidation from moisture in air environments. The observed results indicate that the AZO layer improves the light trapping capability of a potential cell as well as offering additional structural protection for the CuNWs.

## 1. Introduction

Solar energy is a promising avenue for South Africa to pursue as the country is one of the top ten sunniest countries in the world and allows us to reduce our usage of coal. One of the newer types of solar cells, perovskite based solar cells, is a promising alternative to the current type of solar cell that is in circulation, with a 20% improvement within the last decade. With its added flexibility it can also be used in far more situations than the previous generations allowing it to be more widely used.

There are specific issues that need to be resolved with regards to using and manufacturing perovskite-based solar cells. The first important issue is the usage of indium tin oxides (ITOs), which are the most common transparent conductive electrode (TCE). However, ITOs have been found to be both expensive, unstable and brittle, which is not ideal for flexible solar cells [1]. A promising alternative to ITOS ARE metal nanowires, due to their high conductivity and excellent optical transmittance.

Copper nanowires (CuNWs) are abundant, conductive and relatively cheaper to be used as bottom electrodes. However, there are issues with CuNWs that prevent them from being widely used, such as how easily they oxidize. Despite this, coating the CuNWs could easily prevent this from happening while also enhancing some of its attributes. This work will present one such method using polycarbonate as the flexible substrate due to its excellent thermal stability [2], and aluminum-doped zinc oxide (AZO) as the protective layer which could also act as the solar cells' electron transporting layer.

## 2. Experimental section

### 2.1. Materials

For the synthesis of the CuNWs, cupric (ii) chloride dihydrate ( $\text{CuCl}_2 \cdot 2\text{H}_2\text{O}$ ) was used as the copper source, ascorbic acid ( $\text{C}_6\text{H}_8\text{O}_6$ ) as the reducing agent, and octadecylamine (ODA)( $\text{C}_{18}\text{H}_{39}\text{N}$ ) as the capping agent. The amount and concentration of each substance was 0.061 g of copper chloride (5.65 mmol/l), 0.039g ascorbic acid (2.8 mmol/l), and 0.571g ODA (26.5 mmol/l).

For the synthesis of the AZO nanoflakes, 2g zinc acetate ( $\text{Zn}(\text{CH}_3\text{CO}_2)_2$ ) (403.739 mmol/l) as the zinc precursor, 0.0835g of aluminium nitrate (iii) nonahydrate ( $\text{Al}(\text{NO}_3)_3 \cdot 9\text{H}_2\text{O}$ ) (2 mol%) (8.239 mmol/l) as the aluminium precursor, and 0.436g of sodium hydroxide (NaOH) (403.734 mmol/l) were used in the process.

## 2.2. Synthesis of CuNWs

The hydrothermal method was used in the synthesis of CuNWs. Initially the copper chloride as the source of copper and ascorbic acid as the reducing agent were stirred together with 40 ml of deionized water until the solution was completely dissolved. The ODA which acts as the capping agent was also stirred in 40 ml of deionized water until it was completely dissolved. The two mixtures were then added together and magnetically stirred for 1 hour until a blue emulsion solution was observed. The mixture was transferred into an autoclave and then placed in an oven heated at 120°C for 20 hours.

CuNWs were then cleaned using deionized water by centrifuging at 2500 rpm for 5 minutes to remove any excess ODA and other chemicals in the solution. Thereafter the solution was mixed with an equal amount of n-hexane and deionized water to separate the CuNWs from the copper nanoparticles (CuNPs) that also would have formed in this reaction. This step was repeated three times before the final product was placed in isopropanol to prevent any oxidation of the CuNWs during the storage.

## 2.3. Synthesis of AZO NFs

For the synthesis of AZO nanoflakes the NaOH and zinc acetate were added to two separate beakers of 10.9 ml of deionized water and mixed until they were completely dissolved. Once this was complete the NaOH solution was added dropwise to the zinc acetate solution. Thereafter the aluminium nitrate nonahydrate was stirred with 5ml of deionized water before it was added to the final solution, which was then stirred at 850 rpm for 4 hours. The final solution was centrifuged to ensure the AZO nanoflakes were cleaned to remove biproducts that might have formed.

## 2.4 Thin films (CuNWs electrodes) preparation

CuNWs were deposited on a polycarbonate (PC) substrate by drop-casting. Thereafter, the PC/CuNW film was treated in an oven for 5 minutes at 100 °C to embed the CuNWs into the PC substrate. The AZO NFs were spin coated onto the CuNWs film at 2000 rpm and the samples obtained for further analysis were bare PC, PC-CuNWs, PC-CuNWs oven treated, and PC-CuNW coated with AZO.

# 3. Results and discussion

## 3.1. XRD analysis

Figure 1 shows XRD analysis of the prepared films. XRD revealed that pure copper had indeed been formed which were identified by the distinguished peaks at  $2\theta = 43.25^\circ$  and  $50.24^\circ$  [3]. These correspond to the crystal planes of face-centered cubic copper with (111) and (200) plane crystal structures respectively with no detection of impurities like copper oxides. The lack of impurities is excellent as the addition of the impurities is undesirable and may reduce the conductivity of the films, making them unusable as electrodes[4]. Similar results were found for the CuNWs treated in an oven.

The XRD analysis for AZO NFs did not yield expected results based on previous XRD studies on AZO films [5], this could be due to interference from the PC substrate broad peak observed at  $2\theta = 18^\circ$ . Regardless of this, it also formed cubic structures with a preferred orientation of (202) plane.

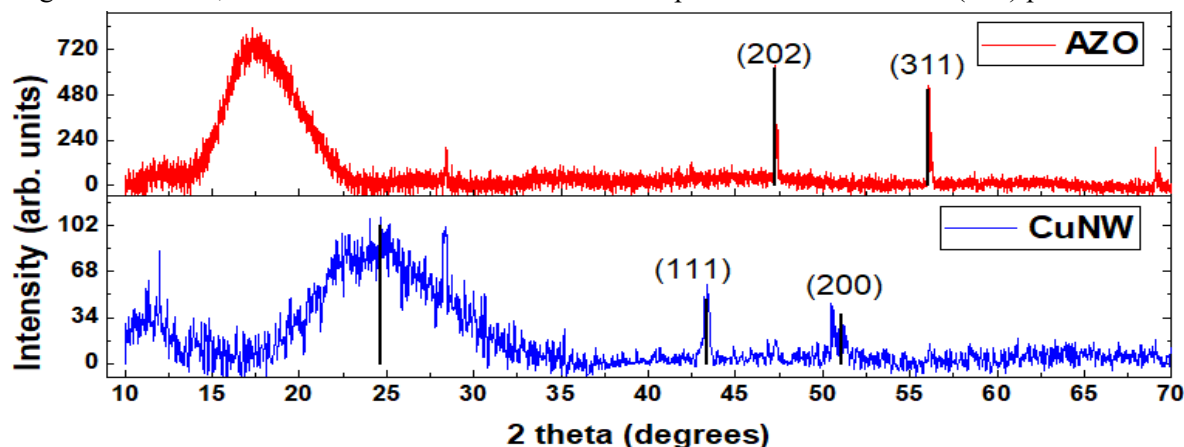
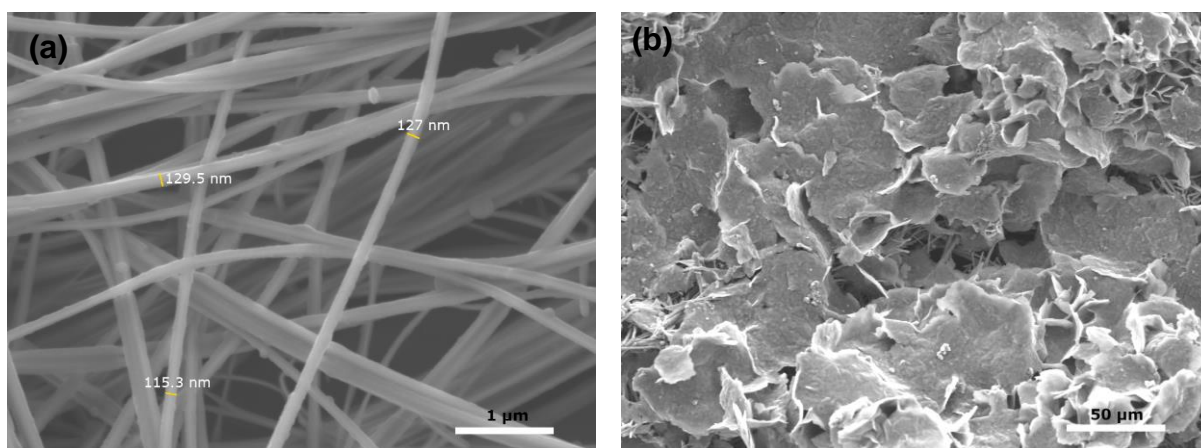


Figure 1: XRD pattern for AZO-NFs and CuNWs.

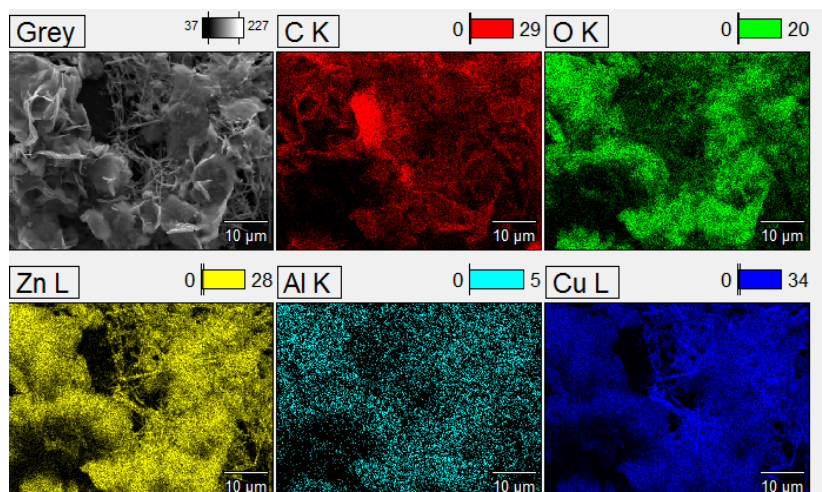
### 3.2. SEM analysis

Figure 2 shows the SEM images and elemental mapping of prepared CuNWs and AZO NFs. From the image shown in Figure 2 (a), it is clear that multiple long and smooth CuNWs were successfully synthesized and that the final cleaning steps were successful in removing the majority of nanoparticles from the CuNWs. This is required to achieve high electrical conductivity and transmittance for the electrodes. The average diameter of the CuNWs was found to be  $\sim 123.93$  nm with an ultra-long length of  $\sim 50$   $\mu\text{m}$ . This is a promising result as previous studies have found that large aspect ratios are ideal for low sheet resistance in electrodes [3]. Smooth CuNWs are also important as smoother CuNWs have been observed to have a reduced light scattering effect, which is important to have for thin films designed to be used in solar cells [3]. The SEM results of the CuNWs after having been treated in the oven did not differ from these images shown here.

As shown in Figure 2 (b), CuNWs were successfully coated with AZO NFs, it can be observed that the AZO NFs managed to remain well layered and coat most of the CuNWs except for a few locations on the film where the CuNWs were still visible. These gaps in the AZO NFs layer could be covered by optimizing the spin-coating process to completely protect the CuNWs from oxidation and prevent harmful chemicals from reaching the CuNWs during the solar cell device fabrication. The elemental mappings in Figure 3 clearly show that the AZO-NFs/CuNWs were composed of the aluminum, zinc, oxygen, and copper elements. This is an indication that the synthesis process was a success, and that the aluminum was successfully doped into zinc oxide. The trace amounts of oxygen were linked to the likelihood of oxidation of CuNWs, which as previously mentioned the CuNWs are easily susceptible to.



**Figure 2:** SEM images of (a) CuNWs and (b) AZO-NFs/CuNWs.



**Figure 3:** Elemental mapping of AZO-NFs

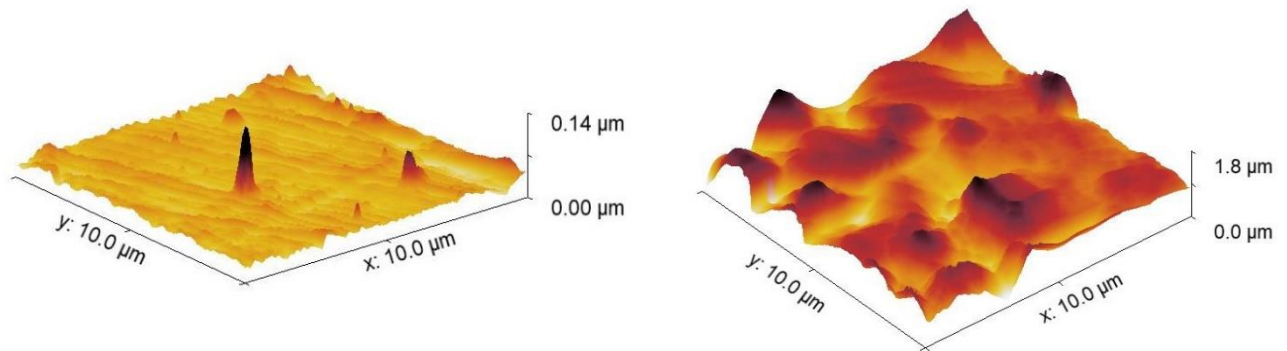


**Figure 4:** AFM images of a) CuNWs and b) AZO NFs.

### 3.3. AFM analysis

Figure 4 shows the AFM of the prepared CuNWs electrodes. AFM was done to study the surface roughness of the prepared CuNWs. The film roughness is reported to have an impact on the solar cell device performance, in terms of layers adherence and light trapping [6].

The results from the CuNWs coated onto the polycarbonate substrate initially showed a relatively smooth surface with a root-mean square (RMS) of  $\sim 6.157$  nm.

However, the AFM of the CuNWs coated with AZO NFs had more surface roughness with the RMS of  $\sim 213.145$  nm. This high surface roughness could be due to the relatively large NFs, as observed in SEM images. The rougher surfaces could be effective for light trapping in the device and thereby promoting high photon absorption (as the surface is more textured and reduces the amount of surface reflection) enhancement of the optical path lengths in the films, and an enhancement of the internal reflections [6].

### 3.4. Tensile strength analysis

The stress – strain analysis was done to determine the parameters governing the flexibility and stretchability of the prepared CuNWs electrodes. The tensile strength technique was used with a Deben Microtester 200N, where prepared CuNWs electrodes were clipped on both ends with the module jaws and the force was applied to pull the electrodes and find the tensile strength at a crosshead speed of 1.00mm/min. Figure 5 shows what happens to the material when this force is applied and is converted to stress-strain. The graph was also broken up as the AZO elongation was double the length of the other experiments.

The yield strength is an important parameter to investigate as it refers to the maximum potential stress that a material can withstand without causing any permanent deformation [7]. It can also be seen as a practical approximation of the elastic limit of the material. The yield strength of a PC substrate was found to be  $\sim 25.721$  MPa, and upon coating with CuNWs it was observed to be  $\sim 25.204$  MPa. This indicates that CuNWs have no effect on substrate deformation and its yield strength still falls under the elastic limit of PC substrates. However, upon treating the PC-CuNWs in an oven, the yield strength was drastically increased to  $\sim 41.274$  MPa. The addition of the AZO NFs coating further showed an increased yield strength of 55.047 MPa. This could be attributed to the fact that coating and heat treatment contribute to the hardening of the PC substrate and thereby reaching its tensile strength which is defined as the maximum stress that a material can undergo before it breaks when it is allowed to be stretched or pulled [8].

Additionally, the resilience of the prepared samples was also examined by considering the total area under the stress-strain curve up to the yield point which was found via integrating using Origin Pro software [9]. The resilience is an indication of the substrate's ability to

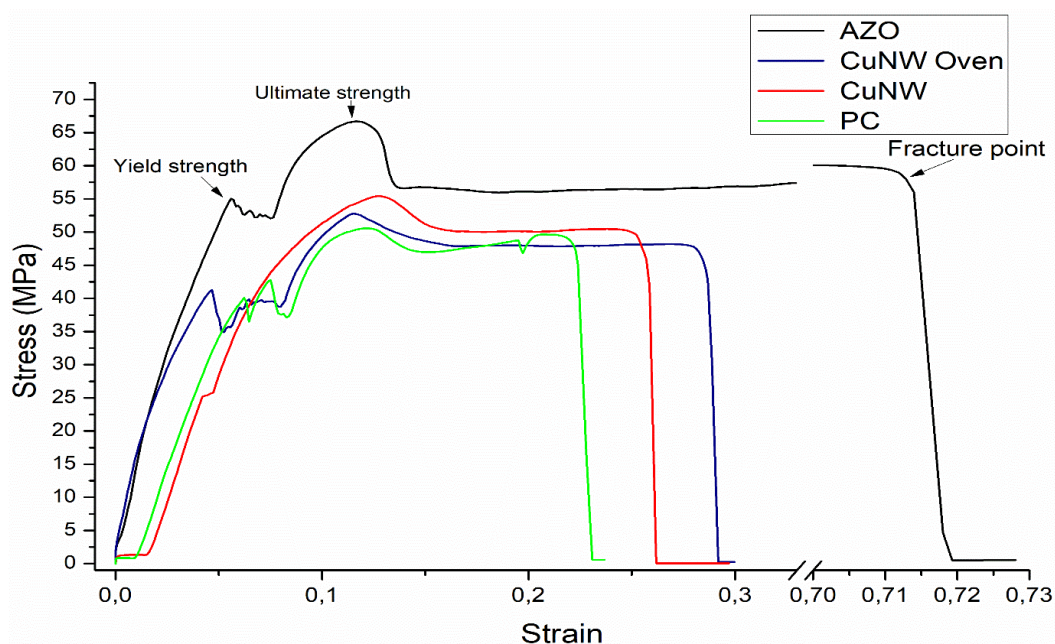


**Figure 5:** Stress-strain graph of the different films studied.

**Table 1:** Summarised data for tensile test

Samples	Yield strength (MPa)	Resilience (MJ/m <sup>3</sup> )	Strain hardening ratio	Fracture strength (MPa)	Young's modulus (N/m <sup>2</sup> )
Bare PC	25.721	0.478	1.743	37.747	706.020
PC-CuNW	25.204	0.498	2.199	47.947	915.451
PC-CuNW-Oven	41.274	1.222	1.279	44.52	820.932
PC-CuNW-AZO	55.047	1.800	1.212	57.994	956.338

withstand taking a shock from possible damage. The addition of the CuNWs onto the PC substrate did not affect its resilience; however, AZO NFs substantially improved the resilience of the substrate. The strain hardening ratio is the ratio of ultimate tensile strength to the yield strength [7]. A low value of the ratio indicates a more brittle material that cannot be stretched as much while a higher value does indicate a greater amount that can be stretched. The larger ratio results in the strain hardening of the substrate having a more obvious effect on the material during the deformation process [10]. As can be observed, after the addition of the CuNWs the strain hardening ratio increased substantially which indicates that the substrate is strengthened and has better formability and not as brittle as the bare PC. This however is changed when the substrate is placed in the oven as the ratio drops below what it previously was. The decrease in the ratio indicates that the substrate is brittle again and more prone to fracture after being treated in the oven. Even the addition of the AZO fails to improve the strain hardening values, which shows that the choice of polymer substrate plays a crucial role on these parameters.

The fracture strength is the strength at which the material physically separates, and the strain reaches its maximum value as the material fractures. It should be noted that more ductile materials will have a fracture strength below the ultimate strength and more brittle materials will have a fracture strength which is closer to the ultimate strength. The CuNWs improved the fracture strength of the bare PC substrate which follows the previous findings of the overall improvement of strength that has been

observed. Note that the oven treatment resulted in the substrate becoming more brittle as can be seen in the drop of fracture strength between the CuNWs and the PC-CuNW sample that had been treated in the oven beforehand. The additional layer of AZO NFs improved the fracture strength.

The Young's modulus is an indication of the stiffness of a material [7]. The larger the value tends to be, the less elastic the material behaves and is generally observed to be stiffer. It is determined by finding the gradient that the stress-strain graph makes from the starting point up until the yield strength. The data indicates that the addition of CuNWs and the AZO NFs layers results in an increase of the Young's modulus resulting in a stiffer and stronger material. This appears to be in line with the other results of this study with an increase in the yield strength of the materials and only a slight increase in the ductility.

#### 4. Conclusion

In conclusion, smooth and long CuNWs were successfully synthesized which have been found to be ideal for the bottom electrodes in solar cells devices. The AZO NFs that were also successfully synthesized have been shown to be able to cover the CuNWs and offer additional protection against tensile stress and potentially against other damages that will occur with daily use of the device using this particular electrode. XRD revealed face-centered cubic structure of these CuNWs and cubic structure for AZO NFs. SEM confirmed the CuNWs and AZO NFs morphology and AFM indicated a higher surface roughness after AZO coating which could be beneficial for light trapping in the solar cell devices thereby promoting enhanced photon absorption. The stress – strain analysis on the CuNWs based electrodes indicated that AZO NFs offer additional protection for electrodes improving resilience, yield strength, and fracture strength.

#### References

- [1] Li X, Wang Y, Yin C and Yin Z 2020 Copper nanowires in recent electronic applications: progress and perspectives *J Mater Chem C Mater* **8** 849–72
- [2] Xiao J, Chen Y, Wang S, Lu P and Hu Y 2016 Thermal degradation mechanism of polycarbonate/organically modified montmorillonite nanocomposites *Polym Compos* **37** 2301–5
- [3] Wang Y, Liu P, Zeng B, Liu L and Yang J 2018 Facile Synthesis of Ultralong and Thin Copper Nanowires and Its Application to High-Performance Flexible Transparent Conductive Electrodes *Nanoscale Res Lett* **13** 1–10
- [4] Chen Z, Ye S, Stewart I E and Wiley B J 2014 Copper Nanowire Networks with Transparent Oxide Shells That Prevent Oxidation without Reducing Transmittance *ACS Nano* **8** 9673–9
- [5] Khan F and Hyun Kim J 2020 Enhanced charge-transportation properties of low-temperature processed Al-doped ZnO and its impact on PV cell parameters of organic-inorganic perovskite solar cells *Solid State Electron* **164**
- [6] Li K, Haque S, Martins A, Fortunato E, Martins R, Mendes M J and Schuster C S 2020 Light trapping in solar cells: simple design rules to maximize absorption *Optica* **7** 1377
- [7] Dupen B 2016 Stress and Strain *Applied Strength of Materials for Engineering Technology* (Purdue University) pp 17–22
- [8] Karakassides A, Ganguly A, Kelly J, Sharma P K and Papakonstantinou P 2021 Radially Grown Graphene Nanoflakes for Tough and Strong Carbon Fiber Epoxy Composites *ACS Appl Nano Mater* **4** 9167–80
- [9] Lin C-Y and Kang J-H 2021 Mechanical Properties of Compact Bone Defined by the Stress-Strain Curve Measured Using Uniaxial Tensile Test: A Concise Review and Practical Guide *Materials* **14** 1–16
- [10] Chen S, Li W-B, Wang X-M, Yao W-J, Song J-P, Jiang X-C and Yan B-Y 2021 Comparative Study of the Dynamic Deformation of Pure Molybdenum at High Strain Rates and High Temperatures *Materials* **14** 4847

# Study of magnetic properties in doped intermediate valent $\text{Ce}_2\text{Rh}_2\text{Ga}$

SP Xhakaza<sup>1</sup> and AM Strydom<sup>1</sup>

<sup>1</sup>Highly Correlated Matter Research Group, Physics Department, University of Johannesburg, PO Box 524, Auckland Park, 2006, South Africa

E-mail: [sxhakaza@uj.ac.za](mailto:sxhakaza@uj.ac.za)

**Abstract.** The magnetic properties of intermediate valent  $\text{Ce}_2\text{Rh}_2\text{Ga}$  were investigated by means of substituting lanthanum (La) and yttrium (Y) into the cerium (Ce) sublattice to achieve negative and positive chemical pressure, respectively. In this study we report on the synthesis, characterization, dc-magnetic susceptibility and magnetization of two doped variants namely,  $\text{Ce}_{1.8}\text{La}_{0.2}\text{Rh}_2\text{Ga}$  and  $\text{Ce}_{1.8}\text{Y}_{0.2}\text{Rh}_2\text{Ga}$ . The doped variants crystallize in the same orthorhombic version of the  $\text{La}_2\text{Ni}_3$ -structure type at room temperature with space group *Cmce*, as the undoped  $\text{Ce}_2\text{Rh}_2\text{Ga}$  compound. The dc-magnetic susceptibility of  $\text{Ce}_{1.8}\text{Y}_{0.2}\text{Rh}_2\text{Ga}$  demonstrates behaviour similar to that of the parent compound with a simultaneous valence and crystal structure transition at  $T_t = 112.29$  K, close to that of  $\text{Ce}_2\text{Rh}_2\text{Ga}$  at  $T_t = 130$  K. However, no transition was observed in  $\text{Ce}_{1.8}\text{La}_{0.2}\text{Rh}_2\text{Ga}$  throughout the accessible temperature range. We discuss our findings in terms of the control that doping exercises over the valence-induced crystal structure instability in  $\text{Ce}_2\text{Rh}_2\text{Ga}$ .

## 1. Introduction

Cerium-based compounds are known to show varying ground states as a result of hybridization between the single 4f electron of nominally trivalent Ce and the conduction electrons in a metal [1-2]. Cerium-based compounds usually have their magnetism dominated by the localized spin- and orbital magnetic moment of the 4f electron. In the strongly correlated electron class of materials however, conditions may be favourable for the 4f electron band to be in close proximity to the metallic Fermi energy, in which case the 4f electron of Cerium acquires a degree of itineracy, with concomitant instability in the Cerium valence. This phenomenon has become known as intermediate or fluctuating valence, and it leads in many cases to heavy-fermion behaviour in Kondo systems [3]. Given this propensity to valence instabilities however, remarkably few Ce compounds are known for temperature-driven valence transitions. In this work we focus on such rare example, namely the ternary intermetallic compound  $\text{Ce}_2\text{Rh}_2\text{Ga}$ .  $\text{Ce}_2\text{Rh}_2\text{Ga}$  was reported to exhibit dimorphism, with the crystal structure outcome associated with the annealing temperature administered during synthesis [4]. When the sample is melted in an arc furnace and subsequently annealed at a temperature of 900°C, it forms in the orthorhombic (space group *Cmce*) crystal structure of  $\text{La}_2\text{Ni}_3$  type (high-temperature variant, henceforth termed as HT- $\text{Ce}_2\text{Rh}_2\text{Ga}$ ). This dimorphic variant is at the focus of this study. By contrast, when annealed at the lower temperature of 700°C the compound adopts a monoclinic structure with space group, *C2/c* of the nominal  $\text{Pr}_2\text{Co}_2\text{Al}$  type [4].

In our initial study [4] on HT- $\text{Ce}_2\text{Rh}_2\text{Ga}$ , a robust anomaly was found consistently in the temperature dependencies of the specific heat and magnetic susceptibility at 130 K. Even though this apparent phase

transition was shown to be temperature hysteretic, it was presumed to characterize a long-range paramagnetic-to-antiferromagnetic phase transition by virtue of the shape of the anomaly in magnetic susceptibility together with the observation that the phase transition was accompanied by an amount of spin-configurational entropy being released at the transition. However, further studies on this compound have shown the 130 K anomaly to be of a more complex nature than a long-range magnetic phase transition. Firstly, our muon spin-resonance study on HT- $\text{Ce}_2\text{Rh}_2\text{Ga}$  [*A. M. Strydom, ISIS  $\mu\text{SR}$  Experimental Report No. 2010475 (unpublished)*] failed to detect any time-dependent oscillations in the muon spin relaxation, which argued against the involvement of any spin ordering in HT- $\text{Ce}_2\text{Rh}_2\text{Ga}$  down to 0.3K. Second, in a resonant X-ray emission spectroscopy experiment [5] persuasive evidence was found for a reconstruction of the Fermi surface and a slight increase of the Ce valence beyond 3+ at 130 K. The average Ce valence  $\nu$  increases by  $\sim 0.7\%$  from the higher temperature orthorhombic phase ( $\nu \sim 3.053$ ) to the  $T < 130$  K monoclinic phase ( $\nu \sim 3.075$ ). Finally, in  $^{69,71}\text{Ga}$  nuclear quadrupole resonance studies [6] the possibility of quenching of charge degrees freedom at the 130 K anomaly was also ruled out, and instead the data formulated evidence for a highly unusual two-ion Kondo state that forms at low temperatures in HT- $\text{Ce}_2\text{Rh}_2\text{Ga}$ .

The aim of this work is to report on the first doping studies of HT- $\text{Ce}_2\text{Rh}_2\text{Ga}$ , namely,  $\text{Ce}_{2-x}\text{T}_x\text{Rh}_2\text{Ga}$  ( $T = \text{Y, La}$ ) in which 10% of the cerium sublattice is being replaced. The two doped compounds were conformed to form in the expected orthorhombic with space group *Cmce*,  $\text{La}_2\text{Ni}_3$ -structure type at room temperature. From our magnetic measurements we derived the behavior of the paramagnetic Weiss temperature and the effective magnetic moment values of the cerium ions in the pair of doped compounds in order to shine a light on the electronic dispensation and the chemical pressure stability of the 130 K simultaneous valence and crystal structure transition.

## 2. Experimental details

Polycrystalline samples of two  $\text{Ce}_{1.8}\text{T}_{0.2}\text{Rh}_2\text{Ga}$  ( $T = \text{Y, La}$ ) compounds were prepared from high purity (weight-%) elements of Ce (99.99), Y (99.99), La (99.9), Rh (99.97), and Ga (99.9999). Owing to a weak oxidative reactivity of metallic Ce and La in air, extra precautions were taken to limit the exposure of these two reactants before melting the samples under Zr-gettered ultra-high purity argon in the arc-furnace enclosure. Stoichiometric ratios of the elements were used. The sample ingots were flipped over and remelted at least three times to promote homogeneity. Weight losses attributable to the arc-melting procedure were confined to within 0.5 weight-%. The as-cast samples were characterized by powder X-ray diffraction at room temperature. A Rigaku SmartLab powder diffractometer was used in the Bragg-Brentano geometry, the scan used  $\text{CuK}_\alpha$  scattering radiation collected in the  $2\theta$  diffraction interval between  $10^\circ$  and  $90^\circ$ ,  $2\theta$  with stepsize of  $0.02^\circ$ . The resulting X-ray diffraction spectra were analyzed using a FullProf suite of programs for full-profile Rietveld refinement [7]. The dc-magnetic measurements on the polycrystalline samples were carried out using the vibrating sample magnetometer platform of a PPMS Dynacool system from Quantum Design, San Diego, in the sample temperature range of 1.8 - 330 K, and with applied magnetic fields up to 9 T.

## 3. Results and discussion

### 3.1. Crystallography

The profile analyses of the powder X-ray diffractograms collected for  $\text{Ce}_{1.8}\text{Y}_{0.2}\text{Rh}_2\text{Ga}$  and  $\text{Ce}_{1.8}\text{La}_{0.2}\text{Rh}_2\text{Ga}$  confirmed that both compounds crystallize in the desired orthorhombic ordered version of the  $\text{La}_2\text{Ni}_3$ -structure type at room temperature with space group *Cmce*, similar to that of the undoped  $\text{Ce}_2\text{Rh}_2\text{Ga}$  compound. The refinement fits yielded values of the lattice parameters which are  $a = 5.85466(3)$  Å,  $b = 9.61734(6)$  Å, and  $c = 7.47766(2)$  Å for  $\text{Ce}_{1.8}\text{Y}_{0.2}\text{Rh}_2\text{Ga}$  and  $a = 5.86116(4)$ ,  $b = 9.66798(3)$  Å, and  $c = 7.48185(1)$  Å for  $\text{Ce}_{1.8}\text{La}_{0.2}\text{Rh}_2\text{Ga}$ . These values are in good agreement with an earlier report [4]. The refined atomic positions are summarized in table 1. Fig. 1 shows the powder X-

ray diffraction pattern obtained together with the full-profile least-squares refinement fit to the data for the representative compound  $\text{Ce}_{1.8}\text{Y}_{0.2}\text{Rh}_2\text{Ga}$ .

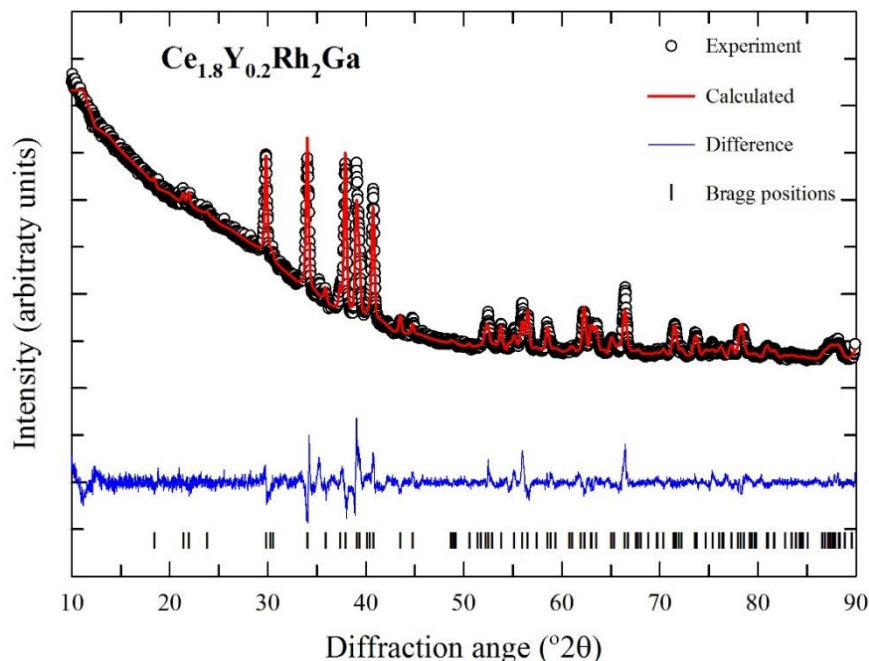


**Figure 1.** Experimental powder X-ray diffraction spectrum of  $\text{Ce}_{1.8}\text{Y}_{0.2}\text{Rh}_2\text{Ga}$  at room temperature denoted by open-circle symbols, Rietveld refinement denoted by a red line, theoretical Bragg positions corresponding to the theoretical  $Cmce$  space group denoted by vertical bars, and the blue line denoting the difference curve between experimental, and Rietveld calculated intensities.

**Table 1.** Crystallographic details obtained from powder X-ray diffraction analyses of  $\text{Ce}_{1.8}\text{Y}_{0.2}\text{Rh}_2\text{Ga}$  and  $\text{Ce}_{1.8}\text{La}_{0.2}\text{Rh}_2\text{Ga}$ .

Comp.	Atom	Wyckoff sites	x	y	z	Occupation ( $\times 100\%$ )
$\text{Ce}_{1.8}\text{Y}_{0.2}\text{Rh}_2\text{Ga}$	Ce	$8f$	0	0.34103	0.09336	0.9
	Y	$8f$	0	0.34103	0.09336	0.1
	Rh	$8e$	0.25000	0.08920	0.25000	1.0
	Ga	$4a$	0	0	0	1.0
$\text{Ce}_{1.8}\text{La}_{0.2}\text{Rh}_2\text{Ga}$	Ce	$8f$	0	0.34149	0.08818	0.9
	La	$8f$	0	0.34149	0.08818	0.1
	Rh	$8e$	0.25000	0.08228	0.25000	1.0
	Ga	$4a$	0	0	0	1.0

### 3.2. Magnetic properties

The temperature dependencies of dc-magnetic susceptibility,  $\chi(T)$  of both title compounds were measured in the field-cooled protocol (data collected while cooling the sample in the excitation field from high to low temperatures) in a magnetic field of 0.1 T for  $\text{Ce}_{1.8}\text{Y}_{0.2}\text{Rh}_2\text{Ga}$  and 0.5 T for  $\text{Ce}_{1.8}\text{La}_{0.2}\text{Rh}_2\text{Ga}$ . Fig. 2(a) and 2(b) show  $\chi(T)$  for these compounds, normalized on a per-mole Ce basis.

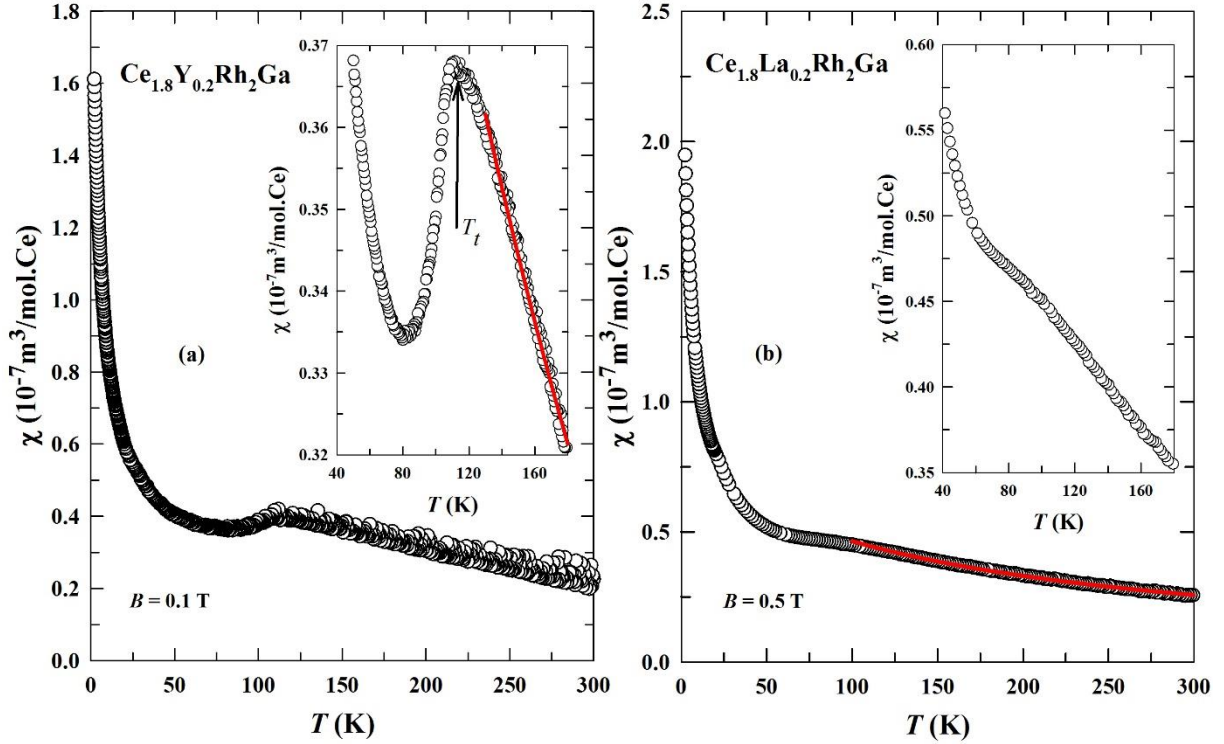


**Figure 2.** (a): Temperature dependent dc-magnetic susceptibility  $\chi(T)$  of  $\text{Ce}_{1.8}\text{Y}_{0.2}\text{Rh}_2\text{Ga}$  measured from 300 K to 1.8 K in a constant applied magnetic field of  $B = 0.1$  T. (inset) Magnified view of  $\chi(T)$ , which displays a cusp-like anomaly at  $T_t = 112.4$  K. (b): dc- magnetic susceptibility  $\chi(T)$  of  $\text{Ce}_{1.8}\text{La}_{0.2}\text{Rh}_2\text{Ga}$  measured from 330 K to 1.8 K in a constant applied magnetic field of  $B = 0.5$  T. (inset) Magnified view of  $\chi(T)$ , which displays the absence of a cusp-like anomaly as compared to the data in Fig. 2(a).

The inset of Fig. 2(a) displays a magnified view of the susceptibility with a red line obtained by fitting the data to the Curie Weiss expression [8]:

$$\chi(T) = \frac{N_A \mu_{\text{eff}}^2}{3k_B(T - \theta_p)}, \quad (1)$$

where  $N_A$ ,  $\mu_{\text{eff}}^2$ ,  $k_B$ , and  $\theta_p$  are Avogadro's number, the effective magnetic moment, Boltzmann's constant and the paramagnetic Weiss temperature, respectively. The best fit was achieved in the temperature range of 130 - 180 K and from the fit values of  $\mu_{\text{eff}} = 2.26(3) \mu_B/\text{Ce}$  and  $\theta_p = -286.98(5)$  K were obtained. The data below 120 K deviates from the Curie Weiss law prediction due to the maximum reached in  $\chi(T)$  at 112.4 K. The observed changes of  $\chi(T)$  on  $\text{Ce}_{1.8}\text{Y}_{0.2}\text{Rh}_2\text{Ga}$  were comparable to that of HT- $\text{Ce}_2\text{Rh}_2\text{Ga}$  looking at the  $\chi(T)$  values at the maximum peak. By contrast, in  $\text{Ce}_{1.8}\text{La}_{0.2}\text{Rh}_2\text{Ga}$  no anomaly is found in  $\chi(T)$  – see Fig. 2(b). The  $\chi(T)$  data of  $\text{Ce}_{1.8}\text{La}_{0.2}\text{Rh}_2\text{Ga}$  followed equation 1 in the range 330 - 100 K; see red line in the inset to Fig. 2(b). The least-squares fit yielded an effective moment value  $\mu_{\text{eff}} = 2.02(5) \mu_B/\text{Ce}$  and a paramagnetic Weiss temperature  $\theta_p = -148.61(4)$  K. By contrast to what was reported on the undoped  $\text{Ce}_2\text{Rh}_2\text{Ga}$  [4], we note that the effective moment values for both doped compounds are somewhat reduced from that of the full free-ion Ce value of  $2.54 \mu_B$ .

The dc-magnetization isotherms of  $\text{Ce}_{1.8}\text{Y}_{0.2}\text{Rh}_2\text{Ga}$  measured at a number of fixed temperatures between 2 - 140 K are presented in Fig. 3(a). The magnetization at 9 T attains a value of  $\sim 0.11 \mu_B/\text{Ce}$  at 10 K which is less than the expected saturation value of free-ion Ce which is  $2.14 \mu_B/\text{Ce}$ . However, the

magnetization isotherms of  $\text{Ce}_{1.8}\text{La}_{0.2}\text{Rh}_2\text{Ga}$  between 2 - 90 K presented in Fig. 3(b) attain a high-field magnetization  $\sim 0.15 \mu_B/\text{Ce}$  at 2 K in 9 T. These small magnetization values are often observed in correlated electron Ce-based compounds [9-10] and are typically caused by crystal-electric field effects associated with the  $L = 3$  orbital angular momentum of the  $4f$  electron of a trivalent Ce ion.

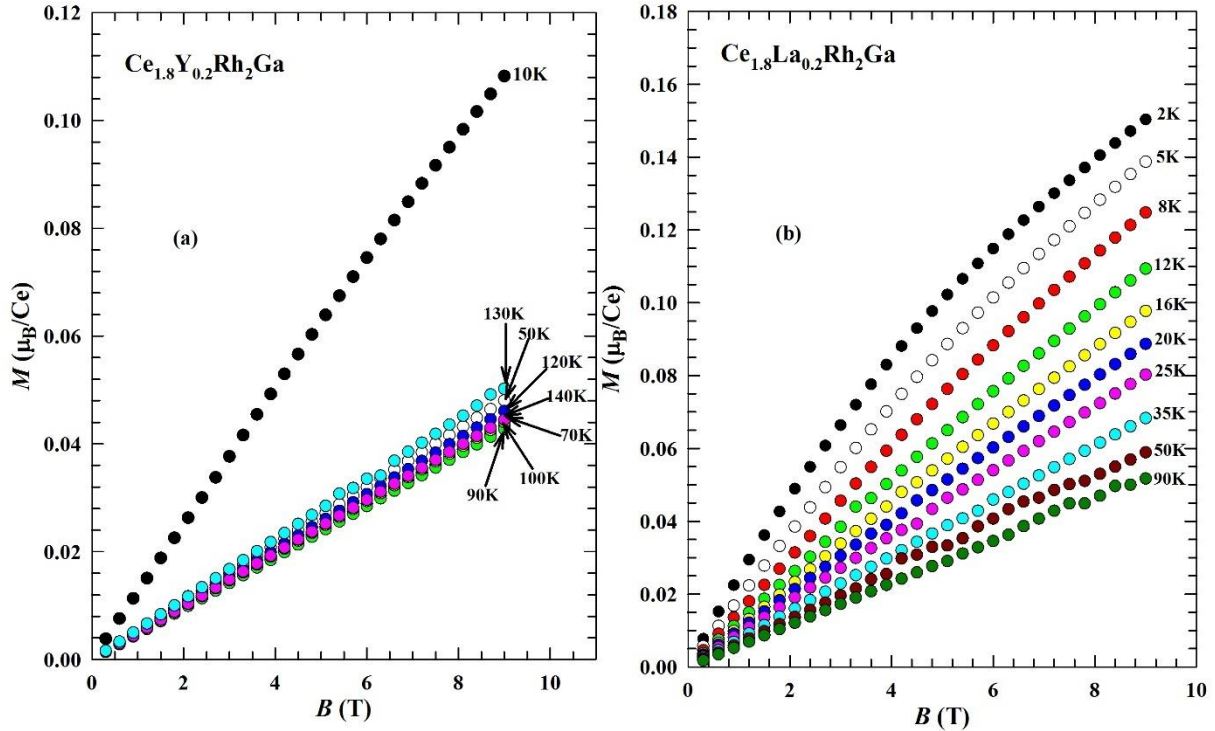


**Figure 3.** Isothermal magnetization per Ce of (a)  $\text{Ce}_{1.8}\text{Y}_{0.2}\text{Rh}_2\text{Ga}$  and (b)  $\text{Ce}_{1.8}\text{La}_{0.2}\text{Rh}_2\text{Ga}$  at temperatures close to the expected valence transition temperature ( $\sim 100$  K) and at low temperature.

#### 4. Conclusion

This study investigated the magnetic properties in the pair of doped compounds  $\text{Ce}_{1.8}\text{Y}_{0.2}\text{Rh}_2\text{Ga}$  and  $\text{Ce}_{1.8}\text{La}_{0.2}\text{Rh}_2\text{Ga}$ . We anticipated to observe effects of a simultaneous dilution of the  $4f$ -electron density at the Fermi energy and lattice expansion (La) and contraction (Y). Although the crystal structure at room temperature was found to remain invariant upon doping, the two doped compounds revealed unexpected variations in the (undoped) valence transition at 130 K. The combined valence and crystal structure transition is retained in  $\text{Ce}_{1.8}\text{Y}_{0.2}\text{Rh}_2\text{Ga}$ , albeit with a huge increase in the antiferromagnetic Weiss exchange parameter ( $-287$  K) compared to that of the undoped compound ( $-120$  K, [4]). In  $\text{Ce}_{1.8}\text{La}_{0.2}\text{Rh}_2\text{Ga}$  on the other hand the Weiss temperature is largely unchanged ( $-148$  K) but the transition has practically disappeared from the temperature progression of  $\chi(T)$ . These findings support the notion that hybridization between the Ce  $4f$  electrons and the conduction electrons play a dominant role over that of  $4f$  electron density of states at the Fermi energy, and that the combined valence and structure transition at 130 K may be manipulated in a facile manner through varying chemical pressure. Further studies are needed in order to disambiguate the influences of positive versus negative pressure in  $\text{Ce}_2\text{Rh}_2\text{Ga}$  and in particular the apparent rapid demise of the phase transition upon application of negative chemical pressure. Further studies are planned to achieved isoelectronic doping and co-doping aimed at keeping the unit cell volume invariant.

**Acknowledgments**

SPX thanks the UJ-GES for financial support, and AMS thanks the SA-NRF (93549) and the FRC/URC of UJ for financial assistance

**References**

- [1] Hauser, R., Michor, H., Bauer, E., Hilscher, G., and Kaczorowski, D., 1997. *Physica B: Condens. Mat.*, **230**, 211-213.
- [2] Löhneysens, H. v., Rosch, A., Vojita, M., and Wölfle, P., 2007, *Rev. Mod. Phys.* **79**, 1015
- [3] Hewson, A. C., 1993 *The Kondo Problem to Heavy Fermions*, (Cambridge University Press, Cambridge)
- [4] Nesterenko, S., Tursina, A., Pasturel, M., Xhakaza, S., and Strydom, A., 2020 *J. Alloys Compd.*, **844**, 155570
- [5] Sato, H., Matsumoto, T., Kawamura, N., Maeda, K., Takabatake, T., and Strydom, A. M., 2022 *Phys. Rev. B* **105**, 035113
- [6] Yamamoto, Sh., Fujii, T., Luther, S., Yasuoka, H., Sakai, H., Bärtl, F., Ranjith, K. M., Rosner, H., Wosnitza, J., Strydom, A. M., Kühne, H., and Baenitz, M., 2022 *Phys. Rev. B*, **106**, 115125
- [7] Young, R. A., 1993 *The rietveld method* (International union of crystallography, Oxford University Press), Vol. 5
- [8] Kittel, C., 2005 *Introduction to Solid State Physics*, (John Wiley and sons, United States of America)
- [9] Janka, O., Niehaus, O., Pöttgen, R., and Chevalier, B., 2016 *Z. Naturforsch.*, **71b**, 737-764
- [10] Pöttgen, R., and Chevalier, B., 2015 *Z. Naturforsch.*, **70b**, 289-304

# Mechanical properties of $\text{Ti}_{50-x}\text{Hf}_x\text{Pt}_{50}$ , ( $0 < x < 50$ ) for high shape memory alloys applications

M Mashamaite, P Ngoepe and H Chauke

Materials Modelling Centre, School of Physical and Mineral Sciences, University of Limpopo, Private Bag X1106, Sovenga 0727, South Africa

Email: [mordecai.mashamaite@ul.ac.za](mailto:mordecai.mashamaite@ul.ac.za)

**Abstract.** Shape memory alloys (SMAs) are metallic materials that can revert to their original shape when exposed to various temperatures. These materials are used in applications such as actuators and aerospace due to their remarkable properties shape memory effect and pseudo-elasticity which occurs as a result of phase transformation. TiPt undergoes a reversible martensitic transformation from B2  $\leftrightarrow$  B19 at elevated temperatures. Previous studies showed that the TiPt alloy is mechanically unstable with the negative shear modulus ( $C' = -32$ ) and soft modes in the negative frequency of the phonon dispersion curves along the gamma region at 0 K. The supercell approach was used to substitute Ti with Hf on TiPt structure to evaluate their mechanical stability from elastic properties and the phonon dispersions curves. The elastic properties suggest that an increase in Hf concentration enhances the mechanical stability of ternary systems. The  $C'$  becomes positive and larger at  $25 < x < 50$ , which suggests a reduced martensitic transformation at  $x \geq 43.75$ . The  $\text{Ti}_{50-x}\text{Hf}_x\text{Pt}_{50}$  systems become more ductile with the increase in Hf concentration, which suggests that Hf stabilizes the system at a higher concentration. The analyses of the vibrational properties of  $\text{Ti}_{50-x}\text{Hf}_x\text{Pt}_{50}$  structures with respect to phonon dispersion are also discussed.

## 1. Introduction

Shape memory alloys (SMAs) have found universal applications in the fields of automotive, aerospace, medicine and engineering [1]. This is due to two special properties pseudo-elasticity or super-elasticity and shape memory effect (SME), which come as a result of phase transformation [2]. Pseudo-elasticity is an elastic response to applied stress, while the SME of these materials is identified with a reversible martensitic transformation (MT), which is a sort of non-diffusive structure phase change including both atomic rearrangements of positions and change in cell volume [3]. The study of phase stability has been an interesting subject [4]. In addition, the main SMAs available are those dependent on NiTi composites, which are utilized in medical industries for dental devices, stents, bone plates, eyeglass casings and in robotics where the application temperature does not exceed 373K [5]. NiTi keeps on overwhelming the developing business sector due to their attractive mechanical properties in their capacity to accomplish functionality when compared with different SMAs, great corrosion resistance and biocompatibility [6].

The search for better SMAs is increasing rapidly for the development of new systems [7]. However, huge advancement has been made in expanding the reach of NiTi-based alloys in actuator-based applications through ternary alloying [8]. A few alloying additions, for example, Au, Pd, Pt, Zr and Hf, have appeared to establish the martensitic transformation temperatures for the shape memory alloys of NiTi SMAs [9]. Some of these ternary alloys were reported to have successfully increased the

transformation temperature of NiTi [10]. High temperature shape memory alloys (HTSMAs) are costly and are still under investigation due to their great functionality and high martensitic transformation temperatures of up to 800 K. However, the most attention was focused on Ni-Ti-Zr, and Ni-Ti-Hf HTSMAs mainly due to the generally low costs for crude materials as compared with the Nobel metals (Au, Pd, and Pt) [11].

Possible elective systems for NiTi can be TiPd and TiPt. TiPd undergoes a B2 (cubic crystal structure) to B19 (orthorhombic) martensite phase transformation with martensite start temperature ( $M_s$ ) between 783 and 836 K [12]. Moreover, equiatomic TiPt exhibits martensitic transformation temperature much higher than NiTi and its ternaries above 1200 K [13]. Various reports have demonstrated that TiPt alloy exhibited negligible shape memory effect (11%), due to the low critical stress for slip deformation compared to the stress required for martensitic reorientation [14]. Newer SMAs systems are being developed for extremely high temperature applications. Investigations of ternary shape memory alloys dependent on TiPd have been growing rapidly, for instance, studies on Ti-Pd-M, (where M = Ni, Pt, Ir, Co or Ru) alloys show high work output and good workability [15]. Ru was found to be effective in hardening and increasing resistance to heat and corrosion [16]. For this reason, TiPt and its ternary have been investigated to improve its mechanical workability [17].

Equiatomic TiPt is even more promising as a very HTMSA since it is reported to undergo a B2 to B19 martensite phase transformation with a  $M_s$  of approximately 1323 K [18]. However, TiPt based alloys have their drawbacks which limit their possible usage, upon the improvement of shape memory properties, the alloy could be used for various temperature applications [19, 20].

In this work, Hf was selected as the third element to improve the properties of the B2 TiPt, particularly because Hf has a greater atomic radius and melting point than both Ti and Pt. The first-principle method was used to investigate the effect of Hf on equiatomic TiPt, utilizing thermodynamic and mechanical properties (elastic and phonon dispersion curves).

## 2. Methodology

The first-principles calculations were performed using density functional theory (DFT) [21, 22] formalism as incorporated with a plane-wave basis in the Vienna *ab initio* Simulation Package (VASP). The projector augmented wave (PAW) was used to treat core-electron interaction [23]. The exchange-correlation functional generalized gradient approximation (GGA) of the Perdew-Burke-Ernzerhof (PBE) [24] was chosen. The plane wave cut-off energy was set at 500 eV to converge the total energy of the binary TiPt alloys. The geometry optimization and the energy were carried out using a  $k$ -spacing of 0.25 equivalent to the  $k$ -point mesh of  $8 \times 8 \times 8$  according to Monkhorst and Pack [25]. A  $2 \times 2 \times 2$  supercell of TiPt was employed to substitute Ti with Hf. In the elastic constant calculations, a strain of 0.005 was used for  $\text{Ti}_{50-x}\text{Hf}_x\text{Pt}_{50}$  systems. The PHONON code was used to investigate the phonon dispersion spectra and the phonon Density of State (phonon DOS). The phonon scatterings for the structures were determined in the system of the direct technique, for which the force constants were inferred by a supercell approach [26].

## 3. Results and Discussion

### 3.1. Lattice parameter and heats of formation

Figure 1 presents the change in (a) lattice parameter and (b) heats of formation against composition of  $\text{Ti}_{50-x}\text{Hf}_x\text{Pt}_{50}$  where,  $0 < x < 50$ . The current findings show that the lattice parameter increases with an increase in Hf content. This is due to the large atomic radius of Hf (0.155nm) as compared to both Ti (0.140nm) and Pt (0.135nm). The binary  $\text{Ti}_{50}\text{Pt}_{50}$  gave an equilibrium lattice parameter and the lowest value of  $a = 3.180 \text{ \AA}$  after optimization, which is in agreement with experimental findings of  $3.192 \text{ \AA}$  [18] followed by  $\text{Hf}_{6.25}\text{Ti}_{43.75}\text{Pt}_{50}$  with the value  $a = 3.196 \text{ \AA}$ . It is also observed the lattice parameter that the volume ( $\text{\AA}^3$ ) increases with an increase in Hf content.

The heats of formation ( $\Delta H_f$ ) of the intermetallic systems can be calculated from the following equation [27]:

$$\Delta H_f = E_{\text{TiPtHf}} - \sum_i x_i E_i, \quad (1)$$

where  $E_{TiPtHf}$  total energy of an intermetallic system, and  $E_i$  is the total energy of the individual elements in the system.

The calculated  $\Delta H_f$  in Figure 1 (b) show that TiPt becomes stable with an increase in Hf content.  $Hf_{50}Pt_{50}$  is the most thermodynamically stable structure, and the most stable ternary being  $Hf_{43.75}Ti_{6.25}Pt_{50}$  (-0.966 eV/atom).

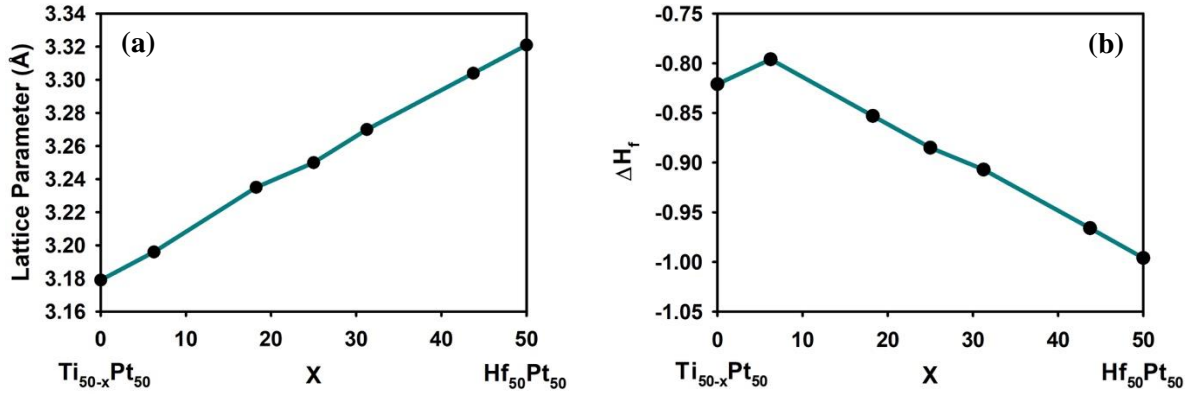


**Figure 1.** Change in (a) Lattice parameter and (b) Heats of formation ( $\Delta H_f$ ) against composition  $Ti_{50-x}Pt_{50}Hf_xPt_{50}$ ,  $0 < x < 50$

### 1.2. Elastic constants

Elastic constants are vital material parameters, the investigation of elastic constants gives a connection between the mechanical properties and dynamic data concerning the idea of the forces working in solids, particularly for the solidness and stiffness of materials. Brittleness, ductility, stiffness, stability and anisotropy ( $A$ ) of material are some of the key fundamental solid-state phenomena of elastic constants. Since the intermetallic compound TiPt belongs to the cubic crystal, it has three independent elastic constants  $C_{11}$ ,  $C_{12}$  and  $C_{44}$ . This system has been adequately used to consider the elastic properties of various metallic structures [28].

For a cubic system, the mechanical stability conditions are given by [29];

$$C_{11}, C_{44}, C_{11} > |C_{12}| \text{ and } C_{11} + 2C_{12} > 0, \quad (2)$$

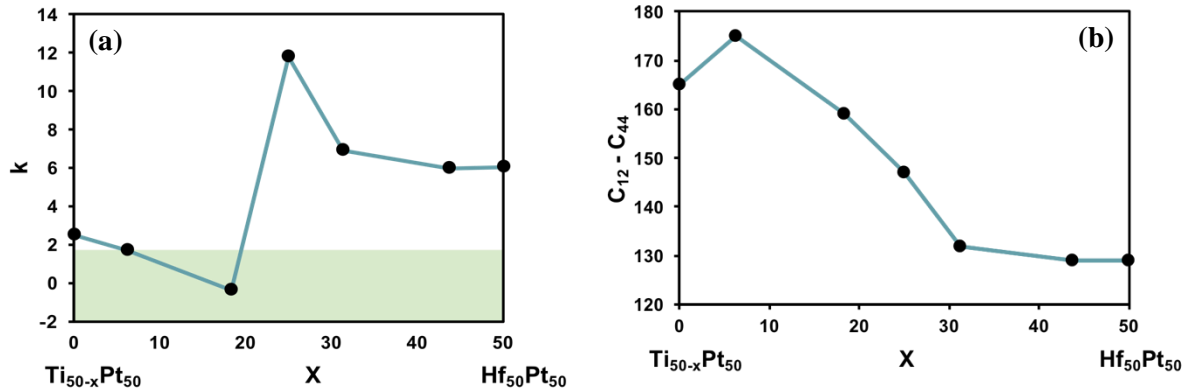
The elastic constants were evaluated to observe the effect of 0.005 strain when substituting Ti with Hf. All the independent elastic constants  $C_{11}$ ,  $C_{12}$ , and  $C_{44}$  for  $Ti_{50-x}Hf_xPt_{50}$  were positive which indicates the mechanical stability of the system. The  $C_{11} < C_{12}$  from 6.25 – 18.75 at.% which gives a negative  $C'$ . Furthermore,  $C_{11} > C_{12}$  from 25 – 43.75 at.% contributes to a positive  $C'$ . The positive  $C'$  suggests that the ternary at 25 – 43.75 at.% Hf, the compositions satisfy the stability conditions. The  $C'$  increases with the addition of Hf to the system, it is also observed that positive and larger  $C'$  leads to  $A > 1$ . Elastic anisotropy of crystals is significant since it associates with the possibility to instigate miniature breaks in materials. The anisotropy factor is the proportion of the level of anisotropy in solid materials [30]. For a completely isotropic material  $A = 1$ , whereas the degree of elastic anisotropy is  $A > 1$  or  $A < 1$ . As shown in Table 1, the value of  $A$  for  $x > 25$  is greater than 1, which indicates that the ternaries can be regarded as an elastically anisotropic material. The martensitic transformation temperature of  $Ti_{50-x}Pt_{50}$  is lowered with an increase in Hf up to 43.75 at. %, which is due to  $C'$ . Contrary to the rise in martensitic transformation at Hf 6.25 at. % due to low  $C'$ .

**Table 1.** The elastic constants  $C_{ij}$  (GPa), shear moduli  $C'$  and anisotropy  $A$  for  $\text{Ti}_{50-x}\text{Hf}_x\text{Pt}_{50}$ ,  $0 < x < 50$ .

Structure	$C_{11}$ (GPa)	$C_{12}$ (GPa)	$C_{44}$ (GPa)	$C'$	$A$
$\text{Ti}_{50}\text{Pt}_{50}$	145	210	45	-32.5	-1.38
$\text{Hf}_{6.25}\text{Ti}_{43.75}\text{Pt}_{50}$	105	229	54	-62	-0.87
$\text{Hf}_{18.75}\text{Ti}_{31.25}\text{Pt}_{50}$	147	206	47	-30	-1.59
$\text{Hf}_{25}\text{Ti}_{25}\text{Pt}_{50}$	192	187	40	2.5	16
$\text{Hf}_{31.25}\text{Ti}_{18.75}\text{Pt}_{50}$	202	178	46	12	3.83
$\text{Hf}_{43.75}\text{Ti}_{6.25}\text{Pt}_{50}$	209	173	44	18	2.44
$\text{Hf}_{50}\text{Pt}_{50}$	209	172	43	19	2.32

Another index to describe the brittleness or ductility of a system is Pugh's ratio ( $k$ ) which is defined as Bulk ( $B$ ) to shear ( $G$ ) ratio,  $k = B/G$ , the  $B/G$  ratio must be  $> 1.75$  for the material to be regarded as ductile, if  $< 1.75$  then the material is brittle [31]. In Figure 2 (a), the structures displayed ductility with an increase in Hf content, since  $B/G > 1.75$ . The dip at 18.75 at.% of Hf was caused by lower values of  $G$ . Furthermore, 6.25 at.% Hf is brittle with  $k = 1.68$ .

Cauchy pressure can be portrayed as  $C_{12} - C_{44}$ , which may be utilized to portray the angular character of atomic bonding in different metals and compounds. The negative estimation of Cauchy pressure demonstrates that the material is non-metallic with directional bonding and while for positive estimation of the material; it is required to be metallic. [32]. From Figure 3 (b), it is evident that the values of  $C_{12} - C_{44}$  of  $\text{Ti}_{50-x}\text{Hf}_x\text{Pt}_{50}$  are positive, which indicates the metallic behavior of the compound. Furthermore, according to  $C_{12} - C_{44}$ , it is noticeable that the metallic behavior of  $\text{Ti}_{50-x}\text{Hf}_x\text{Pt}_{50}$  is getting weaker with an increase in Hf content. Therefore, the  $\text{Ti}_{50-x}\text{Hf}_x\text{Pt}_{50}$  maintained a metallic behavior as Hf is introduced to the system.

**Figure 2.** (a) Pugh's ratio  $k$  and (b) Cauchy pressure against composition  $\text{Ti}_{50-x}\text{Hf}_x\text{Pt}_{50}$ ,  $0 < x < 50$ 

### 1.3. Thermal properties

It is imperative to appreciate the Debye temperature, chemical bonds, and the mechanical solidness of materials. The Debye temperature ( $\theta_D$ ) is firmly identified with numerous actual properties, for example, versatile consistent, explicit warmth and melting point and it can be assessed through the mean sound speed utilizing the accompanying condition [33],

$$\theta_D = \frac{h}{k_B} \left( \frac{3n}{4\pi\Omega} \right)^{1/3} \times v_m, \quad (3)$$

where  $h$  is the Planck constant,  $n$  is the number of atoms in the unit cell. The average sound velocity in a system,  $v_m$  is given by:

$$v_m = \left[ \frac{1}{3} \left( \frac{2}{v_t^3} + \frac{1}{v_l^3} \right) \right]^{-1/3}, \quad (4)$$

where  $v_t$  and  $v_l$  are the transverse and longitudinal elastic wave velocities, respectively, which can be written as:

$$v_t = \left( \frac{G}{\rho} \right)^{1/2} \text{ and } v_l = \left( \frac{3B+4G}{3\rho} \right)^{1/2}. \quad (5)$$

The calculated Debye temperature of the  $\text{Ti}_{50-x}\text{Hf}_x\text{Pt}_{50}$  compositions is summarized in Table 2. The density of the TiPt increases with an increase in Hf, this is deduced from the lattice parameter in section 3.1. The  $\Theta_D$  can also be used to describe the strength of covalent bonds in solid materials [34]. The obtained results indicate that the covalent bonds in  $\text{Hf}_{6.25}\text{Ti}_{43.75}\text{Pt}_{50}$  are greater than all other compositions. The Debye temperature increases in the sequence  $\text{Hf}_{18.75}\text{Ti}_{31.25}\text{Pt}_{50} < \text{Hf}_{25}\text{Ti}_{25}\text{Pt}_{50} < \text{Hf}_{50}\text{Pt}_{50} < \text{Hf}_{31.25}\text{Ti}_{18.75}\text{Pt}_{50} < \text{Hf}_{43.75}\text{Ti}_{6.25}\text{Pt}_{50} < \text{Ti}_{50}\text{Pt}_{50} < \text{Hf}_{6.25}\text{Ti}_{43.75}\text{Pt}_{50}$ .

**Table 2.** The density  $\rho$  (Mg/m<sup>3</sup>), transverse  $v_t$ , longitudinal  $v_l$  and mean elastic wave velocity  $v_m$  (m/s) and Debye temperature  $\Theta_D$  (K) for  $\text{Ti}_{50-x}\text{Hf}_x\text{Pt}_{50}$ ,  $0 < x < 50$ .

Composition	$\rho$	$v_t$	$v_l$	$v_m$	$\Theta_D$
$\text{Ti}_{50}\text{Pt}_{50}$	12.614	2553	4854	2855	337
$\text{Hf}_{6.25}\text{Ti}_{43.75}\text{Pt}_{50}$	12.614	2916	5054	3237	380
$\text{Hf}_{18.75}\text{Ti}_{31.25}\text{Pt}_{50}$	13.210	871	3728	995	115
$\text{Hf}_{25}\text{Ti}_{25}\text{Pt}_{50}$	14.324	1026	3746	1171	135
$\text{Hf}_{31.25}\text{Ti}_{18.75}\text{Pt}_{50}$	14.917	1329	3799	1511	173
$\text{Hf}_{43.75}\text{Ti}_{6.25}\text{Pt}_{50}$	15.411	1372	3709	1557	177
$\text{Hf}_{50}\text{Pt}_{50}$	16.441	1343	3647	1525	172

#### 1.4. Phonon dispersion curves

The scattering relations display two kinds of phonons in particular the optical and acoustic modes corresponding to the upper and lower sets of bands in the chart, respectively. The analyses of the vibrational properties concerning the phonon dispersion curves and the phonon density of states (DOS) of the  $\text{Ti}_{50-x}\text{Hf}_x\text{Pt}_{50}$  ( $x = 6.25, 18.75, 25, 31.25$  and  $43.75$ ) are shown in Figure 3. Previous reports show that the B2 TiPt has soft modes due to Pt contribution and while Ti contributes to the acoustic mode in the positive direction [35]. In addition, on Pt substitution with Hf,  $\text{Ti}_{50}\text{Pt}_{31.25}\text{Hf}_{18.75}$  and  $\text{Ti}_{50}\text{Pt}_{25}\text{Hf}_{25}$  were found to be vibrational stable due to the absence of soft modes in the negative direction of phonon dispersion curves [36]. Interestingly, from Figure 3, it is observed that the soft mode along all the high symmetry directions has the lowest frequency at approximately -3 THz and a slight shift in the acoustic region since Ti was substituted with Hf. The phonon dispersion curves are highly unstable due to the presence of soft modes along with the high symmetry directions. A similar trend is observed in all compositions. The phonon DOS of the  $\text{Ti}_{50-x}\text{Hf}_x\text{Pt}_{50}$   $x = 6.25, 18.75, 25, 31.25$  and  $43.75$  is plotted on each right side of the phonon spectra. The Phonon DOS shift minimally with an increase in Hf content. This is due to the high Pt content in the ternary system. The Pt element contributes more towards the soft modes in the negative direction [36]. In addition, from all the concentrations below the Pt atoms vibrate at lower frequencies, while on the contrary, Ti atoms vibrate towards higher frequencies.

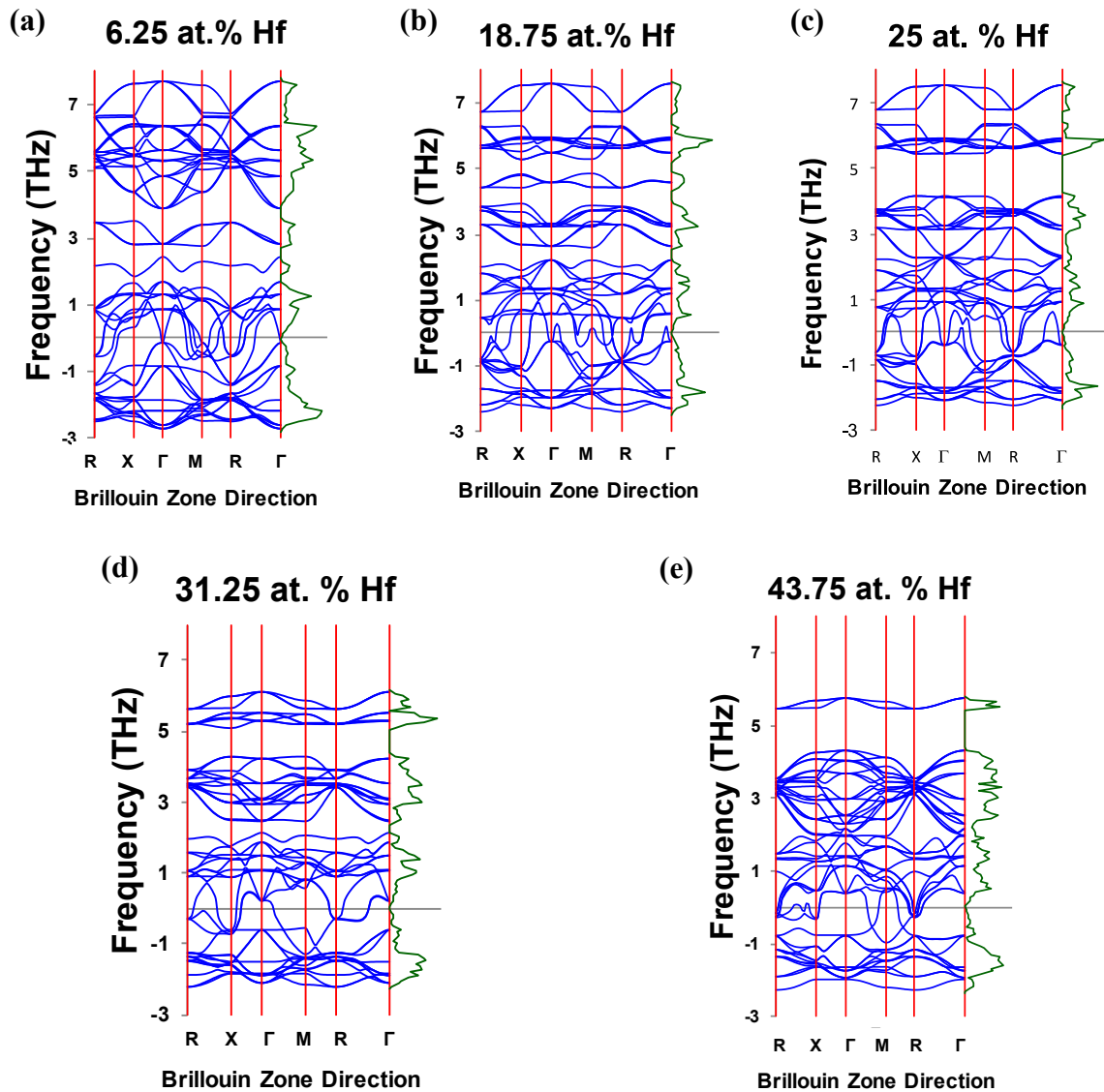


**Figure 3.** Phonon dispersion curves and phonon DOS for  $\text{Ti}_{50-x}\text{Hf}_x\text{Pt}_{50}$ ,  $0 < x < 50$

#### 4. Conclusions

First-principle was used to investigate the structural, thermodynamic and mechanical properties in  $\text{Ti}_{50-x}\text{Hf}_x\text{Pt}_{50}$  where  $0 < x < 50$ . The lattice parameter behaviour depends on the type of the third element, atomic radius, density and sub-lattice. The addition of Hf displayed an increase in lattice parameters due to the atomic radii and densities. Thermodynamic stability for the ternary system was investigated by partially substituting some of the Ti with Hf, it was observed that Hf (-0.966 eV/atom) at 43.75 at.% the substitutions were the most stable structures. The  $C_{44}$  decreases slightly which leads to an increase in transformation temperature. The  $C'$  of the  $\text{Ti}_{50-x}\text{Hf}_x\text{Pt}_{50}$  compound is raised with the increase in Hf content, which leads to positive and larger anisotropy. Cauchy pressure confirmed metallic behavior of the  $\text{Ti}_{50-x}\text{Hf}_x\text{Pt}_{50}$  ( $0 < x < 50$ ) systems. The calculated structures show good thermal conductivity as deduced by the Debye temperature. The phonon dispersion curves were also calculated and suggest that the addition of Hf needs more strain to stabilize TiPt at compositions greater than 6.25 at. % or some substitution to Pt sub-lattice.

### Acknowledgements

This research was supported by the Materials Modelling Centre at the University of Limpopo and the Centre for High Performance Computing. M. P Mashamaite, H. R Chauke and P. E Ngoepe also acknowledge the TiCoC the financial support.

### References

- [1] Wanhill R J H, Ashok B 2017 *Aerospace Mater. Mater. Tech.* Singapore: Springer, **467**
- [2] Jani J M, Leary M, Subi A and Gibson M A 2014 *Mater. Des.* **56** 1078
- [3] Majid T, Vijay G and Mohammad H E 2012 *J. Med. Devices* **6** 034501
- [4] Cai J, Wang D S, Liu S J, Duan S Q and Ma B K 1999 *Phys. Rev. B* **23** 15691
- [5] Nematollahi M, Baghbaderani K S, Amerinatanzi A, Zamanian H and Elahinia M 2019 *Bioengineering* **6** 37
- [6] Morgan N B 2004 *Mater. Sci. Eng. A* **378** 16
- [7] Chowdhury P 2018 *Shap. Mem. Superelasticity* **4** 26
- [8] Bozzolo G, Mosca H O and Noebe R D 2007 *Intermetallics* **15** 901
- [9] Firstov G S, Van Humbeeck J and Koval Y N 2004 *Mater. Sci. Eng. A* **378** 2
- [10] Suzuki Y, Xu Y, Morito S, Otsuka K and Mitose K 1998 *Mater. Lett.* **36** 85
- [11] Ma J, Karaman I and Noebe R 2010 *Int. Mater. Rev.* **55** 257
- [12] Cai W, Tanaka S, Otsuka K 2000 *Mater. Sci. Forum* **279** 327
- [13] Kawamura T, Tachi R, Inamura T, Hosoda H, Wakashima K, Hamada K and Miyazaki S 2006 *Mater. Sci. Eng.* **A438** 383
- [14] Yamabe-Mitarai Y, Hara T, Miura S and Hosoda H 2010 *Intermetallics* **18** 2275
- [15] Yamabe-Mitarai Y 2020 *Metals* **10** 1531
- [16] Hammond C R 2005 *The elements. Boca Raton, FL: CRC*
- [17] Mashamaite M P, Chauke H R and Ngoepe P E 2019 *IOP Conf. Ser.: Mater. Sci. Eng.* **655** 012011
- [18] Donkersloot H C and van Vucht J H N 1970 *J. Less-Common Metals.* **20** 83
- [19] Yamabe-Mitarai Y, Hara T, Miura S, Hosoda H 2006 *Mater. Trans.* **47** 650
- [20] Wadood A, Takahashi M, Takahashi S, Hosoda H and Yamabe-Mitarai Y 2013 *Mater. Sci. Eng.* **A564** 34
- [21] Hohenberg P and Kohn W 1964 *Phys. Rev. B.* **136** 864
- [22] Kohn W and Sham L J 1965 *Phys. Rev.* **140** A1133
- [23] Blöchl P E 1994 *Phys. Rev. B.* **50** 17953
- [24] Perdew J P, Burke K and Ernzerhof M 1996 *Phys. Rev. Lett.* **77** 3865
- [25] Monkhorst H J and Pack J D 1976 *Phys. Rev. B.* **13** 5188
- [26] Parlinski K, Li Z Q and Kawazoe Y 1997 *Phys. Rev. Lett.* **78** 4063
- [27] Fernando G W, Watson R E and Weinert M 1992 *Phys. Rev. B* **45** 15 8233
- [28] Zhang J M and Guo G Y 1997 *Phys. Rev. Letters* **78** 4789
- [29] Mehl M J, Klein B M and Papaconstantopoulos D A 1994 *Inter. Comp.* **1** 1
- [30] Goumri-Said S and Kanoun M B 2007 *Comp. Mat. Sci.* **43** 243
- [31] Pugh S F 1954 *Philos. Mag.* **45** 823
- [32] Pettifor D G 1992 *J. Mater. Sci. and Tech.* **8** 345
- [33] Schreiber E, Anderson O L and Soga N *McGraw-Hill Companies, Inc., New York, 1973.*
- [34] Huang Z W, Zhao Y H, Hou H, Han P D 2012 *Phys. B (2012)* **407** 1075 [34]
- [35] Mahlangu R, Phasha M J, Chauke H R, Ngoepe P E 2013 *Intermetallics*, **3** 31 [35]
- [36] Baloyi M E, Modiba R, Ngoepe P E and Chauke H R 2019 *SAIP Proceedings* 18 [36]



DIVISION

— B —

NUCLEAR, PARTICLE, AND RADIATION  
PHYSICS

# Design and development of the ALICE common readout unit user logic firmware for the Muon Identifier readout chain

D O Thys-dingou<sup>1</sup> A Raji<sup>1</sup>, E Z Buthelezi<sup>2,3</sup> and S V Förtsch<sup>2</sup>

<sup>1</sup> Department of Electrical, Electronic and Computer Engineering, Cape Peninsula University of Technology, Bellville South Industrial, Cape Town, 7530, South Africa

<sup>2</sup> Department of SSC lab, iThemba LABS, Faure, Cape Town, 7100, South Africa

<sup>3</sup> School of Physics, University of the Witwatersrand, Johannesburg, 2000, South Africa

E-mail: dieuveil.orcel.thys-dingou@cern.ch

**Abstract.** A Large Ion Collider Experiment (ALICE) at the Large Hadron Collider (LHC) at CERN went through a major upgrade in which some of its subdetectors were replaced with new ones, while others are equipped with new electronics. The aim of the upgrade is to withstand higher collision rates during the third running period (Run 3), which started in 2022. As part of the upgrade, certain subdetectors such as the Muon Trigger, renamed to Muon Identifier, now operate in a continuous, triggerless readout mode, in addition to the previous triggered readout mode. Due to the increased quantity of data, typical methodologies are impossible to employ without massive efforts to expand the processing capacity. Since the new ALICE computing system cannot keep up with the increased data flow of the Muon Identifier, a new processing algorithm has been established. These proceedings provide a insight to the new approach of processing the Muon Identifier readout data based on a customized user logic FPGA firmware.

## 1. Introduction

ALICE [1] is one of the four main experiments at the LHC. It is designed to study the strongly interacting matter, namely the quark-gluon plasma (QGP) [2] and its properties. In order to unravel the enigma of the universe, the ALICE detector records data during lead-lead (Pb-Pb), proton-lead (p-Pb), and proton-proton (pp) collisions. Based on data collected during Runs 1 and 2, ALICE is the leading heavy-ion experiment in the world and is quickly expanding the knowledge gathered in previous experiments all over the world. The LHC completed the three-year planned second Long Shutdown, which started at the end of 2018 to prepare for Run 3. In line with the LHC upgrade, the ALICE detector had a major upgrade [3]. This upgrade addresses the challenge of reading out Pb-Pb collisions at a rate of 50 kHz, pp, and p-Pb collisions at 200 kHz and higher. At the center of the ALICE upgrade strategy, is a high-speed readout approach based on a Common Readout Unit (CRU), which has been developed for detector data readout, reconstruction, multiplexing, and data decoding on the Online-Offline (O<sup>2</sup>) computing system.

Many of the proposed physics observables require a change in the data-taking strategy, moving away from triggering a small subset of events to continuous online processing and recording of

all events. To achieve these goals, ALICE has been upgraded in such a way that all interactions will be scrutinized with online precision. The upgrade entailed the replacement of some subdetectors with new ones, making use of new technologies, while others are now equipped with new front-end and readout electronic systems [4]. Thus far, the selection of single muon and dimuon events with a maximum trigger rate of 1 kHz, limited by readout capabilities, was provided by the Muon Trigger (MTR), as well as muon identification. However, the upgrade strategy described in the Letter of Intent (LoI)[3] does not require a muon trigger since all events of interest are now read out upon the interaction trigger before online selections. For this reason, as part of the upgrade, the new Muon Identifier (MID) subdetector plays the role of muon identifier.

## 2. Muon Identifier

The MID [5] is based on 72 single-gap Resistive Plate Chamber (RPC) detectors, arranged in 2 stations of 2 chambers, each at a distance of about 16 m and 17 m from the interaction point, respectively. Its readout chain block diagram is shown in Fig. 1.

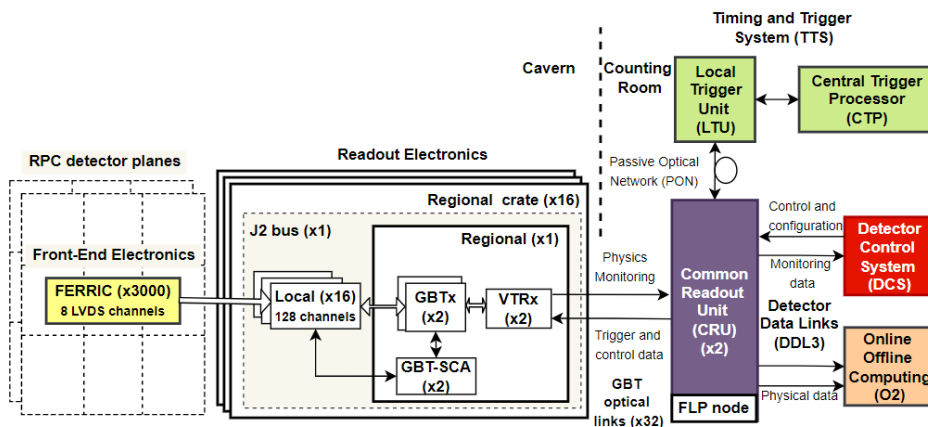


**Figure 1.** A schematic description of the MID readout chain architecture for LHC Run 3.

The MID readout chain consists of about 21,000 strips connected to the 72 RPC detectors spread over multiple Front-End Electronic Rapid Integrated Circuit (FEERIC) cards equipped with one or two customized Application-Specific Integrated Circuits (ASICs). The strip signals from the FEERICs are propagated to the readout electronics using high-speed Low-voltage Differential Signaling (LVDS) channels. The readout electronics (local and regional cards) act as interface between the on and off-detector electronics. They are mounted inside the cavern a little further away from the detector stations, where the radiation is lower. Since the colliding beams will produce a lot of radiation in the area around the ALICE detector in the cavern, the regional cards are equipped with a radiation hardening Gigabit Transceiver set of chips (GBTx and GBT-SCA) [6, 7] used to facilitate the bidirectional connections between the readout electronics and CRUs through optical links, namely, GBT links. The CRUs are the key components of the chain. They combine and multiplex data from multiple readout electronic cards as well as timing and trigger information generated from the Central Trigger Processor (CTP) via the Local Trigger Unit (LTU) before transmitting the data to the O<sup>2</sup> computing facility for processing and storage. The CRUs are mounted on computers housed in the intermediary computer room, called the counting room, tens of meters above the ALICE cavern and thus do not require to be protected from the radiation, as is the case for the readout electronics. These computers can be reached over the network from the main Detector Control System (DCS). The DCS manages the readout

chain by sending commands and monitoring the system. Experimental data are moved from the First Level Processor (FLP) to the Event Processing Node (EPN) for processing and storage. The EPN is an internal component of the O<sup>2</sup> computing system [8].

### 3. CRU firmware

The standard approach of delivering raw data to the O<sup>2</sup> system is no longer sufficient to meet the needs of the newly enhanced MID subdetector. As a result, an alternative option was presented to the ALICE collaboration [9]. Since the release of its first official version in 2018, the CRU firmware provides basic functionalities allowing to interact with multiple systems via a variety of interfaces and read out any subdetector without conducting any first stage data analysis. However, the CRU firmware can be customised to meet the demands of different subdetectors in the ALICE experiment. In particular, a first stage data analysis can be implemented before online and offline reconstruction. This customisation is referred to as "User Logic". It is the responsibility of the MID specialists to decide how data should be handled in their user logic.

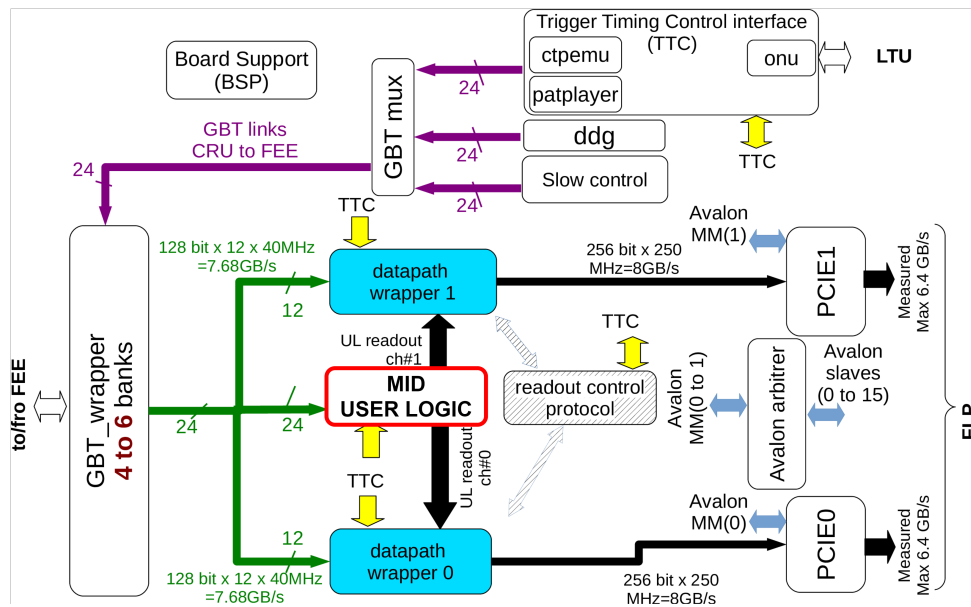


Figure 2. CRU firmware architecture. Adapted from [10].

The CRU firmware architecture is illustrated in Fig.2. It is composed of several modules interacting with several interfaces. From left to right, the main interfaces are the GBT wrappers, Board Support Package (BSP), Datapath Wrappers (DWs), Timing and Trigger Control (TTC), Dedicated Data Generator (DDG), slow control, and PCIe endpoints. All of these interfaces provide indispensable functionalities to the CRU firmware, and at the heart of it is a tailored user logic component with functionalities that are unique to MID.

The key general requirements of the user logic component are derived from several articles and are cited in this paper, but not duplicated. These requirements are described in [10, 11] and [12]. One of the main functional requirements of the user logic component is to reduce the data rates transmitted to the O<sup>2</sup> system by performing zero suppression. It also has to carefully handle the readout electronics anomalies and errors, without stopping the data acquisition of the readout chain. Transient losses of payload (physics) data are not tolerated. This means that at all cost, every level of the user logic hierarchy must be able to identify anomalies from the levels below and continue to transmit packets and follow the communication rules with the levels

above. The violation of communication protocols, corruption of data, and unresponsiveness of the system in case of errors shall be prevented.

**4. Architecture and design of the user logic component**

The user logic is designed in a sequential manner, with all processing occurring one after another from an input-output perspective. The objective of this approach is to facilitate error tracking. The user logic consists of three main segments, each of which is linked to a specific interface of the CRU firmware (see Fig.2). A representation of the user logic block diagram and its interfaces is shown in Fig.3. Starting from the top is the TTC segment (grey), which receives data from the timing and trigger system through the TTC interface. Next is the GBT segment (blue), which receives data from the readout electronics via the GBT wrappers, analyses them then combines them with the Raw Data Header (RDH) extracted from timing and trigger information before transmitting them to the O<sup>2</sup> system via the datapath wrappers. The GBT segment is the only part of the design that can be duplicated through parameterization. Hence, enabling the possibility to process multiple GBT links, allows for improvement and adaption to diverse testing scenarios. The last segment is the Avalon (orange), which provides configuration and monitoring through the PCIe interface.

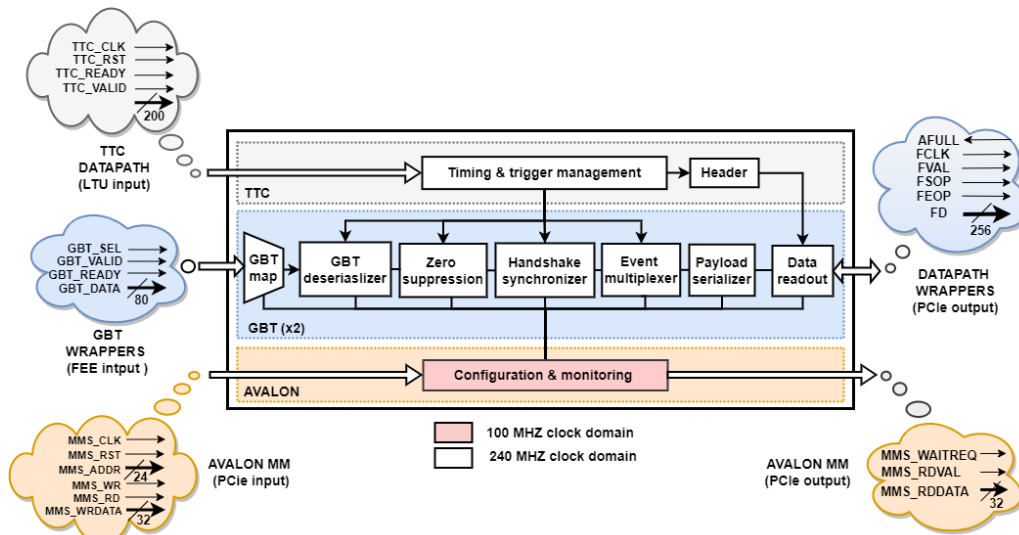


**Figure 3.** Structure of the user logic design showing the three main segments and data flow.

**5. Test-bench layout**

A test bench at iThemba LABS was implemented to extend the capabilities of the user logic and match the test scenarios performed with readout electronics at SUBATECH, Nantes (where the readout electronics cards were designed [13]). The test bench is a scaled-down replica of the MID readout chain without the RPC detectors. It includes a fully-equipped VME crate (16 x local, 1 x regional, and 1 x J2 bus boards), the LTU, CRU, and FLP. Figure 4 depicts the test bench setup and illustrates how various components are linked together. The full setup can be seen on the top left, while in the bottom left the fully-equipped VME crate is shown. The local and regional cards are plugged into the crate via the J2 bus card sitting at the back of the crate. Three cables are exiting the regional card, two of which are optical cables, and connect the regional card to the CRU. The latter is a USB (2.0) cable connected to a CentOS PC, which is used to configure and program the local and regional FPGAs. At the top-right is

the LTU, which can be used to interact with multiple CRUs via a splitter. However, for this application only one CRU is needed. The connection between the LTU and the CRU is done via a single-mode SC to SC optical cable. The LTU uses an Ethernet cable to interact with the FLP software, which runs on CentOS 8. Finally, on the bottom-right is the CRU board housed by the FLP server. The CRU board is internally attached to the FLP via the PCIe connectors, its FPGA can be programmed using the PCIe interface or via its integrated USB blaster programmer, which connects to the FLP server using a micro-USB (2.0) cable.

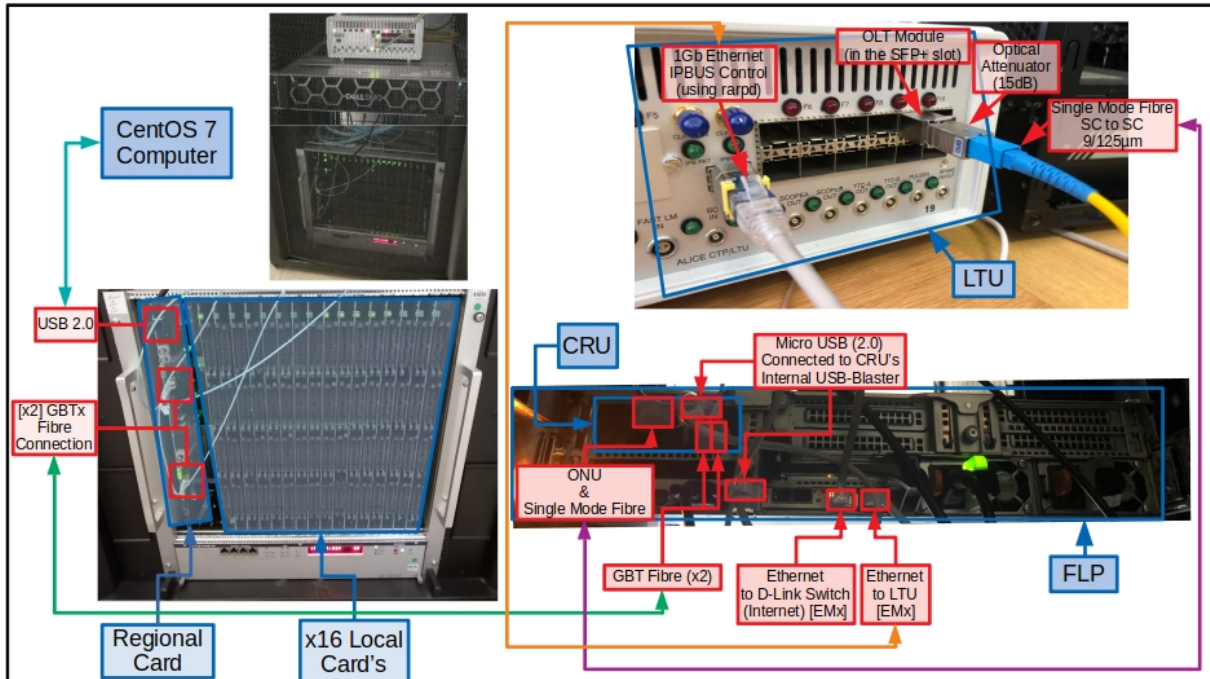


**Figure 4.** New test bench located in the laboratory S64 at iThemba LABS. The diagram shows the readout chain components and how they are connected.

## 6. Results

The simulated results of the working user logic firmware were generated in ModelSim using a simulation framework provided by SUBATECH. A subset of the results is illustrated in Fig.5. As can be observed, the user logic output packets fulfill the readout control protocol criteria specified in [12], which states that packets created by the user logic must begin and terminate with the Start Of Packet (SOP) and End Of Packet (EOP) signals, and each packet must be enclosed by the RDH. The output data format transmitted by the user logic is based on the GBT raw data, pre-analysed and concatenated into multiple data blocks of 256-bit to form the payload included in the packets.

A clear comparison of data before and after being processed by the user logic is illustrated in Figure 5. It shows the outcome result of the data before and after all processing stages the user logic firmware have been completed. These simulation results validate the aim of this research, which is to enhance the way data are processed by only transmitting valuable information to the FLP. The hardware test results did not reflect the simulation results at first, but were refined after each iteration until complete accuracy was achieved. The user logic helped decreasing

the amount of data transmitted from the CRU to the FLP by roughly 80%, and improved the readability of the data at the O<sup>2</sup> level.

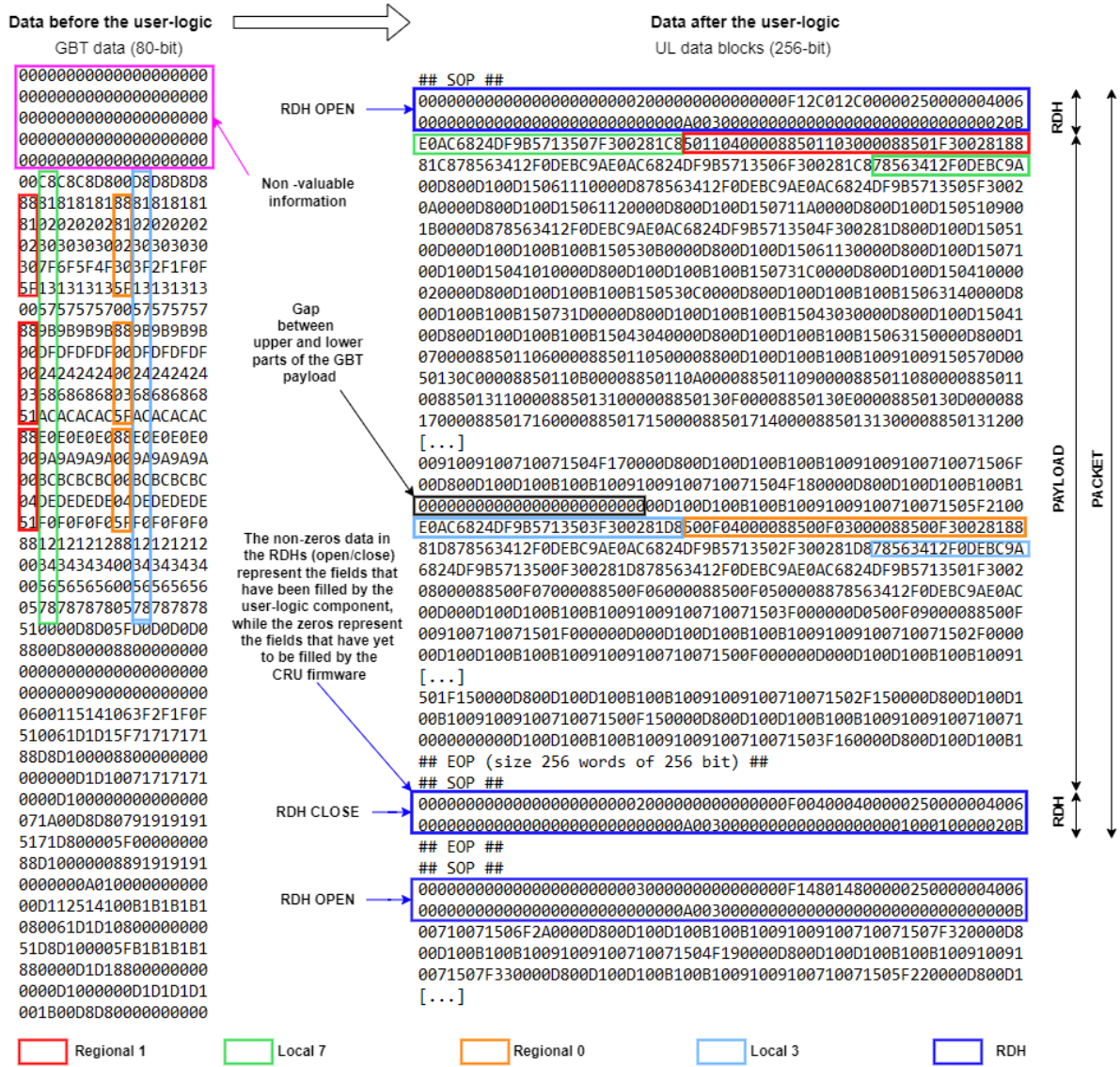


**Figure 5.** Simulation results extracted from ModelSim. This image compares data before and after the user logic processing. As it can be seen, the packets start and end with SOP and EOP signals. Each packet includes RDHs (open and close), that specify the borders of the packet.

**7. FPGA resource usage**

The CRU firmware combined with the user logic component use about 160k (38%) Adaptive Logic Modules (ALMs) and 1355 (50%) RAM blocks of the available resources. These results were obtained after integrating and compiling the CRU firmware with the user logic component. Table 1 provides a summary of the total FPGA resource used. The user logic consumes around 37k (9%) ALMs and 271 (10%) RAM blocks of the overall resources. These findings meet the

requirement of this study, but are not good enough as the long-term aim is to process data from 16 GBT links while maintaining the overall RAM consumption below 75%.

**Table 1.** FPGA resource usage of the CRU firmware after insertion of the user logic component.

Resource name	Total in ratio	Total in percentage
Logic utilization (in ALMs)	160,282 / 427,200	38%
Pin	369 / 960	38%
Block memory bits	19,982,660 / 55,562,240	36%
RAM blocks	1,355 / 2,713	50%
RX channels	41 / 72	57%
TX channels	41 / 72	57%
Phase Locked Loops (PLLs)	59 / 144	41%

## 8. Conclusion

The user logic firmware performed reasonably well during the simulation and hardware tests. The findings shown in these proceedings demonstrate that the user logic is stable, reliable, and built to read out Pb-Pb collisions at a rate of 50 kHz, and pp and p-Pb collisions at 200 kHz and higher without any issues. The methodology implemented shows that it is feasible to considerably reduce the data bandwidth transmitted from the CRU to the FLP by roughly 80%. The user logic has passed the validation tests and so fulfils the MID requirements. The results obtained also indicate that with some optimizations, the user logic can immensely contribute to the development of a full scale user logic component capable of processing data from the complete MID system during the LHC Run 3.

## References

- [1] ALICE Collaboration 2008, The ALICE experiment at the CERN LHC, *Journal of Instrumentation*, **3**: S08002. DOI:10.1088/1748-0221/3/08/S08002
- [2] Graczykowski L. 2016, Soft QGP probes with ALICE, *Acta Physica Polonica B* **47**, pp. 1473-1487. DOI:10.48550/arXiv.1608.00040
- [3] ALICE Collaboration 2014, Upgrade of the ALICE Experiment: Letter of Intent, *Journal of Physics G: Nuclear and Particle Physics* **41**. DOI:10.1088/0954-3899/41/8/087001
- [4] Antonioli P., Kluge A. and Riegler W. 2013, Upgrade of the ALICE Readout and Trigger System, CERN-LHCC-2013-019, ALICE-TDR-015.
- [5] Terlizzi L., The ALICE Muon Identifier (MID), *Journal of Instrumentation*, 2020, **15** C10031. DOI:10.1088/1748-0221/15/10/C10031
- [6] Moreira P. et al. 2009, The GBT Project, *Topical Workshop on Electronics for Particle Physics*. DOI:10.5170/CERN-2009-006.342
- [7] Caratelli A. et al. 2015, The GBT-SCA: A radiation tolerant ASIC for detector control and monitoring applications in HEP experiment, *Journal of Instrumentation*, **10** C03034. DOI:10.1088/1748-0221/10/03/C03034
- [8] Buncic P., Krzewicki M. and Vande Vyvre P. 2015, Technical Design Report for the Upgrade of the Online-Offline Computing System, CERN-LHCC-2015-006, ALICE-TDR-019.
- [9] David E. et al. 2015, ALICE COMMON READ-OUT UNIT, *ALICE internal report*, (Geneva: CERN). [https://www.phenix.bnl.gov/WWW/publish/mxliu/sPHENIX/Readout/CRU/CRU\\_Specification\\_v0.7.pdf](https://www.phenix.bnl.gov/WWW/publish/mxliu/sPHENIX/Readout/CRU/CRU_Specification_v0.7.pdf)
- [10] Bourrion O., Bouvier J. et al. 2021, Versatile firmware for the Common Readout Unit (CRU) of the ALICE experiment at the LHC, *Journal of Instrumentation*, **15** P05019. DOI:10.1088/1748-0221/16/05/P05019
- [11] Kvapil J. et al. 2021, ALICE Central Trigger System for LHC Run 3, *Conference on High-Energy Physics*, **251** 04022. DOI:10.1051/epjconf/202125104022
- [12] Bourrion O. et al., CRU firmware gitlab project. <https://gitlab.cern.ch/alice-cru/cru-fw>
- [13] Renard C., MID Readout electronics project. <http://www-subatech.in2p3.fr/~electro/projets/alice/dimuon/trigger/upgrade/index.html>

# Search for dark sector showering in ATLAS using semi-visible jets

**Sukanya Sinha, Deepak Kar**

School of Physics, University of Witwatersrand, Johannesburg, South Africa

E-mail: [sukanya.sinha@cern.ch](mailto:sukanya.sinha@cern.ch)

**Abstract.** Recent studies in particle physics have shown that there are myriad possibilities for strong dark sector studies at the LHC. One signature is the case of semi-visible jets, where parton evolution includes dark sector emissions, resulting in jets overlapping with missing transverse energy. Owing to the unusual MET-along-the-jet event topology, this is mostly an unexplored domain within ATLAS. In this talk, I will discuss the public results of the first  $t$ -channel ATLAS search for semi-visible jets, that focussed on overcoming the performance and optimisation challenges associated with such a unique final state, specifically looking at the angular difference between the hardest jet and the missing transverse energy.

## 1. Introduction

Collider searches for Dark Matter (DM) until this date have mostly focussed on scenarios where DM particles are produced in association with either heavy Standard Model (SM) particles, photons or jets. However, no confirmed evidence of DM has been observed so far. Several models [1, 2, 3, 4] have been proposed that include a strongly-coupled dark sector, giving rise to unusual and unexplored collider topologies. Semi-visible jets (SVJ) [5] is one such example. A result in the  $s$ -channel production mode has been presented by the CMS collaboration [6]. Here, a preliminary result from the ATLAS search for the  $t$ -channel production mode [7] is presented. Searches for  $t$ -channel production modes allow to probe a broad class of non-resonant signals and can potentially have higher mass reach, as they are not limited only to finding resonance peaks as in the  $s$ -channel searches.

## 2. Signal and background modelling

In the  $t$ -channel production mode, the scalar bi-fundamental mediator ( $\Phi$ ) acts as a portal between SM and dark sectors. The hadronisation process involves dark quarks as well as SM quarks as shown in Fig. 1. The ratio of the stable dark hadrons over the total number of hadrons in the event is termed  $R_{\text{inv}}$ , which can be set in the model. This results in reconstructed jets geometrically encompassing the dark hadrons, termed semi-visible jets (SVJ). The resultant missing transverse momentum ( $E_{\text{T}}^{\text{miss}}$ ) direction is aligned along one of the jets. As this is also a signature of mis-measured jets in a detector, this class of jets as new physics signal has been mostly unexplored at the Large Hadron Collider (LHC).

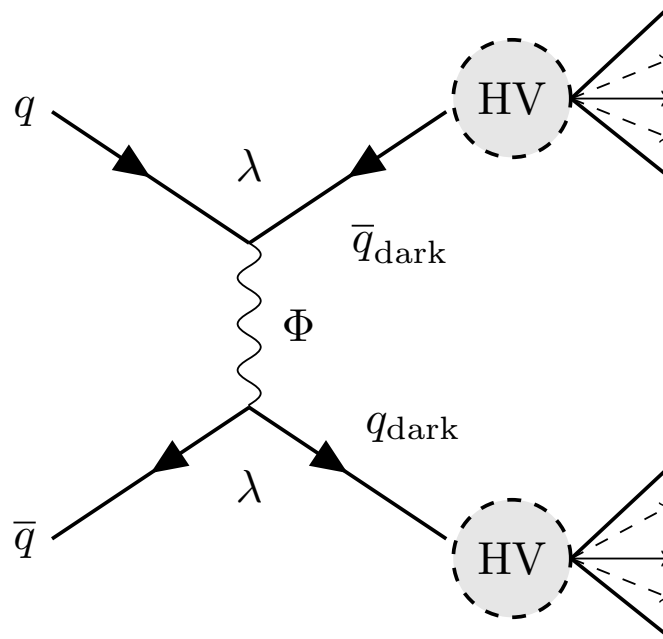


**Figure 1.** The Feynman diagram and subsequent production mechanism for semi-visible jets. The mediator  $\Phi$  decays to two dark quarks, and the hadronisation process involves dark hadrons, and partially SM hadrons, governed by  $R_{\text{inv}}$  fraction. The coupling is denoted by  $\lambda$ . HV denotes the Pythia8 Hidden Valley module interactions connecting the dark sector with the SM sector.

The Madgraph [8] event generator at leading order, with up to two extra jets was used to generate matrix element (ME) level signal events with the DMsimp\_tchannel model [9] and NNPDF30LO [10] PDF. The pair production of mediators with their decays governed by the same  $R_{\text{inv}}$  fraction would result in roughly back-to-back semi-visible jets. The addition of extra jets boosts the hadronic activity, and consequently the  $E_{\text{T}}^{\text{miss}}$  in the event, thereby making the search viable over the Standard Model background. The dark hadron mass is set to be 10 GeV based on [5], while the mediator mass is varied within the range of 1000 - 5000 GeV in 500 GeV intervals. Another free parameter in the model is the coupling connecting the SM and DM sectors,  $\lambda$  (as shown in Fig. 1). The nominal samples are generated with  $\lambda = 1$  but  $\lambda$  can be varied between  $10^{-4} - 4\pi$  [11, 12]. The cross-section is scaled as  $\lambda^4$  without having any impact on the kinematic distributions or on the validity of the model if the mediator mass is 2.5 TeV or higher, as at lower mediator masses, there are contributions from  $s$ -channel processes as well. The Hidden Valley (HV) module [13] of Pythia8 [14] is used to shower the ME level event, using the NNPDF2.3LO [10] parton distribution function (PDF) set and the A14 set of tuned parameters [15]. The MLM [16] jet matching scheme, with xqcut of 100, is employed. The samples were generated with  $R_{\text{inv}}$  values of 0.2, 0.4, 0.6 and 0.8 for each mediator mass.

The contributing background processes are multijet,  $t\bar{t}$ , single top,  $Z/W$ +jets, and diboson, generated using Pythia8.230, PowhegBoxV2 [17, 18, 19] plus Pythia8.230 for showering, and Sherpa2.2.11 [20, 21] respectively. The Monte Carlo (MC) simulated samples are processed through the full ATLAS detector simulation [22] based on Geant4 [23], and then reconstructed and analysed using the same procedure and software that are used for the data.

### 3. Analysis Strategy

This analysis uses  $139 \text{ fb}^{-1}$  of proton-proton collision data with 25 ns bunch spacing collected by ATLAS from 2015 to 2018. The description of the ATLAS detector can be found elsewhere [24]. The  $E_T^{\text{miss}}$  is defined as the negative vectorial sum of the transverse momenta of all selected objects. Events in the analysis are selected with the un-prescaled  $E_T^{\text{miss}}$  trigger having the lowest threshold [26]. Events with  $E_T^{\text{miss}} > 200 \text{ GeV}$  are selected in order to be on trigger efficiency plateau. Particle-flow (PFlow) jets are constructed using the anti- $k_t$  algorithm [27, 28] with a radius parameter of  $R = 0.4$ , using charged constituents associated with the primary vertex and neutral PFlow constituents as inputs [29]. Events are required to have at least two jets within  $|\eta| < 2.8$ , the leading jet is required to have  $p_T > 250 \text{ GeV}$ , while other jets are required to have  $p_T > 30 \text{ GeV}$ . Events are also required to have at least one jet within  $\Delta\phi < 2.0$  of  $E_T^{\text{miss}}$  direction, as the distance of the closest jet to  $E_T^{\text{miss}}$  direction depends somewhat on the  $R_{\text{inv}}$  fraction. Jets are considered tagged as b-jets if they pass the 77% efficiency working point of the  $DL1r$  algorithm [30]. Events with two or more b-tagged jets are vetoed to reduce  $t\bar{t}$  background contributions.

As the signal does not have any leptons, Any events with a  $\tau$ -lepton candidate with  $p_T > 20 \text{ GeV}$  and  $|\eta| < 2.5$  are rejected. Events with any electrons or muons satisfying  $p_T > 7 \text{ GeV}$  and within the tracking volume  $|\eta| < 2.5$  are discarded for the nominal analysis. However, for estimation of leptonic backgrounds, additional leptonic selections are defined. In all cases,  $E_T^{\text{miss}}$  trigger is employed, and  $E_T^{\text{miss}}$  is recalculated considering muons to be invisible, to mimic the nominal analysis trigger level  $E_T^{\text{miss}}$  definition. Events with any electron with  $p_T \geq 7 \text{ GeV}$  are discarded. The muons must have  $p_T \geq 7 \text{ GeV}$ . The 1L selection requires exactly one muon and no b-tagged jet. The 1L1B selection requires exactly one muon as before, but exactly one b-tagged jet in addition. Finally, the 2L selection requires two opposite charged muons with the pair's invariant mass between 66 GeV and 116 GeV, and no b-tagged jets. The 1L-region is dominated by  $W$ +jets events, the 1L1B-region is dominated by semi-leptonic  $t\bar{t}$  and single top quark induced processes, and the 2L-region almost exclusively contains  $Z$ +jets events.

The analysis uses  $E_T^{\text{miss}}$  and  $H_T$ , the latter defined as the scalar sum of  $p_T$  of jets in the event. The region with  $E_T^{\text{miss}} > 600 \text{ GeV}$  and  $H_T > 600 \text{ GeV}$  after the pre-selection is defined as the signal region (SR). The corresponding 1L, 1L1B and 2L control regions (CR) are defined using the muon and b-tagged jet requirements with the same  $E_T^{\text{miss}}$  and  $H_T$  requirements as in the SR. Low and intermediate  $E_T^{\text{miss}}$  validation regions (VR) for multijet process are defined by requiring  $E_T^{\text{miss}}$  to be between 250 GeV to 300 GeV and between 300 GeV to 600 GeV respectively, with the same  $H_T > 600 \text{ GeV}$  requirement after the pre-selection. The CR and VRs have negligible signal contamination.

The search then makes use of two other key observables, which are found to be largely uncorrelated:

- (i) the  $p_T$  balance between the closest jet ( $j_1$ ) and farthest jet ( $j_2$ ) from  $E_T^{\text{miss}}$  direction, termed as  $p_T^{\text{bal}}$ , defined using two-dimensional  $p_T$  vectors:

$$p_T^{\text{bal}} = \frac{|\vec{p}_T(j_1) + \vec{p}_T(j_2)|}{|\vec{p}_T(j_1)| + |\vec{p}_T(j_2)|}.$$

- (ii) the difference in the azimuthal angle between  $j_1$  and  $j_2$  as defined above, termed  $|\phi_{\text{max}} - \phi_{\text{min}}|$ :

Fig. 2 shows the signal against total background shape comparison for  $p_T^{\text{bal}}$  and  $|\phi_{\text{max}} - \phi_{\text{min}}|$  distributions for the nominal selection. There is a distinct shape difference between the different signal benchmark points, and the total background, which is utilised in designing the fit strategy. The  $|\phi_{\text{max}} - \phi_{\text{min}}|$  and the  $p_T^{\text{bal}}$  distributions are divided into nine bins as seen in Fig. 3. These bins are defined identically in SR and in each CR. Yields in these nine bins in each case are treated as the observables.

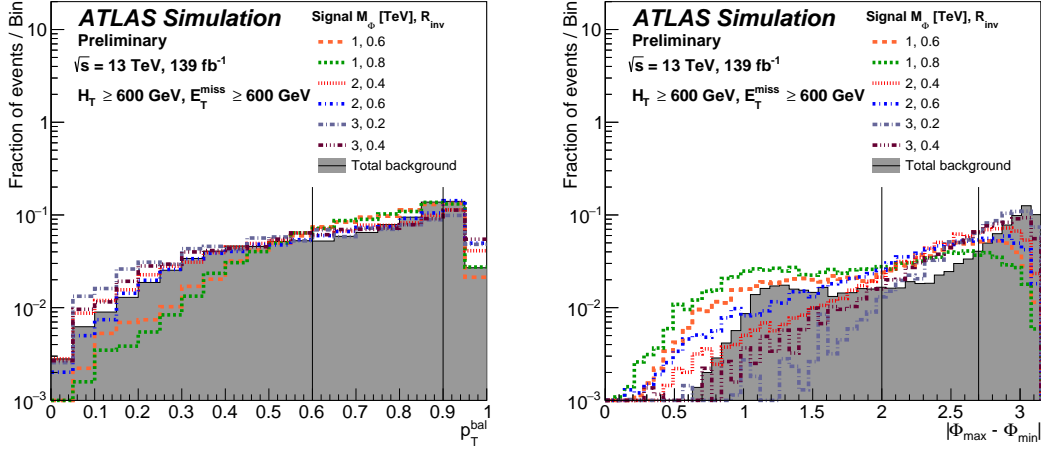


**Figure 2.** Comparisons of shape of  $p_T^{\text{bal}}$  (a) and  $|\phi_{\text{max}} - \phi_{\text{min}}|$  (b) distributions between the total background before the fit and six signal predictions covering a representative mediator mass and invisible fraction range. The solid vertical lines represent how these distributions are divided to form the nine-bin grid subsequently.

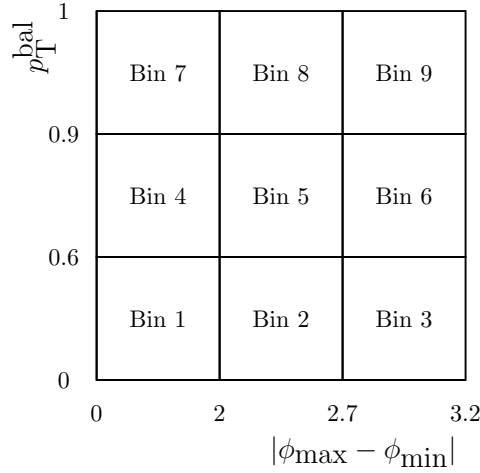


**Figure 3.** The definition of the 9-bins in  $|\phi_{\text{max}} - \phi_{\text{min}}|$  and  $p_T^{\text{bal}}$ , defined identically in SR, VR and in each CR.

The background contributions are from multijet processes with mis-measurement of jet momenta and angles, and from  $W/Z$ +jets, diboson and semi-leptonic top processes with real  $E_T^{\text{miss}}$ . In order to address the known mismodelling in multijet MC samples, reweighting factors using an additional low  $E_T^{\text{miss}}$  VR of 250–300 GeV were derived in multijet-rich bins 3, 6 and 9 and applied to the rest of the bins in the same  $p_T^{\text{bal}}$  range. The background from  $t\bar{t}$  and  $W$ +jets arises either because an electron or a muon is not detected or a hadronically decaying  $\tau$  lepton is misidentified as a jet.

The systematic uncertainties on signal and background yields and shapes result from experimental uncertainties and theoretical modelling effects. The former are due to the jet energy scale (JES) and resolution (JER), computation of the  $E_T^{\text{miss}}$  soft term, flavour-tagging

performance, rescaling of simulation to match the pile-up profile in data, and an absolute uncertainty on the luminosity estimation. Uncertainties in the reconstruction, identification, isolation and trigger efficiencies of muons, electrons and  $\tau$ -leptons and on their energy scale and resolution are also considered. Theoretical uncertainties common on the MC samples are due to renormalisation and factorisation scales and due to PDF choices. Additionally, initial and final state radiation scale uncertainties were assessed for  $t\bar{t}$  and single-top processes as well, treated as uncorrelated between them.

#### 4. Results

In order to estimate the background, a simultaneous binned maximum likelihood function fit is performed using all the nine bin yields, using the MC templates, by employing the SR and the corresponding CRs (1L, 1L1B, and 2L). This is done to simultaneously search for the signal while improving the background prediction in the SR. The scale factors for the individual backgrounds are determined from the fit: The post-fit distributions of  $H_T$ ,  $E_T^{\text{miss}}$ ,  $|\phi_{\text{max}} - \phi_{\text{min}}|$  and  $p_T^{\text{bal}}$  observables are shown in Fig. 4 for the SR. Excellent agreement of data with SM background predictions are seen for all the observables.

Upper limits on the contribution of events from new physics are computed by using the modified frequentist approach  $CL_s$  based on asymptotic formulas at 95% confidence level [31]. The nominal signal cross-sections for each signal mass point can be scaled by  $\lambda^4$  for mediator masses larger than 2.5 TeV, as below that mediator mass it was seen the the twisted  $s$ -channel diagrams contribute non-negligibly.

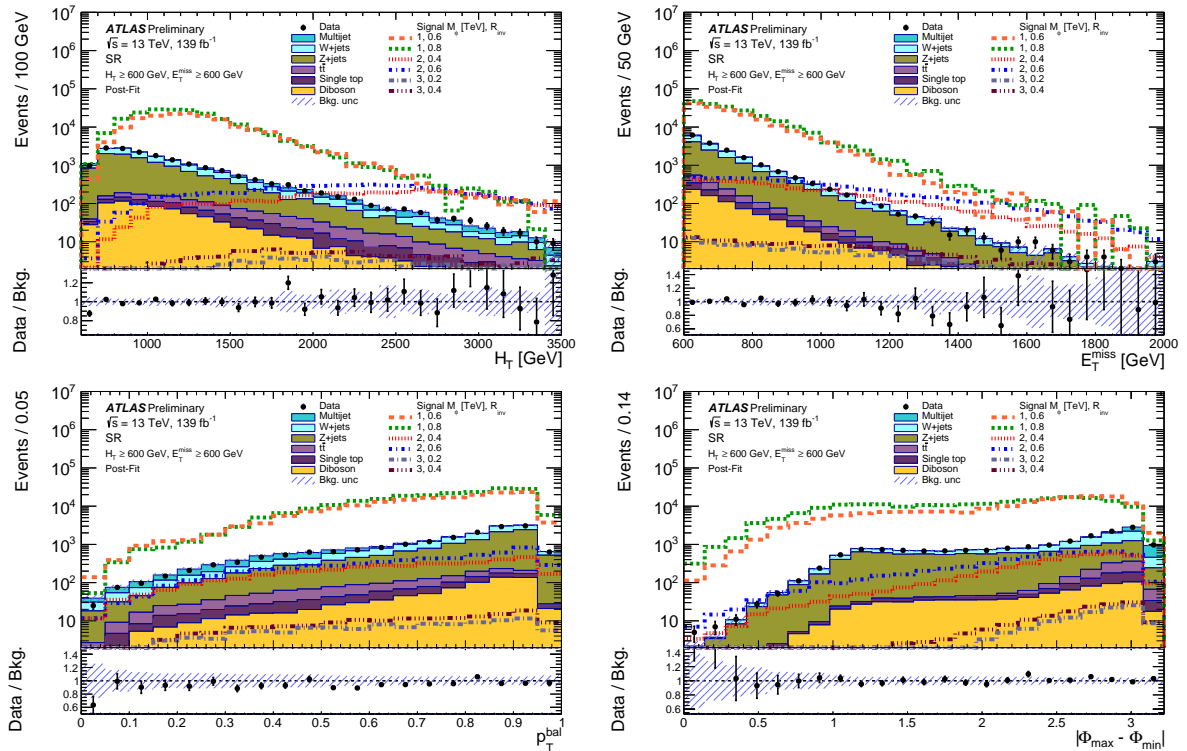


**Figure 4.** The post-fit distributions for  $H_T$  (a),  $E_T^{\text{miss}}$  (b),  $p_T^{\text{bal}}$  (c), and  $|\phi_{\text{max}} - \phi_{\text{min}}|$  (d) are shown for the SR. Data is compared against background predictions, and six signal predictions covering a representative mediator mass and invisible fraction range are overlaid. The uncertainties include all systematic and statistical components. The last bin in (a) and (b) contains the overflow.

For each mediator mass point, the limit on the cross-section is obtained, and the corresponding  $\lambda$  is calculated. This  $\lambda$  value corresponding to the cross-section upper limit is presented for the SR in Fig. 5. It can be seen that for lower mass points, the nominal cross-sections are excluded, whereas for higher mass points only higher values of cross-sections can be excluded. The advantage of this representation is that it sets stringent limits on the signature in general for a wide range of  $\lambda$  values, and can help in recasting this analysis for future model predictions.

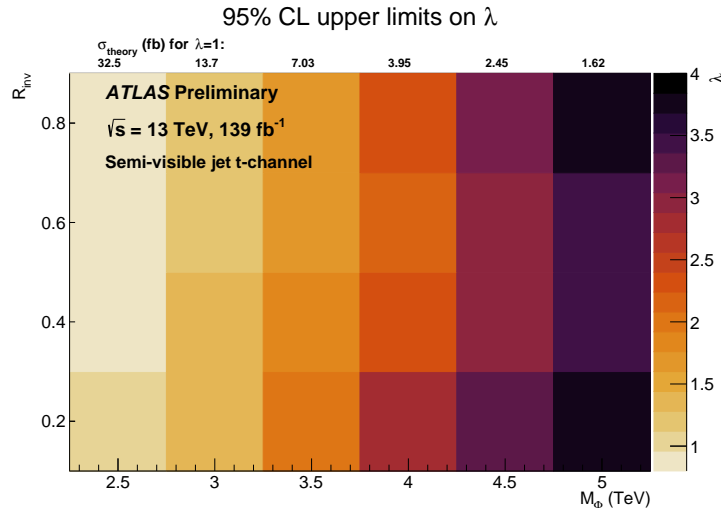


**Figure 5.** The grid shows the observed 95% CL upper limit on  $\lambda$  with  $M_\phi$  on the  $x$ -axis,  $R_{\text{inv}}$  on the  $y$  axis. It also includes over each  $M_\phi$  column the predicted cross-section for that specific mass value as a reference.

## 5. Summary

This article presents the first limits on the SVJ  $t$ -channel production for mediator masses ranging from 1000–5000 GeV, and for  $R_{\text{inv}}$  of 0.2–0.8. The observed yields are in agreement with the SM background expectations. The upper limits at the 95% confidence level on the mediator mass range from 2.4 TeV to 2.7 TeV, depending on the values of the invisible energy fraction. They are translated into upper limits on the coupling strength between the mediator, a Standard Model quark and a dark quark. This is the first result in this topology, but should lead to exploration of other SVJ final states with leptons, or heavy flavours, as well as server a test-bed for machine learning based anomaly detection methods.

## 6. Acknowledgments

SS thanks University of Witwatersrand Research Council for Sellschop grant and NRF for Extension Support Doctoral Scholarship.

## 7. References

- [1] Schwaller P, Stolarski D and Weiler A 2015 *JHEP* **05** 059 (*Preprint* 1502.05409)
- [2] Cohen T, Lisanti M and Lou H K 2015 *Phys. Rev. Lett.* **115** 171804 (*Preprint* 1503.00009)
- [3] Park M and Zhang M 2019 *Phys. Rev. D* **100** 115009 (*Preprint* 1712.09279)
- [4] Bernreuther E, Kahlhoefer F, Krämer M and Tunney P 2020 *JHEP* **01** 162 (*Preprint* 1907.04346)
- [5] Cohen T, Lisanti M, Lou H K and Mishra-Sharma S 2017 *JHEP* **11** 196 (*Preprint* 1707.05326)
- [6] CMS Collaboration 2021 (*Preprint* 2112.11125)

- [7] ATLAS Collaboration 2022 Search for non-resonant production of semi-visible jets using Run 2 data in ATLAS ATLAS-CONF-2022-038 URL <http://cds.cern.ch/record/2815284>
- [8] Alwall J, Frederix R, Frixione S, Hirschi V, Maltoni F, Mattelaer O, Shao H S, Stelzer T, Torrielli P and Zaro M 2014 *JHEP* **07** 079 (*Preprint* 1405.0301)
- [9] Dmsimp model <https://github.com/smsharma/SemivisibleJets> accessed: 2020-11-10
- [10] Ball R D *et al.* (NNPDF) 2015 *JHEP* **04** 040 (*Preprint* 1410.8849)
- [11] Cohen A G, Kaplan D B and Nelson A E 1997 *Phys. Lett. B* **412** 301–308 (*Preprint* hep-ph/9706275)
- [12] Colucci S, Fuks B, Giacchino F, Lopez Honorez L, Tytgat M H G and Vandecasteele J 2018 *Phys. Rev. D* **98** 035002 (*Preprint* 1804.05068)
- [13] Seth M S 2011 *A first study of Hidden Valley models at the LHC* Bachelor thesis Lund Observ. (*Preprint* 1106.2064)
- [14] Sjöstrand T, Ask S, Christiansen J R, Corke R, Desai N, Ilten P, Mrenna S, Prestel S, Rasmussen C O and Skands P Z 2015 *Comput. Phys. Commun.* **191** 159 (*Preprint* 1410.3012)
- [15] ATLAS Collaboration 2014 ATLAS Pythia 8 tunes to 7 TeV data ATL-PHYS-PUB-2014-021 URL <https://cds.cern.ch/record/1966419>
- [16] Mangano M L, Moretti M, Piccinini F and Treccani M 2007 *JHEP* **01** 013 (*Preprint* hep-ph/0611129)
- [17] Nason P 2004 *JHEP* **11** 040 (*Preprint* hep-ph/0409146)
- [18] Frixione S, Nason P and Oleari C 2007 *JHEP* **11** 070 (*Preprint* 0709.2092)
- [19] Alioli S, Nason P, Oleari C and Re E 2010 *JHEP* **06** 043 (*Preprint* 1002.2581)
- [20] Bothmann E *et al.* 2019 *SciPost Phys.* **7** 034 (*Preprint* 1905.09127)
- [21] Schumann S and Krauss F 2008 *JHEP* **03** 038 (*Preprint* 0709.1027)
- [22] ATLAS Collaboration 2010 *Eur. Phys. J. C* **70** 823 (*Preprint* 1005.4568)
- [23] GEANT4 Collaboration, Agostinelli S *et al.* 2003 *Nucl. Instrum. Meth. A* **506** 250
- [24] ATLAS Collaboration 2008 *JINST* **3** S08003
- [25] ATLAS Collaboration 2018 *Eur. Phys. J. C* **78** 903 (*Preprint* 1802.08168)
- [26] ATLAS Collaboration 2020 *JHEP* **08** 080 (*Preprint* 2005.09554)
- [27] Cacciari M, Salam G P and Soyez G 2008 *JHEP* **04** 063 (*Preprint* 0802.1189)
- [28] Cacciari M, Salam G P and Soyez G 2012 *Eur. Phys. J. C* **72** 1896 (*Preprint* 1111.6097)
- [29] ATLAS Collaboration 2017 *Eur. Phys. J. C* **77** 466 (*Preprint* 1703.10485)
- [30] ATLAS Collaboration 2020 *JHEP* **03** 145 (*Preprint* 1910.08447)
- [31] Cowan G, Cranmer K, Gross E and Vitells O 2011 *Eur. Phys. J. C* **71** 1554 (*Preprint* 1007.1727)

# Studying the Production of a Singlet Scalar at Future $e^+e^-$ Colliders with Deep Neural Networks

Anza-Tshilidzi Mulaudzi<sup>a</sup>, Mukesh Kumar<sup>a</sup>, Bruce Mellado<sup>a,b</sup> and Abhaya Kumar Swain<sup>a</sup>

<sup>a</sup>School of Physics and Institute for Collider Particle Physics, University of the Witwatersrand, 1 Jan Smuts Avenue, Johannesburg, 2050, South Africa

<sup>b</sup>iThemba LABS, National Research Foundation, PO Box 722, Somerset West, 7129, South Africa

E-mail: anza-tshilidzi.mulaudzi@cern.ch

**Abstract.** Motivated by the multi-lepton anomalies, a search for narrow resonances with  $S \rightarrow \gamma\gamma, Z\gamma$  in association with light jets,  $b$ -jets, or missing transverse energy was reported by arXiv:2109.02650. In this paper, we search for scalar resonances in the  $e^+e^-$  environment. We consider  $Z\gamma \rightarrow jj, l^+l^-$  and  $S \rightarrow \gamma\gamma$  as the final states and make use of machine learning tools to determine the final state with the most significance. A classification model is developed to distinguish between the signal and background processes through the use of a Deep Neural Network (DNN) which is constructed using a dataset that consists of the energy, the pseudo-rapidity, and the invariant mass of the final state particles. The parameters of the DNN are tuned using a hyperparameter optimisation algorithm so that the convergence of the receiver operating characteristic (ROC) curve is achieved.

## 1. Introduction

The discovery of the Higgs boson [1, 2, 3] at the Large Hadron Collider (LHC), through the ATLAS [4] and CMS [5] experiments, has broadened the field of particle physics. Based on measurements at a mass of 125 GeV for the Higgs, it is seen that it is consistent with Standard Model (SM) predictions which allows us to consider the existence of additional or Higgs-like scalar bosons but be mindful that the mixing with the SM must be adequately small. The multi-lepton anomaly final states at the LHC are observed in refs [6, 7]. They are studied in a two-Higgs doublet model with an additional singlet scalar (2HDM+ $S$ ), where the masses of the  $CP$ -even scalars  $h, S, H$  are to be 125, 150 and 270 GeV, respectively. The presumed dominant decays were  $H \rightarrow Sh, SS$ , which encourages us to search for scalar resonances concerning  $S \rightarrow \gamma\gamma, Z\gamma$  in association with missing transverse energy, light- and  $b$ -jets. The coupling information between the scalar  $S$  and vector boson pairs is established through the observed decays of  $S$  via  $WW, ZZ, Z\gamma$  or  $\gamma\gamma$  channels.

Ref [8], an alternative lepton production mechanism is discussed. The scalar  $S$  may decay as  $S \rightarrow NN$  where  $N$  contains the quantum numbers of the right-handed neutrinos. In this configuration, the 2HDM+ $S$  is extended with right-handed neutrinos and this is used to further explain the anomalous muon  $g - 2$  measurement through the chiral enhancement as discussed in Refs. [9, 10]. Keeping this in mind, we can review a diegesis where the mixing of the scalar with SM is insignificantly small. The couplings of  $S$  to the electroweak gauge bosons are loop

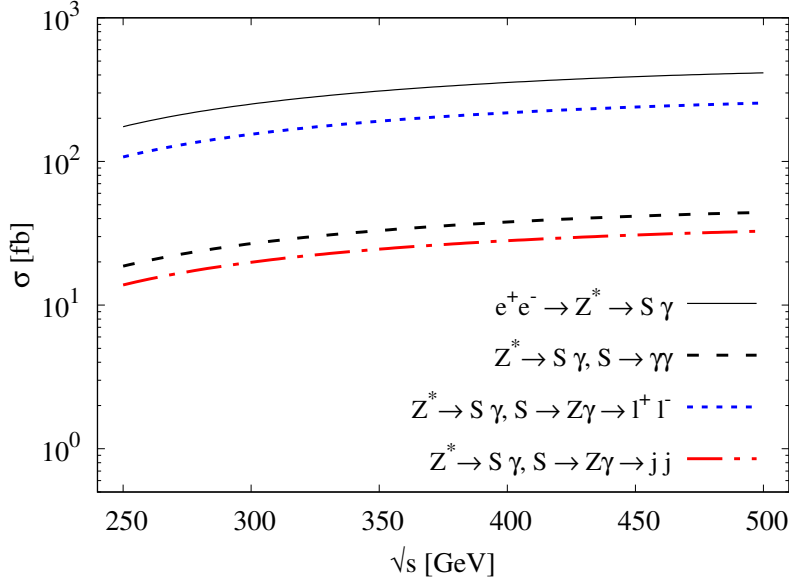


**Figure 1.** The cross-sections for the production of the singlet scalar of a mass  $m_S = 151.5\text{GeV}$  as a function of the centre of mass energy  $\sqrt{s}$  in the  $e^+e^-$  environment. The solid black line represents the production of  $S$  through an off-shell  $Z^*$  gauge boson. The dashed blue, black, and red lines represent the cross-sections for the  $S$  decays where  $S \rightarrow \gamma\gamma$  and  $S \rightarrow Z\gamma, Z \rightarrow jj, l^+l^-$ .

induced, opening up a pathway to the production of  $S$  at future  $e^+e^-$  colliders. Subsequently, it allows an opportunity to study the properties of  $S$  in final states that are strenuous to isolate in pp collisions. In Figure 1, we the cross-sections of the  $S\gamma$  production mechanism. In this proceedings, we aim to show that the cross-section of the singlet scalar is large enough to be detected in future  $e^+e^-$  colliders.

## 2. Model

The electroweak quantum number of  $S$  dictates the coupling of  $S$  with the electroweak gauge bosons  $WW, ZZ, Z\gamma, \gamma\gamma$ . The leading order  $SV_1V_2$  couplings originate from the following two five-dimensional operators [11]:

$$\mathcal{L}_{D5} = \kappa_2 \frac{S}{4m_S} W_{\mu\nu}^a W^{a\mu\nu} + \kappa_1 \frac{S}{4m_S} B_{\mu\nu} B^{\mu\nu}, \quad (1)$$

where  $\kappa_{1,2}$  are the coupling strengths. In terms of mass eigenstates

$$W^\pm = \frac{1}{\sqrt{2}}(W^1 \mp iW^2), \quad (2)$$

and

$$\begin{pmatrix} W^3 \\ B \end{pmatrix} = \begin{pmatrix} c_w & s_w \\ -s_w & c_w \end{pmatrix} \begin{pmatrix} Z \\ A \end{pmatrix}, \quad (3)$$

these operators can be written as,

$$\begin{aligned} \mathcal{L} = & \kappa_2 \frac{S}{2m_S} W_{\mu\nu}^+ W^{-\mu\nu} + (\kappa_2 c_w^2 + \kappa_1 s_w^2) \frac{S}{4m_S} Z_{\mu\nu} Z^{\mu\nu} \\ & + 2c_w s_w \frac{S}{4m_S} (\kappa_2 - \kappa_1) Z_{\mu\nu} F^{\mu\nu} + (\kappa_2 s_w^2 + \kappa_1 c_w^2) \frac{S}{4m_S} F_{\mu\nu} F^{\mu\nu}. \end{aligned} \quad (4)$$

The cosine and sine of the weak mixing angle are  $c_w = g/\sqrt{g^2 + g'^2}$  and  $s_w = g'/\sqrt{g^2 + g'^2}$ , respectively. From Eq. 4 we can write the couplings as:

$$\Gamma_{SV_1V_2}^{\mu\nu} = \frac{g_{SV_1V_2}}{m_S} (p_{V_1} \cdot p_{V_2} g^{\mu\nu} - p_{V_1}^\nu p_{V_2}^\mu), \quad (5)$$

where  $g_{SWW} = \kappa_2$ ,  $g_{SZZ} = (\kappa_2 c_w^2 + \kappa_1 s_w^2)$ ,  $g_{SZ\gamma} = c_w s_w (\kappa_2 - \kappa_1)$ , and  $g_{S\gamma\gamma} = \kappa_2 s_w^2 + \kappa_1 c_w^2$ .

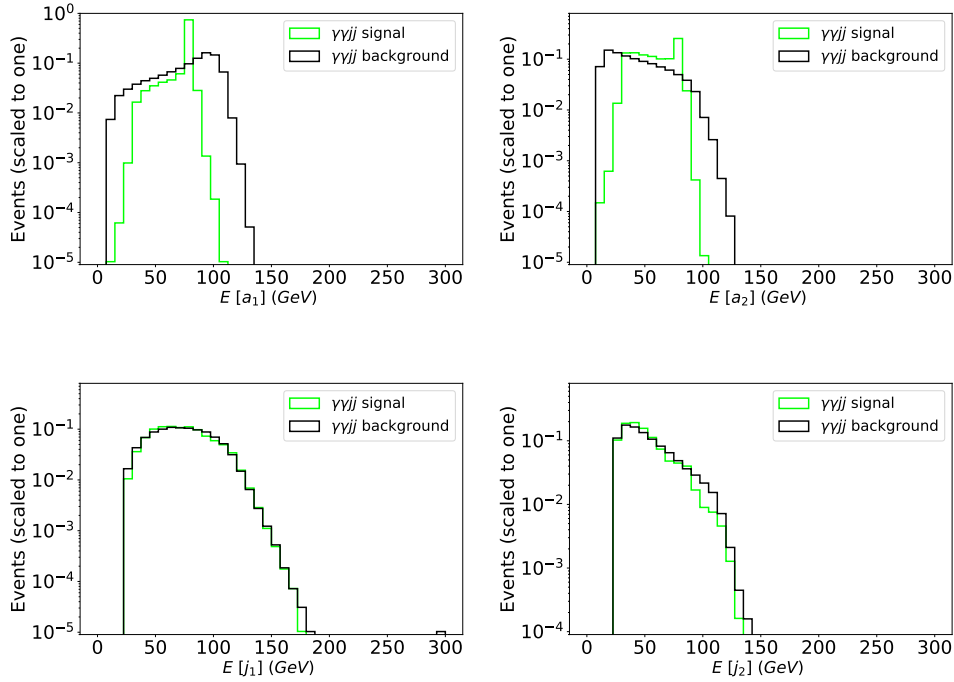


**Figure 2.** Normalised differential distributions for the energies of the di-jet: the leading and sub-leading photon (top row) and jet energy (bottom row).

### 3. Simulation and results

In order to simulate the  $S$  production in association with photon through off-shell  $Z$  boson in  $e^+e^-$  environment, the Lagrangian 4 are implemented in `Feynrules` [12]. Nine hundred thousand background and five hundred thousand signal events are generated using `Madgraph5_aMC@NLO` [13]. Further parton-level events are showered through `Pythia8` [14] to take care of fragmentation and hadronisation. The detector level simulation is performed through `Delphes` [15]. The construction of jets at this level was performed using `Fastjet` [16] which utilizes the anti- $k_T$  jet algorithm with a radius  $R = 0.5$  and  $p_T > 20$  GeV. In this work, the singlet scalar mass is  $m_S = 151.5$  GeV.

The signal process is  $e^+e^- \rightarrow Z^* \rightarrow S\gamma$ , where  $S$  further decays to  $Z\gamma$ ,  $Z \rightarrow jj$  and the background process is  $e^+e^- \rightarrow \gamma\gamma jj$ . The di-jet channel produces the largest cross-section, thus being the dominant final state. The calculations for the production of the SM Higgs boson and other scalars in the context of the Minimal Supersymmetric Model (MSSM) in association with a photon are done in ref. [17, 18, 19]. They show that this process, although it is rare, it produces a clean final state due to suppressed backgrounds. Excesses in the  $Z(\rightarrow \ell^+\ell^-)\gamma$  final state in Ref [8] indicates that the branching ratio of  $S \rightarrow \gamma\gamma$  is significantly lower than that of  $S \rightarrow Z\gamma$ . As such, we choose  $\kappa_W = -0.014$  and  $\kappa_B = 0.028$  ( $\kappa_W/\kappa_B = -0.5$ ) for this study.

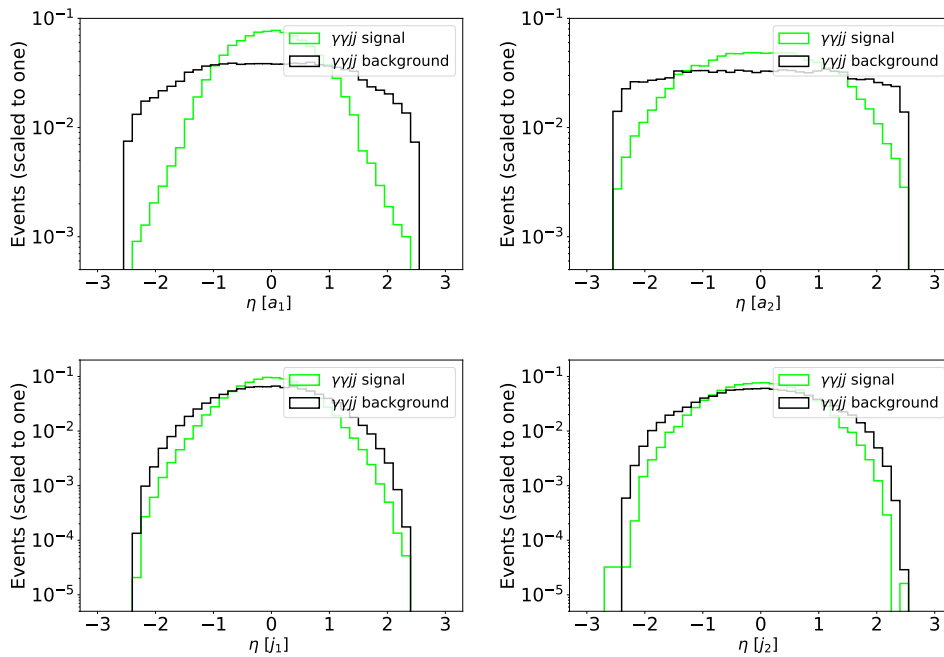


**Figure 3.** Normalised differential distributions for the pseudorapidities of the di-jet: the leading and sub-leading photon (top row) and jets (bottom row).

### 3.1. Optimization of the di-jet channel using ML technique

In machine learning, various tools and systems are used depending on what task one wants to complete. Based on the data from the kinematic distributions (Figures 2, 3), this study makes use of a Sequential Machine Learning model. This model is appropriate for a plain stack of layers where each layer has exactly one input tensor and one output tensor and is essential for developing a Deep Neural Network (DNN). A DNN contains a set of significant parameters that allow us to input and output a series of data sequences. The parameters we use are the number of epochs, neurons, layers, batch size, and the learning rate. Each has a definite contribution to how well the DNN model performs. The DNN is used to train our sequential model and test how it efficiently discriminates the events from signal and background processes.

In these proceedings, we show the results for the di-jet channel. The energy, pseudorapidity, and invariant mass of the final state particles are the input variables for the DNN dataset. After cleaning the dataset, only 592 965 signal and background (combined) samples are present. We split the dataset into 70% training and 30% testing data. The DNN consists of 11 layers, each with 32 neurons. We set the batch size to 32, with the number of epochs being 280. The model learns at a rate of 0.000768. The optimizer of choice was Adamax. The ROC curve in Fig 4 shows an accuracy of 97.6%. Although the model accuracy is good, it contains fluctuations in the plateau for the validation accuracy curve. This could be caused by a low batch size which would be the prime suspect in fluctuations because the accuracy would normally depend on what examples the model sees at each batch. However, that should affect both the training and validation accuracies. Another parameter that usually affects fluctuations is a high learning rate. The weights change much in each epoch, resulting in the model changing its prediction on many examples. Normally this should affect both training and validation sets.

The receiver operating characteristic (ROC) curve depicts the 1:1 ratio of background rejection to signal efficiency. The DNN outputs for the training and testing samples illustrate a distinct separation of the signal and background events. To ensure that our model converges, we

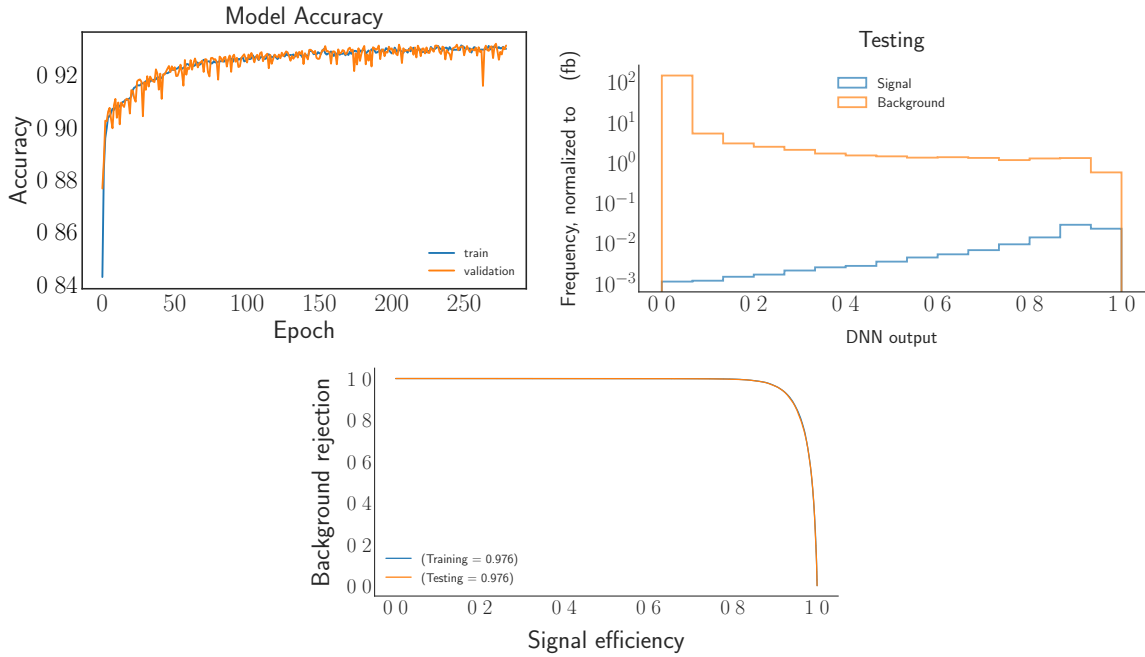


**Figure 4.** The accuracy (left), DNN output (right) and ROC curve (bottom) of the DNN model, are depicted. An accuracy of 97.6% is achieved with the test sample.

develop a hyperparameter optimisation algorithm to tune the parameters of our DNN model. The hyperparameter algorithm has the same structure as the DNN, but we set a range of values for the parameters so that each run takes place with random set parameter values. We can monitor each hyperparameter run using Weights & Biases (Wandb), a Python package that allows us to monitor our training in real-time. It outputs model accuracy and loss plots (figure 5) in real-time and allows us to compare multiple runs in the same project using a Parallel Coordinate Chart (figure 5). It represents the model's performance, in terms of minimum loss or maximum accuracy, with the neural network's hyperparameters.

In our analysis, we also perform cut-flow analysis, to improve the signal significance. The table 1 shows that the significance increases after applying cuts, compared to when there are no cuts.

Cuts	Signal ( $S$ )	Background ( $B$ )	$S$ vs $B$
Initial (no cut)	107	155914	0.272
Energy (leading photon)	$63.6 \pm 5.1$	$20282 \pm 132$	$0.446909 \pm 0.000251$
Energy (sub-leading photon)	$9.2 \pm 2.9$	$918.2 \pm 30.2$	$0.30462 \pm 0.00312$
$\eta$ (leading photon)	$8.40 \pm 2.78$	$667.1 \pm 25.8$	$0.3253 \pm 0.0041$
$\eta$ (sub-leading photon)	$7.9 \pm 2.7$	$519.2 \pm 22.7$	$0.34617 \pm 0.00509$
Invariant mass $\gamma_1\gamma_2$	$7.9 \pm 2.7$	$518.2 \pm 22.7$	$0.3465 \pm 0.0051$

**Table 1.** Table of the background and signal cross-sections for the di-photon, di-jet and di-lepton channels.

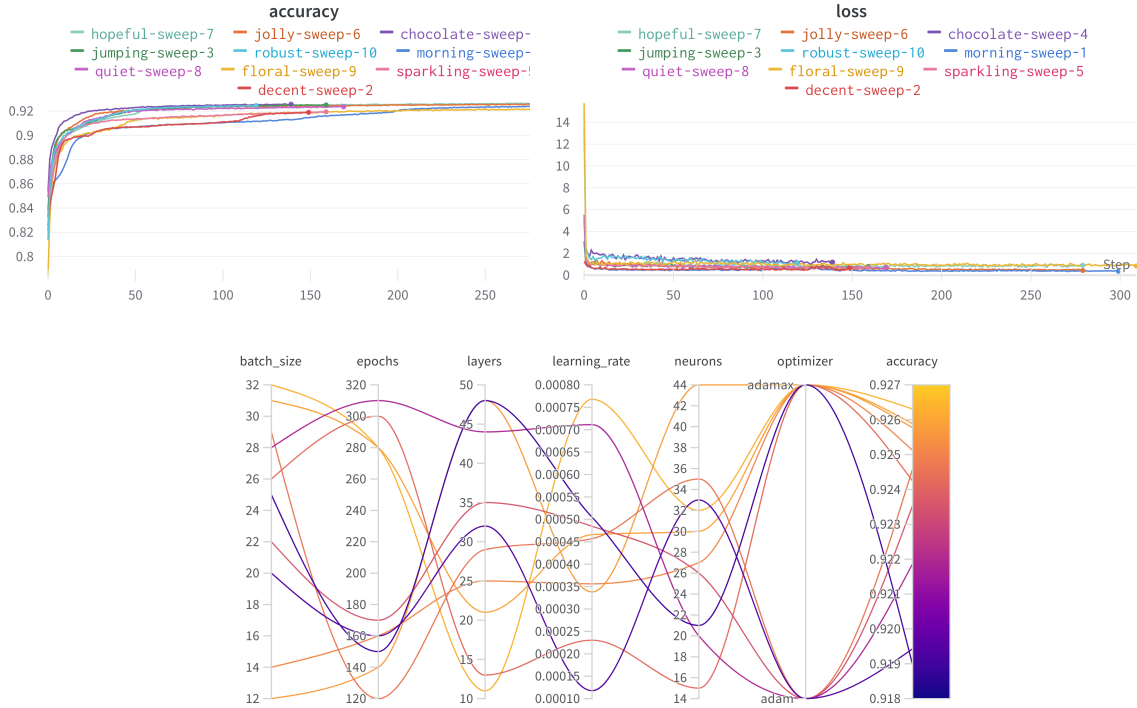


**Figure 5.** This is one of the multiple Wandb sweeps model accuracy (top) and loss(centre) plots are outputted using Wandb. Multiple runs are represented by Parallel Coordinate Chart (bottom).

#### 4. Summary and outlook

In this proceedings, we reported a search strategy of a singlet scalar mass  $m_S = 151.5$  GeV that couples to SM gauge bosons through dimension five operators in  $e^+e^-$  colliders. We consider the associate production of  $S$  with a photon via an off-shell  $Z^*$  where  $S \rightarrow Z\gamma, \gamma\gamma$ . Further, we reported an accuracy of 97.6% for the discrimination of signal and background events for the three-photon channel and a subsequent significance of 0.44 from our analysis. This work is in progress where we will also consider two other  $S$  decay channels, where  $S \rightarrow Z\gamma, l^+l^-$ . We will compare the optimisation of signal over potential backgrounds using conventional and ML techniques and also study the limits on couplings and the potential of future  $e^+e^-$  colliders at different centre-of-mass energies to discover the singlet scalar  $S$ .

#### References

- [1] Englert F and Brout R 1964 *Physical review letters* **13** 321
- [2] Guralnik G S, Hagen C R and Kibble T W 1964 *Physical Review Letters* **13** 585
- [3] Higgs P W 1964 *Phys. Lett.* **12** 132–133
- [4] Aad G, Abajyan T, Abbott B, Abdallah J, Khalek S A, Aben R, Abi B, Abolins M, AbouZeid O, Abramowicz H *et al.* 2013 *Physics Letters B* **726** 120–144
- [5] Chatrchyan S, Khachatryan V, Sirunyan A M, Tumasyan A, Adam W, Aguilo E, Bergauer T, Dragicevic M, Erö J, Fabjan C *et al.* 2013 *Physical Review Letters* **110** 081803
- [6] Von Buddenbrock S, Cornell A S, Mohammed A F, Kumar M, Mellado B and Ruan X 2018 *Journal of Physics G: Nuclear and Particle Physics* **45** 115003
- [7] von Buddenbrock S, Chakrabarty N, Cornell A S, Kar D, Kumar M, Mandal T, Mellado B, Mukhopadhyaya B, Reed R G and Ruan X 2016 *The European Physical Journal C* **76** 1–18

- [8] Crivellin A, Fang Y, Fischer O, Kumar A, Kumar M, Malwa E, Mellado B, Rapheeha N, Ruan X and Sha Q 2021 *arXiv preprint arXiv:2109.02650*
- [9] Crivellin A, Hoferichter M and Schmidt-Wellenburg P 2018 *Physical Review D* **98** 113002
- [10] Chun E J and Mondal T 2020 *Journal of High Energy Physics* **2020** 1–20
- [11] Low I and Lykken J 2010 *Journal of High Energy Physics* **2010** 1–20
- [12] Alloul A, Christensen N D, Degrande C, Duhr C and Fuks B 2014 *Computer Physics Communications* **185** 2250–2300
- [13] Alwall J, Frederix R, Frixione S, Hirschi V, Maltoni F, Mattelaer O, Shao H S, Stelzer T, Torrielli P and Zaro M 2014 *Journal of High Energy Physics* **2014** 1–157
- [14] Sjöstrand T, Mrenna S and Skands P 2008 *Computer Physics Communications* **178** 852–867
- [15] De Favereau J, Delaere C, Demin P, Giammanco A, Lemaitre V, Mertens A and Selvaggi M 2014 *Journal of High Energy Physics* **2014** 1–26
- [16] Cacciari M, Salam G P and Soyez G 2012 *The European Physical Journal C* **72** 1–54
- [17] Barroso A, Pulido J and Romao J 1986 *Nuclear Physics B* **267** 509–530
- [18] Abbasabadi A, Bowser-Chao D, Dicus D A and Repko W W 1995 *Physical Review D* **52** 3919
- [19] Djouadi A, Driesen V, Hollik W and Rosiek J 1997 *Nuclear Physics B* **491** 68–102

# Evaluation and Optimisation of a Generative-Classification Hybrid Variational Autoencoder in the Search for Resonances at the LHC

Finn Stevenson<sup>1</sup>, Benjamin Lieberman<sup>1</sup>, Abhaya Swain<sup>1</sup>, Bruce Mellado<sup>1,2</sup>

<sup>1</sup>School of Physics and Institute for Collider Particle Physics, University of the Witwatersrand, Johannesburg, Wits 2050, South Africa

<sup>2</sup>iThemba LABS, National Research Foundation, PO Box 722, Somerset West 7129, South Africa

E-mail: [finn.david.stevenson@cern.ch](mailto:finn.david.stevenson@cern.ch)

**Abstract.** This proceedings depicts the optimisation and evaluation of a Variational Auto-encoder plus Discriminator model used for  $Z\gamma$  background final state event generation. This work has been completed to evaluate the use of deep learning models instead of traditional computationally expensive Monte Carlo physics event production mechanisms and classification mechanisms.

## 1 Introduction

This proceedings documents the secondary phase, evaluation and optimisation, of the development of a deep generative neural network model for production of  $Z\gamma$  final state data for physics analysis. The discovery of the Higgs boson in 2012 [1, 2] completed the Standard Model (SM) of particle physics. There are still phenomena and anomalies to the SM seen in the data that prompt searches for new bosons. The work described in this paper fits into the bigger picture of searching for new bosons as this work can affect the efficiency and accuracy of the search within the  $Z\gamma$  final state [3, 4]. A main limiting factor related to completing the aforementioned search is the requirement of a large quantity of  $Z\gamma$  final state background events. Traditionally in similar searches, the requirement of copious amounts of data is satisfied through the use of computationally expensive Monte Carlo (MC) production mechanisms. Using pre-trained deep learning models to produce data instead can help alleviate some of the finite CPU resources used in the analysis and reduce the overall time taken for analyses. Furthermore, the aforementioned data generation models can also be used for event classification purposes. Variational Auto-encoders (VAEs) are a type of deep learning model that can somewhat uniquely be used as both a data generation and event classification model, using the same trained model. This bi-functionality again adds to the efficiency and time improvement. The aim of this work is to evaluate the use of deep generative models, specifically variational auto-encoders and derivatives for both data generation and signal classification tasks in the search for new

bosons. This proceedings specifically concentrates on the evaluation and optimisation of the VAE based generative capacity of the model, further work will be completed to evaluate the classification capability.

### 1.1 MC $Z\gamma$ Final State Data

In this work, simulated  $Z\gamma$  background data has been used, which contributes to 90% of the total backgrounds in the production of the Higgs like heavy scalar decaying to  $Z\gamma$  ( $pp \rightarrow H \rightarrow Z\gamma$ ) events, where  $Z \rightarrow e^+e^-$  or  $Z \rightarrow \mu^+\mu^-$ . The  $Z\gamma$  MC events were generated using **Madgraph5** [5] with the **NNPDF3.0** parton distribution functions [6]. Here, the Standard Model (SM) of particle physics has been utilized for which the UFO model files required by the Madgraph are from **FeynRules** [7]. The parton level generation is followed by the parton showering and hadronization by **Pythia** [8] and then the detector level simulation is performed using **Delphes(v3)** [9]. The jets at this level has been constructed using **Fastjet** [10] which involves the anti- $K_T$  jet algorithm with  $P_T > 20$  GeV and radius  $R = 0.5$ . While generating the sample, the  $Z\gamma$  boson was decayed to leptons. Some baseline cuts have also been applied on the leptons and photons at the Madgraph level to enhance the statistics.

### 1.2 Centre of Mass and Kinematic Features

The analysis focuses on the centre of mass of 150GeV ( $132\text{GeV} < m_{\ell\ell\gamma} < 168\text{GeV}$ ). The kinematic features used in the study are  $Z\gamma$  invariant mass,  $m_{\ell\ell\gamma}$ ; the transverse momentum, azimuthal angle, pseudo-rapidity and energy of the leading lepton, sub-leading lepton and photon respectively,  $P_{t_{\ell_1\ell_2\gamma}}$ ,  $\Phi_{\ell_1\ell_2\gamma}$ ,  $\eta_{\ell_1\ell_2\gamma}$  and  $E_{\ell_1\ell_2\gamma}$ ; missing transverse energy  $E_T^{miss}$  and the azimuthal angle,  $\Phi_{E_T^{miss}}$ ; the number of jets,  $N_j$ , the number of central jets,  $N_{cj}$ ; and  $\Delta R_{\ell\ell}$  ( $\Delta R \equiv \sqrt{(\Delta\eta)^2 + (\Delta\phi)^2}$ ),  $P_{t_{\ell\ell}}/m_{\ell\ell\gamma}$ ,  $\Delta\Phi_{\ell\ell}$  and  $\Delta\Phi(E_T^{miss}, Z\gamma)$ .

## 2 Hypothesis

A well trained Variational Auto-encoder can aid in the search for new bosons in the  $Z\gamma$  final state for both data generation and signal classification purposes. The work presented in this proceedings has a more specific hypothesis as follows: The addition of a discriminator network to the overall VAE model as well as a notion of adversarial training similar to that of a Generative Adversarial Network can aid in the training of the model and produce better generated events.

## 3 Methodology

Previous proceedings works have described the initial development of the base VAE model and therefore the base model will only be briefly described here. Concentration will be on the addition of the discriminator network to the VAE overall model that aids in the training of the overall model to produce better generated events in terms of a number of selected metrics.

### 3.1 Variational Auto-encoder

A VAE is an modified version of a classic autoencoder (AE). Architectural changes and an additional component added to the loss function facilitate regularised training and improves the generative capability of the model by ensuring appropriate latent space properties. As shown in Figure 1, the VAE architecture is composed of two main composite networks, the encoder, and the decoder. The VAE is trained to minimise the loss between the input data (kinematic variable event) and the encoded-decoded output (reconstructed event). However, in the case of the VAE, instead of encoding an input event as a single vector, the input is encoded as a distribution over the latent space of the VAE. This allows for some regularisation of the latent space.

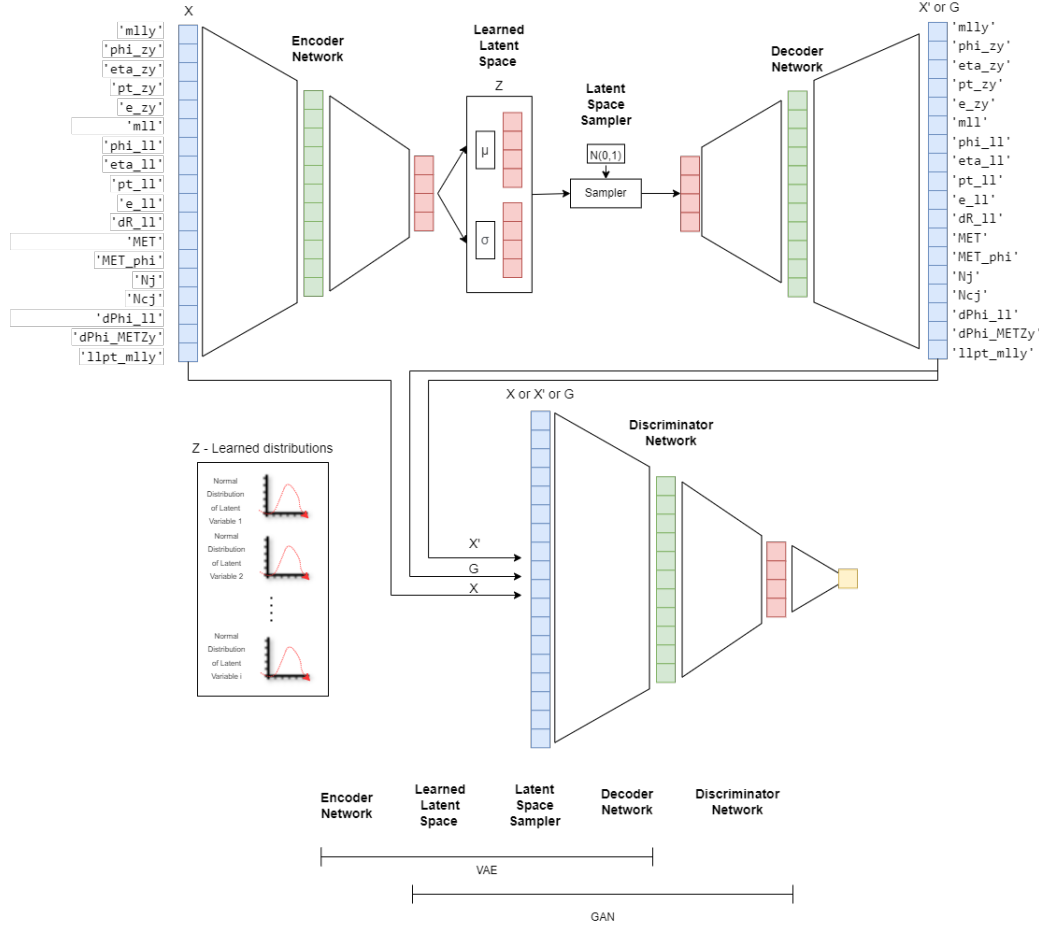


**Figure 1.** Diagram of VAE Base and greater VAE+D model Architecture, showing encoder network, decoder network, learned latent space and discriminator network.

These latent space distributions are forced to be normal Gaussian so that the encoder can be configured to return latent space vectors that represent the mean  $\mu$  and the covariance  $\sigma$  of the normal Gaussian distributions because the Kullback-Leibler divergence between two the Gaussian distributions has a form that can be directly expressed in terms of the means and the covariance matrices of the two distributions. As a result of encoding an input event to a distribution rather than a single vector, it is possible to regularise the latent space. The loss function that is minimised when training a VAE is composed of a reconstruction loss component that is responsible for forcing the output of the decoder to be as close to the input, and secondly, a regularisation loss component, that serves to regularise the organisation of the latent space by making the distributions returned by the encoder close to a standard normal distribution. The loss function also contains a coefficient for the KL-Divergence loss term,  $\beta_V$ . This can be used during optimisation to weigh the importance of the KL-Divergence loss term against that of the reconstruction loss term.

$$L_{VAE} = L_R + \beta_V * L_{KL} \quad (1)$$

$$L_R = \overline{((X' - X)^2)} \quad (2)$$

Where  $X$  is the input event and  $X'$  is the reconstructed event.

$$L_{KL} = \sum (\sigma^2 + \mu^2 - \log \sigma - 1) \quad (3)$$

### 3.2 Variational Auto-encoder + Discriminator (VAE+D)

The addition of a discriminator and the notion of adversarial training network helps in the training of the VAE encoder-decoder network. Figure 1 shows the architecture diagram of the VAE+D model. The VAE+D loss functions seen below are slightly different to the VAE, whilst still including the main loss components of the original VAE. Unlike the VAE, the VAE+D has a loss function for each individual network, the encoder, decoder and discriminator and each network's weights are updated individually at different times during a forward pass of the overall VAE+D. Similar to a GAN, the discriminator and the VAE are trained simultaneously, with the discriminator learning to distinguish fake events from real events and the VAE learning to reproduce real events accurately. The VAE+D loss functions and components are as follows:

$$L_{disc} = BCE_{real} + BCE_{recon} + BCE_{gen} \quad (4)$$

$$L_{dec} = \gamma * Loss_R - Loss_{disc} \quad (5)$$

$$L_{enc} = Loss_{KL} + \gamma * Loss_R \quad (6)$$

Where  $criteria_{BCE}$  is the binary cross entropy between either the actual data against actual data, reconstructed data or generated data. The final discriminator loss function,  $L_{disc}$  is obtained as the sum of the three  $BCE$  based losses.  $\gamma$  is a coefficient of the reconstruction loss, similar to the variational beta parameter in the VAE.

## 4 Model Optimisation

VAEs have many hyper-parameters that can be optimised in order to achieve the best model. This hyper-parameter optimisation can be done using a variety of methodologies and available libraries, however in this work a manual optimisation loop was created. The optimisation loop was created to loop through each of the parameters shown in Table 1, on each iteration building, training and evaluating a model with the loop iteration parameters. There have also been some other considerations taken into account in the code involving looping through the architectural based parameters because of the fact some architectural parameters are constrained by others in order to achieve a plausible architecture.

**Table 1.** Table showing VAE Selected Hyper-parameters and value options

Hyper-parameter	Model	Value Options	Brief Description
Learning Rate	VAE, VAE+D	[0.01, 0.001, 0.0001]	Standard machine learning hyper-parameter that determines how drastically the model changes its weights each iteration in attempt to minimise the loss function and achieve convergence.
Batch Size	VAE, VAE+D	[1, 16, 64, 256, 512]	The batch size refers to the number of training examples used in one training iteration of the model.
Latent Dimension Size	VAE, VAE+D	[8, 16, 32, 64]	Number of latent dimensions variables.
Number of Hidden Layers	VAE, VAE+D	[1, 2, 3]	Number of hidden layers in between input and latent layers.
Number of Nodes in the Hidden Layers	VAE, VAE+D	[16, 32, 64, 128, 256, 512]	Number of nodes in the hidden layers
Variational Beta	VAE, VAE+D	[1, 10, 100, 500, 1000, 5000]	Coefficient of the KL-Divergence loss term in loss function.

After running of the aforementioned hyper-parameter optimisation loop, the best parameters were found for both the VAE and the VAE+D models.

### 5 Results

The Results of the addition of the discriminator network to the VAE can be seen in the figures below. It can be seen that the optimised VAE+D model is a better generative model for the chosen  $Z\gamma$  data.

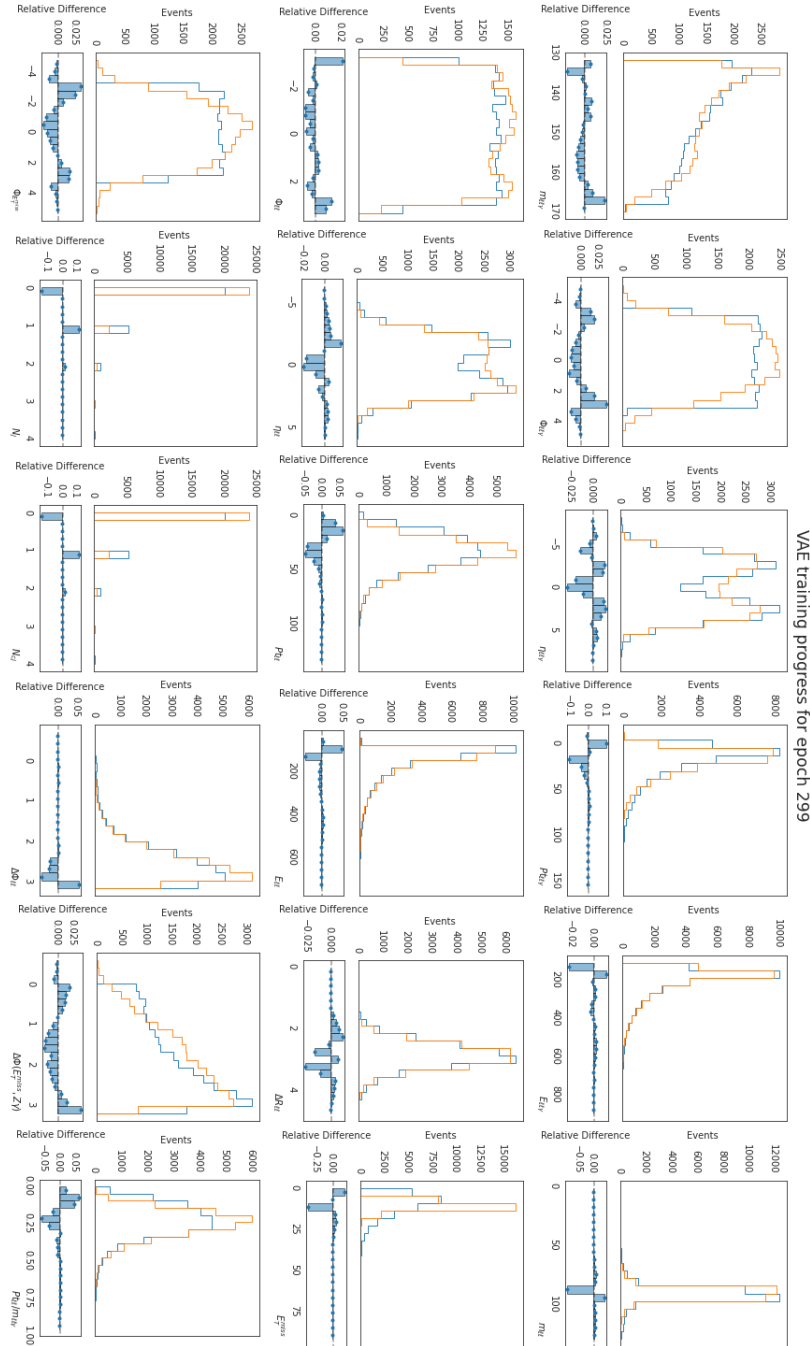


Figure 2. Distribution Graph of Generated Event Features vs. MC Data for VAE Model.

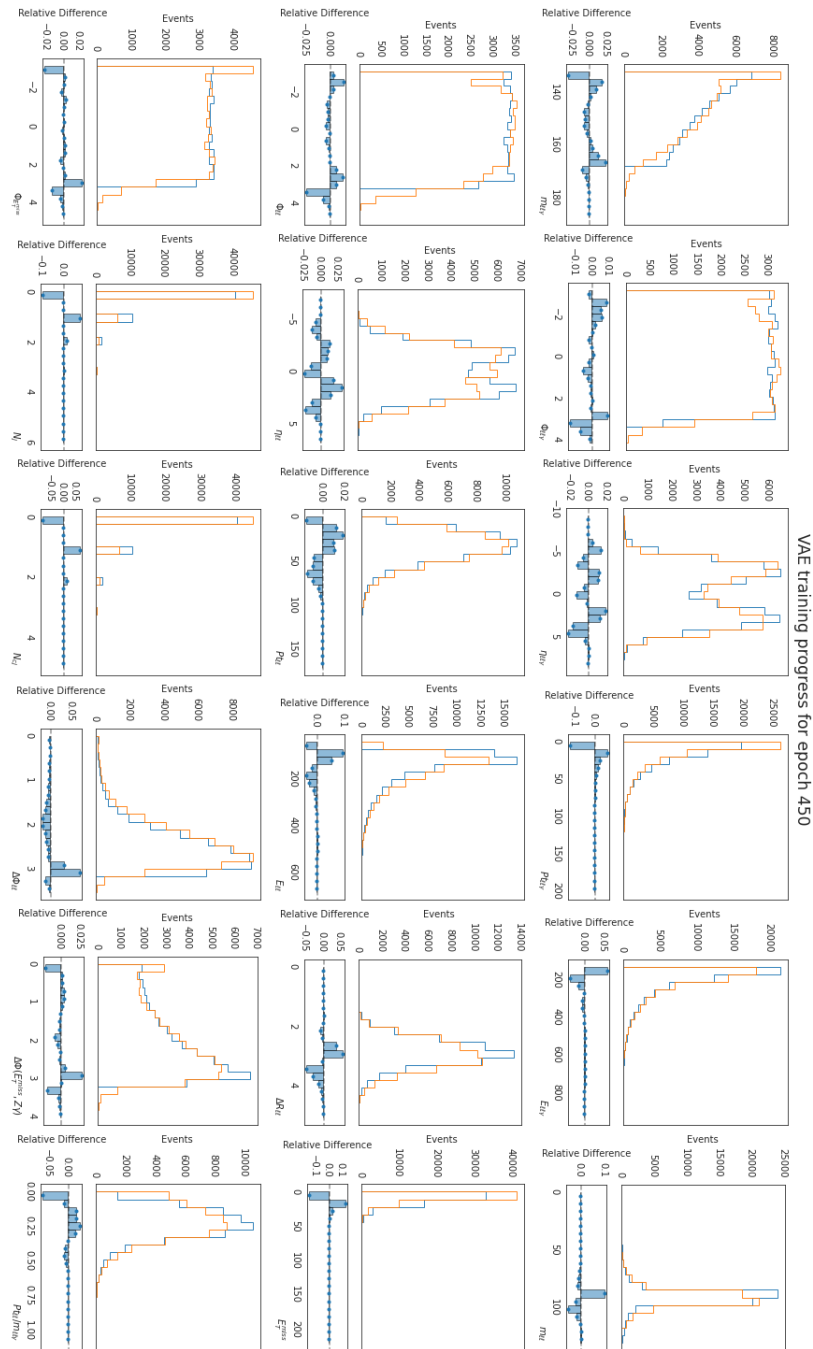
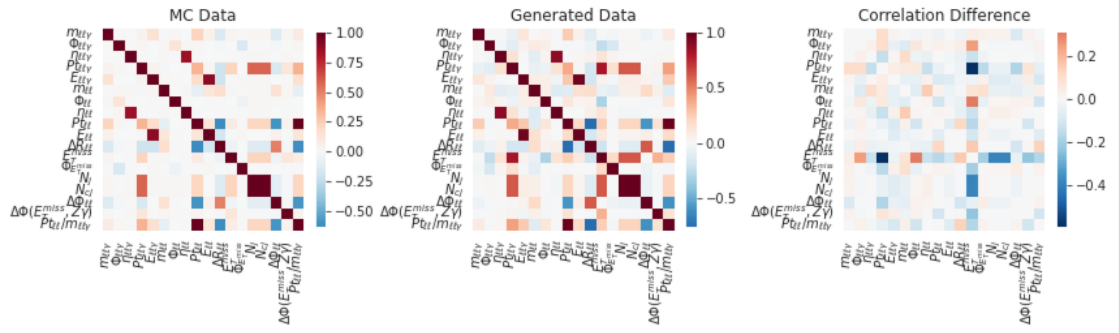
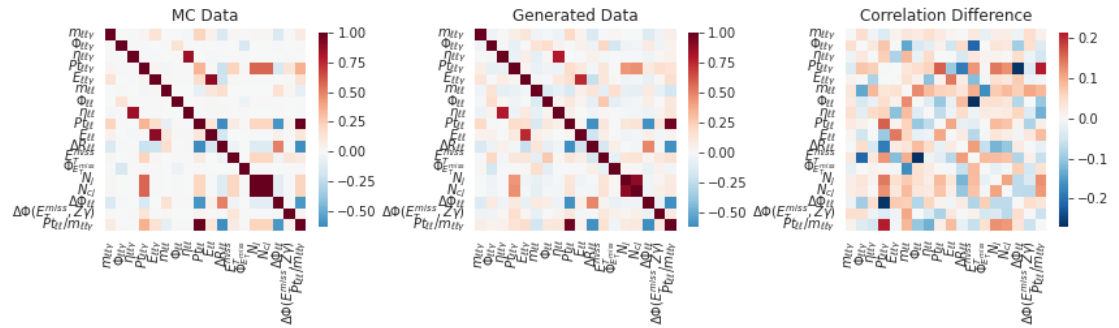


Figure 3. Distribution Graph of Generated Event Features vs. MC Data for VAE+D Model.



**Figure 4.** Correlation Comparison of Generated Event Features vs. MC Data for VAE Model.



**Figure 5.** Correlation Comparison of Generated Event Features vs. MC Data for VAE+D Model.

## 6 Conclusion and Further Work

The addition of the discriminator network to the VAE model has improved the generation results with limited initial optimisation. With further adjustments and hyper-parameter optimisation, the results could achieve better convergence than shown in the results section. A further adjustment that may yield significant improvements is the addition of normalising flows to the VAE model. The addition of normalising flows to the model will allow for more complicated probability distributions to be retained in the latent space, instead of simply forcing the latent space distributions to be normal Gaussian.

## References

- [1] Aad G *et al.* (ATLAS) 2012 *Phys. Lett. B* **716** 1–29 (*Preprint* 1207.7214)
- [2] Chatrchyan S *et al.* (CMS) 2012 *Phys. Lett. B* **716** 30–61 (*Preprint* 1207.7235)
- [3] von Buddenbrock S, Chakrabarty N, Cornell A S, Kar D, Kumar M, Mandal T, Mellado B, Mukhopadhyaya B and Reed R G 2015 (*Preprint* 1506.00612)
- [4] von Buddenbrock S, Chakrabarty N, Cornell A S, Kar D, Kumar M, Mandal T, Mellado B, Mukhopadhyaya B, Reed R G and Ruan X 2016 *Eur. Phys. J. C* **76** 580 (*Preprint* 1606.01674)
- [5] Allwell J, Frederix R, Frixione S, Hirschi V, Maltoni F, Mattelaer O, Shao H S, Stelzer T, Torrielli P and Zaro M 2014 *JHEP* **07** 079 (*Preprint* 1405.0301)
- [6] Ball R D *et al.* (NNPDF) 2015 *JHEP* **04** 040 (*Preprint* 1410.8849)
- [7] Alloul A, Christensen N D, Degrande C, Duhr C and Fuks B 2014 *Comput. Phys. Commun.* **185** 2250–2300 (*Preprint* 1310.1921)
- [8] Sjostrand T, Mrenna S and Skands P Z 2006 *JHEP* **05** 026 (*Preprint* hep-ph/0603175)
- [9] de Favereau J, Delaere C, Demin P, Giammanco A, Lemaître V, Mertens A and Selvaggi M (DELPHES 3) 2014 *JHEP* **02** 057 (*Preprint* 1307.6346)
- [10] Cacciari M, Salam G P and Soyez G 2012 *Eur. Phys. J. C* **72** 1896 (*Preprint* 1111.6097)

# Time stability of the response of gap and crack scintillators of the Tile Calorimeter of the ATLAS detector to isolated muons from $W \rightarrow \mu\nu_\mu$ events

Ntsoko Phuti Rapheeha<sup>1</sup>, Bruce Mellado<sup>1,2</sup>

<sup>1</sup> School of Physics and Institute for Collider Particle Physics, University of the Witwatersrand, Johannesburg, Wits 2050, South Africa

<sup>2</sup> iThemba LABS, National Research Foundation, PO Box 722, Somerset West 7129, South Africa

E-mail: ntsoko.phuti.rapheeha@cern.ch

**Abstract.** The Tile Calorimeter of the ATLAS experiment at the Large Hadron Collider is a hadronic sampling calorimeter that is designed for the reconstruction of hadrons, jets, tau-particles and missing transverse energy. In this study, the response of the gap and crack scintillators of Tile calorimeter is measured using isolated muons from  $W \rightarrow \mu\nu_\mu$  events. The response of the scintillating cells is quantified by measuring the amount of energy deposited per unit length in both data and Monte Carlo simulations to evaluate the stability of the response over time to quantify how well the calibration compensates for time-dependent effects of the calorimeter.

## 1. Introduction

This study aims to determine the time stability of the response of gap and crack scintillators of the response of gap and crack scintillators of the Tile Calorimeter (TileCal) [1] of the ATLAS detector [2] to isolated muons originating from the decay of the  $W$  boson to a muon and a muon neutrino  $W \rightarrow \mu\nu_\mu$ . The response of a cell is quantified as the amount of energy ( $\Delta E$ ) deposited per unit length ( $\Delta x$ ) in that particular cell. The energy loss of muons as they transverse through matter is a well understood process [3]. Ionisation is the dominant energy loss in muons with energies below 100 GeV and the probability distribution of the response follows the Landau function for thin scintillators. The  $W \rightarrow \mu\nu_\mu$  events used in this study are produced during proton-proton ( $pp$ ) collisions at the Large Hadron Collider (LHC) [4].

Muons originating from the  $W \rightarrow \mu\nu_\mu$  processes, as shown in Figure 1, are chosen for their relatively clean experimental signature in the detector. Contribution of muons originating from background processes can be suppressed with relative ease. The electroweak background in the  $W \rightarrow \mu\nu_\mu$  channel is dominated by  $W \rightarrow \tau\nu_\tau$  and  $Z/\gamma^* \rightarrow \mu^+\mu^-$  processes. Background events from the  $Z/\gamma^* \rightarrow \mu^+\mu^-$  process are suppressed by requiring that the selected events have exactly one muon candidate. The leptonic decay of the  $\tau$ -lepton into muon and a  $\tau$  neutrino is a multi-body decay process, resulting in a displaced  $\tau$  decay vertex and on average a muon with a low transverse momentum,  $p_T$  [5, 6]. The  $p_T$  of the selected muon candidates and the position of the primary vertex is used to reject background events. In events where heavy quarks have semi-leptonic decays, hadrons may be misidentified as leptons. These multi-jet background

processes are the ones that contribute significantly to the total background, the presence of missing transverse energy ( $E_T^{\text{miss}}$ ) is used to suppress these Quantum Chromodynamics multi-jet backgrounds.  $E_T^{\text{miss}}$

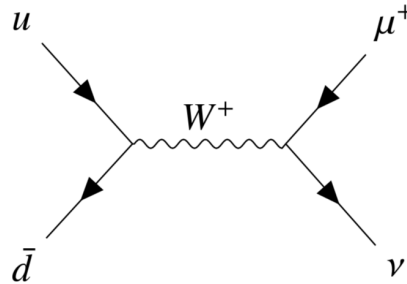


**Figure 1.** Feynman diagram of the leptonic decay of a  $W^+$  boson produced in  $pp$  collisions. The diagram for the decay of  $W^-$  boson is identical, with the only difference being the electric charge.

The study is performed using muons produced during  $pp$  collision observed by the ATLAS detector during the Run 2 data taking period (2015-2018) at a centre-of-mass energy of  $\sqrt{s} = 13$  TeV with  $139 \text{ fb}^{-1}$  integrated luminosity.

## 2. The ATLAS Tile Calorimeter

The ATLAS experiment at the LHC is one of the two general-purpose detectors designed to reconstruct events from  $pp$  or heavy ion collisions. The hadronic calorimeter system of the ATLAS detector is formed by the Tile Calorimeter, which plays a major role in the reconstruction of hadrons, jets,  $\tau$ -leptons and  $E_T^{\text{miss}}$ . It is made up of the fixed long barrel (LB) located at the central area of the collision point  $|\eta| < 1.0$  and two extended barrels (EB) at the forward and backward region  $0.8 < |\eta| < 1.7$ . Figure 2 shows the schematic layout and the scintillator structure of the TileCal cell assembly on the A-side of the detector, a side with positive  $\eta$ .

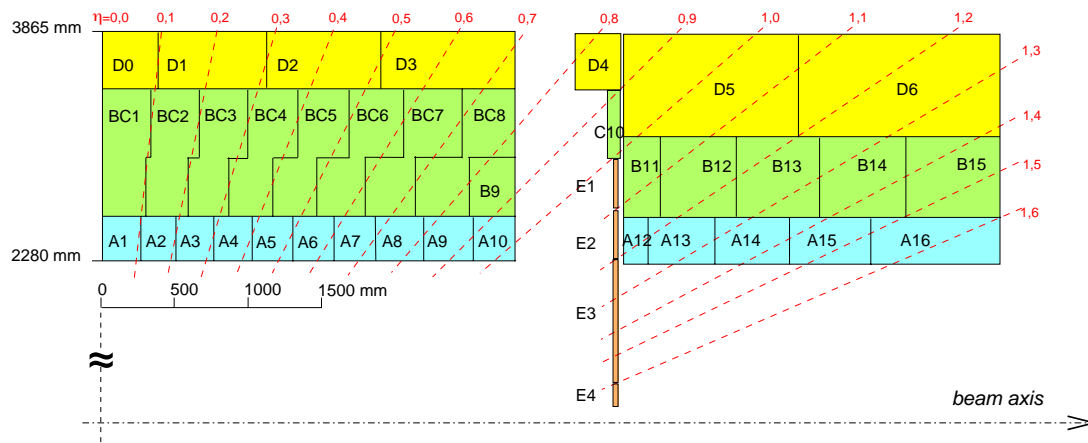


**Figure 2.** Schematic of the TileCal cell layout in a plane parallel to the beam axis [7] and scintillator structure on the A-side of the detector (positive  $\eta$ ). The gap and crack scintillators are shown in orange.

The full azimuthal ( $\phi$ ) coverage around the beam axis is achieved using 64 wedge-shaped modules, a schematic of such module of the TileCal is shown in Figure 3. Each module is made out of alternating layers of steel and scintillating tiles which act as absorber and active material, respectively. It is only gap and crack modules that lack layers of steel. The light generated in the scintillating tiles is collected at the edges, and transported to photomultiplier tubes (PMTs) by wavelength shifting fibres [8].

The region between  $0.8 < |\eta| < 1.6$  is covered by the Intermediate Tile Calorimeter (ITC). The ITC is a plug detector designed to fill the gap between the central and extended barrel calorimeters with the aim of correcting for the energy lost in the passive material that fills the gap region. The region  $0.8 < |\eta| < 1.0$  of the ITC is called the plug. It is made of 311 mm thick steel-scintillator stacks (D4) in the region  $0.8 < |\eta| < 0.9$  which are similar in design to the regular TileCal submodules. The region between  $0.9 < |\eta| < 1.0$  has 96 mm stacks (C10) in the  $z$ -direction. The reduced thickness of the C10 and D4 cells or their special geometry is to accommodate services and read-out electronics for other ATLAS detector systems [9, 10]. The gap and crack region of the ITC is located in the region  $1.0 < |\eta| < 1.6$  and the cells in this region are only made of scintillating tiles due to space limitation. The scintillators in the region  $1.0 < |\eta| < 1.2$  are called gap scintillators, made of E1 and E2 cells while those in the region  $1.2 < |\eta| < 1.6$  are called crack scintillators made of E3 and E4 cells. The gap scintillators primarily provide hadronic shower sampling, while the crack scintillators play an important role in sampling electromagnetic showers.

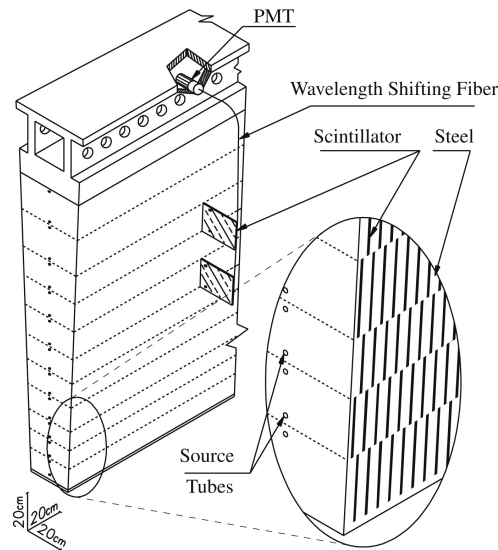


**Figure 3.** Schematic of one TileCal wedge [11], showing the mechanical assembly and optical readouts.

### 3. Event Selection

Table 1 summarises the selected events used in this analysis. The selection was chosen to optimise the number of events with a single muon originating from the  $W \rightarrow \mu\nu_\mu$  process while minimising the number of events from background processes. The selected events are required to contain a single reconstructed muon candidate that passes either the "medium" or "tight" identification requirement [12] to eliminate electroweak background events. A cut on the  $E_T^{\text{miss}}$  is required to exclude the multi-jet background processes. Cuts on the track ( $\sum p_T |_{\Delta R=0.4}$ )

and calorimeter ( $E_{\text{LAR}}|_{\Delta R=0.4}$ ) isolation variables are applied to ensure that the selected muon candidate is well isolated from the hadronic activity around it.

**Table 1.** Event selection based on the  $W$  decays

Variable	Requirement
1 Number of Muons	$N_{\text{muons}} = 1$
2 Transverse invariant mass	$40 < M_{\text{T}} < 140 \text{ GeV}$
3 Missing transverse energy	$30 < E_{\text{T}}^{\text{miss}} < 120 \text{ GeV}$
4 Track isolation	$\sum p_{\text{T}} _{\Delta R=0.4} < 1 \text{ GeV}$
5 Calorimeter isolation	$E_{\text{LAR}} _{\Delta R=0.4} < 1.5 \text{ GeV}$
6 Momentum of the muon	$p^{\mu} \leq 80 \text{ GeV}$
7 Transverse momentum of the muon	$p_{\text{T}}^{\mu} > 28 \text{ GeV}$
8. Average interactions per bunch crossing	$10 < \mu < 40$

In addition to the event selections listed in Table 1, the energy deposited by the passing muon candidate in the gap and crack cells is required to be above 60 MeV in order to suppress signals that are caused by electronic noise. The muon is required to traverse a minimum path length of 11 mm in gap cells and 5 mm in crack cells. The absolute azimuthal angle between the muon's track and cell's centre  $|\Delta\phi(\mu, \text{cell})| < 0.046$ .

The experimental  $pp$  data collected during the LHC Run 2 data taking at  $\sqrt{s} = 13 \text{ TeV}$  is used. Table 2 shows the data taking years of Run 2 and their corresponding integrated luminosity. Monte Carlo (MC) simulated samples of the  $W \rightarrow \mu\nu_{\mu}$  events are used as a reference when studying the response from experimental data. Three sets of MC event samples are generated to match pile-up conditions of the three data taking periods: 2015-2016, 2017, and 2018. The event generator SHERPA [13] was used to generate the  $W$  boson production events which are then interfaced with PYTHIA8 [14] for parton showering.

**Table 2.** Data taking periods of LHC Run 2 and the corresponding integrated luminosity

Period	$\int \mathcal{L} dt \text{ [fb}^{-1}\text{]}$
2015	3.2
2016	33.0
2017	44.3
2018	58.5

The event selection from Table 1 are applied to both the data and MC samples. The events from the simulated samples are normalised to the  $W \rightarrow \mu\nu_{\mu}$  production cross-section multiplied by the integrated luminosity of the corresponding data taking period. The simulated events are also reweighted to account for the different pile-up conditions.

#### 4. Results

The ratio between the deposited energy  $\Delta E$  and the path length that the muon traverse inside the calorimeter cell  $\Delta x$  is used to determine the cell response to the passing muon. The ratio, is denoted as  $dE/dx$ . In an ideal environment,  $dE/dx$  can be described by the Bethe Bloch

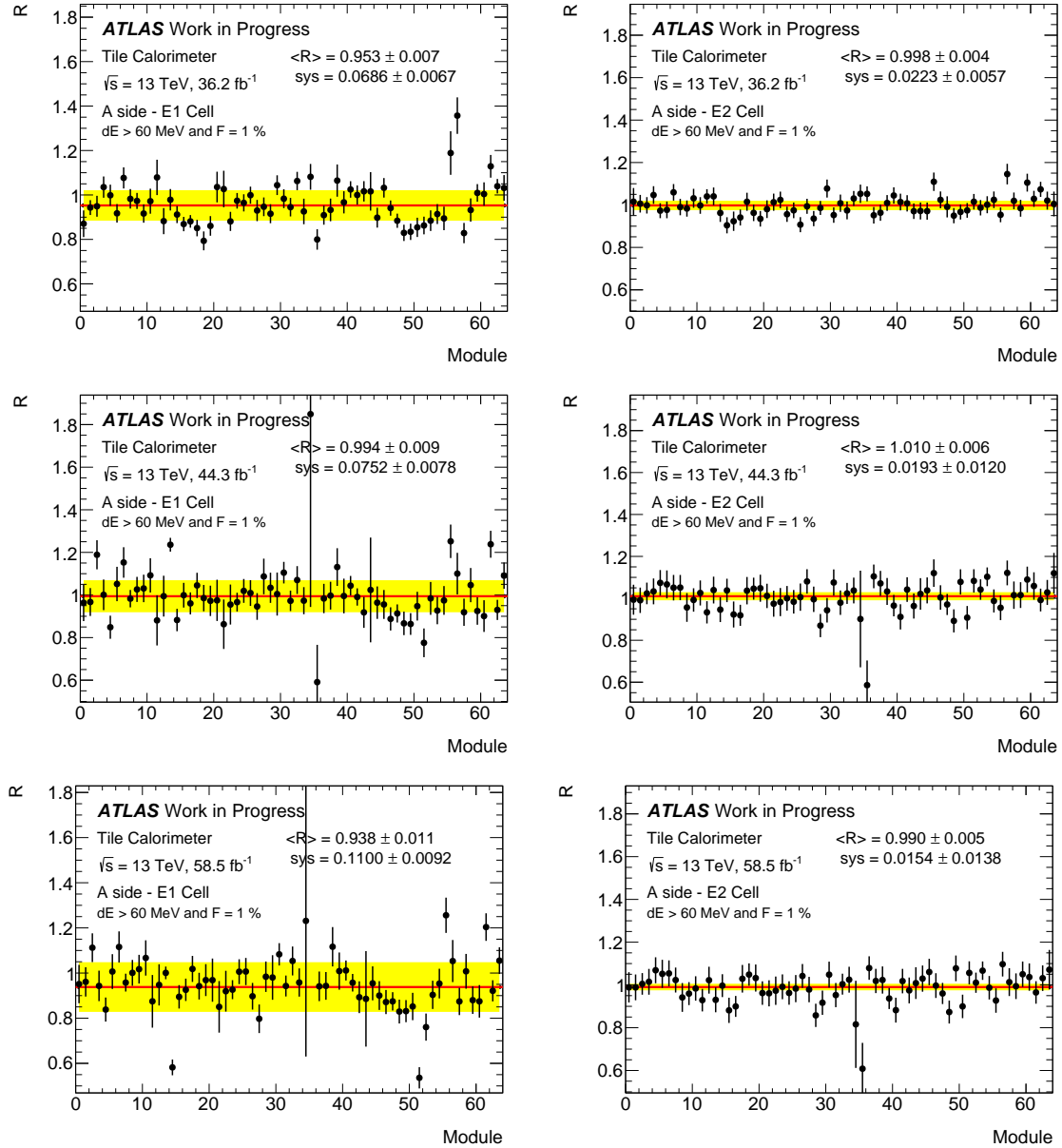


**Figure 4.** Distribution of module number vs  $dE/dx$  in E1 and E2 cells. The red line represents the fitted average response across all modules and the yellow band is the systematic uncertainty associated the fitted average value of  $R$ . The plots show results for 2015-2016 (top), 2017 (middle) and 2018 (bottom) data taking periods.

formula [15] and its probability follows a Landau function [16]. There are noise factors that convolute with the Landau making it difficult to perform fits. The truncated mean of the  $dE/dx$  distribution is used to measure the cell response. In this study, 1% of the events at the higher tail are truncated. The response of a given cell is obtained by taking the ratio of the observed truncated mean  $dE/dx$  with the one from the MC simulation,

$$R \equiv \frac{\langle dE/dx \rangle_F^{\text{Data}}}{\langle dE/dx \rangle_F^{\text{MC}}}, \quad (1)$$

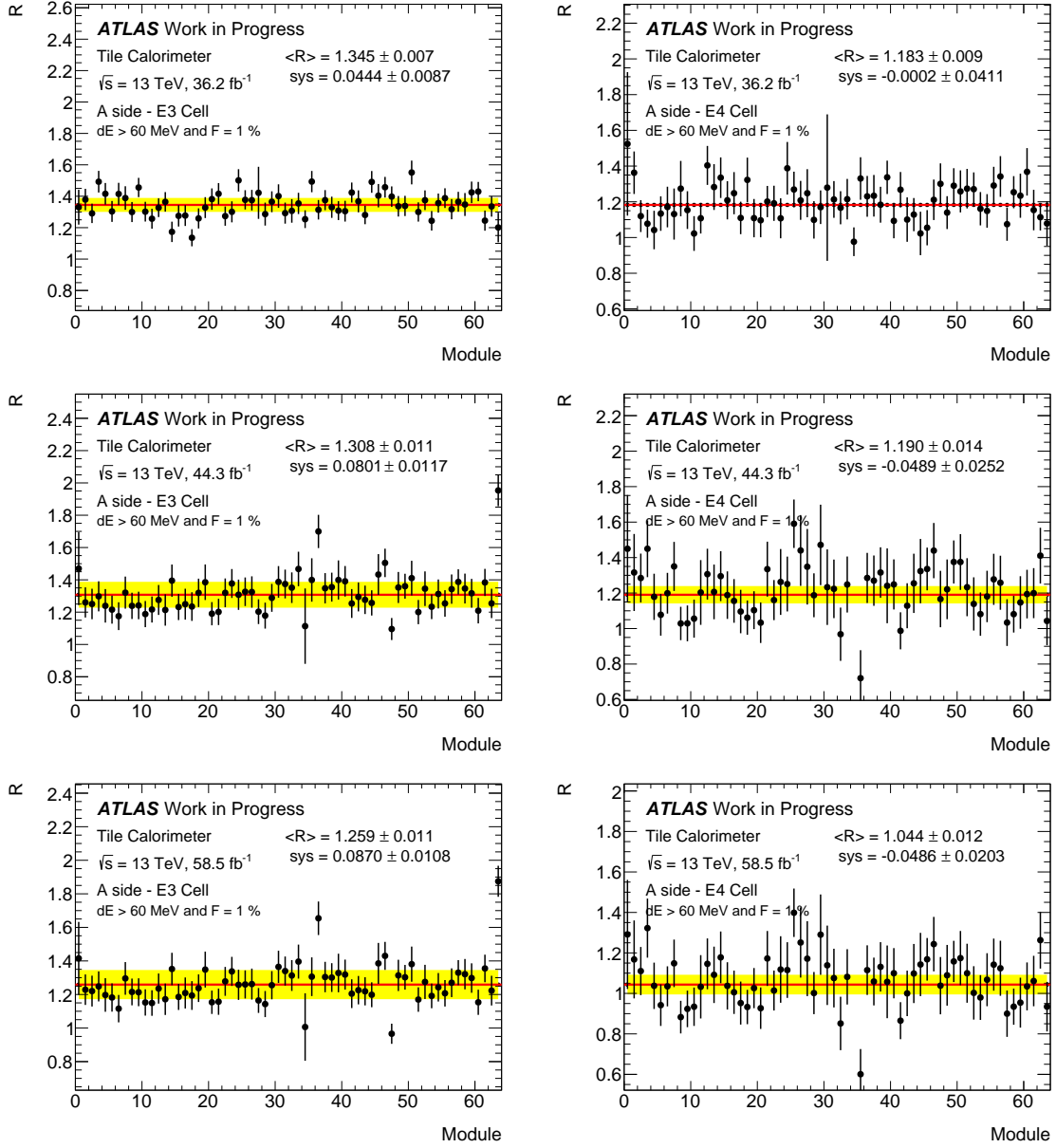


**Figure 5.** Distribution of module number vs  $dE/dx$  in E3 and E4 cells. The red line represents the fitted average response across all modules and the yellow band is the systematic uncertainty associated the fitted average value of  $R$ . The plots show results for 2015-2016 (top), 2017 (middle) and 2018 (bottom) data taking periods.

where  $F$  is the fraction of events truncated, which is set to be 1%. The response ( $R$ ) uniformity of each cell is evaluated over the entire azimuthal direction of the detector on the A-side. The response uniformity of the C-side of the detector will form part of further studies. A Gaussian likelihood function,

$$\mathcal{L}_c = \prod_{m=1}^{64} \frac{1}{\sqrt{2\pi} \sqrt{\sigma_{c,m}^2 + s_c^2}} \exp \left[ -\frac{1}{2} \frac{(R_{c,m} - \mu_c)^2}{\sigma_{c,m}^2 + s_c^2} \right], \quad (2)$$

where  $R_{c,m}$  and  $\sigma_{c,m}$  are the observed  $R$  and its statistical uncertainty for a given cell ( $c$ ) in module  $m$ . The unbinned log likelihood  $-2\log\mathcal{L}$  is minimised using minuit [17] to find  $\hat{\mu}_C$  and  $\hat{\sigma}_C$  which are the average response  $\langle R \rangle$  and the systematic uncertainty attributed to the non-uniformity across the modules.

The response of the cells could change over time due to factors like PMT drift response, ageing effects of the scintillators and wavelength shifting fibres [18]. The average response of each calorimeter cell is compared between different years. The E1 cells show a significant drop in the response during the 2018 data taking period. The drop in the average response can be attributed to the degraded response in modules 12, 35 and 51. The maximum deviation of 2% in the response in E2 cells is observed between 2017 and 2018 data taking periods. The deviation is not as significant as the one observed in the E1 cells. E3 cells show a drop in the response over time. Cells in module 25 and 47 show the most damage as the years increased. Module 32 and 34 in E4 show a drop in response during the 2017 and 2018 data taking periods.

## 5. Conclusions

Isolated muons from  $pp$  collision recorded by the ATLAS detector collected during the 2015-2016, 2017 and 2018 data taking periods were used to measure the response of gap and crack cells of the Tile Calorimeter. An unbinned negative log likelihood function was minimised to obtain the average response of each cell during different data taking years. In the preliminary results, the E1 scintillator cells show the biggest drop in response of 6.18%. This is due to a drop in the response of modules 12, 35 and 51. In further studies, maximum likelihood methods are to be employed in understanding the relative difference of the response in each cell.

## References

- [1] Henriques Correia A M (for the ATLAS collaboration) 2015 The ATLAS Tile Calorimeter Tech. rep. CERN Geneva URL <https://cds.cern.ch/record/2004868>
- [2] Collaboration T A 2008 *Journal of Instrumentation* **3** S08003–S08003 also published by CERN Geneva in 2010 URL <https://doi.org/10.1088/1748-0221/3/08/s08003>
- [3] Zyla P *et al.* (Particle Data Group) 2020 *PTEP* **2020** 083C01 and 2021 update
- [4] Evans L and Bryant P 2008 *Journal of Instrumentation* **3** S08001–S08001 URL <https://doi.org/10.1088/1748-0221/3/08/s08001>
- [5] Belous K *et al.* (Belle) 2014 *Phys. Rev. Lett.* **112** 031801 (*Preprint* 1310.8503)
- [6] Feldman G J *et al.* 1982 *Phys. Rev. Lett.* **48**(2) 66–69 URL <https://link.aps.org/doi/10.1103/PhysRevLett.48.66>
- [7] Manzoni S 2019 *Electron and Photon Energy Calibration* (Cham: Springer International Publishing) pp 115–148 ISBN 978-3-030-24370-8
- [8] Abdallah J *et al.* (ATLAS) 2013 *Journal of Instrumentation* **8** P01005–P01005 URL <https://doi.org/10.1088/1748-0221/8/01/p01005>
- [9] Abdallah J *et al.* (ATLAS) 2013 *Journal of Instrumentation* **8** T11001–T11001 URL <https://doi.org/10.1088/1748-0221/8/11/t11001>
- [10] 1996 *ATLAS tile calorimeter: Technical Design Report* Technical design report. ATLAS (Geneva: CERN) URL <http://cds.cern.ch/record/331062>
- [11] Aad G *et al.* (ATLAS) 2010 *Eur. Phys. J. C* **70** 1193–1236 (*Preprint* 1007.5423)
- [12] Aad G *et al.* (ATLAS) 2016 *Eur. Phys. J. C* **76** 292 (*Preprint* 1603.05598)
- [13] Bothmann E *et al.* (Sherpa) 2019 *SciPost Phys.* **7** 034 (*Preprint* 1905.09127)
- [14] Sjostrand T, Mrenna S and Skands P Z 2008 *Computer Physics Communications* **178** 852–867 ISSN 0010-4655 (*Preprint* 0710.3820)
- [15] Bethe H 1932 *Zeitschrift fur Physik* **76** 293–299
- [16] Landau L D 1944 *J. Phys.* **8** 201–205 URL <https://cds.cern.ch/record/216256>
- [17] James F and Roos M 1975 *Comput. Phys. Commun.* **10** 343–367
- [18] Aaboud M *et al.* (ATLAS) 2018 *Eur. Phys. J. C* **78** 987 (*Preprint* 1806.02129)

# Study of systematic uncertainties and spurious signals of resonant $H \rightarrow Z\gamma$ production at ATLAS Experiment

G Mokgatitswane<sup>1</sup>, J Choma<sup>1</sup>, S Dahbi<sup>1</sup>, X Ruan<sup>1</sup> and B Mellado<sup>1,2</sup>

<sup>1</sup> School of Physics and Institute for Collider Particle Physics, University of the Witwatersrand, Johannesburg, Wits 2050, South Africa

<sup>2</sup> iThemba LABS, National Research Foundation, PO Box 722, Somerset West 7129, South Africa

E-mail: gaogalalwe.mokgatitswane@cern.ch

**Abstract.** This work examines the assessment of systematic uncertainties and quantification of probable false signals on the fitting signal yield to Higgs-like production in the  $Z\gamma$  final state, where the  $Z$  boson decays leptonically. Several sources of systematic uncertainties for the measured observables are considered such as detector systematic uncertainties from detector effects and modelling systematic uncertainties due to modelling of signal and the background processes. To estimate the contribution of each source in the overall uncertainty, large-scale Monte Carlo events simulation has been performed where the events correspond to an integrated luminosity of  $139 \text{ fb}^{-1}$  dataset recorded by the ATLAS experiment in proton-proton collisions during the LHC Run 2.

## 1. Introduction

The recent emergence of multi-lepton anomalies as deviations from Standard Model (SM) predictions in several ATLAS and CMS analyses of Large Hadron Collider (LHC) data, may point to the existence of physics beyond the Standard Model (BSM) [1–4]. An explanation to these anomalies is well demonstrated by the decay of a heavy scalar  $H$  into a lighter one  $S$  and a SM Higgs boson,  $H \rightarrow SS, Sh$ , as per the 2HDM+ $S$  framework which requires the mass of  $S$  to be in the range of 130 GeV to 160 GeV. The ATLAS and CMS have previously studied the signatures of  $S$  in the side-band of the kinematics region in searches for the SM Higgs. In addition, an evidence for the associate production of  $S$  has been accumulated with a mass of 151.5 GeV in Ref. [5], where it is assumed to be through the decay of Higgs-like scalar  $H$ .

In this context, it is anticipated that the production of  $H$  and excesses in the multi-lepton final states at the LHC will have a significant production rate in a number of channels (i.e.  $\gamma\gamma, Z\gamma$ ). Motivated by this, a search for resonances with mass  $m_s = 150 \text{ GeV}$  is performed in the  $Z\gamma$  final state where  $Z$  boson decays to lepton-antilepton pairs,  $\mu^+\mu^-$  and  $e^+e^-$ . Here the  $Z\gamma$  channel is taken into consideration because, compared to the di-photon final state, a Higgs-like boson ( $H$ ) may have a relatively higher likelihood of decaying into a  $Z\gamma$  final state. Because the expected signal excesses are overlaid with background processes that have similar signatures, accurate and precise measurement of signal and background distributions is required.

However, the precision of the measurements is significantly impacted by a number of anticipated systematic uncertainties resulting from biases in experimental measurements as well as Monte Carlo modeling of physical processes such as Standard Model (SM) backgrounds, Beyond Standard Model (BSM) signals, and particle-detector interactions. Understanding the systematic uncertainties for both our SM backgrounds and the BSM signals is crucial for accomplishing this. Within the framework of ATLAS collaboration, a thorough analysis of the systematic uncertainty sources is carried out taking into consideration the Combined Performance group recommendations which is dedicated to object optimisation, identification and selection. Moreover, the impact from spurious signal, fake signals systematics created by the choice of the functional forms for background modeling will also be reviewed.

## 2. Experimental systematic uncertainty

The sources of systematic uncertainties taken into account in this study, for the expected number of signal events include the following nuisance parameters (NP) for the  $\mu\mu\gamma$  channel: 10 muon uncertainties, photon ID/Isolation/Trigger efficiency uncertainties and Pile-up. For the  $ee\gamma$  channel we have: electron ID/Isolation/Reconstruction/Trigger, photon ID/Isolation/Trigger efficiency uncertainties and pile-up.

### 2.1. Pileup re-weighting

Because the simulated pileup overlays the simulated process, the amount of pileup in each simulated event is determined by drawing from a reference distribution of the mean number of interactions per bunch crossing. This distribution may differ from the measured distribution and need to be corrected by re-weighting simulated events with scale factors, which improves the agreement. In order to estimate the uncertainty associated with pileup re-weighting, events are also re-weighted with  $\pm 1\sigma$  variations of the nominal scale factor, where  $\sigma$  is its uncertainty provided by the CP group in Refs. [6–8]. The difference in the event yield between re-weighting with the nominal and the UP(DOWN) variation is taken as the UP(DOWN) uncertainty on the signal yield.

### 2.2. Electrons

The  $e/\gamma$  energy scale, resolution and electrons reconstruction/identification/isolation efficiencies in simulation are corrected in order to improve agreement with data. Energy scale and electron resolution corrections are applied to each electron and reconstruction/identification/isolation efficiency corrections are applied through event re-weighting. Uncertainties associated with electron corrections are evaluated by varying the trigger, reconstruction, isolation and identification scale factors of the leptons by  $\pm 1\sigma$ , and then recompute  $m_{\ell\ell\gamma}$  distribution after varying the uncertainty sources.

- Energy resolution all: uncertainty related to electron energy smearing in simulation to enhance resolution agreement between data and simulation.
- Energy scale all (AFS): uncertainty associated with calibration of electron energy scale in simulation. A special set of calibrations and uncertainties are applied for samples simulated with the Atlfast-II (AF2) parametrization instead of with GEANT4.
- Electron efficiency (ID, Iso, Reco): uncertainties associated with re-weighting of simulated events such that identification, isolation, and reconstruction efficiencies in simulation agree with those in data. Identification efficiency uncertainty is approximately  $\pm 3\%$  on the signal region yield and is the dominant systematic uncertainty.

### 2.3. Muons

The momentum scale,  $e/\gamma$  resolution and isolation/reconstruction/track-to-vertex association efficiencies of muons in simulation are also corrected. Muon resolution and momentum scale corrections are applied to each muon, and isolation/reconstruction/track-to-vertex association (ttva) efficiency corrections are applied through event re-weighting. The same procedure used to assess uncertainties for electrons is followed to assess uncertainties associated with these corrections.

- Muon ID: uncertainty associated with charge-agnostic smearing of simulated muon  $p_T$  in the Inner Detector (ID) in order to improve muon ID  $p_T$  resolution agreement between data and simulation.
- Muon scale: uncertainty associated with calibration of the muon momentum scale in simulation.
- Muon eff. Iso(Reco)(ttva) stat(sys) lowpt: similar to the efficiency uncertainties for electrons but broken up into statistical and systematic errors on the weights.
- Muon sagitta rho: uncertainty associated with correction of muon momenta for charge-dependent sagitta biases in simulation. Geometric deformations of the detectors affect the sagitta measurement and consequently the momentum.
- Muon sagitta resbias: uncertainty associated with correction of muon momenta for residual sagitta bias in simulation.
- Muon MS: uncertainty associated with charge-agnostic smearing of simulated muon  $p_T$  in the Muon Spectrometer (MS) in order to improve muon MS  $p_T$   $e/\gamma$  resolution agreement between simulation and data.

### 2.4. Photons

The same procedure implemented in Subsec. 2.1 is applied to the photon isolation and identification efficiency scale factors to estimate their uncertainty impact on the signal efficiency. The signal efficiencies for each systematic variation corresponding to all samples  $m_x$  in  $ee$  and  $\mu\mu$  channels are computed as:

$$SigEff = \frac{\Sigma(year^n passcut(with weight) * lumi(year) * xsec) / Sum_w}{lumi_{all} * xsec}. \quad (1)$$

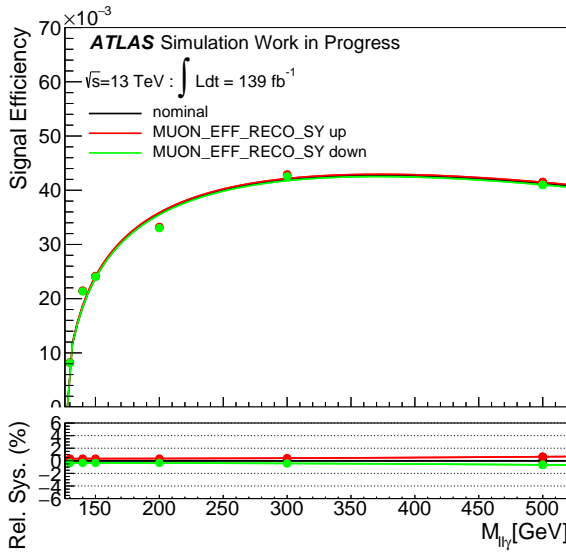
The relative systematic uncertainties on signal efficiency are summarised in Table 1 and the corresponding plots illustrating their impact are presented as shown in Figure 1. A fit to the systematic variations and nominal as a function of  $m_X$  is performed in the top pad (red and green curves) using a sum of first-order polynomial and logarithmic function:  $f = a + b*x + c*log(x+d)$ . The relative difference of the two curves computed in the bottom pad is fitted with a second-order polynomial function, where the smallest and largest absolute numbers are extracted in percentage and used as an estimate. The systematic uncertainties of less than 5% are not considered significant in the analysis.

## 3. Spurious signal study

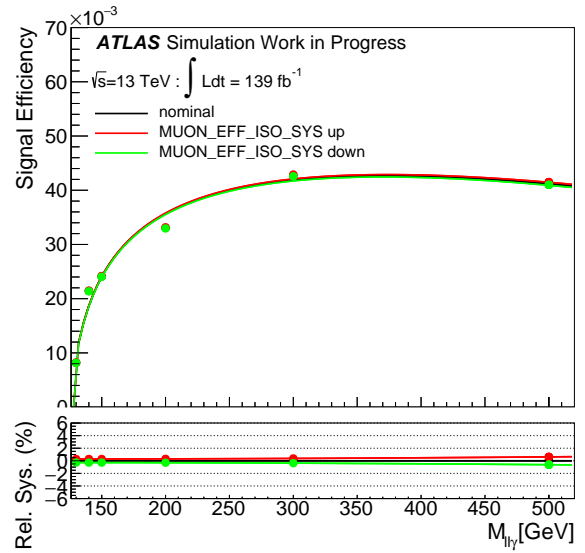
This section estimates the uncertainty of the various functions used to describe the background shape. This uncertainty, referred to as spurious signal  $N_{sig}$ , arises from fitting a pure background template using a given signal plus background functional forms. It is defined as the bias on the signal yield caused by the choice of a particular background function. It is evaluated [9] by fitting a high statistics background-only distributions, scaled to the luminosity of the data but without introducing corresponding statistical fluctuations [10], with a signal plus background model. The fitted signal yield is actually the bias caused by choice of such background model,

Table 1: Summary of the main sources of systematic uncertainty for the measurement of  $\sigma(pp \rightarrow X \rightarrow Z\gamma)$  and of their contribution to the measurement uncertainty.

Category	$\mu\mu\gamma$	$ee\gamma$
<i>Signal Efficiency</i>		
Photon ID efficiency uncertainty	0.497 – 1.051%	0.541 – 1.064%
Photon isolation efficiency uncertainty	0.591 – 0.925%	0.637 – 0.897%
Photon trigger efficiency uncertainty	0.000 – 0.028%	0.000 – 0.000%
Pile-up	0.000 – 0.028%	0.000 – 0.000%
Muon isolation efficiency (stat.)	0.034 – 0.190%	0.000%
Muon isolation efficiency (sys.)	0.278 – 0.624%	0.000%
Muon reconstruction efficiency (stat.)	0.121 – 0.132%	0.000%
Muon reconstruction efficiency (sys.)	0.342 – 0.649%	0.000%
Muon reconstruction efficiency (stat. lowpt)	0.012 – 0.033%	0.000%
Muon reconstruction efficiency (sys. lowpt)	0.023 – 0.048%	0.000%
Muon efficiency (ttva stat.)	0.065 – 0.120%	0.000%
Muon efficiency (ttva sys.)	0.059 – 0.137%	0.000%
Muon efficiency (trig. stat. uncertainty)	0.091 – 0.190%	0.000%
Muon efficiency (trig. sys. uncertainty)	0.970 – 1.665%	0.000%
Electron ID efficiency (total)	0.000%	2.314 – 2.758%
Electron Iso. efficiency (total)	0.000%	0.103 – 0.168%
Electron Reco. efficiency (total)	0.000%	0.485 – 0.538%
Electron Trig. efficiency (total)	0.000%	0.079 – 0.088%
Electron TrigEff. efficiency (total)	0.000%	0.002 – 0.003%



(a)



(b)

Figure 1: Illustration of the impact of systematic uncertainty on signal efficiency resulting from uncertainty in muon reconstruction efficiency (a) and muon isolation efficiency (b).

denoted as spurious signal  $SS$  in the study. The error of fitted signal yield is denoted as  $\Delta S$ , used to judge whether the background function satisfies selection criteria.

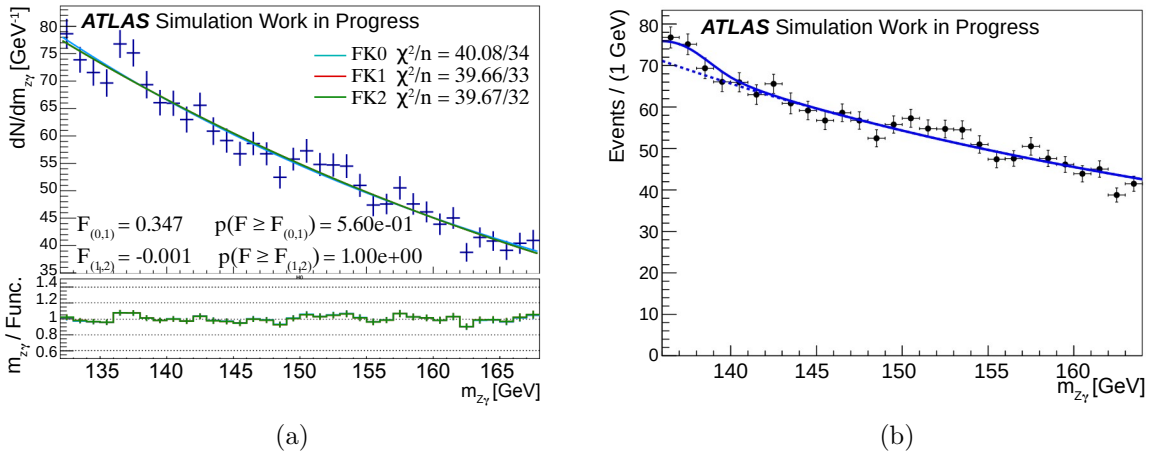


Figure 2: Fitting on the background MC template (a) and fitting with S+B functions (b) for 150 GeV.

Name	S/ $\Delta$ S in %	Spurious signal	N par	Chi2 Prob	Pass selection
150 GeV					
Category H0					
FK0	72.3	18.6	2	14.8	PASS
FK1	136	38.7	3	11.9	PASS

Table 2: Spurious signal yield and fit properties of tested functions at 150 GeV.

The background template is constructed using a combination of SM  $Z\gamma$  (Sherpa\_CT10) MC sample and  $Z$ +jets, which are the main dominant background processes. From previous  $H \rightarrow Z\gamma$  high mass analysis, the data in control region can describe  $Z$ +jet shape well, and the statistical error in control region data is much smaller than  $Z$ +jet simulation. In this context, the background MC sample ( $Z\gamma$ ) is normalised to 90% of real data in the signal region and combined with 10% of reverse photon identification data sample ( $Z$ +jet) in the control region, based on the purity analysis from the previous  $Z\gamma$  papers. The following high-mass function of different functional forms is used for fitting:  $f_k(x; b, \{a_k\}) = (1 - x)^b x^{\sum_{j=0}^k a_j \log(x)^j}$ ,  $k = 0, 1, 2$ , noted as FK0, FK1 and FK2.

The template sample is saved in the histogram with 1 GeV per bin from 130 GeV to 1000 GeV. A scan of the existence of signal with 1 GeV step is performed with the signal shape varying as a function of mass. To find the suitable functional form that best describes background in the data and avoid the spurious signal, ‘‘F-test’’ technique is introduced and a function with a p-value smaller than 5% is selected. The results for VBF category at 150 GeV resonant mass point are shown in Figure 3 and summarised in Table 2, and the yield of spurious signal over its background fluctuations ( $S/\delta S$ ) is expected to be less than 50%.

### Conclusion and outlook

We successfully estimated the experimental systematic uncertainties and spurious signal of the Higgs-like scalar  $H$  production at a mass interest of 150 GeV at the LHC. The study was performed using Monte Carlo (MC) simulated VBF signal samples and background MC samples ( $Z\gamma$ ) corresponding to an integrated luminosity of  $139 \text{ fb}^{-1}$  dataset recorded by the ATLAS experiment in proton-proton collisions during the LHC Run 2. According to preliminary results,

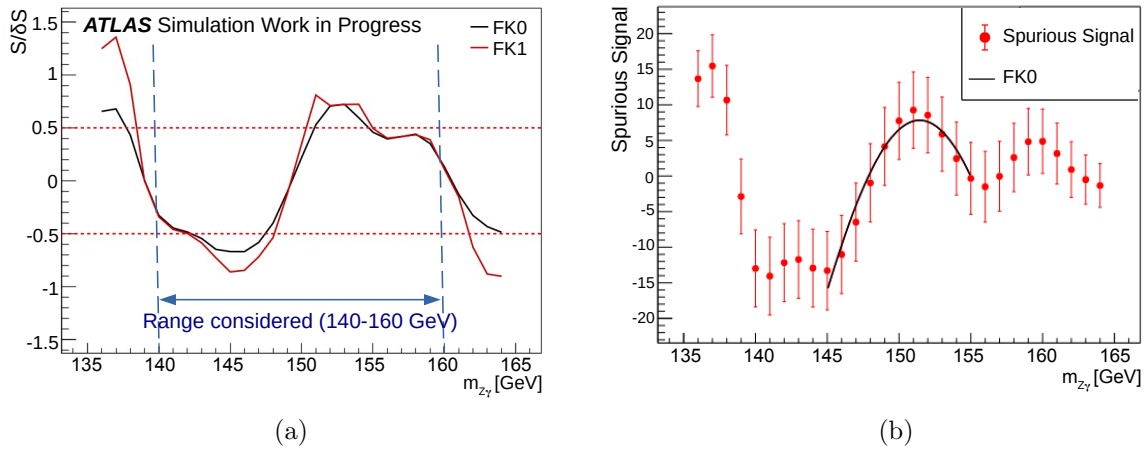


Figure 3: The  $N_{spurious}/\delta N_{spurious}$  as a function of mass for each functional (a) form and spurious signal parametrisation fit (b) at 150 GeV

these uncertainties are relatively small ( $< 5\%$ ) and are not a limiting factor for this study. Consequently, this study will move forward in terms of developing the statistical interpretation.

## References

- [1] von Buddenbrock S, Cornell A S, Iarilala E D R, Kumar M, Mellado B, Ruan X and Shrif E M 2019 *J. Phys. G* **46** 115001 (*Preprint 1809.06344*)
- [2] von Buddenbrock S, Cornell A S, Fang Y, Mohammed A F, Kumar M, Mellado B and Tomiwa K G 2019 *Journal of High Energy Physics* **2019** ISSN 1029-8479 URL [http://dx.doi.org/10.1007/JHEP10\(2019\)157](http://dx.doi.org/10.1007/JHEP10(2019)157)
- [3] von Buddenbrock S, Ruiz R and Mellado B 2020 *Phys. Lett. B* **811** 135964 (*Preprint 2009.00032*)
- [4] Hernandez Y, Kumar M, Cornell A S, Dahbi S E, Fang Y, Lieberman B, Mellado B, Monnakgotla K, Ruan X and Xin S 2021 *Eur. Phys. J. C* **81** 365 (*Preprint 1912.00699*)
- [5] Crivellin A, Fang Y, Fischer O, Kumar A, Kumar M, Malwa E, Mellado B, Rapheeha N, Ruan X and Sha Q 2021 (*Preprint 2109.02650*)
- [6] 2015 Electron and Photon Calibration for Run2 (energy scale and resolution) URL <https://twiki.cern.ch/twiki/bin/view/AtlasProtected/EGammaCalibrationRun2>
- [7] 2015 The ElectronPhotonFourMomentumCorrection tool URL <https://twiki.cern.ch/twiki/bin/view/AtlasProtected/ElectronPhotonFourMomentumCorrection>
- [8] 2016 The MCP Moriond 2016 Recommendation URL [https://twiki.cern.ch/twiki/bin/view/AtlasProtected/MCPAnalysisGuidelinesMC15#Final\\_recommendations\\_for\\_Moriond](https://twiki.cern.ch/twiki/bin/view/AtlasProtected/MCPAnalysisGuidelinesMC15#Final_recommendations_for_Moriond)
- [9] Petit E *et al.* (ATLAS Collaboration) 2016 Supporting note: Selection and performance for the  $Hgg$  and  $HZg$  analyses Tech. rep. CERN Geneva URL <https://cds.cern.ch/record/2130656>
- [10] Aad G *et al.* (ATLAS Collaboration) 2020 Recommendations for the Modeling of Smooth Backgrounds Tech. rep. CERN Geneva

# Compatibility of the CMS dilepton spectra with the Neutral Scalar with Mass around 151 GeV

Srimoy Bhattacharya<sup>1</sup>, Abhaya Kumar Swain<sup>1</sup>, Mukesh Kumar<sup>1</sup>,  
Bruce Mellado<sup>1,2</sup>, Xifeng Ruan<sup>1</sup>

<sup>1</sup> School of Physics and Institute for Collider Particle Physics, University of the Witwatersrand, Johannesburg, Wits 2050, South Africa.

<sup>2</sup> iThemba LABS, National Research Foundation, PO Box 722, Somerset West 7129, South Africa.

E-mail: bhattacharyasrimoya@gmail.com

**Abstract.** The measurements related to the different properties of the newly discovered Higgs boson ( $h$ ) at the LHC by ATLAS and CMS indicate that this 125 GeV boson is compatible with the one predicted by the Standard Model (SM). However, this does not exclude the existence of additional scalar bosons as long as their possible mixing with the SM Higgs is sufficiently small, such that the properties of the latter remain to a good approximation unchanged. In a recent phenomenological analysis, a search for narrow resonances with  $S \rightarrow \gamma\gamma, Z\gamma$  along with leptons, di-jets, bottom quarks and missing energy was reported. The global significance of the excess at  $m_S = 151.5\text{GeV}$  is  $4\sigma$ , whereas a combination with the multi-lepton anomalies gives a significance larger than  $5\sigma$ . Moreover, a recent CMS study in the W boson pair in proton-proton collisions presented an excess in dilepton channel associated with the 0, 1 jet  $ggH$  tagged categories. There it shows an excess around 150 GeV. With this motivation, in this analysis, we consider a new physics model, namely, 2HDM+S, containing two new hypothetical scalar bosons,  $H$  and  $S$  and check the compatibility of this CMS di-lepton spectra with the scalar mass around 150 GeV.

## 1. Introduction

With the discovery of a Higgs-like boson at the Large Hadron Collider (LHC) by ATLAS and CMS collaboration, the Standard Model (SM) of particle physics was complete. However, this compatibility of the measurement with the SM does not exclude the possibility of additional scalar bosons as long as the mixing with the SM higgs is small. In recent times, several investigations of multi-lepton final states from ATLAS and CMS have revealed the so-called “multi-lepton anomalies” as departures from the predictions of the Standard Model [1, 2, 3, 4].

These anomalous features of the LHC data can be explained well with singlet scalar bosons extended to the SM. The full model that describes this signal is known as 2HDM+S, where the 2HDM model is extended by a real singlet scalar. The scalar spectrum in the 2HDM+S model has two CP-even ( $h, H$ ), one CP-odd ( $A$ ), and charged scalar bosons ( $H^\pm$ ), providing ample area to examine the structure of scalar spectrum. Recently, a potential candidate for  $S$  with a mass of 151.5 GeV was published in Ref. [5], where by integrating the side-band data from the CMS and ATLAS searches (several analysis from di-photon,  $Z\gamma$  and  $b\bar{b}$  resonances [6, 7, 8, 9]) for the SM Higgs, they have gathered evidences for the associated generation of new

scalar particle  $S$  (perhaps via the decay of a heavier boson  $H$ ) with a mass  $m_S = 151.5$  GeV. The global significance of the excess at  $m_S = 151.5$  GeV is  $4\sigma$ , whereas a combination with the multi-lepton anomalies gives a significance larger than  $5\sigma$ . Furthermore, if a dark matter candidate is included with this 2HDM+ $S$  model, it is possible to account for a variety of astrophysical anomalies [10]. It is interesting that it may be simply extended to account for the muon  $g - 2$  anomaly [11, 12].

Moreover, the Higgs decays into a pair of  $W$  bosons is one of the most important channels for measuring the Higgs boson production cross section and couplings to SM particles since it has the second-highest branching fraction (21.5%) of all the Higgs boson decay channels predicted by the SM. The CMS collaboration recently published measurements of the Higgs boson properties in the  $H \rightarrow W^+W^-$  decay channel considering the Vector Boson Fusion (VBF) and gluon fusion (ggH) production mechanism. They have also considered the associated production with a vector boson with the final states with at least two charged leptons [13]. Here they presented an excess around 150 GeV in dilepton channel associated with the 0, 1 jet ggH tagged categories.

With this motivation, we have considered these dilepton channels and studied the transverse mass distribution of Higgs in light of the 2HDM+ $S$  model. We here studied the Observed distributions of the  $m_{TH}$  in the 0-jet and 1-jet ggH  $p_{T2} > 20$  GeV and  $p_{T2} < 20$  GeV different flavor (DF) categories.

## 2. The Model

Here, we provide a quick overview of the 2HDM+ $S$  model. We have expanded a Type-II two Higgs doublet model 2HDM with a real singlet scalar,  $\Phi_S$ ; the notation is maintained from the reference, [14]. The model's potential is indicated by:

$$\begin{aligned}
V(\Phi_1, \Phi_2, \Phi_S) &= m_{11}^2 |\Phi_1|^2 + m_{22}^2 |\Phi_2|^2 - m_{12}^2 (\Phi_1^\dagger \Phi_2 + h.c.) \\
&+ \frac{\lambda_1}{2} (\Phi_1^\dagger \Phi_1)^2 + \frac{\lambda_2}{2} (\Phi_2^\dagger \Phi_2)^2 + \lambda_3 (\Phi_1^\dagger \Phi_1) (\Phi_2^\dagger \Phi_2) \\
&+ \lambda_4 (\Phi_1^\dagger \Phi_2) (\Phi_2^\dagger \Phi_1) + \frac{\lambda_5}{2} [(\Phi_1^\dagger \Phi_2)^2 + h.c.] \\
&+ \frac{1}{2} m_S^2 \Phi_S^2 + \frac{\lambda_6}{8} \Phi_S^4 + \frac{\lambda_7}{2} (\Phi_1^\dagger \Phi_1) \Phi_S^2 + \frac{\lambda_8}{2} (\Phi_2^\dagger \Phi_2) \Phi_S^2.
\end{aligned} \tag{1}$$

The  $SU(2)_L$  Higgs doublets in this case are  $\Phi_1$  and  $\Phi_2$ , while the singlet field is  $\Phi_S$ . The first three lines of eqn. 1 are the 2HDM potential. The singlet scalar field is represented by the final four terms. By enforcing a  $Z_2$  symmetry, which causes all the quarks of a given charge to couple to a single Higgs doublet, the tree-level FCNCs may be avoided. The  $m_{12}^2$  term softly breaks the  $Z_2$  symmetry. Additionally, the extension of the  $Z_2$  symmetry to the Yukawa sector guarantees the absence of FCNC at tree level. In this work, we suppose that the real singlet scalar obtains a vacuum expectation value ( $v_{ev}$ ) and satisfies the  $Z_2$  symmetry. This makes the singlet scalar a strong candidate for dark matter. We assumed  $\lambda_i$  to be real as the explicit CP violation is not considered. The minimization conditions then obtained by minimizing the potential with the three Higgs fields with  $v_{ev}$ s.  $\Phi_1 \rightarrow v_1/\sqrt{2}$ ,  $\Phi_2 \rightarrow v_2/\sqrt{2}$  and  $\Phi_S \rightarrow v_S$ . The conditions are,

$$\frac{\partial V}{\partial [v_1, v_2, v_S]} = 0. \tag{2}$$

Which then results in the following three relations:

$$m_{11}^2 = -\frac{1}{2}(v_1^2 \lambda_1 + v_2^2 \lambda_{345} + v_S^2 \lambda_7) + \frac{v_2}{v_1} m_{12}^2, \tag{3}$$

$$m_{22}^2 = -\frac{1}{2}(v_2^2 \lambda_2 + v_1^2 \lambda_{345} + v_S^2 \lambda_8) + \frac{v_1}{v_2} m_{12}^2, \tag{4}$$

$$m_S^2 = -\frac{1}{2}(v_1^2 \lambda_7 + v_2^2 \lambda_8 + v_S^2 \lambda_6), \tag{5}$$

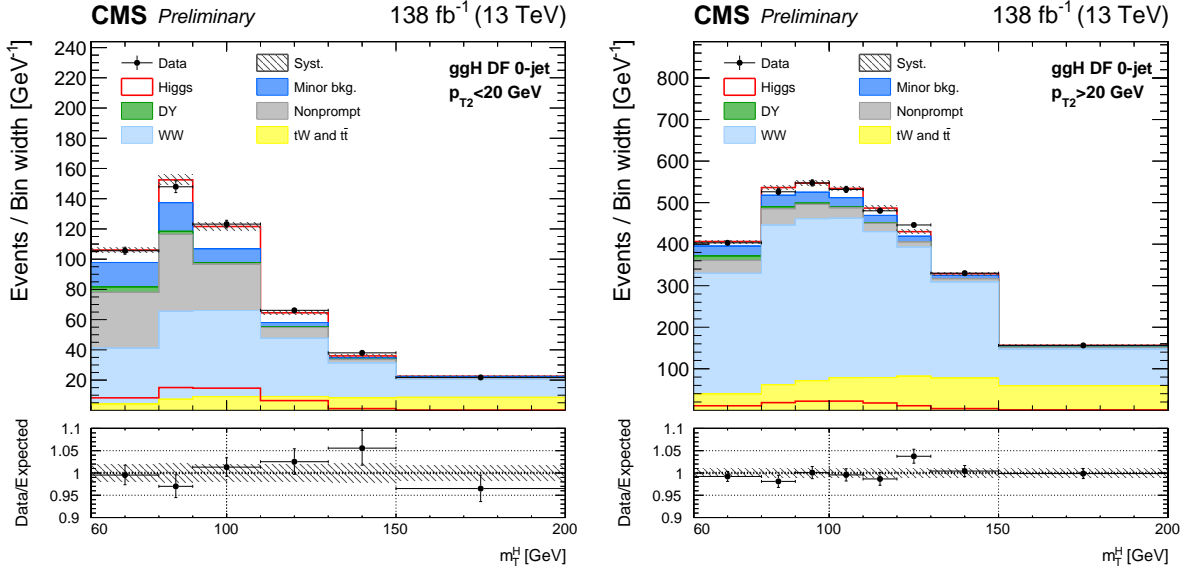


**Figure 1.**  $m_T^H$  distributions for 0-jet ggH  $p_{T2} < 20$  GeV (left) and  $p_{T2} > 20$  GeV (right) DF Categories [13].

where  $\lambda_{345} = \lambda_3 + \lambda_4 + \lambda_5$ .

Then, in order to determine the relationship between the physical parameters and the masses of the neutral and charged higgses, we solve these conditions in addition to the ones that were obtained after diagonalizing the mass matrices of the CP-even, CP-odd, and charged higgs. For further information, see the Ref. [14] and the references there in.

### 3. Simulation and Event selection

The Monte Carlo simulation of proton - proton collisions at the LHC is simulated with CM energy of 13 TeV. The model file for the 2HDM+S is implemented with FeynRules [15]. Using Madgraph5 [16] and the NNPDF3.0 parton distribution functions [17], the parton level signal events are produced. After this parton level event simulation, we have used Pythia8 [18] for the showering and hadronization. The detector level simulation is conducted using Delphes(v3) [19].

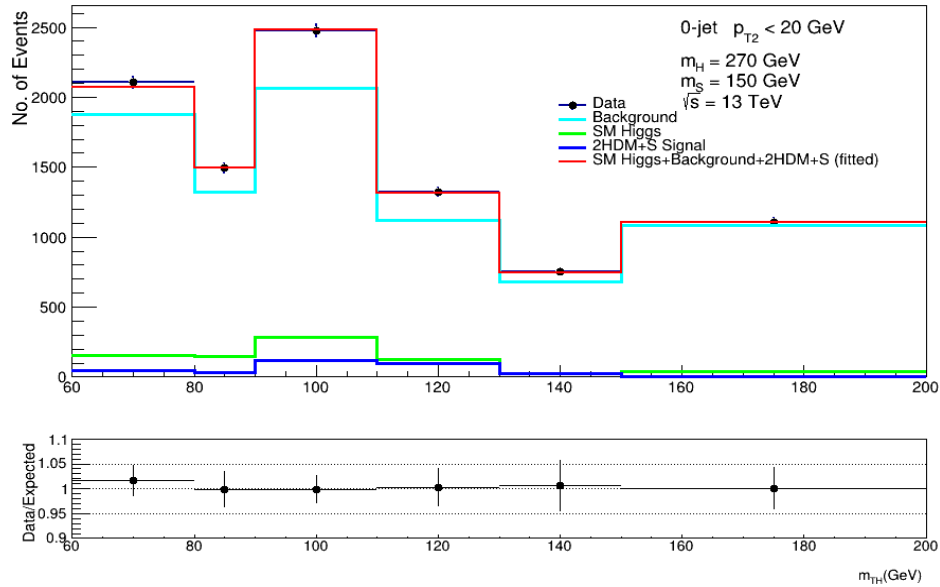
In this analysis, the events are chosen by necessitating the presence of at least two charged leptons (electron or muon) with high  $p_T$ , high  $p_T^{miss}$ , and a varying number of hadronic jets. Through out the analysis, only hadronic jets with  $p_T > 30$  GeV are considered. The highest  $p_T$  (leading) lepton in the event is required to be greater than 25 GeV and for sub-leading leptons, the minimum  $p_T$  requirement is of 10 GeV. On top of these basic selection criteria, the leading leptons must join up to produce an opposite-charged  $e\mu$  pair. By vetoing events that contain any b-jet with  $p_T > 20$  GeV, contributions from top quark production are minimised. To minimize QCD events with multiple misidentified jets, the dilepton invariant mass  $m_{\ell\ell}$  must be larger than 12 GeV. The  $p_T$  of the dilepton system  $p_T^{\ell\ell}$  is considered to exceed 30 GeV. Moreover, the transverse mass built with  $p_T^{miss}$  and the momentum of the subleading lepton  $m_T(\ell_2, p_T^{miss})$  is needed to be higher than 30 GeV. Here  $m_T$  for a group of particles  $\{P_i\}$  with transverse momenta  $\vec{p}_{T,i}$  is identified as :

$$m_T(\{P_i\}) = \sqrt{(\sum |\vec{p}_{T,i}|)^2 - |\sum \vec{p}_{T,i}|^2} \quad (6)$$

The events with zero and one hadronic jets are subdivided into two distinct categories. Finally, these sub-categories are further separated based on whether the sub-leading lepton's

**Table 1.**

	Parameter	Fit Result
$p_{T2} < 20$ GeV	$N_{SM}$	$0.98 \pm 0.02$
	$N_{BSM}$	$3.86 \pm 1.72$

**Figure 2.** The SM+BSM fit result for the transverse mass spectrum of Higgs .

$p_T$  is more than or less than 20 GeV.

#### 4. Results

As mentioned in the previous section, in this analysis we have selected events for the dilepton final states, based on the cuts and analysis techniques given in the experimental search results [13]. The SM background predictions and their related systematic uncertainties were obtained straight from the experimental papers to ensure agreement with the experimental findings. As the mass of Higgs boson cannot be reconstructed in the  $W^+W^-$  channel because of the existence of neutrinos in the final state, the Higgs's Boson transverse mass  $m_T^H = m_T(\ell\ell, p_T^{miss})$  is chosen as a good observable to discriminate the signal from different background processes, such as  $DY \rightarrow \tau^+\tau^-$  and  $V\gamma$ . The distributions of  $m_T^H$  for 0-jet category are given in fig. 1 [13]. Each figure's bottom panel displays the comparison between the total SM prediction and the number of events observed in the data. It is quite apparent from the left panel of fig. 1 that, there exists an excess in the transverse mass distribution of Higgs at around 150 GeV. To address this excess, a fit has performed to the data using the SM+BSM hypothesis. Here, we consider a single degrees of freedom, namely  $N_{SM}$  which normalizes the SM components of the fit (SM Higgs + SM background). On the other hand, another degree of freedom  $N_{BSM}$  is considered, which maps directly to the normalisation of BSM signal. As a representative case, we here discuss the fit for 0-jet,  $p_{T2} < 20$  GeV category. The preliminary result of this fit is given in Table 1 corresponding to a significance of  $3.38 \sigma$ . The distribution overlaid with the SM+BSM

fit is shown in the upper panel of Figure 2. The fit for  $p_{T2} > 20$  GeV will be done later. However,  $p_{T2} < 20$  GeV fit has the largest sensitivity.

## 5. Summary and Conclusion

In this analysis, we have studied the dilepton anomalies reported in recent CMS analysis in the W boson pair in proton-proton collisions. We investigated the transverse mass distribution of Higgs,  $m_T^H$  as an important kinematic observable in various signal regions. The events with zero and one hadronic jets are subdivided into two distinct categories depending on the value of the  $p_T$  of subleading lepton. As a representative case, we here present the preliminary result of the fit for 0-jet with  $p_{T2} < 20$  GeV category. The fitted distribution is in good agreement with the data. Therefore, in conclusion we found that the signal from the 2HDM+S model explain the data reasonably well.

## References

- [1] von Buddenbrock S, Cornell A S, Fadol A, Kumar M, Mellado B and Ruan X 2018 *J. Phys. G* **45** 115003 (*Preprint 1711.07874*)
- [2] Buddenbrock S, Cornell A S, Fang Y, Fadol Mohammed A, Kumar M, Mellado B and Tomiwa K G 2019 *JHEP* **10** 157 (*Preprint 1901.05300*)
- [3] von Buddenbrock S, Ruiz R and Mellado B 2020 *Phys. Lett. B* **811** 135964 (*Preprint 2009.00032*)
- [4] Hernandez Y, Kumar M, Cornell A S, Dahbi S E, Fang Y, Lieberman B, Mellado B, Monnakgotla K, Ruan X and Xin S 2021 *Eur. Phys. J. C* **81** 365 (*Preprint 1912.00699*)
- [5] Crivellin A, Fang Y, Fischer O, Kumar A, Kumar M, Malwa E, Mellado B, Rapheeha N, Ruan X and Sha Q 2021 (*Preprint 2109.02650*)
- [6] Sirunyan A M *et al.* (CMS) 2021 *JHEP* **07** 027 (*Preprint 2103.06956*)
- [7] Aad G *et al.* (ATLAS) 2020 *Phys. Rev. Lett.* **125** 061802 (*Preprint 2004.04545*)
- [8] Sirunyan A M *et al.* (CMS) 2020 *Phys. Rev. Lett.* **125** 061801 (*Preprint 2003.10866*)
- [9] Sirunyan A M *et al.* (CMS) 2018 *JHEP* **09** 046 (*Preprint 1806.04771*)
- [10] Beck G, Kumar M, Malwa E, Mellado B and Temo R 2021 (*Preprint 2102.10596*)
- [11] Abi B *et al.* (Muon g-2) 2021 *Phys. Rev. Lett.* **126** 141801 (*Preprint 2104.03281*)
- [12] Aoyama T *et al.* 2020 *Phys. Rept.* **887** 1–166 (*Preprint 2006.04822*)
- [13] CMS Collaboration, CMS-HIG-20-013 (*Preprint 2206.09466*) URL <https://cds.cern.ch/record/2812784>
- [14] von Buddenbrock S, Chakrabarty N, Cornell A S, Kar D, Kumar M, Mandal T, Mellado B, Mukhopadhyaya B, Reed R G and Ruan X 2016 *Eur. Phys. J. C* **76** 580 (*Preprint 1606.01674*)
- [15] Alloul A, Christensen N D, Degrande C, Duhr C and Fuks B 2014 *Comput. Phys. Commun.* **185** 2250–2300 (*Preprint 1310.1921*)
- [16] Alwall J, Frederix R, Frixione S, Hirschi V, Maltoni F, Mattelaer O, Shao H S, Stelzer T, Torrielli P and Zaro M 2014 *JHEP* **07** 079 (*Preprint 1405.0301*)
- [17] Ball R D *et al.* (NNPDF) 2015 *JHEP* **04** 040 (*Preprint 1410.8849*)
- [18] Sjostrand T, Mrenna S and Skands P Z 2006 *JHEP* **05** 026 (*Preprint hep-ph/0603175*)
- [19] de Favereau J, Delaere C, Demin P, Giammanco A, Lemaître V, Mertens A and Selvaggi M (DELPHES 3) 2014 *JHEP* **02** 057 (*Preprint 1307.6346*)

# A study of top quark pair production in association with a high energy photon at the LHC

Thuso Mathaha<sup>1</sup>, Abhaya Kumar Swain<sup>1</sup>, Bruce Mellado<sup>1,2</sup>

<sup>1</sup>School of Physics and Institute for Collider Particle Physics, University of the Witwatersrand, Johannesburg, Wits 2050, South Africa

<sup>2</sup>iThemba LABS, National Research Foundation, PO Box 722, Somerset West 7129, South Africa

E-mail: 1144845@students.wits.ac.za

**Abstract.** We conducted a study of the ratio of the top quark pair in association with a photon to the top quark pair at the precision of NLO QCD predictions at the LHC with the top quark decay leptonically. This channel is selected because it provides a clean signal while limiting all the background contamination. The top quark pair production cross-section has been measured at LO and NLO in proton-proton collisions at  $\sqrt{s} = 13$  TeV. The events with exactly one electron and one muon, at least two jets, one of which is a b-tagged, are selected. Monte Carlo simulations at leading-order and next-to-leading-order accuracy are used to construct many relevant kinematic observables. These observables are the kinematic variables involving the photon, the angular separation between the two leptons, and the angular separation between the photon and leptons etc.

## 1. Introduction

The top quark is the heaviest known fundamental particle, with a mass  $m_t$  that is significantly greater than any of the other quarks and very close to the scale at which electroweak symmetry breaks. A crucial element of the Large Hadron Collider (LHC) physics program is the study of top quark production and decay characteristics. Top quarks are primarily produced from gluon-gluon fusion in quark-antiquark pairs ( $t\bar{t}$ ) and the precise prediction of the corresponding inclusive cross-section depends on both the top quark mass and the gluon parton distribution function (PDF). This poses a significant challenge for QCD calculational methods. The rate at which the top quark pair is produced can be enhanced in physics beyond the standard model (BSM). For evaluating the predictions of the Standard Model (SM) and its potential extensions, precise measurements of top-quark production are needed. Since its mass is at electroweak scale and in order to understand its electroweak interaction, the production of top-quark pair associated with a high-energy photon can be used to explore the  $t\gamma$  electroweak coupling. Additionally, the measurements of the cross-sections of these processes are particularly important since these topologies are delicate to BSM physics. Thus the purpose of this study can be broken into two parts, first is to provide a systematic analysis in the dilepton top quark decay channel for both processes;  $pp \rightarrow t\bar{t}$  and  $pp \rightarrow t\bar{t}\gamma$ , while we aim to find the most detailed NLO prediction for the cross section ratio. The second part is looking at potential correlations between the two processes in different regions of phase space in an effort to reduce any theoretical uncertainties, it will be feasible to determine whether differential cross section ratios have

improved predictive capacity for new physics searches. The ATLAS and CMS experiments at the LHC are actively driving top quark studies, which are crucial for understanding the basic interactions. The top quarks are dominantly produced in pairs at the LHC through strong interactions, although they can also be produced individually by electroweak interactions. The top quark therefore enables various testing of the underlying forces depending on the production mode. The measurements of top quark parameters, such as top quark mass, width, charge, total and differential cross sections, top quark spin correlations, and top quark charge asymmetry, including differential top quark charge asymmetries, are the main focus for both experiments.

The final state topologies in the top-quark pair production depend on the decay modes of the  $W$  bosons since the top quark decays  $\sim 99\%$  of the time in the SM to a  $W$  boson and a  $b$ -quark [1]. The channel with two leptons (electron and muon pair) with opposite electric charges referred to as  $e\mu$  channel is considered in this study because of the  $W$  boson decaying leptonically. This channel provides a clean signal and it contains less background contamination. The measurement of the top quark pair cross section has been measured at center of mass energy  $\sqrt{s} = 7, 8$  and  $13$  TeV [2, 3, 4] using the events with opposite-sign  $e\mu$  pair and one or two  $b$ -tagged jets. The CDF Collaboration presented the first evidence for the production of  $t\bar{t}$  in association with a high energy photon ( $t\bar{t}\gamma$ ) and the ATLAS Collaboration confirmed the observation of this process in proton-proton collisions at  $\sqrt{s} = 7$  TeV [5]. The top pair cross-section was measured by the ATLAS and CMS Collaborations at  $\sqrt{s} = 8$  TeV [6, 7]. The ATLAS Collaboration made the first measurements of the inclusive and differential cross sections at  $\sqrt{s} = 13$  TeV [8]. In this study were present a ratio measurement between the LO and NLO production of the top quark pair and top quark in association with a high energy photon. The ratio will be measured as a function of angular variables associated to the photon and the leptons together with angular separations between the two leptons in the event.

At  $\sqrt{s} = 8$  TeV, ATLAS has previously reported measurements of the absolute and normalized differential cross-sections as functions of the transverse momentum  $p_T^l$  ( $l = e, \mu$ ) and absolute pseudorapidity  $|\eta^l|$  of the single leptons. This also includes the transverse momentum  $p_T^{e\mu}$ , invariant mass  $m_{e\mu}$  and absolute rapidity  $|y^{e\mu}|$  of the  $e\mu$  system, the absolute azimuthal angle  $|\Delta\phi|$  amongst the two leptons in the transverse direction. These distributions were found to be typically well represented by predictions from next-to-leading order (NLO) fixed-order QCD computations and leading order (LO) multileg. In this study we intend to measure the above mentioned kinematic distributions using the two processes,  $t\bar{t}$  and  $t\bar{t}\gamma$  generated at LO and NLO, while selecting events with opposite sign  $e\mu$  and  $b$ -tagged.

The reason for selecting the  $e\mu$  channel is not only because of its clean final state with minor background contamination but also not requiring multivariate analysis technique to separate the signal and background processes. In order to compare the cross-sections with the theoretical calculation in Ref. [8], the cross-sections are also measured at the parton level rather than the particle level. The calculation represents the first comprehensive computation for  $t\bar{t}$  production with and without a hard final-state photon in hadronic collisions at NLO, taking into account all resonant and non-resonant diagrams, interferences, and off-shell effects of the top quarks and the  $W$  bosons.

## 2. Monte Carlo and Event selection

To generate event samples for both signal processes we use Monte Carlo (MC) generator Madgraph5 [9], interfaced with Pythia 8 [10] for parton showers. The detector simulation is performed using Delphes [11]. The NNPDF2.3LO PDF [12] set was used to produce more  $pp$  interactions that crossed through or were adjacent to bunch crossing. The  $t\bar{t}\gamma$  and  $t\bar{t}$  processes were gen-

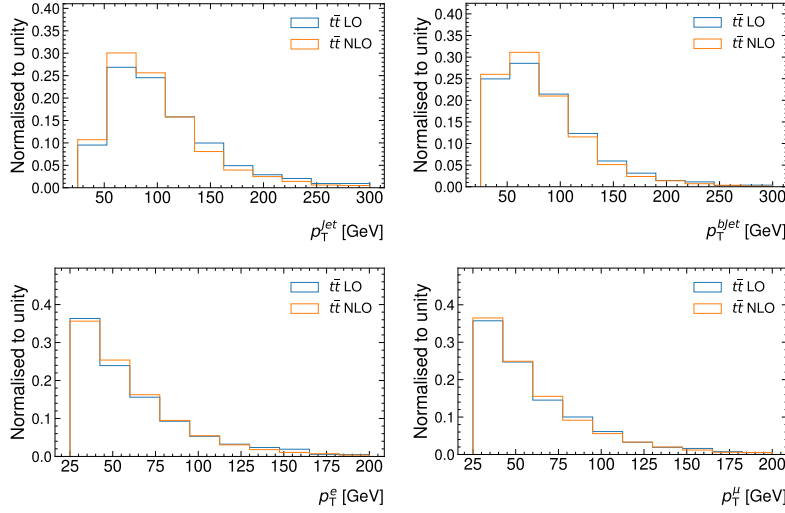


**Figure 1.** Distributions of the transverse momentum of jets and  $b$ -jets in the top row and the transverse momentum of electron and muon in the bottom row for  $t\bar{t}$  signal. The LO distributions are in blue and the NLO distributions are in orange.

erated independently at matrix-element level with and without a photon at both the LO and NLO in QCD.

The ATLAS detector collected the  $139 \text{ fb}^{-1}$  integrated luminosity data that was used in this analysis during the period of Run 2. The main physics objects taken into account in this study are photons, jets,  $b$ -jets, missing transverse momentum and leptons in the form of electrons and muons. With the assistance of reconstructed tracks in the ID system, the energy deposits in the electromagnetic calorimeter are used to reconstruct the electrons. They are chosen using a tight working point from a combined likelihood approach [13], and they must be separated based on the calorimeter and tracking quantities. The selected electrons must be within  $|\eta| < 2.5$  GeV and  $p_T > 25$  GeV. Muons are reconstructed using an algorithm that integrates the track segments from the muon spectrometer and the ID tracks. The same isolation criteria has been applied for muons and electrons in the track and calorimeter. Where the track must start from the primary collision vertex, muons that satisfy  $|\eta| < 2.5$  and  $p_T > 25$  GeV are selected.

Energy accumulated at the electromagnetic calorimeter's core is used to reconstruct photons. If the candidates match one or two reconstructed tracks that are compatible with coming from a photon conversion, they are selected. The selection requirements are met by photons with  $p_T > 25$  GeV and  $|\eta| < 2.37$ . Their energies are calibrated as shown in Ref. [14], and they are reconstructed and identified as described there. The anti- $k_t$  algorithm is used with the topological cluster of cells in the calorimeter to reconstruct jets [15] with a distance  $\Delta R \leq 0.4$  [16]. The selected jets need to have  $p_T > 25$  GeV and  $|\eta| < 2.5$ . By using the  $b$ -jets tagging algorithm (MV2c10) [17] to the jets,  $b$ -quark hadronization jets known as  $b$ -tagged jets are identified. The MV2c10 algorithm is a multivariate discriminant that makes use of the track impact parameters and secondary vertices. The selection criteria for both signal processes employed in this study are the same, except for  $t\bar{t}\gamma$  there is an extra requirement; events must contain at least one photon that meets the aforementioned photon criterion. The generated samples are examined through the comparison of distributions as shown in Figure 1 for  $t\bar{t}$  process and Figure 2 for  $t\bar{t}\gamma$  process.

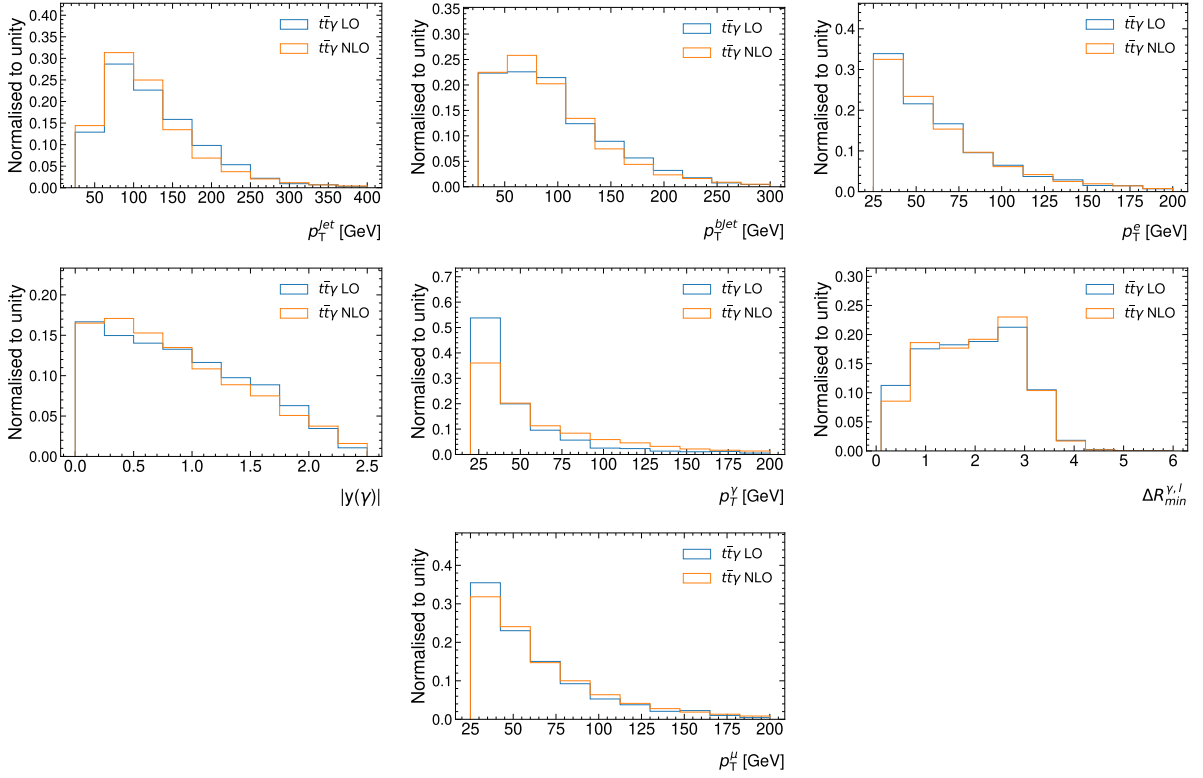


**Figure 2.** Distributions of the transverse momentum of jets,  $b$ -jets and electron in the 1<sup>st</sup> row. The 2<sup>nd</sup> row is the distributions of the rapidity of the photon, transverse momentum of the photon and the separation in the rapidity-azimuthal angle plane between a photon and a lepton for  $t\bar{t}\gamma$ . The transverse momentum of the muon is in the 3<sup>rd</sup> row. The LO distributions are in blue and the NLO distributions are in orange.

### 3. Results

At the center-of-mass energy of  $\sqrt{s} = 13$  TeV for Run II of the LHC, the distributions for the  $pp \rightarrow t\bar{t}$  and  $pp \rightarrow t\bar{t}\gamma$  processes were determined. We find the dominant partonic subprocesses is useful for determining the correlations and any differences between the two production processes. The scattering of two gluons contributes 79% (88%) of the LO  $pp \rightarrow t\bar{t}$  ( $pp \rightarrow t\bar{t}\gamma$ ) cross section, while the quark antiquark makes up the remaining portion 21% (12%) [18]. The kinematics of the final states in  $pp \rightarrow t\bar{t}$  and  $pp \rightarrow t\bar{t}\gamma$ , with two charged leptons, their transverse momentum and  $b$ -tagged jets, should be similar due to the domination of the  $gg$  production process in both instances. The NNPDF2.3 set has been used for all of the differential cross sections that are shown in the following. For both production processes, we use the kinematic-independent renormalization and factorizationscales  $\mu_R = \mu_F = \mu_0$  with the central value  $m_t$  since both processes are comparable from the perspective of QCD, as indicated by the kinematic distributions in figure 1 and 2. In order to highlight shape similarities and differences between the two processes, the distributions are normalized to unity. The distributions do not significantly change between the two processes although in some kinematic variables we do see change. This is because  $gg$  production predominates, favoring jet emissions at slower rates [18].

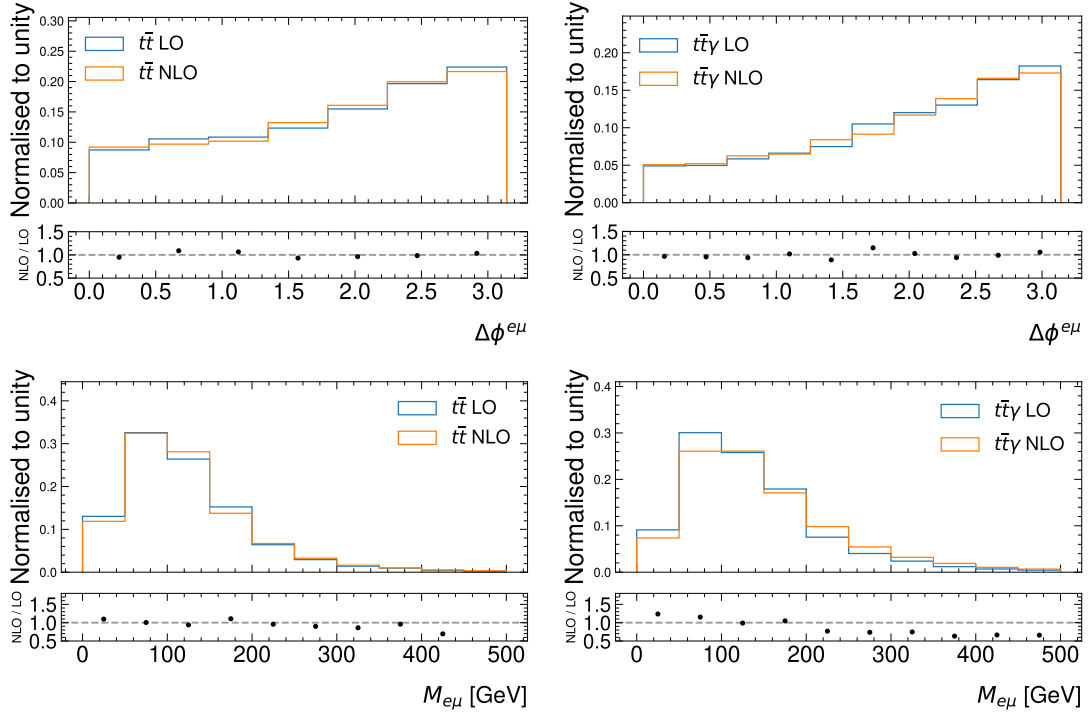


**Figure 3.** Distributions of  $\Delta\phi^{e\mu}$  in the top row and the invariant mass of the two leptons in the bottom row. The are also accompanied by the ratio plots of NLO to LO distributions.

### 3.1. Ratio of cross-section

We would like to see if the theoretical forecasts accuracy can be improved. We also wish to examine whether theoretical uncertainties rely on certain fixed scales. The cross-section ratio equations (Eqn 1 and 2) will be used to describe any deviations between the LO and NLO processes. Ratio of both processes are calculated using the total cross section measured at LO and NLO matrix element.

$$\mathfrak{R}_{LO} = \frac{\sigma_{t\bar{t}\gamma}}{\sigma_{t\bar{t}}} = \frac{0.2298}{59.9} = 0.0038 \quad (1)$$

$$\mathfrak{R}_{NLO} = \frac{\sigma_{t\bar{t}\gamma}}{\sigma_{t\bar{t}}} = \frac{0.2489}{76.54} = 0.0033 \quad (2)$$

To be more precise, we want to see if the theoretical uncertainties for the fixed scale choice can be maintained to around 10%. On the other hand, we would want to examine if a few percent precision, or accuracy similar to that of NNLO calculations for  $t\bar{t}$  production, can be attained in the case of the dynamical scale choice used in this study. From an experimental standpoint, measurements in the regions of phase space defined by selection cuts that closely mimic detector response are more appropriate, simply because such measurements do not introduce extra uncertainties due to model-dependent extrapolations to parton level of  $t\bar{t}$  objects and to the regions of phase space outside the detector sensitivity. Reduced final state decay products paired with photon emission from charged leptons and  $b$ -jets drastically alter the ratio. Figure 3 displays the ratio of NLO to LO as a function of the azimuthal angle shift and the invariant mass of two leptons in the  $e\mu$  channel. According to the ratio plots in Figure 3, the products at LO and NLO do not differ much from one another, with the exception of higher momentum values for  $t\bar{t}$  process, particularly for the invariant masses of the two charged leptons. Precise

generations of  $t\bar{t}$  and  $t\bar{t}\gamma$  at high order are expected to reduce the discrepancies seen at high momentum values.

#### 4. Conclusion

The main objective of this work is to get more accurate theoretical predictions for top quark pair  $t\bar{t}$  production in the di-lepton channel. In order to achieve this, meaningful cross-section ratios for  $t\bar{t}$  and  $t\bar{t}\gamma$  production have been investigated using completely realistic NLO simulations. These cross sections are based on LO and NLO matrix components for the  $2\rightarrow 6$  and  $2\rightarrow 7$  production processes, which contain interference for all top quark and W boson interactions. It is believed that different parton distribution functions are expected to measure the cross section precisely and in this study we have only considered one parton distribution function named NNPDF3.0 pdf collection. Other pdf sets can be examined in future studies to enhance the cross-section measurements, which might reduce the discrepancy between the two LO and NLO process generation.

#### References

- [1] Tanabashi M, Hagiwara K and Hikasa K (Particle Data Group) 2018 *Phys. Rev. D* **98**(3) 030001 URL <https://link.aps.org/doi/10.1103/PhysRevD.98.030001>
- [2] Collaboration A *et al.* 2014 *arXiv preprint arXiv:1406.5375*
- [3] Collaboration A 2016 *Eur. Phys. J. C* **76** 642
- [4] Avdeeva E, Bartek R, Dominguez A, Fangmeier C, Gonzalez Suarez R, Kamalieddin R, Kravchenko I, Malta Rodrigues A, Meier F, Monroy J *et al.* 2017
- [5] Aad G, Abbott B, Abdallah J, Khalek S A, Aben R, Abi B, Abolins M, AbouZeid O, Abramowicz H, Abreu H *et al.* 2015 *Physical review D* **91** 072007
- [6] Demir D A, Collaboration C *et al.* 2011 *European Physical Journal C*
- [7] Aguilar-Saavedra J A 2018 *The European Physical Journal C* **78** 1–8
- [8] Berlendis S, Cheu E, Delitzsch C, Johns K, Jones S, Lampl W, LeBlanc M, Leone R, Loch P, Nayyar R *et al.* 2019
- [9] Alwall J, Herquet M, Maltoni F, Mattelaer O and Stelzer T 2011 *Journal of High Energy Physics* **2011** 1–40
- [10] Sjöstrand T, Ask S, Christiansen J R, Corke R, Desai N, Ilten P, Mrenna S, Prestel S, Rasmussen C O and Skands P Z 2015 *Computer physics communications* **191** 159–177
- [11] De Favereau J, Delaere C, Demin P, Giammanco A, Lemaitre V, Mertens A and Selvaggi M 2014 *Journal of High Energy Physics* **2014** 1–26
- [12] Pumplín J, Stump D R, Huston J, Lai H L, Nadolsky P and Tung W K 2002 *Journal of High Energy Physics* **2002** 012
- [13] collaboration A *et al.* 2011 *arXiv preprint arXiv:1110.3174*
- [14] Aad G, Aggarwal A, Caron S, Colasurdo L, Fabiani V, Gottardo C, Ilic N, König A, Pedraza Diaz L and Schouwenberg J 2019
- [15] Collaboration A *et al.* 2015 Properties of jets and inputs to jet reconstruction and calibration with the atlas detector using proton–proton collisions at  $\sqrt{s}=13$  tev Tech. rep. ATL-PHYS-PUB-2015-036
- [16] Cacciari M, Salam G P and Soyez G 2008 *Journal of High Energy Physics* **2008** 063
- [17] Collaboration A *et al.* 2018 *arXiv preprint arXiv:1805.01845*
- [18] Bevilacqua G, Hartanto H, Kraus M, Weber T and Worek M 2019 *Journal of High Energy Physics* **2019** 1–29

# Kernel Density Estimation-based simulation of Monte-Carlo events at LHC

Nidhi Tripathi<sup>1</sup>, Salah-Eddine Dahbi,<sup>1</sup> Abhaya Kumar Swain<sup>1</sup>, Xifeng Ruan<sup>1</sup>, Bruce Mellado<sup>1,2</sup>

<sup>1</sup>School of Physics and Institute for Collider Particle Physics, University of the Witwatersrand, Johannesburg, Wits 2050, South Africa

<sup>2</sup>iThemba LABS, National Research Foundation, PO Box 722, Somerset West 7129, South Africa

E-mail: [nidhi.tripathi@cern.ch](mailto:nidhi.tripathi@cern.ch)

**Abstract.** We have developed a machine learning-based generative model to estimate the kernel density of the data using the Gaussian kernel and then have generated additional samples from this distribution. This model uses scikit-learn to generate a list of particle four-momenta from the proton-proton collisions produced at the Large Hadron Collider (LHC). We demonstrate the ability of this approach to reproduce a set of kinematic features, that are used for the search for new resonances decaying to  $Z\gamma$ , final states at the LHC. This model is constructed to take the pre-processed  $Z\gamma$  events and generate sample data with accurate statistics mimicking the original distributions and achieving better performances compared to the standard event Monte-Carlo generators.

## 1. Introduction

In the modern era, machine learning generative models are a widely used technology around the world for synthetic data generation. A team of high energy physicist uses these techniques to increase the efficiency of data analysis and event generation at Large Hadron Collider (LHC) [1]. Variational Auto Encoders (VAE) [2, 3] and Generative Adversarial Networks (GAN) [4] are two widely used fast simulation deep generative algorithms in HEP. They two models illustrate the process of generating simulated events more rapidly and precisely reproduce the sample data distribution. However, focus of GAN and VAE is to generate data mostly in image form. These models are difficult to train and need a large amount of data for the purpose [5].

In this paper we investigate the performance of a non-deep machine learning model based on Kernel Density Estimation (KDE) [6], which is a well-known method for density estimation. This model, whose traditional name was the Parzen-Rosenblatt Windows method, learns the distribution of events in a non-parametric manner. The model estimates the density of real data distribution and generates sample data out of that distribution [7].

At the LHC, the ATLAS [8] and CMS experiments made the Higgs boson discovery in 2012 [9, 10]. Many experiments, including those at the LHC, are now devoted to search for direct evidence of physics beyond the Standard Model (SM) in the wake of this finding. The experimental results allow for a better understanding of the SM's limitations, which is a theoretical model developed to understand elementary particles and their interactions [11]. Most of the experiments at the LHC depend on Monte Carlo (MC) simulator for data generation,

which is a time consuming and CPU expensive process. Machine learning based generative models has been integrated with MC generators accelerate the efficiency of generating simulated events. The High-Luminosity Large Hadron Collider (HL-LHC) projects are aimed to increase the luminosity in the future. As a result, it will increase the demand of machine learning based generative models to handle the challenge.

## 2. Method

In this paper we chose KDE for our study because it is a non-parametric methodology that necessitates no previous assumption of a distribution function for probabilities and relies on only one parameter, known as bandwidth, to accurately estimate the density. Usually small tabular data sets requires simple modeling methods based on density estimation. There are numerous density estimation methods, such as KDE [12] the Gaussian mixture model [13], and copulas [14].

### 2.1. Kernel density estimation

To find the shape of the estimated density function, we generate a set of points equidistant from each other and estimate the kernel density at each point. Kernel Density is a non-parametric technique for determining the probability density function of a random sample  $(x_1, x_2, \dots, x_n)$  from a distribution with unknown density function  $f(x)$ . The kernel density estimation is defined as follows:

$$p(x) = \frac{1}{nh} \sum_{j=1}^n K \left( \frac{x - x_j}{h} \right) \quad (1)$$

where  $h$  is the bandwidth parameter that enforces the smoothness of density estimation. The only parameter that impacts the model's accuracy is bandwidth [15, 16]. This model learns the density of the given data and generates synthetic data based on the same distribution. To generate synthetic data, we used the python libraries scikit-learn and NumPy, which implement the Ball Tree or KD Tree algorithm [17]. KDE can be implemented in any dimension, however, its performance degrades at high dimensionality. Which is known as the curse of dimensionality. The scikit-learn library allows cross-validation tuning of the bandwidth parameter to obtain the best model and returns the parameter value that maximizes the log-likelihood of data. GridSearchCV is the function we can use to accomplish this, and it requires different bandwidth parameter values [17].

### 2.2. Dataset

The  $Z_\gamma$  SM MC samples used in this analysis have been generated using Madgraph5 [18] and the detector level simulation is performed using Delphes(v3) [19]. The MC-simulated Higgs Boson signal used in this study for analysis purpose. The analysis focuses around the centre of mass of 150 GeV ( $132 \text{ GeV} < m_{U\gamma} < 168 \text{ GeV}$ ). The simulated  $Z_\gamma$  background data was used, Higgs-like heavy scalar decaying to  $Z_\gamma$  ( $pp \rightarrow H \rightarrow Z_\gamma$ ) events, where  $Z \rightarrow e^+e^-$  or  $Z \rightarrow \mu^+\mu^-$ . The kinematic features used in the study are  $Z_\gamma$  invariant mass  $m_{\ell\ell\gamma}$ , the transverse momentum, azimuthal angle, pseudo-rapidity and energy of the leading lepton, sub-leading lepton and photon respectively,  $P_{t_{\ell_1|\ell_2|\gamma}}$ ,  $\Phi_{\ell_1|\ell_2|\gamma}$ ,  $\eta_{\ell_1|\ell_2|\gamma}$ ,  $E_{\ell_1|\ell_2|\gamma}$ , missing transverse energy  $E_T^{miss}$  and it's azimuthal angle  $\Phi_{E_T^{miss}}$ , the number of jets  $N_j$ , the number of central jets  $N_{cj}$ ,  $\Delta R_{\ell\ell}$  ( $\Delta R \equiv \sqrt{(\Delta\eta)^2 + (\Delta\phi)^2}$ ),  $P_{t\ell\ell}/m_{\ell\ell\gamma}$ ,  $\Delta\Phi_{\ell\ell}$ , and  $\Delta\Phi(E_T^{miss}, Z_\gamma)$ .

## 3. Results

Colab, a free Jupyter notebook environment, was used to run the model, which is powered by an NVIDIA Tesla K80 GPU. A generative model is built using the Scikit-learn and NumPy libraries

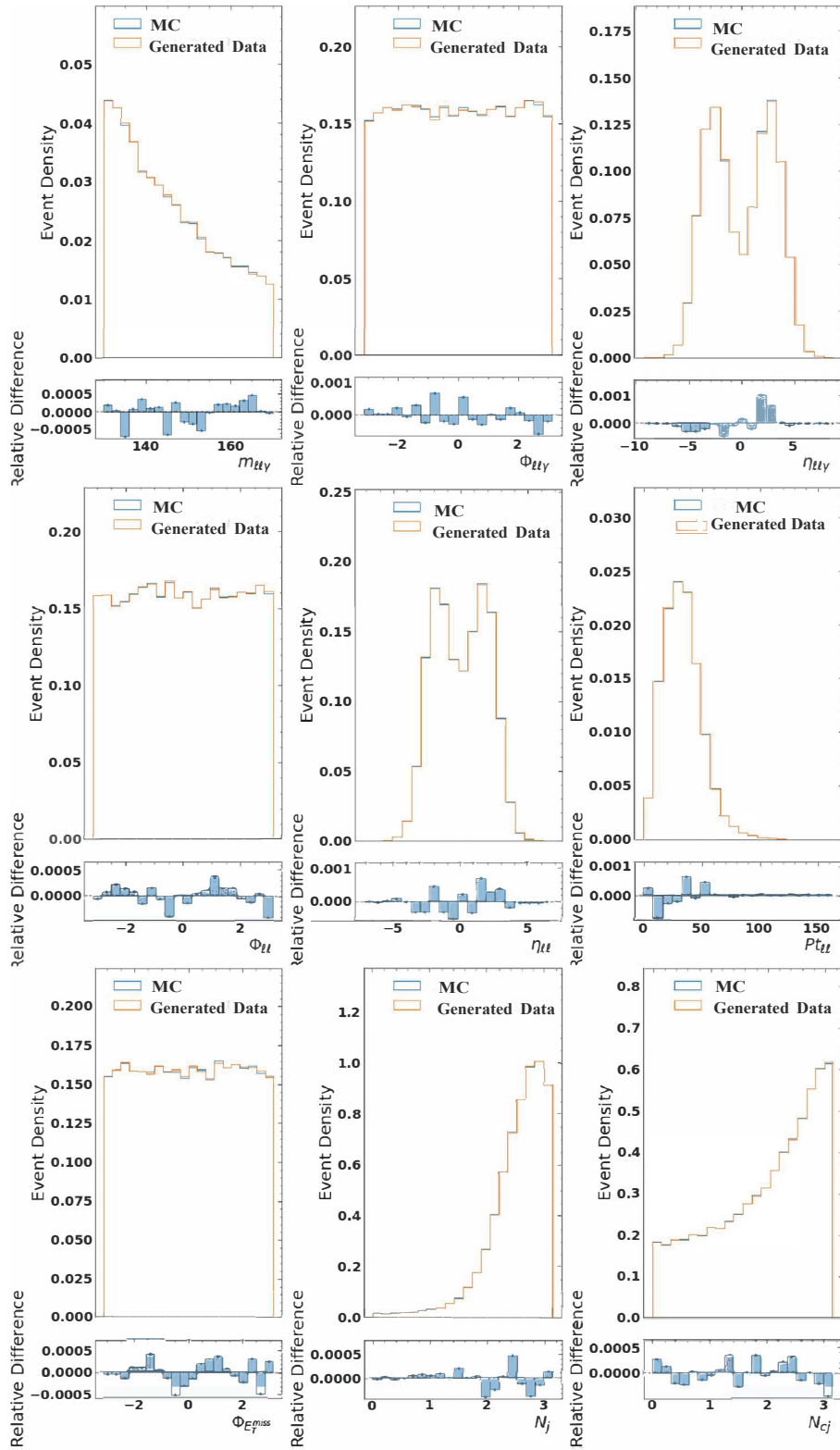


**Figure 1.** Plots comparing Monte Carlo (MC) and generated data from the  $Z\gamma$  data set based on the best selected hyper parameter. Blue and orange plots depict MC and generated data, respectively. The blue columns beneath the data plots show the relative difference ratio.

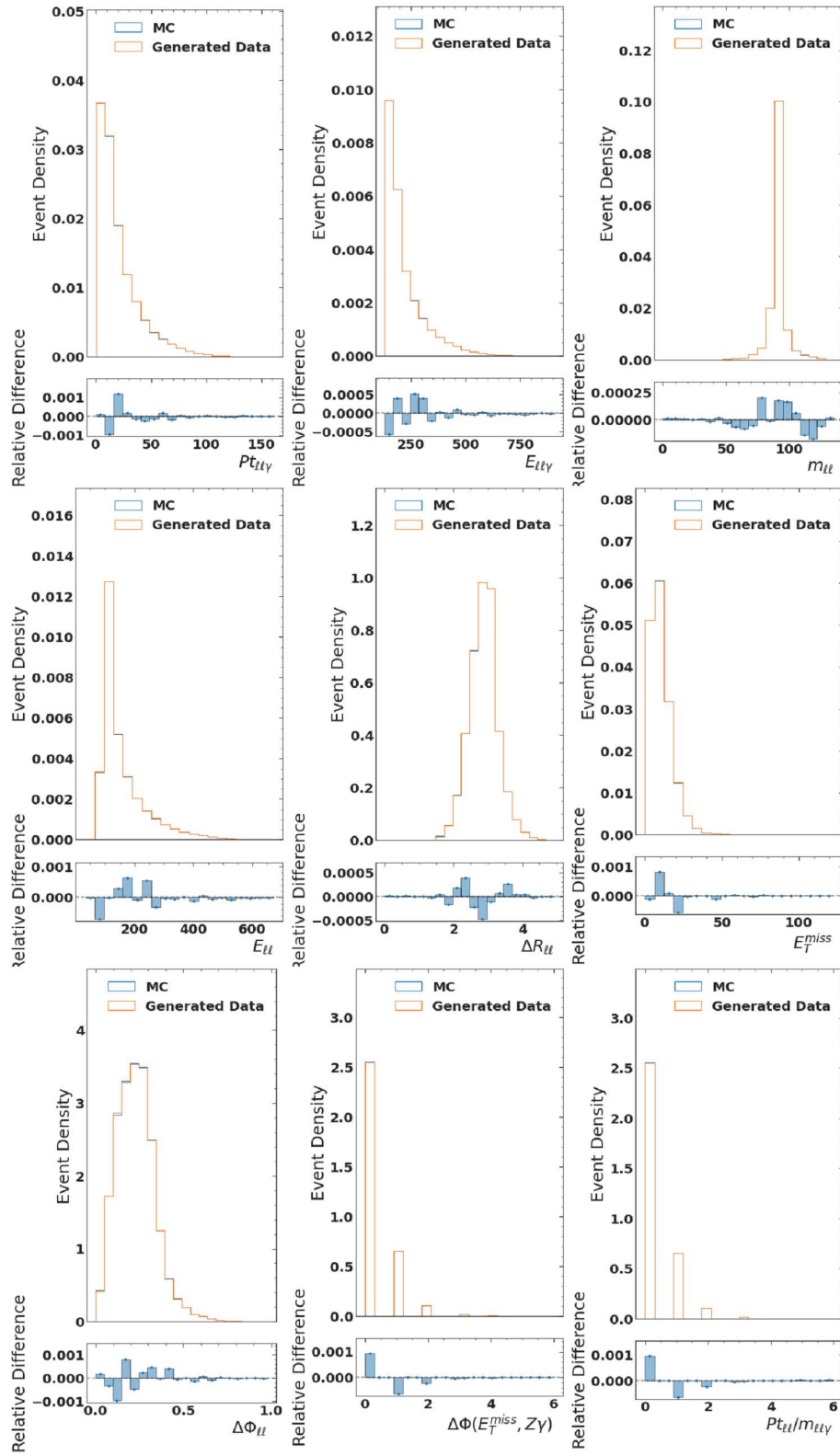


**Figure 2.** Plots comparing Monte Carlo (MC) and generated data from the  $Z\gamma$  data set based on the best selected hyper parameter. Blue and orange plots depict MC and generated data, respectively. The blue columns beneath the data plots show the relative difference ratio.

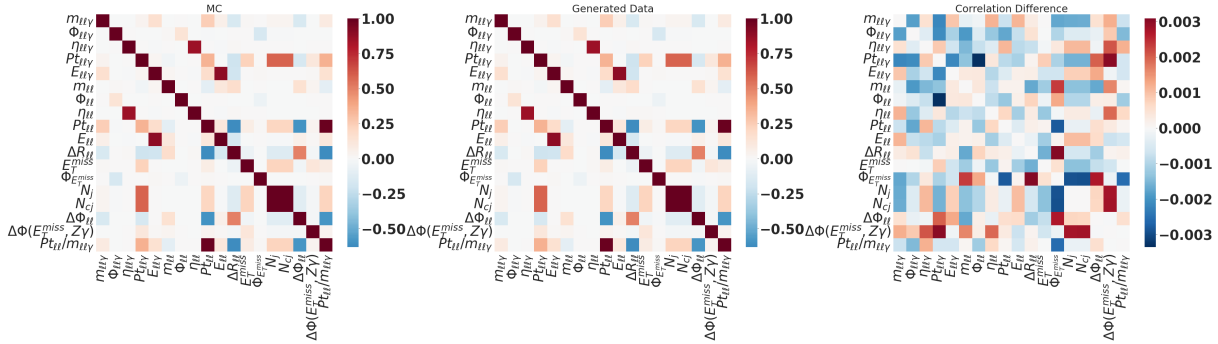


**Figure 3.** Comparison of correlation heatmap plots for Monte Carlo, synthetic data, and the correlation difference between  $Z\gamma$  data sets. The plots indicate a good correlation.

to take pre-processed  $Z\gamma$  data and generate data with accurate statistics that mimic MC data samples from the ATLAS experiment. All the features of both generated and MC data has been compared with their corresponding local relative difference in Figures 1 and 2. The results show that generated model works reasonably and it is able to mimic the real MC samples with a local relative difference that fluctuates between 0.25% and 0.5%. The features correlation heat-map plots for Monte Carlo, generated data, and the correlation difference between  $Z\gamma$  data sets is visualised in, Figure 3.

#### 4. Conclusion

The study presented in this paper describe the performance of Kernel Density Estimation generated synthetic data. The results show that our model generates synthetic data reasonably well. Further efforts are being made to improve the model's consistency and correlation.

#### References

- [1] Dittmaier S, Mariotti C, Passarino G, Tanaka R, Baglio J, Bolzoni P, Boughezal R, Brein O, Collins-Tooth C, Dawson S *et al.* 2011 *arXiv preprint arXiv:1101.0593*
- [2] Kingma D P and Welling M 2013 *arXiv preprint arXiv:1312.6114*
- [3] Rezende D J, Mohamed S and Wierstra D 2014 Stochastic backpropagation and approximate inference in deep generative models *International conference on machine learning* (PMLR) pp 1278–1286
- [4] Goodfellow I, Pouget-Abadie J, Mirza M, Xu B, Warde-Farley D, Ozair S, Courville A and Bengio Y 2014 *Advances in neural information processing systems* **27**
- [5] Gramacki A 2018 *Nonparametric kernel density estimation and its computational aspects* vol 37 (Springer)
- [6] Kamalov F 2020 *Information Sciences* **512** 1192–1201
- [7] Fowler E E, Berglund A, Schell M J, Sellers T A, Eschrich S and Heine J 2020 *Journal of biomedical informatics* **105** 103408
- [8] Aad G *et al.* (ATLAS) 2012 *Phys. Lett. B* **716** 1–29 (*Preprint 1207.7214*)
- [9] Chatrchyan S *et al.* (CMS) 2012 *Phys. Lett. B* **716** 30–61 (*Preprint 1207.7235*)
- [10] Higgs P W 1964 *Physical Review Letters* **13** 508
- [11] Vannerem P, Müller K R, Schölkopf B, Smola A and Soldner-Rembold S 1999 *arXiv preprint hep-ex/9905027*
- [12] Plesovskaya E and Ivanov S 2021 *Procedia Computer Science* **193** 442–452
- [13] Chokwitthaya C, Zhu Y, Mukhopadhyay S and Jafari A 2020 Applying the gaussian mixture model to generate large synthetic data from a small data set *Construction Research Congress*
- [14] Tang X S, Li D Q, Cao Z J and Phoon K K 2017 *Computers and Geotechnics* **87** 229–240
- [15] Scott D W 2015 *Multivariate density estimation: theory, practice, and visualization* (John Wiley & Sons)
- [16] Silverman B W 2018 *Density estimation for statistics and data analysis* (Routledge)
- [17] Pedregosa F, Varoquaux G, Gramfort A, Michel V, Thirion B, Grisel O, Blondel M, Prettenhofer P, Weiss R, Dubourg V, Vanderplas J, Passos A, Cournapeau D, Brucher M, Perrot M and Duchesnay E 2011 *Journal of Machine Learning Research* **12** 2825–2830

- [18] Alwall J, Frederix R, Frixione S, Hirschi V, Maltoni F, Mattelaer O, Shao H S, Stelzer T, Torrielli P and Zaro M 2014 *Journal of High Energy Physics* **2014** 1–157
- [19] Mandrik P, theFCC study group *et al.* 2019 Prospect for top quark fnc searches at the fcc-hh *Journal of Physics: Conference Series* vol 1390 (IOP Publishing) p 012044

# Search for resonant production of strongly-coupled dark matter in proton-proton collisions

**Hannah van der Schyf**

School of Physics, University of Witwatersrand, 1 Jan Smuts Avenue, Braamfontein, Johannesburg, 2000, South Africa

E-mail: 1586749@students.wits.ac.za

**Abstract.** A search for semi-visible jets arising from dark matter, using Run 2 data recorded with the ATLAS detector at the LHC with a center-of-mass energy of 13 TeV is presented. For this search the hidden sector is hypothesized to couple to the standard model (SM) via a heavy leptophobic  $Z'$  mediator via a resonant production  $q\bar{q} \rightarrow Z' \rightarrow \chi\chi$ . Semi-visible jets present an unusual topology, where the visible states in the shower are standard model hadrons and the strongly coupled hidden sector contains dark quarks which result in dark hadrons. This gives a final state consisting of a jet aligned with missing transverse energy due a mixture of stable, invisible dark hadrons and visible hadrons from an unstable subset of dark hadrons that promptly decay to SM particles. The resonant production and decay of such a mediator will result in a dijet system of semi-visible jets, a signature ignored by most dark matter searches.

## 1. Introduction

The study of particle physics is focused on our understanding of elementary particles and the means by which they interact. The Standard Model of particle physics describes the fundamental particles and their interactions, and has so far been highly consistent with experimental data. This sophisticated model gives a complex explanation of 17 fundamental particles in nature, from the vector ( $g, \gamma, W, Z$ ) and scalar ( $H$ ) bosons to the three generations of fermions (quarks and leptons) [1]. Despite this the Standard Model is incomplete as it does not give a truly sufficient description of the universe. As such, it would not be unreasonable to suspect the existence of new physics at the energy scales explored at the LHC.

One enduring question we have long been faced with is dark matter, it is well known that dark matter is an obscure and mysterious highly gravitational substance whose evidence is undeniable. Dark matter does not interact with normal matter yet the mere existence of galaxies and the occurrence of gravitational lensing, its presence is indisputable. Dating back to the 1930's there have been theories postulating the existence of dark matter, expressing the curiosity of an unknown form of non-baryonic matter influencing the structure of the universe. Over decades of questioning and observing there has been indirect evidence through astrophysical and cosmological studies such as those of the cosmic microwave background (CMB) [2].

Over time there has been an growing interest in dark matter and recent years have seen an increase in searches exploring the dark sector, yet there is still no direct evidence of dark matter. There is no suitable particle in the standard model which fits the role of dark matter and with it making up 27% of the universe, the exploration of dark matter a necessity in furthering our understanding of physics. In general most dark matter searches at the Large Hadron Collider

(LHC) are focused on Weakly Interacting Massive Particles (WIMPs). Since standard searches are yet to yield substantial evidence, there are a number of phenomenological papers exploring the possibility of approaching the dark sector through unique collider topologies.

Alternative scenarios for dark matter are hidden valley theories[3] which propose dark sectors with potentially multiple new particles and new forces which are decoupled from the SM except for the mediator particles. The dark sector may contain a new confining force analogous to that of quantum chromodynamics (QCD) in the SM. These models are of interest as they are relatively unexplored experimentally but may present a range of novel kinematic signatures as they generate dark showers [4].

There are a number of considerations which may motivate the search for strongly-coupled dark sectors at the LHC. Because of baryon asymmetry an abundance of visible matter arises, this may be the case for dark matter as well, where a similar mechanism may explain the abundance of dark matter observed in our universe [5]. Cosmological measurements of the dark matter density have been identified to be similar to visible matter, however, approximately five times larger [6]. This points to the idea that dark matter may consist of composite particles, and in some scaled the new confining force, referred to as dark QCD, may have a relation to SM QCD [7], which favours scales of the order of 10 GeV and in the TeV scale for the mediator mass. In general terms, these models have the ability to produce the correct DM relic density[8].

## 2. Semi-Visible Jets

In this preceeding a search for semi-visible jets is performed, where semi-visible jets are jet-like collider objects, and the visible states in the shower are Standard Model hadrons, and the strongly coupled hidden sector contains dark quarks. These dark quarks decay and hadronize to stable and unstable quarks. The unstable quarks then decay to SM quarks, giving a final state jet aligned with missing energy. The dark sector contains many flavours of dark quarks ( $\chi_1, \chi_2, \chi_3, \dots$ ) which form bound states referred to as dark hadrons, and these dark hadrons may be stable or unstable. The unstable dark hadrons decay promptly to SM quarks, however the stable dark hadrons are the DM candidates and pass the detector without interacting. This leads to a collimated mixture of visible and invisible particles, which are termed as semi-visible jets. Thus, the signature will be a pair of jets where if the jets are aligned to the missing transverse energy, and the amount of missing transverse energy is expected to be moderate, because both of the jets contain visible particles, meaning that a portion of the transverse component of the overall MET will cancel out when the jets are produced back to back.

The number of dark-matter particles produced in the shower impacts the amount of missing transverse energy, this effect is parametrised by the fraction of stable and unstable invisible dark hadrons, given by  $r_{inv} = N_{stable}/N_{total}$  [9]. The paramter  $r_{inv}$  can have a value between 0 and 1 and since events containing jets aligned with missing transverse momentum are explicitly rejected from the signal regions of existing collider DM searches, a large portion of the parameter space of this model has not yet been covered, in particular events with intermediate values of  $r_{inv}$ .

Current DM searches are more sensitive to dark sector models having an  $r_{inv} \approx 1$  yielding events having high missing energy and some initial-state radiation [10]. Note that current dijet searches favour dark sector models having  $r_{inv} \approx 0$ , which yield events having two jets but low missing energy [11]. Thus this search supplements these efforts. We consider the resonant production process where two quarks decay to a leptophobic  $Z'$  boson mediator giving two dark quarks,  $q\bar{q} \rightarrow Z' \rightarrow \chi\chi$  [9]. The leptophobic  $Z'$  boson mediator arises from broken a U(1) symmetry, with couplings to SM quarks  $g_q$  and dark quarks  $g_\chi$ . The leptophobic  $Z'$  gauge boson couples to the SM baryon current  $J_{SM}^\mu$ [12]:

$$\mathcal{L} \supset \frac{1}{4} Z'^{\mu\nu} Z'_{\mu\nu} - \frac{1}{2} M_{Z'}^2 Z'_\mu Z'^\mu - g_{Z'}^{SM} Z'_\mu J_{SM}^\mu. \quad (1)$$

The  $Z'$  gauge boson is responsible for linking the dark and visible sector, producing the  $Z'$  portal [13]. As mentioned, the  $Z'$  mediator arises from a U(1) symmetry breaking, and the simulated signal samples are passed through a hidden valley model, where by the one employed for this search is based on Ref [12]. The SM jets then arise from a multi-step process; the dark quarks shower and hadronize in the dark sector and the unstable dark hadrons then decay promptly to SM quarks, and finally the SM quarks shower and hadronize visibly. Since the SM quarks are much less massive than the dark hadrons, they are produced in the intermediate decay step with a much higher relative momentum because the SM particle showers to spread out. Thus the jets are expected to be wider than typical SM jets.

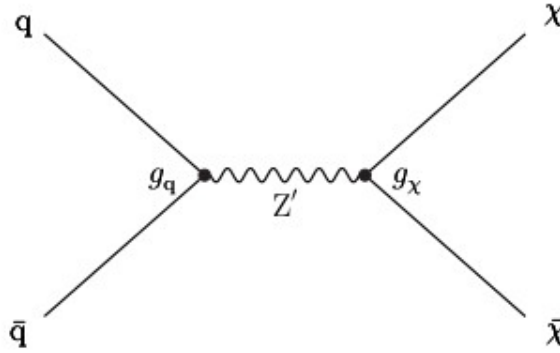


**Figure 1.** Feynman diagram of the leading-order resonant production of dark quarks through a  $Z'$  mediator, with relevant couplings to SM quarks ( $g_q$ ) and dark quarks ( $g_\chi$ ) indicated at the vertices.

The cross section  $\sigma_{Z'}$  is determined by the mediator mass  $m_{Z'}$  and the SM coupling  $g_q$ , but the branching fraction  $\mathcal{B}_{dark} = \mathcal{B}(Z' \rightarrow \chi\chi)$  depends on both couplings  $g_q$  and  $g_\chi$  [9], and the production rate is defined as  $r_{Z'} = \sigma_{Z'} \mathcal{B}_{dark}$ . For  $\mathcal{B} \approx 100\%$ , we assume  $g_\chi \gg g_q$ , where the dark gluon is the dark QCD force carrier, binding the dark quarks into dark hadrons. These may be vectors ( $\rho$ ) or pseudoscalars ( $\pi$ ).

The stable dark hadrons are  $(\pi_{dark}^{DM})$  and  $(\rho_{dark}^{DM})$  and the unstable dark hadrons are  $(\pi_{dark})$  and  $(\rho_{dark})$ , respectively. The dark hadrons are assumed to be degenerate in mass having a small scale  $m_{dark}$ . The dark QCD force coupling strength,  $\alpha_{dark}$ , is an undetermined parameter which primarily influences the dark shower dynamics, where it modifies the transverse momentum  $p_T$  as well and multiplicity of the dark hadrons, as well as the width of the resulting particle shower. The invisible fraction  $r_{inv}$  is a varied parameter, where in previous theories the variation of this fraction has not been considered, making this the most novel parameter.

### 3. Analysis Strategy and Signal Selection

In this search a benchmark model the leptophobic  $Z'$  boson having a mass of 1500 GeV is chosen, the jets are reconstructed using the anti- $k_t$ 10 algorithm and the fraction of stable vs invisible dark hadrons in this case is 0.3. The signal generation is done using MadGraph [14] for the matrix element, and Pythia8 [15] for shower and hadronisation using the hidden valley model, as it uses dark sector showering. For our signal selection, since for our final state is jets we require a lepton veto of no electrons or muons with transverse momentum  $p_T > 7$  GeV, as the detector cannot distinguish at low  $p_T$  values. The leading jet transverse momentum must be greater than 250 GeV, without this selection there are too many initial-state radiation jets polluting the topology. Since we will have a jet aligned with the MET, we require that the  $\Delta\phi$  between the missing energy (MET) and the closest jet must be less than 2, and we require

that the number of b-jets are less than 2. The signal has two jets produced back to back both containing invisible particles, the semi-visible jet (svj) is chosen as the jet closest to the MET.

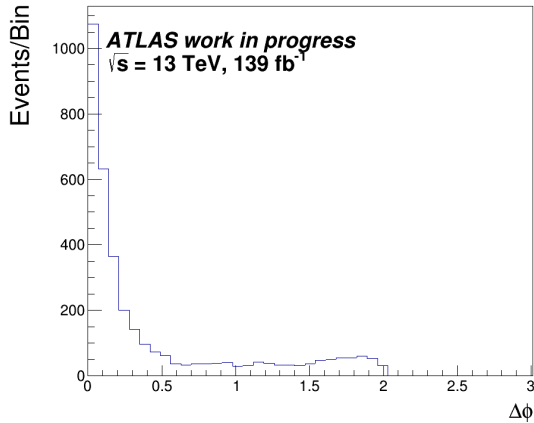


**Figure 2.** The  $\Delta\phi$  between the closest jet and MET which selects the svj.

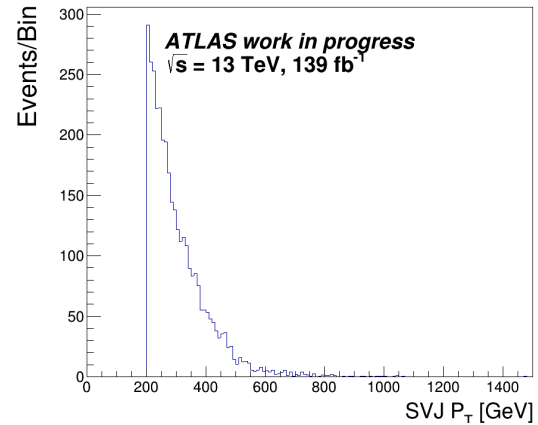


**Figure 3.** The  $p_T$  distribution of the svj.

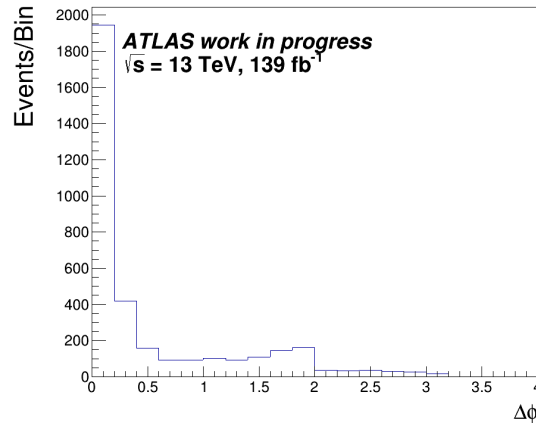


**Figure 4.** The  $\Delta\phi$  between the subleading jet and MET.

It is interesting to note that for most cases considered, the subleading jet is tagged as the svj, as shown in Figure 4. The anti-svj is jet produced back to the svj, which is thus the jet farthest from the MET. Again we see that in most cases the leading jet is tagged as the anti-svj as shown in Figure 6.

The goal is to construct the resonant mass peak accounting for the invisible fraction, Figure 11 shows the invariant mass of the leading and sub-leading jet mass without accounting for the invisible fraction, where the mass peak is around 800 GeV and not the 1500 GeV mass of the mediator  $Z'$  boson.

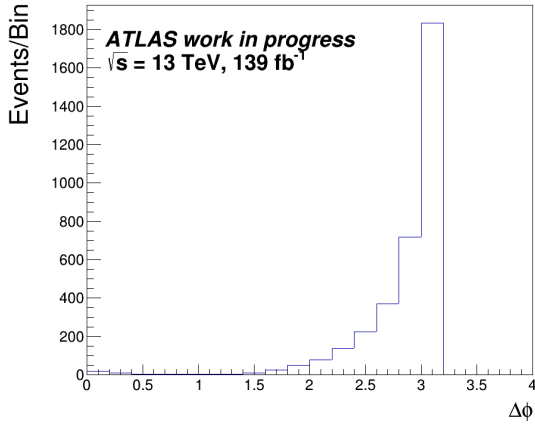


**Figure 5.** The  $\Delta\phi$  between the farthest jet and MET, which selects the anti-svj.

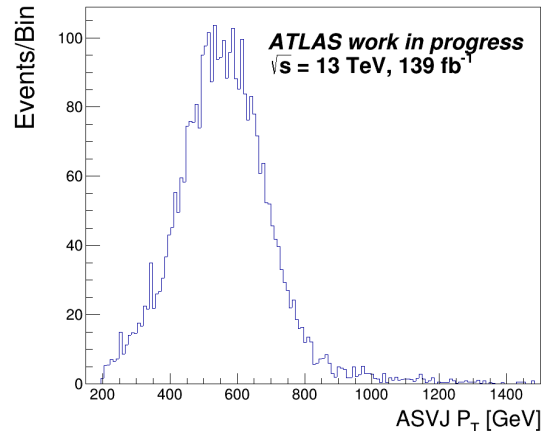


**Figure 6.** The  $p_T$  distribution of the anti-svj.

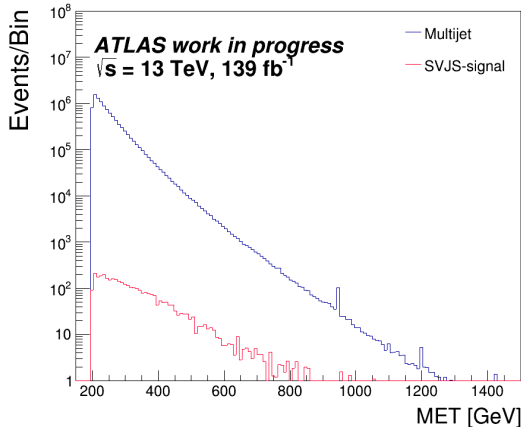


**Figure 7.** MET for signal against multijet background.

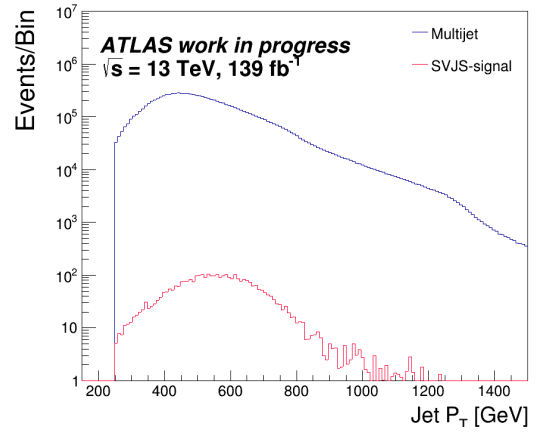


**Figure 8.** Leading-jet  $p_T$  distribution for signal against multijet background.

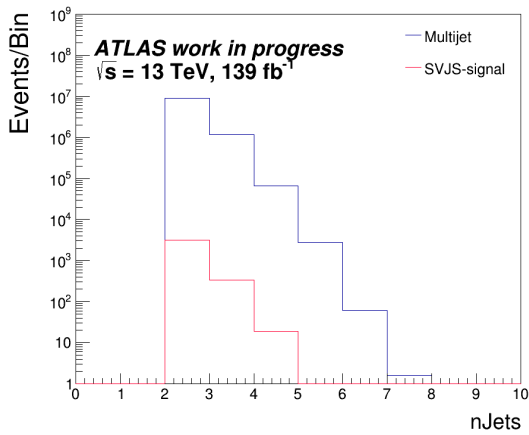


**Figure 9.** Number of jets for signal against multijet.

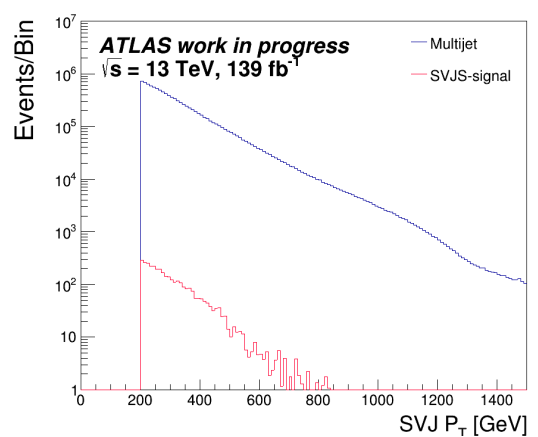


**Figure 10.** Svj transverse momentum for signal against multijet.

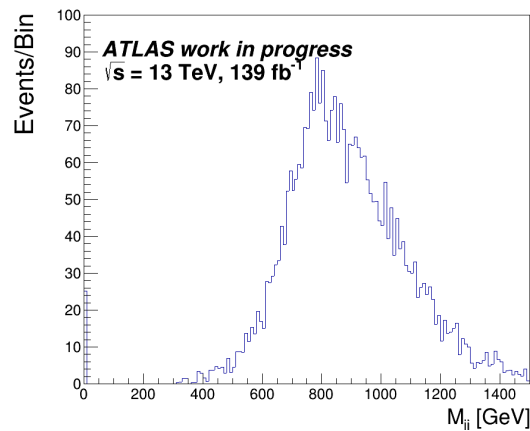


**Figure 11.** Invariant mass of leading and sub-leading jets.

#### 4. Conclusions

A preliminary study of semi-visible jet searches in a resonant production mode was presented. The distributions describing signal characteristics are shown, with an initial look at the largest background. The current invariant mass peak for the leading and sub-leading jet is contrary to mass of the  $Z'$  mediator boson, where the mass peak needs to be reconstructed accounting for the  $r_{inv}$  fraction. The largest background is multijet, reducing the background is the greatest challenge due to lack of discriminating values. This search is ongoing in ATLAS.

#### References

- [1] Weinberg S 2004 *The European Physical Journal C-Particles and Fields* **34** 5–13
- [2] Garrett K and Duda G 2011 *Advances in Astronomy* **2011**
- [3] Strassler M J and Zurek K M 2007 *Physics Letters B* **651** 374–379
- [4] Alimena J, Beacham J, Borsato M, Cheng Y, Vidal X C, Cottin G, Curtin D, De Roeck A, Desai N, Evans J A *et al.* 2020 *Journal of Physics G: Nuclear and Particle Physics* **47** 090501
- [5] Petraki K and Volkas R R 2013 *International Journal of Modern Physics A* **28** 1330028
- [6] Ade P A, Aghanim N, Arnaud M, Ashdown M, Aumont J, Baccigalupi C, Banday A, Barreiro R, Bartlett J, Bartolo N *et al.* 2016 *Astronomy & Astrophysics* **594** A13
- [7] Bai Y and Schwaller P 2014 *Physical Review D* **89** 063522
- [8] Beauchesne H, Bertuzzo E and Grilli di Cortona G 2019 *Journal of High Energy Physics* **2019** 1–24
- [9] CMS collaboration and others 2021 *arXiv preprint arXiv:2112.11125*
- [10] Cohen T, Lisanti M, Lou H K and Mishra-Sharma S 2017 *Journal of High Energy Physics* **2017** 1–32
- [11] CMS Collaboration 2020 *Journal of High Energy Physics* **2020** 1–45
- [12] Cohen T, Lisanti M and Lou H K 2015 *Physical review letters* **115** 171804
- [13] Alves A, Profumo S and Queiroz F S 2014 *Journal of High Energy Physics* **2014** 1–29
- [14] Alwall J, Frederix R, Frixione S, Hirschi V, Maltoni F, Mattelaer O, Shao H S, Stelzer T, Torrielli P and Zaro M 2014 *Journal of High Energy Physics* **2014** 1–157
- [15] Sjöstrand T, Ask S, Christiansen J R, Corke R, Desai N, Ilten P, Mrenna S, Prestel S, Rasmussen C O and Skands P Z 2015 *Computer physics communications* **191** 159–177

# A search for $tWZ$ production with the ATLAS detector using the three and four lepton final states in proton-proton collisions at $\sqrt{s} = 13$ TeV

Alexander Veltman, James Keaveney

Department of Physics, University of Cape Town, South Africa, 7701

E-mail: vltale001@myuct.ac.za

**Abstract.** The production of a single top quark in association with a  $W$  and  $Z$  boson ( $tWZ$ ) is a rare Standard Model process which has never before been detected. This process is sensitive to the top quark electroweak coupling found in some Beyond Standard Model theories such as Standard Model Effective Field theory and may hold information for constraining these theories. A previous search has been performed for  $tWZ$  production using  $139 \text{ fb}^{-1}$  of proton-proton collision data at a centre of mass energy of 13 TeV recorded at the ATLAS detector. The search was performed across the tetralepton and trilepton final states and have been combined to further increase the sensitivity of the analysis. This analysis was expanded to include a comprehensive set of systematic uncertainties. The work presented will include new preliminary blinded results for the cross section of  $tWZ$  production.

## 1. Introduction

The production of a single top quark in association with a  $W$  and  $Z$  boson ( $tWZ$ ) is a rare Standard Model process which has never before been measured. Due to the electroweak vertices involved in the radiation of the  $W$  and  $Z$  boson, the rate of production of the  $tWZ$  process is dependent on how the top quark couples to the electroweak force. The top-electroweak coupling has been identified [1] as a possible area for constraining new beyond Standard Model theories. A precise measurement of the cross-section of the  $tWZ$  process will provide more information regarding the coupling.

However, the measurement of the cross section of the  $tWZ$  process is difficult. The required experimental signatures used to measure  $tWZ$  production are particularly rare due to the prevalence of electroweak interactions. The rarity of the production causes a limiting of available event statistics even when considering a large dataset such as the ATLAS Run 2 dataset. The more impactful factor in the measurement is the similarities between the diagrams of  $tWZ$  and  $t\bar{t}Z$  production. When the next-to-leading order diagrams are considered, the  $tWZ$  diagram has major overlaps with that of  $t\bar{t}Z$  in which the diagrams differ by only a single lepton originating from a top quark. This issue results in  $t\bar{t}Z$  being a major background in the analysis as well as requiring additional steps to perform diagram removal in order to differentiate these processes.

This analysis of the  $tWZ$  process uses two possible experimental signatures which are the trilepton and tetralepton channels. Both channels require that the  $Z$  boson in the event decays leptonically to pairs of electrons or muons. These experimental signatures have previously been investigated [2, 3] where these analyses have been extended. The trilepton channel requires

one of the  $W$  bosons (either the radiated  $W$  or the  $W$  produced by the top decay) to decay hadronically with the other  $W$  decaying leptonically. The tetralepton channel requires both of the  $W$  bosons to decay leptonically. These channels are used in a combined fit in order to produce a combined result for the  $tWZ$  cross section. The analysis in the tetralepton channel has been extended to account for a wider collection of systematic uncertainties as well as updated simulated samples. The details of the tetralepton analysis and its results will be presented in this proceedings. The analysis of the trilepton channel is in the process of a similar extension but full results are not available at this time.

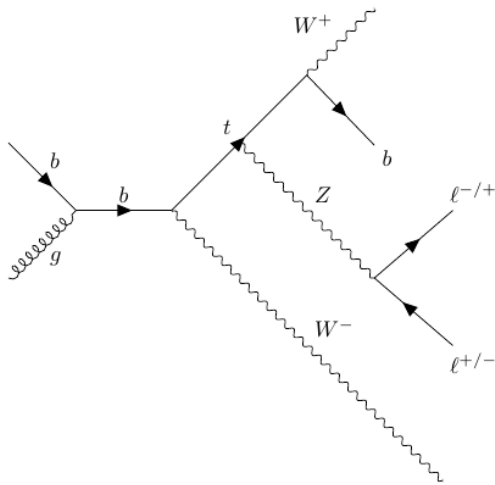


**Figure 1.** An example of a leading order Feynman diagram of  $tWZ$  production where the  $Z$  boson decays leptonically.

## 2. Datasets and Event Selection

This analysis utilises the full  $139 \text{ fb}^{-1}$  Run 2 proton-proton collision dataset taken using the ATLAS detector at the Large Hadron Collider between the years of 2015 and 2018. A comparable set of simulated samples were generated for the  $tWZ$  process as well as any relevant background processes in order to compare the ATLAS data to Standard Model predictions.

A summary of the baseline requirements for lepton and jet objects in each event is present in Table 1. Any leptons which meet these requirements are considered loose leptons. A loose lepton which passes an extra set of isolation and identification criteria is considered to be a tight lepton. A fake lepton is an object which has incorrectly been misidentified as the expected lepton or a lepton from a process which is not the process of interest. The classification of jets containing  $b$ -hadrons, known as  $b$ -jets, is done using a machine learning algorithm DLR1 [4] which uses various working points to describe the likelihood for a jet to contain a  $b$ -hadron. In the analysis, a jet is defined as tight if it passes the 77% DLR1 working point while it is defined as loose if it passes the 85% DLR1 working point but not the 77% DLR1 working point. A  $Z$  boson candidate is defined as any pair of oppositely signed same flavoured (OSSF) leptons in an event which have a reconstructed mass which is within 30 GeV of the  $Z$  boson mass.

The definitions of the signal regions (SR) and control regions (CR) for the analysis are shown in Table 1. Signal regions are constructed to maximise the presence of the signal process with

respect to the background processes. The control regions are constructed to provide estimations for the contributions of the various backgrounds so as to control for them when performing the fitting procedure. The analysis uses two signal regions,  $tWZ$  OF SR and  $tWZ$  SF SR, which differ only by a requirement on the two leptons which did not originate from a  $Z$  boson. The region in which the two non- $Z$  leptons are the same flavour,  $tWZ$  SF SR, is designed to try isolate contributions from the  $ZZ$  background process in the signal regions. Three control regions,  $t\bar{t}Z$  CR,  $ZZb$  CR and  $(tWZ)_{\text{fake}}$ , are used in the analysis. The  $t\bar{t}Z$  CR and  $ZZb$  CR regions are constructed to control for the background contributions from the  $t\bar{t}Z$  and  $ZZ$  processes respectively. The  $(tWZ)_{\text{fake}}$  region requires 3 tight leptons and an additional loose lepton where the region is designed to estimate the contribution of  $t\bar{t}Z$  events which contain a fake lepton.

Baseline selections				
$N_\ell = 4$ $p_T(\ell_1, \ell_2, \ell_3, \ell_4) > (28, 18, 10, 10) \text{ GeV}$ $p_T(\text{jet}) > 20 \text{ GeV},  \eta(\text{jet})  < 4.5, \text{jvt} > 0.5$ $ \eta(\ell_e)  < 2.47$ excluding $1.37 <  \eta(\ell_e)  < 1.52$ $ \eta(\ell_\mu)  < 2.5$ $\sum_{i=1}^4 \text{charge}(\ell_i) = 0$ All OSSF lepton pairs require $m_{\text{OSSF}} > 10 \text{ GeV}$				
Regions				
$tWZ$ OF SR	$tWZ$ SF SR	$t\bar{t}Z$ CR	$ZZb$ CR	$(tWZ)_{\text{fake}}$ CR
$N_\ell^{\text{tight}} = 4$	$N_\ell^{\text{tight}} = 4$	$N_\ell^{\text{tight}} = 4$	$N_\ell^{\text{tight}} = 4$	$N_\ell^{\text{tight}} = 3$ $N_\ell^{\text{loose}} = 1$
$N_Z \text{ candidate} = 1$	$N_Z \text{ candidate} = 1$	$N_Z \text{ candidate} = 1$	$N_Z \text{ candidate} = 2$	$N_Z \text{ candidate} = 1$
$N_{\text{jet}} \geq 1$	$N_{\text{jet}} \geq 1$	$N_{\text{jet}} \geq 2$	$N_{\text{jet}} \geq 1$	$N_{\text{jet}} \geq 1$
$N_{\text{b-jet}}^{\text{tight}} = 1$	$N_{\text{b-jet}}^{\text{tight}} = 1$	$N_{\text{b-jet}}^{\text{tight}} \geq 1$ $N_{\text{b-jet}}^{\text{loose}} \geq 0$ $N_{\text{b-jet}}^{\text{loose}} + N_{\text{b-jet}}^{\text{tight}} = 2$	$N_{\text{b-jet}}^{\text{tight}} = 1$	$N_{\text{b-jet}}^{\text{tight}} = 1$
Opp. Flavour Non- $Z \ell$	Same Flavour Non- $Z \ell$	-	-	-

**Table 1.** A summary of the baseline selections for object definitions and the requirements for the signal and control regions.

### 3. Background Discrimination

In order to differentiate the signal and background within the signal regions, a discriminating variable is determined with a focus on separating  $tWZ$  events from major contributing background processes, particularly  $t\bar{t}Z$  events. This variable is calculated per event and is produced by using the output of a scanning algorithm, the Two Neutrino Scanning Method ( $2\nu SM$ ), as an input into a broader machine learning model, a boosted decision tree (BDT), along with other event properties.

### 3.1. Two Neutrino Scanning Method

The Two Neutrino Scanning Method ( $2\nu SM$ ) algorithm is constructed to produce a weight between 0 and 1 which indicates the likelihood that an event contains a  $t\bar{t}$  pair. The  $2\nu SM$  score helps discriminate between the signal  $tWZ$  events and background  $t\bar{t}Z$  since only the  $t\bar{t}Z$  events will have a  $t\bar{t}$  system. The algorithm tries to reconstruct the  $t\bar{t}$  system by considering different neutrino kinematics.

The algorithm relies on knowing probability distributions for kinematic observables of the top quarks and their neutrino decay products. A sample of simulated  $t\bar{t}$  events is used to construct these distributions using generator-level information where the following variables are calculated:

$$\begin{aligned} m_{t_1}^2 &= \ell_1^2 + b_1^2 + \nu_1^2 & \Delta E_x &= (p_{T,\nu_1})_x + (p_{T,\nu_2})_x - (E_T^{\text{miss}})_x \\ m_{t_2}^2 &= \ell_2^2 + b_2^2 + \nu_2^2 & \Delta E_y &= (p_{T,\nu_1})_y + (p_{T,\nu_2})_y - (E_T^{\text{miss}})_y \end{aligned} \quad (1)$$

where  $\ell_i$  are the 2 non- $Z$  leptons and the  $b_i$  are the 2 highest weighted jets according to the DL1r algorithm. The product of these distributions are then used to define the  $2\nu SM$  weight:

$$\omega_{2\nu SM} = Pr[m_{t_1}]Pr[m_{t_2}]Pr[\Delta E_x]Pr[\Delta E_y] \quad (2)$$

where  $Pr[X]$  is the probability distribution function of  $X$  which results in a value between 0 and 1. A higher score indicates a more suitably reconstructed  $t\bar{t}$  system. In order to calculate the maximum  $\omega_{2\nu SM}$  for some event, different possible configurations of neutrino pairs are considered. Different values of angular components of the neutrino 4-vectors are scanned over with the  $m_{t_1}$ ,  $m_{t_2}$ ,  $\Delta E_x$  and  $\Delta E_y$  being calculated for each configuration. These kinematic variables are then evaluated on the generated distributions and the  $\omega_{2\nu SM}$  weight is found using equation 2. Only the maximum  $\omega_{2\nu SM}$  weight is used to label the likelihood of a  $t\bar{t}$  system being in an event.

### 3.2. Event-Level BDT

A binary classification boosted decision tree (BDT) was created to provide the required discriminating variable. The input features of the model include the scalar sum of the transverse momenta of the leptons, jets and  $b$ -jets, the angular differences between the two non- $Z$  leptons and the maximum  $\omega_{2\nu SM}$  score of the event. Since the objective of the model is binary classification, the output of the model is a number between 0 and 1 where 0 is labelled a background event and 1 is labelled a signal event. The model was trained using simulated samples of  $tWZ$ ,  $t\bar{t}Z$  and  $ZZ$  where  $tWZ$  is labelled as examples of signal events and  $t\bar{t}Z$  and  $ZZ$  are labelled as examples of background events. An investigation of the feature importance of the model found that the maximum  $\omega_{2\nu SM}$  score had the highest importance in the model.

## 4. Extraction Method

The rate of  $tWZ$  production is determined by the signal strength  $\mu(tWZ)$  which is defined as the ratio between the measured  $tWZ$  cross section and the Standard Model prediction for the  $tWZ$  cross section. A signal strength of  $\mu(tWZ) = 0$  represents no detection of any  $tWZ$  production while  $\mu(tWZ) = 1$  represents the Standard Model prediction for  $tWZ$  production. The signal strength is determined using a binned profile likelihood fit [5]. The signal regions and the  $t\bar{t}Z$  control region are treated as histograms of the BDT discriminating variable while the  $ZZb$  control region uses the scalar sum of all jet and lepton  $p_T$  and  $E_T^{\text{miss}}$ . The  $(tWZ)_{\text{fake}}$  region uses the  $p_T$  of the loose lepton in the event. During the fitting procedure,  $\mu(tWZ)$  is considered a parameter of interest while the weights of each histogram bin and each systematic uncertainty are treated as nuisance parameters and are allowed to vary.

### 5. Extracting the signal strength in the tetralepton channel

The analysis was first conducted using a fully blinded Asimov dataset which assumes that the data within all regions appears exactly like the simulated samples. This toy dataset is useful for making comparisons between different analysis strategies without exposing the analysis to possible biases introduced by using the ATLAS dataset. The fully blinded fit result for the  $tWZ$  signal strength  $\mu_{Asimov}^{stat}(tWZ)$  which allowed only statistical nuisance parameters to vary was  $1.00 \pm 0.93$ . When the systematic uncertainties were included, the fit result for  $\mu_{Asimov}(tWZ)$  was  $1.00^{+1.25}_{-1.02}$ . The comparison between the fit with only statistical uncertainties and the fit with both statistical and systematic uncertainties shows that the analysis is mainly dominated by statistical uncertainties. This is unsurprising due to the limited number of  $tWZ$  events available in the tetralepton channel. However, the introduction of a wider set of systematic uncertainties related to new calibrations increased the contributions of systematic uncertainties more than expected. This may indicate that some precision may be gained by attempting to mitigate these systematic contributions.

A fit was also performed using a mixed dataset where blinded Asimov data is only used in the signal regions while the actual ATLAS data is used in the control regions. The fit result for the  $tWZ$  signal strength  $\mu(tWZ)$  using a mixed dataset was  $2.00^{+1.61}_{-1.20}$  which agrees with the Standard Model prediction. This result has an associated expected significance of  $Z_{\mu}^{exp} = 0.95\sigma$  with respect to the Standard Model prediction. The measurement shows no significant deviation from the Standard Model prediction.

The major contributing systematic uncertainties can be seen in the ranking plot in Figure 2. When considering each of these systematic uncertainties, the uncertainty with the largest impact on the fit result is that associated with the  $t\bar{t}Z$  cross section. This is expected since  $t\bar{t}Z$  is the largest background process in the analysis and the ability to constrain its contribution should greatly affect the fit result. Other notable systematic variables are those associated with the tracking and reconstruction of jets and parton distribution function (PDF) calculations. These are relevant due to the number of jets present in the various regions.

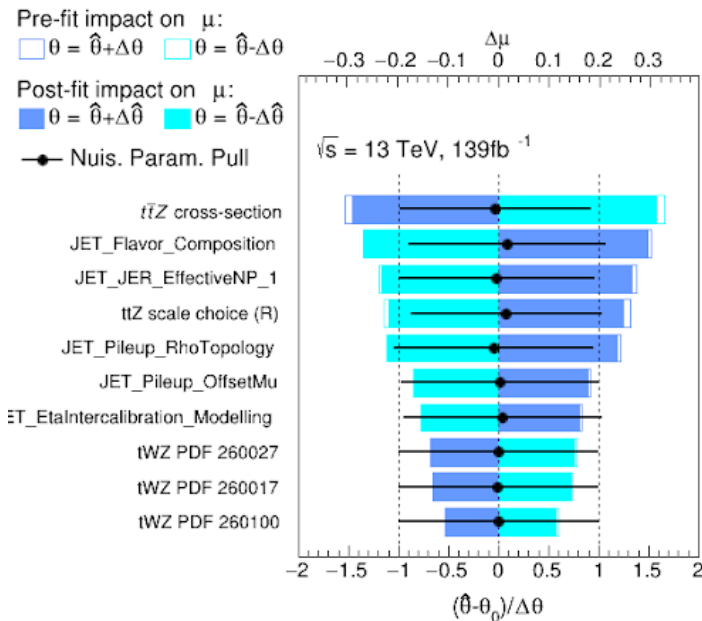


**Figure 2.** Ranking plot for the variations of the systematic uncertainties involved in the mixed data profile likelihood fit. The black points (bottom axis) represent the pull associated with each nuisance parameter. The impact of each nuisance parameter associated with the systematic uncertainties (top axis) is shown using the blue bars. Only the nuisance parameters with the ten highest impact values are shown.

## 6. Conclusion

The single top quark production with an associated  $W$  and  $Z$  boson is a rare Standard Model process which has not been detected. A search for  $tWZ$  production was performed which investigated the tetralepton and trilepton final states where only the blinded results for the tetralepton channel were presented. The best fit value for the signal strength of  $tWZ$  production in the tetralepton channel with respect to the Standard Model prediction was  $\mu(tWZ) = 2.00^{+1.61}_{-1.20}$  where Asimov data was used in the signal regions of the analysis. The result had an associated expected significance of  $Z_{\mu}^{exp} = 0.95\sigma$  with respect to the Standard Model prediction. No deviation from the Standard Model prediction was found. This result will be extended through combination with the measurement in the  $tWZ$  trilepton channel.

## References

- [1] Maltoni F, Mantani L and Mimasu K 2019 *Journal of High Energy Physics* **2019** URL <https://doi.org/10.1007/jhep10/82019/9004>
- [2] Warren B 2021 A search for  $twz$  production in the trilepton channel using run 2 data from the atlas experiment URL <http://hdl.handle.net/11427/36228>
- [3] Reich J 2021 A search for  $twz$  production in the full run 2 atlas dataset using events with four leptons URL <http://hdl.handle.net/11427/36050>
- [4] Aad G *et al.* 2019 *The European Physical Journal C* **79** URL <https://doi.org/10.1140/epjc/s10052-019-7450-8>
- [5] Cowan G, Cranmer K, Gross E and Vitells O 2011 *The European Physical Journal C* **71** URL <https://doi.org/10.1140/epjc/s10052-011-1554-0>

# Characterisation of a new LSO block detector for Positron Emission Particle Tracking

Alice McKnight, R S van der Merwe and T W Leadbeater

Department of Physics, University of Cape Town, South Africa

E-mail: MCKALI012@myuct.ac.za

**Abstract.** The University of Cape Town Physics Department recently acquired a Siemens Biograph 16 HiRez combined PET/CT scanner manufactured in 2005. Unlike older scanner models utilized by the department in Positron Emission Particle Tracking (PEPT), the Biograph scanner uses modern lutetium oxyorthosilicate (LSO) scintillators with a rapid response time, pixelated into a finer spatial grid. The new scintillating material promises an increased light output and faster decay time resulting in improved spatial resolution and reduced dead time compared to the conventional bismuth germanium oxide (BGO) crystals. Advanced front end data acquisition and processing compliment the new detector physics enabling high (energy, timing, & spatial) resolution measurements with low distortion. The LSO crystal dimensions are  $4 \times 4 \times 20 \text{ mm}^3$  arranged in blocks of  $13 \times 13$  optically coupled to 4 photomultiplier tubes. Groups of 12 blocks are serviced by a detector controller responsible for analogue front end data acquisition and digitisation. The full scanner contains 12 controllers totalling 24336 crystals arranged in rings of 39 axially and 624 transaxially. Detector blocks and controllers have been extracted from the original device and reconfigured with a customised data acquisition system. Characteristics such as detector efficiency, temporal resolution, energy resolution, and spatial resolution have been investigated and are compared to performance of previous models for further use in PEPT and positron imaging applications.

## 1. Introduction

Positron Emission Particle Tracking (PEPT) is a nuclear radiation imaging-based technique to measure the dynamics of physical processes [1]. The University of Cape Town Physics Department has a dedicated facility for PEPT at iThemba Labs which currently employs a Siemens HR++ PET camera. The department recently acquired a Siemens Biograph 16 HiRez combined PET/CT scanner manufactured in 2005. Unlike older scanner models, such as the HR++, the Biograph uses modern lutetium oxyorthosilicate (LSO) scintillators with a rapid response time, pixelated into a finer spatial grid. This new scanner will ultimately replace the HR++ at iThemba Labs but must first be characterised and studied to understand its performance from a physics perspective. Once this is achieved the scanner can be modified for further PEPT research, such modifications include developing a means of acquiring list-mode data, implementing higher resolution timestamping, and encoding other data streams such as telemetry from pumps and mass flow controllers [2].

The Siemens 2005 Biograph 16 HiRez is a combined Positron Emitting Tomograph (PET) and X-ray Computed Tomography (CT) scanner which uses advanced gamma ray detection technology to image not only the structure of a system (CT), but also its function (such as metabolic

activity in a medical scenario - PET). The PEPT facility at iThemba labs has historically used positron imaging implemented on modified ex-clinical PET systems to study and characterise functional processes, granular systems, and multiphase flow. By replacing the HR++ scanner at the lab with the newer Biograph, future PEPT research will have access to more advanced PET technology with higher spatial, temporal and energy resolutions and the ability to correlate structure (CT) and function (PET/PEPT) for the first time [3].

To characterise the scanner, detector blocks and controllers were extracted from the original device and reconfigured with a customised data acquisition system. Characteristics such as detector efficiency, temporal, energy, and spatial resolution were investigated and compared to performance of existing detector systems used in PEPT and positron imaging applications.

## 2. Functional Description

The key physical process that PET technology relies on is the electron-positron annihilation. Positrons are emitted by the breakdown of a proton rich radionuclide taking the form of a substance administered to the patient for conventional PET scans, or the tracer particles used in PEPT. Positrons collide with an electron and annihilate near the site of the decay, with the positron range between emission and annihilation contributing a fundamental limit to the spatial resolution in imaging. The annihilation results in two gamma rays, conserving energy and momentum with emission in opposite directions in the reference frame of the electron-positron system. The angle with which the photons are observed in the laboratory frame has slight variability ( $\pm 0.5^\circ$ ) known as noncollinearity, contributing further spatial resolution limits. The emitted gamma rays are measured by the rings of detectors surrounding the system, enabling the time of arrival (ns), energy (keV), and position (mm) of incidence to be determined and stored as raw data from which an image or PEPT analysis can be reconstructed [4].

Each individual detector block within the scanner utilizes a scintillating material which, when ionized by incoming radiation, produces a high energy electron via the photoelectric effect. Energy deposition by this electron excites the atoms in the material to luminescence. A segmented array of these crystals is connected to 4 photomultiplier tubes which output an electronic pulse proportional to the absorbed scintillation light intensity (and hence energy). The crystal elements are optically separated by a reflecting material, the depth of which is empirically determined to share the scintillation light linearly between the four photomultiplier tubes [5]. Comparison of the relative scintillation light intensities enables the exact crystal element illuminated to be determined. A flood histogram illustrating the crystal array of the new LSO detector can be seen in figure (1a) below. The composite signal from the block detector is passed through a single channel analyser (SCA) to determine energy qualified events valid in the range 425 - 650 keV as set by the upper and lower level discriminators. A fast branch of the composite signal is passed to a constant fraction discriminator (CFD) to determine the time of arrival for the event at ns resolution. Singles event data are transmitted to a central coincidence processing unit, where a timing gate system is used on energy qualified events to determine pairs of events assumed to be from the same annihilation. Events from different detectors are regarded as simultaneous (in coincidence) if they both occur within a fixed time window  $2\tau$ , with the rate of random coincidences scaling linearly with the gate duration  $\tau$  [3]. Simultaneous events are known as coincidence pairs and allow the reconstruction of a line of response drawn between the two detectors. Many pairs allow an image map to be created by localising the position of annihilation corresponding to the activity in the organ of the patient, or the location of the tracer particle allowing for particle tracking.

### 3. Experimental Method

A single module consisting of twelve detectors and the associated readout electronics was extracted from the scanner and reconfigured in the lab. The detectors require a split rail power supply providing reference ground (0 V), positive 5.0 V, and negative 5.2 V. Once functional, a means of communicating with the module was developed. The electronics board utilises three communication ports. One is for communications between the detector and the main controller board, carrying a master synchronisation clock (62.5 MHz), a strobe used to parse data words (8.00 MHz), and RS232 standard serial communications enabling calibration and event statistics readout. The other two ports carry singles event data from the module in emitter coupled logic (ECL) over twisted pair conductors. Each event is digitised and transmitted as a parallel set of six 8-bit words with each bit presented at the master clock frequency, and end of word parsed by the strobe. A dedicated translating circuit was built to convert from ECL to transistor transistor logic (TTL) and event words were captured using a custom data acquisition system [6]. Each of the six 8-bit words contains the data representation of a single event in the module, including the time of arrival (ns) relative to the master clock, the energy of the event (keV), and position of the event (block in module; row in block; column in block). The energy calibration and position correction table are determined from the data as presented in figure 1 below.

The front-end electronic processing system was used to query the LSO block detectors for event information. These data included pulse height spectra which was subsequently calibrated in terms of photon energy, position calculations per event used to calculate the absolute crystal positions, and CFD timing encoding time of arrival of energy qualified events. In order for comparison, Nuclear Instrumentation Modules (NIM) were used to obtain singles data for the BGO block detector; signals from each PMT were read-out with individual NIM pre-amplifiers and amplifiers and then summed and digitised. The summed signals were digitised using a multichannel analyser and the pulse height spectrum generated for multiple radioactive sources including  $^{22}\text{Na}$  (511 keV),  $^{137}\text{Cs}$  (662 keV) and  $^{60}\text{Co}$  (1173 and 1332 keV).

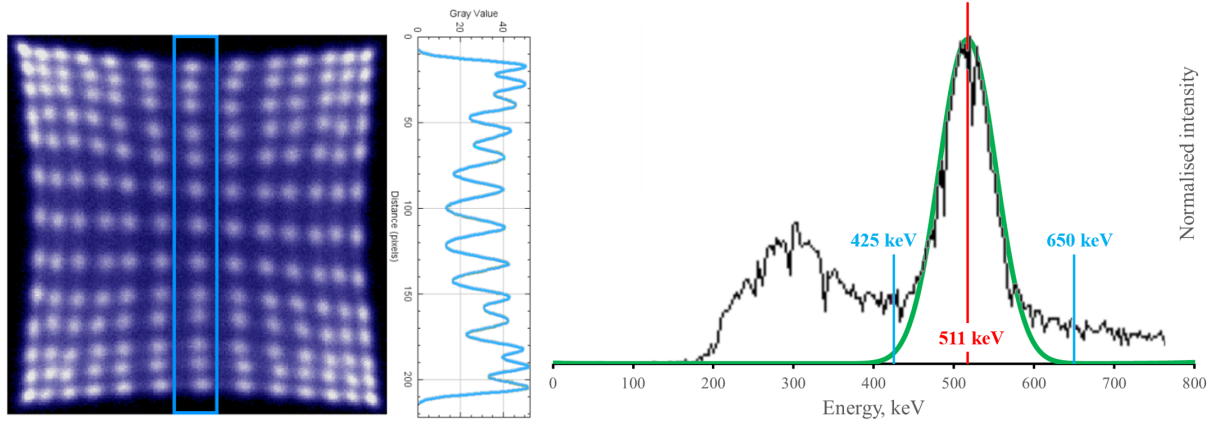
### 4. Results

Characteristics of the LSO crystals used in the Biograph are compared directly against those of the BGO crystals used in the HR++ in order to gauge the similarities and differences expected in their behaviour. Table 1 shows that the LSO detectors have a factor of three higher light output and are expected to yield a correspondingly higher energy resolution of order 1.75 ( $\sqrt{3}$ ). The scintillation light decay time is a factor of six improved on BGO with similar factor improvement expected in time resolution and dead-time factors. Despite the higher material density, LSO is expected to have lower intrinsic photopeak efficiency due to the lower effective atomic number and higher proportion of Compton events relative to photoelectric absorption.

**Table 1.** Crystal properties for both BGO and LSO [7] [4].

Material property	BGO	LSO
Density (g/cc)	7.13	7.40
Effective atomic number	75	66
Decay time (ns)	300	~47
Linear attenuation at 511 keV ( $\text{cm}^{-1}$ )	0.96	0.88
Ratio between photoelectric and Compton at 511 keV	0.78	0.52
Light output (photons/511 keV)	4200	~13000

Results using the on-board analysis capability were retrieved from the Biograph detector controllers and are illustrated in figure 1. The figure contains a flood histogram (a, left) produced by uniformly illuminating the entire face of a detector block, in which each of the  $13 \times 13$  crystals are clearly distinguishable. The histogram illustrates the selectivity in identifying the excited crystal element, from which a correction table can be built. Figure (1b) contains the calibrated pulse height spectrum for the summed PMT signals from an LSO detector block, illustrating the annihilation photopeak at 511 keV and the upper and lower discriminators applied at 425 keV and 650 keV respectively.



(a) Flood histogram of the  $13 \times 13$  crystal array in the an LSO detector block.

(b) Calibrated pulse height spectrum of a  $^{22}\text{Na}$  source from the summed PMT signals of an LSO detector block.

**Figure 1.** Results obtained from the on-board analysis of the Biograph system.

Numerical results from analysis of LSO (Biograph) and BGO (HR++) detector blocks are documented in Table 2 below:

**Table 2.** Results obtained from systematic study of LSO and BGO detector blocks, numerical data from Table 1 where appropriate.

Property (at 511keV)	BGO	LSO
Measured energy resolution (%)	33	17
Calculated energy resolution (%)	30	17
Manufacturer energy resolution (%)	30	16
Calculated intrinsic peak efficiency (%)	41	32
Calculated total interaction efficiency (%)	94	93
Measured intrinsic photopeak efficiency (%)	60	-

The measured 511 keV annihilation photopeaks were characterised by numerically fitting a Gaussian function and parameterising in terms of area, centroid, and standard deviation  $\sigma$ . The energy resolution function was determined as  $R = \Delta E/E$  and measured as the photopeak FWHM / centroid where the Full Width at Half Maximum (FWHM) is  $2.35 \sigma$ . The resolution is reported as a percentage of the full energy at 511 keV.

Photopeak resolutions for BGO and LSO were measured to be 33% and 17% respectively,

in agreement with the expectation calculated using the Poissonian uncertainty relation and a photomultiplier tube quantum efficiency of 25%. The measured and calculated values are in agreement with the manufacturer specifications for these detector materials, which is somewhat surprising given the additional complexity of the segmented block detector design.

The measured intrinsic photopeak efficiency for the BGO detector was determined through comparing annihilation photopeak areas over a range of source-detector separation distances allowing normalisation by the projected solid angle. The intrinsic photopeak efficiency was measured to be slightly higher than expected, however these data may include some contribution from Compton scattering over the energy window chosen to define the peak as well as down-scattering from an associated high energy photon. The intrinsic peak efficiencies are in broad agreement within the range expected numerically.

The efficiency of the detector is influenced by the scintillating material density and linear attenuation coefficient, and a high ratio between the photoelectric and Compton interactions. Photoelectric interactions are favoured as they result in the total absorption of the incoming photon energy, while Compton interactions may only absorb a fraction of the energy and the resultant scattered photon might lead to further interactions in the adjacent detectors, making it difficult to locate the primary interaction. The photoelectric microscopic cross-section scales with the effective atomic number to the power of four, while the Compton scattering cross-section being only linearly proportional to it; a material with a higher effective atomic number therefore yields an improved ratio and higher efficiency. The total macroscopic cross-section scales linearly with material density, thus higher density materials are preferred [7].

The integration of the composite light signal is a direct measure of the energy deposited by the annihilation photons, and is dominated by Poisson statistics in the scintillation light intensity. Higher light output scintillators therefore improve the energy resolution of the detector, as evidenced by the improved energy resolution of the LSO scintillator compared to the lower light output BGO devices.

A smaller decay time allows for higher precision in measuring the time of arrival of the incoming radiation, and reduced front end detector deadtime implying overall higher event rates. Advantageously, the faster decay time of the LSO scintillator allows a reduced coincidence window ( $2\tau = 4\text{ns}$ ) compared to the BGO system ( $2\tau = 12\text{ns}$ ) thereby reducing the relative fraction of random coincidences in the recorded data stream. High speed timing potentially enables measurement of the time-of-flight for the photon pairs.

## 5. Conclusion

Properties of the recently acquired Siemens Biograph 16 HiRez combined PET/CT scanner were determined through a systematic investigation of the characteristics possessed by the LSO crystals utilised within the scanner detectors. These properties include the detector energy, spatial, and timing resolution, and efficiency. The results were compared directly against characteristics of BGO crystals used by models preceding the Biograph, such as the HR++ and demonstrated an improved energy resolution in the LSO crystals at 17% compared to 30% in BGO, with a decreased intrinsic photopeak efficiency at 32% compared to 41% in BGO. These results agree with theoretical expectations deduced from physical properties of the crystals as described in Table 1 and 2. Numerical results of the measured characteristics, together with estimated values for other properties such as intrinsic resolution and efficiency are in broad agreement.

## References

- [1] Parker, D., Broadbent, C., Fowles, P., Hawkesworth, M. and McNeil, P. 1993 Positron emission particle tracking - a technique for studying flow within engineering equipment. *Nuclear Instruments and Methods in Physics Research Section A: Accelerators, Spectrometers, Detectors and Associated Equipment*. **326** 592-607
- [2] Buffler, A. & Cole, K. & Leadbeater, T. & van Heerden, M. 2018 Positron emission particle tracking: A powerful technique for flow studies *International Journal of Modern Phys.: Conf. Series* **48** 1860113
- [3] van der Merwe, R & Peterson, S & Buffler, A & van Heerden, M & McKnight, A & Leadbeater, T. 2022 MicroPEPT: A step towards hybrid PEPT detectors *The Proceedings of SAIP22*
- [4] Bailey, D. L., Townsend, D. W., Valk, P. E., Maisey, M. N., 2005 *Positron Emission Tomography, Basic Sciences* 13-39
- [5] Casey, M., Nutt, R., 1986 A Multicrystal Two Dimensional BGO Detector System for Positron Emission Tomography *IEEE Transactions on Nuclear Science* **33** 460-463
- [6] Leadbeater, T. *et al.* 2012 Positron imaging systems for studying particulate, granular and multiphase flows. *Particuology* **10** 146-153.
- [7] Phelps, M. 2004 *PET: Physics, Instrumentation, and Scanners* New York, (Springer), 14-19

# Search for new spin-1 boson using ATLAS detector data

**XG Mapekula**

University of Johannesburg, Johannesburg, Department of Mechanical Engineering, Corner Kingsway and University Road, Johannesburg, South Africa.

E-mail: [xmapekul@cern.ch](mailto:xmapekul@cern.ch)

**Abstract.** We present a search for a new spin-1 or spin-0 boson where the Standard Model Higgs boson decays into a four lepton final state ( $l = \mu$  or  $e$ ) corresponding to the  $H \rightarrow Z_d Z_d \rightarrow 4l$ . In this scenario,  $Z_d$  is the new boson found in the intermediate state, having a mass range of between 15 - 60 GeV. The search is conducted using pp collision data collected using data collected at the ATLAS experiment. The data corresponds to a total integrated luminosity corresponds of  $139 \text{ fb}^{-1}$  where the centre of mass energy was  $\sqrt{s}=13 \text{ TeV}$ . The observed data was consistent with Standard Model. However, an improvement of a factor between two and four from the previous iteration of the analysis was observed for the limits that were set on the fiducial cross-section and the branching ratio of the Higgs boson. Limits were also set on the mixing parameter related to the Beyond Standard Model framework used in this analysis.

## 1. Introduction

Observations of dark matter in the cosmos suggest that, because dark matter is not accounted for in the Standard Model (SM), the SM remains an incomplete description. Therefore, extensions to the SM via the Higgs sector favouring the existence of dark matter are highly motivated.

One way of extending SM is through exotic Higgs boson decays, where precision measurements have shown that Higgs boson properties allow for branching ratio  $BR < 13\%$  for non-standard Higgs boson decays [1–4]. It is also shown that since the Higgs Boson has a very narrow width, small couplings to a lighter state should lead to a sizeable branching ratio. Furthermore, certain theories within the hidden sector state hidden sector particles may favour coupling to the Higgs boson [5–8]. This scenario makes the Higgs boson the preferred mediator between SM particles and the Hidden sector.

In the Hidden sector scenario [9–18], combining the SM with the addition of a  $U(1)_d$  gauge symmetry [13–17] would mix kinetically with the SM  $U(1)_Y$  hypercharge gauge with a coupling strength  $\epsilon$  field. The dark photon  $Z_d$  would then be this symmetry's gauge boson. The  $Z_d$  boson's coupling strength to the SM is determined by the kinetic mixing parameter  $\epsilon$ . The branching ratio for  $Z_d$  decaying to muon and electron pairs could be in the range 10%-15% [13] between  $1 \text{ GeV} < m_{Z_d} < 60 \text{ GeV}$ . The decays are prompt where  $\epsilon \sim 10^{-5}$  [13] while for smaller values,  $Z_d$  decays would be significantly displaced. Furthermore, the decay width of the  $Z_d$  boson is very small for  $\epsilon \leq 1$  and  $m_{Z_d} < 60 \text{ GeV}$ .

Published Run 2 results for the search of the Higgs boson decaying to a pair of  $Z_d$  boson which decay further into a four lepton final state are presented in this paper [19] where  $pp$  data at  $\sqrt{s} = 13 \text{ TeV}$  with an integrated luminosity of  $139 \text{ fb}^{-1}$  collected using the ATLAS

detector [20] was used. This analysis considers dark vector bosons decaying to same flavor muon and electron pairs, where  $4e$ ,  $2e2\mu$ , and  $4\mu$  final states are included.

A brief description of the ATLAS detector, triggers, Monte Carlo simulation, pre-selection and event selection used in this analysis are given in Section 2. Contributions made by various background processes and the systematic uncertainties attached to them are described in Section 3. The results obtained from the analysis are described in Section 4 while Section 5 presents the paper's conclusion.

## 2. Experimental Setup

The ATLAS detector, which covers a  $4\pi$  solid angle with its cylindrical geometry, is a general-purpose detector situated on one of the four interaction points of the LHC.

Monte Carlo simulations are made with the ATLAS detector's components in mind. In order to determine the expected shapes and yields of the signal and background events, we use Monte Carlo simulated samples. The simulations include pile-up and detector effects. The detector effects [21] are simulated using GEANT4 [22]. The signal samples related to the HAHM model [13, 14, 16, 17] under consideration are simulated using MadGraph5 while the background events are simulated using Powheg box [23–27], Pythia [28], Madgraph5 [29] and Sherpa [30]. Small differences in data reconstruction, impact parameter efficiencies and isolation are corrected by applying weights to the simulated events.

### 2.1. Event Selection

We use event selection cuts to sift the signal events from the background events. We first require electrons to be located within the detector's central region where  $|\eta| < 2.47$  and  $|z_0 \sin \theta| < 0.5 \text{ mm}$ . The transverse momentum of each selected electron must be  $p_T > 7 \text{ GeV}$ . We require that muons be situated within  $|\eta| < 2.7$ , which is the muon spectrometer's acceptance region. Similarly to the baseline electron requirements,  $p_T > 5$  (15) GeV and  $|z_0 \sin \theta| < 0.5 \text{ mm}$  for stand-alone (calo tagged) muons. We then look for quadruplets that have same flavor opposite sign pairs where the quadruplet with the smallest difference between the leading dilepton mass and the sub-leading dilepton mass is the one that is selected. The deposits made by the quadruplet leptons in the inner detector and calorimeter have to be isolated from other deposits. The quadruplet's invariant mass must be within the Higgs window where  $115 \text{ GeV} < m_H < 130 \text{ GeV}$ . Finally, the quadruplet must comply with the medium signal region (MSR) requirement, which was previously defined by  $m_{34}/m_{12} > 0.85$ . This requirement was redefined in this iteration of the analysis because the background was sufficiently low at low energies ( $\langle m_{\ell\ell} \rangle < 30 \text{ GeV}$ ) to search for a possible broader  $Z_d$  than was expected in the HAHM model. The MSR was then modified so that the  $Z_d$  width would be  $3.5\sigma$  for lower dilepton masses and decrease to  $2.0\sigma$  at the higher end of the mass spectrum using Equation 1.

$$m_{34}/m_{12} > 0.85 - 0.1125f(m_{12}) \quad (1)$$

Where  $f(m_{12})$  is the modulating function.

### 2.2. Signal

We generate the  $H \rightarrow Z_d Z_d \rightarrow 4\ell$  process using the Hidden Abelian Higgs Model (HAHM) [17] with MADGRAPH5 [31] in conjunction with PYTHIA8 [32] which models hadronization, underlying event and parton shower. The dark vector boson  $Z_d$  mass is generated for values in the range 15 GeV and 60 GeV for various mass hypothesis values in steps 5 GeV for the process under consideration using the gluon-gluon fusion (ggF) production mode. The Higgs boson mass was set to 125 GeV. The cross-sections of the samples, which are next-to-next-to-leading-order, are normalized using  $\sigma_{SM}(ggF) = 48.58 \text{ pb}$  as recommended in [33].

### 2.3. Background processes

- $H \rightarrow ZZ^* \rightarrow 4\ell$ : We simulated Higgs production using POWHEG-BOX v2 MC event generator [26] for ggF [23], PDF4LHC NLO PDF set [34] for vector boson fusion [35] and vector boson [36]. We then used MADGRAPH5\_AMC@NLO [29] to simulate events produced via heavy quark annihilation while CT10nlo PDF set [37] and the NNPDF23 PDF set [38] are used to simulate events where the production mechanisms are  $t\bar{t}H$  and  $b\bar{b}H$  respectively. Events produced via ggF,  $VBF$ ,  $VH$  and  $b\bar{b}H$  were modelled using PYTHIA8 [39] for the  $H \rightarrow ZZ^*$  decay process while the AZNLO parameter set was used to model the parton shower, multiple parton interactions and hadronization related to the decay process.  $t\bar{t}H$  showering is modelled using HERWIG++ [40] and the UEEE5 parameter set [41].
- $ZZ^* \rightarrow 4\ell$ : SHERPA 2.2.2 together with the NNPDF3.0 NNLO PDF set were used to model the Quark anti-quark annihilation associated with the non-resonant SM  $ZZ^* \rightarrow 4\ell$  process [42–44].  $ZZ^*$  production initiated by the loop-induced  $gg$  process was modelled using GG2VV interfaced with PYTHIA8. To avoid double counting, we omitted the s-channel H diagrams were using CT10 PDF's. The latter process was then calculated at LO. The latter process was multiplied by a K-factor of  $1.70 \pm 0.15$  [45] because it received large QCD corrections. 30% of the total background prediction comes from the  $ZZ^* \rightarrow 4\ell$  process.
- $VVV/VBS$ : This process is modelled using SHERPA 2.1 with the CT10 PDF's. The cross-sections of the processes, which include vector boson scattering and triboson production, are proportional to  $\alpha^6$  at leading order (LO). The results are four lepton final states, including two additional particles (electrons, quarks or muons). The Higgs production through VBF is subtracted from estimates obtained with this generator to avoid duplicates. This background contributed 17% of the total background.
- $Z + (t\bar{t}/J/\psi/\Upsilon) \rightarrow 4\ell$ : We simulate the process where Z bosons are produced via a quarkonium state that decay to four leptons with PYTHIA8 with the NNPDF 2.3 PDF while POWHEG-BOX interfaced to PYTHIA6 [46] were used to simulate the  $t\bar{t}H$  background.
- **Other Background**: Fake leptons produced from  $Z + jets$ ,  $t\bar{t}$  and  $WZ$  decay to less than four prompt leptons including jets. These are modeled using SHERPA 2.2 for  $Z + jets$ , POWHEG-BOX interfaced to PYTHIA6 [46] for  $t\bar{t}$  production and POWHEG-BOX interfaced to PYTHIA8 and the CTEQ6L1 for  $WZ$  production.

## 3. Analysis procedure

### 3.1. Systematic uncertainties

Systematic uncertainties which were found to be dominant in this analysis include:

- **Luminosity and pileup**: We used the LUCID-2 detector [47] to obtain the uncertainties related to luminosity. This was found to be 1.7% [48] for the direct measurements of the luminosity. The measured and predicted inelastic cross section differences are used to determine the uncertainty due to pile-up, which accounts for about 1%.
- **Lepton-related uncertainties**: The event selection efficiency is dependent on lepton identification and reconstruction efficiencies and how well their momentum scale is determined. Resolutions for muons and electrons, momentum scales and efficiencies are measured by applying tag-and-probe techniques to the  $Z \rightarrow \ell^+\ell^-$ ,  $J/\psi \rightarrow \ell^+\ell^-$ , and  $\Upsilon \rightarrow \mu^+\mu^-$  dilepton resonances. Accounting for differences observed between simulation and data together with residual uncertainty estimations [49, 50] leads to corrections in the region of a percentage point. Small, single-lepton uncertainties in the final yield can lead to uncertainties in the region of 15% because the final state contains four leptons. These uncertainties are usually dominated by electron identification and reconstruction efficiency.

- Theoretical uncertainties:** In order to model uncertainties related to simulated signal and background processes, we vary the factorization, parton distribution functions, QCD scales, renormalization, and modelling the underlying event and hadronization. This leads to a total uncertainty in signal acceptance of around 3 % while the background yield uncertainty is between 3–9% for  $H \rightarrow ZZ^* \rightarrow 4\ell$  [51], and 5 % for  $ZZ^* \rightarrow 4\ell$  [43–45, 52–54]

#### 4. Results

This analysis has shown no significant excesses beyond SM. Therefore, limits were set on the fiducial cross-section, which are model independent in order to interpret the results. We set model-dependent limits on the benchmark model parameters mentioned Section 1. The generator-level quantities that are defined are used to derive the analysis' model-independent cross-section limits. The fiducial event selection cuts are designed in such a way as to mimic the selection cuts for the signal region. Events selection effects are factorized into a primarily model-independent a model-dependent acceptance and efficiency using the fiducial event selections. The efficiency is thus used to determine the model-independent cross-section limit shown in Figure 3.

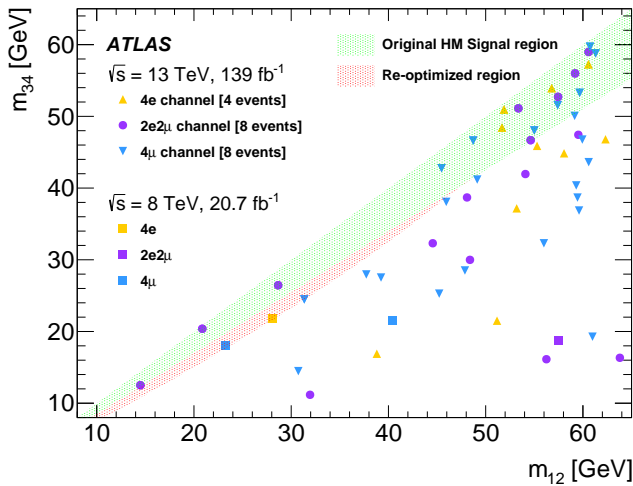


**Figure 1.** Distribution of  $m_{12}$  vs  $m_{34}$  spectrum where the green region represents the previous MSR and the red region represents the new modulated MSR. The square marker represent the events from  $\sqrt{s} = 8 \text{ TeV}$  data while the square and circle markers represent the  $\sqrt{s} = 13 \text{ TeV}$  data.

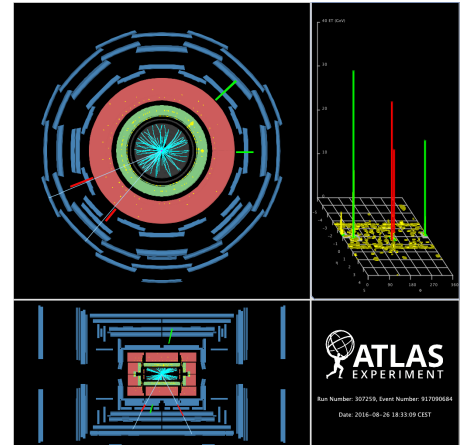


**Figure 2.** Event display of one of the  $2e2\mu$  events from the  $\sqrt{s} = 13 \text{ TeV}$  data with  $\langle m_{\ell\ell} \rangle = 27.5 \text{ GeV}$  that correspond to a global significance of  $1.9\sigma$

Although the analysis is statistically consistent with the SM, there is one event where  $\langle m_{\ell\ell} \rangle < 15 \text{ GeV}$  and another two where  $\langle m_{\ell\ell} \rangle > 60 \text{ GeV}$  which are possible candidates for  $Z_d$ . These are plotted in Figure 1 which shows the  $m_{12}$  vs  $m_{34}$  distribution. The largest deviations from the SM were found at  $\langle m_{\ell\ell} \rangle = 28 \text{ GeV}$  and  $\langle m_{\ell\ell} \rangle = 20 \text{ GeV}$  which have a local significance of  $2.5\sigma$  and  $1.9\sigma$ . The global significance of the event at  $\langle m_{\ell\ell} \rangle = 28 \text{ GeV}$  was found to be  $1.9\sigma$ . A similar analysis at the CMS collaboration also observed an event at  $20 \text{ GeV}$  with a higher significance, shown in Figure 5b of in [55]. This is an interesting result which motivates a further probe for Run3. The profile likelihood ratio  $\left( -2 \log \frac{L(\mu=0, \hat{\theta})}{L(\hat{\mu}, \hat{\theta})} \right)$  was used as the test statistic to determine the significance values. The  $m_{12}$  vs  $m_{34}$  distribution shown is a new plot

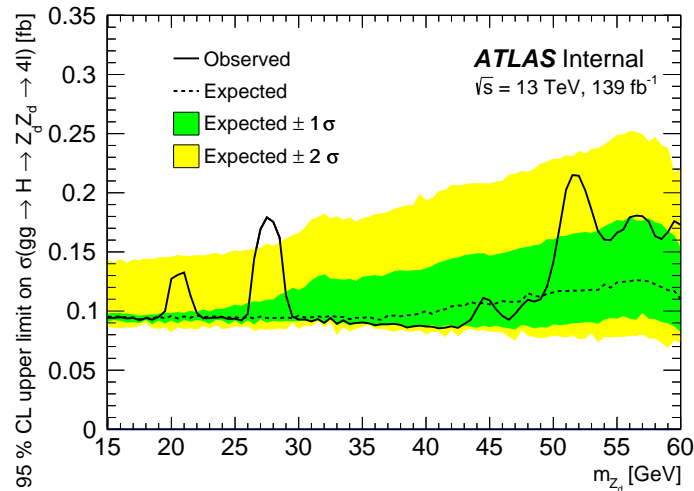


**Figure 3.** 95% CL expected and observed upper limits  $H \rightarrow Z_d Z_d \rightarrow 4\ell$  cross section. These limits assume that the SM Higgs boson is produced via the gluon-gluon fusion process. All final states are combined.

which includes the results for a previous search at 8 TeV [56]. This search also had  $Z_d$  candidates at a similar level of significance. In this paper, we have focused on the possible  $Z_d$  candidates, and so the event display of a typical one is also shown in Figure 2.

## 5. Conclusion

This paper presents the search for the exotic decay of the 125 GeV SM Higgs Boson to two dark vector bosons, which decay into a four-lepton final state. Data from the ATLAS experiment from the LHC, corresponding to  $139 \text{ fb}^{-1}$  of pp collision data at  $\sqrt{s} = 7 \text{ TeV}$  was used in this analysis. This search was conducted in the mass range  $15 \text{ GeV} < m_{Z_d} < 60 \text{ GeV}$ . The data was found to be consistent with SM as no significant deviations from the backgrounds were observed. Therefore limits were set on various parameters in the model.

## References

- [1] ATLAS Collaboration 2016 *Eur. Phys. J. C* **76** 6 (Preprint 1507.04548)
- [2] CMS Collaboration 2015 *Eur. Phys. J. C* **75** 212 (Preprint 1412.8662)
- [3] ATLAS and CMS Collaborations 2016 *JHEP* **08** 045 (Preprint 1606.02266)
- [4] ATLAS Collaboration 2020 A combination of measurements of Higgs boson production and decay using up to  $139 \text{ fb}^{-1}$  of proton-proton collision data at  $\sqrt{s} = 13 \text{ TeV}$  collected with the ATLAS experiment ATLAS-CONF-2020-027 URL <https://cds.cern.ch/record/2725733>
- [5] Shrock R E and Suzuki M 1982 *Phys. Lett. B* **110** 250
- [6] Strassler M J and Zurek K M 2007 *Phys. Lett. B* **651** 374–379 (Preprint hep-ph/0604261)
- [7] Schabinger R M and Wells J D 2005 *Phys. Rev. D* **72** 093007 (Preprint hep-ph/0509209)
- [8] Patt B and Wilczek F 2006 "" (Preprint hep-ph/0605188)
- [9] Fayet P 2004 *Phys. Rev. D* **70** 023514 (Preprint hep-ph/0403226)
- [10] Finkbeiner D P and Weiner N 2007 *Phys. Rev. D* **76** 083519 (Preprint astro-ph/0702587)
- [11] Arkani-Hamed N, Finkbeiner D P, Slatyer T R and Weiner N 2009 *Phys. Rev. D* **79** 015014 (Preprint 0810.0713)
- [12] Dudas E, Mambrini Y, Pokorski S and Romagnoni A 2012 *JHEP* **10** 123 (Preprint 1205.1520)
- [13] Curtin D, Essig R, Gori S and Shelton J 2015 *JHEP* **02** 157 (Preprint 1412.0018)
- [14] Curtin D, Essig R, Gori S, Jaiswal P, Katz A *et al.* 2014 **90** 075004 (Preprint 1312.4992)
- [15] Davoudiasl H, Lee H S, Lewis I and Marciano W J 2013 **88** 015022 (Preprint 1304.4935)
- [16] Wells J D 2008 "" (Preprint 0803.1243)
- [17] Gopalakrishna S, Jung S and Wells J D 2008 *Phys. Rev. D* **78** 055002 (Preprint 0801.3456)

- [18] Alexander J *et al.* 2016 Dark Sectors 2016 Workshop: Community Report (*Preprint* 1608.08632)
- [19] ATLAS Collaboration 2021 (*Preprint* 2110.13673)
- [20] ATLAS Collaboration 2008 *JINST* **3** S08003
- [21] ATLAS Collaboration 2010 *Eur. Phys. J. C* **70** 823 (*Preprint* 1005.4568)
- [22] GEANT4 Collaboration, Agostinelli S *et al.* 2003 *Nucl. Instrum. Meth. A* **506** 250
- [23] Hamilton K, Nason P, Re E and Zanderighi G 2013 *JHEP* **10** 222 (*Preprint* 1309.0017)
- [24] Hamilton K, Nason P and Zanderighi G 2015 *JHEP* **05** 140 (*Preprint* 1501.04637)
- [25] Alioli S, Nason P, Oleari C and Re E 2010 *JHEP* **06** 043 (*Preprint* 1002.2581)
- [26] Nason P 2004 *JHEP* **11** 040 (*Preprint* hep-ph/0409146)
- [27] Frixione S, Nason P and Oleari C 2007 *JHEP* **11** 070 (*Preprint* 0709.2092)
- [28] Sjöstrand T, Ask S, Christiansen J R, Corke R, Desai N, Ilten P, Mrenna S, Prestel S, Rasmussen C O and Skands P Z 2015 *Comput. Phys. Commun.* **191** 159 (*Preprint* 1410.3012)
- [29] Alwall J, Frederix R, Frixione S, Hirschi V, Maltoni F, Mattelaer O, Shao H S, Stelzer T, Torrielli P and Zaro M 2014 *JHEP* **07** 079 (*Preprint* 1405.0301)
- [30] Bothmann E *et al.* 2019 *SciPost Phys.* **7** 034 (*Preprint* 1905.09127)
- [31] Alwall J, Herquet M, Maltoni F, Mattelaer O and Stelzer T 2011 *JHEP* **06** 128 (*Preprint* 1106.0522)
- [32] Sjöstrand T, Mrenna S and Skands P Z 2008 *Comput. Phys. Commun.* **178** 852–867 (*Preprint* 0710.3820)
- [33] Andersen J R *et al.* (LHC Higgs Cross Section Working Group) 2013 Handbook of LHC Higgs Cross Sections: 3. Higgs Properties (*Preprint* 1307.1347)
- [34] Butterworth J *et al.* 2016 *J. Phys. G* **43** 023001 (*Preprint* 1510.03865)
- [35] Nason P and Oleari C 2010 *JHEP* **02** 037 (*Preprint* 0911.5299)
- [36] Luisoni G, Nason P, Oleari C and Tramontano F 2013 *JHEP* **10** 083 (*Preprint* 1306.2542)
- [37] Lai H L *et al.* 2010 *Phys. Rev. D* **82** 074024 (*Preprint* 1007.2241)
- [38] Ball R D *et al.* 2013 *Nucl. Phys. B* **867** 244 (*Preprint* 1207.1303)
- [39] Sjöstrand T, Mrenna S and Skands P 2008 *Comput. Phys. Commun.* **178** 852–867 (*Preprint* 0710.3820)
- [40] Bähr M *et al.* 2008 *Eur. Phys. J. C* **58** 639 (*Preprint* 0803.0883)
- [41] Seymour M H and Siodmok A 2013 *JHEP* **10** 113 (*Preprint* 1307.5015)
- [42] Gleisberg T *et al.* 2009 *JHEP* **02** 007 (*Preprint* 0811.4622)
- [43] Gleisberg T and Höche S 2008 *JHEP* **12** 039 (*Preprint* 0808.3674)
- [44] Cascioli F, Maierhöfer P and Pozzorini S 2012 *Phys. Rev. Lett.* **108** 111601 (*Preprint* 1111.5206)
- [45] Caola F, Melnikov K, Rötsch R and Tancredi L 2015 *Phys. Rev. D* **92** 094028 (*Preprint* 1509.06734)
- [46] Sjöstrand T, Mrenna S and Skands P Z 2006 *JHEP* **05** 026 (*Preprint* hep-ph/0603175)
- [47] Avoni G *et al.* 2018 *JINST* **13** P07017
- [48] ATLAS Collaboration 2019 Luminosity determination in  $pp$  collisions at  $\sqrt{s} = 13$  TeV using the ATLAS detector at the LHC ATLAS-CONF-2019-021 URL <https://cds.cern.ch/record/2677054>
- [49] ATLAS Collaboration 2019 *JINST* **14** P12006 (*Preprint* 1908.00005)
- [50] ATLAS Collaboration 2021 *Eur. Phys. J. C* **81** 578 (*Preprint* 2012.00578)
- [51] Dittmaier S *et al.* (LHC Higgs Cross Section Working Group) 2011 *CERN-2011-002* (*Preprint* 1101.0593)
- [52] ATLAS Collaboration 2017 Multi-Boson Simulation for 13 TeV ATLAS Analyses ATL-PHYS-PUB-2017-005 URL <https://cds.cern.ch/record/2261933>
- [53] Schumann S and Krauss F 2008 *JHEP* **03** 038 (*Preprint* 0709.1027)
- [54] Höche S, Krauss F, Schönherr M and Siegert F 2013 *JHEP* **04** 027 (*Preprint* 1207.5030)
- [55] CMS Collaboration 2020 Search for a low-mass dilepton resonance in Higgs boson decays to four-lepton final states at  $\sqrt{s} = 13$  TeV CMS-PAS-HIG-19-007 URL <https://cds.cern.ch/record/2718976>
- [56] ATLAS Collaboration 2015 *Phys. Rev. D* **92** 092001 (*Preprint* 1505.07645)

# Geant4 Analysis of Secondary Neutrons in Proton Therapy

**Alice Roux, Steve Peterson and Tanya Hutton**

Department of Physics, University of Cape Town, South Africa, 7700

E-mail: rxxali002@myuct.ac.za

**Abstract.** In proton therapy, secondary radioactive particles are produced along the beam line and within the patient due to proton interactions with nuclei in their path. Secondary neutrons are of particular concern, as they are hard to detect and have a high biological effectiveness which causes more damage than other particles to tissues. The Geant4 simulation toolkit was used to model the path of a 191 MeV proton beam through a copper collimator with an inner radius of 50mm, and into a water phantom, which mimics the 24cm proton beam at iThemba LABS. Most internal neutron production was found to occur before the Bragg peak once the proton energies have lowered and the cross section for neutron producing reactions is maximised. For a beam with radius 60mm, 40% of the neutron current comes from external sources. These external neutrons contributed 63% of the neutron associated dose which comprised 95% of the total absorbed dose. The simulation is able to measure the neutron energy fluence through various planes corresponding to the placement of neutron detectors for future experiments. This shows where neutron production and attenuation occurs within a treatment scenario.

## 1. Introduction

When compared to traditional radiotherapy, proton therapy delivers more precise positioning of the dose to the treatment area and a reduction in harm caused to surrounding healthy tissue. As protons have both charge and mass, when they enter a material they lose energy by interacting with the electrons in the material via the Coulomb force. When the protons slow down, they deposit energy into the surrounding tissues. The amount of energy transferred increases as the speed of the protons decrease. Once the protons have stopped completely, all of their energy will be lost, the bulk of which is at the end of their journey, this point is known as the Bragg peak. The distance the protons travel is directly proportional to their initial energy and two protons with the same initial energy will travel the same distance in a reasonably straight line, due to their higher momenta compared to electrons[1].

In an exception to the rule described above, some of the protons will interact directly with nuclei in their path, whether within the target or the proton beam line. These interactions result in the production of various secondary radioactive particles such as gamma rays, electrons, heavy ions and neutrons. Neutrons are of particular interest as they are difficult to detect due to a lack of charge and because they have high biological effectiveness[1]. Simulating a proton therapy scenario and observing the production and behaviour of neutrons sheds a light on what would otherwise be hard to observe, particularly within the target.

## 2. Monte Carlo Proton Therapy Simulation

The Geant4 simulation toolkit allows one to design a detector geometry, in this case a water phantom and copper collimator mimicking a proton therapy scenario, and then begin a Run. Within the Run a number of Events, where a proton enters the geometry from just behind the collimator as if it were part of a beam[2]. As the proton moves through the geometry, its behaviour is dictated by how likely it is for an interaction to take place. The resulting behaviours, such as energy deposition or secondary particle production, from each event can therefore be normalised per source proton to compare to experimental results.

Figure 1 shows a 3D representation of the geometry used to replicate a proton therapy experiment. The target is a water phantom that is 15cm long, 17cm high and 16cm wide these dimensions are chosen to replicate a previous experiment undertaken at iThemba LABS[3]. The copper collimator has an inner radius of 50mm and an outer radius of 70mm and set is into a steel plate with an outer radius of 300mm. The collimator and plate are 80mm thick and are placed 50mm edge to edge from the water phantom.

To produce a beam, protons are created -300mm away from the world isocenter within a prescribed radius of either 60 or 39mm. The protons are generated randomly within this radius so that the entire beam area will be populated.

As Geant4 can be used to model interactions at vastly different energy scales from the high energy collisions at the LHC to lower energy medical physics. The correct physics list is selected to describe the energy scale and particles being observed. Here QGSP\_BIC\_HP is used which models neutrons under 20MeV as well as the rest of the physics needed for this setup[4].

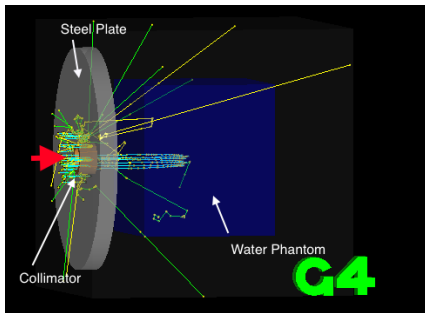


**Figure 1.** 3D representation of the Geant4 model, the red arrow depicts the beam direction. Tracks from 20 protons are shown in cyan, secondaries produced in the collimator and phantom are visible in other colours.

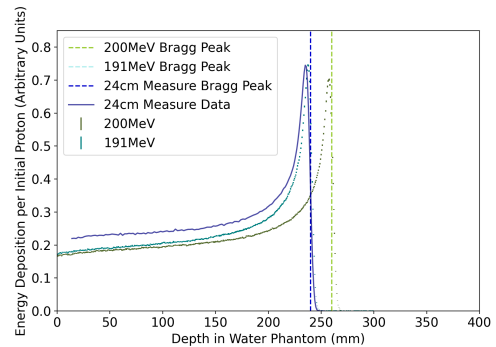


**Figure 2.** Figure showing the proton energy depositions of 200 and 191 MeV energy runs, compared to measured data with a 24cm Bragg peak at iThemba LABS.

## 3. Verification of the Model

### 3.1. Bragg Peak

As all results would need to be comparable to experimental data in the future, the initial energy of the protons was set to match the 24cm Bragg peak at iThemba LABS. To get the position of the Bragg peaks the following equation [5] was used with `scipy.optimize.curve_fit`[6]:

$$D(x) = \begin{cases} a + \alpha e^{\frac{\tau^2 \sigma^2}{2} + \tau(x-\mu)} & x < \mu \\ \text{Erfc}\left(\frac{x-\mu}{\sigma\sqrt{2}} + \frac{\tau\sigma}{\sqrt{2}}\right) & x > \mu \end{cases} \quad (1)$$

Here  $a$  is a constant used to describe the near constant dose deposited before the Bragg peak. Setting  $D(x) = 0$  after the Bragg peak describes the lack of dose after this point. The value  $\mu$  is

the position of the peak. This equation, when fitted to the measured 24cm data, gives a Bragg peak of  $24.009 \pm 0.003$  cm which agrees with the  $24.0 \pm 0.3$  cm measured before. It should be noted that the uncertainties are due to the fit and not from the data, which explains why they are so small.

Initial 200 MeV protons were used, but produced a peak around 26 cm. A value of 191 MeV was found to produce a Bragg peak at  $24.01 \pm 0.01$  cm which can be seen in Figure 2. This was chosen as the energy for all protons from this point forward[7].

### 3.2. Lateral Profiles

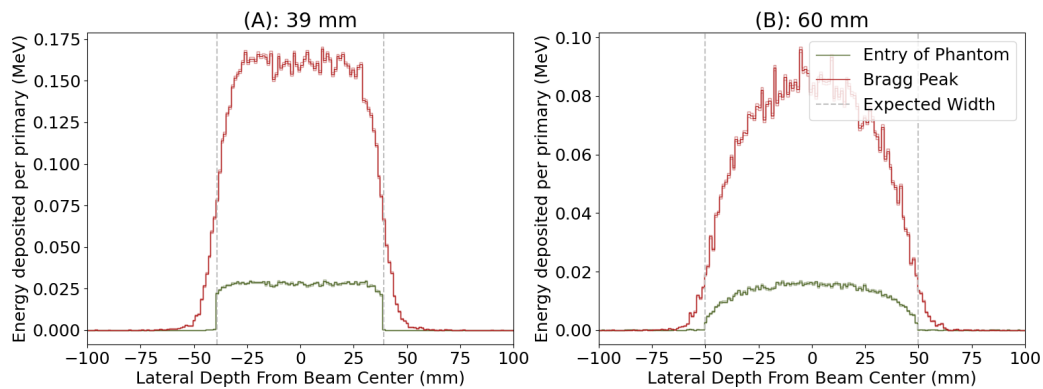


**Figure 3.** Lateral profiles of energy deposition by protons along the width of the water phantom at both the entry to the phantom and the Bragg Peak. (A) depicts a 39mm beam radius and (B) a 60mm beam radius.

To verify the shape of the beam, the energy deposited by protons at the entrance to the phantom and Bragg peak is examined. This is shown in Figure 3 for a beam with a radius of 39mm which passes through the copper collimator and a collimated 60mm beam. It can be seen that on entry of the phantom, the beam width is as expected. At the Bragg peak it has spread so that 6% and 2% of the proton dose is delivered outside original beam for the 39mm and 60mm beams respectively. The difference in results is because the narrower beam is not collimated and at the entry of the water phantom its profile is flat rather than dome shaped like the wider beam. As more of protons are at the beam's edge, they are more likely to exit the original beam profile when they scatter. These two beam diameters are used throughout the analysis to determine the effects of the collimator. This is done by scaling the results from the 39mm beam run per proton incident on the water phantom. This returns the internal components of the measurements as the narrower beam does not interact with the copper collimator. Internal measurements are scaled per proton incident on the phantom from the 60mm beam and subtracted to return the effects of the collimator in that run. Even though the shape of the 39mm beam is not realistic, it will not cause problems in later analysis.

## 4. Neutron Effects

Neutrons do not deposit their energy directly, but interact with nuclei in their path to cause cascades of secondary particles. Unlike for protons, to measure the effect of neutrons a comparison between total energy deposition in runs where neutrons and their secondaries are removed from the model and regular runs. Figure 4 shows the difference between proton energy deposition with and without neutrons to highlight how neutrons cause increased energy deposition throughout the model.

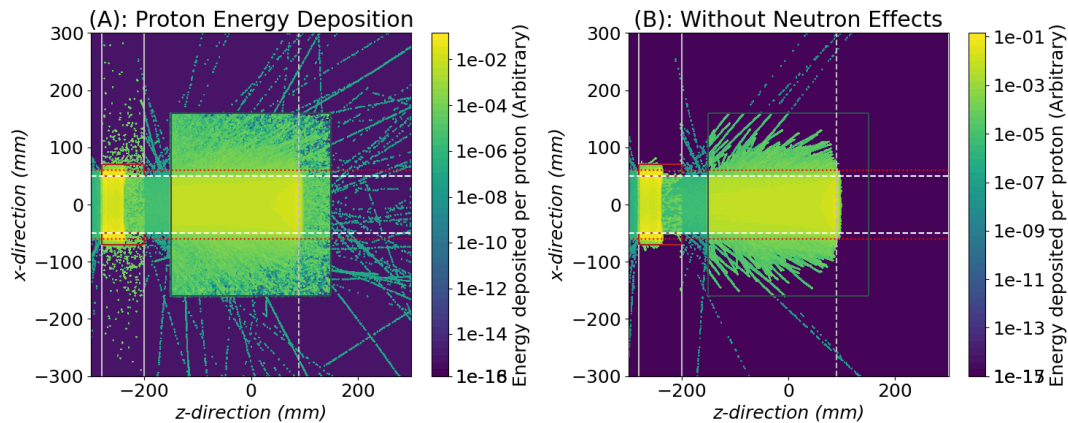


**Figure 4.** Plots of 2D energy deposition by protons with a 60mm beam, (A) shows the regular proton energy deposition whereas in (B) neutrons and their secondaries are removed.

The neutron populations for 39mm and 60mm proton beams are described in Figure 5 showing where neutron production takes place in the model. It can be seen in the 39mm beam that most of the neutrons are produced before the Bragg peak, where the protons' interaction cross sections with the water are at a maximum[8]. Whereas for the 60mm beam, most of the neutron production occurs within the collimator. This first point of interaction is caused as the beam is wider than the collimator as seen in Figure 4.

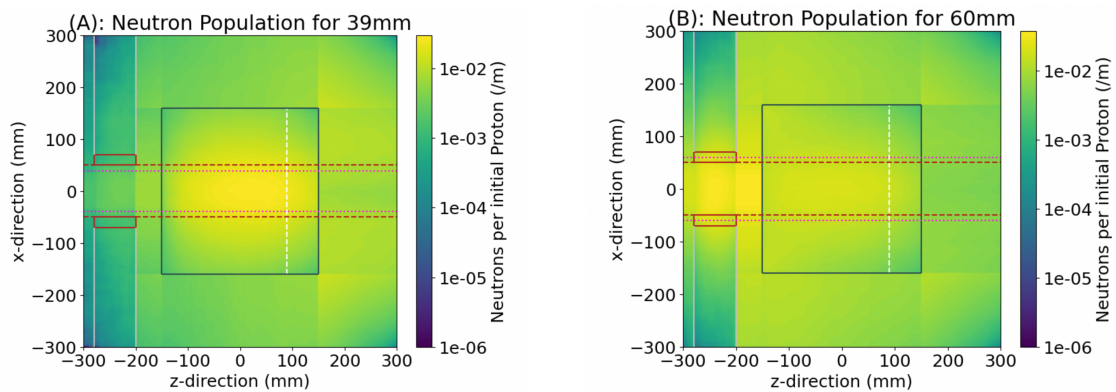


**Figure 5.** Plots showing the number of neutrons flowing through lines of constant  $x$  and  $z$  for a 39mm (A) and a 60mm (B) beam. The white line shows the position of the Bragg peak and the inner of the two red lines shows the width of the beam after passing through the collimator.

The 1D neutron current in the  $z$  direction is shown in Figure 6 for each of the two runs, depicting how neutrons produced in the collimator enter the water phantom. The neutron current for the 60mm beam is split into internal and external components as seen in Figure 7. The internal component is calculated by dividing the neutron current from the 39mm beam by the number of protons entering the phantom and then scaling it to the proton current from the 60mm beam. The external component is therefore the difference between the internal and the total currents. By integration, it is found that 60% of the neutron population is produced internally to the phantom.

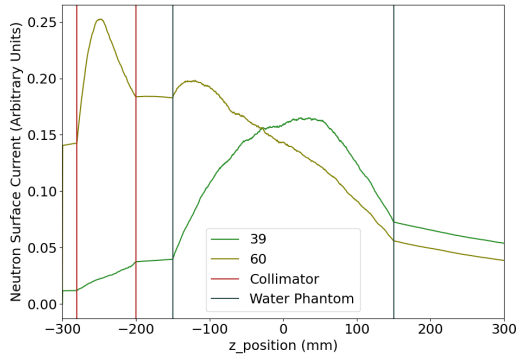


**Figure 6.** The neutron surface currents through the  $z$  direction for the 60mm and 39mm beams.

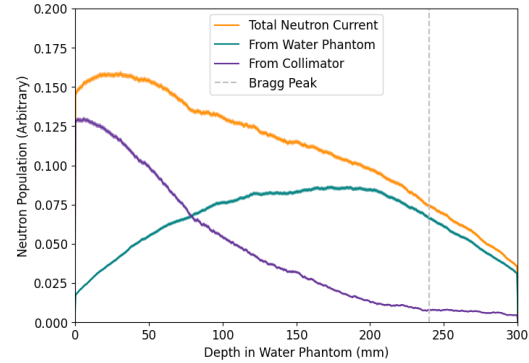


**Figure 7.** The neutron current from the 60mm beam split into the external and internal neutron components

## 5. Dosimetry Results

Dose is the standardised measure for the amount of radiation a person or object receives. The unit for absorbed dose is the Gray (Gy) given in  $\text{J.kg}^{-1}$  and it is the measure of the amount of energy deposited by ionising radiation per kilogram. The absorbed dose is obtained from the Geant4 simulation by summing the energy deposited from particles in each event in the run and dividing by the mass of the water phantom.

**Table 1.** Table showing different components of the total absorbed dose in the phantom as a percentage

	<b>Dose Component (%)</b>	<b>39mm</b>	<b>60mm</b>
A	<i>Therapeutic</i>	$73.79 \pm 0.03$	$90.14 \pm 0.04$
B	<i>Total Secondary</i>	$26.21 \pm 0.03$	$09.86 \pm 0.04$
C	<i>Off-Beam Proton</i>	$23.92 \pm 0.03$	$07.23 \pm 0.04$
D	<i>Neutron Assoc.</i>	$00.62 \pm 0.04$	$00.95 \pm 0.06$
E	<i>Other Secondary</i>	$01.67 \pm 0.06$	$01.67 \pm 0.09$

Table 1 shows the different components of the total absorbed dose of the phantom as a percentage. The therapeutic dose (A) is the absorbed dose delivered by protons within the beam width, this is higher for the 60mm beam as there is less lateral spread of the protons as mentioned in Section 3.2.

The total secondary dose (B), is the sum of all of the non therapeutic dose components. This is split into off-beam proton (C) which is the scattered proton dose taken from a run where neutrons and their secondaries are killed off. The neutron associated dose (D) is the difference between the secondary doses when neutrons are present in the simulation and when they are absent. Finally the other secondary dose (E) is the dose due to heavy ions, gamma rays and anything not a proton or a neutron.

Most importantly, the neutron associated dose is larger for a wider beam, due to external neutrons produced in the collimator, as well as a lower percentage of protons making it to the phantom which causes a decrease in the total proton dose. By scaling the doses from the 39mm beam per proton incident on the phantom, the percentage of the neutron dose produced externally for the 60mm beam is found to be:  $63.8 \pm 4.7$  %.

## 6. Future Work

When designing experiments, using a simulation to shape the planning process and to benchmark expected outcomes is a valuable process. This simulation can be applied in two ways: firstly one can place smaller volumes inside the phantom and measure the dose deposited in them which can be separated into different components as done in Section 5. This can then be compared to experimental results and the results from previous simulations as done in [9].

The simulation can also be used to measure neutron fluences through areas where neutron detectors could be placed in an experimental setup as shown in Figure 8. Figures 9 and 10 show the neutron energy fluences through each possible detector placement. This sort of analysis is useful in comparing to measured neutron data, however it does not include any detector effects caused by the proton beam which would need to be accounted for.

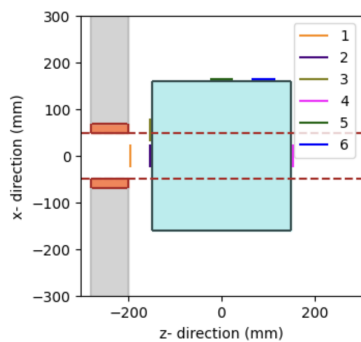


**Figure 8.** Schematic of possible neutron detector placements.

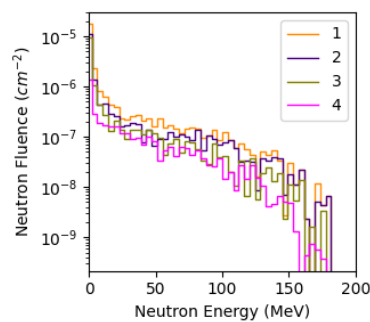


**Figure 9.** The neutron energy fluences through vertical planes in Figure 8

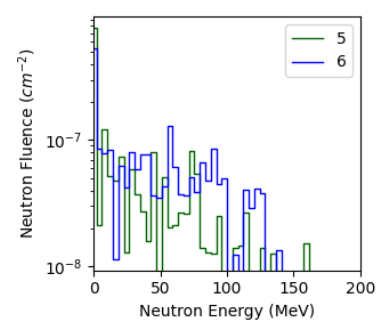


**Figure 10.** The neutron energy fluences through horizontal planes in Figure 8

## 7. Conclusion

The use of a Geant4 model in determining the effects of neutrons during proton therapy was shown. The simulation showed how the peak of neutron production is before the Bragg peak. Through comparison of the 39mm and 60mm runs it was shown the effects of the collimator on external neutron behaviour and dose. The model can be used to aid in experimental design and understanding results.

## References

- [1] Knoll G 2010 *Radiation Detection and Measurement* (Wiley) ISBN 9780470131480
- [2] Unknown 2003 Basic structure of basic structure of the geant4 simulation toolkit the geant4 simulation toolkit URL <https://www.ge.infn.it/geant4/training/portland/basicStructure.pdf>
- [3] Personal Communications with Charlot van der Voorde at iThemba LABS
- [4] Unknown Reference physics lists URL <https://geant4.web.cern.ch/node/155>
- [5] Lambrechts K 2015 Fitting the bragg peak for accurate proton range determination URL [https://fse.studenttheses.ub.rug.nl/13103/1/eindversie\\_bacheloronderzoek\\_K1.pdf](https://fse.studenttheses.ub.rug.nl/13103/1/eindversie_bacheloronderzoek_K1.pdf)
- [6] Community T S 2022 scipy.optimize.curve\_fit documentation URL [https://docs.scipy.org/doc/scipy/reference/generated/scipy.optimize.curve\\_fit.html](https://docs.scipy.org/doc/scipy/reference/generated/scipy.optimize.curve_fit.html)
- [7] Jeyasugiththan J, Camero J N, Symons J, Jones P, Buffler A, Geduld D and Peterson S W 2021 *Biomedical Physics Engineering Express* **7** 025013 URL <https://dx.doi.org/10.1088/2057-1976/abe33d>
- [8] Jia S B, Hadizadeh M H, Mowlavi A A and Loushab M E 2014 *Reports of Practical Oncology And Radiotherapy* **19** 376–384 ISSN 1507-1367
- [9] van Deventer S 2021 *UCT Honors Project - Investigation of secondary neutron production during proton therapy- Unpublished*

# Investigating the effect of neutrons on cadmium zinc telluride Compton camera

**J de Klerk, A Buffler, T Hutton and S Peterson**

Department of Physics, University of Cape Town, Rondebosch 7700, South Africa

E-mail: [dkljos001@myuct.ac.za](mailto:dkljos001@myuct.ac.za)

**Abstract.** During proton therapy (PT), excited-nuclei decay via emission of characteristic prompt gamma rays along the beam path within the target tissue. These gamma rays are detectable via a Compton camera and can be used for *in vivo* proton beam range verification using a technique called prompt gamma imaging (PGI). The detection efficiency of a PGI device can be negatively affected by additional secondary radiation (primarily neutrons). The UCT prompt gamma imaging system “Polaris” is a room temperature solid state Compton camera detector. The imaging device comprises of two independent detection platforms with each consisting of two cadmium zinc telluride crystals ( $20 \times 20 \times 10 \text{ mm}^3$ ) arranged side-by-side. The goal of the project is to better understand the effect of neutrons on the Polaris detectors during PT and compare its responses to NaI, LaBr<sub>3</sub> and BC-501A. The more traditional detectors act as means of calibration for expected gamma ray spectra in the Polaris detectors and to highlight any effect of neutrons on the cadmium zinc telluride crystals. Preliminary results are presented from measurements conducted at the UCT n-lab MeASURE facility (neutrons up to 14 MeV) and at iThemba LABS (66 MeV proton beam).

## 1. Introduction

### 1.1. Proton therapy

Proton therapy (PT) continues to be used effectively in cancer treatment [1]. The benefits of PT lie fundamentally in how energetic protons interact with matter : as protons transverse through matter, energy is lost predominantly through Coulombic interactions with atomic electrons and atomic nuclei [2]. The majority of the proton’s kinetic energy is transferred toward the end of its trajectory, and the point where the maximum amount of energy is transferred occurs at the Bragg peak [3]. Beyond the Bragg peak, the rate of ionisation slows down to a point where the proton’s path comes to an end [4]. The characteristics of the Bragg peak and finite range allows proton therapy to produce high conformal treatment [5], reduce large exposure to healthy tissue and minimise treatment side effects (acute and late) [6].

### 1.2. Compton camera (CC)

During PT, atoms in an excited energy state are produced from reactions between the proton and nucleus of the tissue. The excited atoms decay within less than a nanosecond, emitting a characteristic prompt gamma ray (PG) in the process referred to as ‘prompt emission’ [7]. The energies of PGs are dependent on the atomic composition of the tissue [8]. PGs may be detected by a device known as a Compton camera (CC). A traditional CC consists of at least two detectors, one acting as a scatterer and the other as an absorber, that operate coincidentally

(figure 1). The key interactions for Compton imaging are Compton scattering and photoelectric absorption. PGs incident on a CC scatterer at an angle  $\theta$ , undergoing a Compton interaction where some energy is transferred to a recoil electron. Here, the deposited energy and position of the PG is recorded. Compton scatter can be described by the following relationship of an incident gamma ray energy  $E_0$ , the deposited energy  $E_1$  and the angle of scatter  $\theta_1$  [9]:

$$\cos(\theta_1) = 1 + m_e c^2 \left( \frac{1}{E_0} - \frac{1}{E_0 - E_1} \right). \quad (1)$$

The second detector absorbs the scattered gamma ray by means of photoelectric absorption.

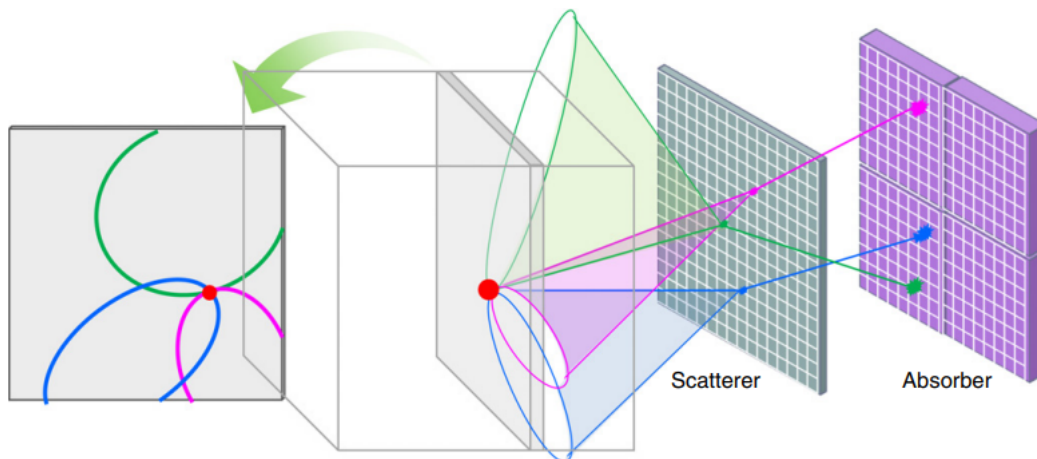


**Figure 1.** Traditional Compton camera with a scatterer and an absorber. The image displays several prompt gammas being projected onto their respective cones [10].

Capturing two or more interactions enables the calculation of the incident PG energy and the construction of a cone of origin. This calculation restricts the PG to the surface of the constructed cone with the intersection of several cones resulting in an image of the source location (figure 1)[10]. Compton cameras have been used as a means for *in vivo* proton beam range verification of a patient through prompt gamma imaging for clinical use [12]. In a study conducted at the University of Maryland School of Medicine, the results for a cadmium zinc telluride (CZT) PG imaging (PGI) system have successfully produced three-dimensional images [9].

### 1.3. UCT PGI system

The UCT Compton camera ‘Polaris’ is a room temperature solid-state detector built by H3D Inc. [Ann Arbor, MI USA]. The CC consists of two independent detection platforms (figure 2). Each platform consists of two CZT crystals ( $20 \times 20 \times 10 \text{ mm}^3$ ) arranged side-by-side for a total of four crystals. The crystals are pixilated  $11 \times 11$  in the  $x$  and  $y$  directions with depth of interaction in the  $z$ -direction. The aforementioned features provides position-sensitive gamma detection in three-dimensions, an energy resolution of 0.8% FWHM at 662 keV [19] and its compact size is practically suited to be alongside patients during PT.

### 1.4. PGI limitations

For a prompt gamma imaging system to be viable for clinical use, the system needs to have high position and energy resolution, good detection efficiencies for double (triple) scatter events and the capability to manage high energy count rates [13].



**Figure 2.** UCT Polaris detectors

deexcites through emission of a gamma ray [20]. Fast neutrons are detectable in CZT through elastic and inelastic neutron scatters [21]. The detection of inelastic scatters occur through measuring recoiling nucleus that require pulse height spectrum thresholds to be set below 10 keVee [22], previously detected in the 5-15 keV region [21]. The detection of neutrons are of interest since it degrades image quality. This occurs through neutrons being detected in coincidence with gamma rays, resulting in false double (triple) scatters [9], and through the production of more secondary particles (particularly prompt gamma rays) [18]. Particles, such as those produced during PT (neutrons, gamma rays, protons, positrons), detected by Polaris are not distinguishable on an event-by-event basis. This adds to the problem of distinguishing between PGs emitted from proton-nucleus and neutron-nucleus interactions and other secondary particles (in particular neutrons). A starting point to solve the problem at hand is to characterise the capability of Polaris through exposure to both neutrons and gamma ray sources. As a result, a series of measurements have been conducted at the UCT neutron facility (n-lab) and at iThemba LABS, making use of several detectors in conjunction with Polaris.

## 2. Measurements

### 2.1. UCT n-lab facility

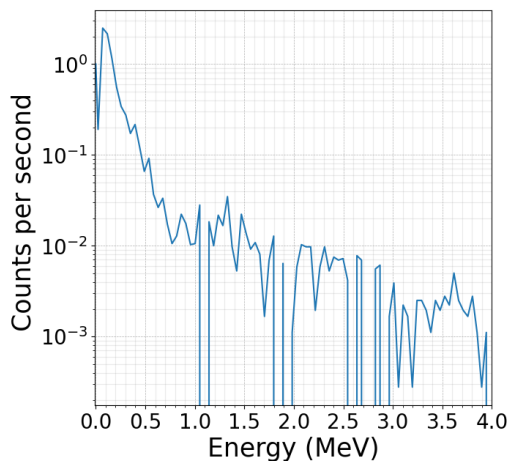


**Figure 3.** STNG energy spectrum from Polaris with  $H_2O$  sample.

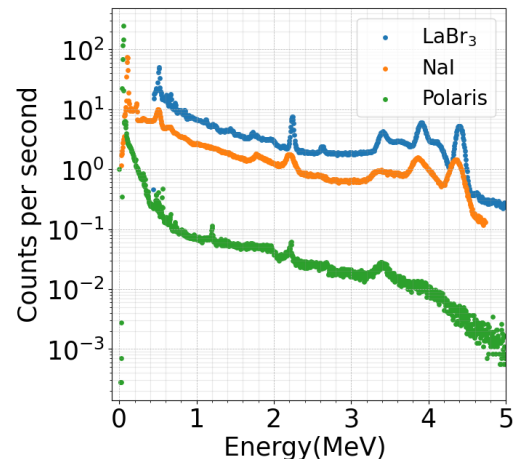


**Figure 4.** Energy spectrum comparison of NaI,  $LaBr_3$  and Polaris from an AmBe source placed inside a HDPE block.

The UCT n-lab houses a Thermo MP-320 Sealed Tube Neutron Generator (STNG) that produces monoenergetic neutrons of 14.1 MeV. Figure 3 displays the Polaris energy spectrum from a water target irradiated with the STNG. The Polaris detectors were placed  $90^\circ$  to the water target with lead shielding to their sides. The expected peak in the 5-15 keV range from nuclei recoils can

not be seen, likely due to low detector count rates and being near the minimum energy threshold of the Polaris detector. Another neutron source available at the n-lab is a 220 GBq americium-beryllium (Am-Be) radioisotope that produces neutrons over a broad energy range from 0 to around 11 MeV. Figure 4 displays the energy spectrum from NaI, LaBr<sub>3</sub> and Polaris detectors of the AmBe source placed inside a HDPE block. The peaks of interest are the annihilation photons (0.511 MeV and 1.022 MeV), 2.2 MeV gamma ray from neutron capture on hydrogen (in water), 3.4 MeV double escape peak, 3.9 MeV single escape peak and a 4.4 MeV gamma ray from the de-excitation of <sup>12</sup>C. At higher energies, peaks are not observed at 3.9 MeV and 4.4 MeV in the Polaris detector.

### 2.2. iThemba LABS measurements

Measurements were made using a 66 MeV pulsed proton beam at iThemba LABS inside the K600 vault (S-line). The targets used in these measurements were a water phantom, carbon and HDPE blocks with several configurations and several detectors including Polaris, BC-501A (liquid organic scintillator) and four LaBr<sub>3</sub> detectors.



**Figure 5.** Detector configuration of 66 MeV proton incident on a water phantom

Unfortunately a few days before the scheduled measurement time, the second Polaris detector stopped working. Figure 5 displays a configuration of a water phantom with BC-501A at 0°, Polaris detector at 90° and LaBr<sub>3</sub> at 135°, 90°, 270° and 315° respectively. After each measurement run, the detectors were changed to encompass a variety of angles (0° being on beam axis with increasing angles in an anticlockwise direction) for each of the targets.

6). What is of interest are the prominent peaks observed in the pulse height (PH) spectrum from BC-501A, figure 6. It is speculated that the two peaks may be due to scattered protons from the beam window. A further case for this is displayed in figure 7 with a high-density line along the same channel number (indicated by the arrow) from BC-501A at 315° to the water phantom. There is no well distinguished peak observed at 0°, potentially due to the detector being shielded by the sample.

There are no prominent peaks at higher energies in the Polaris energy spectrum (figure

### 3. Future work and conclusion

The next step in the project involves producing energy spectrum (neutron and gamma rays) from the BC-501A detector to be compared to Polaris. In order to obtain spectrum from BC-501A one needs to employ a technique called unfolding. Unfolding requires both the PH spectrum of interest and a response matrix for both gammas and neutrons. The responses functions that make up the response matrices will be obtained from previous measurements taken in the D-line at iThemba LABS for neutrons and response functions for gamma rays will be calculated. The PH spectrum of gamma rays and neutrons are obtainable by pulse shape (height) cuts that separate gamma rays and neutrons recorded by the detector. The goal is to discriminate prompt gamma rays from other secondary radiation. Further analysis of the neutron data will provide insights about the future developments of the Polaris system to be able to produce a viable clinical PGI system.

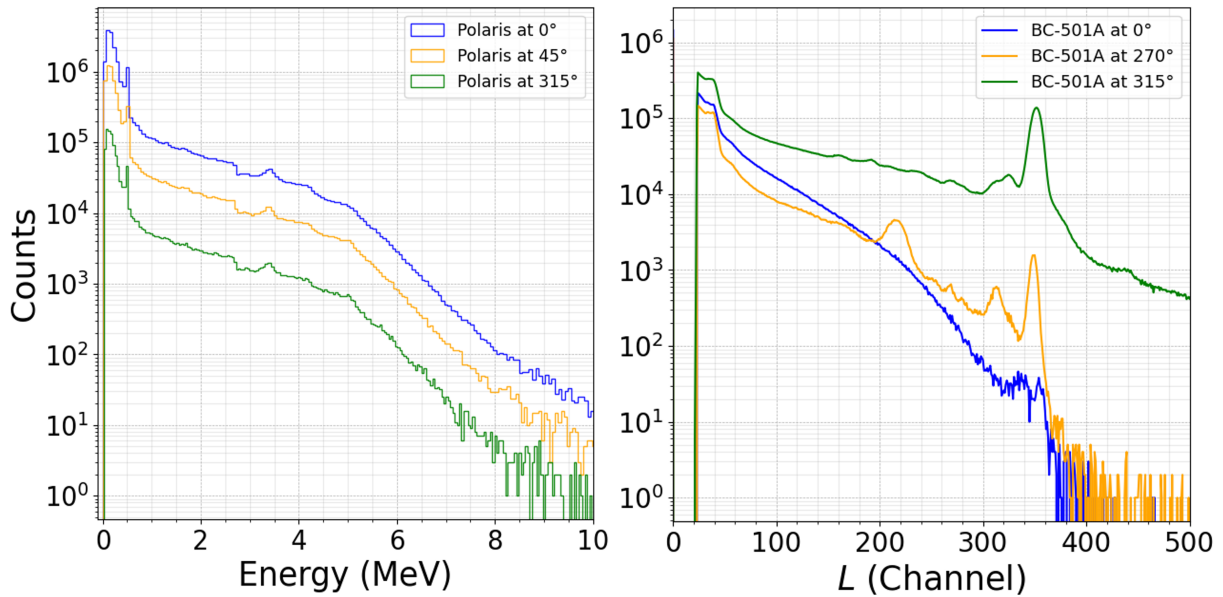


**Figure 6.** Energy spectrum of incident 66 MeV protons on a water target at various angles from (left) Polaris and (right) BC-501A detector respectively.

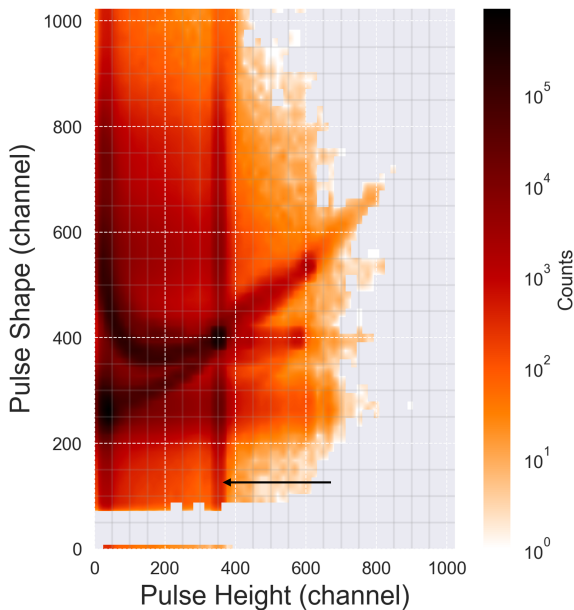


**Figure 7.** 2D pulse shape vs pulse height spectrum of water measured by a BC-501A detector at 315° to a 66 MeV beam incident to the water target.

## References

- [1] Bertolet A and Carabe-Fernandez A 2020 Clinical implications of variable relative biological effectiveness in proton therapy for prostate cancer *Acta Oncol.* **59.10** 1171-1177
- [2] Newhauser W and Zhang R 2015 The physics of proton therapy *Phys. Med. Bio.* **60** R155.
- [3] Leo R W 1994 *Techniques for Nuclear and Particle Physics Experiments* Springer-Verlag Berlin Heidelberg New York p 28
- [4] Martin R B and Shaw G 2019 *Nuclear and particle physics an introduction* John Wiley and Sons Ltd. p 156

- [5] Mackin D, Peterson S, Beddar S and Polf J 2012 Evaluation of a stochastic reconstruction algorithm for use in Compton camera imaging and beam range verification from secondary gamma emission during proton therapy *Phys. Med. Biol.* **57.11** 3537.
- [6] Schneider U, Agosteo S, Pedroni E and Besserer J 2002 Secondary neutron dose during proton therapy using spot scanning *Rad. Oncol. Bio. Phys.* **53.1** 244-251.
- [7] Polf J, Peterson S, McCleskey M, Roeder B, Spiridon A, Beddar S and Trache L 2009 Measurement and calculation of characteristic prompt gamma ray spectra emitted during proton irradiation *Phys. Med. Biol.* **54.22** N519–27.
- [8] Kozlovsky B, Murphy R and Ramaty R 2002 Nuclear deexcitation gamma-ray lines from accelerated particle interactions *ApJS* **141** 523
- [9] Draeger E, Peterson S, Mackin D, Chen H, Beddar S, Polf J 2017 Feasibility studies of a new event selection method to improve spatial resolution of Compton imaging for medical applications *IEEE transactions on radiation and plasma medical sciences* **1.4** 358–367
- [10] Kim S, Seo H, Park J, Kim C, Lee C, Lee S, Lee D, Lee J 2013 Resolution recovery reconstruction for a Compton camera *Phys. Med. Biol.* **58.9** 2823.
- [11] Draeger E, Mackin D, Peterson S, Chen H, Avery S, Beddar S and Polf J 2018 3D prompt gamma imaging for proton beam range verification *Phys. Med. Biol.* **63.3** 035019.
- [12] Maggi P, Peterson S, Panthi R, Mackin D, Yang H, He Z, Beddar S and Polf J 2020 Computational model for detector timing effects in Compton-camera based prompt-gamma imaging for proton radiotherapy *Phys. Med. Biol.* **65.12** 125004.
- [13] McCleskey M, Kaye W, Mackin D, Beddar S, He Z and Polf J 2015 Evaluation of a multistage CdZnTe Compton camera for prompt gamma imaging for proton therapy *Nuclear Instruments and Methods in Physics Research Section A: Accelerators, Spectrometers, Detectors and Associated Equipment* **785** 163–169.
- [14] Panthi R, Maggi P, Peterson S, Mackin M, Polf J and Beddar S 2020 Secondary particle interactions in a Compton camera designed for in vivo range verification of proton therapy *IEEE transactions on radiation and plasma medical sciences* **5.3** 383–391.
- [15] Tuckwell W and Bezak. E 2007 Calculation of the positron distribution from  $^{15}\text{O}$  nuclei formed in nuclear reactions in human tissue during proton therapy *Phys. Med. Biol.* **52.9** 2483.
- [16] Jiang H, Wang B, Xu X, Suit H and Paganetti H 2005 Simulation of organ-specific patient effective dose due to secondary neutrons in proton radiation treatment *Phys. Med. Biol.* **50.18** 4337.
- [17] Streicher M, Goodman D, Zhu Y, Brown S and Kiff S 2017 Fast neutron detection using pixelated CdZnTe spectrometers *IEEE Transactions on Nuclear Science* **64.7** 1920–1926.
- [18] Peterson S, Maggi P, Panthi R, Beddar S, Mackin D, and Polf J, 2020 Investigating the impact of secondaries neutrons on Compton camera for medical imaging [Poster].
- [19] Zhang F, He Z and Seifert C 2007 A prototype three-dimensional position sensitive CdZnTe detector array *IEEE Transactions on Nuclear Science* **54.4** 843–848.
- [20] Martin-Martin A, Iniguez M, Luke P, Barquero R, Lorente A, Morchon J, Gallego E, Quincoces G and Marti-Climent J 2009 Evaluation of CdZnTe as neutron detector around medical accelerators *Radiation Protection Dosimetry* **133.4** 193–199.
- [21] Goodman D, Streicher M, Ahu Y, Brown S and He Z 2017 1-D fast neutron source localization using digital pixelated 3-D position-sensitive CdZnTe Detectors *IEEE Transactions on Nuclear Science* **64.9** 2531-2535.
- [22] Streicher M, Goodman D, Zhu Y, Brown S, Kiff S and He Z 2017 Fast Neutron Detection Using Pixelated CdZnTe Spectrometers *IEEE Transactions on Nuclear Science* **64.7** 1920-1926.

# Higgs boson decays to four leptons and missing transverse momentum via dark vector bosons

MP Connell<sup>1</sup>, X Mapekula<sup>1</sup>

<sup>1</sup>Department of Mechanical Engineering Science, University of Johannesburg, Auckland Park, Johannesburg, South Africa.

E-mail: rsamconn@gmail.com

**Abstract.** Physics beyond the Standard Model (SM) is well motivated and one important search area is to use the Higgs boson as a discovery portal for dark matter. One specialisation of this search is to the exotic decay of the Higgs boson via two dark vector bosons,  $Z_d$ , each of which promptly decay to two leptons, giving a clean four lepton final state. In this search, the SM Higgs boson fluctuates to the dark Higgs boson via Higgs boson mixing at the SM Higgs boson mass. The decay then proceeds via the virtual dark Higgs boson. A variation is that the Higgs boson is produced rather at the dark Higgs boson mass, with the same production mechanism and decay topology. In this case, the search includes  $S$ , the dark Higgs boson, in addition to  $Z_d$ . Previous studies of these channels have shown a search for Higgs boson decays to a  $4\ell + MET$  final state could be another promising avenue. Here  $MET$  refers to missing transverse momentum, meaning there is also an additional dark particle in the modelling. Currently there are no constraints on the dark Higgs boson mass. We introduce this new search, which is still in the initial stages.

## 1. Introduction

The Large Hadron Collider at CERN, Switzerland, is able to produce billions of high energy events in proton-proton collisions. This allows us to search for particles that only occur at such energy scales, including potential candidates for dark matter. There are many theories for what constitutes dark matter but little positive evidence for what it could be [1]. Investigating potential candidates for dark matter and how they interact with normal matter is a crucial part of advancing our understanding of fundamental physics.

## 2. Background

### 2.1. Dark Matter

There is extensive astrophysical evidence for dark matter, including: rotational curve of many galaxies which indicate that normal matter cannot account for the gravitational strength observed, another phenomenon is gravitational lensing by clusters of galaxies, which also requires additional gravitating mass and also mentioned is the observed large scale structure of the cosmos and the microwave background, the modelling of which requires the existence of cold dark matter [2]. Thus, we must search for matter which interacts predominantly via gravity and potentially only very weakly with normal matter [3].

### 2.2. Higgs Portal

The discovery of the Higgs boson in 2012 by the ATLAS and CMS experiments [4, 5] opened up a promising new avenue in the search for dark matter. Because of both the Higgs boson's

high mass and its role as the excitation of the Higgs field, which gives particles mass, it may preferentially couple to exotic, high-mass particles. If this is the case then decays of the Higgs boson could be a rich source of information for production and behaviour of exotic particles, such as dark matter particles [6–8].

### 2.3. Dark Vector Bosons

One branch of exotic Higgs boson decays that has already been investigated is Higgs boson decays via dark vector bosons,  $Z_d$  [9–11]. These studies used the Hidden Abelian Higgs Model (HAHM) [3, 12–14]. This model allows coupling of dark matter to normal matter. This can be represented by the introduction of a kinetic mixing term,  $\epsilon$ , between normal bosons and  $Z_d$ , which would allow for such a weak interaction [1]. The mixing between the SM and dark Higgs boson is also accommodated within this model, via a Higgs portal coupling parameter  $\kappa$  [3]. In the searches discussed above, a Higgs boson is produced by gluon-gluon fusion (ggF) which subsequently mixes to the dark Higgs boson and then decays to two  $Z_d$ , each of which themselves decay into two leptons of opposite sign and opposite flavour, giving a four lepton final state.

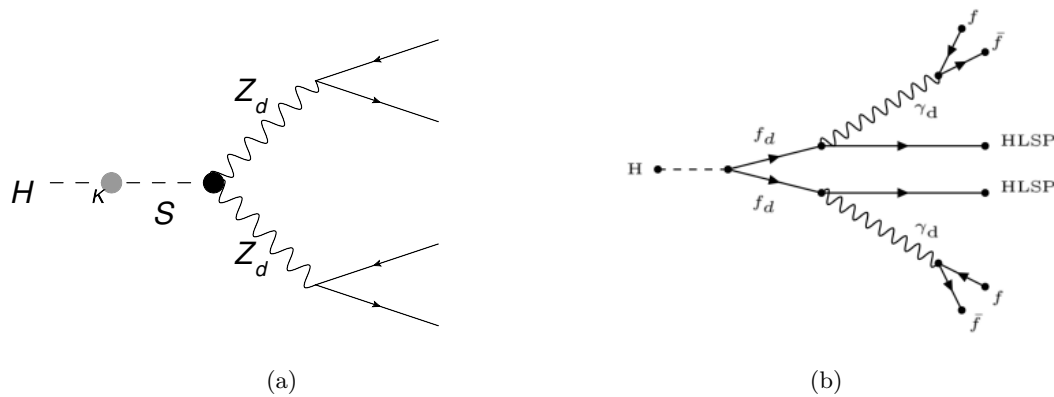


Figure 1: Feynman Diagrams (a) where a Higgs boson is produced by ggF, fluctuating to the dark Higgs boson,  $S$ , which decays via two  $Z_d$  to four leptons and (b) an example where there is also  $MET$  in the final state, in this case represented by the particles labelled HLSP [15].

This scenario is shown in Figure 1(a). Depending on whether the ggF Higgs boson production is on shell for the Higgs boson or the dark Higgs boson (sometimes called more generally the additional scalar), then the invariant mass of either the Higgs boson or the dark Higgs boson can be reconstructed from the kinematics of the four leptons. Higgs boson to  $Z_d$  to four leptons studies allow us to search for  $Z_d$  and possibly also the dark Higgs boson and then study the coupling constants. In Figure 1(b), there is a similar decay where the Hidden Lightest Supersymmetric Particle (HLSP) adds  $MET$  to the final state.

Previous studies have shown  $Z_d$  candidates which are worth investigating [9–11]. Figure 2 shows the 95% confidence level upper bound on the cross section of Higgs boson decays to four lepton final states via  $Z_d$ , for different  $Z_d$  masses. While the results are still consistent with the SM, we can see one distinct region where the observed limit is greater than  $2\sigma$ , at 25–30 GeV.

### 2.4. $4\ell$ and $MET$

A typical final state event display in the high mass scalar search is shown in Figure 3, where  $\langle m_{\ell\ell} \rangle$  is defined as the average invariant mass of the two lepton pairs [9]. Such displays have

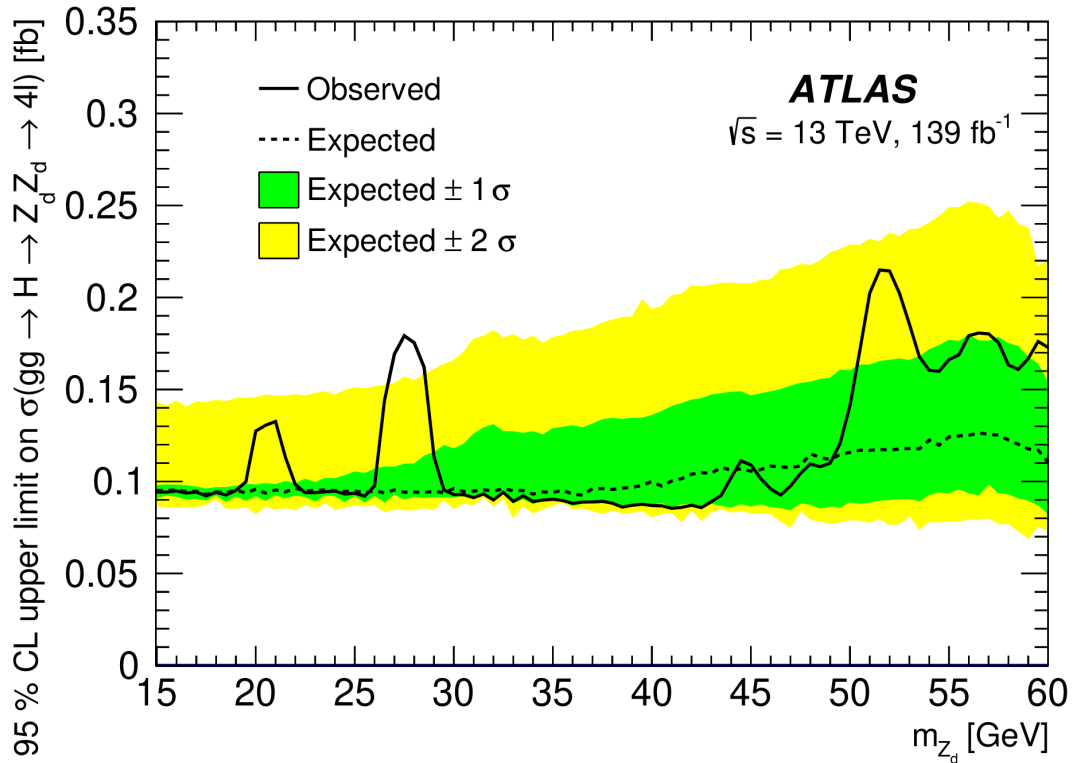


Figure 2: The expected and observed 95% confidence level upper bound on the cross-section of Higgs boson to  $Z_d$  decays for different  $Z_d$  masses, assuming SM Higgs boson production via ggF. This includes the  $4\ell$ ,  $4\mu$  and  $2\ell 2\mu$  decay channels HAHM parameters were set to  $\kappa = \epsilon = 10^{-4}$  [9].

often been found to be accompanied by the presence of  $MET$  in the range 20-80 GeV, which was not accounted for in previous studies. A natural progression of the previous searches is to conduct a search that includes  $MET$  in the four lepton final state and investigate the bumps further. Accordingly we have chosen a model which can generate events in this scenario, as shown in Figure 1(b). The previous studies used the Hidden Abelian Higgs Model (HAHM), which does not include any  $MET$ . This particular model uses the the Falkowski–Ruderman–Volansky–Zupan (FRVZ) model, which introduces lepton jets - events which produce between 4 and 8 collimated leptons in the final state [16, 17]. Lepton jets are predicted by models which posit a massive hidden vector particle in the MeV to GeV range, in this case a dark photon. This dark photon has a small kinetic mixing with the SM photon, which allows it to decay to lighter particles with electric charge.

Including  $MET$  in the kinematics for the signal Monte Carlo (MC) event generation via the above model is not considered a model dependent analysis. This allows one to have signal events, to be added to the MC background events, to facilitate the development of the search algorithm. The actual search will look for excesses which could come from a more general class of models that still conform somewhat to these kinematics.

### 3. Methodology

We will conduct a resonance search where the mass of each  $Z_d$  boson can be reconstructed from the combined invariant mass of the resulting lepton pairs. The search will look specifically in the mass ranges of 20-30 GeV for  $Z_d$ . Currently the analysis is still in the early stages of signal

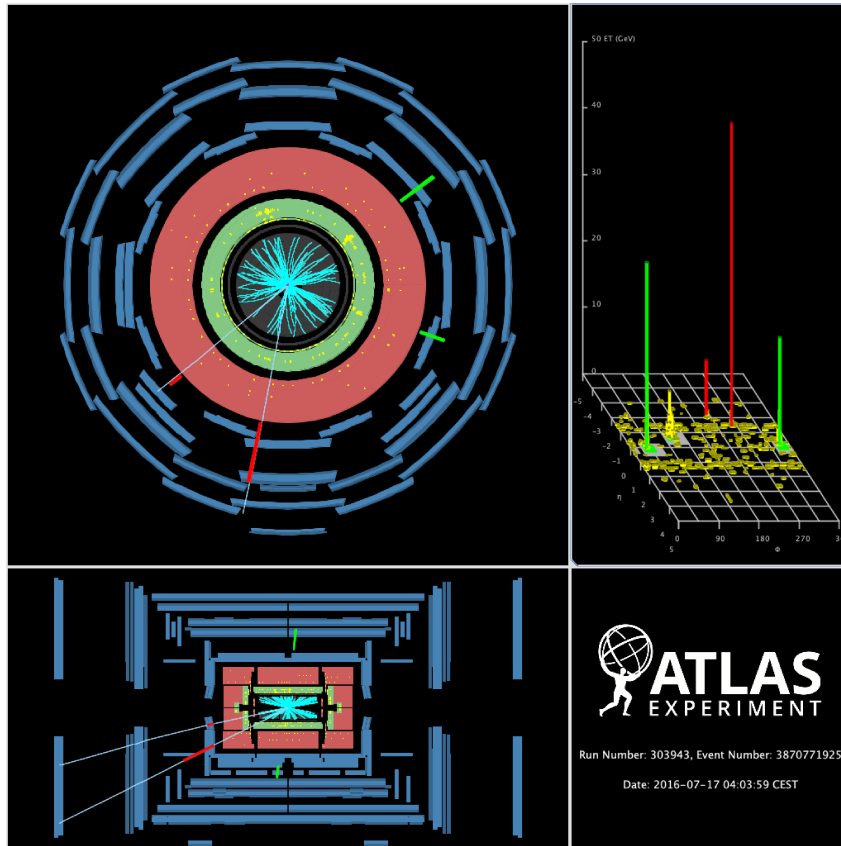


Figure 3: A typical event display for one candidate event in the  $2\ell 2\mu$  channel with  $\langle m_{\ell\ell} \rangle = 20.6$  GeV. Electrons are indicated by green segments/towers, and muons by red segments/towers [9].

generation.

### 3.1. Signal Generation

The first step in the analysis is signal generation. A suitable model must be found to produce the signal for the  $H \rightarrow 4\ell + MET$  decay. This is done using MC programs, such as MadGraph [18] and Pythia [19], which can generate chains of particle interactions starting from a proton-proton collision. These programs generate random sequences of simulated events based on calculated probability distributions of known events, while recording statistics such as particle kinematics. The model used for signal generation must be validated by producing kinematic plots for final state particles in the mass region of interest. Constructing a program to simulate your decay from scratch can be very complex and time-consuming. Thus the best approach is to reuse code from another analysis with a similar decay and final state, by adapting it to be as close as possible to the decay and final state you desire. Because the previous  $Z_d$  studies used the HAHM, they could not be adapted to include  $MET$  in the final state, so a new model had to be found and adapted. A similar model to our decay can be seen in an analysis investigating light long-lived particles that decay to lepton jets [15].

A decay for this model can be seen in Figure 1(b). For the purpose of the  $4\ell + MET$  study, the model can be adapted such that the HLSP would constitute the  $MET$  and each dark photon would become a  $Z_d$ . The fermions would be leptons and the  $f_d$  would be further intermediate dark particles.

One issue with this model is that the particles labelled  $f_d$  are produced back-to-back: their transverse momentum,  $p_T$ , must cancel each other out. This means their subsequent decay products must have a  $p_T$  that also adds up to being effectively back-to-back, which limits the  $MET$  distribution to being quite low - a high  $MET$  requires high  $p_T$  for the other decay products, which is less likely. This limits the  $MET$  to being almost entirely below 50 GeV, which limits the maximum  $MET$  size we can analyse from this model. However, it is worth using this model for validation plots as there could still be interesting information for  $MET$  in this region.

Figure 4 shows typical kinematic distributions as produced by this model. The examples selected are the leading and subleading electron and muon pairs' transverse momenta.

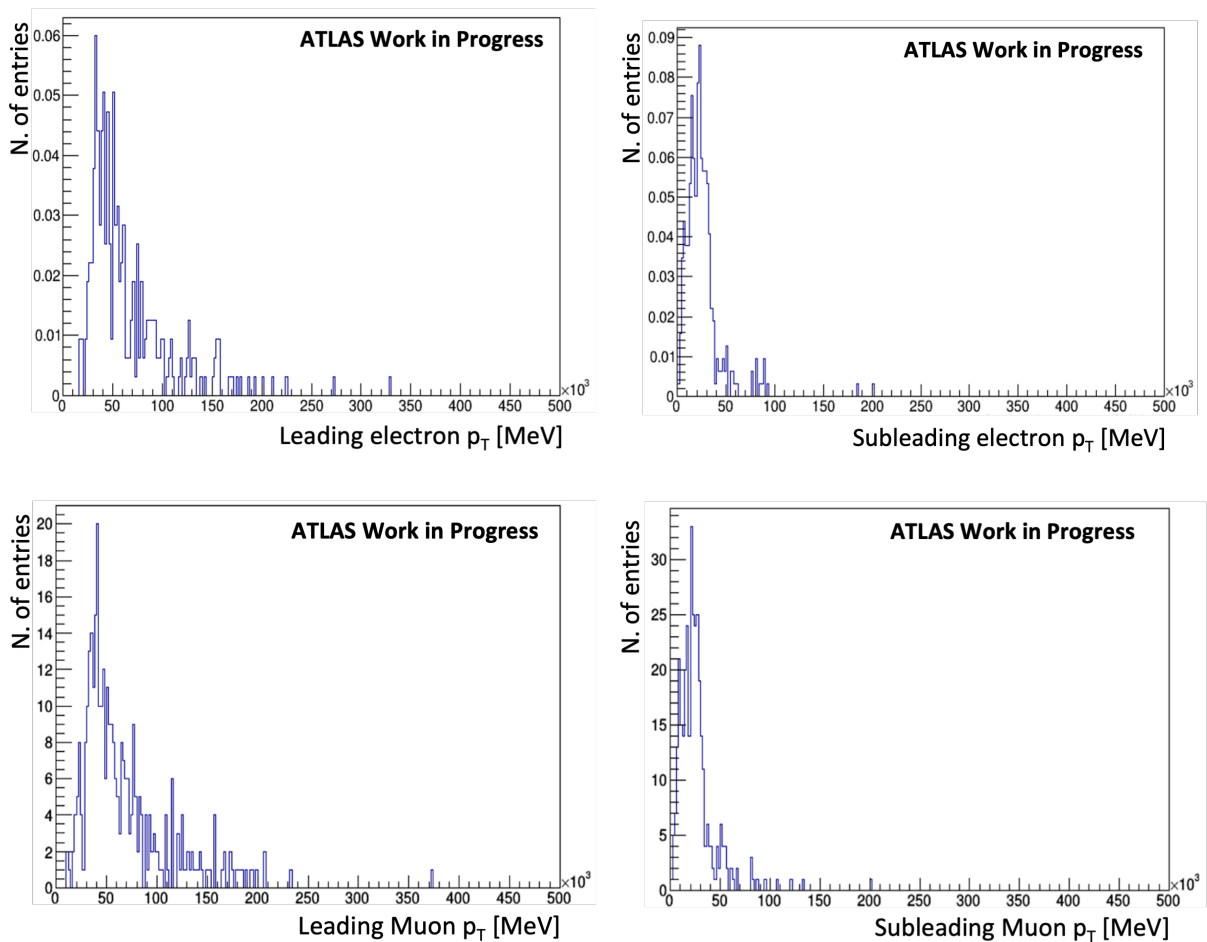


Figure 4: Kinematic plots of leading and subleading electron pair and muon pair transverse momenta produced using the lepton jets model [15].

### 3.2. Background

It is expected that most backgrounds for this analysis will be due to incorrect identification of leptons. Events with more than four lepton final states where some leptons go undetected or are mislabelled could be mistaken as candidate events. Similarly events with leptons plus jets/ photons in the final state where the jets/ photons fake leptons could be mistaken as a four lepton

final state. In the SM,  $MET$  always represents neutrinos so events with four charged leptons plus some neutrinos could be mistaken as candidate events.

#### 4. Conclusions

The aim of the analysis is to investigate a Higgs boson decay via  $Z_d$  to a  $4\ell + MET$  final state, which is motivated by previous studies into a four lepton final state that revealed excesses at certain  $Z_d$  masses. The analysis is still in the early stages: progress has been made in signal generation and a potential model for the signal has been discovered but still needs to be validated. Once signal generation has been completed then the relevant backgrounds will have to be determined and modelled as well. The general statistical analysis must be developed in order to be able to determine signal from background. Looking to the future, we intend to apply machine learning methods, such as boosted decision trees, for reducing background. These and similar methods will be investigated and compared to standard cut-based methods.

#### References

- [1] Curtin D, Essig R, Gori S, Jaiswal P, Katz A, Liu T, Liu Z, McKeen D, Shelton J and Strassler M e a 2014 *Phys. Rev. D* **90**(7) 075004
- [2] Ackerman L, Buckley M R, Carroll S M and Kamionkowski M 2009 *Phys. Rev. D* **79**(2) 023519
- [3] Curtin D, Essig R, Gori S and Shelton J 2015 *JHEP* **02** 157
- [4] ATLAS Collaboration 2012 *Phys. Lett. B* **716** 1
- [5] CMS Collaboration 2012 *Phys. Lett. B* **716** 30
- [6] Shrock R E and Suzuki M 1982 *Phys. Lett. B* **110** 250
- [7] Strassler M J and Zurek K M 2007 *Phys. Lett. B* **651** 374–379
- [8] Schabinger R M and Wells J D 2005 *Phys. Rev. D* **72** 093007
- [9] ATLAS Collaboration 2022 *JHEP* **03** 041
- [10] ATLAS Collaboration 2018 *JHEP* **06** 166
- [11] ATLAS Collaboration 2015 *Phys. Rev. D* **92** 092001
- [12] Davoudiasl H, Lee H S, Lewis I and Marciano W J 2013 *Phys. Rev. D* **88** 015022
- [13] Davoudiasl H, Lee H S and Marciano W J 2012 *Phys. Rev. D* **85** 115019
- [14] Gopalakrishna S, Jung S and Wells J D 2008 *Phys. Rev. D* **78** 055002
- [15] C Sebastiani I Longarini e a 2020 *European Physical Journal C* **80** 450
- [16] Falkowski A, Ruderman J T, Volansky T and Zupan J 2010 *Journal of High Energy Physics* **2010**
- [17] Falkowski A, Ruderman J T, Volansky T and Zupan J 2010 *Physical Review Letters* **105**
- [18] Alwall J, Frederix R and et al S F 2014 *J. High Energ. Phys.* **79**
- [19] T Sjöstrand S M and Skands P 2008 *Comput. Phys. Commun.* **178**

# A frequentist study of the false signals generated in the training of semi-supervised neural network classifiers using a Wasserstein Generative Adversarial Network as a data generator

Benjamin Lieberman<sup>1</sup>, Salah-Eddine Dahbi<sup>1</sup>, Xifeng Ruan<sup>1</sup> and Finn Stevenson<sup>1</sup>, Bruce Mellado<sup>1,2</sup>

<sup>1</sup>School of Physics and Institute for Collider Particle Physics, University of the Witwatersrand, Johannesburg, Wits 2050, South Africa

<sup>2</sup>iThemba LABS, National Research Foundation, PO Box 722, Somerset West 7129, South Africa

E-mail: benjamin.lieberman@cern.ch

**Abstract.** In resonance searches for new physics, machine learning techniques are used to classify signal from background events. When using machine learning classifiers it is necessary to measure the amount of background events being incorrectly labelled as signal events. In this research the  $Z\gamma \rightarrow (\ell + \ell^-)\gamma$  final state dataset focusing around 150 GeV centre of mass is used. A Wasserstein Generative Adversarial Network, WGAN, is used as a generative model and a semi-supervised Deep Neural Network, DNN, is used as a classifier. This study provides a methodology and the results of the measurement of false signals generated during the training of semi-supervised DNN classifiers.

## 1. Introduction

The Standard Model, SM, of particle physics was completed by the 2012 discovery of the Higgs boson, by the ATLAS and CMS collaboration [1, 2]. Since this discovery, developments in machine learning together with increasing luminosity at the Large Hadron Collider, LHC, has advanced searches beyond the SM, BSM. Searches for new BSM bosons is motivated by phenomena such as the matter-anti-matter asymmetry, Dark Matter, and the origin of the neutrino mass, which cannot be explained by the SM. In order to gain insight into these phenomena, machine learning classifiers are used to extract signal from background processes. The semi-supervised machine learning technique is able to reduce training biases by training models using a partially labeled dataset. In this analysis the machine learning method of the semi-supervised classification study, presented in Ref. [3], is investigated. This paper therefore proposes, implements and evaluates a methodology of scrutinising the success of semi-supervised machine learning classification using a Deep Neural network, DNN [4]. This is achieved by quantifying the amount of error, in the form of fake signal events, caused by over-fitting during the training of semi-supervised models that confront side-bands and the signal regions.

When analysing local and global resonances, a extremely large dataset is necessary to overcome the "look elsewhere effect" [5]. This effect can be defined, in searches for resonances

within a given mass range, as the probability of observing a significant local excess of events, elsewhere within the range. To account for this phenomena, machine learning based data generators can be used in conjunction with traditional Monte Carlo (MC) generation to scale datasets. Generative models such as Generative Adversarial Networks (GAN) and Variational Auto-Encoders (VAE) are excellent examples of methodologies commonly used to scale data [6]. Once trained generative models are able to generate events with excellent accuracy at scale with minimal computational resources. While a full evaluation of the different data generators is being conducted in a parallel study, the Wasserstein Generative Adversarial Network, WGAN, is used in this analysis.

In this study, the Run 1 LHC data features and a 2HDM+ $S$  model, where  $S$  is a singlet scalar, is used Ref. [7, 8]. In this model, the heavy scalar,  $H$ , decays predominantly into  $SS, Sh$ , where  $h$  is the SM Higgs boson. A possible singlet,  $S$ , candidate is reported in Ref. [9]. The model exposes multi-lepton anomalies, presented in Refs. [10, 11, 12, 13], astro-physics anomalies, when complemented by a Dark Matter candidate [14], as well as various other anomalies including the  $g - 2$  muon experiment reported by Fermilab [15, 16, 17]. A full review of anomalies can be found in Ref. [18].

### 1.1. $Z\gamma$ Monte Carlo Dataset

In this study, the simulated  $Z\gamma$  background, is considered.  $Z\gamma$  contributes to 90% of the total backgrounds in the production of the Higgs like heavy scalar decaying to  $Z\gamma$  ( $pp \rightarrow H \rightarrow Z\gamma$ ) events, where  $Z \rightarrow e^+e^-$  or  $Z \rightarrow \mu^+\mu^-$ . The  $Z\gamma$  SM MC samples used in this analysis have been generated using `Madgraph5` [19] and the detector level simulation is performed using `Delphes(v3)` [20]. The focus of the analysis is around the centre of mass of 150GeV ( $122\text{GeV} < m_{\ell\ell\gamma} < 178\text{GeV}$ ). The kinematic features used in the study are  $Z\gamma$  invariant mass,  $m_{\ell\ell\gamma}$ , missing transverse energy,  $E_T^{miss}$ , missing transverse energy azimuthal angle,  $\Phi_{E_T^{miss}}$ ,  $\Delta R_{\ell\ell}$  ( $\Delta R \equiv \sqrt{(\Delta\eta)^2 + (\Delta\phi)^2}$ ), the number of jets,  $N_j$ , number of central jets,  $N_{cj}$ , and the transverse momentum,  $P_{t_{\ell_1|\ell_2|\gamma}}$ , azimuthal angle,  $\Phi_{\ell_1|\ell_2|\gamma}$ , and pseudo-rapidity,  $\eta_{\ell_1|\ell_2|\gamma}$ , for each of the leptons and the photon respectively. The feature distributions are shown in Figure 2.

### 1.2. Wasserstein Generative Adversarial Network with gradient penalty

The GAN training strategy is an interaction between two competing neural networks. First, the generator model,  $G$ , maps a source of noise to the input space. Then a discriminator model receives either a generated sample or a MC data sample and must distinguish between the two. The generator is trained to output data of sufficient quality to fool the discriminator into believing it is MC data. The discriminator is simultaneously trained to distinguish MC from generated data. An improved methodology of the GAN, described in Ref. [21], is the Wasserstein GAN, WGAN, which adopts the Wasserstein distance,  $W(q, p)$ , defined as the distance between two probability distributions,  $q$  and  $p$ . The discriminator is replaced in the improved model with a critic,  $C$ , and the gradients are controlled using a gradient penalty,  $GP$ , which penalizes the norm of the critic gradients with respect to the input. An overview of the WGAN with gradient penalty is shown in Figure 1. The generator loss,  $L_g$ , function is defined as

$$L_g = \min_{\tilde{x} \sim \mathbb{P}_g} \mathbb{E} [C(\tilde{x})], \quad (1)$$

where  $\tilde{x} = G(z)$  and  $z$  is the latent space noise and  $\mathbb{P}_g$  is the generator model distribution,  $\tilde{x}$ . The critic loss,  $L_c$ , with gradient penalty is defined as

$$L_c = \max_{x \sim \mathbb{P}_r} \mathbb{E} [C(x)] - \mathbb{E} [C(\tilde{x})] + \lambda * GP, \quad (2)$$

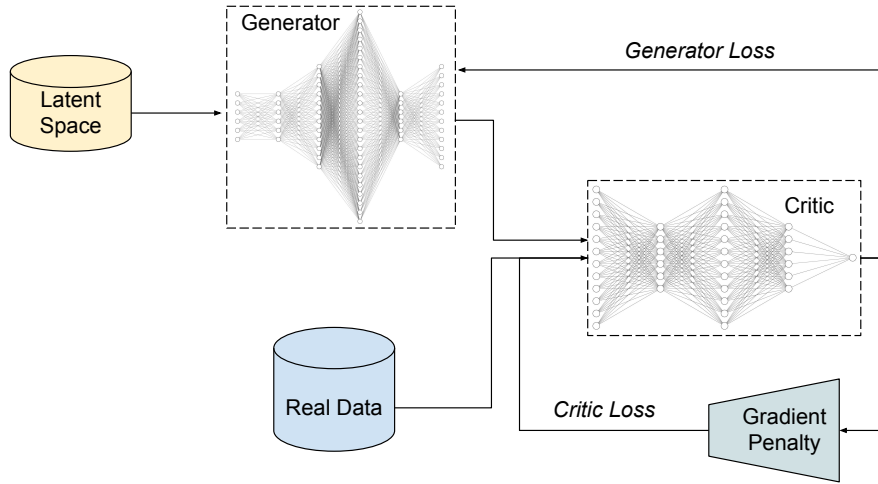


**Figure 1.** Systematic diagram of WGAN with gradient penalty

where  $\lambda$  is the gradient penalty coefficient,  $\mathbb{P}_r$  is the MC data distribution, and the gradient penalty, GP, is defined as

$$GP = \mathbb{E}_{\tilde{x} \sim \mathbb{P}_{\tilde{x}}} [(\|\nabla_{\tilde{x}} C(\tilde{x})\|_2 - 1)^2] \quad (3)$$

## 2. Methodology

The methodology used in this analysis, to quantify fake signal generated in the training of DNN classifiers, can be broken down into three components. These are the WGAN data generator, the semi-supervised DNN and the background rejection scan. In order to conduct a  $3\sigma$  frequentest analysis of fake signal generated, the semi-supervised DNN model must be trained and evaluated on independent datasets more than  $5 \cdot 10^4$  times. For each run, iteration of training and evaluating the DNN, the WGAN is therefore used to generate a statistically distinct dataset.

### 2.1. Data Generation using a WGAN with gradient penalty

The machine learning based data generator used in this analysis, is the WGAN with gradient penalty, which is implemented in Python using pytorch [22]. The model is trained and optimised in order to reproduce the  $Z\gamma$  MC events and as accurately as possible. To this end, the quality of the generated events must be evaluated in terms of the feature distributions as well as the event-wise feature correlations. In order for the generated events to successfully mimic high energy physics events, both the feature distributions and correlations must match the MC data.

The optimisation of the model is therefore achieved by minimising the difference in feature distributions and correlation between the generated data and MC training data. The final model architectures used for the WGAN are summarised in Table 1. The final hyper-parameters used are latent dimension of 18 (equal to number of features), learning rate of  $6 \cdot 10^{-5}$ , batch size of 512 and gradient penalty coefficient,  $\lambda$ , of 0.001. The Critic is trained five times for each Generator training iteration in order to optimised the WGAN training.

### 2.2. Semi-Supervised DNN Training

The DNN model used, is a replica of the optimised model used in Ref. [3]. The model is trained on all of the features except the invariant mass,  $m_{ll\gamma}$ , which is used to define the signal and

**Table 1.** Critic and generator final optimised model architectures.

Model	Layer(s)	Number of nodes	Activation function
Critic	Input Layer	18 (Number of features)	ReLu
	Hidden Layers	[256, 512, 256]	ReLu
	Output Layer	1	Linear
Generator	Input Layer	18 (Latent Space)	BatchNorm, ReLu
	Hidden Layers	[256, 512, 1024, 512, 256]	BatchNorm, ReLu
	Output Layer	18 (Number of features)	BatchNorm, ReLu

background regions. The dataset is divided into two training samples, namely mass-window or signal region, (144GeV to 156GeV), and side-band or background region, (132GeV to 144GeV and 156GeV to 168GeV). As both samples comprise of pure  $Z\gamma$  background, we do not expect the DNN response to find any separation between the two samples.

### 2.3. Quantification of Fake Signal using background rejection scan

For each of the generated datasets that the DNN is trained on, a DNN response, in range (0, 1), is produced. In order to evaluate local and global fake signals, a background rejection scan of the response distribution is used.

The background rejection scan is implemented by extracting batches of events, from the response distribution, to be analysed. The batches extracted make up 50, 60, 70, 80 and 90% of the total events. Each batch is taken starting from the maxima, 1, of the response distribution and moving towards the minima, 0. Once a batch of data is extracted, the events are mapped to their corresponding invariant mass. Each batch's invariant mass distribution is fit with an exponential function,  $f(x)$ , which exposes the distribution of background events. A second fit, using the exponential function with an added Gaussian,  $g(x)$ , is applied with the Gaussian centred at the center of mass, 150 GeV, and  $\sigma$  equal to the resolution of the dataset, 2.4, Ref. [23]. The Gaussian therefore is able to represent any signal events found within the mass window. As there are no signal events within the analysis dataset, any signals found can be assumed to be generated within the training of the DNN. The significance of signal found for each batch can be calculated using Equation 4.

$$\sigma = \frac{\int_a^b [g(x) - f(x)] dx}{\sqrt{\int_a^b [f(x)] dx}} \quad (4)$$

where  $a$  and  $b$  are the minima, 132 GeV, and maxima, 168 GeV, of the invariant mass respectively.

## 3. Results and discussion

The WGAN with gradient penalty converged after 1200 epochs. The feature distributions and corresponding correlations, generated by the model, are visually compared to that of the MC data in Figures 2 and 3 respectively. A visual analysis clearly exposes that the generated feature distributions describe the MC data well, with exception of the  $\phi_{\ell_1|\ell_2|E_T^{miss}}$  distributions. It is important to note that the MC  $\phi_{\ell_1|\ell_2|E_T^{miss}}$  distributions are continuous and uniform. During the optimisation of the WGAN it was made clear that the WGAN model has the most difficulty learning uniform distributions. In the results in Figure 2, these generated feature distributions

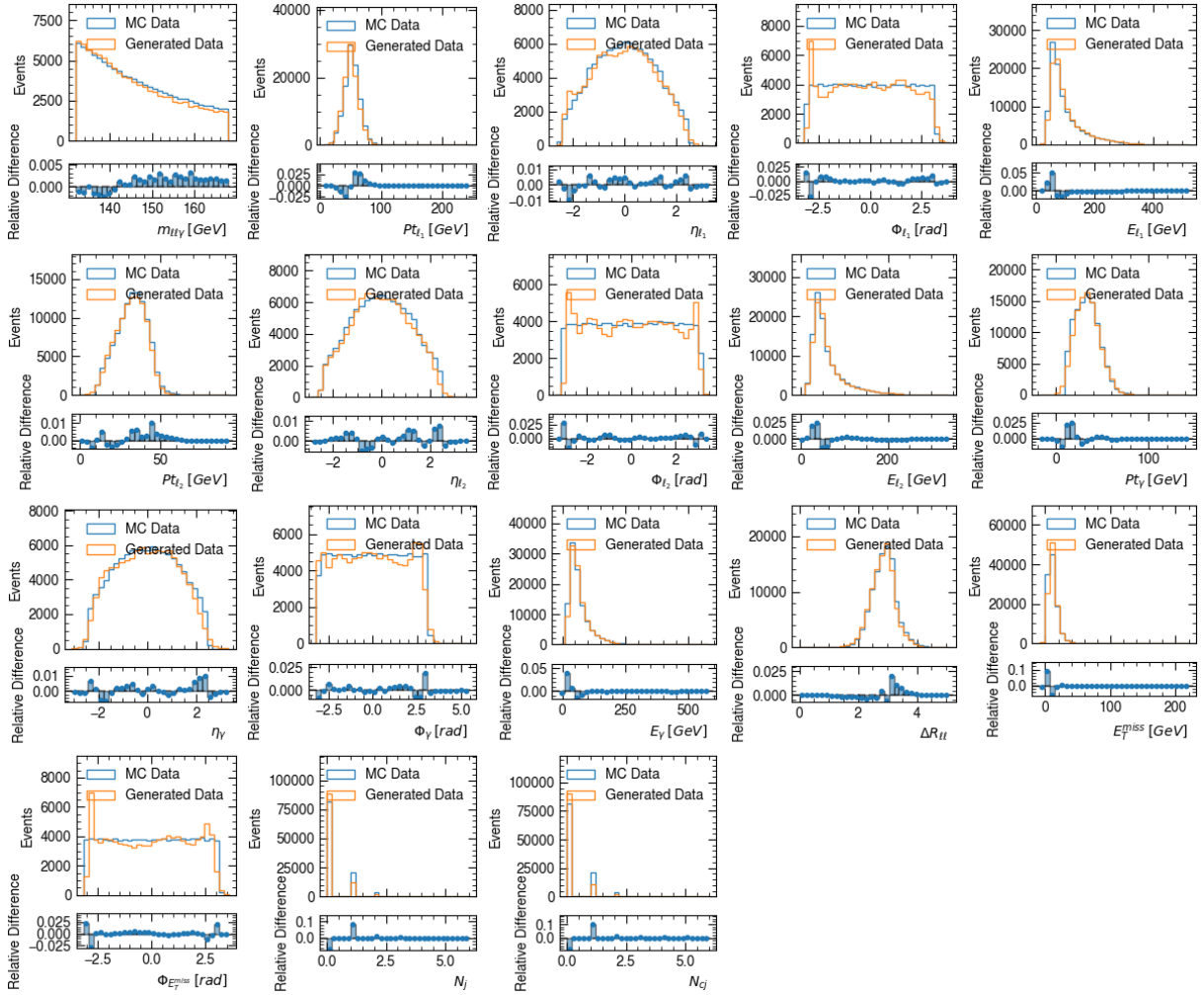


**Figure 2.** Final feature distribution comparison of MC data and WGAN generated data.

still contain undesirable spikes which must be improved in future studies. The Kolmogorov-Smirnov score and bin-wise relative difference scores are used to measure the difference between generated and MC feature distributions. The final model is found to generate data with an average Kolmogorov-Smirnov score of 0.074 and average bin-wise relative difference of 0.021. The event-wise feature correlation of the generated data is shown to excellently mimic that of the MC data using the Spearman correlation and mean correlation difference [24]. The final model achieves a Spearman correlation score of 0.825 and mean correlation difference of 0.023. As most of the feature distributions and correlations of the generated data are of sufficient quality, the pre-trained model can be used in the frequentest study.

A single run of the frequentest study consists of; WGAN generated dataset, training the DNN on the given dataset, mapping the DNN response to invariant mass distribution and applying fits to quantify significance of fake signal for each background rejection. To initially evaluate the extent of false signal, the study is repeated 500 times. The result of these runs is shown in Figure 4. It is important to note that measured significance reflect not only the over-training of the DNN but also the success of the WGAN in synthesising realistic events. This is primarily due to the quality of the generated invariant mass distribution, as the signal and background fits expect the distribution to be a smooth exponential. Therefore if the generated  $m_{ll\gamma}$  distribution

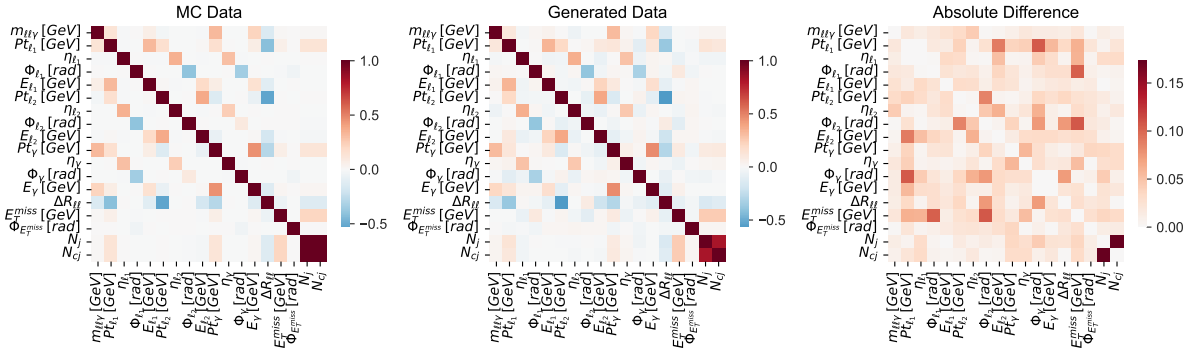


**Figure 3.** Feature correlation heatmaps. Left: MC training data. Centre: WGAN generated data. Right: Difference between MC and generated data.

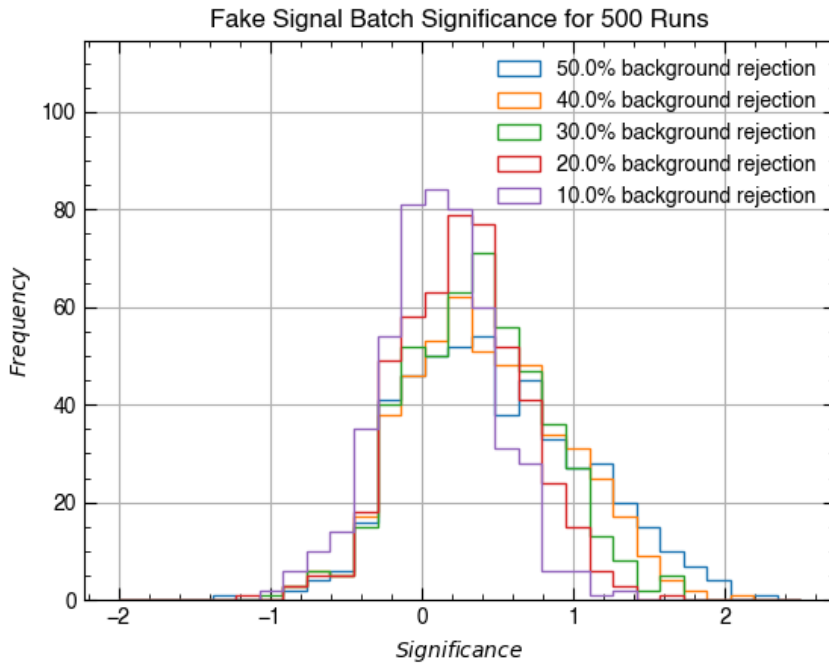


**Figure 4.** Signal significance measured for DNN response event batches on 500 runs of the frequentest study.

is not smooth, these fluctuations can be misinterpreted as signal. However as the final  $m_{ll\gamma}$  distribution generated is smooth, another influence to the results may be the effect of the non-uniformity of  $\phi_{\ell_1|\ell_2|E_T^{miss}}$  distributions on the DNN training.

#### 4. Conclusions

The analysis has shown that, using the above methodology, the extent of fake signal generated in the training of machine learning classifiers can be quantified. The generated dataset show clear evidence that a the WGAN can be used to synthesise high energy physics events. The significance

distributions produced in Figure 4, demonstrates that for 500 runs the significance measured is reasonable, maximum  $2\sigma$ . In order to achieve a  $3\sigma$  analysis, the analysis needs to be repeated for more than 50000 runs. This will allow the significance to be integrated over to quantify the extent of the influence of local and global excesses. By increasing the number of iterations, the accuracy of the final probability distribution improves. The frequentist methodology presented can be used to extract systematic uncertainties, at a fixed mass, using a generalised background dataset.

## References

- [1] Aad G *et al.* (ATLAS) 2012 *Phys. Lett. B* **716** 1–29 (*Preprint* 1207.7214)
- [2] Chatrchyan S *et al.* (CMS) 2012 *Phys. Lett. B* **716** 30–61 (*Preprint* 1207.7235)
- [3] Dahbi S E *et al.* 2021 *International Journal of Modern Physics A* ISSN 1793-656X
- [4] Baldi P, Sadowski P and Whiteson D 2014 *Nature Communications* **5**
- [5] Gross E and Vitells O 2010 *The European Physical Journal C* **70** 525–530
- [6] Otten S and othera 2019 Event generation and statistical sampling for physics with deep generative models and a density information buffer
- [7] von Buddenbrock S, Chakrabarty N, Cornell A S, Kar D, Kumar M, Mandal T, Mellado B, Mukhopadhyaya B and Reed R G 2015 (*Preprint* 1506.00612)
- [8] von Buddenbrock S, Chakrabarty N, Cornell A S, Kar D, Kumar M, Mandal T, Mellado B, Mukhopadhyaya B, Reed R G and Ruan X 2016 *Eur. Phys. J. C* **76** 580 (*Preprint* 1606.01674)
- [9] Crivellin A, Fang Y, Fischer O, Kumar A, Kumar M, Malwa E, Mellado B, Rapheeha N, Ruan X and Sha Q 2021 (*Preprint* 2109.02650)
- [10] von Buddenbrock S, Cornell A S, Fadol A, Kumar M, Mellado B and Ruan X 2018 *J. Phys. G* **45** 115003 (*Preprint* 1711.07874)
- [11] Buddenbrock S, Cornell A S, Fang Y, Fadol Mohammed A, Kumar M, Mellado B and Tomiwa K G 2019 *JHEP* **10** 157 (*Preprint* 1901.05300)
- [12] von Buddenbrock S, Ruiz R and Mellado B 2020 *Phys. Lett. B* **811** 135964 (*Preprint* 2009.00032)
- [13] Hernandez Y, Kumar M, Cornell A S, Dahbi S E, Fang Y, Lieberman B, Mellado B, Monnakgotla K, Ruan X and Xin S 2021 *Eur. Phys. J. C* **81** 365 (*Preprint* 1912.00699)
- [14] Beck G, Kumar M *et al.* 2021 (*Preprint* 2102.10596)
- [15] Sabatta D, Cornell A S, Goyal A, Kumar M, Mellado B and Ruan X 2020 *Chin. Phys. C* **44** 063103 (*Preprint* 1909.03969)
- [16] Abi B *et al.* (Muon g-2) 2021 *Phys. Rev. Lett.* **126** 141801 (*Preprint* 2104.03281)
- [17] Aoyama T *et al.* 2020 *Phys. Rept.* **887** 1–166 (*Preprint* 2006.04822)
- [18] Fischer O *et al.* 2021 *Unveiling hidden Physics Beyond the Standard Model at the LHC* (*Preprint* 2109.06065)
- [19] Alwall J, Frederix R, Frixione S, Hirschi V, Maltoni F, Mattelaer O, Shao H S, Stelzer T, Torrielli P and Zaro M 2014 *Journal of High Energy Physics* **2014**
- [20] de Favereau J, Delaere C, Demin P, Giammanco A, Lemaître V, Mertens A and Selvaggi M (DELPHES 3) 2014 *JHEP* **02** 057 (*Preprint* 1307.6346)
- [21] Gulrajani I, Ahmed F, Arjovsky M, Dumoulin V and Courville A 2017 Improved training of wasserstein gans
- [22] Paszke A and Gross S 2019 *Advances in Neural Information Processing Systems 32* (Curran Associates, Inc.) pp 8024–8035
- [23] Aad G, Abbott B and Abbott D 2020 *Physics Letters B* **809** 135754 ISSN 0370-2693
- [24] Zwillinger D K 2000 *CRC Standard probability and statistics tables and formulae* (CRC Press)

# Simulation of neutron and electron damage in $\text{Al}_2\text{O}_3$ and $\text{MgO}$ using the FLUKA code

TO Mahafa<sup>1,2</sup>, O Mouane<sup>2</sup>, E Sideras-Haddad<sup>2,3</sup> and B Mellado<sup>3</sup>

<sup>1</sup> South Africa Nuclear Energy Corporation, R104 Pelindaba, Madibeng Municipality, Brits, South Africa.

<sup>2</sup> DSI-NRF Centre of Excellence in Strong Materials, University of the Witwatersand, Johannesburg, 2000, South Africa.

<sup>3</sup> School of Physics and Institute for Collider Particle Physics, University of the Witwatersand, Johannesburg, 2000, South Africa.

E-mail: Tshepo.mahafa@necsa.co.za

**Abstract.** We report on the simulation work performed using the FLUKA particle transport code to estimate the damage induced by 1 MeV neutron and 1 MeV electron irradiations in  $\text{Al}_2\text{O}_3$  and  $\text{MgO}$ . The simulation results reveal that both electrons and neutrons can induce damage in our target samples, however at differing rates. The neutron damage rate is higher than that of the electrons in both materials and is constant throughout the materials whilst that of electrons is pronounced at shallow depths and decreases with an increase in depth of the materials. The response of both  $\text{Al}_2\text{O}_3$  and  $\text{MgO}$  to radiation is revealed to be comparable.

## 1. Introduction

One of the key interest pertaining to radiation interaction with matter is on the effect radiation has on materials. Materials operating in high radiation environments get affected by radiation. Empirical evidence obtained from nuclear reactor operation [1] and from experimental campaigns conducted to assess the impact of radiation on materials reveals radiation to have a negative impact on materials [2]. These materials endure undesirable physical and mechanical property changes. When in this state the materials are said to be radiation damaged and are therefore not suitable for optimal and safe running of operations.

The energy transfers that occur from the impinging particle to the target material are the onset of material damage by radiation. The energy transfers, however, have to be above a critical energy threshold value known as the Threshold Displacement Energy (TDE) for the process of material damage to be set in motion [3]. The TDE is the minimum energy required to removing atoms from their sites by radiation [2] and energy transfers below the TDE do not result in materials damage.

The aim of this work was to perform Monte Carlo based simulations to assess the radiation response of metallic oxides  $\text{Al}_2\text{O}_3$  and  $\text{MgO}$  to neutrons and electrons. These investigations are carried out because  $\text{Al}_2\text{O}_3$  and  $\text{MgO}$  are materials considered for use as electron multipliers (dynodes) in photomultiplier tubes (PMT) due to their high secondary electron emission [4, 5]. They are required, however, to be radiation resistant as their exposure to radiation makes them susceptible to radiation damage.  $\text{MgO}$  has a simple cubic crystal structure while  $\text{Al}_2\text{O}_3$  has a hexagonal closely packed structure [6] and their structural makeup maybe key to how each material respond to neutron and electron irradiations.

To achieve our aim, the FLUKA code was used to simulate neutron and electron displacements per atom (dpa) in Al<sub>2</sub>O<sub>3</sub> and MgO. The dpa is an entity used to measure the radiation damage extent in materials and it relates the number of atoms removed in a material over the number of atoms present in that given material. This simulations offer a primary approach in understanding the effects of radiation in materials.

## 2. Materials and Method

We used FLUKA, a multi-particle transport code developed and managed jointly by the Italian National Institute for Nuclear Physics (INFN) and European Organization for Nuclear Research CERN [7] to perform simulation work to assess the damage effect of 1 MeV neutrons and 1 MeV electrons in Al<sub>2</sub>O<sub>3</sub> and MgO. FLUKA Version 2020.0.4 and FLAIR Version 2.3-0 were used for this simulation work. FLUKA uses a card based input system implemented through the advanced graphic interface FLAIR [8] to create the simulation input file. In addition to creating an input file, FLAIR is used for running the simulation, and for visualization of the geometry model and plotting the simulation results. FLAIR uses the gnuplot plotting program to visualize the simulation results.

With regards to the input file, the BEAM card is used to define the source term being the particle type, size and energy with the BEAMPOS card used to define beam positioning and direction of propagation relative to the target. The material type and its composition are defined using the MATERIAL and COMPOUND cards, with allocation of the material type to geometry regions achieved using the ASSIGNMA card. Combinations of cards are used to describe the physics settings and the combination is depended on the problem being simulated. For radiation damage estimation, we used the PHYSICS, MAT-PROP, and IONTRANS cards. The PHYSICS card implements the intra-nuclear cascade model that governs hadrons to nuclear interactions while the MAT-PROP card was used to define the material TDE, with the IONTRANS used for defining the ions transportation. Particle transport thresholds are implemented using the PART-THR and EMFCUT cards for hadrons and electromagnetic radiation respectively. These cards are used to define the energy cut-off values of particles being transported. The USRBIN card was used to score the dpa. USRBIN makes use of a mesh grid that is independent of the geometry to estimate the spatial distribution of the scored quantity.

Figure 1 shows the geometry model of the simulation created with FLAIR. The target is modelled as a 10 mm diameter disc of 1 mm thickness. A 4 mm diameter beam was directed perpendicularly to the target depth in the z-direction as seen in the frontview and sideview of the geometry model in Figure 1(a) and Figure 1(b) respectively.

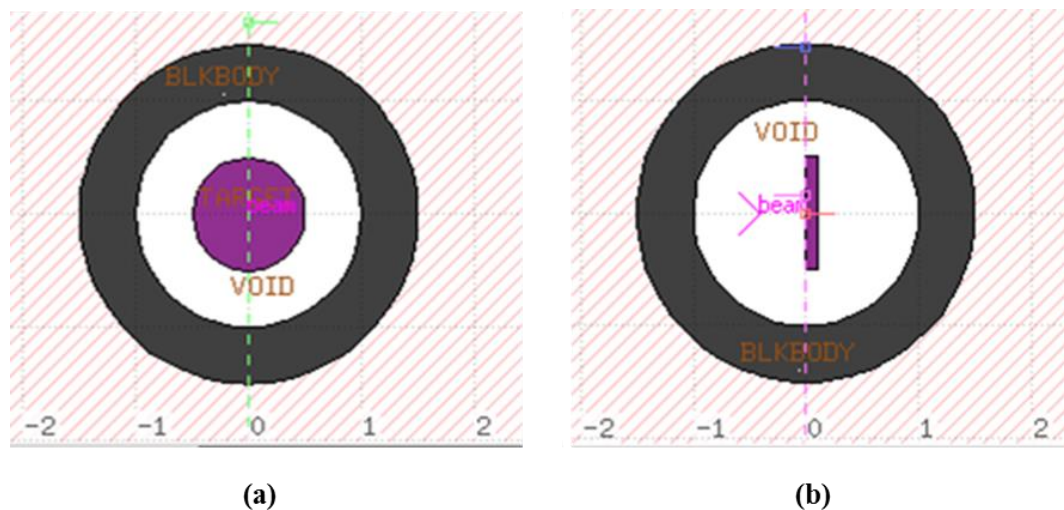


**Figure 1(a).** The frontview of the geometry model showing the beam interacting with the target.

**Figure 1(b).** The sideview of the geometry model showing the beam interacting with the target.

The interaction of the particles with the target occurs in vacuum (VOID) and particles escaping beyond the vacuum into the background (BLKBODY) are not tallied. Simulations were performed separately for both  $\text{Al}_2\text{O}_3$  and  $\text{MgO}$  materials with  $1 \times 10^6$  neutron particles and  $1 \times 10^6$  electron particles simulated respectively. FLUKA calculates the dpa by implementing the Norgett, Robinson, and Torrens (NRT) model [9]. This model is an update on the earliest damage model introduced by Kinchin and Pease [10], and is now the standard used to calculate the defect density introduced in materials by radiation. Table 1 lists the key parameters used in the simulation to calculate the dpa. FLUKA calculates the dpa per bin, with the dpa value for a given bin being the average dpa in that bin. We divided the depth of our target materials into 50 bins of 0.002 cm bin width. The material dpa was calculated as the aggregate of the dpa per bins.

**Table 1.** Material and beam parameters used in the simulation

Parameter	Value
Beam Energy (MeV)	1
Irradiation Fluence ( $\text{n}/\text{cm}^2$ )	$1 \times 10^{15}$ , $1 \times 10^{17}$ , $1 \times 10^{20}$
Irradiation Time (hrs)	8
TDE (eV)	69 for both $\text{Al}_2\text{O}_3$ and $\text{MgO}$

### 3. Results

Figure 2(a) and Figure 2(b) show the dpa/primary result of neutrons and electrons in  $\text{Al}_2\text{O}_3$  respectively. The dpa/primary relates the damage rate per particle interacting with the material. The dpa/primary in  $\text{Al}_2\text{O}_3$  by neutrons is  $1.17 \times 10^{-21}$  while for electrons is  $3.59 \times 10^{-24}$ . The dpa/primary profile of neutrons in  $\text{Al}_2\text{O}_3$  observed in Figure 2 (a) shows the damage caused by 1 MeV neutrons is uniform throughout the material. On the other hand, the dpa/primary profile of electrons in  $\text{Al}_2\text{O}_3$  observed in Figure 2 (b) shows the damage caused by 1 MeV electrons is non uniform in the material.

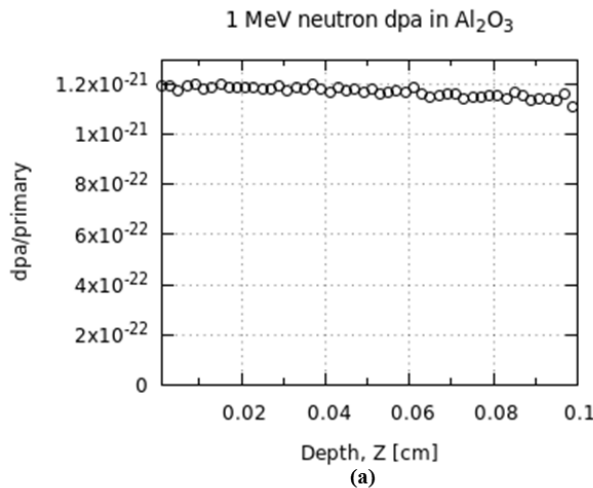


**Figure 2(a).** The dpa/primary profile of 1 MeV neutrons in  $\text{Al}_2\text{O}_3$ .

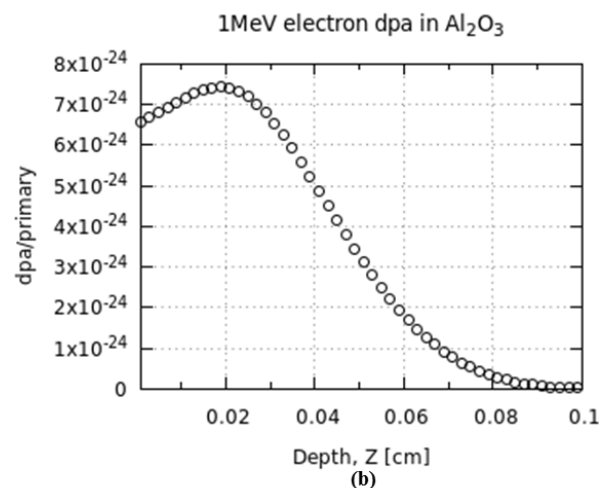


**Figure 2(b).** The dpa/primary profile of 1 MeV electrons in  $\text{Al}_2\text{O}_3$ .

The results observed are consistent with the interaction nature of neutrons and electrons with materials. Neutrons being neutral particles interact directly with the materials nuclei and therefore travel throughout the material. Electrons on the other hand are charged particles that interact through the Coulomb force with the atomic electrons of materials. They get scattered in all directions

depositing most of their energy at shallow depths in the material. Less energy is therefore available to effect any meaningful damage deeper into the material, hence we observe the damage profile shown in Figure 2(b).

Figure 3(a) and Figure 3(b) show respectively the neutron and electron dpa rates in  $\text{Al}_2\text{O}_3$  when bombarded at fluences reported in Table 1. It is observed in both Figure 3(a) and Figure 3(b) that an increase in the particle fluence results in an increase in the dpa rate. This is because over the eight hour irradiation period, more particles interact with the material for particles at higher fluences that result in higher energy transfers from the impinging particles. This then translates to a pronounced displacement of atoms for higher particle fluence as compared to lower particle fluence.

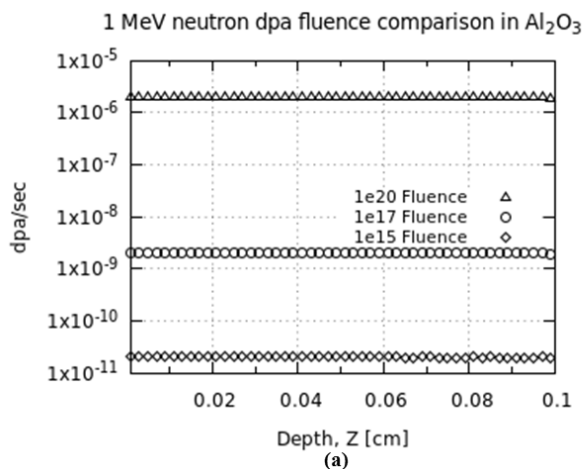


**Figure 3(a).** The dpa rate profiles of 1 MeV neutrons in  $\text{Al}_2\text{O}_3$  at different neutron fluence.

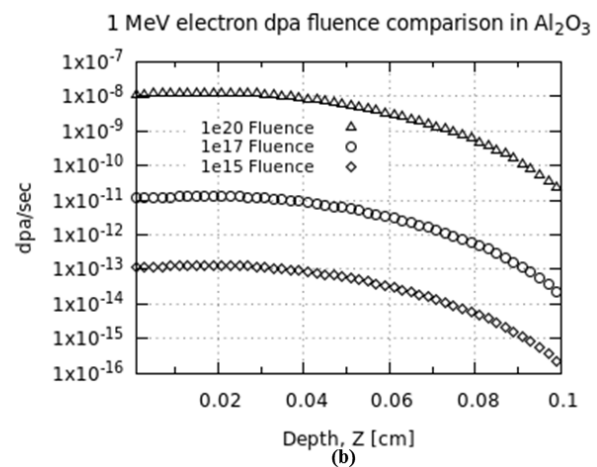


**Figure 3(b).** The dpa rate profiles of 1 MeV electrons in  $\text{Al}_2\text{O}_3$  at different electron fluence.

Figure 4 shows the dpa/primary result of neutrons and electrons in  $\text{MgO}$ . The dpa/primary in  $\text{MgO}$  by neutrons is  $1.1 \times 10^{-21}$  while for electrons is  $4.06 \times 10^{-24}$ . It is observed with  $\text{MgO}$ , as was observed with  $\text{Al}_2\text{O}_3$  that neutron irradiation of  $\text{MgO}$  result in uniform damage throughout the material, whilst the electron damage is not uniform and maximum damage is limited to shallow depths in the material.

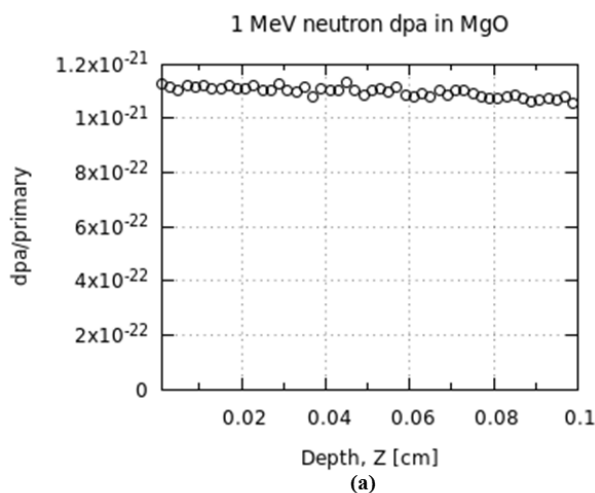


**Figure 4(a).** The dpa/primary profile of 1 MeV neutrons in  $\text{MgO}$ .

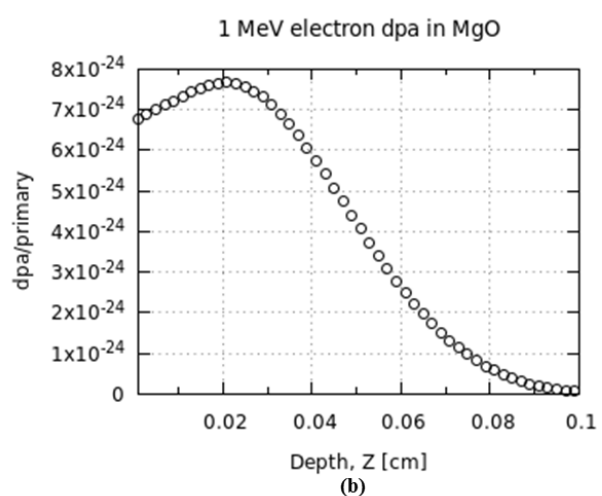


**Figure 4(b).** The dpa/primary profile of 1 MeV electrons in  $\text{MgO}$ .

Figure 5 shows the dpa rate results of MgO when bombarded at neutron and electron fluences reported in Table 1. Both Figure 5(a) and Figure 5(b) show that as the particle fluence increases, the dpa rate in both materials increases as was the case with  $Al_2O_3$ .

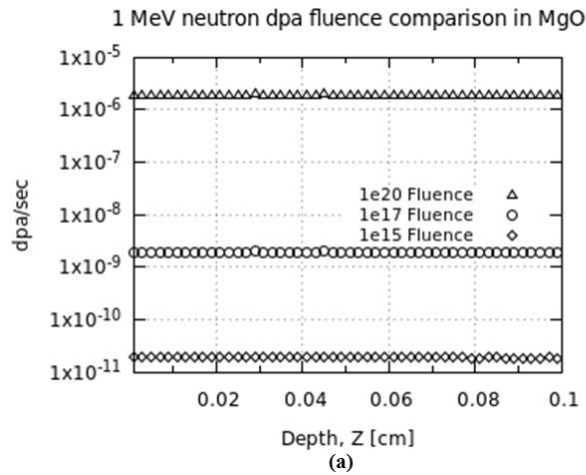


**Figure 5(a).** The dpa rate profiles of 1 MeV neutrons in MgO at different neutron fluence.

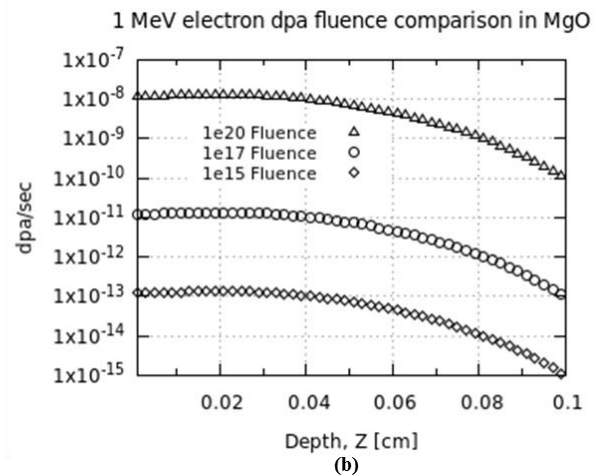


**Figure 5(b).** The dpa rate profiles of 1 MeV electrons in MgO at different electron fluence.

#### 4. Conclusion

In this work, we performed FLUKA simulation of 1 MeV neutron and 1 MeV electron irradiations in  $Al_2O_3$  and MgO to estimate the dpa. We observed that neutron irradiation leads to a high dpa as compared to electron irradiation in both  $Al_2O_3$  and MgO. It was further observed that neutron damage occurs uniformly throughout the materials whilst electron damage is maximized at shallow depths in the materials and is not constant throughout the materials. In terms of their response to electron and to neutron irradiations,  $Al_2O_3$  and MgO dpa rates are comparable. This shows that these materials are most likely to endure similar damage when exposed to radiation. Future work will involve performing experiments of neutron and electron irradiation of  $Al_2O_3$  and MgO to verify the simulation results.

#### References

- [1] Aitkaliyeva A, He L, Wen H, Miller B, Bai X M and Allen T 2017 *Idaho National Laboratory Report MIS-16-37708*
- [2] Yuan Y G, Jiang M, Zhao F A, Chen H, Gao H, Xiao H Y, Xiang X and Zu X T 2017 *Sci. Rep.* **7** 3621
- [3] Nordlund K *et al* 2018 *J. Nucl. Mater.* **512** 450–479
- [4] Zhu X, Guo J, Li X, Zhou R, Wang D and Zhao W 2021 *Appl. Sci.* **11** 4801
- [5] Guo J, Wang D, Xu Y, Zhu X, Wen K, Miao G, Cao W, Si J, Lu M and Guo H 2019 *AIP Adv.* **9** 095303
- [6] Jencic I 2000 *Proc. Int. Conf. on Nuclear Energy in Central Europe* (Bled: Slovenia)
- [7] Ferrari A, Sala P R, Fasso A and Ranft J 2005 “*FLUKA: a multi-particle transport code* CERN-2005-10 INFN/TC\_05/11 SLAC-R-773
- [8] Vlachoudis V 2009 *Proc. Int. Conf. on Mathematics, Computational Methods and Reactor Physics* (Saratoga Springs: New York)
- [9] Guthoff M, de Boer W and Muller S 2014 *Nucl. Instr. Methods. Phys. Res. A* **735** 223–228
- [10] Kinchin G H and Pease R S 1955 *Rep. Prog. Phys.* **18** 1 - 51



DIVISION

C

PHOTONICS

# Towards two-mode mode averaging with Orbital Angular Momentum modes

Alice V. Drozdov and Mitchell A. Cox\*

School of Electrical and Information Engineering, University of the Witwatersrand,  
Johannesburg, South Africa, 2000

E-mail: [mitchell.cox@wits.ac.za](mailto:mitchell.cox@wits.ac.za)

**Abstract.** Higher order structured modes can be used for Mode Division Multiplexing (MDM) in Free Space Optical communication; however, they are highly susceptible to atmospheric turbulence. Atmospheric turbulence causes crosstalk between the modes which decreases the power within the transmitted mode. Mode averaging could assist in mitigating the effects of turbulence by transmitting and receiving two modes, between which crosstalk occurs. Mode averaging used at the receiver and transmitter simultaneously has been shown to increase the performance of a system when used with multiple Orbital Angular Momentum (OAM) modes. Using multiple OAM modes limits the number of modes available for MDM, therefore, it would be more favourable to make use of only two modes. Additionally, modes for mode averaging are often chosen for their simplicity. Choosing more appropriate modes could further improve performance. We investigate the use of OAM modes with un-normalised and normalised beam sizes in two-mode mode averaging by first determining the mode combinations that provide the most received power for each transmitted mode and then using these combinations to compare the total received power of a system using mode averaging to one without averaging. We show that mode averaging can increase the power received by a maximum of 61% at a Strehl Ratio of 0.6 when combining modes optimally.

## 1. Introduction

Free space optical (FSO) communication has become a popular research area due to the promise of fast, cheap and secure internet [1]. FSO transfers information using a laser beam which propagates through the air. This laser beam is usually in the form of a Gaussian or Gaussian-like beam.

There is an interesting alternative to using a Gaussian beam in FSO. Higher order mode sets can be perceived as “patterns of light” with different spatial intensity and phase structures. The Laguerre-Gaussian (LG) and Orbital Angular Momentum (OAM) mode sets are most commonly studied [2; 3]. Higher order modes can be used for Mode Division Multiplexing (MDM), which involves the superposition of orthogonal modes carrying different signals [4]. They are, however, highly susceptible to atmospheric turbulence [5]. As a mode passes through turbulence, turbulence distorts the wavefront and amplitude of the beam, causing crosstalk between different modes [6]. The crosstalk decreases the power and intensity of the transmitted mode. In communication systems, this causes fading errors and thus reduces the data-rate [7].

Multiple methods to prevent these fading errors have been researched. These include adaptive optics [8], spatial diversity [9] and multiple-input-multiple-output digital signal processing [7].

Alternatively, a method known as *Mode Diversity* can be used. By transmitting and/or receiving a number of adjacent modes between which crosstalk occurs, the errors caused by Mode Dependent Loss (MDL) can be mitigated [10]. Since “true” mode diversity as used in communication systems, harnesses the statistical independence of different channels over time [11], we believe that this name is confusing for this particular use case. *Mode Averaging* is more descriptive as there is a similarity to aperture averaging.

Mode averaging has been used at the receiver [12; 13] and transmitter [10] separately as well as at both simultaneously [14; 15]. In this work, we focus on mode averaging used at both the transmitter and receiver. Mode averaging using several OAM modes has shown to increase the performance of a system [14; 15]. However, using many OAM modes can reduce the number of modes available for MDM [16]. More modes could be provided by only using two mode combinations for mode averaging. Mode averaging systems could further be improved by choosing more appropriate modes for the mode combinations. This is in contrast to a simple multi-mode or “bucket”-type receiver. In many of the previous papers, the modes for mode combinations have mainly been chosen for their simplicity. However, in [17], modes are chosen using an exhaustive search and the effective fading figure. Modes could also be chosen by investigating the mode combinations which provide the maximal total received power.

Therefore, we determine the OAM mode combinations that provide the most received power at different turbulence strengths in two-mode mode averaging systems. These combinations are then used to compare the total received power of a system using mode averaging to one without averaging to determine the efficiency of such a system.

## 2. Preliminaries

### 2.1. Orbital Angular Momentum Modes

OAM modes are a subset of LG modes. LG modes are a set of higher-order modes that are solutions to the Helmholtz equation calculated using cylindrical coordinates [2]. The expression for LG modes at  $z = 0$  is given by

$$\text{LG}_p^\ell(\rho, \phi, 0) = C_{l,p}^{\text{LG}} \left( \frac{\rho\sqrt{2}}{w_0} \right)^{|\ell|} L_p^{|\ell|} \left[ \frac{2\rho^2}{w^2(z)} \right] \exp \left( - \frac{\rho^2}{w^2(z)} \right) \exp[-i\ell\phi]. \quad (1)$$

where  $C_{l,p}^{\text{LG}}$  is the normalisation constant,  $L_p^{|\ell|}[\cdot]$  is the generalised Laguerre polynomial and  $w_0$  is the beam waist. LG modes are characterised by two indices namely the azimuthal ( $\ell$ ) and radial ( $p$ ) indices. When  $p = 0$ , the modes are known as OAM modes. In OAM modes, the  $l$  parameter determines the beam propagation factor,  $M^2$ , which affects the beam’s propagation characteristics [18], and is given by

$$M^2 = |\ell| + 1. \quad (2)$$

The diameter of the beam increases according to the second moment radius calculated using  $r^2 = w_0\sqrt{1 + M^2}$  [19]. This diameter can be normalised in the near field using the following equation

$$w_L = \frac{w_0}{\sqrt{1 + M^2}} \quad (3)$$

where  $w_L$  is the radius of a beam with the beam size normalised to the size of the Gaussian beam within the mode set.

### 2.2. Atmospheric Turbulence

Atmospheric turbulence is caused as a result of the mixing of air with different temperatures and pressures, which causes random space and time-varying changes in the refractive index. Turbulence can be simulated by generating random phase screens using statistical models of

which the simplest is the Kolmogorov model [20]. The power spectral density of the refractive index of air is described by

$$\Phi_n^K(\kappa) = 0.033C_n^2\kappa^{-\frac{11}{3}}. \quad (4)$$

In the equation,  $\kappa$  is the angular spatial frequency and  $C_n$  is the refractive-index structure parameter. Turbulence affects beams by distorting their wavefronts (and thus intensities, after propagation). In higher order modes, this causes the spreading of energy or coupling of power between different modes which is known as crosstalk. Crosstalk decreases the amount of power within the transmitted mode. This attenuation is known as Mode Dependent Loss (MDL) and is calculated as

$$\text{MDL}_n = 1 - \frac{S_n}{S_0}. \quad (5)$$

where  $n$  represents the transmitted mode index,  $S_n$  is the intensity of mode  $n$  in the presence of turbulence and  $S_0$  is the intensity of the mode in the absence of turbulence. The MDL is related to the Strehl Ratio (SR) which is a simple measure for turbulence strength defined by

$$\text{SR} = \frac{\langle I(\mathbf{0}) \rangle}{I_0(\mathbf{0})}, \quad (6)$$

where  $\langle I(\mathbf{0}) \rangle$  is the average on-axis intensity of the beam with turbulence and  $I_0(\mathbf{0})$  is the on-axis intensity without turbulence. The angle brackets,  $\langle \cdot \rangle$ , represent an ensemble average. The lower the SR, the greater the turbulence strength.

### 2.3. Modal Decomposition

Any field,  $U$ , can be expressed as a sum of modes that form part of a complete basis, given by

$$U(\mathbf{x}) = \sum_n c_n \Psi_n(\mathbf{x}), \quad (7)$$

where  $\mathbf{x}$  represents the transverse spatial coordinates, and  $\Psi_n(\mathbf{x})$  is the mode  $n$  within the complete basis [21].  $c_n$  is the complex expansion coefficient for mode  $n$  of a particular basis where the amplitude of the expansion coefficient describes the degree to which the field correlates to the basis mode. The crosstalk and MDL measurements are given by this. The phase of  $c_n$  is called the inter-modal phase.

We can determine these expansion coefficients using the inner-product between the initial field and the modes of the complete basis. This so-called modal decomposition of the initial field is given by an inner product

$$c_n = \langle \Psi_n | U \rangle = \int d^2\mathbf{x} \Psi_n^*(\mathbf{x}) U(\mathbf{x}). \quad (8)$$

where  $\Psi_n^*(\mathbf{x})$  is the complex conjugate of  $\Psi_n(\mathbf{x})$ .

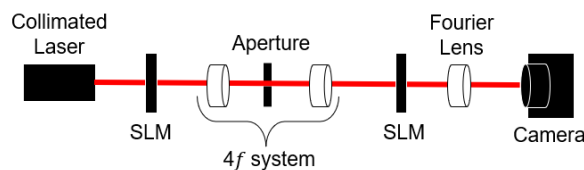


**Figure 1.** Experimental setup that is analogous to the simulation method used (SLM: Spatial Light Modulator)

### 3. Methodology

One of the key performance metrics in a communication system is the signal to noise ratio. If we assume the noise floor is some constant, the greater the received signal power the better the signal to noise ratio. Ignoring other potential complexities which are out of scope, in this work we strive to maximise the received power.

Due to the sheer quantity of data, the results presented here have been acquired using an accurate simulation. We plan to re-measure and verify interesting cases using a physical experimental setup in future. A setup that is analogous to the simulation method can be seen in Fig. 1. In the setup, the collimated laser beam is modulated with a mode combination using the first Spatial Light Modulator (SLM). The modes are combined such that the power within each mode is equal. For modes with normalised beam sizes, their beam sizes are normalised by using Eq. 3 to the size of the Gaussian beam before they are combined and used to modulate the laser beam. Simulated turbulence with turbulence strengths ranging from  $SR=0.1$  to  $0.9$  in steps of  $0.1$  is also added to the laser beam using the first SLM. Turbulence is simulated using a hundred phase screens for each  $SR$ . A  $4f$  system with an aperture is used to acquire the first diffraction order from the SLM. Modal Decomposition is performed using the second SLM and Fourier Lens [21]. The total received power is calculated using the modal decomposition results. The mode combinations which provide the largest received power for a particular  $SR$  are determined by combining all the modes two modes at a time and determining the received power for each combination for that  $SR$ . The best combinations are then used to compare a system with mode averaging to one without mode averaging (i.e. a single mode system).

The method used to determine the best mode combinations is computationally expensive and, thus, only allows for a limited number of OAM modes to be studied. The studied OAM modes have  $\ell$  values ranging from  $-5$  to  $5$  and  $M^2$  values ranging from  $M^2 = 1$  to  $6$ .

### 4. Results and Discussion

In Fig. 2, the total received powers when a single un-normalised or normalised mode is transmitted and combined with other OAM modes at different turbulence strengths are shown. We can see that mode averaging can make a significant improvement on the received power. In Fig. 2(a), it can be seen by taking note of the asterisks (\*) that un-normalised beams with a lower  $M^2$  are best combined with adjacent beams (adjacent  $\ell$  values) with lower beam propagation factors at lower  $SR$ s. This is, however, no longer the case for beams with a higher  $M^2$  which are best combined with Gaussian beams as can be seen in Fig. 2(b).

At lower  $M^2$ , the crosstalk between modes is able to mitigate the MDL of the transmitted beam, however, the strength with which turbulence affects a beam is dependent on its size [6]. Since the beam sizes are not normalised, turbulence will affect the beams with higher  $M^2$  and, thus, larger diameters more. As a result more crosstalk will occur when the  $M^2$  is high. Additionally, the crosstalk of modes with a higher  $M^2$  will spread more [22]. Due to all of this, when the  $M^2$  is high the crosstalk of adjacent modes no longer has the ability to mitigate the effects of MDL. Gaussian beams already have a low MDL, therefore, when the  $M^2$  of a transmitted beam is high it becomes more favourable to combine the beam with a Gaussian beam rather than the adjacent beam. At higher  $SR$ s, beams with a lower  $M^2$  are also combined best with Gaussian beams (Fig. 2(a)). This is as a result of the increase in crosstalk that occurs as the turbulence strength increases [6].

On the other hand, beams with normalised beam sizes are best combined with adjacent beams. It must be noted that both adjacent beams have a similar value for the received power when taking the standard error into account. This is the case for all  $SR$ s and beams with any  $M^2$  as can be seen in Fig. 2(c) and (d). Beams with normalised beam sizes are affected by turbulence similarly. This means that the MDL of all the beams is equal at a particular  $SR$ , therefore, when mode averaging is used, crosstalk between the beams is the only factor that will affect the total

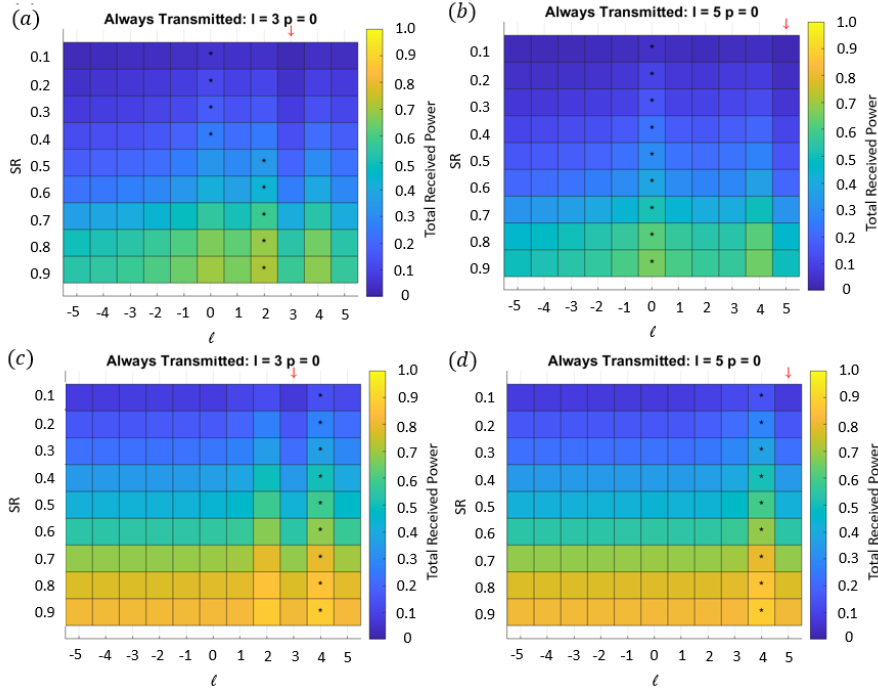


**Figure 2.** Total powers received when a single OAM beam is transmitted and combined with other beams. The mode combined with the transmitted mode which provides the largest received power is shown with an asterisk. In (a) and (c) the transmitted mode is  $\ell = 3$  and has a lower  $M^2$  whereas in (b) and (d) the transmitted mode is  $\ell = 5$  and has a higher  $M^2$ . (a) and (b) show results for un-normalised beams whereas (c) and (d) show results for normalised beams.

received power. Since the most crosstalk occurs between adjacent beams, the OAM modes are best combined with adjacent beams. Using the best mode combinations and comparing the total received power for different modes with and without mode averaging, it was found that mode averaging does improve the total received power. For OAM modes with un-normalised beam sizes at an SR of 0.6 it was found that there was a maximum increase of 61% in the power. Furthermore, for OAM modes with normalised beam sizes this increase was 23%. Un-normalised OAM modes benefit more from mode averaging than normalised OAM modes, however, this is mainly the case for modes with higher  $M^2$ . Nevertheless, the power received for un-normalised modes is always less than the power received for normalised modes in the case of both mode averaging and no mode averaging. However, it must be noted that in this work, we did not take into account the divergence of the beam and its effect on the results. Although the results show that using a normalised beam size provides better performance than un-normalised beam sizes, this is likely to only be the case for short transmission distances. The beams with a normalised second moment radii will diverge to a greater extent than the beams with un-normalised radii as they have been reduced in size [19]. Additionally, beams with different  $M^2$  will diverge at different rates. Since turbulence has a larger effect on larger beams and the turbulence will no longer affect all the normalised beams equally, at larger distances there is likely to no longer be an advantage to using beams with the same radii.

## 5. Conclusion

Mode averaging can mitigate the effects of turbulence on the total received power if the best mode combinations are used. When using OAM modes with un-normalised beam sizes, modes

with a higher  $M^2$  should be combined with a Gaussian beam. On the other hand, modes with a lower  $M^2$  should be combined with its adjacent beam (adjacent  $\ell$  values) at lower SRs and with Gaussian beams at higher SRs. When using OAM modes with normalised beam sizes, modes should always be combined with adjacent modes. There has been much research into the use of OAM modes in mode averaging, however, the work presented in this proceeding, is only preliminary work before studying the full LG basis.

## References

- [1] Trichili A, Cox M A, Ooi B S and Alouini M S 2020 *Journal of the Optical Society of America B* **37** A184–A201
- [2] Allen L, Beijersbergen M W, Spreeuw R J C and Woerdman J P 1992 *Physical Review A* **45** 8185–8189
- [3] Willner A E, Huang H, Yan Y, Ren Y, Ahmed N, Xie G, Bao C, Li L, Cao Y, Zhao Z and et al 2015 *Advances in Optics and Photonics* **7** 66
- [4] Berdagué S and Facq P 1982 *Applied Optics* **21** 1950
- [5] Cox M A, Mphuthi N, Nape I, Mashaba N P, Cheng L and Forbes A 2020 *IEEE Journal of Selected Topics in Quantum Electronics* **27** 1–21
- [6] Anguita J A, Neifeld M A and Vasic B V 2008 *Applied Optics* **47** 2414
- [7] Li S, Chen S, Gao C, Willner A E and Wang J 2018 *Optics Communications* **408** 68–81
- [8] Weyrauch T and Vorontsov M A 2008 *Free-space laser communications with adaptive optics: Atmospheric compensation experiments* vol 2 (Springer) p 247–271
- [9] Navidpour S, Uysal M and Kavehrad M 2007 *IEEE Transactions on Wireless Communications* **6** 2813–2819
- [10] Wang A, Zhu L, Deng M, Lu B and Guo X 2021 *Optics Express* **29** 13171
- [11] Cox M A, Cheng L, Rosales-Guzmán C and Forbes A 2018 *Physical Review Applied* **10**
- [12] Song H, Li L, Pang K, Zhang R, Zou K, Zhao Z, Du J, Song H, Liu C, Cao Y, Willner A N, Bock R, Lynn B, Tur M and Willner A E 2019 *Optics InfoBase Conference Papers Part F160-OFC 2019* 10–12
- [13] Song H, Li L, Pang K and Zhang R 2020 *Optics Letters* **45** 3042–3045
- [14] Li L, Song H, Zhang R, Zhao Z, Liu C, Pang K, Song H, Du J, Willner A N, Almainan A and et al 2021 *Optics Communications* **480** 126488
- [15] Li L, Song H, Zhang R, Zhao Z, Liu C, Pang K, Song H, Du J, Willner A N, Almainan A, Lynn B, Bock R, Tur M and Willner A E 2019 Demonstration of both mode and space diversity in a 100-Gbit/s QPSK free-space optical link to increase system tolerance to turbulence *Optics InfoBase Conference Papers* vol Part F160 pp 4–6 ISBN 9781943580538
- [16] Trichili A, Rosales-Guzmán C, Dudley A, Ndagano B, Salem A B, Zghal M and Forbes A 2016 *Scientific Reports* **6** 27674
- [17] Huang S, Mehrpoor G R and Safari M 2018 *IEEE Transactions on Communications* **66** 2079–2092
- [18] Saghafi S and Sheppard C 1998 *Optics Communications* **153** 207–210
- [19] Phillips R L and Andrews L C 1983 *Applied Optics* **22** 643
- [20] Lane R G, Glindemann A and Dainty J C 1992 *Waves in Random Media* **2** 209–224
- [21] Pinnell J, Nape I, Sephton B, Cox M A, Rodríguez-Fajardo V and Forbes A 2020 *Journal of the Optical Society of America A* **37**
- [22] Mehrpoor G R, Safari M and Schmauss B 2015 *2015 4th International Workshop on Optical Wireless Communications, IWOW 2015* 78–82

# Effects of nanoparticle geometry on photon statistics

Luke C. Ugwuoke<sup>1</sup>, Tjaart P. J. Krüger<sup>1</sup>, and Mark S. Tame<sup>2</sup>

<sup>1</sup> Department of Physics, University of Pretoria, Private Bag X20, Hatfield 0028, South Africa

<sup>2</sup> Department of Physics, Stellenbosch University, Private Bag X1, Matieland 7602, South Africa

E-mail: lcugwuoke@gmail.com

**Abstract.** A quantum study of the geometry-dependent light scattering by a metamolecule weakly driven by a plane-polarized electric field is presented. The metamolecule consists of a semiconductor quantum dot coupled to a silver nanoparticle. We show that a transition from bunching to antibunching of the scattered photons by the metamolecule varies with the quantum dot–nanoparticle distance as the nanoparticle geometry is tuned from prolate to oblate to spheric at constant particle volume. We attribute this to the geometry-dependent quantum dot–nanoparticle coupling, localized surface plasmon resonance, and dipole moment of the nanoparticle.

## 1. Introduction

Metal nanoparticle (MNP)–quantum dot (QD) systems are capable of emitting non-classical light when they interact with the coherent light from a laser source [1–4]. These systems, also referred to as metamolecules [4], have been proposed for various quantum control applications [1, 3]. Furthermore, non-classical light can be used for carrying out quantum communication [5] and refractive index sensing [6].

The QD is usually a photostable, semiconducting emitter, such as cadmium selenide (CdSe), with tunable ground-state, exciton transition frequency,  $\omega_{ex}$ , and spontaneous decay rate,  $\gamma_{ex}$  [7], often modelled as a two-level atom, as shown in Fig. 1(a). Previous studies have considered the interaction between the localized surface plasmon resonance (LSPR) of a spherical MNP and the QD exciton [1–4]. The interaction between the narrow-linewidth exciton and the broad-linewidth LSPR leads to the appearance of a scattering spectrum with a Fano profile — an asymmetric lineshape with both constructive (Fano peak) and destructive (Fano dip) interference regions [1, 2, 7].

Ridolfo et al. [1] have previously shown that the driven metamolecule can exhibit photon antibunching — a quantum effect where a driven scatterer emits photons with a near-regular photocount pattern during absorption–spontaneous emission events [8, 9] — in the weak-driving limit. According to Waks et al. [2], this is the limit where the modified Rabi frequency of the QD,  $\Omega$ , is small compared to the enhanced QD decay rate,  $\Gamma$ , as well as where the semiclassical approximation is valid. In this study, we investigated the photon statistics of both spherical- and spheroidal-based metamolecules. In the latter, the QD exciton interacts with the longitudinal LSPR of the spheroids, as shown in Fig. 1(b). The spherical-based metamolecule is a special case of spheroidal-based metamolecules, whose photon statistics were studied here to ensure that our model is in good agreement with Refs. [1, 2, 4]. In addition, we also investigated the dependence of the photon statistics on the MNP-QD distance.

## 2. Theory

The approach proposed in Ref. [1] is used here to obtain the second-order correlation function for zero-time delay,  $g^{(2)}(0)$  — a statistical parameter that determines whether the scattered photons will arrive

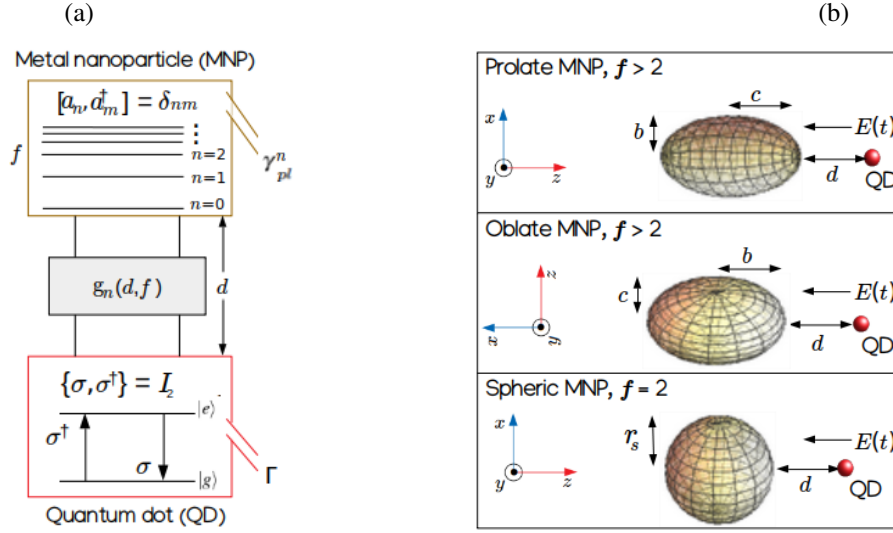


**Figure 1.** (a) Quantum electrodynamics (QED) model of the metamolecule. The MNP has a geometric factor  $f$ , and plasmon modes with angular momentum numbers  $n = 0, 1, 2, \dots$ , corresponding to the plasmon resonances  $0, \omega_{pl}^1, \omega_{pl}^2, \dots$ , with non-radiative decay rates  $0, \gamma_{pl}^1, \gamma_{pl}^2, \dots$ , respectively. The MNP is coupled to the QD through the coupling rate,  $g_n$ , which depends on both  $d$  and  $f$ , where  $d$  is the MNP-QD surface-to-surface distance. The QD is modelled as a two-level atom (with ground state  $|g\rangle$  and excited state  $|e\rangle$ ), which undergoes a decay rate enhancement,  $\Gamma$ , upon interaction with the MNP. The MNP operators,  $a$  and  $a^\dagger$ , obey the commutation rule,  $[a_n, a_m^\dagger] = \delta_{nm}$ , while the QD operators,  $\sigma$  and  $\sigma^\dagger$ , obey the anti-commutation rule,  $\{\sigma, \sigma^\dagger\} = I_2$ . (b) Model geometries of the metamolecule. The incident electric field,  $E(t)$ , is plane-polarized. We assume that the QD dipole couples longitudinally to the MNP dipole, where their dipole orientations lead to maximum effect. Each MNP is modelled as a Drude metal with a frequency-dependent dielectric function,  $\epsilon(\omega)$ . The prolate has semi-axes  $b \times b \times c$ ,  $c > b$ , the oblate has semi-axes  $b \times b \times c$ ,  $b > c$ , and the spheric MNP has an equivalent sphere-volume radius,  $r_s = \sqrt[3]{cb^2}$ , so that while the MNP geometry is tuned through  $f$ , its volume remains constant.

randomly (for coherent light), regularly (for antibunched light), or in bunches (for bunched light), at a detector [9].

In plasmonic cavity QED, the weak-coupling condition,  $g < \gamma_{pl}$ , required for the observation of photon antibunching is easily attainable [1, 3] due to the large value of  $\gamma_{pl}$ . Here,  $g$  is the dipole-dipole coupling rate between the QD and the MNP, and  $\gamma_{pl}$  is the decay rate of the plasmon dipole mode. Hence, we will determine  $g^{(2)}(0)$  in the weak-coupling regime where the rotating-wave approximation is valid.

Finally, only the plasmon dipole mode ( $n = 1$ ) in Fig. 1(a) will be considered here. The plasmon multipolar modes ( $n \geq 2$ ) are dark modes which do not couple to the driving field but couple to the dipole mode. The validity of the dipole approximation has been investigated in Ref. [3], where it was shown that multipolar contributions are not negligible at short MNP-QD distances. However, in Ref. [1], it was shown that the dipole approximation is valid in the distance regime  $d \geq r_{QD} + 2$  nm, where  $r_{QD}$  is the QD radius. Our study will keep to this latter regime.

The driving field of the laser is modelled as a cosine wave:  $E(t) = E_0 \cos \omega t$ , with amplitude,  $E_0$ , and driving frequency,  $\omega$ . In the rotating-frame, the total Hamiltonian of the driven metamolecule is [1, 4]:

$$\mathcal{H} = \hbar \Delta_{pl} a^\dagger a + \hbar \Delta_{ex} \sigma^\dagger \sigma - E_0 \mu (\sigma + \sigma^\dagger) - E_0 (\chi^* a + \chi a^\dagger) + i \hbar g (\sigma a^\dagger - \sigma^\dagger a), \quad (1)$$

where  $\Delta_{pl} = \omega_{pl} - \omega$  and  $\Delta_{ex} = \omega_{ex} - \omega$  are the plasmon-laser detuning and exciton-laser detuning

frequencies, respectively,  $\omega_{ex} = \omega_{pl} - \delta$ ,  $\delta$  is the exciton-plasmon detuning, and

$$\omega_{pl} \approx \sqrt{\frac{\omega_p^2}{\epsilon_\infty + f\epsilon_b} - \gamma_p^2}, \quad \gamma_{pl} \approx \gamma_p + \frac{\gamma_p^3}{\omega_{pl}^2}, \quad (2a)$$

$$\chi \approx -ib(f+1)\epsilon_b\sqrt{2\pi\hbar\epsilon_0c\eta(1-L)}, \quad g \approx \frac{b\mu(f+1)}{(c+d)^3} \sqrt{\frac{c\eta[1-L(v)]}{2\pi\hbar\epsilon_0}}, \quad (2b)$$

where  $\omega_{pl}$  and  $\chi$  are the dipolar LSPR and dipole moment of the MNP, respectively,  $\mu = er_{QD}$  is the dipole moment of the QD,  $e$  is the electronic charge,  $\hbar$  is Dirac's constant,  $\epsilon_0$  is the permittivity of free space,  $\epsilon_b$  is the dielectric constant of the background medium, and  $\epsilon_\infty$  is the high-frequency dielectric constant of silver, where we have ignored radiative damping since we are in the Rayleigh regime [1, 10]. In Eq. 2a,  $\omega_p$  and  $\gamma_p$  are the Drude model parameters for the plasma frequency and free-electron damping rate of silver, respectively,  $f = (1-L)/L$ , where  $L$  is the static geometric factor of the free MNP as given in Ref. [10]. In Eq. 2b,  $c \rightarrow c, b \rightarrow b$  (prolate),  $c \rightarrow b, b \rightarrow c$  (oblate),  $c \rightarrow r_s, b \rightarrow r_s$  (sphere),  $\eta = \omega_p^2/[2\omega_{pl}(\epsilon_\infty + f\epsilon_b)^2]$ , and  $L = L(v) = 1/3$  for a sphere. For the spheroids,  $L(v)$  is the static geometric factor of the MNP-QD system, with a radial coordinate,  $v$ , which we reported previously in Ref. [10].

The equation of motion describing the evolution of the expectation values of the MNP and QD operators,  $a$  and  $a^\dagger$ , and  $\sigma$  and  $\sigma^\dagger$ , respectively, in the Heisenberg picture, is given by [3]:

$$\frac{d\langle \mathcal{O} \rangle}{dt} = \frac{i}{\hbar} \langle [\mathcal{H}, \mathcal{O}] \rangle + \frac{\gamma_{pl}}{2} (a^\dagger \langle \mathcal{O}, a \rangle + \langle a^\dagger, \mathcal{O} \rangle a) + \frac{\gamma_{ex}}{2} (\sigma^\dagger \langle \mathcal{O}, \sigma \rangle + \langle \sigma^\dagger, \mathcal{O} \rangle \sigma), \quad (3)$$

from which we obtain the following coupled equations in the weak-driving limit:

$$\frac{d\langle a \rangle}{dt} = -\left(i\Delta_{pl} + \frac{1}{2}\gamma_{pl}\right)\langle a \rangle + g\langle \sigma \rangle + i\Omega_{pl}, \quad (4a)$$

$$\frac{d\langle \sigma \rangle}{dt} = -\left(i\Delta + \frac{1}{2}\Gamma\right)\langle \sigma \rangle + i\Omega\left(1 - 2\langle \sigma^\dagger \sigma \rangle\right), \quad (4b)$$

$$\frac{d\langle \sigma^\dagger \sigma \rangle}{dt} = -\Gamma\langle \sigma^\dagger \sigma \rangle + i\left(\Omega\langle \sigma^\dagger \rangle - \Omega^*\langle \sigma \rangle\right), \quad (4c)$$

where we have applied the adiabatic approximation [2] (since  $\gamma_{pl} \gg \gamma_{ex}$ ) to obtain Eqs. 4b and 4c. The coupled equations are solved at steady-state conditions to obtain the coherences  $\langle a \rangle, \langle \sigma \rangle$ , the excited state population of the QD  $\langle \sigma^\dagger \sigma \rangle$ , as well as the modified QD parameters  $\Omega = \Omega_{ex}(1 - (\chi/\mu)\sqrt{\mathcal{F}})$  (near-field enhancement),  $\Gamma = \gamma_{ex} + \mathcal{F}\gamma_{pl}$  (Purcell effect),  $\Delta = \Delta_{ex} - \mathcal{F}\Delta_{pl}$  (exciton shift), where  $\mathcal{F} = 4g^2/(\gamma_{pl}^2 + 4\Delta_{pl}^2)$  is the plasmon-induced enhancement factor,  $\Omega_{pl} = E_0\chi/\hbar$  is the driving frequency of the MNP, and  $\Omega_{ex} = \mu E_0/\hbar$  is the Rabi frequency.

### 3. Results and Discussion

In the quantum picture, the dipole moments of the MNP and the QD are defined in terms of the expectation values of their respective operators, as [4]  $\chi\langle a \rangle$  and  $\mu\langle \sigma \rangle$ , respectively, and the total dipole moment operator is  $\mathcal{P}^+ = \chi a + \mu\sigma$ . At steady-state,  $g^{(2)}(0) = \langle (\mathcal{P}^-)^2 (\mathcal{P}^+)^2 \rangle / \langle \mathcal{P}^- \mathcal{P}^+ \rangle^2$ , and the scattering cross-section is proportional to  $\langle \mathcal{P}^- \mathcal{P}^+ \rangle$ , where  $\mathcal{P}^- = (\mathcal{P}^+)^\dagger$  [1, 3].

We have made use of the following model parameters of a CdSe QD and that of a silver nanoparticle from Ref. [1]:  $r_{QD} = 0.7$  nm,  $\gamma_{ex} = 50$   $\mu$ eV,  $\gamma_p = 53.26$  meV,  $\delta = 60$  meV,  $\epsilon_b = 3.0$ ,  $\epsilon_\infty = 3.699$ . The Rabi energy,  $\mu E_0 = 0.01$  meV, ensures that we are in the weak-driving limit:  $\Omega \ll \Gamma$ . The MNP sizes we considered are  $c = 13$  nm,  $b = 12$  nm (prolate),  $c = 12$  nm,  $b = 13$  nm (oblate), and  $r_s \approx 12.32$  nm (spheric). The semi-axes of the spheroids are chosen such that:  $(f_{spheroid} - f_{sphere}) < \frac{1}{8}f_{sphere}$ . This ensures that the respective aspect ratios of the spheroids are very close to that of the sphere, i.e. unity. Some of our analytical results have been verified using the quantum simulation toolbox QuTiP [11].

The scattering cross-section of the metamolecule gradually decreases as the MNP geometry is tuned from  $f = 2.2$  (prolate) to  $f = 2.0$  (spheric), as can be observed from the trend in the scattering peaks in Fig. 2(a). In addition, the wavelengths corresponding to the scattering peaks — the Fano peaks (peaks of the narrow and asymmetric lineshapes in Fig. 2(a)) and the plasmon peaks (peaks of the broad and symmetric lineshapes in Fig. 2(a)) — undergo blueshifts as the MNP geometry is tuned from prolate to spheric, as summarized in Table 1. This shows that each driven metamolecule is a good scatterer depending on the energy region in Fig. 2(a). At far distances,  $d = 10$  nm, the scattering spectra of the metamolecule (broken coloured curves in Fig. 2(a)) approach those of the spectra of the free MNP (broken black curves in Fig. 2(a)), due to huge decreases in the coupling rates.

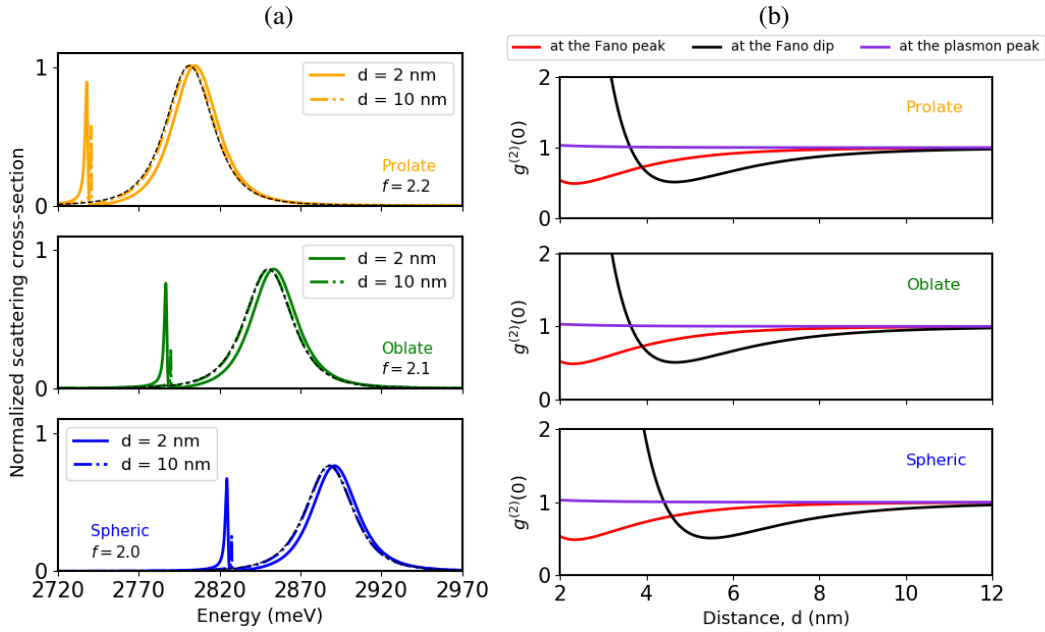


**Figure 2.** (a) Dependence of the scattering cross-section on the geometric factor,  $f$ , and on the MNP-QD distance,  $d$ . (b) Second-order correlation function for zero-time delay,  $g^{(2)}(0)$ , as a function of the MNP-QD distance,  $d$ .

**Table 1.** The Fano peak (Fano resonance), the Fano dip (transparency dip), and the plasmon peak ( $\sim$ plasmon resonance) formed in the scattering spectrum of the metamolecule for each of the MNP geometries at  $d = 2$  nm. (Deduced from Fig. 2(a).)

Metamolecule	$\omega$ (meV)		
	Fano peak	Fano dip	Plasmon peak
Prolate-based	$\sim 2737.77$	$\sim 2739.66$	$\sim 2805.31$
Oblate-based	$\sim 2786.65$	$\sim 2788.54$	$\sim 2853.96$
Spheric-based	$\sim 2824.44$	$\sim 2826.56$	$\sim 2891.27$

Fano interference is responsible for the Fano dips in the scattering spectra in Fig. 2(a), as well as the resonances,  $\omega'_{ex} \approx \omega_{ex} - \mathcal{F} \omega_{pl}$  (Fano resonance) and  $\omega'_{pl} \approx \omega_{pl} + [g^2/(\omega_{pl} - \omega_{ex})]$  (plasmon resonance). The Fano dips are regions in-between the Fano peaks and the plasmon peaks where the metamolecule is transparent to the driving frequency, i.e, frequencies where  $\langle \mathcal{P}^- \mathcal{P}^+ \rangle \rightarrow 0$ . The interference effect weakens at long distances (such as at  $d = 10$  nm in Fig. 2(a)), leading to:  $\omega'_{ex} \rightarrow \omega_{ex}$  and  $\omega'_{pl} \rightarrow \omega_{pl}$  since  $g \rightarrow 0$ . These resonances and the Fano dips are presented in Table 1 as driving frequencies,  $\omega$ , where the metamolecule exhibits different photon statistics as shown in Fig. 2(b).

When driven at the plasmon peak, the metamolecule emits only coherent light ( $g^{(2)}(0) = 1$ ), regardless of the distance,  $d$ , and the MNP geometry (Fig. 2(b), blue-violet curves). This is because, driving the metamolecule at the plasmon peak causes elastic scattering by the MNP to dominate the photon statistics. Hence, the square of one-photon scattering probability,  $\langle \mathcal{P}^- \mathcal{P}^+ \rangle^2$ , is the same as the two-photon scattering probability,  $\langle (\mathcal{P}^-)^2 (\mathcal{P}^+)^2 \rangle$ .

At the Fano dip, the scattered photons are heavily bunched ( $g^{(2)}(0) > 1$ ) at short distances,  $d \leq 4$  nm, and antibunched ( $g^{(2)}(0) < 1$ ) at  $4 \text{ nm} < d \leq 8$  nm, but coherent scattering ( $g^{(2)}(0) \rightarrow 1$ ) dominates at long distances,  $d > 8$  nm (Fig. 2(b), black curves). Though the scattering of an incident photon is suppressed at the Fano dip due to destructive interference, a pair of simultaneous incident photons will saturate the metamolecule's ground state transition, thereby increasing the two-photon scattering probability,  $\langle (\mathcal{P}^-)^2 (\mathcal{P}^+)^2 \rangle$ . Thus, at short distances, driving at the Fano dip leads to a bunching effect because the metamolecule acts as a saturable scatterer. The transition from bunched to antibunched light between  $d > 4$  nm and  $d = 8$  nm is due to a frequency shift, i.e, the Fano dip at  $d = 2$  nm is a Fano peak between  $d > 4$  nm and  $d = 8$  nm. At  $d > 8$  nm, the Fano effect disappears and the response returns to that of the MNP, which gives coherent scattering. In Fig. 2(b), the photon statistics of the prolate- and oblate-based metamolecules are very similar irrespective of their different driving frequencies because the difference in their geometric factors is not sufficient to cause a noticeable change in  $g^{(2)}(0)$ .

Driving the metamolecule at the Fano peak leads to the emission of antibunched light ( $g^{(2)}(0) < 1$ ) at short distances,  $d \leq 4$  nm, which gradually transitions to coherent light ( $g^{(2)}(0) \rightarrow 1$ ) at long distances,  $d > 4$  nm (Fig. 2(b), red curves). At the Fano peak, driving the metamolecule at short distances leads to an antibunching effect as a result of constructive interference, i.e, the spontaneous emission of an absorbed incident photon is enhanced due to the Purcell effect [1, 2]. The saturation of the metamolecule by a photon pair leads to a decrease in the two-photon scattering probability,  $\langle (\mathcal{P}^-)^2 (\mathcal{P}^+)^2 \rangle$ , at the Fano peak. As in the case of the dip, at the Fano peak, the transition from antibunched to coherent light at long distances is due to the vanishing Fano profile in Fig. 2(a).

#### 4. Conclusion

We have shown that the driving frequencies (Fano peak, Fano dip, and plasmon peak), the MNP-QD distance, and the MNP geometry are all important factors to consider when designing metamolecules that exhibit different photon statistics. Our model shows that for a constant MNP volume, the choice of MNP geometry might affect the distance regimes where the metamolecule transitions from bunching to antibunching of the scattered photons, but not those where it transitions from antibunching to coherent emission. Fano interference makes it possible for the driven metamolecule to act as a saturable scatterer for photon statistics control.

#### Acknowledgments

The authors are grateful for the financial support from the South African Quantum Technology Initiative (SA QuTI), the department of science and innovation (DSI), and the national research foundation (NRF).

#### References

- [1] Ridolfo A, Stefano O D, Fina N, Saija R and Savasta S 2010 *PRL* **105** 263601
- [2] Waks E and Sridharan D 2010 *PRA* **82** 043845
- [3] Zhao D, Gu Y, Chen H, Ren J, Zhang T and Gong Q 2015 *PRA* **92** 033836
- [4] McEnergy K R, Tame M S, Maier S A and Kim M S 2014 *PRA* **89** 013822
- [5] Gisin N and Thew R 2007 *Nat. Photon.* **1** 165
- [6] Lee C, Dieleman F, Lee J, Rockstuhl C, Maier S A and Tame M 2016 *ACS Photonics* **3** 992
- [7] Wu X, Gray S K and Pelton M 2010 *Optics Express* **18** 23633
- [8] Steck D A 2017 *Quantum and Atom Optics* (Available online at <http://steck.us/teaching>)
- [9] Walls D F and Milburn G J 2008 *Quantum Optics, 2nd Edition* (Springer)
- [10] Ugwuoke L C, Mančal T and Kruger T P J 2020 *JOSA B* **37**
- [11] Johansson J R, Nation P D and Nori F 2013 *Comput. Phys. Commun.* **184** 1234

## ***In vitro* effects of aluminium (iii) phthalocyanine chloride tetra sulphonic acid-mediated photodynamic therapy on oesophageal cancer**

**OC Didamson<sup>1</sup>, R Chandran<sup>1</sup> and H Abrahamse<sup>1</sup>**

Laser Research Centre, Faculty of Health Sciences, University of Johannesburg P. O. Box 17011, Doornfontein 2028, South Africa

E-mail: habrahamse@uj.ac.za

**Abstract.** Oesophageal cancer is an aggressive and lethal malignancy accounting for the eighth leading cause of cancer and sixth cause of cancer-related death globally. Conventional treatments for oesophageal cancer are characterised by suboptimal efficiency resulting in treatment resistance and relapse. Photodynamic therapy (PDT), a non-invasive modality, has emerged as a potential alternative cancer therapy. Growing evidence has shown that aluminium (III) Phthalocyanine Chloride Tetra sulfonic Acid (AlPcS<sub>4</sub>Cl) is a promising photosensitiser in PDT owing to its photochemical and photophysical features. This study examined *in vitro* impacts of AlPcS<sub>4</sub>Cl-mediated PDT in an oesophageal cancer cell line (HKESC-1). The HKESC-1 cells were grown and maintained in a culture medium incubated at 37° C, with 5% CO<sub>2</sub> and 85% humidity. The cells were treated with increasing dose concentrations of AlPcS<sub>4</sub>Cl and irradiated at a fluence of 5 J/cm<sup>2</sup> using a diode laser at 673.2nm wavelength. The cellular activities following 24 hours post-PDT were evaluated using microscopy and biochemical tests (such as cell viability and cytotoxicity assay) to determine the response of HKESC-1 cells to treatments. Results from treated cells displayed a dose-dependent response as shown by the significant morphologic changes, increased cytotoxic damage, and reduced cell viability. The study showed that AlPcS<sub>4</sub>Cl mediate PDT is an efficient treatment modality for oesophageal cancer. Further research on the mechanism of cell death pathways in oesophageal cancer could enhance and translate the potential application of AlPcS<sub>4</sub>Cl mediated PDT of cancer in clinical settings.

### **1. Introduction**

Oesophageal cancer is an aggressive and lethal malignancy accounting for the eighth leading cause of cancer and the sixth cause of cancer-related death worldwide [1]. Conventional treatments for oesophageal cancer consist of surgery, chemotherapy, and radiotherapy [2], and recently immunotherapy has also been employed for the treatment of oesophageal cancer [2, 3]. However, these conventional therapies are characterised by suboptimal efficiency resulting in treatment resistance, relapse, and severe adverse effects. Also, not all patients are eligible for immunotherapy. Photodynamic therapy (PDT), a non-invasive modality, has emerged as a potential alternative cancer therapy for either curative or palliative purposes. PDT has gained much attention due to its effectiveness, limited toxicity, compatibility with other treatments, can be repeated several times, and cost-effectiveness [4].

PDT is made up of three crucial components, photosensitiser (PS), light and oxygen. The PS, a light-activated agent, is first administered and internalised within the tumour cells, then irradiated with suitable light at a particular wavelength, resulting in reactive oxygen species (ROS) generation,

oxidative stress, damage to cellular organelles /membranes and ultimately the death of cancer cells [5]. Growing evidence indicates that Aluminium (III) Phthalocyanine Chloride Tetra Sulfonic Acid (AlPcS<sub>4</sub>Cl) is a promising photosensitiser in PDT for various tumours due to its distinct photochemical and photophysical features [6]. However, its cellular impacts on HKESC-1 oesophageal cancer cells are limited. This study examined the *in vitro* impacts of AlPcS<sub>4</sub>Cl-mediated PDT in an oesophageal cancer cell line (HKESC-1).

## 2. Method

### 2.1. Cell culture

A human oesophageal cancer cell line (HKESC-1) used in this study was purchased from Cellonex (South Africa), a distributor of AddexBio. HKESC-1 cells were maintained in T75 culture flasks in Dulbecco's modified Eagle's medium (DMEM) (Sigma-Aldrich, D5796) with the addition of 10% Fetal Bovine Serum (FBS) (Biochrom, S0615), 1mM sodium pyruvate 1% antibiotic: 0.5% Amphotericin B and 0.5% Penicillin-streptomycin. The cells were maintained under 5% CO<sub>2</sub>, 37°C and 80% humidity.

### 2.2. Photodynamic Treatment

Photodynamic therapy was conducted as previously described [6]. Triplicate experimental and control cells were cultured with a seeding density of  $5 \times 10^5$  in culture petri dishes of 3.4 cm<sup>2</sup> diameter until cells attain 90 percent confluence. The cells then received different concentrations of the PS (AlPcS<sub>4</sub>Cl) (1.25, 2.5, 5, 10 & 20µM) and were incubated for four hours at 37°C and 5% CO<sub>2</sub> to allow cellular localisation of the PSs. After incubation, the cells were subjected to irradiation using a continuous wave semiconductor diode laser (Oriel Corporation) at 673.2 nm and 5 J/cm<sup>2</sup> fluence. After that, the irradiated culture plates were incubated for 24 hours before biochemical assays were conducted.

### 2.3. Cell Morphology

Cellular morphological changes were visualised and examined with an inverted light microscope (Olympus CKX41Q4), and six images per sample were captured with 10X at a scale of 200µm with an Olympus digital camera using the CellSens software.

### 2.4. Cell Viability Assay

#### 2.4.1. ATP Cell Viability Assay

Cellular ATP examination was conducted using the CellTiter-Glo® 3D luminescence reagent (Promega, G968A) to determine the level of ATP in live cells. Briefly, 100µL cell suspension and 100µL (100µM) of the reconstituted reagent were added into an opaque-walled 96 well plate and carefully mixed. The plate was placed on a shaker for 2 minutes to facilitate lysis and kept in the dark at ambient temperature for 10 minutes. The ATP luminescence generated was quantified using the PerkinElmer, VICTOR Nivo™.

#### 2.4.2. Trypan Blue Exclusion Assay

Cell viability assay was performed using the Trypan blue exclusion test to determine the proportion of live cells. Ten microlitres of 0.4% Trypan blue (Sigma Aldrich, T8154) were added to an equivalent volume of cell suspension and mixed properly. Then, the 10µL volume each was pipetted to both sides of a counting chamber slide and slotted into an automated cell counter (Countess®).

### 2.5. Cytotoxicity

A cytotoxicity assay was conducted to measure the lactate dehydrogenase (LDH) enzyme released by the damaged cell membrane. The test was achieved using the Cyto Tox 96® Non-Radioactive Cytotoxicity assay (Promega, G179A). Briefly, 50µL of reconstituted substrate mix and 50µL of cell suspension were added into a 96 multi-well plate and mixed. The plate was wrapped with foil and kept

in the dark for 30 minutes at 25°C. The absorbance at 490 nm was measured using PerkinElmer, VICTOR Nivo™ and is a measure of the amount of LDH in the sample.

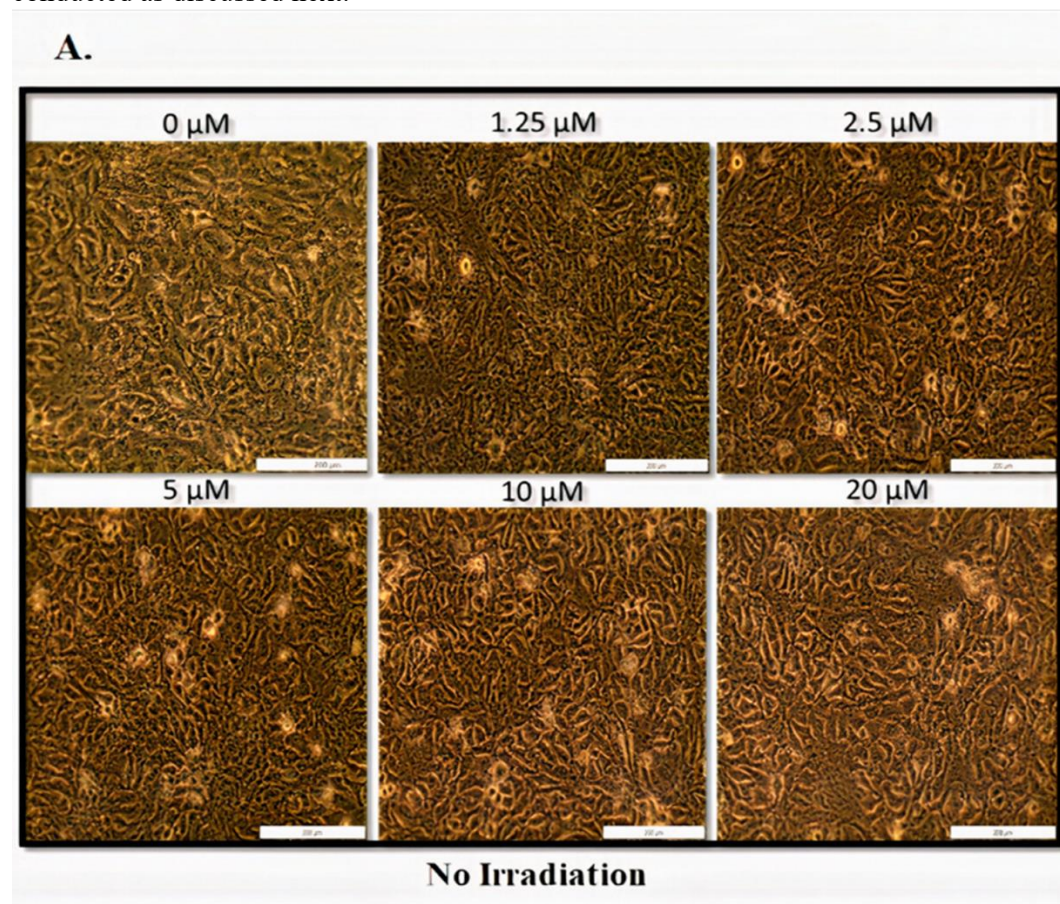
## 2.6. Data Analysis

All experiments were conducted in three technical repeats and in biological triplicates ( $n=3$ ). All results were collated and analysed using GraphPad Prism (v5). The mean values of test groups were evaluated in relation with the mean value of control cells. One-way ANOVA was employed, and a statistical significance was defined as  $p < 0.05$  (\*),  $p < 0.01$  (\*\*), and  $p < 0.001$  (\*\*\*)).

## 3. Result and Discussion

### 3.1. Cellular Morphology

We studied the effect of AlPcS<sub>4</sub>Cl-PDT on the morphology of HKESC-1 cells by examining the cellular alterations after incubation with varying concentrations of AlPcS<sub>4</sub>Cl (1.25-20  $\mu$ M) pre and post irradiation. Six fields were captured per samples at a scale of 200 $\mu$ m. Our findings from HKESC-1 cells receiving AlPcS<sub>4</sub>Cl without irradiation showed no significant cytotoxic effects when compared with the untreated control (Figure 1A). No significant morphological changes were observed in the absence of light. No differences were seen between the control cells with no PS and cells with PS. However, the irradiated cells with AlPcS<sub>4</sub>Cl at 5J/cm<sup>2</sup> showed significant cellular morphological changes (Figure 1B). Morphological impairments showed 24 hours after treatment was shrinkage of cells, membrane integrity distortion, and floatation of cells in culture plates. The morphological changes in the treated irradiated group were indicative of cell death. To confirm this claim further quantitative biochemical analysis were conducted as discussed next.



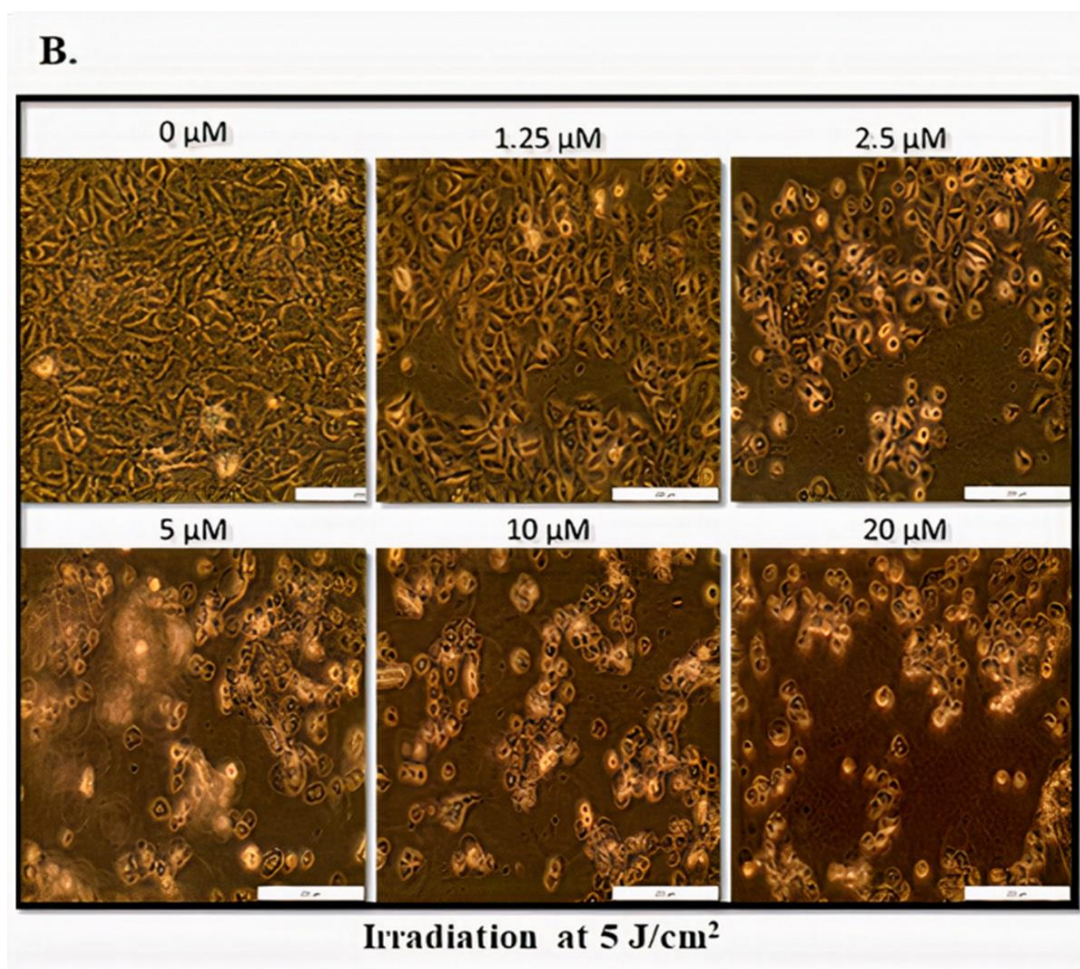


**Figure 1.** Cellular morphological changes in HKESC-1 cells 24 hours post treatments. (A) The morphological changes in the presence of different concentrations of AlPcS<sub>4</sub>Cl (without irradiation). (B) The morphological changes of AlPcS<sub>4</sub>Cl-PDT at 5 J/cm<sup>2</sup> irradiation. The images are representative of six images per sample captured at a scale of 200μm.

### 3.2. Cell Viability Assay

#### 3.2.1. ATP Cell Viability Assay

We evaluated the effects of AlPcS<sub>4</sub>Cl-PDT on HKESC-1 cells viability by measuring the ATP levels, which is a function of cell viability. Damage cell membrane results in the inability to produce ATP, and the intracellular ATPases rapidly diminish the ATP in the cytoplasm [7]. The ATP levels were quantified using CellTiter-Glo® 3D luminous assay after incubation with varying concentrations of AlPcS<sub>4</sub>Cl (1.25-20 μM) without irradiation and with irradiation. Our results revealed high ATP levels in non-irradiated both in the control cells and the cell receiving AlPcS<sub>4</sub>Cl (Figure 2A). The findings showed that the PS does not affect the proliferation rate of the cancer cells when in an un-activated state.

In contrast, the combination of AlPcS<sub>4</sub>Cl with irradiation at 5 J/Cm<sup>2</sup> significantly showed a dose-dependent reduction of ATP levels and high antiproliferative effects on HKESC-1 cells (\*\**p* < 0.001) when compared with the control cells (Figure 2B). This finding is in concordance with the results from Crous and coworkers, who investigated the effect of AlPcS<sub>4</sub>Cl-PDT on lung cancer [6] and Kresfelder et al. (2009) who examined the effects of AlPcSmix on oesophageal cancer [8].

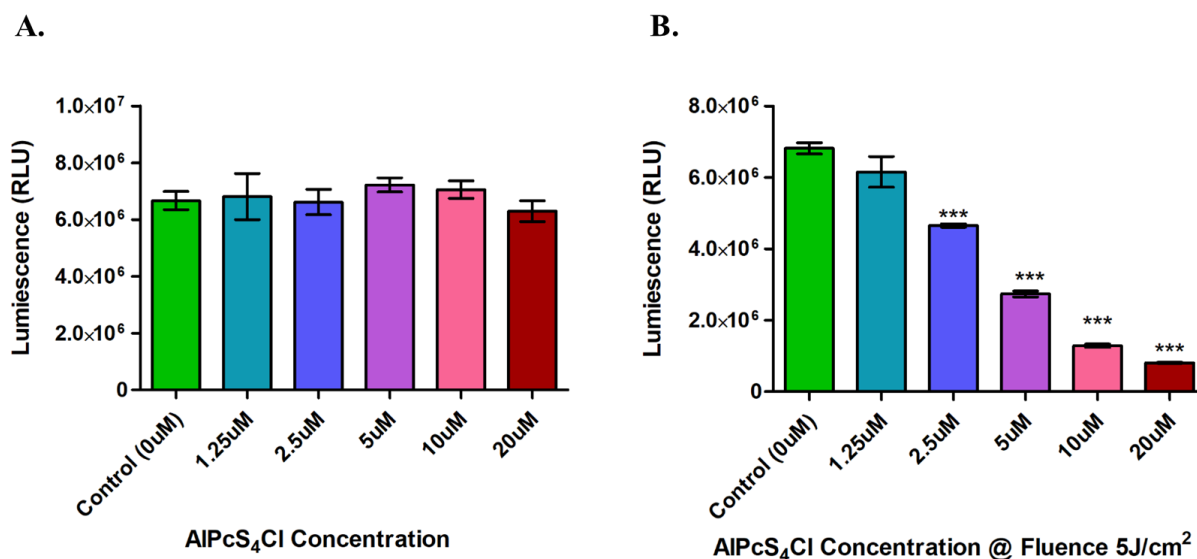


Figure 2. The effects of AlPcS<sub>4</sub>Cl on HKESC-1 cells on cell viability. (A) Non-irradiated cells showed high levels of ATP with no significant difference between the control cells and cells administered with AlPcS<sub>4</sub>Cl. (B) The irradiated cells at 5 J/cm<sup>2</sup> displayed reduced viability with a reduction in ATP levels (\*\**p* < 0.001). The values shown are ± SEM (standard error of the mean) (n=3).

### 3.2.2. Trypan Blue Exclusion Assay

Trypan blue exclusion test was conducted to determine the proportion of live cells present after 24-hour administration of AlPcS<sub>4</sub>Cl and AlPcS<sub>4</sub>Cl-PDT on HKESC-1 cells. Trypan blue exclusion test is based on the mechanism that the cell membrane integrity of viable cells is intact and therefore expels the Trypan blue dye. In contrast, dead cells retain the stain due to damaged cell membrane [7, 9]. The proportion of live cells was measured using an automated cell counter. The result showed that cells treated with different concentrations of AlPcS<sub>4</sub>Cl without irradiation had a high percentage of viable cells which was similar to the untreated control cells (Figure 3A). The findings showed that the PS does not inhibit cell viability in the cancer cells without irradiation. However, substantial differences were seen between the control and the PDT groups, as depicted in Figure 3B (\**p* < 0.05, \*\*\**p* < 0.001). The results demonstrated that the PS substantially decreased cell viability rate post-PDT as observed in ATP viability assay. Comparable findings have been reported on aluminium phthalocyanines based PS on various cancers such as oesophageal cancer [8], lung cancer [6], breast cancer [10], and cervical cancer [11].

### 3.3. Cytotoxicity

Cytotoxicity assay using lactate dehydrogenase (LDH) release method was employed to quantify the amount of LDH enzyme leakage in the cell culture media. Cells that have damaged cell membrane release LDH, which indicates cytotoxic effects [7, 12]. We found that no statistically significant differences were observed in the non-irradiated (between the control cells and the cells administered with PS) (Figure 4A). Although the non-irradiated cells showed some slight cytotoxic effect compared with the cytotoxicity positive control, a common feature of tumour cells undergoing constant proliferation, and so experiencing minor cell death. This observation is consistent with findings from Robertson and colleagues, who examined the cytotoxic effect of metallophthalocyanine (MPc) on human metastatic melanoma cells [13]. The LDH released from damaged cells from the irradiated cells administered with 0–20 μM of PS at 5 J/cm<sup>2</sup> were compared to the control receiving no PS and cytotoxicity positive control. The AlPcS<sub>4</sub>Cl-PDT induced significant cytotoxicity compared to the control receiving no PS (\**p* < 0.05, \*\**p* < 0.01) (Figure 4B), which is also in agreement with a study reported by Crous et al. (2019) who

investigated the cytotoxic effect of this PS on lung cancer[6]. In addition, similar results were shown by studies that examined the cytotoxic of AlPcSmix on oesophageal cancer cells [8] and cervical cancer[11].

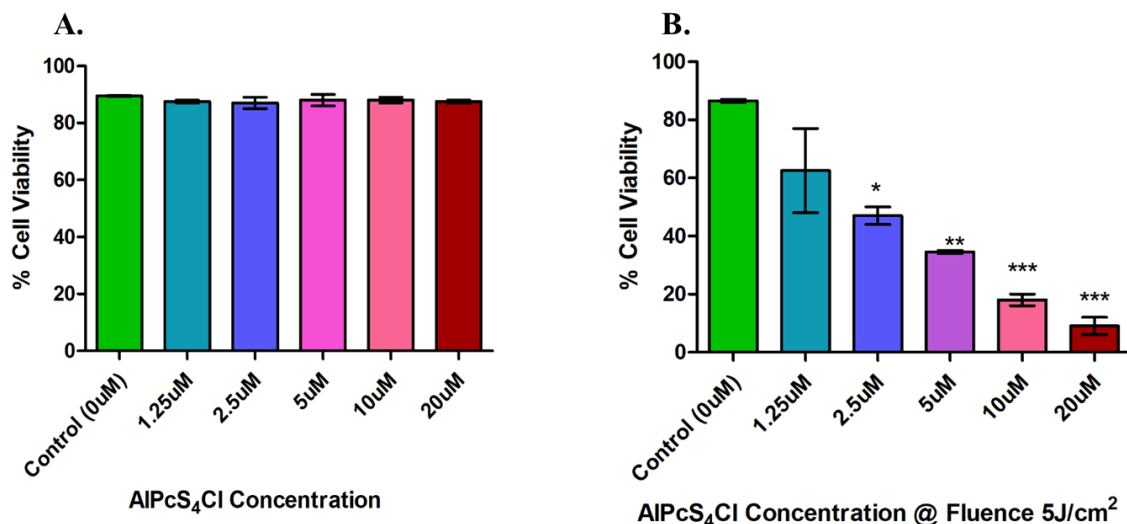


**Figure 3.** Fig. 1. Cell viability effect of AlPcS<sub>4</sub>Cl ON HKESC-1 using Trypan blue exclusion assay. (A) The percentage of cell viability of non-irradiated cells in different concentrations of AlPcS<sub>4</sub>Cl. (B) The percentage of cell viability irradiated with 5 J/cm<sup>2</sup> after AlPcS<sub>4</sub>Cl -PDT treatment. The findings are shown as  $\pm$  SEM (n = 3); (\*p < 0.05, \*\*p < 0.01, \*\*\*p < 0.001).

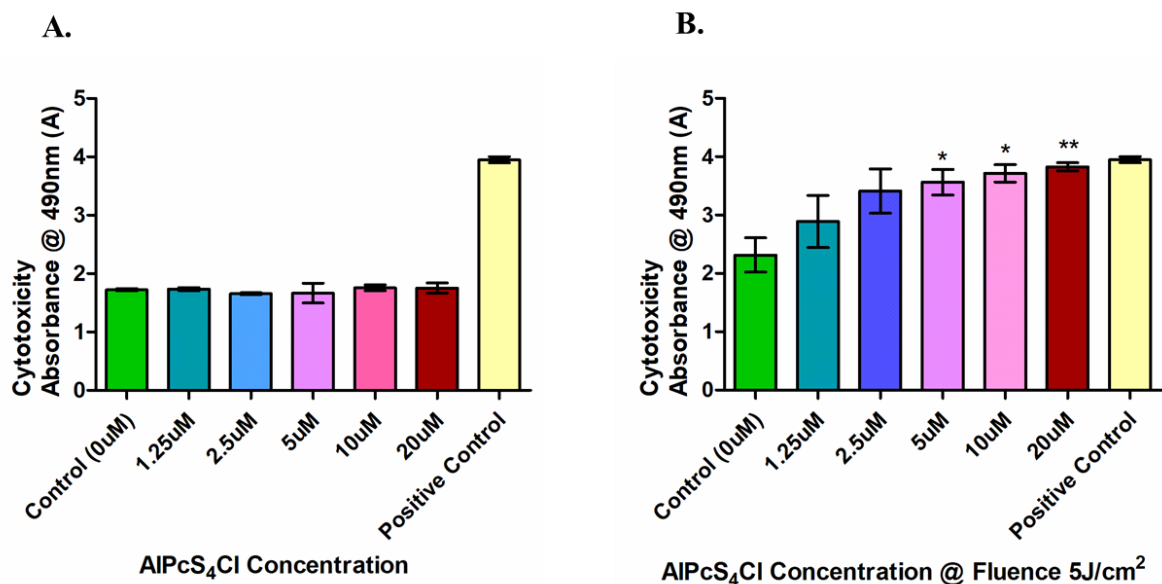


**Figure 4.** The cytotoxic effects of AlPcS<sub>4</sub>Cl and AlPcS<sub>4</sub>Cl-PDT were determined 24 hours after treatments by LDH release cytotoxicity assay on HKESC-1 cells. (A) The levels of LDH leakage in the presence of varying concentrations of AlPcS<sub>4</sub>Cl (non-irradiation). (B) The levels of LDH release after AlPcS<sub>4</sub>Cl-PDT with 5 J/cm<sup>2</sup> irradiation. The results are depicted as  $\pm$  SEM (n = 3); (\*p < 0.05, \*\*p < 0.01).

#### 4. Conclusion

Photodynamic therapy, a non-invasive and non-toxic treatment modality, has emerged as an effective alternative treatment modality required to overcome the challenges associated with the current

conventional therapy for various malignancies. Aluminium phthalocyanine and its derivatives have been investigated in different tumours with promising outcomes. The findings from this study revealed that ALPcS<sub>4</sub>Cl mediated PDT can significantly reduce cell viability and increase the cytotoxic effects on oesophageal cancer. Also, the result showed a negligible dark-cytotoxicity activity on oesophageal cancer, therefore ALPcS<sub>4</sub>Cl-PDT offers a promising treatment modality for oesophageal cancer. Further investigation is needed to determine the cell death mechanism and pathways.

### Acknowledgements

This research is supported by the South African Research Chairs Initiative of the Department of Science and Technology National Research Foundation of South Africa (Grant No 98337). Onyisi Christiana Didamson has been supported financially by the Global Excellence and Stature, Fourth Industrial Revolution (GES 4.0) Doctoral Scholarship from University of Johannesburg. The authors sincerely thank the University of Johannesburg, the National Laser Centre, and the National Research Foundation of South Africa (CSIR-DST) for their financial grant support.

### References

- [1] Ferlay, J., et al., *Cancer statistics for the year 2020: An overview*. International Journal of Cancer, 2021. **149**(4): p. 778-789.
- [2] Obermannová, R., et al., *Oesophageal cancer: ESMO Clinical Practice Guideline for diagnosis, treatment and follow-up*. Annals of Oncology, 2022.
- [3] DaSilva, L.L., P.N. Aguiar, Jr, and G. de Lima Lopes, *Immunotherapy for Advanced Esophageal Squamous Cell Carcinoma—Renewed Enthusiasm and a Lingering Challenge*. JAMA Oncology, 2021. **7**(11): p. 1613-1614.
- [4] Didamson, O.C. and H. Abrahamse, *Targeted Photodynamic Diagnosis and Therapy for Esophageal Cancer: Potential Role of Functionalized Nanomedicine*. Pharmaceutics, 2021. **13**(11): p. 1943.
- [5] Kwiatkowski, S., et al., *Photodynamic therapy - mechanisms, photosensitizers and combinations*. Biomed Pharmacother, 2018. **106**: p. 1098-1107.
- [6] Crous, A., S.S. Dhilip Kumar, and H. Abrahamse, *Effect of dose responses of hydrophilic aluminium (III) phthalocyanine chloride tetrasulphonate based photosensitizer on lung cancer cells*. J Photochem Photobiol B, 2019. **194**: p. 96-106.
- [7] Aslantürk, Ö.S., *In vitro cytotoxicity and cell viability assays: principles, advantages, and disadvantages*. Genotoxicity-A predictable risk to our actual world, 2018. **2**: p. 64-80.
- [8] Kresfelder, T.L., M.J. Cronjé, and H. Abrahamse, *The effects of two metallophthalocyanines on the viability and proliferation of an esophageal cancer cell line*. Photomed. Laser Surg., 2009. **27**(4): p. 625-631.
- [9] Strober, W., *Trypan Blue Exclusion Test of Cell Viability*. Curr Protoc Immunol, 2015. **111**: p. A3.B.1-a3.B.3.
- [10] Muehlmann, L.A., et al., *Aluminium-phthalocyanine chloride nanoemulsions for anticancer photodynamic therapy: Development and in vitro activity against monolayers and spheroids of human mammary adenocarcinoma MCF-7 cells*. J Nanobiotechnology, 2015. **13**: p. 36.
- [11] Chizenga, E.P., R. Chandran, and H. Abrahamse, *Photodynamic therapy of cervical cancer by eradication of cervical cancer cells and cervical cancer stem cells*. Oncotarget, 2019. **10**(43): p. 4380-4396.
- [12] Riss, T.L., et al. *Cytotoxicity Assays: In Vitro Methods to Measure Dead Cells*. 2019.
- [13] Robertson, C.A., H. Abrahamse, and D. Evans, *The in vitro PDT efficacy of a novel metallophthalocyanine (MPc) derivative and established 5-ALA photosensitizing dyes against human metastatic melanoma cells*. Lasers Surg Med, 2010. **42**(10): p. 766-76.

# Recombinant antibody-conjugated silver nanoparticles for improved drug delivery in photodynamic therapy for metastatic melanoma

Zaria Malindi<sup>1,2\*</sup>, Stefan Barth<sup>2</sup> and Heidi Abrahamse<sup>1</sup>

<sup>1</sup>Laser Research Centre, University of Johannesburg, Beit Street, Doornfontein, 2028 Johannesburg, South Africa

<sup>2</sup>Medical Biotechnology and Immunotherapy Research Unit, University of Cape Town, Anzio Road Observatory, 7925 Cape Town, South Africa

E-mail: [222116639@student.uj.ac.za](mailto:222116639@student.uj.ac.za)

**Abstract.** New treatments are needed to overcome melanoma's inherent drug resistance. Immunotherapy uses antibodies to target cancer; photodynamic therapy uses light to produce cytotoxic singlet oxygen and reactive oxidative species; and nanomedicine uses nanocarriers to enhance pharmacokinetics. We aim to establish a chemical conjugation model allowing for directional attachment of SNAP-tag-based recombinant antibodies (rAbs) to silver nanoparticles carrying the photosensitizer ZnPCS<sub>4</sub> for the photoimmunotheranostic management of melanoma. The initial aim was to engineer and purify rAbs comprising anti-CSPG4 single-chain variable fragments (scFv) and SNAP-tag and to validate rAb selective binding to melanoma cells. HEK293T cells were transfected with plasmids containing the scFv and SNAP-tag gene sequences. Secreted protein was purified using immobilised metal affinity chromatography and characterised using SDS-PAGE and Western blot. The rAb was then conjugated to fluorescent markers to confirm selective binding to target cells by flow cytometry and confocal microscopy. These preliminary results indicate the feasibility of this rAb as a targeting ligand for antibody-mediated nano-PDT against melanoma.

## 1. Background

The gold standard for melanoma treatment is resection, but this only provides local control of early-stage disease; in late-stage disease, no satisfactory treatment exists and recurrence becomes probable[1]. Despite advances in cancer drug development, most clinical trials have produced suboptimal outcomes, with many drugs exhibiting poor or non-specific effects[2]. Furthermore, melanoma cells are inherently resistant to treatment owing to their highly developed antioxidant system[3,4]. New therapies are needed to address these patients' unmet clinical requirements.

In photodynamic therapy (PDT), a photosensitizer (PS) is irradiated, inducing cell death. When a photon is absorbed by ground state PS, the PS enters an excited singlet state (PS<sub>es</sub>). Subsequent decay to the ground state causes fluorescent emission. At peak absorption, PS<sub>es</sub> undergoes intersystem crossing, entering an excited triplet state (PS<sub>et</sub>). PS<sub>et</sub> interacts with neighbouring molecules through 1) the type I photo-oxidative pathway in which PS<sub>et</sub> transfers electrons or H<sup>+</sup> ions to proximate biomolecules, which react with oxygen and produce various reactive oxygen species or 2) the type II pathway in which energy released when PS<sub>et</sub> decays is transferred to ground state oxygen, creating

singlet oxygen[5]. PDT has been approved for certain cancers[6], though research on its use in melanoma is ongoing. PDT utilises passive tissue localisation[7], which can lead to off-target accumulation and side effects, but photoimmunotherapy (PIT) provides a targeting strategy for PDT.

SNAP-tag is an engineered enzyme derived from the human DNA repair enzyme O<sup>6</sup>-alkylguanine-DNA alkyltransferase, which removes DNA alkyl adducts from O<sup>6</sup>-alkylated guanine, transferring the alkyl group to its Cys145 reactive cysteine residues and releasing guanine. SNAP-tag mimics this chemistry, reacting readily with benzylguanine (BG). In this single-step protein labelling process, SNAP-tag and any BG-modified substrate bond covalently; the benzyl alkyl group is transferred to the reactive cysteine residue of the SNAP-tag and guanine is released, producing a stable thioether [8,9]. SNAP-tag can be used as a fusion protein with any ligand of choice. In this study, we cloned the single chain variable fragment (scFv) of the anti-chondroitin sulphate proteoglycan-4 (CSPG4) antibody, mAb2.9.27, at the N-terminus. The scFv is one of the smallest functional antibody formats in which the antigen-binding function can be preserved[10]. The scFv-SNAP recombinant antibody's (rAb) reduced size compared to the full-length mAb enhances the degree of penetration into tumorous tissue[8] and facilitates rapid tumour uptake[11]. SNAP-tag further ensures the preservation of antibody integrity and functionality during conjugation because labelling with the payload occurs distal to the antibody fragment[9,12]. Furthermore, since SNAP-tag coupling occurs in a site-specific 1:1 stoichiometry, homogeneous products are generated with a known configuration and drug-to-antibody ratio[9], and because SNAP-tag is of human origin[13], it is not immunogenic. PIT combines the phototoxicity of PDT with the targeting precision of antibody technology to form an antibody-photoabsorber conjugate[14].

The CSPG4 antigen is commonly overexpressed in melanoma. It plays an important role in tumour cell survival, proliferation, migration and invasion, facilitating cancer progression[15]. During embryonic development, CSPG4 expression is seen in several motile tissues; however, expression is limited in the terminally differentiated melanocytes of normal adult tissue due to post-translationally down-regulation[16]. The differential expression of CSPG4 on malignant melanoma cells vs healthy skin tissue and its limited secretion into circulation as a permanently membrane-bound transmembrane protein make CSPG4 a good candidate for targeted therapy[15].

Nanoparticles (NPs) are organic or inorganic structures of up to 100 nm, the physiochemical properties of which can enhance biodistribution and uptake of drugs that are surface-immobilised on or encapsulated within them[17]. Their hydrophilicity improves drug solubility and, thus, pharmacokinetics[18]; they can be easily functionalised[19,20]; they mimic biomolecules, allowing them to go undetected by the host immune system[19]; and they have large aspect ratios, allowing for reduced minimal effective doses due to their high drug loading[21]. In particular, inorganic NPs are easily modified to possess optimal size, shape, and optical properties[22]. Studies have shown that various NP formats can be used as PS drug carriers to augment PDT effects *in vitro*[23]. Silver (Ag) NPs are non-toxic, biocompatible and exhibit antimicrobial and anti-inflammatory properties [24], and these NPs have antitumour effects when used as PSs in PDT[25,26]. However, while gold (Au) NPs have been well-studied[27], the use of AgNP-drug conjugates is limited in the literature, particularly for PS-loaded AgNPs in PDT. Similarly, the use of antibody-NP drug delivery systems has been increasingly examined for AuNPs [28,29], but not for AgNPs.

This project aims to establish a chemical conjugation model allowing for directional attachment of SNAP-tag-based rAbs to nanobioconjugates composed of the PS zinc phthalocyanine tetra-sulphonic acid attached to silver nanoparticles for the photoimmunotheranostic management of melanoma. The initial aim, herein reported, was to engineer and purify rAbs comprising the anti-CSPG4 mAb9.2.27 scFv and the SNAP-tag enzyme and to validate rAb selective binding to CSPG4-positive melanoma cells.

### 3. Methods and Materials

#### 3.1 *In silico* vector design

SnapGene® software (GSL Biotech, Chicago, IL USA) was used for *in silico* design of the mammalian vector system for transient expression of the SNAP-tag fusion protein, and all necessary production vectors were purchased from GenScript (NJ USA).

#### 3.2 Molecular cloning

Plasmid DNA was incorporated into chemically competent DH5a *Escherichia coli* (*E. coli*) cells (NEB, MA United States) using a heat shock method, then inoculated into Luria Bertani (LB) broth (Sigma-Aldrich) and placed at 37°C on a shaker overnight. DNA was isolated using the NucleoBond Plasmid Purification Kit (Macherey-Nagel GmbH & Co, Düren, Germany), and DNA concentration was quantified using a NanoDrop ND-2000 (Thermo Fisher Scientific, DE USA). Restriction enzyme (RE) digests were performed using the NEB Double Digest protocol, and agarose gel electrophoresis was performed to confirm digestion. Agarose bands containing the DNA fragments of interest were excised using the QIAquick Gel Extraction Kit (QIAGEN, Hilden, Germany) and subsequently ligated using the NEB T4 Ligase kit and overnight protocol (NEB). Recombinant plasmid DNA was incorporated into chemically competent *E. coli* cells, and the mixture was spread on LB agar plates supplemented with ampicillin and placed at 37°C overnight. Single colonies were picked and amplified in LB broth. Recombinant plasmids were purified from the *E. coli* using the Zippy Plasmid Miniprep Kit (Zymo Research, CA USA), and the eluted DNA concentration was then quantified using a NanoDrop ND-2000. Single enzyme digest simulations were performed on SnapGene to predicate the cutting patterns for the original and recombinant plasmids, after which RE digest reactions were set up. Agarose gel electrophoresis was performed, and gels were analysed to confirm correct ligation of recombinant plasmids, as predicted by the simulation. Recombinant clones confirmed by restriction mapping were purified using the NucleoBond Plasmid Purification midiprep protocol. Samples were sent to Inqaba Biotec as a pay-for-service to confirm the accuracy of the open reading frame (ORF) sequence.

#### 3.3 HEK293T cell culture and transfection

HEK293T cells were cultured in RPMI-1640 medium supplemented with 10% foetal bovine serum (FBS) and 1% penicillin-streptomycin (Gibco by Life Technologies, CA USA) and incubated at 37°C in 5% CO<sub>2</sub>. The XtremeGENE HP DNA Transfection Reagent Quick Protocol (Sigma-Aldrich, MO USA) was used for transfection, and cells were treated with Zeocin to enrich the Zeocin-resistant transfected population co-expressing the eGFP reporter gene.

#### 3.4 Protein purification

Cell-free supernatant containing the secreted his<sub>6</sub>-tagged fusion protein (mAb9.2.27(scFv)-SNAP) was purified using immobilized metal ion affinity chromatography (IMAC) on an ÄKTA FLPC system (GE Healthcare Europe GmbH, Freiburg, Germany) with a Ni<sup>2+</sup>-NTA Superflow cartridge column. Elution was achieved through binding competition when applying an imidazole gradient to separate elution peaks; 5 mL fractions were collected throughout. Amicon Ultra-15 Centrifugal Filter Units (Merck Milipore, MA USA) were used to further concentrate purified protein and remove imidazole. The concentration of purified mAb9.2.27(scFv)-SNAP rAb was determined using a NanoDrop ND-2000.

#### 3.5 Protein characterisation

Protein samples were separated by size using SDS-PAGE to identify fractions containing protein of the correct weight (~53 kDa). Protein bands were visualised using Coomassie Staining Solution. Western blotting was then used to detect functional his<sub>6</sub>-tag protein. 1:1000 anti-His<sub>6</sub>-tag rabbit primary antibody and 1:5000 goat anti-rabbit IgG horse radish peroxidase-conjugated secondary antibody (Bio Rad) were used to detect proteins on a Gel Doc™ XR Gel Documentation System (Bio Rad).

#### 3.6 Mammalian cell culture

Cancer cell lines were cultured in DMED medium supplemented with 10% FBS and 1% penicillin-streptomycin and incubated at 37°C in 5% CO<sub>2</sub>.

### 3.7 Immunoassays: Binding validation

The NEB Protein Labelling *in vitro* protocol was used to label mAb9.2.27(scFv)-SNAP with BG-modified SNAP-Surface® Alexa Fluor®488. Binding of the final labelled construct to CSPG4-positive cells was assessed quantitatively through flow cytometry using a FACSCalibur system and FlowJo software for analysis (Be ction & Dickinson, Heidelberg, Germany) and qualitatively using confocal microscopy on the Zeiss LSM880 Airyscan (Oberkochen, Germany) with the 40× air objective. The 488 nm (FITC green) and 405 nm (DAPI blue) lasers were used to excite the samples, and the AlexaFluor-488 and Hoechst fluorescent signals were captured accordingly in the green and blue emission channels.

## 4. Results and discussion

### 4.1 *In silico* vector design

Figure 1 shows the *in silico* design of the plasmid generated on SnapGene. Annotated nucleotide and amino acid sequences (not shown) were used to order production vectors.

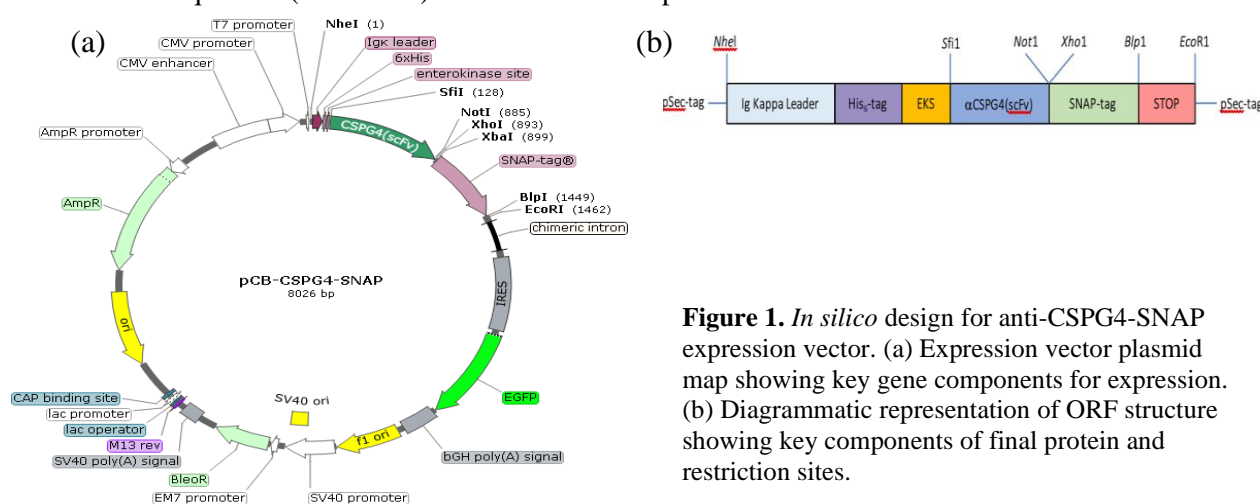


**Figure 1.** *In silico* design for anti-CSPG4-SNAP expression vector. (a) Expression vector plasmid map showing key gene components for expression. (b) Diagrammatic representation of ORF structure showing key components of final protein and restriction sites.

### 4.2 Molecular cloning

After transformation in *E. coli* cells, extraction and purification, all DNA samples were within the acceptable purity ranges. RE digestion of the production and expression vectors was successful, and agarose gel electrophoresis showed DNA fragments correlating to the expected sizes. The backbone and the insert were both digested with *SfiI* and *NotI* and could thus be ligated in frame. After gel extraction, samples with the highest concentrations were used for subsequent ligation. The vector-only ligation control showed only minimal autoligated clones, indicating minimal partial digestion in the previous step. The bacteria only control showed no colony formation, confirming that all colonies contained the vector. *In silico* and *in vitro* restriction mapping confirmed that DNA fragments were successfully ligated and that no autoligated clones were selected. The clone sequences were confirmed to be accurate for further application.

### 4.3 Transfection and protein expression

With the ORF sequence confirmed, the plasmid was introduced into a HEK293T cells. eGFP reporter gene expression confirmed successful transfection and expression.

### 4.4 Protein purification

Collection of the eluted fractions during IMAC was monitored at wavelength 280 nm (Figure 2). Peak 1, seen before the application of the imidazole gradient was non-specific run-through containing BSA. Peaks 2-4, seen after the imidazole gradient, were considered to potentially contain the rAb and were collected for further analysis.

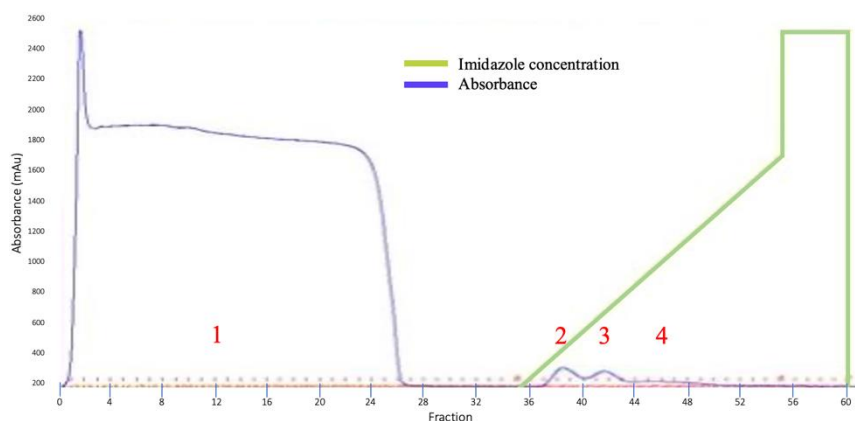


**Figure 2.** Chromatogram from IMAC purification of His<sub>6</sub>-tagged mAb9.2.27(scFv)-SNAP fusion proteins.

#### 4.5 Protein characterisation

The collected peaks above were run on an SDS-PAGE gel to identify the presence of protein corresponding to the weight of mAb9.2.27(scFv)-SNAP (53.13 kDa). Peak 2 contained BSA contaminant; peaks 3 and 4 showed a single band each of an appropriate weight and were thus pooled for further analysis. During Western blotting, peaks 2 and 3 were confirmed to contain his<sub>6</sub>-tag rAb, indicating that functional rAb was retained during purification.

#### 4.6 Immunoassays: binding validation

Figure 3 shows binding of labelled mAb9.2.27(scFv)-SNAP to the CSPG4-positive SK-MEL-28 melanoma cell line (other CSPG4-positive cell lines across all melanoma stages and pigmentation levels not shown) with no binding to MDA-MB-468 negative control cells. These results confirm a) that the rAb exhibits selective binding to CSPG4-positive cells and can thus be used for precise, target drug delivery and b) that CSPG4 is over-expressed in melanoma cells in all growth stages, with and without pigmentation, and in its chemoresistant form; therefore, CSPG4 is a suitable therapeutic target for all forms of melanoma. Figure 4 further demonstrates, using confocal microscopy, that the rAb exhibited significant surface binding to SK-MEL-28 cells but not to the CSPG4-negative control. These results confirm that mAb9.2.27(scFv)-SNAP is suitable for molecular imaging and photodiagnosis of melanoma.

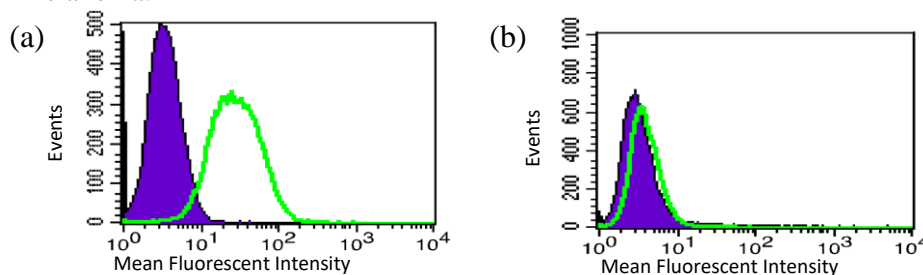


**Figure 3.** Quantitative binding validation via flow cytometry. (a) CSPG4-positive SK-MEL-28 cell line. (b) MDA-MB-468 negative control.

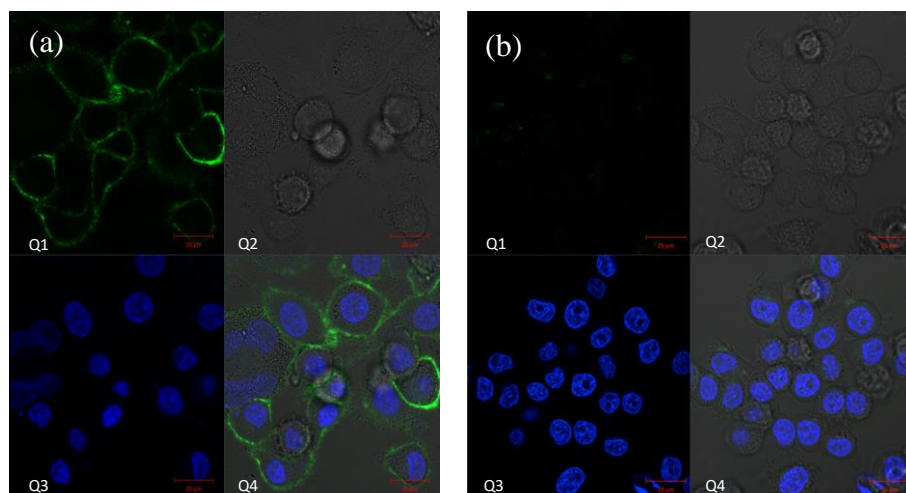


**Figure 4.** Qualitative binding validation via confocal microscopy. (a) CSPG4-positive SK-MEL-28 cell line. (b) MDA-MB-468 negative control. Q1 = FTIC green channel (ex 488 nm, em 519 nm); Q2 = brightfield; Q3 = Hoechst channel (ex 405 nm, em 461 nm); Q4 = merge image. Blue shows Hoechst staining of nuclei; green shows AlexaFluor-488 staining of the CSPG4 antigen. Scale bar = 20  $\mu$ m.

## 5. Conclusion

In summary, using SNAP-tag technology we were able to generate a next generation photoimmunotherapeutic in the form of an rAb fusion protein. The conjugate shows retained functionality of the scFv binding region, with antigen-specific binding to CSPG4-positive melanoma cells. Further steps will include the development of a chemical conjugation model to create rAb-NP conjugates for targeted delivery of PSs in PDT for melanoma, internalisation and trafficking studies and assessment of cytotoxicity after PDT application.

## 6. References

- [1] Rutkowski P, Zdzienicki M, Nowecki ZI, van Akkooi ACJ 2010 Surgery of primary melanomas. *Cancers* **2** 824–41
- [2] Lin A, et al. 2019 Off-target toxicity is a common mechanism of action of cancer drugs undergoing clinical trials. *Sci. Transl. Med.* **11**(509) 8411
- [3] Yuan L, Mishra R, Patel H, Alanazi S, Wei X, Ma Z, Garrett J 2020 BRAF Mutant melanoma adjusts to BRAF/MEK inhibitors via dependence on increased antioxidant SOD2 and increased reactive oxygen species levels. *Cancers* **12** 1661
- [4] Amawi H, Sim HM, Tiwari AK, Ambudkar SV, Shukla S 2019 ABC transporter-mediated multidrug-resistant cancer. *Adv. Exp. Med. Biol.* **1141** 549–80
- [5] dos Santos AF, de Almeida DRQ, Terra LF, Baptista MS, Labriola L 2019 Photodynamic therapy in cancer treatment - an update review. *J. Cancer Metastasis Treat.* **5** 25
- [6] National Cancer Institute 2020 Photodynamic therapy to treat cancer [cited 2022 Aug 5]. Available from: <https://www.cancer.gov/about-cancer/treatment/types/photodynamic-therapy>
- [7] Castano AP, Demidova TN, Hamblin MR 2005 Mechanisms in photodynamic therapy: Part three—Photosensitizer pharmacokinetics, biodistribution, tumor localization and modes of tumor destruction. *Photodiagnosis Photodyn. Ther.* **2**(2) 91
- [8] Keppler A, Kindermann M, Gendreizig S, Pick H, Vogel H, Johnsson K 2004 Labeling of fusion proteins of O6-alkylguanine-DNA alkyltransferase with small molecules in vivo and in vitro. *Methods* **32**(4) 437–44
- [9] Kampmeier F, Ribbert M, Nachreiner T, Dembski S, Beaufilet F, Brecht A, Barth S 2009 Site-specific, covalent labeling of recombinant antibody fragments via fusion to an engineered version of 6-O-alkylguanine DNA alkyltransferase. *Bioconjug. Chem.* **20**(5) 1010–5
- [10] Rodrigo G, Gruvegård M, van Alstine JM 2015 Antibody fragments and their purification by protein L affinity chromatography. *Antibodies* **4**(3) 259–77
- [11] Oliveira S, van Dongen GAMS, Stigter-Van Walsum M, Roovers RC, Stam JC, Mali W, van Diest PJ Van Bergen En Henegouwen P 2012 Rapid visualization of human tumor xenografts through optical imaging with a near-infrared fluorescent anti-epidermal growth factor receptor nanobody. *Mol. Imaging* **11**(1) 33–46
- [12] Puettmann C, Kolberg K, Hagen S, Schmies S, Fischer R, Nachring J, Barth S 2013 A monoclonal antibody for the detection of SNAP/CLIP-tagged proteins. *Immunol. Lett.* **150**(1–2) 69–74
- [13] Juillerat A, Gronemeyer T, Keppler A, Gendreizig S, Pick H, Vogel H, Johnsson K 2003 Directed evolution of O6-alkylguanine-DNA alkyltransferase for efficient labeling of fusion proteins with small molecules in vivo. *Chem. Biol.* **10**(4) 313–7
- [14] Maruoka Y, Wakiyama H, Choyke PL, Kobayashi H. Near infrared photoimmunotherapy for cancers: A translational perspective. *EBioMedicine* **70** 103501
- [15] Price MA, Colvin Wanshura LE, Yang J, Carlson J, Xiang B, Li G, Ferrone S, Dudek AZ, Turley EA, McCarthy JB 2011 CSPG4, a potential therapeutic target, facilitates malignant progression of melanoma. *Pigment Cell Melanoma Res.* **24**(6) 1148–57
- [16] Ghosh A, Syed SM, Kumar M, Carpenter TJ, Teixeira JM, Houairia N, et al. In Vivo Cell Fate Tracing Provides No Evidence for Mesenchymal to Epithelial Transition in Adult Fallopian Tube and Uterus. *Cell Reports*. 2020 May 12;31(6):107631.
- [17] Kruger C, Abrahamse H 2012 Utilisation of targeted nanoparticle photosensitiser drug delivery systems for the enhancement of photodynamic therapy. *Molecules* **23**(10) 2628–49
- [18] Mohanraj VJ, Chen Y 2006 Nanoparticles – A review. *Trop. J. Pharm. Res.* **5**(1) 561–73
- [19] Zolnik BS, González-Fernández A, Sadrieh N, Dobrovolskaia MA 2010 Nanoparticles and the immune system. *Endocrinology* **151** 458–65

- [20] Lim CK, Heo J, Shin S, Jeong K, Seo YH, Jang WD, Park CR, Park SY, Kim S, Kwon IC 2013 Nanophotosensitizers toward advanced photodynamic therapy of cancer. *Cancer Lett.* **334** 176–87
- [21] Liu Y, Yang G, Jin S, Xu L, Zhao CX. Development of high-drug-loading nanoparticles. *ChemPlusChem.* **85**(9) 2143–57
- [22] Mfouo-Tynga I, El-Hussein A, Abdel-Harith M, Abrahamse H 2014 Photodynamic ability of silver nanoparticles in inducing cytotoxic effects in breast and lung cancer cell lines. *Int. J. Nanomedicine* **9**(1) 3771–80
- [23] Nicol JR, Dixon D, Coulter JA. 2015 Gold nanoparticle surface functionalization: A necessary requirement in the development of novel nanotherapeutics. *Nanomedicine* **10** 1315–26
- [24] Kumar SSD, Houreld NN, Kroukamp EM, Abrahamse H 2018 Cellular imaging and bactericidal mechanism of green-synthesized silver nanoparticles against human pathogenic bacteria. *J. Photochem. Photobiol. B, Biol.* **178** 259–69
- [25] Pradeep Chandran C, Mani Rahulan K, Ganesan S 2010 Synthesis and study of photodynamic activity of silver nanoparticles. *Photonics 2010: 10th International Conference on Fiber Optics & Photonics*
- [26] Erdogan O, Abbak M, Demirbolat GM, Birtekocak F, Aksel M, Pasa S, Cevik O 2019 Green synthesis of silver nanoparticles via *Cynara scolymus* leaf extracts: The characterization, anticancer potential with photodynamic therapy in MCF7 cells. *PLOS One.* **14**(6) e0216496–511
- [27] Mohd-Zahid MH, Mohamud R, Che Abdullah CA, Lim J, Alem H, Wan Hanaffi WN, Iskandar ZA 2020 Colorectal cancer stem cells: A review of targeted drug delivery by gold nanoparticles. *RSC Adv.* **10**(2):973–85
- [28] Naidoo C, Kruger CA, Abrahamse H 2012 Targeted photodynamic therapy treatment of in vitro A375 metastatic melanoma cells. *Oncotarget* **10**(58):6079–95
- [29] Crous A, Abrahamse H 2020 Effective gold nanoparticle-antibody-mediated drug delivery for photodynamic therapy of lung cancer stem cells. *Int. J. Mol. Sci.* **21**(11) 3742–65

# ***In vitro* antiproliferative effects of berberine in phthalocyanine-mediated photodynamic therapy on MCF-7 breast cancer cells with overexpressed P-Glycoprotein**

**Alexander Chota, Blassan P. George \*, and Heidi Abrahamse**

Laser Research Centre, Faculty of Health Sciences, University of Johannesburg  
P.O. Box 17011, Doornfontein 2028, South Africa.

E-mail: [blsassang@uj.ac.za](mailto:blsassang@uj.ac.za)

**Abstract.** Multidrug resistance (MDR) is one of the common challenges seen in cancer therapy. This phenomenon has led to the development of novel therapeutic strategies in which chemotherapeutic drugs are administered in combination with photodynamic therapy (PDT). Conventional therapeutic strategies employed in cancer treatment have been reported of yielding good prognosis which is accompanied with undesirable adverse effects. As a result, effective treatments with no potentially catastrophic side effects are required. PDT is a non-invasive phototherapeutic method in which a specific wavelength of light is used to activate photosensitizer (PS), to generate cytotoxic reactive oxygen species (ROS). The combination of PDT with other chemotherapeutic drugs has been studied for many years. The aim of this study was to enhance PDT using a chemotherapeutic drug, berberine (BBR) in combination with zinc phthalocyanine tetrasulfonic acid (ZnPcS<sub>4</sub>) on MDR MCF-7 breast cancer cells with overexpressed P-glycoprotein (P-gp). MDR MCF-7 breast cancer cells were treated with optimized concentrations of BBR and ZnPcS<sub>4</sub> and later irradiated by using a 680 nm diode laser at a fluency of 10 J/cm<sup>2</sup>. The established 50 % inhibitory concentration (IC<sub>50</sub>) was used to evaluate antiproliferative effects induced by individual IC<sub>50</sub> as well as in combination therapy. Morphological changes, adenosine triphosphate (ATP) proliferation, and live/ dead assay were performed to determine the cell cytotoxicity 24 h post-treatment. The results revealed a dose-dependent cytotoxicity in both monotherapy and combination therapy of BBR and ZnPcS<sub>4</sub> mediated PDT on MDR MCF-7 cells with significant morphological changes in combination therapy. In conclusion, the results from the present study suggest the use of BBR as an anticancer agent in ZnPcS<sub>4</sub> mediated PDT. Furthermore, the combination of the two IC<sub>50</sub>'s revealed a dose-dependent cytotoxicity in both monotherapy as well as combination therapy as it led to significant morphological changes accompanied with decreased ATP levels.

## **1. Introduction**

Breast cancer (BC) is the second leading cause of cancer related deaths after lung cancer. This form of cancer primarily originates from the breast tissue. According to the Global Cancer Observatory (GCO) 2020 to 2040 report, the global incidence rate of BC is estimated to increase from 2.26 million to 3.19 million by 2040 while the mortality rate is estimated to increase from 685 thousand to 1.04 million by 2040 [1]. The development of BC can be attributed to several factors e.g., excessive alcohol intake, inflammation, age, genetic mutations, radiation, hormones, body mass index etc. [2]. Surgery, radiation, chemotherapy, hormonal, and immunotherapy are some of the conventional therapeutic options for BC

treatment. However, these modalities have been reported of inducing undesirable side effects [3]. Therefore, novel treatment modalities with improved therapeutic outcomes are worth exploring. It's worth noting that the choice of these therapies is determined by the tumor stages and progression. In order to overcome some of these side effects, many researchers are working on novel therapeutic strategies which include the combination of PDT with chemotherapeutic drugs.

Photodynamic therapy (PDT) is a novel therapy that uses non-ionizing radiation to induce tumor cell death [4]. This form of therapy involves the application, or intravenous injection of a phototoxic drugs known as photosensitizers (PSs) on affected body sites e.g., skin. The principle behind PDT is based on the molecular interactions of preferentially co-localized PS with laser, and molecular oxygen ( $O_2$ ), thus leading to the generation of cytotoxic reactive  $O_2$  species (ROS) [5]. In addition, there is an increased number of research are focusing on enhancing PDT by use of chemotoxic drugs such as berberine (BBR) [6]. Herein, we evaluated the anticancer effects of BBR in combination with  $ZnPcS_4$  mediated-PDT on MDR MCF-7 breast cancer cells using a 680 nm diode laser at  $10 J/cm^2$  *in vitro*. A 680 nm diode laser was chosen for  $ZnPcS_4$  mediated-PDT. This is because metallic phthalocyanines exhibit maximum optical excitation wavelength in the range of 650-800 nm [7].

## 2. Methods and materials

### 2.1. Cell culture, and treatments

MCF-7 human breast cancer cells (ATCC<sup>®</sup> HTB-22) purchased from American Type Culture Collection (ATCC), were used in the present study. This cell line developed resistance for doxorubicin (DOX) as reported in a previous study from our laboratory [8]. MCF-7 cells were maintained in Dulbecco's Modified Eagle's Medium (DMEM), supplemented with 1% Penicillin-streptomycin, 1% Amphotericin B, and 10% Fetal Bovine Serum (FBS). Cells were then incubated for 24 h at 37°C, 85% humidity, and 5% carbon dioxide ( $CO_2$ ). A seeding density of  $3 \times 10^5$  cells/mL was used to plate cells in a 3.4 cm<sup>2</sup> diameter culture plates for *in vitro* studies. Simple linear regression was used to determine the relationship between the dependent variable (y) e.g., relative light unit (%) and the independent variable (x) e.g., concentration. In addition, the regression line equation was used to determine the 50% inhibitory concentration ( $IC_{50}$ ) for both BBR and  $ZnPcS_4$ , 24 h post-treatment using different concentrations of BBR (100, 200, 300, and 400  $\mu M$ ) and  $ZnPcS_4$  mediated-PDT (10, 20, 40, and 80  $\mu M$ ) respectively.

### 2.2. Cell proliferation (ATP luminescence assay)

CellTiter-Glo<sup>®</sup> ATP luminescence assay kit (Promega, G968A) was used in the present study. Briefly, about 50  $\mu L$  of cell suspension was suspended to an equal of reconstituted ATP reagent, mixed thoroughly and incubated for 10 min at room temperature and pressure (rtp). Post-incubation, the homogenous colorimetric mixture was then measured for ATP luminescence using PerkinElmer, VICTOR Nivo<sup>™</sup>.

### 2.3. Morphological analysis and cell viability/ cytotoxicity (LIVE/DEAD<sup>™</sup> assay)

Morphological changes were visualized under an inverted light microscope (Wirsan, Olympus CKX 41) with attached digital camera (Olympus C5060-ADUS). Following the manufacturer's instructions, the LIVE/DEAD<sup>™</sup> assay kit (Cat. No. L3224) (Life Technologies Corporation) was used to qualitatively visualize the distribution of viable and non-viable MDR MCF-7 cells 24 post-treatment with  $IC_{50}$  concentrations of BBR and  $ZnPcS_4$  mediated-PDT. Briefly, the cells (i.e., untreated and treated) were washed thrice by using ice cold 1X PBS (1 mL) and resuspended in 1 mL of 1X PBS. Thereafter, cells were stained with calcein (1  $\mu L$ ), ethidium homodimer-1 (EthD-1) (1  $\mu L$ ) and incubated for 30 min at rtp. Cells were then rinsed thrice with 1 mL 1X PBS after incubation, resuspended in 1 mL 1X PBS, and visualized with Alexa Fluor 488 and EtBr filters using a Carl Zeiss Axio Z1 live imaging microscope.

### 2.4. Statistical analysis

All experiments were performed four times ( $n=4$ ). IBM SPSS version 27 software was used to analyse the mean difference and statistical significance between the control and experimental groups. Mean values plotted as mean  $\pm$  standard error (SE) and statistical significance is represented as ( $p < 0.05$  (\*),  $p < 0.01$  (\*\*), or  $p < 0.001$  (\*\*\*)).

### 3. Results and discussion

#### 3.1. Cell proliferation

Energy levels of untreated and treated MDR MCF-7 cells were determined by measuring the levels of ATP luminescence. A dose-dependent decrease in cell proliferation was observed in cells treated with BBR, ZnPcS<sub>4</sub> mediated-PDT (Figure 1 A and C). As shown in Figure 1 B and D, simple linear regression shows a negative relationship between the relative light unit and concentration. This clearly suggest that the relative light unit (%) decreases, as the concentration increases. Using the linear regression equation, the IC<sub>50</sub> for BBR treated cells was 314.5  $\mu$ M, whereas in ZnPcS<sub>4</sub> mediated-PDT the established IC<sub>50</sub> was at 57.1  $\mu$ M. In addition, it was also observed that both established IC<sub>50</sub>'s in combination therapy significantly decreased cell proliferation levels (Figure 2 B). However, ATP levels were higher in MDR MCF-7 cells that received laser treatment only, and cells that were treated with ZnPcS<sub>4</sub> but did not receive laser treatment (Figure 1 C). These findings are in line with those reported by Uprety et al., [9] and Loonat et al., [10].

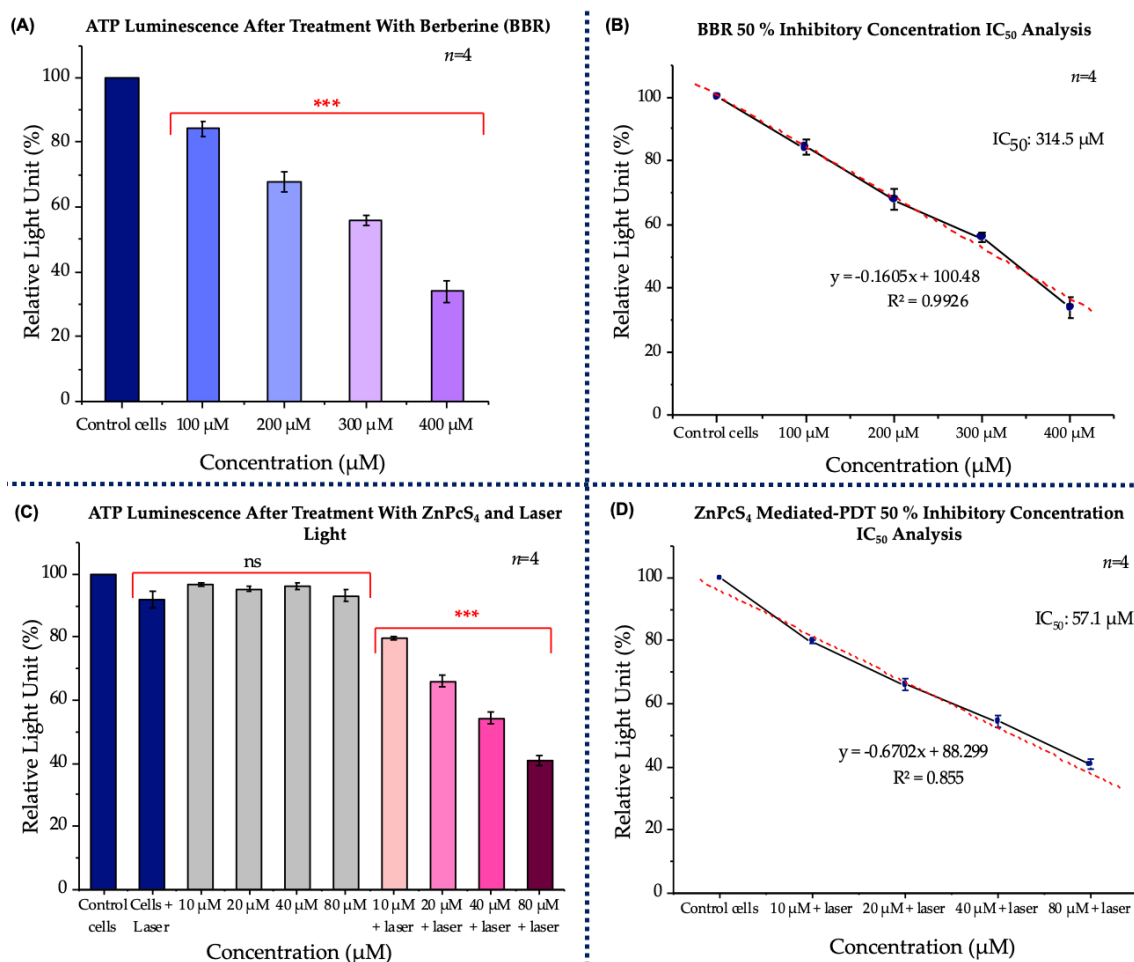


**Figure 1.** ATP luminescence of the control and experimental groups of BBR and ZnPcS<sub>4</sub> 24 h post-treatment (A and C). Linear regression for IC<sub>50</sub> calculations; BBR IC<sub>50</sub> (314.5  $\mu$ M) (B), and ZnPcS<sub>4</sub> mediated PDT IC<sub>50</sub> (57.1  $\mu$ M) (D). Significance  $p < 0.001$  (\*\*\*)).

### 3.2. Morphological analysis and cell viability/ cytotoxicity (LIVE/DEAD™ assay)

Morphology of untreated and treated MDR MCF-7 cells (Figure 2 A). No alterations in morphology was displayed by laser treated cells without a PS (Figure 2, A 2) when compared control cells (Figure 2, A 1). This suggests that 680 nm diode laser alone has no phototoxic effect on cancer cells. However, changes in morphology were observed in MDR MCF-7 cells treated with BBR IC<sub>50</sub>, and ZnPcS<sub>4</sub> mediated-PDT in monotherapy and combination therapy (Figure 2, A 3-5). The results of the present study are similar to those reported by Tynga et al., [11] and Mkhobongo et al., [12].

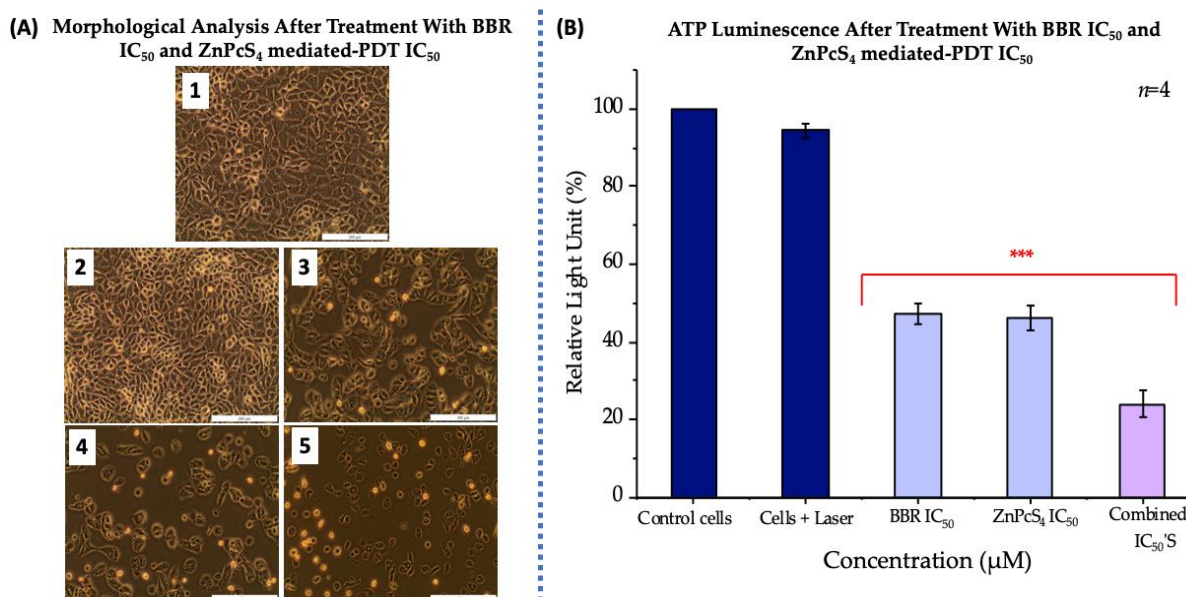


**Figure 2.** Cellular morphology of untreated cells (A 1); cells + laser (A 2); cells + BBR IC<sub>50</sub> (A 3); cells + ZnPcS<sub>4</sub> IC<sub>50</sub> + laser (A 4); and combination of IC<sub>50</sub>'s (A 5). ATP luminescence of the control, IC<sub>50</sub>'s of BBR and ZnPcS<sub>4</sub> mediated PDT (A). Significance  $p < 0.001$  (\*\*\*) ( $n = 4$ ). ( $\times 200$  magnification).

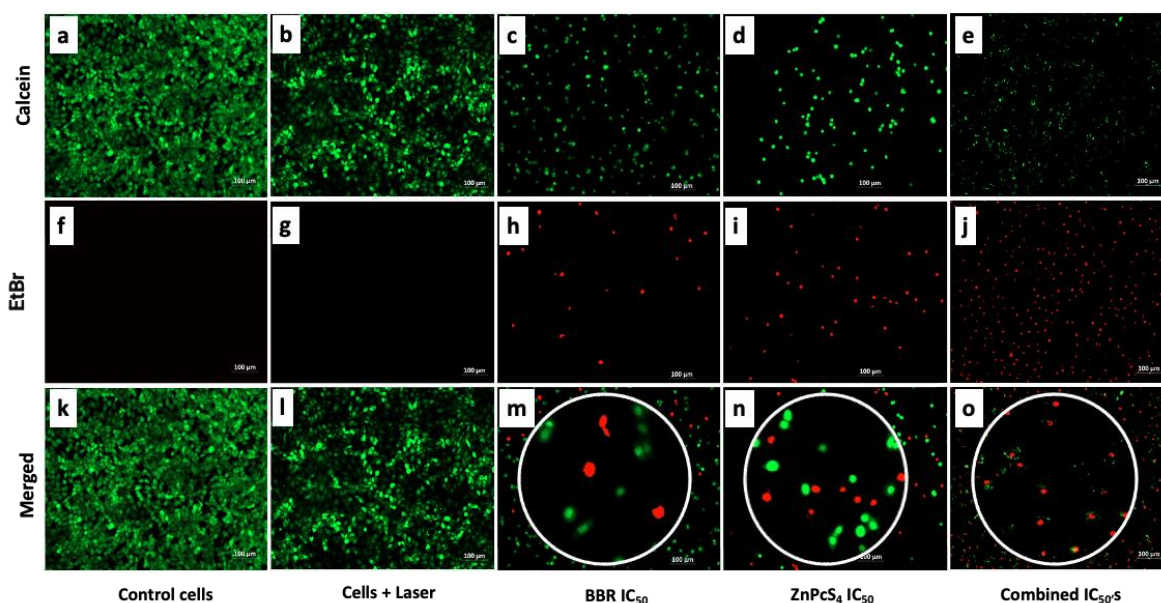


**Figure 3.** LIVE/DEAD™ assay. Live cells stained with calcein (green fluorescence) (a-e) and dead cells stained with EtBr (red fluorescence) (f-j). ( $\times 200$  magnification).

Additionally, the LIVE/DEAD™ assay qualitatively displayed an increase in the number of dead cells in combination of the two IC<sub>50</sub>'s when compared individual treatments (Figure 3 h-j). Interestingly, MDR MCF-7 cells that were treated with laser light did not stain with EtBr. This suggests that the cells membrane of the cells was intact and could not allow the penetration of the stain. Overall, the results obtained from this assay are in support with those reported by Hassan et al., [13].

#### 4. Conclusion

In conclusion, BBR has demonstrated antiproliferative effects in individual treatments as well as in combination with ZnPcS<sub>4</sub> mediated PDT on MDR MCF-7 breast cancer cells *in vitro*. Although conventional treatment modalities for breast cancer often result in cancer recurrences with undesired side-effects. The present study suggests the use of BBR in combination with ZnPcS<sub>4</sub> to overcome the above highlighted limitations seen in breast cancer treatment. In addition, to clearly understand the mechanisms behind BBR and ZnPcS<sub>4</sub>, a detailed cell death analysis will be warranted to give a comprehensive mode of cell death induced by the two drugs in individual treatments and in combination therapy.

#### Acknowledgments

The authors sincerely thank the South African Research Chairs initiative of the Department of Science and Technology and National Research Foundation of South Africa, South African Medical Research Council (SAMRC), African Laser Centre (ALC), and Laser Research Centre (LRC), and the University of Johannesburg.

#### Funding

This research was funded by the South African Research Chairs initiative of the Department of science and technology and National Research Foundation of South Africa (Grant No98337), South African Medical Research Council (Grant No. SAMRC EIP007/2021) as well as grants received from the University Research Committee (URC), African Laser Centre (ALC), University of Johannesburg and the Council for Scientific and Industrial Research (CSIR)-National Laser Centre (NLC).

#### Conflict of interest

Authors declare no conflict of interest.

#### References

- [1] WHO *Cancer Tomorrow*; World Health Organization, 2020. Accessed on 18<sup>th</sup> February 2022
- [2] Zakhari, S.; Hoek, J.B. Epidemiology of Moderate Alcohol Consumption and Breast Cancer: Association or Causation? *Cancers* **2018**, *10*, 349, doi:10.3390/cancers10100349.
- [3] Abbas, Z.; Rehman, S. *An Overview of Cancer Treatment Modalities*; IntechOpen, 2018; ISBN 978-1-78923-778-8.
- [4] Wang, K.; Yu, B.; Pathak, J.L. An Update in Clinical Utilization of Photodynamic Therapy for Lung Cancer. *J. Cancer* **2021**, *12*, 1154–1160, doi:10.7150/jca.51537.
- [5] Li, J.; Meng, X.; Deng, J.; Lu, D.; Zhang, X.; Chen, Y.; Zhu, J.; Fan, A.; Ding, D.; Kong, D.; et al. Multifunctional Micelles Dually Responsive to Hypoxia and Singlet Oxygen: Enhanced Photodynamic Therapy via Interactively Triggered Photosensitizer Delivery. *ACS Appl. Mater. Interfaces* **2018**, *10*, 17117–17128, doi:10.1021/acsami.8b06299.
- [6] An, Y.-W.; Jin, H.-T.; Yuan, B.; Wang, J.-C.; Wang, C.; Liu, H.-Q. Research Progress of Berberine Mediated Photodynamic Therapy (Review). *Oncol. Lett.* **2021**, *21*, 1–10, doi:10.3892/ol.2021.12620.
- [7] Güzel, E.; Atsay, A.; Nalbantoglu, S.; Şaki, N.; Dogan, A.L.; Gül, A.; Koçak, M.B. Synthesis, Characterization and Photodynamic Activity of a New Amphiphilic Zinc Phthalocyanine. *Dyes Pigments* **2013**, *97*, 238–243, doi:10.1016/j.dyepig.2012.12.027.

- [8] Chekwube, A.E.; George, B.; Abrahamse, H. Phototoxic Effectiveness of Zinc Phthalocyanine Tetrasulfonic Acid on MCF-7 Cells with Overexpressed P-Glycoprotein. *J. Photochem. Photobiol. B* **2020**, *204*, 111811, doi:10.1016/j.jphotobiol.2020.111811.
- [9] Uprety, B.; Chandran, R.; Arderne, C.; Abrahamse, H. Anticancer Activity of Urease Mimetic Cobalt (III) Complexes on A549-Lung Cancer Cells: Targeting the Acidic Microenvironment. *Pharmaceutics* **2022**, *14*, 211, doi:10.3390/pharmaceutics14010211.
- [10] Loonat, A.; Chandran, R.; Pellow, J.; Abrahamse, H. Photodynamic Effects of Thuja Occidentalis on Lung Cancer Cells. *Front. Pharmacol.* **2022**, *13*.
- [11] Tynga, I.M.; Houreld, N.N.; Abrahamse, H. The Primary Subcellular Localization of Zinc Phthalocyanine and Its Cellular Impact on Viability, Proliferation and Structure of Breast Cancer Cells (MCF-7). *J. Photochem. Photobiol. B* **2013**, *120*, 171–176, doi:10.1016/j.jphotobiol.2012.11.009.
- [12] Mkhobongo, B.; Chandran, R.; Abrahamse, H. Effects of Photodynamic Therapy on A375 Melanoma Cells Using Aluminium Phthalocyanine Photosensitizer. In Proceedings of the Effects of photodynamic therapy on A375 Melanoma cells using aluminium phthalocyanine photosensitizer; SA Institute of Physics: South Africa, 2021; pp. 290–295.
- [13] Hassan, W.; Dong, Y.; Wang, W. Encapsulation and 3D Culture of Human Adipose-Derived Stem Cells in an in-Situ Crosslinked Hybrid Hydrogel Composed of PEG-Based Hyperbranched Copolymer and Hyaluronic Acid. *Stem Cell Res. Ther.* **2013**, *4*, 32, doi:10.1186/scrt182.

# Investigating the morphology of an optically trapped particle using Mie scattering

**A Erasmus, GW Bosman, PH Neethling and EG Rohwer**

Laser Research Institute, Physics Department, Stellenbosch University, Private bag X1,  
Matieland, 7602, South Africa

E-mail: 16529138@sun.ac.za

**Abstract.** Microscopic polystyrene particles suspended in water are trapped by optical tweezers and we determine their diameter and refractive index using Mie scattering theory. A near infrared laser is used to form the optical trap near the focus by a high numerical aperture lens. The individual trapped particle is illuminated with broadband white light. The scattered light from the particle is collected in the epi-direction and measured with a spectrometer. The measured spectrum is compared to theoretical simulations using Mie theory. An iterative optimization procedure is implemented in order to determine the diameter and refractive index of the particle in the trap. This technique leads to precise measurements of the diameter of the particle with an uncertainty of less than a nanometer on a micron sized particle. In addition, the refractive index per individual particle was determined within a measurement uncertainty of  $10^{-4}$ .

## 1. Introduction

Mie scattering theory can be used to determine an individual particle's diameter and refractive index [1, 2]. Studying an individual particle negates ensemble averaging and one is able to probe local changes in the sample's diameter and refractive index. To study the individual particle, it is isolated and trapped using the optical tweezers system. Here, a polystyrene bead suspended in water is optically trapped using optical tweezers [3]. To create the optical trap, a microscope objective with an numerical aperture (NA) of 1.25 was used to focus the light (wavelength of 975 nm), resulting in a calculated spot size (lateral diameter) of 390  $\mu\text{m}$  [4]. The ray diagram description of optical trapping forces in figure 1 shows the refraction of light by a particle with a higher refractive index than the surrounding medium. The change of momentum that the light experiences creates a net force towards the focus of the light. This is the gradient force and is proportional to the gradient of the electric field.

Once a particle is isolated by the optical tweezers, white light illuminates it and Mie scattering from the particle is used to determine the particle's diameter and refractive index, approximated here by the Cauchy expression [1],

$$n = A + \frac{B}{\lambda^2} + \frac{C}{\lambda^4} \quad (1)$$

When broadband white light is incident on the spherical particle, specific wavelengths will be resonant within the sphere. These resonant modes are known as whispering gallery modes

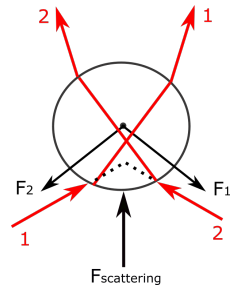


**Figure 1.** Rays 1 and 2 are refracted by the particle and result in a net gradient force towards the focus of the light. Due to the tight focusing of the light, the gradient force is larger than the scattering force, creating a stable optical trap.

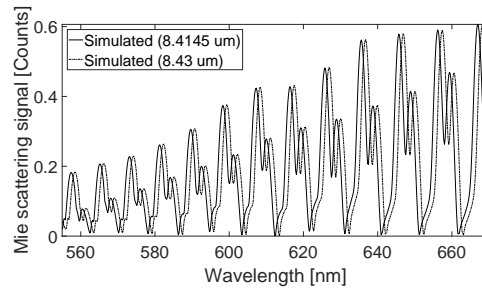


**Figure 2.** Simulated spectra for the scattering of light from a polystyrene particle in water shows a difference in the peak positions between particles with a diameter of 8.4145  $\mu\text{m}$  (solid) and 8.43  $\mu\text{m}$  (dotted).

and correspond to the peaks seen on the spectrum of the scattered light. The positions of these peaks can be calculated using Mie theory [5]. Mie theory solves Maxwell's equations for a plane wave incident on a spherical particle. By solving these equations and including the boundary conditions of the sphere, the spectrum of the scattered light is simulated, (figure 2).

Using this technique, for a similar sample of polystyrene particles, Jones, King and Ward [1] determined the refractive index within  $\pm 0.0005$  and the particle radius within  $\pm 0.4$  nm. In comparison, optical imaging yields a limited lateral resolution on the order of approximately 167 nm using a NA of 1.5 at 500 nm [4]. Combined with optical trapping, the Mie scattering technique described here is not limited to polystyrene particles. It can also be used to spatially manipulate and study individual aerosol droplets [6, 7] which is useful in climate studies. For similar sized water droplets, accurate sizing of the droplets was demonstrated to within  $\pm 2$  nm [5].

## 2. Methodology

The optical trap is constructed based on the Thorlabs Optical Tweezers Module (OTKB/M), figure 3. The trapping laser (975 nm) is focused into the sample by a high numerical aperture microscope objective, (NA 1.25, 100X oil immersion objective). The samples used here are polystyrene particles (diameter 8.9  $\mu\text{m} \pm 0.66$   $\mu\text{m}$ ) suspended in water. The trapped particles are imaged in transmission with a white light LED. A condenser lens (NA 0.4, 10X air objective) collects the light and the image is formed on a CMOS camera. Light from the white light LED scatters from the trapped particle and is collected in the epi-direction by the NA 1.25 objective lens. This scattered light is measured with a spectrometer (Ocean Optics USB4000) with a spectral resolution of 0.2 nm. The integration time for collecting the spectrum of the scattered light was 5 ms and averaged over 10 measurements. To reduce background noise in the spectrum of the scattered light, an aperture is introduced and imaged into the trapping plane. This reduces the scattering from the water surrounding the particle and ensures that the majority of the scattered light is from the trapped particle.

We simulate the Mie scattering for various particle diameters and refractive index iteratively as described by Jones, King and Ward [1]. The software [8] used here allows the user to select the refractive index of a sphere and the size parameter. Given the refractive index of water [9], it computes total scattering, total extinction and angular distribution of the scattered light.

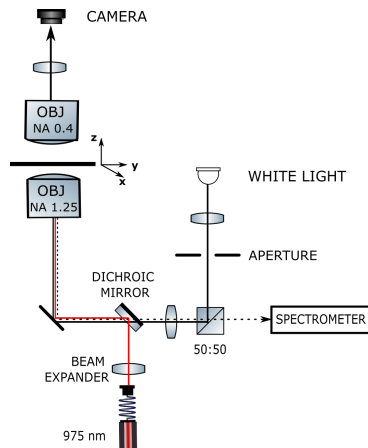


**Figure 3.** The trapping laser is focused by a high numerical aperture objective (OBJ NA 1.25). The sample is illuminated by a white light LED and imaged on a CMOS camera. The back scattered white light from the trapped particle is measured using a spectrometer.

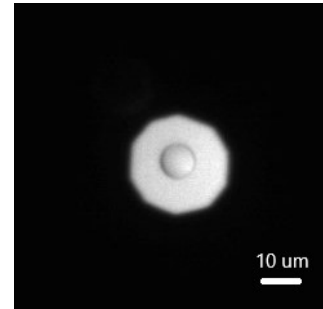


**Figure 4.** A polystyrene particle is trapped in water using the optical tweezers system and imaged on a CMOS camera as shown here. An aperture is also imaged into the trapping plane to reduce scattering from water and increases signal to noise ratio in the measured spectrum.

### 2.1. Experimental details and data analysis

We demonstrated optical trapping of polystyrene particles suspended in water as shown in figure 4. Limiting the illumination to the particle by imaging an aperture onto the trapping plane, reduces the background in the acquired spectrum.

The Mie resonances from the trapped particle are measured with the spectrometer and shown in figure 5. To compare these measurements to simulated Mie scattering from a polystyrene particle in water with varying diameters, the residual background is removed. First, the scattering of white light from water was subtracted, after which the remaining background was removed by fitting a polynomial to the minima in the spectrum and dividing the spectrum by the polynomial, normalising the background.

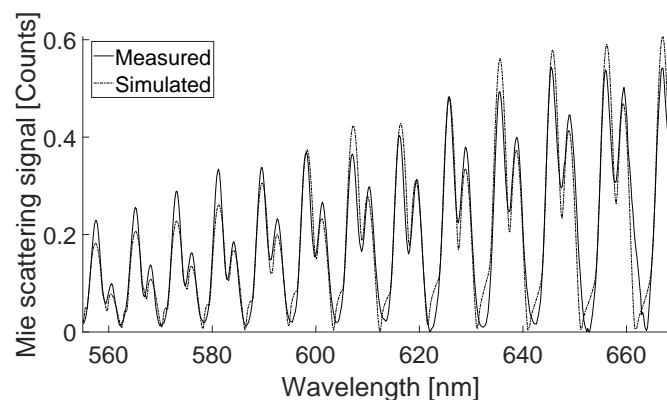


**Figure 5.** The measured Mie resonance structure (solid line) from an optically trapped polystyrene particle suspended in water is compared to simulated scattering (dotted line) for a particle with diameter  $8.4145 \mu\text{m}$ .

To determine the particle diameter and refractive index, the simulated spectrum is varied iteratively by adjusting the diameter and refractive index until it best represents the measurement. Peak positions are used to compare the spectra, because the signal to noise is better for the peaks than the valleys.

As a starting point, representative refractive index values for polystyrene are used to initially estimate the particle's diameter. Using the chosen refractive index values, the diameter is found that results in the simulation best matching the measured spectrum. This is used as the initial diameter of the particle.

Using this estimated particle diameter the refractive index is then adjusted until individual peaks of the simulated and measured spectrum overlap optimally in wavelength. The refractive index required for the individual peaks to align are recorded and a dispersion curve for this particle diameter is plotted. The Cauchy equation is fit (using MATLAB's Trust Region algorithm [10]) and the root mean square error (RMSE) from the fit is indicated in table 1 as an estimate of the uncertainty on the refractive index of the polystyrene particle.

The estimated particle diameter is then varied by 1 nm increments and the process is repeated. Figure 6 shows the RMSE for various particle diameters used for particle 1. The minimum RMSE from the quadratic fit indicates a particle diameter of  $8.4145 \mu\text{m} \pm 0.0001 \mu\text{m}$ . This corresponds to the diameter and refractive index that best describes the measured experimental scattering. The refractive index dispersion for this particle diameter is obtained from a fit resulting in a  $R^2 = 0.9807$  (bead 1 in figure 7),

$$1.583 + \frac{2806}{\lambda^2} + \frac{3.817 \times 10^8}{\lambda^4} \quad (2)$$

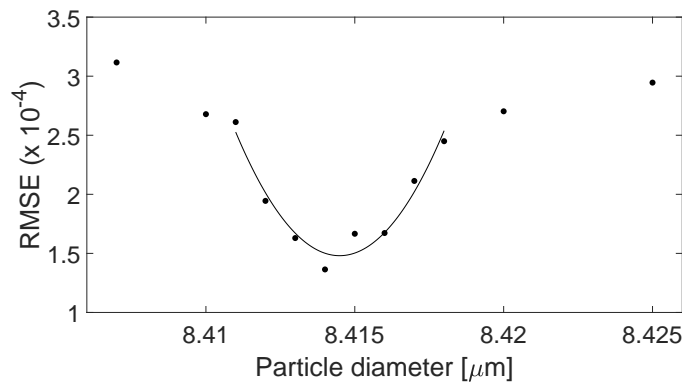


**Figure 6.** The refractive index dispersion is fit using the Cauchy relation and the resulting root mean square error (RMSE) of the fit is shown here for various particle diameters. The minimum of the quadratic fit to the RMSE values corresponds to a particle diameter of  $8.4145 \mu\text{m} \pm 0.0001 \mu\text{m}$ .

### 3. Results and discussion

This protocol described in the section above was repeated for three similar polystyrene particles and the results are summarised in table 1. The technique is highly sensitive and able to distinguish between the refractive indices of individual particles. The refractive index dispersions for the three particles are plotted in figure 7. The average for this limited sample size is also shown.

This work was done under the assumption that the particles can be treated as spherical particles (in order for the Mie theory to apply conveniently). Non-spherical deformities in the

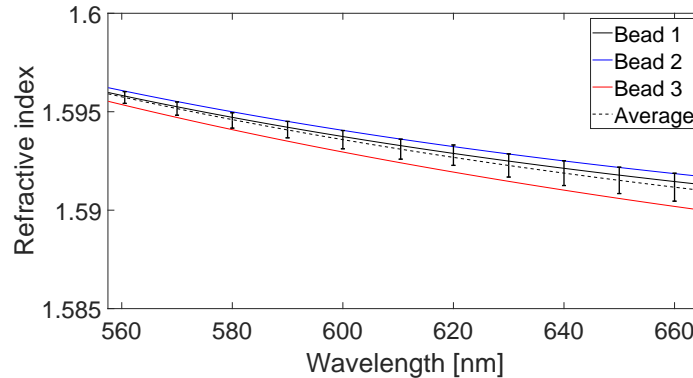


**Figure 7.** A plot of the refractive index dispersion for three polystyrene particles suspended in water along with their average. The standard deviation at selected wavelengths is also shown.

**Table 1.** Three polystyrene particles were trapped in water and investigated for their individual diameter and refractive index. The table shows their diameter and Cauchy terms  $A$ ,  $B$  and  $C$  representing the refractive index of the individual particles.

Particle	Diameter [ $\mu\text{m}$ ]	$A$	$B$ [ $\text{nm}^2$ ]	$C$ [ $\text{nm}^4$ ]	RMSE	$R^2$
Particle 1	$8.4145 \pm 0.0001$	1.583	2806	$3.817 \times 10^8$	$1.48 \times 10^{-4}$	0.9807
Particle 2	$8.4035 \pm 0.0001$	1.584	2484	$4.088 \times 10^8$	$0.99 \times 10^{-4}$	0.9842
Particle 3	$8.4267 \pm 0.0004$	1.578	4964	$1.508 \times 10^8$	$3.85 \times 10^{-4}$	0.9273

particle shape will lead to splitting or broadening of the peaks, which was not observed. The uncertainty in the measurement is a result of the absolute spectral resolution, the accuracy of the calibration of the spectrograph, and the signal to noise. The limited spectral resolution and relatively large background that was removed from the measured spectrum causes the small structures near the minima of the spectrum in figure 5 to be less visible compared to the theoretically calculated spectrum. However, the peak positions are used when comparing the two spectra and hence give the information regarding the particle size and refractive index.

#### 4. Conclusion

In this work, an optical tweezers system was used to trap micron-sized polystyrene particles suspended in water. By doing so, individual particles could be targeted to determine their diameter and refractive index using Mie theory. An existing methodology was adapted to determine these properties from the spectrum of back scattered white light from a trapped particle. The spectrum showed strong resonance peaks that were compared to simulated Mie resonance spectra. The peak positions were used to determine the particle's diameter and refractive index using an iterative protocol. The diameter of the micron sized particles was determined with an uncertainty of less than a nanometer. In addition, it was demonstrated that the technique is sensitive to changes in the refractive index per individual particle.

#### Acknowledgments

The authors are thankful to Dr A.D. Ward, STFC, Rutherford Appleton Laboratories for his knowledge and assistance over the course of this work.

**References**

- [1] Jones S, King M and Ward A 2013 *Phys. Chem. Chem. Phys.* **15** 20735-41
- [2] Chylek P, Ramaswamy V, Ashkin A and Dziedzic JM 1983 *Applied Optics* **22** 2302-7
- [3] Ashkin A, Dziedzic, JM, Bjorkholm JE and Chu S 1986 *Optics Letters* **11** 288-90
- [4] Huszka G and Gijs MAM 2019 *Micro and Nano Engineering* **2** 7-28
- [5] Ward A, Zhang M and Hunt O 2008 *Optics Express* **16** 16390-403
- [6] Mitchem L, Hopkins RJ, Buajarern J, Ward AD and Reid JP 2006 *Chemical Physics Letters* **432** 362-6
- [7] King MD, Thompson KC and Ward AD 2004 *J. Am. Chem. Soc.* **126** 16710-11
- [8] Mie scattering demo program written by Martin Fierz (martin@fierz.ch), August 2005. The Dynamic Link Library was adapted by Dr AD Ward and is based on Bohren and Huffman Mie code.
- [9] International Association for the Properties of Water and Steam, IAPWS R7-97(1997), Release on refractive index of ordinary water substance as a function of wavelength, temperature and pressure (1997)
- [10] MATLAB R2020a and Curve Fitting Toolbox 3.5.11. Copyright 2001 – 2019 The Mathworks, Inc.

# Photobiomodulation at 830 nm modulates proliferation and migration of wounded fibroblast cells

TS Leyane, SW Jere and NN Houreld<sup>1</sup>

Laser Research Centre, Faculty of Health Sciences, University of Johannesburg, P.O. Box 17011, Doornfontein, South Africa, 2028

E-mail:nhoureld@uj.ac.za

**Abstract.** Wound healing is a complex and dynamic process that involves restoring damaged tissue structure and function. Delayed wound healing often advances to chronic non-healing wounds due to reduced cellular proliferation and migration. Photobiomodulation (PBM) involves the application of low-powered light typically in the visible red and near-infrared (NIR) spectrum to modulate cellular mechanisms and has been shown to speed up healing *in vivo*. However, the underlying mechanisms are not well understood. This study aims to determine the effect of PBM using NIR light at 830 nm with 5 J/cm<sup>2</sup> on the proliferation and migration of wounded human fibroblasts. Commercially acquired human fibroblast cells (BJ-5ta, ATCC<sup>®</sup> CRL-4001<sup>™</sup>) were utilized, and two cell models, namely, normal and wounded (central scratch assay), were designed. Cell models were incubated for 24 and 48 h post-irradiation, followed by different investigational tests for cellular morphology and migration rate (inverted microscopy), and proliferation (BrdU, flow cytometry). PBM at 830 nm with 5 J/cm<sup>2</sup> modulates cell proliferation and migration and may aid in the enhanced wound repair process observed *in vivo*.

## 1. Introduction

The prevalence of chronic wounds is rising at a perturbing rate due to populations undergoing industrialization, aging, and becoming more sedentary, and pose a fundamental global economic public health burden [1]. Wounds arise as a result of traumatic injuries, including abrasions and lacerations. Ordinarily, wounds heal in a timely (within a few days/weeks, typically in 3 months) and orderly frame; however, due to underlying pathologies such as keloids, uremia, fibrosis, jaundice, and hereditary healing disorders, some wounds fail to do so and develop into chronic wounds. Wound healing involves a systematized integration of biological and molecular systems that induce a predictable progression of tissue repair. Wound healing is orchestrated via four fundamental and spatially overlapping cascades: hemostasis, inflammation, proliferation, and maturation. For optimum healing of cutaneous wounds, fibroblasts, immune surveillance cells, platelets, keratinocytes, and microvascular cells play vital roles in restoring damaged tissue structure and function and reinstating tissue integrity [2]. Fibroblasts are the primary reconstructing cells involved in critical processes such as breaking down the fibrin clot, constricting the wound, secreting and depositing new extracellular matrix (ECM) proteins, and providing collagen and granulation tissue. They are responsible for secreting essential cytokines and growth factors for cell proliferation and differentiation conducive to wound repair [3]. Impaired fibroblast functionality in diabetic patients often leads to decreased collagen synthesis and wound strength. According to You *et al.* [4], chronic wounds are onerous to treat due to their diminished response to conventional treatments.

Photobiomodulation (PBM) employs specific wavelengths of visible red and near-infrared (NIR) light to expiate specific cellular and tissue impairments. This therapeutic technique is a non-invasive, non-thermal therapy that involves the application of low-powered light sources such as lasers, light-emitting diodes (LEDs), and broadband light using appropriate filters, in the visible light (400- 800 nm) and infrared (760- 1400 nm) spectrum to promote tissue regeneration [5,6]. Several studies have demonstrated PBM as a promising therapeutic method that elicits healing [7] and advances the proliferation phase of wound healing [8].

Additionally, studies have demonstrated different physiological effects when comparing PBM in the visible red light and NIR spectrum, indicating that PBM has biostimulatory effects in a dose and wavelength-dependent manner [9,10]. An optimal dosage of PBM evokes cellular activity, including cell proliferation, viability, migration, and growth factor production, which enhances the wound repair process in non-healing chronic wounds. Based on the optical window model, NIR light has been reported to penetrate tissues deeper than red light, which is ascribed to the reduced absorption by hemoglobin and melanin [11]. Despite NIR light having a deeper penetration into the tissue, most *in vitro* studies use visible red light, leaving a knowledge gap in the NIR range. Despite global interest in PBM therapy, the application of this therapy has not been acclimatized or routinely practiced in South Africa.

This study aimed to determine the effects of PBM at 830 nm on the proliferation and migration of fibroblast cells, which are principal contributing aspects to wound healing.

## 2. Methodology

Commercially purchased human fibroblast cells (BJ-5ta, ATCC® CRL-4001™) between passages 8 and 11 were utilized and cultured under standard guidelines. Two cell models were designed: normal (N) and wounded (W). Briefly, cells were incessantly grown in minimum essential media (MEM) supplemented with 10% Fetal Bovine Serum (FBS), 1% amphotericin B, 1% penicillin-streptomycin, 2 mM L-glutamine, 0.1 mM non-essential amino acids (NEAA), and 1 mM sodium pyruvate. Cells were then rinsed twice with pre-warmed Hank's Balanced Salt Solution (HBSS) and subsequently detached with 1 mL/25 cm<sup>2</sup> of TrypLE™ Express. Cell quantification was conducted, and cells were seeded at a density of  $6 \times 10^5$  (morphology and migration rate) or  $1 \times 10^6$  for flow cytometry (proliferation assay) into 3.4 cm diameter cell culture dishes in 3 mL supplemented MEM and were incubated at 37°C (5% carbon dioxide (CO<sub>2</sub>); 85% humidity) overnight to facilitate cellular attachment.

Post-incubation, the culture media was discarded, and cells were rinsed twice with 1 mL HBSS and replaced with fresh media. To achieve a wounded cell model (W), a sterile 1 mL disposable pipette was used to create a central scratch (CS), or "wound," in a confluent cell monolayer [12]. The CS method is based on the observation that upon creating a cell-free zone across the center of the cell monolayer, the cells on the "wound" margins will migrate towards the center to close the created gap [13]. Post-wounding, the cells were incubated for 30 min to allow them to settle [12]. Cells were irradiated with a continuous wave diode laser at a wavelength of 830 nm, and a fluence of 5 J/cm<sup>2</sup>. Laser parameters are summarized in Table 1. Post-irradiation, cells were incubated at 37°C (5% CO<sub>2</sub>; 85% humidity) for 24 and 48 h.

Post-irradiation, an inverted light microscope (Olympus CKX41) was used to determine morphological changes in both experimental models, and images were captured using the AnalySISgetIT software at 0 h, 24 h and 48 h to assess wound closure. The distance between the wound margins was measured from three experimental repeats and used to quantify the rate of cell migration, which was expressed in percentages using the following equation:

$$\frac{At_{0h} - At_{time}}{At_{0h}} \times 100$$

where  $At_{0h}$  is the distance between wound margins of the central scratch at 0 h, and  $At_{time}$  is the successive distance between the wound margins of the central scratch at various time points [14]. The same position on each plate/model (n=3) was measured over the 48 h period. The position on the plates were marked and the position on the XY axis on the microscope noted.

Flow cytometry using the BD Pharmingen fluorescein isothiocyanate (FITC) 5-Bromo-2'-deoxyuridine (BrdU) Flow Kit (The Scientific Group, BD Sciences, 559619/557891) was used to

evaluate cell proliferation. BrdU, an analog of thymidine, a DNA precursor, is integrated into newly synthesized DNA in cells acceding and advancing through the S phase of DNA replication (DNA synthesis). In this procedure, the quantification and categorization of cells actively synthesizing DNA, as related to their cell cycle position (i.e., S phase) explicated by their 7-ADD staining intensities, is accomplished by a two-color cytometric analysis. The test was conducted using the manufacturer's instructions. Unstained cells were used to establish easy visualization and gating of cells on forward scatter (FSC) and side scatter (SSC) plots.

Experiments were performed three times ( $n=3$ ), and statistical analysis was done using SigmaPlot version 14.0 (SYSTAT). Differences between groups were determined using the Student t-test and One-Way Analysis of Variance (ANOVA) for each independent variable and were considered statistically significant when  $p < 0.05$ .

**Table 1.** Laser irradiation parameters.

Variables	
Light source	Diode laser
Wavelength (nm)	830
Emission	Continuous wave
Power output (mW)	114
Spot size (cm <sup>2</sup> )	9.1
Power density (mW/cm <sup>2</sup> )	12.53
Irradiation exposure (s)	399
Fluence (J/cm <sup>2</sup> )	5
Energy (J)	45.5

### 3. Results and Discussion

Chronic or non-healing wounds fail to progress through the wound healing phases in a timely reparation process primarily due to impaired wound oxygenation, infections, venous insufficiency, and diseases that interrupt the normal physiological condition, predisposing it to impaired wound healing. PBM imparts an array of therapeutic interventions, such as activating different intracellular signaling pathways involved in cellular proliferation, migration, and wound healing [15]. Optimal use of PBM augments cell viability and the rate of proliferation in various cell types, including but not limited to fibroblasts [16], mesenchymal stem cells [17], and epithelial cells [18]. Hehenberger and colleagues [19], suggested that fibroblasts from chronic wounds demonstrate a decreased proliferation rate. Therefore, therapeutic methods inciting increased fibroblast activity are essential for advancing wound healing.

In this study, microscopically, fibroblast cells displayed the typical elongated and spindle shape, with multi-polar projections (Figure 1). In W irradiated (5 J/cm<sup>2</sup>) cell models, the findings demonstrated increased haptotaxis (an outgrowth of cells along the wound margins) and chemotaxis (movement of cells towards the central scratch) when compared to the W non-irradiated (0 J/cm<sup>2</sup>) controls.

W irradiated (5 J/cm<sup>2</sup>) cells exhibited a significant increase ( $p < 0.05$ ) in migration rate at 24 h, suggesting that PBM effectively induces chemotaxis and haptotaxis, and accelerates fibroblast cell migration in wound healing. However, at 48 h, the increase in the rate of cell migration observed in W irradiated (5 J/cm<sup>2</sup>) cells was not statistically significant ( $p=0.943$ ) when compared to their non-irradiated (0 J/cm<sup>2</sup>) control cells (Figure 2). These results correspond with Ayuk and colleagues' [20] study using diabetic wounded fibroblast cells (WS1). The fibroblasts exhibited evidence of haptotaxis and chemotaxis when irradiated at 660 nm (5 J/cm<sup>2</sup>). In this study, W irradiated (5 J/cm<sup>2</sup>) cells migrated faster, which is verified by the significant increase in migration rate at 24 h. These results are supportive of the incomplete wound closure observed in W irradiated (5 J/cm<sup>2</sup>) cells, which contradicts the results when the fibroblast cells are irradiated at a red wavelength of 632 nm [9] and 660 nm [21]. Additionally, comparing W cell models at 24 h with their respective models at 48 h demonstrated a statistical difference ( $p < 0.01$ ).

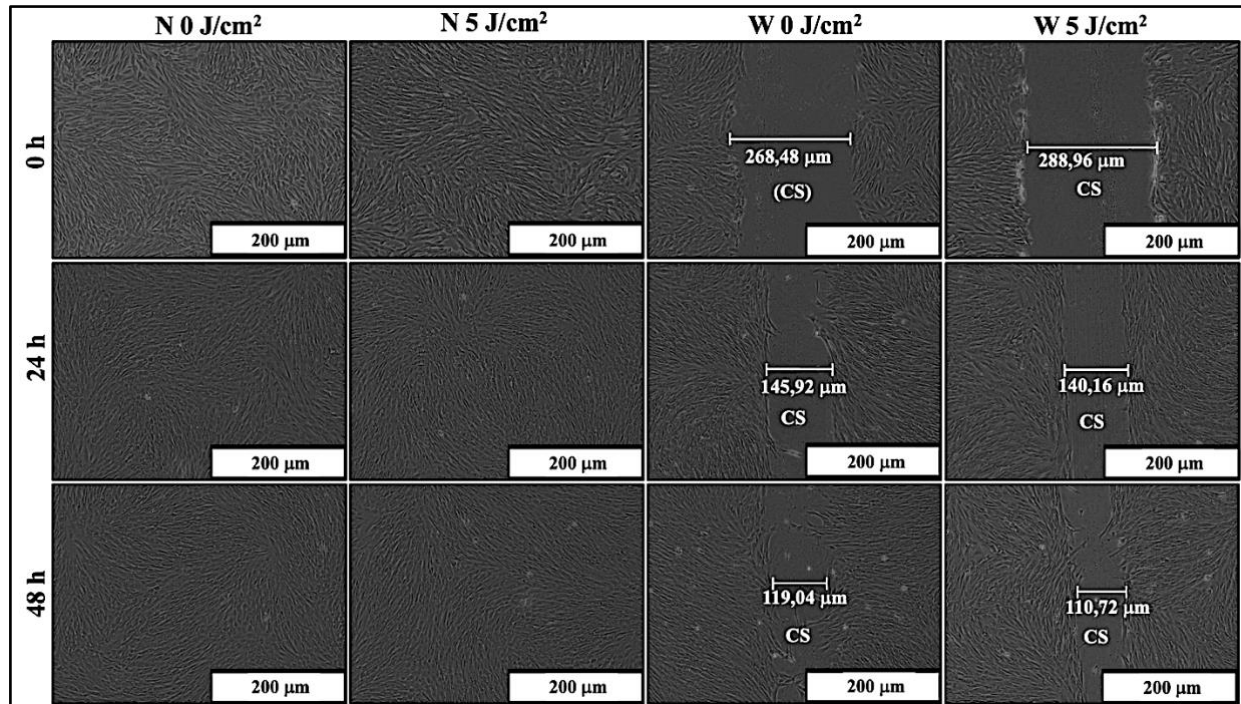


**Figure 1.** Micrographs displaying the morphology of normal (N) and wounded (W) cell models *in vitro* at 0 h, 24 h and 48 h post-irradiation. Cells retained their well-known elongated and spindle-shaped fibroblast morphology. At the same time, cells in the W model demonstrated a change in direction and migrated towards the central scratch (CS) to enable wound closure. Scale bar 200 μm (40x magnification).

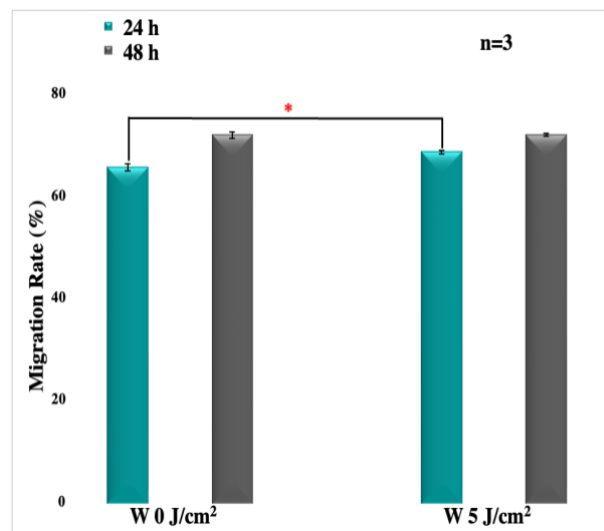


**Figure 2.** Percentage (%) migration rate in wounded (W) cell models at 24 h and 48 h post-irradiation. W irradiated (5 J/cm²) cells at 24 h demonstrated a significant increase in migration rate when compared to their non-irradiated (0 J/cm²) controls. Statistical significance is presented as \*p<0.05 (±SEM).

At 24 h post-irradiation, N irradiated (5 J/cm²) cells demonstrated a significant decrease in cell proliferation ( $p < 0.01$ ), while W irradiated (5 J/cm²) cells exhibited a significant increase ( $p < 0.05$ ) when compared to their control cells (Figure 3). At 48 h post-irradiation, N irradiated (5 J/cm²) cells exhibited a non-significant increase ( $p = 0.067$ ) in cell proliferation when compared to their non-irradiated (0 J/cm²) controls. W irradiated (5 J/cm²) cells exhibited a significant increase ( $p < 0.05$ ) in cell proliferation compared to their non-irradiated (0 J/cm²) controls. Thus, demonstrating a significant acceleration in

cellular proliferation in W irradiated cell models as revealed by BrdU staining for cells acceding and advancing through the S-phase of DNA replication. N irradiated ( $5 \text{ J/cm}^2$ ) cells displayed no propitious effect of PBM, signifying that PBM therapy is more beneficial for stressed cells and/or cells with impaired growth. Therefore, PBM alters the physiological state of stressed cells, restoring tissue homeostasis and healing responses [21]. On the contrary, Pogrel and colleagues [22], reported that Ga-Al-As lasers at 830 nm and a fluence that ranged from 0.12 to  $4.24 \text{ J/cm}^2$  could not augment the proliferation of keratinocytes and fibroblasts. A study by Almeida-Lopes *et al.* [16], demonstrated that PBM in the NIR spectrum (780 nm;  $2 \text{ J/cm}^2$ ) increased cell proliferation of human gingival fibroblasts.

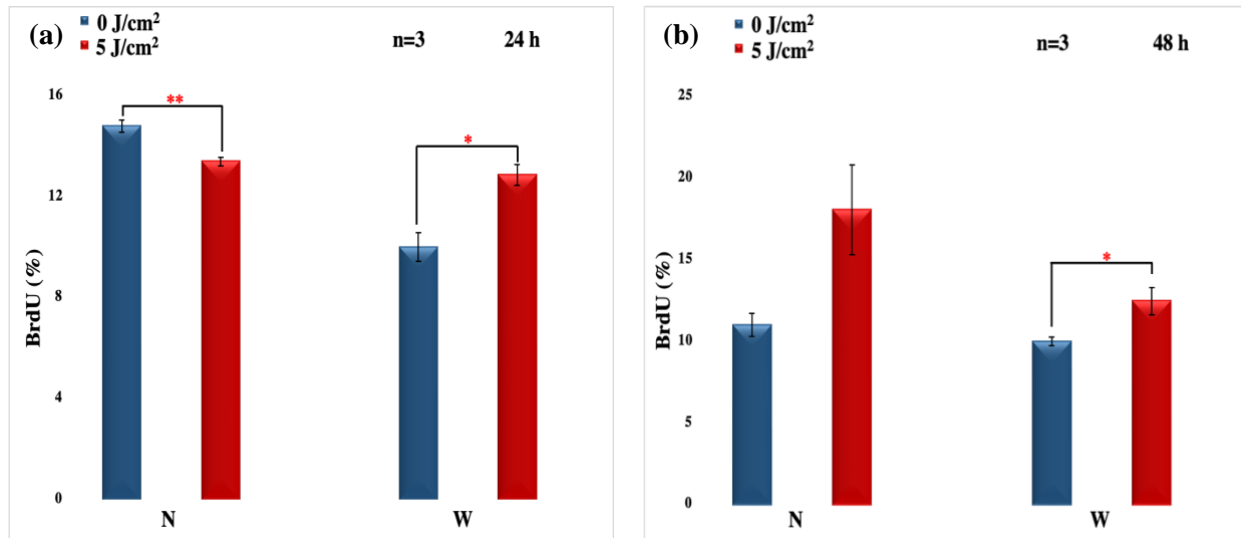


**Figure 3.** Percentage of cells in proliferative S- (DNA synthesis) phase as measured by flow cytometry in normal (N) and wounded (W) cell models (a) 24 h, and (b) 48 h post-irradiation. Statistical significance is presented as \* $p < 0.05$  and \*\* $p < 0.01$  ( $\pm$ SEM).

#### 4. Conclusion

In conclusion, the present study's findings suggest that PBM at 830 nm using  $5 \text{ J/cm}^2$  has a photobiostimulatory effect on cellular migration and proliferation and has the potential to augment wound healing. Our results demonstrate that at 24 h after irradiation PBM had no effect on the proliferation of normal cells and may suggest that extended incubation post-irradiation is necessary to reap the full effects of PBM. However, no complete wound closure was detected at 48 h, which contradicts the results when fibroblast cells are irradiated at a red wavelength of 660 nm. These findings suggest that although there is a significant improvement in cell migration and wound closure at 830 nm, PBM of cells *in vitro* in the visible red region appears to be more effective and pronounced. To verify these discrepancies, more comparative research on PBM at 660 nm and 830 nm should be conducted in both *in vitro* and *in vivo* studies.

#### Acknowledgements

This work was supported by the South African Research Chairs Initiative of the Department of Science and Technology and the National Research Foundation of South Africa (Grant No 98337), as well as grants received from the University of Johannesburg (URC), the National Research Foundation (NRF), and the Council for Scientific and Industrial Research (CSIR)-National Laser Centre (NLC) Laser Rental Pool Programme.

#### References

- [1] Sen C K 2021 *Advances in Wound Care* **10** 281-92.
- [2] Falanga V 2005 *The Lancet* **366** 1736-43
- [3] Monsuur H N, Boink M A, Weijers E M, Roffel S, Breetveld M, Gefen A, van den Broek L J and Gibbs S 2016 *J. Biomech.* **49** 1381-87

- [4] You H-J, Namgoong S, Han S-K, Jeong S-H, Dhong E-S and Kim W-K 2015 *Cytotherapy* **17** 1506–13
- [5] Heiskanen V and Hamblin M R 2018 *Photochem. Photobiol. Sci.* **17** 1003-17
- [6] Avci P, Gupta A, Sadasivam M, Vecchio D, Pam Z, Pam N and Hamblin M R 2013 *Semin. Cutan. Med. Surg.* **32** 41–52
- [7] Hamblin M R 2018 *Photochem. Photobiol.* **94** 199–212
- [8] Kuffler D P 2016 *Regen. Med.* **11** 107–22
- [9] Houeild N N and Abrahamse H 2007 *Lasers Med. Sci.* **23** 11–18
- [10] Hawkins D and Abrahamse H 2006 *Photomed. Laser Surg.* **24** 705–14
- [11] Chung H, Dai T, Sharma S K, Huang Y-Y, Carroll J D and Hamblin M R 2012 *Ann. Biomed. Eng.* **40** 516–33
- [12] Houeild N and Abrahamse H 2007 *Diabetes Technol. Ther.* **9** 451-459
- [13] Liang C-C, Park A Y and Guan J L 2007 *Nat. Protoc.* **2** 329–33
- [14] Felice F, Zambito Y, Belardinelli E, Fabiano A, Santoni T and Di Stefano R 2015 *Int. J. Biol. Macromol.* **76** 236–41
- [15] Leyane T S, Jere S W and Houeild N N 2021 *Int. J. Mol. Sci.* **22** 11223
- [16] Almeida-Lopes L, Rigau J, Amaro Zângaro R, Guidugli-Neto J and Marques Jaeger M M 2001 *Lasers Surg. Med.* **29** 179–84
- [17] Ginani F, Soares D M, Barreto M P eV and Barboza C A G 2015 *Lasers Med. Sci.* **30** 2189–94
- [18] Ejiri K, Aoki A, Yamaguchi Y, Ohshima M and Izumi Y 2014 *Lasers Med. Sci.* **29** 1339–47
- [19] Hehenberger K, Kratz G, Hansson A and Brismar K 1998 *J. Dermatol. Sci.* **16** 144–51
- [20] Ayuk S M, Houeild N N and Abrahamse H 2012 *Diabetes Technol. Ther.* **14** 1110–17
- [21] Ayuk S M, Houeild N N and Abrahamse H 2018 *Lasers Med. Sci.* **33** 1085–93
- [22] Pogrel M A, Chen J W and Zhang K 1997 *Lasers Surg. Med.* **20** 426–32

# Simulation of a malaria nanoplasmonic biosensor based on extraordinary optical transmission

A. S. Kiyumbi and M. S. Tame

Department of Physics, Stellenbosch University, Private Bag X1, Matieland 7602, South Africa

E-mail: akiyumbi@gmail.com

**Abstract.** In this study, we present the theoretical analysis and optimization of a 2D metasurface made from gold for sensing *Plasmodium falciparum* (Pf) parasites. The sensor is made of equal-distance periodic circular nanoholes on a gold planar surface. Specifically, it is an array of nanoholes patterned in a 100 nm thick gold film where the diameter of nanoholes is 150 nm and the center-to-center separation is 400 nm. When probed by light, these nanoholes give rise to extraordinary optical transmission resonant peaks resulting from the hybridization between surface plasmons and optical modes inside nanoholes. By monitoring the shift of transmission peaks or transmission intensity, the induced refractive index perturbation due to Pf-antibody-antigen interactions can be accurately measured. We report, based on refractive index unit (RIU), a minimum limit of detection of  $3.19 \times 10^{-4}$  RIU using spectral interrogation and  $1.00 \times 10^{-4}$  RIU using intensity interrogation. These sensor properties can be useful for the diagnosis of malaria at an early stage.

## 1. Introduction

Malaria, a mosquito-borne disease has infected humans for centuries. In 2020, malaria resulted in 627,000 deaths globally. Africa made up 96% of global malaria deaths and about 80% of all deaths in the region were children under 5 years [1]. Conventional malaria diagnosis is based on empirical therapy, antibody rapid diagnostic tests (mRDTs), nucleic acid-based molecular analysis, and/or microscopic analysis [2]. These methods are limited in precision, affordability, integration, or portability. They also require long detection times, sophisticated infrastructure, and trained personnel [3]. For example, mRDTs have various well-known detection problems [4]. To overcome these diagnosis limitations, researchers are interested in designing different kinds of optical biosensors to in-vitro detect malaria parasites [5]. For example, 1D and 2D photonic crystal biosensors and surface plasmon resonance biosensors are compact, robust, and can label-free detect low malaria parasitemia using a small sample size [6–9]. Recent progress in the development of malaria diagnostic tests, potential biomarkers, and their applications are summarised in reviews by Ragavan et al. [5] and Priyamvada et al. [10].

In this work, we design, simulate, and analyze a malaria plasmonic biosensor based on extraordinary optical transmission (EOT) that operates in the visible and near infra-red optical regime ( $\lambda = 450$  nm to 850 nm). The biosensor is made up of a metasurface with periodic nanoholes 150 nm in diameter and 400 nm apart patterned in a gold film (100 nm thick) and deposited onto a glass substrate. The finite element numerical method, using COMSOL Multiphysics has been utilized for modeling and simulation. The spectral sensitivity and limit of detection are calculated and their contribution to sensing is discussed.

## 2. Theoretical background

Surface plasmon resonance (SPR) biosensing is a practical and commercial label-free diagnostic technique that enables the investigation of ligand-receptor interactions by utilizing surface plasmon waves [11]. The technique offers real-time analysis and immediate recognition of biomolecular species and their interactions. Surface plasmons (SPs) are electromagnetic excitations propagating and evanescently confined at a metal-dielectric interface. They arise due to the coupling of an incident transverse electromagnetic wave to oscillations in the metal's electron plasma [12]. These surface modes are a self-consistent solution of the 3D Maxwell equations and are characterized in terms of their dispersion according to [12]

$$k_{sp} = k_0 \sqrt{\frac{\epsilon_m \epsilon_d}{\epsilon_m + \epsilon_d}}. \quad (1)$$

Here,  $k_{sp}$  is the propagation constant of surface plasmons,  $k_0 = \frac{2\pi}{\lambda}$  the propagation constant of an incident photon in free space,  $\lambda$  is the excitation wavelength, and  $\epsilon_m$  and  $\epsilon_d$  are the permittivity of the metal and the adjacent dielectric. Due to momentum mismatch,  $k_{sp} > k_0$ , it is difficult to excite SPs by directly probing the metal surface.

Periodic nanohole arrays structured on metals are a class of 2D photonic grating that allows the direct excitation of SPs. When a wave polarised along one of the array axes is incident on this structure, the array exhibits EOT. The phenomenon was first reported by Ebbesen [13]. The name EOT is used because the amount of transmitted light ( $T$ ) through a sub- $\lambda$  hole (diameter  $d \ll \lambda$ ) is much higher than what could be expected by Bethe's classical aperture theory [14]. The EOT phenomenon is the result of a hybridization between SPs, quasi-cylindrical waves, and optical modes inside nanoholes [15, 16]. Plasmon properties of the film material ("metal transparency window") in the spectral range of measurement are also important to realize the EOT effect and hence EOT is sometimes related to the excitation of a Fabry-Perot resonance in holes. The physics and detailed explanation of EOT through periodic nanohole arrays in real metals have been examined in Refs. [17, 18]. Analytical derivations and models that provide deeper insight are also formulated to capture the essential mechanisms involved in this phenomenon [19]. At resonance, the wavelength of light that can be transmitted,  $\lambda_{sp}$ , through periodic nanoholes is given by

$$\lambda_{sp} = \frac{a_0}{\sqrt{i^2 + j^2}} \sqrt{\frac{\epsilon_m \epsilon_d}{\epsilon_m + \epsilon_d}}, \quad (2)$$

where  $a_0$  is the lattice constant (i.e. distance between nanoholes), and  $i$  and  $j$  are non-zero integer numbers representing scattering orders of the surface wave.

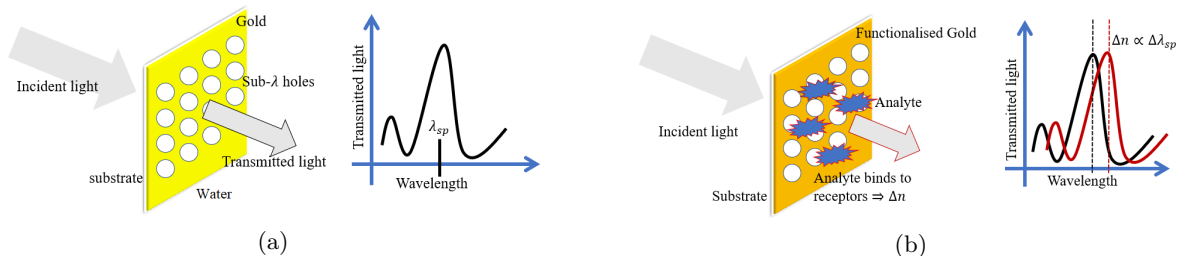


Figure 1: (a) A schematic drawing of the designed EOT-based SPR sensor showing the main three components of the sensor, the substrate layer (glass), nanohole array (optical transducer), and the analyte layer (e.g. water). (b) The working principle of the sensor. When the target analyte (in water or blood) binds to the receptors immobilized on the gold surface, the refractive index  $n$  near the metal surface is altered. A change in  $n$  results in a change of maximum transmission wavelength  $\lambda_{sp}$ . By monitoring this change, EOT-based sensing is attained.

From Eq. (2), the adsorption of ligand molecules to immobilized receptors in the vicinity of a metal-dielectric interface alters the dielectric refractive index  $n = \sqrt{\epsilon_d}$ , which then alters the coupling condition and hence shifts the resonant wavelength  $\lambda_{sp}$  of transmission maximum(s). The ligand molecules (or target analytes) are then detected based on the shift of  $\lambda_{sp}$ . However, EOT resonances are also tunable through the engineering of hole shape, hole size, and periodicity [20,21], this adds another avenue for designing EOT-based sensors. Fig. 1(a) shows the designed EOT-based SPR sensor. The working principle of the sensor is summarised in Fig. 1(b).

### 3. Modeling and simulation

The finite element method was performed using COMSOL multiphysics to simulate the optical transmission response of the periodic nanohole array patterned on a gold film, as shown in Fig. 2(a). The model geometry is discretized into finite elements formed by 2D and/or 3D meshing. At points where these elements meet (nodes), a set of linear partial differential Maxwell equations are iteratively solved. Solutions of individual elements need to converge to obtain the whole model solution. Floquet periodic boundary conditions are usually used to address periodic nanoholes but due to the symmetry of the modeled geometry and to save computational time, a quarter of the unit cell is simulated. The two boundaries perpendicular to the x-axis and y-axis were set as perfect electric conductors (PEC) and perfect magnetic conductors (PMC), respectively. They work as absorbing layers for an incident p-polarised or s-polarised light propagating into unbounded space. The top and bottom domains of the sensor structure are declared as the analyte layer ( $n_d = 1.33$  to  $n_d = 1.41$ ) and the substrate layer (glass,  $n_s = 1.52$ ), respectively. The middle domain is the gold film perforated with subwavelength holes. The adhesion layer between glass and gold film and the analyte binding layer between gold and a bioreceptor are both ignored in this model because their inclusion only slightly affects the spectral locations of the resonances. The choice of  $n_d$  for the analyte layer is practical in malaria diagnosis since the refractive index of whole blood lysate in different stages of malaria lies in that range. Normal stage  $n = 1.408$ , ring stage  $n = 1.396$ , trophozoite stage  $n = 1.381$  and schizont stage  $n = 1.371$  [22]. However, these values are just baseline values. When the analyte in the blood binds to receptors, the baseline values would change by a small amount  $\delta n$ , which is more important in SPR biosensing as it corresponds to a specific binding process [9]. The modified Lorentz-Drude model was used to include the frequency-dependent  $\epsilon_m$  of gold [23]. A normal TM-polarized plane wave incident from the substrate side is used as an optical excitation. To avoid undesired numerical reflections back into the interior of a computational region, the top, and bottom boundaries of the model system are terminated by strong absorbing perfectly matched layers (PML).

### 4. Result and Discussion

To determine the sensitivity and the limit of detection, we modeled the expected experimental response of our sensor by imposing an experimental white light spectrum into the simulated spectra shown in Fig. 2(b). The spectrum of a white light LED source adds the necessary noise to our simulated spectra. This noise stems from the spectrometer and shot noise from the statistical nature of the light. We are interested in the total noise as this is what puts a lower bound on the limit of detection in a real experiment. The transmission spectra in Fig. 2(c) are the expected experimental results when a MBB1F1 fiber-coupled light emitting diode (LED) from Thorlabs is used to illuminate the sensor. Using a moving standard deviation algorithm, the fluctuation of intensity  $\Delta I$ , which represents noise in the sensor output was plotted against  $\lambda$ , see inset in Fig. 2(c). Our analysis focuses on the first and second peaks at around 650 nm and 740 nm respectively. The peak around 500 nm is ignored in sensing analysis because is an intrinsic property of the gold film associated with the interband transition.

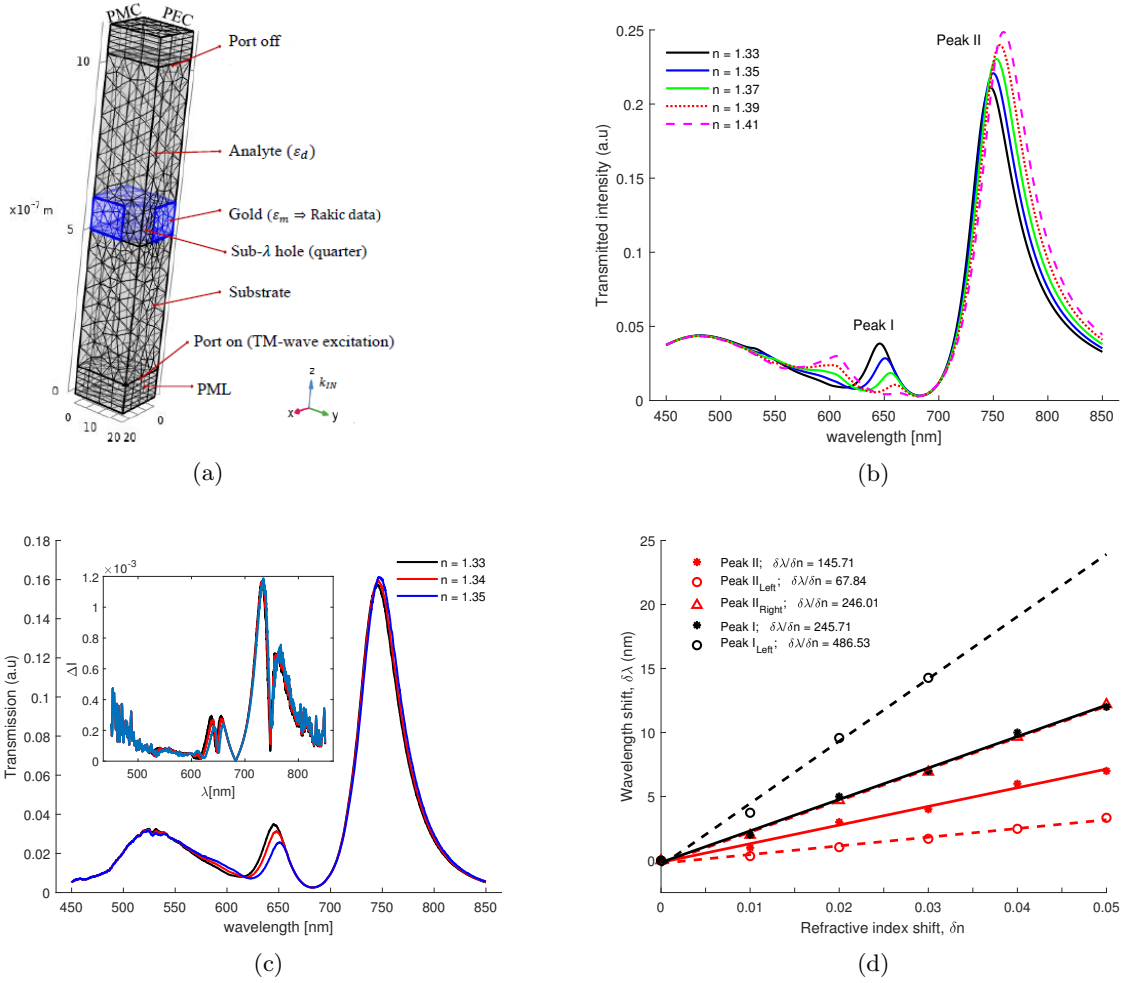


Figure 2: (a) A COMSOL model of the sensor system showing a quarter of the unit cell. PEC and PMC boundary conditions are applied perpendicular to the x and y-axes. (b) The simulated transmission spectra of the gold nanohole array in liquid analyte with a refractive index ranging from  $n = 1.33$  to  $n = 1.41$ . (c) Modeled experimental transmission spectra of the sensor (representatives) and the associated intensity fluctuation  $\Delta I$  (inset figure) plotted against  $\lambda$ . Both the main figure and its inset share the same legend. (d) Spectral sensitivity  $\delta\lambda/\delta n$  (where  $\delta n = n - 1.33$ ) around peak I and peak II shows that the left of peak I is the most sensitive region.

From Fig. 2(d), a small change in refractive index  $\delta n$  from a baseline of  $n = 1.33$  linearly shifts the position of the transmission maxima by  $\delta\lambda$ . One can also fix the wavelength and monitor changes in the transmitted intensity  $\delta I$  at that wavelength. Therefore, the sensitivity  $S_{RI}$  of our sensor is defined as the extent to which the intensity or wavelength changes for a given change of the refractive index  $\delta n$  when  $\lambda$  or  $I$  is fixed. The limit of detection (LOD), the minimum detectable change of the refractive index  $\Delta n$ , is linked to  $S_{RI}$  by [24, 25]

$$\text{LOD} = \Delta n = \frac{\Delta Y}{S_{RI}}. \quad (3)$$

Here,  $Y$  is an explicit observable parameter (intensity or wavelength) that changes with respect to  $\delta n$ , and  $S_{RI} = \left| \frac{\delta Y}{\delta n} \right|$  at a fixed  $\lambda$  or  $I$  and  $\Delta Y$  is the noise associated with the measurement of  $Y$ . Therefore, the practical functionality of the SPR sensor depends on the sensitivity  $S_{RI}$

and the noise  $\Delta Y$  in the sensor output which depends on the system parameters,  $\lambda$  and  $n$ . The inset of Fig. 2(c) shows a strong  $\lambda$  dependence of  $\Delta I$  and by changing  $n$  we found a weak  $n$  dependence of  $\Delta I$ . Furthermore, we found that the sensitivity  $S_{RI}$  weakly depends on the baseline  $n$  for intensity or wavelength sensing and that  $\frac{dY}{dn} = \lim_{\delta n \rightarrow 0} \frac{\delta Y}{\delta n}$ , we then have for intensity or wavelength sensing

$$\text{LOD} = \left| \frac{\delta n}{\delta I} \right|_{\lambda} \Delta I = \left| \frac{\delta I}{\delta n} \right|_{\lambda}^{-1} \Delta I, \quad (4)$$

or

$$\text{LOD} = \left| \frac{\delta n}{\delta \lambda} \right|_I \Delta \lambda = \left| \frac{\delta n}{\delta \lambda} \right|_I \left| \frac{\delta \lambda}{\delta I} \right|_I \Delta I = \left| \frac{\delta \lambda}{\delta n} \right|_I^{-1} \left| \frac{\delta I}{\delta \lambda} \right|_I^{-1} \Delta I. \quad (5)$$

In Fig. 3(a), we show a linear relation between  $\delta I$  and  $\delta n$  at a fixed  $\lambda = 645$  nm and extract out the intensity sensitivity  $S_{RI}^I = \left| \frac{\delta I}{\delta n} \right|_{\lambda=645\text{nm}} = 0.6366$  RIU<sup>-1</sup>. Using this value in Eq. (4) together with the noise  $\Delta I(\lambda)$  shown in the inset of Fig. 2(c), the LOD at 645 nm is calculated as  $1.52 \times 10^{-4}$  RIU. The LOD data plotted against  $\lambda$  shown in Fig. 3(b) is obtained based on this procedure. We estimate the minimum LOD around peak I as  $1.00 \times 10^{-4}$  RIU. On the other hand in Eq. (5),  $\left| \frac{\delta \lambda}{\delta n} \right|_I$  and  $\left| \frac{\delta I}{\delta \lambda} \right|_I$  are the spectral sensitivity  $S_{RI}^{\lambda}$  shown in Fig. 2(d) and the gradient of the spectral profile shown in Fig. 2(b) at a fixed intensity, respectively. Values of  $S_{RI}^{\lambda}$  and their LOD are calculated and shown in Table. 1. The minimum LOD is  $3.19 \times 10^{-4}$  RIU on the left of peak I where the best  $S_{RI}^{\lambda}$  is 486.53 nm RIU<sup>-1</sup>.

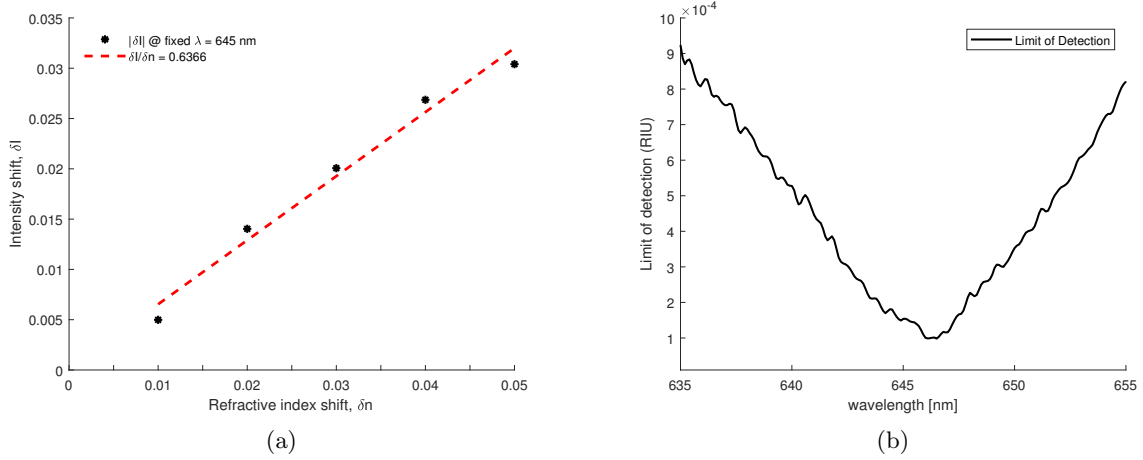


Figure 3: (a) Refractive index sensitivity based on intensity  $S_{RI}^I$  at a fixed wavelength  $\lambda = 645$  nm. (b) The calculated LOD as a function of  $\lambda$  based on Eq. (4). The LOD at  $\lambda = 645$  nm is  $1.52 \times 10^{-4}$  RIU and the minimum LOD for the 635 nm - 655 nm band is  $1.00 \times 10^{-4}$  RIU.

Table 1: Spectral sensitivity and LOD values calculated using Eq. (5).

Parameters	Peak I( $\lambda_{sp}$ )	Peak I(left)	Peak II( $\lambda_{sp}$ )	Peak II(right)	Peak II(left)
$S_{RI}^{\lambda}$ (nm RIU <sup>-1</sup> )	245.71	486.53	145.71	246.01	67.84
LOD (RIU)	$6.30 \times 10^{-4}$	$3.19 \times 10^{-4}$	$1.09 \times 10^{-3}$	$6.71 \times 10^{-4}$	$2.36 \times 10^{-3}$

## 5. Conclusion

We studied an SPR plasmonic sensor based on EOT for the diagnosis of malaria. In this biosensor, the liquid analyte of refractive index ranging from 1.33 (water) to 1.38 (trophozoite stage of malaria infection) is taken to mimic the refractive index of blood cells at different stages of malaria infection. Since the diagnosis technique is based on the principle of variation of a biophysical parameter (refractive index), the shift of maximum transmission peak is monitored, and the spectral sensitivity and LOD thereof are calculated. The transmission resonance peak shifts  $\delta\lambda_{sp}$  around the two EOT peaks are linear with the refractive index shifts  $\delta n$  of the analyte. The highest spectral sensitivity and LOD of the sensor is 486.53 nm RIU<sup>-1</sup> and  $3.19 \times 10^{-4}$  RIU on the left of the first peak (635 nm to 655 nm band). On the other hand, based on intensity interrogation, the sensor can attain the minimum LOD of  $1.00 \times 10^{-4}$  RIU. The device shows a good sensing performance and thus there is a potential for detecting low percentages of malaria antigens from an infected blood sample. For example, according to Ref. [9], when 10% of red blood cells were infected with plasmodium parasites, the binding of monoclonal antibodies against plasmodium lactate dehydrogenase (a malaria biomarker) produced a 0.004 RIU shift on the sensor surface. The sensor (LOD  $\approx 10^{-4}$  RIU) can easily detect this change ( $\Delta n = 0.004$ ) with high resolution. For classical SPR sensors, the current LOD state-of-the-art range between  $10^{-6}$  RIU to  $10^{-7}$  RIU [25, 26]. However, SPR sensors are more complicated to operate than the EOT-based sensor studied here.

## Acknowledgments

This project is supported by the African Laser Centre (ALC) grant (ALC-R016) at the South African Council for Scientific and Industrial Research (CSIR). We also acknowledge support from the University of Dar es Salaam, Tanzania, the Laser Research Institute (LRI) of the University of Stellenbosch, the Department for Science and Innovation (DSI), and the National Research Foundation (NRF) of the Republic of South Africa.

## References

- [1] World Health Organization 2021 *World malaria report 2021* (Geneva, World Health Organization)
- [2] Fitri L, Widaningrum T, Endharti A, Prabowo M, Winaris N, Nugraha R 2022 *J. Clin. Lab. Anal.* **36** (4)
- [3] Bronzan R N, McMorrogh M L and Patrick K S 2008 *Mol. Diag. Ther.* **12** 299–66
- [4] Ranadive et al. 2017 *Clin. Inf. Dis.* **64** 1221
- [5] Ragavan K, Kumar S, Swaraj S and Neethirajan S 2018 *Biosensors and Bioelectronics* **105** 188–210.
- [6] Ankita, Suthar B and Bhargava A 2021 *Plasmonics* **16** 59–63
- [7] Rashidnia A, Pakarzadeh H, Hatami, M and Natesan A 2022 *Opt. Quant. Electron* **54** 38.
- [8] Briand V, Thilakarathne V, Kasi, R and Kumar C 2012 *Talanta* **99** 113–18
- [9] Cho S, Briscoe J, Hansen I, Smith J, Chang Y, and Brener I 2014 *IEEE Sensors Journal* **14**(5) 1399–84
- [10] Priyamvada J, Babina C, Sanjukta P and Pranab G 2014 *BioMed Research International* **2014**
- [11] Vasimalla Y, Himansu S P and Rahul J P 2021 *Heliyon* **7**(3)
- [12] Maier S A 2007 *Plasmonics: fundamentals and applications* (Berlin Heidelberg: Springer)
- [13] Ebbesen T, Lezec H, Ghaemi H, Thio T and Wolff P A 1998 *Nature* **391** 667–69
- [14] Bethe H A 1944 *Phys. Rev.* **66** 163–82
- [15] Liu H and Lalanne P 2008 *Nature* **452**(7188) 728–31.
- [16] Liu H and Lalanne P 2010 *J. Opt. Soc. Am. A* **27** 2542–50
- [17] Popov E, Nevierne M, Enoch S and Reinisch R 2000 *Physical Review B.* **62** 16100–08
- [18] Martín-Moreno L et al. 2001 *Phys. Rev. Lett.* **86** 1114–17
- [19] Zyablovskii A A et al. 2017 *J. Exp. Theor. Phys.* **125** 175–88
- [20] Monteiro J P et al. 2013 *Sensors and Actuators B: Chemical* **178** 366–70
- [21] Yue W, Wang Z, Yang Y, Li J, Wu Y, Chen L, Ooi B S, Wang X and Zhang X 2014 *Nanoscale* **6**(14) 7917–23
- [22] Akpa M A, Konan K, Tokou Z, Kossonou Y, Dion S, Kaduki K and Zoueu J 1996 *Sensors* **19** 3045
- [23] Rakić A, A B Djurišić, J Elazar and M L Majewski 1998 *App. Opt.* **37** 5271–83.
- [24] Homola J 2008 *Chem. Rev.* **108**(2) 462–93.
- [25] Lee C et al. 2021 *Chem. Rev.* **121**(8) 4743–4804
- [26] Piliarik M and Homola J 2009 *Opt. Express* **17** 16505–17

# Wavelength calibration of a monochromator system

I Rabe, P J W du Toit and R H Sieberhagen

National Metrology Institute of South Africa, Meiring Naude Road, Pretoria, SA

E-mail: [irabe@nmisa.org](mailto:irabe@nmisa.org)

**Abstract.** A new system for measurement of spectral power responsivity of detectors, utilising a monochromator system, was implemented at NMISA and characterised. The monochromator system includes sources of optical radiation, input optics, order sorting filters, a scanning double monochromator, diffraction gratings and output optics. As part of the characterisation, wavelength calibrations were performed in the wavelength regions of 200 nm to 400 nm and 600 nm to 1 100 nm. This was done by measuring the relevant spectral lines of wavelength standards selected from the NIST Atomic Spectra Database, and applying corrections for ambient conditions using the Engineering Metrology Toolbox of NIST. The monochromator steps corresponding to the spectral peaks measured were determined using the steep-side method. A linear fit of the spectral peaks versus the corresponding monochromator steps provided the wavelength calibration equations. These were then used when scanning the wavelength regions with the monochromator software. Uncertainty of measurement analyses were performed for each of the wavelength calibrations to determine the uncertainty associated with the wavelength position of the monochromator and its influence on the spectral power responsivity of a detector.

## 1. Introduction

A new system for measurement of spectral power responsivity of detectors was implemented at NMISA. This measurement system consists of a scanning double monochromator and other components selected based on the system's requirements. For this measurement system where a low uncertainty of measurement is required, it is critical to have good wavelength accuracy of the double monochromator. In this case, a double monochromator should be calibrated for wavelength before any measurement is performed and with each change in the monochromator setup, such as a change in diffraction gratings. This is done to determine the true position of the wavelength spectrum with an associated uncertainty. The wavelength calibration produces a wavelength calibration equation, which may be used by the monochromator software when scanning through a wavelength region to record data.

A wavelength calibration is performed with spectral line sources used as wavelength standards. These are lamps that contain specific elements and through electrical discharge in such a gas or vapour, emissions lines occur at known wavelengths [1]. The NIST Atomic Spectra Database [2] lists the wavelengths of these emissions and also indicates the stronger emission spectral lines. Figure 1 provides an example of the emission spectral lines of the argon spectral line source used in the wavelength region of 600 nm to 1 100 nm.

## 2. Determining the wavelength calibration equation

The appropriate spectral line source should be selected for the wavelength region in which the calibration is to be performed. At first, a large spectral area scan should be performed to determine which spectral lines to use, as shown in Figure 1. Good spectral lines will be those free of line blending. Spectral lines that are in the noise level should also be avoided. For a monochromator system with symmetric bandpass, the wavelength of the peak of the spectral line may be determined using the steep-side method described in Kostkowski [1]. This method determines the wavelength of the peak of the spectral line by averaging the wavelengths at the steep sides of the spectral line at 10 % of the maximum signal,  $\lambda_1$  and  $\lambda_2$ , refer to Figure 2. The wavelength of the peak or center wavelength is given by

$$\lambda_c = \frac{\lambda_1 + \lambda_2}{2} \quad (1)$$

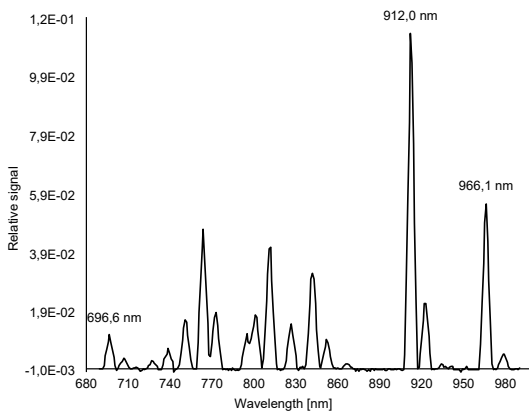


**Figure 1.** Emission spectral lines of the argon spectral line source used for the wavelength calibration in the visible to near-IR region.

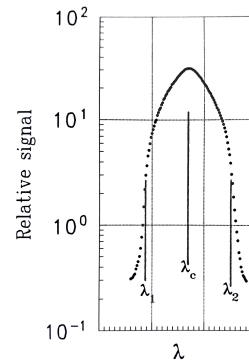


**Figure 2.** Excerpt from Kostkowski [1] demonstrating the steep-side method for a wavelength calibration.

The atomic emission spectral lines in vacuum should be corrected for ambient conditions. This may be done with the NIST Engineering Metrology Toolbox [3] which utilises the modified Edlén equation to calculate the index of refraction of ambient air,  $n$ , from the supplied laboratory air temperature, relative humidity and air pressure. It calculates the wavelength in ambient air,  $\lambda_{air}$ , from the wavelength in vacuum,  $\lambda_{vac}$ , and the refractive index using the relationship:

$$\lambda_{air} = \frac{\lambda_{vac}}{n} \quad (2)$$

Once the spectral lines in ambient air are obtained, the monochromator steps versus the wavelength of the peak of each corrected spectral line are plotted. The appropriate fit for the data is derived to obtain the expected wavelength calibration equation.

## 3. Method

A wavelength calibration was performed for the double monochromator in the wavelength regions of 200 nm to 400 nm and 600 nm to 1 100 nm using the standard laboratory procedure. The relevant spectral line sources were used, together with a silicon photodiode detector

and a variable gain low noise current amplifier connected to a multimeter operated with the monochromator software. The spectral lines were obtained from the NIST Atomic Spectra Database. To find the monochromator steps corresponding to the peak wavelength of each spectral line, the steep-side method as described in Section 2 was used. The ambient conditions were measured during each calibration and a correction was applied for temperature, atmospheric pressure and relative humidity, to each spectral line wavelength using the Engineering Metrology Toolbox of NIST. A linear fit of the spectral peaks versus the corresponding monochromator steps provided the wavelength calibration equations.

Verification of the wavelength calibration equations obtained in each wavelength region was performed by calculating the corresponding monochromator steps and moving the scan controllers of the monochromator to the laser lines at 543 nm and 632,8 nm, respectively. The peak signal of each laser line was found at the monochromator position within the stated wavelength uncertainty.

Uncertainty analyses were performed based on JCGM 100:2008 (GUM) [4], see the dissertation [5] for a detailed analysis. During calibration there are many factors that influence the measurement result and therefore contribute to the measurement uncertainty. These sources of uncertainty are called input quantities,  $X$ , or uncertainty contributors, and their estimates are combined to produce the uncertainty of measurement. An uncertainty calculation starts with the estimated uncertainty,  $u_e(x)$ , of the value,  $x$ , of these input quantities or uncertainty contributors, each of which has a defined probability distribution with an associated coverage factor,  $k$ . From this, the standard uncertainty,  $u(x)$ , is calculated as the quotient of the estimate of the uncertainty contributor and the coverage factor. A sensitivity coefficient,  $c$ , may have to be obtained to determine the sensitivity of the standard uncertainty to its contribution to the combined uncertainty, due to a change in the input quantity. The contribution to the combined standard uncertainty,  $u(y)$ , is therefore calculated as the product of the standard uncertainty and the sensitivity coefficient. These contributions,  $u(y)$ , are appropriately combined to obtain the combined standard uncertainty,  $u_c(y)$ . The expanded uncertainty,  $U$ , is reported and determined by multiplying the combined standard uncertainty with the appropriate coverage factor.

Several uncertainty contributors were considered and quantified for the wavelength calibrations performed in both wavelength regions. The complete uncertainty calculations on both wavelength regions are provided in Appendix A and Appendix B.

### *3.1. Wavelength region of 200 nm to 400 nm*

A set of 1 200 g/mm ruled gratings blazed at 300 nm was installed in the double monochromator, and a mercury spectral line source was used. A large spectral area scan was performed with the monochromator from 233 nm to 552 nm in 1 nm intervals using a bandwidth of 5 nm. From this scan, the spectral lines used for this calibration were selected. These spectral lines, in vacuum, were 253,7283 nm, 296,8149 nm and 435,9560 nm. Each of these spectral lines were scanned three times using a smaller wavelength interval of 0,2 nm. The scans were performed over a wavelength range of  $\pm 5$  nm of the spectral line.

When 10 % of the maximum signal is calculated, there is not necessarily a signal measured at the scanning steps that matches this value. Instead of selecting the closest value of monochromator steps, a linear fit was used on each steep side of the spectral line. The recorded signal closest to the calculated 10 % of the maximum signal was used as the midpoint of five data points on each steep side of the spectral line, respectively. The five data points were used to determine the linear fit, shown in blue in Figure 3. The linear fits were used to calculate the monochromator steps corresponding to the calculated 10 % of the maximum signal on each steep side of the spectral line and Equation 1 was applied to determine the monochromator steps corresponding to the peak of the spectral line. This procedure was followed for each of the three scans performed to determine the average step position for each respective spectral line.

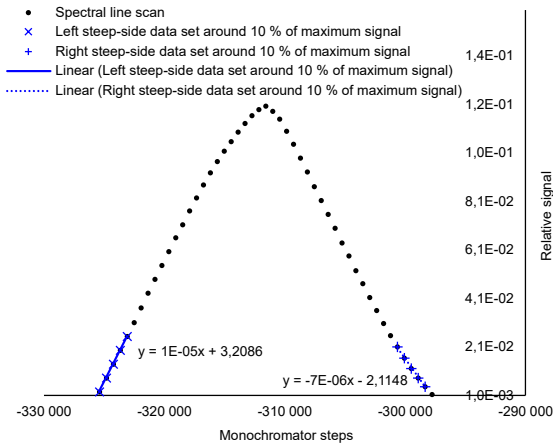


**Figure 3.** An example of the steep-side method and linear fits of data points around 10 % of maximum signal to determine the monochromator steps of the peak of a spectral line.

Corrections for ambient air using the NIST Engineering Metrology Toolbox is limited to the wavelength region of 300 nm to 1 700 nm. Two of the spectral lines selected for this wavelength region, 253,7283 nm and 296,8149 nm, therefore fall outside this range. The correction applied to these two wavelengths was the refractive index determined for the ambient air as specified in the laboratory procedure for temperature,  $24\text{ }^{\circ}\text{C} \pm 2\text{ }^{\circ}\text{C}$ , relative humidity,  $50\text{ \%RH} \pm 15\text{ \%RH}$ , and an atmospheric pressure of 86 kPa at 300 nm. This approximation was applied as a best estimate and found to be sufficient as the results were within the stated uncertainty for the verification performed.

The monochromator steps were plotted against each corrected spectral line and a linear fit was applied to the data to obtain the wavelength calibration equation.

### 3.2. Wavelength region of 600 nm to 1 100 nm

A set of 600 g/mm gratings blazed at 800 nm was installed in the double monochromator, and an argon spectral line source was used. A large spectral area scan was performed with the monochromator from 690 nm to 990 nm in 1 nm intervals, see Figure 1, using a bandwidth of 4 nm. The spectral lines selected from this scan were, in vacuum, 696,7352 nm, 912,5471 nm and 966,0435 nm. Each of these spectral lines were scanned using a smaller wavelength interval of 0,1 nm. The scans were performed over a wavelength range of  $\pm 5$  nm of the spectral line.

The closest value of monochromator steps at the steep sides of each spectral line corresponding to 10 % of the maximum signal was determined. The largest difference between the closest value and calculated value of monochromator steps using the linear fits as in Figure 3, was approximately 36 monochromator steps. This is equal to approximately 0,025 nm, which is small in comparison with the wavelength uncertainty of  $\pm 0,2$  nm obtained.

The monochromator steps were plotted against each corrected spectral line and a linear fit was applied to the data to obtain the wavelength calibration equation.

## 4. Results

The wavelength calibration equation for the 200 nm to 400 nm region was found to be:

$$y(\lambda) = 288,047\lambda - 855\,187 \quad (3)$$

where  $y(\lambda)$  is the monochromator steps and  $\lambda$  is the wavelength in Angstrom [ $\text{\AA}$ ], see Figure 4. The uncertainty of measurement in wavelength was  $\pm 0,3$  nm.

The wavelength calibration equation for the 600 nm to 1 100 nm region was found to be:

$$y(\lambda) = 144,028\lambda - 1\,003\,276 \quad (4)$$

See Figure 5. The uncertainty of measurement in wavelength was  $\pm 0,2$  nm.

The uncertainty calculations are provided in Appendix A and Appendix B. For a more detailed description, refer to the dissertation by Rabe [5].

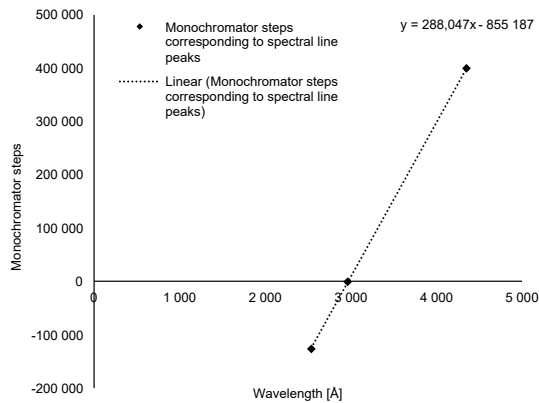


**Figure 4.** A plot of the monochromator steps corresponding to spectral lines peaks with a linear fit for the wavelength calibration in the region 200 nm to 400 nm.

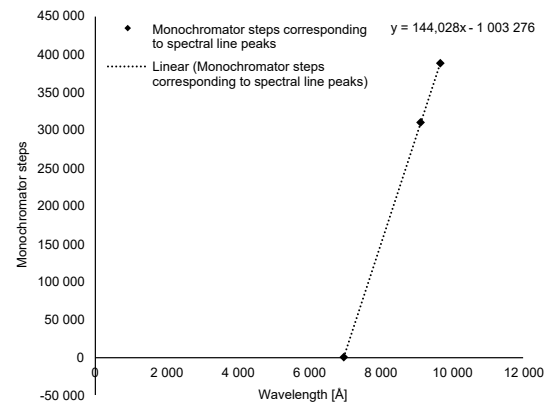


**Figure 5.** A plot of the monochromator steps corresponding to spectral lines peaks with a linear fit for the wavelength calibration in the region 600 nm to 1 100 nm.

## 5. Conclusion

As part of the characterisation of the new measurement system for spectral power responsivity of detectors implemented at NMISA, wavelength calibrations were performed in the wavelength regions of 200 nm to 400 nm and 600 nm to 1 100 nm. This was done by measuring the relevant wavelength standards for spectral lines selected from the NIST Atomic Spectra Database, and applying corrections for ambient conditions using the Engineering Metrology Toolbox of NIST. The monochromator steps corresponding to the spectral peaks measured were determined using the step-side method. A linear plot of the spectral peaks versus the corresponding monochromator steps was used to obtain the wavelength calibration equations to be used in the respective wavelength regions when operating the monochromator. The uncertainty of measurement was calculated for each of the wavelength calibrations. The verifications performed in each wavelength region were successful when compared with the uncertainty of measurement obtained.

**Appendix A. Uncertainty of measurement for the wavelength calibration in the 200 nm to 400 nm region**

**Appendix B. Uncertainty of measurement for the wavelength calibration in the 600 nm to 1 100 nm region**

## References

- [1] Kostkowski H J 1997 *Reliable Spectroradiometry* (Maryland: Spectroradiometry Consulting)
- [2] NIST 2019 *Atomic Spectra Database Lines Form* [Online] Available at: <https://www.nist.gov/pml/atomic-spectra-database>
- [3] NIST 2004 *Engineering Metrology Toolbox* [Online] Available at: <https://emtoolbox.nist.gov/Wavelength/Edlen.asp>
- [4] JCGM 2008 *JCGM 100:2008 Evaluation of measurement data — Guide to the expression of uncertainty in measurement* 1st ed

- [5] Rabe I 2022 *Characterisation and uncertainty of measurement analysis of a detector spectral power responsivity measurement system* Master's thesis University of Pretoria

## Appendix A

**Table A1.** Uncertainty of measurement calculated for the wavelength calibration in the wavelength region of 200 nm to 400 nm.

No.	Input quantity	Estimated uncertainty		Probability distribution	Coverage factor	Standard uncertainty		Sensitivity coefficient		Uncertainty contribution	
i	$X_i$	$u_e(x_i)$	unit		k	$u(x_i)$	unit	$c_i$	unit	$u_i(y)$	unit
1	Theoretical value spectral line in vacuum	1,73E-04	nm	Normal	1	1,73E-04	nm	1,00E+00		1,73E-04	nm
2	Modified Edlen equation calculation	7,39E-08	1	Normal	2	3,70E-08	1	-3,29E+03	nm/1	1,21E-04	nm
3	Laboratory temperature effect	4,00E+00	°C	Triangular	$\sqrt{6}$	1,63E+00	°C	3,53E-04	nm/°C	5,76E-04	nm
4	Laboratory humidity effect	3,00E+01	%RH	U-shaped	$\sqrt{2}$	2,12E+01	%RH	4,50E-06	nm/%RH	9,55E-05	nm
5	Laboratory air pressure effect	4,00E+00	kPa	Rectangular	$\sqrt{3}$	2,31E+00	kPa	1,17E-03	nm/kPa	2,71E-03	nm
6	Wavelength calibration equation offset	2,87E+02	steps	Normal	1	2,87E+02	steps	3,47E-04	nm/steps	9,95E-02	nm
7	Wavelength reproducibility	5,00E-03	nm	Rectangular	$\sqrt{3}$	2,89E-03	nm	1,00E+00		2,89E-03	nm
8	Mechanical resolution of monochromator	2,50E-02	nm	Rectangular	$\sqrt{3}$	1,44E-02	nm	1,00E+00		1,44E-02	nm
9	Resolution used in calibration	1,00E-01	nm	Rectangular	$\sqrt{3}$	5,77E-02	nm	1,00E+00		5,77E-02	nm
10	Repeatability	8,37E+01	steps	Normal	1	8,37E+01	steps	3,47E-04	nm/steps	2,91E-02	nm
										$u_c(y)$	1,20E-01 nm
										U (k=2)	3,00E-01 nm

## Appendix B

**Table B1.** Uncertainty of measurement calculated for the wavelength calibration in the wavelength region of 600 nm to 1 100 nm.

No.	Input quantity	Estimated uncertainty		Probability distribution	Coverage factor	Standard uncertainty		Sensitivity coefficient		Uncertainty contribution	
i	$X_i$	$u_e(x_i)$	unit		k	$u(x_i)$	unit	$c_i$	unit	$u_i(y)$	unit
1	Theoretical value spectral line in vacuum	1,00E-04	nm	Normal	1	1,00E-04	nm	1,00E+00		1,00E-04	nm
2	Modified Edlen equation calculation	4,20E-08	1	Normal	2	2,10E-08	1	1,00E+00	nm/1	2,10E-08	nm
3	Laboratory temperature effect	4,00E+00	°C	Triangular	$\sqrt{6}$	1,63E+00	°C	6,81E-04	nm/°C	1,11E-03	nm
4	Laboratory humidity effect	3,00E+01	%RH	U-shaped	$\sqrt{2}$	2,12E+01	%RH	9,29E-06	nm/%RH	1,97E-04	nm
5	Laboratory air pressure effect	4,00E+00	kPa	Rectangular	$\sqrt{3}$	2,31E+00	kPa	2,26E-03	nm/kPa	5,21E-03	nm
6	Steep-side method offset	3,60E+01	steps	Normal	1	3,60E+01	steps	6,94E-04	nm/steps	2,50E-02	nm
7	Wavelength calibration equation offset	7,20E+01	steps	Normal	1	7,20E+01	steps	6,94E-04	nm/steps	5,00E-02	nm
8	Wavelength reproducibility	5,00E-03	nm	Rectangular	$\sqrt{3}$	2,89E-03	nm	1,00E+00		2,89E-03	nm
9	Mechanical resolution of monochromator	5,00E-02	nm	Rectangular	$\sqrt{3}$	2,89E-02	nm	1,00E+00		2,89E-02	nm
10	Resolution used in calibration	5,00E-02	nm	Rectangular	$\sqrt{3}$	2,89E-02	nm	1,00E+00		2,89E-02	nm
11	Repeatability	1,56E+01	steps	Normal	1	1,56E+01	steps	6,94E-04	nm/steps	1,08E-02	nm
										$u_c(y)$	7,03E-02 nm
										U (k=2)	2,00E-01 nm

# Photonic quantum entanglement

A I Smith, C M Steenkamp and M S Tame

Department of Physics, SU, Matieland 7602, RSA

E-mail: andre12smith@gmail.com

## Abstract.

Path entanglement is an essential tool in quantum information and quantum communication protocols. We study the generation and measurement of path entangled photon states using pairs of single photons generated by spontaneous parametric down-conversion (SPDC). Path entanglement is generated using a Mach-Zehnder (MZ) interferometer in one arm of the SPDC setup. We characterise the MZ interferometer as well as perform standard tests to indicate whether entanglement is present, including protocols on determining the quality of the photons generated. These tests include a second-order correlation measurement and a visibility measurement. These two tests determine the quality of the single photons being generated and the quality of interference of a photon with itself, respectively. This method of entanglement quantification is tested for SPDC single photons for the first time and demonstrated to be successful.

## 1. Introduction

Entanglement is a valuable resource in the development of quantum computers and quantum information systems [1]. It has two common definitions: the first states that a composite system which forms some state is entangled if it is not separable [2]. The second states that entangled states are states that cannot be simulated by classical correlations [3].

In terms of the example given in Fig. 1 the first definition would say the system is entangled if the state of photon 1 could not be separated from the state of photon 2. This is the case in this example as when one of the photons is measured as  $|H\rangle$  the other must be measured as  $|V\rangle$  and vice versa, where  $|H\rangle$  and  $|V\rangle$  correspond to a horizontal and vertical polarised photon, respectively. This means that the measured outcomes are necessarily dependant on each other.

For the second definition the example given in Fig. 1 would be considered entangled if the

### Measuring a Pair of *Entangled* Photons

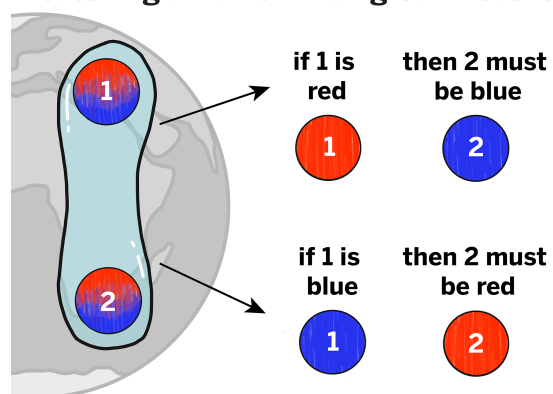


**Figure 1.** Example image of two photons generated in the state  $|\Psi\rangle = \frac{1}{\sqrt{2}} (|H\rangle |V\rangle + |V\rangle |H\rangle)$  being measured. Here  $|H\rangle$  is shown as red and  $|V\rangle$  is shown as blue. Image taken from <https://quantumatlas.umd.edu/entry/entanglement>.

measured outcome of the system could not be simulated by a classical system. A classical equivalent for this system would be a system where randomly one photon is produced in the state  $|H\rangle$  and based on this the other is in the state  $|V\rangle$ . Any set of measurements on this classical state will show only classical correlations, whereas for the state  $|\Psi\rangle$  in Fig. 1, there are measurements outcomes that cannot be simulated classically [3].

The scenario shown in Fig. 1 is an example of polarisation entanglement. For this research, single-photon entanglement, also known as path entanglement is used.

Path entanglement is a form of entanglement which instead of making use of two photons that can be measured in  $|H\rangle$  or  $|V\rangle$ , makes use of two paths. Each path can be measured in the states  $|1\rangle$  and  $|0\rangle$ , where  $|1\rangle$  denotes a photon detection and  $|0\rangle$  denotes no photon detection or a vacuum detection. An example setup for producing this entanglement can be seen in Fig. 2.

The state created in the example in Fig. 2 is  $|\Psi\rangle = \frac{1}{\sqrt{2}}(|1\rangle_1|0\rangle_2 + |0\rangle_1|1\rangle_2)$ , where the subscripts denote the path the detection is made in. This system is known to be an entangled system [4, 6]. In this case the polarisation of the photon is not indicated as the photon has the same polarisation in each path.

This study is the first to quantify entanglement for SPDC single photons.

## 2. Setup

The setup in Fig. 3 was built to generate single-photon path entanglement. In the figure, the single-photon source is a BBO crystal. Detector  $A$  is used as a heralding detector to infer the existence of a photon which can be measured by either detector  $B$  or  $C$ . A Mach-Zehnder (MZ) interferometer is placed in the heralded arm. The MZ interferometer consists of two 50/50 beamsplitters as well as two mirrors, one of which is placed on a translation stage, and is set such that the two paths interfere coherently.

In the image a line can be seen drawn through the MZ interferometer. This is used to distinguish the generation and analysis part of the interferometer. This line can also be used to represent where entanglement is present.

It should also be noted that there are three neutral density (ND) filters present. These filters are added as the beamsplitters used are not exactly 50/50, thus the ND filters are added to compensate for the beamsplitters. The ND filter labelled ND 1 is used to compensate for BS 1 which has a higher transmission than reflectance in the generation half of the MZ interferometer. The filter ND 2 is used to compensate for BS 2, which also has a higher transmission than reflectance, in the analysis half of the MZ interferometer. The final filter ND 3 is used to compensate for the polarising beamsplitter, which is used when probing the state.

The half-wave plates (HWP) are used to probe the generated path entangled state together with the polarising beamsplitter, and initially all have their fast axes set to zero degrees to the vertical direction in the lab.

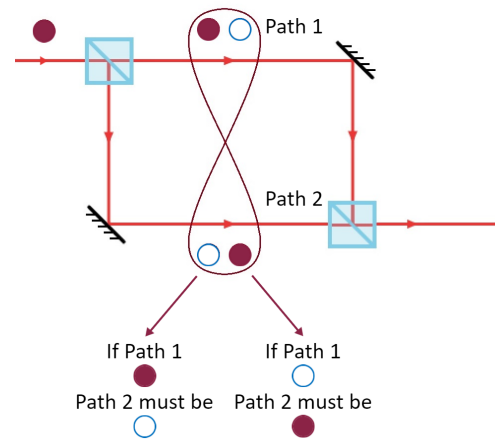


**Figure 2.** Example setup for producing path entanglement inside a Mach-Zehnder interferometer.

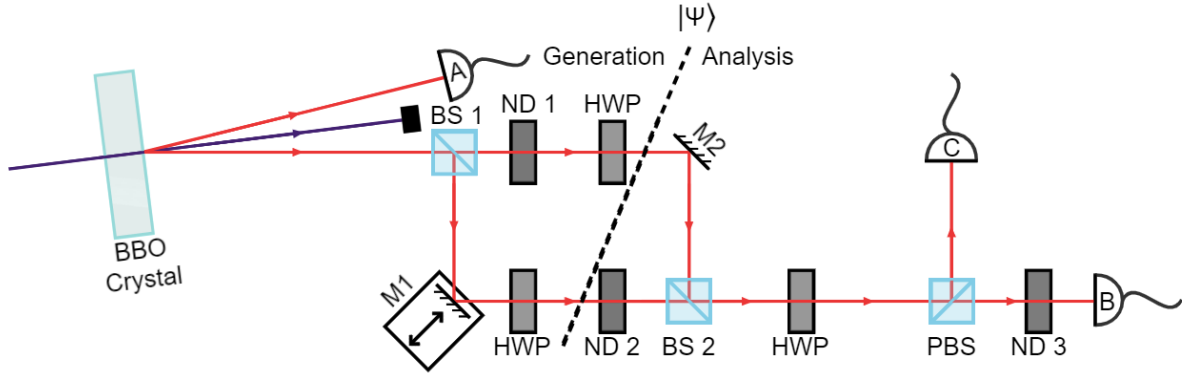


**Figure 3.** A simplified diagram of the setup used to generate single-photon entanglement.

### 3. Method

The ND filters are set such that the outputs of each of the beamsplitters are equal to generate single-photon path entanglement. Single photons are sent through the setup and the mirror mounted on the translation stage is then set such that the two arms of the MZ interferometer interfere coherently.

We follow the method outlined in Ref [4] to probe the state. The two paths within the MZ interferometer are set to be distinguishable. This is done using two HWP's within the interferometer, one of which, the lower path, has fast axis its set to a  $45^\circ$  angle with respect to vertical. This results in the two arms within the MZ interferometer having orthogonal polarisations and  $|\Psi\rangle = \frac{1}{\sqrt{2}} (|H\rangle_1 |0\rangle_2 + |0\rangle_1 |V\rangle_2)$ . When recombining the two paths at the analysis stage the output state after BS 2 is given by

$$|\Psi'\rangle = \frac{1}{\sqrt{2}} (|H\rangle + e^{i\phi} |V\rangle), \quad (1)$$

where  $\phi$  is the phase gained inside the MZ. However, since the paths were set such that they interfere coherently,  $\phi = 0$ . This results in equal detections in detectors *B* and *C*. Since equal frequency of detection is present, equal probability can be inferred for detection. The HWP located outside of the MZ interferometer is then used to interfere the output of the two paths to analyse the state further by rotating the angle of the HWP with respect to vertical. This produces the final state

$$|\Psi''\rangle = \frac{1}{\sqrt{2}} \left( (\cos 2\theta |H\rangle + \sin 2\theta |V\rangle) + (\sin 2\theta |H\rangle - \cos 2\theta |V\rangle) \right), \quad (2)$$

where  $\theta$  is the change of the angle of the fast axis of the HWP.

### 4. Results and Discussion

A second-order correlation ( $g^{(2)}$ ) test is performed to ensure all experiments are done using single photons. This test found  $g^{(2)} = 0.0043 \pm 0.0019$  which is well within the bound  $g^{(2)} \leq 0.5$  to ensure single photons are present [5].

When interfering the output of the two paths it is expected that the output state  $|\Psi''\rangle$  will behave as shown in Table 1. In Table 1 the output state fluctuates from equal detections in *B* and *C* to full detections in one, back to equal detections and then full detections in the other.

Comparing the prediction in Table 1 to the data obtained in Fig. 4, the same oscillation can be seen where the number of detected photons alternates between  $|H\rangle$  polarisation to  $|V\rangle$

**Table 1.** Theoretical prediction of what is expected when sending the  $|\Psi'\rangle = |+\rangle$  state through a HWP at angle  $\theta$ . Where  $|+\rangle = \frac{1}{\sqrt{2}}(|H\rangle + |V\rangle)$ .

$\theta$	$ H\rangle$ mapping	$ V\rangle$ mapping	$ \Psi''\rangle$
$0^\circ$	$ H\rangle$	$- V\rangle$	$ -\rangle$
$22.5^\circ$	$ +\rangle$	$ -\rangle$	$ H\rangle$
$45^\circ$	$ V\rangle$	$ H\rangle$	$ +\rangle$
$67.5^\circ$	$- -\rangle$	$ +\rangle$	$ V\rangle$
$90^\circ$	$- H\rangle$	$ V\rangle$	$ -\rangle$

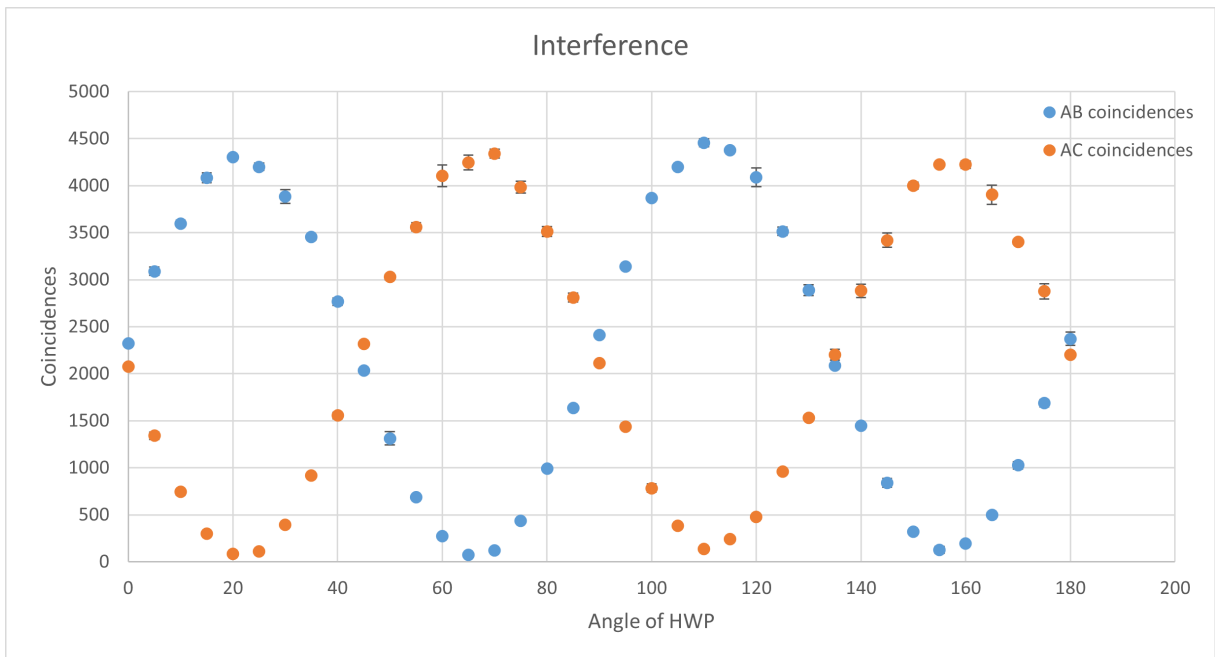


**Figure 4.** Interference data captured by increasing angle  $\theta$  by  $5^\circ$  increments over a 5s interval. Error bars represent the standard deviation of data at each angle.

polarisation, as seen by the change in number of detections in detectors  $B$  and  $C$  (coincidences with  $A$  within  $8ns$ ), which represent the detection of  $|H\rangle$  and  $|V\rangle$  polarisation photons.

The concurrence ( $C_N$ ) is determined to test the presence and the quality of the entanglement in the system. This is done using

$$C_N = V - \sqrt{y_c}, \quad (3)$$

for post-selected entanglement. In Eq. 3,  $V$  represents the visibility, which is a measure of the quality of the interference observed in Fig. 4, and  $y_c$  is a measure of the degree of contamination due to higher order interactions [4]. The visibility ( $V$ ) is determined by using

$$V = |P_{01} - P_{10}|, \quad (4)$$

where  $P_{10}$  and  $P_{01}$  are the normalised probabilities of a photon detection in path 1 or 2, respectively [4]. Determining  $y_c$  is done by using

$$y_c = 2 \left( \frac{N}{N-1} \right) \frac{p_0 p_2}{p_1^2}, \quad (5)$$

where  $N$  is the number of modes present in the system, in this case 2, and  $p_0$ ,  $p_1$  and  $p_2$  represent the probability of no photons, one photon and two photons being present in the MZ interferometer [4].

When using the data in Fig. 4 along with the given equations it is found that  $V = 0.9647 \pm 0.5684 \times 10^{-3}$ , which implies high quality interference and  $y_c = 0.001284 \pm 0.003032$ . For entanglement to be present it is required that  $y_c \leq V^2$  [4]. The experimental value obtained for  $y_c$  is several orders of magnitude smaller than the required boundary for entanglement to be present. This implies the existence of entanglement in the system with low higher-order contamination. Finally it is found that  $C_N = 0.9499 \pm 0.03325$ , this implies the existence of high quality entanglement which could be used in quantum information protocols.

## 5. Conclusion

The results obtained imply the generation of high quality path entanglement, showing the setup was successful in its aim to generate path entanglement. This form of entanglement can now be applied in quantum communication, quantum sensing and quantum imaging applications.

Additionally, this shows that the method used here for the first time to quantify entanglement of SPDC single photons works well. This is proof that the method can now be applied to other types of single photon sources and multimode cases.

## References

- [1] Nielsen M A, Chuang I L 2010 *Quantum computation and quantum information* (Cambridge: Cambridge press).
- [2] Horodecki R, Horodecki P, Horodecki M and Horodecki K 2009 *Rev. Mod. Phys.* **81**, 865–942.
- [3] Masanes L, Liang Y and Doherty A C 2008 *Phys. Rev. Lett.* **100** 090403.
- [4] Papp S B, Choi K S, Deng H, Lougovski P, van Enk S J and Kimble H J 2009 *Science* **324**, 764–68.
- [5] Loudon R 2000 *The Quantum Theory of Light* (Oxford: Oxford University Press).
- [6] van Enk S J 2006 *Phys. Rev. A* **74** 026302.

## Photobiomodulation at 830 nm influences diabetic wound healing *in vitro* through modulation of inflammatory cytokines

T N Mgwenya, H Abrahamse and N N Houreld

Laser Research Centre, Faculty of Health Sciences, University of Johannesburg, P.O Box 17011, Doornfontein, South Africa, 2028

E-mail: [nhoureld@uj.ac.za](mailto:nhoureld@uj.ac.za)

**Abstract.** Diabetes remains a global challenge, associated with delayed wound healing due to increased oxidative stress and pro-inflammatory cytokines. Photobiomodulation (PBM) induces wound healing through diminishing inflammation and oxidative stress and has been successfully used for healing diabetic ulcers *in vivo*. This study investigated the effects of PBM at 830 nm and a fluence of 5 J/cm<sup>2</sup> on inflammation in an *in vitro* diabetic wounded cell model. To achieve this, fibroblast cells were cultured under hyperglycaemic conditions, wounded via the central scratch, irradiated, and incubated for 24 h and 48 h. Pro-inflammatory cytokines (interleukin-6, IL-6; tumour necrosis factor-alpha, TNF- $\alpha$ ; and cyclooxygenase-2, Cox-2) were measured using ELISA. Post-PBM there were no significant changes in IL-6 and Cox-2 at both 24 and 48 h; the only significant change was the increase in TNF- $\alpha$  at 24 h. Despite TNF- $\alpha$  and Cox-2 being pro-inflammatory cytokines, they have been found to promote healing in the early stages of wound healing. PBM at 830 nm with 5 J/cm<sup>2</sup> does not appear to influence inflammation in a diabetic wounded cell model as measured by IL-6 and Cox-2.

### 1. Introduction

Diabetes Mellitus (DM) remains a global health concern. According to the International Diabetes Federation (IDF), 537 million adults between the ages of 20 and 79 were living with diabetes worldwide in 2021, and this is predicted to reach 643 million by 2030 and 783 million by 2045 [1]. DM is linked to complicated wound healing. Diabetic foot ulcers (DFUs) are common in patients living with type-2 DM. Infection, ulcer formation, and deep-tissue necrosis are the most common complications that contribute to chronic wounds in type-2 DM patients due to the combination of neuropathy and various degrees of peripheral vasculopathy [2]. A high glucose environment causes difficulty in wound healing [3]. Diabetic wounds are often associated with increased inflammation, reduced fibroblasts (essential cells for wound repair) and cellular proliferation, and decreased cytokine and growth factor production [4].

Current treatments for chronic wounds remain ineffective to some degree, with a high rate of failure and relapse. Only a 50% healing rate is achieved [5]. This demonstrates the need to research and develop new therapies, including photobiomodulation (PBM), and a better understanding of their underlying cellular and molecular effects on diabetic wound healing. Several studies have been conducted on PBM, and many of these have demonstrated the benefits of PBM on wound healing [6,7,8,9]. However, the accepted working parameters of PBM (wavelength/s, fluencies, and duration) on wound healing have

not been adequately optimized. PBM is typically used in the red and near-infrared (NIR) electromagnetic spectrum, with most *in vitro* studies conducted in the red spectrum [7]. There are few reports on PBM at 830 nm as an approach to enhance wound healing in diabetic patients [10]. The current study investigates the effects of PBM at 830 nm with a fluence of 5 J/cm<sup>2</sup> on a diabetic wounded cell model with a specific focus on three inflammatory markers (Cox-2, TNF- $\alpha$ , and IL-6). The study will contribute to a better understanding of the underlying molecular mechanisms of PBM and provide an understanding of the role of PBM at 830 nm on inflammatory cytokines in diabetic wound healing.

## 2. Materials and methods

### 2.1. Cell culture

A human skin fibroblast cell line, commercially purchased from the American Type Culture Collection (WS1, ATCC® CRL-1502™) was used in this study. The cell line was cultured under standard conditions in minimum essential medium (MEM) supplemented with 1 mM sodium pyruvate, 0.1 mM non-essential amino acids (NEAA), 2 mM L-glutamine, 1% penicillin-streptomycin, 1% amphotericin B, and 10% fetal bovine albumin (FBS) and incubated at 37°C, 5% CO<sub>2</sub> and a humidity of 85%.

The study focused on the influence of PBM on a diabetic wounded cell model. To achieve a diabetic cell model *in vitro*, WS1 cells were continuously grown in supplemented MEM (basal glucose concentration of 5.6 mM) with an additional 17 mM D-glucose [7, 8, 9, 11]. Thus, cells are grown for several passages before experiments in 22.6 mM glucose. Cell passages from 9 to passage 15 were used. For experiments, cells were seeded at a density of  $6 \times 10^5$  into 3.4 cm diameter culture dishes for 24 h to allow for attachment. To achieve a diabetic wounded model, a ‘wound’ was created by the central scratch assay [8, 12, 13]. A cell-free zone (‘wound’) with cells on either side and a wound margin was created in the cell monolayer by scraping the confluent cell layer with a 1 mL sterile pipette.

### 2.2. Laser irradiation

Thirty minutes post ‘wounding’, cells were irradiated using a laser in the Laser Research Centre (LRC) laboratory, set up by the Council for Scientific and Industrial Research (CSIR)/National Laser Centre (NLC), at an emission wavelength of 830 nm. Laser irradiation at 830 nm and a fluence of 5 J/cm<sup>2</sup> stimulates WS1 cells [9]. Table 1 provides the laser parameters used in this study.

**Table 1.** Laser parameters. Irradiation time is based on the calculation Dose (J/cm<sup>2</sup>) = Intensity (W/cm<sup>2</sup>) x Time (s).

Variables	Diode Laser
Wavelength (nm)	830
Wave emission	Continuous wave
Power output (mW)	106
Power output density (mW/cm <sup>2</sup> )	11.65
Spot size (cm <sup>2</sup> )	9.1
Irradiation time (s)	429
Fluence (J/cm <sup>2</sup> )	5
Energy (J)	45.5

WS1 human fibroblast cells were irradiated via fiber optics from above with the culture dish lid off and in the dark to prevent any light interference. Non-irradiated cells (0 J/cm<sup>2</sup>) served as controls. The laser irradiation effects were determined by looking at various cellular responses analyzed after 24 h and 48 h incubation. This was evaluated by studying the morphology and migration of cells and conducting biochemical assays to determine levels of inflammatory cytokines.

### 2.3. Morphological changes and migration rate

Morphological changes were determined using inverted light microscopy (Olympus CKX41), and images were taken using analysis getIT software. Three biological repeats ( $n=3$ ) were performed for this experiment per time interval (0 h, 24 h, and 48 h). The distance/wound gap width ( $\mu\text{m}$ ) between the edges/wound margins of the cell free zone was measured three times in each cell culture plate in the same position and cellular migration rate was determined [13, 14].

### 2.4. Quantitative analysis of inflammatory cytokines

The Enzyme-Linked Immunosorbent Assay (ELISA) was used to detect levels of the inflammatory markers (Cox-2, IL-6, and TNF- $\alpha$ ) released by cells ( $n=3$ ) into the surrounding culture media. The human Cox-2 ELISA kit (Sigma-Aldrich, RAB1034), human TNF- $\alpha$  ELISA kit (Sigma-Aldrich, RAB0476), and human IL-6 ELISA kit (Sigma-Aldrich, RAB0306) were used to determine the levels of the three inflammatory cytokines as per the manufacturer's instructions. All reagents and samples were brought to room temperature (18–25°C) to thaw before use. The standards and culture media samples (100  $\mu\text{L}$ ) were added in duplicate to their appropriate wells on a coated 96-well microplate, covered with microplate sealer, and incubated at 4°C with gentle shaking overnight.

Following overnight incubation, the standards and samples were discarded, and the plates washed four times with sample wash buffer (diluted 5-fold in distilled water). A biotinylated detection antibody (100  $\mu\text{L}$  diluted 80-fold in assay diluent buffer) was added to each well, and plates were incubated for 1 h at room temperature with gentle shaking. The wash step was repeated as described previously, and freshly prepared horseradish peroxidase (HRP)-Streptavidin solution (diluted 600-fold in assay diluent buffer) was added (100  $\mu\text{L}$ ) to each well and incubated for a further 45 min at room temperature with gentle shaking. The wash step was repeated and ELISA colorimetric 3,3',5,5'-tetramethylbenzidine (TMB) reagent (100  $\mu\text{L}$ ) added to each well. The plates were incubated for 30 min in the dark with gentle shaking at room temperature. To each well, 50  $\mu\text{L}$  of stop solution was added and absorbance was read immediately at 450 nm using a multiplate reader (Perkin Elmer, Victor<sup>3</sup> 1420).

### 2.5. Statistical analysis

Experiments were conducted in triplicate (biological repeats,  $n = 3$ ), and assays in duplicate (technical repeats). SigmaPlot version 12.0 was used for statistical analysis and to create graphs showing the mean and standard error of the biochemical assay conducted. To identify statistical variances between the experimental and control groups, the student t-test was applied. When values were less than 0.05, the results were deemed significant ( $P < 0.001^{***}$ ,  $P < 0.01^{**}$ , and  $P < 0.05^*$ ).

## 3. Results and discussion

### 3.1. Morphological changes and migration rate

Skin can regenerate and create a collagenous scar to replace lost or damaged tissue. Fibroblast cells follow the patterns of migration as a loosely connected population. Figure 1 depicts typical fibroblast morphology, with cells appearing long and spindle shaped. At 0 h non-irradiated (0  $\text{J}/\text{cm}^2$ ) and irradiated (5  $\text{J}/\text{cm}^2$ ) cells did not show morphological changes. At 24 h both models showed changes in growth direction and cellular projections towards the central scratch, however the irradiated cell model started to show increased cell confluency with fewer gaps compared to non-irradiated cells. At 48 h the central scratch was completely closed with increased cell confluence in irradiated cells, while open gaps were still visible in the control cells. The irradiated DW model at 48 h showed an increase in cell orientation and cell movement across the central scratch when compared to all other time intervals.

The migration rate of irradiated cells was increased as compared to their controls across all time intervals (figure 2). At 24 h (figure 2a), a significant ( $P < 0.001$ ) increase in cell migration rate was noted in irradiated cells compared to non-irradiated cells. The migration rate in irradiated cells was 75%

as compared to 49% in control cells. Although not significant ( $P = 0.124$ ), at 48 h irradiated cells showed a migration rate of 100% compared to non-irradiated cells which were at 95 % migration rate (figure 2b).

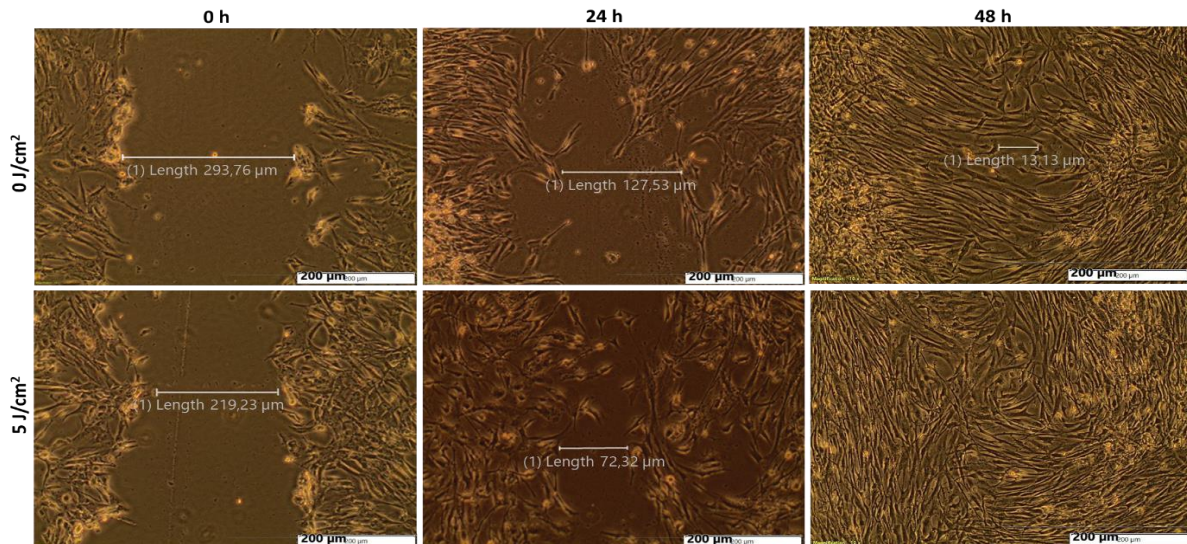


**Figure 2.** Morphological changes and cellular migration of diabetic wounded (DW) cell models post-irradiation captured at. Non-irradiated cells showed no significant morphological changes while irradiated cells showed an increase in migration and projection towards the central scratch, with increased cell movement at 48 h.

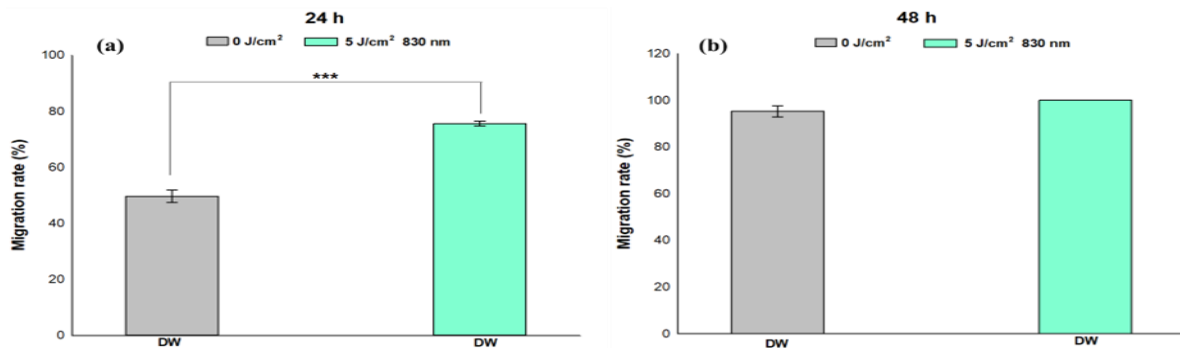


**Figure 1.** Migration rate (%) of diabetic wounded (DW) cell models. Cells showed a higher migration rate at 24 h in irradiated cells compared to non-irradiated cells. Statistical significance is presented as \*\*\* $P < 0.01$  ( $\pm$ SEM).

### 3.2. Quantitative analysis of inflammatory cytokines

ELISA was used to quantitatively measure the levels of human Cox-2, human IL-6, and human TNF- $\alpha$ . There were no significant changes in Cox-2 at 24 h ( $P = 0.642$ ) and 48 h ( $P = 0.137$ ) post-irradiation (figure 3a and b). Despite being a pro-inflammatory cytokine, Cox-2 has been found to promote healing in the early stages of wound healing [16, 17], and the Cox-2 pathway is an integral component of inflammation. Cox-2 is also thought to be an immediate gene product that can be produced quickly but only temporarily [18]. IL-6 levels in irradiated cells initially increased ( $P = 0.842$ ) at 24 h, but this increase was not statistically significant (figure 3c). Although not statistically significant ( $P = 0.680$ ), the levels of IL-6 decreased at 48 h (figure 3d).

TNF- $\alpha$  levels were initially increased in irradiated DW cells at 24 h ( $P < 0.05$ ), however, these levels decreased at 48 h, but the difference was not significant ( $P = 0.541$ ) (figures 3e and f). Like Cox-2, TNF-

$\alpha$  is a pro-inflammatory cytokine that has been found to promote healing in the early stages of wound healing [19]. A similar study conducted by our research group on WS1 human fibroblast cells at a wavelength of 660 nm with a fluence of 5 J/cm<sup>2</sup> also found a decrease in TNF- $\alpha$  levels in diabetic wounded groups at 48 h post-irradiation [19]. TNF- $\alpha$  is released by cells like endothelial cells, keratinocytes, and fibroblasts in the injured area immediately when an injury occurs to promote healing [20], which could explain the rise in TNF- $\alpha$  levels observed at 24 h.

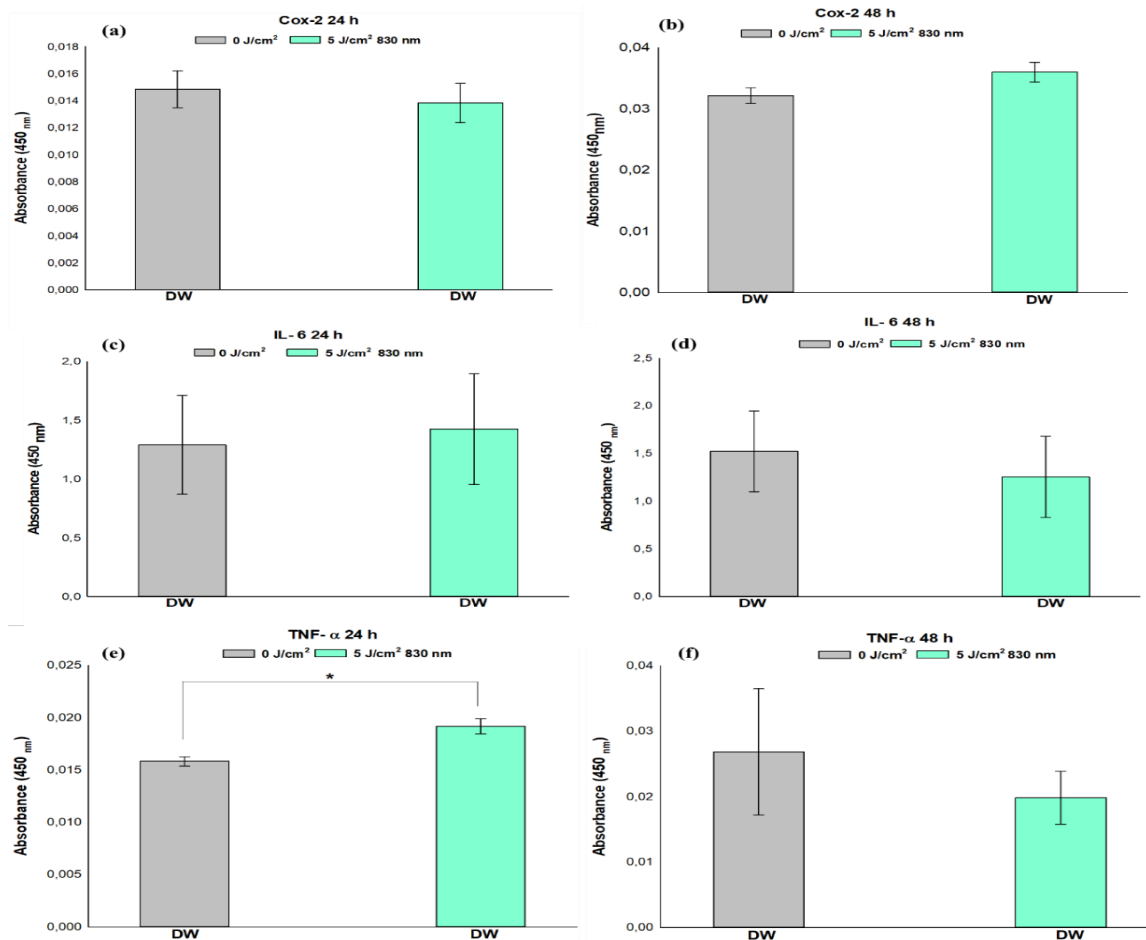


**Figure 3.** Post-irradiation analysis of the inflammatory cytokines human Cox-2, human IL-6, and human TNF- $\alpha$  in a diabetic wounded (DW) cell model at 24 h and 48 h. Non-irradiated samples served as controls. Statistical significance is presented as \* $P < 0.05$  ( $\pm$ SEM).

The creation of extracellular matrix proteins and matrix metalloproteinase, essential for the repair of injured tissues, as well as the activity of fibroblasts, vascular endothelial cells, and keratinocytes are predominantly regulated by elevated TNF- $\alpha$  levels [20]. Additionally, during the inflammatory phase, the primary cellular sources of TNF- $\alpha$  are converted into recruited neutrophils and macrophages, and this process results in a positive recruitment boost for extending the inflammatory responses [20]. This is supported by the decreased TNF- $\alpha$  levels seen at 48 h in the current study, which is also supported by the wound closing observed in the morphological and migration studies. Although our current study was conducted *in vitro*, the results obtained are similar to the *in vivo* study by Ritsu *et al* [20] which used a mouse model with full-thickness skin wounds to examine the role of TNF- $\alpha$  in the early process of wound healing. TNF- $\alpha$  was detected shortly after the creation of the wound, increased after the first few hours, peaked in 24 h, and then decreased to the basal level.

#### 4. Conclusion

The study observed migratory effects on the DW cell model exerted by the administration of PBM at 830 nm with a fluence of 5 J/cm<sup>2</sup>. This was observed in the irradiated diabetic wounded model as they showed more cell presence in the central scratch and a higher migration rate. PBM at 830 nm with 5 J/cm<sup>2</sup> had no effect on Cox-2 and IL-6 in diabetic wounded cells *in vitro*. PBM may exert healing by stimulating the early phases of wound healing by increasing TNF- $\alpha$  levels, which decrease with the passage of time.

#### Acknowledgments

This work is based on the research supported by the South African Research Chairs Initiative of the Department of Science and Technology (DST) and National Research Foundation (NRF) of South Africa (Grant No 98337), the NRF (Grant No 129327), as well as grants received from the University of Johannesburg research council (URC), and the Council for Scientific and Industrial Research (CSIR) /National Laser Centre (NLC) Laser Rental Pool Program.

#### References

- [1] International Diabetes Federation, IDF 2021 Diabetes Atlas, 10th edition, available from <https://https://diabetesatlas.org/> Accessed on 16/08/22
- [2] Baig M S, Banu A, Zehravi M, Rana R, Burle S S, Khan S L, Islam F, Siddiqui F A, Massoud E E S, Rahman M H and Cavalu S 2022 *Life* **12** doi: 10.3390/life12071054
- [3] Spampinato SF Caruso GI De Pasquale R Sortino MA and Merlo S 2020 *Pharmaceuticals (Basel)* **13** 60 doi: 10.3390/ph13040060
- [4] Patel S, Srivastava S, Singh M R and Singh D 2019 *Biomed. Pharmacother.* **112** 108615
- [5] Frykberg R G and Banks J 2015 *Adv. Wound Care* **4** 560-82
- [6] Mignon C Uzunbajakava NE Castellano-Pellicena I Botchkareva NV Tobin DJ 2008 *Lasers Surg. Med.* **50** 859–882
- [7] Ayuk S M, Houreld N N and Abrahamse H 2012 *Diabetes Technol. Ther.* **14** 1110–7
- [8] Houreld N and Abrahamse H. 2010. *Diabetes Technol Ther.* **12** 971-78
- [9] Houreld N and Abrahamse H 2008 *Lasers Med Sci.* **23** 11-18
- [10] Tsai S R and Hamblin M R 2017 *J. Photochem Photobiol B* **170** 197-207
- [11] Houreld NN Sekhejane PR and Abrahamse H 2010 *Lasers Surg. Med.* **42** 494–502
- [12] Houreld N, Sekhejane P R and Abrahamse H 2010 *Proc. Int. Conf. on WALT (Norway)* **1** (Bologna/ ScienceMED) 23-26
- [13] Liang C C, Park A Y and Guan J L 2007 *Nat. Protoc.* **2** 329-33
- [14] Felice F, Zambito Y, Belardinelli E, Fabiano A, Santoni T and Di Stefano R 2015 *Int. J. Biol. Macromol.* **76** 236–241
- [15] Wilgus T A, Bergdall V K, Tober K L, Hill K J, Mitra S, Flavahan N A and Oberyzyzn T M 2004 *Am J. Pathol.* **165** 753-61
- [16] Szweda M, Rychlik A, Babińska I and Pomianowski A 2019 *J. Vet Res.* **63** 215-24
- [17] Piipponen M, Li D and Landén N X 2020 *Int J Mol Sci.* **21** 8790 doi: 10.3390/ijms21228790
- [18] Ashcroft G S, Jeong M J, Ashworth JJ, Hardman M and Jin W 2013 *Wound Repair Regen.* **20** 38-49
- [19] Shaikh-Kader A, Houreld N N, Rajendran N K and Abrahamse H 2021 *Oxid. Med. Cell. Longev.* **2021** doi:10.1155/2021/6667812
- [20] Ritsu M, Kawakami K, Kanno E, Tanno H, Ishii K, Imai Y, Maruyama R and Tachi M 2017 *J. Dermatology Dermatologic Surg.* **21** 14-19



DIVISION

D

ASTROPHYSICS AND SPACE SCIENCE

# Interacting viscous dark cosmology

B.G Mbewe<sup>1</sup>, A Abebe<sup>2,3</sup>

<sup>1</sup>Centre for Space Research, North-West University, Potchefstroom 2520, South Africa

<sup>2</sup> Centre for Space Research, North-West University, Mahikeng 2745, South Africa

<sup>3</sup> National Institute for Theoretical and Computational Sciences (NITheCS), South Africa

E-mail: bonang.mbewe@gmail.com

**Abstract.** Observational data show that the universe is dominated by the dark sector, which is comprising of dark matter  $\rho_m$  and dark energy  $\rho_\Lambda$ . This is with a budget allocation of 25% to dark matter while dark energy is about 70%. Since most of the existing work in the literature is limited to the study of background cosmological dynamics, this project aims at deriving the equations that govern the evolution of a universe filled with interacting viscous dark fluids and analyzing their behaviour as compared to  $\Lambda$ CDM universe. The approach will be to model and derive the background cosmological equations of interacting viscous fluids using the little rip, pseudo rip and bounce cosmology models and compare the results obtained with that of  $\Lambda$ CDM cosmology.

## 1. Introduction

Studies show that the present universe is expanding in an accelerated fashion and this poses a great deal of great challenges to fundamental physics as well as cosmology [1, 2, 3]. The challenge of cosmic acceleration of the universe is due to the belief that most of the energy that exists in the universe, exists by a form of a new ingredient called dark energy which has a negative pressure. This notion has made its way into various theoretical models of dark energy being proposed, with the simplest model being the cosmological constant  $H_0$  with constant dark energy density and equation of state as  $w_\Lambda = \frac{p}{\rho_\Lambda} = -1$  [3].

The  $\Lambda$ CDM model is by far the simplest and observationally supported model, although it has two challenges being the fine-tuning problem and coincidence problem [1, 2, 4]. In fine-tuning the problem is that the the value of  $\Lambda$  is quite small as compared to the expectations of particle physicists, while in the coincidence problem we have, the fractional magnitude of the present energy density of dark matter  $\Omega_m$  and dark energy  $\Omega_\Lambda$  being of the same order [3, 5].

The coincidence problem can be alleviated by consideration of interaction of fluids amongst one another since dark components are expected to not evolve separately. However, the interaction is supposed to be negligible at high redshifts and to be important or significant at lower redshifts in a sense that it enables us to choose the correct form of interaction term that leads to an almost constant ratio between the energy density of dark matter and dark energy at low redshifts [2, 5].

The  $\Lambda$ CDM model is an idealized model which in practice is useful in many instances but in some instances incorrect such as coincidence and fine-tuning problems. This then gives way for taking into account the viscous effects more especially when considering turbulence effects; or many other relativistic situations [6]. Taken from a hydrodynamic stance, the viscosity effect describes the deviation of system from thermal equilibrium to the first order. Bulk viscosity in the cosmic fluid plays a significant role, even more so in the singularity phenomenon.

The objective of this article is to obtain the analytical solutions of the cosmological models that are induced by an inhomogeneous viscous fluid coupled with dark matter [7]. The article is structured as follows. In Section 2, we give equations that govern the evolution for viscous cosmological fluid coupled with dark matter. In Section 3, we discuss the little rip model and compare it to standard  $\Lambda$ CDM model. In Section 4, we discuss pseudo rip model in comparison to  $\Lambda$ CDM model. In Section 5 we discuss bounce cosmology and compare it to the  $\Lambda$ CDM model. We then present our concluding remarks in the last section.

## 2. Background equations for viscous coupled dark fluids

The background equations for viscous interacting dark fluids in FLRW metric is given in the following form as [7]:

$$\dot{\rho}_\Lambda + 3H(p + \rho_\Lambda) = -Q, \quad (2.1a)$$

$$\dot{\rho}_d + 3H\rho_d = Q, \quad (2.1b)$$

$$\dot{H} = -\frac{\kappa^2}{2}(\rho_d + \rho_\Lambda + p), \quad \text{with } \kappa^2 = 8\pi G. \quad (2.1c)$$

Here  $\rho$  denotes energy density of dark fluid components and  $p$  the isotropic pressure, while the subscripts ‘‘ $\Lambda$ ’’ and ‘‘ $d$ ’’ refer to dark energy and dust matter (comprising of dark matter and baryonic matter) respectively. A dot represents a differentiation with respect to cosmic time while exchange of energy between dark energy and dust matter is denoted by  $Q$  given by

$$Q = \delta H \rho_d, \quad (2.2)$$

with  $\delta > 0$  a constant.

We also have the expression for equation of state (E.O.S) given in inhomogeneous form as:

$$p = w\rho_\Lambda - 3H\zeta, \quad (2.3)$$

where  $\zeta$  is the bulk viscosity and  $w$  being the E.O.S parameter which is given by

$$w = A_0\rho_\Lambda^{\alpha-1} - 1, \quad (2.4)$$

with  $A_0 \neq 0$  and  $\alpha \geq 1$  being constants.

The Hubble parameter in terms of the scale factor is given as follows:

$$H = \frac{\dot{a}}{a}, \quad (2.5)$$

$$a = \frac{a_0}{1+z} = \frac{1}{1+z}, \quad \text{where } a_0 = 1.$$

Here  $z$  is the cosmological redshift while  $a_0$  is the scale factor evaluated at present time ( $z = 0$ ). Substituting equation (2.2) into (2.1) we obtain:

$$\dot{\rho}_\Lambda + 3H(p + \rho_\Lambda) = -\delta H \rho_d, \quad (2.6a)$$

$$\dot{\rho}_d + 3H\rho_d = \delta H \rho_d, \quad (2.6b)$$

$$\dot{H} = -\frac{\kappa^2}{2}(\rho_d + \rho_\Lambda + p), \quad (2.6c)$$

and equation (2.4) into (2.3)

$$\begin{aligned} p &= A_0 \rho_\Lambda^\alpha - \rho_\Lambda - 3H\zeta, \\ p + \rho_\Lambda &= A_0 \rho_\Lambda^\alpha - 3H\zeta. \end{aligned} \quad (2.7)$$

And finally, substituting equation (2.7) into (2.6)

$$\dot{\rho}_\Lambda + 3H(A_0 \rho_\Lambda^\alpha - 3H\zeta) = -\delta H \rho_d, \quad (2.8a)$$

$$\dot{\rho}_d + 3H\rho_d = \delta H \rho_d, \quad (2.8b)$$

$$\dot{H} = -\frac{\kappa^2}{2}(\rho_d + \rho_\Lambda + p). \quad (2.8c)$$

We parametrize bulk viscosity as given by [5, 8]:

$$\zeta = \eta H_0 \left( \frac{\rho_d}{\rho_{d0}} \right)^m. \quad (2.9)$$

Here  $m$ ,  $\eta$  are positive dimensionless quantities with  $\eta$  being a coefficient of bulk viscosity and  $H_0$  is the Hubble constant. From Friedmann-Lemaître-Robertson-Walker (FLRW) metric the Friedmann equation for a universe composed of only dark fluid components, reads as follows for a flat universe:

$$3H^2 = \kappa^2(\rho_d + \rho_\Lambda) \implies 1 = \frac{\kappa^2}{3H^2}(\rho_d + \rho_\Lambda). \quad (2.10)$$

Substituting equation (2.9) into equation (2.8a) we obtain the generalized conservation equation of dark energy in redshift space as:

$$\rho'_\Lambda - \frac{3A_0}{1+z}\rho_\Lambda^\alpha = \frac{\delta}{1+z}\rho_d - \frac{9\eta H_0^2}{1+z} \left( \frac{\rho_d}{\rho_{d0}} \right)^m h, \quad (2.11)$$

and conservation equation of dust matter in redshift space as:

$$\rho'_d = \frac{3-\delta}{1+z}\rho_d. \quad (2.12)$$

Here superscript  $'$  represents differentiation with respect to redshift,  $h \equiv \frac{H}{H_0}$  is a normalized Hubble parameter and in this paper we will be solving equation (2.11), for  $\alpha = 1$  to simplify and reduce our equation such that the solution to it can be easily obtained analytically, otherwise ( $\alpha \neq 1$ ) numerical methods will need to be used. By inspection from equations (2.8,2.9), the  $\Lambda$ CDM model can be recovered if and only if, the following conditions are met:

- $\delta = 0 \implies Q = 0$ . This takes care of decoupling the fluids so that they can evolve separately.
- $\eta = 0 \implies \zeta = 0$ . The exotic fluid is allowed/permitted to be non-viscous.
- $A_0 = 0 \implies w = -1$ . Dark energy is now having a negative pressure together with the above condition 2, which is the driving force behind the accelerating expansion of the universe.

### 3. Little rip model

Little rip is characterized by an increasing Hubble parameter but in an asymptotic sense in remote time [7]. We have chosen a toy model for the Hubble parameter that describes little rip attributes as follows:

$$H(z) = H_0 - \lambda \ln(1+z) \implies h \equiv \frac{H}{H_0} = 1 - h_1 \ln(1+z), \quad (3.1)$$

where  $\lambda > 0$  and  $h_1 = \frac{\lambda}{H_0}$  are constants. By integrating equation (2.11,2.12), the analytical expression for dust matter and dark energy is given by:

$$\left\{ \begin{array}{l} \rho_d = \rho_{d0}(1+z)^{3-\delta}, \\ \rho_\Lambda = \delta\rho_{d0} \left\{ \frac{(1+z)^{3-\delta}}{3(1-A_0) - \delta} \right\} \\ \quad - 9\eta H_0^2 \left\{ \frac{(1+z)^{m(3-\delta)}}{[3(m-A_0) - m\delta]^2} \left[ 3(m-A_0) - m\delta - h_1 \left( \ln |(1+z)|^{3(m-A_0)-m\delta} - 1 \right) \right] \right\} \\ \rho_{\Lambda 0}(1+z)^{3A_0} - \frac{\delta\rho_{m0}}{3(1-A_0) - \delta} (1+z)^{3A_0} + \frac{9\eta H_0^2}{[3(m-A_0) - m\delta]^2} [3(m-A_0) - m\delta + h_1] (1+z)^{3A_0}. \end{array} \right. \quad (3.2)$$

Using fractional energy density parameter  $\rho_i = 3H^2\Omega_i$  where  $i = d, \Lambda$ , equation (3.2) can be given in dimensionless form as:

$$\left\{ \begin{array}{l} \Omega_d = \frac{1}{h^2} (1+z)^{3-\delta}, \\ \Omega_\Lambda = \frac{1}{h^2} \left\{ \frac{\delta\Omega_{d0}(1+z)^{3-\delta}}{3(1-A_0) - \delta} - \frac{3\eta(1+z)^{m(3-\delta)}}{[3(m-A_0) - m\delta]^2} \left[ 3(m-A_0) - m\delta - h_1 \left( \ln |(1+z)|^{3(m-A_0)-m\delta} - 1 \right) \right] \right\} \\ \quad + \Omega_{\Lambda 0}(1+z)^{3A_0} - \frac{\delta\Omega_{d0}(1+z)^{3A_0}}{3(1-A_0) - \delta} + \frac{3\eta(1+z)^{3A_0}}{[3(m-A_0) - m\delta]^2} [3(m-A_0) - m\delta + h_1] \left. \right\}. \end{array} \right. \quad (3.3)$$

It can be noted with equations (3.2,3.3) that once we let  $\delta = 0, A_0 = 0$  and  $\eta = 0$  then the  $\Lambda$ CDM case is recovered as  $\rho_d \approx a^{-3}$ . Also, for dark energy, we obtain  $\rho_\Lambda \approx \rho_{\Lambda 0} = \text{constant}$ . For a flat universe composed entirely of dark components the fractional energy density is given by ( $\Omega_d + \Omega_\Lambda = 1$ ). Using this relation of fractional energy density, we obtain the expression of Hubble parameter for little rip as:

$$\begin{aligned} h^2 = & \Omega_{d0} \left( \frac{3(1-A_0)}{3(1-A_0) - \delta} \right) \left( (1+z)^{3-\delta} - (1+z)^{3A_0} \right) \\ & - \frac{3\eta}{[3(m-A_0) - m\delta]^2} \left[ (1+z)^{m(3-\delta)} \left( 3(m-A_0) - m\delta - h_1 \left( \ln |(1+z)|^{3(m-A_0)-m\delta} - 1 \right) \right) \right. \\ & \left. - (1+z)^{3A_0} \left( 3(m-A_0) - m\delta + h_1 \right) \right] + (1+z)^{3A_0}. \end{aligned} \quad (3.4)$$

It can be seen that once again, that when the  $\Lambda$ CDM condition are called, then equation (3.4) takes the form,  $h^2 = \Omega_{d0}(1+z)^3 + \Omega_{\Lambda 0}$ . Furthermore, the equation that governs the evolution of deceleration parameter for the model is given by:

$$\begin{aligned}
q = & -1 + \frac{1}{2h^2} \left[ \Omega_{d0} \left( \frac{3(1-A_0)}{3(1-A_0)-\delta} \right) \left\{ (3-\delta)(1+z)^{3-\delta} - 3A_0(1+z)^{3A_0} \right\} + 3A_0(1+z)^{3A_0} \right. \\
& - \frac{3\eta}{[3(m-A_0)-m\delta]^2} \left\{ m(3-\delta)(1+z)^{m(3-\delta)} \left( 3(m-A_0) - m\delta - h_1 \left( \ln |(1+z)^{3(m-A_0)-m\delta}| - 1 \right) \right) \right. \\
& \left. \left. + (1+z)^{m(3-\delta)} \left( -h_1(3(m-A_0)-m\delta) \right) - 3A_0(1+z)^{3A_0} (3(m-A_0) - m\delta + h_1) \right\} \right]. \tag{3.5}
\end{aligned}$$

When we apply the  $\Lambda$ CDM conditions mentioned in Section 2, indeed the deceleration parameter for  $\Lambda$ CDM is recovered which is of the form  $\left( q = \frac{\frac{3}{2}\Omega_{d0}(1+z)^3}{\Omega_{d0}(1+z)^3 + \Omega_{\Lambda 0}} - 1 \right)$ .

#### 4. Pseudo rip model

The pseudo rip model is a model characterized by the Hubble parameter that tends to a de Sitter space in the remote future [7]. We take a toy model to represent the analogue of pseudo rip as given below:

$$h = \frac{H}{H_0} = \sqrt{2 \left[ 1 + \ln \left( \frac{H_1}{H_0} \right) - \frac{H_1}{H_0} + \frac{\lambda \ln(1+z)}{H_0} \right]}, \tag{4.1}$$

where  $H_0 > H_1$  and  $\lambda$  are positive constants. By integrating equation (2.11,2.12), the analytical expression for dust matter and dark energy is given by:

$$\left\{ \begin{aligned}
& \rho_d = \rho_{d0}(1+z)^{3-\delta}, \\
& \rho_\Lambda = \frac{\delta\rho_{d0}}{3(1-A_0)-\delta} \left[ (1+z)^{3-\delta} - (1+z)^{3A_0} \right] + \rho_{\Lambda 0}(1+z)^{3A_0} \\
& \quad - 9\eta H_0^2 (1+z)^{3A_0} \left[ \frac{\exp \left[ \frac{3(m-A_0)-m\delta}{2h_1} \right]}{h_1 \exp(2(1+\ln h_2 - h_2))} \right] \\
& \quad \left\{ \sqrt{2 \left( h_1 \ln(1+z) + \ln h_2 - h_2 + 1 \right)} \exp \left[ 2 \left( h_1 \ln(1+z) + \ln h_2 - h_2 + 1 \right) \right] \right. \\
& \quad \left. - \sqrt{2 \left( \ln h_2 - h_2 + 1 \right)} \exp \left[ 2 \left( \ln h_2 - h_2 + 1 \right) \right] \right\}.
\end{aligned} \right. \tag{4.2}$$

Here  $h_2 = \frac{H_1}{H_0}$  and  $h_1 = \frac{\lambda}{H_0}$ . Using fractional energy density parameter, equation (4.2) can be

given in dimensionless form as:

$$\left\{ \begin{array}{l} \Omega_d = \frac{1}{h^2}(1+z)^{3-\delta}, \\ \Omega_\Lambda = \frac{1}{h^2} \left\{ \frac{\delta\Omega_{d0}}{3(1-A_0)-\delta} \left[ (1+z)^{3-\delta} - (1+z)^{3A_0} \right] + \Omega_{\Lambda 0}(1+z)^{3A_0} \right. \\ \quad \left. - 3\eta \left[ \frac{\exp\left(\frac{3(m-A_0)-m\delta}{2h_1}\right)}{h_1 \exp[2(1+\ln h_2 - h_2)]} \right] \right. \\ \quad \left. \left( \sqrt{2\left(h_1 \ln(1+z) + \ln h_2 - h_2 + 1\right)} \exp\left[2\left(h_1 \ln(1+z) + \ln h_2 - h_2 + 1\right)\right] \right) \right. \\ \quad \left. \left. - \sqrt{2\left(\ln h_2 - h_2 + 1\right)} \exp\left[2\left(\ln h_2 - h_2 + 1\right)\right] \right) \right\}. \end{array} \right. \quad (4.3)$$

It can be seen that by calling all the conditions required to recover the  $\Lambda$ CDM case, that indeed equations (4.2,4.3) reduce to  $\Lambda$ CDM case, where  $\rho_d \approx a^{-3}$  and  $\rho_\Lambda \approx \rho_{\Lambda 0} = \text{Constant}$ . For a flat universe composed of dark components only, we have the Hubble parameter given by:

$$\begin{aligned} h^2 = & \frac{\Omega_{d0}}{3(1-A_0)-\delta} \left[ 3(1-A_0)(1+z)^{3-\delta} - \delta(1+z)^{3A_0} \right] + \Omega_{\Lambda 0}(1+z)^{3A_0} \\ & - 3\eta \left[ \frac{\exp\left(\frac{3(m-A_0)-m\delta}{2h_1}\right)}{h_1 \exp[2(1+\ln h_2 - h_2)]} \right] \\ & \left\{ \sqrt{2\left(h_1 \ln(1+z) + \ln h_2 - h_2 + 1\right)} \exp\left[2\left(h_1 \ln(1+z) + \ln h_2 - h_2 + 1\right)\right] \right. \\ & \left. - \sqrt{2\left(\ln h_2 - h_2 + 1\right)} \exp\left[2\left(\ln h_2 - h_2 + 1\right)\right] \right\}. \end{aligned} \quad (4.4)$$

Once again, when the  $\Lambda$ CDM conditions are called, then equation (3.4) takes the form,  $h^2 = \Omega_{d0}(1+z)^3 + \Omega_{\Lambda 0}$ . Furthermore, the equation that governs the evolution of deceleration parameter for the model is given by:

$$\begin{aligned} q = & \frac{1}{2h^2} \left\{ \frac{\Omega_{d0}}{3(1-A_0)-\delta} \left[ 3(1-A_0)(3-\delta)(1+z)^{3-\delta} - 3A_0\delta(1+z)^{3A_0} \right] \right. \\ & \left. + 3A_0\Omega_{\Lambda 0}(1+z)^{3A_0} - 3\eta \left[ \frac{\exp\left(\frac{3(m-A_0)-m\delta}{2h_1}\right)}{h_1 \exp[2(1+\ln h_2 - h_2)]} \right] \right. \\ & \left\{ \frac{h_1}{2\sqrt{2\left(h_1 \ln(1+z) + \ln h_2 - h_2 + 1\right)}} \exp\left[2\left(h_1 \ln(1+z) + \ln h_2 - h_2 + 1\right)\right] \right. \\ & \left. \left. + 2h_1 \sqrt{2\left(h_1 \ln(1+z) + \ln h_2 - h_2 + 1\right)} \exp\left[2\left(h_1 \ln(1+z) + \ln h_2 - h_2 + 1\right)\right] \right) \right\} - 1. \end{aligned} \quad (4.5)$$

When we apply the  $\Lambda$ CDM conditions we indeed retrieve  $\Lambda$ CDM deceleration parameter which is of the form  $\left( q = \frac{\frac{3}{2}\Omega_{d0}(1+z)^3}{\Omega_{d0}(1+z)^3 + \Omega_{\Lambda0}} - 1 \right)$ .

### 5. Bounce cosmology model

Bounce cosmology is a model where singularities do not occur but instead the model behaves in a cyclic manner [9]. In that regard the model goes from accelerated collapse era to an accelerated expansion era without any display of singularities [7]. Taking the scale factor in an exponential form as a toy model, we have the Hubble parameter given as follows:

$$H = 2n\beta \left[ -\frac{1}{\beta} \ln(1+z) \right]^{\frac{2n-1}{2n}}, \quad (5.1)$$

with  $n > 0$  a constant and  $\beta > 0$  a dimensional constant. By integrating equation (2.11,2.12), the analytical expression for dust matter and dark energy is given by:

$$\left\{ \begin{array}{l} \rho_d = \rho_{d0}(1+z)^{3-\delta}, \\ \rho_\Lambda = \frac{\delta\rho_{d0}}{3(1-A_0) - \delta} \left( (1+z)^{3-\delta} - (1+z)^{3A_0} \right) + \rho_{\Lambda0}(1+z)^{3A_0} \\ - \frac{9\eta H_0^2(2n\beta_0)}{3(m-A_0) - m\delta} \left[ -\frac{1}{\beta_0[3(m-A_0) - m\delta]} \right]^{\frac{2n-1}{2n}} \left[ \frac{2n-1}{2n} \right] \left\{ (1+z)^{3A_0} \right. \\ \left. + (1+z)^{m(3-\delta)} \left( \ln|(1+z)|^{3(m-A_0) - m\delta} - 1 \right) \right\}. \end{array} \right. \quad (5.2)$$

Using fractional energy density parameter, equation (5.2) can be given in dimensionless form as:

$$\left\{ \begin{array}{l} \Omega_d = \frac{1}{h^2}(1+z)^{3-\delta}, \\ \Omega_\Lambda = \frac{1}{h^2} \left\{ \frac{\delta\Omega_{d0}}{3(1-A_0) - \delta} \left[ (1+z)^{3-\delta} - (1+z)^{3A_0} \right] + \Omega_{\Lambda0}(1+z)^{3A_0} \right. \\ - 3\eta \left[ \frac{2n\beta_0}{3(m-A_0) - m\delta} \right] \left[ -\frac{1}{\beta_0[3(m-A_0) - m\delta]} \right]^{\frac{2n-1}{2n}} \left[ \frac{2n-1}{2n} \right] \\ \left. \left[ (1+z)^{m(3-\delta)} \left( \ln|(1+z)|^{3(m-A_0) - m\delta} - 1 \right) + (1+z)^{3A_0} \right] \right\}. \end{array} \right. \quad (5.3)$$

Also to note is that by calling all the conditions required to recover the  $\Lambda$ CDM case, that indeed equations (5.2,5.3) reduce to  $\Lambda$ CDM case, where  $\rho_d \approx a^{-3}$  and  $\rho_\Lambda \approx \rho_{\Lambda0} = \text{Constant}$ . For a flat universe composed of dark components only, we have the Hubble parameter given by:

$$h^2 = \frac{\Omega_{d0}}{3(1-A_0) - \delta} \left[ 3(1-A_0)(1+z)^{3-\delta} - \delta(1+z)^{3A_0} \right] + \Omega_{\Lambda0}(1+z)^{3A_0} \\ - 3\eta \left[ \frac{2n\beta_0}{3(m-A_0) - m\delta} \right] \left[ -\frac{1}{\beta_0[3(m-A_0) - m\delta]} \right]^{\frac{2n-1}{2n}} \left[ \frac{2n-1}{2n} \right] \\ \left\{ (1+z)^{m(3-\delta)} \left( \ln|(1+z)|^{3(m-A_0) - m\delta} - 1 \right) + (1+z)^{3A_0} \right\}. \quad (5.4)$$

It can be seen that once again, when the  $\Lambda$ CDM conditions are invoked then equation (5.4) takes the form,  $h^2 = \Omega_{d0}(1+z)^3 + \Omega_{\Lambda0}$ . Furthermore, the equation that governs the evolution of deceleration parameter for the model is given by:

$$\begin{aligned}
q = \frac{1}{2h^2} & \left\{ \frac{\Omega_{d0}}{3(1-A_0)-\delta} \left[ 3(1-A_0)(3-\delta)(1+z)^{3-\delta} - 3A_0\delta(1+z)^{3A_0} \right] \right. \\
& - 3\eta \left[ \frac{2n\beta_0}{3(m-A_0)-m\delta} \right] \left[ \frac{2n-1}{2n} \right] \left[ -\frac{1}{\beta_0[3(m-A_0)-m\delta]} \right]^{\frac{2n-1}{2n}} \\
& \left[ m(3-\delta)(1+z)^{m(3-\delta)} \left( \ln |(1+z)|^{3(m-A_0)-m\delta} - 1 \right) + [3(m-A_0)-m\delta](1+z)^{m(3-\delta)} \right. \\
& \left. \left. + 3A_0(1+z)^{3A_0} \right] + 3A_0\Omega_{\Lambda 0}(1+z)^{3A_0} \right\} - 1. \tag{5.5}
\end{aligned}$$

When we apply the  $\Lambda$ CDM conditions mentioned in Section 2, indeed the deceleration parameter for  $\Lambda$ CDM is recovered which is of the form  $\left( q = \frac{\frac{3}{2}\Omega_{d0}(1+z)^3}{\Omega_{d0}(1+z)^3 + \Omega_{\Lambda 0}} - 1 \right)$ .

## 6. Conclusions

In this work we studied late-time cosmology, where the viscous dark fluid components were coupled together and allowed to exchange energy amongst one another in a flat FLRW universe. Three models were investigated namely two models of late-time singularity and one that does not exhibit the singularity behaviour which are as follows; little rip, pseudo rip and bounce cosmology.

In this paper, the solutions are obtained analytically as a consequence from reducing equation (2.11) by assuming ( $\alpha = 1$ ), otherwise numerical methods would have to be applied if ( $\alpha \neq 1$ ). All the models are in accord with  $\Lambda$ CDM case when the requirements for  $\Lambda$ CDM are brought into play, which made the study interesting. Furthermore, it is noted that the effects of bulk viscosity and coupling tends to prolong/delay the equality epoch of the dark fluids components.

In little rip model, we see the effects of bulk viscosity delaying the equality epoch when compared with the  $\Lambda$ CDM model. For standard  $\Lambda$ CDM the equality epoch occurs about  $z \approx 0.32$  while for little rip is at about  $z \approx 0.12$  (that is, when taking  $A_0 = 0.5$ ,  $n = 1$ ,  $\eta = 1$ ,  $h_1 = 1e - 5$ ). However, values of these parameters are randomly chosen and does not imply that they may be observationally correct. Also to note is the effects of coupling strength parameter  $\delta$  (that is, when only considering coupling parameter and not viscosity and  $A_0$  from EoS parameter), that also tends to either delay or speed up the equality epoch depending on the sign of  $\delta$ , for  $\delta > 0$ , we see the equality epoch delayed as it occurs about  $z \approx 0.16$  in comparison to the standard  $\Lambda$ CDM model. When the coefficient of bulk viscosity, coupling strength and  $A_0$  (which is part of EoS parameter) are taken to be non-zero, the effects they have on the overall evolution of energy densities is that they tend to delay equality epoch as well. With all these said, the model also tends to predict a universe that in late-time will be dominated by dark energy fluid component. The same behaviour is seen in pseudo rip model as well.

For bounce cosmology model the behaviour noticed is different from the above rip models, as the evolution of dark fluids components are cyclic. At  $z > 0.019$  we note the dominance epoch of dark energy fluid component over dust fluid, followed by an equality epoch at  $z \approx 0.019$ , then in region ( $0.015 < z < 0.019$ ) we find dust fluid dominated epoch. At  $z \approx 0.015$  we see an equality epoch once again, followed by dark energy fluid dominated epoch at ( $-0.015 < z < 0.015$ ) then the equality epoch at  $z \approx -0.015$  and the pattern seems to be cyclic as the dark fluid components interchange the dominance epochs.

As a continuation of this work, we will be constraining the parameter space of these models to see if so that they can be viable cosmological solutions in agreement with observational data. We also intend to study the cosmological density perturbations of these models in order to understand the matter growth and structure formation of large-scale structures in the universe.

### Acknowledgements

BGM and AA acknowledge funding for this work through the National Astrophysics and Space Science Program (NASSP) and the National Research Foundation (with grant number 112131).

### References

- [1] Liddle A 2015 *An introduction to modern cosmology* (John Wiley & Sons)
- [2] Ryden B 2017 *Introduction to cosmology* (Cambridge University Press)
- [3] Shi K, Huang Y and Lu T 2012 *Monthly Notices of the Royal Astronomical Society* **426** 2452–2462
- [4] Ellis G F, Maartens R and MacCallum M A 2012 *Relativistic cosmology* (Cambridge University Press)
- [5] Kremer G M and Sobreiro O A 2012 *Brazilian Journal of Physics* **42** 77–83
- [6] Brevik I, Myrzakulov R, Nojiri S and Odintsov S D 2012 *Physical Review D* **86** ISSN 1550-2368 URL <http://dx.doi.org/10.1103/PhysRevD.86.063007>
- [7] Brevik I, Obukhov V V and Timoshkin A V 2014 *Astrophysics and Space Science* **355** 399403 ISSN 1572-946X URL <http://dx.doi.org/10.1007/s10509-014-2163-9>
- [8] Tiwari R K, Alfedeeel A H, Sofuoğlu D, Abebe A and Hassan E I 2022 *arXiv preprint arXiv:2208.13736*
- [9] Bamba K, Makarenko A N, Myagky A N, Nojiri S and Odintsov S D 2013 Bounce cosmology from  $F(R)$  gravity and  $F(R)$  bigravity (*Preprint* 1309.3748)

# Probing dark matter in 2HDM+S with MeerKAT

**N Lavis and G Beck**

School of Physics, University of the Witwatersrand, Private Bag 3, WITS-2050,  
Johannesburg, South Africa

E-mail: 1603551@students.wits.ac.za, geoffrey.beck@wits.ac.za

**Abstract.** The unknown nature of dark matter remains an eyesore on our cosmological paradigm. Much of the previous work done to probe its properties have used gamma-ray studies, but the impressive sensitivities of new radio instruments are allowing them to become the frontrunners in dark matter searches. MeerKAT is the best instrument of its kind in the southern hemisphere, making it a prime candidate for dark matter indirect hunts. By measuring diffuse synchrotron emission within galaxy clusters observed in the MeerKAT Galaxy Cluster Legacy Survey (MGCLS) we are able to probe the properties of a dark matter model. In this work the 2HDM+S model as well as a sample of generic WIMP channels are considered. The former was developed to explain various anomalies observed in Large Hadron Collider (LHC) data from runs 1 and 2. The use of public MeerKAT data allows us to present some of the first WIMP dark matter constraints produced using this instrument.

## 1. Introduction

While indirect evidences such as gravitational lensing, galactic rotation curves, and anisotropies in the cosmic microwave background (CMB) indicate the presence of dark matter in our Universe, its composition remains unknown. Candidates take many forms, with one of the current favoured forms being WIMPS. For a review of evidences and candidates see Bertone et al. [1]. Methods of investigation include collider searches, attempted direct detections and indirect searches via decay/annihilation products. This work utilizes the latter. The two-Higgs doublet model with an additional singlet scalar (2HDM+S) is a beyond standard model hypothesis that contains a hidden sector dark matter candidate. The model was proposed as an explanation for various anomalies observed in Large Hadron Collider data from runs 1 and 2 [2, 3]. The conjectured mass range of this candidate overlaps with that of astrophysically motivated dark matter models for the Payload for Antimatter Exploration and Light-nuclei Astrophysics (PAMELA) [4] anti-particle excesses and gamma-ray excesses observed by Fermi-LAT [5] at the galactic centre. In prior indirect dark matter searches gamma-ray experiments, such as Fermi-LAT [6] and the High Energy Stereoscopic System (H.E.S.S) [7], have taken preference. This is due to their low attenuation and high detection efficiency. With the introduction of new highly capable radio interferometers such as MeerKAT, the precursor to the Square Kilometre Array (SKA), radio frequency dark matter searches are expected to gain prevalence, as there are indications that radio data analysis is an effective method for producing dark matter constraints [8]. The superior angular resolution of such instruments limits confusion between diffuse emission and point sources. Predictions of the sensitivity of the upcoming SKA1-MID to annihilating TeV dark matter have been produced by Cembranos et al [9]. By the comparison of measured diffuse synchrotron emission in galaxies from the MeerKAT Galaxy Cluster Legacy Survey

(MGCLS) [10] to the predictions produced by modelling the dark matter annihilation within the cluster environments we are able to produce limits for the annihilation cross sections of various annihilation channels for a range of masses.

In this work we extend the results presented in [11] by considering five additional clusters and producing the statistically stacked results of the annihilation cross section upper limits produced with the results of all twelve clusters. These proceedings are structured as follows: Section 2 briefly discusses the 2HDM+S formalism and the dark matter sector it introduces. Section 3 introduces the synchrotron emission formalism with which the simulations are performed. Section 4 introduces MGCLS and the potential benefits of MeerKAT. In section 5 we present and discuss our results.

## 2. 2HDM+S and Dark Matter

Numerous multi-lepton anomalies have been observed in both run 1 and 2 data from the LHC [2] [3] since the discovery of the Higgs boson [12, 13, 14, 15]. An analysis of the multi-lepton final states indicates a deviation from the Standard Model (SM) predictions. This alludes to the existence of physics beyond the SM. One implication of the 2HDM+S model is the production of multiple leptons via its decay chain  $H \rightarrow Sh, SS$  [3], where  $h$  is the Higgs boson. The heavy Higgs  $H$  and scalar boson  $S$  have masses fixed to  $m_H = 270$  GeV and  $m_S = 150$  GeV respectively [16] within the model. There have been statistically compelling excesses reported for opposite and same sign di-leptons as well as the three lepton channel both with and without the presence of b-tagged jets [17] [18] [19]. In addition, evidence for the production of the scalar  $S$  with mass 151 GeV was obtained by combining side band data from SM Higgs searches [20]. When all decay channels are included a global significance of  $4.8 \sigma$  was reported for the required mass range (130 -160 GeV) to explain the anomalies [20]. This validates some of the assumptions within the model. The scalar  $S$  can potentially act as a mediator between SM particles and the dark matter candidate that is introduced within the hidden sector of the model.

## 3. Synchrotron emission model

The formalism for predicting the surface brightness of synchrotron emission within a given halo environment is outlined by Beck et al in [21]. The power of synchrotron emission produced by an electron of energy  $E$  within a magnetic field of strength  $B$  is given by [22] as:

$$P_{\text{sync}}(\nu, E, r, z) = \int_0^\pi d\theta \frac{\sin^2 \theta}{2} 2\pi \sqrt{3} r_e m_e c \nu_g F_{\text{sync}}\left(\frac{\kappa}{\sin \theta}\right), \quad (1)$$

where  $\nu$  is the observed frequency,  $z$  is the redshift of the source,  $m_e$  is the mass of an electron,  $\nu_g = \frac{cB}{2\pi m_e c}$  is the non-relativistic gyro-frequency and  $r_e = \frac{e^2}{m_e c^2}$  is the classical radius of an electron [21].

The parameter  $\kappa$  is defined as

$$\kappa = \frac{2\nu(1+z)}{3\nu_0\gamma} \left( 1 + \left( \frac{\nu_p\gamma}{\nu(1+z)} \right)^2 \right)^{3/2}, \quad (2)$$

where  $\nu_p$  is the plasma frequency, which is directly dependent on the electron density of the environment. The parameter  $F_{\text{sync}}$  describes the synchrotron kernel and is defined as

$$F_{\text{sync}}(x) = x \int_x^\infty dy K_{5/3}(y) \approx 1.25x^{1/3} e^{-x} (648 + x^2)^{1/12}. \quad (3)$$

The synchrotron emissivity at a radial position  $r$  within a halo is then found to be

$$j_{\text{sync}}(\nu, r, z) = \int_{m_e}^{M_x} dE \left( \frac{dn_{e^-}}{dE} + \frac{dn_{e^+}}{dE} \right) P_{\text{sync}}(\nu, E, r, z). \quad (4)$$

The factor  $\frac{dn_e}{dE}$  describes the particle (electron and positron respectively) equilibrium distribution. When considering dark matter induced radio emission the diffusion and energy loss experienced by the resultant electrons must be considered. This is due to the fact that position and energy distributions of the electrons will influence the subsequent synchrotron emission [21]. The equilibrium distributions can be found by solving the diffusion-loss equation under the assumption of vanishing time derivatives,

$$0 = \frac{\partial}{\partial t} \frac{dn_e}{dE} = \nabla \left( D(E, \mathbf{x}) \nabla \frac{dn_e}{dE} \right) + \frac{\partial}{\partial E} \left( b(E, \mathbf{x}) \frac{dn_e}{dE} \right) + Q_e(E, \mathbf{x}). \quad (5)$$

In equation 5  $\frac{dn_e}{dE}$  is the electron equilibrium distribution, the spatial diffusion is described with  $D(E, \mathbf{x})$ ,  $b(E, \mathbf{x})$  describes the rate of energy loss and the electron source function is given by the function  $Q_e(E, \mathbf{x})$ . The per annihilation electron yield function for the 2HDM+S channel can be found in [23]. For the other annihilation channels see [24]. Typical methods for solving the diffusion equation are outlined in [21]. The Green's function method is used in this work. The flux density spectrum within a radius  $r$  of the halo centre is then found to be

$$S_{\text{sync}}(\nu, z) = \int_0^r d^3 r' \frac{j_{\text{sync}}(\nu, r', z)}{4\pi D_L^2}, \quad (6)$$

where  $D_L$  is the luminosity distance to the source in question [21].

#### 4. MGCLS

Galaxy clusters are the largest gravitationally bound structures in their universe. The matter budget within them is dominated by dark matter. This makes them promising astrophysical laboratories for the search for potential dark matter signatures. A fraction of clusters contain a detectable diffuse radio source. This component can be used to place constraints on a dark matter model, by comparing the measured values to predictions. Observational data indicates that the spectrum of the emission is steep (see reviews [25],[26]). This information can potentially be used to probe the distributions of the cosmic ray particles as well as the cluster magnetic fields [10]. More accurate representations of cluster magnetic fields will reduce the uncertainties of the modelled dark matter signals. In turn this could lead to more reliable constraints on the dark matter properties within the test model. As found in this study and others [27], a limited number of clusters have well studied magnetic fields. Thus MeerKAT's potential for studying magnetic fields may greatly benefit attempts at constraining dark matter. The data used in this work is obtained from the MeerKAT Galaxy Cluster Legacy Survey (MGCLS). Detailed information of MGCLS can be found in Knowles et al [10]. The procedure used to obtain the integrated fluxes of the radio halos is outlined in [11]. The use of the SAOImageDS9 radio flux measurement is acknowledged [28].

#### 5. Results and Discussion

The sample size of clusters investigated in this work is twelve. For seven clusters the virial mass and radius was found in literature. This information was used to simulate the halo environments. These properties are listed in Table 1. For the remaining clusters the only available mass information found was  $M_{500}$ . From this information the characteristic density and scale radius can be found. This is done by solving

$$\int_0^{r_{500}} \rho(r) 4\pi r^2 dr = M_{500}, \quad (7)$$

and

$$\int_0^{r_{500}} \rho(r) dr = 500\rho_c \frac{4\pi r_{500}^3}{3}, \quad (8)$$

simultaneously by assuming the NFW density profile, as there appears to be some evidence of NFW-like density profiles in clusters [29, 30, 31].

$$\rho(r) = \frac{\rho_0}{\frac{r}{r_s} \left(1 + \frac{r}{r_s}\right)}. \quad (9)$$

The modelled signals consider that the dark matter distribution is smooth. It is known that physical halos have a more clumpy distribution due to the presence of substructure as predicted through the bottom-up formation model. The more concentrated regions are expected to enhance the signal [32, 33]. This is due to the signal's proportionality to the square of the density. The boost effect is more enhanced in larger halos, as they contain more hierarchical levels of structure formation. The total halo boost factors can be calculated using the parametric equation in [33] with  $\alpha = 2$ . For the masses of the clusters considered the total boost factor is approximately 60. However this factor is produced mainly for a  $\gamma$ -ray signal. Synchrotron emissions will not experience this full boost factor, as sub-halos are more common around the outskirts of the host halo. In these regions the magnetic fields are generally much weaker. Thus it is necessary to calculate a scaled boost factor. This can be accomplished by multiplying the distribution of the host halo with a modification function from [34] in order to obtain the mass distribution of the sub-halos. This density is then normalized to produce a probability distribution. The scaled boost factor is then the sub over the probability of a sub-halo being at the given radius multiplied by the magnetic scaling factor at that point.

Table 1: Physical characteristics of the clusters. Column 2: redshift. Column 3: virial mass. Column 4: halo scale radius- defined as the virial radius divided by the virial concentration. Common alternate names are provided in column 5 and the scaled boost factor is given in column 6.

Cluster name	z	$M_{\text{vir}}$ ( $10^{15} M_{\odot}$ )	$R_s$ (Mpc)	Alternate name	Scaled Boost	References
Abell 209	0.206	1.35	0.62		5.69	[10] [35]
Abell 370	0.375	3.03	0.36	G172.98-53.55	5.78	[10] [36] [37]
Abell 2813	0.29	1.241	0.61	J0043.4-2037	2.84	[10] [35]
Abell S295	0.3	0.51	0.44	J0245.4-5302	5.58	[10] [35]
Abell S1063	0.348	1.49	0.66	J2248.7-4431	5.74	[10] [35]
J0528.9-3927	0.284	1.64	0.65		1.82	[10] [38]
J0645.4-5413	0.167	1.24	0.61	Abell 3404	4.27	[10] [35]

The mass range that has been considered is 75-200 GeV in order to overlap with the mass range of the 2HDM+S dark matter candidate expected from kinematic considerations [3], and fitting to the astrophysical excesses. The simulated fluxes are compared to the measured values with a  $2\sigma$  confidence level. The error in the measured value is estimated with a sum of squares value of a 5% systematic error due to the calibration of the equipment as well a statistical error given by SAODS9 in the flux measurement. The results of the twelve individual clusters are stacked. The tightest constraints arise from Abell 370, the largest and most distant cluster. The least constraining results are found in Abell 545, one of the closest and smallest clusters. The remaining results lie between these two ends.

The cross section limits produced are above the thermal relic value,  $\langle\sigma V\rangle \approx 10^{-26}$ . Thus the dark matter model can not be ruled out as a candidate for all dark matter, as its present

Table 2: Physical characteristics of the clusters. Column 2: redshift. Column 3: characteristic density. Column 4: halo scale radius. Common alternate names are provided in column 5 and the scaled boost factor is given in column 6.

Cluster name	$z$	$\rho_s$ ( $10^{14} M_\odot/\text{Mpc}$ )	$R_s$ (Mpc)	Alternate name	Scaled Boost	References
Abell 545	0.154	1.23	0.99	J0532.3-1131	2.24	[10] [39]
Abell 2667	0.230	2.91	0.89	J2351.6-2605	1.08	[10] [40]
J0303.7-7752	0.274	2.97	0.8	G294.66-37.02	2.57	[10] [40]
J0638.7-5358	0.233	3.86	0.82	Abell S592	2.76	[10] [40]
J1601.7-7544	0.153	3.46	0.76	G313.88-17.12	1.78	[10] [40]

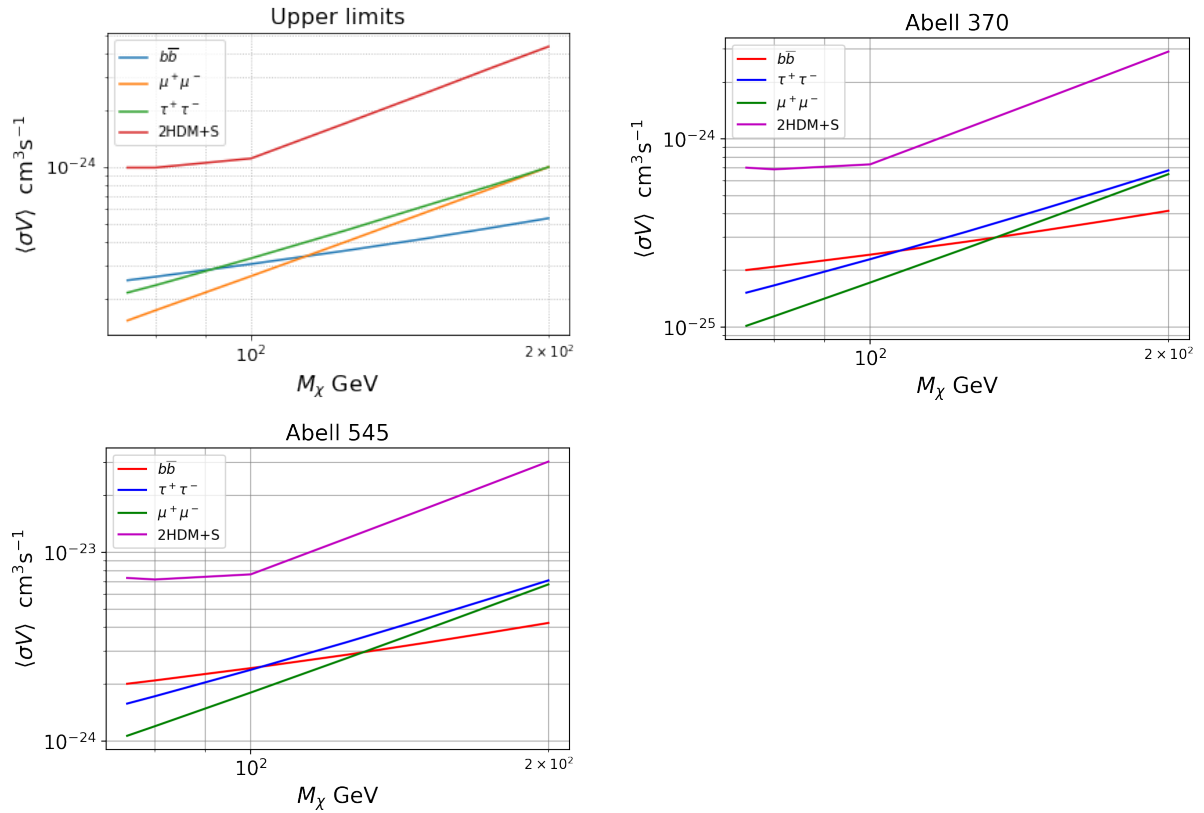


Figure 1: Annihilation rates at a  $2\sigma$  confidence level for the annihilation channels over the mass range 75-200 GeV. The statistically stacked results of the 12 clusters are shown in figure (a). These results are dominated by the most constraining results of Abell 370, which are shown in figure (b), but are slightly skewed by other underperforming clusters such as Abell 545, figure (c).

abundance may be less than what is required to agree with present cosmological abundance. Future work will consider the cases of faint mini halos as well as non-detection of diffuse emission. This will lower the surface brightness values that the dark matter signal will be constrained by.

### Acknowledgments

N.L acknowledges the financial assistance of the South African Radio Observatory (SARAO) towards this research ([www.sarao.ac.za](http://www.sarao.ac.za)).

- [1] Bertone G, Hooper D and Silk J 2005 *Physics reports* **405** 279–390
- [2] Von Buddenbrock S, Chakrabarty N, Cornell A S, Kar D, Kumar M, Mandal T, Mellado B, Mukhopadhyaya B and Reed R G 2015 *arXiv preprint arXiv:1506.00612*
- [3] von Buddenbrock S, Chakrabarty N, Cornell A S, Kar D, Kumar M, Mandal T, Mellado B, Mukhopadhyaya B, Reed R G and Ruan X 2016 *The European Physical Journal C* **76** 1–18
- [4] Picozza P, Galper A, Castellini G, Adriani O, Altamura F, Ambriola M, Barbarino G, Basili A, Bazilevskaia G, Bencardino R *et al.* 2007 *Astroparticle physics* **27** 296–315
- [5] Fermi-LAT <https://fermi.gsfc.nasa.gov/>, (Accessed 2021-03-24)
- [6] Atwood W, Abdo A A, Ackermann M, Althouse W, Anderson B, Axelsson M, Baldini L, Ballet J, Band D, Barbiellini G *et al.* 2009 *The Astrophysical Journal* **697** 1071
- [7] Foo H.E.S.S. <https://www.mpi-hd.mpg.de/hfm/HESS/>, (Accessed 2021-03-01)
- [8] Chan M H 2021 *Galaxies* **9** 11
- [9] Cembranos J A, de la Cruz-Dombriz Á, Gammaldi V and Méndez-Isla M 2020 *Physics of the Dark Universe* **27** 100448
- [10] Knowles K, Cotton W, Rudnick L, Camilo F, Goedhart S, Deane R, Ramatsoku M, Bietenholz M, Brüggem M, Button C *et al.* 2022 *Astronomy & Astrophysics* **657** A56
- [11] Lavis N and Beck G 2022 *arXiv preprint arXiv:2208.06813*
- [12] Higgs P W 1964 *Physical Review Letters* **13** 508
- [13] Higgs P W 1964 *Phys. Lett.* **12** 132–133
- [14] Englert F and Brout R 1964 *Physical review letters* **13** 321
- [15] Guralnik G S, Hagen C R and Kibble T W 1964 *Physical Review Letters* **13** 585
- [16] Von Buddenbrock S, Cornell A S, Mohammed A F, Kumar M, Mellado B and Ruan X 2018 *Journal of Physics G: Nuclear and Particle Physics* **45** 115003
- [17] von Buddenbrock S, Cornell A S, Fang Y, Mohammed A F, Kumar M, Mellado B and Tomiwa K G 2019 *Journal of High Energy Physics* **2019** 1–41
- [18] von Buddenbrock S, Ruiz R and Mellado B 2020 *Physics Letters B* **811** 135964
- [19] Hernandez Y, Kumar M, Cornell A S, Dahbi S E, Fang Y, Lieberman B, Mellado B, Monnakgotla K, Ruan X and Xin S 2021 *The European Physical Journal C* **81** 1–13
- [20] Crivellin A, Fang Y, Fischer O, Kumar A, Kumar M, Malwa E, Mellado B, Rapheeha N, Ruan X and Sha Q 2021 *arXiv preprint arXiv:2109.02650*
- [21] Beck G 2019 *Galaxies* **7** 16
- [22] Longair M S 2010 *High energy astrophysics* (Cambridge university press)
- [23] Beck G, Kumar M, Malwa E, Mellado B and Temo R 2021 *arXiv preprint arXiv:2102.10596*
- [24] Cirelli M, Corcella G, Hektor A, Hütsi G, Kadastik M, Panci P, Raidal M, Sala F and Strumia A 2011 *Journal of Cosmology and Astroparticle Physics* **2011** 051
- [25] Feretti L, Giovannini G, Govoni F and Murgia M 2012 *The Astronomy and Astrophysics Review* **20** 1–60
- [26] Van Weeren R, de Gasperin F, Akamatsu H, Brüggem M, Feretti L, Kang H, Stroe A and Zandanel F 2019 *Space Science Reviews* **215** 1–75
- [27] Storm E, Jeltama T E, Profumo S and Rudnick L 2013 *The Astrophysical Journal* **768** 106
- [28] SAODS9- radio flux measurements
- [29] Beck G and Sarkis M 2022 *arXiv preprint arXiv:2210.00796*
- [30] Mamon G, Cava A, Biviano A, Moretti A, Poggianti B and Bettoni D 2019 *Astronomy & Astrophysics* **631** A131
- [31] He Q, Li H, Li R, Frenk C S, Schaller M, Barnes D, Bahé Y, Kay S T, Gao L and Dalla Vecchia C 2020 *Monthly Notices of the Royal Astronomical Society* **496** 4717–4733
- [32] Sánchez-Conde M A and Prada F 2014 *Monthly Notices of the Royal Astronomical Society* **442** 2271–2277
- [33] Moliné Á, Sánchez-Conde M A, Palomares-Ruiz S and Prada F 2017 *Monthly Notices of the Royal Astronomical Society* **466** 4974–4990
- [34] Jiang F and van den Bosch F C 2017 *Monthly Notices of the Royal Astronomical Society* **472** 657–674
- [35] Klein M, Israel H, Nagarajan A, Bertoldi F, Pacaud F, Lee A T, Sommer M and Basu K 2019 *Monthly Notices of the Royal Astronomical Society* **488** 1704–1727
- [36] Lee J H, Kang J, Lee M G and Jang I S 2020 *The Astrophysical Journal* **894** 75
- [37] Bartelmann M 1996 *arXiv preprint astro-ph/9602053*
- [38] Foëx G, Chon G and Böhringer H 2017 *Astronomy & Astrophysics* **601** A145
- [39] Mantz A B, Allen S W, Morris R G, von der Linden A, Applegate D E, Kelly P L, Burke D L, Donovan D and Ebeling H 2016 *Monthly Notices of the Royal Astronomical Society* **463** 3582–3603
- [40] Rossetti M, Gastaldello F, Eckert D, Della Torre M, Pantiri G, Cazzoletti P and Molendi S 2017 *Monthly Notices of the Royal Astronomical Society* **468** 1917–1930

# A Closer Look at Potential Exoplanets Targets from the Nooitgedacht Observatory

**Henriëtte Vorster, Bruno Letarte**

Centre for Space Research, North-West University, 11 Hoffman Street, Potchefstroom 2531, South Africa

E-mail: [h.vorster01@gmail.com](mailto:h.vorster01@gmail.com), [Bruno.Letarte@nwu.ac.za](mailto:Bruno.Letarte@nwu.ac.za)

**Abstract.** Surveys like KELT and TESS search for transiting extrasolar planets, and have found many potential candidates. The optical telescope at the Nooitgedacht Observatory is ideal for follow-up observations of these candidates, and to collect more data of specific promising candidates. Candidates that are suitable for observations were identified. The suitability of candidates depends on the magnitude of the host star, the decrease in magnitude during the transit, and the angle at which the star is located when the transit begins. From numerous observations, the limitations of the optical telescope at the Nooitgedacht Observatory, with respect to the various properties of an exoplanet system, are established and refined. The data collected from the suitable candidates was processed using aperture and differential photometry and compiled as a light curve. The light curve was then analysed to study the transits and compared them to published data obtained from previous observations. We present the light curve of exoplanet WASP 80-b and conclude that it is the ideal type of exoplanet to observe from the Nooitgedacht Observatory.

## 1. Introduction

Since the discovery of the first exoplanet, 51 Pegasi b [1] the interest in extra-solar planets has increased exponentially, as well as the discoveries thereof. As of August 2021, 5071 exoplanets have been confirmed by NASA [2]. Multiple space based surveys like NASA's TESS (Transiting Exoplanet Survey Satellite) and the Kepler space telescope are used to find exoplanets. Ground based surveys like KELT (The Kilodegree Extremely Little Telescope) and HATNet (Hungarian-made Automated Telescope Network) were also on the hunt. There are multiple methods of detection and confirmation. These methods include the transit method, the radial velocity method, gravitational microlensing and direct imaging, which are the four main methods used. In this project we use the transit method to observe known exoplanets and compare the data to published work; to determine the limitations of the equipment at the North-West University's Nooitgedacht Observatory, with respect to the system properties of the exoplanet system.

## 2. Nooitgedacht Observatory

The Nooitgedacht Observatory is located approximately 35km outside of Potchefstroom on a farm in the Vredefort Dome at  $26^{\circ}54'0.09\text{S}$ ,  $27^{\circ}10'0.05\text{E}$  which is at an elevation of 1448m. This observatory was used for the observations for the duration of the project. The telescope is a Meade LX200 16" f/10 ACF Schmidt-Cassegrain. Its mirror has a diameter of 40.6 cm and a focal length of 4064mm. This all brings about the telescope's resolving power of 0.285

arc-seconds. The mount that moves telescope is a Paramount ME German equatorial mount controlled by TheSkyX software by Software Bisque. The main imaging CCD camera is the Quantum Scientific Imaging (QSI) 540wsi, with a field of view of approximately  $15 \times 15$  arc-minutes. It has internal cooling and can take a color filter wheel. The guiding telescope that is used is the Williams Optics ZenithStar 70 mm Doublet ED APO. It is a refracting telescope with a focal length of 420 mm. The camera connected to the guide telescope is the Atik Titan, which has a field of view of approximately  $30 \times 30$  arc-minutes. The guide telescope was mainly used for auto-guiding purposes.

### 3. Transit method

#### 3.1. Overview

The movement of a planet when it first moves in front of the disk of the host star, until the planet leaves the disk, is called the transit. If an observer has a line of sight on the planet as it moves across the disk of the host star, the observer will see a decrease in the flux of the star. The transit method entails observing the host star and continuously taking images before the transit starts until after the transit ends. Using aperture and differential photometry the flux of the star is then obtained from each of the images. The value of the flux is plotted against time and the resulting graph is called the light curve, which shows the diminishing flux of the host star during the transit.

#### 3.2. Selection of Targets

To acquire potential targets available for observation from the Nooitgedacht Observatory we used the Exoplanet Transit Database [3]. This database gives transit predictions that are visible from your location, as well as the variables of each exoplanet. These variables include the start time, end time and duration of the transit, the magnitude of the host star, the dip in magnitude of the star during the transit and it gives the angle between the horizon and the host star at the beginning and end of the transit. Due to limitations of the Nooitgedacht telescope there are three criteria the target needs to meet to be a good candidate for observation. The first criterion is the magnitude of the host star. The optimal range for the telescope is between 8 and 12. This range is an approximation because it also depends on the relative change in the host star's magnitude during the transit. This is the second criterion. The fainter stars need a larger depth to obtain usable light curves. The third criterion is the angle at which the target will be when the transit starts and ends. These angles need to be above 30 degrees, as a consequence of the telescope being located inside a building where the roof opens. From the horizon, this obscures about 25 degrees of the sky and the observation has to start at least 30 minutes before the transit starts.

#### 3.3. Image Capturing

When a target is selected, four types of images are taken - the light images and three types of calibration images. The light images are processed to obtain the the flux of the host star. We need to select an exposure time for these images to optimize the signal-to-noise ratio (SNR). The selection of exposure time is also important to prevent saturation or underexposure. The highest analog-to-digital unit (ADU) in the image must be below 75% of the saturation point of the imaging camera's detector. Prior to the start of the observation images are taken at different exposure times and then an exposure time is chosen where the SNR is highest and the ADU is in the correct range. The position of the star also need to be taken into account. As the star moves during the observation the airmass will change, which will affect the apparent magnitude of the stars in the image and in turn will affect the the ADU of the images. From the information obtained from the Exoplanet Transit Database, the observation needs to start

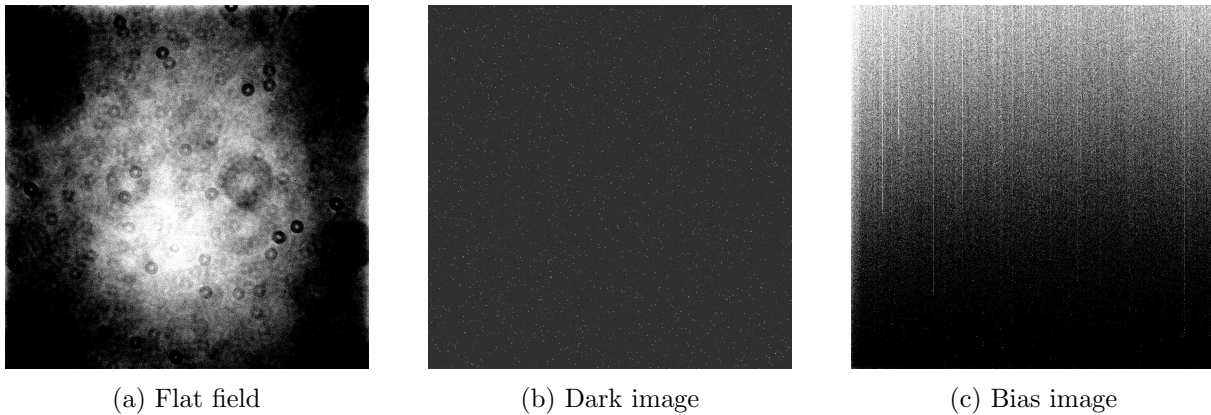


Figure 1: Example of calibration images taken on 27/07/2021 for WASP-80 b

at least 30 minutes pre-ingress and end 30 minutes post-ingress.

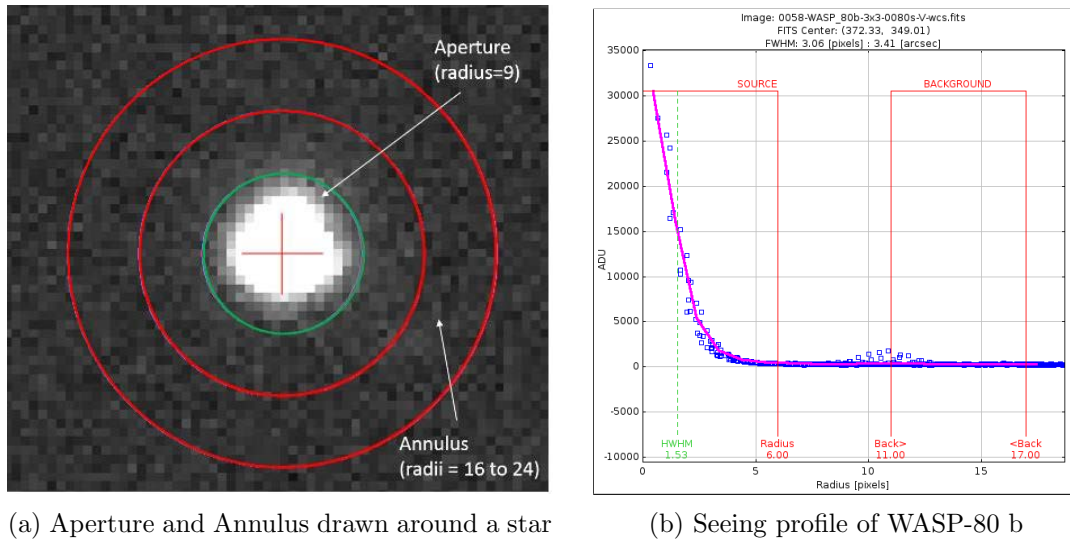
The first of the calibration images is called flat fields. These images are taken after sunset but before any stars are visible. These images are used to correct the light images to mitigate the effects of dust donuts (caused by dust on the equipment) and vignetting. The exposure times for these images must be short enough to prevent saturating the images. Dark images, the second calibration image, are taken after the observation in the same conditions as the light images, including the exposure time and temperature. These images are taken with the mirror of the telescope covered and the camera shutter closed so no light can reach the camera's detector. These images capture any thermal noise due to the equipment and are used to remove the noise from the light images. Because every pixel of the camera is different, they read the incoming signal differently.

The final calibration image that needs to be taken is the bias. These are taken at a exposure time of zero seconds; with the lens of the telescope covered and the camera shutter closed. These images capture any readout noise from the camera sensor and are taken after the observation. The three calibration images, shown in figure 1, are used to correct the light images during the data processing. At least ten images are needed for each type of calibration image are taken and combined together.

#### 3.4. Image Processing

After the observation the images are imported to an application known as AstroImageJ (AIJ). This software is specifically used for processing and analyzing astronomical images, and light curve extracting by using differential and aperture photometry [4]. The images are processed in three different phases using AIJ, the preparation, calibration and differential photometry phase. In the first phase the light images are scanned through to look for any unusable images, this includes images where meteor or satellite trails are visible. These images are then removed from the data set. This is also where we check if a meridian flip has occurred.

The calibration phase is where the images are prepared for differential photometry. AIJ is used to correct the light images with the flat fields, dark and bias images. The calibration images are combined to create a master file for each type of image. The master files are then used to correct all the light images. After the correction the light images are also plate solved. By using a local install of astronomy.net, the star field in the images is compared to a database



(a) Aperture and Annulus drawn around a star

(b) Seeing profile of WASP-80 b

Figure 2

of star positions. This is done to determine the right ascension and declination of the center of the image. The plate solving is necessary because of misaligned images and drifting during the observation, it helps AIJ during the next phase to keep track of the stars in the images throughout the processing.

During the differential photometry phase, aperture photometry is applied to determine the flux of a star. When an aperture is drawn around a star, as seen in figure 2a, there is background sky contribution. To compensate for this an annulus is also drawn around the star, also seen in figure 2a. The ADU count in the annulus is used to adjust the ADU in the aperture and remove the contribution of the background. To obtain the values of the radius of the source (star) and the radii of the inner and outer annulus the seeing profile function of AIJ is used. This gives a graph as shown in figure 2b.

The flux of the host star also changes during the observation due to atmospheric extinction. To correct this comparison stars in the field-of-view are selected. It is important that these stars are not inherently variable and their magnitude is close to that of the host star. The aperture function is also applied to these stars, and their flux is adjusted to be constant. The adjustments made to the flux of the comparison stars are then used to normalize the flux of the host star, to compensate for atmospheric extinction. The predicted ingress and egress points are added, the data prior and after these points is used to establish a baseline of the flux of the host star. AIJ then outputs a measurements table which is used to plot the light curves.

### 3.5. Model Fit

AIJ creates a model fit on the data, firstly it takes into account the predicted ingress and egress points of the transit and the radius and spectral type of the host star when creating the model. The model fit can then be modified by selecting certain detrend parameters to include in the model. These parameters are included or excluded to get the Bayesian Information Criterion value as low as possible for the best possible model fit[4]. This value is calculated as follow:

$$BIC = \chi^2 + k \ln N; \quad (1)$$

where  $k$  is the number of fitted parameters and  $N$  is the number of data points. When the best possible combination of detrend parameters are selected, the ingress and egress points of the model are added to the plot. From the resulting light curve, the radius and composition of the planet can be inferred if certain variables are known. Assuming the flux from the planet is negligible and the host star and planet are spherical we have the following approximation [5]:

$$\Delta F \equiv \frac{F_{\text{no transit}} - F_{\text{transit}}}{F_{\text{no transit}}} = \left( \frac{R_p}{R_*} \right)^2 \quad (2)$$

Where  $R_p$  is the radius of the exoplanet and  $R_*$  is the radius of the host star and  $\Delta F$  is the observed change in flux of the host star. AIJ provides the value of  $\Delta F$  and if the radius of the host star is known we can approximate the radius of the planet using equation 2.

#### 4. Results

WASP-80 b satisfied all conditions mentioned in section 3.2. The observation of this exoplanet was done on the 27th of July 2021 from 21:07 until 23:59 SAST. The host star has a magnitude of 11.881 and a change in magnitude of 0.0310. This is a rather faint star, but the size of the change in magnitude made it a good target.

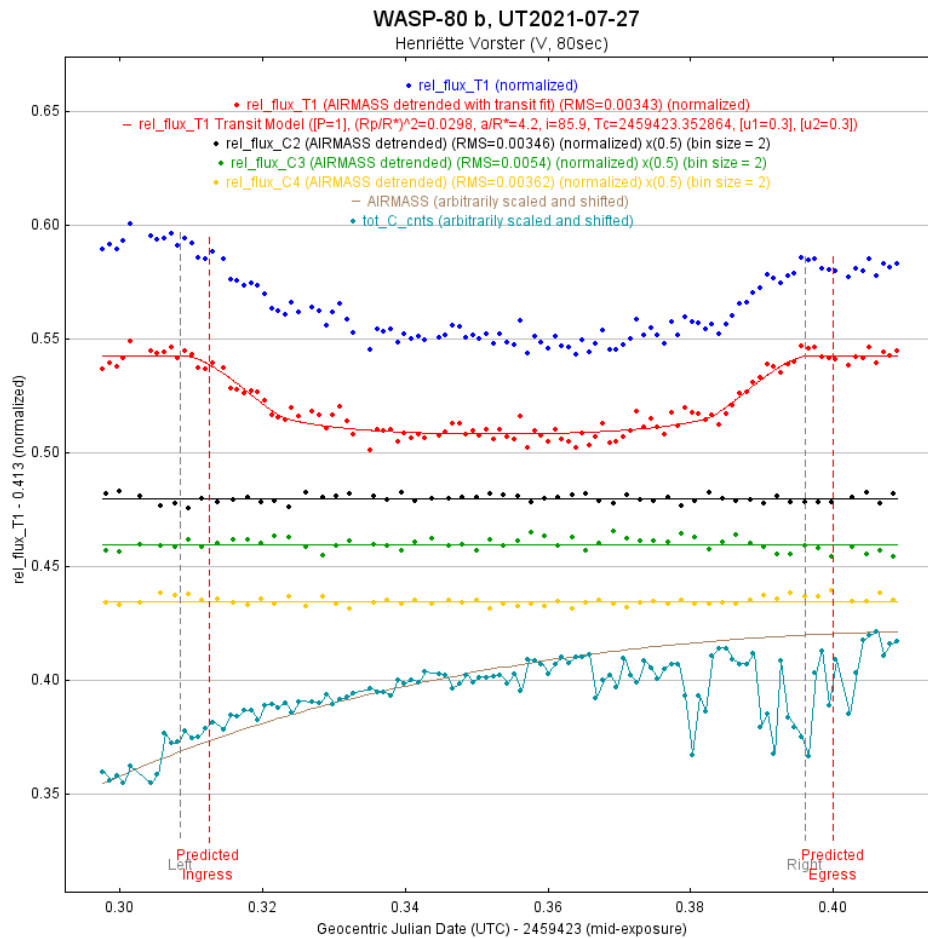


Figure 3: Plot for WASP-80 b (blue), comparison stars (black, green and yellow) and airmass (brown), including the AIJ model fit (red)

According to the Exoplanet Transit Database the transit started at 21:30 and ended at 23:36 SAST. We therefore had 23 minutes of data prior to and after the transit. The images were taken with an exposure time of 80 seconds, in the V-filter. It was three days after full moon, the humidity was at 50% and the temperature was at about 4°C. The light curve for this observation is given in figure 3.

This plot includes the normalized flux for the host star (blue), the model fit for the transit (red), and the relative flux for three comparison stars (black, green and yellow), as well as the airmass (brown line) throughout the observation paired with the total background sky counts for all the comparison stars (teal) which is arbitrarily scaled. As can be seen from figure 3 the predicted ingress and egress times do not match that of the model, this can be due to various reasons. Because the moon was bright the night of observation the background sky contribution might have influenced the data. The observation also started only 23 minutes before the transit started, this means there is only 17 data points before the transit, which might not be enough to establish an accurate baseline for the flux, the same goes for the data points after the transit ended. The value for  $\Delta F$  is measured as  $0.0298$  and using the radius of the host star  $R_* = 0.586_{-0.018}^{+0.017} R_\odot$  [6]. We used equation 2 to calculate the radius of the exoplanet as  $R_p = 0.9854_{-0.0303}^{+0.0286} R_{\text{Jup}}$ , The radius of WASP-80 b was  $R_p = 0.95 \pm 0.03 R_{\text{Jup}}$  as reported in literature [6]. The radius calculated from the model is in close proximity to the published radius, this can be due to the same reasons given above.

## 5. Conclusions

We are capable of doing differential photometry at Nooitgedacht. We still need to process all the data taken throughout the project to conclude on the full limitations of the telescope at Nooitgedacht when observing exoplanets. WASP-80 b is a good candidate to observe from Nooitgedacht, and targets with similar attributes can be considered as good exoplanets to observe.

## References

- [1] Mayor M and Queloz D 1995 *Nature* **378** 355
- [2] Brennan P 2019 Exoplanet exploration: Planets beyond our solar system <https://exoplanets.nasa.gov/>
- [3] Poddaný S, Brát L and Pejcha O 2010 Exoplanet transit database. reduction and processing of the photometric data of exoplanet transits <http://var2.astro.cz/ETD/index.php>
- [4] Collins K A, Kielkopf J F, Stassun K G and Hessman F V 2017 *The Astronomical Journal* **153** 77
- [5] Seager S and Mallen-Ornelas G 2003 *The Astrophysical Journal* **585** 1038
- [6] TriAUD A H, Anderson D, Cameron A C, Doyle A, Fumel A, Gillon M, Hellier C, Jehin E, Lendl M, Lovis C *et al.* 2013 *Astronomy & Astrophysics* **551** A80

# Primordial black holes and the Sunyaev-Zel'dovich effect

**Justine Tarrant and Geoff Beck**

University of the Witwatersrand, 1 Jan Smuts Avenue, Braamfontein, South Africa, 2000

E-mail: [justine.tarrant@wits.ac.za](mailto:justine.tarrant@wits.ac.za), [geoffrey.beck@wits.ac.za](mailto:geoffrey.beck@wits.ac.za)

**Abstract.** Primordial black holes are a popular candidate for dark matter. In the mass regime where their conjectured Hawking evaporation is significant, they have been subject to many constraints via X-rays, gamma-rays, and even radio emission. Previously the Sunyaev-Zel'dovich effect has been considered to place further limits on the  $M > 10M_{\odot}$  primordial black hole abundance via the effects of their accretion of ambient gas. In this work we will present a novel and robust means of placing abundance limits on low-mass black holes, using the Sunyaev-Zel'dovich effect induced by electrons produced via their Hawking radiation within galaxy clusters.

## 1. Introduction

Recently, the study of primordial black holes (PBHs) has gained significant attention due to the possibility that they could constitute dark matter (DM) [1, 2]. Aside from its gravitational interaction, very little is known about DM. PBHs interact almost entirely via gravitation, as does DM. This strengthens the link between DM and PBHs and the possibility of a PBH-DM fraction that is non-zero. PBHs are unique in that they are not formed from stellar collapse. They are created in the early universe within the first second after the big bang. Furthermore, the mass of the PBHs depends on the time at which they were created. Those that formed at the Planck time ( $t \sim 10^{-43}$ s) have masses around  $10^{-5}$ g, whilst a mass of  $10^{38}$ g occurs at  $t \sim 1$ s. This broad mass range might indicate that extended mass functions are more realistic [3]. The mass range considered here is subject to astrophysical and cosmological constraints. For example, large masses ( $m \geq 10^{38}$ g) are subject to dynamical constraints and strong lensing [4, 5, 6], whilst masses below  $m = 4 \times 10^{14}$ g are excluded because they would have already evaporated due to Hawking radiation. Observations using the Voyager 1 spacecraft [3], lensing [7, 8] and gamma-rays [9, 10] have been used to further constrain PBH-DM abundance [7]. Therefore, we consider the range of masses:  $m \in [4 \times 10^{14}, 10^{17}]$ g. The upper bound in this mass range results from the Hawking flux being very small for  $m > 10^{17}$ g.

Black holes are conjectured to undergo Hawking radiation, as do PBHs, and when these black holes are large they emit low-energy charged particles like electrons. At sub-GeV energies, these electrons are influenced by the Sun [3]. This meant that probing the low-energy scales was not feasible. As already mentioned, the low-energy electrons correspond to large masses meaning that it is difficult to determine PBH abundance for larger masses [3]. Fortunately, the Voyager 1 spacecraft has left the heliopause threshold, making it possible to detect low-energy electrons,

which are no longer being heavily influenced by the Sun [11, 12]. Boudad & Cirelli 2019 [3], in their work, used the Voyager 1 data to place constraints on the PBH abundance.

On the other hand, when PBHs are small enough they have a high temperature [13]. This means that they can emit a population of fast, energetic electrons. These electrons from PBH evaporation are likely to emit synchrotron radiation in the presence of a magnetic field [7]. Chan & Lee 2020 [7] focus on radio data (and synchrotron radiation) from the inner Galactic Centre. Finally, one may also place constraints on the PBH abundance using the SZ effect to study the effects of the accretion of ambient gas [14]. The SZ effect considers cosmic microwave background photons that get up-scattered by energetic electrons in the intervening space. This has the virtue of being far less uncertain than the method of Chan & Lee, which depends very strongly upon the assumptions used to derive the magnetic field profile within the Milky-Way galactic centre (for which only a few data points and weak theoretical constraints exist [15]). In addition to this, a single radio data point is all that is used for synchrotron constraints [7]. In the SZ case, we depend only on the well-characterised large-scale structure of the magnetic field within Coma [16] and have a variety of high-precision data on the SZ effect within galaxy clusters (particularly Coma) available [17, 18]. When studying realistic astrophysical environments, magnetic fields are usually present and are needed to account for energy losses occurring due to synchrotron radiation.

In this work, we use the SZ effect in a novel way to place constraints on PBH abundance. We shall consider the induced SZ effect from electrons created by PBHs via Hawking radiation, in galaxy clusters. In particular, we are looking for cases where the SZ effect from PBHs is brighter than the X-ray inferred electron population in Coma.

## 2. Methodology

Firstly, we determine the number of electrons a PBH produces via Hawking radiation. This radiation has a quasi-thermal spectrum [19] with temperature  $T$  and the standard thermal shape

$$\frac{dN}{dE} = \left( \frac{E}{8\pi k_B T} \right)^2 \frac{p_a}{2\pi} \left( e^{\frac{E}{k_B T}} + 1 \right)^{-1}, \quad (1)$$

where the numerical coefficients  $p_a$  vary slightly for lower and higher-energy electrons

$$p_a = \begin{cases} 27/h & E \geq 8\pi k_B T \\ 16/h & E < 8\pi k_B T \end{cases}. \quad (2)$$

Here,  $dN/dE$  has units of inverse energy, inverse time. The fact that the temperature of the radiation is proportional to the average energy  $\langle E \rangle$  of the electron means that an average galaxy cluster (with  $k_B T = 10$  keV) can host a large number of energetic electrons, depending on the number of PBHs which undergo Hawking radiation in the beginning. To find the corresponding electron equilibrium distribution we need to solve the steady-state diffusion-loss equation

$$\vec{\nabla} \cdot \left( D(E, \vec{x}) \vec{\nabla} \frac{dn_e}{dE} \right) + \frac{\partial}{\partial E} \left[ b(E, \vec{x}) \frac{dn_e}{dE} \right] + Q_e(E, \vec{x}) = 0, \quad (3)$$

where  $D$  is the diffusion function,  $b$  is the loss function, and  $Q_e$  is the ‘‘source term’’ (i.e. the rate of electron injection by PBHs). The loss function is given by

$$\begin{aligned} b(E) &= b_{\text{IC}} E_{\text{GeV}}^2 + b_{\text{sync}} E_{\text{GeV}}^2 B_{\mu\text{G}}^2 \\ &+ b_{\text{Coul}} \bar{n}_{\text{cm}3} \left( 1 + \frac{1}{75} \log \left[ \frac{\gamma}{\bar{n}_{\text{cm}3}} \right] \right) \\ &+ b_{\text{brem}} \bar{n}_{\text{cm}3} E_{\text{GeV}}, \end{aligned} \quad (4)$$

where  $\gamma = \frac{E}{m_e c^2}$  with  $m_e$  being the electron mass,  $\bar{n}$  is the average gas density, and  $\bar{n}_{\text{cm}3} = \left(\frac{\bar{n}}{1 \text{ cm}^{-3}}\right)$ . The coefficients  $b_{\text{IC}}$ ,  $b_{\text{sync}}$ ,  $b_{\text{Coul}}$ ,  $b_{\text{brem}}$  are the energy-loss rates from ICS, synchrotron emission, Coulomb scattering, and bremsstrahlung. These coefficients are given by  $0.25 \times 10^{-16}(1+z)^4$  (for CMB target photons),  $0.0254 \times 10^{-16}$ ,  $6.13 \times 10^{-16}$ ,  $4.7 \times 10^{-16}$  in units of  $\text{GeV s}^{-1}$ .

We specify  $Q_e$ :

$$Q_e = \frac{dN}{dE} \frac{\rho_{\text{PBH}}}{M_{\text{PBH}}}, \quad (5)$$

where the density profile is the DM distribution of the target object (i.e. the Coma cluster). If PBHs are to make up the entirety of DM, then they should be distributed in the same manner as the DM. A general profile is the Zhao-Hernquist case

$$\rho_{\text{PBH}}(r) = \rho_s \left(\frac{r}{r_s}\right)^{-\alpha} \left(1 + \frac{r}{r_s}\right)^{-3+\alpha}, \quad (6)$$

where  $r$  is the radial coordinate and  $r_s$ ,  $\rho_s$ , and  $\alpha$  are the characteristic values that describe a given halo. For galaxy clusters, the diffusion length is much smaller than the scale of the cluster. Therefore, for the simplest case, we are able to ignore diffusion. This leaves only the loss-function  $b(E)$  to be calculated, see [20] for details and the definition of the loss-function (we use the properties of the Coma cluster from [16, 21]). For this case, our solution for the differential electron equilibrium distribution looks like

$$\frac{dn_e}{dE}(r, E) = \frac{1}{b(E)} \int dE' Q_e(r, E'). \quad (7)$$

Integrating over the energy  $E$  we find the electron distribution created by PBHs via Hawking radiation, where diffusion is insignificant

$$n_{e,\text{PBH}}(r) = \int dE \frac{\rho_{\text{PBH}}}{M_{\text{PBH}} b(E)} \int dE' \frac{\Gamma(E')}{\exp[E'/T_{\text{PBH}}] + 1}. \quad (8)$$

The electron absorption probability is given by  $\Gamma(E)$ . We note that  $\rho_{\text{PBH}} = f\rho_{\text{DM}}$ , where  $f$  is the amount of DM in the form of PBHs. The electrons, created by Hawking radiation, scatter CMB photons and lose energy. This will result in a change of energy and therefore a change in temperature. The total change in temperature requires we use

$$\Delta T(x) = y g_{sz}(x), \quad (9)$$

where  $x = \frac{h\nu}{k_B T_{\text{CMB}}}$ ,  $\nu$  is the frequency of interest and  $g_{sz}$  is the spectral distortion function [20]. The Compton- $y$  parameter is given by

$$y = \sigma_T \int dl n_e(r) \frac{k_B T}{m_e c^2}, \quad (10)$$

where  $l$  is the line of sight through the target halo. In the simplest case (the diameter line)  $r = l$ . Note, we will need to integrate our equilibrium solution  $\frac{dn_e}{dE}$  over  $E$  as well as  $l$ .

Next, we calculate the change in temperature due to a PBH population that constitutes all of the DM within the Coma cluster  $\Delta T_{\text{PBH}}$  and compare it to the data presented in [17]. We may then use

$$f \Delta T_{\text{PBH}} < \Delta T_{\text{Coma}}, \quad (11)$$

to limit the allowed values of  $f$  at 95% confidence interval by using the  $2\sigma$  upper limit on  $\Delta T_{\text{Coma}}$ .

Note that, in the case of Planck data [18], we compare the SZ  $y$  values in the centre of the cluster, as their temperature profile is not easily resolved by frequency (due to details of their analysis).

### 3. Results and discussion

First, we will discuss the monochromatic case, where all the PBHs were created with the same mass. The most stringent constraints, in the studied mass range, for the monochromatic case are those by Boudad & Cirelli 2019, see Figure 1. The constraints of Chan & Lee 2020 and those in this work are a lot weaker, however, we found that our results are comparable to Chan & Lee 2020. In Figure 1, our constraints are given by the solid black and yellow lines. The yellow line is associated with the Planck data and is thus likely more representative of an accurate physical picture due to the superiority of the instrument. The black line corresponds to the MITO data [17], which resulted in slightly better results than Planck. For both our data sets we see that, while our results are slightly weaker for masses below  $10^{15}$  g, we can constrain PBHs of larger mass better than Chan & Lee 2020. Importantly, we do not suffer from their systematic uncertainties in the magnetic field modeling and our limits are 95% confidence interval, whereas theirs are naive upper limits.

Additionally, from Figure 1, we can see that our constraints are not as stringent as those from Boudad & Cirelli 2019. Low-energy electrons are difficult to study since they are affected by the sun as they move through space. Recently, however, the Voyager 1 spacecraft left the sun's heliopause thereby lifting the limitation on studying low-energy electrons. Boudad & Cirelli 2019 were then able to find constraints that were based on a more comprehensive study.

Next, we consider the extended mass distribution. There are three commonly used: log-normal, power-law, and critical collapse. In this work, a log-normal mass distribution is used. It is given by

$$\frac{dn}{dM} = \frac{f}{\sqrt{2\pi}\sigma M} \exp\left(-\frac{\log^2(M/\mu)}{2\sigma^2}\right), \quad (12)$$

where each set  $(\mu, \sigma)$  provides a model represented by part of a parameter space corresponding to an  $f$ . Here,  $\mu$  is the mass for which the density is a maximum and  $\sigma$  is the width around the peak. For a large  $\mu$  and small  $\sigma$ , for example, we can see that the parameter space is largely a dark green. Dark green indicates a large fraction  $f$ , i.e. close to  $f \sim 1$ . Considering the entire parameter space, we notice that dark green covers a very small patch. Therefore, the darker the green, the more poorly constrained the model. This is encouraging since most of the models (i.e. the parameter space) are well-constrained as can be seen by lighter greens. For the extended case  $3 \times 10^{15}$ g corresponds to the range  $f \in [10^{-4}, 10^{-3}]$  g across all values of  $\sigma$ . This range is much smaller than unity, so it reasonably constrains the PBH abundance. Interestingly, our results for extended distributions are slightly more comparable to those presented by Boudad & Cirelli 2019 than in the monochromatic case.

Boudad & Cirelli 2019 used the full, general diffusion-convection-reacceleration model to study propagation [3]. This yielded well-constrained PBH-DM abundances due to Voyager 1's access to low-energy electrons. On the other hand, Chan & Lee 2020 considered synchrotron emission from the galactic centre, where the magnetic field is quite uncertain [15] and is highly important to their results. In our case, the results are weaker than Boudad & Cirelli 2019 but provide a novel and robust means to derive constraints on PBH populations, without the serious systematic concerns of the method of Chan & Lee 2020. One caveat on these results is that we have used the non-relativistic SZ effect throughout. Whereas, the high temperatures for lower mass PBHs would necessitate the considerably more complex relativistic approach. This will be explored in future work and may enhance the limits for PBH masses below  $10^{15}$ g.

### 4. Conclusion

We present a novel means of constraining the abundance of PBHs as DM by considering the electrons produced via Hawking radiation of the PBHs. These energetic electrons provided the necessary electron population required to scatter photons from the CMB. We used the SZ effect to calculate a temperature change due to a population of PBHs and compared this to SZ data

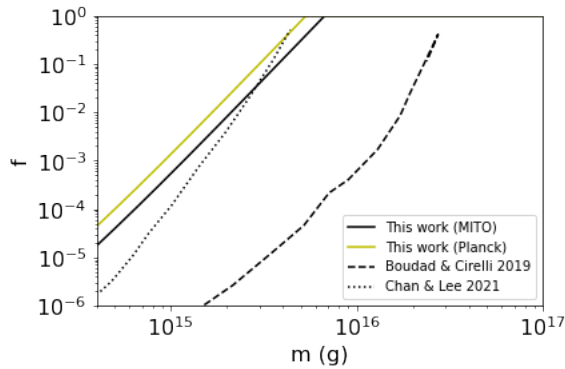


**Figure 1.** Constraints on PBH abundance for the monochromatic mass function.

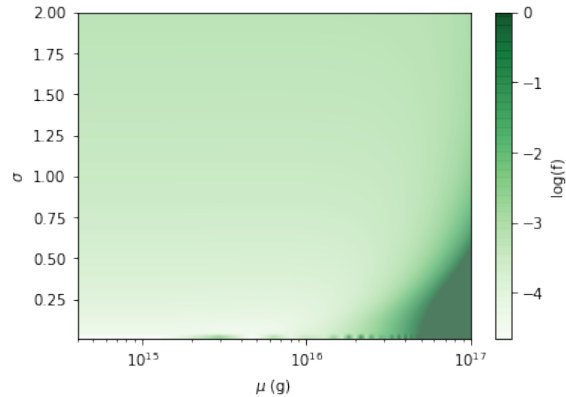


**Figure 2.** Constraints on PBH abundance for the extended mass function.

for the Coma cluster. Constraints on  $f$ , which is the amount of DM consisting of PBHs, could be placed with a 95% confidence level. We considered two mass functions. The monochromatic results were comparable to Chan & Lee with a slight advantage toward higher masses. The extended case placed better constraints. The resulting parameter space was mostly light green giving  $f < 10^{-2}$  and only a small corner with  $f \sim 1$  was poorly constrained. One advantage of this method is that it is more robust than the synchrotron approach and should be applicable in a larger number of environments.

### Acknowledgments

JT acknowledges the support of the SARA0 post-doctoral fellowship initiative.

### References

- [1] Zel'dovich Y B and Novikov I D 1967 *Sov. Astron.* **10** 602
- [2] Hawking S 1971 *Mon. Not. R. Astron. Soc.* **152** 75
- [3] Boudaud M and Cirelli M 2019 *Phys. Rev. Lett.* **122** 041104
- [4] Brandt T D 2016 *Astrophys. J. Lett.* **824** L31
- [5] Koushiappas S M and Loeb A 2017 *Phys. Rev. Lett.* **119**(4) 041102
- [6] Gaggero D *et al.* 2017 *Phys. Rev. Lett.* **118**(24) 241101
- [7] Chan M H and Lee C M 2020 *Mon. Not. Roy. Astron. Soc.* **497** 1212–16
- [8] Montero-Camacho P *et al.* 2019 *J. Cosmol. Astropart. Phys.* **08** 031
- [9] Carr B J *et al.* 2016 *Phys. Rev. D* **94** 044029
- [10] Carr B *et al.* 2021 *Rept. Prog. Phys.* **84** 116902
- [11] Stone E *et al.* 2013 *Science* **341** 150–153
- [12] Cummings A C *et al.* 2016 *Astrophys. J.* **831** 18
- [13] Hawking S 1974 *Nature* **248** 30
- [14] Abe K T *et al.* 2019 *Phys. Rev. D* **99** 103519
- [15] Bringmann T *et al.* 2014 *Phys. Rev. D* **90**
- [16] Bonafede A *et al.* 2010 *Astron. Astrophys.* **513** A30
- [17] de Petris M *et al.* 2002 *Astrophys. J. Lett.* **574** L119–L122
- [18] Planck Collaboration *et al.* 2013 *Astron. Astrophys.* **554** A140
- [19] Corda C 2012 *Int. J. Mod. Phys. D* **21** 1242023
- [20] Beck G 2019 *J. Cosmol. Astropart. Phys.* **08** 019
- [21] Chen Y *et al.* 2007 *Astronomy and Astrophysics* **466** 805–812

# Studying gas flows in the SUNBIRD starburst galaxies and LIRGs: Preliminary results of NGC 6000

P. Janse van Rensburg<sup>1, 2</sup>, K. M. Mogotsi<sup>1, 3</sup>, P. Väisänen<sup>1, 3</sup>, and M. A. Bershad<sup>1, 2, 4</sup>

<sup>1</sup>South African Astronomical Observatory, PO Box 9, Observatory, 7935 Cape Town, South Africa

<sup>2</sup>Astronomy Department, University of Cape Town, Private Bag X3, Rondebosch 7701, South Africa

<sup>3</sup>Southern African Large Telescope, PO Box 9, Observatory, 7935 Cape Town, South Africa

<sup>4</sup>University of Wisconsin, Department of Astronomy, 475 North Charter Street, Madison, WI 53706, USA

E-mail: [petro@sao.ac.za](mailto:petro@sao.ac.za)

**Abstract.** Gas flows are an important aspect of galactic feedback and the regulation of star formation in galaxies. Nearby starburst galaxies and Luminous Infrared Galaxies (LIRGs) provide an extreme environment where feedback and the changes due to it can be studied in great detail. The aim of this project is to search for traces of outflows and inflows in a sample of nearby starburst galaxies and LIRGs in the SuperNovae and starBurst in the InfraReD (SUNBIRD) survey, and to characterize them using observations of the stellar, and neutral and ionized gas kinematics. As a first step, the gas flows were studied using long-slit spectra from the Southern African Large Telescope. We present preliminary results from this data for one of the SUNBIRD galaxies NGC 6000. The neutral and ionized gas kinematics can be traced through the sodium doublet (NaD) absorption lines and H $\alpha$  emission line, respectively. In this proceeding, we modeled the ionized gas with multiple components of Gaussian and Gaussian-Hermite functions and compared best-fit models as an initial step to identify and characterize the gas flows in and around this galaxy. In NGC 6000, a double Gaussian and Gaussian-Hermite function modeled the H $\alpha$  emission line better which indicates that there could be outflowing, inflowing or extraplanar gas.

## 1. Introduction

Galaxies display a bimodal distribution in colour: red, early-type galaxies with a low star formation rate and blue, late-type galaxies with a high star formation rate [e.g., 1]. This bimodality originates because star formation can either be enhanced or quenched depending on the inflow and outflow of gas in the galaxy as well as gas heating. The inflow and outflow of gas is often referred to as the baryon cycle. Gas accreting onto the galaxy from the intergalactic medium makes it possible for more stars to form. Gas that is flowing out of the galaxy can either leave the galaxy completely if it has a velocity greater than the escape velocity of the galaxy, flow to the circumgalactic medium, or it can be recycled back into the galaxy. Galaxies with a high star formation rate create an extreme environment where the baryon cycle is easier to study and

observe with earth-based observations [2; 3].

Galactic outflows or winds are one of the primary feedback mechanisms in galaxies. Outflows are mainly driven by star formation or active galactic nuclei (AGN) activity and are important in the regulation of star formation. They are also multi-phase and can be studied with various tracers [2]. For example, in the optical regime, stellar absorption and outflowing neutral gas can be traced with the sodium doublet (NaD) absorption lines and ionized gas with the H $\alpha$  emission line [e.g., 4; 5]. Outflow velocities can also range from tens to a few hundred km/s [e.g., 4; 6].

In this project, we study the gas flows in nearby starburst galaxies and Luminous Infrared Galaxies (LIRGs) in the SUPERNOVAE and starBURST in the INFRAReD (SUNBIRD) survey [7]. The SUNBIRD survey has two science goals: to calculate the total SFR in the nearby universe by looking at dust-enshrouded core-collapse supernovae in star forming galaxies, and to perform an in-depth study of star formation in LIRGs.

## 2. Observational Methods and Data Analysis

### 2.1. Sample and Observations

The SUNBIRD survey contains more than 40 galaxies. For this project, we focused on a sub-sample of 24 galaxies based on the availability of lower ( $R \sim 1000$ ) and higher ( $R \sim 3000$ ) resolution long-slit spectra from previous studies [10; 6]. The lower resolution data can be used for stellar population and kinematics modelling, as well as using the emission lines for line diagnostics and characterisation of the interstellar medium. The line diagnostics can be used to characterise the outflowing gas and determine if the outflow is driven by star formation, AGN activity or both. The higher resolution data is useful for more complex multi-component fitting of the emission and absorption lines which traces the ionized and neutral gas, respectively. The sub-sample includes isolated galaxies, Seyferts, AGNs, and galaxies in group/cluster environments, all covering a wide range of interaction stages. Figure 1 shows the interaction stages of the sub-sample and the general properties of the galaxies in the sub-sample are shown in Table 1.

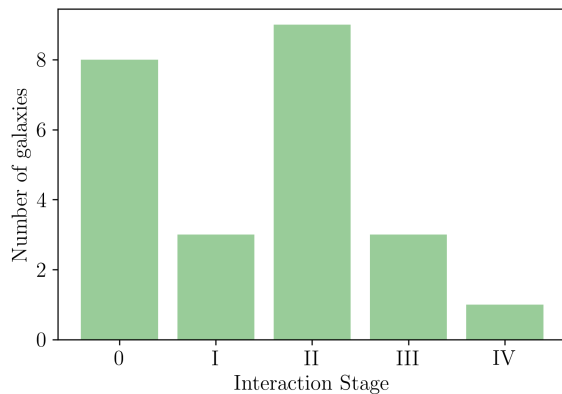


**Figure 1:** The interaction stages of the sub-sample ranging from isolated galaxies (0) to galaxies in a post-merger phase (IV). The interaction stages are defined in [8; 9].

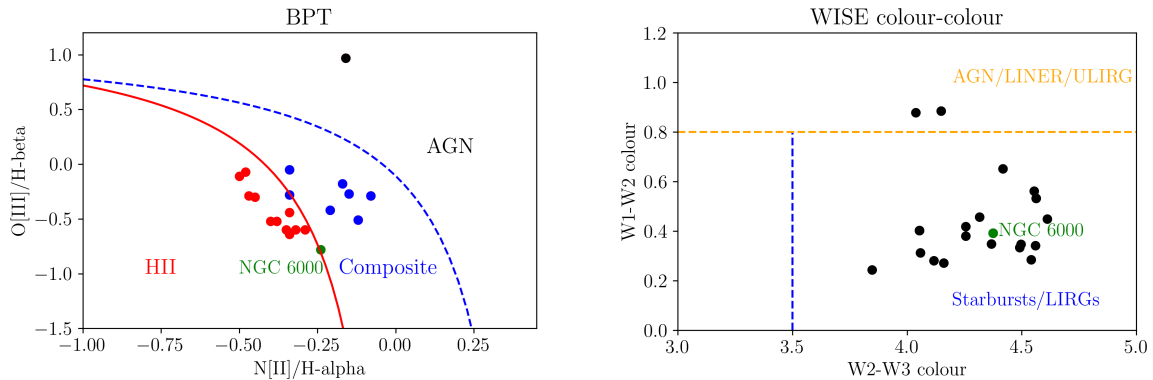
Table 1: Properties of the galaxies in the sub-sample.

<b>Redshift</b>	$0.0073 \leq z \leq 0.0482$ ( $34 < D_L \leq 217$ Mpc)
<b>Infrared (IR) luminosity</b>	$10^{10.76} L_{\odot} \leq L_{IR} \leq 10^{11.81} L_{\odot}$
<b>Near-Infrared (NIR) star formation rate (SFR)</b>	$10^{0.99} M_{\odot} \text{yr}^{-1} \leq \text{SFR} \leq 10^{2.04} M_{\odot} \text{yr}^{-1}$

The starburst galaxies and LIRGs in the SUNBIRD survey have been studied with long-slit spectra from the Southern African Large Telescope Robert Stobie Spectrograph [SALT, RSS; 11; 12] in two previous studies. In the study by [10], the author studied 52 SUNBIRD galaxies

by looking at their stellar populations and the properties of the interstellar medium using spectra with a grating of PG0900 ( $R \sim 1000$ ), which covered a wavelength range of approximately 3640–6740 Å. In the study by [6], 40 SUNBIRD galaxies were studied using higher resolution ( $R \sim 3000$ ) spectra (PG1800 grating), covering a wavelength range of about 5600–6930 Å. In [6], outflows were studied by looking at the kinematics of the ionized and neutral gas traced through the  $H\alpha$  emission line and NaD absorption lines, respectively. The kinematics were determined through fitting Gaussian and Gauss-Hermite models. If outflows were present in the galaxy, these were detected as deviations from regular galaxy rotation as well as differences between the  $H\alpha$  and NaD rotation curves. That work did not model the stellar contribution to the spectra. We aim to improve and extend the work done by [6] by performing more complex emission line fitting and modeling the stellar kinematics with a Penalized Pixel-Fitting method [pPXF, 13].

In order to get a better understanding of the properties of the sub-sample, we plotted the BPT [Baldwin, Phillips, and Terlevich; 14] diagram using the spatially integrated line ratios calculated in the two previous studies. This allowed us to differentiate the star-forming galaxies from the AGN in the sub-sample. This is shown in Figure 2a. In addition, we also plotted a Wide-field Infrared Survey Explorer [WISE; 15] colour-colour plot (W1-W2 vs W2-W3), shown in Figure 2b, to differentiate between the star-forming galaxies and LIRGs, and AGN. Figure 2a shows that the majority of the galaxies in the sub-sample are either star-forming (HII) galaxies or they are in the composite region, where the power source can be star formation, an AGN or even shock excitation [16]. The WISE colour-colour plot shows a similar result with only two galaxies in the AGN/LINER/ULIRG region.



(a) BPT diagram of the sub-sample. The solid red line is from [17] and the dashed blue line from [18]. (b) WISE colour-colour plot of the sub-sample. Refer to [15; 19] for a description.

**Figure 2:** BPT diagram and WISE colour-colour plot of the sub-sample showing the differentiation between the star-forming galaxies and AGNs.

In this proceeding, we present preliminary results of one galaxy in the sub-sample: NGC 6000. All of the data were reduced using IRAF<sup>1</sup> by [10]. NGC 6000 is a nearby star-forming spiral galaxy at  $z = 0.007$ . It has an IR SFR of  $10^{1.2} M_{\odot} \text{yr}^{-1}$  and an IR luminosity of  $10^{10.97} L_{\odot}$ . In the BPT diagram (Figure 2a), it is on the border between the HII and composite region and in the WISE colour-colour plot (Figure 2b) it is classified as a starburst/LIRG. Based on its IR luminosity, NGC 6000 would be classified as a starburst galaxy since LIRGs have an IR luminosity of  $10^{11} L_{\odot} \leq L_{\text{IR}} < 10^{12} L_{\odot}$  [20]. The rotation curve of the ionized (red) and neutral

<sup>1</sup> Image Reduction and Analysis Facility, distributed by the National Optical Astronomy Observatory.

(black) gas in this galaxy calculated by [6] is shown in Figure 3. The author of [6] also calculated an offset velocity between NaD and H $\alpha$  of 140 km/s. This galaxy was chosen because of the large outflow velocity determined by [6]. In [6], only a single Gaussian and Gaussian-Hermite was fitted and the velocities were calculated with the overall best-fit model.

## 2.2. Emission line modeling

In order to build and improve on the work done by [6], three models were fitted to the SALT RSS long-slit spectra of the sub-sample to obtain the kinematics of the galaxies. Instead of selecting one model overall, we compare the three different models at each spatial row of the 2D spectrum. We first focused on obtaining the kinematics of the ionized gas, traced by the H $\alpha$  emission line. Three emission lines were fitted: the two [NII] lines and the H $\alpha$  line in the region between approximately 6550Å and 6700Å. Three models were fitted to the emission lines:

- (i) A single Gaussian model on each emission line,
- (ii) a single Gaussian model on the two [NII] emission lines and a double Gaussian model on the H $\alpha$  emission line, and
- (iii) a single Gaussian-Hermite model on each emission line.

The Gaussian-Hermite has two additional parameters: skewness, which fits the wings and heaviness of the tails, and kurtosis, which fits the peak. The Gaussian-Hermite function becomes a normal Gaussian when these two parameters are 0.

An automated Python code was written to fit these three models to the emission lines and calculate the rotation curve of each galaxy based on the best fit at each spatial row along the 2D spectrum. Before the emission lines were fitted, the continuum around H $\alpha$  and [NII] was modeled with a polynomial using the `specutils` Astropy package<sup>2</sup> and subtracted from the spectrum. The emission line modelling was performed through the non-linear least squares `kmpfit` package from the Kapteyn Python module<sup>3</sup>. We find that other Python-based software do not have the flexibility to easily adjust the models for the analysis we want to perform. An example of the double Gaussian model at two spatial rows is shown in Figure 4.

The initial parameters were determined based on the position (centroid) of the H $\alpha$  line and known proximity of the two [NII] lines. We also added bounds to limit the standard deviation (width) of each emission line. Widths smaller than 0.422 Å would not be sensible because of the wavelength dispersion and widths larger than 20 Å would include regions outside the emission lines. We also applied a  $4\sigma$  cut to exclude any rows where the noise were modeled. A combined rotation curve was calculated by using the velocity from the best-fit model at each spatial row,

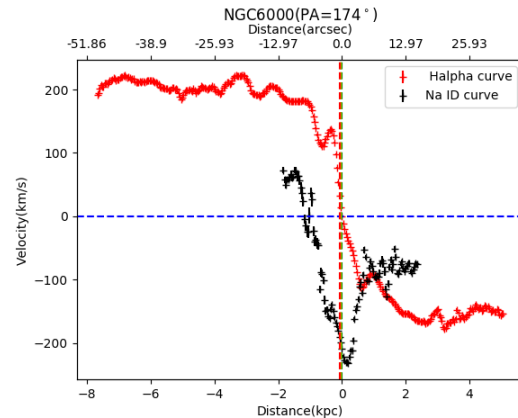
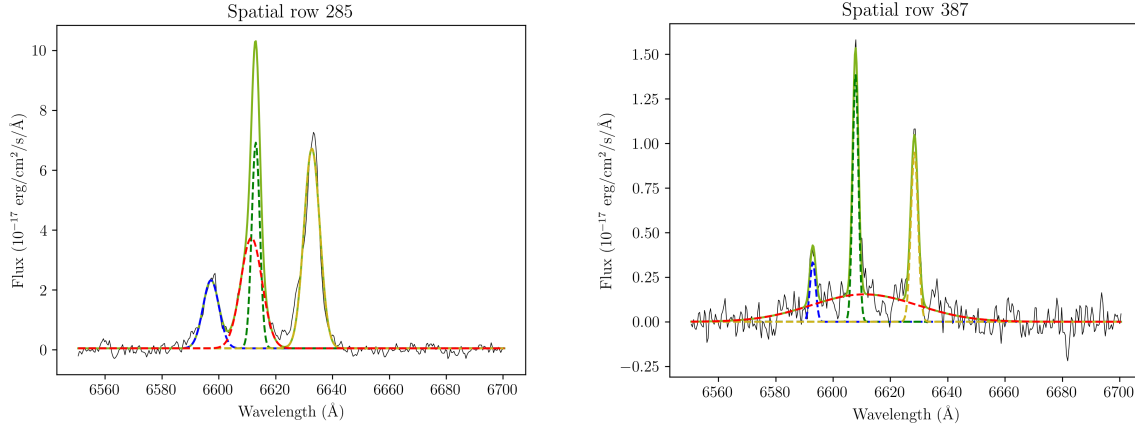


**Figure 3:** The rotation curve of NGC 6000 from [6]. The ionized gas traced by H $\alpha$  is shown in red and the neutral gas traced by NaD is shown in black.

<sup>2</sup> <https://specutils.readthedocs.io/en/stable/index.html>

<sup>3</sup> <https://www.astro.rug.nl/software/kapteyn/index.html>

determined from the chi-squared value. A heliocentric velocity correction was also applied to the velocities.



(a) Double Gaussian fit at spatial row 285 ( $\sim 5$  arcseconds from the centre of the galaxy).

(b) Double Gaussian fit at spatial row 387 ( $\sim 21$  arcseconds from the centre of the galaxy).

**Figure 4:** Double Gaussian fit of the  $H\alpha$  and  $[NII]$  emission lines near the centre of the galaxy (a) and in a region where the velocity is constant (b).

### 3. Results

A preliminary rotation curve for NGC 6000 is shown in Figure 5. At each spatial row, the velocity was determined by the model that fitted the best (smallest reduced chi-square value). The single Gaussian model fitted the best at the edge of the galaxy. A double Gaussian function and Gaussian-Hermite (asymmetric profile) had the best fit in the rest of the galaxy. An example of a double Gaussian fit near the centre of the galaxy is shown in Figure 4a. The secondary, blue-shifted component in the double Gaussian suggests that there could be inflowing, outflowing or extraplanar gas. This can also be seen in the rotation curve (Figure 5) where the gas traced by the secondary (broad) Gaussian component lags behind the gas traced by the primary (narrow) component near the centre of the galaxy. The velocity offset between the broad and narrow component at the centre of the galaxy is about half of what was calculated in [6] (60 km/s), however it is still in agreement with other galaxy outflow velocities (see Section 1). In the work of [6], they only showed the rotation curve based on a single Gaussian component (refer to Figure 3), which only shows gas flows as deviations from regular galaxy rotation. By fitting an additional component, we can not only determine whether there are multiple gas components (i.e., outflow, inflow or extraplanar gas), but also study the properties of the gas flows. These properties include using emission line ratios to study the ionization and determine if the outflow is driven by star formation, AGN activity or both [16].

We note that there are some areas where better constraints are needed, especially in the broad component (cyan dots). There are also regions where the broad component velocity seems to remain constant (e.g., at 20 arcseconds). An example of a double Gaussian fit at this region is shown in Figure 4b. The narrow component velocity is not affected by the broad component, but the broad component has a velocity much greater than what we would expect in a secondary component. This suggests that it could be extraplanar gas or scattered light from the instrument. It will be investigated in further analysis.

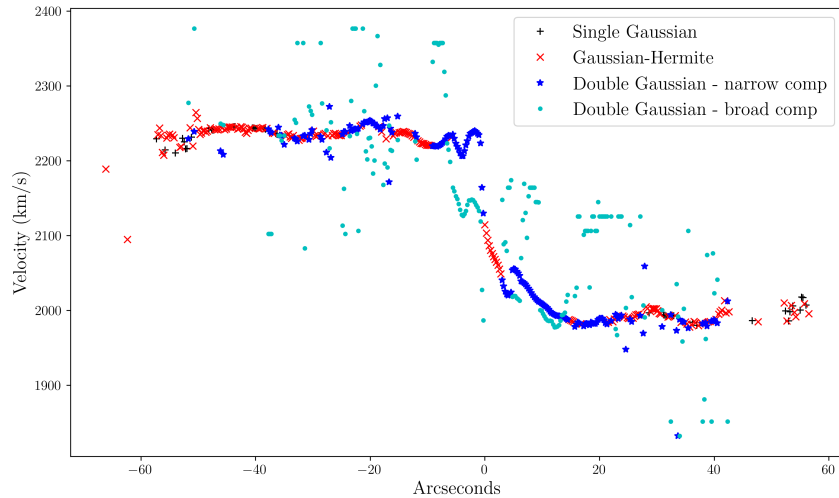


**Figure 5:** The rotation curve of NGC 6000. The velocity of the best fit is shown as black plus signs for a single Gaussian, red crosses for a Gaussian-Hermite function, and cyan dots and blue stars for the broad and narrow component of the Double Gaussian, respectively.

#### 4. Conclusion

We have shown preliminary results of a study of the gas flows in galaxy NGC 6000 based on long-slit spectra from the RSS on SALT. From the rotation curve, we showed that a double Gaussian and Gaussian-Hermite fit the spectrum better, especially near the centre of the galaxy. These asymmetric functions indicate that there is some outflowing, inflowing or extraplanar gas. In the future, this analysis will be repeated for all other galaxies in the sub-sample and we will also model the NaD absorption lines in order to trace the kinematics of the neutral gas. The stellar component to NaD will be subtracted by modeling the stellar kinematics with pPXF. We will also study some of the galaxies with multi-wavelength data including data from the Atacama Large Millimeter/submillimeter Array (ALMA), the Multi Unit Spectroscopic Explorer [MUSE; 21] and the SALT NIR Integral Field Unit [IFU; 22]. In order to verify our analysis, we will also do a similar analysis with other software like Bayesian active galactic nucleus (AGN) Decomposition Analysis for Sloan Digital Sky Survey (SDSS) Spectra [BADASS; 23].

#### Acknowledgments

PJ acknowledges the support from the National Research Foundation of South Africa (NRF, Partial Postgraduate Scholarship UID: 142477) and the South African Astronomical Observatory (SAAO). The results presented in this proceedings are based on observations made with the Southern African Large Telescope (SALT) under the program 2013-1-RSA\_OTH-024.

#### References

- [1] Strateva I *et al.* 2001 *AJ* **122** 1861–74
- [2] Veilleux S, Cecil G and Bland-Hawthorn J 2005 *ARA&A* **43** 769–826
- [3] Tumlinson J, Peeples M S and Werk J K 2017 *ARA&A* **55** 389–432
- [4] Cazzoli S, Arribas S, Maiolino R and Colina L 2016 *A&A* **590** A125
- [5] Fluetsch A *et al.* 2021 *MNRAS* **505** 5753–83
- [6] Tafere M S 2018 *UCT* Master’s thesis
- [7] Väisänen P *et al.* 2014 ed Y D Mayya D R G and Terlevich E (INAOE & AMC) pp 185–9

- [8] Miralles-Caballero D, Colina L, Arribas S and Duc P A 2011 *AJ* **142** 79
- [9] Veilleux S, Kim D C and Sanders D B 2002 *ApJS* **143** 315
- [10] Ramphul R A 2018 *UCT* Ph.D. thesis
- [11] Burgh E B *et al.* 2003 ed Iye M and Moorwood A F M (SPIE) pp 1463–71
- [12] Kobulnicky H A *et al.* 2003 ed Iye M and Moorwood A F M (SPIE) pp 1634–44
- [13] Cappellari M and Emsellem E 2004 *PASP* **116** 138–147
- [14] Baldwin J A, Phillips M M and Terlevich R 1981 *PASP* **93** 5–19
- [15] Wright E L *et al.* 2010 *AJ* **140** 1868–1881
- [16] Kewley L J, Nicholls D C and Sutherland R S 2019 *ARA&A* **57** 511–570
- [17] Kauffmann G *et al.* 2003 *MNRAS* **346** 1055–1077
- [18] Kewley L J, Dopita M A, Sutherland R S, Heisler C A and Trevena J 2001 *ApJ* **556** 121
- [19] Jarrett T H *et al.* 2017 *ApJ* **836** 182
- [20] Sanders D B and Mirabel I F 1996 *ARA&A* **34** 749–792
- [21] Bacon R *et al.* 2010 vol 7735 ed McLean I S, Ramsay S K and Takami H (SPIE) pp 131–139
- [22] Wolf M J *et al.* 2018 vol 10702 ed Evans C J, Simard L and Takami H (SPIE) pp 854–873
- [23] Sexton R O, Matzko W, Darden N, Canalizo G and Gorjian V 2020 *MNRAS* **500** 2871–2895

# From setting up a new telescope to optimizing astrometric solutions

**Jane Mankhubu Letsoalo, Bruno Letarte**

Centre for Space Research, North-West University, 11 Hoffmann Street, Potchefstroom 2531, South Africa.

E-mail: [janemankhubu88@gmail.com](mailto:janemankhubu88@gmail.com), [Bruno.Letarte@nwu.ac.za](mailto:Bruno.Letarte@nwu.ac.za)

**Abstract.** A new optical telescope has been set up at the North-West University (NWU) Potchefstroom campus, on the roof of the physics building (G5). It is the old 30 cm Meade that used to be at the Nooitgedacht observatory until around 2010, when it was replaced by a 40 cm. It was decided to refurbish the optical tube and purchase a new mount. It will mostly be used for public outreach purposes. The project was to setup a new telescope, starting with a custom-made steel pier anchored to the roof, extending an electrical connection, and the balancing plus polar alignment of the telescope. This required the software and all other components of the telescope to function together. The observatory is now in the final phase of being ready for the public by making the roof safe. For scientific observations, a tested conducted and optimized methods of plate solving for accurate astrometric solutions. It will be discussed how to go from detector coordinates (X, Y) to astronomical coordinates (RA, DEC) on images taken at the Nooitgedacht observatory.

## 1. Introduction

An optical telescope is an essential tool for astronomers, used to collect images of distant objects through their emission, absorption, or reflection of visible light. They have been in existence since the 17<sup>th</sup> century and have been used for many discoveries. Since then, other scientists have begun creating and building different types of telescopes, covering the electromagnetic spectrum. Having a site accessible to the public, where people can learn the basics, and get hands-on experience using a small telescope will provide a great opportunity for both upcoming student scientists and the public at large.

## 2. The Roof Observatory

The roof observatory is located at coordinates  $26^{\circ}41'11''S$   $27^{\circ}5'37''E$ . The telescope has a Schmidt-Cassegrain design and is seen in Figure 1. The tube is portable, and easy to assemble and disassemble. It has a 30 cm (12") aperture, with a light-collecting area of  $225\pi$  cm<sup>2</sup> and resolving power of 0.38 arc-seconds [1]. The telescope focal ratio of  $f/10$  makes it ideal for planet and moon gazing. The focal length of the telescope is 3048 mm, and the eyepiece is 40 mm, giving a magnification of 76.2. The mount chosen is an iOptron CEM60, Central Equatorial mount (see Figure 1). The mount has a payload capacity of  $\sim 27$  kg, high precision tracking, and provides a slew speed of 3.75°/sec [2]. The CEM60 comes with an iPolar scope incorporated within it. It is used for the polar alignment, while pointing at the celestial pole, it will detect star patterns and guide the alignment process with the provided software. Once the mount has



**Figure 1.** (a) The image shows the optical tube for the observatory. (b) The image of the iOptron CEM60 mount on the steel pier.

the polar alignment done, we can start to point and track properly.

The first step was to remove the U-fork anchor of the old alt-azimuth mount from the 30 cm optical tube and replacing it with a new mount, an iOptron CEM60. An adapter was made so that the tube fits on the new mount. In March of 2021, a steel pier was installed on the roof. An electrical connection was brought to the side of the telescope to be able to drive the motors and power the computer. The mount came with a 9.5 kg counterweight. This was not enough to balance the telescope; a second counterweight was added and modified to fit the shaft. This was also not enough, so the counterweight shaft was extended by more than 30 cm to achieve balance. To allow proper tracking and operation, the mount was set to an angle of  $26.4^\circ$  corresponding to our latitude.

Figure 2 depicts the telescope's final setup, well-balanced and properly polar-aligned. There is still a main broad connection problem preventing perfect pointing. However, this is a documented problem, which will require a firmware upgrade, to be done soon. The telescope can still observe under the current conditions. For the site to be ready, a rolling protective metal cover has been designed and manufactured and should be delivered soon. It will be used during the dry season so that the telescope can be kept outside. It will protect the telescope from dust, humidity, and heat, and will ensure quick access to it throughout the whole of the season, from May to November. It can be rolled away to allow easy access for stargazing.

### 3. Astrometric Calibration

Images taken with a CCD camera on a telescope have an X and Y pixel axis, a grid based on the physical size of the detector. These images can also have the approximate celestial coordinates, Right Ascension (RA) and Declination (DEC) of where the telescope was pointing while imaging the sky. An astrometric solution is the addition of the RA and DEC information, at a sub-pixel level, to the image header. This is called the World Coordinate System (WCS). Before processing any data, basic data reduction has to be done by taking flat, bias, and dark frames. The flat frames are taken immediately after the sunset in all filters for variations in the sensitivity of the individual pixels. Then, with the shutter closed, dark frames are taken with an image of noise from the dark current, followed by bias or zero frames used to eliminate read-out noise in the CCD. These tasks can be carried out using AstroImageJ. AstroimageJ is an open-source



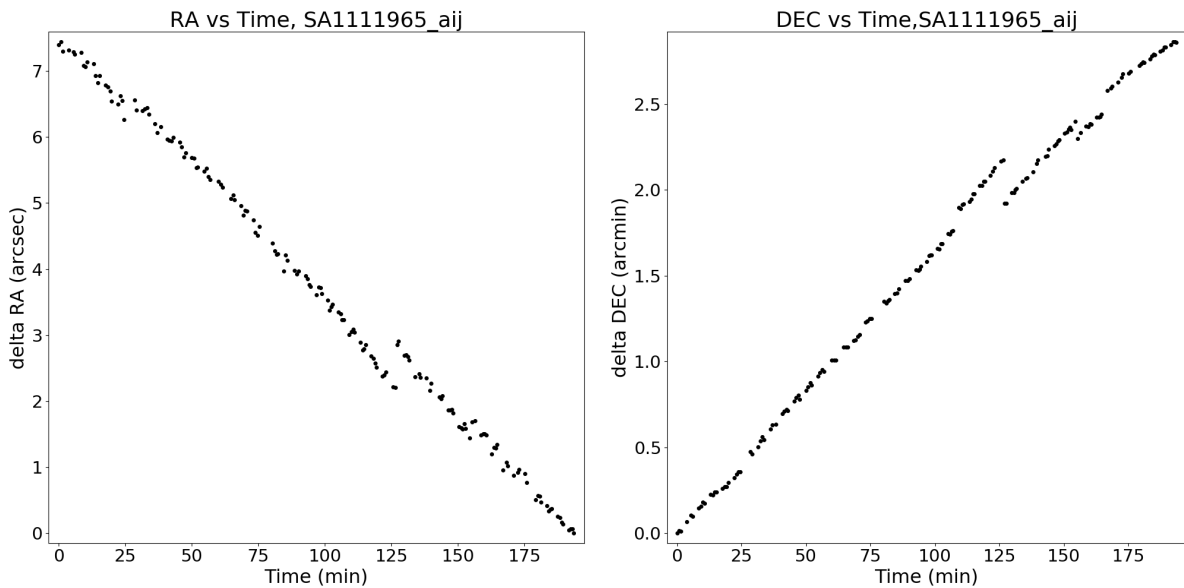
**Figure 2.** Image (a) and (b) shows the full operating telescope with counterweights, properly aligned and well-balanced.

software incorporating components of ImageJ which are in the public domain [3]. Once the basic reduction is done, an open source software such as Astrometry.net can be used to get astrometric solutions [4]. In each image, stars will be detected, and their relative position in X and Y will be compared to catalog data that has full WCS information to try to find a match. This information is saved in the FITS files header. FITS is a file format designed to store, transmit, and manipulate scientific images and associated data. Astrometry.net can be installed locally on a computer without requiring internet access, or used via an online interface from AstroImageJ. The online version is slower and has access to fewer options, but it works very well and without any configuration. The goal was to compare the suitability of the two different methods.

Using data collected over a three-hour long session of the random star field SA1111965 in the wide-band filter UBVRI, containing approximately 225 FITS images. The data was processed with AstroImageJ to get the first astrometric calibration. The same procedure was followed using the local installation of Astrometry.net, where few parameters were changed in both methods to obtain desirable results. The first round of plate-solving with AstroImageJ produced 114 fits over 13.30 hours, and the second round gave an additional 49 fits over 163 runs over approximately 6.23 hours. Running the files using Astrometry.net installed locally returns 179 successful files in 0.27 hours. The software returns 100 times faster results. The same case applies when using Astrometry.net with a combination of sextractor software [5], which optimally detects, measures, and classifies sources from astronomical images. It runs slightly longer (0.37 hours) with more successful files solved (196), and these results can be seen in Table 1.

**Table 1.** Summary of plate-solving methods.

<b>Astrometry.net (via AstroImageJ) online</b>						
	Time(hrs)	Total	Success	Still fail	New success	Seconds/solve
round 1	13.30	225	114	111	114	420.00
round 2	6.23	225	163	62	49	457.96
<b>Astrometry.net, local with ImageXY</b>						
	0.27	225	179	46	179	5.36
<b>Astrometry.net, local with sexttractor</b>						
	0.37	225	196	29	196	6.73

**Figure 3.** Plot (a) and (b) is the drift in RA and DEC with time using AstroimageJ.

To examine the drift in the RA and DEC of the reference pixel with time for each image, Figure 3 was constructed using the RA and DEC of the reference point with FITS keywords (CRVAL1 and CRVAL2), which are the world coordinates that corresponds to the pixel value and time taken from the FITS header. The drift seen in the figure is the slow movement of the telescope over time. According to the estimates, the drift in RA and DEC with time is 0.0421 and 0.0144 arcseconds per minute, respectively. The jump in the sequence corresponds to the time when we manually re-centered the field. A spacial distribution plot of RA vs DEC was then constructed for both methods, as seen in Figure 4.

While not totally identical, they are more, or less the same for both methods. In both cases, there is a slow drift of the reference pixel of the image, corresponding to the telescope's imperfect tracking. Tracking refers to the movement of the telescope's axis at a sidereal rate. A plot of that difference per image processed by the two different methods can be seen in Figure 5. There is no systematic difference observed; therefore both methods are comparable. Considering the time difference in processing the solutions, and the higher rate of success, a local installation of astrometry.net is preferable.

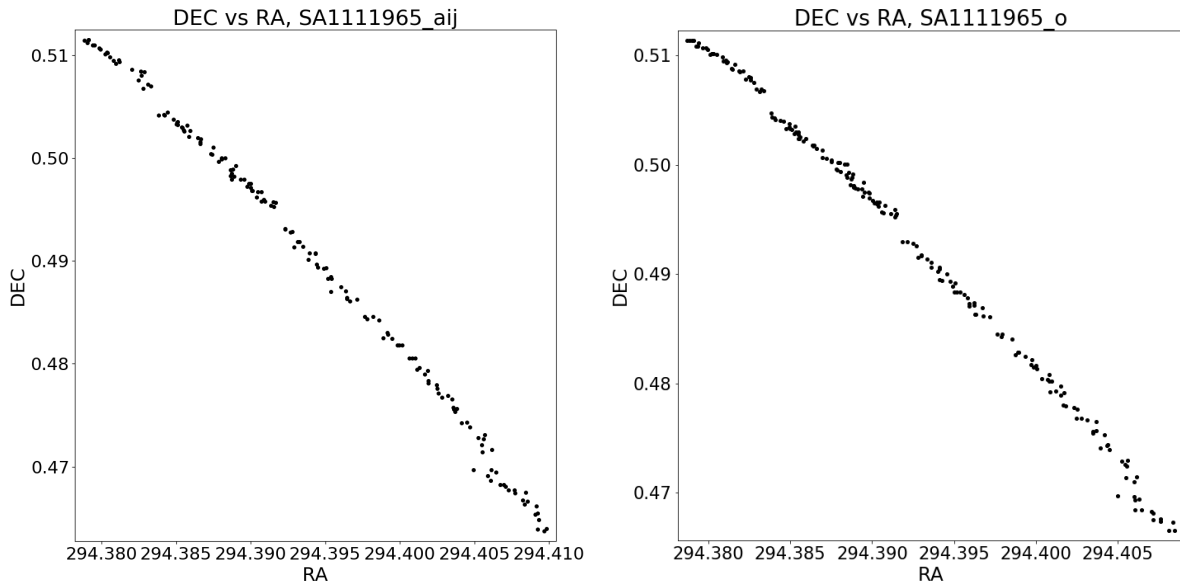


**Figure 4.** Images (a) and (b) shows comparison in RA and Dec of AstroImageJ and Astrometry.net .

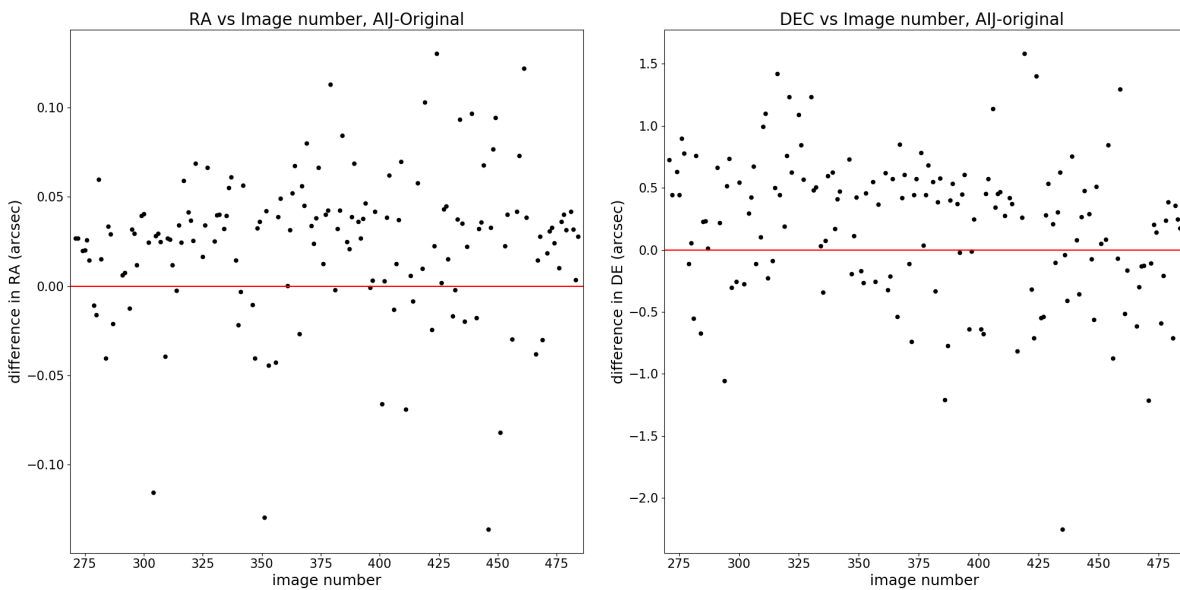


**Figure 5.** The images (a) and (b) shows the difference between AstroImageJ and Astrometry.net local for each individual image.

#### 4. Conclusion

In summary, the telescope has been setup; it is well-balanced and polar aligned, and almost ready for the public. A method was also developed to do astrometric calibration on images taken at the Nooitgedacht observatory without an internet connection. The best method is using the optional sextractor software to do the source detection on a local installation of astrometry.net.

**Acknowledgement:**

This research is supported by the National Research Foundation of South Africa, the National Astrophysics and Space Science Programme (NASSP, Grant number UID36279) and the Centre for Space Research at the NWU.

**References**

- [1] Corporation M I 2003 8",10",12",14",16" lx200gps schmidt-cassegrain telescopes 7" lx200gps maksutov-cassegrain telescope with autostar ii hand controller [https://www.meade.com/downloadEntityFile/assets/product\\_files/instructions/LX200GPS\\_manual.pdf](https://www.meade.com/downloadEntityFile/assets/product_files/instructions/LX200GPS_manual.pdf) accessed: 2022-06-10
- [2] iOptron 2008 ioptron cem60 center-balanced equatorial mount [https://tejraj.com/pdf/CEM60\\_Manual.pdf](https://tejraj.com/pdf/CEM60_Manual.pdf) accessed: 2022-06-04
- [3] Collins K A, Kielkopf J F, Stassun K G and Hessman F V 2017 *The Astronomical Journal* **153** 77
- [4] Lang D, Hogg D W, Mierle K, Blanton M and Roweis S 2010 *The Astronomical Journal* **139** 1782
- [5] Bertin E and Arnouts S 1996 *Astronomy and astrophysics supplement series* **117** 393–404

# Investigating HI size-mass relation in TNG50 and MIGHTEE-HI

O Rabyang<sup>1\*</sup>, A Gebek<sup>2</sup>, LL Leeuw<sup>1</sup> and M Baes<sup>2</sup>

1. Department of Physics and Astronomy  
University of the Western Cape

South Africa, Bellville, Cape Town, 7535

2. Department of Physics and Astronomy

Ghent University

Belgium, B-9000, Ghent, Sint-Pietersnieuwstraat, 25

E-mail: \*4115981@myuwc.ac.za

**Abstract.** Cosmological simulations of galaxy formation have been pivotal in advancing our understanding of structure and galaxy formation in the Universe. These simulations follow the nonlinear evolution of galaxies, modelling a variety of physical processes over an enormous range of time and length scales. Many of these physical processes are implemented through sub-grid prescriptions to alleviate the computationally expensive nature of simulations and deal with some of the complex physics and processes, which are not fully understood. As a result, discrepancies between observational and simulated data can arise. In this study, our goal is to investigate to which extent TNG50 galaxies follow the MIGHTEE-HI observations. We use the HI size-mass relation to study the consistency of the TNG50 galaxies in comparison to the MIGHTEE-HI galaxies. The TNG50 sample follows the same logarithmic relation derived from observation by previous work, between the diameter ( $D_{HI}$ ) and the mass ( $M_{HI}$ ) of HI discs. We measure a slope of  $0.478 \pm 0.004$ , an intercept of  $-3.172 \pm 0.030$  and a scatter of 0.29 dex. In future work, we intend on investigating the large scatter in our results as well as predict the cosmic evolution of the HI size-mass relation.

## 1. Introduction

Atomic hydrogen (HI) provides the primordial gas that serves as the raw material for the build-up of stellar mass. Observations of HI in galaxies provide a powerful probe to study galaxy formation and evolution mechanisms. Improvements in the sensitivity of observational surveys have made it possible to detect fainter HI structures than previous surveys could. Consequently, allowing for a better census of the total HI content in galaxies but also elucidates the interactions they have with their environment and their importance in galactic evolution.

Global HI relations, such as the HI mass vs stellar mass, neutral hydrogen mass function (HiMF), neutral hydrogen velocity function (HiVF) and the Tully-Fisher relation place constraints on cosmological models of galaxy formation and evolution. HI scaling relations in nearby disc galaxies, especially the tight HI size-mass relation, also provide important constraints. In this study, we will reproduce this relation for the TNG50 HI discs and test their consistency towards the MIGHTEE-HI observed galaxies.

The HI size-mass relation was first investigated by [2] and parametrised as follows:

$$\log(R_{HI}) = \alpha \times \log(M_{HI}) - \beta \quad (1)$$

where  $\alpha$  and  $\beta$  represent the slope and intercept, respectively.  $R_{HI}$  is in units of kpc and  $M_{HI}$  is in units of  $M_{\odot}$ . A slope of  $0.510 \pm 0.04$  and an intercept of  $-3.27 \pm 0.06$  was determined, suggesting that the average HI surface density in these galaxies is nearly constant.

A study by [6] reproduced the relation using the largest HI observational work-to-date. A galaxy collection of over 500 galaxies from different surveys, ranging over five decades in  $M_{HI}$  was studied. Consequently, they reported a slope of  $0.506 \pm 0.003$  and an intercept of  $-3.25 \pm 0.009$ . These results produced a noteworthy tight scatter relation of 0.06 dex. Other studies of observational galaxies have also reproduced the HI size-mass relation (e.g. [7], [8]). The general consensus is that the relation implies that HI galaxy discs of different types of galaxies are very self-similar, suggesting that all galaxies experience a similar evolutionary process so long as they remain gas-rich. This contradicts what was reported by [9], which equally noted that low-mass galaxies have denser HI discs in comparison to their more massive counterparts. This is a natural consequence due to the smaller galaxies having lower angular momentum.

A more recent study by [3] presented the homogeneous MIGHTEE (MeerKAT International GHz Tiered Extragalactic Exploration)-HI EARLY Science data. This sample consisted of 276 galaxies, ranging 4 orders of magnitude in HI mass at redshift zero. The study reported a slope of  $0.501 \pm 0.008$ , an intercept  $-3.252^{+0.073}_{-0.074}$  and corresponding observed scatter of 0.057 dex. These results are in good agreement with what is currently reported in the literature. This makes the HI size-mass relation a good candidate to place a strong constraint on the way that different processes, including gas inflow, star formation and feedback balance in numerical models of galaxy formation and evolution.

In this work, we present the HI size-mass relation for galaxies from the TNG50 cosmological simulation. We will be using simulated data produced by [13] to study the correlation between TNG50 galaxies and that of MIGHTEE-HI. Our goal is to investigate how well the TNG50 simulation predicts observations (i.e. MIGHTEE-HI).

### 1.1. TNG50

IllustrisTNG [5] is a suite of cosmological magnetohydrodynamical simulations of different volumes and resolutions, which constitutes of TNG100, TNG300 and TNG50. TNG50 is the last of the three projects, consisting of over 20 billion resolution elements and capturing spatial scales of  $\sim 100$  parsecs. The 50 Mpc box is sampled by  $2160^3$  dark matter particles, with masses of  $4 \times 10^5 M_{\odot}$  and  $2160^3$  initial gas cells, with masses of  $8 \times 10^4 M_{\odot}$ . Furthermore, TNG50 incorporates the comprehensive TNG model for galaxy formation and evolution physics, subsequently occupying a unique combination of large volume and high resolution. The large volumes feature allow for statistically robust comparison of entire galaxy populations whereas the high resolution more reliably model the cold, star-forming gas. TNG50 has proven to be an instrumental, theoretical tool for comparison through the production of mock observations and simulated data. Such studies have been recorded in [10] as well as [11] just to name a few. In this project we will exploit the statistical and resolution capabilities of TNG50 and compare them against the MIGHTEE-HI Early Survey data.

### 1.2. MIGHTEE-HI

Additionally, important to this work is the MIGHTEE-HI observational survey. MIGHTEE is one of eight Large Survey projects of MeerKAT [14]. The HI survey, MIGHTEE-HI, focuses on HI emission, absorption and polarisation in galaxies. MIGHTEE-HI is one of the first deep, blind, medium-wide interferometric surveys for HI. We have used the Early Science data [12] and have followed [3] to reproduce the observed MIGHTEE-HI size-mass relation. A 4k spectral line correlator mode was used to collect the data. The correlator had a channel width of 209 kHz and a velocity resolution of  $44.1 \text{ km.s}^{-1}$  at redshift zero. Two of the four MIGHTEE fields were used to carry out these observations. Namely; XMMLSS -covering approximately  $3.5 \text{ deg}^2$  of the sky - and COSMOS which covers  $1.5 \text{ deg}^2$  of the sky.

## 2. Methodology

[13] undertook a systematic study of models that predict the HI and  $H_2$  fraction and applied them to the TNG50 simulation galaxies. The modelling of the HI-to- $H_2$  transition and the relevant details of the TNG50 simulations are discussed at length in the paper previously mentioned. The HI-to- $H_2$  model by [4] has been implemented as the partitioning scheme of choice to produce the moment0 maps used in this study. The model from relies on surface densities rather than volume densities. The moment0 maps were produced by applying the HI-to- $H_2$  model. The UV field plays an important part in the destruction of hydrogen which is required for the HI-to- $H_2$  transition partitioning process. The radiative transfer code SKIRT has been employed to estimate the UV radiation field. The UV field is calculated by propagating light from star-forming regions and evolved stars through the dusty interstellar medium, taking dust attenuation into account.

### 2.1. Galaxy selection

TNG50 can fully represent simulated galaxy populations spanning  $10^7 < \frac{M_*}{M_\odot} < 10^{11.5}$  where  $M_*$  and  $M_\odot$  are the stellar mass and solar mass, respectively. However, in our study we worked with a base sample of  $M_* > 10^7 M_\odot$  and  $M_g > 10^6 M_\odot$  is imposed on the galaxies, where  $M_g$  is the gas mass. Correspondingly, these criteria produced feasible result when estimating the UV radiation field in SKIRT.

The size of the HI galaxy disc is conventionally defined as  $\Sigma_{HI} \sim 1 M_\odot pc^{-2}$ . Furthermore, an advantage of measuring  $R_{HI}$  at  $1 M_\odot pc^{-2}$  is that it is more easily measurable for small HI discs that are close to being unresolved. Some of the galaxies in this sample have surface densities lower than  $1 M_\odot pc^{-2}$ , these are thus negated. A stellar-mass-selected and HI-rich-selected samples of 12 611 and 10 652 is obtained respectively. For the purpose of this study we will only focus on the HI-rich-selected sample, which is a sample retention of 83.35 % from the stellar-mass-selected sample. We do not cut the galaxy sample any further at this point.

### 2.2. Determine the size of the TNG50 galaxies

In this section we apply the 2D Gaussian fit presented in equation (2), to determine the HI size of the galaxy

$$f(x, y) = A \exp(-(a(x - x_0))^2 + 2b(x - x_0)(y - y_0) + c(y - y_0)^2), \quad (2)$$

where A is the amplitude of the Gaussian peak in  $M_\odot pc^{-2}$ ,  $(x_0, y_0)$  represents the central position in pixels. We acknowledge that the HI radial distribution is not Gaussian, and that HI radial profiles often reveal a depletion at the center. However, for the purpose of this study we are

only interested in the outer part of the HI disc where the size is measured. The parameters  $a$ ,  $b$  and  $c$  are defined as:

$$a = \frac{\cos^2(\theta)}{2\sigma_X^2} + \frac{\sin^2(\theta)}{2\sigma_Y^2}, \quad (3)$$

$$b = \frac{\sin 2(\theta)}{4\sigma_X^2} + \frac{\sin 2(\theta)}{4\sigma_Y^2}, \quad (4)$$

$$c = \frac{\sin^2(\theta)}{2\sigma_X^2} + \frac{\cos^2(\theta)}{2\sigma_Y^2}. \quad (5)$$

The position angle is represented as  $\theta$  in radians,  $\sigma_X$  and  $\sigma_Y$  are the semi-major and semi-minor axis of the disk, respectively.

This study applies a framework which automatically calculates the size and mass of the individual HI disc galaxies. We select galaxies which have surface densities larger than  $1M_\odot.pc^{-2}$ . The sample then undergoes the 2D Gaussian fitting process. Similarly, the initial conditions for the amplitude,  $a, b, c$  and  $\theta$  parameters are calculated for all the individual galaxies. A python package called differential evolution is used for this role. This package looks for the optimal initial conditions by searching for the global minima within a given parameter space. These are then assigned as the initial conditions. This helps decrease the run time of the code as well as saves the memory due to the sheer quantity of the galaxy sample.

### 3. Results and discussion

In this section we will be discussing the results obtained from this study. Figure (1) and Figure (2) show the HI moment0 map of a HI-rich galaxy from our sample set and the TNG50 HI size-mass relation at  $z \sim 0$ , respectively. The red contour line seen in Figure (1) demarcates the region at which  $\Sigma_{HI} \sim 1M_\odot.pc^{-2}$ , which defines the  $R_{HI}$  of the galaxy disc. The blue points represent the galaxy population and the green shaded area represents the  $3\sigma$  region of this sample. Additionally, the two straight lines represented in black and red denote the MIGHTEE-HI[3] and TNG50 HI size-mass relation, respectively. These lines are represented by the the best-fit seen in equation (1). Our sample selection includes galaxies of different orientation and morphology. Nonetheless, a line of best fit through our data parametrises the TNG50 HI size-mass relation as follows

$$\log(D_{HI}) = 0.48 \pm 0.004 \times \log(M_{HI}) - 3.17 \pm 0.030. \quad (6)$$

Observationally the relation is extremely tight, with only 0.06 dex [6] and 0.057 dex scatter [3]. Likewise, our simulated galaxies reproduce the same general trend seen in observations. This trend depicts that larger HI size discs correspond to a higher HI mass which is in agreement with other studies.

The authors of [3] reported a sample galaxy population of  $M_{HI}$  ranging from  $M_{HI} \sim 10^8 - 10^{11.5}M_\odot$  with corresponding size ranges between  $D_{HI} \sim 1 - 2.3$  kpc. In this study a similar mass range,  $\sim 10^8 - 10^{10}M_\odot$ , was investigated. In this study we report HI disc galaxies size ranging between 0.1 – 2 kpc which are slightly lower than what was reported in [3].

Nevertheless, the TNG50 HI size-mass relation is in slight tension with what has been reported in other studies. Although our results show more scatter the best-fitting parameters are consistent with the observational findings of the literature such as [3] and [6]. This implies

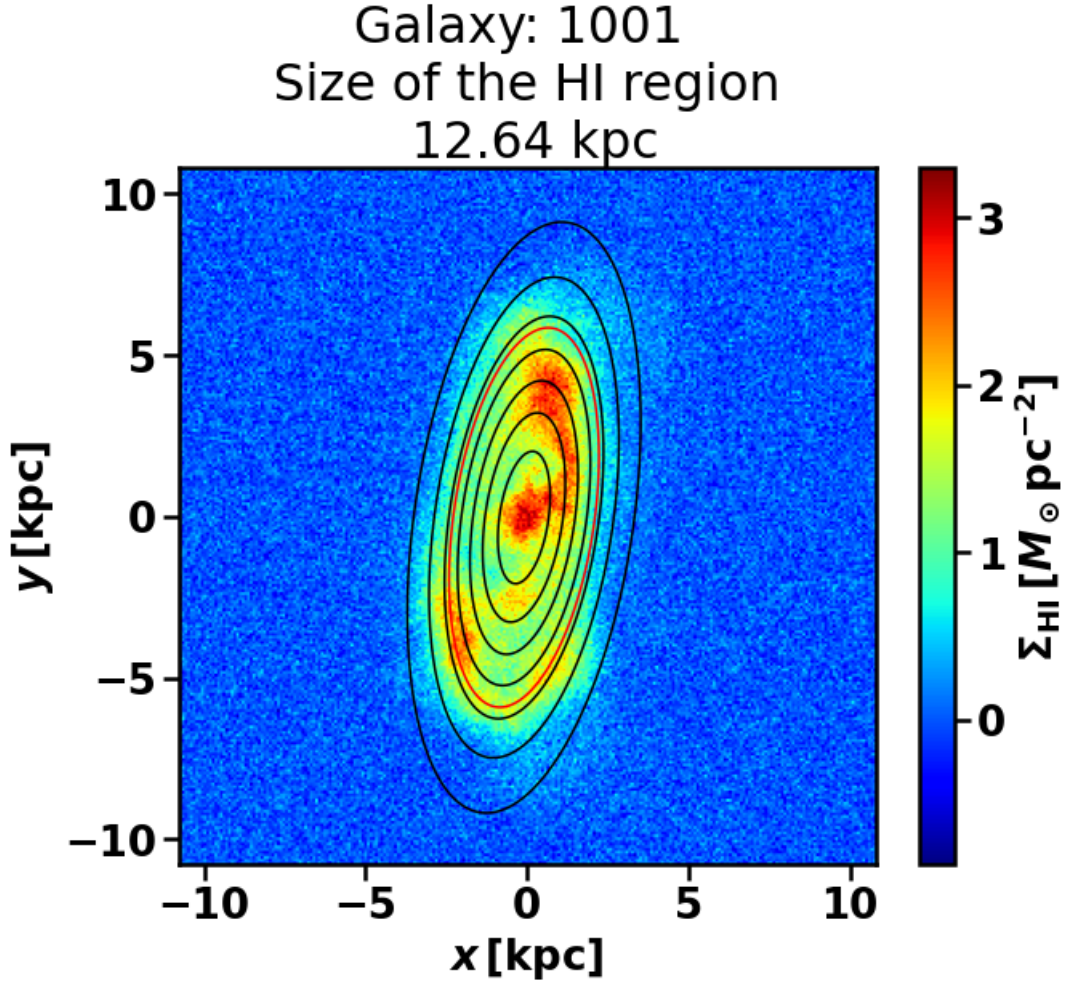


**Figure 1.** This HI moment0 map shows an example of a galaxy in our TNG50 sample. The red contour demarcates the region at which  $\Sigma_{HI} \sim 1M_{\odot}.pc^{-2}$ . The size and mass of this galaxy are  $D_{HI} \sim 12.68$  kpc and  $M_{HI} \sim 3 \times 10^8 M_{\odot}$  respectively.

that the average HI surface densities within TNG50 galaxies is an approximate constant and thus the mechanisms which balance the HI distribution in all the galaxies. Further investigation of the feedback mechanisms could improve on these results.

#### 4. Conclusions

We have presented the HI size-mass relation of the TNG50 HI galaxy discs. The sample contained  $\sim 10000$  HI-rich galaxies at redshift zero. The predictability of the HI size-mass relation makes it a good candidate for testing the accuracy or consistency of any model or simulation of galaxy evolution.

We measured galaxy HI masses and used the 2D Gaussian fitting method to estimate the size of the HI galaxy discs. The main results of our study are as follows :

- In our analysis we have reported a  $R_{HI}$  within the 1 – 10 kpc range with corresponding  $M_{HI}$  ranges from  $\sim 8.5 \times 10^7$  to  $\sim 1.3 \times 10^9 M_{\odot}$ .

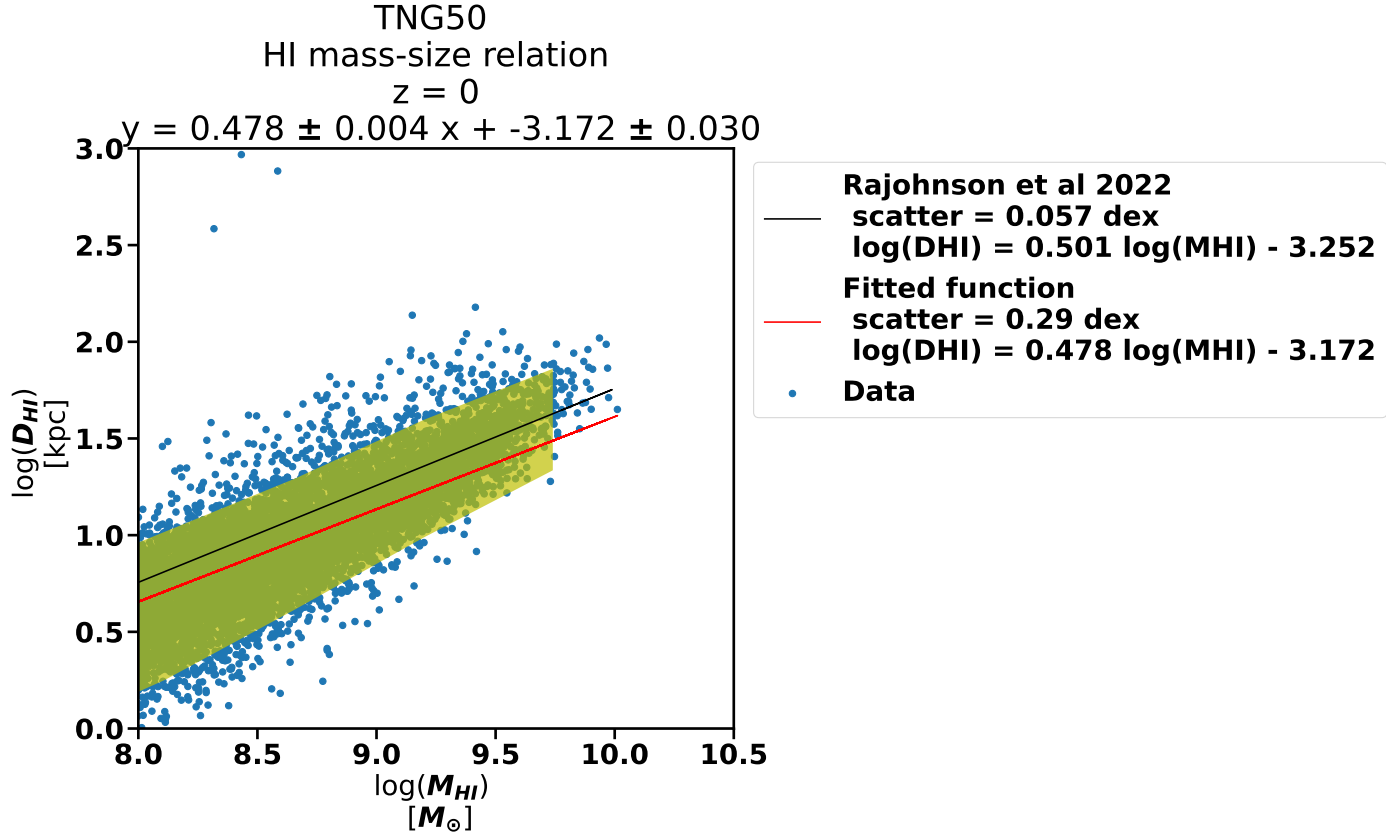


**Figure 2.** This plot shows the TNG50 size-mass relation. In the y-axis we have the size of the galaxy in kpc and in the x-axis we represent the HI size in  $M_{\odot}$ .

- We obtained a line-of-best fit of  $\log(D_{HI}) = 0.478 \pm 0.004 \times \log(M_{HI}) - 3.172 \pm 0.030$  for the TNG50 HI disc galaxies. There is slight tension between our results and Rajohnson [3] (as seen in Figure (2)). This maybe due to an underestimate of the total neutral gas abundance at  $z = 0$  by about a factor of two. we intend on investigating other HI scaling relations to verify this claim as well as look at how the spatial resolution of TNG50 HI maps affects the HI size-mass relation.
- Galaxies in hydrodynamical simulations and semi-analytical models have an analytically derived limit on its scatter of  $\leq 0.1$  dex. In this study a scatter of 0.29 dex was obtained. Our next task is to understand the reason behind this large scatter and improve this relation.

In this work we have successfully showed that the HI size mass relation can be used as a tool to investigate the agreeability of simulated galaxies.

## 5. Acknowledgments

We thank Gauri Sharma, Sambatriniaina Rajohnson, Natasha Maddox and Mekuanint Kifle for useful discussions. We also thank the NFR and SARAO for funding this project.

**References**

- [1] Stevens, A.R., Diemer, B., Lagos, C.D.P., Nelson, D., Pillepich, A., Brown, T., Catinella, B., Hernquist, L., Weinberger, R., Vogelsberger, M. and Marinacci, F., 2019. Atomic hydrogen in IllustrisTNG galaxies: the impact of environment paralleled with local 21-cm surveys. *Monthly Notices of the Royal Astronomical Society*, **483**(4), pp.5334-5354.
- [2] Broeils, A.H. and Rhee, M.H. Short 21-cm WSRT observations of spiral and irregular galaxies. HI properties, 1997. *Astronomy and Astrophysics*, **324**, pp.877-887.
- [3] Rajohnson, S.H., Frank, B.S., Ponomareva, A.A., Maddox, N., Kraan-Korteweg, R.C., Jarvis, M.J., Adams, E.A., Oosterloo, T., Baes, M., Spekkens, K. and Adams, N.J. MIGHTEE-HI: the HI size–mass relation over the last billion years, 2022. *Monthly Notices of the Royal Astronomical Society*, **512**(2), pp.2697-2706.
- [4] Gnedin, N.Y. Cosmic reionization on computers. I. Design and calibration of simulations, 2014. *The Astrophysical Journal*, **793**(1), p.29.
- [5] Springel, V., Pakmor, R., Pillepich, A., Weinberger, R., Nelson, D., Hernquist, L., Vogelsberger, M., Genel, S., Torrey, P., Marinacci, F. and Naiman, J. First results from the IllustrisTNG simulations: matter and galaxy clustering , 2018. *Monthly Notices of the Royal Astronomical Society*, **475**(1), pp.676-698.
- [6] Wang, J., Koribalski, B.S., Serra, P., van der Hulst, T., Roychowdhury, S., Kamphuis, P. and N. Chengalur, J. New lessons from the HI size–mass relation of galaxies, 2016. *Monthly Notices of the Royal Astronomical Society*, **460**(2), pp.2143-2151.
- [7] Marinacci, F., Grand, R.J., Pakmor, R., Springel, V., Gómez, F.A., Frenk, C.S. and White, S.D. Properties of HI discs in the Auriga cosmological simulations , 2017. *Monthly Notices of the Royal Astronomical Society*, **466**(4), pp.3859-3875.
- [8] Bahé, Y.M., Crain, R.A., Kauffmann, G., Bower, R.G., Schaye, J., Furlong, M., Lagos, C., Schaller, M., Trayford, J.W., Vecchia, C.D. and Theuns, T. The distribution of atomic hydrogen in eagle galaxies: morphologies, profiles, and HI holes, 2016. *Monthly Notices of the Royal Astronomical Society*, **456**(1), pp.1115-1136.
- [9] Lelli, F., McGaugh, S.S. and Schombert, J.M. SPARC: mass models for 175 disk galaxies with Spitzer photometry and accurate rotation curves, 2016. *The Astronomical Journal*, **152**(6), p.157.
- [10] Diemer, B., Stevens, A.R., Lagos, C.D.P., Calette, A.R., Tacchella, S., Hernquist, L., Marinacci, F., Nelson, D., Pillepich, A., Rodriguez-Gomez, V. and Villaescusa-Navarro, F. Atomic and molecular gas in IllustrisTNG galaxies at low redshift, 2019. *Monthly Notices of the Royal Astronomical Society*, **487**(2), pp.1529-1550.
- [11] Stevens, A.R., Diemer, B., Lagos, C.D.P., Nelson, D., Obreschkow, D., Wang, J. and Marinacci, F. Origin of the galaxy HI size–mass relation, 2019. *Monthly Notices of the Royal Astronomical Society*, **490**(1), pp.96-113.
- [12] Maddox, N., Frank, B.S., Ponomareva, A.A., Jarvis, M.J., Adams, E.A.K., Davé, R., Oosterloo, T.A., Santos, M.G., Blyth, S.L., Glowacki, M. and Kraan-Korteweg, R.C. MIGHTEE-HI: The H I emission project of the MeerKAT MIGHTEE survey, 2021. *Astronomy Astrophysics*, **646**, p.A35.
- [13] Andrea Gebek, Maarten Baes, Benedikt Diemer, Erwin de Blok, Dylan Nelson, Anand Utsav Kapoor, Peter Camps, Omphile Rabyang, Lerotherdi Leeuw. The atomic-to-molecular hydrogen transition in TNG50: Exploration of HI maps using realistic UV fields. *Unpublished manuscript*.
- [14] Jonas, J. MeerKAT Team, 2016. *MeerKAT Science: On the Pathway to the SKA*, **1**.

# Spectral and temporal analysis of short gamma-ray bursts detected by the *Fermi* space telescope with known redshift

D J Maheso<sup>1</sup>, S Razzaque<sup>1</sup> and F F Dirirsa<sup>2</sup>

<sup>1</sup> Centre for Astro-Particle Physics (CAPP) and Department of Physics, University of Johannesburg, PO BOX 524, Auckland Park 2006, South Africa

<sup>2</sup> Astronomy and Astrophysics Department, Entoto Observatory and Research Center, Space Science and Geospatial Institute, Addis Ababa, Ethiopia

E-mail: d.j.maheso@gmail.com

**Abstract.** Gamma-ray bursts (GRBs) are highly energetic impulses of  $\gamma$  rays that are classified into two major categories, namely the long and short GRBs. Their distinction lies in their duration ( $T_{90}$ ) which is calculated from the photon flux accumulation over time. Long GRBs lasts for more than 2 seconds whilst short GRBs lasts for less than 2 seconds with their prompt emission being in the keV to GeV energy band. Short GRBs are typically spectrally hard and the relation between their duration and spectral index depicts a weak inverse correlation. In this study, a sample of sources with known redshift made up of 15 short GRBs detected by *Fermi* Gamma Ray Burst Monitor (GBM) and one intermediate GRB, GRB100816A were selected for spectral studies in the energy range 10 - 900 keV. Most sources in the sample have photons detected by the *Fermi*-Large Area Telescope (LAT) low energy event (LLE) selection except for GRB090510A which is the brightest source in the sample. As a result it has a considerable number of high energy photons with the highest energy photon energy of 29.9 GeV. The counts obtained from the GBM data were binned and their most prominent pulses were selected for spectral and temporal analysis. Only 12 sources from the sample had prominent pulses including the double peaked GRB111117A. The pulses were fitted using the Norris function. The rise times of the pulses are compared with the rise time of a magnetar giant flare, in order to distinguish between the two  $\gamma$ -ray transients.

## 1. Introduction

Gamma-ray bursts (GRBs) are among the most luminous sources in the universe [1, 2]. They occur at cosmological distances hence they could be used as cosmological probes. In this study, short GRBs (SGRBs) with 90% of their  $\gamma$ -ray fluence being in the interval less than 2 seconds (i.e.  $T_{90} < 2$  seconds) detected by the *Fermi* telescope are selected. These sources could be treated as cosmological standard candles, similar to Type-Ia supernovae, by using various phenomenological relations among observed parameters [3]. Sources from star forming galaxies are also detected as  $\gamma$ -ray transients which are not cosmological. These are called magnetar giant flares (MGFs) which are associated with magnetars.

Magnetars are neutron stars (NSs) that are extremely magnetized and are produced by 0.5% of core collapse SNe (CCSNe) [4]. MGFs can be easily mistaken for cosmological SGRBs. For

instance, GRB790305 was detected in 1979 which was the first giant flare to be observed [5] hence the aim to further make their criteria clearer. MGFs arise from star forming galaxies and they tend to look like the cosmological hard SGRBs hence fake SGRBs [6] whilst cosmological SGRs which will be refereed to as real SGRBs originate from the merging of compact binary systems [7] including NS–NS binary systems, white dwarfs and BH–NS systems.

Fake SGRB pulses depict numerous milliseconds (ms) for their rise time which is much shorter in comparison to cosmological SGRBs [4]. MGFs are however spectrally hard [4] which is similar to the spectral hardness of real SGRBs [8] hence it is often difficult to distinguish between the two. A recent study [9] showed that the  $T_{90}$  interval is not sufficient to distinguish between the two hence the attention to the  $\gamma$ –ray pulse properties. Moreover, MGFs are less energetic compared to their cosmological counterparts having emissions within the energy range  $\approx 10^{43} - 10^{46}$  erg [4, 5] whilst the energy of cosmological short bursts can go up to  $10^{53}$  erg .

These mistaken short bursts have posed a number of questions as their variations with cosmological bursts is significant thus their classification should be revised. Zhang et al. [6] asserts that these events are actually different from cosmological short bursts which have varying cosmological progenitors. One characteristic that distinguishes MGFs from cosmological short bursts is their multiple pulse events.

In this work, pulse fitting will be used to retrieve properties of SGRBs with known redshift. These properties will be compared to those of MGFs hence make it easy to distinguish the two. As a result, allow the study of these intriguing sources in detail.

## 2. Observations and Analysis

In the investigation of finding the distinction between cosmological SGRBs and MGFs a sample of 367 SGRBs with known redshift detected by the *Fermi* Gamma-Ray Burst Monitor (*Fermi* GBM) were selected. *Fermi* GBM is one of the two instruments of the *Fermi* space telescope which also consists of the major instrument; the Large Area Telescope (LAT). *Fermi* LAT is a pair-conversion instrument which is sensitive to  $\gamma$ -rays in the energy range of  $\approx 30$  MeV to  $> 300$  GeV [8] with a low FoV of 2.4 sr [10].

GBM is the minor instrument which has 14 detectors consisting of 2 BGO and 12 Thallium doped Sodium Iodide (NaI[Tl]) scintillation detectors and both detectors are utilised in spectroscopy [8]. The NaI detectors are sensitive in the energy range from 8 keV to 1 MeV and are utilised to obtain a full unocculted view of the sky. In the presence of a GRB event, they get triggered thus can approximate the location of the bursts by using relative count rates [8] making them ideal for triggering and localising GRB events [10]. BGO detectors are best for detecting high energy  $\gamma$ -ray photons and their sensitivity ranges from  $\approx 200$  keV–40 MeV [8].

The GRB signals in GBM are recorded as three data types; CTIME, CSPEC and TTE. CTIME has a high 256 ms temporal resolution with 8 energy channels [8], CSPEC data has a low 4 s spectral resolution with full spectral resolution of 128 energy channels that are used for spectroscopy [8] and TTE data has a  $2\mu\text{s}$  temporal resolution and 128 energy channel spectral resolution. The temporal resolution can be adjusted to an optimal value with enough statistics during the analysis [8], hence TTE data was utilised in this study.

From the sample consisting of 367 sources, only sources with prominent peaks were of interest. This brought down the number to 16 SGRBs. These sources possessed prominent peaks when their rate counts from different detectors are summed up. However, looking only at the data for each individual detector, some signals were not strong hence their pulses were faint. Therefore, those sources were not considered during pulse fitting and sources with high count rates without the summation of the data were chosen. Hence individual detector data was used instead. This allowed to clearly observe which detectors got triggered hence fit the pulse for the detector that has more counts. These resulted in having a sample of 12 sources. All detectors were chosen based on their rate counts, with the highest one being favourable.

The TTE data was refined using the *RMFIT* package<sup>1</sup>. The background of the data was fitted with a polynomial of degree 1. The 30 - 40 keV energy channel was excluded as it corresponds to the iodine K-edge. The pulses were binned with 16 ms resolution. Finer binnings revealed significant features for GRB 090510 and GRB201221D, see figures 1 and 3.

The pulses were fit with the so-called Norris function [11] and a  $\chi^2$  test was done to determine the pulses goodness of fit.

$$I(t) = \begin{cases} A \exp \left[ - \left( \frac{|t-t_{peak}|}{t_{rise}} \right)^{\nu_1} \right]; & t < t_{peak} \\ A \exp \left[ - \left( \frac{|t-t_{peak}|}{t_{fall}} \right)^{\nu_2} \right]; & t > t_{peak} \end{cases} \quad (1)$$

The function is mathematical and it gives the rising ( $t_{rise}$ ) and falling times ( $t_{fall}$ ) of the pulses which are the free parameters. The amplitude of a pulse is given by  $A$  and is fixed for each source alongside the pulse peak time  $t_{peak}$ ,  $\nu_1$  and  $\nu_2$ . The exponential parameters describes the shape of the fit. The former is responsible for the exponential shape whilst the latter is dominant when the fit has a Gaussian shape.

After careful analysis, two sources were removed from the sample consisting of SGRBs with prominent peaks, hence only 10 cosmological SGRB sources were left for analysis. Their analysis was done alongside the recent MGF, GRB200415A. All bursts were analysed in five varying energy channels; 25 - 50, 50 - 100, 100 - 300 and > 300 keV as in the Norris et. al. paper [12] and an addition of 10 - 25 keV energy channel which is the minimum sensitivity of the GBM instrument.

### 3. Results and discussion

The results of the pulse fitting with the Norris function are summarised in table 1 to table 4. Only the results of 4 brightest SGRBs are presented in this work including that of GRB200415A, the MGF. A typical feature of MGFs is a multi-peaked spectra with a main prominent pulse followed by an oscillating pulse that is weak [6]. The oscillations explain NS rotational period. The rising pulse time of the main prominent pulse is usually tens of ms, see table 2. The fake GRB200415A emerged from a nearby galaxy and its most prominent first pulse was detected which resembles short hard GRBs [13] see figure 2. Hence the the distinction cannot be made from just looking at the spectra. Moreover, SGRB spectra are usually hard [10], which is not an ideal property to differentiate MGFs from cosmological SGRBs as they also have hard spectra. GRB200415A's pulse is non existent in the 10 - 25 keV energy range hence prominent pulses are observed at higher energies.

<sup>1</sup> [https://fermi.gsfc.nasa.gov/ssc/data/analysis/scitools/rmfit\\_tutorial.html](https://fermi.gsfc.nasa.gov/ssc/data/analysis/scitools/rmfit_tutorial.html)

GRB090510 is a bright short burst with a rising time in the range 22 - 43 ms (see table 1) which does not vary significantly from the 5 - 35 ms rising pulse time of the MGF, GRB200415A (see table 2). The detector selected for GRB090510 was NaI 6 which showed high rate counts amongst others. Although GRB090510 has multiple peaks (see figure 1), the observed multi-peaks are due to the small binnings and have no association with a MGF' origin as they are not oscillating nor appear in the background.

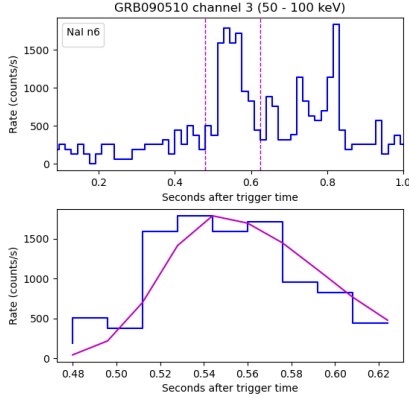


**Figure 1.** GRB090510,  $z = 0.903$ , NaI 6 detector.

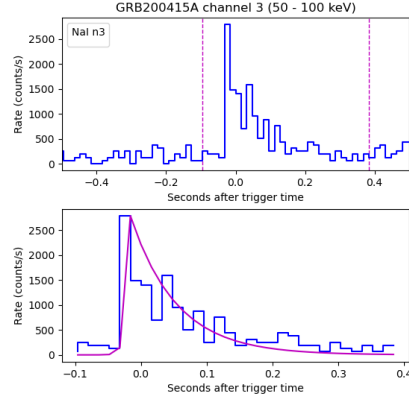


**Figure 2.** GRB200415A, NaI 3 detector.

**Table 1.** GRB090510 pulse fit results within the peak interval, 0.480 - 0.624 seconds.

Parameter	Channel number				
	1 (10 - 25 keV)	2 (25 - 50 keV)	3 (50 - 100 keV)	4 (100 - 300 keV)	5 (> 300 keV)
A (counts/s)	1276.99	1211.12	1787.80	2553.98	1213.14
$\nu_1, \nu_2$	1,1	1,1	2,2	2,2	1,1
Peak time (s)	0.544	0.528	0.544	0.544	0.544
Rise time (s)	$0.043 \pm 0.010$	$0.026 \pm 0.009$	$0.033 \pm 0.004$	$0.031 \pm 0.005$	$0.022 \pm 0.005$
$\chi^2/dof$	0.57/8	1.60/8	13.87/8	56.56/8	4.87/8

The intermediate source, GRB200826A has its duration  $T_{90}$  ranging from 1 to 2 seconds as observed with varying detectors [9] therefore, making  $T_{90}$  insufficient to distinguish GRBs from MGFs alongside spectral hardness. The pulses vary from one energy channel to another hence there is no particular pattern in its rising and falling times from energy channel 1 to channel 5 (table 3). The rising and falling times are a few 100 ms which varies significantly from that of the MGF. The pulses were best fitted with an exponential fit ( $\nu_1, \nu_2 = 1, 1$ ) of the Norris function except for channel 3 which is a combination of Gaussian ( $\nu_1 = 2$ ) and exponential ( $\nu_2 = 1$ ) fit. Table 2 shows that this trend is also shown by the MGF for energy channels 4 and 5.

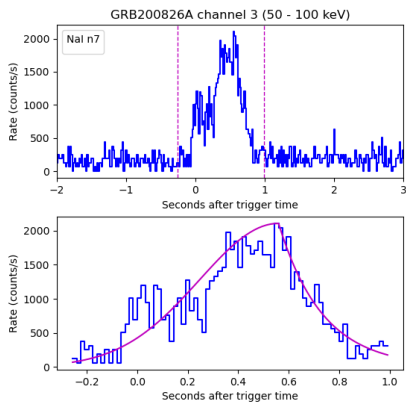
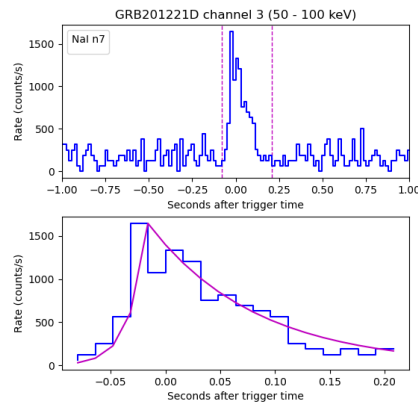
**Table 2.** GRB200415A pulse fit results within the peak interval, -0.096 - 0.384 seconds.

Parameter	Channel number				
	1 (10 - 25 keV)	2 (25 - 50 keV)	3 (50 - 100 keV)	4 (100 - 300 keV)	5 (> 300 keV)
A (counts/s)	—	1290.29	2788.55	6549.85	2580.54
$\nu_1, \nu_2$	—	1,1	1,1	2,1	2,1
Peak time (s)	—	0.00	-0.016	-0.016	0.00
Rise time (s)	—	$0.035 \pm 0.009$	$0.005 \pm 0.004$	$0.010 \pm 0.001$	$0.023 \pm 0.003$
Fall time (s)	—	$0.087 \pm 0.014$	$0.070 \pm 0.007$	$0.061 \pm 0.002$	$0.036 \pm 0.004$
$\chi^2/dof$	—	168.92/31	181.98/31	80.45/31	179.03/31

**Table 3.** GRB200826A pulse fit results within the peak interval, -0.128 - 0.896 seconds.

Parameter	Channel number				
	1 (10 - 25 keV)	2 (25 - 50 keV)	3 (50 - 100 keV)	4 (100 - 300 keV)	5 (> 300 keV)
A (counts/s)	1911.66	2357.30	2105.26	1973.12	317.30
$\nu_1, \nu_2$	1,1	1,1	2,1	1,1	1,1
Peak time (s)	0.496	0.400	0.560	0.448	0.288
Rise time (s)	$0.570 \pm 0.046$	$0.327 \pm 0.023$	$0.443 \pm 0.017$	$0.235 \pm 0.020$	$0.103 \pm 0.023$
Fall time (s)	$0.466 \pm 0.048$	$0.409 \pm 0.030$	$0.175 \pm 0.015$	$0.178 \pm 0.017$	$0.235 \pm 0.036$
$\chi^2/dof$	140.76/77	138.22/77	120.46/27.14/77	185.36/77	96.00/77

Both GRB200415A and GRB201221D have pulse rising and falling times in tens of ms range which is an observed feature of MGFs. The former is a MGF [6] however the latter suggests that it has a MGF origin as opposed to compact binary merger origin [14] due to its maximum pulse rising time of 87 ms, see table 4. Furthermore, the association of GRB201221D with a core-collapse origin is highly improbable [15] hence further raising the question regarding its progenitor.

**Figure 3.** GRB200826A,  $z = 0.748$ , NaI 7 detector.**Figure 4.** GRB201221D,  $z = 1.046$ , NaI 7 detector.

**Table 4.** GRB201221D pulse fit results within the peak interval, -0.080 - 0.208 seconds for n6 detector.

Parameter	Channel number				
	1 (10 - 25 keV)	2 (25 - 50 keV)	3 (50 - 100 keV)	4 (100 - 300 keV)	5 (> 300 keV)
A (counts/s)	1518.99	1203.42	1643.98	1393.80	—
$\nu_1, \nu_2$	1,1	1,1	1,1	2,1	—
Peak time (s)	0.016	0.032	-0.016	0.032	—
Rise time (s)	$0.047 \pm 0.011$	$0.087 \pm 0.016$	$0.016 \pm 0.003$	$0.070 \pm 0.009$	—
Fall time (s)	$0.106 \pm 0.017$	$0.114 \pm 0.016$	$0.098 \pm 0.007$	$0.051 \pm 0.010$	—
$\chi^2/dof$	8.43/17	1.26/17	2.35/17	42.08/17	—

#### 4. Conclusion

MGFs appear in nearby and star forming galaxies. They are associated with multi-peak signals that oscillate. However they are observed as single peaked sources hence commonly mistaken as cosmological SGRBs. From this work, the pulse fitting mechanism enabled to find the rising time of the pulses and it is observed that GRB200415A depicts a MGF rising time which ranges from 5 to 35 ms. GRB201221D also poses a challenge as it is known to be a cosmological SGRB however its pulse rising time suggests otherwise. GRB200826A's light curve pulse profile is protruding (figure 3) and there is no evidence of non-negligible signals outside the main peak hence this is a real SGRB. GRB090510 on the other hand depicts multiple pulses, however they are not above the background hence proving that it is also a genuine GRB despite its questionable rising and falling times. For future work, more MGF sources are to be studied including the GRB051103 and GRB070201 amongst other sources. Therefore allowing comprehensive studies on MGFs and cosmological SGRBs properties. [1]

#### References

- [1] T. Piran, "The physics of gamma-ray bursts," *Reviews of Modern Physics*, vol. 76, no. 4, p. 1143, 2005.
- [2] P. Meszaros, "Gamma-ray bursts," *Reports on Progress in Physics*, vol. 69, no. 8, p. 2259, 2006.
- [3] F. F. Dirirsa, S. Razzaque, F. Piron, M. Arimoto, M. Axelsson, D. Kocevski, F. Longo, M. Ohno, and S. Zhu, "Spectral analysis of fermi-lat gamma-ray bursts with known redshift and their potential use as cosmological standard candles," *The Astrophysical Journal*, vol. 887, no. 1, p. 13, 2019.
- [4] E. Burns, D. Svinkin, K. Hurley, Z. Wadiasingh, M. Negro, G. Younes, R. Hamburg, A. Ridnaia, D. Cook, S. Cenko, *et al.*, "Identification of a local sample of gamma-ray bursts consistent with a magnetar giant flare origin," *The Astrophysical Journal Letters*, vol. 907, no. 2, p. L28, 2021.
- [5] E. Mazets, S. Golenetskii, V. Il'Inskii, R. Aptekar, and Y. A. Guryan, "Observations of a flaring x-ray pulsar in dorado," *Nature*, vol. 282, no. 5739, pp. 587-589, 1979.
- [6] H.-M. Zhang, R.-Y. Liu, S.-Q. Zhong, and X.-Y. Wang, "Magnetar giant flare origin for grb 200415a inferred from a new scaling relation," *The Astrophysical Journal Letters*, vol. 903, no. 2, p. L32, 2020.
- [7] D. Eichler, M. Livio, T. Piran, and D. N. Schramm, "Nucleosynthesis, neutrino bursts and  $\gamma$ -rays from coalescing neutron stars," *Nature*, vol. 340, no. 6229, pp. 126-128, 1989.
- [8] P. N. Bhat, C. A. Meegan, A. von Kienlin, W. S. Paciesas, M. S. Briggs, J. M. Burgess, E. Burns, V. Chaplin, W. H. Cleveland, A. C. Collazzi, *et al.*, "The third fermi gbm gamma-ray burst catalog: the first six years," *The Astrophysical Journal Supplement Series*, vol. 223, no. 2, p. 28, 2016.
- [9] A. Rossi, B. Rothberg, E. Palazzi, D. Kann, P. D'Avanzo, L. Amati, S. Klose, A. Perego, E. Pian, C. Guidorzi, *et al.*, "The peculiar short-duration grb 200826a and its supernova," *The Astrophysical Journal*, vol. 932, no. 1, p. 1, 2022.
- [10] M. Ajello, M. Arimoto, M. Axelsson, L. Baldini, G. Barbiellini, D. Bastieri, R. Bellazzini, P. Bhat, E. Bissaldi,

- R. Blandford, *et al.*, “A decade of gamma-ray bursts observed by fermi-lat: the second grb catalog,” *The Astrophysical Journal*, vol. 878, no. 1, p. 52, 2019.
- [11] J. Norris, R. Nemiroff, J. Bonnell, J. Scargle, C. Kouveliotou, W. Paciesas, C. Meegan, and G. Fishman, “Attributes of pulses in long bright gamma-ray bursts,” *The Astrophysical Journal*, vol. 459, p. 393, 1996.
- [12] J. P. Norris, J. T. Bonnell, D. Kazanas, J. D. Scargle, J. Hakkila, and T. W. Giblin, “Long-lag, wide-pulse gamma-ray bursts,” *The Astrophysical Journal*, vol. 627, no. 1, p. 324, 2005.
- [13] K. Hurley, S. Boggs, D. Smith, R. Duncan, R. Lin, A. Zoglauer, S. Krucker, G. Hurford, H. Hudson, C. Wigger, *et al.*, “An exceptionally bright flare from sgr 1806–20 and the origins of short-duration  $\gamma$ -ray bursts,” *Nature*, vol. 434, no. 7037, pp. 1098–1103, 2005.
- [14] H.-Y. Yuan, H.-J. Lü, Y. Li, B.-B. Zhang, H. Sun, J. Rice, J. Yang, and E.-W. Liang, “Probing the progenitor of high-z short-duration grb 201221d and its possible bulk acceleration in prompt emission,” *Research in Astronomy and Astrophysics*, vol. 22, no. 7, p. 075011, 2022.
- [15] K. Misra, D. Kann, K. Arun, A. Ghosh, R. Gupta, L. Resmi, J. Fernández, C. Thöne, A. Postigo, S. Pandey, *et al.*, “Multi-wavelength analysis of short grb 201221d and its comparison with other high\& low redshift short grbs,” *arXiv preprint arXiv:2206.08947*, 2022.

# Spatially-resolved stellar kinematics of the CLoGS brightest group early-type galaxies

CD Stevens<sup>1</sup>, SI Loubser<sup>1</sup>

1. Centre for Space Research, NWU, Potchefstroom, 2520, South Africa

E-mail: [clinton.stevens.7@gmail.com](mailto:clinton.stevens.7@gmail.com)

**Abstract.** Galaxy groups within the local Universe contain over half of all observable galaxies. Furthermore, galaxy groups host the majority of both baryonic and dark matter content in the Universe. Therefore galaxy groups are excellent laboratories for studying galaxy evolution. Of particular importance are the brightest group early-type galaxies (BGEs) roughly located at the centre of each group's gravitational potential well. By studying the stellar kinematics of these BGEs, we hope to better understand the mass-assembly histories of these galaxies. The Complete Local-Volume Groups Sample (CLoGS) is a statistically complete survey of 53 galaxy groups in the optical, X-ray, and radio bands. We measure the spatially-resolved stellar kinematics of the BGEs of 18 of these groups. The spectra of these galaxies were obtained via optical spectroscopy with the Southern African Large Telescope (SALT). The stellar kinematics are obtained with full-spectrum fitting software. The radial profiles of both the stellar velocity dispersion and stellar rotational velocity of some of these BGEs are presented. We find a diverse range of stellar kinematics for the BGEs, for example, some BGEs show strong rotation and others no rotation. We further measure the stellar velocity dispersion slopes of these BGEs and compare them to other galaxy surveys and galaxy evolution simulations.

## 1. Introduction

Galaxies can be found within a variety of different environments such as clusters, groups, fields and voids, each with a different concentration of baryonic and dark matter. Of particular importance are galaxy groups which host over 60 % of all observable galaxies [1]. The dominant, central galaxy within each group is typically found close to the centre of the group's dark matter halo [2]. The mass assembly histories of brightest group early-type galaxies (BGEs) are strongly tied to their group environment's baryonic and dark matter content and are understood to result from prior merging processes [3]. However, the exact mass assembly histories of BGEs are still poorly understood and more unique than previously thought [4] [5] [6]. To constrain the mass profiles of BGEs and their group environments, the dynamical mass of these galaxies can be determined by measuring their stellar kinematics [5] [6]. These mass profiles can in turn be used to build galaxy evolution models and simulations, which improve our understanding of how galaxies evolve within group environments [7]. In this study, we will measure the spatially-resolved stellar kinematics of 18 of the Complete Local-Volume Groups Sample (CLoGS) BGEs. Our results will be compared with other galaxy surveys and galaxy evolution simulations to complement existing data.

CLoGS is a sample of 53 optically-selected galaxy groups located within 80 Mpc [8]. As part

of the selection criteria, these groups are fully virialised and contain a central early-type galaxy (BGE) [8]. 23 of these BGEs, observable from the Northern hemisphere, have already been studied with the Hobby-Eberly Telescope [9]. To complement this, we study 18 CLoGS BGEs observable from the Southern hemisphere with the Southern African Large Telescope (SALT). These BGEs are: ESO 507-25, NGC 128, NGC 193, NGC 1395, NGC 1550, NGC 2292, NGC 2911, NGC 3078, NGC 3325, NGC 3923, NGC 4697, NGC 5044, NGC 5084, NGC 5153, NGC 5903, NGC 7252 and NGC 7377 as originally presented by O’Sullivan *et al.* (2017).

## 2. Method

We obtain spatially-resolved optical spectra for our subsample of CLoGS BGEs using the SALT Robert Stobie Spectrograph (RSS). To measure the stellar kinematics of these BGEs, these spectra are fitted with the full-spectrum fitting software pPXF [10]. To constrain these measurements, pPXF is performed as a Monte-Carlo simulation of 50 iterations. An example pPXF fit is shown in Figure 1. We measure different apertures to create stellar velocity dispersion and stellar rotational velocity profiles. The slopes of the stellar velocity dispersion profiles are fitted with the function:  $\log(\frac{\sigma}{\sigma_0}) = \eta \cdot \log(\frac{R}{R_0}) + c$ , with  $c, \eta \in \mathbb{R}$ ,  $R_0 = 1$  kpc and  $\sigma_0$  is the central velocity dispersion measured up to  $R_0$ .

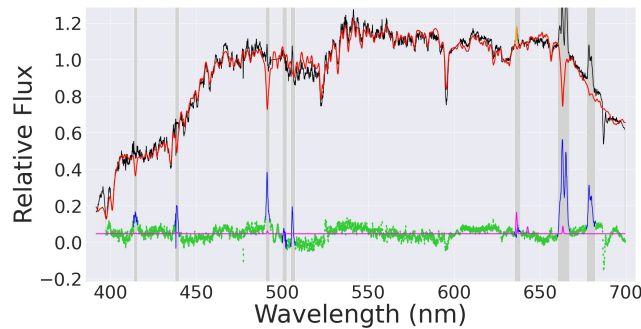


Figure 1: First iteration pPXF fit of ESO 507-25 using the MILES stellar library [11]. The observed spectrum is shown in black. The best pPXF fit is shown in red. The deviations are shown in green. The gas emission lines (shown in orange and blue) are masked in grey.

## 3. Results

We show the stellar velocity dispersion slopes and stellar rotational velocity profiles of NGC 193 and NGC 5084 to illustrate the diversity of stellar kinematics observed.

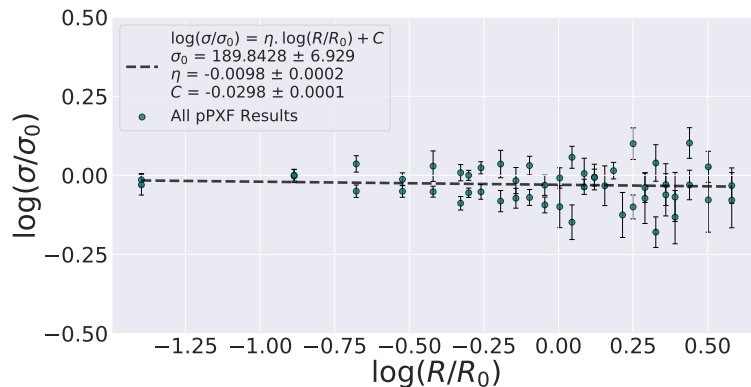


Figure 2: Stellar velocity dispersion slope of NGC 193. The slope is close to zero. The radial profile can be interpreted as flat with reasonable certainty.

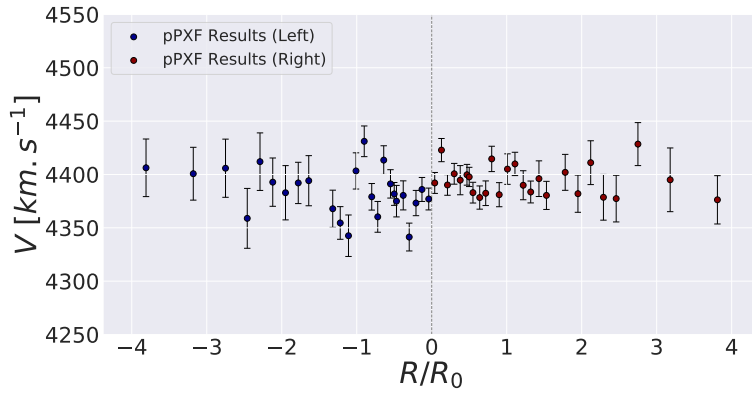


Figure 3: Rotational velocity profile of NGC 193. The pPXF results show that NGC 193 has no clear discernible rotation.

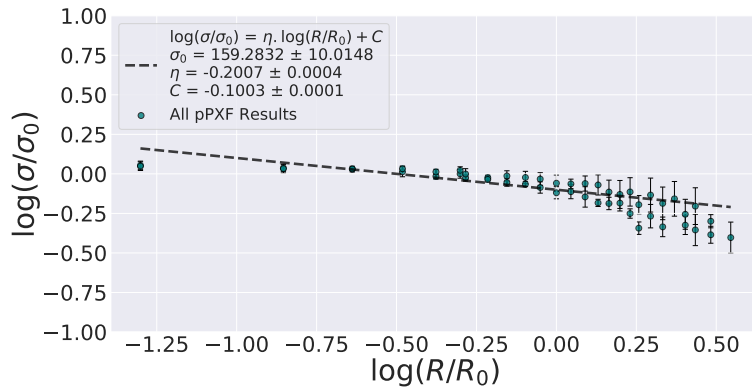


Figure 4: Stellar velocity dispersion slope of NGC 5084. The slope is small and negative. The radial profile can be interpreted as decreasing.

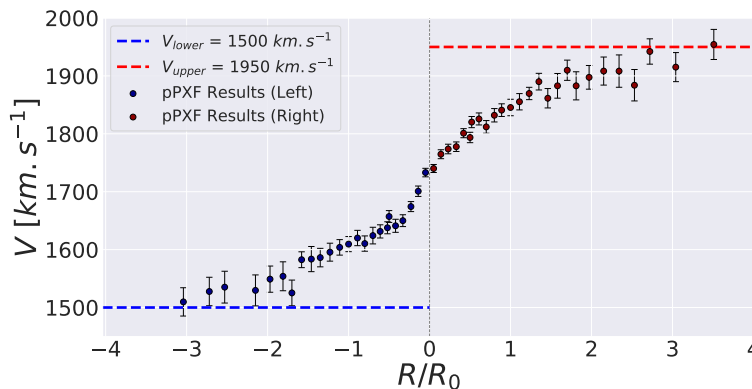


Figure 5: Rotational velocity profile of NGC 5084. The pPXF results show that NGC 5084 has very strong rotation with  $V_{\max} = (V_{\text{upper}} - V_{\text{lower}})/2 \approx 225 \text{ km s}^{-1}$ .

We summarise our results by comparing the velocity dispersion slopes measured for our sample of CLoGS BGEs against other complementary galaxy surveys and simulations. We firstly compare our observational results with other field early-type galaxies (ETGs) and brightest cluster galaxies (BCGs), similar to Loubser *et al.* (2018), as shown in Figure 6. In particular, we compare the 18 CLoGS BGEs from our study and the 23 CLoGS BGEs studied by Loubser *et al.* (2018), with similarly bright early-type galaxies (with  $-25.5 \text{ mag} \lesssim M_K \lesssim -21.5 \text{ mag}$ ) within the local Universe (within 80 Mpc). These ETG samples are documented in Cappellari *et al.* (2006) and Mehlert *et al.* (2000). In addition we compare the CLoGS BGEs with BCGs of similar redshift ( $z \lesssim 0.1$ ). The Multi-Epoch Nearby Cluster Survey (MENeACS) BCG sample and Canadian Cluster Comparison Project (CCCP) BCG sample are used, as similarly presented in Loubser *et al.* (2018). These BCGs, with a luminosity of  $-27.8 \text{ mag} \lesssim M_K \lesssim -25.7 \text{ mag}$ , are notably brighter than the CLoGS BGEs with a luminosity of  $-26 \text{ mag} \lesssim M_K \lesssim -24.2 \text{ mag}$  [9] [12]. Additionally these BCGs, with a cluster halo mass between  $1.6 \times 10^{14} M_\odot \lesssim M_{500} \lesssim 1.7 \times 10^{15} M_\odot$ , are more massive than the CLoGS BGEs, with a group halo mass between  $3.6 \times 10^{12} M_\odot \lesssim M_{500} \lesssim 4.4 \times 10^{13} M_\odot$  [9] [12].

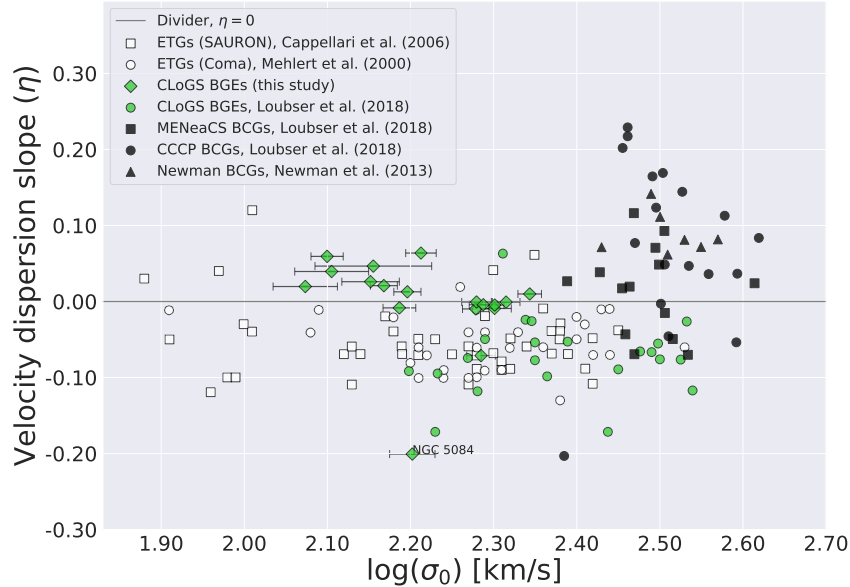


Figure 6: Velocity dispersion slope vs. central velocity dispersion. The ETGs from Cappellari *et al.* (2006) and Mehlert *et al.* (2000) are shown in white. The CLoGS BGEs are shown in green. The BCGs from Loubser *et al.* (2018) and Newman *et al.* (2013) are shown in black.

From figure 6 it can be seen that the stellar kinematics of the CLoGS BGEs closely resemble the field ETGs within the central velocity dispersion range  $2.1 \leq \log(\sigma_0) \leq 2.4$ . Figure 6 further shows that the MENeACS and CCCP BCGs have an overall higher velocity dispersion slope. This is unsurprising, since the dark matter haloes of clusters have the highest gravitational potential. However, the relationship between velocity dispersion slope and halo mass (from BGEs to BCGs, i.e. from group to cluster) is discontinuous. This implies that brightest central galaxies in groups and clusters evolve differently from one another.

Secondly, we compare our observational results with some of the latest galaxy evolution simulations, such as the Romulus suite of simulations performed by Jung *et al.* (2022) and the DIANOGA simulation performed by Marini *et al.* (2021). These simulations both assume a  $\Lambda$ CDM Universe with similar cosmological parameters. The Romulus suite of simulations as-

sume:  $\Omega_m = 0.309$ ,  $\Omega_\Lambda = 0.691$ ,  $\Omega_b = 0.0486$ ,  $H_0 = 67.8 \text{ km s}^{-1}\text{Mpc}^{-1}$  and  $\sigma_8 = 0.82$  and the DIANOGA simulation assumes:  $\Omega_m = 0.24$ ,  $\Omega_b = 0.037$ ,  $H_0 = 72 \text{ km s}^{-1}\text{Mpc}^{-1}$  and  $\sigma_8 = 0.8$  [13] [14]. In particular, we compare the 18 CLoGS BGEs from our study and the 23 CLoGS BGEs studied by Loubser *et al.* (2018) with the 107 Romulus brightest group galaxies (BGGs) presented by Jung *et al.* (2022) and the 60 DIANOGA Hydro BCGs presented by Marini *et al.* (2021) as shown in Figure 7. The 107 Romulus BGGs are divided into two categories: Romulus (Heavy) BGGs with a halo mass of  $\log(M_{200}/M_\odot) \geq 12.5$  and Romulus (Light) BGGs with a halo mass between  $12 \leq \log(M_{200}/M_\odot) < 12.5$ .

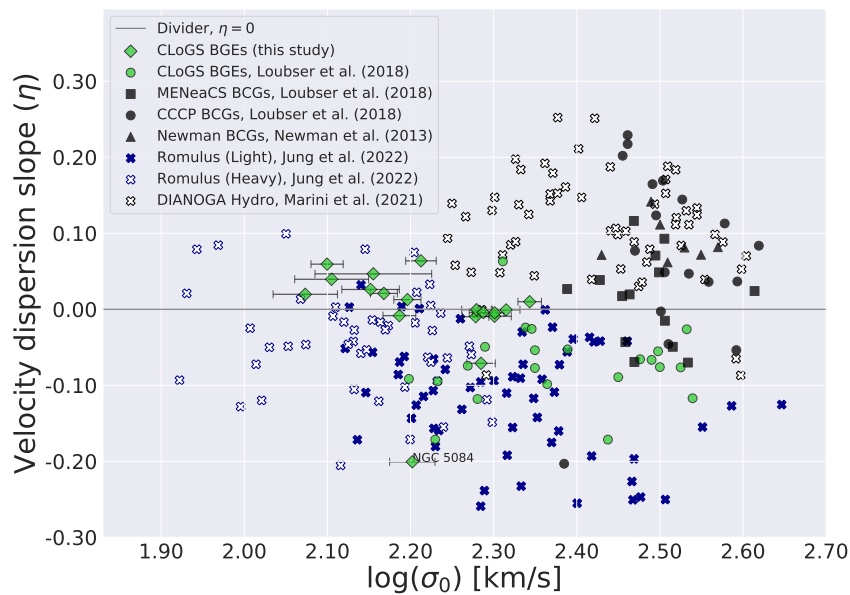


Figure 7: Velocity dispersion slope vs. central velocity dispersion. The CLoGS BGEs are shown in green. The results are compared with the latest simulation results: Romulus (shown in blue) and DIANOGA Hydro (shown in white).

From figure 7 it can be seen that the range of velocity dispersion slopes measured for the BGEs vastly differ from the results of the Romulus and DIANOGA simulations. This implies that the unique hydrodynamic and baryonic processes present in group environments are poorly understood or that the resolution of current simulations are too poor for group environments.

#### 4. Concluding Remarks and Future Work

We measure a variety of different stellar velocity dispersion and stellar rotational velocity profiles for our subsample of CLoGS BGEs. Out of the 18 CLoGS BGEs from our study, 8 are marginally rotating and 10 are non-rotating. All 18 BGEs have a nearly flat velocity dispersion slope, with  $-0.10 \leq \eta \leq 0.10$ , save NGC 5084 which has a slope of  $\eta \sim -0.20$ . As can be seen from Figure 6, the stellar kinematics of the CLoGS BGEs seem to more closely reflect field ETGs than that of BCGs. From Figure 7, it can be seen that our measured range of velocity dispersion slopes significantly differ from the simulation results of Marini *et al.* (2021) and Jung *et al.* (2022). This implies that our current galaxy evolution simulations are insufficient in modelling the stellar kinematics of BGEs. This discrepancy might be caused by the resolution of these simulations. We invite those building galaxy evolution simulations to make use of our observational data to test their results. Future work would involve a similar study of the remaining CLoGS BGEs and their stellar kinematics. These CLoGS BGEs include: NGC 252, NGC 1106, NGC 1167, NGC 1407, NGC 4956, NGC 5322, and NGC 5444.

## 5. Acknowledgements

This work is based on the research supported wholly by the National Research Foundation of South Africa (CDS: Grant Number 134198; SIL: Grant number 120850). Opinions, findings and conclusions or recommendations expressed in this publication is that of the author(s), and that the NRF accepts no liability whatsoever in this regard.

## References

- [1] Eke VR, Baugh CM, Cole S, Frenk CS and Navarro JF 2006 Galaxy groups in the 2dF Galaxy Redshift Survey: the number density of groups, *Monthly Notices of the Royal Astronomical Society*, 370, p. 1147-58
- [2] Shen, S., Yang, X., Mo, H., Van den Bosch, F. and More, S., 2014. The statistical nature of the brightest group galaxies. *The Astrophysical Journal*, 782(1), p.23.
- [3] Bezanson, R., Van Dokkum, P.G., Tal, T., Marchesini, D., Kriek, M., Franx, M. and Coppi, P., 2009. The relation between compact, quiescent high-redshift galaxies and massive nearby elliptical galaxies: Evidence for hierarchical, inside-out growth. *The Astrophysical Journal*, 697(2), p.1290.
- [4] Von Der Linden, A., Best, P.N., Kauffmann, G. and White, S.D., 2007. How special are brightest group and cluster galaxies?. *Monthly Notices of the Royal Astronomical Society*, 379(3), p.867-893.
- [5] Loubser, S.I., Lagos, P., Babul, A., O'Sullivan, E., Jung, S.L., Olivares, V. and Kolokythas, K., 2022. Merger histories of brightest group galaxies from MUSE stellar kinematics. *Monthly Notices of the Royal Astronomical Society*, 515(1), p.1104-1121.
- [6] Jung, S.L., Rennehan, D., Saeedzadeh, V., Babul, A., Tremmel, M., Quinn, T.R., Loubser, S.I., O'Sullivan, E. and Yi, S.K., 2022. Massive central galaxies of galaxy groups in the Romulus simulations: an overview of galaxy properties at  $z = 0$ . *Monthly Notices of the Royal Astronomical Society*, 515(1), p. 22-47
- [7] Springel, V., White, S.D., Jenkins, A., Frenk, C.S., Yoshida, N., Gao, L., Navarro, J., Thacker, R., Croton, D., Helly, J. and Peacock, J.A., 2005. Simulations of the formation, evolution and clustering of galaxies and quasars. *Nature*, 435(7042), p.629-636.
- [8] O'Sullivan, E., Ponman, T.J., Kolokythas, K., Raychaudhury, S., Babul, A., Vrtiliek, J.M., David, L.P., Giacintucci, S., Gitti, M. and Haines, C.P., 2017. The Complete Local Volume Groups Sample-I. Sample selection and X-ray properties of the high-richness subsample. *Monthly Notices of the Royal Astronomical Society*, 472(2), p.1482-1505.
- [9] Loubser, S.I., Hoekstra, H., Babul, A. and O'Sullivan, E., 2018. Diversity in the stellar velocity dispersion profiles of a large sample of brightest cluster galaxies  $z \leq 0.3$ . *Monthly Notices of the Royal Astronomical Society*, 477(1), p.335-358.
- [10] Cappellari, M., 2012. pPXF: Penalized Pixel-Fitting stellar kinematics extraction. *Astrophysics Source Code Library*, p.ascl-1210.
- [11] Falcón-Barroso, J., Sánchez-Blázquez, P., Vazdekis, A., Ricciardelli, E., Cardiel, N., Cenarro, A.J., Gorgas, J. and Peletier, R.F., 2011. An updated MILES stellar library and stellar population models. *Astronomy and Astrophysics*, 532, p.A95.
- [12] Kolokythas, K., O'Sullivan, E., Raychaudhury, S., Giacintucci, S., Gitti, M. and Babul, A., 2018. The Complete Local-volume Groups Sample-II. A study of the central radio galaxies in the high-richness subsample. *Monthly Notices of the Royal Astronomical Society*, 481(2), pp.1550-1577.
- [13] Tremmel, M., Karcher, M., Governato, F., Volonteri, M., Quinn, T.R., Pontzen, A., Anderson, L. and Bellovary, J., 2017. The Romulus cosmological simulations: a physical approach to the formation, dynamics and accretion models of SMBHs. *Monthly Notices of the Royal Astronomical Society*, 470(1), pp.1121-1139.
- [14] Bassini, L., Rasia, E., Borgani, S., Granato, G.L., Ragone-Figueroa, C., Biffi, V., Ragagnin, A., Dolag, K., Lin, W., Murante, G. and Napolitano, N.R., 2020. The DIANOGA simulations of galaxy clusters: characterising star formation in protoclusters. *Astronomy & Astrophysics*, 642, p.A37.
- [15] Cappellari, M., Bacon, R., Bureau, M., Damen, M.C., Davies, R.L., De Zeeuw, P.T., Emsellem, E., Falcón-Barroso, J., Krajnovic, D., Kuntschner, H. and McDermid, R.M., 2006. The SAURON project—IV. The mass-to-light ratio, the virial mass estimator and the Fundamental Plane of elliptical and lenticular galaxies. *Monthly Notices of the Royal Astronomical Society*, 366(4), pp.1126-1150.
- [16] Mehlert, D., Saglia, R.P., Bender, R. and Wegner, G., 2000. Spatially resolved spectroscopy of Coma cluster early-type galaxies-I. The database. *Astronomy and Astrophysics Supplement Series*, 141(3), p.449-468.
- [17] Newman, A.B., Treu, T., Ellis, R.S. and Sand, D.J., 2013. The density profiles of massive, relaxed galaxy clusters. II. Separating luminous and dark matter in cluster cores. *The Astrophysical Journal*, 765(1), p.25.
- [18] Marini, I., Borgani, S., Saro, A., Granato, G.L., Ragone-Figueroa, C., Sartoris, B., Dolag, K., Murante, G., Ragagnin, A. and Wang, Y., 2021. Velocity dispersion of brightest cluster galaxies in cosmological simulations. *Monthly Notices of the Royal Astronomical Society*, 507(4), p. 5780-5795.

# MeerChoirs: Preliminary neutral gas kinematics of interacting galaxies in the J1250-20 group

Sriram Sankar<sup>1,2</sup>, Moses Mogotsi<sup>1,3</sup>, Amidou Sorgho<sup>4</sup>, and Bradley S. Frank<sup>2,5,6</sup>

<sup>1</sup> South African Astronomical Observatory, Observatory 7925, Cape Town, SA

<sup>2</sup> Department of Astronomy, University of Cape Town, Private Bag X3, Rondebosch 7701, SA

<sup>3</sup> Southern African Large Telescope, Observatory, Cape Town 7925, SA

<sup>4</sup> Instituto de Astrofísica de Andalucía (IAA), Granada, Andalucía, ES

<sup>5</sup> South African Radio Astronomy Observatory, 2 Fir Street, Observatory, 7925, SA

<sup>6</sup> The Inter-University Institute for Data Intensive Astronomy (IDIA), Department of Astronomy, University of Cape Town, Private Bag X3, Rondebosch, 7701, SA

E-mail: [sriram@sao.ac.za](mailto:sriram@sao.ac.za)

**Abstract.** We present preliminary results from our study of the distribution and kinematics of the neutral gas in a low-inclination, late-type galaxy that is residing in a group environment and is undergoing a minor merger. We report the kinematics of the extended, warped, asymmetric, and lopsided HI disc of ESO575-006 which is part of the J1250-20 group observed with MeerKAT. The sensitivity and wide field-of-view of MeerKAT enable us to probe HI in a major extent of the group down to  $N_{\text{HI}} \sim 2.6 \times 10^{19} \text{ cm}^{-2}$  with a spatial resolution of  $47''$  and a spectral resolution of  $17.4 \text{ km s}^{-1}$ . We take advantage of MeerKAT's high spatial & spectral resolution, by producing a high-resolution cube for kinematic analysis, which probes down to  $N_{\text{HI}} \sim 4 \times 10^{19} \text{ cm}^{-2}$  with a spatial resolution of  $16''$  and a spectral resolution of  $5.8 \text{ km s}^{-1}$ . We see indications of Extra-Planar Gas (EPG), tidal interactions with neighbouring galaxies, lagging rotation in the extended disc, and an HI plume. We also detect five previously unknown dwarfs in the extended field that can potentially be part of the group. Resolved studies of such unique laboratories that encapsulate several key processes of the baryon cycle spanning the Interstellar Medium (ISM), Circumgalactic Medium (CGM), and Intra-Group medium (IGrM) are crucial for constraining galaxy evolution models.

## 1. Introduction

The hydrogen 21 cm line (hereafter HI) in the radio regime is a remarkable tracer for studying various processes in galaxies; offering unique insights about the structure, kinematics, and dynamics of the neutral gas, galaxies, and their environments. The HI discs of galaxies often extend to several times the radii of the optical disc and thus presents the potential to directly study mergers, accretion, interactions, and other environmental effects [1]. High sensitivity observations of lower column density HI makes it possible to study the extended disc, disk-halo-interface, inner CGM and even the neutral IGrM. Furthermore, resolved observations of these discs also provide rotation curves out to large radii, which can probe the underlying dark matter [2]. However, the extended gas distribution is far from a simple axi-symmetric, thin, differentially rotating disc. The outer HI discs of spiral galaxies are known to be warped but the drivers

and timescales of these warps are not well-established [1]. Warps, lopsidedness in the morphology and kinematics of HI discs as well as asymmetric global spectral profiles in most cases have been attributed to interactions. The HI disc is also expected to be flared in the outer parts, although, this can only be observed in the Milky-Way and highly inclined galaxies. Extra-planar gas (EPG) with radial and vertical velocity lags have also been observed directly in edge-on galaxies [3] and kinematically in certain nearly face-on [4] and intermediately inclined galaxies [5]. EPG in the Milky-Way has been observed in the form of High-velocity Clouds (HVCs) and Intermediate Velocity Clouds (IVCs) in HI emission and absorption signatures on background QSOs and halo stars [6]. A fraction of the EPG is expected to originate from the stellar disc as galactic fountains and another fraction from accretions stemming from interactions or infall from the cosmic web. Resolved and sensitive observations of galaxies at a range of inclination angles are required to understand the kinematics and origins of EPG. Most of the EPG reported to date have been from observations of highly inclined systems. A low-inclination perspective can be useful to link structures in the stellar disc with the observed EPG and also to explore various motions in the HI disc with reduced projection effects. The unparalleled combination of high sensitivity, large field of view, and high spatial & spectral resolution offered by MeerKAT makes it the optimal instrument to study HI gas kinematics in nearby galaxies and groups.

MeerChoirs (PI: Moses Mogotsi, 2020 & 2022 Open Time Proposal) is a deep HI study of the Choirs group sample [7] from the SINGG catalog (Survey for Ionization in Neutral Gas Galaxies; [8]). SINGG is an optical R-band and H $\alpha$  imaging follow-up to HIPASS (HI Parkes All-Sky Survey; [9]). The Choir sample consists of 15 late type dominated, gas rich groups that are thought to be in the early stages of assembly. About half of the sample contain two large spirals and a number of dwarf galaxies making them morphological analogs of the local group that are in a more compact state. The selection criteria for the Choir groups employed in [7] was constrained to a  $\sim 15'$  field because of field of view considerations of SINGG and HIPASS. The wider field of the groups were studied in Dz21[10] by querying NASA/IPAC Extragalactic Database (NED) for sources in a  $\sim 4^\circ$  field around each Choir group and cross matching the obtained catalogue with the 2MASS Extended Source Image Server in order to make a magnitude limited sample. They also use a catalogue of filaments in the local universe curated by [11] to estimate distances to the nearest filament for the Choir Groups. MeerChoirs will be the deepest and highest resolution HI study of the Choir groups to date. We aim to study the impact of the environment on galaxy evolution by mapping galaxy interactions, detecting previously undetected group members, and looking at the resolved HI-properties of individual galaxies within the groups. This work reports the preliminary kinematic analysis of a low-inclination, late-type galaxy (S1) in one of the Choir groups, HIPASS J1250-20 (hereafter J1250). Throughout this work, we use the cosmological parameters from Planck 2018 data[12]  $H_0 = 67.7 \text{ km s}^{-1} \text{ Mpc}^{-1}$ ,  $\Omega_m = 0.310$ , and  $\Omega_\Lambda = 0.69$ .

## 2. HIPASS J1250-20

J1250, within a projected radius of  $\sim 250$  kpc, hosts two large spiral galaxies (ESO575-G006 or S1 and ESO575-G004 or S2), three dwarf galaxies (S3, S4, and S5), and two compact H $\alpha$  emitters (S6 and S7; [7], Dz19[13]). In previous work, Dz21[10] conclude that J1250 is embedded in a low density environment and that its distance to the nearest filament is about  $\sim 4$  Mpc. Subsequently, they classify J1250 as an isolated group (See panel (c) and (d) of Appendix H figure 17 in D21). The neutral hydrogen content of the central region of the group, was mapped with ATCA and was presented in Dz19[13]. They report a possible interaction between the HI-rich galaxy, S1 and the HI-poor galaxy, S2. The dwarf galaxy S3 and the compact H $\alpha$  emitters, S6 and S7 were found to be within the HI envelope of S1. The HI associated with S2 was found to be off-center and gas content of the dwarf galaxy S4 was reported to be associated with S2. They conclude that the ongoing minor merger in S1 and the tidal interaction between S1 and S2

could be responsible for the increased HI content of S1 and the decreased HI content of S2. They also recover an HI mass of  $M_{\text{HI}}[M_{\odot}] = 10.53 \pm 0.2$  for a group distance of 114 Mpc, comparable to the mass of  $M_{\text{HI}}[M_{\odot}] = 10.39 \pm 0.11$  quoted in the HIPASS catalogue for a group distance of 110 Mpc [9]. However, due to the target's declination ( $\sim -20^{\circ}$ ), the synthesized beam for their observation was unevenly elongated in the direction of the beam major axis ( $30.79'' \times 102.8''$ ) causing spurious emission features as a result of beam smearing. Their observations, although smeared, probe HI down to a column density of  $\sim 3.5 \times 10^{19} \text{ cm}^{-2}$  with a velocity resolution of  $15 \text{ km s}^{-1}$ . But the reported  $N_{\text{HI}}$  is likely not at the  $3\sigma$  level since, the reported single channel RMS of  $2 \text{ mJy beam}^{-1}$  seem to be underestimated from  $2.9 \text{ mJy beam}^{-1}$ , which we recover from their primary beam corrected cube. Nonetheless, our observations detect gas down to their reported  $3\sigma_{\text{chan}}$  level with a higher spatial resolution. Moreover, we define our base contour at  $\sqrt{N}\sigma_{\text{chan}}\Delta v$ , where,  $N$  is the number of channels spanned by the source signal,  $\sigma_{\text{chan}}$  is the average noise per channel at the source position, and  $\Delta v$  is the channel width. The high noise, low resolution of the ATCA data, and the non-uniform beam renders it difficult to extract reliable gas kinematics.

### 2.1. MeerKAT observations and data reduction

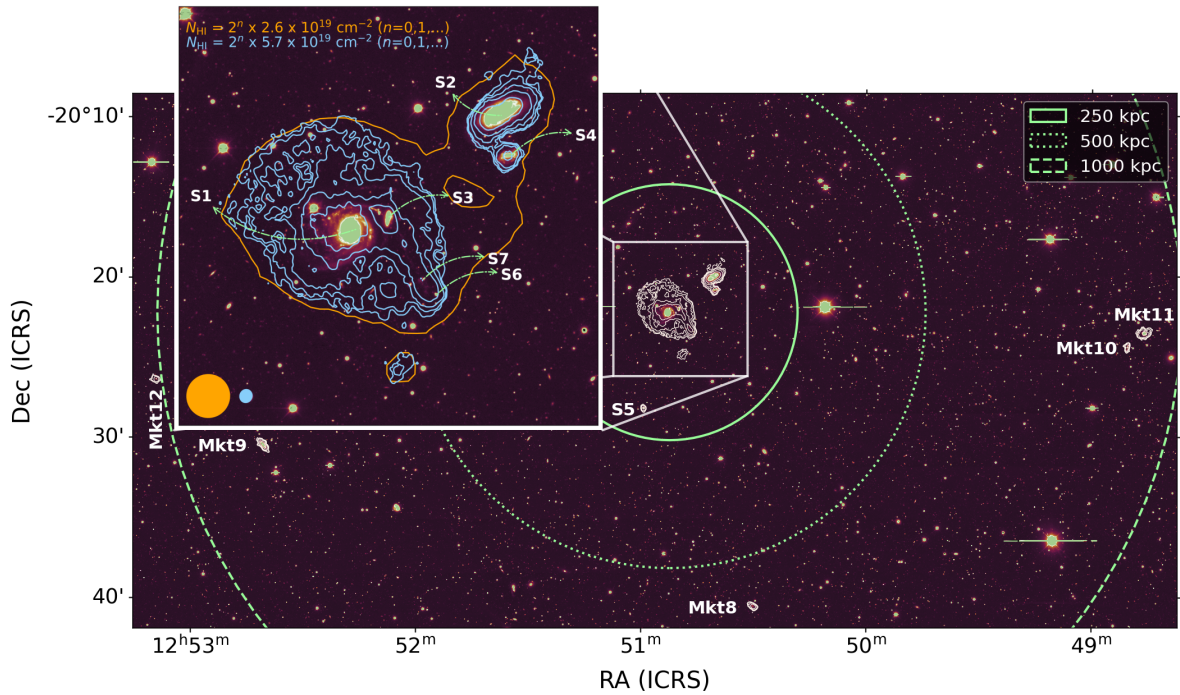


**Figure 1.** DECAM g band image of MeerKAT's 1 degree field centered at J1250-20 S1. The green circles correspond to 250, 500, and 1000 kpc projected distance from the center of the field. The inset highlights galaxies S1, S2, S3, S4, and H $\alpha$  emitters S7 and S6. The orange contour & beam is from the  $47''$  smoothed cube and the light blue contours & beam are from the  $16''$  cube. Both cubes were spectrally smoothed to  $17.42 \text{ km s}^{-1}$  to account for the inherent dispersion of HI. The base contour level is  $\sqrt{N}\sigma\Delta v$ .

J1250 was observed with MeerKAT in L-band with the 32k correlator mode in late February and April 2021. The full track of 4.78 hours was split into two blocks, a rising block and a setting block, to ensure efficient scheduling and to increase the uv coverage. The radio bright

QSO *B1245-197*,  $\sim 42'$  offset from the phase centre contaminates the field by inducing artefacts and disproportionately increasing the noise. The channels affected by strong RFI attributed to GPS L3 are ignored while imaging. After both the blocks have been observed, the two visibility sets from the correlator were fed to the SARA0 SDP calibration pipeline individually. The pipeline flags RFI signals, computes various calibration solutions (flux, phase, gain, bandpass) and applies the corrections to the data. We utilize the CASA[14] task `tclean` for continuum and spectral line imaging, `SoFiA2`[15] for producing clean-masks, `CARTA`[16] and `SoFiA-Image-Pipeline`[17] for inspection. The continuum of 15 MHz chunks centered at the redshifted HI emission extracted from the resulting gain-corrected, bandpass, and flux calibrated Measurement Sets (L1 visibility) are modelled and subtracted independently before being concatenated. This was to ensure optimal subtraction of the artefacts induced by the bright sources in the field. The final concatenated Measurement Set (MS) is imaged to produce  $12''$  and  $16''$  cubes with the latter being used for kinematic analysis. The final cubes with an RMS of  $\sim 0.2\text{mJy beam}^{-1}$ , which is 10 times lower than the reported noise of the ATCA cube, detect HI down to a column density of  $\sim 4 \times 10^{19} \text{ cm}^{-2}$  with a spectral resolution of  $5.8 \text{ km s}^{-1}$ . In MeerKAT's  $\sim 1^\circ$  field-of-view ( $\sim 1.9 \text{ Mpc}$ ; see figure 1), we detect HI in 5 other dwarf galaxies with optical counterparts in the deep DECam images (Mkt8 - Mkt12), which we could be potential group members. Only Mkt11 (2MASS J12484609-2023346) was reported in Dz21[10]. Mkt9 (2MASS J12524037-2030315 or LEDA 840758) does not have a redshift in the literature and the other three (Mkt8, Mkt10, Mkt12) have not yet been identified as sources let alone dwarf galaxies. We recover an HI mass for S1 and S2 of  $M_{\text{HI}}[M_\odot] = 10.61 \pm 0.01$  for a group distance of  $\sim 116 \text{ Mpc}$ , consistent with previously reported masses. The distance is the luminosity distance at the systemic velocity obtained from kinematic modelling.

## 2.2. Gas Kinematics in S1

The HI disc of S1 is extended, asymmetric, warped, and lopsided. Most of the rotating gas associated with S3 is distinctly seen in the emission line profiles. We see indications of EPG near the center, S3, and along the SW stellar stream. We also see an HI plume South-East of the SW stellar stream. Within the resolution of our data, we do not see any distinct kinematic signatures associated with the  $\text{H}\alpha$  emitters, S7 and S6. These Tidal Dwarf Candidates are still within the extended HI disc of S1 and there also seem to be signatures of EPG in the region. From the kinematics, it is evident that the HI disc is affected by the interaction between S1 and S3. S1's interactions with S2 and S4 could also be contributing to the observed gas distribution. Although, the resolved and uniformly sampled  $16''$  cube reveals the absence of a tidal bridge connecting S1, S4, and S2, at the same column density levels as that of the ATCA data (Dz19[13]). We smooth our data to  $47''$  resolution to detect faint emission in the bridge connecting the galaxies down to  $N_{\text{HI}} 2.6 \times 10^{19} \text{ cm}^{-2}$ . Furthermore, two other considerations lend credence to the argument of a low column density interaction between S1, S2, and S4. Firstly, the velocity centroids in the SW stellar stream, the approaching side of S4, and the receding side of S2 appear to be comparable. Secondly, the kinematic center of the gas envelope of S4 seem to be offset from the optical center in the SE direction, the direction corresponding to S1. The kinematic offset in S4 is not surprising given its proximity to and clear interaction with S2, but the direction of the offset bolsters the scenario of another interaction with S1. Since the interactions are mostly confined to the receding side, we model each side independently to attempt to isolate the influence of these interactions on the extended disc.

We perform 3D tilted ring modelling using `3D BAROLO` [18] to extract the kinematic and geometric parameters of the neutral gas envelope of S1. In panel (b) of figure 2, we compare three tilted ring models of the disc: (I) Receding side, (II) Approaching side, and (III) Both sides. In the Position-Velocity-Diagram (PVD; panel (a) of figure 2), we overlay the contours (green) of

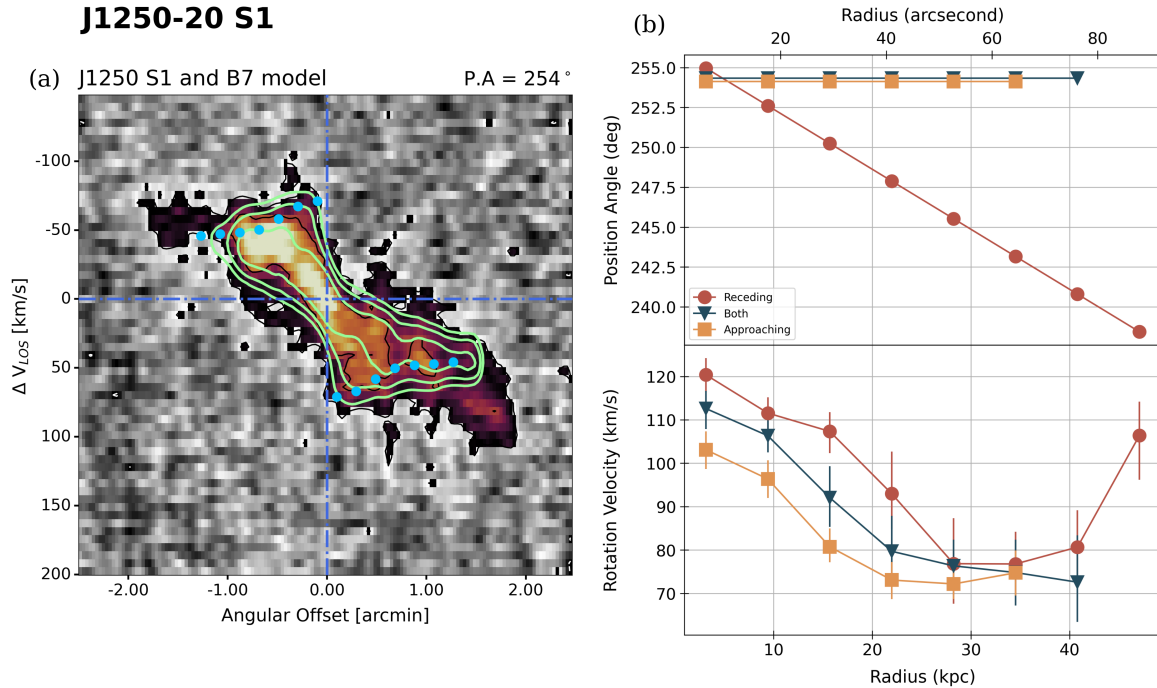


**Figure 2.** Panel (a): S1 major axis PVD extracted along a length of  $5'$  with a width of  $3'$  roughly spanning the minor axis. The green contours denote the model obtained from 7 ring tilted ring modelling of both sides. The slice was extracted with a position angle of  $254^\circ$ , the average P.A. of the model. Panel (b): Comparison of P.A. and rotation velocity obtained from tilted ring modelling of the receding side (SW), approaching side (NE), and both sides. The approaching and both side were modelled with constant inclinations  $\sim 41^\circ$  &  $39^\circ$  respectively and a constant P.A. of  $\sim 254^\circ$ . Whereas the receding side was modelled with an increasing inclination and a decreasing P.A.

the 7-ring model extracted from both sides of the disc. From the model we recover an average position angle of  $254^\circ$  measured from N to receding side. The P.A. extracted from R-band data in the SINGG catalog was  $\sim 304^\circ$ . The inclination obtained from the tilted ring modeling of both sides and just the approaching side is  $\sim 39^\circ$  &  $41^\circ$  respectively. The receding side of the disc is more warped than the approaching side and the obtained inclination increases from  $37^\circ$  in the inner ring to  $42^\circ$  in the outer ring. We recover a falling rotation curve from all three of our models of the warped disc. The slow rotating extended gas on the receding side also shows up as beard gas in the PVD.

We also perform Gaussian decomposition to study the component structure and to separate planar gas, extraplanar gas, and gas associated with S3. We utilize the machine learning assisted automated fitting tool, Gausspy+ [19] to decompose the spectra along each spaxel into either single or multiple Gaussian components. To avoid over-fitting and un-physical components we specify a maximum of 3 components per spaxel. The use of the corrected Akaike Information Criterion (AICc) for model selection also ensures that the model with the least number of components has a higher propensity for being selected. The fitting also takes into account spatial coherence due to the beam as well as the physical distribution of gas. The recovered component map and some example fitted spectra are shown in figure 3.

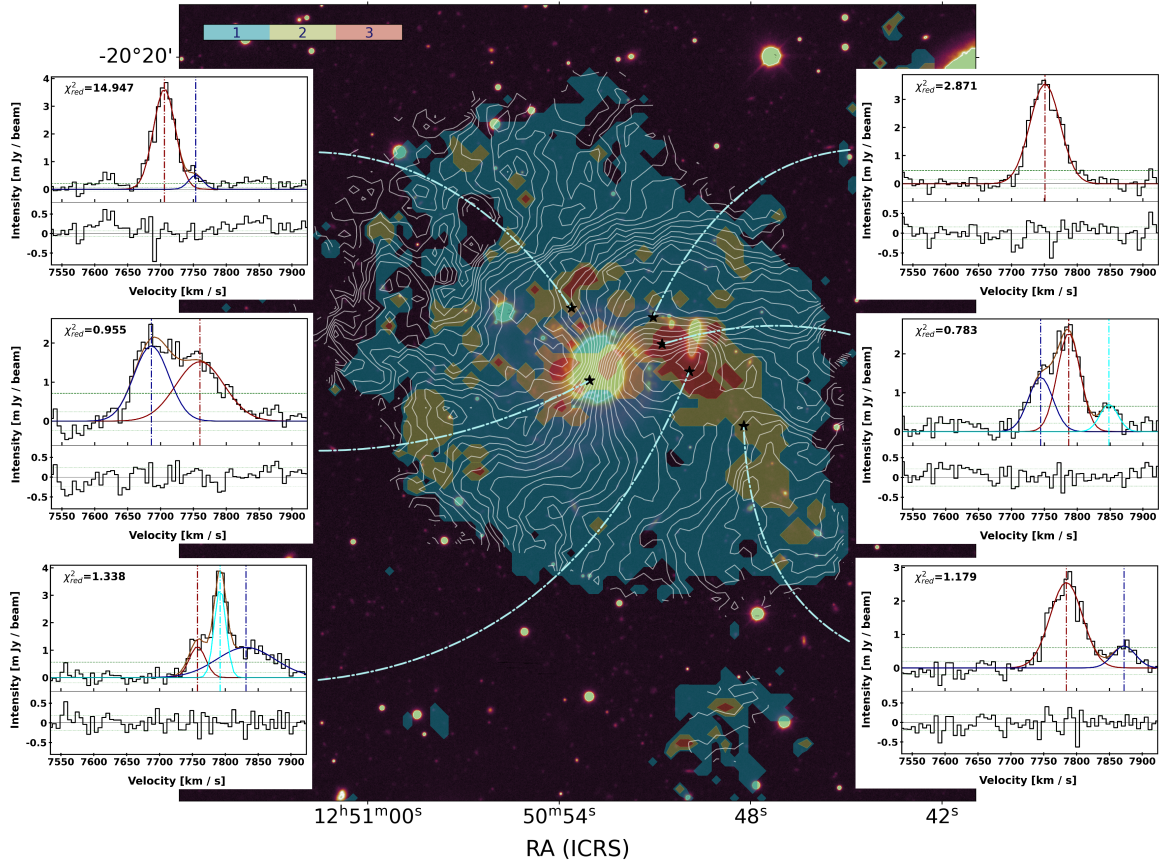


**Figure 3.** HI moment 1 contours and map of the number of fitted Gaussian components overlaid on DECam g band image. The plot also shows the spectrum of some select voxels fitted with either single or multiple Gaussian components.

### 3. Conclusion

In this era of high sensitivity, spatially resolved spectroscopy facilitated by modern day interferometers and integral field spectrographs, we can now study the resolved kinematics and disc dynamics of multi-phase gas in galaxies residing in various environments. Our preliminary analysis of the neutral gas kinematics of a low-inclination, late-type galaxy with ongoing minor and major interactions in a group, reveal a warped, lopsided, and asymmetric disc with extensive extra-planar gas, an HI plume, slow rotating extended gas, and possible deviations from circular motion. In a future work, we will report the detailed gas kinematics of the main group members along with an evaluation of galaxies in the extended field.

### Acknowledgments

We thank the referees for their helpful comments that helped improve the quality of this manuscript. SS and MM thank the South African Astronomical Observatory and the Southern African Large Telescope for funding this work. The MeerKAT telescope is operated by the South African Radio Astronomy Observatory, which is a facility of the National Research Foundation, an agency of the Department of Science and Innovation. The authors acknowledge the contribution of those who designed and built the MeerKAT instrument and the data processing pipelines. We acknowledge the use of the ilifu cloud computing facility - [www.ilifu.ac.za](http://www.ilifu.ac.za), a partnership between the University of Cape Town, the University of the Western Cape, the

University of Stellenbosch, Sol Plaatje University, the Cape Peninsula University of Technology and the South African Radio Astronomy Observatory. We also acknowledge various software and packages that facilitated this work including but not limited to Astropy, SoFiA2, CASA, CARTA, SoFiA Image Pipeline, Gausspy+, SlicerAstro, 3DBarolo, SpectralCube, etc.

## References

- [1] Sancisi R, Fraternali F, Oosterloo T and van der Hulst T 2008 *The Astronomy and Astrophysics Review*, Volume 15, Issue 3, pp.189-223 **15** 189 ISSN 0935-4956
- [2] de Blok W J G, Walter F, Brinks E, Trachternach C, Oh S H and Kennicutt R C 2008 *The Astronomical Journal* **136** 2648–2719 ISSN 0004-6256, 1538-3881
- [3] Zschaechner L K, Rand R J, Heald G H, Gentile G and Kamphuis P 2011 *The Astrophysical Journal* **740** 35 ISSN 0004-637X
- [4] Boomsma R, Oosterloo T A, Fraternali F, van der Hulst J M and Sancisi R 2008 *Astronomy and Astrophysics*, Volume 490, Issue 2, 2008, pp.555-570 **490** 555 ISSN 0004-6361
- [5] Marasco A, Fraternali F, Heald G, de Blok W J G, Oosterloo T, Kamphuis P, Józsa G I G, Vargas C J, Winkel B, Walterbos R a M, Dettmar R J and Jütte E 2019 *Astronomy & Astrophysics*, Volume 631, id.A50, 27 pp. **631** A50 ISSN 0004-6361
- [6] Marasco A and Fraternali F 2011 *Astronomy and Astrophysics* **525** A134 ISSN 0004-6361
- [7] Sweet S M, Meurer G, Drinkwater M J, Kilborn V, Dénes H, Bekki K, Hanish D, Ferguson H, Knezek P, Bland-Hawthorn J, Dopita M, Doyle-Pegg M T, Elson E, Freeman K, Heckman T, Kennicutt R, Kim J H, Koribalski B, Meyer M, Putman M, Ryan-Weber E, Smith C, Staveley-Smith L, Wong O I, Webster R, Werk J and Zwaan M 2013 *Monthly Notices of the Royal Astronomical Society* **433** 543–559 ISSN 0035-8711
- [8] Meurer G R, Hanish D J, Ferguson H C, Knezek P M, Kilborn V A, Putman M E, Smith R C, Koribalski B, Meyer M, Oey M S, Ryan-Weber E V, Zwaan M A, Heckman T M, Kennicutt Jr R C, Lee J C, Webster R L, Bland-Hawthorn J, Dopita M A, Freeman K C, Doyle M T, Drinkwater M J, Staveley-Smith L and Werk J 2006 *The Astrophysical Journal Supplement Series* **165** 307–337 ISSN 0067-0049
- [9] Meyer M J, Zwaan M A, Webster R L, Staveley-Smith L, Ryan-Weber E, Drinkwater M J, Barnes D G, Howlett M, Kilborn V A, Stevens J, Waugh M, Pierce M J, Bhathal R, de Blok W J G, Disney M J, Ekers R D, Freeman K C, Garcia D A, Gibson B K, Harnett J, Henning P A, Jerjen H, Kesteven M J, Knezek P M, Koribalski B S, Mader S, Marquarding M, Minchin R F, O'Brien J, Oosterloo T, Price R M, Putman M E, Ryder S D, Sadler E M, Stewart I M, Stootman F and Wright A E 2004 *Monthly Notices of the Royal Astronomical Society* **350** 1195–1209 ISSN 0035-8711
- [10] Džudžar R, Kilborn V, Sweet S M, Meurer G, Jarrett T H and Kleiner D 2021 *Monthly Notices of the Royal Astronomical Society* **500** 3689–3710 ISSN 0035-8711
- [11] Kleiner D, Pimblet K A, Jones D H, Koribalski B S and Serra P 2017 *Monthly Notices of the Royal Astronomical Society* **466** 4692–4710 ISSN 0035-8711
- [12] Planck Collaboration 2020 **641** A6 (*Preprint* 1807.06209)
- [13] Džudžar R, Kilborn V, Meurer G, Sweet S M, Drinkwater M, Bekki K, Audcent-Ross F, Koribalski B, Kim J H, Putman M, Ryan-Weber E, Zwaan M, Bland-Hawthorn J, Dopita M, Doyle-Pegg M T, Elson E, Freeman K, Hanish D, Heckman T, Kennicutt R, Knezek P, Meyer M, Smith C, Staveley-Smith L, Webster R and Werk J 2019 *Monthly Notices of the Royal Astronomical Society* **483** 5409–5425 ISSN 0035-8711
- [14] McMullin J P, Waters B, Schiebel D, Young W and Golap K 2007 **376** 127
- [15] Westmeier T, Kitaeff S, Pallot D, Serra P, van der Hulst J M, Jurek R J, Elagali A, For B Q, Kleiner D, Koribalski B S, Lee-Waddell K, Mould J R, Reynolds T N, Rhee J and Staveley-Smith L 2021 *Monthly Notices of the Royal Astronomical Society* **506** 3962–3976 ISSN 0035-8711
- [16] Comrie A, Wang K S, Hsu S C, Moraghan A, Harris P, Pang Q, Pińska A, Chiang C C, Chang T H, Hwang Y H, Jan H, Lin M Y and Simmonds R 2021 CARTA: The Cube Analysis and Rendering Tool for Astronomy Zenodo
- [17] Hess K M, paoloserra, Boschman L, Shen A and H J 2022 Kmhess/SoFiA-image-pipeline: SoFiA Image Pipeline v1.2.0 Zenodo
- [18] Di Teodoro E M and Fraternali F 2015 *Monthly Notices of the Royal Astronomical Society* **451** 3021–3033 ISSN 0035-8711
- [19] Riener M, Kainulainen J, Beuther H, Henshaw J D, Orkisz J H and Wang Y 2020 *Astronomy & Astrophysics*, Volume 633, id.A14, 25 pp. **633** A14 ISSN 0004-6361

# Tracing Water Masers at their Smallest Scale with VLBI

J M Vorster<sup>1,\*</sup>, J O Chibueze<sup>1,2</sup>, T Hirota<sup>3,4</sup>, G C MacLeod<sup>5,6</sup>

<sup>1</sup>Centre for Space Research, Potchefstroom campus, North-West University, Potchefstroom 2531, South Africa

<sup>2</sup>Department of Physics and Astronomy, Faculty of Physical Sciences, University of Nigeria, Carver Building, 1 University Road, Nsukka 410001, Nigeria

<sup>3</sup>National Astronomical Observatory of Japan, National Institutes of Natural Sciences, 2-21-1 Osawa, Mitaka, Tokyo 181-8588, Japan

<sup>4</sup>Department of Astronomical Sciences, SOKENDAI (The Graduate University for Advanced Studies), Osawa 2-21-1, Mitaka-shi, Tokyo 181-8588, Japan

<sup>5</sup>The Open University of Tanzania, P.O. Box 23409, Dar-Es-Salaam, Tanzania

<sup>6</sup>Hartebeesthoek Radio Astronomy Observatory, PO Box 443, Krugersdorp, 1741, South Africa

E-mail: [jobvorster8@gmail.com](mailto:jobvorster8@gmail.com)

**Abstract.** The high-mass star-forming region NGC6334I-MM1 underwent an energetic accretion event in January 2015. We report the large-scale (10 – 100 AU) and small-scale ( $\sim 1$  AU) changes in spatial and velocity structures of 22 GHz water masers as observed with VERA before and during the accretion burst. The masers in the northern bow-shock CM2-W2 brightened, and better traced a bow structure during the burst. In the southern regions, there was both activation and disappearance of associations before and during the burst. We measured the amplitudes, central velocities and FWHMs of about 20 features in each epoch. We found that the linear scale of the brightest feature in CM2-W2 grew from 0.6 AU before the burst to 1.4 AU after the burst, possibly indicating that a larger volume of gas was able to sustain masing action as a consequence of the accretion burst. This feature also had a rapid (0.2 yr) brightness increase by a factor of four, which has been previously reported in long-term single-dish monitoring. We propose that the water maser flare could be explained by an increase of the collisional pump rate due to radiative heating of H<sub>2</sub> by increased high energy radiation (UV or X-ray) from the inner protostellar core. We also describe the spot and spectral method of maser proper motion calculations. We argue that for high spectral resolution observations the spectral method is more robust for calculating proper motions than the spot method.

## 1. Introduction

The 22 GHz water maser transition is an important tracer of star-forming regions and evolved stars. These masers are known to be highly variable and to sustain population inversion in high-density turbulent or shocked environments [1]. Individual water maser cloudlets have been observed in W49N with typical linear sizes of 1 AU, and Full Width at Half Maximums (FWHMs) of  $0.5 \text{ km s}^{-1}$  to  $3 \text{ km s}^{-1}$  [2]. The association between shocks and 22 GHz water masers makes them good tracers of high-velocity protostellar jets.

An important application of water masers is proper motion and parallax measurements through multi-epoch Very Long Baseline Interferometry (VLBI) observations [3, 4]. The variability of water masers can make it difficult to identify persistent water masers which trace the same gas. Two assumptions are commonly made in water maser proper motion observations. Firstly, that the proper motions of water masers trace gas motions and not just the propagation of pumping conditions [5]. Secondly, that there is little or no acceleration in the water masers [6]. The second assumption is equivalent to assuming a near constant radial velocity,  $V_{\text{LSR}}$ , for

the maser features, and linear displacement over time in right ascension and declination. The time dependant environment in the high-mass star-forming region NGC6334I-MM1 due to the recent accretion burst [7, 8] might serve as a novel physical environment in which to test these assumptions.

NGC6334I is a high-mass star-forming region which contains nine-millimetre cores and is at a distance of 1.3 kpc [9]. In January 2015, the largest millimetre core, MM1, underwent flaring in multiple maser species and had an increase in luminosity by a factor of  $16.3 \pm 4.4$  [7, 10]. The region hosts multiple outflows, with bright water masers at the edges of an NW-SE bipolar outflow [8, 11]. There is still uncertainty about the exact mechanism that caused the flaring of water masers  $\sim 2700$  AU away from the accretion bursting source, given that the masers of this transition are understood to be collisionally pumped [12]. Looking closely at individual maser features before and after the accretion burst might shed some light on the physical mechanisms at work in the water maser flare.

The aim of this experiment is to study the spatial and velocity structure of water masers in NGC6334I at a high angular resolution with VERA before and during the accretion burst.

## 2. Observations and Data Reduction

We did seven epochs of observations of 22 GHz water masers with the VERA VLBI array [4]. The observations were on epochs 2014.7, 2014.9, 2015.1, 2015.3, 2015.9, 2016.1 and 2016.2. The phase tracking centre was  $(\alpha, \delta) = (17^{\text{h}}20^{\text{m}}53.377^{\text{s}}, 35^{\circ}46'55.808'')$ , J2000). The channel width of our observations was  $0.44 \text{ km s}^{-1}$ . The correlated visibilities were calibrated and imaged with the Astronomical Image Processing System (AIPS), with the same procedure than is described in [11]. The synthesized beam size was  $1.3 \times 3.3$  milliarcseconds. Self-calibration was used on a bright velocity channel to improve the dynamic range of the images. After the data was imaged, the SAD task was used to fit 2D Gaussians to each channel, to get the positions and radial velocities of the maser spots. Spatial precision smaller than the beam width can be obtained for bright maser emission, as spatial precision in VLBI is inversely proportional to the signal-to-noise ratio of a source [13]. In this work a maser ‘‘spot’’ refers to a single 2D Gaussian fit in a single channel map, while a maser ‘‘feature’’ refers to a collection of maser spots, with a velocity gradient in space and a Gaussian spectral distribution. It has been argued that a feature represents a single physical maser cloudlet [2].

## 3. Results

We detected water masers in CM2-W1, CM2-W2, MM1-W1, UCHII-W1, UCHII-W2 and UCHII-W3 according to the nomenclature of [8]. Figure 1 shows the positions and radial velocities of the maser spots for each epoch. Note that some of the spots in Figure 1 are likely spurious detections from imaging artefacts. Imaging artefacts can be identified as one or two faint isolated maser spots with a symmetric spatial distribution around brighter spots.

We identified features that were a cluster of spatially close ( $\sim 1$  AU) maser spots which have a Gaussian spectral distribution. The requirement for maser spots in a feature to have Gaussian spectral distributions filter out spurious detections. We fit Gaussian functions to the maser features’ spectral distributions. We detected 15, 23, 28, 27, 22, 21 and 22 features in the seven epochs respectively. The brightest maser feature in the burst epochs (after 2015.1) is shown in Figure 2. The intensity, velocity and FWHM ranges of all the maser features were highly variable between epochs. In 2014.9 the brightest maser feature had an amplitude of  $55 \text{ Jy beam}^{-1}$ , while in 2015.3 the feature flared to  $729 \text{ Jy beam}^{-1}$ . Between the features in all the epochs, the centre velocity  $V_{\text{centre}}$  ranged from  $-49 \text{ km s}^{-1}$  to  $0.92 \text{ km s}^{-1}$ . The FWHMs of single features ranged from  $0.62 \text{ km s}^{-1}$  to  $2.5 \text{ km s}^{-1}$ . Some maser clusters had a double Gaussian spectral distribution.

In CM2-W1, only 1 – 3 features with  $V_{\text{LSR}} \sim -8 \text{ km s}^{-1}$  were detected in the early epochs, before and at the onset of the accretion burst. In CM2-W2, the masers were initially only features in the range of  $-5 \text{ km s}^{-1} \leq V_{\text{LSR}} \leq -12.5 \text{ km s}^{-1}$ , and the size of the bow shock traced by the water masers was  $\sim 120 \text{ AU}$ . In the later epochs, highly blue-shifted features with  $V_{\text{LSR}} \sim -50 \text{ km s}^{-1}$  were detected at the northern part of the bow structure. The masers also traced a more well-defined bow shape with a size of  $\sim 420 \text{ AU}$  in later epochs. This is seen in the top of Figure 1, where the maser spots become a straight line over time. CM2-W2 was the region containing the brightest masers, and also the masers which had the most significant flares due to the accretion burst [7]. In the epochs 2014.7 – 2015.3, the masers in MM1-W1 form a linear structure on a milliarcsecond scale with a size of  $\sim 15 \text{ AU}$  and velocity range  $-4 \text{ km s}^{-1} \leq V_{\text{LSR}} \leq 0 \text{ km s}^{-1}$ . After epoch 2015.3, the masers in MM1-W1 are displaced and the maser spots have a smaller linear structure, with size  $\sim 7 \text{ AU}$ . The velocity range stayed the same.

The masers in the southern regions near the UCHII region NGC6334F displayed variability. UCHII-W1, the southernmost maser association, consists of multiple subclusters distributed over 600 AU with a velocity range spanning  $-37 \text{ km s}^{-1} \leq V_{\text{LSR}} \leq -5 \text{ km s}^{-1}$ . Most of the clusters consisted of single maser features. The clusters show normal proper motion in the epochs 2014.7 – 2014.9. At 2015.1, one of the clusters at  $-33.7 \text{ km s}^{-1}$  disappears. Between 2016.1 and 2016.2, three clusters disappeared, and only three clusters were detected. The brightest cluster, with a constant radial velocity range  $-16 \text{ km s}^{-1} \leq V_{\text{LSR}} \leq -8 \text{ km s}^{-1}$  was detected in all epochs. There were some morphological changes in this cluster, with maser features excited and disappearing between 2015.1 and 2016.2. UCHII-W2 consisted of a single feature at  $-30 \text{ km s}^{-1}$  between 2014.7 and 2015.1, which was not detected in subsequent epochs. In 2016.1 and 2016.2 a new feature was detected which showed a double-peaked spectral profile in the velocity range  $-31 \text{ km s}^{-1} \leq V_{\text{LSR}} \leq -26 \text{ km s}^{-1}$ . UCHII-W3 had no detections before 2015.1, with detections of a  $-31 \text{ km s}^{-1}$  feature in 2015.1 and 2015.3. This feature was not detected in 2015.9 and two new features, with  $V_{\text{LSR}} -36 \text{ km s}^{-1}$  and  $-49 \text{ km s}^{-1}$  were detected in the final two epochs.

Figure 2 shows the spot positions and spectral profile of the single maser feature throughout all the epochs. This feature was in the bow shock CM2-W2. The spatial distributions of the pre-burst maser spots are compact with a size of  $470 \mu\text{as}$  corresponding to a linear scale of 0.6 AU. After the burst, the feature subtended an angle of  $1060 \mu\text{as}$ , corresponding to a linear scale of 1.4 AU. The feature's spectral profile also shows significant variability. Table 1 shows the Gaussian parameters for the feature. The feature changed from a single to a double Gaussian between 2014.7 and 2014.9, and back to a single Gaussian in 2015.3. The feature intensity was also variable and was the brightest feature in the field for all epochs. HartRAO monitoring observations have shown a high cadence time series which can be attributed to this feature [7]. The time series shows that the maser flux density sharply rose during the onset of the accretion burst, then dimmed slightly, after which the flux density was relatively constant. We see the same behaviour in our observations.

## 4. Discussion

### 4.1. Large and small scale effects of the accretion burst on the water masers

There were changes both in the spatial and velocity distribution of the water masers on a large (10 – 100 AU) and small (0.5 – 5 AU) scale. The masers in CM2 flared significantly, and appear to trace the bow-shaped shock front more closely. In the southern regions, some associations disappeared, and new features were activated [12]. In all epochs, the large-scale bipolar spatial distribution was visible.

The  $-7.6 \text{ km s}^{-1}$  feature shown in Figure 2 is the brightest in the field in the epochs after 2015.3. The interval between 2015.1 and 2015.3 was a time when the maser flared rapidly [7]. The change in the linear size of the feature possibly indicates that an increased volume

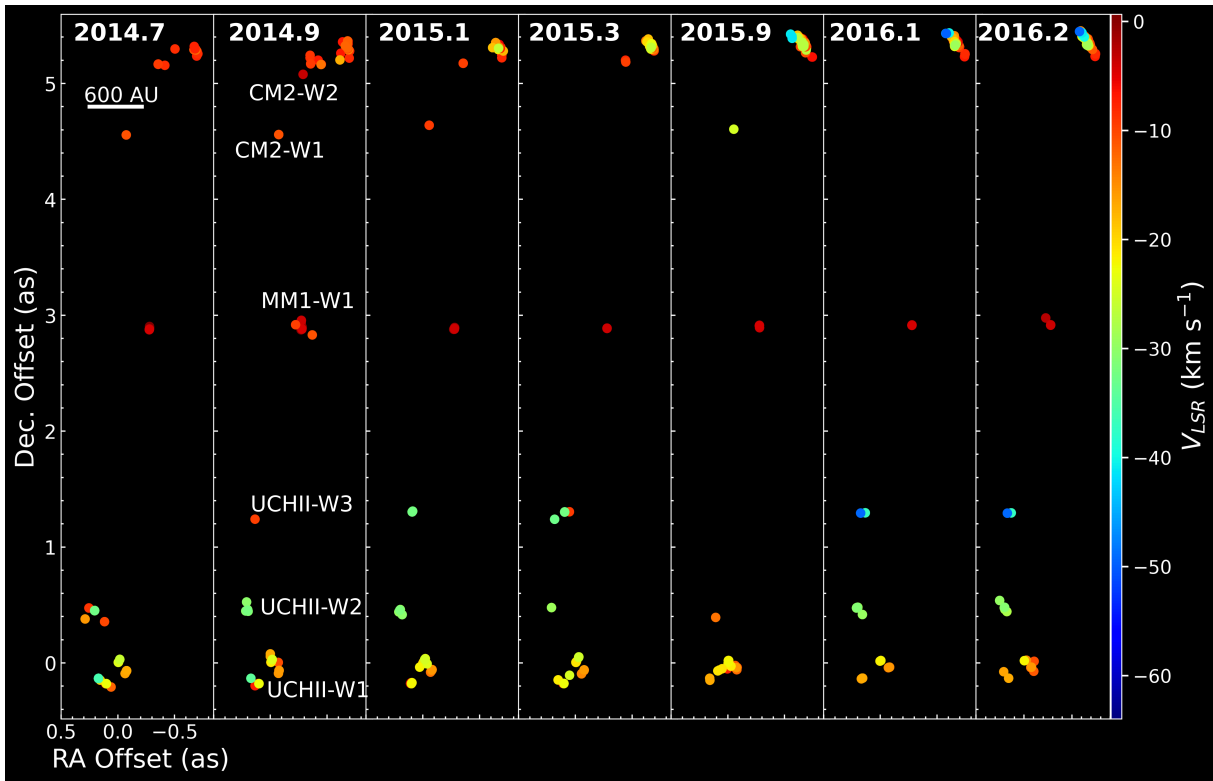


**Figure 1.** Positions of the water masers as detected by VERA for each epoch. The position of the spots indicates the position of the maser spots while the colour indicates the radial velocity according to the colour scale shown at the right of the figure. The text in the upper left of each panel indicates the date of the observation. The white reference line shows the linear distance scale assuming  $d = 1.3$  kpc. The names of each region are shown in white text in the second panel.

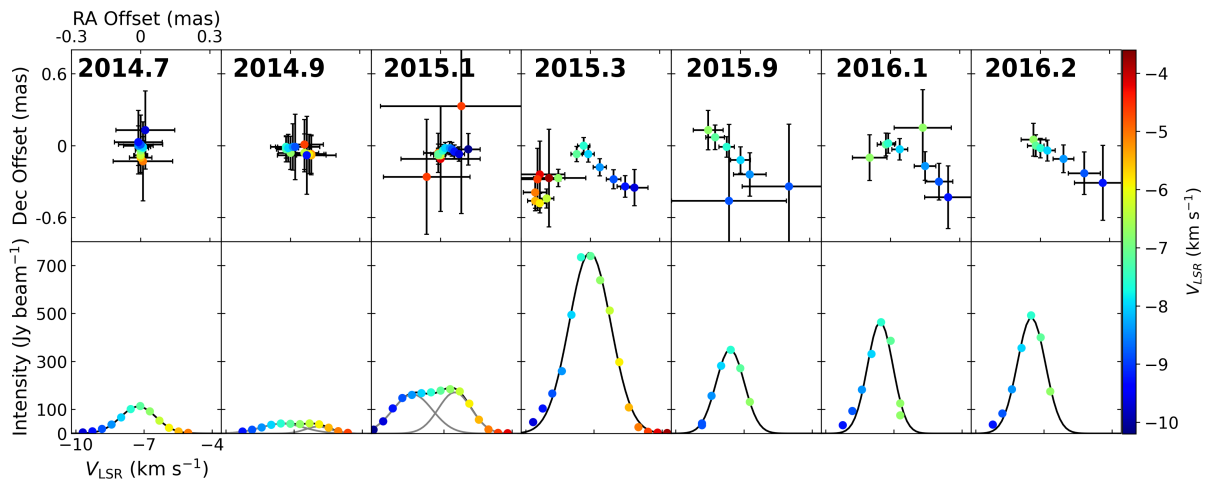


**Figure 2.** Top: Positions and radial velocities of spots in the brightest maser feature in CM2-W2 over time. The offsets are in terms of the centre position of the feature. The scale is the same for each panel. Bottom: The spectral profile of the feature for each epoch. The black lines show the Gaussian fit to the maser spots. The colour of the spots in each panel indicates the radial velocity according to the colour bar on the right-hand side.

Epoch	$A$ (Jy beam <sup>-1</sup> )	$V_{\text{centre}}$ (km s <sup>-1</sup> )	FWHM (km s <sup>-1</sup> )
2014.7	112 (2)	-7.26 (0.02)	1.84 (0.04)
2014.9	41 (1)	-7.52 (0.04)	2.24 (0.08)
	29 (2)	-5.95 (0.03)	1.30 (0.05)
2015.1	163 (6)	-8.38 (0.09)	2.05 (0.16)
	172 (10)	-6.53 (0.07)	1.70 (0.10)
2015.3	755 (19)	-7.18 (0.03)	2.17 (0.06)
2015.9	351 (7)	-7.61 (0.01)	1.46 (0.03)
2016.1	465 (38)	-7.61 (0.05)	1.32 (0.12)
2016.2	483 (19)	-7.55 (0.03)	1.46 (0.07)

**Table 1.** Gaussian fit parameters for the maser feature shown in Figure 2. The values in parenthesis are the uncertainties on the fit. Epochs 2014.9 and 2015.1 had a double Gaussian feature, and the parameters of both Gaussians are shown in this table.

of water molecules had a pumping rate able to sustain maser action. There are some possible explanations. Water masers are known to support population inversion by collisions with H<sub>2</sub> and emission at specific “sink” transitions [1]. The accretion burst could amplify the collisional pump either mechanically or radiatively. CM2-W2 is  $\sim 3000$  AU from the accretion bursting source MM1B, with an excavated cavity along the jet axis [8]. Material ejected by the burst with a speed of  $150 \text{ km s}^{-1}$  would take 95 years to reach CM2-W2, ruling out mechanical amplification [11]. With regards to radiative amplification, a stronger radiation field could cause the maser flare if the collisional partner has a high opacity to the radiation, and if a portion of the energy from the radiation is converted to kinetic energy in the collisional partner H<sub>2</sub> [14]. At high densities ( $n \geq 10^6 \text{ cm}^{-3}$ ) H<sub>2</sub> can be thermally heated by high-energy radiation [15]. It is possible that high-energy radiation propagated freely through the excavated cavity, heating up the H<sub>2</sub> which would in turn increase the pump rate. Our proposal builds on the proposal of [8].

Recently, a radiative pumping scheme for 22 GHz water masers was proposed [16]. They showed that population inversion can be sustained radiatively for dust temperatures  $\sim 1400$  K, water number densities  $10^{4-6} \text{ cm}^{-3}$  and hydrogen kinetic temperatures  $< 500$  K. The density and kinetic temperature requirements are reasonable if you take the shock model of [1] into account, but it would have to be shown that CM2-W2 is under the effect of a 1400 K dust temperature radiation field for this explanation to be valid.

#### 4.2. Identifying maser features and the spectral method of proper motion calculation

In water maser proper motion measurements, an important step after calibration and imaging is identifying the persistent object that you are tracking over time. There are two main approaches to identifying persistent water masers. These approaches can be called the “spot” and the “spectral” method.

The spot method consists of using individual maser spots in a single velocity channel as a persistent object. The foundational assumption of the spot method is that the velocity drifts are smaller than the instrument’s channel width throughout the observations. This approach was used in proper motion calculations by e.g. [11]. The spectral method involves using the intensity-weighted centroid position of the three brightest spots in a maser spectral feature. The feature method assumes that a single Gaussian spectral profile indicates a single masing cloud. This method has been used by e.g. [3].

We argue that the feature method is the most reliable and robust method of calculating proper motions for masers. Some data sets have calibration errors leading to spurious detections due to side lobes. The spot method has no built-in way to discern these spurious detections. On the

other hand, the spectral method requires a Gaussian spectral distribution, which is not found for side-lobe detections. Further, the spectral method does make an assumption about the velocity drift and can take velocity drift into account if the feature can be identified to be persistent. The requirement for the spectral method is that the spectral resolution of the observations must be much smaller than the line width. For observations with a coarse spectral resolution, the spectral and spot methods are equivalent, as no Gaussian will be seen in the spectral profile.

In summary, calculating the proper motion with the intensity-weighted centroid position of multiple maser spots which are spatially close on the order of 1 AU and which show a single Gaussian in its spectral profile, is a more robust and reliable way to calculate proper motions than by using spots in a single channel.

## 5. Conclusion

We report multi-epoch VLBI observations of 22 GHz water masers with VERA before and during the recent accretion burst in NGC6334I. We identified around 20 clusters of individual maser spots with a Gaussian spectral distribution and calculated their amplitudes, centre velocities and FWHMs. We found all these parameters to be variable between pre-burst and burst epochs in all regions where we detected water masers. The brightest maser feature in CM2-W2 was found to have a variable linear scale, with a pre-burst scale of 0.6 AU and a burst scale of 1.4 AU. This possibly indicates that a larger volume of gas had the correct pumping conditions to sustain masing action. We proposed that the water maser flare could be explained by the amplification of the collisional pump rate through radiative heating of H<sub>2</sub> by increased high-energy radiation (UV or X-ray). Lastly, we also argued that proper motions are more reliably calculated with the intensity-weighted centroid of the brightest maser spots in a spectral feature, rather than using single spots.

## Acknowledgements

JMV acknowledges the National Research Foundation of South Africa for funding this research (Grant Number: 134192). JOC acknowledges support from the Italian Ministry of Foreign Affairs and International Cooperation (MAECI Grant Number ZA18GR02) and the South African Department of Science and Technology's National Research Foundation (DST-NRF Grant Number 113121) as part of the ISARP RADIOSKY2020 Joint Research Scheme. T. Hirota is financially supported by the MEXT/JSPS KAKENHI Grant Number 17K05398. This research made use of NASA's Astrophysics Data System Bibliographic Services. VERA is operated by Mizusawa VLBI Observatory, a branch of the National Astronomical Observatory of Japan.

## References

- [1] Hollenbach D *et al* 2013 *ApJ* **773** 70
- [2] Gwinn C R 1994 *ApJ* **429** 253
- [3] Burns R A *et al* 2017 *MNRAS* **467** 2367–2376
- [4] Hirota T R *et al* 2020 *PASJ* **72** 50
- [5] Goddi C *et al* 2006 *A&A* **447** L9–L12
- [6] Sanna A *et al* 2010 *A&A* **517** A71
- [7] MacLeod G C *et al* 2018 *MNRAS* **478** 1077–1092
- [8] Brogan C L *et al* 2018 *ApJ* **866** 87
- [9] Brogan C L *et al* 2016 *ApJ* **832** 187
- [10] Hunter T R *et al* 2021 *ApJL* **912** L17
- [11] Chibueze J O *et al* 2021 *ApJ* **908** 175
- [12] Vorster J M *et al* 2021 *SAIP* p 358
- [13] Pradel N *et al* 2006 *AA* **452** 1099–1106
- [14] Burke B F *et al* 1978 *ApJL* **226** L21–L24
- [15] Sternberg A *et al* 1989 *ApJ* **338** 197
- [16] Gray M D *et al* 2022 *MNRAS* **513** 1354–1364

# Simulating the radio emission of dark matter for new high-resolution observations with MeerKAT

**M Sarkis and G Beck**

School of Physics, University of the Witwatersrand, Private Bag 3, WITS-2050, Johannesburg, South Africa

E-mail: [michael.sarkis@students.wits.ac.za](mailto:michael.sarkis@students.wits.ac.za)

**Abstract.** Recent work has shown that searches for diffuse radio emission by MeerKAT - and eventually the SKA - are well suited to provide some of the strongest constraints yet on dark matter annihilations. To make full use of the observations by these facilities, accurate simulations of the expected dark matter abundance and diffusion mechanisms in these astrophysical objects are required. However, because of the computational costs involved, various mathematical and numerical techniques have been developed to perform the calculations in a feasible manner. Here we provide the first quantitative comparison between methods that are commonly used in the literature, and outline the applicability of each one in various simulation scenarios. These considerations are becoming ever more important as the hunt for dark matter continues into a new era of precision radio observations.

## 1. Introduction

Despite decades of work, indirect Dark Matter (DM) searches – those that look for emission from the annihilation and decay products of DM particles – are yet to find a signal that can be solely attributed to DM. Until such a detection is made, and as our observing capabilities improve with newer and more sophisticated telescopes, we continue to methodically move through the parameter spaces of candidate DM models and eliminate those that conflict with the data. The recent public release of the MeerKAT Galaxy Cluster Legacy Survey data [1], together with recent studies that show the competitiveness of using DM radio emission for indirect detection [2, 3, 4], provides strong motivation for a renewed and continued effort in radio DM searches. In this work we take a brief but detailed look at the various theoretical aspects involved in the modelling of the radio emission from DM, and comment on how the choice of model will likely play an important role in indirect searches with high-resolution instruments.

Our analysis includes simulations of the DM host environments for two source targets, the Coma galaxy cluster and the M31 galaxy, and a calculation of the synchrotron emission resulting from the annihilation of Weakly Interacting Massive Particles (WIMPs) therein. We model our DM halos with a set of reasonable source parameters and find the emission after solving the electron propagation equation in each environment. The methods of solving this equation are a major focus point of this work, as the choice of technique used can lead to a non-negligible change in the observed emission, particularly in smaller source targets where diffusion effects are significant. With  $< 10$  arcsecond resolution capabilities, observations with MeerKAT (and soon the SKA) are for the first time able to probe the inner regions of these targets, which is where the strongest constraints on DM can be found. Therefore, accurate spatial modelling of these targets is essential for us to make full use of the new data.

## 2. Modelling

The two source targets in this work, the Coma galaxy cluster and the M31 galaxy, were chosen for their well-characterised properties in the literature. Of particular importance are the profiles of their magnetic fields and thermal gas densities; as these quantities appear in the modelling process (but are often underspecified), the uncertainty of the final solution depends strongly on the treatment of these factors [5]. However, since the simulation of the halo environment is not the central focus of this work (and for the sake of brevity), we refer the reader to the following sources for details regarding the parameters in the Coma cluster [6, 7] and in the M31 galaxy [8, 9].

In each halo environment, the emission of synchrotron radiation will be determined by the spatial and energy equilibrium distribution of charged annihilation products,  $\psi(\mathbf{x}, E)$ . In this work the products considered are electrons and positrons. The evolution of these distributions over time is then given by the following propagation equation, which includes the dominant effects of energy losses and spatial diffusion:

$$\frac{\partial \psi(\mathbf{x}, E)}{\partial t} = \nabla \cdot [D(\mathbf{x}, E) \nabla \psi(\mathbf{x}, E)] + \frac{\partial}{\partial E} [b(\mathbf{x}, E) \psi(\mathbf{x}, E)] + Q(\mathbf{x}, E). \quad (1)$$

Here  $D$ ,  $b$  and  $Q$  are the diffusion, energy-loss and DM annihilation source functions respectively, and the determination of the exact forms of these functions follows the methods laid out in [5].

### 2.1. Solving the propagation equation

We determine the equilibrium electron distribution  $\psi$  using two independent techniques. The first, referred to here as the ‘Green’s Function (GF) method’ [2, 10], uses a Green’s function with simplified forms of  $D$  and  $b$  to solve Eq. 1 semi-analytically. The second, referred to as the ‘Alternating Direction Implicit (ADI) method’ [11, 12], uses a numerical approach to solve Eq. 1 iteratively. In both methods we consider the halo environment to be spherically symmetric, so that  $\mathbf{x}$  may be replaced by  $r$  in Eq. 1. We also note here that we have assumed a simplified form of  $D$ , which would be a tensor in a more general case. As our methodology closely follows the above-mentioned literature, we only summarise these methods and point out any major differences in the following sections.

*GF method* If the forms of the diffusion and energy-loss functions are simplified so that they have no spatial dependence, a solution to Eq. 1 can be found directly with the use of Green’s functions and image charges. However, these simplifications often have an impact on the calculated emission (for a review on this topic, see [5]). In this work we use non-weighted averages for the magnetic field and thermal gas densities, found using an averaging scale radius that matches the scale radius of the DM halo. This choice encapsulates the region in the halo that contains the majority of WIMP annihilations – and thus best represents the spatial structure of the halo – while allowing us to forgo any explicit spatial dependence in Eq. 1. Now, the equilibrium distribution of electrons in the halo can be calculated using

$$\psi(r, E) = \frac{1}{b(E)} \int_E^{m_\chi} dE' G(r, \Delta v) Q(r, E'), \quad (2)$$

with  $m_\chi$  as the WIMP mass and the Green’s function ( $G$ ) given by

$$G(r, \Delta v) = \frac{1}{\sqrt{4\pi\Delta v}} \sum_{n=-\infty}^{\infty} (-1)^n \int_0^{r_{\max}} dr' \frac{r'}{r_n} \left[ \exp\left(-\frac{(r' - r_n)^2}{4\Delta v}\right) - \exp\left(-\frac{(r' + r_n)^2}{4\Delta v}\right) \right] \frac{Q(r')}{Q(r)}. \quad (3)$$

Here  $r_{\max}$  is the maximum radius for any diffusion processes and  $r_n = (-1)^n r + 2nr_{\max}$  is the location of the  $n^{\text{th}}$  image charge. The quantity  $\Delta v$  is calculated as

$$\Delta v = v(E) - v(E'), \quad (4)$$

where

$$v(E) = \int_E^{m_\chi} dx \frac{D(x)}{b(x)}. \quad (5)$$

*ADI method* In this method, we discretise Eq. 1 and solve for the equilibrium distribution iteratively. Since the ADI method retains the radial dependence in the diffusion and energy loss functions (where the GF method does not), the problem becomes 2-dimensional in energy and space. Using a traditional finite-difference technique in this scenario could be computationally expensive, which is why we opt for a method that uses so-called ‘operator splitting’ to treat each dimension separately and divide the problem into smaller, more manageable pieces. Thus, during each step of the method, we use a general form of the 1-dimensional Crank-Nicolson (CN), scheme (see, for instance, [13]) which is a finite-differencing technique that includes the average of second-order implicit and explicit terms in the updating equation, thereby leveraging the unconditional stability of a fully implicit method while maintaining second-order accuracy in space and time. This scheme is relatively easy to solve, as the updating equation turns out to be a set of linear equations with tridiagonal coefficient matrices. We write this, as in [11, 12], as

$$-\frac{\alpha_1}{2}\psi_{x-1}^{n+1} + \left(1 + \frac{\alpha_2}{2}\right)\psi_x^{n+1} - \frac{\alpha_3}{2}\psi_{x+1}^{n+1} = \frac{\alpha_1}{2}\psi_{x-1}^n + \left(1 - \frac{\alpha_2}{2}\right)\psi_x^n + \frac{\alpha_3}{2}\psi_{x+1}^n + Q_x \Delta t. \quad (6)$$

Here  $n$  is the temporal grid index (with the spacing between indices given by  $\Delta t$ ) and  $x$  represents either the energy or spatial grid index. The forms of the  $\alpha$  coefficients, which encapsulate the diffusion and energy loss effects, need to be found by discretising the relevant operators from Eq. 1. The scheme we have used for this is as follows:

$$\frac{1}{r^2} \frac{\partial}{\partial r} \left( r^2 D \frac{\partial \psi}{\partial r} \right) \xrightarrow{\text{discretisation}} C_{\tilde{r}}^{-2} \left[ \frac{\psi_{i+1} - \psi_{i-1}}{2\Delta\tilde{r}} \left( \log(10)D + \frac{\partial D}{\partial\tilde{r}} \right) \Big|_{\tilde{r}=\tilde{r}_i} + \frac{\psi_{i+1} - 2\psi_i + \psi_{i-1}}{\Delta\tilde{r}^2} D \Big|_{\tilde{r}=\tilde{r}_i} \right] \quad (7)$$

for the radial operator and

$$\frac{\partial}{\partial E} (b\psi) \xrightarrow{\text{discretisation}} C_{\tilde{E}}^{-1} \left[ \frac{b|_{\tilde{E}=\tilde{E}_j} (\psi_{j+1} - \psi_j)}{\Delta\tilde{E}} \right] \quad (8)$$

for energy operator, where  $C_{\tilde{r}} = (r_0 \log(10) 10^{\tilde{r}_i})$ ,  $C_{\tilde{E}} = (E_0 \log(10) 10^{\tilde{E}_j})$  and  $\Delta\tilde{r}$ ,  $\Delta\tilde{E}$  represent the radial and energy grid spacings, respectively. We use  $i$  and  $j$  to denote positions in the radial and energy grids, and have omitted the temporal indices as these forms will apply to both implicit and explicit terms in the same way. The vertical bars denote that the functions which they are attached to are evaluated at the given grid index. We have also made the variable transformations  $\tilde{r} = \log_{10}(r/r_0)$  and  $\tilde{E} = \log_{10}(E/E_0)$  (similarly to [12], except with base 10 instead of e), which allows us to more accurately track the electron distribution in our grids when the involved processes operate over a wide range of physical scales. Finally, note that in the case of energy losses, we only consider upstream differencing.

The  $\alpha$  values can now be found by taking Eqs. 7 and 8 and equating coefficients with Eq. 6; once these are found, the updating equation can be solved with some matrix solution algorithm. If we represent the discretisation schemes shown above by the symbol  $\Psi$ , the overall iterative solution can be summarised with the steps

$$\begin{aligned}\psi^{n+1/2} &= \Psi_{\hat{E}}(\psi^n) \\ \psi^{n+1} &= \Psi_{\hat{r}}(\psi^{n+1/2}),\end{aligned}\tag{9}$$

which are repeatedly solved (using Eq. 6) until the value of  $\psi$  has converged to the equilibrium value. The other minutiae of this method, including initial and boundary conditions, convergence criteria and stability considerations, can be found in [11, 12].

### 2.2. Synchrotron emission

Once found via the GF or ADI methods, the equilibrium distribution is used to calculate the radio emissivity, given by

$$j_{\text{sync}}(\nu, r) = \int_0^{m_x} dE \psi_{e\pm}(E, r) P_{\text{sync}}(\nu, E, r),\tag{10}$$

where  $\nu$  is the synchrotron frequency,  $\psi_{e\pm}$  is the sum of electron and positron equilibrium distributions and  $P_{\text{sync}}$  is the power emitted by an electron with an energy of  $E$  (this is calculated as in [2]). The emissivity is then used to calculate the two main results in this work. Firstly, the azimuthally averaged surface brightness curves,

$$I_{\text{sync}}(\nu, r, \Theta, \Delta\Omega) = \int_{\Delta\Omega} d\Omega \int_{l.o.s.} dl \frac{j_{\text{sync}}(\nu, l)}{4\pi},\tag{11}$$

where *l.o.s.* is the line-of-sight to a point in the halo at radius  $r$ , which makes an angle of  $\Theta$  with the centre of the halo, and  $\Delta\Omega$  is the solid angle over which the surface brightness is calculated. In this work we show results for a single representative frequency of  $\nu = 0.5$  GHz. Secondly, we calculate the integrated flux density by

$$S_{\text{sync}}(\nu, R) = \int_0^R d^3r' \frac{j_{\text{sync}}(\nu, r')}{4\pi d_L^2},\tag{12}$$

where the emissivity is integrated over the region enclosed by  $R$  and  $d_L$  is the luminosity distance to the target. For the results shown in this work we consider  $R$  to be the virial radius of the halo.

## 3. Results

Here we provide the details of the simulations we have performed, and show the results for two observables: the radio surface brightness (Eq. 11) and integrated flux (Eq. 12). We use a set of reasonable source parameters for the halo environments that respect observational constraints, and aim to use WIMP parameter values that are representative of the many viable candidates. We thus consider a large range of particle masses, from 10 to 1000 GeV, and use a set of four annihilation channels,  $\{b\bar{b}, e^+e^-, \mu^+\mu^-, \tau^+\tau^-\}$ . Since the focus of this work is on a comparison between the two solution methods, particularly in the way that they differ with various source targets, we show the results side-by-side and in the same manner for both targets. In Fig. 1 we show the surface brightness curves for the Coma cluster (left-hand panels) and M31 (right-hand panels), and Fig. 2 shows the integrated fluxes from the same targets for a range of frequencies.

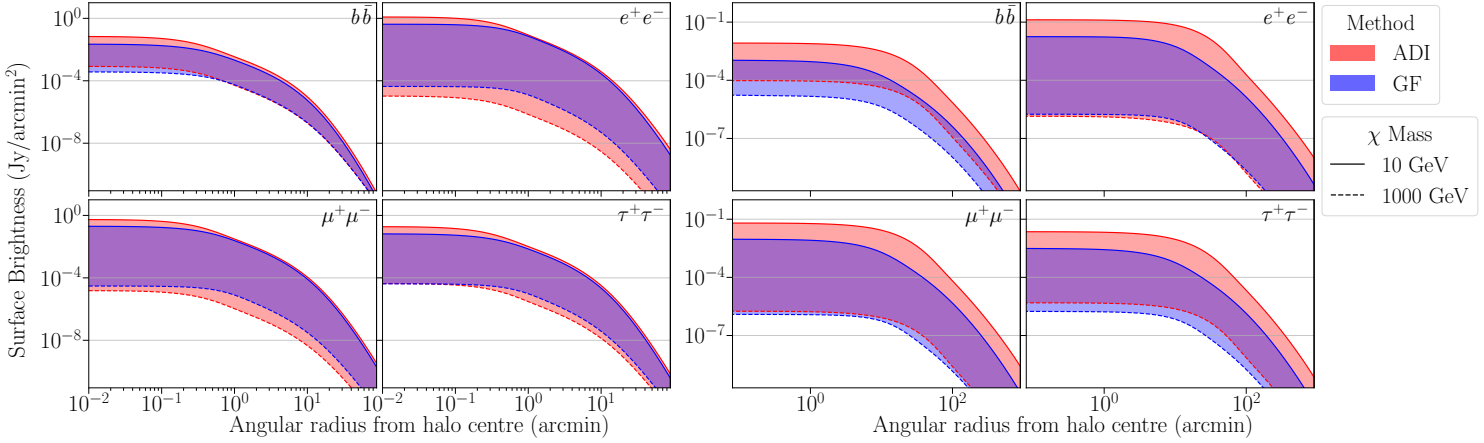


**Figure 1.** Surface brightness curves for the Coma galaxy cluster (left-hand panels) and the M31 galaxy (right-hand panels). Each of the four panels show different annihilation channels, given by the label in the top right of each plot. The ADI and GF methods are represented by the red and blue colours respectively, and the region in which the results overlap are given by the combination of these (the purple colour). These shaded regions represent the full mass range of the WIMPs (from 10 to 1000 GeV), and the domain of each panel runs up until the halo’s virial radius  $R$  (in angular units).

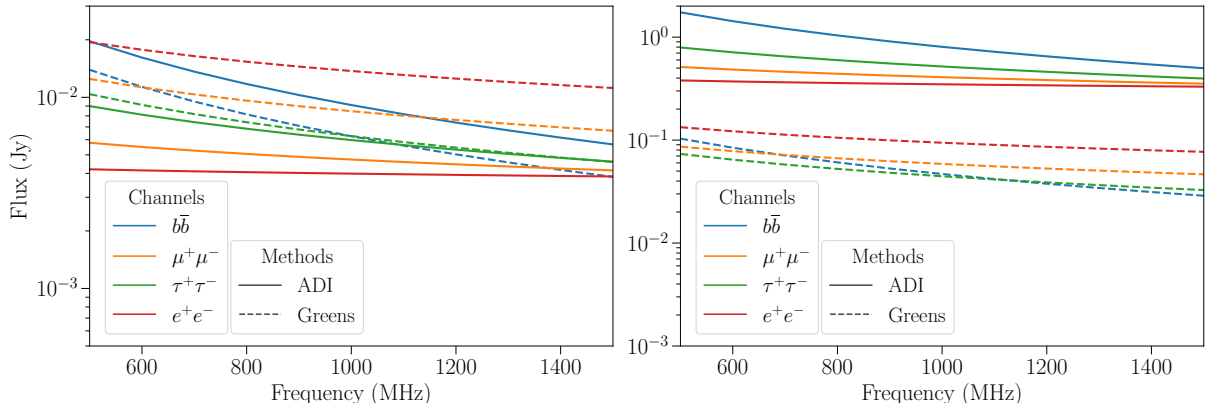


**Figure 2.** The integrated fluxes, calculated using Eq. 12, for the Coma galaxy cluster (left) and the M31 galaxy (right). The different linestyles represent the two solution methods presented in Sec. 2.1, and each colour indicates the use of a different annihilation channel.

#### 4. Discussion and conclusions

In Figs. 1, we see generally good agreement between the GF and ADI methods, which can be inferred from the significant amount of overlap between the curves in each panel. Noticeably however, we see more disagreement (less overlap) between the methods in the M31 galaxy than we do for the Coma galaxy cluster. Our explanation for this lies in the mathematical techniques employed by each method, and how they each treat the spatial dependence of the diffusion function in particular. In the galaxy cluster environment of Coma, diffusion effects are negligible on sufficiently large scales [10, 5], whereas in the physically smaller galaxy, diffusion effects start to influence the surface brightness distribution at all relevant scales. Since the GF and ADI methods leverage a spatially independent and dependent diffusion function (respectively), the resulting equilibrium distributions will tend to differ in the environments where the length

scales in question do not greatly exceed the diffusion length, as is the case for M31. This trend is also seen in the fluxes from Fig. 2, which show a clear disagreement in all channels for the M31 galaxy, and relative agreement in all channels in the Coma cluster. Based on these results and the comparison of target environments presented in [5], we also expect that smaller target environments (like the dwarf spheroidal satellite galaxies of the Milky Way) would show further disagreement between the solution methods, as diffusion effects would be even more significant in these environments.

The other notable result we see from these simulations is that the methods differ on small scales, even in the large Coma cluster. This is significant, as the inner regions of the DM halos are where we would observe the strongest emission. With high-resolution radio interferometers allowing us to resolve these smaller scales, our models could be tested against the strongest possible DM emission, allowing us to find more stringent constraints on DM properties than previously possible. In this regard, the surface brightness curves displayed here would be especially valuable results when determining new observational limits, as their emission profiles are highly dependent on the spatial structure of the DM halo.

With the impressive spatial resolution of telescopes like MeerKAT and the SKA, we are now able to probe the inner regions of these DM halos – regions which have formerly been hidden from our view. The need for accurate modelling techniques is thus more necessary than ever before, and the considerations presented in this work should help inform the modelling choices made in future radio searches for DM.

### Acknowledgments

This work is based on the research that was supported by the National Research Foundation of South Africa (Bursary No. 112332). G.B. acknowledges support from a National Research Foundation of South Africa Thuthuka grant no. 117969.

### References

- [1] Knowles K, Cotton W D, Rudnick L *et al.* 2022 *Astronomy & Astrophysics* **657** A56
- [2] Beck G 2019 *Galaxies* **7** 16
- [3] Regis M, Reynoso-Cordova J, Filipović M D *et al.* 2021 *Journal of Cosmology and Astroparticle Physics* **2021** 046
- [4] Chan M 2021 *Galaxies* **9** 11
- [5] Sarkis M and Beck G 2022 *The Proceedings of SAIP2021* ed Prinsloo A (UJ) pp 316–322 ISBN 978-0-620-97693-0
- [6] Bonafede A, Feretti L, Murgia M *et al.* 2010 *Astronomy and Astrophysics* **513** A30
- [7] Łokas E L and Mamon G A 2003 *Monthly Notices of the Royal Astronomical Society* **343** 401–412
- [8] Ruiz-Granados B, Rubiño-Martín J A, Florido E *et al.* 2010 *The Astrophysical Journal* **723** L44–L48
- [9] Tamm A, Tempel E, Tenjes P *et al.* 2012 *Astronomy & Astrophysics* **546** A4
- [10] Colafrancesco S, Profumo S and Ullio P 2006 *Astronomy & Astrophysics* **455** 21–43
- [11] Strong A W and Moskalenko I V 1998 *The Astrophysical Journal* **509** 212–228
- [12] Regis M, Richter L, Colafrancesco S *et al.* 2015 *Monthly Notices of the Royal Astronomical Society* **448** 3747–3765
- [13] Press W H, Teukolsky S A and Vetterling W T 2007 *Numerical Recipes: The Art of Scientific Computing* 3rd ed (Cambridge University Press) ISBN 978-0-521-88068-8

# MeerKAT's view on galaxy clusters: Diffuse radio emission in MeerKAT Galaxy Cluster Legacy Survey

K Kolokythas,<sup>1</sup> T Venturi,<sup>2</sup> I Loubser<sup>1</sup> and K Knowles<sup>3,4</sup>

<sup>1</sup>Centre for Space Research, North-West University, Potchefstroom 2520, South Africa

<sup>2</sup>INAF, Istituto di Radioastronomia di Bologna, via Gobetti 101, 40129 Bologna, Italy

<sup>3</sup>Centre for Radio Astronomy Techniques and Technologies, Department of Physics and Electronics, Rhodes University, PO Box 94, Makhanda 6140, South Africa

<sup>4</sup>South African Radio Astronomy Observatory, 2 Fir Street, Observatory 7925, South Africa

## Abstract.

Galaxy clusters are the largest gravitationally-bound structures in the Universe, with their baryonic mass distributed between the constituent galaxies and the ionized plasma of their intracluster medium (ICM). As such, radio observations of galaxy clusters are powerful tools for the detection of diffuse cluster-scale synchrotron emission, which carries information about the cluster formation history. Observations using Square Kilometre Array (SKA) precursor and pathfinder instruments are now opening up a new window on diffuse cluster sources and challenging our simple classification scheme (radio halos, mini-halos, and radio relics), making clear the need for an update of our current knowledge. Towards this direction the MeerKAT telescope carried out a program of long-track observations of galaxy clusters in L-band which became the MeerKAT Galaxy Cluster Legacy Survey (MGCLS), consisting of  $\sim 1000$  hours, observing 115 galaxy clusters at 1.28 GHz spread out over the Southern sky.  $\sim 54\%$  (62/115) of the MGCLS clusters are found to present some kind of diffuse emission, hosting a total of 99 diffuse cluster structures or candidates with 57% (56/99) of these structures being new. As the majority (66%; 37/56) of new structures are discovered in the X-ray selected sample we suggest that X-ray selected cluster samples are more likely to reveal new radio structures that have been missed by earlier surveys/studies opening up new areas of investigation in cluster formation and evolution.

## 1. Introduction

One of the most important aspects in the observations of galaxy clusters is the search for diffuse cluster-scale radio synchrotron emission. The detection of such structures plays a key role as it can reveal information regarding the evolution and the formation history of a cluster (for an observational detailed review see e.g., [1], and for a theoretical one see [2]). A great variety of low surface brightness and steep radio spectra ( $\alpha < -1.0$ ) diffuse radio morphologies has been detected to date in clusters (e.g., [3],[4],[5],[6]); however, historically, there are three dominant classes that almost every detected diffuse cluster radio emission falls into: *a) radio halos, b) radio mini-halos, and c) radio relics.*

*Radio halos* are diffuse sources that are typically correlated with the morphology of the X-ray emitting intracluster medium (ICM). The main mechanism that gives rise to these structures that span scales of  $>500$  kpc (up to few Mpc scales), is particle reacceleration as a result of massive cluster mergers, with radio halos exhibiting observed correlations between the radio source's power and its host cluster mass as well as with its thermal properties (e.g., [7],[8],[9]).

*Radio mini-halos* on the other hand, are smaller structures than radio halos with their projected sizes spanning between few tens to few hundreds of kpc situated in the central area of dynamically relaxed, cool-core clusters ([10]) and most of the time are found to be confined within cold fronts that are observed at the cluster core. A radio-loud active brightest cluster galaxy (BCG) is always present in mini-halo clusters that is contributing, at minimum, part of the seed electrons necessary to generate the observed diffuse emission (e.g., [11]). As is the case in radio halos, particle reacceleration induced by gas sloshing is most likely the driving mechanism for the production of radio mini-halos (e.g., [12], [13]).

*Radio relics* are the last class where elongated kpc to Mpc-scale structures are included that are usually observed at the outskirts of merging galaxy clusters. One of the main observed properties of radio relics is that they present a high degree of polarization (e.g., [14]) which denotes that their origin is closely related to the presence of merger-induced shocks in the ICM. For this reason, numerous clusters exhibit relics at opposite directions in the periphery of a cluster, also known as double radio relics (e.g., Abell 3667; [15]) either with the detection of a radio halo in between them or not (see [16], [17]). In this class is also included a sub-class of revived fossil emission from radio-loud active galactic nuclei (AGN) in the region of the cluster known as radio phoenixes ([1]).

Due to their detectable surface brightness from current radio telescopes, the number of detected radio halos and relics in merging clusters has been continuously rising to date, over a broad range of cluster masses ([18]) and a wide range of redshifts ([19]). However, the detection of radio mini-halos still remains at low numbers as a result of current radio observational constraints. Recently, the number of detected radio sources with very steep-spectrum filaments has been significantly rising (e.g., Abell 2034; [20]), introducing a necessity to further investigate the link between radio galaxies and the particle reservoir they deposit into the ICM, but also in general, the mechanism of cluster merger events (see e.g., [21]).

Therefore, with the advent of radioastronomy and the operation of new era radiotelescopes (such as LOFAR, uGMRT, JVLA, ASKAP and MeerKAT) a unique opportunity arises in the study of galaxy clusters from MHz to GHz frequencies opening up new areas of investigation in cluster formation and evolution.

## 2. The MGCLS sample and data

The first step towards the SKA era was made in 2018 with the commissioning of the L-band of the MeerKAT radio telescope. Between June 2018 and June 2019 using the full MeerKAT radio-telescope array, (minimum of 59 antennas per observation) utilising the L-band receiver (nominal radio frequency band 900–1670 MHz) in the 4K correlator mode (4096 channels across the digitised band of 856–1712 MHz) and a dump rate of 8 seconds, 115 clusters were observed. This is the MeerKAT Galaxy Cluster Legacy Survey (MGCLS). MGCLS is a sample of 115 galaxy clusters with a mean redshift of  $\sim 0.14$  (only four clusters have  $z > 0.4$ ) that spans over a large area in the Southern sky between declination  $-80^\circ$  and  $\sim 0^\circ$ . A detailed description of the sample, the observations, and its data are presented at the MGCLS survey paper in [22].

For the MGCLS sample no specific selection criteria were applied, either in mass, redshift or luminosity, which makes MGCLS an inhomogeneous sample consisting of clusters that were drawn either from a group of ‘radio-selected’ clusters or a group of ‘X-ray-selected’ ones. The radio sub-sample consists of 41 clusters with known diffuse cluster radio emission from earlier studies (e.g., [10], [23], [24]). Due to this selection, this sub-sample contains only high mass clusters and is strongly biased towards clusters with radio halos and relics. On the other hand, the rest of the clusters (74 clusters or 65% of the MGCLS sample), are the X-ray sub-sample, that was selected from the MCXC catalog ([25]), in an effort to balance cluster selection and avoid any prior biases towards or against cluster radio properties.

All MGCLS datasets were calibrated and imaged with the basic procedure described in [26]

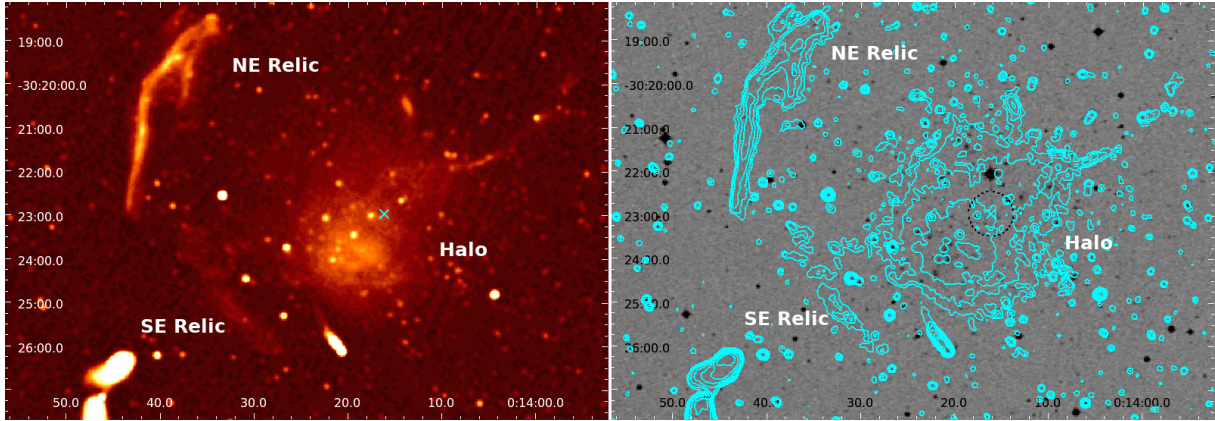


**Figure 1. A 2744.** *Left:* MeerKAT 1.28 GHz radio image at normal resolution ( $\sim 7.8''$ ). *Right:* MeerKAT 1.28 GHz contours in cyan ( $1\sigma = 5 \mu\text{Jy beam}^{-1}$ ), overlaid on the *DSS* optical image. The radio contours are spaced by a factor of two, starting from  $3\sigma$ . For this source the scale at the cluster redshift is  $4.536 \text{ kpc arcsec}^{-1}$ . The size of the radio halo extends  $\sim 2 \text{ Mpc}$ , the NE Relic  $\sim 1.6 \text{ Mpc}$  and the SE one  $\sim 1.2 \text{ Mpc}$ .

using the Obit package 2 ([27]). The images were corrected for the primary beam at each frequency, as described in [26], both at the full resolution of the image ( $\sim 7.5 - 8''$ ), and at a convolved  $15''$  one in order to aid the recovery of low surface brightness features. The very good short baseline spacing of MeerKAT (29 m minimum baseline length) is key for the detection of diffuse radio structures, and allows the full recovery of up to  $10'$  extended emission in angular scales (for more details on the data and their analysis see [22]).

### 3. First results from the MGCLS diffuse radio emission catalog

The galaxy clusters that have been observed in the MGCLS provide only a glimpse of the many diffuse cluster emission discoveries that are most likely to be made in the SKA era. We provide here an overview of the first results from the detected diffuse radio emission sources to the best of our knowledge so far. For a detailed description of all clusters with detected diffuse radio sources and a full analysis of their properties see the MGCLS diffuse emission catalog paper II (Kolokythas et al. 2023 in prep.)

For each of the diffuse sources, the emission classification in [22] was based on a combination of the full  $7''$  and  $15''$  resolution MeerKAT data products with candidate structures being classed those which presented either a marginal detection or an uncertain feature and as ‘unknown’ those whose the diffuse source wouldn’t fit into any of the current classes.

We used a similar strategy as in [22] for the calculation of the flux densities of the diffuse radio sources by estimating the total flux density of a radio structure using the  $15''$  resolution image and then extracting the contribution of background point radio sources within this region using the full  $7''$  resolution image. The physical projected sizes mentioned here refer to the largest linear sizes of the structures and were calculated based on the  $15''$  resolution image based on the redshift of each cluster. Figure 1 shows an example of a radio halo and relics emission from cluster A 2744.

#### 3.1. Statistical analysis

We find that more than half ( $\sim 54\%$ ; 62/115) of the observed MGCLS clusters in this Legacy Survey present some kind of diffuse cluster emission, with the total number of diffuse cluster structures or candidates detected being 99 as several clusters are found to host more than one.

57% (56/99) of these structures are noted as new ([22]). Examining the MGCLS sample in more detail, we find that 34% of these new structures are discovered in the radio selected sample (19/56) whereas the majority (66%; 37/56) of the newly detected radio structures are seen in the X-ray selected sample. This suggests that X-ray selected cluster samples are more likely to ‘reveal’ new radio structures that have been missed by earlier surveys/studies. However we also note that a significant number of new faint radio structures have also been confirmed/found in the radio selected sample due to the much improved surface brightness sensitivity of the MGCLS at 1.28 GHz.

Our diffuse cluster emission detections can be summarised as follows: 3 new mini-halos and 7 new mini-halo candidates, 25 halo detections and 6 candidates (of which 13 are new), 28 relics and 18 relic candidates (of which 26 are new), 2 new phoenix candidates, one known revived fossil plasma, and 9 diffuse sources with ambiguous or unknown classifications, 6 of which are new. This shows that (including the candidates -c-) only  $\sim 9\%$  (10/115) of the observed clusters present a radio mini-halo whereas the rate for radio halos in clusters is much higher at 27% with the rate of clusters that exhibit at least one relic being 25% (29/115) (as some clusters present more than one relic). Having a look only at the detected radio structures, we see that radio relics are the most commonly detected diffuse structures in MGCLS at 47% (46/99) followed by halos at 32% (31/99) and mini-halos at 11% (10/99). 10% (9/99) of the detected structures are ambiguous/unknown with only 3% (2/99) being candidate Phoenixes and just 2% listed as revived fossil plasma (1/99).

The detected MGCLS diffuse radio structures vary significantly in size, flux density, spectral index and radio power, indicating the variety of their properties. We find that the projected sizes in the MGCLS sample range from as small as  $\sim 80$  kpc (Abell 2751; cRelic) to as big as  $\sim 2.3$  Mpc (Abell 3667; Relic). The estimated flux densities at 1.28 GHz range between as faint as  $\sim 0.4$  mJy (c radio mini-halo) and as strong as  $\sim 400$  mJy (A3667; Relic), with the radio power ( $P_{1.28GHz}$ ) of the detected structures spanning from  $\sim 10^{22}$  W Hz $^{-1}$  to greater than  $10^{25}$  W Hz $^{-1}$ . Examining the in-band radio spectral index distribution between 900 and 1400 MHz we find structures that have regions with relatively flat spectral index ( $\alpha_{908}^{1656} \sim -0.50$ ) with radio relics exhibiting as steep spectra indices as  $-3.5^1$ .

#### 4. Conclusions

The first results from the detected diffuse radio emission sources in MGCLS galaxy clusters provide a glimpse of the many diffuse cluster emission discoveries that are most likely to be made in the SKA era that open up new areas of investigation in cluster formation and evolution. One such example is the very faint (low luminosity) radio relic candidates detected by exploiting the excellent surface brightness sensitivity of the MGCLS with another example being the ambiguous diffuse structures in several clusters that do not belong to any of the typical existing classes, a finding which reveals the need for new dynamical, particle acceleration, or field amplification processes in the ICM.

#### 5. Acknowledgments

This work is based on the research supported by the National Research Foundation of South Africa (KK & SIL: Grant number 120850). Opinions, findings and conclusions or recommendations expressed in this publication are that of the author(s), and the NRF accepts no liability whatsoever in this regard. MGCLS data products were provided by the South African Radio Astronomy Observatory and the MGCLS team and were derived from observations with the MeerKAT radio telescope. The MeerKAT telescope is operated by the South African Radio

<sup>1</sup> The radio spectral index  $\alpha$  is defined as  $S_\nu \propto \nu^\alpha$ , where  $S_\nu$  is the flux density at frequency  $\nu$

Astronomy Observatory, which is a facility of the National Research Foundation, an agency of the Department of Science and Innovation.

## References

- [1] van Weeren R J, de Gasperin F, Akamatsu H, et al 2019 *Space Sci. Rev.* **215** 16
- [2] Brunetti G and Jones T W 2014 *Int. J. Mod. Phys. D* **23** 1430007
- [3] Giacintucci S, Venturi T, Brunetti G, Bardelli S, Dallacasa D, et al 2005 *A&A* **440** 867
- [4] Venturi T, Giacintucci S, Dallacasa D, et al 2008 *A&A* **484** 327
- [5] Macario G, Venturi T, Brunetti G, Dallacasa D, Giacintucci S et al 2010 *A&A* **517** 43
- [6] Kale R, Venturi T, Giacintucci S, et al 2013 *A&A* **557** A99
- [7] Brunetti G, Setti G, Feretti L and Giovannini G 2001 *MNRAS* **320** 365
- [8] Kale R, Venturi T, Giacintucci S, et al 2015 *A&A* **579** A92
- [9] Cuciti V, Cassano R, Brunetti G, et al 2021a *A&A* **647** A51
- [10] Giacintucci S, Markevitch M, Cassano R, et al 2017 *ApJ* **841** 71
- [11] Richard-Laferrere A, Hlavacek-Larrondo J, Nemmen R S et al 2020 *MNRAS* **499** 2934
- [12] ZuHone J A, Markevitch M and Lee D 2011 *ApJ* **743** 16
- [13] ZuHone J A, Markevitch M, Brunetti G and Giacintucci S 2013 *ApJ* **762** 78
- [14] van Weeren R J, Rttgering H J A, Brggen M and Hoeft M 2010 *Science* **330** 347
- [15] Rottgering H J A, Wieringa M H, Hunstead R W and Ekers R D 1997 *MNRAS* **290** 577
- [16] Bonafede A, Brggen M, van Weeren R et al 2012 *MNRAS* **426** 40
- [17] Lindner R R, Baker A J, Hughes J P et al 2014 *ApJ* **786** 49
- [18] Cuciti V, Cassano R, Brunetti G et al 2021b *A&A* **647** A50
- [19] Di Gennaro G, van Weeren R J, Brunetti G et al 2021 *Nature Astronomy* **5** 268
- [20] Shimwell T W, Luckin J, Brggen M et al 2016 *MNRAS* **459** 277
- [21] de Gasperin F, Intema H T, Shimwell T W et al 2017 *Sci. Adv.* **3** e1701634
- [22] Knowles K, Cotton W D, Rudnick L, Camilo F et al 2022 *A&A* **657**, A56
- [23] Kale R, Wik D R, Giacintucci S et al 2017 *MNRAS* **472** 940
- [24] Parekh V, Dwarakanath K S, Kale R and Intema H 2017 *MNRAS* **464** 2752
- [25] Piffaretti R, Arnaud M, Pratt G W, Pointecouteau E and Melin J B 2011 *A&A* **534** A109
- [26] Mauch T, Cotton W, Condon J et al 2020 *ApJ* **888** 61
- [27] Cotton W D 2008 *PASP* **120** 439

# Collimation of Ion Density Distribution of Vacuum Arc Thrusters with Axial Magnetic Fields

T M Rencken<sup>1</sup>, R T Paton<sup>1</sup> and P Ferrer<sup>2</sup>

<sup>1</sup> Department of Mechanical, Aeronautical and Industrial Engineering, University of the Witwatersrand, Johannesburg, South Africa

<sup>2</sup> Mandelstam Institute for Theoretical Physics, University of the Witwatersrand, Johannesburg, South Africa

E-mail: [tristanrencken@gmail.com](mailto:tristanrencken@gmail.com)

**Abstract.** The implementation of a pulsed axial magnetic field to the plasma of a Vacuum Arc Thruster collimates the ions within the plasma plume which increases ion density distribution along the normal. The magnetic field is generated by a capacitive discharge coil which generates magnetic field strengths up to 50 mT (millitesla). A first order numerical model was developed to determine whether the influence of magnetic fields on ion density distributions could be predicted accurately. Numerical simulations using particle-in-cell methods show a close correlation with experimental methods. The correlation between the experimental and numerical method for describing the plasma plume ion density distribution for various magnetic field strengths are discussed.

## Acknowledgements

This work is supported and funded by the SITA Aero Foundation.

## 1. Introduction

Vacuum Arc Thrusters (VATs) use plasma propulsion techniques to generate thrust through vacuum arc technology. The highly ionised and directional plasma generated by the vacuum arc creates minuscule, precise amounts of thrust. VATs were originally studied in the 1960s-70s [1] and have regained attention due to the improvements in electrical and mechanical systems available today. The VAT may very well be the next major step in electrical propulsion systems that drive unmanned exploration into the solar system. VATs have proven to be a desirable method of propulsion for nanosats (nanosatellites) due to its high thrust efficiencies, low overall mass (< 1 kg) and low power usage (1 - 100 W) in comparison to conventional combustion engines. These micro-thrusters have lower weight requirements due to the absence of propellant storage tanks and flow control valves. Nanosats are loosely defined as a satellite that weighs between 1 kg to 10 kg.

This paper introduces a study conducted in describing the effects of pulsed magnetic fields on the ion density distribution of VATs both experimentally and numerically. Understanding the influence of pulsed magnetic fields on ion density distributions allows for potential thrust improvements on current VAT designs and ion contamination of the nanosat.

## 2. VAT Design Theory and Performance

The VAT performance relies on a high current arc discharge between two metallic electrodes separated by a dielectric. The arc discharge between these electrodes is initiated by a momentary high voltage pulse triggered by a PPU (Power Processing Unit). Once the discharge is triggered, the high current arc vapourises and ionises the cathode material which accelerates into free space from the cathode spot in the form of a highly ionised plasma [2]. Once triggered, the discharge is sustained. The acceleration of the plasma from these cathode spots (where the arc terminates plasma on the cathode) results in an emission of ions at very high speeds, on the order of  $10^4$  m/s [3].

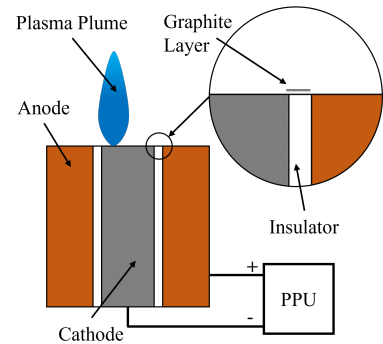


**Figure 1.** VAT Plasma

Two different research methodologies were applied; an experimental and a numerical simulation approach.

## 3. Experimental Approach

The Ion Density Distribution (IDD) about the central emission spot on the plasma was measured for various magnetic field strengths to quantify its influence on the ion distribution properties of the ions within the plasma.

### 3.1. Thruster Design

The VAT design was based on a coaxial design, with a solid iron cathode rod placed within an alumina ceramic insulation tube surrounded by a solid copper anode ring, as shown in Figure 2. This design was implemented due to its high degree of symmetry along the centre line of the thruster. The generation of the initial arc between the cathode and anode was achieved by coating the surface of the insulator with a thin conductive graphite layer which provides a momentary path of low resistance between the anode and the cathode. When a relatively low voltage of several hundred volts is applied between the anode and cathode, breakdown occurs at imperfections along the conductive surface. These tiny discharges generate enough metal vapor to initiate a larger arc discharge. Once the main arc has been initiated, the metal droplets from the cathode redeposit on the surface of the insulator and replenish the conductive layer on the insulator surface. This method allowed for the vacuum arc thruster to operate between 3500 - 4500 pulses before the graphite layer had to be reapplied.

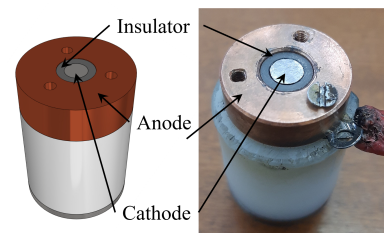


**Figure 2.** VAT design

### 3.2. Experimental Electrical Setup

The VAT plasma was generated by a Power Processing Unit (PPU). A schematic of the PPU is shown in Figure 3. When designing the PPU it was important to build a reliable circuit capable of creating high density vacuum arc discharges with long discharge periods (2.0 - 2.5 ms). The operation of the VAT discharge was dependent on several circuit parameters, namely the capacitance and inductance of the components used. A range of circuit parameters were tested; the capacitance, inductance and supply voltage. A more capacitive circuit produced greater reliability in triggering and thus it was decided that the inductance would be approximately  $50 \mu\text{H}$ .

The inductance was generated with a toroidal inductor with a ferrite core. When testing the capacitance, it was decided to use a capacitance of 1.1 mF. The pulse length and pulse frequency was controlled with a standard microcontroller with a high voltage insulated-gate-bipolar-transistor (IGBT).

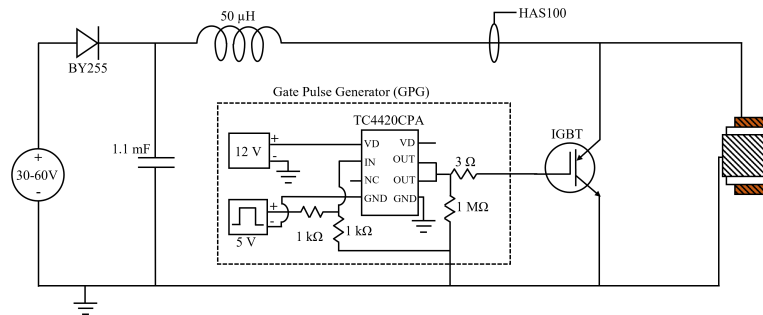


Figure 3. Power Processing Unit circuit

The implementation of a pulsed magnetic field was achieved with a capacitive discharge circuit capable of generating high currents through a magnetic coil, see Figure 4. The circuit was designed to discharge the built up charge through the coil for a desired pulse length. An important aspect of the design was the ability to control the pulse length of the magnetic field to ensure that the plasma discharge experiences a constant magnetic field during the arc discharge. The magnetic field coil was then placed around the VAT such that the plasma experienced the greatest magnetic field induction through the centre line of the coil.

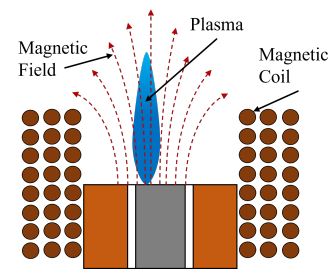


Figure 4. Magnetic coil

3.3. Ion Density Distribution Measurements

The IDD was measured using a Faraday cup probe within the low pressure vacuum chamber. The main purpose of the Faraday cup probe was to measure the IDD at various angles about the plasma and at various distances from the plasma, as shown in Figure 5. These measurements would provide insight into the ion distribution and the shape of the thrust-producing plasma plume. The determination of the IDD allowed for a detailed description on the extent to which the magnetic field collimates the ions within the plasma.

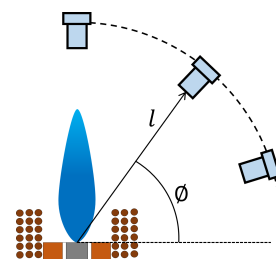


Figure 5. Faraday cup setup

4. Numerical Simulation

In addition to the experimental approach, a numerical first-order, particle-in-cell (PIC) model was developed with MATLAB. This particle in-cell-model was used to determine whether a numerical algorithm could be used to predict the ion density distribution of a VAT plasma. As a first order approximation, the effects of self-consistent electromagnetic fields were assumed to be negligible, as well as any particle-particle collisions. These assumptions were made on the basis that the initial particle positions were generated based on empirical experimental results for ion density distributions, and based on the fact that any of the self-magnetic field doesn't substantially affect the plasma jet for arc currents  $I < 200$  A [4]. The model generates particle positions which follow a typical cosine distribution which has been experimentally validated [5]. For a cosine distribution in polar coordinates, the current density at a radius,  $l$ , and angle,  $\phi$ ,

defined from the surface normal of the cathode surface due to mass generated in area  $dA$  on the surface is:

$$j_{ip}(l, \phi) = \frac{j_{ic} \cos \phi}{\pi l^2} dA \quad (1)$$

where  $j_{ic}$  is the ion current flux from the cathode surface.

Once the particles had been generated and placed within the simulation domain, a Boris particle push was performed. The Boris method is the de facto standard for particle pushing in plasma physics codes. This method is phase space volume conserving which is used to advance a charged particle within electromagnetic fields [6]. To conserve momentum throughout, appropriate boundary conditions were chosen. Particles which had been pushed passed a specified distance were re-injected into the simulation domain at the cathode spot with its original starting orientation. This ensured momentum conservation and allowed the model to reach stability once each particle had been re-injected into the domain.

## 5. Results

### 5.1. Experimental Results

When conducting the experiment, two significant measurements were taken, the arc discharge current  $I_{arc}$ , measured with a high current transducer, and the ion current  $I_{ion}$ , measured with the Faraday cup probe. The ion current was used to describe the IDD about the plasma emission spot. These measurements were taken simultaneously with a sampling rate of 200

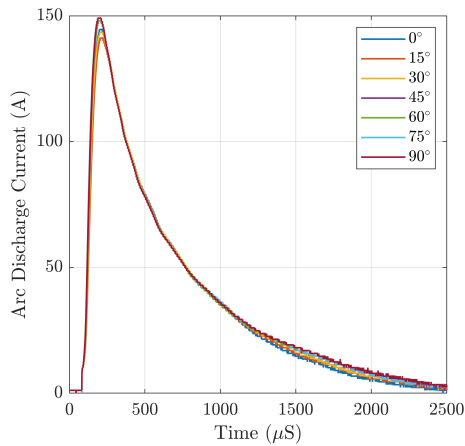


**Figure 6.** Arc current measurements

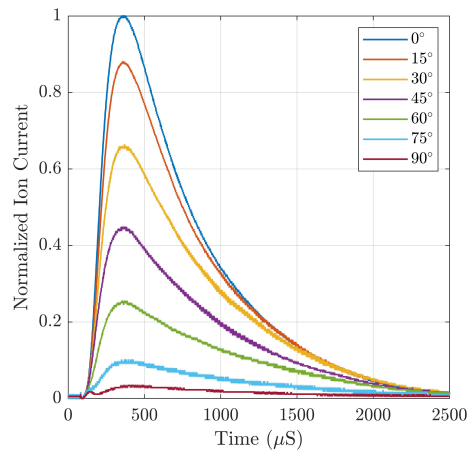


**Figure 7.** Normalised ion current

Mega Samples Per Second (MSa/s). Figures 6 and 7 show a typical measurement result. The behavior of a vacuum arc discharge is inherently stochastic, hence a general pulse averaging scheme was implemented over a series of 128 consecutive pulses. The ion current readings are proportional to the arc discharge current (typically 10% of the arc discharge current[7]), and thus it was important to normalise the ion current with its associated arc discharge current. The arc discharge current is constant throughout all measurements taken for various angles as shown in Figure 6. After performing a statistical analysis of the experimental results it was found that there was a maximum standard deviation of  $\sigma = 14.802$  A and a maximum standard error of  $SE = 0.6436$  A and a maximum percentage error of 1.26%. However, as the angle about the centre line of the thruster increases, the ion current measurement decreases significantly, see Figure 7. This suggests that the majority of the ions emitted from the cathode spot are directed along the centre line of the thruster. The experimental procedure was then repeated after introducing the magnetic field intending to collimate the ions along the centre line.

By normalizing the results of the magnetised ion current to the unmagnetised ion current, it is evident that the ion distribution is significantly influenced by the magnetic field, as shown in Figure 8. The variation in distribution is relatively low between magnetic field strengths of 20-50 mT, however with a significant increase in all peak ion distributions in comparison to the unmagnetised distribution. The magnetic field results in an increase in ion distribution at low angles and a decrease in ion distribution at higher angles. There is a major deviation from the theoretical distribution around 45 degrees. This deviation is as a result of the magnetic coil obstructing the path of the ions emitted from the cathode spot. The theoretical distribution shown is based on the empirical ion density distribution from Equation 1.

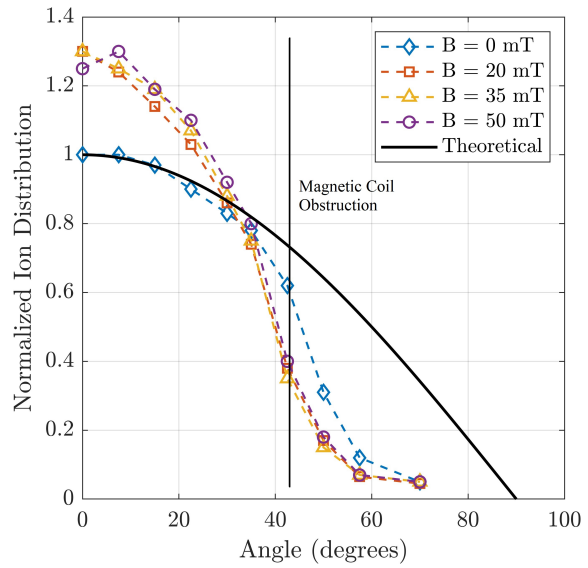


**Figure 8.** Ion current density for given angles about the plasma plume

5.2. Numerical Simulation Results

With the application of a 50 mT magnetic field, shown in Figure 10 there was a significant increase in ion collimation along the normal where ion density is presented as  $n_i / \text{m}^3$ . It was then possible to quantify the density differential as a result of the magnetic field using the unmagnetised plasma in Figure 9.

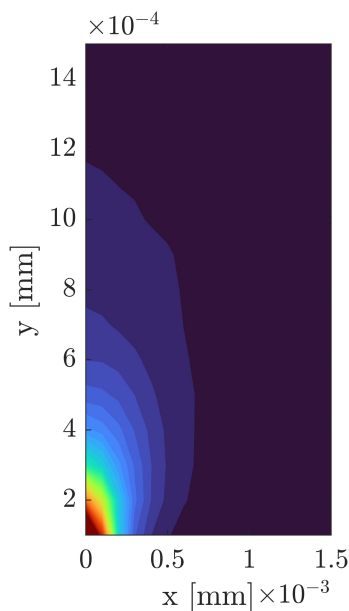


**Figure 9.** Unmagnetised plasma

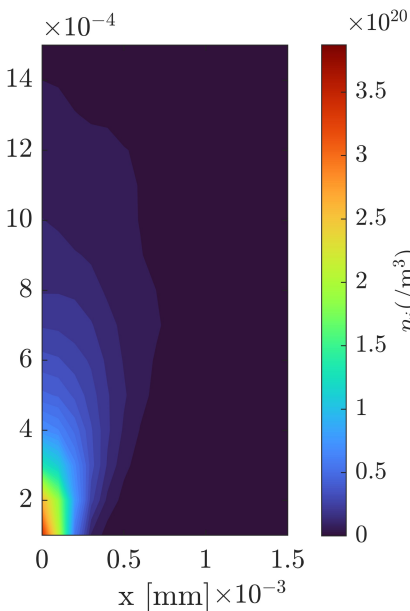


**Figure 10.** Magnetised plasma

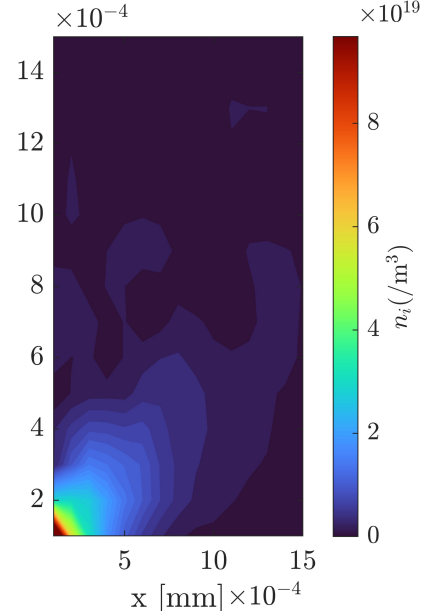


**Figure 11.** Density differential contour

A significant difference can be found near to the cathode spot at the origin, and at the

edge of the plasma plume, as shown in Figure 11. The difference at the edge of the plasma plume is a result of the magnetic field having a greater influence on the ions with a velocity vector directed away from the centre line of the plasma plume. Using these results, it was then possible to compare the simulated results with the results obtained from the experiment. When comparing the experimental and numerical simulation results in Figure 12, the unmagnetised distribution correlates closely with the theoretical curve, with the exception of high angles where there is a more gradual drop in ion density. The magnetised distribution, however, follows a similar trend to that of the experimental distribution despite having a lower peak ion density closer to the centre line. These discrepancies could be attributed to several factors. The particle motion is dependent on the mass and charge of the ions. These variables are inherently arduous to determine for any given material, and ion mass and charge selection within the simulation which may have resulted in this error. Additionally, due to the negated parameters within the study, it is possible that the self-consistent electromagnetic fields may cause a higher electric potential closer to the cathode spot which would result in particles being subjected to an increased acceleration due to like-like charge interactions.

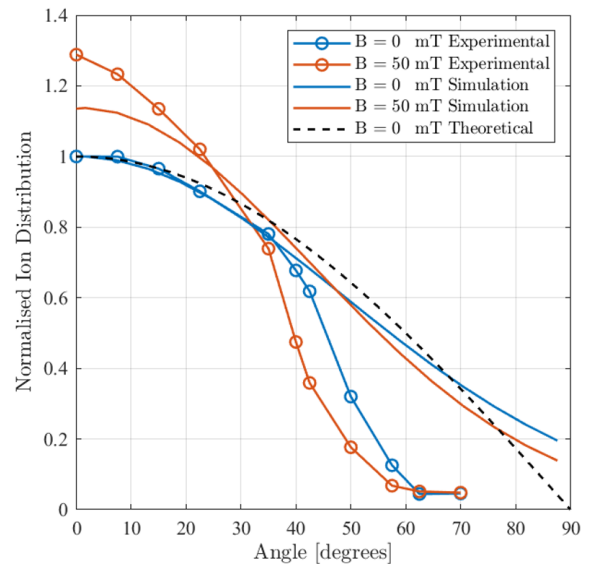


**Figure 12.** Experimental and numerical ion density distribution results

## 6. Conclusions

A study on the influence of pulsed magnetic fields on ion density distributions was conducted through experimental and numerical methods. The magnetic field has an effect on the overall ion density distribution. The numerical model closely follows the trends obtained from the experiment, however discrepancies exist in peak ion distributions at higher angles. The increase in magnetic field strengths results in an increase in ion density distribution along the centre line of the thruster. Further studies should be carried out to determine the effects and extent thereof of the mass and charge assignment of the ions in the simulation. The possibility of reducing any error by including the self-consistent electromagnetic fields due to ion and electron distributions within the numerical simulation should also be explored.

## 7. References

- [1] Lun J 2008 *Development of a Vacuum Arc Thruster for Nanosatellite Propulsion*
- [2] Polk, J.E. et al. 2008 *A theoretical analysis of vacuum arc thruster and vacuum arc ion thruster performance*, *IEEE Transactions on Plasma Science*, 36(5 PART 1), pp. 2167–2179.
- [3] Anders, A. and Yushkov, G.Y. 2002 *Ion flux from vacuum arc cathode spots in the absence and presence of a magnetic field*, *Journal of Applied Physics*, 91(8), pp. 4824–4832.
- [4] Beilis, I.I., Keidar, M. and Boxman, R.L. (1998) *Theoretical study of plasma expansion in a magnetic field in a disk anode vacuum arc*, *Journal of Applied Physics*, 83, p. 709.
- [5] Tuma D, Chen C, and Davies D 1978, *Erosion products from the cathode spot region of a copper vacuum arc* *J. Appl. Phys.*, vol. 49, no. 7, pp. 3821–3831.
- [6] Zenitani, S. and Kato, T.N. (2020) *‘Multiple Boris integrators for particle-in-cell simulation’*, *Computer Physics Communications*, 247.
- [7] C. Kimblin 1973, *Erosion and ionization in the cathode spot regions of vacuum arcs*, *J. Appl. Phys.*, vol. 44, no. 7, pp. 3074–3081.

# Compact stars: Numerical solutions to the structure equations using python

Luyanda Mazwi<sup>1</sup>, Dawit Worku<sup>2</sup>, Thuthukile Khumalo<sup>3</sup>

<sup>1</sup>Centre of Astro-Particle Physics, University of Johannesburg, Auckland Park Kingsway Campus, Johannesburg

<sup>2</sup>Department of Mathematics and Physics, Faculty of Applied Sciences, Cape Peninsula University of Technology

<sup>3</sup>School of Physics, University of the Witwatersrand, Johannesburg 2050, South Africa

E-mail: luyandamazwi10@gmail.com

**Abstract.** The study of compact stars is a topic very valuable for the testing of modern physics in order to better understand the behaviour of cold dense nuclear matter. Compact stars have no fusion processes occurring within them. The only way these stars are then capable of supporting themselves is through the degeneracy pressure of the fermions that constitute these objects. These stars can then be modelled as a degenerate Fermi gas of either electrons or neutrons. This study aimed to solve for the Newtonian and Tolman-Oppenheimer-Volkoff (TOV) structure equations through a numerical approach using Python in order to model the behaviour of these stars. White dwarfs were modelled as a Fermi gas of electrons while the neutron star was modelled first as a pure neutron gas and then as a mix of neutrons, protons and electrons. It was found that within certain limits, the results obtained particularly for the neutron stars, compared well to expected values for the mass of these objects in literature.

## 1. Introduction

Compact stars (white dwarfs or neutron stars) are the final stage of a star's lifetime. A star powers itself through nuclear fusion, in which lighter elements are combined to form heavier elements. After hydrogen and helium burning, the star's core consists largely of carbon or oxygen. As a result, nuclear fusion processes stop and the star's temperature decreases [2]. The star no longer is able to maintain hydro-static equilibrium and the core contracts, resulting in an increase in temperature and pressure. For Zero Age Main Sequence (ZAMS) stars with an initial mass of less than  $4M_{\odot}$ , the carbon-oxygen core will not be large and hot enough to reinitialize nuclear fusion in the star. For a ZAMS star with an initial mass between  $4 - 8M_{\odot}$ , additional nucleosynthesis is now possible, resulting in carbon burning [1]. Due to the high core temperature, the outer regions of the star expand. The outer layer eventually expands to the point where it becomes optically thin, revealing the remnant object which will eventually cool to become a white dwarf [1]. This resulting object consists of largely carbon and oxygen which is the old star's core with no fusion processes taking place [1]. Through the degeneracy pressure of the electrons present in the core, the star is able to maintain hydro-static equilibrium [2].

Similarly, neutron stars are stabilised by the degeneracy pressure of neutrons. As noted above, for a star with initial mass greater than 8 solar masses, carbon and oxygen fusion is now possi-

ble. Note that one would expect that for ZAMS stars with an initial mass greater than  $8 M_{\odot}$ , catastrophic collapse would occur once the core is largely composed of carbon and oxygen. The maximum mass a degenerate core can have is  $1.4 M_{\odot}$ , the Chandrasekhar limit. However, these stars undergo a significant amount of mass loss preventing this catastrophic collapse [1]. Around this core of heavier elements, are layers of hydrogen and helium that also undergo fusion. As long as these fusion processes produce the required heat for fusion, fusion to heavier elements will continue in the core along with the fusion of lighter elements in the outer shell. However, once iron is produced in the core, no more fusion processes accompanied with the release of energy will occur in the core [2]. This iron core then increases in mass while its radius shrinks as there is insufficient thermal energy that is produced to support its structure. At some critical mass, the iron core collapses. The density increases so much that electron capture occurs to form neutrons out of protons [2]. The atomic nuclei becomes more and more neutron rich with increasing density. Eventually, at some critical density, the nuclei are unable to bind neutrons and the neutrons drop out of the nuclei to form a neutron liquid that surrounds the nuclei. For even greater density, a dense in-compressible core of neutrons with a small number of protons and electrons present will form [2]. The collapse is rapid and the outer layers fall and bounce off the in-compressible, core leaving behind the remnant neutron star. The study of these stars is very valuable as they provide a means of studying the behaviour of dense, cold nuclear matter in conditions that are close to the density of or even exceeding the density of atomic nuclei [4]. Currently, the Equation of State (EoS) of neutron stars is not known. The only way we can then study them is through comparison of generated models and observed data [3].

### 1.1. Structure equation for a polytrope

The structure of a star is maintained through a balancing act between the outward thermal pressure and the inward gravitational pull. The structure equations describing this balancing act are given by  $\frac{dm}{dr} = \rho(r)4\pi r^2$  and  $\frac{dp}{dr} = -\frac{Gm(r)\rho(r)}{r^2}$ . Rewriting these equations in terms of energy density,  $\epsilon(r)$ , we find

$$\frac{dm}{dr} = \frac{\epsilon(r)4\pi r^2}{c^2} \quad (1)$$

$$\frac{dp}{dr} = -\frac{G\epsilon(r)m(r)}{c^2 r} \quad (2)$$

These coupled equations need to be solved simultaneously to determine the relationship between mass, pressure and radius. Because these equations are coupled, by making use of an equation of state, ie. an equation describing the relationship between pressure and energy density, it becomes possible to numerically solve these equations. The potential distribution of the energies fermions can occupy as an ideal gas in thermal equilibrium is given by the Fermi-Dirac statistic[6]

$$f(E) = \frac{1}{e^{(E-\mu)/k_B T} + 1} \quad (3)$$

Where  $E$  is energy,  $\mu$  is the chemical potential,  $k_B$  and  $T$  the temperature. The number density of the Fermi gas in phase space is given by  $n_i = \frac{dN}{dV}$ . For a degenerate ideal Fermi gas (meaning  $T \rightarrow 0$ ), the distribution function will have a value of either be 1 or 0. By ignoring electrostatic interactions, the number density for a degenerate Fermi gas is given by  $n_e = \frac{k_F^3}{3\pi^2\hbar^3}$ . Given that the mass density of the star in terms of nucleon mass is given by  $\rho = n_e m_n \frac{A}{Z}$  with  $A$  and  $Z$  being the atomic mass and atomic number, we find that the Fermi momenta of the constituent particles is given by  $k_F = \hbar \left( \frac{3\pi^2 \rho Z}{m_n A} \right)^{1/3}$ .

The total energy density of the star is given by  $\epsilon = nm_N \frac{A}{Z} c^2 + \epsilon_i(k_F)$  with  $i$  being the particle species. The energy of the particle species is given by  $E(k) = \sqrt{k^2 c^2 + m_e^2 c^4}$ . The energy density contributions due to the Fermi momenta and the pressure of a system with an isobaric distribution of pressure is given by [2]

$$\epsilon_i = \frac{8\pi}{(2\pi\hbar)^3} \int_0^{k_F} \sqrt{k^2 c^2 + m_i^2 c^4} k^2 dk \quad (4)$$

$$p = \frac{1}{3} \frac{8\pi}{(2\pi\hbar)^3} \int_0^{k_F} k v k^2 dk \quad (5)$$

Where  $v = \frac{kc^2}{E} = \frac{kc^2}{\sqrt{k^2 c^2 + m_e^2 c^4}}$ . Simplifying these integrals based on whether the fermions are moving relativistically or not, we find a simple relation between energy density and pressure. For both cases we find that  $p \approx K_{non-rel} \epsilon^{5/3}$  and  $p \approx K_{rel} \epsilon^{4/3}$ .

Where  $K_{non-rel} = \frac{\hbar^2}{15\pi^2 m_e} \left( \frac{3\pi^2 Z}{m_N c^2 A} \right)^{5/3}$  and  $K_{rel} = \frac{\hbar c}{12\pi^2} \left( \frac{3\pi^2 Z}{m_N c^2 A} \right)^{4/3}$  which correspond to the non-relativistic and relativistic cases respectively. The above equations are called polytropes which refers to an equation of state that can be expressed as  $p = K\epsilon^\gamma$ . Due to the formulation of energy density and pressure we use the dimensionless quantities  $\bar{\epsilon}$  and  $\bar{p}$  such that  $p = \epsilon_0 \bar{p}$  and  $\epsilon = \epsilon_0 \bar{\epsilon}$  where  $\epsilon_0$  has the dimensions of energy density  $erg.cm^{-3}$ . We can then rewrite our polytrope in dimensionless form as  $\bar{p} = \bar{K} \bar{\epsilon}^\gamma$ . This allows us to rewrite the structure equations in dimensionless form as

$$\frac{dp}{dr} = - \frac{GM_\odot}{c^2} \frac{\bar{p}^{1/\gamma} \bar{M}(r)}{r^2 \bar{K}^{1/\gamma}} = - \frac{\alpha \bar{p}^{1/\gamma} \bar{M}(r)}{r^2} \quad (6)$$

$$\frac{\bar{M}}{dr} = \frac{4^2 \bar{p}^{1/\gamma} \epsilon_0}{M_\odot c^2 \bar{K}^{1/\gamma}} = \beta r^2 \bar{p}^{1/\gamma} \quad (7)$$

The new defined constants  $\alpha$  and  $\beta$  have dimensions  $km$  and  $km^{-3}$  respectively. Both differential equations carry dimension  $km^{-1}$ . This means these equations need to be integrated with respect to  $r$ .  $\alpha$  is given by  $\epsilon_0 = \left[ \frac{1}{\bar{K}} \left( \frac{R_0}{\alpha} \right)^\gamma \right]^{1-\gamma}$  where  $R_0 = \frac{GM_\odot}{c^2}$ .

For very compact stars (like neutron stars), one has to take into account the effect of space-time curvature[5]. These effects become more pronounced as the quantity  $2GM/Rc^2$  approaches unity. The star then needs to be described using Einstein's equation  $G_{\mu\nu} = -\frac{8\pi G}{c^4} T_{\mu\nu}$ . For an isobaric, static, general relativistic ideal fluid sphere (a star is essentially a fluid sphere) at hydro-static equilibrium, we make use of the Tolman-Oppenheimer-Volkoff (TOV) equation [2]

$$\frac{dp}{dr} = - \frac{G\epsilon(r)M(r)}{c^2 r^2} \left[ 1 + \frac{p(r)}{\epsilon(r)} \right] \left[ 1 + \frac{4\pi r^3 p(r)}{m(r)c^2} \right] \left[ 1 - \frac{2GM(r)}{c^2 r} \right]^{-1} \quad (8)$$

This equation is already in dimensionless form and strengthens gravitational effects.

## 2. Results

In order to solve the dimensionless structure equations, we make use of Ordinary Differential Equation (ODEs) Solvers using Python. This finds a numerical solution to these equations. For this project the `odeint` function from the `scipy.integrate` library was used to solve the polytropic structure equations. Through some elementary coding it is then possible to create plots using the output from the `odeint` function. These plots give an idea of how the solution behaves and are useful for the physical interpretation of the solution. It is also very easy to

extract the pressure, mass and radius of the stars that are solutions to these structure equations. They are simply the maximum values in the arrays for pressure, mass and radius.

In order to use the ODE solvers in Python, we need to choose an initial central pressure that makes physical sense for the situation. Secondly, in the dimensionless structure equations, constants  $\alpha$  and  $\beta$  are present. We also have the liberty of choosing the values of these constants. Note that the choice of  $\alpha$  affects the value of  $\epsilon_0$  which in turn determines the value of  $\beta$ .

### 2.1. White Dwarfs non-relativistic case

In this case, the constituent electrons aren't moving relativistically. This means the polytropic index is given by  $\gamma = 5/3$ . For this case we expect lower pressure values. As a result we expect the star to support less mass than the relativistic case. We choose that  $\alpha = 0.05 \text{ km}$ , implying  $\epsilon_0 = 2.488 \times 10^{37} \text{ erg.cm}^{-3}$  and  $\beta = 0.005924 \text{ km}^{-3}$ . The results for a range of central pressures are as follows

**Table 1.** Mass and Radius for range of central pressures (Non-relativistic case)

Central Pressure (unitless)	Radius (km)	Mass ( $\odot$ )
$\bar{p}_0 = 10^{-15}$	10500	0.39422
$\bar{p}_0 = 10^{-16}$	13500	0.197582
$\bar{p}_0 = 10^{-17}$	16500	0.09900736

### 2.2. White Dwarfs relativistic case

In this case the electrons are moving relativistically. In such a case, the star can support a larger mass but requires a greater central pressure. This large central pressure "squeezes" the electrons into relativistic speeds. In this case the polytropic index is given by  $\gamma = 4/3$ . Here we chose that  $\alpha = 1.473 \text{ km}$ , making  $\epsilon_0 = 7.463 \times 10^{39} \text{ ergs/cm}^3 = 4.17 M_\odot c^2/\text{km}^3$ , and  $\beta = 52.46 \text{ km}$ . The results from the ODE solver are given by the table below

**Table 2.** Mass and Radius for range of central pressures (Relativistic case)

Central Pressure (unitless)	Radius (km)	Mass ( $\odot$ )
$\bar{p}_0 = 10^{-15}$	8500	1.2469
$\bar{p}_0 = 10^{-16}$	13000	1.2456
$\bar{p}_0 = 10^{-17}$	19900	1.2357

### 2.3. Neutron star: Full relativistic case

To set up an equation of state that works for a range of Fermi momenta values, we can write the energy density of the star as a function of pressure. This is given by

$$\bar{\epsilon}(p) = A_{non-rel}\bar{p}^{3/5} + A_{rel}\bar{p} \quad (9)$$

Where  $A_{non-rel}$  and  $A_{rel}$  are constants. The first term dominates in low pressures while the second will dominate in high pressures. We redefine and fix  $\epsilon_0$  as  $\epsilon_0 = \frac{m_n^4 c^5}{(3\pi^2 \hbar)^3} = 5.346 \times 10^{36} \text{ ergs.cm}^{-3} = 0.003006 M_\odot c^2 . km^{-3}$ . Using the equations derived earlier for pressure and energy density, Mathematica can be used to fit the constants  $A_{non-rel}$  and  $A_{rel}$  over a range of Fermi momentum values. These constants were then found to be  $A_{non-rel} = 2.4216$  and  $A_{rel} = 2.8663$ . With the new  $\epsilon_0$ , we chose that  $\alpha = R_0 = 1.476 \text{ km}$  we obtain that  $\beta = 0.03778$ . Now because neutron stars are sufficiently compact and massive enough, one needs to consider relativistic effects. We then need to solve for the TOV equation. For comparison we solved both the Newtonian formalism and the TOV equations. The results for a starting central pressure  $\bar{p}_0 = 0.01$  (which is clearly relativistic) is provided below

**Table 3.** Mass and Radius for different models

Model	Radius (km)	Mass ( $\odot$ )
Newtonian Model	11	1.5312
TOV	9	0.77

#### 2.4. Neutron stars with protons and electrons

Neutron stars realistically don't only consist of neutrons. This is because free neutrons are unstable and undergoes weak decay. A free neutron has a half-life of about 15 minutes before decaying into a proton, electron and electron anti-neutrino. Note that all the decay products (with the exception of the neutrino) are Fermions. This means that at some point, all the lower energy levels of the protons and electrons of the system become filled up. Due to Pauli's exclusion principle, no more protons and electrons can then be added to the system. Once in this state, equilibrium between the rates of electron capture and neutron decay is reached stabilising the number of protons and electrons present in the star. We can perform a very similar analysis as done previously. The total energy density and pressure is simply the sum of the energy and pressure contributions from each particle species that is present. We then can write  $\epsilon_{tot} = A_{non-rel} \bar{p}_{tot}^{3/5} + A_{rel} \bar{p}_{tot}$ . Performing the same fitting procedure on Mathematica, we find  $A_{non-rel} = 2.572$  and  $A_{rel} = 2.891$ . Performing a long string of calculations by varying central pressures, we can create a plot demonstrating how the solutions behave. We vary central pressure and append the mass and radius values at the end of an array. Figure 1 is the plot generated with this analysis for the pure neutron star case and the neutron star with protons and electrons. The central pressure increase from the right to the left. The range of central pressures  $\bar{p}_0$  is 0.01 – 5.

### 3. Conclusion

The mass of neutron stars ranges from about 1-3 solar masses [3]. However, neutron stars have a theoretical lower mass limit of  $1 M_\odot$  [3]. In this study, the masses for the neutron stars lie within this expanded mass range of  $0.1 M_\odot - 3 M_\odot$ . We find comparable results between the pure neutron star and a neutron star with protons and neutrons. The behaviour of the solutions to the equations for a range of central pressures is the same. We find the solutions stabilise around a maximum mass of  $0.77 M_\odot$  for the pure neutron star case (TOV solution considered here due to the compactness of these stars) and for neutron stars with protons and electrons, the solutions stabilise around a maximum mass of  $7.1 M_\odot$ . Note that in this study, no inter-particle

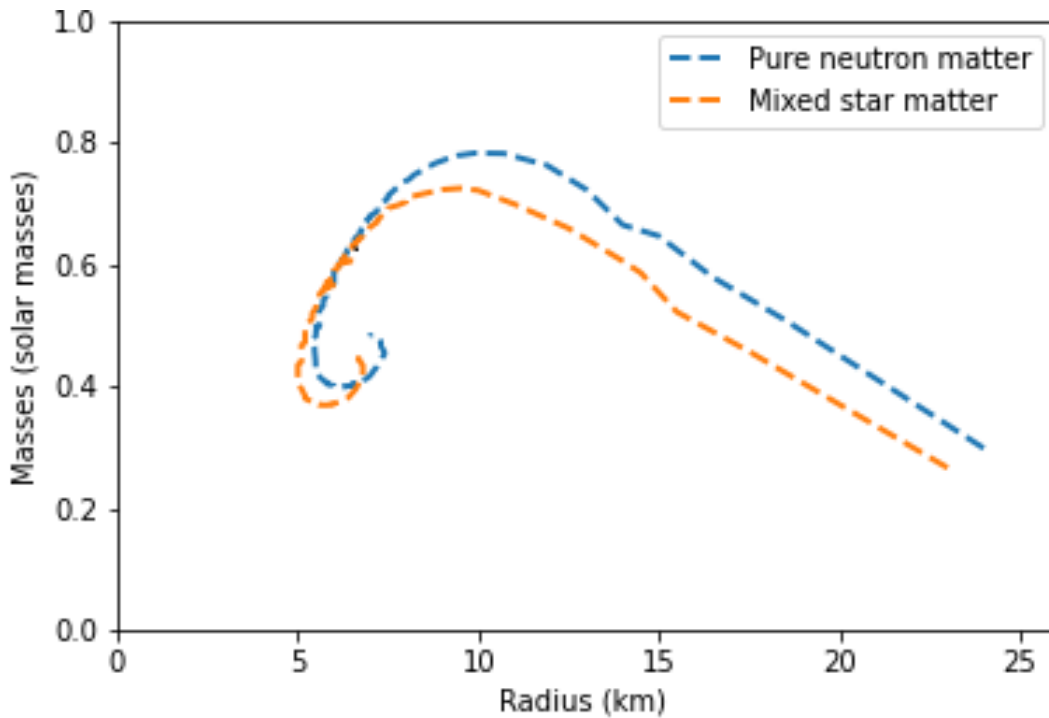


**Figure 1.** Plot of radius and mass parameterised by central pressure

interactions were considered. It is believed that the simplicity of the models used in this study accounts for the unrealistically low maximum mass of these stars. . The maximum mass of a neutron star is expected to be  $2.5 M_{\odot}$  due to constraints placed by the stiffness of the EoS [3]. As a future work, these interactions will be included in the model. Secondly spin effects were not considered in this study. The inclusion of spin in the model is expected to increase the maximum mass the star can support. Spin can increase the maximum mass of a neutron star by 25% [7]. With recent developments in the field of gravitational waves, another means of probing the equation of state is provided. By studying the wave forms produced by merging neutron stars it becomes possible to determine the properties of the neutron star through studying the effect of tidal forces on the generated wave forms. We hope to improve current models of neutron stars with the added information from the gravitational wave analysis.

#### 4. Acknowledgements

The work presented here was completed as part of the NMU-NITheCS internship program in 2021/2022. I'd like to thank Prof. Azwinndini Muronga for hosting the internship, as well as Dr. Dawit Worku and Ms. Thuthukile Khumalo for their help. Finally, I'd like to thank NITheCS for providing financial support and establishing this initiative, which I consider invaluable to aspiring researchers like myself. The skills and knowledge gained during the internship have been extremely beneficial to my primary research area.

#### References

- [1] D.A Ostlie B.W Carroll. *An introduction to modern astrophysics*. Pearson, 2014. ISBN: 10: 1-292-02293-0.

- 
- [2] Irina Sagert *et al.* “Compact stars for undergraduates”. In: (July 2005). DOI: <https://arxiv.org/abs/astro-ph/0506417v1>.
  - [3] Lex Kaper *et al.* “Measuring the Masses of Neutron Stars”. In: *The Messenger* 126 (Dec. 2006), pp. 27–30.
  - [4] Riccardo La Placa *et al.* “Neutron Star Radius-to-mass Ratio from Partial Accretion Disc Occultation as Measured through Fe K Line Profiles”. In: (July 2003). DOI: <https://arxiv.org/abs/2003.07659>.
  - [5] Richard.R Silbar *et al.* “Neutron stars for undergraduates”. In: (July 2003). DOI: <https://arxiv.org/abs/nucl-th/0309041v2>.
  - [6] E.M Lifshitz L.D Landau. *Statistical Physics*. Course of Theoretical Physics. Elsevier, 1980.
  - [7] J.M Miller M.C Miller. “The Masses and Spins of Neutron Stars and Stellar-Mass Black Hole”. In: (Aug. 2014). DOI: <http://arxiv.org/abs/1408.4145v1>.



DIVISION

— E —

PHYSICS FOR DEVELOPMENT,  
EDUCATION, AND OUTREACH

## The inclusion of nature of science in grade 12 high-stakes physics assessments in South Africa

**Umesh Ramnarain**

University of Johannesburg, Kingsway Avenue, Auckland Park, 2006

E-mail: [uramnarain@uj.ac.za](mailto:uramnarain@uj.ac.za)

**Abstract.** This research explores the representation of Nature of Science (NOS) in three national high-stakes grade 12 physics examinations. A recent characterization of NOS is called the Family Resemblance Approach (FRA). This study adopted a FRA as a conceptual framework in guiding the analysis of grade 12 physics items for the representation of NOS. FRA offers 11 categories that consolidate the epistemic, cognitive and social aspects of science in a holistic, flexible and descriptive way. The findings of this study suggest that greater attention needs to be paid to the representation of NOS in both the cognitive-epistemic and social-institutional systems. A particular concern is the weak representation of NOS in the socio-institutional dimension. An implication of this is that learners are not tested on higher-order skills such as critical thinking that would inform their decision-making on socio-scientific issues related to physics. This is therefore a call for deliberation amongst stakeholders on the tasks that are set in physics examinations.

### 1. Introduction

The construct ‘nature of science’ (NOS) has been regarded as a key purpose for studying science for more than 100 years [1]. NOS forms the foundation of science curriculum documents worldwide [2]. In the South African Curriculum and Assessment Policy Statement (CAPS) Physical Sciences, NOS is addressed through Specific Aim number 3 where it is stated that “an understanding of the nature of science and its relationships to technology, society and environment” [3]. Due to this curriculum emphasis, NOS formed the focus of this research.

NOS is an encompassing and multifaceted concept and cannot be defined by a single term or a statement. Nature of science does not describe how the natural world works, but is rather a description of how the scientific enterprise works [4]. McComas, Clough and Almazroa [5] describe a ‘consensus view’ of the nature of science extracted from eight international science standards documents. According to this view, scientific knowledge is tentative and subject to change; it is subjective; people from all cultures contribute to science; and scientific ideas are affected by their social and cultural milieu.

An understanding of the nature of the science is critical to science learning. McComas and Clough [4] put it that “NOS is fundamental to any conception of a science education” (p. 11). Incorporating the nature of science in teaching also conveys to learners a view of science as a human endeavour steered by our sense of curiosity in trying to understand the physical world. This view of

science can enhance interest in the subject [6]. An understanding of the nature of science has also been presented as essential for informed decision-making, especially in evaluating the effect of technological innovations on society [7].

This research explored the representation of Nature of Science (NOS) in three national high-stakes grades 12 physics examinations. These were examinations administered by the Department of Basic Education for the years 2018, 2019 and 2020. It is maintained that these three papers will provide a representative sample. This study has particular significance due to curriculum reform that deliberately attempted to transform the previous curriculum that depicted to the learner and teacher a view of science which was not compatible with the afore-mentioned tenets of the nature of science. Science curricula worldwide have given more emphasis to NOS, and this goal was also set by curriculum developers in post-Apartheid South Africa. It is therefore of interest to know whether this curriculum intent translates into the assessment of learners in high stakes physics examinations.

The ‘consensus’ view of the nature of science has been criticized, with one of the criticisms being that “the consensus view simplifies the NOS but does not illustrate the detailed process and actions in science [8]. A recent characterization of NOS is called the Family Resemblance Approach (FRA) (Figure 1). FRA is a holistic perspective that supports the understanding of science as the conception of dynamic cognitive, epistemic, and social-institutional systems [9]. FRA offers a comprehensive framework for NOS-related issues [10]. The FRA wheel consists of 11 categories, with the inner-most level depicting the cognitive and epistemic aspects of science and the outer levels indicating social-institutional elements. The cognitive-epistemic system comprises the following categories: aims and values, scientific practices, methods and methodological rules, and scientific knowledge. Within the social-institutional system, the following categories are identified: professional activities, scientific ethos, social organizations and interactions, social values, political power structures, social certification and dissemination, and financial systems.



**Figure 1:** The FRA Wheel: Science as cognitive, epistemic and social institutional system [10]

The following research question was investigated: How are the FRA NOS categories represented in three Physics papers in high-stakes matric examinations?

## 2. Method

The units of analysis included all questions except MCQ that appear in three national high-stakes grade 12 physics examination papers. Each examination paper contained 10 MCQ that were excluded from the analysis. A high-stakes exam is written at the end of grade 12 and the results are used in applying for university entrance. Questions relating to NOS were coded according to the FRA NOS

categories as reflected in the FRA wheel. A statement in the question was regarded as conforming to a category, if it related to the description of the category. For some questions, it was realised that multiple codes could apply and so this was allowed. The coding was conducted independently by the author and a researcher in science education. To measure the interrater reliability, Cohen's kappa coefficient [11] was computed. The inter-rater agreement was  $K = .85$  for the statements, and this was considered good [12]. Eventually, after discussion on the discrepancy in coding, full agreement was reached between the coders.

### 3. Results

The frequency distribution of the NOS categories depicted in all three physics examination papers is shown in Table 1 below.

**Table 1:** Frequency distribution of the NOS categories in FRA framework

Aims and values	Scientific practices	Methods and methodological rules	Scientific knowledge	Professional activities	Scientific ethos	Social certification and dissemination	Social values of science	Social organizations and interactions	Political power structures
0	14	11	62	0	0	0	0	0	0

In total there were 87 NOS coded items with all codes (100%) related to the cognitive-epistemic system. Within the cognitive-epistemic system, scientific knowledge (62 out of 87), scientific practices (14 out of 87), and methods and methodological rules (11 out of 87) had the highest proportion of codes. An example of question that was classified as "scientific knowledge" was question 2.1 of the 2018 physics examination paper. Here is the question: 2.1 State Newton's Second Law in words. (2) This trend of questions predominantly addressing the cognitive-epistemic system was consistent for all three question papers. NOS was absent in other categories.

The strongest interconnectedness amongst codes was revealed for the categories of scientific practices, and methods and methodological rules, where 10 statements in examination questions were coded to both categories. In other words, each of these 10 statements could be coded to the two categories, and this suggests some relationship between the categories.

### 4. Discussion and conclusion

The results of this study inform on the extent to which NOS is represented in grade 12 physics examinations. A critical finding of this study is that NOS representation in the social-institutional system is absent. If the important categories such as social values of science and political power structures in this system were more strongly represented, this could give impetus to classroom instruction that engages learners in socio-scientific issues. Various studies have alluded to how focusing on socio-scientific issues (SSI) can enable understanding of nature of science. This need to address socio-scientific issues with learners is addressed in CAPS where an important thrust of the curriculum is for learners to be empowered in responsible decision-making on issues related to science, society and technology [3].

## 5. Recommendations

Greater attention needs to be given to the formulation of assessments tasks that address the social-institutional system. This could have implication for classroom practices because assessments tend to influence learning experiences afforded to learners ('teach to the test') by teachers. Examination questions on the nature of science can be formulated according to test items that have been used for research such as items in the Views of Nature of Science Questionnaire (VNOS) [13]. Teacher professional development needs to focus on assessing for NOS understanding in all dimensions of NOS.

## References

1. Lederman N G and Lederman J S 2014 *Research on Teaching and Learning of Nature of Science* ed N G Lederman and S K Abell eds (New York: Routledge) pp 600-620
2. Lederman N G, Lederman J S and Antink A 2013 Nature of science and scientific inquiry as contexts for the learning of science and achievement of scientific literacy. *International Journal of Education in Mathematics, Science and Technology*, **1**(3), 138-147.
3. Department of Basic Education 2011 Curriculum and assessment policy statement grades 10–12: physical sciences. Pretoria: Government Printer.
4. McComas W F and Clough M P 2020 Nature of Science in Science Instruction: Meaning, Advocacy, Rationales, and Recommendations. In: McComas W.F., editor. *Nature of science in science instruction* (pp. 3–22). Springer: Dordrecht.
5. McComas W F, Clough M P and Almazroa H 1998 The role and character of the nature of science in science education. In *The nature of science in science education* (pp. 3-39). Dordrecht: Routledge
6. Matthews, M.R. (1994). *Science Teaching: The Role of History and Philosophy of Science*. Dordrecht: Routledge.
7. Driver R, Leach J and Millar R 1996 *Young people's images of science*. McGraw-Hill Education (UK).
8. Jho H 2019 A comparative study on the various perspectives on the nature of science through textbook analysis centering on the consensus view, Features of Science, and Family Resemblance Approach. *Journal of The Korean Association for Science Education*, **39**(5), 681-694.
9. Akgun S and Kaya E 2020 How do university students perceive the nature of science? *Science & Education*, **29**, 1-32.
10. Erduran S and Dagher Z 2014 *Reconceptualizing the nature of science for science education: Scientific knowledge, practices and other family categories*. Dordrecht: Springer.
11. Cohen J 1960 A Coefficient of Agreement for Nominal Scales. *Educational and Psychological Measurement*, **20**, 37-46.
12. Miles M B and Huberman A M 1994 *Qualitative Data Analysis: An Expanded Sourcebook*. Thousand Oaks, CA: Sage Publications.
13. Lederman N G, Abd-El-Khalick F, Bell R L and Schwartz R S 2002 Views of Nature of Science Questionnaire: Toward Valid and Meaningful Assessment of Learners' Conceptions of Nature of Science. *Journal of Research in Science Teaching*, **39**, 497-521.

## Exploring the impact of teacher education programme on the development of pre-service science teachers' TPACK

**S Ramaila and E Ndumanya**

Department of Science and Technology Education  
University of Johannesburg, South Africa

E-mail: samr@uj.ac.za

**Abstract.** Technology integration is central to the improvement of teaching and learning especially in science education. This study explored the impact of teacher education programme on the development of pre-service science teachers' technological pedagogical content knowledge (TPACK) by adopting a generic qualitative design located within the interpretivist paradigm. The empirical investigation involved six purposively selected pre-service science teachers enrolled for a Bachelor of Education degree at a South African university. Qualitative data was collected through analysis of lesson plans, evaluation of micro lesson presentations, and semi-structured interviews. The study is underpinned by TPACK framework as a theoretical lens. The findings revealed that forms of knowledge developed by the preservice science teachers were mostly technological knowledge (TK), content knowledge (CK) and technological pedagogical content knowledge (TPACK). Findings further demonstrated that the training programme provided meaningful opportunities for pre-service science teachers to use various technologies as learning tools. It is recommended that sustainable professional development opportunities ought to be provided to implore science teachers to fully embrace digital transformation as a key imperative associated with the advent of the Fourth Industrial Revolution. Theoretical implications for technology-enhanced teaching and learning are discussed.

**Keywords:** TPACK, professional development, digital transformation

### 1. Introduction

The effective integration of educational technologies has gripped the attention of researchers and teacher educators in recent years. The integration of educational technologies is primarily geared towards the accomplishment of curriculum reforms aimed at preparing individuals for 21st century competencies and skills (i.e. critical thinking, creative, collaborate, communicate and problem solving) in order to survive, make informed decisions and realise future career aspirations [1]. Technology integration has been recommended both in South African educational system and all over the world in the past years [2]. Therefore, there is a need for the new generation of teachers to effectively integrate and use educational technologies in teaching and learning. The international Society for Technology in Education (ISTE) [3] puts considerable emphasis on the standard for teachers' competence with regard to the use of technology in education. Thus, teacher education programme ought to respond to the need to equip teachers with this competence. Currently, teacher education programmes are promoting and providing meaningful opportunities that will enhance pre-service teachers' knowledge and skills

in developing essential competencies in using technologies in education [4,5]. The extent to which technology integration is harnessed in teacher training programmes informs pedagogical practices adopted by pre-service teachers (PSTs) when integrating technology in science teaching and learning. Developing pre-service teachers' competencies in the effective use of technologies in education requires enhancement of their Technological Pedagogical Content Knowledge (TPACK) [6]. Various studies have examined the impact of teacher training programs on pre-service teachers' TPACK in teaching and learning with educational technologies in developing countries [1,4]. However, there is a need for more studies to explore the impact of teacher education programmes on development of pre-service science teachers' TPACK within the broader South African context. The empirical investigation is guided by the following research question.

What is the effect of teacher education programme on the development of pre-service science teachers' TPACK?

## **2. Theoretical framework**

The study is underpinned by technological pedagogical content knowledge (TPACK) [13] as the underlying theoretical framework. The TPACK framework is relevant to the study as it puts particular emphasis on the interaction between pedagogical knowledge, content knowledge and technological knowledge [13]. In addition, the TPACK framework advocates that learning can be facilitated when technology is used to complement teaching using appropriate pedagogical approaches [13]. TPACK is defined as the basis of effective teaching with technology which requires an understanding of the representation of concepts using technology [14].

## **3. Research design and methodology**

This study adopted a case study design located within the interpretivist paradigm to explore the impact of teacher education program on development of PSTs' TPACK from multiple data sources [7]. The qualitative data sources were lesson plans, micro lesson presentations and semi-structured interviews. Although the study involved six (two males and four females) purposively selected pre-service science teachers that were enrolled for Postgraduate Certificate in Education (PGCE) majoring in Physical Sciences, the findings have important implications for the development of preservice teachers' TPACK [12]. The pre-service teachers attended a weekly two hour lecture which put emphasis on learning through design of lesson plans. The content-specific course aimed at preparing pre-service science teachers to design learner-centred lessons that support development of learners' 21st century skills and competencies using various pedagogical strategies and the appropriate integration of educational technologies Physical Sciences teaching and learning. The course provides meaningful opportunities such as critical analysis of national school curriculum (known as Curriculum and Assessment Policy Statement), design of lesson plans, teaching strategies, teacher knowledge (content knowledge, pedagogical content knowledge, and technological pedagogical content knowledge), computational thinking, technology-enhanced assessments, and technology integration in teaching and learning. In addition, the pre-service science teachers were required to present micro-lessons after attending six weeks teaching practice known as Work integrated learning (WIL) to experience real-life school context. At the final stage of the course, they submitted e-portfolios and wrote summative examination.

Data collection tools used to follow the development of PSTs were as follows: analysis of lesson plans, evaluation of micro-lesson presentations, and semi-structured interviews. Lesson plans required the PSTs to hand in lesson plans designed for the micro-lesson presentation in order to gain

more detailed information about the lesson and presentation. In terms of its generic structure, the lesson plan included lesson aims and objectives, introduction, engagement (such as big ideas, misconceptions, difficulties/ limitations, teaching procedures, resources, and assessment), and conclusion. The lesson plan was also expected to exhibit coherence and alignment with lesson outcomes. The participants were finally afforded opportunities to reflect on the important aspects of the lesson. Each participant was given 30- 45 minutes to present a micro lesson to peers and researchers. Two researchers observed and evaluated preservice teachers' TPACK development using adapted TPACK-based lesson observation rubric [8]. At the end of micro-lesson presentation, each participation was interviewed to gain more information about their views on teaching and learning, TPACK competencies and rationale, experience and challenges in developing the TPACK during the course of their teacher education programme. The interviews were audio-recorded and each session took 20-30 minutes for each participant. Both lesson plans and micro-lesson presentations were analysed by two researchers using a TPACK-based lesson observation rubric. The adapted rubric consisted of three sections lesson plan, evidence of seven competencies of TPACK in the lesson presented, and general evaluation in terms of ability to use technology and interaction in using technology along three levels: low (1), moderate (2), and high (3). The two researchers evaluated and scored each lesson plans and micro-lesson presentations individually during the presentation. Thereafter, the scores were reviewed for differences and consensus was reached. Finally, the internal consistency was determined using Cronbach Alpha coefficient between the items of the rubric (see Table 2).

**Table 2: Internal consistency coefficient of micro-lesson presentation and lesson plan**

<b>Cronbach alpha</b>	<b>PST1</b>	<b>PST2</b>	<b>PST3</b>	<b>PST4</b>	<b>PST5</b>	<b>PST6</b>
	<b>0.821</b>	<b>0.852</b>	<b>0.764</b>	<b>0.863</b>	<b>0.901</b>	<b>0.885</b>

The data obtained from the semi-structured interviews was analysed using content analysis procedure. This procedure involved transcribing, coding and categorizing the transcription into thematic items in relation two seven constructs (competencies) of TPACK. First, each researcher coded data obtained from each pre-service science teachers' interview separately. Thereafter, the researchers had a discussion on each interview code to address differences to reach consensus. The researchers calculated a measurement of consistency by determining the amount of coded data as different and the same to represent the percentage agreement. The results are given in Table 3.

**Table 3: Percentage agreement of semi-structured interview data analysis**

<b>% Agreement</b>	<b>PST1</b>	<b>PST2</b>	<b>PST3</b>	<b>PST4</b>	<b>PST5</b>	<b>PST6</b>
	<b>83%</b>	<b>84%</b>	<b>91%</b>	<b>79%</b>	<b>85%</b>	<b>88%</b>

To ensure reliability, the internal consistency coefficient was determined and the percentage agreement was calculated. To ensure validity, the triangulation of data was realised through multiple data collection sources (i.e. micro-lesson presentations, lesson plans and semi-structured interviews).

#### **4. Results**

TPACK development of the preservice science teachers from micro-lesson presentations and lesson plans is depicted in Table 4.

**Table 4: TPACK development of the preservice science teachers from micro-lesson presentation and lesson plans.**

<b>TPACK development</b>	<b>Lesson plans, micro lesson presentations</b>
<b>Highest knowledge developed</b>	Technological Knowledge (TK) Content Knowledge (CK) Technological Pedagogical Content Knowledge (TPACK)
<b>Moderate knowledge developed</b>	Technological Content Knowledge (TCK) Technological Pedagogical Knowledge (TPK) Pedagogical Content Knowledge (PCK)
<b>Least knowledge developed</b>	Pedagogical Knowledge (PK)

The highest forms of knowledge developed were CK, TK, and TPACK. Moderate forms of knowledge developed were TPK, TCK and PCK. The least form of knowledge developed was PK. The result obtained from semi-structured interviews were consistent with the level of PSTs TPACK seven competencies revealed in the micro lesson presentation and lesson plans. For example, the high-level forms of knowledge developed (TK, CK and TPACK) were also obtained in semi-structured interviews because the PSTs appropriately mentioned the various digital technologies used, the reason for choosing these technologies and how they intended to use it in the science classroom to foster meaningful teaching and learning. They also explained the topic, lesson aims, and objectives as well as the big ideas appropriately. The PSTs' ability to integrate technologies such as projector, laptops, PowerPoint presentations, Phet simulations, videos and Kahoot in achieving the lesson objectives through observations, discussion and asking and/or answering questions were highly mentioned as reflected in the following excerpts.

The use of technology helps in engaging the learners to conceptualise the concept of Doppler effect by using picture of sonar process of a pregnant woman. Engaging them in the picture helped to relate what they are learning in school to real life experience and it simulates them to ask and answer questions about what they observe in the picture. This also help them to actively participate in learning (Participant 1).

Using technology in teaching science concepts have really helped me because learners have this attitude that science is a difficult subject because it is abstract. But using technology help learners to gain interest and enjoy the learning because they visualise the concept. This actually trigger their imagination and visualisation, and in developing skills in using technologies in learning and communicating in our current digital society (Participant 4).

The moderate level knowledge developed in these teachers was also reflected in their interviews as PSTs used the various technologies in facilitating the lesson objectives and implementation of various teaching strategies to help the learners to understand the concepts being taught. Moderate knowledge developed was evidenced by preservice teachers' inability to appropriately elicit learners' prior knowledge and misconceptions as illustrated in the following excerpts.

Using technology helps me as a teacher in planning and teaching easily such as the You-tube because in using slides it enable me to engage the learners in better understanding of the abstract concept such as electric circuits, identify their misconceptions and how to address them (Participant 5).

Technology makes teaching easier because it helps me to have enough time to engage the learners using PowerPoints presentation, simulation and pictures than when I write on board. It also gives me the opportunity to easily access my note on the laptop whenever the learner come to me for more explanation (Participant 6).

The least knowledge developed was evidenced by preservice teachers' inability to coherently implement adopted teaching strategies. For instance, preservice teachers encountered fundamental challenges with the implementation of inquiry-based learning. The preservice teachers expressed fundamental appreciation of the impact of the teacher education programme on their TPACK development. This sentiment is encapsulated in the following excerpts.

This course has helped in developing knowledge and skills in using technology in teaching science. Integrating technology requires the teacher to promote learner-centred learning where I use various technology such as video, pictures etc. to engage the learners in constructing their own learning while I facilitate the teaching and learning process rather than the teacher-centred or traditional learning method (Participant 2).

This course has taught me how to prepare my lesson using technology which I was not exposed or using before. I have benefited also in learning different teaching strategies e.g. questioning and inquiry-based learning, and to integrate different technological tools and software in teaching science because using technology help the learners to engage more on the activity and interact better. It enables the learners also to ask questions based on what they observed using technology (e.g. video and pictures) than when teach them using only textbook and writing on the chalkboard (Participant 4).

## **5. Discussion**

The study revealed a positive impact of the teacher education programme on preservice teachers' TPACK development. The preservice teachers' forms of knowledge that were significantly developed were TK, CK and TPACK. The preservice teachers' forms of knowledge that were moderately developed were TPK, TCK and PCK with the least form of knowledge developed being PK. The teacher education programme served to enhance preservice teachers' ability to design proper lesson plans. In addition, the participants indicated that the programme provides meaningful opportunities to sharpen their professional skills required to foster inclusive learning through pedagogic innovation. The participants further indicated that the programme enhanced the development of 21<sup>st</sup> century skills and competencies. Key findings in this study strongly suggest that the activities implemented added an innovative dimension to the coordination of work integrated learning as an integral part of preservice teacher training. The findings are consistent with previous studies conducted on preservice teacher training programmes [4,9,10]. The need to bridge theory-practice gap through development of preservice teachers' TPACK is paramount [11]. The study has profound implications for provision of authentic opportunities that would enable pre-service science teachers to acquire knowledge and skills required for coherent integration of technology to foster technology-enhanced science teaching and learning in diverse contexts.

## **5. Conclusion**

The key findings of the study suggest that the teacher education programme holds promise as a means to develop preservice teachers' TPACK. There is a crucial need for teacher education programmes to promote holistic teacher professional development. Sustainable professional development opportunities ought to be provided to encourage science teachers to fully embrace digital transformation as a key imperative associated with the advent of the Fourth Industrial Revolution.

**References**

- [1] Can B Erokten S and Bahtiyar A 2017 An investigation of pre-service science teachers' technological pedagogical content knowledge *Euro. J. Ed. Res.* **6(1)** 51
- [2] Jita T 2016 Pre-service teachers' competence to teach science through information and communication technologies in South Africa *Pers. in Ed.* **34(3)** 15
- [3] International Society for Technology in Education 2008 NETS for Teachers
- [4] Aktas I and Ozmen H 2020 Investigating the impact of TPACK development course on pre-service science teachers' performances *Asia Pac. Ed. Rev.* **21** 667
- [5] Tondeur J Scherer R Siddiq F and Baran E 2019 Enhancing pre-service teachers' technological pedagogical content knowledge (TPACK): A mixed-method study. *Ed. Tech. Res. and Dev.* **68(1)** 319
- [6] Mishra P and Koehler M J 2006 Technological pedagogical content knowledge: A new framework for teacher knowledge. *Teac. Col. Rec.* **108(6)** 1017
- [7] Creswell J W 2014 *Research design: Qualitative, quantitative, and mixed methods approaches* (4th ed). Thousand Oaks, CA: Sage.
- [8] Hoffer M Grandgenett N Harris J and Swan K 2011 Testing a TPACK-based technology integration observation instrument. Teacher Education Faculty Proceedings & Presentations, Paper 19.
- [9] Canbazoglu-Bilici S Guzey S and Yamak H 2016 Assessing pre-service science teachers' technological pedagogical content knowledge (TPACK) through observations and lesson plans. *Res. in Sci. and Tech. Ed.* **34(2)** 237
- [10] Maeng J L Mulvey B K Smetana L K and Bell R L 2013 Preservice teachers' TPACK: using technology to support inquiry instruction *J.l of Sci. Ed. Tech.* **22** 838
- [11] Shinas VH Karchmer-Klein R Mouza C Yilmaz-Ozden S and Glutting JJ 2015 Analyzing preservice teachers' technological pedagogical content knowledge development in the context of a multidimensional teacher preparation program *J. Dig. Learn. Teach. Ed.* **31(2)** 47
- [12] Fraenkel JR Wallen NE and Hyun HH 2012 How to design and evaluate research in education (8<sup>th</sup> ed.). New York: Mc Graw Hill
- [13] Koehler M and Mishra P 2009 What is Technological Pedagogical Content Knowledge (TPACK)? *Contemp. Iss. in Tech. and Teac. Edu.* **9(1)** 60
- [14] Koehler MJ Mishra P and Cain W 2013 What is Technological Pedagogical Content Knowledge (TPACK)? *J. of Ed.* **193(3)** 13

# Correlations between matriculation marks and mechanics misconceptions

Emanuela Carleschi<sup>1</sup>, Anna Chrysostomou<sup>1,2</sup>, Alan S. Cornell<sup>1</sup> and Wade Naylor<sup>3,1</sup>

<sup>1</sup> Department of Physics, University of Johannesburg, PO Box 524, Auckland Park 2006, South Africa

<sup>2</sup> Institut de Physique des Deux Infinis de Lyon, Université de Lyon, UCBL, UMR 5822, CNRS/IN2P3, 4 rue Enrico Fermi, 69622 Villeurbanne Cedex, France

<sup>3</sup> National School of Education, Faculty of Education & Arts, Australian Catholic University, Brisbane Campus, 1100 Nudgee Road, Banyo QLD 4014, Australia

E-mail: [acornell@uj.ac.za](mailto:acornell@uj.ac.za), [ecarleschi@uj.ac.za](mailto:ecarleschi@uj.ac.za), [achrysostomou@uj.ac.za](mailto:achrysostomou@uj.ac.za), [wade.naylor@acu.edu.au](mailto:wade.naylor@acu.edu.au)

**Abstract.** In this proceeding we discuss the initial stages of how using ‘dominant misconceptions’, as derived from the pre-test part of the Force Concept Inventory (FCI) assessment tool, can give informative data on how to proceed with teaching practices on a classical mechanics course, as taught in the Physics Department of the University of Johannesburg (UJ). We also briefly discuss some language correlations between high school matriculation marks and FCI scores, and how this may prepare faculty members when considering their teaching andragogy. In conclusion, the academic and language backgrounds of students enrolled on classical mechanics courses at UJ can have an impact on pre-test ability.

## 1. Introduction

In a recent work by the authors, reference [1], we have looked through the ‘misconception’ lens at how undergraduate students on a classical mechanics course perform on the *Force Concept Inventory* (FCI) assessment tool [2–5]. The FCI is a 30-minute multiple-choice test comprised of 30 questions on elementary principles and applications of classical mechanics; *viz.* circular motion, Newton’s three laws, etc. The recommended means of administering this assessment tool is as a strictly closed-book test held at the beginning of the semester (the *pre-test*), to provide instructors with an indication of their students’ baseline mechanics skills. Students are not expected to prepare for the assessment and once the pre-test is completed it is not reviewed in class nor do students receive feedback on their attempts.

However, adaptive physics pedagogy/andragogy has become a topic of interest in recent years [6], with a particular focus on confronting persistent or ‘dominant misconceptions’ generally held by incoming undergraduate students as has been argued in references [7–13]. Martin-Blas et al. [10] and Bani-Salameh [12] have suggested that these flaws in understanding should be diagnosed as early as possible by looking at these ‘dominant misconceptions’ in the pre-test. If effective teaching is to take place [12], then a primary objective at the start of teaching mechanics is to identify these misconceptions. A number of diagnostic tools have been developed for the various physics sub-disciplines. A subset of these have been designed to gauge student

comprehension at the onset of an introductory university course, and then to assess their progress at the end of the course.

As such, we shall discuss in this proceedings some further work we have undertaken with the first year undergraduates taking physics at the University of Johannesburg (UJ). In particular, we will see that for the 2021-2022 cohorts at UJ, see figure 1, questions 5, 11, 17, 19, 26 and 30 were the questions where dominant misconceptions lay. Note that questions 5 and 17 relate to questions on gravity (for example question 5 asks about the forces exerted on a circular frictionless channel), question 11 relates to Newton's third law, question 26 to Newton's first law and question 30 to impetus.\*

Given these ideas we would like to ask the following research question: How do high school matriculation scores in mathematics, science and languages affect the pre-test scores of the FCI? Our preliminary investigations conducted with the first-year engineering and physics students at UJ in 2020 [1] seemed to support this, where one particularly popular incorrect response was that “a force in the direction of motion” was partially responsible for the action described in the corresponding FCI question. The belief that “motion requires an active force” was flagged as a misconception as identified in references [10, 12, 13].

In our present study, we have performed a question-by-question analysis on the FCI pre-test responses for the 2021 and 2022 first-year physics cohorts, with  $N = 313$  students in the 2021 cohort and  $N = 337$  students in the 2022 cohort, see tables 1 and 2.† We begin with a description of the student participants and the manner in which their responses were collected in section 2. We then present our results in section 3, with a focus on the ‘dominant misconceptions’. We also include a preliminary look at correlations between matriculation marks and FCI scores in section 4, followed by conclusions and future work in section 5.

## 2. Methodology

Due to the ongoing nature of the COVID-19 pandemic, South African institutions of tertiary education were expected to function mostly – if not entirely – online [1]. The delayed release of the 2020 Grade 12 results further derailed the 2021 academic programme, with first-year academic activities only beginning on March 8<sup>th</sup> at UJ in 2021, leading to a first semester shortened by several weeks and the pre-test deployment delayed until March, see table 1. The 2022 cohort started on schedule as can be seen from the February deployment of the pre-test in table 2.

With the permission of the various lecturers involved in each of the courses that participated in this study (see table 1 for details) and ethical clearance from UJ's ethics committee, we launched the FCI test via the Blackboard interface – using the valuable lessons learnt during lockdown where we found it became easier to deploy this inventory test online – and made it available to students for a total of five days, using the module page corresponding to each of the courses.

Whilst we shall leave this for future work, it is interesting to note that through this platform we were able to track student activity (to determine whether test-takers left the browser page during the course of the test), time their test attempt, and force submission after an allotted time. We were also able to make a test visible for a set period of time. For our data collection, we enabled these features to reduce cheating and to ensure students submitted their responses after 30 minutes. Once the deployment period was over and each class had completed the assignment, the data was downloaded and processed within a single Excel spreadsheet for each

\* Access to this inventory and more information about other types of physics & astronomy tests can be found in reference [14] and at the following website <https://www.physport.org/>.

† In this case we include all students who sat the pre-test, regardless of whether they fully answered all questions or not.

**Table 1.** Course codes, their associated entry-level requirements (Grade 12 mathematics and physical sciences scores), FCI deployment period, number of student responses per class, and average scores for five first-year classes involved in the 2021 FCI pre-testing:  $N = 313$ .

Course (Physics for...)	Ent. % Math.	Ent. % Phys. Sci.	Deployment period	Responses/ class	Mean (%)
PHYS1A1 (Majors)	70	60	13/04 - 17/04	19/70	33.2
PHY1EA1 (Physics Ext.: Sem1)	60	50	09/04 - 13/04	187/306	30.1
PSFT0A1 (Education)	50	50	05/04 - 09/04	62/91	29.9
PHYG1A1 (Earth Sci.)	60	50	05/04 - 09/04	13/17	28.2
PHYL1A1 (Life Sci.)	70	50	07/04 - 11/04	32/64	28.6

**Table 2.** Course codes etc. as in table 1 for five first-year classes involved in the 2022 FCI pre-testing:  $N = 337$ .

Course (Physics for...)	Ent. % Math.	Ent. % Phys. Sci.	Deployment period	Responses/ class	Mean (%)
PHYS1A1 (Majors)	70	60	21/02 - 25/02	28/55	36.7
PHY1EA1 (Physics Ext.: Sem1)	60	50	21/02 - 25/02	176/250	26.7
PHYG1A1 (Earth Sci.)	60	50	21/02 - 25/02	9/9	33.3
PHYL1A1 (Life Sci.)	70	50	21/02 - 25/02	19/40	30.0
PHYE0A1 (Engin. Phys.)	60	60	24/02 - 28/02	105/500	33.3

of the individual classes. All data was anonymised in accordance with the requirements of the protection of personal information act.

In what follows we will present preliminary comparisons for the FCI pre-test data for the 2021 and 2022 cohorts at UJ. The analyses break down the responses for each question to look for ‘dominant misconceptions’ [10]. This can be very useful in gauging how an initial cohort, and indeed different subgroups, need different teaching pedagogies. We then also present some initial results relating to correlations between FCI performance and high school matriculation results (this was part of the ethics clearance which had been obtained for this work from 2021 onwards).

Note that in tables 1 and 2 ‘Ext.’ refers to the extended courses, where students who do not meet entry-level requirements for introductory physics classes can complete a four-year Bachelor of Science in which the traditional first-year physics course is taught over a three-semester period. We have also included a third semester course result for comparison in table 1. In relation to both years (2021 and 2022) in tables 1 and 2 the number of students who sat the pre-test were 313 and 337, respectively. This is less than the number of students who take the course. For example, in table 2, the number of Engineering Physics students for 2022 was 500, but only 105 attempted the pre-test.

### 3. Pre-test analyses and results - 2021 vs. 2022

The preliminary analyses of the pre-tests for the 2021 and 2022 cohort at UJ, for each of the 30 questions, is summarised in figure 1. The green shaded % shows the percentage of students

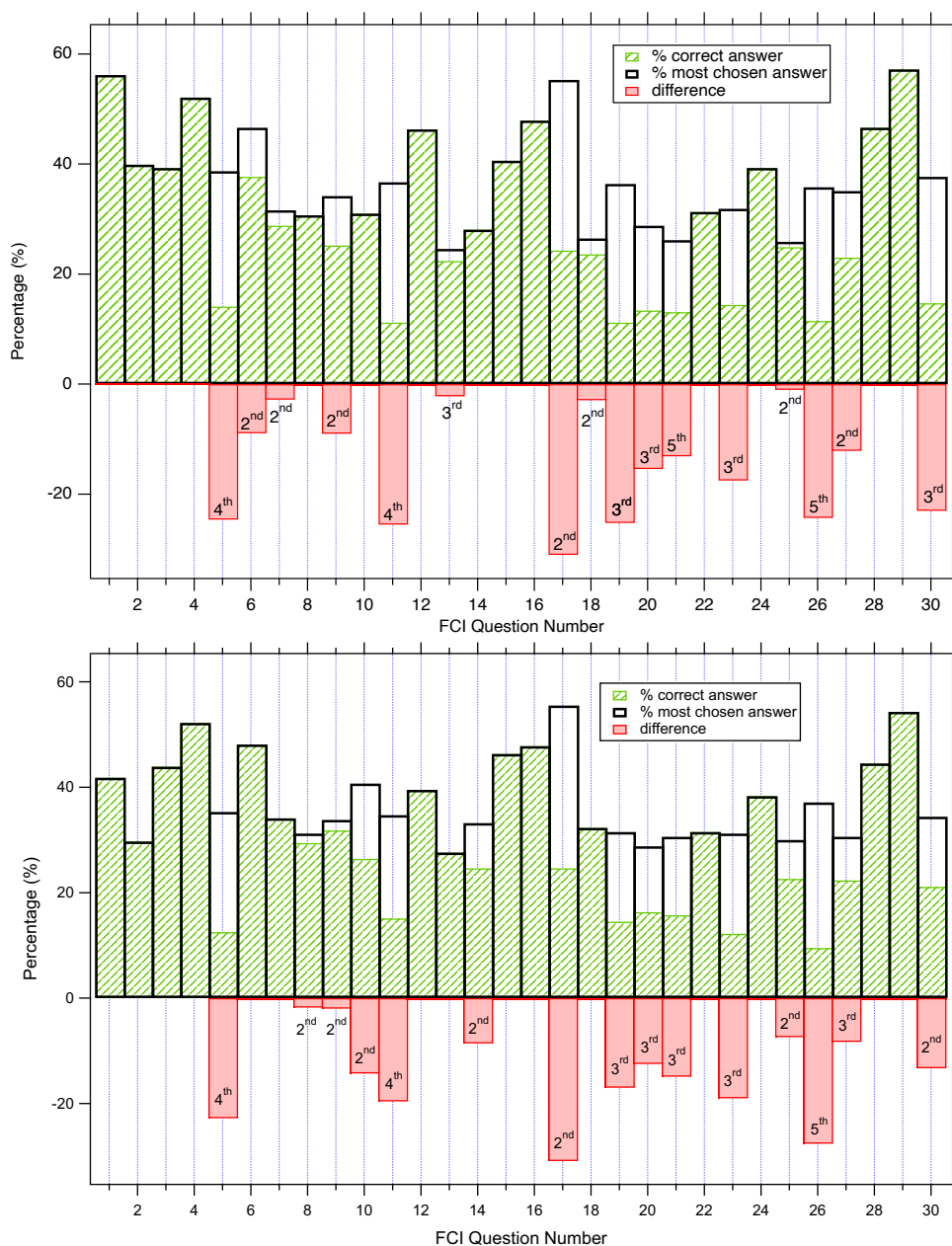


**Figure 1.** Comparison of pre-test scores for 2021 and 2022 cohorts. Top panel: Breakdown of pre-test questions for the 2021 UJ students sitting an introductory physics course,  $N = 313$ . The labels on the red % differences, such as  $4^{th}$ ,  $2^{nd}$  etc., label the most commonly chosen (incorrect) response. Lower panel: Breakdown of pre-test questions for the 2022 students sitting an introductory physics course,  $N = 337$ .

who got the correct answer, with the black outline showing the % for the most commonly chosen answer. For example, questions 1 – 4 have all of the responses as correct. The choices where the majority response was incorrect correspond to those questions with a larger red % difference showing that more students chose the wrong answer. For these cohorts of students this corresponded to questions 5, 11, 17, 19, 26, and 30, respectively. Given that this information was collected at the pre-test stage, the course instructors could attempt to adjust the teaching

**Table 3.** Pearson’s correlation coefficients for different classes in the 2022 cohort. The course codes are discussed in table 2, where ‘Eng’ implies English was the main language spoken at home and ‘Other’ implies another language aside from English was spoken at home.

Matric / Pretest Corr Coeff	PHYS1A1		PHYS1EA1		PHYG1A1		PHYE0A1	
	Eng	Other	Eng	Other	Eng	Other	Eng	Other
Phys Sci	0.375	0.683	0.125	0.314	-0.945	-0.445	0.060	0.303
Maths	0.147	0.707	0.338	0.220	-0.979	-0.559	0.562	0.521
English	0.293	-0.157	0.214	0.103	0.645	-0.614	0.099	-0.054

and learning to try to reinforce a given concept as deduced from the relevant question.‡

These questions appear to show what Martin-Blas *et al.* call ‘dominant misconceptions’ [10] For example, question 5 focuses on circular motion and we can see here that this question was not well understood by most of the cohort. Given that this information was collected at the pre-test stage, the course instructors could attempt to adjust the teaching and learning to try to reinforce such a concept.

A comparison of tables 1 and 2 for the mean scores, and figure 1 for the amount of red % differences observed, allows one to infer that the 2022 cohort has performed better on the pre-test. Quite interestingly, the dominant incorrect answer (labelled in the red shaded region) is the same in all but a few of the questions.§ Besides using ‘dominant misconceptions’ we have also started to investigate correlations between high school matriculation results (in various subjects) and pre-test FCI results.

#### 4. Correlations between high school matriculation marks and FCI pre-test scores

As well as considering ‘dominant misconceptions’ we may also look for correlations between high school matriculation results and the FCI pre-test. Table 3 summarises some of our initial investigations into correlations among the different cohorts for 2022. For example, 9 students were in the PHYG1A1 cohort and the number who spoke English at home was three. As such, the study could benefit from increased group sizes, and will be left for future work.

However, one can infer an overall trend that correlations between English scores and the FCI pre-test are more positive for students whose language spoken at home is English. This is in agreement with the observations made in reference [15], where FCI gains were found to have a dependence on English reading ability. Table 3 also shows that mathematics and physical sciences matriculation scores also have a positive correlation with pre-test scores. Though this is with an exception for PHYG1A1, which only had 9 students, in which case we cannot say too much here, due to the validity of the statistics for such a small sample.¶

#### 5. Concluding remarks

In these proceedings, we have used the pre-test part of the FCI to evaluate the baseline comprehension of Newtonian mechanics presented to first-year students enrolled in introductory physics courses over a two year period from 2021-2022. From the method of ‘dominant misconceptions’ we are able to see how a whole cohort compares, see figure 1 for a comparison of 2021 and 2022 cohorts. By displaying a question-by-question breakdown on the pre-test we can see what % of each question is answered incorrectly and also confirm if similar cohorts answer

‡ It should be noted that the post-test and hence the gain generally shows improvement [5].

§ This may not just be that the ‘misconceptions’ are the same but also possibly that the design of the inventory itself is also slightly flawed, e.g., see reference [16].

¶ For reasons of brevity we have not included Life sciences PHYL1A1, although similar correlations are found.

with the same “wrong-answer” type, see figure 1. Quite interestingly both cohorts answered the same set of questions incorrectly, see figure 1. In particular, questions 5, 11, 17, 26 and 30. As such, these two cohorts share similar ‘dominant misconceptions’.

We have also started looking at how possible correlations with given subjects in high school matriculation results can be used to predict how well a given student will perform. Although this work is in its preliminary stages, table 3 shows correlations between the different cohorts sitting first year classical mechanics at UJ; where a clear positive correlation can be seen for mathematics and physical sciences scores. || The subgroups for each cohort have been divided into English being spoken at home or another language spoken at home and in general we see a negative correlation for those whose main language is ‘other’. The FCI does have different language versions, see the discussion of the PhysPort system in reference [14], but no Afrikaans, isiZulu, isiXhosa, and many of the other languages spoken in South Africa are not available.\*\*

Although this is only a preliminary study, in relation to our recent work focusing on the 2020 cohort [1], we hope to combine our data from across all three years: 2020-2022 and then look at how high school matriculation performance data (as briefly discussed in section 4) correlates to student performance on the FCI and given the possible issues around the first languages of our participants, a translation of the FCI into all official languages of South Africa could be considered.

### Acknowledgements

EC and ASC are supported in part by the National Research Foundation of South Africa (NRF). AC is supported by the NRF and Department of Science and Innovation through the SA-CERN programme, as well as by a Campus France scholarship. WN is supported by a Faculty of Education and Arts Grant, ACU: Project Code No: 50-905300-111.

### References

- [1] Carleschi E, Chrysostomou A, Cornell A S and Naylor W 2022 *Eur. J. Phys.* **43** 035702.
- [2] Halloun I. A. and Hestenes D 1985 *Am. J. Phys.* **53** 1043.
- [3] Hestenes D, Wells M and Swackhamer G 1992 *Phys. Teach.* **30** 141.
- [4] Hestenes D 1998 *Am. J. Phys.* **66** 465.
- [5] Hake R 1998 *Am. J. Phys.* **66** 64.
- [6] Yasuda J, Mae N, Hull M M and Taniguchi M 2021 *J. Phys.: Conf. Ser.* 1929 012009.
- [7] Hammer D 1996 *Am. J. Phys.* **64** 1316.
- [8] Obaidat I M and Malkawi E 2008 *Int. J. Scholarship Teach. Learn.* **3** 19.
- [9] Bayraktar S 2009 *Int. J. Sci. Math. Educ.* **7** 273.
- [10] Martin-Blas T, Seidel L and Serrano-Fernandez A 2010 *Eur. J. Eng. Educ.* **35** 597.
- [11] Savinainen A and Viiri J 2008 *Int. J. Sci. Math. Educ.* **6** 719.
- [12] Bani-Salameh H N 2016 *Phys. Educ.* **5** 2014003.
- [13] Bani-Salameh H N 2016 *Phys. Educ.* **5** 2015006.
- [14] McKagan S B, Strubbe L E, Barbato L J, Mason B A, Madsen A M, and Sayre E C 2020 *The Physics Teacher*, **58** (7), 465-469.
- [15] Alinea A L and Naylor W 2015 *Phys. Educ.* **50** 210.
- [16] Yasuda J, Mae N, Hull M M, and Taniguchi M 2018 *Phys. Rev. Phys. Educ. Res.* **14**, 010112.
- [17] FEBE Annual Report, University of Johannesburg 2019 <https://www.uj.ac.za/wp-content/uploads/2022/03/febe-ar2020-final-report-final-to-meca.pdf> [Date of last access: July 19, 2022].

|| The smaller cohorts such as PHYG1A1 have smaller numbers making statistical inferences more difficult.

\*\* The physics department at UJ is in general comprised of students from various diverse cultural and linguistic backgrounds, see for example [17].

## Language in learning. Does teaching Physics in isiZulu aid students' understanding?

**D B Fish**

Director: Unizulu Science Centre, University of Zululand, KwaDlangezwa, South Africa

E-mail: [thefish@iafrica.com](mailto:thefish@iafrica.com)

**Abstract.** The language of learning has long been an important and controversial topic – especially in South Africa with 11 official languages but matric science available in only two of them. The author considered this issue in the refinement of a science show presented at Unizulu Science Centre. The show uses music and musical instruments to introduce students to topics around sound and waves. In a previous presentations at SAIP conference [1], the author has reported on an extensive study of this show (conducted towards a master's degree) which measured what students learned from the show and which revealed difficulties for students coming from rural schools when contrasted with those from urban and township schools. As an extension to this study (conducted towards a doctoral degree) the show was presented to the weaker rural group in isiZulu (their home language), while the survey instruments used were kept in English. The aim of this exercise was to establish whether home language instruction aided the students in understanding the concepts better. The science show was presented in isiZulu to a group of 40 Grade 9 students and multi-mode pre- and post-tests were used to assess students' understanding. Significant gains in student learning were measured, compared with that previously achieved by similar rural groups. While performed in the context of science shows in science centres, this study nevertheless has relevance to all educational interventions in physics. Whatever the challenges, it may be argued that mother-tongue instruction is preferable wherever possible for maximizing student understanding and engagement.

### 1. Review of Research into Language and Culture

Constructivism [2] stresses that learning is a different experience for each student and that they understand things with reference to their own life experiences and cultural backgrounds. South Africa is characterized by marked differences in the provision of resources and suitably qualified teachers. These factors contribute significantly towards comprehension. Furthermore, because science is taught primarily in English, second or third-language speakers are consequently disadvantaged. Student home environment also makes a big difference to how science is learned [3]. In light of the above, we need to consider the influence that culture, background and language have on learning in science.

Science achievement is a controversial issue across the globe as “science assessments often contain a high level of linguistically and culturally dependent content that can exacerbate the persistent gaps in science achievement and professions” [4]. Being raised in different language and cultural settings clearly gives students different points of origin for learning science. Solano-Flores and Nelson Barber [5] identified five areas in which culture affects a student's performance in science in addition to their life context and values. These include: the student's epistemology, their language ability, their cultural worldview, cultural communication and socialization styles.

Lee [3] asserts that students from different language and cultural backgrounds come to school with their own prior knowledge assimilated from their language, home, culture and community. This is often quite different to that of traditional “Western” science curricula, which can sometimes lead to a disconnection. As stated by Lee [3], “Recent efforts to provide culturally congruent science instruction indicate that when linguistic and cultural experiences are used as intellectual resources, students from diverse backgrounds are able to engage in scientific practices and show significant achievement gains.” The challenge for the student is to make the transition from their own prior knowledge to the new, possibly unexplored, world of science. These transitions have also been depicted as “border-crossings” [6] [7] and students’ achievement in science often depends on how well they can cross these borders. Phelan *et al.* [8] constructed a model to describe how students may move from one world to another, identifying at least four patterns of border crossings between different worlds, stressing that teachers should strive to make these crossings as painless and permanent as possible.

Finally, Dempster and Zuma [9] investigated reasoning used by isiZulu-speaking children in responding to science questions in English (from TIMSS studies), finding that these children relied heavily on translation into mother-tongue (in this case isiZulu) in order to tackle these questions. Thus, a study on the influence of language of instruction in science seemed to be pertinent for our context.

## 2. Methodology

This study is an extension of a more comprehensive study of student perceptions on sound and waves conducted (by the author) towards a Masters and then a Doctoral degree. *Originally*, three groups of 40 Grade 9 students were presented with a science show (“Good Vibrations, the science of sound!”) under controlled conditions. Students were drawn from three schools with differing socio-economic circumstances: urban, township and rural. A set of mixed mode probes was designed and implemented to test for gains in student understanding after the show. *Subsequently*, the show (and the probes) was modified in light of the first study with the view to improve learning gains. After obtaining some encouraging results showing improvements for the rural group based on the *subsequent* show (and probes), one final change was made to see if further improvement was possible for this group. In light of: language concerns which emerged from analysis of answers, the language issues affecting validation and the results of an English Language Test conducted, it was decided to test what effect the language in which the show was presented would have on students’ achievement. After much discussion and debate with (isiZulu-speaking) colleagues and my supervisors, I decided to have the *show* translated into isiZulu but to keep the *probes* in English, for the following reasons:

- 1) Matric final exams being written in English;
- 2) Non-existence of technical terms in isiZulu;
- 3) Coding by myself and supervisors can only be done in English;
- 4) Controlling of issues if altering the language of both the intervention (the show) and the instrument (the survey) at the same time;
- 5) Making a comparison with previous studies (conducted in English) possible.
- 6) Making a comparison with overseas studies possible.
- 7) Zuma and Dempster’s [10] demonstration that achievement amongst isiZulu-speaking children was not significantly improved if the probe items were translated into isiZulu (even though students revealed a positive attitude towards tests in isiZulu).

Issues of the language of instruction and testing are naturally very contentious and merit much more attention than this study will allow.

The science show and slides were translated by one of our student interns and checked by three other isiZulu speaking science teachers. The process was complex and served to underline the numerous difficulties involved in translating science in South Africa. Apart from alterations to the words on the slides, the whole show was presented in isiZulu, but the pre- and post-tests presented and

written in English (although instructions for these were given in isiZulu). This testing was done 4 months after the *subsequent* tests, with a group of 42 different Grade 9 pupils from the same rural school as used previously. The show was presented in isiZulu, but otherwise conditions and day-programme were identical.

### 3. Results

The first rather unexpected result which emerged was the increase in confidence for the later rural group instructed in *isiZulu* (compared with the *original* rural group, instructed in English). An increased confidence to attempt drawings was shown in the vastly reduced number of drawings left blank. Figure 1 below compares number of drawings left blank for the *original* rural group (English instruction), and later group (*isiZulu* instruction):

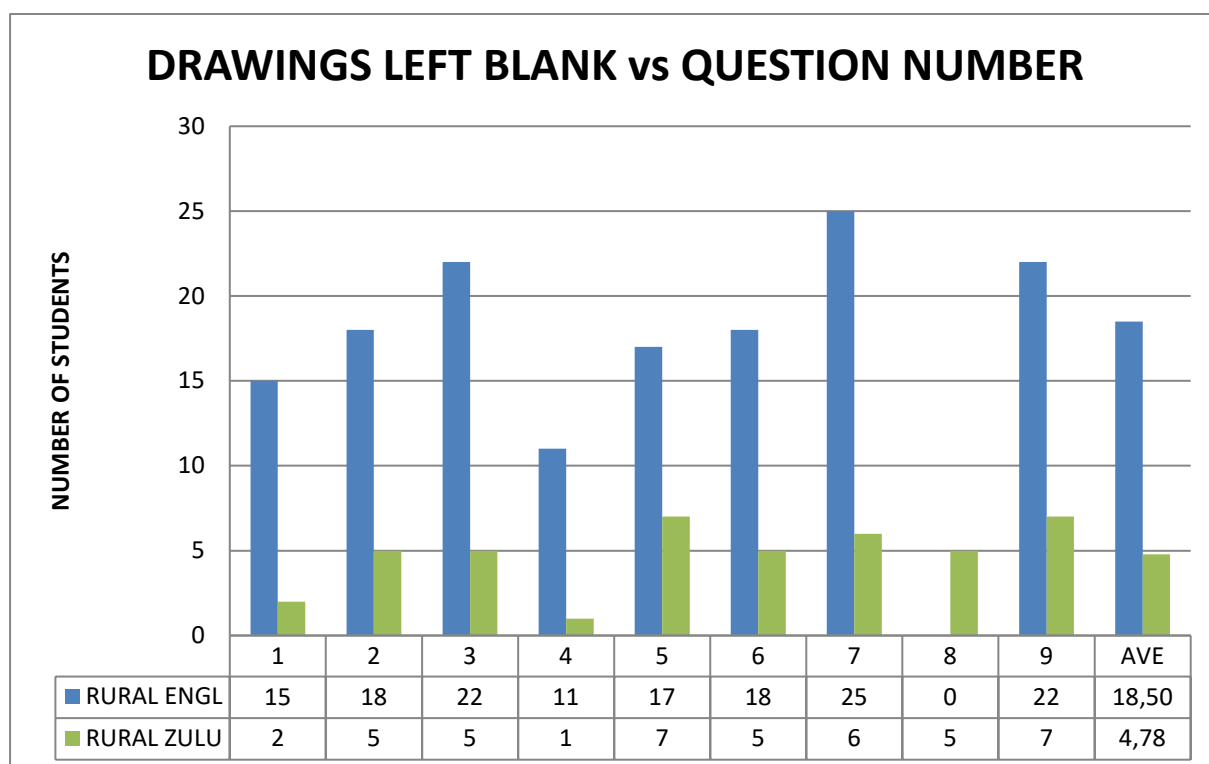


**Figure 1.** Number of drawings left blank by the two rural groups for each question (1 – 9).

The drawings themselves were very similar to those of the original rural group, and the written answers again were almost unusable because of the very weak English language ability of the students. Nevertheless, it was pleasing to see the greater confidence to at least attempt the drawings. This is clear from the greatly reduced number of answers which were left blank.

The difference in results for this later *isiZulu* group was most marked in the multiple-choice post-test. Figure 2 below compares pre-test and post-test percentages, as well as differences (improvement: post minus pre) for the groups in the *original* study (Urban, Township and Rural, conducted in the English language), with the later rural group (with *isiZulu* instruction).

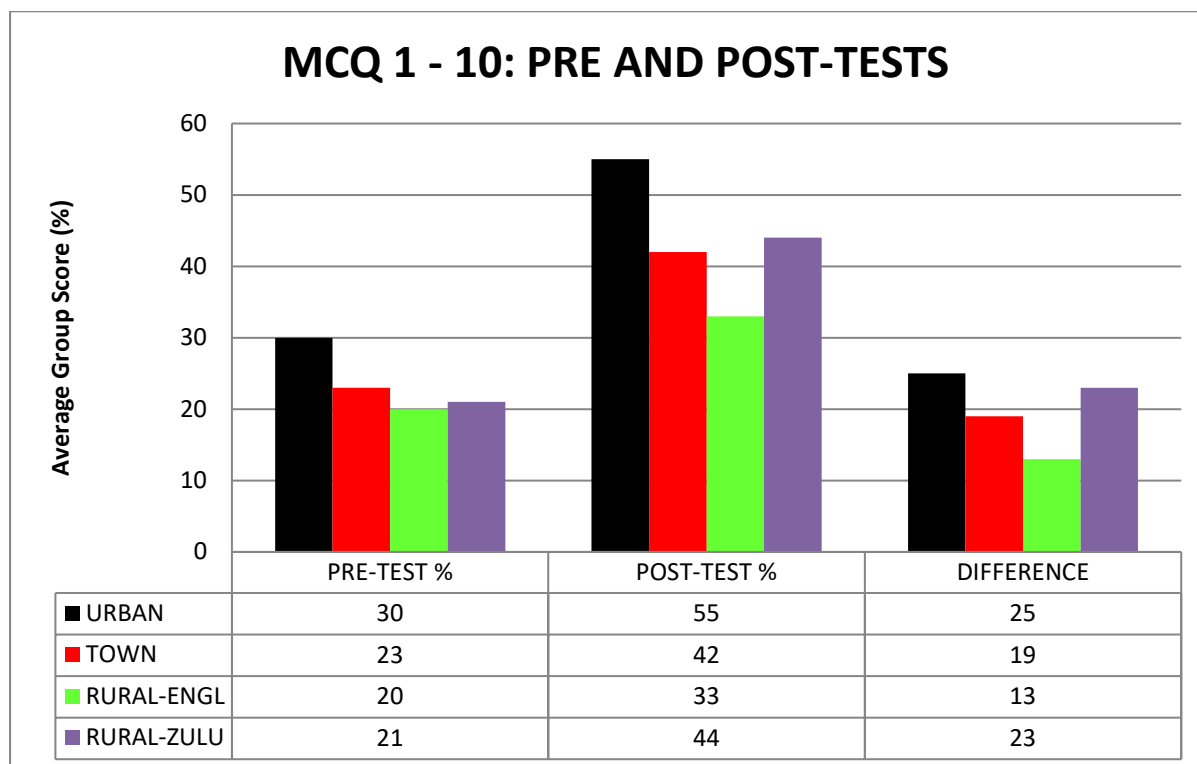


**Figure 2.** Graphs of MCQ's average group scores for four groups.

The difference which home language instruction made to the Rural (isiZulu) group can be clearly seen. Their pre-test mark is almost identical to that of the previous Rural (English) group (21 and 20 %), but their post-test mark (44 %) and difference (23 %) is much better, and even better than the township group. Table 1 below indicates that their t-test value comparing pre- to post-test scores was even lower than before, confirming the hypothesis that this pre- to post-test improvement was not by chance. The standard deviations of pre- and post-test scores were very similar to the rural ones indicating an increase in mean score, rather than just a greater spread. Even the average discrimination index for all 10 questions was improved.

**Table 1.** Statistics for rural and isiZulu pre- and post-tests (MCQ).

	AVERAGE %	STANDARD DEVIATION %	T-TEST SCORE	AVERAGE DISCRIM. INDEX
RURAL (ENGL) PRE-TEST	20.0	13.8	2.4 E-5	0.51
RURAL (ENGL) POST-TEST	33.1	17.3		
RURAL (ZULU) PRE-TEST	21.4	13.2	2.1 E-9	0.57
RURAL (ZULU) POST-TEST	44.5	18.5		

What was of concern in the *original* Rural (English) group was that almost a quarter of students actually got worse results in the post test than in the pre-test, indicating that they had little grasp of the questions. Figure 3 below shows that there was a significant improvement for the Rural (isiZulu) group, supporting the fact that the show is now more understandable.

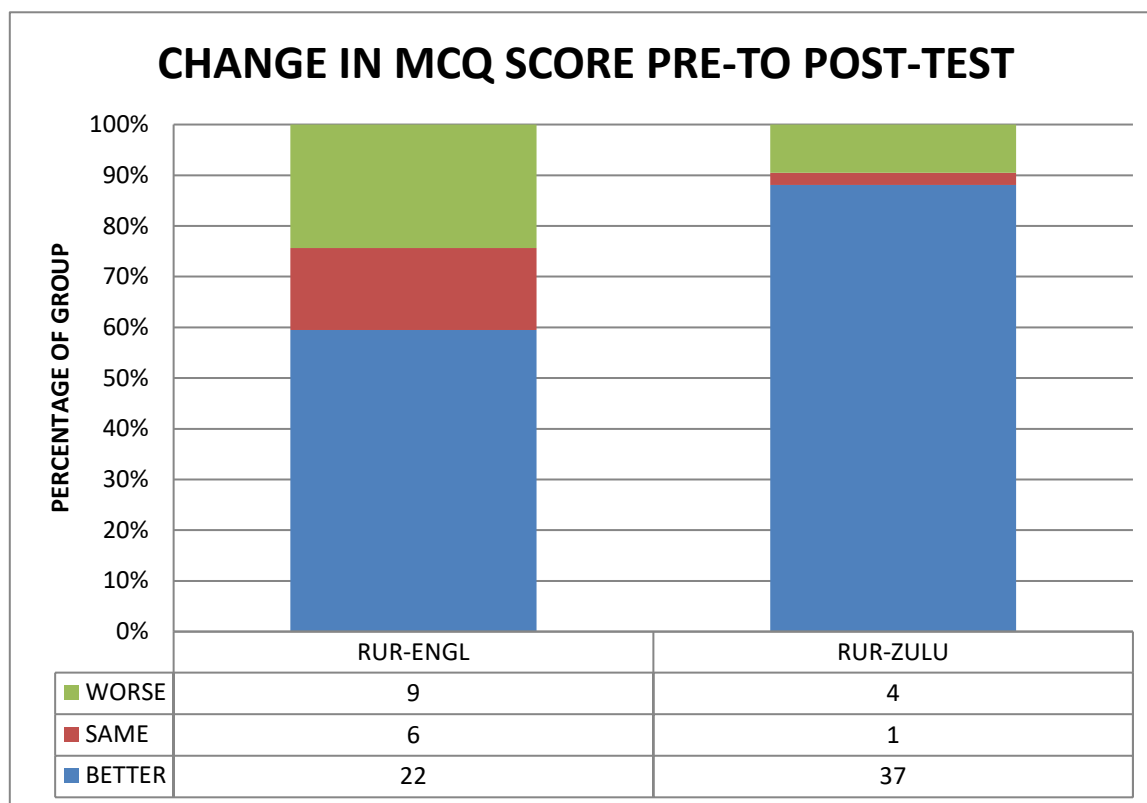


**Figure 3.** Graph of change in MCQ scores pre- to post-test for the two rural groups.

#### 4. Conclusion

The follow up study test done with the presentation in isiZulu revealed marked improvements as shown especially in the MCQ where this group (instructed in isiZulu) actually overtook the township group and more than doubled their class average pre- to post-test, despite the test being in English, and their general English language ability being weak. Furthermore they showed that many incorrect prior conceptions were effectively dealt with, including the understanding of English terminology like volume and pitch. This was less evident in their Open Ended Survey results, where they were still hampered in writing verbal explanations by their very weak English language ability. Despite this, their confidence to attempt the drawings was significantly improved.

It is evident that the greatest improvement for the weakest group (rural) in terms of overall score increase (pre- to post-test MCQ), and confidence in attempting drawings, is achieved by presenting the show in their home-language of isiZulu. While this is a very limited study (in terms of scope, subject matter, grades, sample size, iterations etc) these results suggest that further work on home language instruction in other areas would be valuable. With 11 official languages in South Africa and the final matric exam available in just two of these, the issue of language is both pertinent and contentious. Having seen learning gains with home language instruction in this study, further studies on the influence of language of assessment (questions) and response (student answers) is needed. Such studies should also consider the desires of the students themselves and investigate to what extent proficiency in matric science, or preparation for global citizenry, is more important to them.

## References

- [1] Fish, Anderson, Aalih and Pelaez (2021), "Classification of sound conceptions.", in *The Proceedings of SAIP2019, the 65th Annual Conference of the South African Institute of Physics*, edited by Prof. Aletta Prinsloo, (UJ). ISBN: 978-0-620-97693-0
- [2] Driver, R. (1989). "Students' conceptions and the learning of science." *International Journal of Science Education* **11**: 481-490
- [3] Lee, O. (2003). "Equity for Linguistically and Culturally Diverse Students in Science Education: A Research Agenda." *Teachers College Record* **105**(3): 465-489.
- [4] Penfield, R.D., Lee, O. (2009) "Test-Based Accountability: Potential Benefits and Pitfalls of Science Assessment With Student Diversity." *Journal Of Research In Science Teaching*. **47** (1), 6–24 (2010)
- [5] Solano-Flores, G., and Nelson-Barber, S. (2001). "On the cultural validity of science assessments." *Journal of Research in Science Teaching*, **38**, 553–573.
- [6] Giroux, H. (1992). "Border crossings: Cultural workers and the politics of education." New York: Routledge.
- [7] Aikenhead, G. S., and Jegede, O. J. (1999). "Cross-cultural science education: A cognitive explanation of a cultural phenomenon." *Journal of Research in Science Teaching*, **36**(3), 269-287.
- [8] Phelan, P., Davidson, A., and Cao, H. (1991). "Students' multiple worlds: Negotiating the boundaries of family, peer, and school cultures." *Anthropology and Education Quarterly*, **22**, 224-250.
- [9] Dempster, E., & Zuma, S. (2010). "Reasoning used by isiZulu-speaking children when answering science questions in English." *Journal of Education*, **50**, 35-59.
- [10] Zuma, S.C. and Dempster, E.R. (2008). "isiZulu as a language of assessment in science." *African Journal of Research in Mathematics, Science and Technology Education*, **12**, 31–46.

# The impact of simulation experiments on the understanding of the concepts of acceleration and energy

**OO Ewuola<sup>1</sup>, CJ Sheppard<sup>2</sup> and ARE Prinsloo<sup>2</sup>**

<sup>1</sup> Department of Physics, University of Johannesburg, P.O Box 524 Auckland Park, Johannesburg, Gauteng, South Africa

<sup>2</sup> Cr Research Group, Department of Physics, University of Johannesburg, P.O Box 524 Auckland Park, Johannesburg, Gauteng, South Africa

E-mail: [oewuola@uj.ac.za](mailto:oewuola@uj.ac.za), [cjsheppard@uj.ac.za](mailto:cjsheppard@uj.ac.za), [alettap@uj.ac.za](mailto:alettap@uj.ac.za)

**Abstract.** Despite how easy teaching acceleration and energy might seem to academics at first glance, studies have shown that not only are there difficulties in teaching these concepts, but students also struggle in learning them sometimes. While the expert easily perceives a concept mathematically, conceptual understanding in nature may become complex for the lay-man. As a result, misunderstanding of such concepts is observed in learners understanding of these concepts at various levels. Studies have however shown computer simulations to improve the understanding and perceptions of physics concepts for students. Therefore, the present study investigates the use of computer simulations on the understanding as well as learning of acceleration and energy concepts under first year science and engineering students. The students already completed the theoretical work on acceleration, potential and kinetic energy, the work-energy theorem and the effect of friction on the energy of the system. A short online BlackBoard based pre-test, an online computer based Simulation and a BlackBoard based post-test were administered to evaluate the impact of the simulation experiment on the understanding of the students. The Blackboard based pre-test and post-test consisted of basic multiple choice and short questions related to acceleration, various forms of energy, energy conversion and the impact of friction on a system. The simulation experiment was based on an existing PhET Interactive Simulation that offered the opportunity to engage with a simulated controlled reality, as well as investigate concepts related to acceleration and energy. The experimental procedure and answer sheet was hosted on Leybold Didactic's Leydocs platform. A practical report based on the results of the simulation as well as graphs plotted using the data from the simulation were uploaded by the students at the end of the simulation. Detailed analyses of the student answers and the statistics for the various groups will be addressed. Results show that both science and engineering students gained a greater understanding of the concepts after completion of the computer simulation and accompanied report in an era of the Fourth Industrial Revolution (4IR).

## 1. Introduction

Traditional methods of teaching involved students gathering in classrooms for lecture sessions with faculty where physical concepts are taught to students. Tutorial sessions and hands-on practical sessions are then used to reinforce the concepts that have been taught in the lecture classes. Some physical concepts like acceleration and energy have however proved to be difficult to teach not only due to some

of the complexities in the understanding and expressions of such concepts but also due to the expertise of the individual trying to teach such concepts [1,2] and the background knowledge of the student.

Previous studies have suggested that computer simulations could be great tools to aid the understanding of students in certain taught concepts [3–5]. Despite this, face-to-face teaching was usually the preferred mode of instruction for most aspect of teaching. The arrival of COVID-19 however changed the landscape of education and educational instructions all over the world as the realities of faculties and students not being able to gather together in the same room hit educators and students alike in 2020. It soon became clear that something had to be done quickly to ameliorate the sudden disruption to the educational calendar. While it was easy to record and share videos where concepts are taught to students, the challenge swiftly became how practical sessions would be held, especially for modules like Physics that has practical components.

The initial response was to share data from previous practical sessions with students so that they could write reports based on the data given to them. It however soon became evident that providing data to students to use in writing practical reports was not sufficient enough in training the students especially on concepts that required practical understanding. It then became important to find a model that would work best to help the students in understanding physical concepts and also help train the students in other important skills like gathering data, interpreting them, correctly analyzing them and presenting the reports of the analyzed data.

Computer simulation was chosen as the medium to present practical sessions with the students. Computer simulations were expected to help the students to have better interactions with the concepts that had been taught in class. Even though some studies have reported that computer simulations based learning helped improve the self-efficacy of some students [6], it was important to evaluate the impact of simulation experiments on the understanding of the students that were partaking in the simulation experiments.

Previous investigations have emphasized that there are many difficulties not only in the teaching of acceleration [7,8] and energy [1,9,10], but also in the students learning thereof. As in many other instances, the perceptions regarding these concepts again illustrates that what an expert considers as straightforward mathematical concepts can become rather complex phenomena once it needs conceptual understanding within physical environments [1]. This frequently leads to misunderstanding regarding these concepts amongst learners at various levels. Previous studies suggest that computer simulations can improve the understanding of physics concepts [11]. This current study therefore evaluated the understanding of the students on the concepts of acceleration and energy before and after one of the online simulation experiments.

## 2. Method

After completing the theoretical classes on acceleration, potential and kinetic energy, the work energy theorem and the effect of friction on the energy of the system, a group of first year science and engineering physics students were informed of the tasks for the practical session for the week a day before the practical session. The students are normally informed of the topic for the simulation for the next practical session so that they can prepare ahead for the practical session. However, to evaluate the effect of the simulation on the knowledge of the students, they were not informed on the topic for the simulation for the particular practical session.

A pre-evaluation test comprising of 14 conceptual basic multiple choice and short answer questions related to acceleration, various forms of energy, energy conversion and the impact of friction was administered to the students on the Blackboard testing platform. These are questions with varying levels of difficulty that were designed based on the some of the situations that the students would encounter in the computer based experimental simulation. The test was timed and designed to display only one question at a time without the option to go back to a previously completed question. Students were informed that they would have another opportunity to do another test after the simulation and that the better of the two Blackboard tests would be used in determining their performances.

After the pre-evaluation test, the students were given access to the computer simulation experiment which was prepared based on the PhET Energy Skate Park simulation [12]. An experimental set-up and answer sheet was designed detailing the steps students were to take in carrying out the experiment. The experiment was hosted on Leybold Didactic's Leydocs platform [13] and shared with the students. The Leybold Didactic's Leydocs platform gives the students the opportunity to follow instructions in order to proceed with the embedded PhET simulations, complete tables and fill in answers to the questions as they proceed – finally compiling a report in portable document format (PDF) to be uploaded.

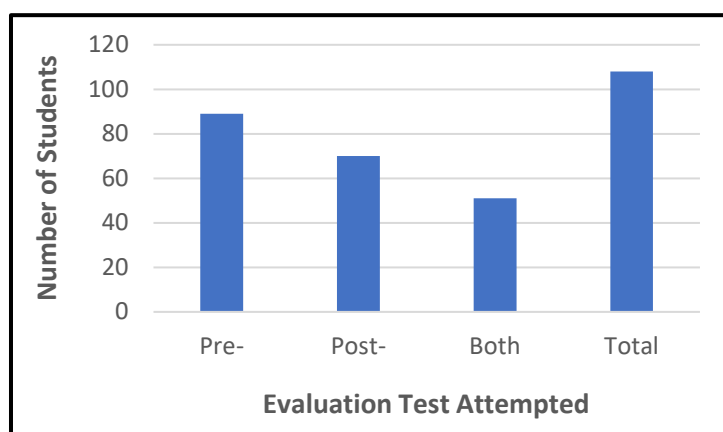
Students gathered data from the PhET simulation, completed the tables, answered the experimental questions, plotted graphs, interpreted the data and drew conclusions based on the results obtained from the simulation experiment and data obtained. The final experimental report as well as the prepared graphs were uploaded on the Blackboard platform to be graded.

A post-evaluation test comprising the same fourteen conceptual basic multiple choice and short answer questions that were tested in the pre-evaluation test was administered to the students 30 minutes after the computer simulation experiment was concluded. The post-evaluation test was designed with the same settings as the pre-evaluation test. Both the pre- and post-evaluation tests were then graded and the performances analyzed.

The data from the Blackboard based pre-and post-evaluation tests were analyzed with RStudio Version 1.1.453 (© 2009-2018 RStudio, Inc) to evaluate the performances of the students in the tests. In grading the Blackboard based evaluation tests, a student who got a question correctly is awarded the full marks for such question. Students who did not get a question correctly but gave answers that indicated that such student had an idea of the way the question should be answered were awarded partial marks. This included questions with more than one part that were graded as a single question. Questions that were not attempted by the students were recorded as “unanswered”.

### 3. Results

A total of 108 students comprising of 77 engineering and 31 science students attempted at least one of the Blackboard based evaluation tests. 89 students (58 engineering and 31 science) attempted the pre-evaluation test, 70 students (53 engineering and 17 science) attempted the post-evaluation test while 51 students (34 engineering and 17 science) attempted both the pre- and post-evaluation tests. Figure 1 shows the distribution of students who attempted the tests. An overview of the attempts for the evaluation tests is presented in Table 1.

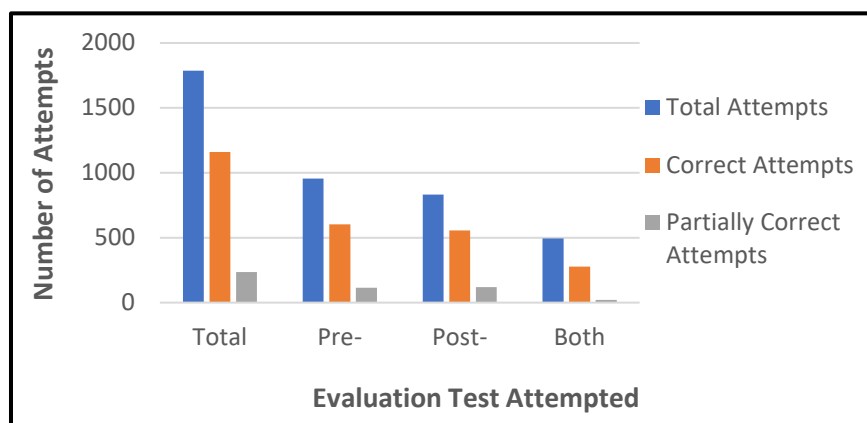


**Figure 1.** Student attempts for the evaluation tests.

**Table 1.** An overview of attempts for the pre- and post-evaluation tests.

	All Students	Engineering Students	Science Students
Students that attempted at least one evaluation test	108	77	31
Students that attempted pre-evaluation test	89	58	31
Students that attempted post-evaluation test	70	53	17
Students that attempted both evaluation tests	51	34	17
Total number of questions attempted	1787	1305	482
Number of questions attempted in pre-evaluation test	955	679	276
Number of questions attempted in post-evaluation test	832	626	206
Number of questions attempted in both evaluation tests	494	356	138
Number of questions correctly answered overall	1159	872	287
Number of questions correctly answered in pre-evaluation test	603	444	159
Number of questions correctly answered in post-evaluation test	556	428	128
Number of questions correctly answered in both evaluation tests	278	210	68

A total of 2226 questions were made available to the students altogether in both tests while 1787 questions were attempted by the students. 955 questions were attempted in the pre-evaluation test while 832 were attempted in the post-evaluation test. Of the 1787 questions attempted, 603 and 556 were correctly answered in the pre- and post-evaluation tests respectively while 115 and 120 were partially correctly answered in the pre- and post-evaluation tests respectively as shown in Figure 2.

**Figure 2.** Overview of student performances in the evaluation tests.

The highest possible score for the test was 25. The test score frequency pattern had a Gaussian distribution with an overall total mean score for both evaluation tests of  $14.82 \pm 5.74$  (15.58 for engineering and 13.06 for science students). The mean scores for the pre- and post-evaluation tests (without considerations for whether students did both pre- and post-evaluation tests) were  $13.12 \pm 5.02$  and  $16.97 \pm 5.91$  respectively. The mean score for the post-evaluation tests was significantly higher than

the mean score pre-test ( $t^1 = -4.3495$ ;  $df^2 = 135.43$ ;  $p\text{-value}^3 < 0.001$ ). Of the 51 students that did both the pre- and post-evaluation tests, the mean scores for the tests were  $13.82 \pm 4.78$  and  $17.41 \pm 6.16$ , respectively. The mean score for the post-evaluation tests for this group was significantly higher than the mean score pre-test ( $t = -3.2843$ ;  $df = 94.234$ ;  $p\text{-value} = 0.001$ ). Majority of the students (75%) had higher marks in the post-evaluation test compared with the pre-evaluation as shown in Figure 3.

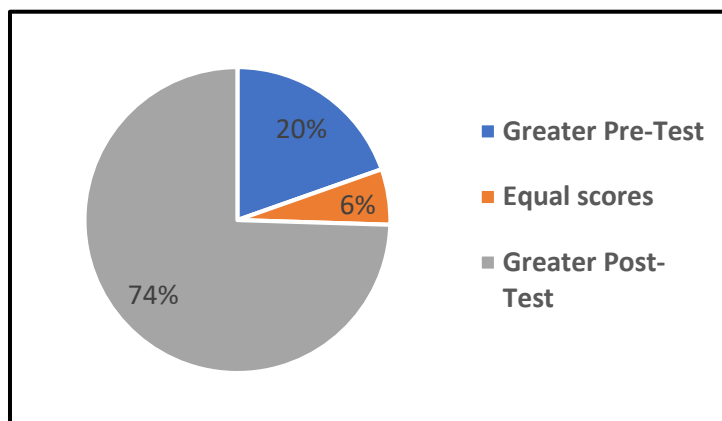


**Figure 3.** Comparison between Pre- and Post-evaluation test scores per student.

#### 4. Discussion

With about half (47%) of the study population attempting both the pre- and post-evaluation tests, the results from the study is representative of both the engineering and science students that registered for the module. With the students attempting 80% of the entire questions made available to them, the authors conclude that the spread of the attempts of the students was very good. Time could have been a factor for the inability to attempt all the questions as the evaluation tests were both timed.

A mean score of 52% in the pre-evaluation test indicates that the average student already had some knowledge of the concepts being tested before going into the study. This is because the lecturers had already taught these concepts in class before the study was carried out. As a result, the lecturers are commended for the class lecturing sessions. The mean score for the post-evaluation test increased to 68% after the students completed the online simulation. This suggests that the online simulation further enhanced the understanding of the students on the concepts of acceleration and energy. These results are for all the students that took part in the study, irrespective of whether they did only one or both evaluation tests.

The results from the group that did both the pre- and post-evaluation test is even more interesting as this group allows us to compare the performances and knowledge of specific students before and after the simulation. The engineering students had some improvements in their scores (from 60% to 71%) while the science students had big improvements in their scores (from 46% to 67%). Despite the levels of improvements in the scores of both groups, the engineering students had a mean score that is higher than that of the science students. This is probably because different faculty members are responsible for each group of students. However, both groups had comparable post-evaluation test mean scores.

For the entire group that attempted both the pre- and post-evaluation tests, the pre-evaluation mean score of 55% significantly improved to 70% in the post-evaluation test after the students had gone through the simulation experiment. This improvement strongly suggests that the students benefitted well from the online simulation and had improved marks in the post-evaluation test as a result of their encounter with the simulation experiment. This is consistent with results from other studies that confirmed that computer simulations improved the understanding of students in physics [11,14,15]. This

<sup>1</sup> t – Student's t-test statistics

<sup>2</sup> df – Degree of Freedom in Students' t-Test

<sup>3</sup> p-value - Level of significance

is further confirmed by looking at the individual performances of students since majority of the students had much improved scores in the post-evaluation test, compared with the pre-evaluation tests.

## 5. Conclusion

The current study concludes that the use of computer simulation experiments significantly enhanced the understanding, as well as learning, of acceleration and energy concepts under first year science and engineering students. The results from the group of students that completed both the pre- and post-evaluation tests showed an increase of 15% in the mean score after completion of the simulation experiment. This substantial increase in the mean score leads to the conclusion that using computer simulations along with traditional teaching and practical methods will further enhance the learning of concepts related to acceleration and energy for first year science and engineering students. In line with other previous studies, we conclude that the use of computer simulation in experiments is beneficial to the understanding and learning experience of students.

## 6. Funding

No external funding was required for this study.

## Acknowledgements

The authors thank the University of Colorado for providing the PhET simulations that were used for the simulation experimental sessions as open source simulations. We also appreciate Drs Ogunsanya, Baruwa and Abima for marking the scripts of the pre- and post-evaluation tests.

## References

- [1] Kruger C 1990 Some primary teachers' ideas about energy *Phys Educ* [Internet]. [cited 2022 Aug 27];**25** 2:86. Available from: <https://iopscience.iop.org/article/10.1088/0031-9120/25/2/002>
- [2] Pendrill AM 2019 Understanding acceleration: An interplay between different mathematics and physics representations *J Phys Conf Ser.* **1286** 1.
- [3] Wieman CE, Adams WK, Loeblein P, and Perkins KK 2010 Teaching Physics Using PhET Simulations *Phys Teach* [Internet]. [cited 2022 Aug 27];**48** 4:225–7. Available from: [https://www.researchgate.net/publication/238560172\\_Teaching\\_Physics\\_Using\\_PhET\\_Simulations](https://www.researchgate.net/publication/238560172_Teaching_Physics_Using_PhET_Simulations)
- [4] Finkelstein ND, Perkins KK, Adams W, Kohl P, and Podolefsky N 2005 Can computer simulations replace real equipment in undergraduate laboratories? *AIP Conf Proc* [Internet]. [cited 2022 Aug 27];**790**:101–4. Available from: [https://www.researchgate.net/publication/253189513\\_Can\\_Computer\\_Simulations\\_Replace\\_Real\\_Equipment\\_in\\_Undergraduate\\_Laboratories](https://www.researchgate.net/publication/253189513_Can_Computer_Simulations_Replace_Real_Equipment_in_Undergraduate_Laboratories)
- [5] Prima EC, Putri AR, and Rustaman N 2018 Learning solar system using PhET simulation to improve students' understanding and motivation *J Sci Learn* [Internet]. [cited 2022 Aug 27];**1** 2:60. Available from: [https://www.researchgate.net/publication/324122357\\_Learning\\_solar\\_system\\_using\\_PhET\\_simulation\\_to\\_improve\\_students'\\_understanding\\_and\\_motivation](https://www.researchgate.net/publication/324122357_Learning_solar_system_using_PhET_simulation_to_improve_students'_understanding_and_motivation)
- [6] Trongtirakul T, Pusorn K, and Peerawanichkul U 2022 Computer Simulation-Based Learning: Student Self-Efficacy During COVID-19 Outbreak In: 2022 International STEM Education Conference (iSTEM-Ed 2022), July 6-8, 2022, Sukhothai, Thailand. Sukhothai, Thailand
- [7] Liu G and Fang N 2016 Student Misconceptions about Force and Acceleration in Physics and Engineering Mechanics Education [Internet] *International Journal of Engineering Education*. Available from: <https://www.researchgate.net/publication/295010239>
- [8] Taşar MF 2010 What part of the concept of acceleration is difficult to understand: The mathematics, the physics, or both? *ZDM - Int J Math Educ* [Internet]. [cited 2022 Aug 27];**42** 5:469–82. Available from: [https://www.researchgate.net/publication/225823875\\_What\\_part\\_of\\_the\\_concept\\_of\\_acceleration\\_is\\_difficult\\_to\\_understand\\_The\\_mathematics\\_the\\_physics\\_or\\_both](https://www.researchgate.net/publication/225823875_What_part_of_the_concept_of_acceleration_is_difficult_to_understand_The_mathematics_the_physics_or_both)
- [9] Saglam-Arslan A, Altan Kurnaz Kastamonu Üniversitesi M, and Altan Kurnaz M 2011 Students' conceptual understanding of energy: Do the learning difficulties in energy concept discovered in

- the 1990s persist still? [Internet] Vol. 3, Energy Education Science and Technology Part B: Social and Educational Studies. Available from: <https://www.researchgate.net/publication/297687666>
- [10] Sefton IM 2004 Understanding Energy In: Proceedings of 11th Biennial Science Teachers' Workshop. The University of Sydney;
- [11] Sarabando C, Cravino JP, and Soares AA 2014 Contribution of a Computer Simulation to Students' Learning of the Physics Concepts of Weight and Mass *Procedia Technol.* **13**:112–21.
- [12] Energy Skate Park - Conservation of Energy | Kinetic Energy | Potential Energy - PhET Interactive Simulations [Internet] [cited 2022 Aug 27]. Available from: <https://phet.colorado.edu/en/simulations/energy-skate-park>
- [13] LeyLab [Internet] [cited 2022 Aug 27]. Available from: <https://leylab.de/>
- [14] Kabigting LDC 2021 Computer Simulation on Teaching and Learning of Selected Topics in Physics *Eur J Interact Multimed Educ.* **2** 2:e02108.
- [15] Ouahi M Ben, Hou MA, Bliya A, Hassouni T, Mehdi E, and Ibrahmi A 2021 The Effect of Using Computer Simulation on Students' Performance in Teaching and Learning Physics: Are There Any Gender and Area Gaps? [cited 2022 Nov 12]; Available from: <https://doi.org/10.1155/2021/6646017>

# Students' understanding of physical components of electrical circuits

M.N. Khwanda<sup>1</sup>; P. Molefe<sup>1</sup> and B.M. Sondezi<sup>1</sup>

<sup>1</sup>Physics Department, University of Johannesburg, Auckland Park 2006, South Africa.

E-mail: [mkhwanda@uj.ac.za](mailto:mkhwanda@uj.ac.za)

**Abstract.** In many cases, the teaching of electricity starts from the basic use of ohms law and its mathematical interpretations. Less is done in terms of defining and explaining qualitatively the role of the electric circuit elements like a resistor, a conductor, a switch and lastly a battery. Since the learning of electricity is predominantly conceptual, it is perceived as difficult because it cannot be physically touched or seen, and those physical components are less dealt with qualitatively. The physical components are used during representations to explain the conceptual interactions of what takes place in each component in terms of current, resistance and potential difference. This research is aimed at determining how students define and explain the role of some basic electric circuit elements, that is, resistors, conductors, batteries and a switch. In addition, this work aims to determine how the knowledge of these physical components can enhance the understanding of electricity.

## 1. Introduction and theoretical background

In many cases, teaching electricity begins with the basic application of Ohm's law and its mathematical interpretation. Less effort is done to define and qualitatively explain the role of the electrical circuit elements such as resistor, conductor, switch and finally battery. Since learning electricity is predominantly conceptual, it is found to be difficult in that it cannot be physically touched or seen, and these physical components are treated in a less qualitative manner. Students' understanding of electricity is usually poor and dominated by misunderstandings [1]. To bridge the gap, a suggestion was made to review teaching strategies. Furthermore, literature advised physics teachers in secondary or high school to take a concrete action by involving the students to empirical learning experience [2].

The grand challenge identified in science education is to improve students' conceptual development of scientific concepts [3], while at the same time, the ongoing agenda is to help students to obtain high quality learning [4]. To improve students' conceptual development of scientific concepts, this research adopted the back to basic approach consisting of two parts, namely: identifying students' knowledge of physical components and their roles in electric circuit, which function as a system and is usually overlooked [5]. These physical components were a battery, a bulb, a conductor, and a switch. The second part focussed on how students use the knowledge of the physical components to answer questions dealing with electric circuit. Literature grounded by constructivism recommended the teachers' awareness of students' prior knowledge and possible misunderstandings [1] as a key in planning for designing classroom activities to enhance conceptual development.

Guided by the phenomenographically approach on classifying students' understanding, this research aims to present how students define and explain the role of some basic electrical circuit elements, i.e., resistors, conductors, batteries, and a switch. In addition, this work aims to determine whether the knowledge of these physical components has an impact on students' understanding of electricity.

## 2. Research Design and procedures

The research was a qualitative pre-post instruction design in which interventions were conducted using a whole class discussion of the physical components of electrical circuits: battery, conductor, resistor, and the switch, followed by an introduction of the field model as a strategy of explaining the dynamics of electrical circuits. A pre-post instruction study measures the occurrence of an outcome before and after a particular intervention is implemented [6]. The field model explains the movement of charges in a circuit under the influence of electric field created when charges are separated in a battery. Students' knowledge and understanding were assessed by phenomenography both before and after the intervention. The phenomenographic method was regarded as a useful tool for evaluating students' comprehension of scientific ideas and locating the root causes of misunderstandings. One of the advantages of phenomenography method is that the phenomenographic data not only provide rich and contextual descriptions of students' understanding but are also capable of holistic understanding to unpack into different patterns of consciousness and non-consciousness of components [4]. Follow-up treatment took place after eight weeks.

### 2.1 Participants and instruments used for data collection.

The participants were Bachelor of Education (B.Ed) second year preservice students (44 wrote pre-intervention: 42 post-intervention) who were deliberately chosen considering that they had learnt the subject in high school and the subject was about to be repeated at the tertiary level. Being guided by phenomenography, pre-instructional data were collected using a semi-structured, open-ended questionnaire [4] with an additional confidence question. The semi-structured questionnaire was chosen because of its convenient deployment and allows a wider range of experiences with a phenomenon to be captured. Post-test instrument had no confidence questions. The questions were divided into two parts, namely:

*Part 1: Pre-instruction questions targeting students' knowledge of the physical components and their roles as follows:*

*The diagram in figure 1 represents a longitudinal cross area of a torch with different parts labelled A to D.*

1.1 Name the parts labelled A to D and their roles in electric circuit.

1.2 How confident are you about the answers you gave in 1.1? Select from the following:

A: Very Confident with the name and the explanation of the role

B: Very Confident with the explanation but not sure about the role

C: Very confident with the role but not sure about the explanation of the role

D: I guess all

E: I don't have a clue

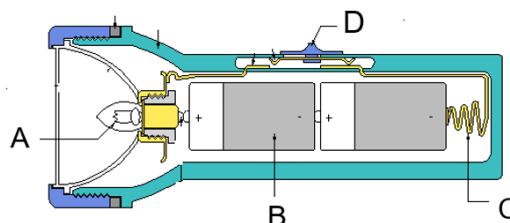


**Figure 1.** Longitudinal section of the torch taken from meritnation.com.

*Part 2: Post instruction questions to determine if the knowledge of the physical components and their roles impacts their conceptual understanding of electricity circuit dynamics.*

The post-intervention questions were aimed at understanding how students use their knowledge of physical components to answer conceptual understanding questions. Conceptual questions require students to understand how both physical and conceptual components work as a system to fulfil a specific role. Questions were the following:

2. Use the diagram in figure 2 to answer the following questions.

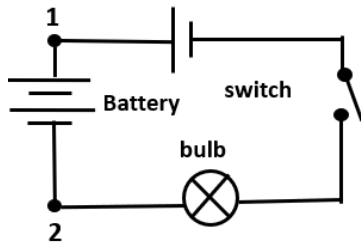


**Figure 2.** Electric circuit 1.

2.1 What causes the bulb to glow in figure 2 when the switch is on? Explain.

2.2 What will happen to the resistance of the bulb if another battery is added in series in figure 2?

2.3 Why bulbs in our lecture room glow almost at the same time when the switch is put on?

3. The diagram in figure 3 shows an electric circuit with three different light bulbs X, Y and Z. When the switch is on, bulbs X and Y were glowing, but bulb Z was not glowing. From the following options, select the reason why bulb Z is not glowing. Explain your choice.

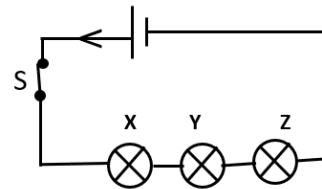


**Figure 3.** Electric circuit 2.

- A. the resistance of Z is too low
- B. the resistance for Z is too high
- C. the current is too weak by the time it reaches Z
- D. bulb Z is nearer the negative terminal

### 3. Data analysis

The main goal of the study is to identify several qualitatively distinct categories that represent variations in individual experience [4] of parts of an electrical circuit and their roles. The phases used in data analysis were as follows: identification, sorting, comparison, and categorisation [7]. Both questions from parts 1 and 2 were phenomeno-graphically analysed using data collected from after Google form. The first question was just to name the physical object (part) of the torch and the role of each. The answers to the role of each part were then sorted and categorized to explain the students' knowledge of the role of each component. Finally, the students' confidences were compared to their explanations of the role of each component.

### 4. Results and discussions

The presentation and discussion of the results were done in two parts. Part 1 focused on the result of students' knowledge of the physical components and their roles, while Part 2 focused on whether knowledge of the physical components has an impact on their conceptual understanding of basic electrical circuitry.

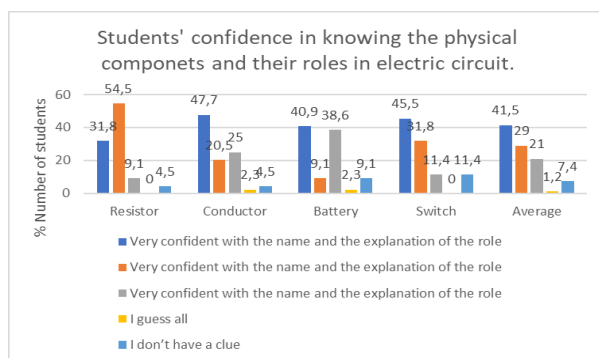


**Figure 4.** Students' confidence.

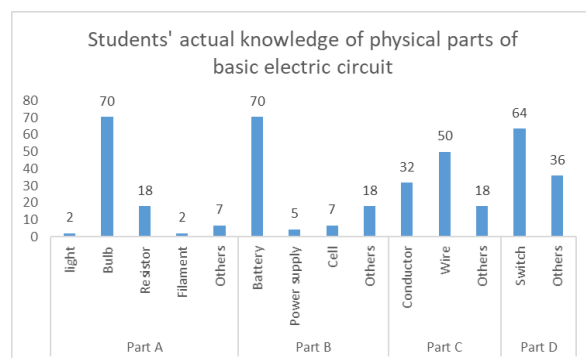


**Figure 5.** Students' knowledge of the physical components.

#### 4.1 Part 1: students' knowledge of the physical components *and* their roles.

Figure 4 shows that 31.8% of students are very confident with naming and explaining the role of resistor. While 54.5% of the students are very confident with the explanation, they are unsure about the role of the resistor. However, the average of student confidence across the components shows that student confidence levels are less than 50%. This result shows that many students still had misconceptions or were unaware of the physical components and their role in the circuit.

Figure 5 shows positive results from more than 50 % of the students in each part, correctly naming the physical parts of the circuit. There are still a handful of students who confuse the lightbulb and the resistor, affecting their confidence in naming and explaining the roles of the physical parts.

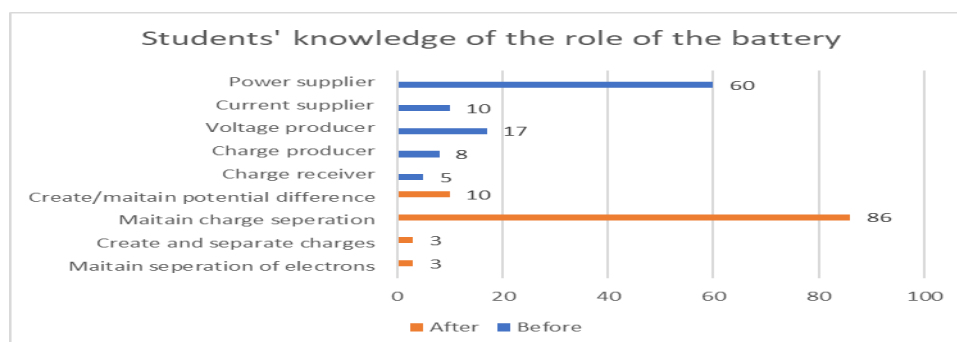


**Figure 6.** Students' knowledge of the role of the battery before and after intervention.

Figure 6 shows that after the intervention, students greatly improved their knowledge of the role of the battery. The most appropriate role of the battery, which helps explain circuit dynamics, is to maintain charge separation, since an electric field is created when charges are separated. This idea combines static electricity with electrodynamics, which saw the field model as a powerful tool to meet the great challenge in electricity [8].

#### 4.2 Part 2: The impact of students' knowledge of physical components on their conceptual understanding.

To determine if students' knowledge of the physical components affects how they answer qualitative questions about basic electrical circuits, the following results per question are presented.

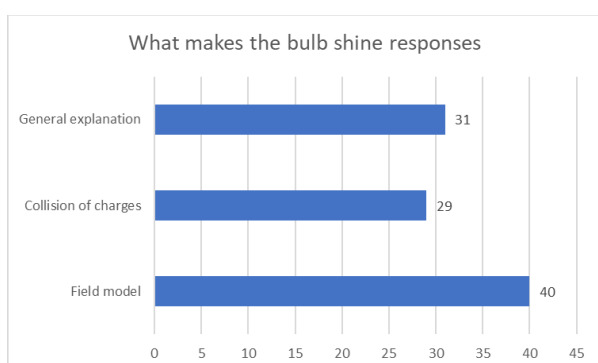


**Figure 7.** Question 2.1 responses.

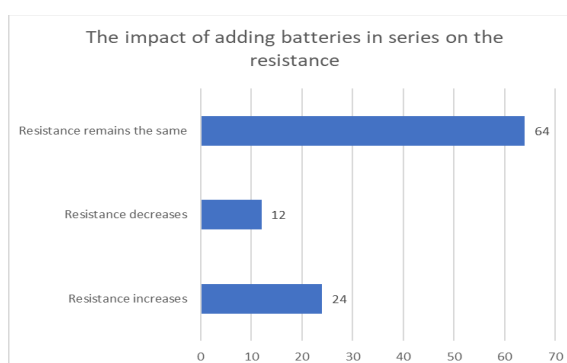


**Figure 8.** Question 2.2 responses.

#### Question 2.1: What causes the bulb to shine when connected to electric circuit?

Two questions related to the causes of the glow of the lightbulb in a circuit. The first question only referred to an incandescent bulb connected in series with the battery and switch. Students' answers to the question of what makes the light bulb glow or not glow are shown. Common explanations were those

that were not 100% scientifically based, for example: “*It is lit because the circuit is on*”. This type of explanation does not help assess understanding when presenting just one idea among many. Those who used collisions of charges correctly explained and showed their understanding of the difference between a conductor and a resistor. Some of the misconceptions identified: “*The bulb glows when electric current interacts with the resistance of the bulb*” and “*The resistor converts current to electricity.*”

One of the promising answers given by student, was based on the field model as follows: “When the switch is on, *electric field are established throughout the circuit at approximately the speed of light*, the electric fields are directed from positive terminal and negative terminals separated by the battery through the conductor and at this moment charges start to move *creating current and potential difference simultaneously*, the electric field are closer to each other in the resistor meaning *the electric field force is stronger*. According to Newton's second law of motion, the charges gain more acceleration causing them to move *faster colliding with each other and the particles of the filament*, due to this collision the average kinetic energy increases and according to collision theory the *temperature will also increase*, thus converting electrical energy to heat energy which is later dissipated as light.”

Knowing the role of each physical component helped students re-explain, including using mechanical concepts (Newton's second law) to show why the temperature increases and ultimately why the lightbulb glows. Another explanation by student: “As soon as the circuit is closed and *there's charge separation in the battery*, potential difference is established instantaneously then the charges will start to move. When the charges reach the bulb, there is a *filament in the bulb that acts as a resistor and since it is very thin* the rate at which the charges will move, and kinetic energy will also increase as *the electric field lines are close to one another and the increase in kinetic energy will lead to an increase in temperature* hence heat and light will be produced that's where the bulb shines.” The statements above prove that the students used the knowledge of the role of the battery and the resistor to explain why the bulb emit light, therefore this knowledge enabled them to explain how the light bulb in a circuit glow

*Question 2.2: The impact of adding the number of batteries in series on the resistance of the bulb.*

During the intervention, the roles of each physical component were discussed, for example, resistance was also discussed as a physical component with predefined resistance. The chart above (see figure 8) shows that most students 64% retained the role discussed in class. Some examples of explanations that show the improved understanding in terms of students' knowledge of the role of each physical component are as follows:

*Student 1:* The resistance of an electrical component of a circuit is fixed immediately after the component is manufactured at the store and it is never affected by anything happening in the circuit, thus it remains the same regardless of the times and seasons.

*Student 2:* The bulb is manufactured to have a specific resistance; hence it will not be affected by the emf the battery can supply.

The students' reasoning above shows that their understanding of the role of resistance allowed them to answer questions correctly without applying Ohm's law. However, some students retained their misconceptions and explained incorrectly using Ohm's law as their justification as follows:

*Student 3:* Resistance is directly proportional to the voltage. Increasing the number of cells increases the voltage and hence increases the resistance.

*Student 4:* If the total potential difference in the circuit increases it will reduce the resistance of the bulb when the switch is ON because when the switch is ON the current is produced due to the movement of the charges, since resistance is indirectly proportional to the current flowing in the circuit it will decrease when the current increases.

The two sample answers imply that some of the students do not understand Ohm's law correctly. Similar results where Ohm's law was misinterpreted was previously reported [10].

*Question 2.3: Bulbs in the lecture room shining almost at the same time.*

Figure 9 and figure 10 below show the results of question 2.3 and question 3 that will be discussed in the next sections.

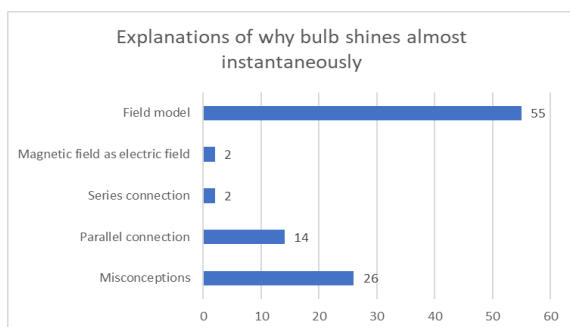


**Figure 9.** Question 2.3 responses.

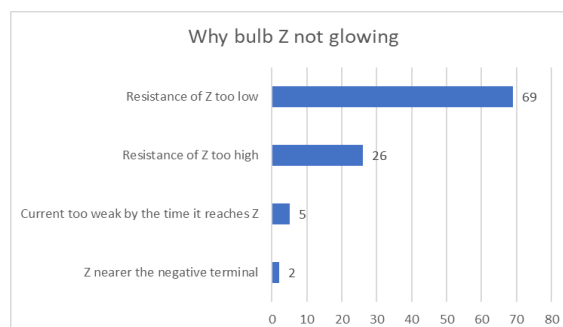


**Figure 10.** Question 3 responses.

In general, students think that charges travel at the speed of light, which is why light bulbs glow almost simultaneously. Most students explained using the field model (The battery maintains the separation of charges during the process, an electric field is built up throughout the circuit at almost the speed of light, that's why the charges start moving almost simultaneously: that's why the light bulbs shine at the same time) as reflected in figure 9. Once students understand the battery's role as that of maintaining charge separations, it becomes easier to explain using the field model. The common misconception has been that charges travel at the speed of light and that non-distinction between the magnetic field and electric field will be treated with the concept substitution strategy in the future [9]. The fact that most students (55%) explained using the field model is also a positive contribution towards teaching electricity using the field model as advocated by Stocklmayer [8].

*Question 3: Why bulb Z is not glowing?*

The results of question 3 shown in figure 10 revealed that 69 % students understood the impact of resistance on the brightness of the bulb in series circuit, however few misconceptions still exist which is consistent with that found by Aisahsari and Ermawati [2].

## 5. Conclusion

Many students do not know the names and roles of the physical parts of electrical circuits but are expected to know the conceptual elements. That explains why the understanding of electricity is difficult. In this research, phenomenography was helpful in showing how students understand the names and roles of parts in the basic electrical circuit, and misunderstandings were identified and presented to share with others. Based on the explanation given by most students when answering Part 2, the study claimed that knowledge of the physical components: battery, resistor, conductor, and switch can have a positive impact on students' understanding of basic DC circuits. However, further exploration is required to investigate other topics in an attempt to reach the goal of the science agenda [3] and to continuously tackle the great challenge [4] in science teaching and learning. The implication or recommendation is that teachers should first ensure that students know and understand the role of the physical parts of the circuit before introducing the concepts of current, resistance, and potential difference. This can be done using a phenomenographic approach, classifying students' experiences with the phenomenon.

## References

- [1] Turgut U, Gürbüz, F and Turgut, G 2011 An investigation 10th grade students' misconceptions about electric current. *Procedia-Social and Behavioral Sciences*. **15**, p. 1965–1971
- [2] Aisahsari R and Ermawati F 2020 Evaluating students' misconceptions and the causes on direct current concepts by means of four-tier multiple choice test. *J. Phys.: Conf. Ser* **1491** 012009
- [3] Osborne J, Henderson J, MacPherson A, Szu E and Wild A Y 2016 The development and validation of a learning progression for argumentation in science. *J. Res. Sci. Teach*, **53**, pp. 821-846.
- [4] Han F, and Ellis R 2019 Using Phenomenography to tackle key challenges in science education. *Frontiers in Psychology:Methods*. **10**, 1414, pp. 1-10
- [5] Rainson S, Tranströmer G and Viennot L 1994 Students' understanding of superposition of electric fields., " *Am. J. of Phy.* **62**, 6, pp. 1026-1032
- [6] These M 2014 Observational and interventional study design types; an overview," *Biochemia Medica* **24**, 2, pp. 199-10
- [7] Marton F, Carlsson M and Halasz L 1992 Differences in understanding and the use of reflective learning in reading. *Br. J. Educ. Psychol*, **62**, pp. 1-16
- [8] Stocklmayer S 2010 Teaching direct current theory using a field model. *International Journal of Science Education*, **32**, 13, pp. 1801-28
- [9] Grayson D 1994 Concept substitution: Instructional strategy for promoting conceptual change. *Research in Science Education*, **24**, pp. 102-111
- [10] Khwanda M and Kriek J, 2020 An evaluation of students' understanding of DC circuit concepts through students' written explanations. *J. Phys.: Conf. Ser* **1512** 012020

# The effects of monitored peer teaching and learning on the understanding of basic Physics concepts

B M Sondezi<sup>1</sup>, M Khwanda<sup>1</sup> and P Molefe<sup>1</sup>

<sup>1</sup>University of Johannesburg, Physics Department, P.O. Box 524, Auckland Park, Johannesburg, 2006, South Africa.

E-mail: [bmsondezi@uj.ac.za](mailto:bmsondezi@uj.ac.za)

**Abstract.** Learners and students alike are always seeking alternative ways of learning and understanding the concepts of most Science, Technology, Engineering and Mathematics (STEM) courses. Among these clusters of STEM courses, a sub-branch of Physics has been the most challenging one for both learners at the school level as well as for students at the university level. The challenge is particularly prominent in the first few years of their university experience. This is the stage where students deal with both misconceptions and concepts they need to understand. In an endeavour to deal with this challenge, lecturers are forever seeking ways and strategies of effective methods that could be used to make the delivery of this course easy and manageable for students. Peer teaching has been adopted as one of the methods to be explored in teaching a specific topic to a specific group of first-year students, to enhance their involvement, understanding and ownership of their learning. This work reports on the findings of this method as investigated on to first-year students at the university. Conclusions were drawn from well-analysed thematic data collected from questionnaires ministered to students.

## 1. Introduction and Background

The success of teaching and learning can also be measured by how students understand, interpret and apply learned concepts in an acceptable way. Teachers and lecturers would always strive to teach and impart knowledge the best way they can, but the work of imparting knowledge is not effective if the students do not learn anything from the concepts provided. For effective learning, students are expected to be active participants and there must be an emphasis on developing students' skills, including exploring their own attitudes and values [1]. One of the barriers to learning is the student's attitude towards the topic and the facilitator. This is the reason why presenters are always looking for new ways to convey their topics in interesting ways that allow students to easily convey their knowledge. However, the subject of physics, with its difficulties due to its complexity and poor conception, seems to have fewer methods to teach it, slightly changing the attitude that learners and students already have about it.

In order for active learning to take place, three basic factors are required, i.e., basic elements, learning strategies; and teaching materials must be well coordinated [2]. These elements are; speaking, listening, reading, writing and reflecting, which involve cognitive activities that allow students to gain clarity about questions; consolidate and acquire new knowledge. Furthermore; learning strategies need to be integrated into these five elements to encourage active learning. This is the part where facilitators have to continuously explore different methods and find out which ones work better for a specific group of students. Reported teaching strategies include small groups, collaborative work, case studies, simulation, discussion, problem-solving, and journaling [2]. With the understanding that basic theories are used to describe how students process, absorb and retain knowledge in the teaching/learning process [1], specific teaching and learning strategies for a certain group of students at the university were investigated. This strategy is based on the philosophy of social constructivism and the theory of variations. These formed the core of this study as they are seen as relevant guides to how the learning process will take place in a classroom where students interact with each other. While knowledge is

viewed as a human product that is socially and culturally constructed [3], its reality is assumed to be constructed through human activity and not discoverable. In other words, the members of society create their reality. The theory of variations explains how a learner comes to see, understand, or experience a certain phenomenon in a certain way, and why two students in a class sitting next to each other might understand a concept differently [4]. According to this theory, learning occurs when students see or experience critical aspects of the subject matter through the learning space [5]. On this basis, peer teaching and learning were employed, and the effectiveness of this method was measured in terms of understanding the concepts learned, as later assessed through this group of students.

To meet the daunting demands of improving the quality of teaching and learning while doing more with less, there has been an increasing interest in involving students as partners in learning and teaching. A peer teacher is anyone who has a status similar to that of the person being taught and who acts as a complement and active partner of university teachers in the process of learning and teaching. It is important to be clear that student partners, often a senior student, involved in academic support programs such as peer-to-peer instructors are not teachers and are not expected to teach and present new material. However, they make learning easier for their peers. Peer-to-peer education is not uniformly defined, and a number of terms are used interchangeably by authors [6]. More learning than Elaborative Study with Concept Mapping, by [7], states that students practice retrieval by remembering information. It is concluded that peer retrieval practice is a powerful tool to promote the learning of complex concepts [7]. It has been claimed that the act of reconstructing knowledge in itself enhances learning, and tutoring itself can have an important positive impact on knowledge retention. Therefore, learning the material in order to teach it to another student can be a particularly effective way to improve mastery of the content [8]. How, then, can student retrieval practice, reconstructing knowledge, be used in higher education when students teach each other? John Hattie states that the greatest impact on student learning occurs when teachers become learners of their own lessons and when students become their own teachers [9]. As learners move from being recipients to being productive teachers, it is likely that they need to understand the material at a deeper level in order to be effective teachers. According to [10], many students focus on learning recipes or problem-solving strategies without understanding the underlying concepts; A focus on memorization does not always lead to understanding. On the other hand, students who become teachers of their own learning tend to self-assess, self-evaluate, self-monitor, and self-learn.

## **2. Research Design and Experimental Methods**

Data collection was carried out through detailed semi-structured interview-like questionnaires administered via Google forms. This method was chosen because it manages to understand the participant's unique perspective better than a general understanding of a phenomenon [11]. Its open nature allowed the subject under study to be explored further and provided an opportunity to discuss the subject in more detail [12] in order to provide better recommendations.

### *2.1 Participants and instruments used for data collection.*

The participants were a group of life sciences students enrolled in a four-year extended degree and in their second year of the university experience, although in their first year of the university curriculum. These students are in their final physics experience as they will no longer enrol in other physics modules as per the requirements of their degree. A class of 86 students received a Google Form with semi-structured interview-like questionnaires through the university's online teaching and learning platform, Blackboard. The form was handed out in June 2022 at the end of the module, just before they could write their final exam. Only 53 (62%) students took part in the survey. Selected questions from the interview guide are exhibited and the students' answers are shown verbatim. The data obtained were collected and analysed using the thematic approach and recommendations were made.

Two months prior to execution of this activity, the purpose of the strategy used in teaching and learning a part of the module under study was explained to the students. Students were also mentally prepared a month in advance to give them time to participate as group members. This included the assignment of the members to the groups and the assignment of the sections to be dealt with. They then had time for 4 weeks to research the topic, shared the work among themselves, and prepared their presentations using PowerPoint slides. The presentations took two weeks, that is, a total of eight hours, where each student had a section to present from their respective groups. The survey was then performed at the end of the semester, where all participating students consented to the interview conditions.

## 2.2 Interview Questions

2.2.1 How did you find the teaching of Physics this year, 2022?

2.2.2 Did the lecturer allow a good environment for teaching and learning and understanding?

2.2.2.1 Elaborate on your response given in 2.2.2.

2.2.3 Comment on the teaching strategy used by your lecturer.

2.2.4 Comment on the learning approach used to learn Chapter 24 (X-RAYS). Do you feel you learnt better with this approach? Explain.

2.2.5 Was teaching and learning from peers through presentations beneficial for you?

2.2.6 Explain your choice on this question: Was peer teaching and learning (from presentations) beneficial for you?

## 3. Results

In this section, the answers to the respective interview questions are given, analysed and discussed.

These were thematically analysed based on the observations from the interview results of the students.

### Interview Question 1: How did you find the teaching of Physics this year, 2022?

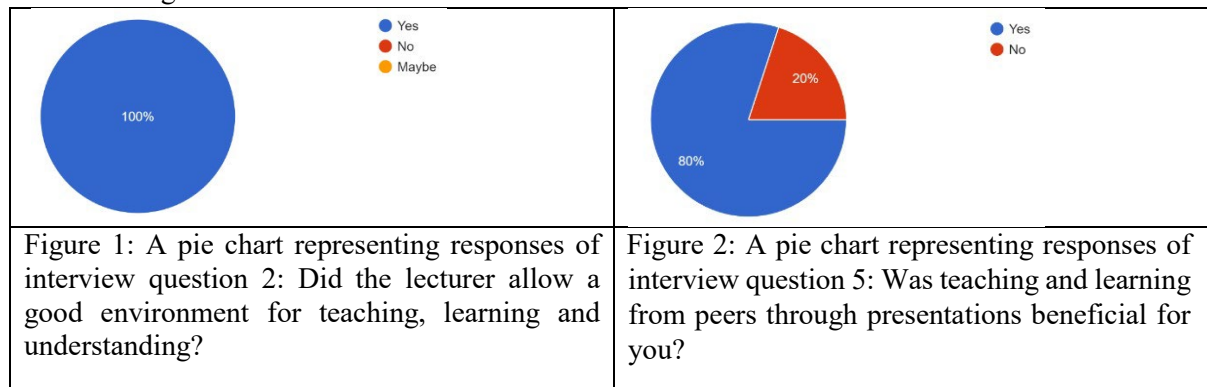
#### Responses

R1.1: It wasn't anything like 2021 when I attended online. It was actually interactive, enjoyable and difficult with the fact that I struggle with physics, not that I am not getting help but I am not putting much effort.

R1.2: The teaching of physics this year was very easy to understand, and the lecture made it easy for us to engage in class

R1.3: It was good, the lecturer went over all concepts and ensured we understood the core ideas of the topic before moving on.

### Interview Question 2: Did the lecturer allow a good environment for teaching, learning and understanding?



**Elaboration of Interview Question 2:** *Did the lecturer allow a good environment for teaching, learning and understanding?*

**Responses**

R2.1: The lecturer provided chances for questions from us to ask her and also made practical examples which made sense. She would ask questions about what we heard, and we would discuss and try to recall. She would help us along the discussion.

R2.2: The lecturer let all of us engage meaningfully with the content.

R2.3: The lecturer allowed us to present our understanding by doing a presentation on a certain chapter.

R2.4: Both students and lecturer were engaging in the content.

**Interview Question 3:** *Comment on the teaching strategy used by your lecturer.*

**Responses**

R3.1 It is very exciting when we present and the notes, she gives are understandable when we learn. I personally feel that way. On my side, I am not doing that well because of a lack of commitment and strategy but for the exam, things will be different.

R3.2 She doesn't do everything by herself. We engage with lecture slides while incorporating any crucial information we as students might have acquired during our own time of study.

R3.3 She taught in different approaches like presentation notes, dividing us into groups and giving us tasks, which were easier to go about.

**Interview Question 4:** *Comment on the learning approach used to learn Chapter 24 (X-RAYS). Do you feel you learnt better with this approach? Explain.*

**Responses**

R4.1: Yes, students understand something better when it is explained by other students. The students really enjoyed presenting, I wish it could be done even in other modules.

R4.2: Yes, I did. It was exciting and nerve-wracking getting in front of a bunch of students whom I had never personally interacted with. It was fun to learn this way. This made me research and watch YouTube videos on a section of the topic I was presenting. It made me understand and retain information. Yes, I personally think the research part urged us to get more information which made us a bit excited to share with others. Being taught by fellow classmates made it interesting because they break it down to our level of thinking as a unit thus, I enjoyed that method of teaching as well.

R4.3: Having other students teach us made it easy to understand and made us comfortable with each other so we can work together.

R4.4: Some of my peers were very much prepared for their presentations and that resulted in me having a better understanding but for some, I couldn't understand a thing.

R4.5: No, I didn't I only understood that part that I covered for my presentation when other groups presented, I usually went blank and I blame no one but myself.

**Interview Question 5:** *Was teaching and learning from peers through presentations beneficial for you?*

**Explanations of the interview question 5:** *Explain your choice on this question: Was peer teaching and learning (from presentations) beneficial for you?*

**Responses**

R5.1: I learnt a lot from my peers as they researched and made demonstrations. Looking at the visuals they obtained and using them to explain and ask us questions. It was an exciting moment.

R5.2: The peer teaching and learning helped me understand certain things because they were well-researched and taught from the basics of the topic.

R5.3: Our peers understand the way in which we receive a concept, so when they are presenting they know which points to highlight.

R5.4: I prefer learning from the lecturer because she gives better explanations

R5.5: No, the first groups were ill-prepared which ruined the rest of the group because I was lost at the beginning which made the rest hard to understand.

#### **4. Analysis and Discussion**

##### *4.1 Analysis and discussion based on Interview Question 1: How did you find the teaching of Physics this year, 2022?*

The students' answer to the question of how physics was taught this year, i.e., 2022, is very interesting. This response is attributed to COVID-19, which has hit various sectors very hard all around the world, including education. Schools and colleges were forced to adopt online teaching and learning to avoid wasting time, but the transition has not been easy for many, especially those with fewer resources [13]. Understanding that this group of students were in 12<sup>th</sup> grade in 2020 puts them at a disadvantage as they had lost some contact time with teachers due to the pandemic. It is then understandable why they found the teaching and learning very interesting this year, considering that in 2021 these students were fully tutored through online teaching and learning throughout the year. Lack of physical contact is the main reason behind the loss of effective learning for these students [13]. Employing better strategies that differed from traditional teaching methods made a big difference in the understanding of physics concepts for this group.

##### *4.2 Analysis and discussion based on Interview Question 2: Did the lecturer allow a good environment for teaching, learning and understanding?*

The whole class confirms the quality of the environment in which the lectures were taught. It is this environment that encourages students to attend and engage in class. A safe and positive learning environment is also characterized by the relationship between a teacher and their students. When students understand that their teacher cares about them and wants them to perform well, they feel comfortable asking questions, making mistakes, and taking risks to learn something new [14]. To build these types of relationships, the instructor took an interest in each student's strengths and interests, as well as their struggles and frustrations. The freedom to participate without fear of making mistakes has enhanced student learning. The responses suggest that allowing students to take ownership of their learning makes them active participants and forces them to know and understand.

##### *4.3 Analysis and discussion based on Interview Question 3: Comment on the teaching strategy used by your lecturer.*

It is interesting to learn that students recognized the strategy used by the lecturer to convey the content of the module, which is more of an interactive approach. The response stating that students would engage with lecture slides while discussing their views learned in preparation for class and with other peers is indicative of the unique approach used in these lectures. This approach is considered by [15] as a teaching and learning method that is social and takes place through interaction between teachers and students and between the students themselves. The way students react to the teaching activities is the most important element of the quality of teaching [15] and this seems to have been achieved in this module through such approaches.

##### *4.4 Analysis discussion based on Interview Questions 4, 5 and 6: Comment on the learning approach used to learn Chapter 24 (X-RAYS). Do you feel you learnt better with this approach? Explain.*

The students' answers to this question are an indication of the success of the method used. Interactive teaching and learning have proven to be one of the most effective methods as it enables and enforces student participation. This is done in a variety of approaches, including peer teaching and learning, which

have been studied. When students are given hands-on experiences, they take full responsibility for their learning. The use of different strategies, including peer teaching, provided students with an opportunity to explore their current knowledge, attitudes and values, which fit well with their current knowledge, as explained by social constructivism pedagogy [16]. In this case, the student's strengths were utilized while at the same time improving their research and presentation skills, all of which contributed to their understanding of the concepts. While concerns were raised about mistreatment of other groups in the preparation of their presentations, the benefits of the interactive approach to learning played a major role, as the lecturer filled in these gaps by constantly explaining and correcting misunderstandings throughout the process. The 20% of students who do not support the strategy, understandably come from the students who were discouraged due to factors such as; ill-prepared presentations, lack of cooperation from other group members, and possibly time wasted in preparing the work, as others have indicated that they would prefer the lecturer to deliver the chapter.

#### 4. Recommendations and Conclusion

The peer teaching and learning approach has proven to be a more effective tool with more benefits for both the teacher and the students. The teacher immediately learns about the students' understanding of the concept and can deal with the challenge immediately on-site. Students learn new skills to find information for themselves. They learn to be independent and also to work in groups. It has been observed that students understand more quickly and better when they learn from their peers, which they testified to. It is important to mention that this method works effectively for smaller groups compared to larger ones as it allows for thorough monitoring of each student in relation to their work. It is recommended that the teacher or lecturer remain alert at all times during presentation times and be ready to correct errors and misrepresentations of the concepts. What was learned from this study is that physics can be made easier by involving students in their own learning, which also inspires more interest and enthusiasm for the subject. It is therefore advisable to use these interactive learning approaches in particular for subjects that are perceived as difficult. The study needs to further analyse the direct impact of peer teaching by analysing the understanding of concepts directly learnt through this approach. However, a 100% pass rate and throughput obtained in this module could be used to draw the conclusion of the success rate.

#### References

- [1] Sivan A, Leung R, Woon C and Kember D 2000 An implication of active learning and its effect on the quality of student learning," *Innovative Education Training International* **37** pp. 381-389
- [2] Meyers C and Jones T 1993 *Promoting active learning, strategies for college classroom* (San Francisco: Jossey- Bass Publishers)
- [3] Enerst P 1999 Social Constructivism as a Philosophy of Mathematics *Radical Constructivism* **23**
- [4] Orgill M 2012 *Phenomenography* (New York: Springer)
- [5] Marton F 2015 *Necessary Conditions of Learning* (New York: Routledge)
- [6] Dawson P, van der Meer J, Skalicky J and Cowley K 2014 On the effectiveness of supplemental instruction: A systematic review of supplemental instruction and peer-assisted study sessions literature between 2001 and 2010," *Review of Educational Research* **84** pp. 609-639.
- [7] Karpicke J D and Blunt J R 2011 Retrieval practice produces more learning than elaborative *Science* **331** pp. 772-775
- [8] Astin A 1993 *What matters in college? Four critical years revisited* (San Francisco, CA: Jossey-Bass).

- [9] Hattie J 2009 *Visible learning. A synthesis of over 800 meta-analyses relating to achievement.* (New York, NY: Routledge)
- [10] Mazur E 2014 *Peer instruction: A user's manual* (Essex: Person New International Edition)
- [11] Adeoye-Olantunde O A and Olenik N 2012 Research on scholarly methods: Semi-structured interview *Journal of the American College of Clinical Pharmacy*, pp. 1358-1367
- [12] Mathers, N., Fox, N. and Amanda, H., *Using Interviews in Research Projects*, Radcliffe: Radcliffe Medical, 2021.
- [13] Donnelly R, Patrinos H. and Gresham J 2021 *The impact of COVID-19 on education – Recommendations and opportunities for Ukraine* [Online] Accessed 2.08.2021 Available: <https://www.worldbank.org/en/news/opinion/2021/04/02/the-impact-of-covid-19-on-education-recommendations-and-opportunities-for-ukraine>
- [14] Hendrix E 2019 *How your surroundings affect the way you study* [Online]. Available: <https://www.ucas.com/connect/blogs/how-your-surroundings-affect-way-you-study>.
- [15] Tomljenovic Z 2015 An Interactive Approach to Learning and Teaching in Visual Arts Education *C.E.P.C. Journal* **5** 3 pp. 73- 93
- [16] Senthamarai S 2018 Interactive Teaching Strategies *Journal of Applied and Advanced Research* **3** 1 pp. S36-S38

# Teach electronics to applied physics students: Prototyping, design and research on a printed circuit board.

Marco Mariola<sup>1</sup>

<sup>1</sup>University of KwaZulu-Natal, Durban, 4000, South Africa.

E-mail: mariolam@ukzn.ac.za

**Abstract.** In science and engineering, practical activities are necessary to test theoretical knowledge in a natural environment. Modules like applied physics do not have enough time to teach the students how to work on a printed circuit board or modify an existing circuit. This paper presents an alternative way of training using a reconfigurable and low-cost PCB board. The experiments are generally conducted using an experimental breadboard, where the components are placed, following a schematic. The intention is not to replace the breadboard from the student curriculum, but the proposed system can be implemented. Given the versatility of the PCB, the proposed system can also be used for fast prototyping in research.

## 1. Introduction

Through the practical activities in electronics, students can better understand the theory and the challenges related to assembling an electronic circuit. Generally, the practical exercises consist of making and testing a circuit on a breadboard. More specialised academic courses in electronics have several modules to improve the industrial technical skills of the students. Contrary to purely scientific disciplines, the number of modules in electronics is minimal to be practically used in the industry without further training. The classical approach using the breadboard is still a valid teaching instrument. Still, in the proposed method, the experiments will be performed using a set of reconfigurable circuits mounted on a Printed Circuit Board (PCB). In the proposed novel training approach, the students start with studying the schematic to figure out how to change the existing circuit to perform the designed task scheduled for a specific day. The student can modify the circuit using appropriate components without soldering from the schematic since a suitable socket can insert the electronic components.

## 2. The experimental board

The experimental prototyping board consist of four operational amplifiers, two passive filters, a pair of transistor circuits, one digital to analogue circuit, and a slot for a comparator compatible with the LM393. The different components of the system are highlighted in Figure 1.

### 2.1. Operational amplifier block

The circuit was inspired by an article in an old electronic magazine called Nuova Elettronica, which proposed a universal operational amplifier board to fast realise operational amplifier

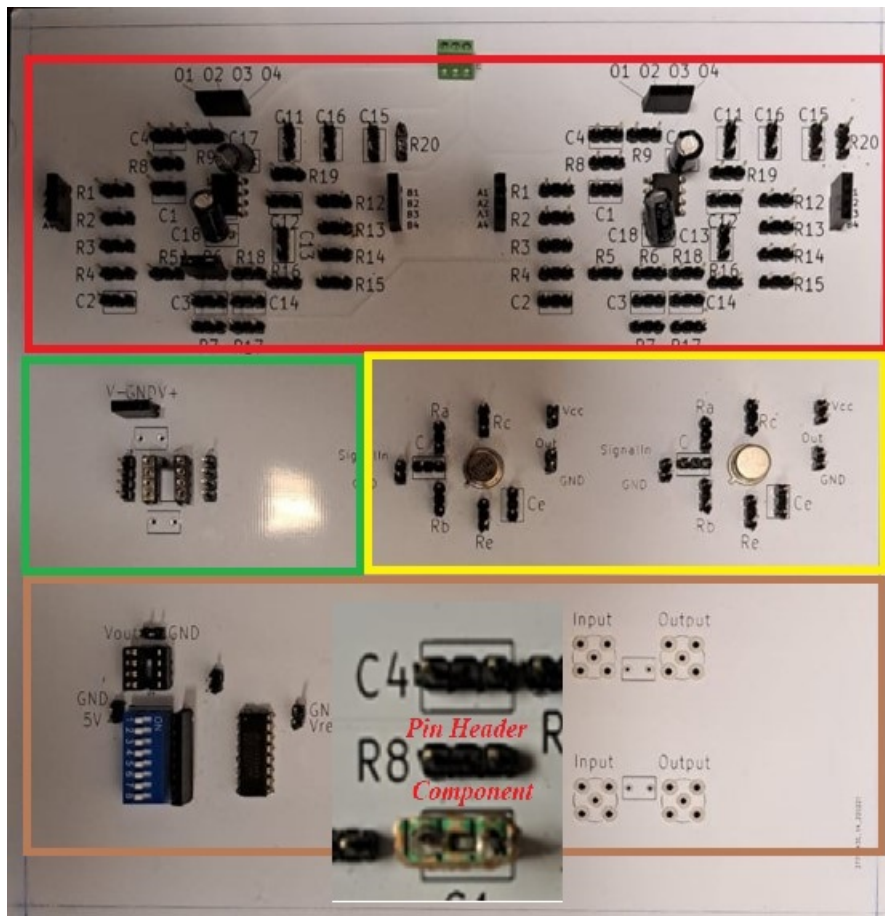


**Figure 1.** The sub-circuit of the reconfigurable board. The red area indicates the four operational amplifier circuits. The yellow area includes the transistor pair circuits. The green domain shows the comparator. In the last brown area, from right to left, the ADC and the passive filters are shown, respectively.

circuits for general applications [1]. The original schematic was adapted for training purposes and the routed circuit was designed to be student-friendly. The schematic is depicted in Figure 2. The operational amplifier used is the LM358 [2]. This component has two internal operational amplifiers and can operate with a single or dual power supply. The students can work directly on the schematic by replacing the component with the appropriate values, leaving a space or a shortcut. Suppose, for example, the students need to test a simple noninverting operational amplifier circuit. The students can modify the circuit by the schematic inspection, as depicted in Figure 3. The electronic components are placed on a female pin socket, as represented in Figure 1. The component will be inserted in a male pin header, which takes the place of the component represented in the schematic. Except for the operational amplifier integrated circuit (IC), the other components are not placed on the board, providing a set of open circuits. On the left side of Figure 3, the inverting amplifier is shown. In order to replicate the circuit on the left, the only resistance placed on the PCB are the resistance  $R_{22}$  and  $R_{28}$ , and the other socket are left empty, except the resistor  $R_{26}$  which is replaced by a jumper. The input signal will be placed in  $A_{21}$ , and the output signal can be measured at the pin  $O_{22}$ . In alternative some of the students can choose the path  $R_{21}$ - $C_{21}$ , and place the resistor  $R_{22}$  and the jumper at  $C_{21}$  respectively. In the last case, the lecturer can evaluate a different mark, since the modification

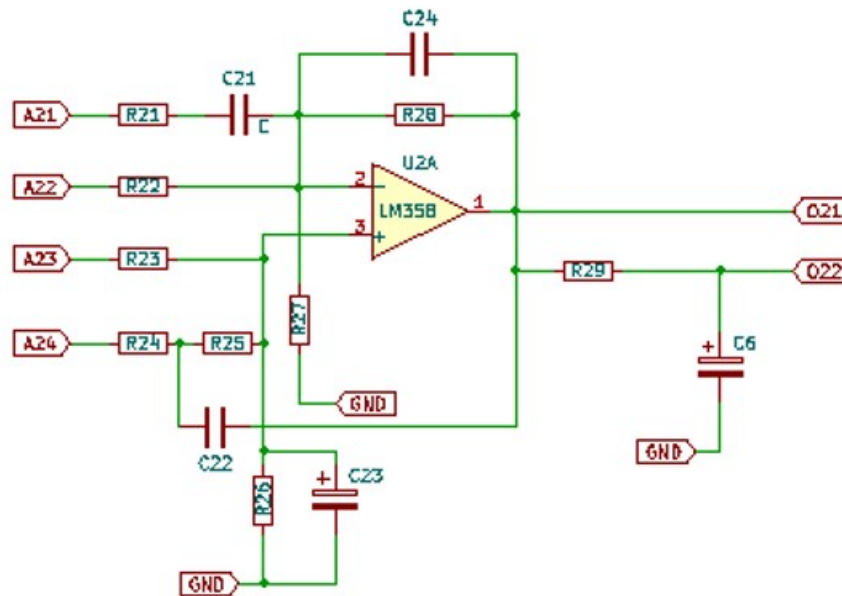


**Figure 2.** Schematic of the universal operational amplifier, which is related to one of the two operational amplifiers in the LM358.

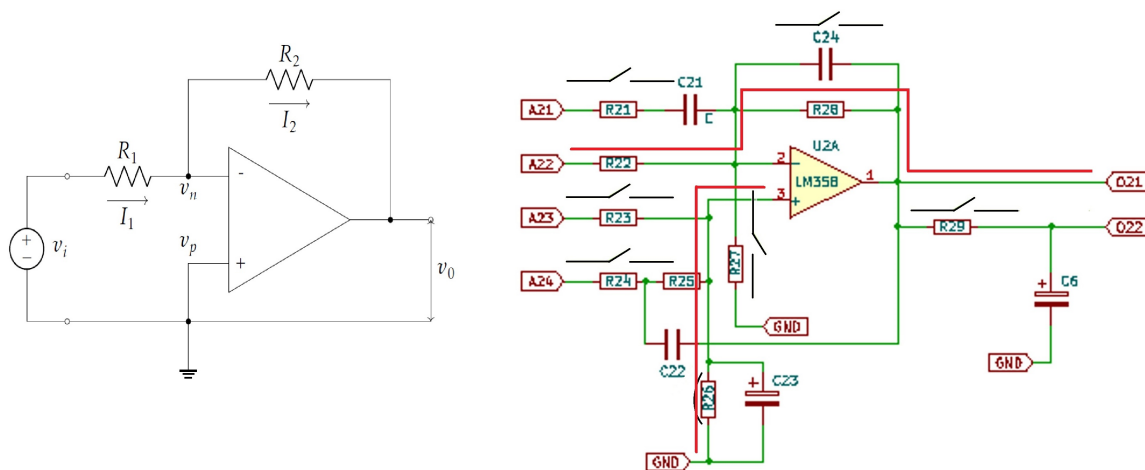


**Figure 3.** The preliminary work of the students to adapt the board to the appropriate circuit.

is not optimal<sup>1</sup>. The students need to be aware that each LM358 includes two operational amplifiers and the unused operational amplifier need to be configured as a voltage follower with positive input connected to the ground.

<sup>1</sup> The alternative path require more components.

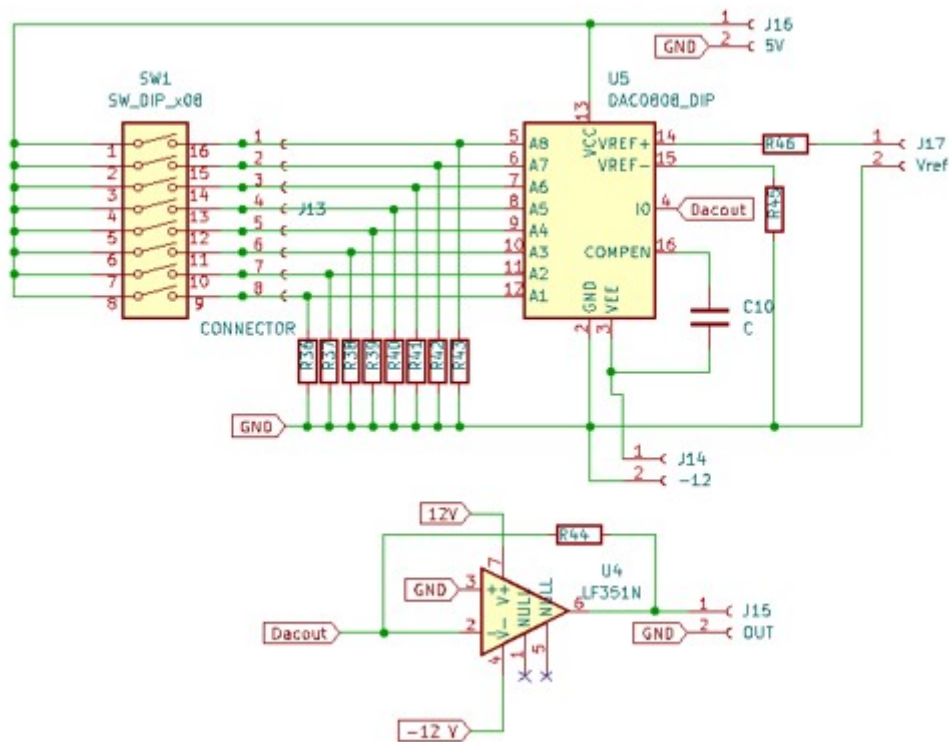


**Figure 4.** DAC implementation.

### 2.2. The comparator

The operational amplifier is not generally optimal to work as a comparator since the slow-rate [3]. For this component only an 8-DIP socket and the power connection are provided<sup>2</sup>. The comparator should be a replacement for the LM393 [4].

### 2.3. Digital to Analogue Converter (DAC)

This sub-circuit is a plug-and-play block to training analogue to digital conversion. The students insert the digital code through the 8-DIP switch to obtain the desired analogue value. As seen in Figure 4, an external power supply should deliver 5V and the reference voltage. The digital input can also be externally set through an eight-pin socket<sup>3</sup>.

### 2.4. Filters and transistors blocks

The transistor pair circuit is made of two NPN circuits reconfigurable using the same philosophy of the operational amplifier circuits. One of the classical experiments in applied physics, and engineering modules, is the definition and characterisation of high and low-pass passive filters [5]. Since the filter blocks are not specified on the PCB, the task for the students will be to identify if the chosen filter is low or high-pass [6].

## 3. Use of the board for research

The proposed board is designed to perform several experiments by changing the configuration of the circuits. This property makes our board useful for teaching and learning and fast prototyping.

<sup>2</sup> The teacher/lecturer can choose the favourite component.

<sup>3</sup> This is useful when the DAC is controlled by a microcontroller, or other external digital devices.

By looking at the board, it is possible to observe that each block can cooperate with the other available blocks to realise a more complex circuit. The IC on the board are mounted on sockets and can be replaced with the most updated one<sup>4</sup>.

#### 4. Conclusion

The proposed board is designed to be implemented in the practical activities for applied physics and engineering modules. The purpose of the board is a suitable training device to place students in front of an actual device and train them to modify and analyse a ready-produced PCB board. We believe this training approach can help the students' careers in industry and research fields and does not exclude the classical method of using the breadboard. Due to the board flexibility of the board, the system can use for fast prototyping in research.

#### Acknowledgments

This work is based on research supported by the South African Research Chair Initiative of the Department of Science and Technology and National Research Foundation and the Technology Innovation Agency, South Africa.

#### References

- [1] Elettronica N 2011 *Scheda universale con doppio operativa* RNuova Elettronica Editore Bologna, Italy
- [2] Texas Instruments 2000 *LMx58-N Low-Power, Dual-Operational Amplifiers*
- [3] Horowitz P and Hill W 2015 *The Arts of Electronics* 3rd ed (new York: Cambridge University Press)
- [4] Texas Instruments 2000 *LM393 and LM2903 Dual Comparators*
- [5] Jamerson T High- and low-pass RC filters [http://www.phy.olemiss.edu/~thomas/weblab/222%20Lab%20Manual/Highpass\\_lowpass.pdf](http://www.phy.olemiss.edu/~thomas/weblab/222%20Lab%20Manual/Highpass_lowpass.pdf) [Online; accessed 26-August-2022]
- [6] Bringardner J Electronic Filters [https://manual.eg.poly.edu/index.php/Electronic\\_Filters](https://manual.eg.poly.edu/index.php/Electronic_Filters) [NYU Tandon School of Engineering,Online; accessed 26-August-2022]

<sup>4</sup> The IC LM358, can be replaced for example by an LM082, LM072 etc.

## High school learners' difficulties with Kinematics graphs

**Itumeleng Phage**

Central University of Technology, Free State, Bloemfontein Campus

E-mail: [phageh@gmail.com](mailto:phageh@gmail.com)

**Abstract.** Kinematics is one of the topics taught at high school, from Grade 10 to Grade 12. This study was conducted with Grade 11 learners with the view to determine their understanding of Kinematics graphs in physical science. A questionnaire consisting of Algebraic graphs in Mathematics and Kinematics graphs were distributed to 98 Grade 11 learners. The responses were analysed statistically. The results showed that majority of learners have difficulties in the construction, analysis, and interpretation of not only Kinematics graphs but Algebraic graphs. The learners' prior knowledge of Algebraic graphs and functions were supposed to assist them in the comprehension of Kinematics graphs and equations. They had difficulties with variables also in Algebra; as a result, became more difficult for them to understand and relate variables in Algebra with those in Kinematics. Though learners could answer questions in Algebra, they struggled to connect the meaning of the variables and to relate them to the meaning of underlying Kinematics concepts. Among other difficulties they encountered was setting up a scale for Kinematics when constructing them. In this regard, the learners performance demonstrated that they lacked scientific knowledge or literacy to comprehend Kinematics graphs. The study also agreed with previous studies that learners are unable to integrate their Mathematics knowledge with the Physics concepts or transfer their Kinematics knowledge to Algebra.

### 1. Introduction

Learners in schools, including undergraduate students, in the science fields have difficulty to identify and apply their prior learning of basic Algebraic knowledge to solve Physics problems such as Kinematics graphs (Freitas et al., 2004). Observation yielded that undergraduate Physics students lacked the ability to apply their knowledge and skills of prior learning in linear Algebraic graphs (Mathematics) that could help them solve and present Kinematics graphs in Physics. The whole scenario raises the importance of Mathematics. This Discipline is known and reported to be an essential tool in the study of Physics; that is to say, studying Physics without the sound basics of Mathematics might prove very difficult (Pietrocola, 2008). In light of the above, Mathematics is even referred to as the "language of Physics" (Redish, 2005). Physicists blend conceptual Physics with mathematical skills and use them to solve and interpret equations and graphs (Redish, 2005).

A high failure rate of first year undergraduate Physics students often appears to be blamed on their lack of high school content knowledge and conceptual understanding in both Mathematics and physical science (Semela, 2010). The use and application of Kinematics equations and graphs also seems to be one of the Physics content knowledge areas which high school learners struggle or have difficulty with at tertiary or undergraduate level, even though they have learnt this in their high school curriculum (Phage, Lemmer & Hitge, 2017).

Previous studies such as Beichner (1990 and 1994), McDermott, Rosenquist and Zee, (1987), Brasell and Rowe, (1993), Woolnough, (2000), have reported that learners in Grade 10 to 12, including undergraduate learners, are still struggling with and have the inability in the understanding and interpretation of Physics graphs. The introduction of the concept of line graphs in Algebra (Mathematics) to Kinematics (Physics) was meant to equip Physics learners with graph skills as learnt from the Mathematics class.

Though, against the educators' beliefs, learners perform better in Algebra questions than in Kinematics. This means that their poor performance and inability to interpret graphs in Kinematics is not due to lack of Algebra knowledge (Phage, Lemmer & Hitge, 2017). Planinic et. al., (2011) and

Phage, (2015) stated that learners have difficulties with the interpretation of the slope of a line graph. Learners have also been observed to have challenges with interpretation of line graph in Algebra, but more in Kinematics context (et. al., 2011).

This study will therefore determine what factors causes high school Physical Science learners to perform poorly in Kinematics graphs. The researcher would be able to determine their perceptions on the teaching and learning as well as their conceptual understanding that underpins the topic and what Algebraic knowledge do they need to comprehend Algebraic graphs. Further to that, he would also be in a position to establish what Algebraic knowledge they need in order to comprehend Algebraic graphs. In so doing, the researcher would be able to, firstly, propose a model of teaching and learning of Kinematics graphs that could not only enhance the comprehension of Kinematics graphs by high school physical science learners. Secondly, this would result in competency in the topic. Consequently, this would boost their moral as they develop more interest in the subject. And finally, the outcome would be improved results. The study will have a greater significance in the development and improved curriculum in the Further Education and Training (FET) subjects of Physics (Physical Science) and Algebra (Mathematics).

## 2. Theoretical framework

According to Curriculum and Assessment Policy Statement (CAPS) Grades 10-12 Physical Sciences (DBE, 2011), learning Sciences requires a learner-centered approach in the delivery of learning and teaching methodology (DBE, 2008) as well as strategy. This is an active and constructivist approach, in which a learner will develop an inquiry - based mind and hands-on activity skills (DBE, 2008). In this approach, critical thinking and problem-solving attitudes automatically form part of the basis of learning. It is therefore, necessary and encouraging that high school educators should instill critical thinking and problem-solving attributes among their learners. In so doing, grade 10 – 12 learners will be duly prepared to enter higher education learning and be able to use their prior learning (high school learning) to learn new concepts and ideas.

It is necessary to comprehend what science is and how Physics fits within that field of study. One pertinent area within the study of Physics. According to Nwosu (2019) and Bosman (2006), Science hinges on a thorough understanding of the subject matter. As a result, it is important for teachers to instruct students effectively and to be fully prepared to discuss the nature of Science, its philosophies, and how it relates to culture. These scholars added that, in order for students to develop scientific literacy, teachers must also possess the procedural skills, values, and attitudes that are crucial to the study of Science. According to these authors, only a very small number of Science professors believe that their students lacked scientific literacy, which prevented them from performing scientific experiments. Engineers and physicists hold the belief that problem-solving and critical thinking are tools for Science (Nwosu, 2019; Bosman, 2009).

According to Cen et al., (2016) and Mitnik et al., (2009), the ability to create and comprehend graphs is a crucial skill for understanding science. Its absence might be perceived as a barrier to and handicap for conceptualizing science. Students of all ages cannot relate Kinematics concepts like position, velocity, and acceleration to the prior Algebraic knowledge of graphs that they have (Mitnik et al., 2009).

Previous researches (Redish & Kuo, 2015; Uhden et al., 2012) have reported that graphs in Kinematics as a mathematical-physical models that illustrate the motion of objects. Redish & Kuo, (2015); Uhden et al., (2012) argued that the models assist in the mathematization of physical system or model in order to integrate the physical knowledge of concepts with the technical and structural knowledge in Mathematics. Learners in a Physics class acquire their knowledge to make physical meaning with Mathematics (Redish & Kuo, 2015). Learners therefore are prompted to extract knowledge of relevant subsets in Physics and Mathematics to associate them with the actual meaning of Mathematics symbols and formulae. There are two symbols,  $x$  and  $t$ , that are represented by mathematical functions, and these are Algebraic and graphical symbols. The Algebraic and graphical representations in Physics carry physical meaning of variables used in these functions. According to reports, the understanding of line graphs comes from a combination of several types, such as pattern recognition

that interprets and provides qualitative and quantitative information as indicated by labels and titles (Canham & Hegarty, 2010).

Lemmer and Gunstone (2016) indicate that it is of paramount importance that learners be introduced to real world phenomena before they can be allowed to derive the physical-mathematical models of such phenomena. It is; therefore, that learners use the experiences of real world and laboratory exposure to be acquainted with the relationship between the concepts and Mathematics found in the Physics and Physics-mathematical models (Lemmer, 2013; Zwickl, Hu, Finkelstein & Lewandowski, 2015). Educators are expected to teach their learners to integrate knowledge of Physics and Mathematics as this knowledge does not come to them automatically (Moyo, 2020; Glazer, 2011 & Phage 2015). Phage (2015) even recommended that Physics educators should also be allowed to teach Mathematics in the lower grades in order to enforce this knowledge and review or relate those Algebraic concepts and knowledge with the new Physics concepts to be learned.

Hermida (2014,) argue that, in order for students to learn effectively, they believe that their instructors must be able to communicate with them at a personal level. These authors also stated that it is important to look into how students and institutions perceive effective teaching, how students' perspectives of effective Physics instruction using Mathematics have changed over time, and how their perceptions of good teaching compare. It has been shown that some teachers believe it is simple to teach Physics ideas even when their pupils find it challenging (Gumede, 2020; Rankhumise & Raphoto, 2014; Gunstone, Mulhall, McKittrick, 2009). These authors claimed that the teachers who are knowledgeable and skilled in Physics topics are the ones who comprehend and have feelings regarding the teaching challenges of such concepts.

### 3. Research Method

The participants were comprised of 124 Grade 11 learners from various high schools in the Free State Department of Basic Education, South Africa. The schools were from three districts made up of varied and mixed nature demographic backgrounds such as, viz., rural (farms and villages), semi-rural (township), and urban (city and former Model C). A purposive sampling of all Grade 11 Physical Science learners in these schools was used. All participants belonged in the mainstream of Physical science (Physics and Chemistry) and Mathematics as specialization subjects in their secondary school level. The participant's` biographical information is covered in the results along with reader (participants) characteristics.

A questionnaire (quantitative data) was used to elicit answers for the study topic and research tool, which was then followed by interviews (qualitative data). The questionnaire consisted of two sections of multiple-choice questions, namely one on Kinematics (Beichner, 1994; Susac, Bubic, Kazotti, Planinic, and Palmovic, 2018) with 30 items, and one on corresponding Mathematics graph operations (27 items). The Test of Understanding Graphs in Kinematics (TUG-K), created by Beichner (1994), served as the source for the Kinematics questions on the questionnaire (1994). It was utilized to evaluate the participants' comprehension utilizing various graph operations on the level of the Grade 11 South African school year. Only one-dimensional motion was considered in this study. To test the learners' deeper comprehension of graph operations, the researcher created extra questions. Four graph operations were included in the survey. These were: reading coordinates, comparing, and calculating the area under graphs, graph gradients, and connecting representations (Algebraic equations and shape of graphs). The following step was to create related Mathematics problems on linear functions that need the same operations as the Kinematics problems.

The content of the questionnaire was verified by fellow high school educators in the Physical Science field and teaching the subject. They were piloted with thirsty Grade 12 physical science learners from a different school in one of the selected districts. The necessary changes from their input and recommendations were made, though there were only a few mistakes that were found. The final questionnaire's reliability was confirmed by using the Cronbach's alpha coefficients of 0.69 for the Kinematics portion and 0.75 for the Mathematics section.

Descriptive statistical analysis was used to determine the effect sizes for differences in means of separate groups. The researcher examined the impact of reader characteristics on participant performance in the Mathematics (Algebra) and Kinematics (Physics) sections of the questionnaire (Ellis & Steyn, 2003). A value of  $d=0.2$  implies a little effect,  $d=0.5$  a moderate effect, and  $d=0.8$  a difference of practical importance. The participants' gender, and whether they received the same grade the year before or not (were taken into consideration. Statistical analysis was used to compare the variations in average percentages between the Algebra and Kinematics areas of the Mathematics questionnaire's responses.

Since sampling was done, effect sizes were used in the statistical analysis of the questionnaire results. The McNemar test was used to analyze and interpret the proportional differences between Algebra and Kinematics success rates using Cohen's effect sizes (Stokes, Davis & Koch, 2012). The effect size numbers demonstrates if there is a practically significant difference between the percentages of participants who were able to correctly answer the Algebra questions and those who were able to correctly answer the Kinematics questions.  $W=0.1$  denotes a negligible effect,  $W=0.3$  a moderate effect, and  $W=0.5$  a practically substantial difference between the two factors under consideration.

After completing the questionnaire, twelve randomly chosen respondents with a range of skills participated in a group interview to further explore how past Kinematics knowledge affected their ability to understand graphs. The information elicited was related to:

- The differences and similarities between distance & displacement and speed & velocity
- Naming equations of motion and stating what each symbol stands for
- Between velocity-time and displacement-time graphs, in which one can you obtain average velocity, and in which can you obtain instantaneous velocity?
- Which equation of linear motion can give a straight line on a v-t graph? Explain your answer.
- Given  $v_f = v_i + at$  with constant  $a$ , which symbol represents the gradient, and which one represents the y-intercept on a v-t graph?

The interview transcripts were classified and recorded. In every area of the research investigation, the ethical standards of the research procedures were followed.

#### 4. 1. Findings from an empirical investigation and discussion

##### 4.1. Respondent characteristics

Table 1 below depicts the total number of respondents and their average percentages for each category.

**Table 1.** Comparison of the how respondent characteristics affected their answers to the Kinematics and Mathematics questions:

(a)	Gender	% of participants	Mathematics	Kinematics
	Male	76	67%	38%
	Female	48	58%	32%
	<b>Effect sizes (d-value):</b>		<b>0.58</b>	<b>0.52</b>
(b)	School year gap Grade 11	% of participants	Mathematics	Kinematics
	One year	111	66%	36%
	Two years	13	59%	33%
	More years	0	0	0
	<b>Effect sizes (d-value):</b>		<b>0.43</b>	<b>0.23</b>

The results in Table 1 demonstrate that minor to moderate performance discrepancies were caused by varying respondent attributes. With a medium effect size (0.5), male respondents outperformed

female respondents in the Kinematics and Mathematics parts. Participants who completed grade 10 the previous year performed distinctly better (effect size 0.43) in Mathematics section than those who had a gap of two or more years in comparison with their prior studies of Mathematics, even though only a small effect size (0.23) appeared for Kinematics section.

#### 4.2. Contextual understanding and inferential techniques

Participants did perform better on the Mathematics items than the Kinematics items requiring equivalent processes in both the overall questionnaire and for each component. While the average score in Kinematics was only 35% (standard deviation 12.8 percent), the average score for all Mathematics problems was 63% (standard deviation 16.0 percent).

##### 4.2.1. Reading of the coordinates

In general, participants performed better while reading coordinates, as observable by the high performance (92%) of Figure 1's Kinematics item P6.1. The remaining Kinematics problems and the two Mathematics questions that only required a simple reading of coordinates also had excellent results (> 80%). The McNemar test found no differences between Kinematics and Mathematics coordinate reading performances that were significant ( $w=0,2$ ).

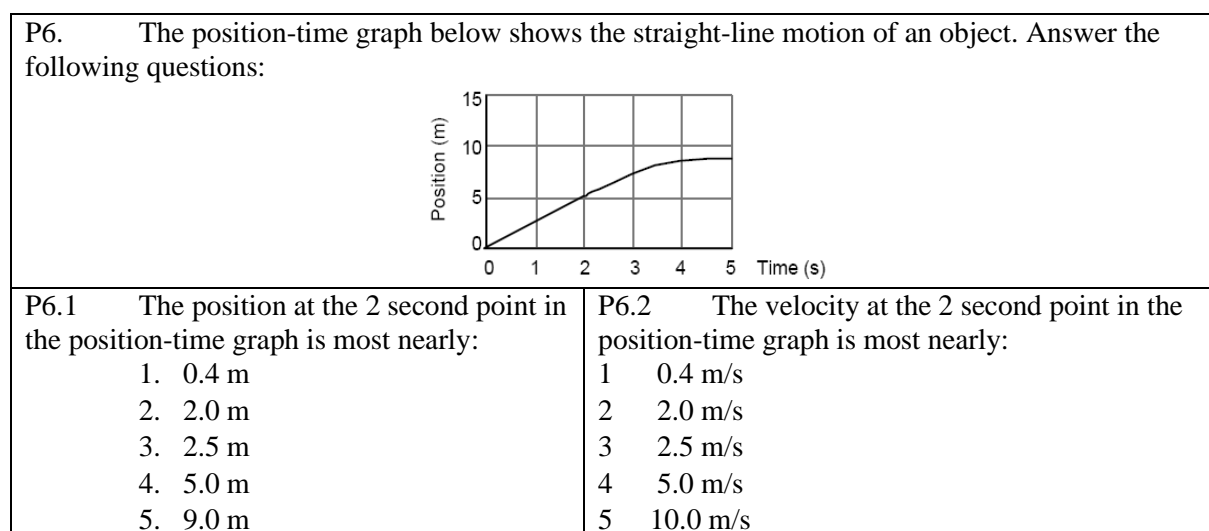


**Figure 1.** An example of items testing for coordinate reading and gradient of Kinematics graphs (Phage et al., 2017)

As demonstrated by the findings of the interviews and other issues included in the questionnaire, the finding that participants were able to recognize coordinate pairs on Cartesian planes in a Kinematics context does not necessarily mean that they had attained knowledge of the Kinematics ideas. For instance, only seven out of the 12 interviewees were able to define velocity in a manner that was acceptable in science language.

4.2.2. *Gradient determining and interpreting.* Further testing was done to determine if learners could deduce the velocity at a certain time point from the position-time graph in Figure 1 by using it (P6.2). Approximately 65% of participants selected option 3 correctly. It's interesting to see that roughly 20% of participants just read the value 5 off the position axis (option 4). The interviews supported the participants' difficulties in relating velocity to the position-time graph's gradient.

The Kinematics graph from Figure 1 was also provided in the Mathematics section, with the main variation being the use of  $y$  and  $x$  variables rather than position and time to determine whether the participants possess the Mathematical ability to determine the gradient at a point. 83% of the participants correctly responded to the question, "What is the gradient of the graph at  $x = 2$ ?" This pair of related

Kinematics and mathematical questions was answered in a different way with a moderate effect ( $w = 0.30$ ). Several participants who did well on the arithmetic test struggled to solve the Kinematics problem.

The participant's comprehension of the fundamental Kinematics concepts of displacement, average and instantaneous velocity, as well as acceleration, was further revealed by the interviews. The ratio of position to time ( $v=s/t$ ) rather than the ratio of change in position to time ( $v=\Delta s/\Delta t$ ) was frequently mistaken for average velocity. This error was also evident in some questions from the questionnaires and the interviews, such as P6.4's calculation of velocity at 5 seconds from the graph in Figure 1. This error was particularly obvious when it came to determining the gradient of kinematic graphs for line graph segments that did not pass through the origin, or in situations where  $\Delta s/\Delta t \neq s/t$ . P6.4 was correctly answered by just 8% of participants, and 17% correctly answered the comparable arithmetic question, with a modest practical meaningful difference of  $w=0.2$ .

4.2.3. *Area under a graph.* Figure 2 illustrates two of the questionnaire questions that assessed learners' capacity to calculate the area under a graph (item M7.2) and apply it to a Kinematics graph (item P1).

The correct response to the math question M7.2 is graph (C), while the correct response to the question P1 is graph (B) with the equivalent form. Only 28% of participants correctly answered the Kinematics question, while 69% of participants correctly answered the Mathematics question. The high  $w$ -value of 0.63 indicates the practical importance of this disparity in their responses. The other matching pairings of items on comparison and area under graphs calculation likewise showed same tendency. All  $w$ -values ranged from medium to large.

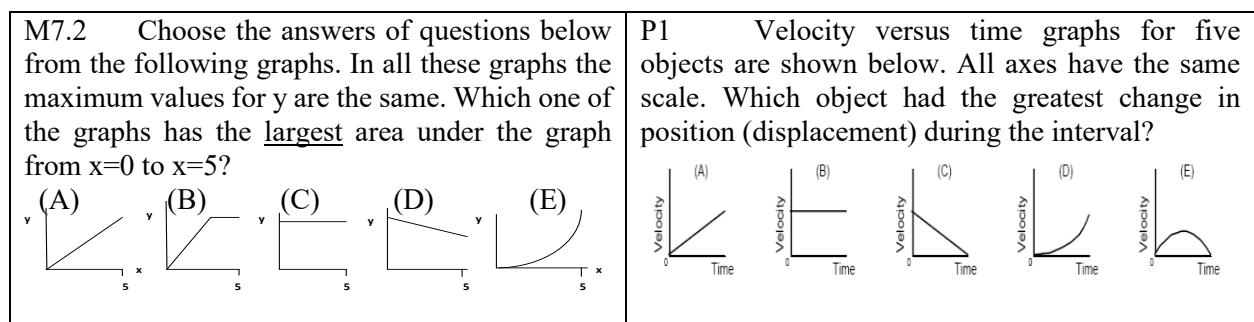


**Figure 2.** An example of corresponding Mathematics and Kinematics items testing for comparison of area under graph lines (Phage et al., 2017).

4.2.4. *Relation in representation.* Five graphs of various types of the corresponding Algebraic and Kinematics items (M4 and P20) on the link between graphic and Algebraic representations are shown in Figure 3 below. Participants had to match a Mathematical function or Kinematics equation to one of the provided graphics using the items M4.1 and P20.1, M4.2 and P20.3, and M4.3 and P20.2.

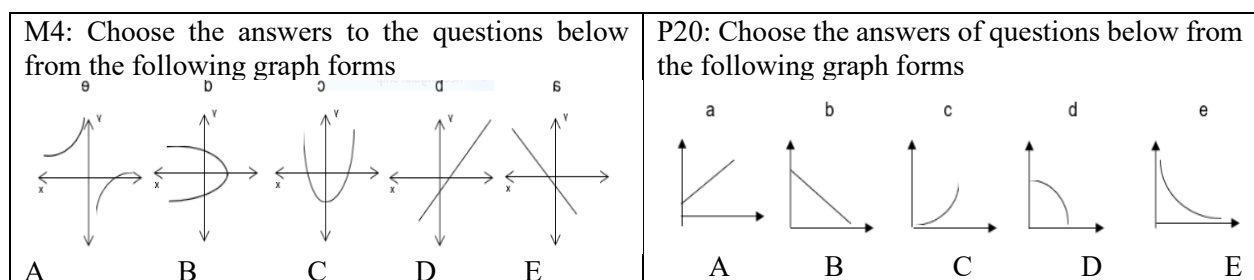


**Figure 3.** An example of corresponding Mathematics and Kinematics items on connection of graphic and Algebraic representations (Phage et al., 2017).

The findings reveal that, in M4.1 (graph (A) and P20.1 (graph (A), respectively, 67% and 65% of participants correctly identified straight lines. A similar percentage of participants correctly identified graph (E) as hyperbolic and connected graph (C) with the provided quadratic function in the following arithmetic questions. Only 27% of participants correctly identified the hyperbolic form of the Kinematics expression in P20.3 and only 38% of participants associated the quadratic equation with graph (C) in the Kinematics item P20.2 (E). While a small  $t$ -value of 0.03 was found for the associated straight-line graphs, the hyperbolic and parabolic equations produced large  $t$ -values (0.58 and 0.44) reflecting medium to practically significant disparities in reactions in the two contexts. The interviews confirmed that participants had trouble making connections among various Kinematics function representations.

## 5. Conclusion and recommendations

Data in this study have demonstrated that some learners do have a limited Algebraic knowledge and they lack conceptual understanding and knowledge, as well as practical use and application in Kinematics graphs. This contributed to the factors that influence high school learners' difficulties with the comprehension of Kinematics graphs. Learners still lack conceptual understanding and knowledge of Kinematics and its graph. They were unable to relate Algebraic concept with Kinematics concepts or find similarity between them especially in terms of graphing and graph skills. Terminology also seems to be an integral contribution to their comprehension of Kinematics graphs. They were unable to define concepts in Kinematics graphs in order to read, plot, analyse and interpret data and graphs, meaning that they were struggling to deduce meaning and information from these data and graphs.

Both Kinematics (Physics) and Algebraic (Mathematics) functions should place more emphasis on the context (interpretation) of graphs in order to improve learning and knowledge transfer. Finding the meaning of graphs and of their characteristics (such as slope, area under the graph) seems to be one of the most challenging areas of graph analysis for these respondents, as evidenced by the study of learners' difficulties with graphs. Another observation, and/or argument we have derived from this study is that, that learners must comprehend graphs during instruction, learn about and debate their meaning through peer cooperation, and, if at all possible, relate graphs to actual examples of motion (for example through the use of motion detectors).

Although it appears that there is not much knowledge transfer from Algebra to Kinematics, this may be because learners do not recognize the similarities between some Algebraic and Kinematics problems. This calls more for reflection of what high school Physics (Physical Science) educators need to do before dwelling into the Kinematics and its graphs concepts. Both the curricula of Mathematics and Physical Science need to be reviewed to accommodate the introductions of what concepts and knowledge is and will be required from Algebra (Mathematics) to Kinematics (Physics).

This conforms with previous studies (McDermott et al., 1987; Redish et al., 2015) that Mathematics is the language and tool for problem-solving in Physics. It is in light of the above therefore that the researcher recommends that the conceptual understanding and interpretation of Kinematics (Physics) and Algebra (Mathematics) quantities by learners, as well as the development of better connections between the two disciplines, are all critical areas for educators to focus on.

## References

- [1] Beichner, R. J. (1990). The effect of simultaneous motion presentation and graph generation in a Kinematics lab. *Journal of Research in Science Teaching*, **27**, 803–815.
- [2] Bosman, L., 2006. The value, place and method of teaching natural science in the foundation phase (Doctoral dissertation, University of South Africa).
- [3] Beichner, R.J. 1994. Testing learner interpretation of Kinematics graphs. *American journal of Physics*, **62**(8): 750-762.
- [4] Brasell, H. M. & Rowe, B. M. (1993). Graphing skills among high school Physics learners. *School Science and Mathematics*, **93**(2), 63–69
- [5] Canham, M. and Hegarty, M., 2010. Effects of knowledge and display design on comprehension of complex graphics. *Learning and instruction*, **20**(2), pp.155-166.

- [6] Cen, S.H. and Newman, P., 2019, May. Radar-only ego-motion estimation in difficult settings via graph matching. In 2019 International Conference on Robotics and Automation (ICRA) (pp. 298-304). IEEE.
- [7] Ellis, S.M., & Steyn, H.S. (2003). Practical significance (effect sizes) versus or in combination with statistical significance (p-values). *Management Dynamics* **12**, 51–53.
- [8] Freitas, I.M., Jiménez, R., Mellado, V. (2004). Solving Physics problems: The conceptions and practice of an experienced teacher and an inexperienced teacher. *Research in Science Education* **34**, 113–133.
- [9] Hermida, A., 2016. Social media and the news. *The SAGE handbook of digital journalism*, pp.81-94.
- [10] Lemmer, M., 2013. Nature, cause and effect of learners' intuitive conceptions regarding changes in velocity. *International Journal of Science Education*, **35**(2), pp.239-261.
- [11] Lemmer, M. and Gunstone, R., 2016, July. Physical models: A crucial link between reality and mathematical models. In SAIP Conference, University of Cape Town, South Africa.
- [12] McDermott, L. C., & Redish, E. F. (1999). Resource letter: PER-1: Physics education research. *American Journal of Physics*, **67**, 755.
- [13] McDermott, L.C., Rosenquist, M.L. and Van Zee, E.H., 1987. Learner difficulties in connecting graphs and Physics: Examples from Kinematics. *American Journal of Physics*, **55**(6), pp.503-513.
- [14] Mitnik, R., Recabarren, M., Nussbaum, M. and Soto, A., 2009. Collaborative robotic instruction: A graph teaching experience. *Computers & Education*, **53**(2), pp.330-342.
- [15] Moyo, N.M., 2020. Mathematical difficulties encountered by Physics learners in Kinematics: a case study of form 4 classes in a high school in Botswana (Doctoral dissertation, Stellenbosch: Stellenbosch University).
- [16] Nwosu, M., 2019. Youth entrepreneurship among university graduates in Anambra, Nigeria (Doctoral dissertation, Walden University).
- [17] Phage, I.B., 2015. An analysis of learners' knowledge of graphs in Mathematics and Kinematics. Masters dissertation, North-West University.
- [18] Phage, I.B., Lemmer, M. and Hitge, M., 2017. Probing factors influencing students' graph comprehension regarding four operations in Kinematics graphs. *African Journal of Research in Mathematics, Science and Technology Education*, **21**(2), pp.200-210.
- [19] Pietrocola, M. (2008). Mathematics as structural language of physical thought. In M. Vicentini & Sassi, Elena (Hrsg.), *Connecting Research in Physics Education with Educator Education* volume **2**, ICPE – book (Bd. 2).
- [20] Planinic, M., Milin-Sipus, Z., Katic, H., Susac, A. and Ivanjek, L., 2012. Comparison of learner understanding of line graph slope in Physics and Mathematics. *International journal of science and Mathematics education*, **10**(6), pp. 1393-1414
- [21] Rankhumise, M.P. and Raphoto, M.S., 2014. The Effect of Inquiry-Based Teaching-Learning Sequence in Ameliorating Alternative Conceptions and Conceptual Difficulties of Conservation of Mechanical Energy. *Mediterranean Journal of Social Sciences*, **5**(15), pp.366-380.
- [22] Redish, E.F. (2005) Problem solving and the use of Mathematics in Physics courses. *Proceedings of the Conference, World View on Physics Education in 2005: Focusing on Change*
- [23] Redish, E.F. and Kuo, E., 2015. Language of Physics, language of math: Disciplinary culture and dynamic epistemology. *Science & Education*, **24**(5), pp.561-590.
- [24] Semela T., 2010. Who is joining Physics and why? Factors influencing the choice of Physics among Ethiopian university learners. *International Journal of Environmental & Science Education* Vol. **5**, No. 3, July 2010, 319-340
- [25] Susac, A., Bubic, A., Kazotti, E., Planinic, M. and Palmovic, M., 2018. Learner understanding of graph slope and area under a graph: A comparison of Physics and nonPhysics learners. *Physical Review Physics Education Research*, **14**(2), p.020109.
- [26] Stokes, M.E., Davis, C.S. and Koch, G.G., 2012. *Categorical data analysis using SAS*. SAS institute.
- [27] Uhden, O., Karam, R., Pietrocola, M. and Pospiech, G., 2012. Modelling mathematical reasoning in Physics education. *Science & Education*, **21**(4), pp.485-506.
- [28] Woolnough, J. (2000). How do learners learn to apply their mathematical knowledge to interpret graphs in Physics? *Research in Science Education*, **30**, 259–267
- [29] Zwickl, B.M., Hu, D., Finkelstein, N. and Lewandowski, H.J., 2015. Model-based reasoning in the Physics laboratory: Framework and initial results. *Physical Review Special Topics-Physics Education Research*, **11**(2), p.020113.

# Using a Mobile Kibble Balance to explain Physics principles in Education

**LF Mndebele, TG Mametja, AE Karsten, C Sonntag, M Sibisi (National Metrology Institute of South Africa)**

Address: CSIR Campus, Building 5, Meiring Naude Road, Brummeria Pretoria 0182, South Africa  
E-mail Address: [lmndebele@nmisa.org](mailto:lmndebele@nmisa.org);

**Abstract.** In metrology, a Kibble balance is an instrument used by metrologists to measure the kilogram which is the SI unit for mass. There are several physics principles used in the operation of this instrument – namely electromagnetism, classical mechanics, electrostatics, electricity, optics, materials science, and metrology. The basis of this investigation is on all these physics disciplines applied for the functionality of the Kibble balance. The National Metrology Institute of South Africa (NMISA) developed a miniature version of the Kibble balance with 3D printed mechanical parts, referred to as the Mobile Kibble Balance (MKB). This version serves the same purpose as a Kibble balance but has less accuracy and precision. Detailed, uncomplicated explanations for all the mechanisms involved in operating the MKB are given. This paper demonstrates the educational value of the MBK in teaching physics and promotes metrology in the community.

## 1. Introduction

A Kibble balance (originally known as a Watt Balance) is an instrument used by metrologists to realize the kilogram with high accuracy. Like most balances, it needs a certain force to counter another force: Thus, an electromagnetic force induced in a current carrying coil immersed in a magnetic field is used to balance out the weight of a test mass.



Figure 1: Kibble balance model of NIST (National Institute of Standards and Technology)

In this paper, the NMISA MKB is used to demonstrate the Kibble balance’s core operation modes for better visualization and understanding. A discussion of the physics principles applied in the MKB and suggestion on how to integrate the instrument in modern education are also given.

**2. NMISA’s mobile Kibble balance and functionality**

A Mobile Kibble balance (MKB) serves the same purpose as a Kibble balance but is a much simplified and less precise version of it. The MKB is used to demonstrate how the actual Kibble balance realizes the kilogram or calibrates mass. In Figure 2(a), the main components of an MKB system are depicted.

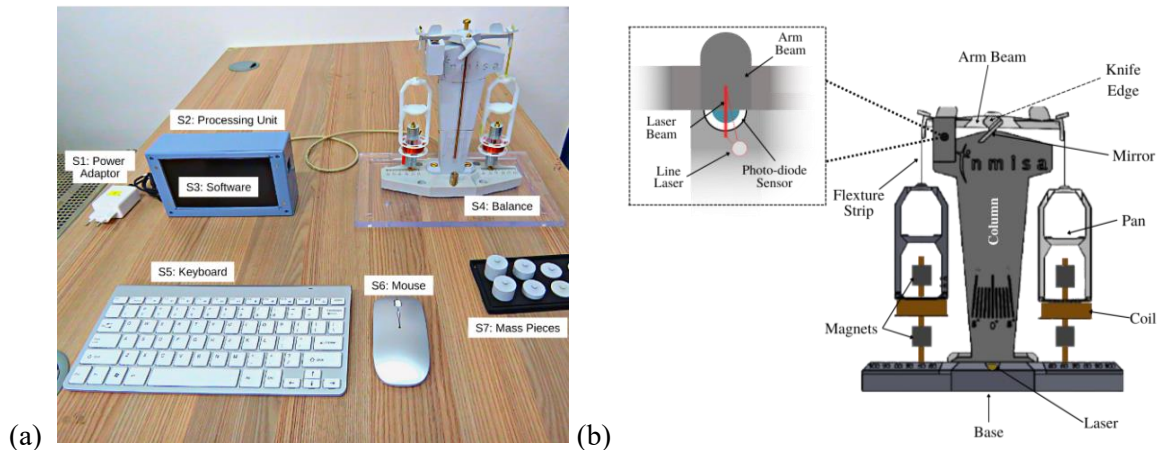


Figure 2: (a) All components that make up the mobile Kibble balance system. (b) A labelled diagram of the balance.

There are two basic operation modes for the MKB – (1) weighing (or force) mode and (2) velocity (or calibration) mode. Before performing any measurements, a driver coil is chosen. The coil will be supplied with current as needed per operation mode requirement. In the weighing mode, a test mass is placed on a pan attached to the coil with a current-carrying wire emersed in a magnetic field (measurement coil). When energized, the measurement coil induces an electromagnetic force that counters the weight of the test mass. It would have been ideal to simply use  $mg = IBL$  (2.1) as a working equation, where  $I$  is the current needed to counter the test mass’s weight,  $B$  is the magnetic field strength and  $L$  is the length of the wire. However, it is challenging to accurately obtain the  $B$  and  $L$  values during measurements.

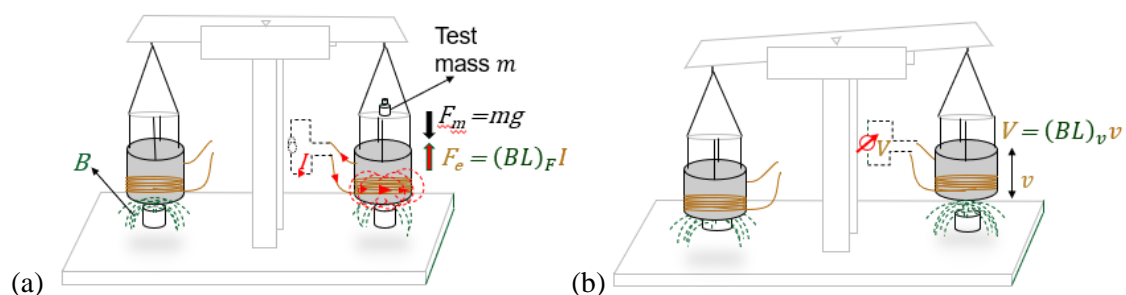


Figure 3: (a) Illustrates the weighing mode of operation. (b) Illustrates the velocity mode of operation.

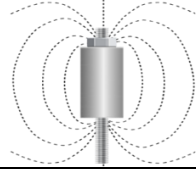
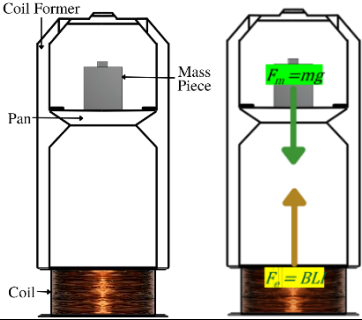
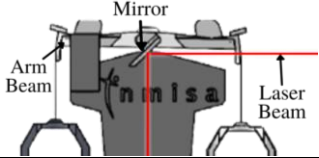
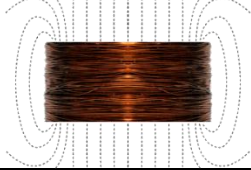
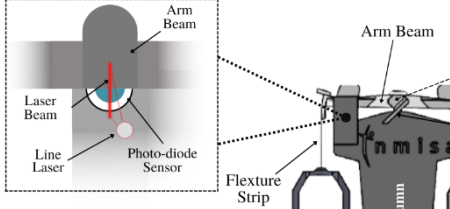
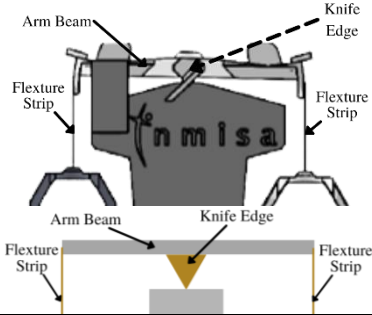
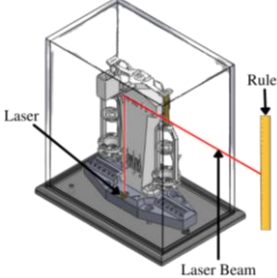
To take care of this we need the velocity mode. This is because it also has these quantities appearing in its working equation i.e.,  $V = vBL$  (from Faraday’s law), where  $V$  is the induced voltage and  $v$  the speed of the coils. The velocity mode can be viewed as a second step in taking measurements with a mobile Kibble balance. Here, the driver coil is supplied with a sinusoidal signal that in turn makes the balance’s coils alternate in a sinusoidal motion at constant average speed  $v$  [2]. Voltage,  $V$ , is thus induced in the coils due to the change in magnetic flux as described by Faraday’s law of induction [3].

In a final step the  $B$  and  $L$  are eliminated, using working equations obtained from the weighing and velocity mode i.e.,  $mg = IBL$  (2.2) and  $V = BLv$  (2.3) to get  $m \approx \frac{VI}{gv}$  (2.4) where  $g$  is the earth’s gravitational acceleration and  $m$  the mass of the test mass. The final approximation is only valid if one

uses the same driver coil for the two modes [2]. Notice that this final expression is free of  $B$  and  $L$  as desired.

### 3. Physics Principles Applied in the Mobile Kibble Balance

Table 1: A table summarizing the physics principles from the MKB mechanical parts with their functions

Name	Part of the system	Function	Physics Principle
1. Magnet		Provides magnet field to coils	Magnetism (Magnetic field)
2. Coil former pans		Platform for mass pieces	Classical Mechanics (Forces)
3. Mirror		Reflects laser light to measure ruler	Optics (Light reflection)
4. Coil wires		Carry current and induce electric field	Electrostatics (Current-carrying conductors)
5. Line laser		System's equilibrium sensing	Optics (Light polarisation)
6. Arm beam and knife edge		Designed for balance	Classical Mechanics (Forces)
7. MKB		Mass calibration	Metrology (Physical Metrology)

This section is the meat of the investigation where the basic physics principles governing the operation of the MKB are clearly summarized (Table 1). Touching on classical mechanics, optics, magnetism, electrostatics, and metrology, this is an ideal educational tool for a physics educator or student. However, before recommending ways to integrate the MKB in a classroom, reasons why physics' teaching methods need to be improved are discussed.

#### 4. Link to Education

With all the theoretical implications above, it is now time to highlight reasons why including a MKB in a classroom would be effective and the specific areas in physics where improvements can be made. In a case study conducted by the University of Liverpool in 2003, the reason why fewer secondary students were interested in physics than in biology was investigated. This investigation involved 317 physics students from six comprehensive secondary schools in Liverpool [1].

The university used short questionnaires to collect data from the same sample of students. A closed-form item was used to ask if students found physics 'very interesting', 'boring' or 'neither interesting nor boring'. Next, in an open-form item, the students were required to substantiate their previous answer with any number of reasons. From that case study the specific areas in the discipline which the uninterested students expressed to be boring are evaluated [1]. In the discussion of results subsection, the link between practical and theoretical learning is made and later we propose a few ways in which the MKB can be used practically in a classroom.

##### 4.1 Results from the case study

Tables 1 to 3 are the results obtained by the University of Liverpool in their investigation as introduced in the beginning of this section. *Disclaimer: we took interest in the following data (Tables 1 to 3) from a paper published by the University of Liverpool as cited in this section.*

Table 2: A table with proportions of the students considering physics boring, interesting or neither

How students find physics	Males (%)	Females (%)	All (%)
Very interesting	8	4	6
Interesting	28	13	20
Neither interesting nor boring	26	25	26
Boring	20	29	25
Very boring	18	20	24

Table 3: A table with categories of reasons for why students find physics boring and their proportions

Category of reason	Percentage of sample (%)
Difficult/hard subject	48
Do not enjoy subject	30
Content of subject	20
Subject irrelevant	14
Subject too easy	11
Too little practical work	7
Subject repetitive/predictable	6

Table 4: A table with the specific content of physics found boring or interesting and their proportions

Specific content of physics found boring or interesting	Boring (%)	Interesting (%)
Mathematical aspects	15	12
Electricity	3	8
Energy	1	8
Forces	2	5
Solar system/universe	-	6
Circuits	-	4
Nuclear energy	-	3
Magnetism	-	3
Colour/spectrum	-	1

**Note:** Percentages may total more than 100% because individual students offered more than one reason and percentages may not total exactly 100% due to rounding. Total number of students who participated, n = 317.

#### 4.2 Discussion of results from case study

As seen in Table 2, about 49% of the 317 students found physics to be either boring or very boring. This alarming percentage alone could justify for the need to improve the way in which teachers present physics in schools.

The University of Liverpool further investigated to see what the reasons were for students to find physics uninteresting. As a result, the reasons were then grouped into categories as seen in Table 3. Further investigations to gauge the effectiveness of the MKB in dealing with the reasons offered by the students can be made.

These reasons only highlight the problems learners are facing in physics as a whole and not necessarily the concerns in specific areas of the study. Therefore, to put a pin to the problem, the university then took the investigation a step further to get the specific areas of physics that were uninteresting to students. According to Table 4, there are four areas listed that the MKB touches on – these are ‘Forces’, ‘Magnetism’, ‘Color/Spectrum’ (Optics) and ‘Electricity’ (Electrostatics). Therefore, considering these results and the summary from the *Physics Principles Applied in the MKB* section, it can be inferred that a substantial number of areas in physics is touched on by the MKB.

This offers physics educators an opportunity to practically demonstrate multiple concepts that they teach. According to Robin Miller who did a study in the role of practical work in the teaching and learning of science, not only can practical work make learning more interesting, but it can develop students’ scientific knowledge. However, to do this there are a few requirements to ensure effectiveness. Firstly, the educators must clearly and concisely define the objectives of the practical task, then plan an explicit strategy that will make students think about the concepts while doing the practical task to create a link between the task and scientific knowledge [5].

Jan Wrenn and Bruce Wrenn of Andrews University re-enforce this idea of practical learning. They did a study on enhancing learning by integrating theory and practice. Using a strategy that compels both students and teacher to assume the role of both teacher and student in separate scenarios. These scenarios included both learning and applying (practising) what has been taught. They found that all participants maximised gaining knowledge through learning, reflecting, interacting, and applying what was learned. The only difficult thing to measure was which party learned more since both the teacher and learners gained knowledge [6]. Therefore, the MKB provides an opportunity for practical learning of physics in schools. The effectiveness of improving learning by introducing the MKB in a classroom can be measured through implementation and evaluating changes in future investigations.

### 5. Prescriptions for integrating a MKB in modern education

This section discusses ways in which teachers can use the MKB in a modern classroom as an attempt to enhance the experience of learning physics. Analogous to having a human skeleton in a biology class or chemicals in a chemistry lab, an MKB can be a prominent teaching tool in a physics classroom. One of the key aspects of this tool is that it touches more than one area of the subject, thus making it multi-purpose in application.

#### 5.1. Education levels recommended for MKB use

From the commencement of the study of physics it is important that students grasp its concepts properly. Hence it is recommended that the MKB gets integrated in a classroom from the first year of learning physics – grade 10 in South Africa. It can be used as an apparatus for experiments or a visualization aid for concepts to improve learning [4].

#### 5.2. Possible experimental projects

As shown under the *Link to Education* section, the MKB has a great span over physics. One can only lack imagination when it comes to the physics projects that can be curated for students using the MKB. In this section, we suggest a few of these projects without imposing limitations to any other ones.

Table 5: A table with proposed investigations for practical tasks using the MKB or its components and their descriptions

Proposed investigation	Description
<i>Balancing forces</i> (Classical mechanics)	In this project, students can explore the concept of weight using the balance and mass pieces. <i>Mass calibration (Application - Metrology)</i> ; Traditional calibration of mass (assigning mass values to mass pieces) can be an extra step for their investigation.
<i>Current carrying coils</i> (Electromagnetism)	The classic right-hand rule is a famous convention in physics, but truth be told it takes some imagination to visualize the result of what happens when we have a current-carrying conductor. This is where the MKB comes in. Electromagnetic force behavior can be studied using the coils of the balance. Balancing the electromagnetic force with a mass piece's weight can be an addition to this project. Coil properties can also be investigated, such as the number of coils, wire thickness and wire material.
<i>Magnetic field properties investigations</i> (Magnetism)	Using the MKB's magnets, students can study the properties of magnets and their fields. This can be further visualized using the magnetic field lines sketches. The concepts of repulsion and attraction can also be seen.
<i>Light reflection investigations</i> (Optics)	<b>Warning: Lasers can lead to blindness; the right goggles must be worn as a safety precaution.</b> The MKB has lasers that can be used for optics observations like light reflection. The laser in the base (see <i>Table 1, no. 7</i> ) can also be used to study how light behaves in other media, for example light refraction.
<i>Determining the experimental value of Planck constant</i> (Application – Metrology)	As an application task, learners can work towards obtaining the Planck constant. The following may be the outline used when curating an investigation: From the weighing and velocity mode's working equation (equations 2.2 and 2.3 respectively). The Planck constant can then be approximated to be $h = \frac{(BL)_w}{(BL)_v} h_{conv} \quad (5.1)$ where $(BL)_w$ the value for $(BL)$ from weighing mode, $(BL)_v$ the $(BL)$ value from the velocity mode and $h_{conv}$ is the conventional Planck constant i.e., $h_{conv} = 6,62607015 \times 10^{34}$ Js, (Refer to <i>section 2</i> for description of symbols)

## 6. Conclusion

This paper has discussed the basic functions of the MKB and its potential for addressing the existing gaps in physics education. It was shown how using an MKB as a visualization tool or experiment apparatus can potentially facilitate the teaching and assessing of physics learners. The instrument is particularly advantageous because it explicitly handles multiple fields in physics which are relevant to school or undergraduate curricula. Lastly, since this is an instrument adapted from an actual instrument used in metrology (the Kibble balance), it does bring about awareness for metrology itself.

## 7. Investigation recommendations

There exists great potential for further study in this field. Additional research could include obtaining feedback from learners to assess the impact of the ideas proposed in this paper. A broader survey can be done to observe if the gaps found in the Liverpool case study apply to other school curricula in different regions. Considering the growing novelty of 3D printing technology, the 3D printed parts of the MKB can be discussed and improved to ensure cost effectiveness and improved functionality of the system. These are a few of many recommendations possible to scale up this investigation.

## References

- [1] Why aren't secondary students interested in physics?, *Department of Physics, University of Liverpool* **32**, 4 (2003); doi 0031-9120/040324
- [2] A LEGO Watt balance: An apparatus to determine a mass based on the new SI, *American Journal of Physics* **83**, 913 (2015); doi 10.1119/1.4929898
- [3] Kinsler, Paul. Faraday's Law and Magnetic Induction: Cause and Effect, Experiment and Theory. *ResearchGate* **2**, 148-161 (2020); doi 10.3390/physics2020009
- [4] Shabiralyani, G., & Hasan, S. K. Impact of Visual Aids in Enhancing the Learning Process Case Research: District Dera Ghazi Khan. *Journal of Education and Practice*, 226-233 (2015).
- [5] Robin Millar, The role of practical work in the teaching and learning of science, *Department of Educational Studies, The University of York*, 1-24 (2004)
- [6] Jan Wrenn and Bruce Wrenn, Enhancing Learning by Integrating Theory and Practice, *International Journal of Teaching and Learning in Higher Education, Andrews University* **21**, 2 (2009)



DIVISION

F

APPLIED PHYSICS

# Synthesis and characterization of adsorbent biopolymer composite pellets and their potential application for VOCs removal from pharmaceutical effluents

NP Simelane<sup>1</sup>, JKO Asante<sup>1</sup>, PP Ndibewu<sup>2</sup>, LL Sibali<sup>3</sup>

<sup>1</sup> Department of Physics, Faculty of Science, Tshwane University of Technology, Private Bag X680, 175 Nelson Mandela Drive, Arcadia, Pretoria 0001, South Africa.

<sup>2</sup> Department of Chemistry, Faculty of Science, Tshwane University of Technology, Private Bag X680, 175 Nelson Mandela Drive, Arcadia, Pretoria 0001, South Africa.

<sup>3</sup> Department of Environmental Sciences, College of Agriculture and Environmental Sciences, University of South Africa, Florida Campus, South Africa.

E-mail: [AsanteJKO@tut.ac.za](mailto:AsanteJKO@tut.ac.za)

**Abstract.** This study focussed on investigating the effectiveness of using a newly prepared pelletized biopolymeric composite material for the adsorption of VOCs pharmaceutical effluents. Composite materials have received a great deal of scientific and technological attention due to the potential benefits associated with their unique properties, such as ease of preparation, high durability, good recyclability and high adsorption capability. In this study, the biosorbent was created by blending/coating a synthetic polymer (carboxen-1000) with activated *Moringa oleifera* seed husks (MOSH) under optimized conditions to create a new biopolymeric composite material. This material was then tested for its effective removal of three selected VOCs (BTE: benzene, toluene and ethylbenzene) in pharmaceutical effluents. Advanced techniques like FTIR, SEM, XRD, N<sub>2</sub>-BET and TGA were used to characterize the material. A recovery efficiency of >98% was recorded for the BTE. The material was also still effective after being used in 3 cycles.

## 1. Introduction

Water pollution caused by toxic organic pollutants found in pharmaceutical effluents is currently a major threat to public health not only in South Africa, but also around the world. Volatile organic compounds (VOCs) such as benzene, toluene and ethylbenzene (BTE) are among the most toxic in this group of compounds, thus, are referred to as emerging dangerous environmental pollutants carried along by pharmaceutical effluents. Human exposure to these VOCs has been linked to the development of various diseases, including cancer (Amann et al., 2014).

To address this issue, the adsorption technique, which employs adsorbent materials such as activated carbons among others (Liew et al., 2018), has received considerable attention. However, traditional adsorbents typically have low adsorption capacity. As a result, biopolymeric composite materials, which combine the benefits of several materials, are gaining attention as potential materials for

addressing global challenges in water purification. Recently, agricultural wastes such as *Moringa oleifera* seed husks (MOSH) have been used in the preparation of these biopolymer composite materials. This is because they are inexpensive, biodegradable, and readily available, making them suitable for use even in developing countries. A study conducted by Ibrahim et al. (2022) reported that biopolymer composite materials have a high adsorption capacity of pollutants such as dyes and heavy metals during wastewater treatment.

Biopolymer composite pellets were created in this study by combining activated MOSH powder with a synthetic polymer (carboxen-1000) powder in an optimized ratio. The pellets were prepared using a Spark Plasma Sintering (SPS) instrument. The pellets were then characterized using a variety of techniques and tested for BTE removal from pharmaceutical wastewater samples.

## 2. Materials and methods

### 2.1. Materials

All chemicals and solvents used in this study were purchased from Sigma-Aldrich (Germany). The synthetic carboxen-1000 polymer was also purchased from Sigma-Aldrich (Germany). The *Moringa oleifera* seed husks (MOSH) were collected from a farm in Zvezda Game Resort, located in the North West province of South Africa.

### 2.2. Methods

#### 2.2.1. Preparation of the biopolymer composite pellets

Activated *Moringa oleifera* (MO) powder was prepared according to a method reported by Bezzera et al. (2020). The activated MO powder was blended with the synthetic polymer powder in optimized ratios; 5 wt%, 3 wt%, and 1 wt% synthetic polymer using a tubular mixer. The mixtures were consolidated by Spark Plasma Sintering (HPD 25, FCT System GmbH Germany) instrument in order to produce the pellets. The powders were loaded into a graphite die, 20 mm diameter and sintered using an optimized temperature and time of 300°C and 5 min., respectively. The mixed powders were uniaxial pressed at 50 Mpa at a heating rate of 100°C/min.

#### 2.2.2. Characterization of the synthesized pellets

The functional groups formed in the material were identified using FTIR. SEM, XRD and the N<sub>2</sub>-BET method coupled with Nitrogen gas were used to investigate the microstructure of the material produced. The thermal stability of the pellets was investigated using TGA.

#### 2.2.3. Batch adsorption studies on the prepared adsorbents

Preliminary experiments were conducted on the pellets in order to investigate the effect of contact time, initial pH, initial concentration and adsorbent dosage. This was not one of the objectives, but it was done to ensure the best possible working conditions for the adsorption studies. One of the primary goals of the study was to investigate the effect of adsorption temperature on the pellets.

Hydrogen chloride (HCl) and formic acid (HCO<sub>2</sub>H) were used to wash the pellets for regeneration and reuse.

## 3. Results and discussion

### 3.1. Characterization results

#### 3.1.1. FTIR analysis

The FTIR spectra of the synthesized biopolymer composite pellets before and after adsorption are shown in Figure 1. The presence of functional groups such as -OH (3680 cm<sup>-1</sup>), C-O stretching vibration (1033 cm<sup>-1</sup>) as well as carbonyl groups can be seen in the spectra. These identified functional groups all play a role during the adsorption process in agreement with similar findings reported in the literature (Ambaye et al., 2021). The FTIR spectra for before and after adsorption were compared to

demonstrate that indeed adsorption occurred and to identify which functional groups were responsible for the VOCs uptake.

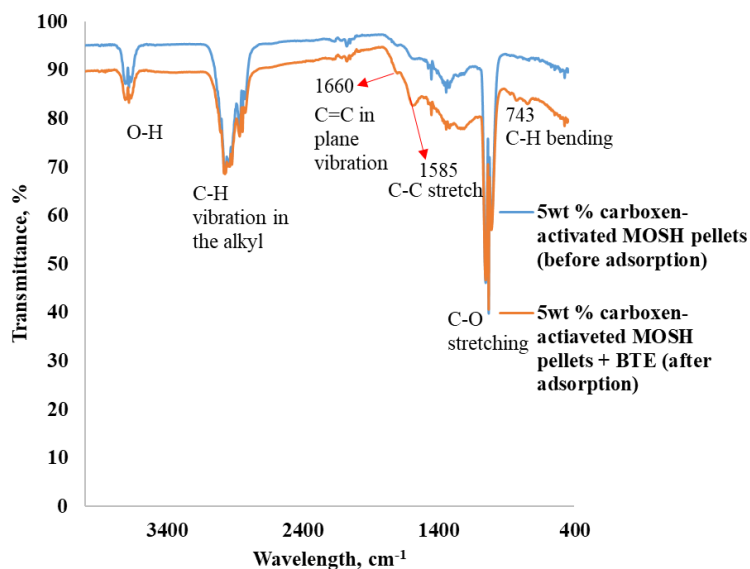


**Figure 1.** FTIR spectra of the synthesized biopolymer composite pellets before and after adsorption

### 3.1.2. SEM analysis

The SEM micrograph of the synthesized biopolymer composite pellets is shown in Figure 2. The pellets, as seen in the image, had a heterogeneous morphology with some well-defined pores. Because of their high porosity, these pellets would therefore make excellent adsorbents according to Avci et al. (2018).

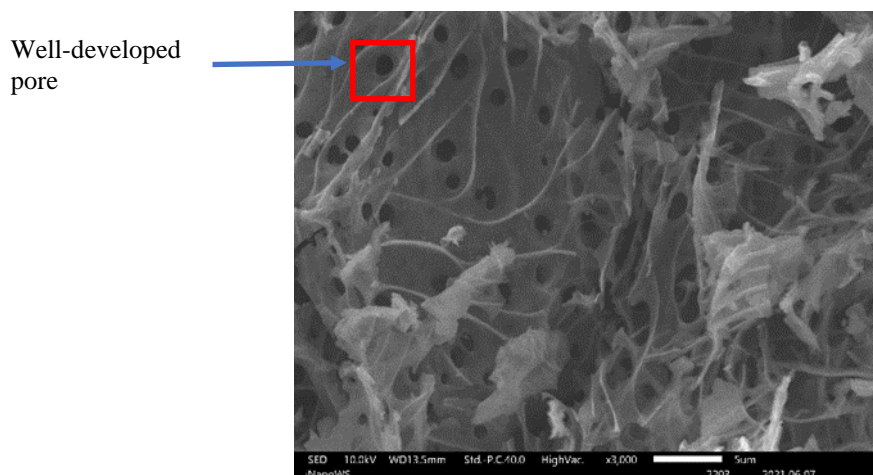


**Figure 2.** SEM image of the biopolymer composite 3000 magnification times

### 3.1.3. XRD analysis

The carboxen-1000 synthetic polymer structure (fig.3a) was very crystalline, as evidenced by the presence of sharp peaks, whereas the structure of activated MOSH (neat pellets powder) (fig.3b) was amorphous. The biopolymer composite pellets powder structure had a few sharp peaks due to the presence of the very crystalline carboxen-1000 synthetic polymer, but their overall structure was amorphous, similar to that of the matrix, which was activated MOSH.

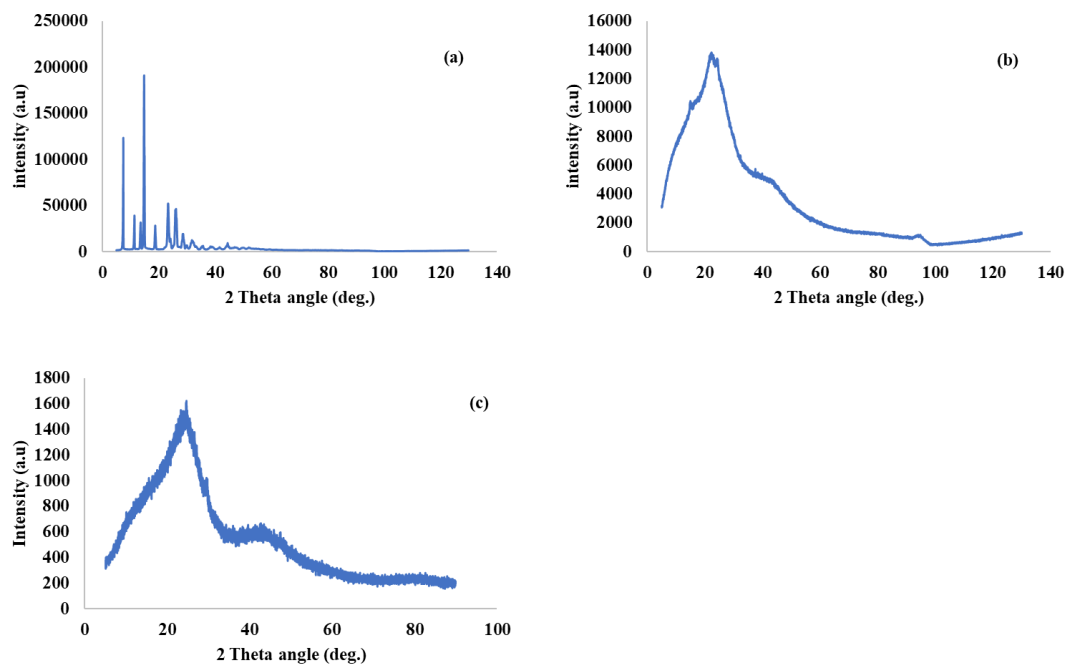


**Figure 3.** X-ray diffractogram of (a) carboxen-1000 powder, (b) activated MOSH (neat pellets powder) and (c) the synthesized carboxen-activated MOSH pellets powder

#### 3.1.4. N<sub>2</sub>-BET analysis

The N<sub>2</sub>-BET method was used to study the micro and mesoporous structure of the pellets in a nitrogen environment. Table 1 compares the particulate structural properties of biopolymer composite pellets to those of neat pellets. The batch adsorption studies revealed that the composite pellets had a higher adsorption capacity than the neat pellets. This could be attributed to their greater specific surface area, pore volume, and smaller pore size (Table 1). Adsorption capacity increases with increasing specific surface area and pore volume (Ma et al., 2014).

**Table 1.** Results of the relative densities and micro hardness of sintered sample.

Sample	Specific surface area (m <sup>2</sup> .g <sup>-1</sup> )	Total pore volume (cm <sup>3</sup> .g <sup>-1</sup> )	Average pore size (nm)
Neat activated MOSH pellets	1.403	0.027	2.259
5 wt.% carboxen-activated MOSH pellets	3.497	0.033	1.927

Not included in Table 1 are the results of 1- and 3-wt% carboxen-activated MOSH pellets. Both have their specific surface areas as well as their total pore volume lying between the values recorded between the neat and the 5 wt.%.

#### 3.1.5. TGA analysis

TGA was then used to investigate the thermal stability of the 5 wt.% synthesized biopolymer composite pellets (sample with best adsorbancy). Figures 4a and b show that the pellets degraded at high temperatures, indicating that they are very thermally stable. The first (low) degradation stage occurred around 428 °C, followed by the second (large) degradation stage at 628 °C. A similar study (Moussout et al., 2016) found that the degradation of their adsorbents occurred at temperatures ranging from 500 to 600 °C, implying that these synthesized biopolymer composite pellets have greater thermal stability. This implies that the synthetic polymer (Carboxen-1000) increased the bond strength of the composite pellets and resulted in a low decomposition rate, making them more thermally stable.

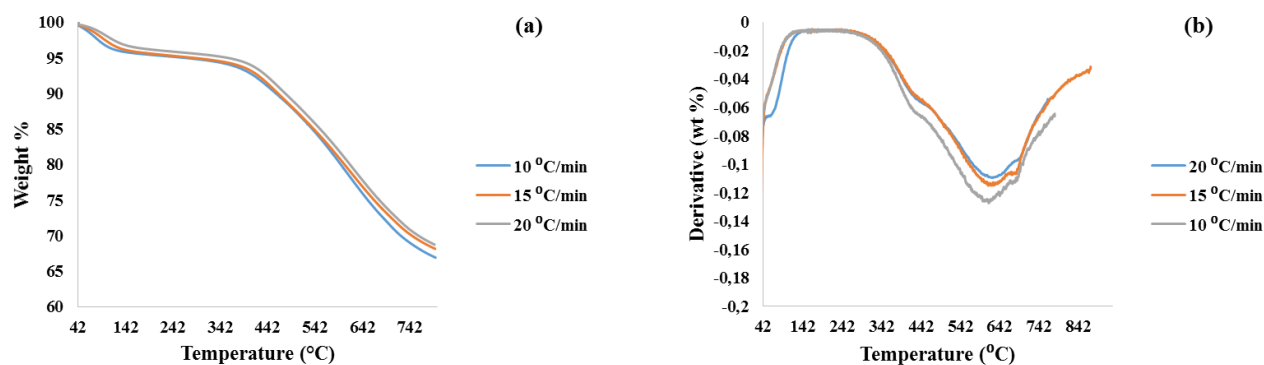


**Figure 4.** (a) TG analysis and (b) derivative thermogravimetry (DTG) thermographs of the 5 wt.% Carboxen-activated MOSH biopolymer composite pellets respectively at different heating rates of 10, 15, and 20 °C/min.

### 3.2. Batch adsorption results

#### 3.2.1. Effect of temperature

The effect of environmental temperature on the pellets was studied at various temperature. Figure 5 shows that the highest removal of BTE occurred at a temperature of 30 °C. Increasing the temperature from 25 to 30 °C increased the adsorption capacity from around 95 % to approximately 99 %. From 30 to 40 °C, the adsorption capacity decreased indicating that the adsorption process is exothermic (Albadarin et al., 2012).

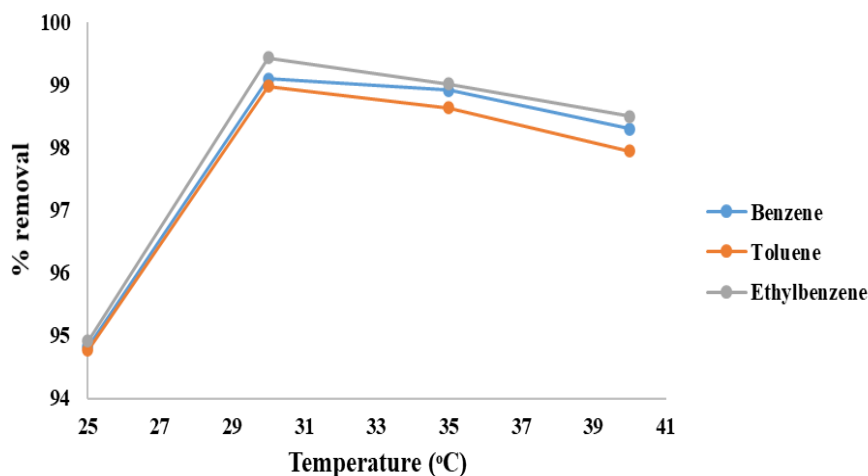


**Figure 5.** Effect of temperature on 5 wt.% biopolymer composite pellets for the removal of BTE

### 3.2.2. Effect of time

Batch adsorption studies of BTE onto biopolymer composite pellets were carried out over a 4-hr period at four different temperatures. After 3 hrs, the highest removal rate was achieved.

The pellets were also regenerated and reused. The biopolymer composite pellets did not disintegrate and were capable of removing more than 90 % BTE even after three cycles of use or three adsorption cycles. The synthetic polymer acted as a scavenger during the adsorption process.

## 4. Conclusion

Biopolymer composite pellets were synthesized and effectively tested for removing three selected toxic VOCs namely: benzene, toluene and ethylbenzene, from pharmaceutical effluents. Characterization results revealed that these pellets contained useful functional groups, which play an important role during the uptake of VOCs. It was also revealed that they had a high surface area and good pore distribution, which are both beneficial during adsorption process. The pellets were very efficient because after batch adsorption studies, it was shown that they were able to remove more than 98 % of BTE from the wastewater samples. In addition, these pellets are economically efficient since they can be regenerated and reused several cycles (at least 3 times) before they become exhausted.

## References

- [1] Albadarin, A.B., Mangwandi, C., Ala'a, H., Walker, G.M., Allen, S.J. and Ahmad, M.N., 2012. Kinetic and thermodynamics of chromium ions adsorption onto low-cost dolomite adsorbent. *Chemical engineering journal*, 179, pp.193-202.
- [2] Amann, A., de Lacy Costello, B., Miekisch, W., Schubert, J., Buszewski, B., Pleil, J., Ratcliffe, N. and Risby, T., 2014. The human volatilome: volatile organic compounds (VOCs) in exhaled breath, skin emanations, urine, feces and saliva. *Journal of breath research*, 8(3), p.034001.
- [3] Ambaye, T.G., Vaccari, M., van Hullebusch, E.D., Amrane, A. and Rtimi, S., 2021. Mechanisms and adsorption capacities of biochar for the removal of organic and inorganic pollutants from industrial wastewater. *International Journal of Environmental Science and Technology*, 18(10), pp.3273-3294.
- [4] Avci, G., Velioglu, S. and Keskin, S., 2018. High-throughput screening of MOF adsorbents and membranes for H<sub>2</sub> purification and CO<sub>2</sub> capture. *ACS applied materials & interfaces*, 10(39), pp.33693-33706.

- 
- [5] Bezerra, C.D.O., Cusioli, L.F., Quesada, H.B., Nishi, L., Mantovani, D., Vieira, M.F. and Bergamasco, R., 2020. Assessment of the use of *Moringa oleifera* seed husks for removal of pesticide diuron from contaminated water. *Environmental technology*, 41(2), pp.191-201.
- [6] Ibrahim, N.A., Abdellatif, F.H., Hasanin, M.S. and Abdellatif, M.M., 2022. Fabrication, characterization, and potential application of modified sawdust sorbents for efficient removal of heavy metal ions and anionic dye from aqueous solutions. *Journal of Cleaner Production*, 332, p.130021.
- [7] Liew, R.K., Azwar, E., Yek, P.N.Y., Lim, X.Y., Cheng, C.K., Ng, J.H., Jusoh, A., Lam, W.H., Ibrahim, M.D., Ma, N.L. and Lam, S.S., 2018. Microwave pyrolysis with KOH/NaOH mixture activation: a new approach to produce micro-mesoporous activated carbon for textile dye adsorption. *Bioresource technology*, 266, pp.1-10.
- [8] Ma, Y., Zhou, Q., Li, A., Shuang, C., Shi, Q. and Zhang, M., 2014. Preparation of a novel magnetic microporous adsorbent and its adsorption behavior of p-nitrophenol and chlorotetracycline. *Journal of Hazardous Materials*, 266, pp.84-93.
- [9] Moussout, H., Ahlafi, H., Aazza, M. and Bourakhouadar, M., 2016. Kinetics and mechanism of the thermal degradation of biopolymers chitin and chitosan using thermogravimetric analysis. *Polymer Degradation and Stability*, 130, pp.1-9.

# Sol-gel derived and electrospun mesoporous TiO<sub>2</sub>: Effects of calcining temperature on the structure, morphology and surface area

DG Tsotetsi, MS Dhlamini and PS Mbule\*

Department of Physics, CSET, University of South Africa, Johannesburg,  
1710, South Africa

Email: [dieketsengklara96@gmail.com](mailto:dieketsengklara96@gmail.com)

**Abstract.** This work report the effect of calcining temperature on the structure, morphology and surface area of mesoporous TiO<sub>2</sub> using sol-gel and electrospinning methods. The particles solution was drop-cast on the glass substrate to make thin films and subsequently calcined at 350°C, 450°C and 550°C for 4hrs. Samples calcined at 550°C were identified to have clear porous morphology compared to other samples while using both sol-gel and electrospinning methods. The mixture of rutile and anatase phase was obtained with XRD technique whereas electrospun samples were more crystalline than sol-gel samples both calcined at 550°C. Nitrogen adsorption – desorption isotherms and Brunnauer–Emmet–Teller (BET) showed increased pore size and surface area for electrospun samples than sol-gel samples.

## 1. Introduction

The optimum scaffold and electron transport layer in perovskite solar cells (PSCs) has specifically been found to be mp-TiO<sub>2</sub> which has a longer optical light path and the capacity to reduce charge recombination [1]. The crystallinity of the mp-TiO<sub>2</sub> nanoparticles is necessary for efficient electron transfer and large pores are desired to enhance diffusion of charge carriers. Anatase, rutile, and brookite are the three main crystalline forms of TiO<sub>2</sub> that can be found in nature. Due of its many vacancies and imperfections that can trap electrons, anatase is advantageous in applications involving photocatalytic activity. When compared to anatase phase, rutile is the most stable crystalline type and has fewer flaws which readily encourage electron-hole recombination and make rutile a poorer photocatalytic movement. When the annealing temperatures are higher than 650°C, rutile is said to replace brookite, a known unstable crystalline phase of TiO<sub>2</sub> [2-4]. Sol-gel, hydrothermal, templates, and solvothermal methods are used to prepare TiO<sub>2</sub> in a variety of morphologies including zero-dimensional (micro/nanospheres), one-dimensional (rods, tubes, and nanowires), two-dimensional (films, layers, and sheets) and three-dimensional (porous spheres, urchin-like spheres) [5-8]. Among the different morphologies that are largely reported in the literature, mesoporous TiO<sub>2</sub> (mp-TiO<sub>2</sub>) architectures prepared with sol-gel followed by electrospinning technique promote porous materials which have recently attracted the attention in both fundamental and applied materials research [9]. Particularly for perovskite solar cells application where infiltration of perovskite materials into pores is a challenge. Therefore, it is important to explore different cost-effective synthesis methods and tune the parameters to evaluate the suitability of mesoporous TiO<sub>2</sub> in devices application, particularly, solar cells. In this study, we synthesized mp-TiO<sub>2</sub> particles by sol-gel method and thereafter electrospun the sol to form spherical porous particles with fiber-like structures. Subsequently, the particles were calcined at different temperatures of 350°C, 450°C and 550°C to evaluate the effects of calcining temperature on

the structure, morphology, porosity and surface area for possible application is photovoltaic devices such as perovskite solar cells.

## 2. Preparation of sol gel and electrospinning of mesoporous titanium dioxide

Sol-gel method was used to prepare mesoporous TiO<sub>2</sub> particles at room temperature. A precursor sol was prepared by the hydrolysis and condensation of titanium tetraisopropoxide (TTIP) in the presence of glacial acetic acid. In a typical sol-gel preparation, a fixed amount of 3 mL TTIP precursor was mixed in 50 mL of ethanol and stirred for 5 minutes. 20 mL of glacial acetic acid was added in TTIP solution and was kept stirring for 30 minutes at room temperature. In a separate beaker 5.6 g of Polyvinylpyrrolidone (PVP) was dissolved in ethanol and mixed in the TTIP solution while continuing to stir for 3 hrs. The prepared solution was transparent yellow and viscous enough for electrospinning process. During electrospinning, the sol flow rate was kept at 3 mL/hour, tip-collector distance was fixed at 12 cm and the transverse speed was set at 15.64 cm/min while syringe pump speed was set 0.200 mm/min. The applied voltage was maintained at 12 kV. In order to make thin films, electrospun nanoparticles were then gathered on aluminum foil, mixed with ethanol, and dropped onto a glass substrate. Following that, samples were calcined for 4 hrs at various temperatures of 350°C, 450°C, and 550°C in a muffle furnace that had been preheated. Obtained samples were films from sol-gel process then followed by films from electrospinning process and thus temperature effects on the structure, morphology, porosity, thermal stability and surface area were investigated. The thin films were then characterized using X-ray diffraction (XRD), field emission scanning electron microscopy (FE-SEM), Fourier Transform Infrared Spectroscopy (FTIR), and Volumetric Micrometrics Tristar II apparatus.

## 3. Results and discussion

### 3.1 XRD analysis

In Figure 1, the XRD pattern of the samples presented a relatively similar diffraction peaks for sol-gel samples compared with samples obtained after electrospinning process showing that the acquired samples are the mp-TiO<sub>2</sub> particles consisting of an intense rutile diffraction peak at approximately  $2\theta = 27^\circ$  and the anatase diffraction peaks at  $2\theta = 25^\circ, 37^\circ$  and  $48^\circ$ . An improved crystallinity was observed from electro-spun samples with an estimation of the phase ratio to be ~95% rutile and ~5% anatase, at 550°C calcining temperature which implies a stable rutile phase for electro-spun mp-TiO<sub>2</sub>. The estimated crystallite size for sol-gel samples was  $\sim 17.32 \pm 0.05$  nm while samples obtained after electrospinning process showed an increase of crystallite size to  $\sim 35.13 \pm 0.05$  nm at 550°C using the rutile peak at  $2\theta = 27^\circ$ . The crystallite size was estimated using Debye-Scherrer equation [10] indicated as follows:

$$D = K\lambda/\beta \cos \theta \quad (1)$$

where D is the crystallite size,  $\lambda$  the wavelength of the X-ray radiation ( $\lambda = 0.15406$  nm) for CuK $\alpha$ , K the constant ( $K = 0.89$ ) and  $\beta$  the full-width at half-maximum of ( $2\theta = 27^\circ$ ) peak.

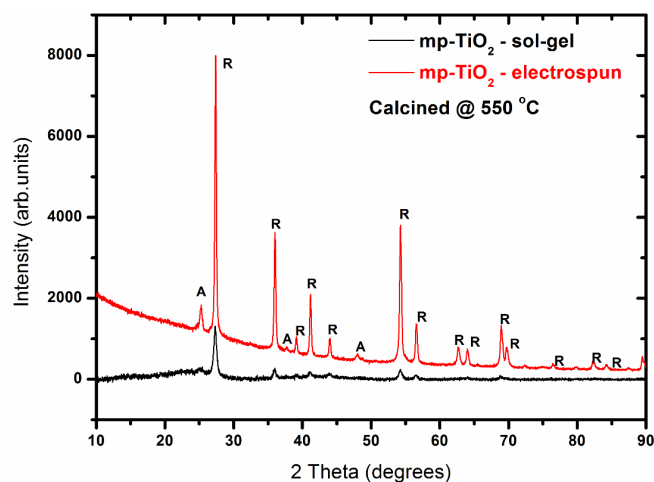
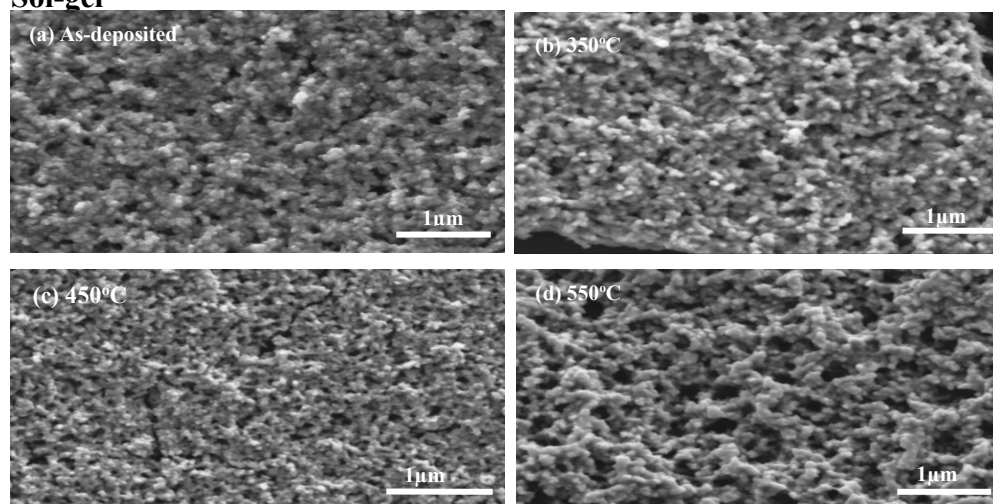


**Figure 1.** XRD patterns of mp-TiO<sub>2</sub> prepared by sol-gel and electrospun calcined at 550°C.

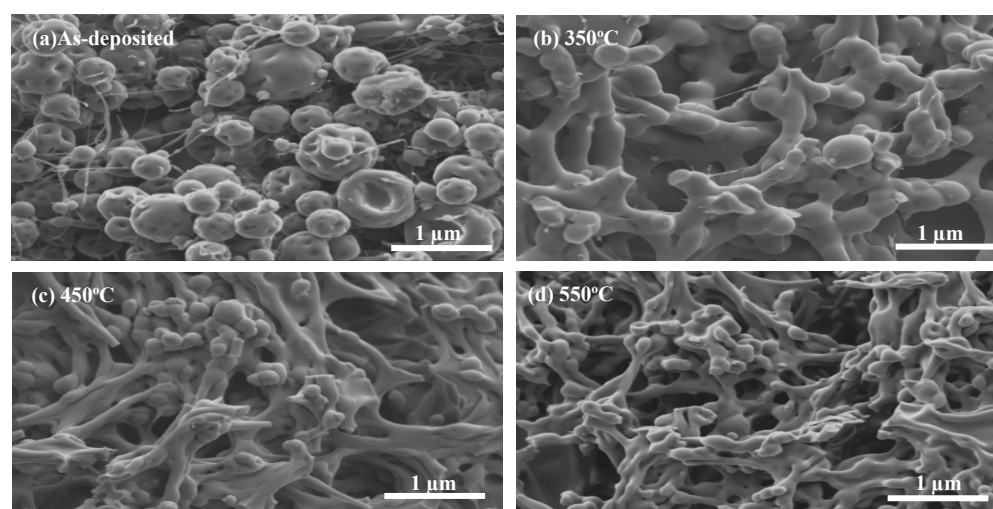
### 3.2 FESEM and particle size analysis

Figure 2(a-d) illustrates FESEM images and particle size analysis of mp-TiO<sub>2</sub> films prepared from sol-gel and those obtained after electrospinning process, respectively. For sol-gel samples, the porous morphology of the as-deposited mp-TiO<sub>2</sub> films was observed with the particle size around 0.017  $\mu\text{m}$ . As the calcining temperature was increased the pore size and particle size seemed to be improved from the calcining temperature of 350°C, 450°C and larger pores were observed when the calcining temperature was increased to 550°C. The particles which appeared to be spherical were observed to be uniform in shape, proving the efficient use of PVP as a capping agent. The particles also showed shape stability and uniformity even after being calcined at high temperature of 550°C which was  $\sim 0.024 \mu\text{m}$ . On the other hand, FESEM images of electro spun TiO<sub>2</sub> samples showed morphology of the as-prepared TiO<sub>2</sub> to have larger spherical particles ( $\sim 1.832 \mu\text{m}$ ) with irregular size pores and unaligned fibre-like structures. The calcination of the porous TiO<sub>2</sub> particles significantly transformed the surface morphology of the samples. As presented from the images, upon calcination at 350°C and 450°C the mesoporous morphology was observed, and spherical particles appears to be interconnected developing pores with irregular diameter size. Again, it is noticeable that the size of spherical particles is reduced and fiber-like structures have completely disappeared forming a smooth surface. As the calcining temperature is further increased to 550°C, the morphology appears to be loosely producing more non-

#### Sol-gel

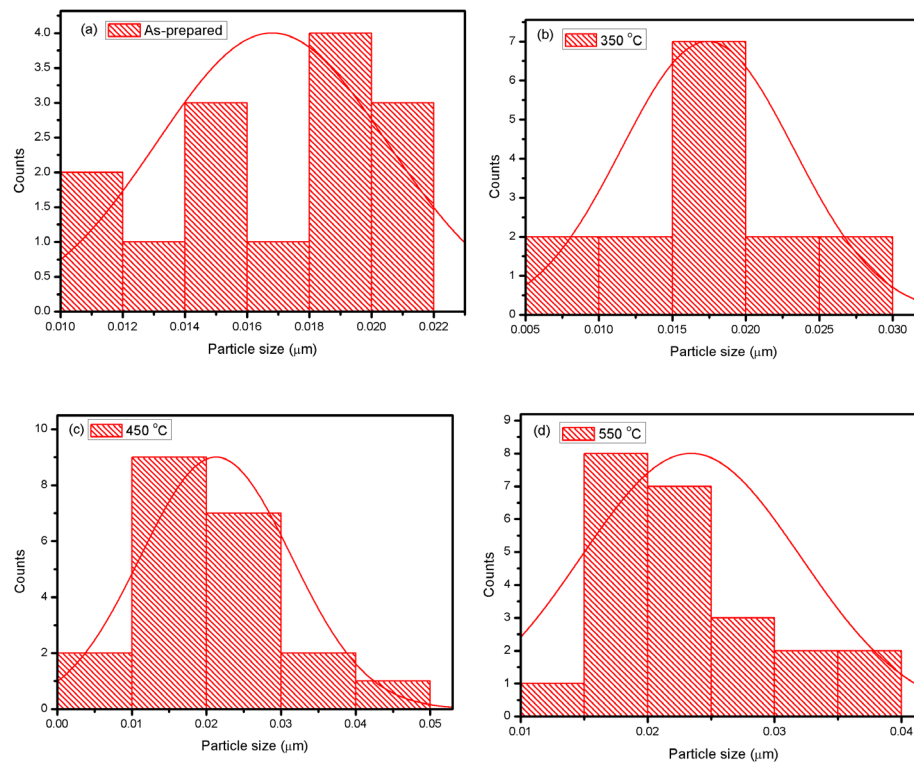


#### Electro spun



**Figure 2.1.** SEM images of mp-TiO<sub>2</sub> for (a) As-prepared, calcined at (b) 350°C, (c) 450°C and (d) 550°C from sol-gel derived and electro spun samples.

### Sol-gel



### Electro spun

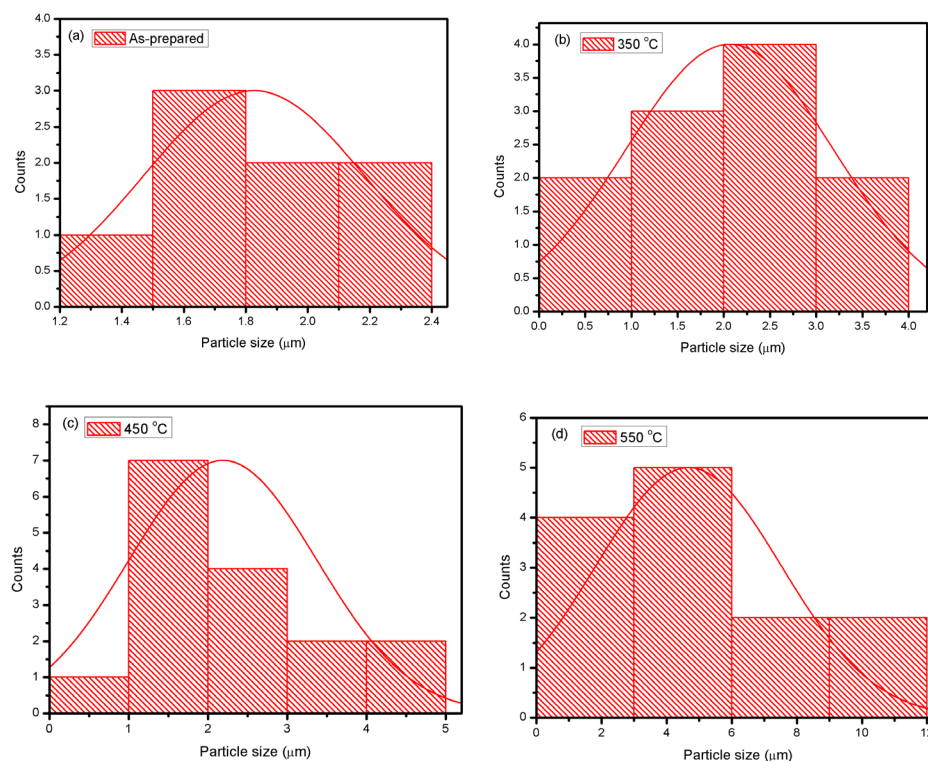


**Figure 2.2.** Particle size analysis of  $\text{mp-TiO}_2$  for (a) As-prepared, calcined at (b) 350°C, (c) 450°C and (d) 550°C from sol-gel derived and electrospun samples.

uniform pores. It is obvious that the calcining temperature promotes the pore formation and calcination at 550°C resulted in better pore formation. It has been reported elsewhere that, the highly porous material becomes a potential to be used as the electron transporting layer and also playing a role of allowing the sun penetration to the perovskite material in solar cells application [11].

### 3.3 BET and BJH analysis

The mesoporous characteristics of the TiO<sub>2</sub> particles were investigated by nitrogen (N<sub>2</sub>) adsorption-desorption isotherm, i.e. the nitrogen adsorbed volume against its relative pressure. Figure 3 depicts the N<sub>2</sub> adsorption and desorption isotherm patterns of the mp-TiO<sub>2</sub> samples prepared from sol-gel and electrospinning. The H3 type was obtained for sol-gel while H1 was observed on electrospun sample calcined 550°C indicating the mesoporous type whereas surface area, pore size, pore volume and average particle size were increased for electrospun sample compared to sol-gel sample as shown in Table 1.

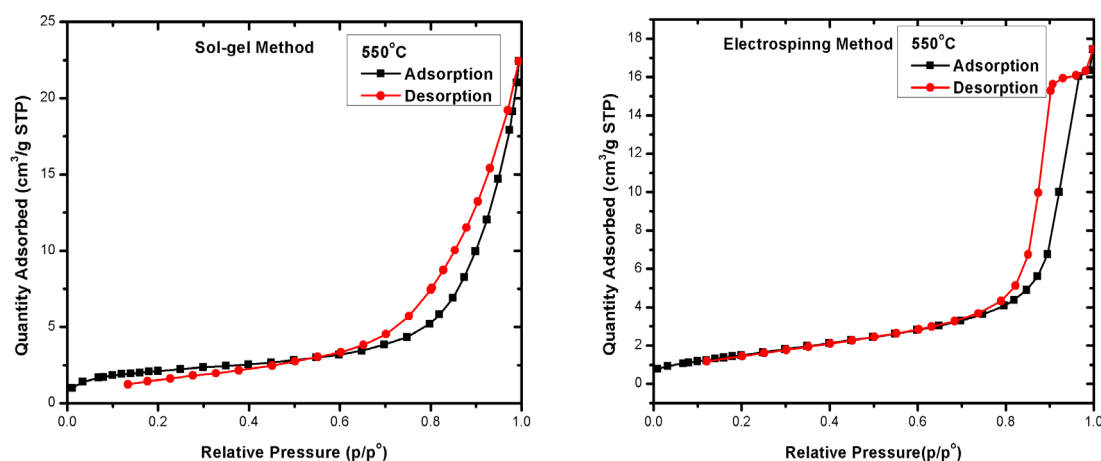


**Figure 3.** Nitrogen adsorption and desorption isotherm patterns and pore size distribution of the mp-TiO<sub>2</sub> for sol-gel and electrospun samples.

**Table 1.** Pore parameters of m-TiO<sub>2</sub> for as-prepared by sol-gel and electrospinning method.

Sample	Surface Area (m <sup>2</sup> /g)	Pore Size (nm)	Pore Volume (cm <sup>3</sup> /g)	Average Particle size (nm)
Mp-TiO <sub>2</sub> -sol-gel	5.83	0.03	17.78	820
Mp-TiO <sub>2</sub> -electrospun	7.32	0.06	18.51	1029

### 3.4 FTIR analysis

Further analysis of electrospun samples was performed and FTIR results are presented in Figure 4, for as-prepared and calcined mp-TiO<sub>2</sub>. The broad band observed at ~3395 cm<sup>-1</sup> and the band at ~2958 cm<sup>-1</sup> are attributed to the O – H hydroxyl groups and C– H stretching vibration, respectively, while the sharp band at ~1661 cm<sup>-1</sup> is allocated to the C=O in the amide group in PVP polymer. The band at around 1445 cm<sup>-1</sup> can be attributed to O – H bending vibrations. The C – N stretching vibration absorption band resulting from PVP was observed at ~1292 cm<sup>-1</sup> and the sharp band at ~1020 cm<sup>-1</sup> show an anhydride stretching mode [12-14]. It can be observed that upon calcining at 350°C, 450°C and 550°C, the FTIR bands intensity were significantly reduced. This may be due to the fact that calcining promotes the reduction of hydroxyl groups.

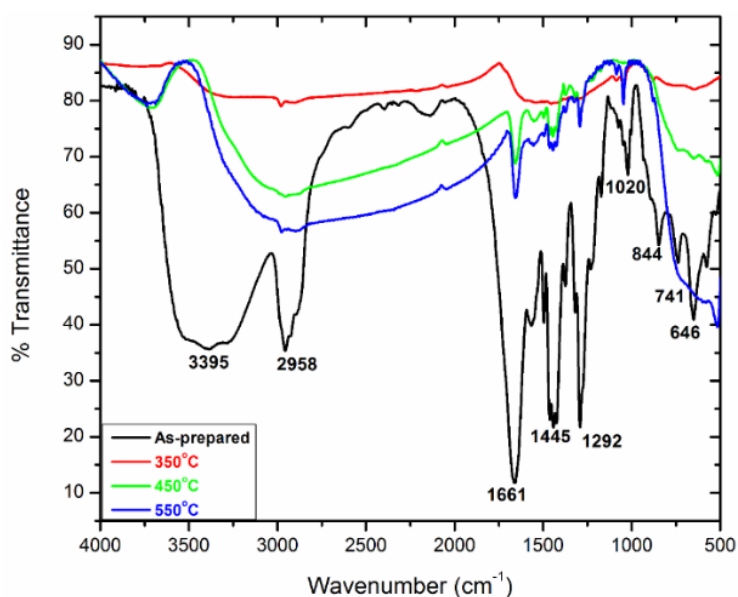


**Figure 4.** FTIR spectra of mp-TiO<sub>2</sub> for As-prepared, calcined at 350 °C, 450 °C and 550 °C from electrospun samples.

#### 4. Conclusion

This work successfully demonstrated mesoporous nature of TiO<sub>2</sub> influenced by the calcining temperature. Furthermore, the effect of calcining temperature on the XRD results indicated that a mixture of two phases, rutile and anatase were formed, with rutile being the dominant phase at 550°C calcining temperature. Similarly, the morphology also evolved with the increase of calcining temperature, showing non-uniform pores. The intensity of the FTIR vibrational modes bands was significantly reduced and this may be due to the fact that calcining mp-TiO<sub>2</sub> particles at high temperatures promotes the reduction of hydroxyl groups. BET surface area was improved with an increase of calcining temperature and relatively larger pore size was obtained from the sample calcined at 550°C indicating a good possibility of efficient perovskite infiltration, which is needed for perovskite solar cells application. This observation was found in both sol-gel and electrospun samples.

#### Acknowledgements

The authors would like to thank the South African National Research Foundation (NRF) for financial support (grant no. 131101) and the University of South Africa for providing research infrastructure.

#### References

- [1] Hernandez-Granados A, A N. Corpus-Mendoza A N et al 2019 *Opt. Mater.* **88** 695-703
- [2] Niu B, Wang X, Wu K et al 2018 *Mater.* **11** 1910
- [3] Scarpelli F, Mastropietro T F et al (2018) DOI: 10.5772/intechopen.74244
- [4] Liu Y C, Lu Y F et al 2011 *Int. J. Photoenergy.* **2011** 619069
- [5] Regonini D, Jaroenworarluck A, Stevensa R and Bowen C R 2010 *Surf. Interface Anal.* **42** 139-144
- [6] Deshmanea V G, Owena S L et al 2015 *J. Mol. Catal A: Chem.* **408** 202-213
- [7] Parida B, Singh A et al 2019 *Mater. Today Commun.* **18** 176-183
- [8] Li H, Liu H et al 2016 *Mater.* **9** 849
- [9] Yina Q, Xiang J et al 2016 *J. Exp. Nanosci.* **11** 1127-1137
- [10] Mahshid S 2007 *J. Mater. Process. Technol.* **189** 296–300
- [11] Mazloun-Ardakani M and Arazi R 2017 *Nanochem Res.* **2** 20-28
- [12] Zhu Z, Zhang Y et al 2019 *Mater(Basel).* **12** 896
- [13] Ramírez-Cedillo E and Ortega-Lara W et al 2019 *Membr(Basel).* **9** 12
- [14] Diantoro M, Istirohah T et al 2018 *J. Phys.: Conf. Ser.* **1040** 012045

# A Nonlinear Logistic Regression Model for the Measurement of Drug Potency in Photodynamic Therapy

EP Chizenga<sup>1</sup> and H Abrahamse<sup>1,2</sup>

<sup>1</sup>Laser Research Centre, Faculty of Health Sciences, University of Johannesburg, P.O. Box: 17011, Johannesburg 2028, South Africa

<sup>2</sup>NRF SARChI: Laser Applications in Health, South Africa

Email: [habrahamse@uj.ac.za](mailto:habrahamse@uj.ac.za)

**Abstract.** Photodynamic Therapy (PDT), a therapeutic modality that uses light to kill cancer by means of a photochemical reaction that is initiated when a photosensitizer (PS) molecule absorbs a photon of light to become phototoxic, is one example where principles of physics have provided cutting-edge solutions in biology. Like all other therapies, the potency of PDT must be determined before confirming its usage and to measure the therapeutic potency of these PSs in PDT, a good model and technique for the accurate measurement of potency is indispensable. In this present study, a design for accurate estimation of PDT potency was therefore developed using regression analysis of the inhibition of proliferation of cells treated with PDT. A cancer cell line, SiHa cells, was cultured and treated with serially diluted PS concentrations for treatment at two different laser fluencies. Using nonlinear regression, the dose-response curve was fitted, and the half growth inhibition (GI50) value was calculated using a Four Parameter Logistic (4PL) Model. The findings showed that GI50 of the PS was 63.426  $\mu\text{M}$  and 40.813  $\mu\text{M}$  for 5  $\text{J}/\text{cm}^2$  and 10  $\text{J}/\text{cm}^2$ , respectively. Of the many important observations in this study, worth noting is the wide difference in PS concentrations with different fluences, a phenomenon that can be explored for dosing preferences in different settings. This work has also provided guiding principles for the accurate estimation of PDT potency for early-stage PDT investigations and includes theoretical considerations for the accurate estimation of the GI50 value.

## 1. Introduction

Accurate estimation of drug effectiveness or inhibition capacity is the single most important aspect of any drug discovery exercise in both academics and industrial research. The value of the concentration corresponding to a response midway between the highest and lowest concentrations i.e., IC50 for half Inhibitory concentration or GI50 for Half Growth Inhibition, which basically are the same thing just different terminology, is used in the early stages of drug discovery to determine the activity of a drug. This value is used to refer to the drugs' potency and is required for the evaluation of the performance and suitability of a drug being investigated [1]. When measuring the IC50/GI50 on any therapeutic compound, the proposition is based on the assumptions that a monotonic relationship exists between

---

2 To whom any correspondence should be addressed.

the dose of the compound and the response in the assay and secondly, that a consistent definition of a particular response at a given concentration is predictable based on this relationship.

Statistically, this value can therefore be determined from analysis of responses at varying concentrations and different ways of achieving this are available for different applications. In Photodynamic Therapy (PDT), however, this important pharmacological factor is not adequately investigated for the confirmation of the most appropriate method for determination of PDT potency *in vitro*, for *in vitro* experimentation. In PDT, photosensitization of a photoactivatable drug, the Photosensitizer (PS), is what causes cytotoxicity. This photosensitization is induced by light of a specific wavelength in the excitation range of the PS [2]. Meaning that there are two variables in the process, both of which need optimization and assessment. Unlike mere synergism, the relationship between the PS and light is inseparable because the PS is an inert molecule in its ground state and only upon excitation to an excited triplet state does it become active to devise a reaction, and similarly the light in the absence of PS does not have any therapeutic significance in PDT. This interrelationship is unlike most in pharmacology where addition of the drug shows a direct effect and the measurement of drug potency is unambiguous and can be achieved by fitting a simple linear or nonlinear regression where concentration is the independent variable, and the response is the dependent variable.

In PDT as explained both variables need to be considered using reliable statistical evaluation. This present study, therefore, sought to investigate the most appropriate way of determining the IC<sub>50</sub>/GI<sub>50</sub> value that is accurate considering the relation between PS and laser, and all the important variables in between PS administration and laser exposure, in an *in vitro* setting, using a monolayer of cells. Different approaches can be used, but the Four Parameter Logistic (4PL) Model is a non-linear regression model that is used for fitting dose-response and concentration-response data and shows a sigmoidal curve to represent the response of cells to a drug [3]. The conventional optimal 4PL model might not be the best for PDT situations hence this investigation reports on a 4PL model design best suitable for PDT, one that not only is accurate, but also cost-effective while meeting the requirements for reporting IC<sub>50</sub>/GI<sub>50</sub> values according to the recommendations of the Assay Guidance Manual.

## 2. Methodology

### 2.1 Sample Preparation and Cell Culture

A commercially procured PS, Al (III) Phthalocyanine Chloride Tetrasulfonic Acid (Frontier Scientific™, Cat# AlPcS-834) with a molecular weight of 895.21 and molecular formula of C<sub>32</sub>H<sub>16</sub>AlClN<sub>8</sub>O<sub>12</sub>S<sub>4</sub>, was used in this investigation. A stock solution of 100 mM was prepared from the solid dye to a final volume of 5 ml in Phosphate Buffered Saline (PBS) at neutral pH (pH 7.4) using the Genway UV-Vis Spectrophotometer (Lasec). Spectrophotometric scanning from 400 to 800 nm at 2 nm wavelength intervals was performed and the obtained data was plotted on a line chart. An adherent cell line, SiHa cells (ATCC® HTB35™) suitable for *in vitro* monolayer experimentation, were procured from Separations Scientific SA (Pty) Ltd. The cells were initially propagated in culture using Dulbecco's Modified Essential Medium (DMEM) (Sigma Aldrich), at 37°C with 5% CO<sub>2</sub> and 85% humidity in a cell culture incubator ((Thermofisher Scientific). Upon reaching the required cell quantity, cells were seeded in tissue culture plates with a diameter of 3.4 cm (Corning Inc.) at a density of  $3 \times 10^5$  cells per plate and incubated as described for propagation. An attachment window of 8 hours was given before addition of PS after which a serially diluted range of PS concentrations were added to the monolayer of cells and left for 18 hours to allow for maximum intracellular uptake and internalization. After 18 hours, the media was removed, and the monolayer was washed three times with pre-warmed Hanks Balanced Salt Solution, HBSS (Sigma Aldrich) to remove unabsorbed PS, in preparation for irradiation

### 2.2 Irradiation

The cells were prepared and cultured in 3.4 cm diameter tissue culture plates, at culture conditions described above. Cells cultured but not treated with either PS or light were included, followed by cells

treated with light only without the addition of PS to show the effects of light in the absence of PS, and finally a plate of cells treated with PS without exposure to light, to indicate the possible effects of PS in the absence of light. The experimental groups were treated with decreasing PS concentrations, using a serial dilution factor of 0.5, starting with 500  $\mu\text{M}$  down to 7.8  $\mu\text{M}$ . Irradiation was done 8 hours after PS treatment, using a monochromatic semiconductor diode laser with a wavelength of 673.2 nm (Oriol, USA), at 5 and 10  $\text{J}/\text{cm}^2$ , in 1 ml of media. Exposure times for each fluence were determined using equation 1 below. After irradiation, all groups were left for 12 hours at culture conditions before the assessment of cellular responses. A summary of the experimental layout is shown in table 1 below.

Table 1. Control and experimental groups

Group	Description	
Control Group One	No Photosensitizer, No Irradiation	
Control Group Two	PS Negative Control	
Control Group Three	Laser Negative Control	
Experimental Groups	500 $\mu\text{M}+5 \text{ J}/\text{cm}^2$	500 $\mu\text{M}+10 \text{ J}/\text{cm}^2$
	250 $\mu\text{M}+5 \text{ J}/\text{cm}^2$	250 $\mu\text{M}+10 \text{ J}/\text{cm}^2$
	125 $\mu\text{M}+5 \text{ J}/\text{cm}^2$	125 $\mu\text{M}+10 \text{ J}/\text{cm}^2$
	62.5 $\mu\text{M}+5 \text{ J}/\text{cm}^2$	62.5 $\mu\text{M}+10 \text{ J}/\text{cm}^2$
	31.3 $\mu\text{M}+5 \text{ J}/\text{cm}^2$	31.3 $\mu\text{M}+10 \text{ J}/\text{cm}^2$
	15.6 $\mu\text{M}+5 \text{ J}/\text{cm}^2$	15.6 $\mu\text{M}+10 \text{ J}/\text{cm}^2$
	7.8 $\mu\text{M}+5 \text{ J}/\text{cm}^2$	7.8 $\mu\text{M}+10 \text{ J}/\text{cm}^2$

$$\frac{X \text{ mW} \times 4}{(\pi) \times 3.4 \text{ cm}^2} \quad (1)$$

Where  $X$  is the power output in mW measured by a power meter and the 3.4 cm is the diameter of light path, which also is equivalent to the diameter of the plates used.

### 2.3 Cellular Responses

After irradiation, the morphological assessment was done first. The plates were taken from the incubator and observed directly before washing, using the inverted light microscope (Wirsam, Olympus CKX41) with a built-in camera. Images were captured at 200 $\times$  magnification, the Olympus cellSens Imaging Software was used for the acquisition of the images, and ImageJ was used for further analysis of the captured images. Following microscopy, the CellTiter-Glo luminescent cell viability assay (AnaTech: Promega, PRG7571) was used for the determination of proliferation. In this assay luminescent signal is detected from the reaction of luciferase enzyme with Adenosine Triphosphate (ATP), at a signal proportional to the amount of ATP in the cells. Cells were washed once with HBSS and suspended in 200  $\mu\text{l}$  of media. An equal volume of the CellTiter-Glo reagent was added to the plates and shaken using a rocking shaker for 2 min to induce lysis. The mixer was then immediately pipetted into an opaque-walled 96 multi-well plate in duplicate, and luminescence in relative light units (RLU) was then measured on the Perkin Elmer, VICTOR Nivo Multimode Microplate Reader, Part # HH35000500).

### 2.4 IC50/GI50 Calculation

To calculate the IC50/GI50, the 4PL model was used as shown in equation 2 below. Experiments were repeated three times ( $n=3$ ) and statistical analysis was performed using SigmaPlot software version 14.0. Student t-test was performed to determine the statistical difference between the control and experimental groups.

$$Y = d + \frac{(a - d)}{1 + \left(\frac{x}{c}\right)^b} \quad (2)$$

Where,  $Y$  = Response (i.e., the dependent variable)  
 $x$  = Concentration (i.e., Dose, the independent variable)  
 $a$  = The Minimum (response at zero dose)  
 $d$  = The Maximum (response at infinite dose)  
 $c$  = Point of inflection (i.e., the EC50/IC50)  
 $b$  = Hill coefficient (i.e., the slope at point  $c$ ).

## 3. Results and Discussion

### 3.1 Morphology and Cell Proliferation

The morphology of cells after treatment indicated alterations as observed in Figures 1A and B below. Changes in morphology were suggestive of an ongoing cell death mechanism, with some apoptotic and some necrotic features. Terminal cell death as seen in floating cells and cellular debris was also evident in higher doses as seen in Figure 1 A and B below. The extent of cell damage was dose-dependent with low doses having little or no damage, followed by progressing cellular damage until the highest dose. Single variable control groups, not included in the figure, showed no changes in morphology, and appeared similar in shape, size, and attachment to the standard control.

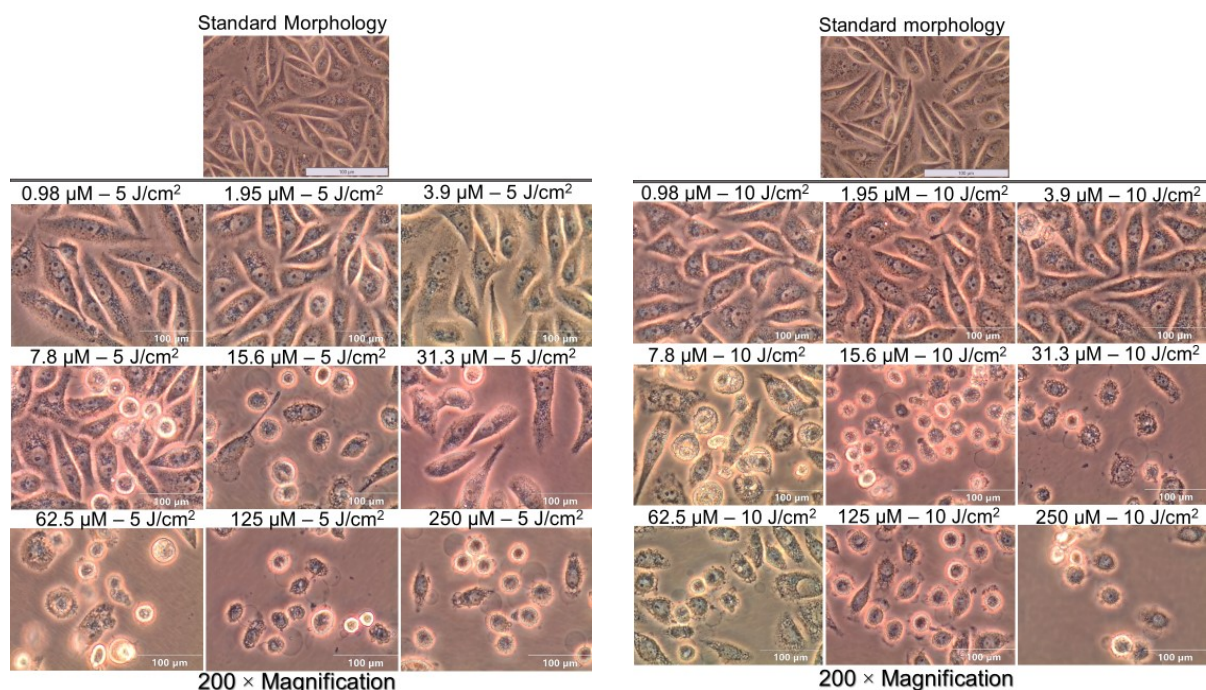


**Figure 1 A.** Cells irradiated with 5 J/cm<sup>2</sup> showing the morphology of PDT treated cell with characteristic changes in a dose-dependent manner

**Figure 1 B.** Cells irradiated with 10 J/cm<sup>2</sup> showing the morphology of PDT treated cell with characteristic changes in a dose-dependent manner

The proliferation rate of cells also indicated similar trends with a proportional decrease of proliferation inversely to the concentration of PS, i.e., dose-dependent decrease. Similarly, control cells were used to measure the maximum ATP concentration from which all other groups are compared. The untreated standard control showed a high ATP concentration which was used to calculate the 100% proliferation. All control groups i.e., either PS alone or laser alone, had increased proliferation at the end of the experimental period. Experimental groups however showed significant decrease in the concentration of ATP ( $p < 0.001$ ), indicated by low luminescence signal. Shown in Figure 2 below is the observed dose-dependent decrease in proliferation of PDT treated cells.

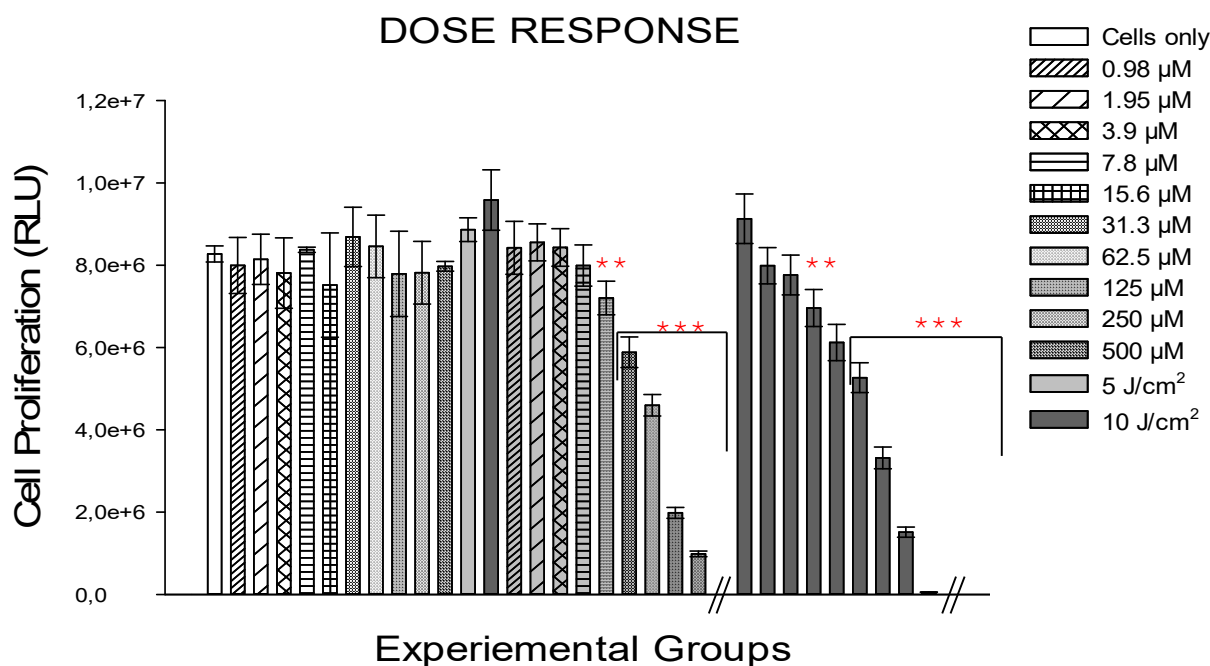


**Figure 2.** Dose-response assessment of cell proliferation using ATP measurement as an indicator of cellular proliferation. Results showing a dose-dependent decrease in ATP, inversely proportional to the concentration used. 5  $\text{J}/\text{cm}^2$  is plotted in light grey and 10  $\text{J}/\text{cm}^2$  in dark grey, with significance shown using \*\* for ( $p < 0.01$ ), and \*\*\* for ( $p < 0.001$ ). The concentration of 500  $\mu\text{M}$  with  $\text{RLU} = 0$  is shown by break lines i.e., // on the x axis

### 3.2 Calculated $\text{IC}_{50}/\text{GI}_{50}$

At the concentration of 500  $\mu\text{M}$ , it was established that the proliferation response had its maximum inhibition, for both 5 and 10  $\text{J}/\text{cm}^2$ . Similarly, the minimum inhibition lies at the same concentration as the 0% plate control. Hence, both 0% and 100% values were determined and confirmed to insert the  $a$  and  $d$  in equation 2 above. By terminology, it is therefore conceivable to calculate the absolute  $\text{IC}_{50}/\text{GI}_{50}$  value for this response [4]. Using equation 2 and by plotting a logistic regression curve, the absolute  $\text{IC}_{50}/\text{GI}_{50}$  was therefore determined at 63.426  $\mu\text{M}$  and 40.813  $\mu\text{M}$  for 5  $\text{J}/\text{cm}^2$  and 10  $\text{J}/\text{cm}^2$ , respectively as shown in Figures 3 A and B below.

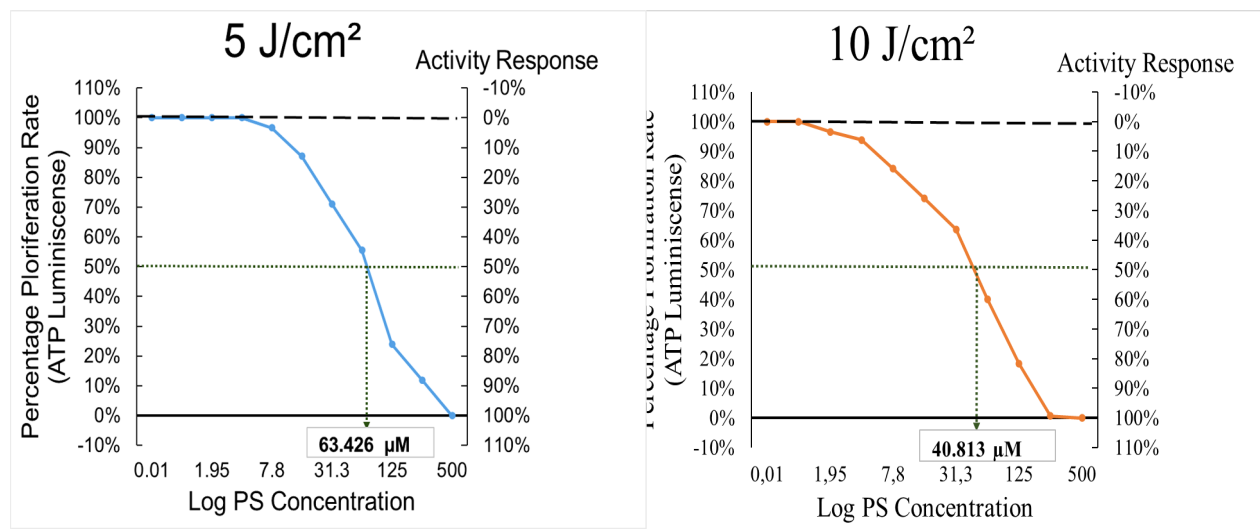


**Figure 3 A.** The IC<sub>50</sub>/GI<sub>50</sub> of 63.426 in cells irradiation with 5 J/cm<sup>2</sup>, plotted using with reference to equation 2

**Figure 3 B.** The IC<sub>50</sub>/GI<sub>50</sub> of 40.813 in cells irradiation with 10 J/cm<sup>2</sup>, plotted using with reference to equation 2

#### 4. Conclusion

Here, we have described for the first time using nonlinear logistic regression, the calculation of the IC<sub>50</sub>/GI<sub>50</sub> for PDT experiments *in vitro*. In therapeutic applications, there are many reasons for clinical failures, but the choices made concerning identification and optimization during the discovery phase is one major contributor. As a vital part of drug discovery, *in vitro* experimentation is the stage where drug potency at cellular level is determined, and the effectiveness and usability of a drug are ascertained. The outcomes of this study show that higher laser fluences achieve better PDT outcomes at lower PS concentrations and this information is important when setting up PDT doses. Moreover, the methods used here are inferable for measurement of GI<sub>50</sub> values when other PSs are used. In the end, it is important to ensure accuracy of the GI<sub>50</sub> by using such reliable methods, because wrongfully reported values are a menace to the process of drug discovery and should be avoided. This present study was performed *in vitro* using monolayer cultured cells, hence the concentration and variables mentioned here are for the purpose of cells treated as a monolayer, to understand the PDT potency at cellular level.

#### 5. Acknowledgements

This work is based on the research supported by the South African Research Chairs Initiative of the Department of Science and Technology and National Research Foundation of South Africa (Grant No: 98337). The authors sincerely thank the University of Johannesburg, the National Research Foundation for their financial grant support, and the National Laser Centre for providing use of their lasers

#### 6. References

- [1] Sebaugh J L 2011. *Pharma. Stat.* **10** 2
- [2] Calixto G M, Bernegossi J, de Freitas L M, Fontana C R and Chorilli M. 2016 *Molecul.* **21** 3
- [3] Markossian S, Grossman A, Brimacombe K, et al. 2004 *Eli Lilly & Co. and NCATS*, **2021**
- [4] Kalliokoski T, Kramer C, Vulpetti A, Gedeck P 2012 Comparability of mixed IC<sub>50</sub> data-a statistical analysis. *PLoS One.* **8** 4

# Implementation of the LED Integrator panel for the Prometeo system in the ATLAS Tile Calorimeter

Onesimo Mtintsilana<sup>1</sup>, Jalal Abdallah<sup>2</sup>, Pavle Tsotskolauri<sup>3</sup> and Bruce Mellado<sup>1,4</sup>

<sup>1</sup>School of Physics and Institute for Collider Particle Physics, University of the Witwatersrand, Johannesburg, Wits 2050, South Africa

<sup>2</sup>Department of Physics, University of Texas, United States

<sup>3</sup>Andronikashvili Institute of Physics, Tbilisi State University, Georgia

<sup>4</sup>iThemba LABS (NRF), Old Faure Rd, Eerste River, Cape Town, 7100, South Africa

E-mail: [onesimo.mtintsilana@cern.ch](mailto:onesimo.mtintsilana@cern.ch)

**Abstract.** The high-luminosity upgrade to the LHC (HL-LHC) poses significant issues for the ATLAS detector, including increased radiation exposure to the on-detector electronics and higher pileup from low momentum collisions compromising the operation of the trigger selection system. Almost every electronic component of the Tile Calorimeter (TileCal) will be upgraded during the ATLAS Phase-II Upgrade. During the assembly, installation, and maintenance phases of the new on-detector readout electronics system, its correct functionality must be validated by a portable system. Prometeo (Portable readout module for tile electronics) is an improvement to the MobiDICK system, which was utilised to assess current electronics during the Long Shutdown 1 and 2. To achieve precise calibration of the Tile calorimeter and to be able to measure individual parts of the detector readout chain, a set of calibration systems is used. Signals from the PMTs are conditioned and digitized by readout electronics, and slow readout measures the integrated current from the PMTs in parallel. This slow readout, known as the integrator, is used for light yield cell calibration and LHC luminosity monitoring. An Integrator Panel has been integrated into the Prometeo web interface and we present the current status and test results.

## 1. Introduction

The Large Hadron Collider (LHC) at CERN will push the limits of particle physics with its unprecedented high energy and luminosity. The upgrade of the Large Hadron Collider (LHC) to the High-Luminosity LHC (HL-LHC) [1] allows for a plethora of physics studies but provides significant challenges to the detector, trigger, and data acquisition systems in the form of increasing trigger rates and detector occupancy.

The ATLAS Tile Calorimeter (TileCal) is the central hadronic calorimeter section of the ATLAS experiment [3] at the LHC as illustrated in Figure 1 and it is made of steel as passive material and scintillator plates (tiles) as active material [4]. In preparation for the HL-LHC, the TileCal will require new electronics to provide a low-latency, high-frequency and fully digital input for ATLAS trigger system. Therefore Test benches, are being developed to validate the assembly of components into the mini-drawers and their installation into the ATLAS detector.

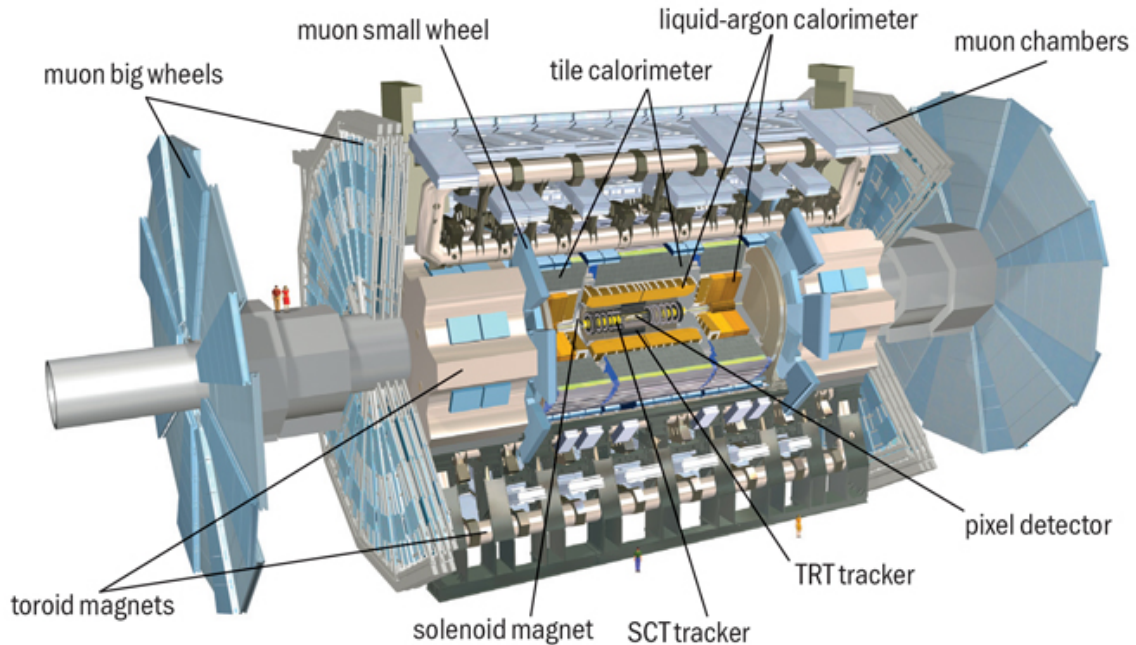


Figure 1: The layout of the ATLAS detector, showing some of the key components. Overall, the detector is 25 m tall and spans some 40 m from end to end. This image was taken from Ref [2]

A lighter more portable Test station, called the Prometeo will be used to validate the installation (see Section 2 ) of the mini-drawer into ATLAS and perform the initial quality assurance.

## 2. Prometeo

The Prometeo is a portable test bench used to certify front-end electronics of the TileCal at the HL-LHC. It is a high-throughput electronic device designed to simultaneously read all digitised samples from 12 channels at the LHC bunch crossing frequency and evaluate the data quality in real time. The design inherits features from the presently-used MobiDICK4 test-bench [5]. Prometeo must be able to test, among many other things, the following: connection with mini-drawers (MD), connection with Daughterboard (DB) and MainBoard (MB), Photomultiplier Tubes (PMT) and Charge Injection Linearity. To test the PMT-Blocks' responsiveness to light pulses, an LED system must generate light pulses that simulate physics pulses. The PMT-Block teststand for testing the response of 12 PMT-Blocks to light (corresponding to one mini-drawer).

### 2.1. Prometeo functions and usage

The PMT-Block teststand shown in Figure 2 is designed to validate the functionality of assembled PMT-Blocks but is not intended to measure PMT properties. The initial step of mini-drawer construction is the production of up to 12 PMT-Blocks, which will be used to populate the mini-drawer. Each PMT-Block includes an active separator and a FENIC card. Once the 12 PMT-Blocks have been built, they are placed and tested on a PMT teststand designed to accommodate the 12 PMT-Blocks shown in Figure 3. The PMT teststand is equipped with its own MB, DB, and High Voltage (HV) distribution board. The portable HV of Prometeo is connected to the HV bus board in order to deliver HV to the 12 PMT-Blocks [6]. The Prometeo LED generates light pulses that are transmitted to the PMTs. The portable LV of Prometeo



Figure 2: Light tight box for the phase-2 PMT teststand showing 12 PMT-Blocks on the tray.



Figure 3: Components of the PMT Block.

transmits LV to the MB, and readout fibres connect Prometeo to the DB.

Throughout the PMT-Block certification process, LED runs are conducted in low gain, high gain, pedestal, and charge injection modes. In addition to measuring linearity, noise, gains, and data transmission errors in slow and fast readout channels, linearity, noise, and gains are also assessed in slow and fast readout channels.

### 3. Prometeo Software

The Prometeo web interface as shown in Figure 4 is the software used to execute certification tests and analyse the results. It is accessible via any web browser, including mobile devices, and is platform independent. The system is based on a client-server architecture, with Prometeo acting as a server that communicates via ethernet through a VHDL module that supports IPbus [7]. The client connects via UDP protocol, employing a modular framework with panel plug-ins for various mini-drawer tests. This architecture is client-driven, meaning the client has direct control over the server's functionalities and can modify them on the go.

Through the IPbus protocol, the software communicates with the server to perform read and write operations on a specific memory address or a FIFO memory [7]. The firmware keeps track of the list of registers so that commands, status, data position, sample count, calibration parameters, etc. can be configured.

#### 3.1. IPBus Server

The IPbus software is written in C++, and a Python extension is provided to enhance the scripting capabilities of the end-user, which is frequently employed for developing new tests. Alternately, the user may also use the Java Graphic User Interface (GUI) (Figure 4) to manage test results interactively. The C++ implementation and Python extension can be compiled on any platform, and a Java graphical user interface is compatible with all operating systems. In any event, the core of the software is a collection of algorithms that transform IPbus protocol commands into functions for mini-drawer testing.

The user is able to test communication with the mini-drawer, operate front-end cards, LEDs, and HV power, and store/retrieve data from FIFO or address-specific memory. In addition, tests for the Integrator for the new system have been rebuilt, and the results are reported in Section 4.1.

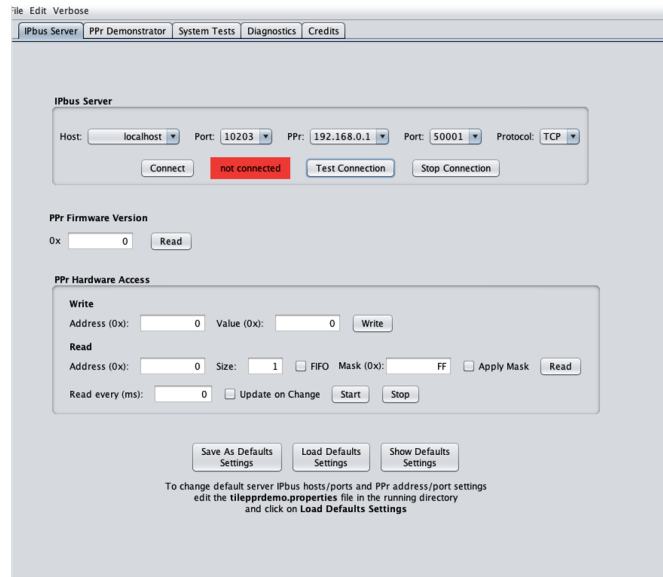


Figure 4: Prometeo Graphic User Interface.

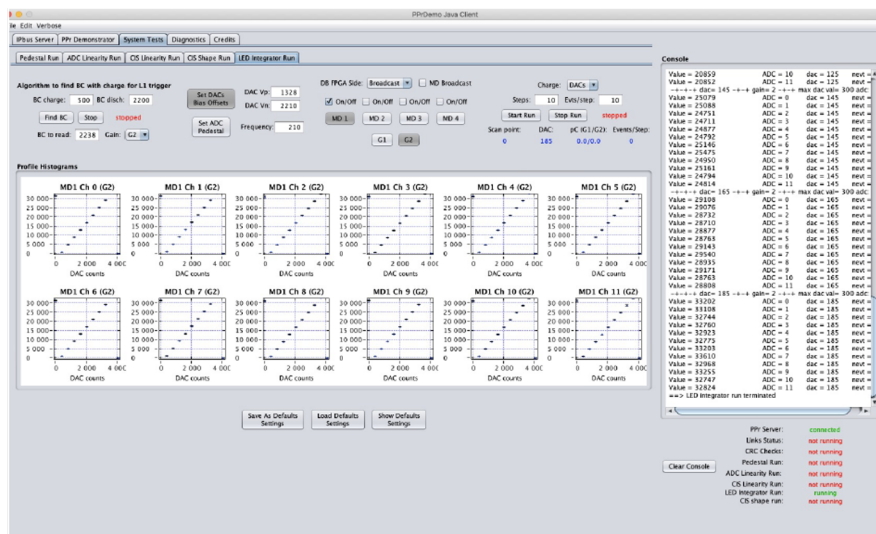


Figure 5: Results of the Integrator Panel installed in the Prometeo GUI.

## 4. System Tests

### 4.1. Integrator

Integrator is printed on a circuit board that is connected to the FENICs card. In addition to the integrator, this board contains a fast digital signal processor for processing collision events of interest in physics, and it delivers a portion of the ATLAS Level 1 Calorimeter trigger signals. A panel for the integrator, as displayed in Figure 5, has been added and tested on the Prometeo GUI. The total number of gains added to this panel is six, but only the results for Gain 2 are shown on the panel (G2). This test was conducted on mini-drawer 1, and all 12 channels produced consistent results. This was then repeated for Gain 2 and the remaining three mini-drawers, for which no deviations were found.

To prevent saturation, the integrator gain can be selected by choosing one of six preconfigured resistors that also specify the integration time. The user can set the frequency, sample number,

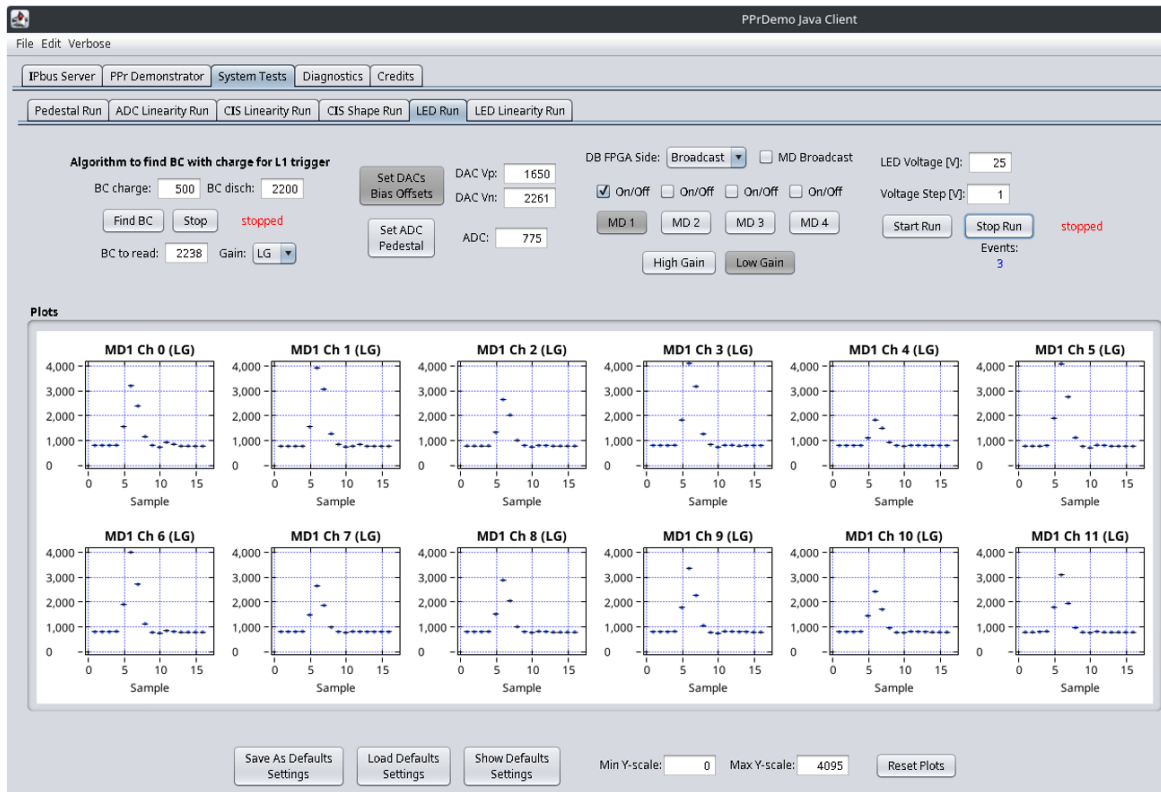


Figure 6: LED Shape panel installed in the Prometeo GUI results after running the system tests.

mini-drawer to read, gains, and events for each measurement step using this panel. All six gains were tested, and no discrepancies were detected.

#### 4.2. LED Shape and LED Linearity

As previously outlined in Section 2.1, one of the submodules for the Prometeo is the LED Driver, which is used to evaluate the functionality of PMT blocks. The LED driver is physically connected to the Compact Processing Module (CPM) and operated from the PC using Prometeo software. A LED Shape panel, as demonstrated in Figure 6, was integrated to and tested on the GUI. This panel uses an LED driver to evaluate the light injection of 12 PMT-Blocks. By adjusting "LED Voltage" from 5 to 30V, the light intensity can be modified. The system tests were conducted for both the High and Low Gain. On the panel, we display the Low Gain (LG) data for mini-drawer 1, for which 11 channels were tested. Similarly, we observed no inconsistencies during the LED Run test.

### 5. Conclusion

The LHC's Phase II Upgrade will enhance instantaneous luminosity by a factor of 5-10. Electronics will have to endure a substantially higher radiation dose and a greater data throughput need. All TileCal on- and off-detector electronics will be replaced between 2025 and 2027 as part of the HL-Phase LHC's II update. Prometeo is designed to certify the phase-II front-end electronics of TileCal. The test-bench, which can conduct a variety of tests, was motivated by the success of the MobiDICK systems in maintaining the TileCal super-drawers.

Each component of this demonstrator is currently being tested as it is incorporated to the system. We have successfully introduced new panels to the GUI, the Integrator, and the LED, and their functionality has been verified by system testing. Since there were no discrepancies, they have been incorporated into the GUI. In addition, pulses, LED shape, and charge-injection tests have been conducted successfully. Concurrently with the development of the demonstrator, more tests are developed and evaluated.

### Acknowledgments

The author was supported by the National Research Fund through the PhD Grant.

### References

- [1] ATLAS Collaboration 2012 Letter of Intent for the Phase-II Upgrade of the ATLAS Experiment Tech. rep. CERN Geneva draft version for comments URL <https://cds.cern.ch/record/1502664>
- [2] Atlas undergoes some delicate gymnastics, howpublished = <https://cerncourier.com/a/atlas-undergoes-some-delicate-gymnastics/>, note = Accessed: 2022-08-30
- [3] Aad G *et al.* (ATLAS Collaboration) 2008 *JINST* **3** S08003. 437 p also published by CERN Geneva in 2010 URL <https://cds.cern.ch/record/1129811>
- [4] Aad G *et al.* (ATLAS Collaboration) 2010 *Eur. Phys. J. C* **70** 1193–1236. 64 p accepted for publication in EPJC (latest version has minor editorial modifications following requests from EPJC referees) (*Preprint* 1007.5423) URL <https://cds.cern.ch/record/1282535>
- [5] Alves J *et al.* 2013 URL <http://cds.cern.ch/record/1558969>
- [6] Adragna P *et al.* *Nuclear Instruments and Methods in Physics Research Section A: Accelerators, Spectrometers, Detectors and Associated Equipment* **564** 597–607
- [7] Bullock D, Carrio F, Hofsajer I, Govender M, Mellado B, Moreno P, Reed R, Ruan X, Sandrock C, Solans C, Suter R, Usai G and Valero A 2014 URL <https://cds.cern.ch/record/1704927>

# Upgrade of ATLAS Tile Calorimeter TTC system for Phase-II test-beam campaigns

Humphry Tlou<sup>1</sup> and Bruce Mellado<sup>1,2</sup>

<sup>1</sup> School of Physics and Institute for Collider Particle Physics, University of the Witwatersrand, Johannesburg, Wits 2050, South Africa

<sup>2</sup> iThemba LABS, National Research Foundation, PO Box 722, Somerset West 7129, South Africa

E-mail: [humphry.tlou@cern.ch](mailto:humphry.tlou@cern.ch)

**Abstract.** The Tile Calorimeter (TileCal) is the central hadronic calorimeter of the ATLAS experiment at the Large Hadron Collider (LHC). The LHC Phase-II upgrades will take place during the Long Shutdown 3 period (2026-2028), leading into the High Luminosity Large Hadron Collider (HL-LHC). The HL-LHC is expected to have the capability to deliver up to five times the LHC nominal instantaneous luminosity in the year 2029. The TileCal Timing, Trigger and Control (TTC) system of the test-beam facility is being upgraded for the Phase-II test-beam campaigns. A new TTC interface module, the ATLAS Local Trigger Interface (ALTI) is being deployed during the Long Shutdown 2 period (2019-2022) of the LHC, as part of Phase-I upgrades. The ALTI is a 6U VME64x module which provides the interface between the Level-1 Central Trigger Processor and the TTC optical broadcasting network, to the Front-End electronics. The ALTI integrates the functionalities of the Local Trigger Processor, Local Trigger Processor interface, TTC VME bus interface and the TTC emitter modules, which are currently used in the experiment. The upgrade involves a new configuration with additional features due to increased amount of programmable logic resources. The status of the upgrade activities is presented.

## 1. Introduction

The Tile Calorimeter (TileCal) is the central hadronic calorimeter ( $|\eta| < 1.7$ ) of the ATLAS experiment at the Large Hadron Collider (LHC) [1]. Its primary purpose is to provide energy and position of hadrons [2]. The TileCal (shown in figure 1) is constructed with iron plates, plastic scintillators, optical fibres and electronics. It is split into three cylinders along the beam axis, and each cylinder is divided into 64 wedge-shaped modules that are staggered in the  $\phi$  direction. It features one central long barrel (LB) with two partitions (one on A-side and the other on C-side) known as LBA and LBC. The other two short extended barrels (EB) are divided into two partitions, EBA and EBC. The Front-End (FE) electronics are placed within the wedge-shaped modules and are linked to the Back-End (BE) read-out electronics through an optical Timing, Trigger and Control (TTC) distribution network. The BE electronics control these four partitions through their corresponding TTC crates. The TileCal system performs several weeks of test-beams each year at the CERN SPS North Area in preparation for the ATLAS Phase-II upgrades. The ATLAS Phase-II upgrades will take place during the Long Shutdown 3 (LS3) period (2026-2028), leading into the High Luminosity Large Hadron Collider (HL-LHC). In the year 2029, the HL-LHC is expected to deliver an instantaneous peak luminosity of up to

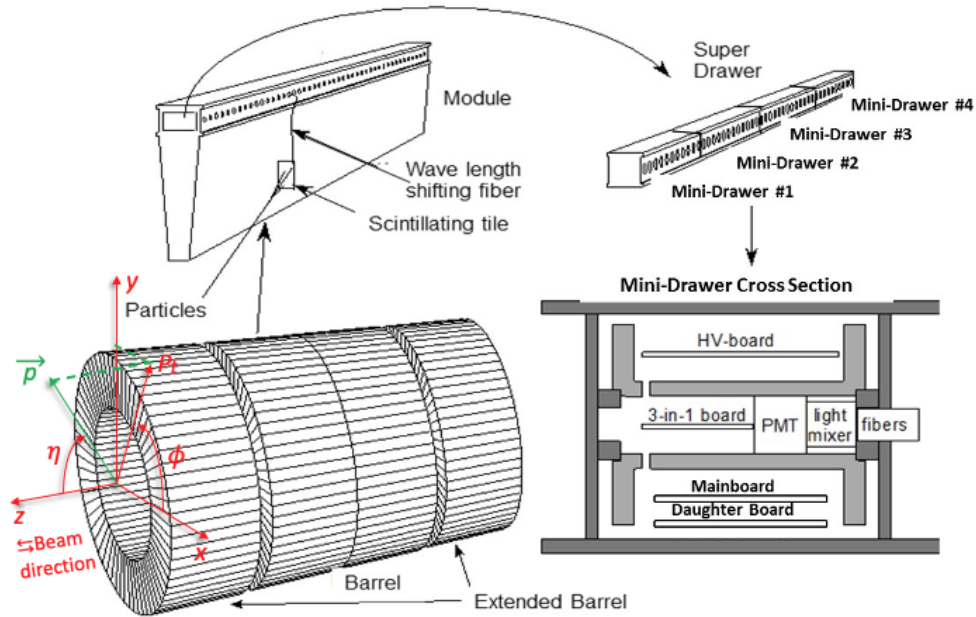


Figure 1: The schematic diagram of the TileCal barrels, showing the module and its components.

$7.5 \times 10^{34} \text{ cm}^{-2}\text{s}^{-1}$ , corresponding to an average of 200 simultaneous proton-proton collisions per bunch crossing. An increase in luminosity will result in higher pile-up, higher trigger rates and higher radiation doses, motivating the upgrade of the ATLAS sub-detectors. As part of the upgrades, the TileCal on- and off-detector electronics will be replaced during LS3. The TileCal data acquisition infrastructure for the test-beam setup is being upgraded with a new TTC interface module, the ATLAS Local Trigger Interface (ALTI).

The TileCal collects data using the ATLAS Trigger and Data Acquisition (TDAQ) system. The TDAQ system selects events with unique characteristics that may be useful for physics analysis. It is built on two levels: the hardware Level-1 and the High Level Trigger (HLT) system. The Level-1 trigger (Level-1 Calo and Level-1 Muon) identifies interesting events promptly based on specific inputs from muon detectors and calorimeters. It uses the Central Trigger Processor (CTP) to lower the acceptable events from 40 MHz (25 ns) to 100 kHz [3, 4]. The corresponding event signal produced by the CTP is known as the Level-1 Accept (L1A). The rate of accepted events is then processed further in the HLT to lower the rate of recorded events from 100 kHz to 1 kHz [3].

## 2. Test-beam setup at the CERN SPS North Area

The Super Proton Synchrotron (SPS) delivers the test beam-line to the setup. In the beam line, a number of detectors are installed to monitor the beam's quality, position, and particle composition [5]. A schematic diagram of the beam elements used in the test-beam area is shown in figure 2. Three Cherenkov Counters (CCs) are installed to aid in data interpretation and particle identification. As part of the beam trigger system, two trigger scintillators S1 and S2 are also included in the beam line. The beam position is measured with a precision of 0.2 mm using two wire chambers [6]. For muon detection, a Muon Hodoscope is used also known as the Muon wall. It is a mobile detector comprised of 12 scintillators installed behind the Tile modules and is largely used in offline analysis to suppress the pions' low energy tail in high energy hadron runs. The legacy readout electronics are installed in two modules and the Phase-II upgrade electronics are installed in the other two modules. The module configuration changes depending

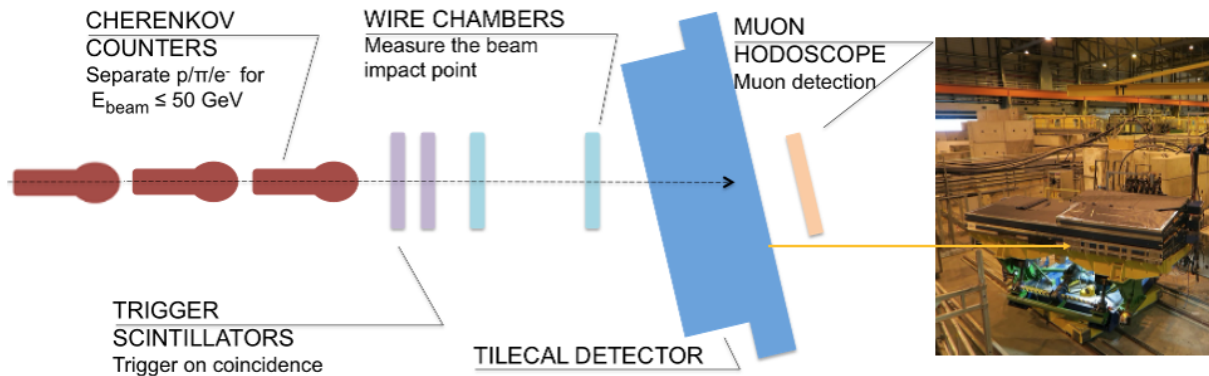


Figure 2: The schematic diagram of the ATLAS TDAQ system, with emphasis on the upgrade of the local TTC system.

on the test-beam program. For interface with the back-end electronics, these modules comprise of Photo-Multiplier Tubes (PMT) blocks with 3-in-1 cards, Digitizer boards, and Interface boards. During test-beams, legacy modules are critical in allowing a comparison between the legacy and new readout electronics. The Demonstrator module incorporates two options: the PMT blocks in the outside minidrawers which are powered by the High Voltage (HV) remote system, while the PMTs in the central minidrawers are powered by the HV internal system. Each upgraded module receives Low Voltage (LV) power from a finger LV power system connected to the module's extreme, and controlled by the legacy detector control system software.

The TileCal modules on top of the scanning table are exposed to low-energy hadrons, electrons and muons in the range of 20–160 GeV. The scanning table is built to rotate the modules at different angles and positions with regard to the incident beam. Data-taking during beam conditions is steered by the DAQ system. The BE electronics are a combination of the legacy and the new upgrade readout electronics. The legacy BE Read-Out Driver (ROD) crate consists of a Single Board Computer, a ROD and a Transition Board Module. The upgrade modules transmit data to two Tile PreProcessor (TilePPr)<sup>1</sup> boards integrated within the legacy TDAQ software through the TTC and ROD interfaces. The TTC system uses the TDAQ software to configure the legacy and upgraded electronics.

### 3. Upgrade of the Test-beam TTC system with the ALTI board

The ALTI module is a new electronic board designed for the ATLAS experiment at CERN as part of the TTC system [8]. It integrates the functionalities of the four existing modules shown in figure 3 (left), which are currently used in the local TTC system of experiment: Local Trigger Processor (LTP), Local Trigger Processor interface (LTPi), TTC VME bus interface (TTCvi) and the TTC emitter (TTCex). The primary function of the ALTI board is to provide interface between the Level-1 CTP and the local TTC system of the sub-detector. It is made of state-of-the-art components and the logic is implemented in a single FPGA, which allows for more flexibility and added functionalities. During the operation of the detector, the ALTI module receives the TTC signals from the CTP through parallel twisted-pair of low voltage differential signaling cables and distributes them to the sub-detector electronics through the optical TTC distribution network. The full LHC turn consists of 3564 bunch crossings (BCs). The signals received from the CTP are the bunch clock, orbit signal, L1A with 8-bit trigger type and the event counter reset. The bunch clock is the main timing signal produced by the LHC and has

<sup>1</sup> The TilePPr Demonstrator [7] is used to run and read out the Demonstrator module, allowing backward compatibility with the current ATLAS TDAQ and TTC system.

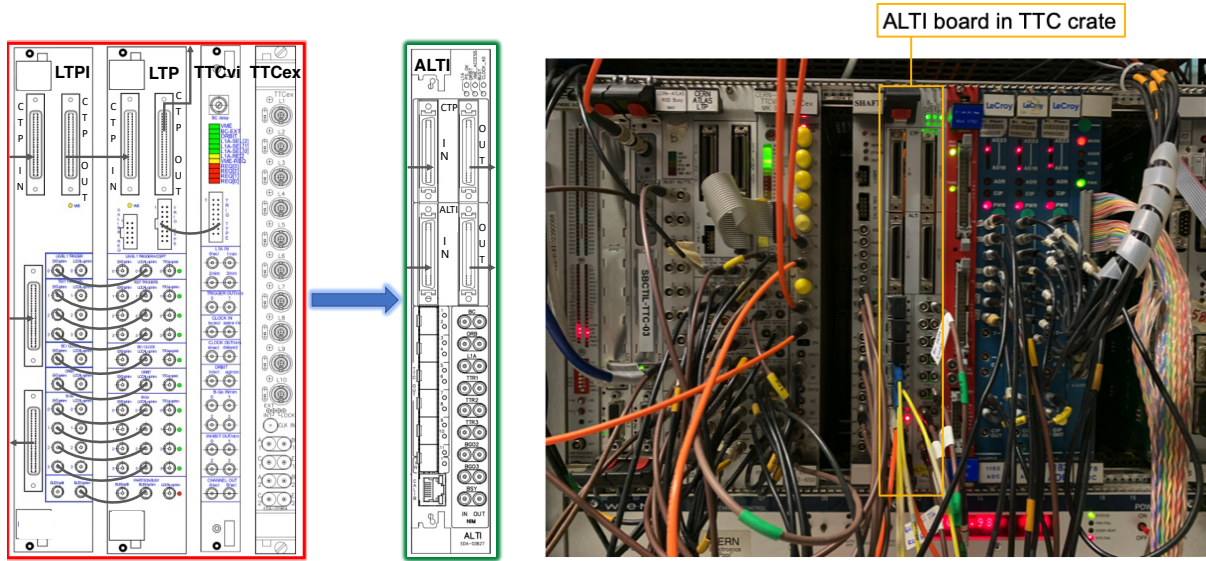


Figure 3: The ALTI module replaces the four legacy TTC modules (left). The ALTI module with new optical fibres integrated in the BE electronics' TTC crate (right).

a frequency of 40 MHz and the orbit signal is the second timing signal that indicates the start of a new LHC turn and allows the identification of the BCs. TileCal ALTI software has been developed, validated and integrated into the Tile online software. The Object Kernel Support (OKS)<sup>2</sup> database for the TileCal test-beam system, has been modified for the ALTI board. The ALTI schema file is loaded in the OKS database and ALTI objects are created from the ALTI classes. In one of the test-beam NIM crates, the beam trigger logic is developed using timer counters, discriminators, and Fan-in/Fan-out modules. When a beam particle creates a signal on the two scintillators, the beam trigger provides a Master trigger signal. The Master signal is then sent to a second NIM crate, which starts the time-to-digital converter measurement of the beam chamber signals and reads out the analog-to-digital converter used for scintillator signal digitization. In addition to generating the Master trigger, the trigger logic sends the L1A signal to the ALTI in the TTC crate, unless the busy signal indicates that the readout path is unavailable. The ALTI then sends the L1A signal to the TilePPr, RODs, and FE electronics.

### 3.1. Calibration systems and the Diagnostics and Verification System

The updated TileCal ALTI software required an upgrade of the calibration systems [9] as well as the Diagnostics and Verification System (DVS) [10]. These systems have been rigorously tested in relation to the legacy TTC system. To achieve good energy determination and to account for changes in the readout electronics caused by irradiation, ageing, and electronic failures, the TileCal utilizes very accurate and precise calibration systems. The calibration systems are the Cesium system, Laser system, Charge Injection Scan (CIS) and the Minimum Bias System. More details about the calibration systems can be found in refs. [9, 11]. Each system checks a different component of the readout electronics chain and the total calibration of each readout channel is provided by a combination of these tests.

<sup>2</sup> OKS is an object-oriented database with storage based on XML

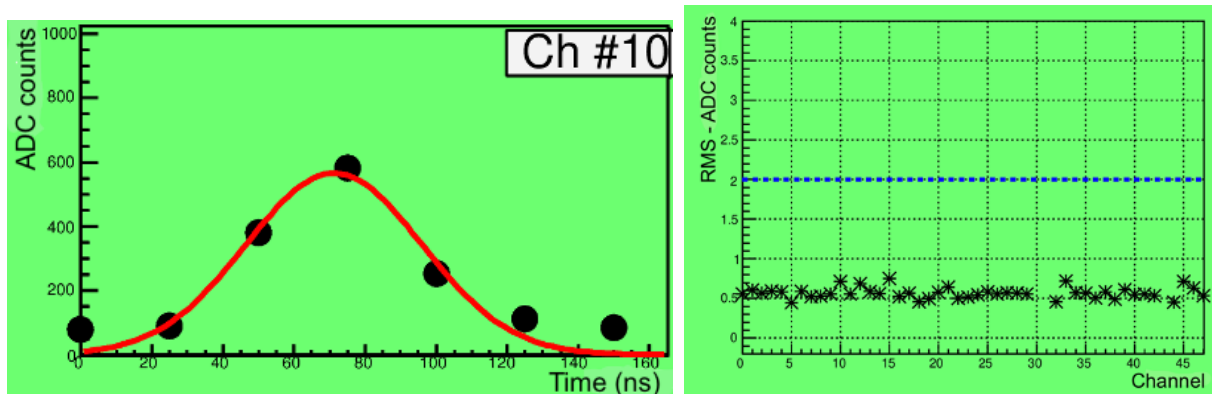


Figure 4: The CIS DVS test performed on one operational read-out module indicates a good reconstructed pulse of ADC counts versus time for seven samples per channel (left). The RMS ADC counts versus the channel number are shown in the pedestal DVS test, and the electronics noise level is below the set RMS ADC threshold of 2 counts for all read-out channels (right).

#### 4. Results

Calibration and DVS results are performed to validate the new TDAQ system using the ALTI board. Seven samples are produced when the DAQ system is well calibrated, the samples result in a Gaussian fit for pulse recognition. The DVS tests are used to check for the digital readout of the super-drawers, and are performed for CIS as shown in figure 4 (left) and Pedestal as shown in figure 4 (right). CIS results show a good pulse shape resulting from good signal reconstruction. Pedestal results show that noise levels are within acceptable levels for module LBA01.

#### 5. Conclusions

Several test-beam campaigns are conducted at the CERN SPS North area in the Prévessin site, to evaluate the TileCal Phase-II upgrade electronics for the HL-LHC project. There are usually two test-beam periods during the year and each test-beam period takes two weeks, with access to the beam line. Data is collected, with Tile modules being sampled with varying energy beams and positioning to the beam line. The TileCal TTC system has been successfully migrated to use the ALTI board. Calibration and DVS results to validate the TDAQ system are shown, in preparation for the upcoming test-beam campaigns using the ALTI system. Results for the first test-beam campaign using the ALTI system, showing the distributions for kaons, pions, and electrons, will be obtained in November 2022.

#### References

- [1] Alici A, Bomben M, Dawson I and Sonneveld J 2021 *CERN Yellow Rep. Monogr.* **1** 23–34
- [2] Hrynevich A (ATLAS) 2017 *JINST* **12** C06021
- [3] Vazquez Schroeder T (ATLAS) 2017 *PoS EPS-HEP2017* 525
- [4] Abolins M *et al.* (ATLAS TDAQ) 2016 *JINST* **11** P06008
- [5] Di Girolamo B, Dotti A, Giangiobbe V, Johansson P, Pribyl L and Volpi M 2005 Beamline instrumentation in the 2004 combined ATLAS testbeam Tech. rep. CERN
- [6] Spanggaard J 1998 Delay Wire Chambers - A Users Guide Tech. rep. CERN Geneva URL <https://cds.cern.ch/record/702443>
- [7] Carrió F, Moreno P and Valero A (ATLAS Tile Calorimeter System) 2016 *JINST* **11** C03047
- [8] Ask S *et al.* 2008 *JINST* **3** P08002
- [9] Aaboud M *et al.* (ATLAS) 2018 *Eur. Phys. J. C* **78** 987 (Preprint 1806.02129)
- [10] Barczyk M *et al.* 2003 *eConf C0303241* TUGP005 (Preprint hep-ex/0305106)
- [11] Cortés-González A (ATLAS) 2018 *EPJ Web Conf.* **170** 01003

# Threading a Laser Through the Eye of a Needle: Multimode Fibre Coupling in Turbulence

**Fortune Iga and Mitchell A. Cox**

School of Electrical and Information Engineering, University of the Witwatersrand,  
Johannesburg, South Africa

E-mail: igakayala@gmail.com

**Abstract.** The unequal access to reliable internet connectivity between urban and peri-urban areas remains a concern in many developing countries, including South Africa. A major reason for this digital divide is the unequal distribution of fibre infrastructure, which is typically caused by economic or geographic factors. Free Space Optical (FSO) communication could be used to mitigate this disparity by extending the optical network without the need for additional fibre installation. This would provide users access to the larger unlicensed spectrum provided by optical networks. However, modern FSO systems remain expensive and inaccessible to low-income residents of peri-urban areas. The cost of such technology could be significantly improved by “hacking” off-the-shelf fibre hardware, such as small form-factor pluggable (SFP) transceiver modules. However, coupling light into fibre hardware is difficult due to the atmospheric factors which attenuate optical signals in free space. Most severe of these factors is atmospheric turbulence which causes beam wander and intensity fluctuations. Literature has shown that optical fibre cables have been used to channel free space light into SFP transceiver modules. However, with the variety of standard “off-the-shelf” fibre cables available, it is unclear which of them would best couple light into fibre hardware. As such, this proceeding proposes research into the optimization of light coupling from free space into fibre hardware, by investigating the coupling performance of OM1, OM4 and OM5 multi-mode fibres cables in the presence of atmospheric turbulence. The received power and scintillation indices are compared. It was found that the OM4 fibre cable coupled the most optical power while the OM1 fibre cable had the least scintillation index. The OM5 fibre cable performed the worst in the conducted experiment.

## 1. Introduction

When compared to other African countries, South Africa has a high concentration of terrestrial fibre installations. This allows 67% of its population to live within 1 km of fibre infrastructure. However, the final connection which links the end-users to fibre infrastructure remains a challenge in many parts of the country. A reason for this is the high costs of drilling and trenching required for the extension of fibre networks. This leads to unequal fibre access between wealthy communities that can afford fibre cable installations and poorer communities whose residents have low disposable income [1]. A possible solution to the last mile fibre access challenge is free space optical (FSO) communication. Free space optical communication is the point-to-point transmission of information encoded on a laser beam which propagates through the atmosphere [2]. This concept could be used to bridge the gaps within the fibre optical network without the use of additional fibre cabling. Modern FSO systems are able to transmit large amounts of data at gigabit speeds across tens of kilometres [3]. However, such technology remains expensive and inaccessible to low-income populations. This is due to the expensive high-power lasers and custom electronics required to overcome the attenuating factors within the atmosphere.

Researchers have explored the use low-cost off-the-shelf fibre hardware, such as small form factor pluggable (SFP) transceiver modules, in FSO applications. This would significantly lower the cost of such technology and allow for easier deployment of FSO systems in different scenarios, including last mile connections. However, the challenge in doing this is coupling light from free space into fibre hardware. Different methods have been used to do this as seen in the following works. Ref. [4] demonstrates a cost-effective FSO system that uses a bidirectional SFP module to transmit data across 125 m. A short single mode fibre with a subscriber connector (SC) is used to guide the light into and out of a bidirectional SFP. In [5], a 1550 nm SFP transceiver module is used to develop a 500 m FSO system. A single mode fibre cable is used on the transmitting part of the SFP module, while a multimode fibre cable is used to receive the signal. A 1 Gbps FSO system is developed using a 1550 nm SFP module in [6]. The link is tested through a 7.2 m atmospheric chamber. The beam is coupled into the SFP using a multimode fibre with a core size of 1 mm for a large field of view. This work emphasized that the dominant power loss was a result of coupling light from free space into the fibre cable at the receiver side. A self-aligning FSO system is presented in [7]. Spatial division multiplexing was used by coupling light beams into eight multimode fibres cables of 50  $\mu\text{m}$  cores which were connected to eight separate SFP transceivers. This link was tested across 210 m.

According to the literature reviewed above, fibre optical cables have been utilized to channel free-space light into fibre hardware. Literature has also shown that fibre coupling in such systems is the main source of power loss due to the inherent difficulty of fibre coupling [6]. There are different types of fibre cables available which have been designed and characterized for fibre network applications. However, little work has been done to characterize the light gathering capabilities of these fibre cables when used in free-space coupling. As such, the performance of fibre cables in free-space coupling remains largely unknown. Such information would be beneficial to designers as it would inform them of which fibre cable would lead to the lowest power loss.

For this reason, this proceeding aims to contribute to the optimized use of low-cost off-the-shelf fibre hardware in FSO systems, by comparing the coupling performance of different fibre cables in the presence of atmospheric turbulence. This is done to determine the optimal fibre cable to use for this application. Experimental testing will be done by coupling light that travels across a 140 m FSO link into various fibre cables and evaluating the results.

## 2. Background

### 2.1. *Effects of Atmospheric Turbulence*

One of the most detrimental factors that affect free space optical communication is atmospheric turbulence [8, 9]. Atmospheric turbulence is caused by random fluctuations in temperature and pressure which form regions of unstable air masses called turbulent eddies. These eddies have independent characteristics and vary in size and density. Turbulent eddies also vary in refractive indices. As such, when light propagates through them refraction takes place.[10]

The effect of turbulence on a propagating light beam is dependent on the size of the turbulent eddies encountered. If a turbulent eddy is larger than the beam diameter, the entire beam deflects. This is known as beam wander (or beam steering) which causes the light beam to have a “cork screw” motion through the atmosphere. This results in lateral displacement and angular misalignment at the receiving aperture. If a small detector is used at the focal point, the misalignment caused by beam wander will attenuate the received power. This is known as signal fading and can lead to loss of information if the power is beneath the link margin. Deep fades refer to situations where the signal power or intensity is too low for reliable communication [11].

If a turbulent eddy is of a similar size to the beam diameter, it focuses or defocuses the light in a lens-like manner. This leads to fluctuations in the light intensity detected at the receiver plane. This is a phenomenon known as scintillation. Scintillation often leads to degradation of the signal-

to-noise ratio and deep random signal fades. The amount of scintillation faced by an optical system is characterized using the normalized variance of intensity, which is known as the scintillation index,  $\sigma_I^2$ . The scintillation index is calculated as

$$\sigma_I^2 = \frac{\langle I^2 \rangle - \langle I \rangle^2}{\langle I \rangle^2} = \frac{\langle I^2 \rangle}{\langle I \rangle^2} - 1. \quad (1)$$

If the eddy is smaller than the diameter of the beam, a portion of the light is deflected away from the rest of the beam. This leads to loss in received power. This effect is minimized by ensuring that the beam diameter is smaller than the coherence length of the atmosphere which is known as the Fried parameter [10]. The coherence length is the radius in which turbulence is correlated. Outside this radius, turbulence is uncorrelated and independent [11].

## 2.2. Optical Fibre Cables

Optical fibres are cylindrical dielectric wave guides used to transport information in the form of optical energy. Optical fibres consist of three main concentric layers which are the core, cladding and coating. The core is the central region in which light is guided through. It is usually made up of low-loss silica glass and index modifying dopants. The core is embedded in the cladding, which is made of a similar material, but with a slightly lower refractive index. Surrounding the cladding is a protective coating, which is the first non-optical layer. It is a cushioning polymer which protects the silica structure against physical and environmental damage. Extra protecting is often added by incorporating an outer coating reinforced with steel or kevlar material. Light travels through the core of an optical cable, where it is confined by the principle of total internal reflection. For this to occur, light within the fibre core should strike cladding boundary at an incident angle which results in a refractive angle greater than  $90^\circ$ . This causes the light beam to reflect back into the core. The maximum angle of incident at the face of a fibre cable which results in total internal reflection is known as the acceptance angle. This angle is characterized by a dimensionless factor known as the numerical aperture (NA), which is a function of the acceptance angle  $\theta_a$  given by [12]

$$NA = \sin(\theta_a). \quad (2)$$

There are two types of fibre cables which are single mode and multi-mode fibres. Single mode fibre cables can only transmit one ray (mode) of light and typically have very small core diameters of about 9 microns. This makes coupling into single mode fibre very challenging and impractical in long range FSO systems. Multi-mode fibre cables have much larger core sizes, with common core diameters being 50 and 62.5 microns. This allows easier coupling of light into a multi-mode fibre cable. For this reason, only multi-mode fibre cables are considered in this research. The effects of modal dispersion are assumed to be negligible in this work because only a short piece of multi-mode fibre is required to couple light into the fibre hardware.

There are five standard classes of multi-mode fibre cables, which are shown in Table 1. All fibre cables in these classes have graded index profiles. In a graded index profile, the refractive index of the fibre core gradually decreases in a concentric manner with the highest value being at the center. This causes the light rays to propagate through the fibre core in sinusoidal shapes, minimizing modal dispersion and allowing for high data rates across longer distances. The different multi-mode classes each have a unique graded-index profile. This is because manufacturers have attempted to improve performance by optimizing the refractive index profile. This has led to improved modal bandwidths in newer multi-mode classes as seen in Table 1. Despite the improved performances, the impact of the different graded-index profiles on free space coupling is unknown. However, through testing, it is possible to determine which fibre cable works best for this application.

OM1 and OM2 fibre cables have similar characteristics and can be used interchangeably in many applications. The same is true for OM3 and OM4 fibre cables. For this reason, only OM1, OM4 and OM5 multi-mode fibre cables were considered at this stage of the research.

Table 1: Characteristics of the 5 Multi-mode fibre cable Classes

Class	Colour Code	Core Diameter	NA	Modal Bandwidth
OM1	Orange	62.5 $\mu\text{m}$	0.275	200 MHz*km
OM2	Orange	50 $\mu\text{m}$	0.2	500 MHz*km
OM3	Aqua	50 $\mu\text{m}$	0.2	2000 MHz*km
OM4	Aqua	50 $\mu\text{m}$	0.2	4700 MHz*km
OM5	Lime Green	50 $\mu\text{m}$	0.2	28000 MHz*km

### 3. Methodology and Data Collection

Atmospheric turbulence leads to power attenuation and scintillation. As such, the optimal fibre cable used for free space coupling should couple the highest amount of optical power and have the least scintillation index. To test this, a 140 m FSO link was established between two buildings at the University of the Witwatersrand. A custom designed optical cage system was used to focus light beams onto the fibre cable tips. A 75 mm plano-convex lens with a focal length of 250 mm is used in the cage system, resulting in an f-number of 3.33. At this f-number, the airy disk diameter focused on the fibre tips is 12.59  $\mu\text{m}$ , as seen in Equation 3, and incoming half angle of 8.53°. This airy disk diameter and half angle are smaller than the fibre core diameters and within the numerical apertures of all three multi-mode fibre cables that will be tested, allowing for effective coupling.

$$\phi = 2.44\lambda F\# \quad (3)$$

A 1510/1590 nm bidirectional small form factor pluggable transceiver module was used as the light source. After propagating through the link, the beam was coupled into a multi-mode fibre cable at the receiver and was measured and recorded using an infrared optical power meter (PM16-122) operating at a sampling time of 90 ms. The power meter used measures wavelengths between 700 nm to 1800 nm with a power range of 50 nW to 40 mW. Power measurements taken for three-minute intervals each, which leads to approximately 2000 samples for each measurement interval as in Figure 1. The fibre cables are tested sequentially and a total of eleven data sets were recorded for each cable at different times of the day.

### 4. Results and Discussion

The above mentioned experiment was carried out to analyse the coupling performance of the different fibre cables in real atmospheric turbulence. As expected, the received optical signal is turbulent and noisy, as seen in Figure 1a, which is an example of the optical power coupled in an OM1 fibre cable. The average for each dataset was calculated as summarized in Figure 1c, with error-bars indicating standard deviation. To measure the fluctuations within the entire optical system, the scintillation indices were calculated using equation 1. This measurement indicates which fibre cable is most resilient to fluctuations caused by different factors including atmospheric turbulence. The scintillation indices are calculated across 50 points within the data, resulting in a moving scintillation index as seen in Figure 1b. The averages of the scintillation indices were calculated for each data set and are summarized in Figure 1d. It can be observed

that data sets of high optical power had low the scintillation indices. Figure 1d shows that the highest scintillation index observed is 0.13, implying weak turbulence at this range.

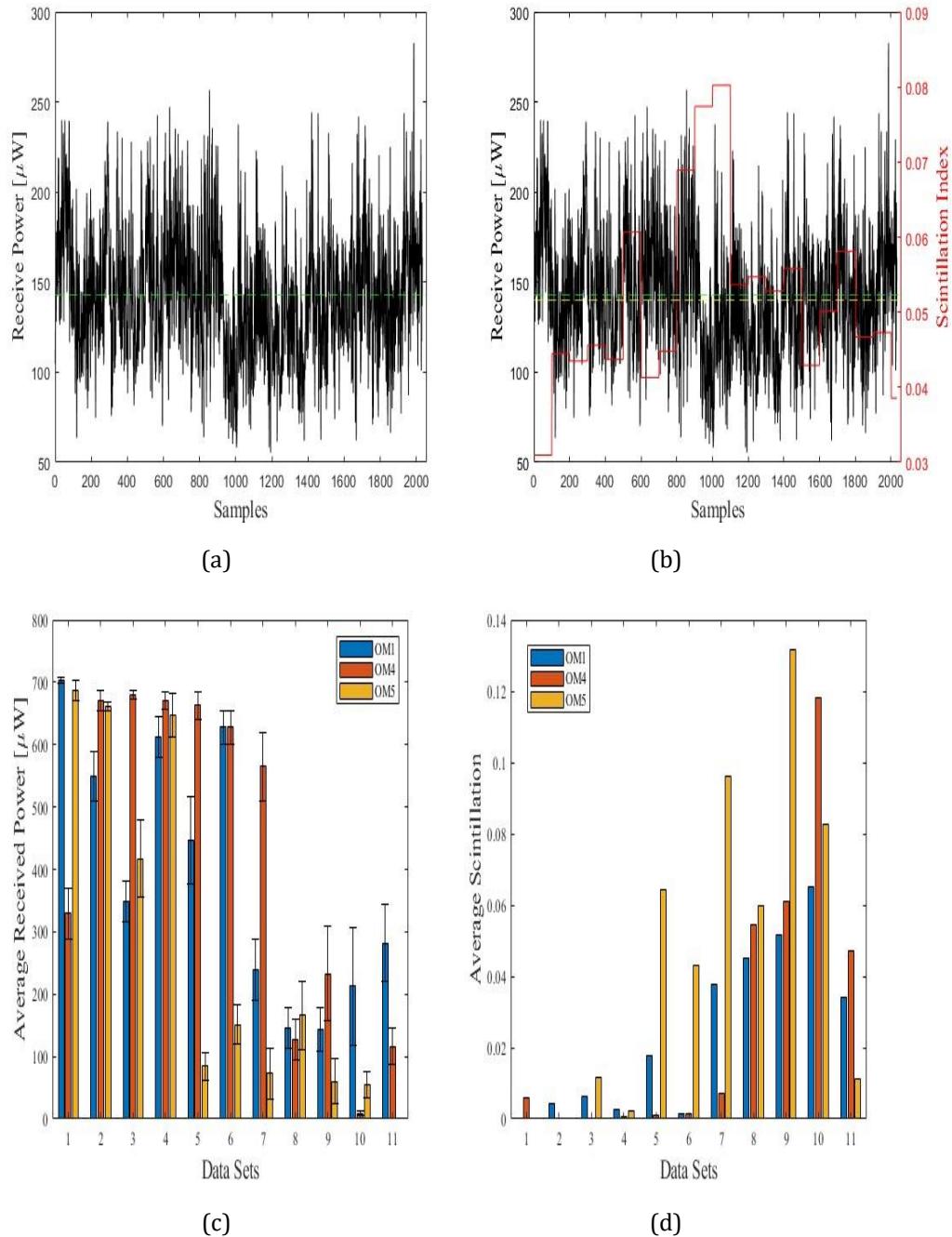


Figure 1: **Optical Power and Scintillation Index** (a) shows the optical power coupled into an OM1 multimode fibre cable with the average power represented by the green dashed line. (b) shows the scintillation index calculated across 50 power samples. The yellow dashed line represents the average scintillation index. (c) shows the average power coupled in each data set. OM1, OM4 and OM5 are represented by the blue, orange and yellow bars. (d) shows the average scintillation index experienced in each data set. Similarly, OM1, OM4 and OM5 are represented by the blue, orange and yellow bars.

The average of the power and scintillation index means was calculated and is shown in Figures 2a and 2b. These graphs show that on average the OM4 multi-mode fibre coupled the most optical power, while the OM1 fibre cable had the lowest scintillation index. However, the error bars of the two fibre cables overlap in each Figure, implying that they performed very similarly. Despite the OM5 cable having the highest modal bandwidth, as seen in Table 1, it performed the worst in this experiment. On average it coupled the lowest optical power and had the highest scintillation index.

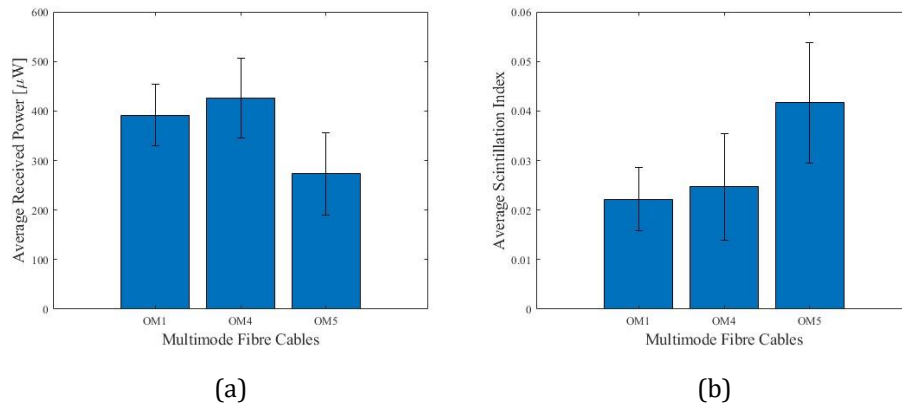


Figure 2: **Average of Power and Scintillation Index** (a) shows the average of the mean power values for each data set and the corresponding error bars. (b) shows the average of the mean scintillation index values of each data set and the corresponding error bars.

## 5. Conclusion

This proceeding has presented an investigation carried out to determine the optimal fibre cable to use for free space light coupling in the presence of atmospheric turbulence. The results have shown that the OM1 and OM4 multi-mode fibre cables had a comparable performance with overlapping error bars. While the OM5 multi-mode fibre cable had the worst results, with the lowest power coupled and the highest scintillation index. This research will be extended upon by increasing the range in order to increase the atmospheric turbulence strength.

## References

- [1] Lavery M P, Abadi M M, Bauer R, Brambilla G, Cheng L, Cox M A, Dudley A, Ellis A D, Fontaine N K, Kelly A E, Marquardt C, Matlhane S, Ndagano B, Petruccione F, Slavík R, Romanato F, Rosales-Guzma'n C, Roux F S, Roux K, Wang J and Forbes A 2018 *Nature Photonics* **12**(5) 249–252 ISSN 17494893
- [2] Ghassemlooy Z and Popoola W O 2010 Terrestrial free-space optical communications URL [www.intechopen.com](http://www.intechopen.com)
- [3] Trichili A, Cox M, Ooi B and Alouini M S 2020 *Journal of the Optical Society of America B* **37**
- [4] Mustafa L and Thomsen B 2013 Reintroducing free-space optical technology to community wireless networks *19th Americas Conference on Information Systems, AMCIS 2013, Chicago, Illinois, USA, August 15-17, 2013* (Association for Information Systems) URL <http://aisel.aisnet.org/amcis2013/ISUsage/RoundTablePresentations/3>
- [5] Sekhar C, Agrawal J and Farook O 2005 Designing a free space optical/wireless link pp 10.416.1–10.416.13

- [6] Abadi M M, Ghassemlooy Z, Mohan N, Zvanovec S, Bhatnagar M R and Hudson R 2019 Implementation and evaluation of a gigabit ethernet fso link for 'the last metre and last mile access network' (Institute of Electrical and Electronics Engineers) ISBN 9781728123738
- [7] Abadi M M, Cox M A, Alsaigh R E, Viola S, Forbes A and Lavery M P 2019 *Scientific Reports* **9**(1) ISSN 20452322
- [8] Hamza A, Deogun J and Alexander D 2018 *IEEE Communications Surveys Tutorials*
- [9] Al-Gailani S, Mohd Salleh M F, Salem A, Shaddad R, Sheikh U, Algeelani N and Almohamad T 2020 *IEEE Access*
- [10] Kaushal H, Jain V and Kar S 2017 *Optical Networks: Free Space Optical Communication* (Springer) ISBN 978-81-322-3689-4 URL <http://www.springer.com/series/6976>
- [11] Cox M A, Gailele L, Cheng L and Forbes A 2019 URL <http://arxiv.org/abs/1907.10519>
- [12] Saleh B E A and Teich M C 1991 *Fiber optics*

# Ion fraction measurements of vacuum arc thrusters

**P Stansell, P Ferrer**

School of Physics, University of the Witwatersrand, Johannesburg, Wits 2050, South Africa

E-mail: prstan2@gmail.com

**Abstract.** The Vacuum Arc Thruster (VAT) is a simple electric propulsion system that produces a metal plasma. The VAT has potential as the plasma source for a high performance gridded ion thruster, the vacuum arc ion thruster VAIT. As the efficiency of such a system ultimately depends on the amount of ion current that the VAT can produce, ion and arc current measurements were made for three different VATs: coaxial thrusters firing steel and bismuth cathodes and a planar steel thruster. A maximum ion to arc current ratio of  $10.27 \pm 0.5\%$  was obtained from the coaxial thruster firing steel, followed by the coaxial bismuth thruster at  $7.5 \pm 0.5\%$  and the planar steel at  $6.73 \pm 0.5\%$ . These results are discussed in the context of the ion thruster, and some drawbacks of the VAT plasma source are presented. It is concluded that the VAT may be suitable as a plasma source as long as the unique demands of high peak ion current and non-uniform plasma density can be accommodated by the grid system.

## 1. Introduction

Gridded ion thrusters operate by accelerating ions from a plasma through a strong electric field, between two or more grids, to very high velocities. These ion thrusters offer some of the highest electrical efficiencies (60–80%) and specific impulses ( $> 5000s$ ) of any practical space propulsion system [1]. This makes them ideal for use on deep space missions, as well as for station keeping applications. Gridded ion thrusters are most commonly fueled by noble gases such as xenon or krypton, which are expensive and require mass-intensive gas handling equipment. The vacuum arc thruster, henceforth abbreviated as VAT, on the other hand, is a very simple low efficiency, low specific impulse propulsion system that uses pulsed arcs to ablate a cathode metal into a plasma [2]. Although the VAT trades performance for simplicity it potentially has many advantages as the plasma source for a high performance two stage system: the vacuum arc ion thruster (VAIT). In this device a VAT would be used to produce a metal plasma from which metal ions would be accelerated through a set of grids. Compared to traditional gas-based plasma sources, the VAT is compact and lightweight and overall much simpler in design. Second, it produces a highly ionised plasma with few neutrals which is desirable for an ion thruster [3]. Finally, it can produce beams of heavy metal ions such as bismuth and uranium - which are 60 and 82 percent heavier than xenon respectively, which is simply not practical with other plasma sources. These higher ion masses mean greater thrust levels are attainable for the same beam current level. As grid erosion is determined ultimately by the beam current, this means a vacuum arc ion thruster could potentially have longer grid lifetimes than gas-based systems [8]. Ultimately the efficiency of the VAT as an ion thruster plasma source depends on how much ion current is produced for a given arc current. This is expressed as the ion fraction  $f_i$ , also known as the ion to arc current ratio; the determination of this value is the key focus of

this work. Basic space propulsion figures of merit for a vacuum arc ion thruster are presented followed by ion current measurement results from three different vacuum arc thrusters. From these measurements the ion fraction is determined. Finally we discuss these results and outline potential challenges of using the VAT as a plasma source.

## 2. Vacuum arc ion thruster figures of merit

In a VAIT, the beam current is the total ion current from the VAT that can be extracted by the grid system. The ion to arc current ratio or ion fraction,  $f_i$ , is simply:

$$f_i = \frac{J_i}{J_d} \quad (1)$$

Where  $J_d$  is the arc discharge current and  $J_i$  is the total ion current. The ion mass flow rate is dependent on the ion to arc current ratio,  $f_i$ , the ion mass  $M_i$  and the average ion charge state  $\langle Z \rangle$ , where  $e$  is the electron charge.

$$\frac{dm_i}{dt} = \frac{M_i f_i J_d}{e} \langle Z^{-1} \rangle \quad (2)$$

The ion current from a VAT is not uniform and has an exponential distribution. Thus a correction factor,  $C_j$ , is applied to take this into account. The effective grid transparency is given by  $\phi_g$ . Therefore the ion beam current,  $J_b$ , is:

$$J_b = f_i J_d C_j \phi_g \quad (3)$$

The ion velocity,  $u_i$ , can then be derived from conservation of energy:

$$\frac{1}{2} M_i u_i^2 = e V_b \langle Z \rangle \quad (4)$$

$$u_i = \sqrt{\frac{2e \langle Z \rangle V_b}{M_i}} \quad (5)$$

Writing the ion beam mass flow rate:

$$\frac{dm_{ib}}{dt} = \frac{dm_i}{dt} \phi_g C_j = \frac{f_i J_d C_j \phi_g M_i}{e} \langle Z^{-1} \rangle \quad (6)$$

The thrust is simply:

$$T = \frac{dm_{ib}}{dt} u_i = f_i J_d C_j \phi_g \sqrt{\frac{2M_i V_b}{e}} \langle Z^{-\frac{1}{2}} \rangle \quad (7)$$

and the specific impulse:

$$I_{sp} = \frac{T}{\frac{dm_t}{dt} g} = \frac{f_i C_j \phi_g \langle Z^{-\frac{1}{2}} \rangle}{E_r g} \sqrt{\frac{2M_i V_b}{e}} \quad (8)$$

Where  $E_r$  is the VAT cathode erosion rate expressed in  $\frac{kg}{C}$  [6]. As shown above, both the thrust and specific impulse ultimately depend on the ion fraction  $f_i$ , equation (1). The determination of this value for a variety of cathode materials and thruster geometries is the focus of this work.

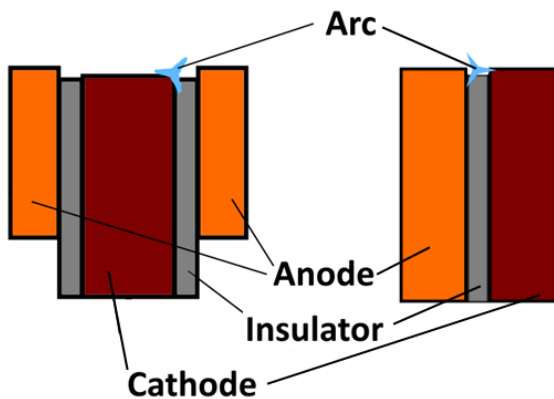


**Figure 1.** Cross section showing the simple geometry of coaxial (left) and planar (right) thrusters.



**Figure 2.** The three VATs used in this work. Left to right: Bismuth coaxial thruster showing clear cathode erosion, coaxial steel thruster with minor erosion and planar steel thruster during arc operation.

### 3. Total Ion Current Measurements

In order to determine the ion fraction,  $f_i$ , the total ion current and arc currents were measured and the ratio between them calculated, see equation (1). A large collector was used to completely encapsulate the VAT so that ions could be captured from all angles surrounding the thruster, including from behind the thruster. Three different thrusters were tested, a coaxial thruster with a bismuth cathode (99.9% Bi), a coaxial thruster with a mild steel (99.6% Fe) cathode and a planar thruster with a mild steel cathode. The coaxial thrusters had cylindrical cathodes 6.25mm in diameter and an alumina ceramic ( $Al_2O_3$ ) tubular insulator 3mm thick. The coaxial thruster anodes were copper. The planar thruster had a 1mm flat borosilicate glass insulator separating the anode and cathode which were both mild steel pieces 20mmx5mmx10mm. The planar glass insulator was recessed by 1mm allowing the cathode direct view of the anode. The coaxial thrusters had no recession and the surfaces of the cathode insulator and anode were all in the same plane. A cross section of the geometry is shown in figure 1 and the thrusters are shown in figure 2. All thrusters were driven by the same circuit which relied on an inductive high voltage spike to initiate the arc [4]. Experiments were conducted at  $1.5 \pm 0.5 \times 10^{-6}$  Torr. A  $0.1\Omega$  resistor was used to measure the ion current, this low value was chosen to prevent a large voltage drop across the collector which could prevent proper repulsion of plasma electrons. The maximum voltage drop the collector would have experienced is  $V = IR = 4 \times 0.1 = 0.4V$ , which should have a negligible impact on electron repulsion. The circuit drive voltage, which is also the anode voltage relative to the cathode, was 48V. In typical VAT drive circuits, the arc energy predominantly comes either from a capacitor or an inductor which leads to a very sharp triangular arc pulse shape [5]. This is undesirable for a plasma source as this arc current shape will produce a highly non-uniform ion current. Thus the circuit used in this work was tuned to better match the impedance of the arc plasma, and operates as a one stage Rayleigh type pulse forming network producing roughly square shaped arc current pulses. In all tests the cathode was grounded and the ion collector plate was biased negative relative to ground to reflect electrons from the plasma plume. The negative bias on the collector plate was varied from -0.8V to -60V. Due to the fact that each arc modifies the cathode surface meaning no two arcs are the same, all results presented were averaged over 20 arc pulses.

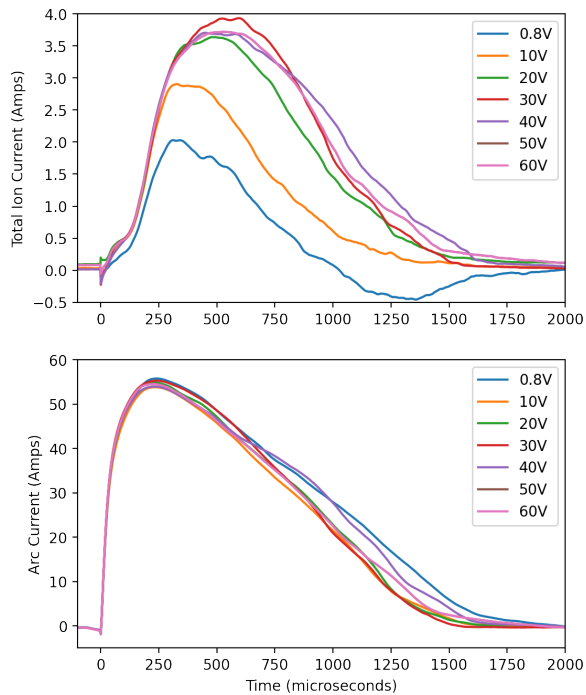


**Figure 3.** Coaxial bismuth thruster ion and arc currents over the range of ion collector negative bias voltages tested.

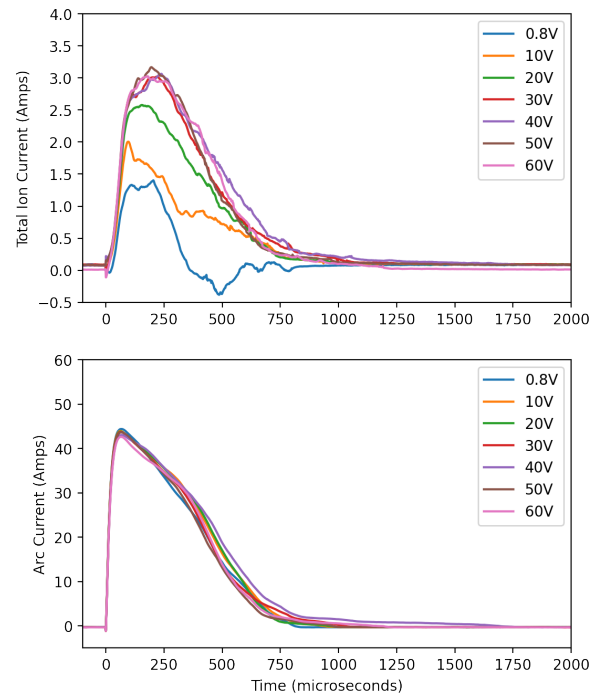


**Figure 4.** Coaxial steel thruster ion and arc currents over the range of ion collector negative bias voltages tested.

## 4. Results

### 4.1. General findings

The averaged arc and ion currents are shown in figures 3, 4 and 5, where the legend denotes the negative bias voltage on the ion collector. The time has been zeroed to the start of the arc pulse. The arc burns until the current drops below the minimum threshold necessary to sustain the arc, the arc chopping current. As bismuth has a lower discharge voltage than iron, it can sustain the arc for longer before reaching the chopping current. This is clearly seen by the difference in arc length in figures 3 and 4. The coaxial bismuth arcs lasted approximately  $1500\mu\text{s}$  while the coaxial steel arcs lasted only  $750\mu\text{s}$ . It is interesting to note that the planar steel thruster arcs also lasted  $1500\mu\text{s}$  despite having the same cathode material as the coaxial steel thruster. This may be due to the fact that the planar geometry, with a 1mm insulator was able to lower the arc chopping current and thus prolong the arc.

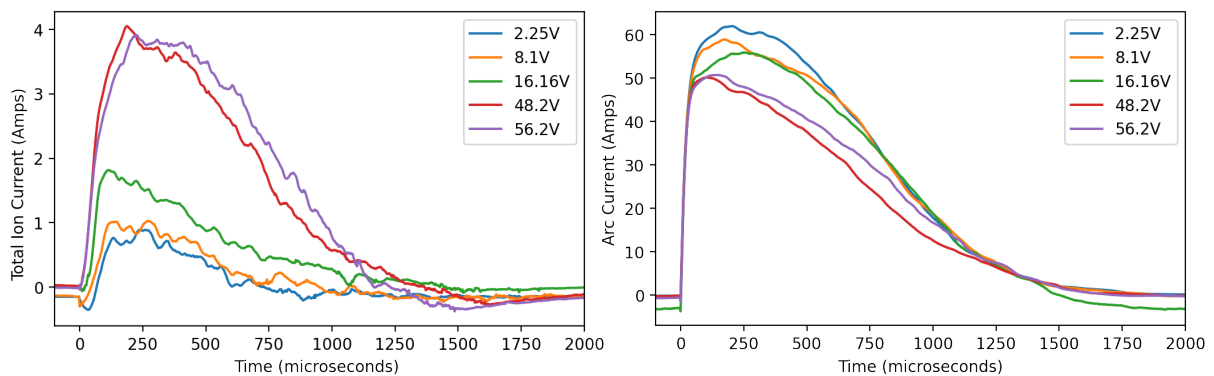
### 4.2. Ion to arc current ratios

Figure 6 shows the ion to arc current ratio expressed as a percentage of the arc current for all three thrusters. As bismuth has a much lower cohesive energy than iron, it was expected that the coaxial bismuth thruster would produce the highest ion to arc current ratio [7]. However, it was the coaxial steel thruster that had the highest ratio measured at  $10.27 \pm 0.5\%$ , followed by the bismuth thruster at  $7.5 \pm 0.5\%$  and finally the planar steel thruster at  $6.73 \pm 0.5\%$ . These values are in broad agreement with the literature where ion fractions of 5 – 10% are commonly observed. However, bismuth is often reported to have a higher ion fraction than other materials, up to about 12% [11, 3, 10]. The fact that the coaxial steel thruster produced significantly more ion current for a given arc current is interesting and warrants further investigation. One possibility is that the bismuth cathode began melting and so produced fewer ions. The fact that

the bismuth arcs burned at higher arc currents and for approximately twice as long as the steel arcs, coupled with bismuth’s much lower melting point lend support to this idea [7, 9].

4.3. Estimation of the plasma electron temperature

The electron temperature in vacuum arc plasmas is known to be on the order of 1 eV [7]. Figure 6 clearly shows a plateau in the ion to arc current ratio as the negative bias is increased beyond -20V. This suggests that the electron temperature is indeed low in all three thrusters regardless of geometry or cathode material.



**Figure 5.** Planar steel thruster ion and arc currents over the range of ion collector negative bias voltages tested.

During the planar steel thruster ion current measurements, there was an issue with the power supply limiting the current. These results were excluded and new tests were repeated with the same supply used for the coaxial thruster tests but at higher voltages. Unfortunately this lead to a lack of data points over the range 20-40V, however the trend of ion current saturation does still appear if somewhat less robustly.

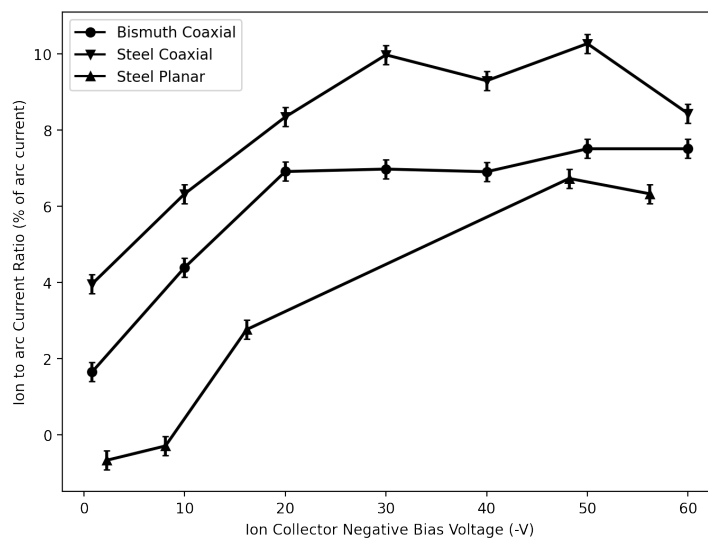


**Figure 6.** Ion to arc current ratio versus ion collector negative bias voltage, expressed as a percentage of the arc current.

## 5. Potential drawbacks of the VAT plasma source

The VAT produces a large ion current pulse of several amps. This places a high peak power demand on the accelerator supply; some 6kW peak power assuming 4A beam current and 1500V acceleration voltage. Alternatively a capacitor bank could be used but must be oversized to prevent significant voltage sag during the pulse. Furthermore the grid area would need to be large enough to accommodate this peak ion current. Another challenge to consider is that the plasma from the VAT has an exponential distribution; with  $C_j \approx 0.67$  as the plume divergence parameter. This means that even if the grid system is capable of extracting the total ion current from the VAT, the space charge limit may be exceeded along the cathode axis. Finally, as the pulse length of the vacuum arc is quite short, in this work some 1-1.5ms; the processes of extraction, acceleration and neutralisation must occur and reach equilibrium very quickly. This situation could be improved by increasing the arc pulse lengths, so long as the cathode can be kept below melting point.

## 6. Conclusion

In conclusion, the vacuum arc thruster was examined as the plasma source for a gridded ion thruster. The relevant spacecraft figures of merit were presented. Total ion currents were measured for three different VATs by encapsulating them in a large negatively biased ion collector and the ion to arc current ratio  $f_i$  was calculated. All thrusters produced ion currents of several amps and ion to arc current ratios above 6%. The coaxial steel thruster produced the highest  $f_i$  of  $10.27 \pm 0.5\%$ . Differences in arc currents, arc burning lengths and ion currents were observed and reasons for these discrepancies discussed. The ion currents began to saturate at -20V bias voltage which implies a low electron temperature in the vacuum arc plasma. These findings show that the VAT can readily produce several amps of metal ions, largely independent of thruster geometry or cathode material. The VAT may be a suitable plasma source if the burdens of high peak ion currents and non-uniform plasma density can be overcome.

## Acknowledgments

This work was supported in part by the South African National Space Agency (SANSA).

## References

- [1] Goebel, D.M. and Katz, I., 2008. Fundamentals of electric propulsion: ion and Hall thrusters. John Wiley Sons.
- [2] Keidar, M., Schein, J., Wilson, K., Gerhan, A., Au, M., Tang, B., Idzkowski, L., Krishnan, M. and Beilis, I.I., 2005. Magnetically enhanced vacuum arc thruster. *Plasma Sources Science and Technology*, 14(4), p.661.
- [3] Brown, I.G. ed., 2004. The physics and technology of ion sources. John Wiley Sons.
- [4] Anders, A., Brown, I.G., MacGill, R.A. and Dickinson, M.R., 1998. Triggerless' triggering of vacuum arcs. *Journal of Physics D: Applied Physics*, 31(5), p.584.
- [5] Kolbeck, J., Anders, A., Beilis, I.I. and Keidar, M., 2019. Micro-propulsion based on vacuum arcs. *Journal of Applied Physics*, 125(22), p.220902.
- [6] Polk, J.E., Sekerak, M.J., Ziemer, J.K., Schein, J., Qi, N. and Anders, A., 2008. A theoretical analysis of vacuum arc thruster and vacuum arc ion thruster performance. *IEEE Transactions on Plasma Science*, 36(5), pp.2167-2179.
- [7] Anders, A., 2008. Cathodic arcs: from fractal spots to energetic condensation (Vol. 50). New York: Springer.
- [8] Qi, N., Gensler, S., Prasad, R., Krishnan, M., Vizir, A. and Brown, I., 1998. A pulsed vacuum arc ion thruster for distributed small satellite systems. In 34th AIAA/ASME/SAE/ASEE Joint Propulsion Conference and Exhibit (p. 3663).
- [9] Lun, J., 2015. Performance improvement of vacuum arc thrusters (Doctoral dissertation, University of the Witwatersrand, Faculty of Engineering and the Built Environment, School of Mechanical, Industrial Aeronautical Engineering).
- [10] Boxman, R.L., Sanders, D. and Martin, P.J. eds., 1996. Handbook of vacuum arc science technology: fundamentals and applications. William Andrew.
- [11] Brown, I.G., 1994. Vacuum arc ion sources. *Review of scientific instruments*, 65(10), pp.3061-3081.

# Comparison between the empirical and machine techniques to predict global solar irradiance for Mutale area in Limpopo Province, South Africa

T.W Murida<sup>1</sup>, T.S Mulaudzi<sup>1</sup>, N.E Maluta<sup>1,2</sup>, N Mphephu<sup>3</sup>

<sup>1</sup>. Department of Physics, University of Venda, Thohoyandou, South Africa

<sup>2</sup>. National Institute for Theoretical and Computational Sciences (NITheCS), Gauteng, RSA

<sup>3</sup>. Standard Bank, South Africa

E-mail: [thaluwhitney@gmail.com](mailto:thaluwhitney@gmail.com)

**Abstract.** The prediction of solar irradiance is of utmost importance in guiding solar power conversion systems with a specific focus on design, modelling, and operation. Availability of solar irradiance data plays a significant role for decision-makers responsible for future investment policies on green energy. The lack of weather stations and measured solar parameters in most areas in the developing countries has led to the development of solar prediction models. However, reliable prediction of solar irradiance is dependent on the availability of quality data and the prediction methods. Empirical models have been developed and used in the past; however, in recent times intelligent algorithms have proved to have more predictive power due to the availability of high-frequency data. The study uses two empirical models namely: the Clemence model and Hargreaves and Samani model to predict the global solar irradiance at Mutale station in the Limpopo province in South Africa. Furthermore, machine learning and deep learning techniques namely: support vector machines, random forest and artificial neural network were also used to predict global solar irradiance in the same area. To assess the predictive power of these empirical and machine models, the estimated values for the global solar radiation were compared with the recorded data from the Mutale weather station. Based on the results that were found on this study, machine learning techniques tend to give better or good result compared with empirical models.

## 1. Introduction

There has been a consensus (United Nations) that several countries across the globe are confronted with significant energy crises. As energy consumption rises, the world will encounter a substantial shortage of fossil fuels in the future decades because such power sources provide most of the world's energy [1]. The existing of consumption energy across the globe is based almost completely on non-renewable resources like oil, gas, and coal. However, in recent times, there has been a call to reduce carbon emissions since these resources are not environmental free. The fundamental issue is the energy crises, particularly acute in emerging countries where there is a need to power families and industries [2]. It is estimated that in the next 30 years, the world will be overpopulated, and the energy demand will also increase [3].

The economy of developing countries that are highly industrialized, for example, South Africa, has a high energy demand. As the primary power provider in South Africa, Eskom relies on fossil fuels as an energy source, which is harmful to the environment. Using fossil fuels increases greenhouse gas emissions, such as carbon dioxide, causing global warming and hurting the ecosystem and biodiversity. The best solution to this challenge is for the world to move away from non-renewable resources and use renewable energy resources. In any given location, the demand for renewable and sustainable energy has increased.

Solar radiation from the sun is quickly becoming a viable alternative source to other traditional energy sources. Solar energy looks to be the most popular alternative among the various forms of clean energy sources because of its endless and non-polluting nature. Precise solar radiation estimation tools (which are the empirical models but due to their deficiencies in predicting solar radiation, machine learning has proved to have more predictive power due to the availability of high-frequency data) are critical in the design of the solar system. However, solar irradiance forecast depends on the available data and the forecasting methodologies used. Empirical models have been developed and used in the past, but due to the availability of high-frequency data, intelligent algorithms have recently proven to have more prediction potential [4].

## 2. Study area

The research area of this project has been selected to be at Mutale area, Limpopo province South Africa. The province experiences high temperatures averaged to 25.2°C in January while the coldest month is June at an average of 12.5°C. The geographic coordinates of the selected station are tabulated in table 1.

**Table 1.** Geographical coordinates Mutale area.

Station	Latitude	Longitude	Altitude
Mutale	-22.73461	30.52188	550

## 3. Methodology

This study employed the historical data that was recorded by Agricultural Research Council (ARC). Two empirical models namely, Clemence and Hargreaves-Samani were employed to evaluate and estimate the global solar radiation for Mutale area. Again, machine learning algorithms was also be utilized for further predictions. The empirical and machine learning models was compared against each other and the performances of empirical models and machine learning algorithms for estimating daily solar radiation will be further evaluated in different areas using statistical equations.

### 3.1. Hargreaves-Samani

Hargreaves-Samani developed a temperature-based model to predict global solar radiation [5]. Based on this principle, he recommended a simple equation defined as

$$H = H_0 * (K_r \sqrt{\Delta T}), \quad (1)$$

where,  $H$  represents daily mean value of global solar radiation ( $MJm^{-2}day^{-1}$ ),  $H_0$  is daily mean value of extraterrestrial radiation ( $MJm^{-2}day^{-1}$ ),  $\Delta T$  is the difference between the maximum temperature ( $T_{max}$ ) and the minimum temperature ( $T_{min}$ ) in ( $^{\circ}C$ ),  $K_r$  is the empirical coefficient respectively.

### 3.2. Clemence Model

Clemence [6] has developed the temperature-based equation for estimating global solar radiation given by

$$H = (1.233 * H_0 * \Delta T + 10.593 * T_{max} - 0.713 * T_{max} * \Delta T + 16.5480) * (0.04184), \quad (2)$$

### 3.3. Random Forest

A random forest model was used to predict global solar radiation in this research work. Random forest is a supervised ensemble machine learning technique that is utilized to solve classification and regression problems [7]. The random forests are a combination of several decision trees that were built using the bootstrapping technique, which involved selecting randomly at each node from samples in the learning dataset for the predictors. It makes use of ensemble learning by constructing a set of predictive models and combine their outputs in to a single prediction, a method for solving complicated issues by combining a number of classifiers.

### 3.4. Support Vector Machine

In this research work another machine learning technique, support vector machine was used to predict solar radiation. A support vector machine (SVM) learning is a supervised machine learning algorithm used for both classification and regression problems [8]. SVM models include a variety of fundamental kernel functions, including polynomial (Poly), Gaussian, exponential radial basis function (ERBF), radial basis function (RBF), sigmoid, and linear kernels (9). The SVR works by mapping the input space into a high-dimensional feature space and constructs the linear regression in it which can be expressed as

$$f(x) = w\psi(x) + b \quad (3)$$

where  $w$  is the weight vector,  $\psi(x)$  maps inputs  $x$  into a high dimensional feature space that is nonlinearly mapped from the input space  $x$  and  $b$  is the threshold that separates the boundary line and the hyperplane. The main aim of using SVM is to minimize the weight. Comparing to the SV formulation for soft margin linear classifiers, the linear regression formulation is given by minimizing:

$$\frac{1}{2}w^T w + C \sum_{i=1}^N (\zeta_i + \zeta_i^*) \quad (4)$$

$$\text{Subject to} \quad y^i - w^T X^i - \omega_0 \leq \varepsilon + \zeta_i; \quad i = 1, \dots, N \quad (5)$$

$$w^T X^i - \omega_0 - y^i \leq \varepsilon + \zeta_i^*; \quad i = 1, \dots, N \quad (6)$$

$$\zeta_i, \zeta_i^* \geq 0, \quad i = 1, \dots, N \quad (7)$$

where  $C$  is the regularization,  $\|w\|$  is the weight,  $\zeta^i$  and  $\zeta^*$  is the errors.

### 3.5. Artificial Neural Network

Another technique was also employed to predict global solar radiation in this work. Artificial neural networks (ANN) are the neural networks that is based on the design of a human neuron. In the domains of artificial intelligence, machine learning, and deep learning, neural networks enable computer programs to identify patterns and resolve common issues by recognizing the behaviour of the human brain [10]. ANNs are comprised of a node layers, containing an input layer, one or more hidden layer and an output layer. Each node or artificial neuron is connected to others and has a weight and threshold that go along with it. For the general neural network model, we let  $N_l$  to denote the number of neurons in the  $l$ -th layer for  $l = 1, 2, \dots, L$ .

$$y_j^{(1)} = \sum_{j=0}^{N_{l-1}} \omega_{ij}^{(1)} a_j^{l-1} \quad (8)$$

where  $y_j$  denotes activation,  $\omega_{ij}$  is the weight and represent the bias neuron.  $g$  is the activation function, in this study (rectified linear unit) relu, sigmoid, softplus, softsign, tanh, (scaled exponential linear units)

selu, (exponential linear unit) elu, exponential, LeakyReLU and were used and through cross validation, the best parameter was relu.

$$a_j^{(i)} = g \left( \sum_{j=0}^{N_{l-1}} \omega_{ij}^{(l)} a_j^{l-1} \right), i = 1, 2, \dots, N_l, l = 2, 3, \dots, L \quad (9)$$

The predicted output layer will be given by

$$y(z, w) = \sum_{j=0}^{\widehat{N_{L-1}}} \omega_{N_{L-1}}^{(L)} a_j^{L-1}. \quad (10)$$

#### 4. Model evaluation metrics

Statistical data analysis was used to test the accuracy and performance of the models. The following statistical data analysis namely: mean absolute error (MAE), coefficient of determination ( $R^2$ ), root mean square error (RMSE) and mean square error (MSE) were employed to evaluate the results.

#### 5. Results and discussion

This section presents the findings from the empirical and machine learning methods used to estimate the daily global solar radiation for the Mutale area. Python was used for all computations for this work, while MATLAB was used to calibrate the empirical models when determining the model coefficients. The subsections below describe and display these results. Results for all methods that are used under this study and the comparison between the observed and estimated are shown and discussed under these subsections. Performance metrics results are also displayed under this section.

The figures below illustrate the observation and the estimated daily global solar radiation for the Clemence, Hargreaves-Samani, random forest, support vector machines and artificial neural network models. It can be observed that solar radiation reaches its peak and lowest points throughout the summer and winter seasons, respectively. Summer is the season with the highest levels of global solar radiation, which coincides with the highest temperatures. Figures 1 and 2 represent the global solar radiation of the observed and estimated data for the Clemence model and Hargreaves-Samani model respectively. Figures 3, 2 and 5 represent global solar radiation for random forest, support vector vector machine and artificial neural networks.

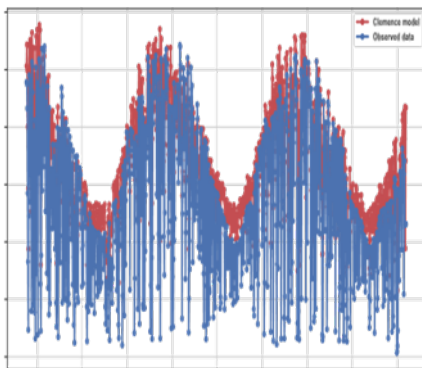


Figure 1. Clemence model.

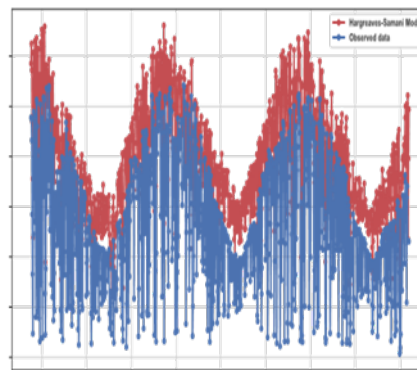
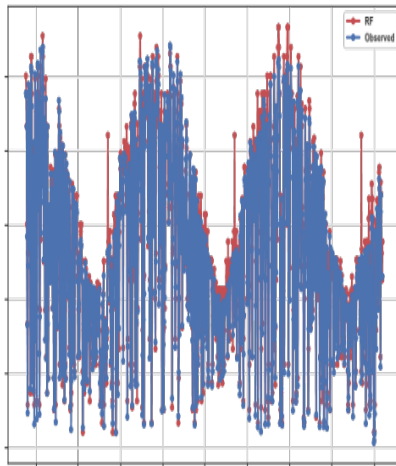
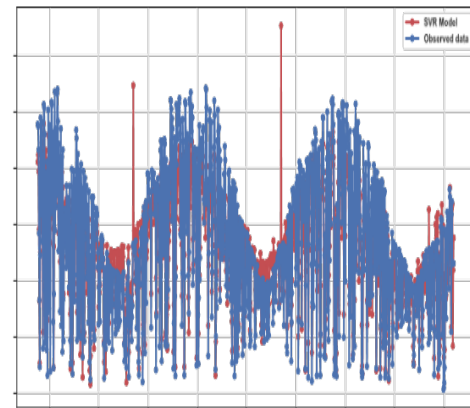


Figure2. Hargreaves-Samani.



**Figure 3.** Random forest.



**Figure 4.** Machine support vector.

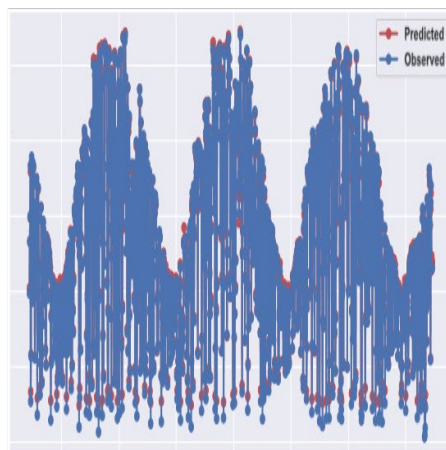


**Figure 5.** Artificial neural network.

Table 2 below shows the statistical analysis for global solar radiation comparing observed and estimated data for the Clemence, Hargreaves-Samani, random forest, support vector machine and artificial neural networks models. It can be observed from the Table 2 that the values of MSE for all the models range from 0.027 to 23.38. RMSE values range from 0.52 to 4.84 which shows a good comparison because the values are close to zero since the values for RMSE ranges from 0.. The coefficient of determination  $R^2$  ranges from 0.40 to 0.99 for all the models. This indicates that deep learning and machine learning techniques perform better for the Mutale area. And the values of MAE ranges from 0.50 to 3.84 for all the models.

**Table 2.** Statistical errors obtained from different models.

Models	MSE	R <sup>2</sup>	RMSE	MAE
Clemence	23.38	0.44	4.84	3.84
Hargreaves-Samani	51.47	0.40	7.17	6.45
Random Forest	1.15	0.97	1.07	0.72
Support vector machine	7.87	0.81	2.81	2.12
Artificial neural network	0.27	0.99	0.52	0.50

## 6. Conclusion

In this study, empirical models, machine and deep learning techniques were employed to estimate the global solar radiation for Mutale area in Limpopo province. Statistical analysis was also utilized to determine the performance measures of the models. It can then be observed that the performance of the empirical models is low compared to machine learning and deep learning. Random forest and support vector machines together with artificial neural networks seems to be the best model for Mutale area since the coefficient of determination ranges from 0.81, 0.97 and 0.99. If the values of  $R^2$  is close to 1 then the model is said to be a perfect fit.

## 7. Acknowledgments

I would like to thank God for giving me strength and wisdom during this study. I would like to extend my acknowledgement to my supervisor Dr TS Mulaudzi and my co-supervisor Mr N Mphephu and Dr NE Maluta for all their tireless effort and encouragement. I would also like to thank university of Venda and ARC for providing with the data to carry out this study. Lastly, I would thank my family and friends for all their endless support.

## References

- [1] Dorian, J., Franssen, H. & Simbeck, D. Global challenges in energy. *Energy Policy*. 34, 1984-1991 (2006)
- [2] Kessides, I. Chaos in power: Pakistan's electricity crisis. *Energy Policy*. 55 pp. 271-285 (2013)
- [3] Field, C.B., Campbell, J.E. and Lobell, D.B. Biomass energy: the scale of the potential resource. *Trends in ecology & evolution*, 23(2), pp.65-72 (2008)
- [4] Puah, B.K., Chong, L.W., Wong, Y.W., Begam, K.M., Khan, N., Juman, M.A. and Rajkumar, R.K. A regression unsupervised incremental learning algorithm for solar irradiance prediction. *Renewable Energy*, 164, pp.908-925 (2021)
- [5] Hargreaves, G. & Samani, Z. Reference crop evapotranspiration from temperature. *Applied Engineering In Agriculture*. 1, 96-99 (1985).
- [6] Clemence, B.S.E., An attempt at estimating solar radiation at South African sites which measure air temperature only. *South African Journal of Plant and Soil*, 9(1), pp.40-42 (1992)
- [7] Ren, Y., Zhang, L. & Suganthan, P. Ensemble classification and regression-recent developments, applications and future directions. *IEEE Computational Intelligence Magazine*. 11, 41-53 (2016)
- [8] Shmilovici, A. Support vector machines. *Data Mining And Knowledge Discovery Handbook*. pp. 231-247 (2009)
- [9] Hofmann, T., Schölkopf, B. and Smola, A.J. Kernel methods in machine learning. *The annals of statistics*, 36(3), pp.1171-1220 (2008)
- [10] Tyagi, A. & Chahal, P. Artificial intelligence and machine learning algorithms. *Research Anthology On Machine Learning Techniques, Methods, And Applications*. pp. 421-446 (2022)

# Investigating the effects of turbulence-induced tilt and lateral displacement on OAM modes

Steven G. Makoni, Ling Cheng, and Mitchell A. Cox

School of Electrical and Information Engineering, University of the Witwatersrand, Johannesburg, South Africa

E-mail: 1935885@students.wits.ac.za

**Abstract.** Free-Space Optical (FSO) communication links have used Orbital Angular Momentum (OAM) modes as channels in Mode Division Multiplexing (MDM) systems. OAM modes suffer from turbulence-induced OAM crosstalk, which degrades the performance of FSO communication links. Turbulence predominantly causes lateral displacement and tilt angle on the beam wavefront. There are analytical models that characterize OAM crosstalk due to lateral displacement and tilt angle. We investigated the OAM spectrum due to lateral displacement and tilt angle for an input beam misaligned from the measurement axis. An experimental setup generated 11 OAM modes,  $\ell \in [-5, 5]$ . We optically imposed these modes with lateral displacement and tilt angles. We present the analytical expression and experimental results which show that our approach does correctly measure the OAM spectrum due to lateral and tilt angle misalignments of the input beam with some adjustments required.

## 1. Introduction

Orbital Angular Momentum (OAM) has been identified as another degree of freedom of light. A beam carrying OAM can be characterized with a complex amplitude term  $\exp(i\ell\theta)$ , where  $\ell$  can take any integer value [1]. Such a beam is an OAM mode and Laguerre–Gaussian (LG) modes are one of the examples of such. OAM modes being orthogonal to each other can be used to multiplex communication channels and hence improving the channel capacity of free-space optical links [2]. These modes have been used for Mode Division Multiplexing (MDM) because of the orthogonality of OAM modes.

In free-space optical links, a light beam propagating through air transfers information. Three primary atmospheric phenomena affect beam propagation, namely absorption, scattering, and turbulence. Absorption and scattering by gases and particles of the atmosphere that causes attenuation are wavelength dependent. The flow of turbulence induces lateral displacement and angle of arrival fluctuations (i.e. tilt angle) as the fundamental aberrations among many effects on the wavefront of beam [3, 4]. Lateral displacement and tilt manifest as a random beam movement at the receiver. Unfortunately, OAM mode propagating through turbulence spreads its energy to neighbouring modes. A phenomenon known as OAM crosstalk causes errors at the receiver in FSO links.

In attempting to investigate the OAM crosstalk due lateral displacement and tilt, an analysis of OAM of a beam misaligned from a reference axis showed that a single OAM state becomes a superposition of a number of states [5]. A theoretical proof and numerical simulations showed the relationship of the dispersed OAM spectrum versus the tilt angle and lateral displacement but without experimental verification [6]. The change in the observed OAM spectrum was experimentally obtained as the input beam was misaligned with respect to the analyser [7].

In this work, we look at this topic from an alternative perspective. By assuming that lateral displacement and tilt angle are the main aberrations of turbulence, we can simplify OAM in turbulence

to OAM in lateral displacement and tilt angle. This work investigates the OAM spectrum due to lateral displacement and tilt angle. The experimentally obtained spectrums are compared with an OAM spectrum analytical expression. This investigation is necessary because allows a way to verify if the experimental setup conforms to the known theory about the relationship between lateral displacement and tilt angle with OAM spectrum. The measurements collected will be used to model the spectrum using machine learning instead of the analytical expression. The rest of this paper contains the background information, followed by the setup and approach used to obtain the measurements. Lastly, a discussion of the preliminary results of the spectrums obtained in the presence of misalignments.

## 2. Background

### 2.1. OAM modes

OAM modes have intensities and phases profiles. The spatial phase is a twisted light spiral staircase. OAM beams are defined by the azimuthal index,  $\ell$ , that can have any number of integer twists. When an OAM mode propagates through turbulence, its energy spreads to the neighbouring modes - OAM crosstalk. OAM modes are a subset of the Laguerre–Gauss (LG) modes that form an orthonormal basis in cylindrical coordinates.

The field of an LG beam, with an azimuthal index,  $\ell$  and a radial index  $p$ , in a cylindrical coordinate system, is given by

$$U(r, \Phi, z) = E_0 (\sqrt{2} \frac{r}{\omega(z)})^\ell L_p^\ell \left( \frac{2r^2}{\omega(z)^2} \right) \frac{\omega_0}{\omega(z)} e^{(-i\Psi_{p\ell}(z))} e^{(i\frac{kr^2}{2q(z)})} e^{(i\ell\Phi)} \quad (1)$$

where  $L_p^\ell(\cdot)$  is the associated Laguerre polynomial,  $E_0$  is a constant electric field amplitude,  $\omega(z)$  is the beam radius,  $\omega_0$  is the beam radius at the beam waist,  $z_0 = \frac{\pi\omega_0^2}{\lambda}$  is the Rayleigh range,  $q(z) = z - iz_0$ , is the complex beam parameter, and the Gouy phase shift is given by  $\Psi_{p\ell}(z) = (2p + |\ell| + 1)\tan^{-1}(\frac{z}{z_0})$ .

### 2.2. OAM in turbulence

As a Gaussian beam propagates through turbulence, three main effects that will take place:- beam spreading causing the beam to get bigger as it propagates, beam wander causing the centroid position of the beam to change at the receiver and scintillation resulting in the beam changing its shape. Additionally, an OAM mode will spread its energy neighbouring modes - OAM crosstalk when propagating in turbulence. Atmospheric turbulence induces mainly tilt and lateral displacement aberrations due to pressure fluctuations and temperature gradients. Fig 1 shows lateral displacement and tilt angle on a beam. Therefore, the system of OAM modes in turbulence is simplified to OAM modes in tilt and lateral displacement, since turbulence is stochastic in nature.

### 2.3. Modal decomposition

Modal decomposition is a standard technique used to retrieve the modal power spectra to fully characterize complex field distributions using a few mode weight coefficients. This technique can be used to reveal the information of crosstalk present in a particular LG field in an optical system. In modal decomposition, an unknown optical field (the mode to be detected) is expressed as a linear combination of orthogonal basis functions.

$$U(x) = \sum_{\ell} c_{\ell} \Phi_{\ell} \quad (2)$$

where  $U(x)$  is the unknown field at the receiver,  $\ell$  are the mode indices,  $c_{\ell}$  is the complex expansion coefficient and  $\Phi_{\ell}$  is the chosen basis function. The main aim is to calculate the complex expansion coefficients,  $c_{\ell}$ . With the aid of a digital hologram encoded on the spatial light modulator (SLM) and a

Fourier lens the complex expansion coefficient measurements can be achieved. The coefficient can be extracted from the optical field intensity at the optical axis of the Fourier plane. This optical field intensity will be directly proportional to the  $c^2$ .

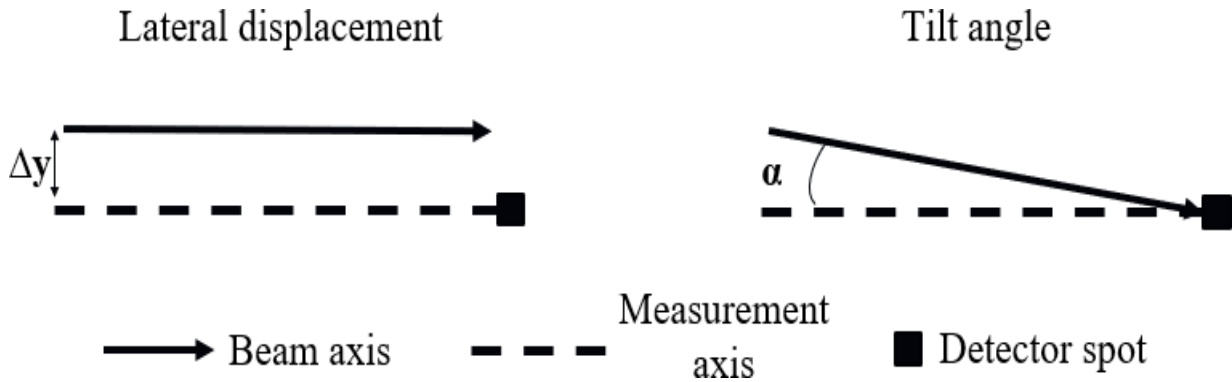


**Figure 1.** Illustration of lateral displacement and tilt angle. The beam axis is the axis the beam propagates through turbulence. The measurement axis is the axis used to measure the intensity of the beam at the detector spot. Lateral displacement,  $\Delta y$  is the offset of the beam axis vertically (or horizontally) parallel to the measurement axis. Tilt,  $\alpha$  is when the beam axis is at an angle upon beam arrival at the detector spot. Therefore, lateral displacement and tilt angle cause the beams axis to be misaligned with the measurement axis.

### 3. Methodology

Figure 2 schematically depicts a standard modal decomposition setup with two SLMs used to perform the experiment [8]. A 632.8 nm collimated Gaussian laser beam is transformed into the required mode using the first SLM. The required mode is imaged onto the second SLM, which performs the modal decomposition to a camera at the Fourier plane of the decomposition lens. The SLM used was a SLM-100-01-0001-01, the all-in-one model for 632.8 nm wavelength.

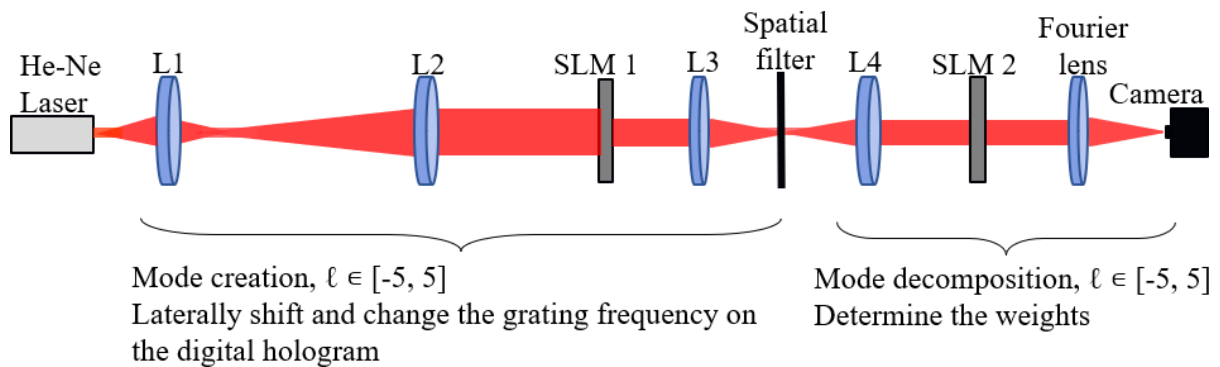


**Figure 2.** Schematic experimental setup: Lens (L1 and L2) enlarges the beam. The first SLM is illuminated with horizontally polarized light and encoded with holograms that perform complex amplitude modulation and impose tilt angle and lateral displacement. An incoming LG mode from SLM 1 selected by the spatial filter is ‘modally’ decomposed by the second SLM addressed by detecting hologram. At the Fourier plane, the camera detects the on-axis intensity.

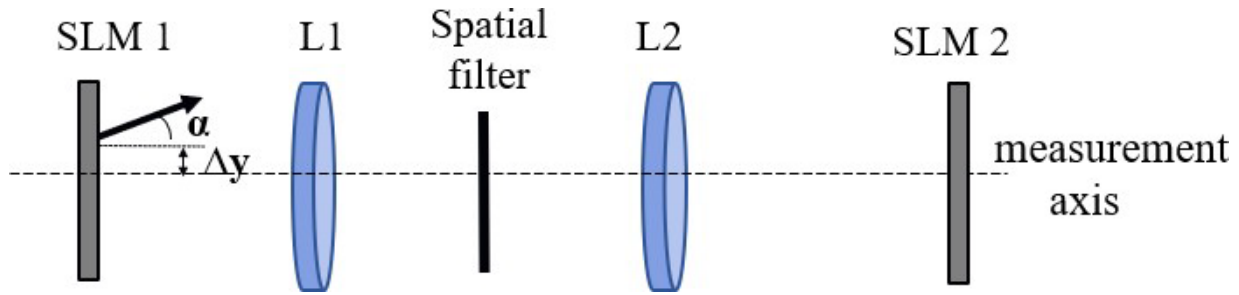


**Figure 3.** Experiment schematic of how the SLM will be used to impose both lateral displacement and tilt angle on the hologram on the first SLM. During mode creation, the center of the mode created is moved by changing the amount of lateral displacement,  $\Delta y$ . The blazed grating on the first SLM varies the amount of tilt imposed. Both lateral displacement and tilt angle are with respect to the measurement axis. The measurement axis is determined before lateral displacement or tilt angle is imposed.

The first SLM was used to laterally displace and tilt the created mode. Figure 3 illustrates how the lateral displacement and tilt were optically imposed by using the first SLM. By offsetting the position of the created mode on the Cartesian plane on the hologram, lateral displacement was imposed. Tilt angles were imposed on the created mode by varying the grating frequency of the blazed grating on the hologram. The setup used, but not limited to 11  $LG^{\ell}_{p=0}$  modes,  $\ell \in [-5, 5]$ .

#### 4. Preliminary results

Several combinations of lateral displacement and tilt angle with respect to the measurement axis for OAM modes were experimentally imposed. Mode index value of  $\ell = 0$  was used to make the comparison between measured spectrums and those calculated using the crosstalk analytical expression, as detailed in [6]. The corresponding results are shown in Fig 4. As expected, individually imposing lateral displacement or tilt angle results in a spectrum symmetrical about the input mode [6]. As the amount of lateral displacement and tilt angle increases, the spectrum broadens. Results show that the mode,  $\ell = 0$ , is more sensitive to tilt angles than displacement. For future work, machine learning will be used to model the spectrum using these measurements instead of the analytical expression. The use of machine learning could model the spectrum in the presence of additional higher order aberrations because of turbulence. Such a model might be useful for combating turbulence in MDM.

However, there are mismatches in the spectrums probably due to the precision of the setup as indicated by the crosstalk present in the aligned setup as shown in Fig 4(a). The additional aberrations arising from the SLMs and the other optical elements used within the experimental setup as well as the orientation of the tilt angle produced by the first SLM.

#### 5. Conclusion

The OAM spectrum of various beams, with lateral displacement and tilt with respect to the measurement axis were analyzed. Results were presented on mode value of  $\ell = 0$  but similar results were obtained for other  $\ell$  values. These results corresponded to the spectra obtained from the crosstalk analytical expression, thereby confirming that our approach yields a useful measurement of the OAM spectrum. An example of this is for analyzing the OAM crosstalk due to turbulence which may reveal interesting features within the OAM spectrum. Future work will be attempting to model the spectrum using machine learning and these measurements instead of the analytical expression. In the presence of additional higher order aberrations machine learning model might be useful for mitigating the effects of turbulence in MDM.

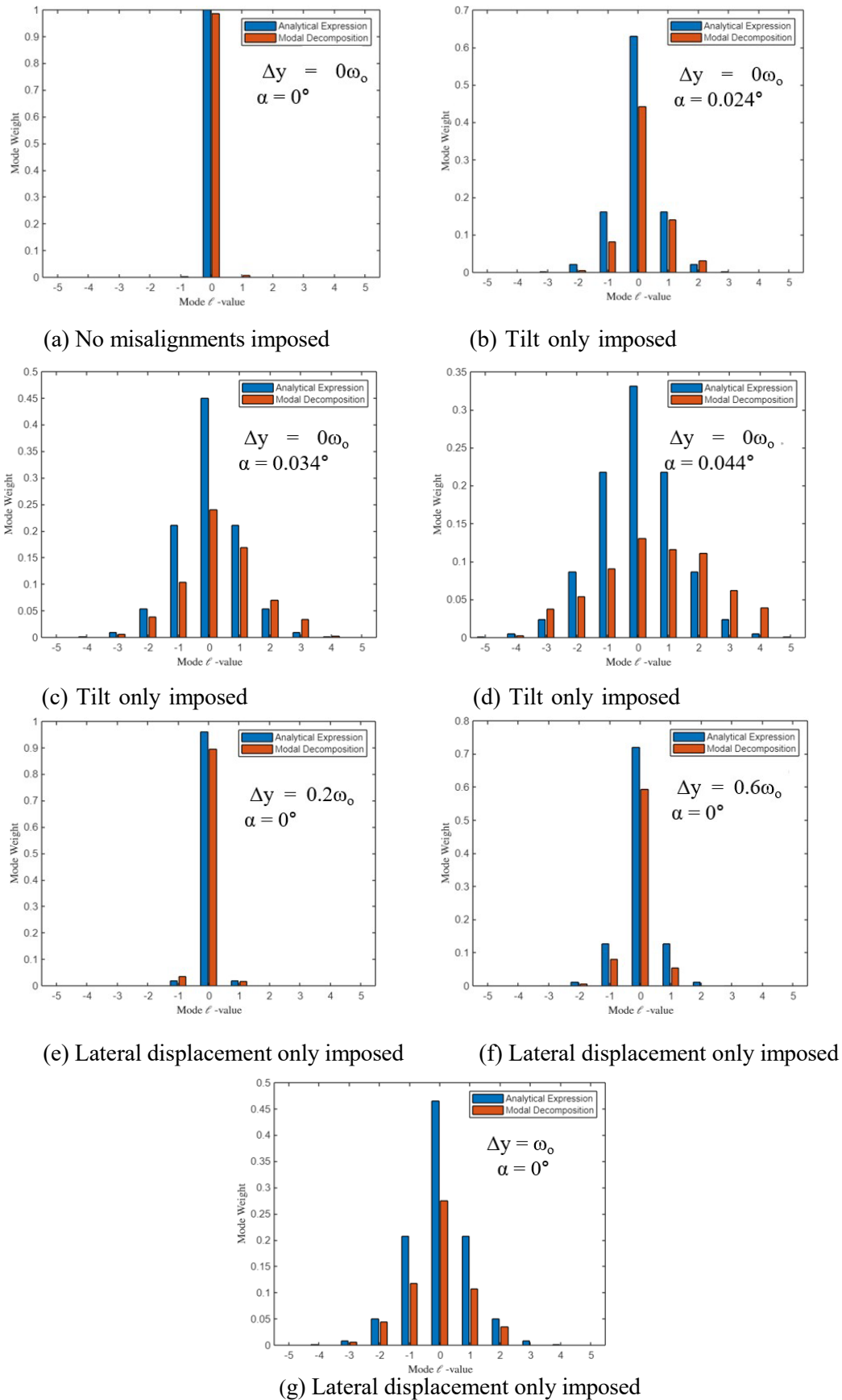


Figure 4. The analytical and experimental spectrums for different misalignments on  $\ell = 0$ .

**References**

- [1] Allen L, Beijersbergen M W, Spreeuw R J C and Woerdman J P 1992 *Phys. Rev. A* **45**(11) 8185–8189  
URL <https://link.aps.org/doi/10.1103/PhysRevA.45.8185>
- [2] Gibson G, Courtial J, Padgett M J, Vasnetsov M, Pas'ko V, Barnett S M and Franke-Arnold S 2004  
*Opt.Express* **12** 5448–5456 URL <http://opg.optica.org/oe/abstract.cfm?URI=oe-12-22-5448>
- [3] Noll R J 1976 *J. Opt. Soc. Am.* **66** 207–211 URL <http://opg.optica.org/abstract.cfm?URI=josa-66-3-207>
- [4] Cox M A, Gailele L, Cheng L and Forbes A 2019 Modelling the memory of turbulence-induced beam wander URL <https://arxiv.org/abs/1907.10519>
- [5] Vasnetsov M V, Pas'ko V A and Soskin M S 2005 *New Journal of Physics* **7** 46–46  
URL <https://doi.org/10.1088/1367-2630/7/1/046>
- [6] Lin J, Yuan X C, Chen M and Dainty J C 2010 *J. Opt. Soc. Am. A* **27** 2337–2343  
URL <http://opg.optica.org/josaa/abstract.cfm?URI=josaa-27-10-2337>
- [7] Lavery M P J, Berkhout G C G, Courtial J and Padgett M J 2011 *Journal of Optics* **13** 064006  
URL <https://doi.org/10.1088/2040-8978/13/6/064006>
- [8] Pinnell J, Nape I, Sephton B, Cox M A, Rodr'iguez-Fajardo V and Forbes A 2020 *J. Opt. Soc. Am. A* **37** C146–C160 URL <https://opg.optica.org/josaa/abstract.cfm?URI=josaa-37-11-C146>

# Environmental Monitoring in the ATLAS ITk Detector

M. P. Connell<sup>1</sup>, M. Bhamjee<sup>1</sup>, T. P. Mafa<sup>2</sup>, S. H. Connell<sup>1</sup>, L. Leeuw<sup>3</sup>

<sup>1</sup>Department of Mechanical Engineering Science, University of Johannesburg, Auckland Park, Johannesburg, South Africa. <sup>2</sup>Department of Mathematical Sciences, UNISA - ATLAS High Energy Physics Group, University of South Africa, Johannesburg, 1710, South Africa

<sup>3</sup>Department of Physics and Astronomy, University of the Western Cape. Belville 7535, Cape Town. South Africa

E-mail: rsamcon@gmail.com

**Abstract.** In the design of the proposed Phase-II Inner Tracker upgrade to the ATLAS detector, humidity and temperature sensors will be placed throughout the volume to monitor environmental conditions. To assist in the placement of these sensors and to better understand the internal fluid environment of the detector under the nitrogen flushing, the Inner Tracker is modelled using Computational Fluid Dynamics. Fluid flow and heat transfer simulations have been completed, revealing key features of the flow distribution during nitrogen flushing. The models also indicate a uniform temperature distribution throughout most of the volume.

## 1. Introduction

The ATLAS Inner Tracker (ITk) is a planned upgrade to the ATLAS detector at the Large Hadron Collider (LHC) in CERN, Switzerland. The purpose of the ITk is to plot the positions and trajectories of charged particles close to the particle interaction point [1]. The ITk will replace the current Inner Detector, which will have suffered accumulated radiation damage, while at the same time improve the coverage, radiation hardness and triggering capabilities in time for the High Luminosity LHC [1]. The internal components of the particle detectors are susceptible to damage due to high humidity: when is high enough, condensation can occur and sensitive electrical equipment can become corroded over time resulting in loss of sensitivity and even complete loss of detection, greatly reducing the effectiveness of the detector [1]. Because the internal environment of a detector is kept at  $-20^{\circ}\text{C}$  for optimal performance, any moisture introduced can be dangerous.

This problem is solved in the ITk in two ways: continual flushing with dry nitrogen ( $\text{N}_2$ ) which will keep the environment dry and humidity and temperature sensors placed throughout the detector which will be able to monitor the environmental conditions and warn if conditions lead to condensation. These "leaks" could be back-diffusion in the dry  $\text{N}_2$  flush exhaust, leaks at the service penetrations. A fault condition in the cooling is envisaged to drop the local temperature, meaning the specification of very low humidity must be sufficient that the dew-point is below the lowest temperature reached in this extreme fault condition ( $T_{dp} < -60^{\circ}\text{C}$ ).

In order to know the best placements for sensors and better understand the fluid environment, a Computational Fluid Dynamics (CFD) simulation is used to calculate flow, temperature and humidity distributions throughout the volume. This paper will address the CFD modelling up to the point of modelling temperature and flow distributions. The results of these models are presented and the next steps in order to model humidity are discussed.

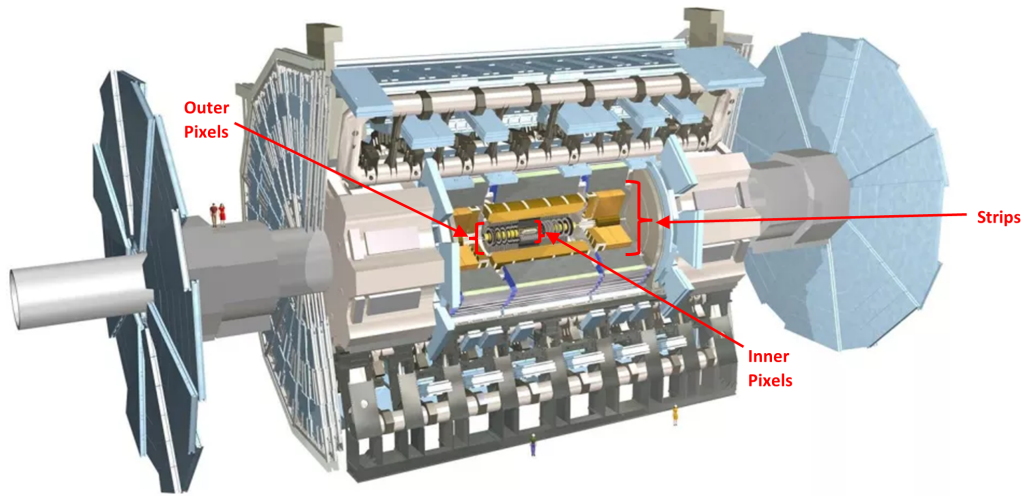


**Figure 1.** Overview of the ATLAS detector showing the Inner Detector to be replaced in the Upgrade by the Inner Tracker (ITk) [1].

## 2. Methodology

The CFD simulation design and execution has 4 stages: simplification and adaption of real geometry to suit the CFD, meshing, executing the simulation and post-processing.

### 2.1. Geometry

For simulation purposes, the ITk volume is split into 3 sections, from outermost to innermost: the Strips, the Outer Pixels and the Inner Pixels, shown in figure 1. The work presented in this paper concerns only the ITk Outer Pixels.

The Outer Pixels can be thought of as a pipe filled with sets of dozens of discs, which detect particles, as well as support cylinders. The main section of the Outer Pixels can be divided into 3 parts: the Left ( $+z$ ) endcap, the outer barrel, and the Right ( $-z$ ) endcap, as can be seen in Figure 2. It widens at each end into the two Patch Panel 1 (PP1) flanges. There are 12 flushing inlets of 10mm wide on the left flange mirrored by 12 similarly sized outlets on the right flange. The outer barrel services envelop the endcaps and then insert into the outer barrel. The Pixel Service Tube (PST) separates the Outer Pixels from the Strips and the Inner Service Tube (IST) separates the Inner and Outer Pixels.

The geometry is made complex by the transitions from large to small length scales. There are many channels on the  $mm$  scale typically between the detector discs and support structures. This becomes especially challenging when meshing for CFD as it requires sudden changes in cell size around these narrow channels.

A cross section of these components in the  $yz$ -plane is shown in Figure 2. The geometry is simplified as much as possible without changing any fundamental features. The Outer Pixels are symmetrical across the  $yz$ -plane so only half of the volume requires meshing. The  $y$  and  $z$  axes are not symmetric due to gravity and flow direction respectively. However, the ITk is still in the design phase, thus, the geometry is always subject to changes.

### 2.2. Meshing

The mesh for the ITk is large at around 60 million cells, which are predominantly tetrahedral. To ensure mesh quality, all cells were required to have a skewness below 0.9. To achieve this the average cell size was set to be 10mm and face meshing was applied to the narrow channels, so that each channel was at least 2 cells wide.

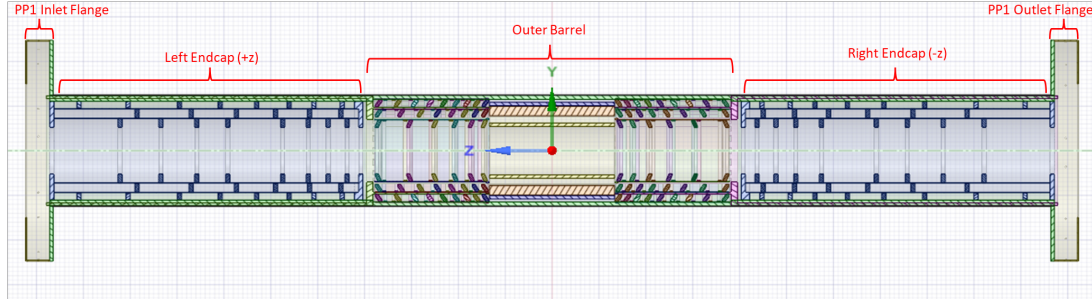


**Figure 2.** Cross section of the ITk Outer Pixels showing the solid components.

### 2.3. Simulation

**2.3.1. Governing Equations** The finite volume method [2] is used to simulate the fluid environment inside the ITk. The governing equations are shown in equations (1) and (2). Equation (1) is the continuity equation and represents conservation of mass. Equation (2) represents conservation of momentum in x, y and z directions [2], [3], [4]. Equation (3) represents the heat transfer equation for the fluid and equation (4) represents the heat transfer equation for solid regions.

$$\nabla(\rho\vec{u}) = 0 \quad (1)$$

$$\rho\nabla\cdot(\vec{u}_i\vec{u}) = -\frac{\partial p}{\partial x_i} + \nabla\cdot(\mu\nabla\vec{u}_i) - B_i \quad (2)$$

for  $i = x, y, z$ . where the body forces are  $B_x = B_z = 0$  and  $B_y = -\rho g$ .

$$\nabla\cdot(\rho\vec{u}) = -P\nabla\cdot(\vec{u}) + \nabla\cdot(k\nabla T) \quad (3)$$

$$\nabla\cdot(\vec{u}\rho h) = \nabla\cdot(k\nabla T) \quad (4)$$

**2.3.2. Boundary Conditions** The boundary conditions for the inlets and outlets are listed in Table 1. The inlets are designed to achieve a flow rate of 500l/hr throughout the full volume.

<b>Table 1.</b> Inlet and Outlet boundary conditions for the Outer Pixels simulation			
<b>Boundary</b>	<b>Type</b>	<b>Flow Rate (<math>kg/s</math>)</b>	<b>Temperature (C)</b>
Inlets	Mass Flow Inlets	$7.9 \times 10^{-5}$ $(6.59 \times 10^{-6} kg/s \text{ per inlet})$	10
Outlets	Pressure Outlets	Atmospheric pressure	Fluent Calculated

The temperature boundary conditions are shown in the Table 2. Most solids are excluded from the simulation to simplify the model and are instead represented as constant boundary conditions. The outer barrel services and bulkheads are deemed to be thick enough to be modelled, thus they are meshed and affect the heat transfer simulations. A coupled boundary condition is applied where the solid regions are in contact with other meshed regions and constant temperature boundary conditions are used where they face an external surface.

All internal detector components are maintained at a temperature of  $-20^\circ\text{C}$  to ensure the optimal functioning of electronics and these are represented by constant temperature walls in

**Table 2.** Temperature boundary conditions for the Outer Pixels simulation

Boundary	Type	Heat Transfer Conditions	Temperature [C]
Flanges	Wall	Const. Temperature	25
PST	Wall	Const. Temperature	20
IST	Wall	Const. Temperature	-20
Detector disks	Wall	Const. Temperature	-20
Bulkhead	Solid region (meshed)	Const. Temperature	25 on external face
		Coupled	Fluent calculated on Outer Pixels side.
Outer Barrel	Solid region	Const. Temperature	20 on PST side
Services	(meshed)	Coupled	Fluent calculated on Outer Pixels side.

the simulation. Temperature boundary conditions at the Outer Pixels boundaries to Strips [5] and Inner Pixels are taken from results of CFD simulations of these regions.

First a flow-only simulation is run to get a flow distribution for the volume. The energy equation is turned off and there is no heat transfer between components. After this a heat transfer simulation is run, giving both flow and temperature distribution. This can effect the flow and allows for the possibility of effects like buoyancy driven flow.

*2.3.3. Convergence* For the flow-only simulations, the standard residuals are used: continuity and velocity in the x, y, and z directions. For the heat transfer simulations, energy is also used as a residual. For both simulations mass imbalance is monitored. Mass imbalance is the difference between net mass in through the inlets and out through the outlets. In some cases continuity may not converge because the mass imbalance is non-zero – however, as long as the mass imbalance is stable the simulation can be considered converged. The tolerance values used for continuity, x, y, and z velocities is  $10^{-3}$  and for energy it is  $10^{-6}$

Once simulations were set up and initialised, they were run on the Centre for High Performance Computing (CHPC) clusters in South Africa. Both flow-only and heat transfer simulations are found to converge within 300 iterations.

*2.3.4. Solver Settings* The solver uses double precision so these values are calculated halfway between each mesh node as well as at each node. Momentum and pressure at nodes shared between cells must match, meaning the equations must all be solved simultaneously. The solver's initial solution is a guess which is then used in the next calculation. The simulation is iterated in this way until it certain variables, called residuals, fall below a set tolerance level. Residuals are dimensionless and can be roughly understood as the difference between a given quantity from one iteration to the next. Once every residual is below its tolerance value in a given iteration, the simulation is considered converged.

Flow is assumed to be incompressible and, for flow and heat transfer simulations, at constant density. A viscous model is used where the flow is assumed to be laminar. This assumption is based on measurement of the flow through the inlets, which is calculated to be laminar. Gravity is set at -9.81m/s in the y-direction. Solid components are modelled as graphite and the fluid environment is assumed to be entirely N<sub>2</sub> for the flow and heat transfer simulations.

### 3. Results

#### 3.1. Flow Results

Velocity magnitude plots indicate low velocity flow throughout the Outer Pixels. The velocity magnitude plot for the left endcap in Figure 3 shows flow is between  $1 - 5\text{mms}^{-1}$  through the majority of the volume. Layer 4, the outermost layer of the endcaps marked by 1 in Figure 3,

demonstrates that this layer has the highest velocity magnitude. This can be seen more clearly in the right-hand image depicting velocity plots for the  $yz$ -plane. This high velocity is due to Layer 4 having more space for fluid to flow through, while Layers 2 and 3 have only narrow  $1-2\text{mm}$  channels. This could be problematic as Layers 2 and 3 may not be flushed as effectively as Layer 4. This pattern of flow is mirrored for the right endcap, while the Outer Barrel region does not show significant flow features for any layer.

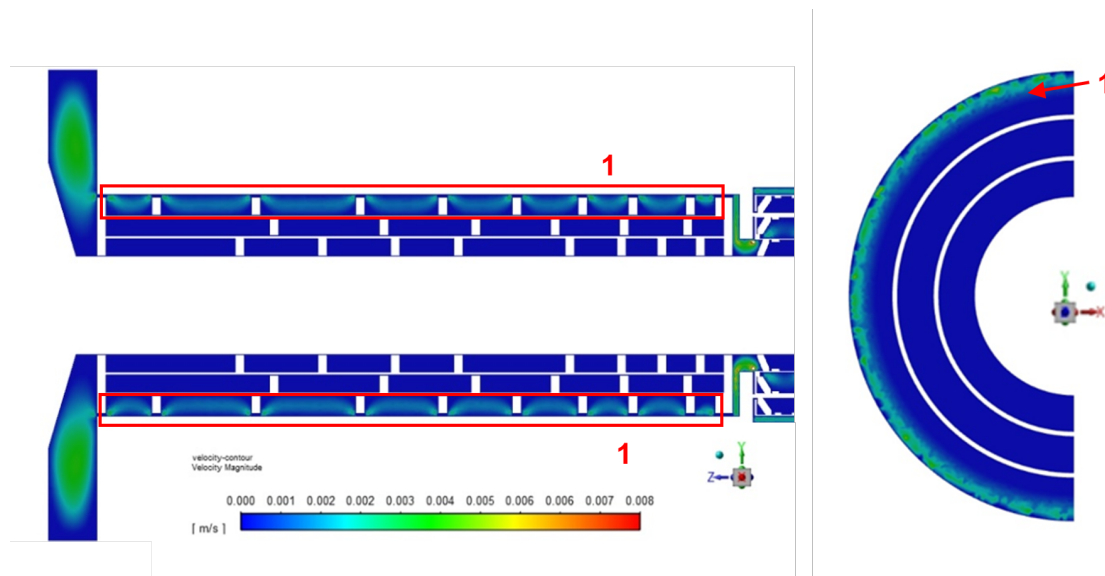


**Figure 3.** Velocity magnitude contours in the Outer Pixels endcap. Left:  $yz$ -plane Right:  $xy$ -plane

### 3.2. Temperature Results

Temperature plots for the Outer Pixels indicate that the temperature is mostly uniform at  $-20\text{C}$  throughout the volume. This is seen most easily in the right-hand image of Figure 4. This uniform distribution is due to cooling from the detector components: each component has its own cooling system.

Layer 4 of the endcap and the outer barrel services are labelled by 1, and this region exhibits a higher temperature due to the external boundary conditions on the services, which conducts heat down to Layer 4. However, this area is subject to a geometry update that will isolate Layer 4 from the services. Once this update is implemented it is expected that Layer 4 will be have the same uniform distribution as Layers 2 and 3 as it will be thermally isolated. The same temperature pattern is mirrored in the right endcap and the outer barrel discs are also at uniform temperature.

These temperature distributions would indicate that there is no preferred position for sensors to be placed based on properties of the fluid environment. As it stands, it would be advised sensors placement can proceed according to considerations of convenience, such as what areas have space, whether it is easy to insert sensors there, and a need to have maximum coverage of the Outer Pixels volume. In regards to the latter, sensors will be placed only in the endcaps and not the outer barrel. This is because leaks are only expected at the flanges and not along the volume. Any moisture due to leaks will have to pass through the endcaps before reaching the outer barrel. However, the addition of air leaks, and the subsequent humidity, into the simulations could affect temperature and flow distributions. Subsequently sensor placement may need to be reconsidered based on future model predictions.

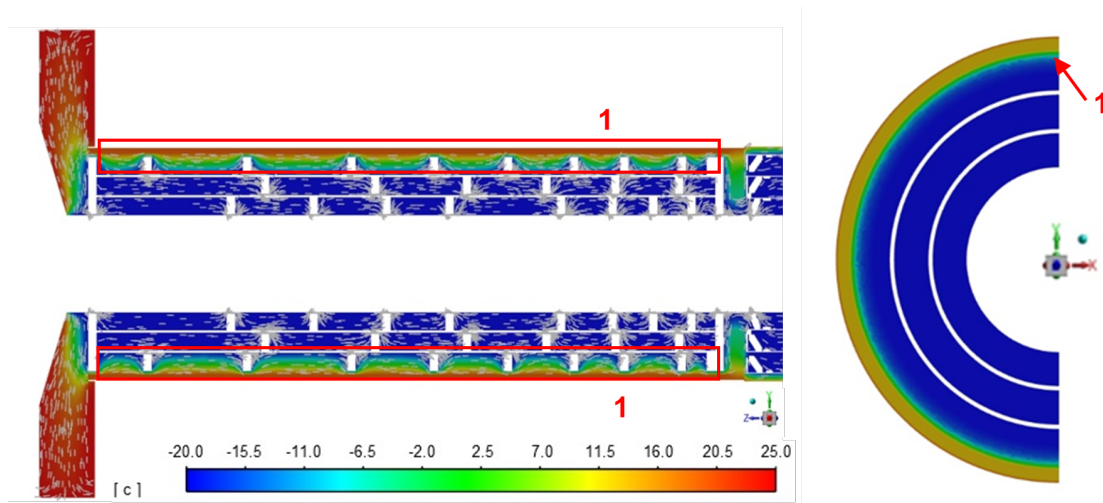


**Figure 4.** Temperature contours in the Outer Pixels endcap. Grey arrows indicate velocity vectors. Left: yz-plane Right: xy-plane

#### 4. Conclusion

The aim of this work was to model the internal fluid environment of the ATLAS ITk using CFD in order to advise on the placement of sensors. Although flow and temperature distributions have been modelled, humidity must still be modelled before we can confidently assess the optimal placement of sensors. Flow distributions have indicated that there may be some areas in the geometry which may hinder flow. On the other hand, temperature distributions are almost entirely uniform throughout the inner layers, implying that there is no preferred location for temperature sensors. However, these adding humidity to the simulations could still affect these results. This will be done by introducing humid air as a new species entering the volume via "leaks" on the flanges and the distribution of densities for each species will be calculated using the species transport equation, allowing calculation of humidity distributions. A user-defined function can be created that takes temperature and humidity values at each point in the volume in order to calculate the Dewpoint. This distribution will allow us to understand at what locations condensation is likely to occur.

#### 5. Acknowledgments

The Centre for High Performance Computing (CHPC) is acknowledged for the use of the CHPC clusters.

#### References

- [1] ATLAS Collaboration 2017 ATLAS Inner Tracker Strip Detector: Technical Design Report URL <https://cds.cern.ch/record/2257755>
- [2] Versteeg H K and Malalasekera W 2007 *An Introduction to Computational Fluid Dynamics: The Finite Volume Method* (Pearson)
- [3] Bhamjee M, Nurick A and Madyira D 2013 *Energy and Buildings* **57** 289–301 ISSN 0378-7788
- [4] ANSYS Inc 2021 ANSYS Fluent Theory Guide
- [5] Mafa T P, Bhamjee M, Connell S H and Leeuw L L 2022 Fluid Flow and Humidity in the ATLAS ITk Studied by CFD

# The investigation between covariability of energy fluxes and CO<sub>2</sub> flux exchanges at Skukuza Kruger National Park by Eddy Covariance technique

LTakalani<sup>1</sup>, T S Mulaudzi<sup>2</sup>, H Thenga<sup>3</sup>, N E Maluta<sup>4</sup>, M Mateyisi<sup>5</sup>

<sup>1,2,4</sup>Department of physics, university of Venda, Limpopo in South Africa, Thohoyandou 0950. <sup>3,5</sup>South African's Council of Scientific and Industrial Research, Pretoria 0001, Brummeria, Meiring Naude Road South Africa. <sup>3</sup>National Institute of Theoretical and Computational Sciences, Stellenbosch Institute for advanced studies in South Africa, Stellenbosch 7600.

E-mail: lufunotakalani@gmail.com/lufuno.takalani@univen.ac.za

**Abstract.** The contribution of the Kruger National Park South Africa ecosystem to Carbon uptake and emission is highly variable across the years due to perturbations in vegetation cover as driven by large herbivores and inter-annual climate variability. The quantification of the contribution from the savanna ecosystems to the global carbon budget is still highly uncertain. This can be accounted for by the unavailability of CO<sub>2</sub> measurements as well as changes in patterns of land use. This study explores the simultaneous changes in CO<sub>2</sub> flux exchanges and energy fluxes to understand the response of vegetation to climate variability. We have investigated the covariability between energy fluxes such as sensible heat flux, latent heat flux, and net radiation and CO<sub>2</sub> flux exchange by the Eddy Covariance technique at Skukuza Kruger National Park, South Africa. The patterns of the energy fluxes and net ecosystem exchange (NEE) during 1<sup>st</sup> January 2017 and 2018 show the ecosystem as a sink of Carbon with an average of  $-11,6177 \text{ } \mu\text{mol.m}^{-2} \cdot \text{s}^{-1}$  daytime,  $+4,6354 \text{ } \mu\text{mol.m}^{-2} \cdot \text{s}^{-1}$  nighttime,  $-8,3959 \text{ } \mu\text{mol.m}^{-2} \cdot \text{s}^{-1}$  daytime,  $+6,3479 \text{ } \mu\text{mol.m}^{-2} \cdot \text{s}^{-1}$  nighttime, respectively. CO<sub>2</sub> fluxes showed similar trends during the hydro-ecological year with an average of  $+0,8455 \text{ } \mu\text{mol.m}^{-2} \cdot \text{s}^{-1}$  and  $+0,1102 \text{ } \mu\text{mol.m}^{-2} \cdot \text{s}^{-1}$  annual increase from 2017 and 2018, respectively. While the energy flux increases with a decrease in carbon sink over that period from  $H = 67,3488 \text{ w/m}^2$ ,  $LE = 78,7404 \text{ w/m}^2$  and  $R_{n-MET} = 86,4002 \text{ w/m}^2$  up to  $H = 82,3075 \text{ w/m}^2$ ,  $R_{n-MET} = 99,0331 \text{ w/m}^2$  and down  $LE = 40,4249 \text{ w/m}^2$  contribution of the change from 2017 dry year to 2018 wet year, respectively. The increase in energy fluxes and CO<sub>2</sub> flux exchanges shows connections that have large implications for the Skukuza area and its response to interannual variability.

## 1. Introduction

The global Carbon dioxide levels today are higher than at any point in the least the past 800,000 years. Human activities have increased the concentration of Carbon dioxide in the atmosphere, amplifying Earth's natural greenhouse effect. Carbon dioxide concentrations are rising mostly because of the fossil fuels that people are burning for energy. Fossil fuels like coal and oil contain carbon that plants pulled out of the atmosphere through photosynthesis over the span of many millions of years; human activities are returning that carbon to the atmosphere in just a few hundred years. Carbon is the fundamental component of all organic compounds. It is one of the primary elements of life, involved in the fixation of energy by photosynthesis.

The biosphere includes a complex mixture of carbon compounds which originate, transform, and decompose within this sphere. Plants absorb CO<sub>2</sub> during photosynthesis, which is active during the daytime. All living organisms always respire and release CO<sub>2</sub>. Thus, Carbon-dioxide is produced and consumed in a cyclic manner. (Rebecca Lindsey et al.2020) A carbon sink is anything that absorbs more carbon than it releases. These sinks keep the levels of carbon dioxide in the atmosphere at manageable levels (e.g., forests and soils, oceans, untapped fossil fuel wells, and photosynthesis of terrestrial plants. The Carbon fluxes from the atmosphere to the ground are given a negative sign (mean down-take can result in sink) and the ground to the atmosphere are given a positive sign (mean uptake which can result in source of carbon), respectively. (Archibald SA, A Kirton, et al. 2008). The energy balance at Earth's land surface requires that the energy gained from net radiation be balanced by the fluxes of sensible and latent heat to the atmosphere and the storage of heat in soil. These energy fluxes are a primary determinant of surface climate. The annual energy balance at the land surface varies geographically in relation to incoming solar radiation and soil water availability. Energy fluxes vary over the course of a day and throughout the year, also in relation to soil water availability and the diurnal and annual cycles of solar radiation. (Gordon Bonan et al. 2015). This paper explores the simultaneous changes in CO<sub>2</sub> flux exchanges and energy fluxes to understand the response of vegetation to climate variability. We have investigated the covariability between energy fluxes such as sensible heat flux, latent heat flux, net radiation, and CO<sub>2</sub> flux exchange by Eddy Covariance technique at Skukuza Kruger National Park, South Africa.

## 2. Methodology

The Carbon dioxide flux measurements using the Eddy Covariance technique generate a raw dataset with a very high temporal resolution (generally 10-20 Hz). The first step in the analysis of these data is to screen them for spurious values, perform various corrections, and then integrate the fluxes over periods of about 30 minutes. An Eddy covariance system was built at a site near Skukuza Camp in Kruger National Park, South Africa, in 2000, with meteorological measurements starting in January 2001, as the first flux measurements are used. The site required that the length of the tower be 22m long, 16 m of height measurements, 10 m vegetation height, (25.0197°S, 31.4969°E), lies at 365 m above the sea level, in an area with 547 mm/year of mean annual rainfall, which falls between November and April and the annual temperature ranges between 14.5 and 29.5 °C. (Scholes, R.; Gureja, N et al.2001).

Data was collected using LI-7500, the open-path analyser that measured in situ gas, instantaneous wind speed, CO<sub>2</sub> concentration, radiation, and latent and sensible heat flux measurements needed for computing the connection between energy fluxes and CO<sub>2</sub> flux exchanges. The turbulence (vertical) fluxes of the carbon dioxide,  $F_c$  (mmol m<sup>-2</sup> s<sup>-1</sup>), the sensible heat flux,  $H$  (W m<sup>-2</sup>), and the latent heat flux,  $\lambda E$  (W m<sup>-2</sup>) for each time step (time scales, daily and diurnal patterns in various seasons, seasonal and inter-annual) were obtained from the flux tower at Skukuza. The eddy flux was calculated as:

$$F = \overline{\rho_a W' S'} \quad \text{General equation} \quad (1)$$

The eddy flux ( $F$ ) was approximately equal to the mean air density multiplied by the mean covariance between deviations in instantaneous vertical wind speed and mixing ratio. Carbon dioxide flux was presented as the mean covariance between deviations in instantaneous vertical wind speed and density of CO<sub>2</sub> in the air. (Grünwald T, Bernhofer C et al.2007, Mauder M, Foken T et al.2011)

$$F_c = \rho_a \overline{W' \rho_c'} \quad \text{Carbon dioxide flux} \quad (2)$$

By analogy, sensible heat flux was equal to the mean air density multiplied by the covariance between deviations in instantaneous vertical wind speed and temperature; conversion to energy units were accomplished by including the specific heat term.

$$H = \rho_a c_p \overline{W' T_a'} \quad \text{Sensible heat flux} \quad (3)$$

Latent heat flux was computed in a similar manner using water vapor and later converted to energy units.

$$\lambda E = \overline{\lambda W' \rho_v'} \quad \text{Latent heat flux} \quad (4)$$

Where  $\rho_a$  was the density of dry air ( $\text{kg m}^{-3}$ ) at a given air temperature,  $c_p$  was the specific heat capacity of dry air at constant pressure ( $\text{J kg}^{-1} \text{K}^{-1}$ ),  $\lambda$  was the latent heat of vaporisation ( $\text{J kg}^{-1}$ ),  $\rho_c$  was the molar density of  $\text{CO}_2$  gas ( $\text{mol m}^{-3}$ ) and  $\rho_v$  was the molar density of water vapour ( $\text{mol m}^{-3}$ ).  $T_a$  was the air temperature derived from the sonic anemometer (K) and  $W$  was the vertical wind velocity component ( $\text{m s}^{-1}$ ), and  $S'$  mixing ratios. Over bars denoted time averages and primes indicated fluctuations about the averages. Energy closure balance was obtained using the energy budget represented by equation 5, parameters data was stored at the eddy covariance flux tower every 30 minutes. Energy balance closure was evaluated by statistical regression of turbulent energy fluxes (sensible and latent heat (LE)) against available energy (net radiation, less the energy stored) and by solving for the energy balance ratio, the ratio of turbulent energy fluxes to available energy.

$$H + \lambda E + R_n + G = 0 \quad \text{Energy closure} \quad (5)$$

### 3. Results and Discussion

Half-hourly fluxes were used to analyze Net ecosystem exchanges (NEE) (Figure 1). Previous studies defined a hydro-ecological year from 1 July to 30 June of the following year according to Archibald et al. 2009. We observed patterns of covariability during the hydro-ecological years (Figure 1), with mean of  $F_C = -0,7349 \text{ umol.m}^{-2} \cdot \text{s}^{-1}$  (2008/09),  $F_C = -03185 \text{ umol.m}^{-2} \cdot \text{s}^{-1}$  (2010/11),  $F_C = -0,8454 \text{ umol.m}^{-2} \cdot \text{s}^{-1}$  (2016/17), and  $F_C = +0,1102 \text{ umol.m}^{-2} \cdot \text{s}^{-1}$  for 2017/2018 with data bias because only values ending in January 2018 is used which does not represent full hydro-ecological year. This can be attributed to vegetation and availability of rain to grow vegetation during the years, although some of the years are regarded as dry/drought years this has not impacted largely on the ecosystem over the years because Skukuza plants regrowth as a form of carbon sequestration. The site has less human carbon footprint. The ecosystem was still able to maintain its reservoirs. Luis A. et.al. 2021 also found results that indicate a shift to a climate into extreme dry and wet seasons might eventually suppress the savanna carbon uptake capacity allowing it to remain as carbon sink. The first results from the project CarboAfrica in 2009 for savanna estimates lead to a moderate carbon sink where the main components were Fires, deforestation and forest degradation were the main contributors to the carbon emissions.

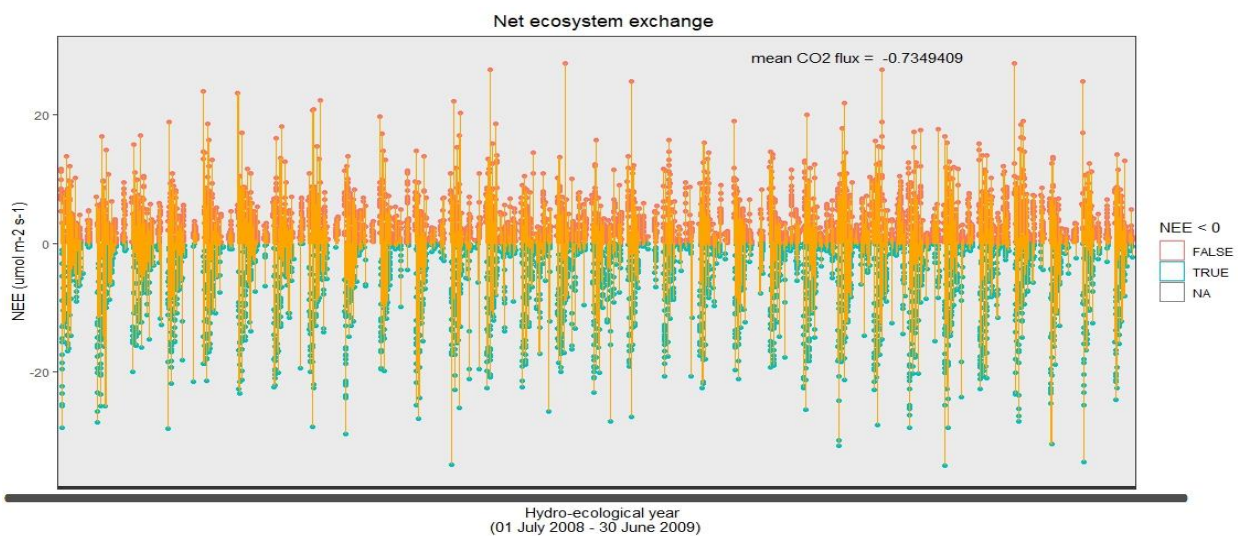


Figure 1 Net ecosystem exchange (NEE) for hydro-ecological years 2008/09.

The scatter plot (Figure 2) explains the correlation between the Net ecosystem exchange (NEE) and sensible heat flux(H). It represents how closely the two variables are connected. There can be three such situations to see the relation between the two variables Positive Correlation is when the values of the two variables move in the same direction so that an increase/decrease in the value of one variable is followed by an increase/decrease in the value of the other variable. Negative Correlation is when the values of the two variables move in the opposite direction so that an increase/decrease in the value of one variable is followed by decrease/increase in the value of the other variable. No Correlation is when there is no linear dependence or no relation between the two variables.

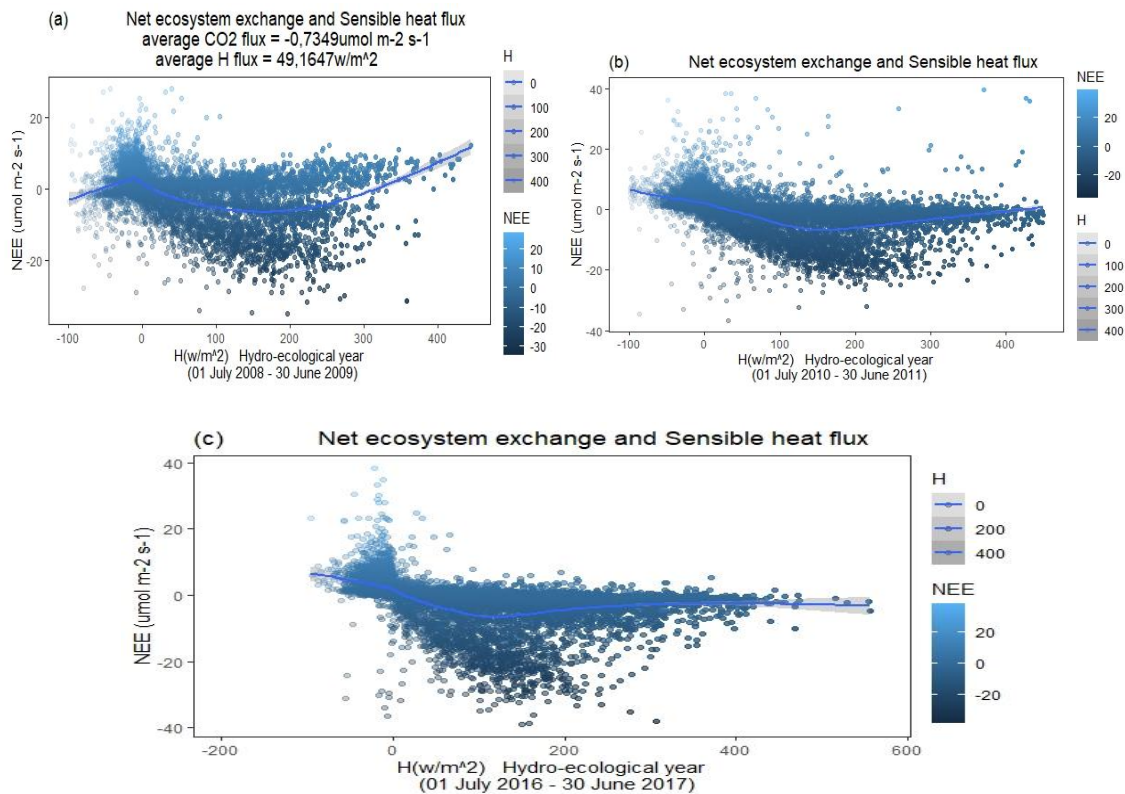


Figure 2 Net ecosystem exchange (NEE) and sensible heat flux(H) for hydro-ecological years 2008/09, 2010/11, 2016/17.

The pattern shown in Figure 2 indicates the relation between NEE and sensible heat flux (a)-(c), where the correlation curving towards the negative. This shows that with an increase in energy flux of sensible heat over the years, the Skukuza ecosystem is impacted negatively. The curve is moving towards average if this uptake is continuous, it may end up becoming a source of Carbon in the future. This pattern is similar for NEE and latent heat flux as well as NEE and net radiation. Similar correlations were found by Wang, W., J. A. et.al.2016, where examined the correlation of water vapor and CO<sub>2</sub> through analyses of high-frequency time series derived from eddy covariance measurements collected over a suburban grass field in Princeton, NJ during a 2-year period (2011–2013). The sensible heat flux (Figure 2) increases with a decrease in carbon sink over that period 2008/09, 2010/11,2016/17 and 2017/18 from **(a)  $H = 49,1647 \text{ w/m}^2$** , **(b)  $H = 58,5849 \text{ w/m}^2$** , **(c)  $H = 67,3488 \text{ w/m}^2$**  and 2017/18 is bias since dataset does not complete for hydro-ecological year with  $H = 82,3076 \text{ w/m}^2$ , respectively. Latent heat fluxes and CO<sub>2</sub> fluxes showed negative correlation during the hydro-ecological years 2008/09,2010/11,2016/17 and 2017/18 was not reliable since its data bias.

While the latent heat fluxes mean for those years measured were,  $LE = 63,0990 \text{ w/m}^2$ ,  $LE = 50,5743 \text{ w/m}^2$ ,  $LE = 78,7404 \text{ w/m}^2$  and  $LE = 40,4249 \text{ w/m}^2$ . Interestingly, maximum  $\text{CO}_2$  uptake occurs during periods of low soil moisture when green leaves are still present. This reduces gross primary production through ecosystem water stress, cause vegetation mortality and further exacerbate climate extremes due to land–atmosphere feedbacks. Previous work has explored the impact of soil-moisture availability on past carbon-flux variability (Green, J.K., et.al.2019). However, the influence of soil-moisture variability and trends on the long-term carbon sink and the mechanisms responsible for associated carbon losses remain uncertain.

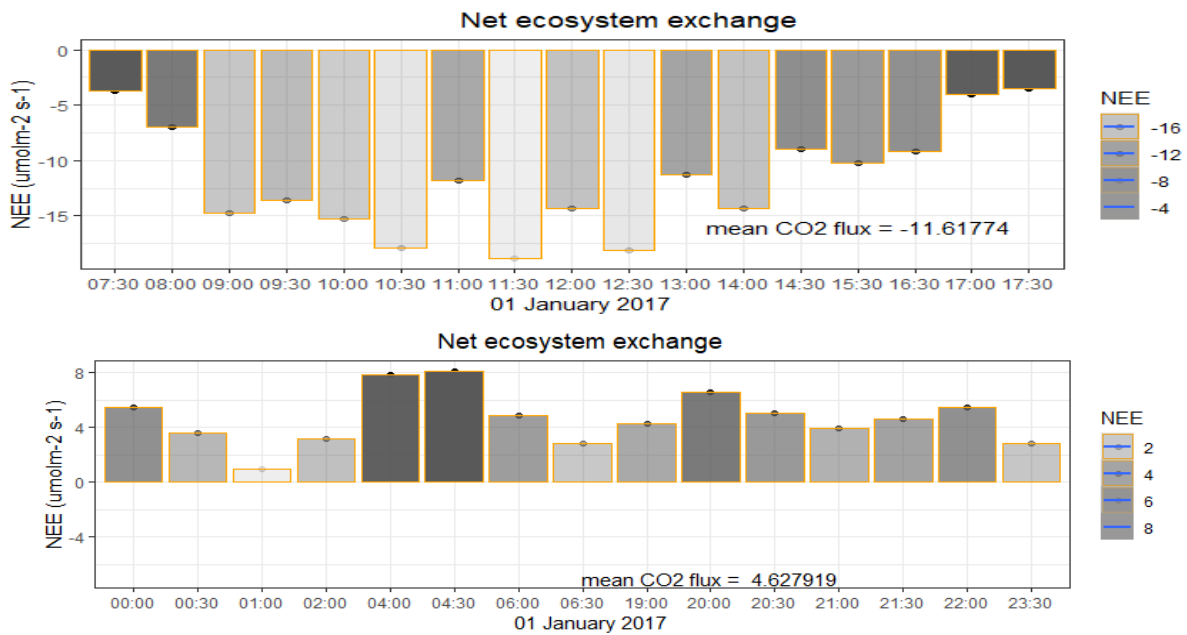


Figure 3 Fluxes Net ecosystem exchange (NEE) daytime and nighttime of 01 January 2017.

The half hourly NEE (Figure 3), during 1st January 2017 shows average of  $-11,6177 \text{ } \mu\text{mol}\cdot\text{m}^{-2}\cdot\text{s}^{-1}$  daytime,  $+4,6354 \text{ } \mu\text{mol}\cdot\text{m}^{-2}\cdot\text{s}^{-1}$  night-time, and 2018 was uptake from 2017 to  $-8,3959 \text{ } \mu\text{mol}\cdot\text{m}^{-2}\cdot\text{s}^{-1}$  daytime,  $+6,3479 \text{ } \mu\text{mol}\cdot\text{m}^{-2}\cdot\text{s}^{-1}$  night-time, respectively.  $\text{CO}_2$  fluxes showed similar trends during the hydro-ecological years with average of  $+0,8455 \text{ } \mu\text{mol}\cdot\text{m}^{-2}\cdot\text{s}^{-1}$  and  $+0,1102 \text{ } \mu\text{mol}\cdot\text{m}^{-2}\cdot\text{s}^{-1}$  increase from 2017 and 2018, respectively. While the energy flux increases with a decrease in carbon sink over that period from  $H = 67,3488 \text{ w/m}^2$ ,  $LE = 78,7404 \text{ w/m}^2$  and  $R_n = 86,4002 \text{ w/m}^2$  up to  $H = 82,3075 \text{ w/m}^2$ ,  $R_n = 99,0331 \text{ w/m}^2$  and down  $LE = 40,4249 \text{ w/m}^2$  contribution of the change from dry year to wet year for 2017 and 2018, respectively. However, to quantify and understand the patterns for analyses we used hydro-ecological years instead of a day. The energy balance closure was 74% but generally, a 100% energy budget closure is not achieved for EC systems, and an average closure of approximately 80% is often observed. Several reasons for the lack of 100% including different sampling scales of the sensors; energy storage; measurement errors; and heterogeneity of the land surface resulting in advective fluxes and transport of large eddies which cannot be measured with the Eddy Covariance method.

These patterns (Figure 4) show that energy cannot be conserved according to the law of conservation in this site by using the eddy covariance method. Since the Skukuza flux tower is a LI-Cor 7500 open path gas analyzer, it has problem with energy closure. This issue can be resolved by looking at closure residual. The energy closure must approach zero. While closure residual is determined with:

$$\text{Closure Residual} = (R_n + G) - (H + \lambda E) \tag{6}$$

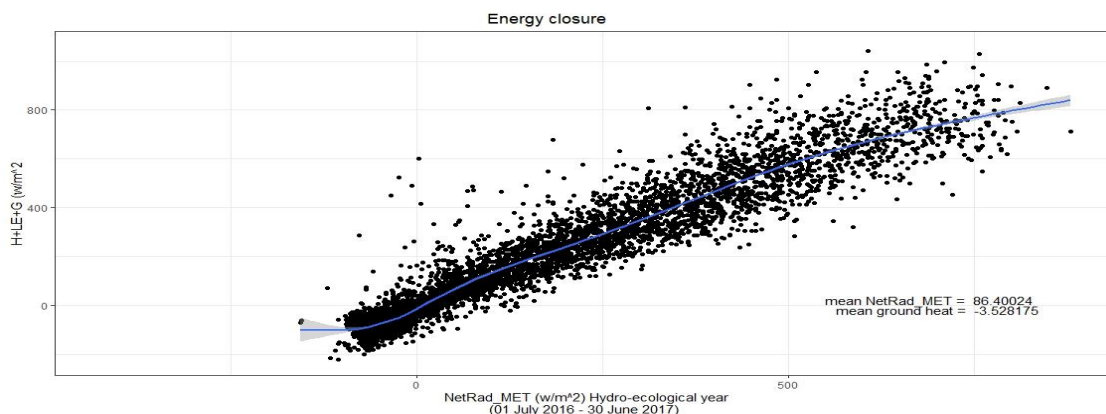


Figure 4 Energy closure with the sum of sensible heat flux (H), latent heat flux (LE) and soil heat flux (G) against net radiation for 2008/09.

#### 4. Conclusion

The increase in energy has large implications to the Skukuza area and its response to interannual climate variability. The covariability can be attributed to perturbations in vegetation cover as driven by interannual climate variability. The variability seems to be largely controlled by variations in the length of time that green leaf is displayed by the trees and grasses, and by changes in seasonal patterns of water availability both ultimately driven by variations in rainfall between years. Similar previous study done by Archibald et al., 2008 revealed same patterns. It became obvious that the energy balance at the Earth's surface could not be closed with experimental data. The available energy, that is, the sum of the net radiation and the ground heat flux, was found in most cases to be larger than the sum of the turbulent fluxes of sensible and latent heat. For the CO<sub>2</sub> flux networks a closure of the energy balance of approximately 80% is usually found.

#### 5. Acknowledgement

We would like to thank the support of University of Venda department of physics. We would like to thank CSIR, SANParks, EMSAfrica, Vuwani science resource centre and Thunen for supporting the science.

#### References

- [1] Archibald, S., Kirton, A., Merwe, M. V. D., Scholes, R. J., Williams, C. A., & Hanan, N. (2008). Drivers of interannual variability in Net Ecosystem Exchange in a semi-arid savanna ecosystem, South Africa. *Biogeosciences Discussions*, 5(4), 3221.
- [2] Green, J.K., Seneviratne, S.I., Berg, A.M. *et al.* Large influence of soil moisture on long-term terrestrial carbon uptake. *Nature* **565**, 476–479 (2019). <https://doi.org/10.1038/s41586-018-0848-x>
- [3] Grünwald, T., & Bernhofer, C. (2007). A decade of carbon, water and energy flux measurements of an old spruce forest at the Anchor Station Tharandt. *Tellus B: Chemical and Physical Meteorology*, 59(3), 387-396.
- [4] Lindsey, R., & Dahlman, L. (2020). Climate change: Global temperature. Available online: *climate.gov* (accessed on 22 March 2021).
- [5] Mauder, M., & Foken, T. (2015). Documentation and instruction manual of the eddy-covariance software package TK3 (update).
- [6] Wang, W., J. A. Smith, P. Ramamurthy, M. L. Baeck, E. Bou-Zeid, and T. M. Scanlon (2016), On the correlation of water vapor and CO<sub>2</sub>: Application to flux partitioning of evapotranspiration, *Water Resour. Res.*, 52, 9452–9469, doi:10.1002/2015WR018161

# Characterisation of bulk materials using fast neutron transmission analysis

Sizwe Mhlongo<sup>1,\*</sup>, Tanya Hutton<sup>1</sup>, Zina Ndabeni<sup>1,2</sup>, Naledi Segale<sup>1</sup> and Andy Buffler<sup>1</sup>

<sup>1</sup>Department of Physics, University of Cape Town, Rondebosch, 7701, South Africa

<sup>2</sup>Department of Subatomic Physics, iThemba LABS, Somerset West, 7129, South Africa

\*E-mail: [mhlsiz016@myuct.ac.za](mailto:mhlsiz016@myuct.ac.za)

**Abstract.** Neutrons and gamma rays are effective probes for the elemental characterization of bulk samples. When a neutron interacts with matter, it does so in a unique way, depending on the energy of the neutron and the nature of the target nucleus. Most nuclides exhibit distinctive structure in their total and differential cross sections, which enhances the probability of certain neutron interactions occurring at specific incident neutron energies and exiting scattering angles. Elements can thus be differentiated via their total, elastic and inelastic scattering cross sections, the energy loss that occurs in neutron scattering and the energies of gamma rays produced in inelastic collisions. In this work we report on the use of the fast neutron transmission analysis technique for the analysis of C and H in graphite and high density polyethylene.

## 1. Introduction

The interrogation of materials to determine their elemental composition is of wide interest in industry. There are many well established techniques that are regularly used for this purpose [1, 2], and in particular neutron-based techniques have seen much development in the past decades [3, 4]. Neutron techniques typically interrogate a material by interacting with atomic nuclei, inducing secondary radiation which are characteristic of the composite nuclei of the material [5]. The types of radiation that can be induced, and measured, include prompt and delayed gamma rays, and scattered neutrons [4, 5]. Alternatively, investigation of neutrons which have not interacted within a material i.e. the transmitted neutrons, relative to knowledge of the incident neutron field, can provide a characteristic signature which can be used to determine the composition of the material [6].

The practical implementation of fast neutron transmission analysis (FNTA) involves irradiating a sample with a well-characterized (energy, intensity and angle) neutron beam, and measuring the transmitted neutron energy spectrum. For a pencil beam of neutrons incident on a bulk sample with thickness  $x$ , the attenuation can be described by Eq. 1 [7], where  $I(x)$  and  $\Sigma_R$  are the energy dependent neutron intensity and removal cross sections [8] respectively:

$$I(x) = I(0) \exp(-\Sigma_R t). \quad (1)$$

For a composite material the removal cross section is a linear combination of the constituents, weighted by their respective mass ratios. Removal cross sections are unique for each constituent and can be determined by measurement, simulation or from literature depending on the application. Previous work has demonstrated the use of FNTA to determine the water content in a concrete sample [6], or the elemental composition of sand [7]. The aim of this work is to investigate FNTA as a technique for elemental analysis, by measuring the microscopic removal cross sections of C in graphite and H in polyethylene ( $(C_2H_4)_n$ ) samples and comparing them to total cross sections in the neutron data libraries. The broader goal is to construct a library of elemental responses which will then be used to elementally characterize materials in bulk.

## 2. Experimental setup and procedure

The measurements were undertaken using a deuterium-tritium (D-T) MP320 (Thermo Fisher) sealed tube neutron generator (STNG) at the n-lab, a fast neutron facility at UCT that was commissioned in 2017 [9]. The D-T STNG produces neutrons of energy 14 MeV at a rate of  $10^8$  neutrons  $s^{-1}$  into  $4\pi$   $sr^{-1}$ , which were collimated into a 0.8 cm diameter pencil beam (Figure 1). A  $\varnothing 2'' \times 2''$  EJ-301 organic liquid scintillator detector was positioned in the beam, and operated at a negative bias of 1100 V. Signals from the anode (fast) and dynode (slow) were acquired with a CAEN DT5370 digitizer coupled to the QtDAQ software [10]. As the detector was sensitive to both neutron and gamma ray radiation, pulse shape discrimination (PSD) was implemented through QtDAQ using the fast anode signal [10,11] in order to select only for events induced by neutrons. Energy information was obtained from the pulse height of the dynode signal after shaping and amplification with an Ortec 113 pre-amplifier and 427A amplifier. The resulting light output ( $L$ ) spectra were calibrated using a series of gamma ray sources to produce an electron equivalent energy ( $MeV_{ee}$ ) scaling. In organic scintillators, gamma rays interact primarily by Compton scattering, and the Compton edges [12] for the gamma rays from  $^{137}Cs$ ,  $^{60}Co$ ,  $^{22}Na$  and  $^{241}Am$ - $^9Be$  were used for calibration.

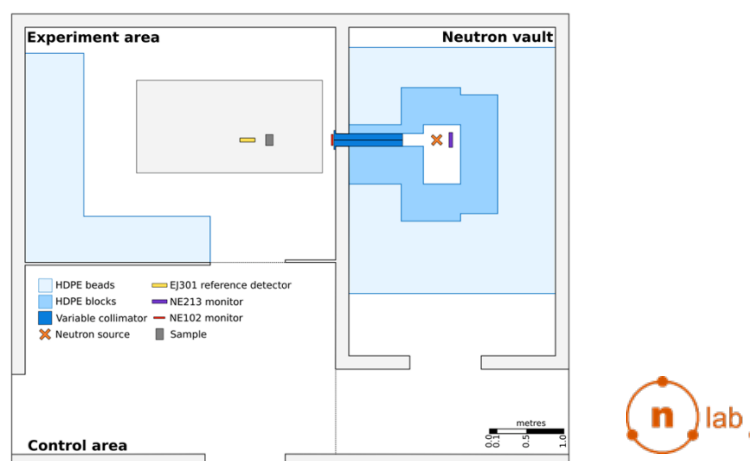


**Figure 1.** Schematic of the n-lab facility showing the neutron vault, where the STNG is well-shielded with high density polyethylene (HDPE) from the control area and the experimental area.

The present measurements used samples of graphite and high density polyethylene (HDPE). Graphite is primarily comprised of  $^{12}C$ , and the samples used in this work consisted of solid blocks with a density of  $1.8$   $g\ cm^{-3}$ , cross sectional area of  $5.0 \times 5.0$   $cm^2$  and thicknesses up to  $14.3$   $cm$ . The HDPE samples had a density of  $0.9$   $g\ cm^{-3}$ , cross sectional area of  $50.0 \times 50.0$   $cm^2$  and thicknesses up to  $5.0$   $cm$ . A typical experimental set up is shown in Figure 2.

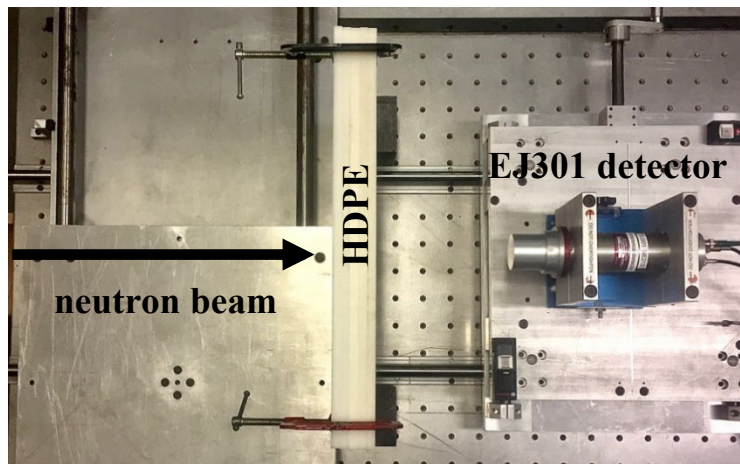


**Figure 2.** Experimental setup for a 0.8 cm diameter pencil beam of 14 MeV neutrons incident on a 5.0 cm thick HDPE sample. Neutrons transmitted through the sample are detected with an EJ-301 organic liquid scintillator.

The samples were positioned at 74.0 cm from the collimator exit, while the reference detector was positioned at 120 cm from the collimator exit, at an angle of  $0^\circ$  with respect to the beam axis. The samples were irradiated until a minimum of  $10^5$  neutron events were recorded. The measured  $L$  spectra were calibrated and normalized with respect to the acquisition time.

### 3. Results and analysis

Measurements of the transmitted neutrons were made for multiple thicknesses of each sample. Figure 3 shows the normalized and calibrated  $L$  spectra measured for graphite and HDPE. As expected from Eq. 1, increasing the amount of material results in a decrease in the transmitted neutron intensity. The no sample case is taken to be representative of the incident neutron intensity  $I(0)$ .

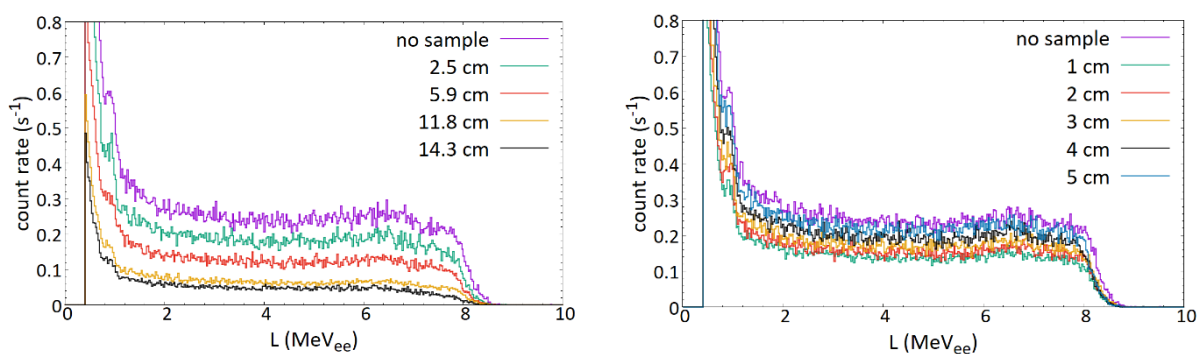


**Figure 3.** Calibrated light output spectra  $L$  of 14 MeV neutrons transmitted through graphite (left) and HDPE (right) samples.

The effective removal cross section at 14 MeV for each sample was obtained from the fit parameters of the transmitted neutron intensity (obtained by integrating count rates within the 1.2 MeV<sub>ee</sub> to 8.4 MeV<sub>ee</sub> range of  $L$ ) with respect to the material thickness (see Figure 4).

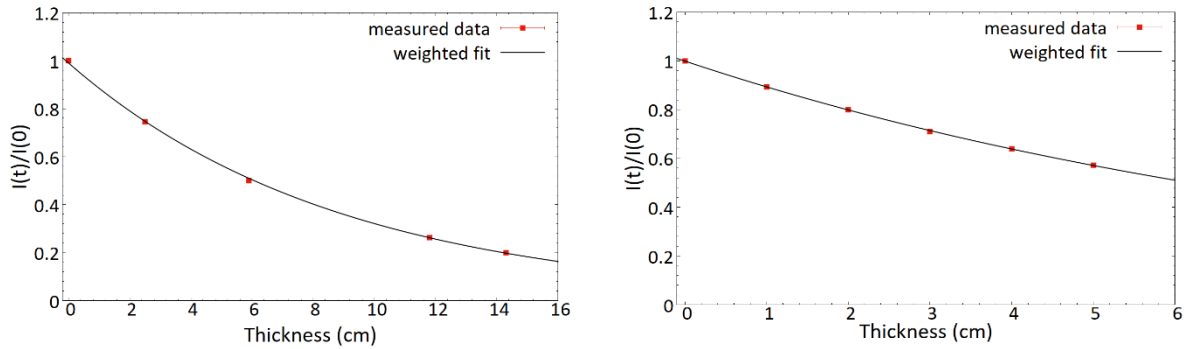


**Figure 4.** Relative neutron intensity as a function of sample thickness at 14 MeV for graphite (left) and HDPE (right). The uncertainties of transmitted neutron intensities for both the materials ranged between 0.3% to 0.5%.

Equation 1 was linearized (Eq. 2) and a weighted linear least squares minimization used to determine  $\Sigma_R$  from the fit parameters:

$$\ln\left(\frac{I(x)}{I(0)}\right) = \Sigma_R x. \quad (2)$$

The data were well-fitted, and the resulting effective removal cross sections for graphite and HDPE are presented in Table 1.

**Table 1.** Effective removal cross sections for 14 MeV neutrons.

Material	$\Sigma_R(\text{cm}^{-1})$
Graphite	$0.1150 \pm 0.0012$
HDPE	$0.1118 \pm 0.0007$

The effective removal cross section  $\Sigma_R$  is regarded as a bulk property and depends on the physical preparation of the sample. In order to develop elemental signatures, it is necessary to define a microscopic effective removal cross section  $\sigma_R$ , which removes the dependence on the physical form of the sample. The microscopic removal cross section is related to  $\Sigma_R$  by:

$$\Sigma_R = \frac{\rho N_A}{A} \sigma_R, \quad (3)$$

where  $\rho$  is the sample density  $N_A$  is Avogadro's number, and  $A$  is the molar mass of the isotope, element, or compound as required. As graphite is comprised solely of C (98.93 %  $^{12}\text{C}$ ), the elemental microscopic removal cross section  $\sigma_{R,C}$  was directly obtained from the measured value for  $\Sigma_R$ . HDPE is comprised of a known ratio of H and C, so the elemental microscopic removal cross section  $\sigma_{R,H}$  for H (99.98 %  $^1\text{H}$ ) can be extracted according to Eq. 4:

$$\sigma_{HDPE} = 2\sigma_{R,C} + 4\sigma_{R,H}. \quad (4)$$

The microscopic removal cross sections  $\sigma_R$  for  $^{12}\text{C}$  and  $^1\text{H}$  are presented in Table 2 together with the total microscopic cross sections  $\sigma_T$  as defined in the ENDF/B-VIII.0 data library [13].

**Table 2.** Microscopic cross sections of C and H for 14 MeV neutrons.

Element	$\sigma$ (b)	
	$\sigma_R$	$\sigma_T$
C	$1.265 \pm 0.037$	$1.298 \pm 0.055$
H	$0.750 \pm 0.002$	$0.676 \pm 0.023$

#### 4. Discussion and Conclusion

The use of fast neutron transmission analysis has been demonstrated, leading to measurements of effective removal cross sections. In order to deconvolve the composition it is necessary to produce a series of unique responses, from transmitted neutron measurements, and measurements of other signatures, for each element of interest. The macroscopic removal cross sections measured at 14 MeV for graphite and polyethylene, were used to extract the microscopic removal cross sections of C and H, which were found to be  $1.265 \pm 0.037$  barn and  $0.750 \pm 0.002$  barn respectively. There is agreement to within experimental uncertainty between the measured (removal) cross section and total microscopic cross section (literature) of carbon [13], but this is not the case for hydrogen, which requires further consideration. Based on the empirical rule that removal cross sections are approximately equal to two thirds of the total cross sections for neutron energies in the 6 MeV to 8 MeV range, we expect our measured values to be less than the total cross sections, this has been shown to also apply to 14 MeV neutron energies [14]. We also expect the ratios of the removal cross sections to total cross sections to be constant for both H and C [14]. While there are still outstanding issues to be resolved, the results presented here show promise with respect to using FNTA for materials analysis. Additional measurements are ongoing to investigate the effective removal cross section over a broader range of neutron energies using an  $^{241}\text{Am-}^9\text{Be}$  radioisotopic source, in combination with gamma ray measurements with the STNG to generate multi-modal elemental response functions.

#### Acknowledgements

The authors would like to thank and acknowledge the National Research Foundation and the Science Faculty at UCT for supporting this work.

#### References

- [1] Rouessac F and Rouessac A 2007, *Chemical Analysis: Modern Instrumentation Methods and Techniques* (Chichester: John Wiley and Sons)
- [2] Mulhauser F 2012 *Neutron Generators for Analytical Purposes* (Vienna: IAEA) pp 15-25
- [3] Valkovic V 2016, *14 MeV Neutrons: Physics and applications* (Boca Raton: CRC Press) p 14
- [4] Elayi A G 1990 *Activation Analysis Vol 2*, ed Z B Alfassi (Boca Raton: CRC Press) p 74
- [5] Buffler A 2004 *Radiation Physics and Chemistry* **71** pp 853-61
- [6] Buffler A 1997 *Int. conf. neutrons in research and industry* (Crete) Vol 2867, ed G Vourvopoulos (Washington:SPIE) pp 192-197
- [7] Hutton T, Buffler A and Alexander A 2022 *EPJ Web Conf.* **261**
- [8] Zoller L K 1964 *Nucleonics* **22** pp 128
- [9] Hutton T and Buffler A 2018 *Proc. of SAIP2017 (Stellenbosch)*, ed Engelbrecht pp 324-330
- [10] Comrie A C, Buffler A, Smit F D and Wortche H J 2015 *Nucl. Instrum. Methods. Phys. Res. A* **772** pp 43-49
- [11] Buffler A, Hutton T, Leadbeater T, Alexander M and Dlamini S 2020 *International Journal of Modern Physics Conference Series* **50**
- [12] Krane K S 1955, *Introductory Nuclear Physics* (New York: John Wiley and Sons) pp 200
- [13] Brown D A et al., 2018 *Nuclear Data Sheets* **148** pp 1-142
- [14] Ku L P and Kolibal J 1983 *Effective dose removal cross section of 14 MeV neutrons* (New Jersey: Princeton University) pp 11-12

# Validation of the Monte Carlo Detector Effects Model for the UCT POLARIS Compton Camera

F S Smuts<sup>1</sup>, N Hyslop<sup>1</sup>, P Maggi<sup>2</sup>, J Polf<sup>3</sup>, T Leadbeater<sup>1</sup>, M Van Heerden<sup>1</sup>, S W Peterson<sup>1</sup>

<sup>1</sup>Department of Physics, University of Cape Town, Rondebosch 7700, South Africa

<sup>2</sup>Lawrence Livermore National Laboratory, Livermore, CA, United States

<sup>3</sup>Department of Radiation Oncology, University of Maryland School of Medicine, Baltimore, MD, United States

E-mail: [frank.s.smuts@gmail.com](mailto:frank.s.smuts@gmail.com)

**Abstract.** The benefit of proton therapy will only truly be realized once an experimental in-vivo dose verification system has been developed. The use of a Compton Camera (CC) allows detection of the secondary radiation, specifically Prompt Gammas (PG), produced at the location of the dose deposition. The UCT Polaris detector is composed of two PolarisJ CC modules with two CdZnTe positron-sensitive crystals per module, configurable in an orthogonal or face-to-face alignment. Previous work has shown that the CdZnTe crystals experience significant deadtime when exposed to a high dose-rate proton beam. The Monte Carlo Detector Effects (MCDE) model was developed to replicate these deadtime effects. The goal of this work was to adapt the MCDE model to the UCT Polaris detection system, to allow for new detector configurations and broaden the applicability of the model to high-activity gamma sources. The MCDE model results are compared to measured data from a short-lived <sup>68</sup>Ga positron source in face-to-face configuration. The observed differences between the measured and simulated results point to an overestimation in the underlying Geant4 model and to a change in one of the timing parameters used in the MCDE model. A two-parameter optimization code was run to improve the overall comparison between simulation and experiment, providing the most extensive validation of the MCDE model to date.

## 1. Introduction

Compton cameras (CCs) have been studied extensively as a tool for imaging the passage of a proton beam through a patient during proton radiotherapy, in order to verify the dose range of the beam as reviewed by Polf and Porodi [1]. This *in vivo* imaging is achieved through tomographic reconstruction of the dose site, using multiple scattering depositions in the CCs by prompt gamma rays emitted during tissue irradiation. Compton cameras with Cadmium-Zinc-Tellurium crystals (CdZnTe) are a popular for use in tomographic reconstruction, due to their high position and energy resolution [2]. Experimental studies conducted with proton beams in laboratories and clinical radiotherapy facilities demonstrate that *in vivo* imaging is feasible [3,4]. However, at clinical dose rates, the detector efficiency for multiple scattering events becomes too low for a functional reconstruction of the dose range.

In order to investigate the detector efficiency, Maggi and Polf developed a quantitative Monte Carlo and Detector Effects (MCDE) model for simulating gamma ray interactions with a CdZnTe CC detector [5]. The MCDE model enabled an analysis of deadtime effects and false coincidence events in the detector, by simulating the effects of detector electronics on data capture. The model was validated through a comparison to a proton beam experiment in a PJ3 detector with 16 PolarisJ CC modules in a two-plane configuration. In the present work, the MCDE model is shown to generalise to arbitrary

detector configurations, through its adaptation to the UCT PolarisJ Compton Camera detector. The broader applicability of the model is demonstrated, by replicating an experiment with a high-activity  $^{68}\text{Ga}$  positron source. The true and simulated detectors are compared with respect to their characteristic deadtime behaviour. The model is further optimised to improve the overall comparison between simulation and experiment.

## 2. Method

### 2.1. MCDE: A Brief Overview

A flowchart diagram of the MCDE model is drawn in Figure 1 [5]. In the data input stage, the experimental setup is replicated with a Geant4 Monte Carlo model, which simulates the interactions of gamma rays with the Compton Camera's CdZnTe crystals after emission from a radioactive source or beam target. The positions and deposited energies of single, double and triple scatter events ( $D_n$ ) are used as idealised raw data for the MCDE model; these have neither preassigned time stamps nor exposure to deadtime effects. In the initialisation stage, the positions are assigned time stamps  $t_n$  drawn from an exponential distribution, with a rate parameter corresponding to a desired dose rate or source activity. The position data is then discretised and indexed by pixel, crystal and module number. During detector timing and readout, the simulation models the detector response as a three-stage cycle: each module first detects a scattering event, then records interactions over a small timing window. The modules enter deadtime to process the event, and subsequently reactivate to listen for new events. The timing and readout section accounts for physical effects that distribute and dampen energy depositions in the CdZnTe crystals, of which dominant factors are the anode potentials, charge drift and the formation of electron clouds. Account is also made for timing delays associated with the proprietary electronics in the PolarisJ modules. The final output of the MCDE model is a list of position data, energy depositions and timestamps for all events recorded by the detector.

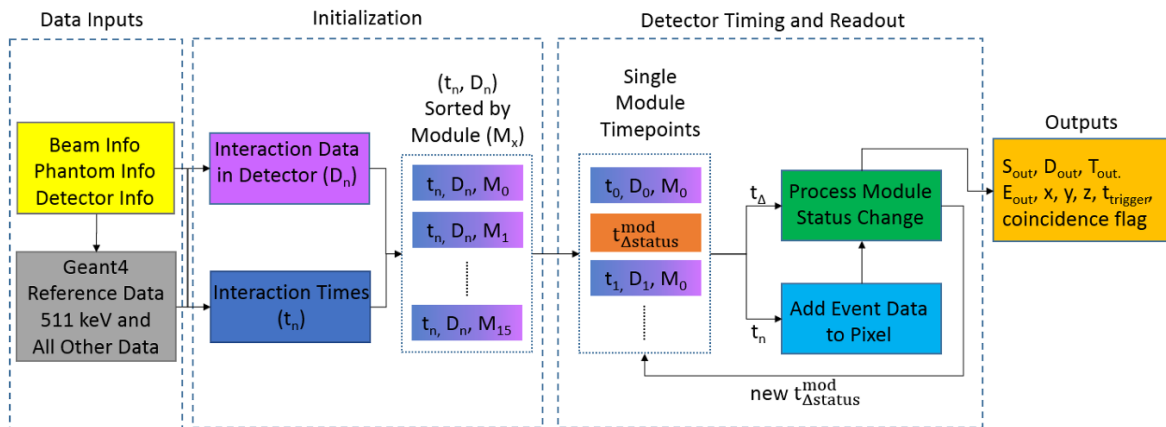


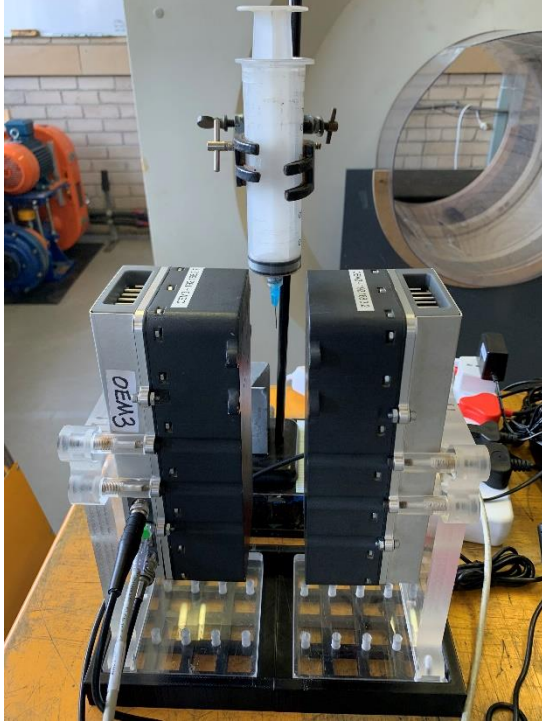
**Figure 1:** High level flowchart for the MCDE model [5].

### 2.2. Adapting MCDE to the UCT PolarisJ Compton Camera

The original MCDE model was hardcoded for a two-plane detector setup [5] as detailed in the introduction. The UCT Polaris detector is composed of two separate PolarisJ modules with two CdZnTe positron-sensitive crystals per module, typically configured in an orthogonal or face-to face alignment. Neither alignment was compatible with the original model. Compatibility was achieved by transforming all position data, from either orthogonal or back-to-back alignments, to a standard configuration with the modules placed side-by-side on a fixed plane. The position discretisation was then adapted for the two-module case. The solution is justified on the basis that the MCDE model is blind to the relative configuration of the modules after simulating the interactions in the Geant4 model, as long as the modules do not intersect. For dose range reconstruction, an inverse transformation was applied to the

event data after simulating detector timing and readout. Additional modifications included the handling of cases where the PolarisJ modules have either two or four crystals, as well as repositioning of the anode planes in the detector.

### 2.3. Recorded Event Rate vs. Activity of a $^{68}\text{Ga}$ Positron Source



A measurement-simulation comparison was drawn for an experiment with a short-lived  $^{68}\text{Ga}$  point source [6] starting at an initial activity of  $4.72 \pm 0.24$  MBq (see Figure 2). The aim of the experiment was to identify the relationship between the expected rate of raw singles events in the CCs ( $n$ ) and the recorded event rate ( $m$ ), as a function of the activity  $A$ . The graph of event rate  $m(A)$  versus  $A$  is called the deadtime curve. The relationship between event rate  $m$  and expected rate  $n$  was captured by a nonparalysable deadtime model based on geometric arguments [7]

$$n = \frac{m}{1 - m\tau_{np}}$$

Here,  $\tau_{np}$  is a non-paralysable deadtime parameter unique to the detector. The setup was replicated with  $5 \times 10^7$  simulated decays in the Geant4 model. The MCDE model was run at 200 source activities evenly spaced between 1 and 5000 kBq, using a small fixed sample

**Figure 2:** Image of the experimental setup for PG imaging of a  $^{68}\text{Ga}$  point source [6].

of the simulated dataset. For the MCDE model, the expected event rate was calculated directly from input parameters, whereas for experiment the expected event rate was estimated with a weighted linear fit to data at low activity (160 to 220 kBq). Scattering events with more than three interactions were excluded from the measured event rate calculation for both cases. The real and simulated detectors were compared with respect to their non-paralysable deadtime parameters  $\tau_{np}$ . This follows from applying a weighted linear fit  $y = am + b$  to the activity function  $m/A$  ( $m$ ), which yields the estimate  $\tau_{np} = -a/b$ .

### 2.4. MCDE Model Optimisation

A two-parameter optimisation was carried out to improve the comparison between measurement and simulation for the MCDE model. One parameter was a linear shift to the total deadtime experienced by the detector for each recorded event, which naturally affects the rate at which events are recorded by the detector. The second parameter is a factor correction applied to the number of scatter events recorded in the Geant4 simulation: this accounts for over – or underestimates in the number of interaction events that take place in the CC for a given activity. The objective function for minimization was the chi-square value of the distance between the simulated deadtime curve and a small sample of data points from the experimental deadtime curve. The local minimum of the objective function was estimated by a brute force evaluation of its value for a small region of the parameter space.

### 3. Results and Discussion

Figure 3a shows a comparison between the measured and simulated deadtime curves for the  $^{68}\text{Ga}$  positron source experiment, and Figure 3b shows the corresponding activity functions along with the fits used for estimating the non-paralyzable deadtime parameters  $\tau_{np}$ . The estimated deadtime parameters are  $\tau_{np} = 2.4544 \pm 0.0016 \times 10^{-5} \text{s}^{-1}$  (Measured),  $\tau_{np} = 2.01 \pm 0.27 \times 10^{-5} \text{s}^{-1}$  (Unoptimised MCDE) and  $\tau_{np} = 2.52 \pm 0.41 \times 10^{-5} \text{s}^{-1}$  (Optimised MCDE). The differing orders of magnitudes in variance for the measured and simulated deadtime parameters result predominantly from a much larger sample size for the measured data.

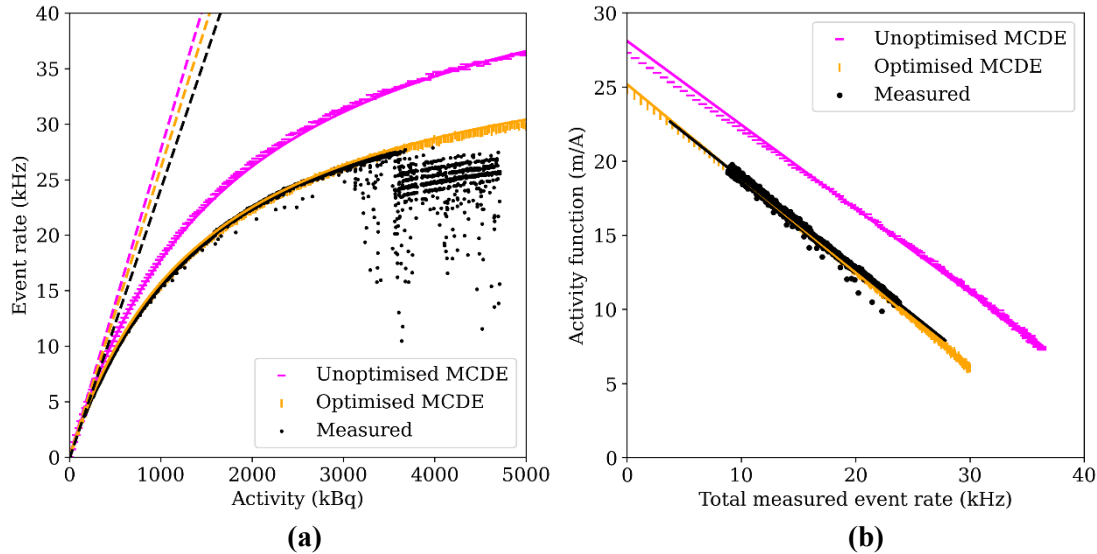


**Figure 3:** (a) Measured and simulated raw singles event rates as a function of activity for a  $^{68}\text{Ga}$  point source. Expected rates  $n$  are drawn with dashed lines, event rates  $m$  with scatter points, and non-paralyzable deadtime model fits with solid lines. (b) Activity functions of measured and simulated event rates.

In the range 0 to 3500 kBq, the measured deadtime curve increases monotonically and plateaus without becoming paralyzed. Beyond this range, the deadtime curve drops sharply and forms a physically implausible set of parallel curves. The effect is conjectured to be an artefact of buffer overflow when streaming the event data to onboard memory, suggesting a saturation point of the detector for sources with high activity. Paralyzable deadtime effects may also play a secondary role in decreasing the measured event rate. To the best of the knowledge of the authors, the observation has not been listed in any previous publications, and the data will be analysed in depth in a future work.

The MCDE model qualitatively reproduces the relationship between activity and event rate for the measured deadtime curve, apart from the region above 3500 kBq; this is anticipated, as the model excludes a mechanism for buffer overflow. A nonparalyzable deadtime model fit closely matches the simulated data, serving as further validation that the MCDE model agrees with standard geometric models of deadtime that are established in literature and applied in the contexts of CCs and [5,7,8]. Quantitatively, the model overestimates the measured event rate by a factor to the order of approximately 20%. Two parameters were identified as explanatory variables that could potentially explain the discrepancy: the time spent by the detector in deadtime, and overestimation of gamma ray interactions with the detector in the Geant4 simulation. In Figure 4, a phase diagram is drawn for the objective function of the discrepancy between simulated and measured deadtime curves, as a function of the two parameters. In order to optimise the comparison, the deadtime tuning factor needs to increase, and the event rate correction factor needs to decrease. The former implies that the MCDE model deadtime per event is too short, and the latter indicates that the Geant4 model simulates too many events for a given source activity. The optimisation yields closely matching event rates between measurement and

simulation, as well as strong agreement between the estimated parameters  $\tau_{np}$ . We attribute the event overestimation to simplifying assumptions in the Geant4 model. In particular, the model excludes the syringe needle used to hold the point source (see Figure 2) which absorbs emissions in a significant solid angle about the source.

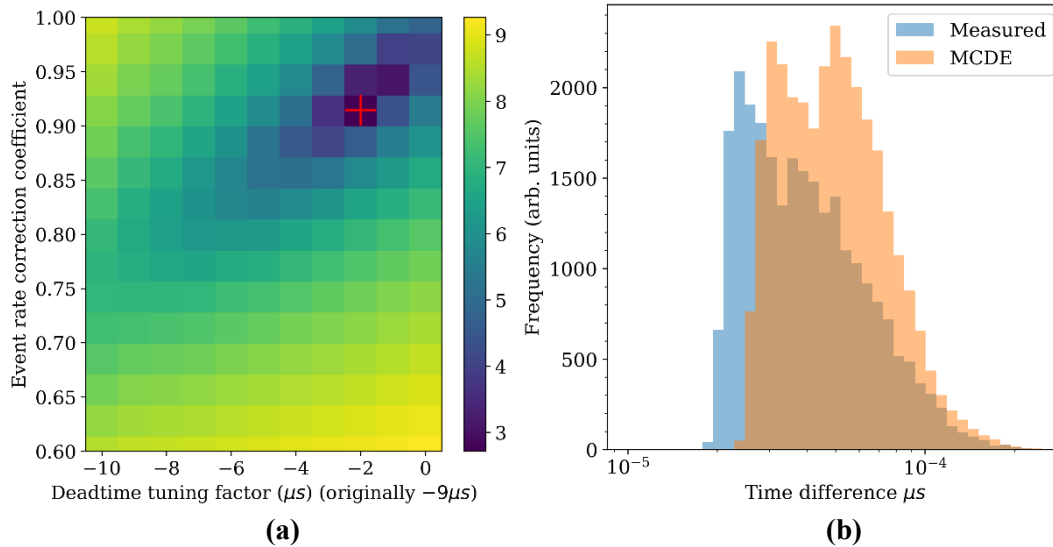


**Figure 4:** (a) Phase diagram of the logscaled weighted chi square value of the difference between the measured and simulated deadtime curves, as a function of the deadtime tuning factor and the event rate correction coefficient. The optimal parameters are a tuning factor of 2  $\mu\text{s}$  and correction coefficient of 0.914. (b) Time differences between subsequent events recorded by the true and optimised MCDE detectors.

In general, the optimisation is not fully explanatory. For example, the change in the deadtime tuning factor results in a mismatch of minimum time differences between the measured and simulated data (Figure 4b). Ongoing work aims to improve the objective function for optimisation, by including additional weighting to minimise deviations between the measured and simulated time difference distributions.

#### 4. Conclusion

The Monte Carlo Detector Effects (MCDE) model was adapted to the UCT Polaris Compton Camera and used to model the detector's deadtime characteristics when exposed to a  $^{68}\text{Ga}$  point source. The unoptimised MCDE model correctly predicts that the Polaris detector is nonparalysable, but overestimates the experimental event rate. A brute force optimization indicates that discrepancies result from event rate overestimation in the initial Geant4 model, as well as biased per-event deadtime during detector timing and readout. The optimised MCDE model closely agrees with an idealised nonparalysable deadtime model fit to the original data. The MCDE model can be further optimized for use in investigating positron sources.

#### References

- [1] Polf J C and Parodi K 2015 *Phys. Today* **68** 28–33
- [2] He Z, Li W, Knoll G F, Wehe D K, Berry J and Stahle C M 1999 *Nuclear Instruments and Methods in Physics Research A* **422** 173–178
- [3] Polf J C, Avery S, Mackin D S and Beddar S 2015 *Phys. Med. Biol.* **60** 7085

- 
- [4] Hueso-Gonzalez F, Pausch G, Petzoldt J, Römer K E and Enhardt W 2017 *IEEE Trans. Radiat. Plasma Med. Sci.* **1** 76–86
- [5] Maggi P, Peterson S, Panthi R, Mackin D, Yang H, He Z, Beddar S and Polf J 2020 *Phys. Med. Biol.* **65** 125004
- [6] Hyslop N, Peterson S and Leadbeater T W 2021 Sub-Millimetre Positron-Emission Particle Tracking Using a CdZnTe Semiconductor Array *UCT Dept. of Physics* 11-54
- [7] Knoll G F 2010 *Radiation Detection and Measurement Wiley* 121–128
- [8] Leadbeater T W 2009 The Development of Positron Imaging Systems for Applications in Industrial Process Tomography, *The University of Birmingham Positron Imaging Centre* 145-149

# Setting up an environment that continuously analyse The ATLAS Tile Calorimeter temperature data

Lungisani S Phakathi<sup>1</sup>, Sanele S Gumede<sup>1</sup>, Betty Kibirige<sup>1</sup>, Juraj Smieško<sup>2</sup> and Filipe Martins<sup>3</sup>

<sup>1</sup>Department of Physics and Engeneering, University of Zululand, kwaDlangezwa campus, kwaZulu Natal, South Africa.

<sup>2</sup>Faculty of Mathematics and Physics, Institute of Particle and Nuclear Physics, Charles University

<sup>3</sup>Laboratório de Instrumentação e Física Experimental de Partículas

E-mail: lungisani.sipho.phakathi@cern.ch

**Abstract.** The purpose of the work is having a stable and flexible environment of web interface, to reach that a well set environment that is invaluable for Tile-in-One (TiO). TiO is a plugin-based approach for evaluating the accuracy of the data and conditions for ATLAS Tile Calorimeters (TileCal). The TiO is a collection of small sized independent web tools called plugins, designed to make it easier for a user to evaluate TileCal data. The TiO platform intends to combine many TileCal web applications into a single standard services and data because outdated interfaces are becoming more difficult to maintain. The TiO web platform should allow large flexibility and ease of maintenance so that it would be friendly to the plugin developers as well. An environment was set up such that it may query the Data Control System (DCS) for temperature data using a special interface called DCS Data Viewer (DDV). The following technique is being used to create a new environment based on the ability to query those data: CentOS 8 was installed inside the virtual box to easily access CERN internal network. This strategy ensures that the DDV tool is effectively used to query the Tile DCS temperature data which is subsequently converted into a format appropriate for the visualizing library. The visualization tool allows user to interact with the plots. Currently the set-up is done for easy access to the network and since this is on the development a status of a drawer is shown. The focus is having stable environment and concentrated on finding an intuitive way to display not only the status of one particular module, but the whole detector as well.

## 1. Introduction

The European Organisation for Nuclear Research (CERN) [1], based in France and Switzerland is Europe's foremost particle physics laboratory. The Large Hadron Collider (LHC) [2] is the world's most powerful particle accelerator, providing high energy proton-proton (p-p) collisions at an energy of 13.6 TeV situated at CERN. The LHC tunnel is located in the French-Swiss border at an average depth of approximately 100 underground and with 27 km in circumference. The paper is focused on finding the solid and flexible environment of web interface that will continuously analyse the temperature of Hadronic Tile Calorimeter (TileCal) sub-detector of the ATLAS experiment. Figures 1 and Figure 2 shows the ATLAS detector and TileCal respectively.

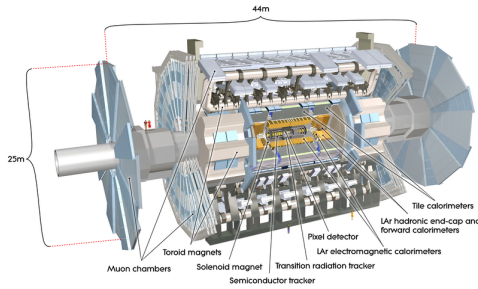


**Figure 1:** ATLAS detector showing all sub-detectors with TileCal in grey colour.

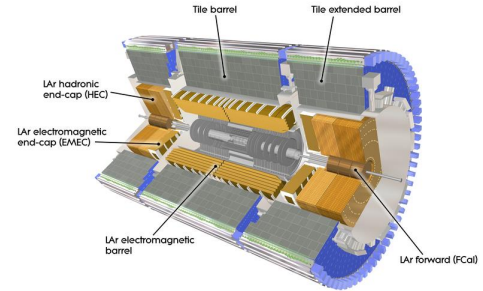


**Figure 2:** ATLAS Tile Calorimeter in conjunction with sub-detectors it surrounds.

The ATLAS [3] detector has numerous sub-detectors arranged in layers that investigate a variety of physics, such as the Higgs boson, additional dimensions, dark matter, and many others. TileCal [3, 4] is the hadronic calorimeter that used to detect hadrons, taus, jets, reconstruction of muons and any missing transverse energy created during the period of collisions. TileCal is a sampling calorimeter that uses steel plates as the absorber and scintillating tiles as the active material. After light is produced in the calorimeter, two Photomultiplier Tubes (PMTs) in the TileCal front-end electronics receive information via Wave Length Shifting Fibers (WLS) [4]. The ATLAS detector is divided into three sections: two extended barrels (EBs) and a long central barrel (LB). For operating purposes, the LB is divided into two divisions, each of which is composed of 64 modules. Each module has its own Front End (FE) electronics, which are used exclusively for data acquisition within the super drawers [5]. Detector Control System (DCS) [6] is responsible for the operation of the detector infrastructure (tracking the low voltage, high voltage, front-end electronics cooling system, and back-end crates in a variety of applications). The TileCal DCS keeps track of the temperature of the front-end electronics with temperature sensors at several locations such as power supplies and monitoring boards. The crucial key monitored by TileCal DCS is the High Voltage applied to each PMTs typically in the range of 650-700 V [7]. According with equation 1, it is very crucial to monitor the temperature in the TileCal, since along with the applied high voltage is one of the parameters which can affect the gain of the PMTs.

$$\frac{\Delta G}{G} = \frac{HV^\alpha(t)}{HV^\alpha(t_r)} \quad (1)$$

The  $HV$  variation over the same period determines the relationship between the relative PMT gain variation  $G$  between a reference time  $t_r$  and a time of interest  $t$ , where the parameter  $\alpha$  is obtained experimentally for each PMT [8]. The temperature of TileCal PMTs have to be monitored, because channel in turn affects the physical variables that is being measured. The purpose of the current study is to have a stable and flexible environment of web interface that will continuously study the variation of the temperature in the drawers of the module over a short period of time, eg few weeks. The work aims to extract, monitor, and finally visualize temperature data for stability in the drawers using the solid tool called Tile-in-One (TiO). The TiO is a collection of small-sized independent web tools called plugins, designed to make it easier for a user to evaluate TileCal data.

## 2. Tile-in-One software

The different group of ATLAS collaborators created several web tools for TileCal data quality by using a variety of technologies and data sources [9]. The use of various technologies, the requirement for specific data recovery techniques, and the poorly unified documentation were drawbacks of those technologies. Several tools were independently created during the development of the TiO program without adhering to a set structure. In order to complete a certain work, collaborators must search through a variety of unique tools, databases, and software, which increases the likelihood of errors and adds time to the process. Plugin based system for assessing the quality of data and conditions for ATLAS TileCal is known as the TiO [10]. TiO is a collection of small sized independent web tools called plugins. As older interfaces become obsolete and become more difficult to maintain, TiO platform intends to combine many TileCal web tools into a single, shared platform that will share the same processing infrastructure and provide access to shared services and data [11].

### 2.1. Tile-in-One architecture

TiO is designed to be flexible and simple to maintain. The goal of this design was to create a user-friendly web platform that could still be flexible enough to collect data from different data sources. Figure 3 shows the architecture of the TiO.

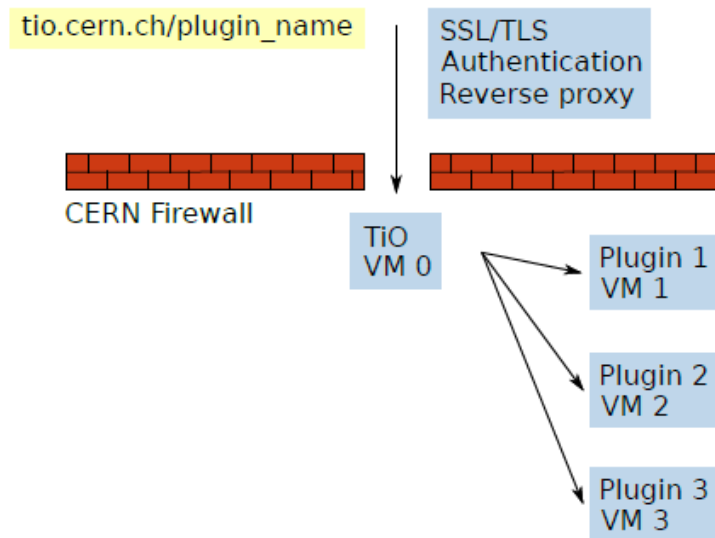


**Figure 3.** The architecture of the TiO web platform.

The web platform is built around a single primary server (TiO/VM0), which is located at `https://tio.cern.ch` and is in charge of routing user requests and responses, authenticating users using the `oauth2proxy` [12], and controlling the secure connection to the web platform. To act as a reverse proxy for each individual plugin so that each plugin runs its own Virtual Machine (VM), the main server runs the `Nginx` server [13]. The VM that operates the primary server is hosted by CERN's `OpenStack`, which serves to enable a specific VM to run its own software for that specific plugin. Multiple pages are handled via the server-side `Bottle` [14] framework and the client-side `Bootstrap` [15] framework, while `uWSGI` [16] is the underlying infrastructure that serves the pages. `Bottle` framework and `Bootstrap` are the two main technologies that describe the design of the TiO.

## 2.2. Template for Plugins

The "Plugin Template" acts as a general template to aid in the creation of new plugins. The developers of the plugin are introduced to Full Stack, meaning they are responsible for the creation of both the web server and the usual web application's web page, as well as other related tasks. The plugin loads data from a csv or JSON file on the server side and generates responses to user requests. The responses could be of several types, most crucial are two:

- The static file response, where the server sends whole files to the client.
- Dynamic response through template, here server dynamically generates web page.

The TiO platform currently has twenty two plugins, of which are run by various CERN network users and two of which have been deprecated. Table 1 displays every finished and maintained plugins.

**Table 1:** All current active plugins

### List of Plugins

#### Active Plugins

Plugin	Current Maintainer	Machine	Git Repository
<a href="#">Monitoring</a>	Juraj Smiesko	<a href="#">tio</a>	<a href="#">tio-config</a>
<a href="#">DQM3</a>	Michal Dubovsky	<a href="#">tio-0002</a>	<a href="#">tio-0002</a>
<a href="#">DQ Validation</a>	Barbora Eckerova	<a href="#">tio-0003</a>	<a href="#">tio-0003</a>
<a href="#">Documentation</a>	Juraj Smiesko	<a href="#">tio-0004</a>	<a href="#">tio-0004</a>
<a href="#">Tile Powercycling</a>	Michal Dubovsky	<a href="#">tio-0005</a>	<a href="#">tio-0005</a>
<a href="#">Plugin Template</a>	Juraj Smiesko	<a href="#">tio-0006</a>	<a href="#">tio-0006</a>
<a href="#">Sample Noise Calibration</a>	(Karl Filip Backman)	<a href="#">tio-0007</a>	<a href="#">tio-0007</a>
<a href="#">Run List</a>	Juraj Smiesko	<a href="#">tio-0008</a>	<a href="#">tio-0008</a>
<a href="#">Read Calibration</a>	Sanya Solodkov	<a href="#">tio-0010</a>	<a href="#">tio-0010</a>
<a href="#">Tile Conditions Web Server Selection</a>	Elliot Parrish	<a href="#">tio-0011</a>	<a href="#">tio-0011</a>
<a href="#">CIS Constant History</a>	(Juraj Smiesko)	<a href="#">tio-0012</a>	<a href="#">tio-0012</a>
<a href="#">Laser Monitoring</a>	(Juraj Smiesko)	<a href="#">tio-0013</a>	<a href="#">tio-0013</a>
<a href="#">TileCal Maintenance Summary</a>	Danijela Bogavac	<a href="#">tio-0014</a>	<a href="#">tio-0014</a>
<a href="#">DQ History</a>	Daniel Scheirich	<a href="#">tio-0015</a>	<a href="#">tio-0015</a>
<a href="#">Detector Plugin</a>	Betty Kibirige	<a href="#">tio-0016</a>	<a href="#">tio-0016</a>
<a href="#">DQ Notes</a>	Juraj Smiesko	<a href="#">tio-0017</a>	<a href="#">tio-0017</a>
<a href="#">Calibration Runs Analysis</a>	Daniel Suchy	<a href="#">tio-0018</a>	<a href="#">tio-0018</a>
<a href="#">Calibration Runs Summary</a>	Daniel Suchy	<a href="#">tio-0019</a>	<a href="#">tio-0019</a>
<a href="#">Tile L1Calo Issue Tracker</a>	Danijela Bogavac	<a href="#">tio-0020</a>	<a href="#">tio-0020</a>
<a href="#">HVAnaMon plugin</a>	Sebastien Binet	<a href="#">tio-0021</a>	<a href="#">tio-0021</a>
<a href="#">TileDAQmon Plugin</a>	Sebastien Binet	<a href="#">tio-0022</a>	<a href="#">tio-0022</a>

#### Deprecated Plugins

Plugin	Last Maintainer	Plugin Type	Machine	Git Repository
Simple Static Plugin Template	Sofia Hyrych	TiO Plugin	<a href="#">tio-0001</a>	<a href="#">tio-0001</a>
DQ History	Sofia Hyrych	TiO Plugin	<a href="#">tio-0009</a>	<a href="#">tio-0009</a>

The plugin makes use of a program named Monitorix [17], which keeps track of the plugin and provides information on the network and virtual machine status. The work is based on Detector plugin (tio-0016), which involve monitoring of temperatures in the TileCal.

### 3. Setting up temperature plugin

An overall work after having a solid and flexible web interface aims to study the variation of the temperature in the drawers of the module over a short time measured using the web platform called TiO, display them to a user in a friendly and intuitive manner using contemporary web technologies and carry out a comparative analysis of temperature data to establish useful patterns for the prediction of the state of the cooling system. To have a stable temperature monitoring plugin, above mentioned technologies and plugin template must be applied. The development of a solid and stable temperature plugin and how it uses various technologies is demonstrated in the following points:

- Installation of virtual Box that will run as local host.
- Installation of the CentOs 8 inside the virtual box for ease access to CERN network.
- The DDV tool is used to query the Tile DCS temperature data.
- Plotly library is used for graphical.
- All the source code is stored in a Git repository

The objective of having a stable and flexible temperature plugin is:

- To develop a temperature plugin (software) tool for easy access to the DCS temperature data from the Oracle databases using DCS Data Viewer (DDV) queries.
- To visualize temperature data in a plugin using browsable interface and interactive plotting library over user defined time period, for example, the time of the run.
- To analyse the temperature data using temperature plugin tool in the drawers by comparing the historical data for checking with the previous periods, for example, of last 24 hrs.
- To display the trends of temperature for individual drawers with the option to show data, for example, for last 24 hrs period. Other periods of time might also be considered.

### 4. Temperature plugin's preliminary results

Preliminary results show the successfulness of querying the Tile DCS temperature data collected from Oracle database using DDV tool. DDV server eases the retrieval of the DCS historical data. HTTP requests are made to the DDV server directly for any temperature probe in a drawer of the module to be visualised and analysed. Figure 4 shows the version of a set temperature plugin on the user side. The user can visualise TileCal temperature data using interactive plotting library such as: capturing data at a point where the cursor is placed, zooming in and out of the plots, downloading .png file for use in reports and many more. Temperature varies in each drawer, each drawer is stable on a different temperature than the other. The graph shows that the temperature at some point increases, decreases and be stable resulting in affecting the gain of the PMTs. The gist of the work is to flag those issues, during the ATLAS experiment. The temperature must be stable over the time period to not affect the data collected. The developed interface is currently flexible.

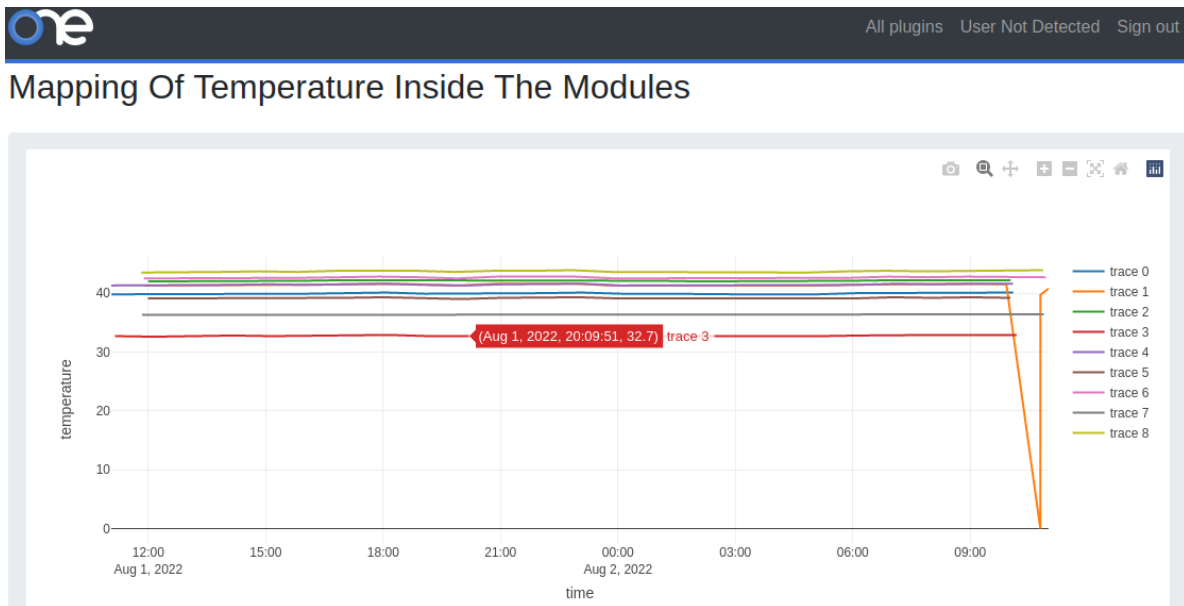


**Figure 4.** Preliminary result of the temperature mapping in the drawers taken in the last 24 hours.

## 5. Summary

The interface is well advance in a way that it can send python requests to the server and archive them in the local host for better visualisation and analysis of temperature. Interface will play a vital role in periodically collecting lot of data for every drawer in a short space of time. Finally, work will study the stability of the temperature and detect issues in the drawers as the temperature is tempered. The quality of the data will be improved.

## References

- [1] Giovanni Calderin et al, “Modelling CO2 cooling of the ATLAS ITk Pixel Detector,” page 1–2, 2019
- [2] F Martins, “The ATLAS Tile Calorimeter DCS for Run 2,” ATL-TILECAL-PROC-2016-001, page 1–3
- [3] Yuri Smirnov and Juraj Smiesko, “Tile-in-One: An integrated system for data quality and conditions assessment for the ATLAS Tile Calorimeter,” ATL-TILECAL-SLIDE-2019-829
- [4] Tile Calorimeter Technical Design Report, CERN/LHCC/9642
- [5] ATLAS Collaboration, “The ATLAS Experiment at the CERN Large Hadron Collider,” Journal of Instrumentation, vol. 3, no. 08, pp. S08003-S08003, 2008
- [6] S. Schlenker, S. Arfaoui, S. Franz, et al., “The ATLAS Detector Control System,” in Proceedings of ICALEPCS, 2011, page. 5–8.
- [7] The ATLAS Collaboration, “Operation and performance of the ATLAS Tile Calorimeter in Run 1,” The European Physics Journal C78 (2018), page. 25
- [8] The ATLAS Collaboration, “Readiness of the ATLAS Tile Calorimeter for LHC collisions,” The European Physics Journal C (2010), pp. 1209
- [9] Yuri Smirnov and Juraj Smiesko, “Tile-in-One: an integrated system for data quality and condition assessment for the ATLAS Tile Calorimeter,” EPJ Web of Conferences 245, page 2-5, 01010 (2020)
- [10] Tile Calorimeter Technical Design Report, CERN/LHCC/9642
- [11] Juraj Smiesko, “An integrated system for data quality and conditions assessment for the ATLAS Tile Calorimeter,” EPJ Web of Conferences 214, pp 2-3, 01030 (2019)
- [12] OAuth2proxy, [https://github.com/bitly/oauth2\\_proxy/](https://github.com/bitly/oauth2_proxy/) (2014), accessed: 2022-08-25
- [13] Nginx, <https://nginx.org/> (2004), accessed: 2022-08-25
- [14] Bottle framework, <https://bottlepy.org/docs/dev/> (2021), accessed: 2022-08-25
- [15] Bootstrap, <https://getbootstrap.com/> (2021), accessed: 2022-08-25.
- [16] uWSGI, <https://uwsgi-docs.readthedocs.io/> (2020), accessed: 2022-08-25.
- [17] J. Sanfeliu, Monitorix (2022), <https://www.monitorix.org/> [last accessed 2022-03-04]

# A modified Zinc oxide gas sensor approach to detect oxidizing gases

**Lungisani S Phakathi, Sanele S Gumede and Betty Kibirige**

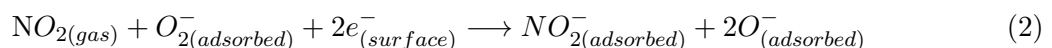
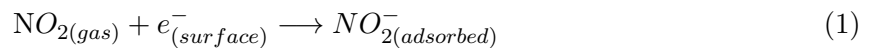
Department of Physics and Engeneering, University of Zululand, kwaDlangezwa campus, kwaZulu natal, South Africa.

E-mail: lungisani.sipho.phakathi@cern.ch

**Abstract.** Selective detection of gases such as nitrogen dioxide ( $NO_2$ ), carbon monoxide (CO), carbon dioxide ( $CO_2$ ), and various volatile organic components is necessary for air quality monitoring and safety. There are several metal oxide gas sensor (MOGS), but the focus of this study was Zinc Oxide (ZnO); an n-type MOGS.  $NO_2$ , an oxidising gas was the target gas. The aim of this study was to establish the possible enhancement of a gas sensor selectivity by the introduction of signal conditioning electronics circuitry such as the Wheatstone bridge in tandem with an operation amplifier circuit. Exposing electronics enhanced ZnO MOGS system to  $NO_2$  resulted in a increasing negative voltage output between 0 and  $-3.5 V$ . This range of voltages is sufficient to run a micro-controller, with the assumption that a reducing gas would result in a positively increasing voltage, a micro-controller could be conditioned to select between an oxidising and a reducing gas.

## 1. Introduction

When a Metal Oxide Gas Sensor (MOGS) is exposed to gaseous chemicals, its resistivity changes with concentration of the gas. ZnO is an n-type MOSG with a band gap of  $3.37 eV$  and that allows for it to work under chemoresistance principle.  $NO_2$  is an oxidising gas of interest. When ZnO is exposed to  $NO_2$  gas, the following chemical reactions take place:



This shows that electrons are taken away from the surface that leads to an increased resistance of the ZnO MOGS. On the other hand, when a reducing gas is introduced to the surface of the ZnO gas sensor, electrons are introduced in the conduction band of ZnO, reducing the resistance of ZnO [1]. For this study, a Wheatstone bridge was designed and introduced to balance with no gas present. The Wheatstone bridge is sensitive to small resistance changes. Thus by using a Wheatstone bridge, changes in resistance of the MOGS due to the gaseous environment can be

easily measured quantitatively. The Wheatstone bridge Equation in (3) was captured in excel to allow comparison between simulated and theoretical results.

$$V_{out} = \left( \frac{1}{1 + \frac{R_2}{R_1}} - \frac{1}{1 + \frac{R_3}{R_4}} \right) \quad (3)$$

A gas sensor is a device which receives a chemical signal and responds by converting it into an electrical signal. A gas sensor is a mandatory tool that is used to identify a specific task assigned to it [1]. In this experiment, the gas sensor was a semiconductor (ZnO) device that would be used to sense toxic gases in industries and general working environments. The aim was not to measure the resistance of the gas sensor in the presence of the targeted gas, but rather measure the output voltage of the gas sensing system.

### 1.1. Zinc Oxide as a gas sensor

Over the past decade, scientists have made important improvements in the quality of ZnO as an electronic material in its own right. The detection of a specific gas is enabled by using semiconductor sensors that are selective to particular chemical species [2]. The existing sensors that have been produced give a response to a mixture of gases. This means that such sensors are not selective enough to a specific chemical species. In order to solve this problem, an array of sensors which are able to simultaneously detect different gaseous chemical species was introduced. This arrangement made it possible to sense a variety of gaseous chemical species by giving the correlation among a large number of sensor outputs [3].

ZnO is a kind of material that is widely used in electronic and opto-electronic applications because of its abundance, non-toxicity and low costs [4]. ZnO is a well-known material that is a II-VI compound semiconductor with a wide band gap energy of 3.37 eV [5]. The response of the ZnO gas sensor towards some targeted gases may be upgraded by doping, reducing grain size or changing the temperature and humidity [6]. The crucial characteristic that manufacturers need in a gas sensor is for it to be selective with respect to the type of the targeted gas that is oxidizing or reducing [7].

The metal oxide gas sensor works on a chemoresistance principle. When the gas molecules interact with a metal oxide surface, it acts as either an acceptor or donor. The resistivity or electrical conductivity of a metal oxide thin film changes as it interacts with the target gas. The resistivity of the metal oxide semiconducting thin film depends on the majority carrier in the film. This happens if it is oxidized or reduced at ambient temperature [8]. The gas molecules undergo Reduction-Oxidation (REDOX) reactions. A surface adsorption site ensures correct interaction of gas molecules with the material. The adsorption can be observed by tempering with temperature. Below 200 °C, oxygen can accept one electron and above it can accept two, as shown by Equations (4) and (5) [9]. In the case of a n-type sensor, the surface gets depleted with electrons by presence of any other ions such as oxygen and upon exposure to a target gas ( $NO_2$ ), these species reacts with the gas molecules to reverse back electron to the conduction band of the surface, resulting in decreasing conductivity [10].



### 1.2. Synthesis of ZnO MOGS thin films

There are many methods used to deposit ZnO for different applications. The chemical bath method is the preferred method because it is simple to follow, requires low temperatures and

low cost of deposition equipment. Chemical bathing [11] is a technique for depositing thin films and nanomaterials over a large surface area. In this paper, thin films of ZnO have been deposited on a silica glass substrate using the chemical bath method. Before introducing it into the gas sensing environment, two aspects were investigated: the chemical composition and the morphology of the film, as well as the energy band gap.

### 1.3. Description of existing gas chamber

The gas testing chamber can endure extremely high temperatures [12]. The temperature was varied in order to establish its effect on the sensitivity of the sensor to the test gas. The test chamber made from brass has a transparent lid to allow for easy visual monitoring of all connections [12].

The gas testing chamber is equipped with a heating stage that is capable of heating the sample to a desired temperature, which varied between 100-400 °C[12]. The heating is with six 33 kΩ resistors with a power rating of 10W and a thermocouple to measure the temperature of the stage. The stage temperature is controlled by adjusting the supply voltage from a power supply [12].

It has two inlet pipes for the introduction of gases, that is the test gas and the flushing gas. It has one pipe outlet that removes the gas from the chamber. The outlet pipe is immersed into water to reduce possibilities of explosion [12].

The stage is made to accommodate the sample for its gas sensing testing. A sample was placed on the substrate that has silver contact with a copper wire connected to a Tru-RMS multi-meter used to measure the test gas effect on the resistance of the samples [12].

### 1.4. Proposed concept

The objective of this study is to modify an existing ZnO gas chamber sensing device [12]. An output voltage in a range of 0 to 5 V is required to run a micro-controller that monitors the test gas as it is introduced in the gas sensing device [14].

### 1.5. The Wheatstone bridge circuit

The Wheatstone bridge circuit diagram is shown below. The Wheatstone bridge [13] was

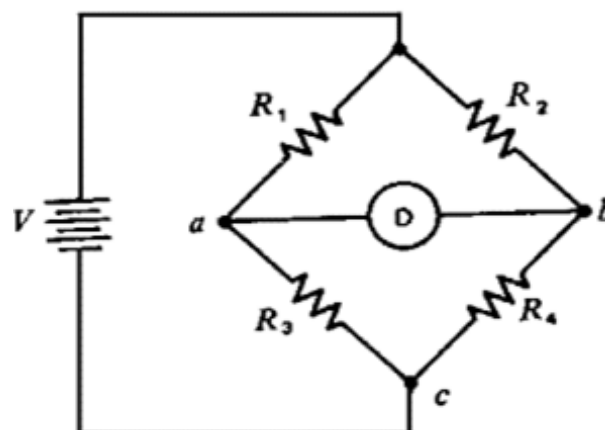


**Figure 1.** The Wheatstone bridge circuit

designed to balance using the gas sensor resistance reading obtained when it is in the air environment. The purpose of using Wheatstone bridge, was to convert the changing in sensor resistance into a changing output voltage of the whole simulation [14]. To monitor the gas inside

and outside of the chamber, two gas sensors are used and placed at the  $R_1$  and  $R_4$ , as in Figure 1. This serves as the normalising resistance and at this resistance value, the output voltage of the bridge is zero. For an oxidising gas, the ZnO gas sensor resistance is at a maximum when it is exposed to air. The resistance decreases to a steady state minimum when an oxidising gas is introduced.

## 2. Design and simulation using PSpice

The Personal Simulation program with integrated circuit emphasis (PSpice) allows a user to capture a circuit diagram, simulate and analyse possible outcomes of the circuit. It has the power to calculate complex node voltages and branch currents across the captured design, allowing a user to generate relevant data for further analysis. The connection is done in port a and b as shown by Figure 1 of the Wheatstone bridge and the circuit with an Operation Amplifier (OpAmp) which amplifies measured voltage is shown in Figure 2 was captured in PSpice. The

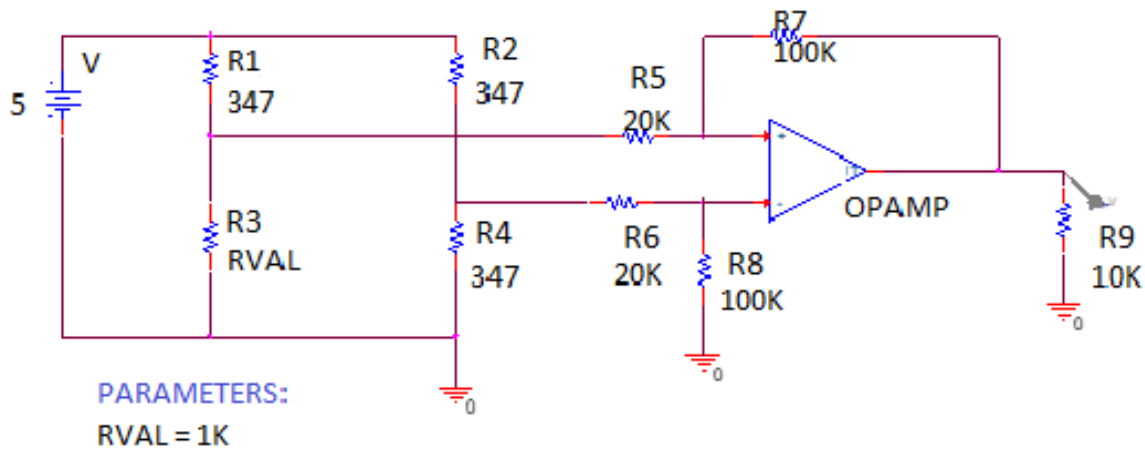


**Figure 2.** The schematic diagram of proposed concept in PSpice.

OpAmp at the output port of the Wheatstone bridge measures the output voltage from the bridge and amplify it to a voltage suitable for micro-controllers [14]. The Wheatstone bridge was designed to be in balance when the gas sensor is not exposed to the target gas. Resistor  $R_1$  and  $R_3$  represent the sensor resistance in air and in a gas chamber, respectively. Resistor  $R_2$  and  $R_4$  acts as a normalising gas sensor, chosen to be equal to  $R_1$  in contemplation of giving zero output voltage when there is no gas present in the chamber. In the circuitry of Figure 2, the ratio  $\frac{R_7}{R_5}$  or  $\frac{R_8}{R_6}$  determines the amplification factor of the amplifier.

$$V_{out_{OpAmp}} = V_{out} \left( \frac{R_7}{R_5} \right) \quad (6)$$

### 2.1. Sensor resistance and the balancing of the Wheatstone bridge

Using the results presented by Shichi Seto et al. [7] on the Mathematical modelling of a semiconductor gas sensor, the change in gas sensing resistance was used to test the proposed concept. At 350 °C, the variable resistor (RVAL), that represented the sensor, was varied between 625 and 347  $\Omega$  in steps of 5  $\Omega$  in the absence and presence of the targeted gas respectively.

### 3. Results and discussion

Figure 3 shows an Excel comparison of the voltage results obtained from the PSpice simulations across the output resistance R9 in Figure 2 and those obtained theoretically using mathematical models of Equation 6.

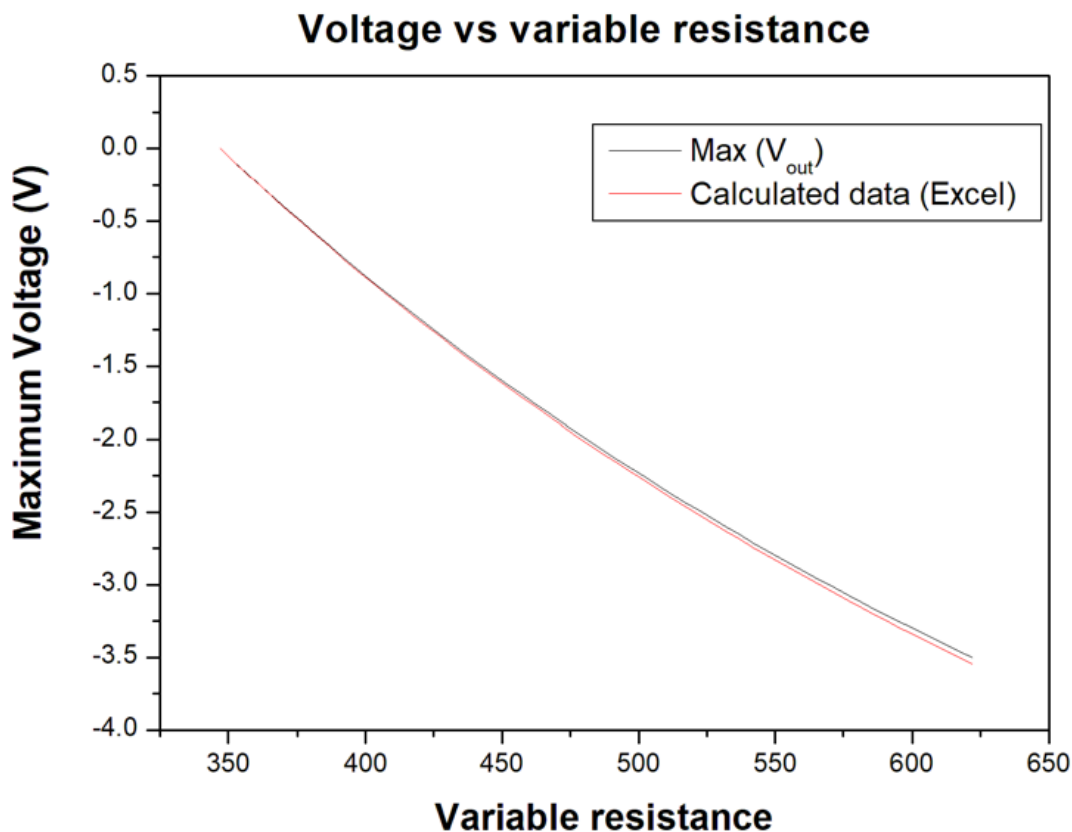


**Figure 3.** Readings of the maximum output voltage in the variable resistor as influenced by oxidizing gas. The graph shows the negative increase as the  $NO_2$  gas enters the chamber.

The graph shows a negative increase of voltage as the gas enters the chamber. The response (variable resistance) vs (maximum voltage) demonstrate that the oxidizing gas increases the resistivity of ZnO, resulting in reducing the output voltage of the system. Results in Figure 3 is in accordance with the proposed solution of the micro-controller as it operate in the range between 0 to 5 V. The output voltage magnitude lies in the range: 0.0 to -3.5 V and that means it is sufficient enough as an input to a micro-controller to function. The introduction of Wheatstone bridge shows the stability in measuring the small change in resistance as the gas enters the chamber. The overlapping of the two curves all the way through the same path, clarifies that the simulated results using the PSpice environment agree well with the calculated results. As mentioned in the introduction, when a reducing gas is introduced to the surface of the ZnO gas sensor, electrons are introduced in the conduction band of ZnO. Therefore, the assumption for the presence of a reducing gas would be a graph showing a positive increase in voltage as the gas enters the chamber.

#### 4. Conclusion

The designed circuit was successful in providing the required voltage that can be used as input to the micro-controller, that requires a voltage between 0.0 and -3.5 V. Results show the correlation with theory of an oxidizing gas leading to a negative output voltage from the ZnO sensor for an oxidizing gas. Results from simulated circuit in PSpice agree with the result from calculated result. This range of voltages is sufficient to run a micro-controller, with the assumption that a reducing gas would result in a positively increasing voltage, a micro-controller could be conditioned to select between an oxidising and a reducing gas.

#### Acknowledgments

Mr Mkwae and Gumede for valuable discussions. This work was supported by the NRF and the Research Committee of the University of Zululand.

#### References

- [1] Sureshkumar N and Dutta A 2020 Environment gas sensors based on nanostructured thin films pp 1–3
- [2] Nakamoto N, Oyabu T and Kimusa H 2001 *5th int. Conf. on engineering design and automation (EDA, las vegas)* **525** p 1110
- [3] Ohashi N et al 1998 *Bonding of Zinc Oxide crystals doped with transition metal ions, Extended abstract of 59th meeting university* p 228
- [4] Mondal S, Bhattacharyya S R and Mitray P 2013 *int. Conf. effect of Al doping on microstructure and optical band gap of ZnO thin film synthesized by successive ion layer adsorption and reaction* vol 80(2) (Pramana J physics) p 315
- [5] Hassan N K and Hashim M R 2013 *structural and properties of ZnO thin film prepared by oxidation of Zn metal powders sains Maysial*, vol 42(2), p 193
- [6] Shankar P and Rayappan J B B 2014 *gas sensing mechanism of metal oxides; the role of ambient atmosphere, type of semiconductor and gases*, p 1
- [7] Shichi Seto et al, 2006 *Mathematical model of semiconductor gas sensor, Sensors and Materials*, Vol 18(1) (MYU Tokyo) pp 1–16
- [8] Yuan W, Liu A, Huang L, Li C and Shi G 2013 *High-performance NO<sub>2</sub> sensors based on chemically modified graphene (Advanced Materials)* vol 25, pp 766–71
- [9] Arafat M M, Dinan B, Akbar S A and Haseeb A S 2012 *Gas sensors based on one dimensional nanostructured metal-oxides (A review) Sensors*. vol 12(6) pp 7207–58
- [10] Sharma S and Madou M 2012 *A new approach to gas sensing with nanotechnology (Philosophical Transactions of the Royal Society A: Mathematical, Physical and Engineering Sciences)* vol 370(1967) page 2448–73
- [11] Nkrumah IN et al 2013 *synthesis and characterization of ZnO thin films deposited by chemical bath technique, int. Engineering and technology* **18** pp 809-810
- [12] Ngqondo ST 2008 *Hydrothermally grown Pb<sup>2+</sup> doped ZnO nanorods for hydrogen and acetylene gas sensing, (Department of physics in University of Zululand)* p 40
- [13] Vordos N, Gkika DA and Bandekas DV, 2020 *Wheatstone bridge and Bio-engineering, (Department of Physics, International Hellenic University Journal of Engineering Science and Technology Review*, p 4–6
- [14] Illyaskutty N et al 2018 *Miniaturized Single Chip Arrangement of a Wheatstone Bridge Based Calorimetric Gas Sensor (Institute for Sensor and Information Systems (ISIS), Karlsruhe University of Applied Sciences)*, p 3–5

# MicroPEPT: A step towards hybrid PEPT detectors

**R van der Merwe\***, S Peterson, A Buffler, M van Heerden, A McKnight and T Leadbeater

Department of Physics, University of Cape Town, South Africa

E-mail: \* VMRR0B003@myuct.ac.za

**Abstract.** Positron Emission Particle Tracking (PEPT) measures the trajectory of a freely moving radioactive tracer particle, and enables the non-invasive study of dynamic systems from engineering to medicine. PEPT performance is limited by the activity achievable in radiolabelling a suitable tracer particle, and the fixed geometry of conventional detector systems. In investigating phenomena on micro-scales, recent development of advanced instrumentation has been required to offset these limitations. A modular bismuth germanate oxide (BGO) scintillator array, with detection modules derived from CTI/Siemens PET scanners, has been constructed and coupled to a recently developed data acquisition system. This array consists of 1024 detector elements (512 pixels of 6.75 x 6.25 x 30 mm and 512 pixels of 4.1 x 4.0 x 30 mm) giving a field of view of 150 mm x 196 mm x 101 mm. Energy and timing resolutions of this system were determined and sensitivity profiles were modelled numerically, informing on optimal system parameters to enable future characterisation of the detector efficiency, spatial resolution and deadtime parameters. These initial results indicate the applicability of modular BGO scintillator arrays in addressing small scale flow phenomena, and lead the direction of future work in combining the BGO system with a pair of high resolution pixelated semiconductor detectors for the first time.

## 1. Introduction

The Positron Emission Particle Tracking (PEPT) technique can be used to non-invasively study dynamic systems, with applications in fields from engineering to medicine [1, 2, 3]. By radiolabeling a suitable tracer particle, tracking can be performed to high spatial and temporal resolution over an extended time, from which the trajectory of the tracer can be determined with an associated uncertainty. Recently, a need to examine more challenging systems on the micro-scale has arisen with PEPT applications in the study of micro-scale flows, such as the flows in biological systems and microfluidic devices, as well as potential applications in beam line tracking in proton radiotherapy [4]. However, PEPT performance of existing systems is limited by the absolute efficiencies of fixed geometries, compounded by low activity in radiolabeling suitable small tracer particles, leading to the requirement of advanced instrumentation development. Previous work with semiconductor detectors has demonstrated the feasibility of applying PEPT to micro-scale systems [4], but the achievable field-of-view (FOV) and location rates were limiting, promoting the benefits of development towards a hybrid detection system accounting for these limitations. In this paper, the development and characterization of a modular scintillator array designed to support a semiconductor detection system is performed, serving as a first step towards the development of hybrid detection systems optimised for micro-scale particle tracking.

## 2. The PEPT technique and spatial resolution

The PEPT technique makes use of proton rich radioisotopes to label a suitable tracer particle for the system of interest. Emitted positrons annihilate with free electrons to produce two approximately back-to-back 511 keV photons due to momentum conservation [5]. When these photons are detected in coincidence, a 3-dimensional line-of-response (LOR) is defined along which the annihilation event occurred. Through the measurement of many such LORs, the position of the tracer can be determined with an associated uncertainty.

However, not all recorded LORs arise from true coincidence events. Random coincidences can occur when a photon originating from another unassociated source is detected within the coincidence window forming one or both parts of a coincident pair. Similarly, scattered LORs occur when one or both coincident photons scattered in surrounding materials before being detected. To account for these issues, an iterative least-squares minimisation algorithm [1] is used to remove corrupt LORs, finding the most likely location of the tracer at a given time.

The spatial resolution of a PEPT system operating as described can be estimated with  $u(\bar{P}) = \frac{w}{\sqrt{T}}$  where  $u(\bar{P})$  is the 3-dimensional location uncertainty on a measured PEPT location  $\bar{P}$ ,  $w$  is the spatial resolution of the positron camera, and  $T$  is the true coincidence rate [6]. For micro-scale tracking, PEPT location uncertainty must be reduced, achieved by either reducing  $w$  or increasing  $T$ . Considering significant changes to tracer choice and production to be beyond the scope of this work, reducing  $w$  can be achieved by reducing the pixel size of the detection system, and improving its energy resolution. Increasing  $T$  can be achieved by increasing the data rate, by increasing either the activity of the tracer or by increasing the absolute efficiency of the detection system. Absolute efficiency is determined by the intrinsic efficiencies of the detector materials and the geometric efficiency of the whole system, assuming no deadtime.

Typical PEPT systems have fixed geometries and detector materials implying fixed efficiencies, energy resolution, and pixel sizes. Significant improvements to the spatial resolution of a PEPT system are achieved with the development of a new detection system optimising these properties for micro-scale measurement, with an emphasis on reduced pixel size and increased energy resolution. Typically however, energy resolution and pixel size improvement is accompanied with reduction in absolute efficiency. A modular detection system allowing adjustment of its geometry and therefore absolute efficiency is ideal, and the use of multiple detection systems with different materials and properties as a hybrid camera allows for the highest degree of optimisation.

## 3. Detector technologies

Noting the significant dependence of the PEPT spatial resolution on pixel size and energy resolution, semiconductor detectors typically offer the best performance. Previous work [4] has investigated the feasibility of the University of Cape Town (UCT) Polaris system [7], consisting of a pair of pixelated room-temperature cadmium zinc telluride (CZT) semiconductor crystals shown in figure 1, with promising results demonstrating sub-millimeter tracking of low activity tracer particles [4]. However, the absolute efficiency and timing resolution of the semiconductor system are both relatively low, negatively impacting the achievable coincidence rates, and hence location frequency. The achievable FOV dimensions of the system were limited by the small detector scale, preventing its use in applications requiring micron precision where system scales are on the order of centimeters. To improve on the FOV scale and location rates, it is natural to turn to larger scintillator detectors, offering improved absolute efficiencies and timing resolutions.

UCT has detector components from a Siemens ECAT 951 and EXACT HR++ PET scanners retired from clinical use, both comprised of detector blocks of bismuth germanate oxide (BGO) segmented into 8x8 scintillator crystals, shown in figure 1. The detector blocks from the HR++ camera are smaller than those from the 951, having pixel dimensions of  $4.1 \times 4.0 \times 30 \text{ mm}^3$  and  $6.75 \times 6.25 \times 30 \text{ mm}^3$  respectively, where the difference implies a trade-off between spatial

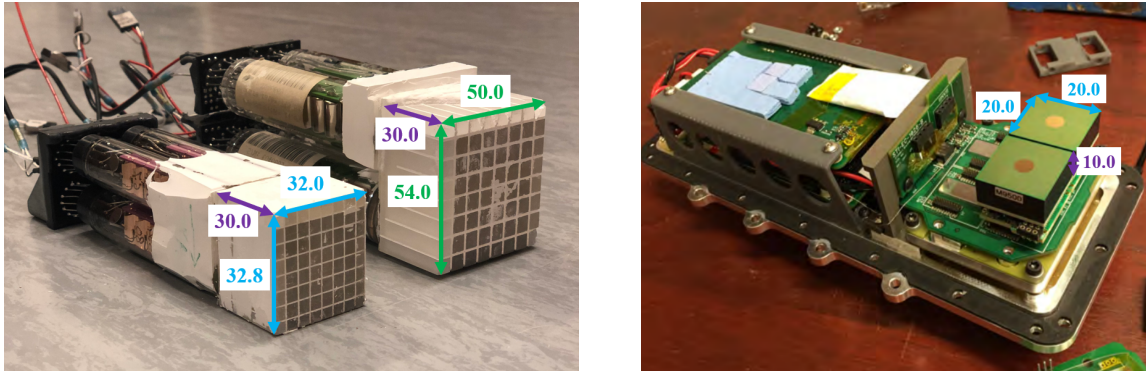


**Figure 1.** (Left) Detector blocks from the EXACT HR++ (left) and ECAT 951 (right) without protective casing. In each, four photomultiplier tubes and their 8x8 segmented crystals can be seen. (Right) The internals of the PolarisJ module, showing the two CZT crystals as the green squares on the right. All dimensions are given in mm.

resolution and absolute efficiency by virtue of their relative pixel densities and overall sizes.

Both of these detector types offer at minimum an intrinsic detection efficiency of 55% at 511 keV, whereas the Polaris system, with its much smaller pixels of  $1.8 \times 1.8 \times 0.5 \text{ mm}^3$ , offers only 15% detection efficiency. Through the development of a modular hybrid system, the trade-offs between all three detector types can be optimised for micro-scale tracking, achieving micro-scale location precision mostly through the use of the semiconductor system while maintaining useful location rates and larger volume FOV through the scintillators.

## 4. Detector characterisation

### 4.1. Energy resolution

Important elements of the PEPT detection system are the lower and upper level discriminators (LLD and ULD respectively), determining the allowed range of measured energy values describing a valid annihilation photon. Setting these limits accurately reduces noise by removing scattered events that are corrupt LORs. The energy resolution of the corresponding detector block is determined by measuring the width of the appropriate 511 keV photopeak. The energy resolution of a 951 detector block was determined in this paper, and similar calculations have been performed for both the HR++ blocks [8] and the Polaris system [4].

The four photomultiplier tubes (PMTs) from each detector block were connected to individual NIM pre-amplifiers and amplifiers, with the signal from each summed and digitised, using a multi-channel analyzer to produce pulse height spectra. However, since the detector PMTs do not provide uniform outputs due to manufacturing and component tolerances, a process of gain-matching was performed with photopeaks from each PMT aligned in pulse height by adjusting the gains of the separate amplifiers producing a single photopeak in the summed output.

Using three calibration sources, Na-22 (511 and 1275 keV), Cs-137 (662 keV) and Co-60 (1173 and 1332 keV)[9], an energy calibration was performed by Gaussian fitting to the appropriate photopeaks and relating them to their expected energies. Due to the poor energy resolution of the BGO crystals, the two independent photopeaks of the Co-60 source could not be separately identified as their Gaussian peaks overlapped. To account for this in the calibration, a single Gaussian was fit to the combined peak using a weighted mean centroid.

The fitting parameters of the 511 keV peak of Na-22 were determined from figure 2 and the energy resolution was calculated to be  $30.51 \pm 0.48\%$  at 511 keV. Repeating the process for the 1275 keV photopeak, an energy resolution of  $28.9 \pm 2.2\%$  was found. Using the computed energy resolution, the optimal lower and upper level discriminators were selected to be the centroid

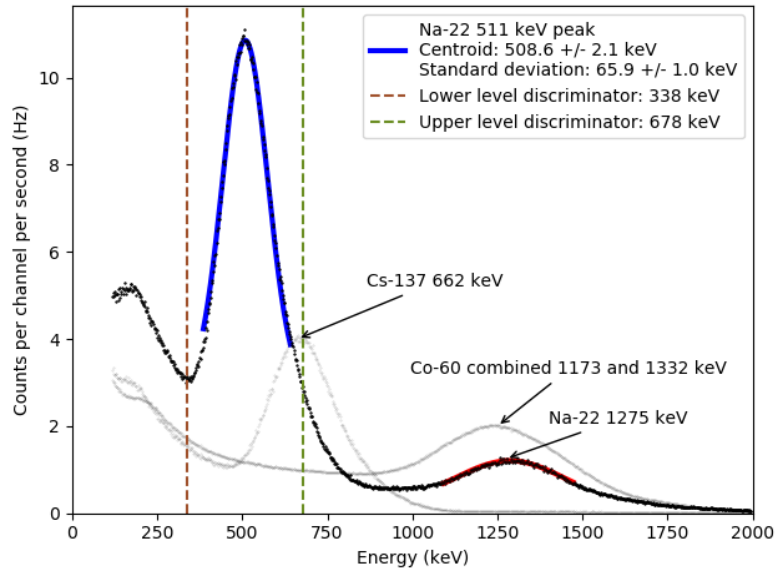


**Figure 2.** Calibrated energy spectra of the three sources as measured by a 951 detector block. The Na-22 spectrum is shown in bold, with Gaussian peaks fitted to each photopeak. Optimal lower and upper level discriminators are shown as dashed vertical lines.

energy  $\mu \pm N\sigma$ , where  $N$  was chosen to include 99% of the photopeak, giving  $338.9 \pm 3.3$  keV and  $678.4 \pm 3.3$  keV respectively. The LLD agrees with the expected energy of the Compton edge, indicating that this choice of  $N$  excludes the Compton scattered photons from the 511 keV peak, reducing the fraction of corrupt LORs.

#### 4.2. Temporal resolution

The temporal resolution describes the precision at which the system can measure the time of arrival for a single detection event. Two single events are regarded as simultaneous, or coincident, if they both occur within a coincidence window of time period  $2\tau$ , where  $\tau$  is limited by the time resolution in resolving an event. When  $\tau$  is greater than the time resolution of the system, all true coincidences will be recorded, and the number of recorded random coincidences increases linearly with  $\tau$ . Knowledge of the time resolution allows for the careful selection of  $2\tau$  which maximises the true coincidence rate while limiting the random coincidence rate, minimising the inclusion of corrupt LORs from random events.

Singles events were recorded for a positron source central to a pair of detector modules operating in coincidence, and a time delay was added to the events in one module. By varying this delay and determining the number of events that were within the same coincidence window, a Gaussian curve representing the system's coincidence timing resolution was plotted. As the delay is increased from zero, fewer true coincidences are detected and beyond a point all measured coincidences are random coincidences. As the size of the coincidence window is increased beyond the system's intrinsic timing resolution, the Gaussian curves reach a maximum and plateau as all true coincidences are fully covered by the chosen window. Increasing the coincidence window beyond that point leads to the inclusion of a higher fraction of corrupt LORs.

In figure 3, these curves are shown for varying coincidence windows, with the flat top visible at large values of  $2\tau$ . Fitting a Gaussian function to each of the curves with coincidence windows of 8 and 24 ns, being the curves with typical Gaussian shapes, the standard deviation of each

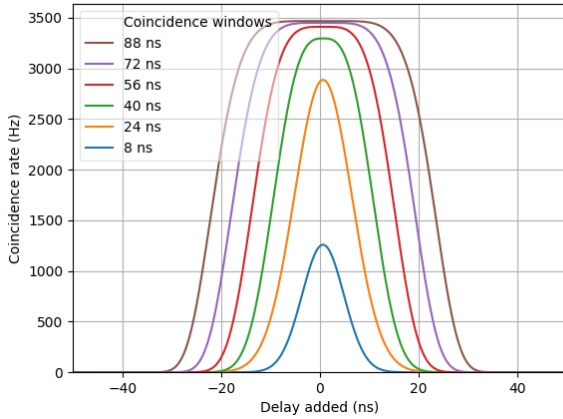


**Figure 3.** The coincidence rate as a function of time delay added to one of the coincident modules. Each curve represents a different coincidence window,  $2\tau$ .

was determined to be  $4.24 \pm 0.03$  ns and  $5.78 \pm 0.03$  ns respectively. The difference arises from the use of different coincidence windows. In the  $2\tau = 24$  ns case,  $\tau$  is greater than the time resolution of the system and the window width is included in the peak, whereas in the 8 ns case  $\tau$  is less than the system's time resolution, being approximately 4.24 ns.

The temporal resolution of PEPT locations can be estimated using the uncertainty estimator. Assuming  $w = 5$  mm for the BGO system, at a 1 MHz acquisition rate a location period of 2.5 ms can be estimated, achieving  $u(\bar{P}) = 100$   $\mu\text{m}$ . This location period implies systems under investigation must be slow moving, which is unsurprising as this system has not been optimised for high rate applications, which may be investigated in future work.

#### 4.3. Geometry definition

The hybrid camera geometry needs to be carefully optimised to leverage the benefits of each detector type if it is to be used for micro-scale PEPT. A BGO system consisting of two modules of four 951-series detector blocks and two modules of HR++ detector blocks was developed.

Clearly, the central region of the detector system is the most significant in measurements of micro-scale phenomena and the Polaris system must be placed there. The placement of the BGO modules is more flexible, and their individual characteristics must be considered. To do this, a Monte Carlo simulation of the sensitivity profile of the system was used for further optimisation, where the Monte Carlo aspects handled the volume effects of the crystals and their intrinsic efficiencies. A uniform sensitivity profile is desired in the central region of interest to avoid dead time limiting hot spots and to allow uniformity of PEPT measurements over the volume, but absolute uniformity is difficult to achieve due to the number of detector types.

In figure 4, the geometry of the hybrid camera system is shown, consisting of 1024 BGO pixels and 9680 CZT pixels, giving a high resolution region of interest between the Polaris modules of  $(62 \times 42 \times 20)$   $\text{mm}^3$  shown as a shaded red region, and a larger FOV between the BGO modules of  $(150 \times 196 \times 101)$   $\text{mm}^3$ . This geometry was selected as the HR++ blocks placed between the 951 blocks allow for the improved spatial resolution of the HR++ blocks to contribute significantly to the central region of interest, while also maintaining improved absolute efficiencies and an increased FOV as offered by the 951 blocks.

The uniformity of the sensitivity profile was validated using the simulation in figure 4, where sensitivity profiles as functions of their corresponding coordinates are shown at different depths along the Z axis in grey, with the mean sensitivity over all depths shown in bold. The uniformity of the central region can be seen in these profiles, although notable variation in uniformity can be seen at varying depths. Several other possible geometries were also tested, with none achieving

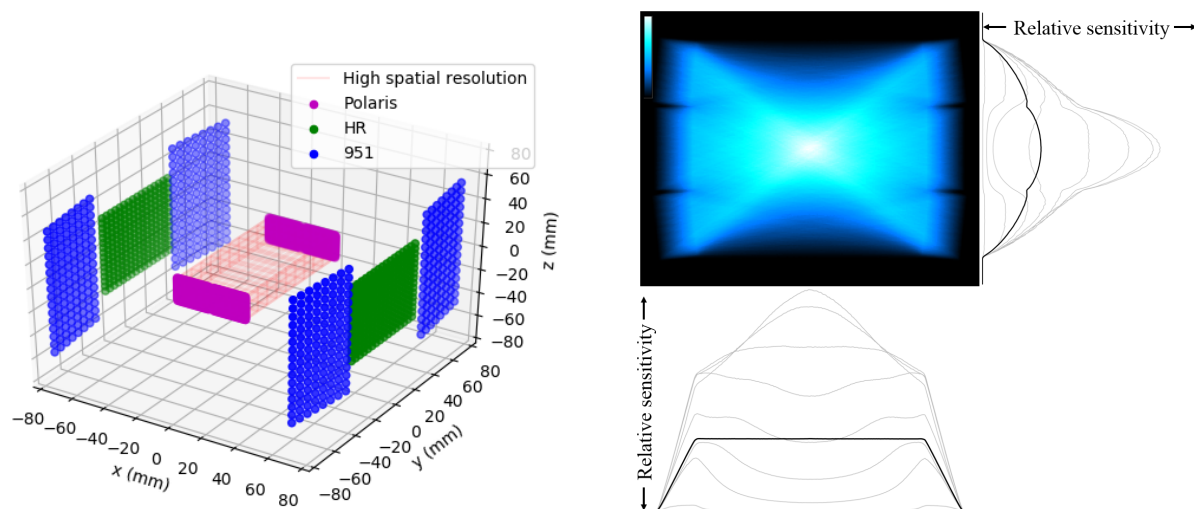


**Figure 4.** (Left) The geometry of the hybrid camera, showing each segmented detector element as a separate pixel with the central shaded high resolution region. (Right) The simulated sensitivity profile in the XY plane integrated along the Z axis, with corresponding profiles along the Y (side) and X (bottom) axis shown at varying depths. All profiles are drawn to scale.

similar central uniformity as in the chosen geometry. Using known deadtime limits of the BGO modules and their estimated efficiencies, a practical activity range of tracer particles was determined for the system, from 50 kBq to deadtime limiting 15 MBq particles.

## 5. Conclusions and future work

A modular BGO scintillator array was constructed to enable the application of PEPT to systems on the small scale, at micron precision. A numerical model of the sensitivity profile of the system was used to optimise the chosen geometry for uniformity within its field of view. Energy and timing resolutions were determined, allowing for the optimisation of system parameters for low noise detection. Precise characterisation of the detection efficiency, spatial resolution and deadtime parameters of the system in the future will lead into the development of a hybrid detector system combining the modular BGO array with a pair of high resolution pixelated semiconductor detectors, enabling the application of PEPT in the study of micro-scale phenomena for the first time.

## References

- [1] Parker D, Broadbent C, Fowles P, Hawkesworth M and McNeil P 1993 *Nuclear Instruments and Methods in Physics Research Section A: Accelerators, Spectrometers, Detectors and Assoc. Equipment* **326** 592 – 607
- [2] Buffler A, Govender I, Cilliers J, Parker D, Franzidis J P, Mainza A, Newman R, Powell M and Van der Westhuizen A 2009 *Int. Topical Meeting on Nuclear Research Applications and Utilization of Accelerators*
- [3] Leadbeater T, Parker D J and Gargiuli J 2012 *Particuology* **10**(2) 146–153
- [4] Hyslop N 2021 *Sub-Millimetre Positron-Emission Particle Tracking Using a CdZnTe Semiconductor Array* Master's thesis
- [5] Knoll G F 2009 *Radiation Detection and Measurement* (John Wiley) pp 12–13 3rd ed
- [6] Leadbeater T and Parker D 2013 *7th World Congress in Industrial Process Tomography* pp 85–94 ISBN 0853163235
- [7] H3D Inc. 2018 *J6400 High-Energy High-Flux Spectrometer* URL <https://h3dgamma.com/J6400Specs.pdf>
- [8] McKnight A, Leadbeater T and van der Merwe R 2022 *Characterisation of a new LSO block detector for Positron Emission Particle Tracking* The Proceedings of SAIP2022
- [9] NuDat database National Nuclear Data Center URL <https://www.nndc.bnl.gov/nudat/>

# Developing an infectiousness model for droplet transmission

**M Ralijaona<sup>1</sup>, E Igumbor<sup>1</sup>, M Bhamjee<sup>1</sup>, S Connell<sup>1</sup>, N Martinson<sup>2</sup>, K Otwombe<sup>2</sup>, H Grobler<sup>1</sup>, F Swanepoel<sup>2</sup>, P Mafa Takisa<sup>3</sup>, J Chewparsad<sup>2</sup>, M Milovanovic<sup>2</sup> and F Nabeemeeah<sup>2</sup>**

<sup>1</sup> Department of Mechanical Engineering Science, Faculty of Engineering and the Built Environment, University of Johannesburg.

<sup>2</sup> Perinatal HIV Research Unit, Chris Hani Baragwanath Academic Hospital, Faculty of Health Sciences, University of the Witwatersrand.

<sup>3</sup> Department of mathematical Sciences and UNISA - ATLAS High Energy Physics Group, University of South Africa, Johannesburg, 1710, South Africa.

E-mail: mralijaona@uj.ac.za

**Abstract.** Modelling of droplet based transmission in clinical spaces guided by a combination of the principles of medicine and physics can produce safer environments. Understanding airborne respiratory disease transmission is essential in light of the recent worldwide SARS-CoV-2 pandemic. This can help define better public health strategies to adopt and to design public spaces in such a way that humanity is less vulnerable to airborne transmission. Airborne infectious saliva droplets are the principal factor of transmission and the infectiousness is associated with the magnitude of the viral load. There is a need to consider the effects of local environmental factors on the evolution of droplet infectiousness. This work presents a computational fluid dynamics (CFD) model that incorporates heat and mass transfer to account for droplet evaporation. An Eulerian-Lagrangian approach was used to simulate air and particle flow. These flows were calculated using a two-way coupling method. Interactions between droplets are captured with coalescence and breakup models. The model assumes infectiousness is proportional to droplet volume which here has a constant pathogen concentration in the saliva. Results from this work show that higher temperature lowers infectiousness of the droplets containing the virus by increasing their evaporation, whereas humidity considerably reduces their evaporation rate and thus sustains their infectiousness. Thus ideally indoor spaces should be warmer, drier and ventilated. The results are benchmarked to measurement and other computational based methods and studies. The aim is to use the model to optimise the design of clinical and public spaces with optimal ventilation to minimise risks of infection.

## 1. Introduction

Airborne respiratory diseases are affecting humanity and can even turn into a global pandemic. Airborne transmission can be identified as the primary way of transmission as the number of infections reduces significantly when mandatory face mask is applied [1]. Policies which ameliorate the infectiousness of the droplets need to be set in public spaces. For that, a better understanding of the physical phenomena occurring during the air-carriage of respiratory droplets responsible of disease transmission is crucial. During the recent SARS-COV-2 pandemic, researchers investigated this matter and different approaches can be found in literature : experimental [2], theoretical [3] and computational studies [4, 5].

In this study, we consider the case of SARS-CoV-2 and Tuberculosis and similar, where pathogens are contained in expelled saliva droplets which are driven by the local air and are influenced by environmental factors. The infectiousness of a SARS-COV-2 droplet is proportional to its viral load count, with higher viral loads increasing ones susceptibility to infection. For a single droplet, the higher the viral load, the

higher its infectiousness. Saliva droplet size decreases with time due to evaporation. Hence, the number of pathogens would decrease as the droplet evaporates, as described in reference [6], where it is assumed that pathogens leave the droplet at the same rate as the fluid, and that dry pathogens are soon rendered harmless. In this study, the main objective is to develop an infectiousness model that accounts decreasing droplet infectiousness due to air flow and environmental factors (temperature and humidity).

## 2. Modeling approach

The model computes air and particles in such a way that air and droplets are coupled. Air motion is impacting on particles and impacts of particles are also incorporated in the air equations.

### 2.1. Euler-Lagrange approach

Air flow and droplet motion are coupled using the Euler-Lagrange approach. Air is considered as a continuum and is computed with the Navier-Stokes equations :

$$\frac{\partial \rho}{\partial t} + \frac{\partial}{\partial x_i} (\rho u_i) = S_m \quad (1)$$

$$\frac{\partial}{\partial t} (\rho u_i) + \frac{\partial}{\partial x_j} (\rho u_i u_j) = -\frac{\partial p}{\partial x_i} + \frac{\partial}{\partial x_j} \left[ \mu \left( \frac{\partial u_i}{\partial x_j} + \frac{\partial u_j}{\partial x_i} - \frac{2}{3} \delta_{ij} \frac{\partial u_l}{\partial x_l} \right) \right] + \frac{\partial}{\partial x_j} (-\rho \overline{u'_i u'_j}) + S \quad (2)$$

where  $\rho$ ,  $u_i$ ,  $S_m$ ,  $p$ ,  $\mu$ ,  $u'_i$  and  $S$  are density, mean velocity, mass source, pressure, dynamic viscosity, velocity fluctuations and momentum source of air respectively ;  $\delta_{ij}$  is the Kronecker delta. Subscripts  $i$ ,  $j$  and  $l$  denote the space coordinates, equation (1) and (2) stands for each space component of the velocity.

Turbulence is treated with the Shear-Stress Transport (SST)  $k - \omega$  model. The Reynolds stresses  $-\rho \overline{u'_i u'_j}$  are modeled with the Boussinesq hypothesis and the turbulent kinetic energy  $k$  and the specific dissipation rate  $\omega$  transport equations are added as described in reference [7].

Droplets are considered as a discrete phase and their trajectories are computed by integrating the force balance on the particles :

$$\frac{d\vec{u}_p}{dt} = \frac{18\mu C_D \rho d_p}{\rho_p d_p^2} \frac{\rho d_p}{\mu} (\vec{u} - \vec{u}_p) + \frac{\rho_p - \rho}{\rho_p} \vec{g} \quad (3)$$

where  $\frac{18\mu C_D \rho d_p}{\rho_p d_p^2} (\vec{u} - \vec{u}_p)$  is the drag force per unit mass,  $C_D$  is the drag coefficient,  $\vec{u}_p$ ,  $\rho_p$  and  $d_p$  are respectively the particle velocity, density and diameter. To account for the effect of turbulence on particle motion, a turbulent dispersion model is used. The fluid velocity  $u$  is then equal to  $\vec{u} + u'$ . More complex particle-particle interactions were also taken into consideration by adding droplet breakup and coalescence models.

The two-way coupling approach is used to enable momentum, heat and mass exchange between air and droplets. While the droplet trajectory is calculated, gain or loss of heat, mass and momentum are tracked. Those quantities are then incorporated in the air equations as sources. Air and droplets are then impacting each other. As described in reference [7] heat and mass transfer law between air and particles depends on the particle temperature  $T_p$ . If the droplet temperature is lower than the vaporization temperature or if the volatile fraction of the droplet is fully consumed, the following equation is solved :

$$m_p C_p \frac{dT_p}{dt} = h A_p (T_\infty - T_p) + \varepsilon_p A_p \sigma (\theta_R^4 - T_p^4) \quad (4)$$

where  $m_p$ ,  $C_p$ ,  $A_p$  and  $\varepsilon_p$  are the particle mass, heat capacity, surface area and emissivity,  $T_\infty$  is the temperature of air,  $h$  is the convective heat transfer coefficient,  $\sigma$  is the Stefan-Boltzmann constant and  $\theta_R$  is the radiation temperature. When the particle temperature reaches the vaporization temperature, the

droplet is vaporizing and transfer mass to the continuous phase. The following equations are computed until the volatile fraction of the droplet is fully drained :

$$N_i = k_c(C_{i,s} - C_{i,\infty}) \quad (5)$$

$$m_p(t + \Delta t) = m_p(t) - N_i A_p M_{w,i} \Delta t \quad (6)$$

where  $N_i$  is the molar flux of vapor,  $k_c$  is the mass transfer coefficient,  $C_{i,s}$  is the vapor concentration of the droplet surface,  $C_{i,\infty}$  is the vapor concentration in the air and  $M_{w,i}$  is the molecular weight of the vapor.

### 2.2. Injection properties

The way droplets are expelled is described by some parameters : the injection velocity and temperature, the size distribution of the droplets, and the droplet flow rate. Those properties depend on the respiratory event taken into consideration, whether it is a breathing, coughing or sneezing. In this study, we are considering a cough as described in reference [8]. The injection surface is rectangular shaped, its sides are 4 cm and 0.48 cm. Droplets are injected at a temperature of 34°C. The cough period is of 0.12 s, and the flow rate is calculated in order to obtain a total injected mass of 7.7 mg. Droplets are injected at a velocity of 11 m/s, which is the average velocity of a cough as indicated in reference [9].

The particle diameter follows a Rosin-Rammler distribution given by the following equation :

$$f(d) = e^{(-d/\bar{d})^n} \quad (7)$$

where  $d$  is the droplet diameter,  $f(d)$  is the cumulative mass fraction corresponding to droplet of diameter  $d$ ,  $\bar{d}$  is the mean diameter and is equal to 80  $\mu m$ ,  $n$  is called the spread parameter and is equal to 8. The minimum and maximum diameter are respectively 10  $\mu m$  and 110  $\mu m$ .

### 3. Results and discussion

For these preliminary studies, for the purpose of model development and benchmarking, the simulation domain is a simple room with an air vent as an inlet and a door as an outlet (Figure 1a). The cough is released from a rectangular shaped face located at 1.7 m height. The domain was meshed using tetrahedral shaped mesh elements, refined at the injection face (Figure 1b and 1c).

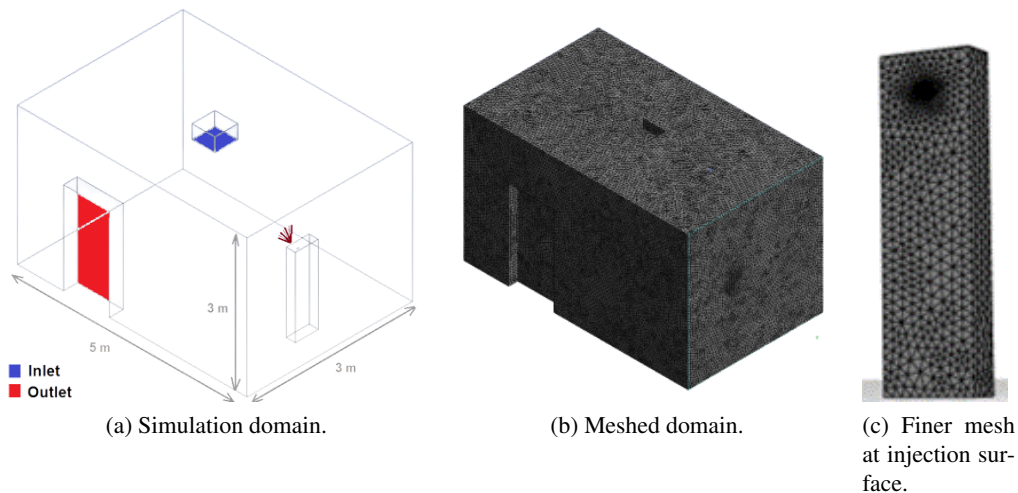


Figure 1: The domain and its treatment

The simulation was run inside this simple room. To highlight the effect of air flow on droplet dispersion, two different cases were investigated. The first one is when there is no air flow inside the room, the other one is when air is flowing. In the last case, the velocity inlet at the air vent was set to 1 m/s. However, the air is experiencing some backflow at the outlet, resulting in the air velocity going up to 5 m/s (Figure 2 (a)). Velocity streamlines from the surface where droplets are injected are plotted in Figure 2 (b), to get an idea of how droplets would be transported.

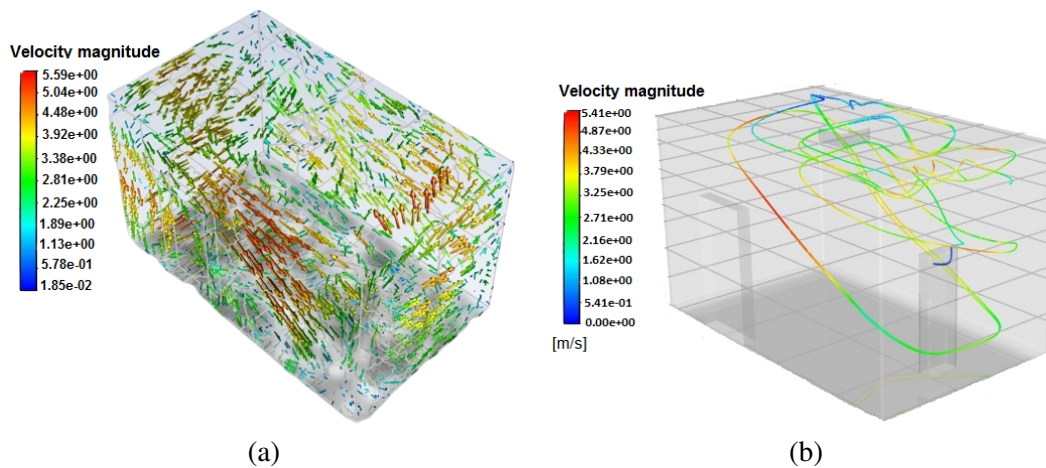


Figure 2: (a) Air velocity field, (b) air velocity streamlines.

When particles are expelled in a room with no air flow, particles of diameter  $d \leq 3\mu m$  are buoyancy driven and remain airborne (Figure 3 (a)) whereas larger ones ( $d \geq 5\mu m$ ) are more affected by gravity and rapidly fall to the ground. When air velocity is substantial, particles are better dispersed throughout the room (Figure 3 (b)).

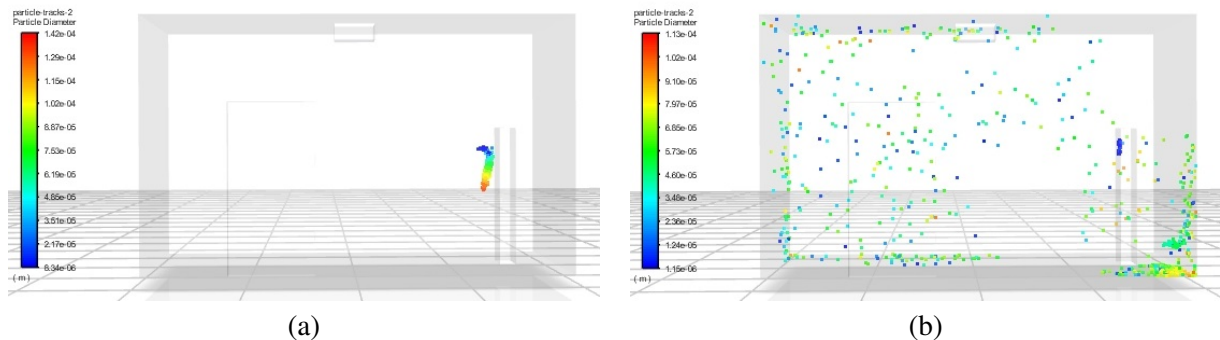


Figure 3: Particle dispersion (a) in a room without air flow, (b) with air flow.

The effect of evaporation is also important. The CFD modelling is able to follow this and show evaporation rate is accentuated by temperature (Figure 4 (a)), it is lowered by humidity (Figure 4 (b)) and it is accentuated by relative air flow.

In Figure 5, the droplet pathlines are tracked. For simplicity the air flow is zero. The droplets are color coded to their diameter, and it can be seen this diameter decreases due to evaporation. In the left part many droplet pathlines are shown and in the right part only a single one for clarity. This decrease in droplet size by evaporation occurs with a loss of virus. This represents the attenuation of infectiousness due to decomposition of dehydrated viruses [6]. This then represents the preliminary goal of the study,

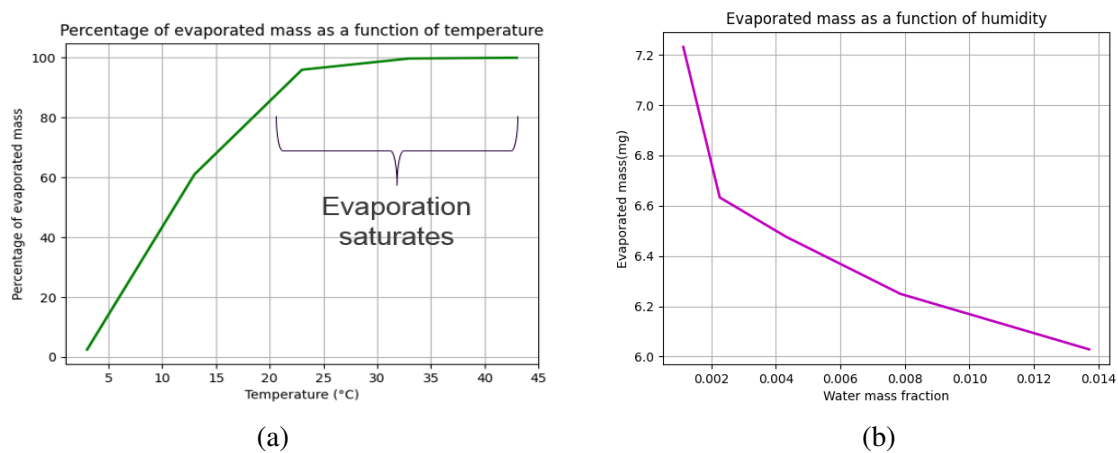


Figure 4: Evaporation rate as a function of (a) temperature, (b) humidity.

to incorporate a model for decreasing droplet infectiousness due to evaporation, and to track this on a per droplet basis.

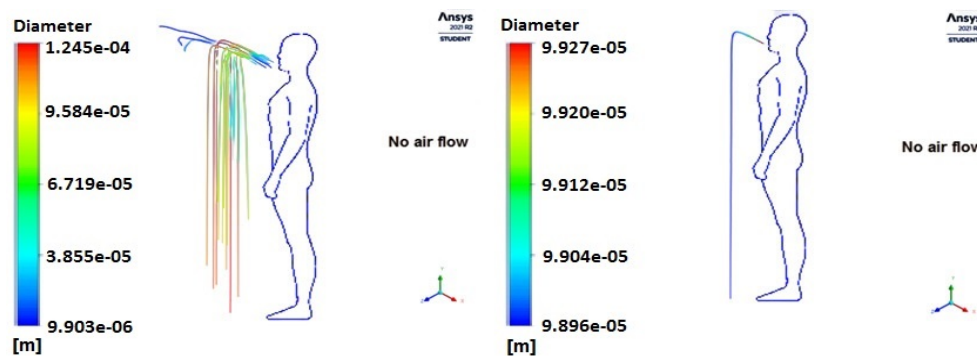


Figure 5: Particle pathlines. In the figure in the right, the decrease in droplet size is shown and therefore infectiousness decreases due to the effect of evaporation.

Thus closed spaces, which are likely to keep moisture, would experience lower evaporation, and small airborne particles would last longer. But in ventilated spaces, evaporation would be higher, in Figures 3 (a) and (b) residence time would be lower and droplet infectiousness would decrease [10].

The model is benchmarked to the CFD model in reference [8]. In this paper, particles are injected in an open environment, with wind coming from behind the coughing person. The mouth is located at 1.63 m. Figure 6 shows a result obtained with our model in the case of wind speed being equal to 4 km/h. Distance travelled by droplets for a given time are consistent with results shown in reference [8]. The difference resides in the fact that in our result, particles are more affected by gravity, due to coalescence.

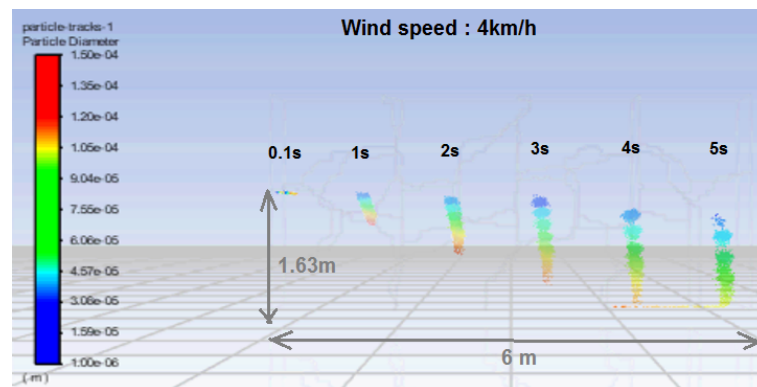


Figure 6: Particle motion in an open space. With wind speed of 4 km/h droplets of diameter  $d \leq 4\mu\text{m}$  remain airborne and the effect of gravity is causing the larger droplets ( $d \geq 100\mu\text{m}$ ) to settle faster.

#### 4. Conclusion

The main goal of this study is to introduce a model for the infectiousness of respiratory diseases transmitted by expelled droplets, into a larger CFD model of the fluid space. The CFD simulates the transport and evolution of droplets expelled from a cough. Particle trajectory is computed in a simplified environment, effect of temperature and humidity of the environment is taken into account by considering droplet evaporation. The influence of air flow on droplet dispersion is also taken into consideration. It is seen that this scheme is able to track the time evolution of infectiousness of individual droplets.

These findings are critical for public health facilities treating patients with airborne transmissible diseases such as SARS-CoV-2, tuberculosis or influenza amongst others. Such facilities need to be designed to incorporate ways of minimizing the risk of disease transmission by improving ventilation and controlling temperature and humidity. Further studies will deploy this model in selected public and clinical spaces. This study can also be extended to other public health concerns like harmful gases transport with or without entrained particles.

#### Acknowledgments

This work is based on the research supported the research grant of the University of Johannesburg. The authors thank the PHRU, its staff for the opportunity to access their facilities and utilise the AVGU equipment. The Centre for High Performance Computing (CHPC) is acknowledged for the use of the CHPC facilities.

#### References

- [1] Zhang R, Li Y, Zhang A L, Wang Y and Molina M J 2020 Identifying airborne transmission as the dominant route for the spread of COVID-19 *Proceedings of the National Academy of Sciences* **117** (26) **14857–14863**
- [2] Shah Y, Kurelek J W, Peterson S D and Yarusevych S 2021 Experimental investigation of indoor aerosol dispersion and accumulation in the context of COVID-19: Effects of masks and ventilation *Phys. Fluids* **33** 073315.
- [3] Agrawal A and Bhardwaj R 2021 Probability of COVID-19 infection by cough of a normal person and a super-spreader *Phys. Fluids* **33** 031704.
- [4] Pendar M-R and Páscoa J C 2020 Numerical modeling of the distribution of virus carrying saliva droplets during sneeze and cough *Phys. Fluids* **32** 083305.
- [5] Wu L, Liu X, Yao F and Chen Y 2021 Numerical study of virus transmission through droplets from sneezing in a cafeteria *Phys. Fluids* **33** 023311.
- [6] Dbouk T and Drikakis D 2020 Weather impact on airborne coronavirus survival *Phys. Fluids* **32** 093312.
- [7] Ansys® fluent theory guide, Release 15.0, November 2013.
- [8] Dbouk T and Drikakis D 2020 On coughing and airborne droplet transmission to humans *Phys. Fluids* **32** 053310.
- [9] Zhu S, Kato S and Yang JH 2006 Study on transport characteristics of saliva droplets produced by coughing in a calm indoor environment *Building and Environment* **41** 1691-1702.
- [10] Mirzaie M, Lakzian E, Khan A, Warkiani M E, Mahian O and Ahmadi G 2021 COVID-19 spread in a classroom equipped with partition – A CFD approach *Journal of Hazardous Materials* **420** 126587.

# Measurement of fast neutron removal cross sections for the elemental analysis of concrete

Naledi Segale<sup>1,\*</sup>, Tanya Hutton<sup>1</sup>, Sizwe Mhlongo<sup>1</sup>, Andy Buffler<sup>1</sup>

<sup>1</sup>Metrological and Applied Sciences University Research Unit (MeASURE),

Department of Physics, University of Cape Town, Cape Town, South Africa, 7700.

\*E-mail: [SGLNXX001@myuct.ac.za](mailto:SGLNXX001@myuct.ac.za)

**Abstract.** Concrete structures in nuclear power plants (NPPs) are exposed to extreme conditions causing degradation and composition changes over the reactor lifetime. To ensure compliance of existing concrete structures to nuclear regulations the radiation shielding properties, and elemental composition, need to be non-destructively determined. In this work we demonstrate the use of fast neutron measurements to investigate the proportions of silicon dioxide (SiO<sub>2</sub>) and calcium carbonate (CaCO<sub>3</sub>) in a well-characterised sample of sand, a key constituent of any concrete. Fast neutron transmission measurements were made with an EJ-301 organic liquid scintillator, and a collimated beam of <sup>241</sup>Am-<sup>9</sup>Be neutrons incident on samples of SiO<sub>2</sub>, CaCO<sub>3</sub> and sand. For each sample, the effective removal cross section was calculated over a broad range of neutron energies. Similar removal cross sections were found for SiO<sub>2</sub> and sand indicating that sand is predominantly made up of SiO<sub>2</sub>, which was in agreement with previous X-ray fluorescence measurements. Based on known mass ratios, the removal cross section for sand was reconstructed from the values for SiO<sub>2</sub> and CaCO<sub>3</sub> and was in agreement with the measured removal cross section for sand.

## 1. Introduction

Concrete is widely used in nuclear power plants (NPPs) because of its mouldability, simple manufacturing process, use of locally available materials, cheap production cost, good compression strength and excellent shielding property against gamma rays and neutrons [1]. The concrete structures in NPPs are often exposed to high stresses, prolonged high temperatures, and high levels of neutron and gamma ray radiation causing the concrete to degrade and change in composition over time. What is of particular concern to neutron radiation shielding is the loss of water [2], and hence hydrogen, which is difficult to quantify non-destructively.

In South Africa, Eskom owns and operates the Koeberg NPP, which features two pressurized water reactors each delivering 970 MW gross power. The two units were commissioned in the 1980s and the current license is set to expire in 2024. There are plans in place to extend the design life of the Koeberg NPP by a further 20 years, overseen by the National Nuclear Regulator (NNR) [3]. Part of the process requires re-evaluation of the existing concrete structures, with respect to radiation shielding and structural properties.

### 1.1 Fast neutron transmission spectroscopy (FNTS)

Fast neutrons are useful for the analysis of bulk materials as they are highly penetrating, produce characteristic radiation signatures for each element and are particularly sensitive to low mass elements such as hydrogen. For beam of neutrons incident on a sample of interest, three major signatures are produced: transmitted neutrons; scattered neutrons; and gamma rays (prompt and delayed) [4, 5]. Measurement of these signatures, both in intensity and energy provides information on the nuclei with which neutrons have interacted. In fast neutron transmission spectroscopy (FNTS), the elemental composition of a sample can be determined from the analysis of transmitted neutron spectra through a sample. For a neutron beam incident on a sample, some fraction of neutrons interact with the material and are subsequently removed from the beam. The neutrons which are transmitted through the sample are then detected. The ratio of the incident and transmitted fluence spectrum can be used to determine the composition of the sample through the use of the effective removal cross section [4].

### 1.2 Effective removal cross section

The effective removal cross section ( $\Sigma_R$ ) provides a measure of the neutron attenuation through a bulk sample and is highly specific for each element. The concept of  $\Sigma_R$  is often associated with the presence of hydrogen in sample of interest, however, it can be extended to non-hydrogenous samples, as long as they provide sufficient moderation of the neutron beam. Furthermore, it is only valid for fast neutrons with neutron energies between 2 MeV and 12 MeV as  $\Sigma_R$  is approximately constant within this range [6]. The attenuation of a beam of fast neutrons through a bulk sample can be modelled by Eq. 1, where  $I(t)$  is the transmitted neutron intensity for a sample of thickness  $t$ , and  $I(0)$  is the incident neutron intensity:

$$I(t) = I(0) \exp(-\Sigma_R t). \quad (1)$$

For a composite material, the effective removal cross section is related to a linear combination of the constituent parts as shown in Eq. 2, where  $m_k$  is the mass fraction of component  $k$ , with density  $\rho_k$  [7]:

$$\Sigma_R / \rho = \sum_k m_k (\Sigma_{R,k} / \rho_k). \quad (2)$$

The use of FNTS for concrete analysis has been previously demonstrated at the University of Cape Town, where the energy dependent effective removal cross sections for sand, cement and water were measured and used to de-convolve the relative ratios in well characterized concrete samples [8]. However, the use of this technique is limited to new concrete installations, as it is necessary to also measure with the composite ingredients which often have a location dependence [9]. Proof-of-concept studies have been undertaken to investigate the use of elemental responses for both transmitted and scattered neutrons to generalize the technique, but experimental validation is still needed [7]. In this work we present the progress towards the experimental implementation of elemental analysis of complex materials such as concrete. In this phase a well-characterised sample of sand is utilised as the exemplar material since it is comprised of known ratios of  $\text{SiO}_2$  and  $\text{CaCO}_3$ .

## 2. Experimental method

The experimental implementation of fast neutron transmission spectroscopy requires: a collimated beam of fast neutrons with a known distribution in energy and intensity; a sample with which the neutrons interact; and a neutron sensitive detector with appropriate acquisition and analysis protocols. All these are available at the n-lab, a fast neutron facility within the Department of Physics, University of Cape Town [10]. Figure 1 illustrates a typical experimental geometry for FNTS measurements at the n-lab, including a pencil beam of  $^{241}\text{Am}$ - $^9\text{Be}$  neutrons, samples of sand,  $\text{SiO}_2$  and  $\text{CaCO}_3$ , and an EJ-301 organic liquid scintillator for neutron detection.



**Figure 1.** Fast neutron transmission experimental set-up. A pencil beam of  $^{241}\text{Am}$ - $^9\text{Be}$  neutrons is incident on the segmented container, where the shaded sections correspond to a measurement of 4.0 cm sample thickness. Transmitted neutrons are incident on a 2" x 2" EJ-301 organic liquid scintillator detector.

### 2.1 $^{241}\text{Am}$ - $^9\text{Be}$ neutron source

An  $^{241}\text{Am}$ - $^9\text{Be}$  radioisotopic source was used, which produces neutrons via the  $(\alpha, n)$  reaction. Americium-241 decays via  $\alpha$ -particle emission with a half-life of 432.2 years. The emitted  $\alpha$ -particles slow down and are captured by  $^9\text{Be}$  to produce  $^{12}\text{C}$ , a neutron and a 4.43 MeV  $\gamma$ -ray. This source produces a broad spectrum of neutrons ranging from thermal to 11 MeV as shown by the distribution in Fig. 2. The 220 GBq  $^{241}\text{Am}$ - $^9\text{Be}$  source at the n-lab produces around  $10^7$  neutrons per second into  $4\pi$  steradians, and is used to produce a pencil beam of neutrons, as indicated by the arrow in Fig. 1, with a 1.0 m long HDPE collimator (0.8 cm internal diameter).

### 2.2 Samples

Samples of  $\text{SiO}_2$ ,  $\text{CaCO}_3$  and sand were prepared in a segmented container (Fig. 1), with cross sectional area of  $5.0 \times 5.0 \text{ cm}^2$  and thicknesses of 2.0, 4.0 and 6.0 cm. The sand used in this work was provided by the Concrete Materials and Structural Integrity Research Unit (CoMSIRU) at University of Cape Town, and is representative of the sand used in local concrete installations, such as Koeberg NPP. A sample of this sand was (destructively) analyzed by X-ray fluorescence (XRF) and was found to contain 78.5 %  $\text{SiO}_2$  and 18.6 %  $\text{CaCO}_3$  by mass. The remaining 2.9 % consisted of several other oxides, with no single one exceeding 0.5 % by mass [8]. The  $\text{SiO}_2$  and  $\text{CaCO}_3$  samples were comprised of glass beads ( $< 1.0 \text{ mm}$  diameter), and a fine powder respectively. As fast neutrons are sensitive to elemental composition and insensitive to chemical bonding, there is no requirement for the physical form of each sample to match that found in the composite sample. For example,  $\text{CaCO}_3$  in powder form and  $\text{CaCO}_3$  from shell fragments (as found in sand) will demonstrate the same neutron attenuation behavior when normalized by their individual densities. For each sample, and thickness, the total mass was recorded to account for changes in sample density between preparations.

### 2.3 EJ-301 neutron detector

Neutrons transmitted through the sample were detected using a 2" x 2" EJ-301 organic liquid scintillator optically coupled to an ETL 9214 12-stage photomultiplier tube and base supplied by Scionix, and operated at a negative bias of 1100 V. Both the anode and dynode signals were acquired using a CAEN DT5730 digitizer [12] and the QtDAQ [13] software. As the detector is sensitive to both neutrons and

gamma rays, pulse shape discrimination (PSD) was implemented through QtDAQ to identify neutron only events using the fast anode signals [14]. Energy information on the recoiling particles was obtained from the pulse height of the dynode signals after amplification and shaping with an Ortec 113 preamplifier and 574 amplifier. A typical PSD plot for an  $^{241}\text{Am-}^9\text{Be}$  source measured with an EJ-301 detector is shown in Fig. 3. The neutron only events are used to produce a neutron light output ( $L$ ) spectrum, after calibration with a series of reference gamma ray sources, which was used as a measure of neutron intensity  $I(t)$  introduced in Eq. 1.

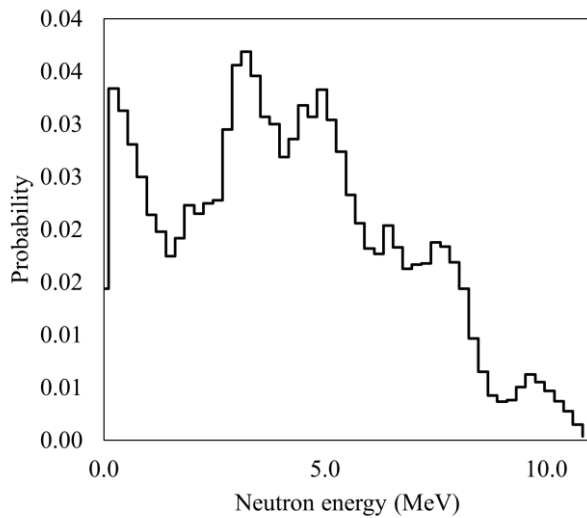


**Figure 2:** Neutron energy spectrum produced by an  $^{241}\text{Am-}^9\text{Be}$  radioisotopic source [11].

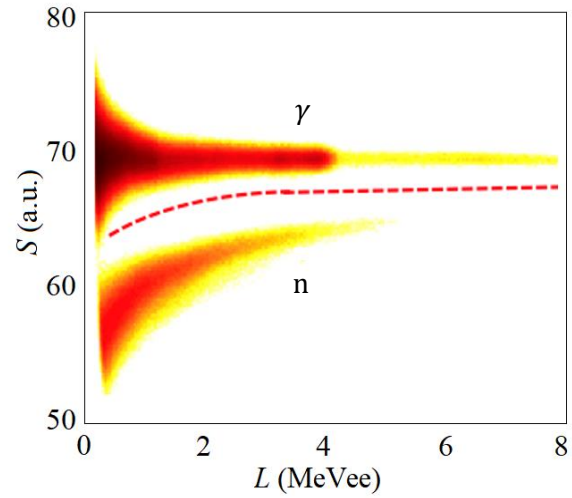


**Figure 3:** Counts as a function of light output parameter  $L$  and pulse shape parameter  $S$  measured with an EJ-301 scintillator for an  $^{241}\text{Am-}^9\text{Be}$  source. Contributions from neutrons ( $n$ ) and gamma rays ( $\gamma$ ), are separated by a software cut (dashed line)

### 3. Results and analysis

Calibrated neutron light output spectra measured for the three samples are shown in Fig. 4. In all instances the 0.0 cm case (empty container) is shown in black. The neutron attenuation is expected to behave according to Eq. 1, where an increase in sample thickness should correspond to an exponential reduction in measured neutron rate. This decrease is clearly evident in the  $\text{SiO}_2$  and sand datasets. The density of the  $\text{CaCO}_3$  sample is much lower than that of  $\text{SiO}_2$  or sand, thus the reduction in transmitted neutron rates is much lower.

To determine the effective removal cross section, the integrals of the measured light output spectra (Fig. 4) in the range of 1.0 – 5.5  $\text{MeV}_{\text{ee}}$  were used as a measure of the transmitted neutron intensity  $I(t)$ . The integrated  $L$  spectrum for  $t = 0.0$  cm was taken to be the incident neutron intensity  $I(0)$  as no sample was present. Using these values  $\Sigma_R$  can be determined using Eq. 1, however as there are small variations in density  $\rho$  between sample preparations it is more useful to consider the parameter  $\Sigma_R/\rho$  for comparison. Table 1 contains a summary of the effective removal cross sections for  $\text{SiO}_2$ ,  $\text{CaCO}_3$  and sand averaged over the three non-zero thicknesses. The uncertainties presented here correspond to the standard deviation about the mean while a full uncertainty analysis is still ongoing.

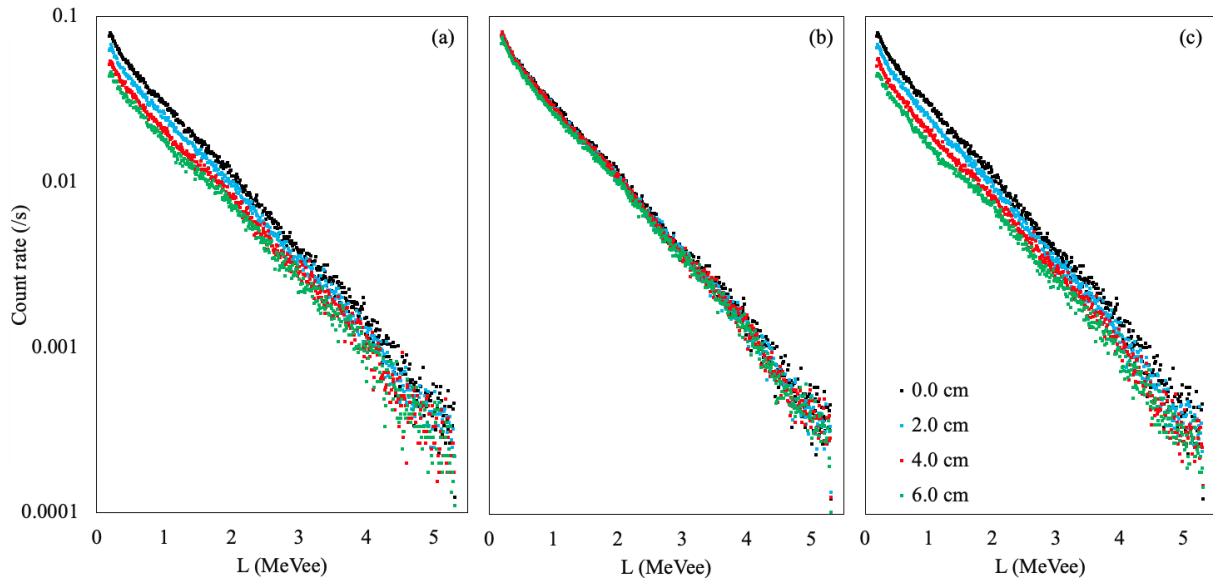


**Figure 4:** Light output spectra measured with an EJ-301 detector for a beam of  $^{241}\text{Am}$ - $^9\text{Be}$  neutrons transmitted through samples of (a)  $\text{SiO}_2$ , (b)  $\text{CaCO}_3$  and (c) sand, and normalised with respect to measurement time. The count rates are presented on a logarithmic scale.

**Table 1:** Summary of measured removal cross section data for  $\text{SiO}_2$ ,  $\text{CaCO}_3$  and sand.

	$\Sigma_R$ [ $\text{cm}^{-1}$ ]	$\rho$ [ $\text{g cm}^{-3}$ ]	$\Sigma_R/\rho$ [ $\text{cm}^2 \text{g}^{-1}$ ]
	2.0 cm : 4.0 cm : 6.0 cm	2.0 cm : 4.0 cm : 6.0 cm	
<b>SiO<sub>2</sub></b>	0.085 : 0.084 : 0.081	1.40 : 1.45 : 1.42	$0.0586 \pm 0.0020$
<b>CaCO<sub>3</sub></b>	0.015 : 0.008 : 0.016	0.37 : 0.38 : 0.36	$0.034 \pm 0.013$
<b>Sand</b>	0.082 : 0.088 : 0.085	1.50 : 1.51 : 1.50	$0.0568 \pm 0.0015$

The removal cross section measured for sand was only slightly less than that measured for  $\text{SiO}_2$ , and notably greater than that for  $\text{CaCO}_3$ , confirming that the sand sample was predominantly made up of  $\text{SiO}_2$  as expected from the XRF measurements. The measured removal cross sections were then used to validate the relationship expected from Eq. 2. The measured  $\Sigma_R/\rho$  values for  $\text{SiO}_2$  and  $\text{CaCO}_3$ , along with their known mass ratios (XRF), were used to reconstruct the density normalised removal cross section for sand, which was determined to be  $0.0539 \pm 0.0030 \text{ cm}^2 \text{g}^{-1}$ . This value agrees with the measured value of  $0.0568 \pm 0.0015 \text{ cm}^2 \text{g}^{-1}$  within experimental uncertainties. It was noted that the removal cross section measured for 4.0 cm  $\text{CaCO}_3$  was lower than expected, and possible causes are still being investigated. As such, the calculated removal cross section for sand is marginally lower than the measured value, though the agreement between the measured and calculated values is considered acceptable, and is within quoted uncertainties.

At this stage there is only a single measured value for the removal cross section for each sample, which means there is no way to solve for the mass ratios of each component. The next phase of this work will be to unfold the neutron energy spectra associated with each sample, and determine energy dependent removal cross sections, from which a unique solution for the mass ratios can be determined from a secondary unfolding procedure.

#### 4. Discussion and conclusion

The fast neutron transmission spectroscopy technique is being developed at the n-lab to non-destructively determine the elemental composition of complex bulk materials such as concrete. In this work, the density normalized removal cross sections were measured for  $\text{SiO}_2$ ,  $\text{CaCO}_3$  and sand with values of  $0.0586 \pm 0.0020 \text{ cm}^2 \text{ g}^{-1}$ ,  $0.034 \pm 0.013 \text{ cm}^2 \text{ g}^{-1}$  and  $0.0568 \pm 0.0015 \text{ cm}^2 \text{ g}^{-1}$  respectively at  $^{241}\text{Am}$ - $^9\text{Be}$  neutron energies. The similarity between the measured values of  $\Sigma_R/\rho$  for sand and  $\text{SiO}_2$  indicates that sand is predominantly made up of  $\text{SiO}_2$ . This is consistent with previous XRF measurements. To validate the relationship between the removal cross sections of individual constituents ( $\text{SiO}_2$  and  $\text{CaCO}_3$ ) and the removal cross section of the composite material (sand), a reconstructed removal cross section for sand was determined to be  $0.0539 \pm 0.0030 \text{ cm}^2 \text{ g}^{-1}$ , which is consistent with the measured value.

The next phase of this research will require the use of spectrum unfolding to determine the energy dependence of the transmitted neutrons, and hence energy dependent removal cross sections. By constructing a database of removal cross sections, by oxide or element, the composition of an unknown sample can be determined via a secondary unfolding process. The results presented here form part of an Honours level research project, which aims to contribute to this database, and further validate the technique for the analysis of sand. Subsequent measurements will determine elemental removal cross sections, and the investigation of more complex media such as concrete.

#### References

- [1] Basu P, Labbe P and Naus D, 2013. Nuclear Power Plant Concrete Structures. In: *Structural Mechanics in Reactor Technology*. IASMiRT, pp1-5
- [2] Peterson E, 1960. *Shielding Properties of Ordinary Concrete as a Function of Temperature*, USAEC, Report HW-65572
- [3] Department of Mineral Resources and Energy, 2019. Integrated Resource Plan (IRP2019)
- [4] Micklich B, Curry B, Fink C, Smith D and Yule T, 1994. System design considerations for fast-neutron interrogation systems. *Proceedings Substance of detection systems*, **2092**, pp3-5
- [5] Buffler A, 1998. *Fast Neutron Scattering Analysis*. PhD thesis, University of Cape Town
- [6] El-Khayatt A, 2010. Calculation of fast neutron removal cross-sections for some compounds and materials. *Annals of Nuclear Energy*, **37**(2), pp218-222
- [7] Hutton T, Buffler A and Alexander M, 2022. Elemental analysis of concrete via fast neutron transmission and scattering spectrometry. *EPJ Web of Conferences*, **261**, 03003
- [8] Buffler A, Hutton T, Leadbeater T, Alexander M and Dlamini S, 2020. Neutron transmission studies for concrete used in the nuclear industry. *International Journal of Modern Physics: Conference Series*, **50**, pp3-8
- [9] Walker B, 2013. *Fine Aggregate Resources in the Greater Cape Town Area*. MSc thesis, University of Cape Town
- [10] Hutton T and Buffler A, 2017. A new D-T neutron facility at UCT. *SAIP2017 Proceedings*, pp324-330
- [11] International Standards Organisation, 1999. Neutron reference radiation fields, ISO 8529-1
- [12] CAEN SpA, 2021. User manual UM3148, DT5730/DT5730S – 8 Channel 14 bit 500/200 MS/s Digitizer
- [13] Comrie A, 2015. QtDAQ git repository, [online] Available: <https://bitbucket.org/veggiesaurus/qtdaq>
- [14] Comrie A, Buffler A, Smit F, and Wortche H, 2015. Digital neutron/gamma discrimination with an organic scintillator at energies between 1 MeV and 100 MeV. *Nuclear Instrumentation and Methods*, **A772**, pp43-49

# Communication distance and security improvement in satellite based quantum key distribution via photon polarization pseudo-random bases encoding

TENE Alain Giresse<sup>1</sup>, YIANDE DEUTO Germain<sup>1</sup>, AZANGUE KOUMETIO Armel<sup>1</sup>, TCHOFFO Martin<sup>1,2</sup>

<sup>1</sup>Department of Physics, Faculty of Science, University of Dschang, Cameroon, P.O.Box 67, Cameroon

<sup>2</sup>Centre d'Etude et de Recherche en Agronomie et en Biodiversité, FASA, Université de Dschang, Cameroun

E-mail: alain.tene@aims-cameroon.org

**Abstract.** New protocol to achieve very long-distance and secure communication between two legitimate users (Alice and Bob) namely, the pseudo-random entangled photon based QKD protocol using a low-earth-orbit (LEO) type satellite as the photon source relay is proposed. We assume the combined type-I and type-II SPDC as photon source distributing entangled photons pairs to Alice and Bob, and the quantum logistic map (QLM) as quantum pseudo-random number generator (QPRNG) in order to randomly select photon polarization states measurement bases. Under these considerations, the secure key rate upper bound is evaluated and numerical simulations show that, the maximum communication distance increases significantly with the photon block size, and with the error correction function. One also observes that the protocol can tolerate a secure communication up to about 19000 km under lower background error (or lower atmosphere diffraction). The secure key privacy is strongly improved since public discussion is avoided due to the use of a QPRNG, which guarantees identical measurement bases choice between Alice and Bob. Based on the above, our protocol is more efficient. In addition, the secure key privacy is significantly amplified.

## 1. Introduction

In our nowadays communication networks, truly secret communication channel between two or more operators has become a major problem with an increasing in computer's power and speed. That is, scientists continuously think about a better way to secretly share sensitive information or a secure and unbreakable key for information encryption. Quantum mechanics properties of particles have been recently presented as a suitable candidate to solve the problem [1, 2, 3, 4]. Based on this idea, several research works have been developed in the past few decades to implement new strategies which employed quantum effects to manipulate and transmit information more secretly, here we refer to quantum cryptography (QC) [5, 6]. The latest mentioned notion mainly focuses on sharing a secret key for information encryption between two or more legitimate users (Alice and Bob), namely quantum key distribution (QKD) and has been proved to significantly improve the security of information, since Alice and Bob could be alert by the presence of any eavesdropper (Eve) intending to intercept their exchanging information.

Indeed, the concept of QKD which was first introduced by Bennett and Brassard in 1984, is nowadays known as the best method of sharing a secret key and has therefore, been successfully implemented [6].

For this reason, numerous QKD protocols have been developed so far, namely: the Ekert91 (proposed by Ekert in 1991, [7]), the B92 (proposed by Bennett in 1992 [8]), the SSP (six-state protocol proposed by Bechmann-Pasquinucci in 1999 [9, 10]) protocols, just to list a few. Despite their huge security, these protocols still present some limits as they require single photon measurement which induces losses due to photon splitting. In addition to the security, two other properties characterizing good QKD protocol are the quantum bit error rate (QBER) and the maximum tolerable communication distance between legitimate users. However, the above mentioned protocols were found to present lower QBER and very limited communication distance. To overcome these drawbacks, new protocols that used entangled photons as well as Bell's entangled states were developed [11, 12, 13]. Whereas, it was demonstrated that, with a spontaneous parametric-down conversion (SPDC) photon source based QKD, one could achieve up to 144 km as communication distance under noisy quantum channels, which is acceptable but not enough for long-distance communication [14, 15]. Experiments proved that for any pure-loss quantum channel with transmittance efficiency  $\eta$ , the secure key rate scales linearly with  $\eta$  [16, 17, 18], inducing a fundamental limit to the maximum tolerable communication distance. Due to this problem, new approaches which are based on sharing a secret key over free space with very lower loss rate using low-earth-orbit (LEO), medium-earth-orbit (MEO) or geostationary orbit (GEO) satellites as an intermediate relay between legitimate communication users were recently introduced [19]. However, LEO and GEO are the most suitable candidates due to their altitude (160 to 3000 km or usually below 900 km for LEO and 35786 km precisely for GEO). Thus, due to the proximity of LEO to the earth's surface, we assume in this work that an entangled photon source will be distributing entangled photon pairs from a LEO-type satellite in order to reduce losses due to beam diffraction.

In fact, satellite based QKD has attracted significant interests of researchers, and has been successfully implemented in real physical experiments [16, 20, 21, 22, 23, 24]. Although significant results have been achieved, the security of the protocol still requires deep studies. Whereas, Jian-Yu *et al.* [25] demonstrated that free-space links could provide the most appealing solution to long-distance and secure communication. The experiment was conducted using a floating platform hot-air balloon fulfilling the conditions of a LEO-type satellite. In similar conditions, Wang *et al.* [25] will later investigate long-distance QKD with the floating hot-air balloon platform under rapid motion, altitude change and they found a quantum bit error rate (QBER) of 4.04%. Moreover, Pan [26] established the space platform with long-distance satellite-to-ground quantum channel and he was able to achieve the BB84 QKD up to 1200 km with a QBER of about 1%. In the same idea, using retro-reflectors in LEO satellite, space-to-ground transmission of quasi-single photon has been investigated by Yin *et al.* [27]. They realized a signal-to-noise ratio of 16:1, sufficient for unconditionally secure QKD links. In addition, Nauerth *et al.* [28] found that, the BB84 QKD between ground station and airplane moving at regular angular velocity similar to LEO-type satellite is feasible, and the experiment demonstrated a QBER of 4.8% at 20 km range. However, the first downlink microsatellite QKD experiment was just realized very recently in 2017 with a QBER less than 3% and  $99.4 \pm 4.4\%$  degree polarization by Takenaka *et al.* [29]. Several authors investigated the protocol using single photons and demonstrated the feasibility of free space satellite-to-ground QKD with significant improvements regarding the QBER, the communication distance and the sifted key rate in the night-time as well as under noisy-like sunlight daytime [20, 22, 30, 31, 32, 33]. Further achievements using entangled photons showed that, the latest can more significantly improve the key rate and the communication distance as well. Moreover, it turns out that downlink QKD in night-time presents lower loss compared to uplink QKD in similar conditions [34, 35]. Nevertheless, all the previously mentioned protocols use most often true random number generators (TRNGs) for photon bases choice. This usually costs sifting in the key raw and may reduce up to half in its size, since the legitimate users (Alice and Bob) must perform their measurement with incompatible bases choices.

To overcome this serious drawback, we suggest in this research paper to use a QPRNGs for photon measurement bases choice to guarantee identical measurement bases selection by Alice and Bob. Similar procedure was very recently studied in our previous works, but in the case of optical link based QKD protocol [36], and the results proved its efficiency. We thus, suggest a new protocol that uses the

quantum kick system, which are very good QPRNGs, easily implementable, and could strongly improve the efficiency of satellite based communication. If this protocol is successfully implemented, it will significantly enhance the maximum communication distance and the efficiency of the security due to random-like behavior and high sensitivity to initial conditions of chaotic systems [37, 38]. We therefore, assume our random bases selection to be guaranteed by the quantum logistic map (QLM) [39] and the SPDC-photon source to be our entangled photons generator located in a LEO-type satellite to ensure downlink communication with lower loss. This is realized following the structure below: Sec. 2 presents in detail the procedure to generate random bases for photons polarization measurement using QLM. In Sec. 3, the SPDC-entangled photons Hamiltonian is presented, following by the derivation of the wave function and the probability distribution. We also present in detail the scheme for photon polarization state measurement in the same section. The satellite-to-ground based QKD protocol using entangled photons and QLM as QPRNG is described in detail in Sec. 4, with the derivation of the QBER and the secure key rate. In addition, numerical simulations of our main results are presented in Sec. 5. We end the work with some concluding remarks and discussion in Sec. 6.

## 2. Pseudo-random bases generation for photon state polarization measurement via quantum logistic map

Existing QKD protocols provide most often the condition to randomly choose photons polarization states measurement bases. This requires the legitimate users to utilize true-random number generators (TRNGs). However, this procedure costs sifting in the key raw and may induces a loss of half in the secure key size. To avoid the problem, other QKD protocols that use quantum pseudo-random number generators (QPRNGs) have been introduced [40, 41, 42]. Using QPRNGs in QKD for photons states measurement bases choice and post-processing procedures can highly improve the secure key security. But, there exist a limited number of QPRNGs. As developed in our previous works [43], chaotic systems have been found to be very efficient for the purpose. This is the reason why in this section we describe in detail the procedure to generate pseudo-random bit sequences (PRBSs) used for photon states polarization bases encoding via quantum logistic map (QLM). Under quantum error corrections, QLM can be assimilated to classical system, where its dynamics is given by [36, 43, 44]:

$$\begin{cases} x_{j+1} = r(x_j - |x_j|^2) - ry_j, \\ y_{j+1} = -y_j e^{-2s} + r e^{-s} [(2 - x_j - x_j^*)y_j - x_j z_j^* - x_j^* z_j], \\ z_{j+1} = -z_j e^{-2s} + r e^{-s} [2(1 - x_j)z_j - 2x_j y_j - x_j], \end{cases} \quad (1)$$

One can observe that, all the values of the variables  $x$ ,  $y$  and  $z$  always belong to the interval  $[0, 1]$  and display period doubling, implying that Eq. (1) displays chaotic behavior, given  $r$  and  $s$  kindly selected such that  $4 \geq r > 3.85$  and  $s \geq 3.5$ . It is important to note that, given real initial conditions, the values of  $x$ ,  $y$  and  $z$  are real too. We notice that, the variables  $x$ ,  $y$  and  $z$  which help to define the set of Eq. (2) are function of the bifurcation parameters  $r$  and  $s$ , which are shared between the communication users before they start running the QKD protocol to provide more security. Whereas, any eavesdropper intending to guess these values will not be able to get the set of Eq. (2), and thus cannot select good bases for photon polarization state measurement. Therefore, system (1) provides an efficient and secure QPRNG for quantum state bases choice in QKD protocols. The procedure to generate these pseudo-random bases choice is described below:

Let  $S$  be a sequence defined by  $S = \{s_k\}_{k=1, \dots, N}$ , with  $s_k = \lceil 1000 * (x_k + y_k + z_k) \rceil \text{mod}(2)$ , which are either 0 or 1, each appearing at random. For example, if  $N = 3000$  then, using system (1), the following sequence is obtained,  $S = \{1111111 \dots 1000110001110111110111011\}$ . Based on the NIST TS<sup>1</sup> randomness test [45], we found a P-value of 0.5347, which is far greater than 0.01 showing that our sequence  $S$  is random with 99.99% confidence. Thus, under the same initial conditions  $x_0, y_0, z_0$

<sup>1</sup> National Institute of Standards and Technology Test Suite

and the same parameters  $r$  and  $s$ , truly random and identical sequences  $S_A$  and  $S_B$  are generated on Alice's and Bob's sides, respectively in order to prepare their random-basis for photon polarization state measurement. For this reason, let  $|\Phi\rangle = \cos(\phi)|0\rangle + \sin(\phi)|1\rangle$ , where  $\{|0\rangle, |1\rangle\}$  is the standard basis. Using the sequences  $S_A$  and  $S_B$ , Alice and Bob can generate the following random sequence bases:

$$B_i = \left\{ |\phi_{s_k^i}\rangle, |\phi_{s_k^i} + \frac{\pi}{2}\rangle \right\}, \quad (2)$$

with  $\phi_{s_k^i} = \frac{s_k^i \pi}{2} 2^{-s_k^i}$ ,  $i = A, B$ , and  $s_k^i$  take its values in  $S_A$  for Alice or  $S_B$  for Bob. It can be observed that, if  $s_k^i = 0$ , then  $\phi_{s_k^i} = 0$  and one get the basis  $\{|0\rangle, |\frac{\pi}{2}\rangle\}$  (rectilinear basis), while for  $s_k^i = 1$ , then  $\phi_{s_k^i} = \frac{\pi}{4}$  and one get the basis  $\{|\frac{\pi}{4}\rangle, |\frac{3\pi}{4}\rangle\}$  (diagonal basis). Therefore, following the sequences  $S_A$  and  $S_B$  obtained respectively by Alice and Bob, the photon state polarization measurement bases are either  $\{|0\rangle, |\frac{\pi}{2}\rangle\}$  or  $\{|\frac{\pi}{4}\rangle, |\frac{3\pi}{4}\rangle\}$  each appearing in a random manner and always coincide for the two legitimate users. Fig.1 illustrates the above described bases rotation:

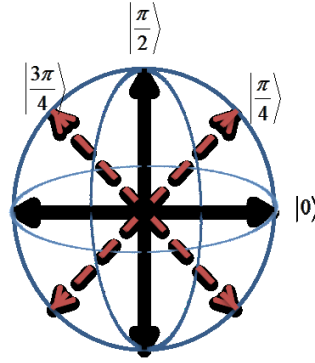


Figure 1: Polarization state measurement pseudo-random rotation bases.

### 3. The combined type-I and type-II spontaneous parametric-down conversion entangled photons pairs source

As previously mentioned, the combined type-I and type-II SPDC is assumed in this work to be the entangled photons pairs generator. It is fully described in our previous works [36], where its degenerated Hamiltonian is derived as:

$$H_I = i\kappa(a_H^\dagger b_H^\dagger + a_V^\dagger b_V^\dagger + a_H^\dagger b_V^\dagger - a_V^\dagger b_H^\dagger) + H.c., \quad (3)$$

with  $\kappa$  describing both the crystal's properties and the field pump amplitude,  $H$  and  $V$  the directions of polarization ( $H$  for horizontal and  $V$  for vertical). Let  $\xi = \kappa t$  the time step, the wave function associated to (3) is derived by:

$$|\Psi\rangle = \frac{1}{\cosh^2(\sqrt{2}|\xi|)} \sum_{n=0}^{\infty} \frac{\xi^*}{|\xi|} \sqrt{(n+1)(\alpha^{2n} + \beta^{2n} + \gamma^{2n} + \vartheta^{2n})} \left( \tanh(\sqrt{2}|\xi|) \right)^n |\Phi_n\rangle, \quad (4)$$

where

$$\begin{aligned} |\Phi_n\rangle = & \frac{1}{(n+1)\sqrt{\alpha^{2n} + \beta^{2n} + \gamma^{2n} + \vartheta^{2n}}} \sum_{k=0}^n [\alpha^n |k, k\rangle_a |n-k, n-k\rangle_b \\ & + \beta^n (-1)^{n-k} |k, n-k\rangle_a |n-k, k\rangle_b \\ & + \gamma^n (-1)^k |(n-k), k\rangle_a |k, n-k\rangle_b \\ & + \vartheta^n |(n-k), n-k\rangle_a |k, k\rangle_b]. \end{aligned} \quad (5)$$

Considering  $P_k$  the density probability to generate  $k$ -entangled photons pairs, we get :

$$P_k = |\langle \Phi_k | \Psi \rangle|^2 = \frac{1}{\cosh^4(\sqrt{2} |\xi|)} (k+1) \tanh^{2k}(\sqrt{2} |\xi|). \quad (6)$$

Letting  $\nu = \sinh^2(\sqrt{2} |\xi|)$ , the photon mean number, which only depends on the light pulse amplitude and the crystal's properties, one obtains:

$$P_k = \frac{\nu^k}{(1+\nu)^{k+2}} (k+1). \quad (7)$$

Fig. 2 presents the comparison between  $P_k$  and Poisson distribution. It can be observed that, the

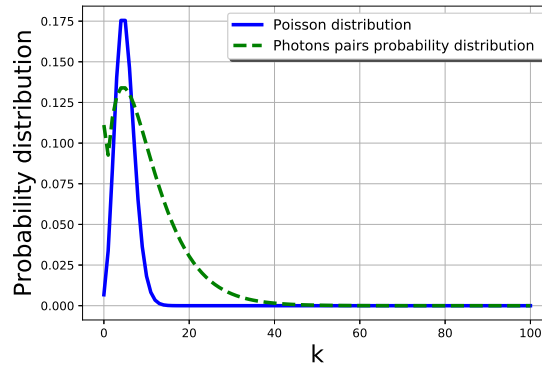


Figure 2: Comparison between the combined type-I and type-II SPDC entangled photons pairs probability density and Poisson distribution.

probability distribution of photons follows Poisson distribution, which implies that the produced photon pairs are non-correlated each to other.

#### 4. Satellite based quantum key transmission with PRB photon polarization state measurement

##### 4.1. Protocol description

As already discussed, we assumed the SPDC-photon source to be located in a LEO-type satellite and emitting a stream of entangled photon pairs directed to the ground by a Cassegrain-type telescope, which are received and redirected to Alice's and Bob's stations installed on the ground, both receiving half of entangled photons pairs. Fig.3 presents the schematic diagram of the process. Here, an entangled photons source located on a satellite emits a stream of entangled photon pairs, directed to the ground by a moving Cassegrain-type telescope. Two other Cassegrain-type telescopes on the ground receive the photons and whatever direction they come from, and send them to the detection apparatus. The Cassegrain-type telescopes are made of pointing mirrors, with the role of ensuring lower change in the photon state polarization. The quantities  $z_1$  and  $z_2$  are respectively the distance between Alice's station and the satellite, and the distance between Bob's station and the satellite respectively, while  $L$  denotes the distance between Alice's and Bob's stations, which will later be considered as the communication distance between both parties.

The strength of the protocol lies on two main fundamental laws of quantum physics namely "*the no-cloning theorem*" and "*the measurement principle*". Based on this idea and assuming that an eavesdropper (Eve) does not have any useful information regarding the characteristics of the QPNG (initial conditions and bifurcation parameters) pre-shared between Alice and Bob, and that is used to encode photons bases, the following steps should therefore be performed to generate the private key:

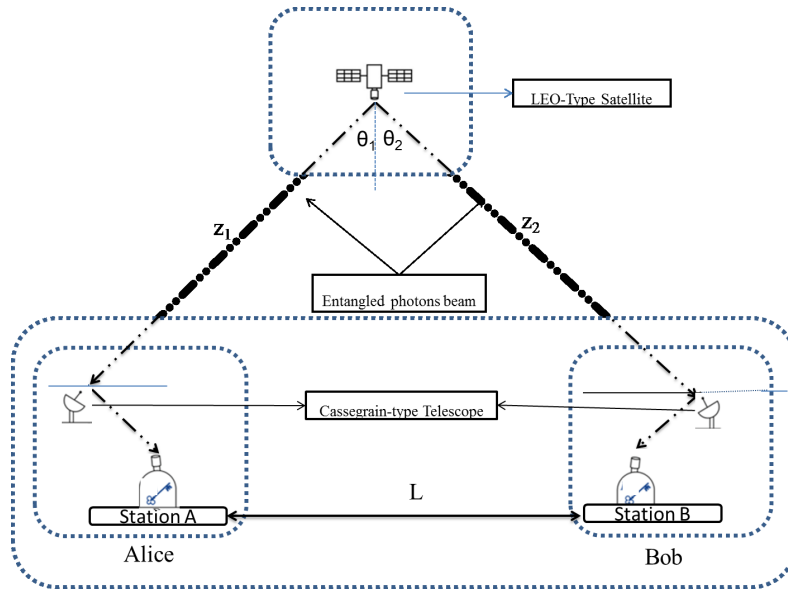


Figure 3: LEO-type satellite based QKD scheme, where each ground station contains a photon detector device, a photon polarization state measurement device and a photon beam splitter as the procedure requires single photon measurement.

**Step 1:** Alice and Bob first agree on the initial conditions ( $x_0$ ,  $y_0$  and  $z_0$ ) and the bifurcation parameters ( $r$  and  $s$ ) of the QLM as presented in Sec. 2.

**Step 2:** Via a SPDC-photon source located in a LEO-type satellite with a launcher commend on Alices possession, she runs the SPDC module and produces a pair of entangled photons at each pulse, which is distributed between her and Bob's stations following the scheme of Fig.3. They also set the value of  $s$  which should be increased by step of  $\epsilon = (s_{max} - s_{min})/N$  in the range of 3.5 to 6 after each pulse as the control parameter.

**Step 3:** They notify each to other after each pulse whether a photon has been detected via classical channel (cellular phone). This step is termed as "information reconciliation", and shall be used for correcting dependencies between Alice's and Bob's key, which may include for example the dependencies arising from errors inflicted by atmosphere diffraction as well as those due to measurements by Eve. In the case, either Alice or Bob does not record a photon detection, they should repeat this step, otherwise, they abort the process.

**Step 4:** After **Step 3** satisfied (i.e. both parties have recorded a photon detection), each party thus runs the QLM module hold in hand and follows the procedure kindly described in Sec. 2 to encode his photon measurement basis, which should be either rectilinear ( $\{|0\rangle, |\frac{\pi}{2}\rangle\}$ ) or diagonal ( $\{|\frac{\pi}{4}\rangle, |\frac{3\pi}{4}\rangle\}$ ) as shown on Fig.1, and perform photon polarization state measurement. It is worth noting that the output result should be identical given the particularity of their measurement bases selection.

**Step 5:** Following the outcome of the basis they obtained in **Step 4**, they perform the measurement on their detected photon to determine the polarization state, which maps bit 0 onto  $90^\circ$ - or  $135^\circ$ -polarization and bit 1 onto  $0^\circ$ - or  $45^\circ$ -polarization.

**Step 6:** Alice and Bob simultaneously increment the value of the control parameter  $s$  with the step of  $\epsilon$ , repeat **Step 2** to **4**. They therefore construct two sequences  $S_A$  for Alice and  $S_B$  for Bob, respectively, which should be identical given that the photons state polarization is not affected by the measurement device. The identical sequences  $S_A$  and  $S_B$  should be only known to Alice and Bob since the photons on which Eve has an information are canceled in **Step 3**.

**Step 7:** In the worse case where Eve may acquire information about the secret key by guessing the measurement basis at each pulse as well as listening to the private information shared during the error reconciliation process, for the sake of reducing this information, the technique of “privacy amplification” is invoked. Explicitly, privacy amplification generates a shorter key from the corrected key of **Step 6**, hence reducing Eve’s information about the shared key.

#### 4.2. Theoretical evaluation of the QBER and the secure key rate

Optical fiber link based QKD systems offer limited communication distance, and thus cannot be applied for long-distance communication, due to attenuation along the fiber. To overcome this drawback, free-space links QKD systems were proposed [24, 43, 46, 47, 48], which uses GEO, MEO or LEO type satellite as relay between the sender (Alice) and the receiver (Bob). Based on this idea, we propose in this section a QKD protocol that uses a LEO-type satellite in which a SPDC entangled photons source is located with the role of producing and distributing entangled photons pairs to Alice and Bob through free-space. It is important to mention that, the almost non-birefringent character of the atmosphere guarantees the preservation of photon pairs polarization state [24, 46, 47]. However, attenuation of photon’s signal is non-negligible due to three main effects, which are: (i) atmospheric propagation, (ii) diffraction and (iii) detector efficiency. As regard to the attenuation due to atmospheric propagation, absorption, scattering and turbulence are the main effects. Thus, atmospheric attenuation can be evaluated taking into consideration the latest effects with the relation:

$$\eta_{atm} = \eta_{abs}\eta_{scatt}\eta_{turb}, \quad (8)$$

with  $\eta_{abs}$ , the attenuation rate due to absorption,  $\eta_{scatt}$  the attenuation rate due to scattering and finally,  $\eta_{turb}$  the attenuation rate due to turbulence. The light is absorbed and scattered by gas molecules and aerosols present in the atmosphere [24, 46, 47]. But, the most relevant contribution to atmospheric propagation attenuation is caused by turbulence, which is due to thermal fluctuations that produce refractive index variations. It is much larger for the uplink than for the downlink. This is caused by the pronounced influence of atmospheric turbulence for the uplink, where the turbulent layers are close to the transmitter. In contrast, for a downlink the effect of the turbulent layer close to the receiver is negligible to first order. It mostly depends on the atmospheric condition and the position of the ground station [47]. It causes divergence rate of the light beam, and is evaluated following the work of Moli-Sanchez *et al.* [47] by:

$$\eta_{turb} = \frac{1}{1 + \frac{\theta_{turb}^2 R_t^2}{\lambda^2}}, \quad (9)$$

with  $\theta_{turb} = \frac{\lambda}{\pi\omega_0}$  the additional divergence angle in radian caused by atmospheric turbulence,  $\lambda$  the signal wavelength,  $R_t$  the radius of the transmitting primary pointing mirror and  $\omega_0$  the beam waist for Gaussian beams. In most of satellite based QKD protocols,  $\eta_{turb}$  is chosen as constant, since it does not depend on the distance satellite-to-ground, but only on atmospheric conditions. It is clear that this relation is similar with that used for uplink, the difference is in the beam waist  $\omega_0$ , which is much smaller for downlinks compared to uplinks. In [49] for example, they considered an empiric formula  $(13/V) * (\lambda/550)^{-q}$ , where V is the visibility to evaluate the atmospheric turbulence for downlinks communication, however, this relation is limited for particular time, while relation (9) is more general.

As regard to signal attenuation due to diffraction, the effect is very important and strongly depends on the satellite-to-ground distance in additional to other telescope’s parameters. The Cassegrain-type telescope is used in the sender’s and receiver’s stations as well as in the satellite to ensure satellite-to-ground downlink transmission. In the present work, we assume such telescope to be used for entangled photons pairs exchange, and also the produced photon beam to be of Gaussian-type [21]. Under these

assumptions, the attenuation rate due to diffraction can be calculated following refs. [21, 50] as:

$$\eta_{diff} = \left[ \exp\left(-2\frac{r_t^2}{\omega_t^2}\right) - \exp\left(-2\frac{R_t^2}{\omega_t^2}\right) \right] \left[ \exp\left(-2\frac{r_{re}^2}{\omega_{re}^2}\right) - \exp\left(-2\frac{R_{re}^2}{\omega_{re}^2}\right) \right], \quad (10)$$

with the subscript  $t$  representing the transmit telescope and  $re$ , the receive one.  $R_{t(re)}$  and  $r_{t(re)}$  refer to the radii of the primary and secondary mirrors, respectively;  $\lambda$  is the light wavelength;  $\omega_{t,re}$  denotes the beam radius at the transmit/receive side, with  $\omega_t = R_t$ ,  $\omega_{re} = \omega(z) = \omega_0 \sqrt{1 + \frac{z^2}{z_R^2}}$ . The quantity  $z_R = \frac{\pi\omega_0^2}{\lambda}$  denotes the so called Rayleigh length or Rayleigh range [51], which is the distance along the propagation direction of the beam from waist to the place where the area of the cross section is doubled.  $z$  is the distance between the telescopes (i.e. the link distance). In satellite based QKD protocols, one has  $z \gg z_R$ , and  $\omega_{re}$  in this case becomes  $\omega_{re} = \frac{\omega_0 z}{z_R} = \frac{\lambda z}{\pi\omega_0}$ , where  $\omega_0$  denotes the minimum value of  $\omega$ .

The telescopes can be also designed as refractors, which is realistic in particular for the transmitter. Eq. (10) is still valid after setting the corresponding value of  $r_{t(re)}$  to zero. The effect of Pointing errors or misalignment of the optics can be readily taken into account by including an additional attenuation term  $\eta_{err}$ , which is constant. Given that the SPDC photon source distributes entangled photons pairs to Alice and Bob situated each to distant stations on the ground, one must define two quantities, namely,  $T_A$  and  $T_B$  representing the overall transmission efficiency on Alice's and Bob's sides respectively as follows:

$$\begin{cases} T_A = \eta_{err} \eta_{atm} \epsilon_A \eta_{diff}^A, \\ T_B = \eta_{err} \eta_{atm} \epsilon_B \eta_{diff}^B, \end{cases} \quad (11)$$

where  $\epsilon_A$  and  $\epsilon_B$  define respectively the detector efficiencies of Alice's and Bob's detectors. From Fig.3 describing the protocol, we have assumed a straight line separating Alice's and Bob's stations by a distance of  $L$ , which can be expressed as a function of  $z_1$ , the distance between Alice's station telescope and the satellite telescope and  $z_2$ , the distance between Bob's station telescope and the satellite telescope as:

$$L = \sqrt{z_1^2 + z_2^2 + 2z_1 z_2 \cos(\theta)}. \quad (12)$$

Inversely, the distances  $z_1$  and  $z_2$  can be expressed as function of  $L$  by:

$$\begin{cases} z_1 = \frac{1}{\cos(\theta_1)} \frac{L}{\tan(\theta_1) + \tan(\theta_2)}, \\ z_2 = \frac{1}{\cos(\theta_2)} \frac{L}{\tan(\theta_1) + \tan(\theta_2)}, \end{cases} \quad (13)$$

In the approximation case (i.e. we assume Alice's and Bob's stations at sea level such that one can have  $z_1 \approx z_2$ ), we also have  $\theta_1 \approx \theta_2 = \frac{\theta}{2}$ , and in this case, we get  $z_1 = z_2 = \frac{L}{\sin(\frac{\theta}{2})}$ . Taking into account the above assumptions, we get the photons transmission efficiencies on Alice's and Bob's sides with respect to the distance  $L$  separating their stations, known as communication distance between legitimate users. Due to the above described phenomena, some photons may thus be lost during the exchanging process and should not be taken into consideration during the secure key extraction process. Below are therefore described in detail the procedure Alice and Bob must perform for the purpose of secure key extraction.

Considering the above relations, the overall transmittance of  $k$ -photons state is defined by:

$$T_k = [1 - (1 - T_A)^k][1 - (1 - T_B)^k] = 1 - (1 - T_A)^k - (1 - T_B)^k + [(1 - T_A)(1 - T_B)]^k, \quad (14)$$

It is important to mention that detection may occur on Bob's and Alice's detectors given zero incoming photon. This is known as dark count in existing QKD protocols. In this case the probability to detect a quantum state given an incoming quantum state, is a conditional probability defined by [52]:

$$\Upsilon_k = [T_k + \Upsilon_{0A} - \Upsilon_{0A} T_k][T_k + \Upsilon_{0B} - \Upsilon_{0B} T_k], \quad (15)$$

with  $\Upsilon_{0A}$  and  $\Upsilon_{0B}$  the dark count probability for the sender's and receiver's detectors, respectively. The overall photon gain can therefore be evaluated as:

$$G_v = \sum_{k=0}^{\infty} P_k \Upsilon_k = 1 + \frac{(1 - \Upsilon_{0A})(1 - \Upsilon_{0B})}{(1 + vT_A + vT_B - vT_A T_B)^2} - \frac{1 - \Upsilon_{0A}}{(1 + vT_A)^2} - \frac{1 - \Upsilon_{0B}}{(1 + vT_B)^2}. \quad (16)$$

During the conversion process into sequence of bits of photons state polarization, an error may occur with probability  $E_0$  due to dark count detection. In addition, due to detector device imperfection, one may also record an error with probability  $E_d$ . Considering both assumptions, an error of detecting  $k$ -photons with probability  $E_k$  may occur given by:

$$E_k = \frac{1}{k+1} \sum_{j=0}^k \left( E_0 - \frac{E_0 - E_d}{\Upsilon_k} \left[ (1 - T_A)^{k-j} - (1 - T_A)^j \right] \left[ (1 - T_B)^{k-j} - (1 - T_B)^j \right] \right). \quad (17)$$

Thus, one can easily evaluate the quantum bit error rate (QBER), which is the probability that detection occurs given erroneous detection as:

$$E_v = \frac{\sum_{k=0}^{\infty} P_k \Upsilon_k E_k}{\sum_{k=0}^{\infty} P_k \Upsilon_k} = E_0 - 2 \frac{E_0 - E_d}{G_v(1+v)} \frac{1}{T_B - T_A} \left( \frac{1 - T_A}{1 + vT_A} - \frac{1 - T_B}{1 + vT_B} \right) - 2 \frac{E_0 - E_d}{G_v(1+v)} \left( \frac{1}{1 - (1 - T_A)(1 - T_B)} + \frac{(1 - T_A)(1 - T_B)(1 - (1 - T_A)(1 - T_B))^{-1}}{1 + v - v(1 - T_A)(1 - T_B)} \right). \quad (18)$$

Analogically to the procedure described in [36], the secure key rate can be derived as:

$$R_n = \frac{1}{N} (NG_v(1 - H_2(E_v + \mu_n)) - K_{\text{leak}} - K_{\text{secure}}), \quad (19)$$

where,

$$K_{\text{secure}} = -\log\left(\frac{2}{\epsilon_{\text{sec}}^2 \epsilon_{\text{co}}}\right), \quad K_{\text{leak}} = NG_v f(E_v) H_2(E_v), \quad (20)$$

with  $\mu_n$  the statistical fluctuation known as the maximum optical tolerable noise defined as,

$\mu = \sqrt{\left(\frac{1}{N} + \frac{1}{n}\right)\left(1 + \frac{1}{n}\right)\log\left(\frac{2}{\epsilon_{\text{sec}}}\right)}$ ,  $N$  the photon pairs block size produced and  $n$  the number of photon pairs involved in the key generation. The terms  $K_{\text{leak}}$  and  $K_{\text{secure}}$  refer to the error correction leakage (i.e. the number of bits published during error correction with the error correction efficiency function  $f(E_v)$ ) and the security bound respectively, with  $\epsilon_{\text{co}}$  introducing the upper bound of secret key correctness probability. This implies that if  $S_A$  and  $S_B$  are the sender's and receiver's secret key respectively, then the protocol is known to be  $\epsilon_{\text{co}}$ -correct providing that  $\text{Probability}(S_A \neq S_B) \leq \epsilon_{\text{co}}$ . In the other words,  $\epsilon_{\text{co}}$  introduces the probability of error induced measurement bases authentication.  $\epsilon_{\text{sec}}$  introduces the upper bound of secret key secrecy probability. It is more smaller in this protocol since public discussion is avoided due to the use of QPRNG instead of TRNG for measurement bases choice, which guarantees identical measurement bases selection for Alice and Bob. The function  $H_2(e) = -e \log_2(e) - (1 - e) \log_2(1 - e)$  defines the binary Shannon entropy.

## 5. Numerical results and discussions

In this section, we numerically present the main results of this research paper. All simulations in this section are subject to the following parameters: wavelength  $\lambda = 650\text{nm}$ , with the telescopes' radii,

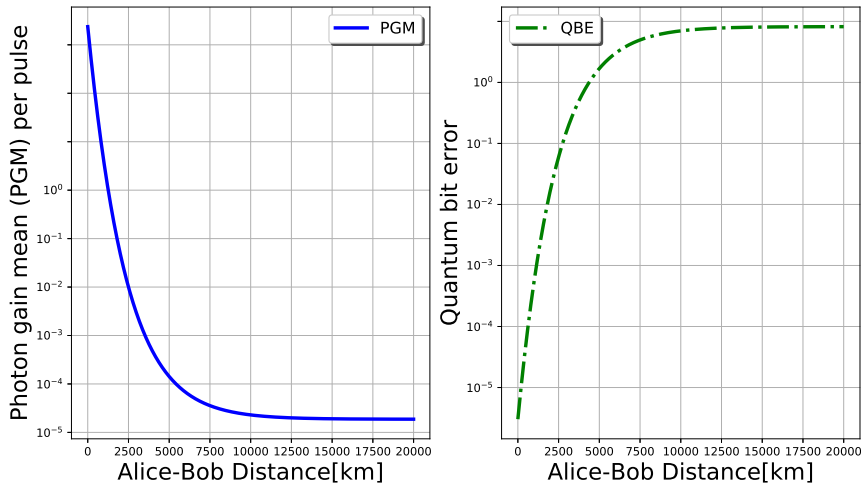


Figure 4: quantum bit error (QBE) and photon gain mean (PGM) per pulse with respect to the communication link distance between Alice's and Bob's stations, taking  $E_0 = 0.5$ ,  $E_d = 0.015$ ,  $\eta_A = \eta_B = 0.9$ ,  $\Upsilon_{0A} = \Upsilon_{0B} = 5.50 \times 10^{-5}$ ,  $\nu = 0.373$ , and with a maximum tolerable atmospheric link loss of  $2 \times 10^{-4} \text{ dB/km}$ ,  $\epsilon_{co} = \epsilon_{sec} = 10^{-14}$ .

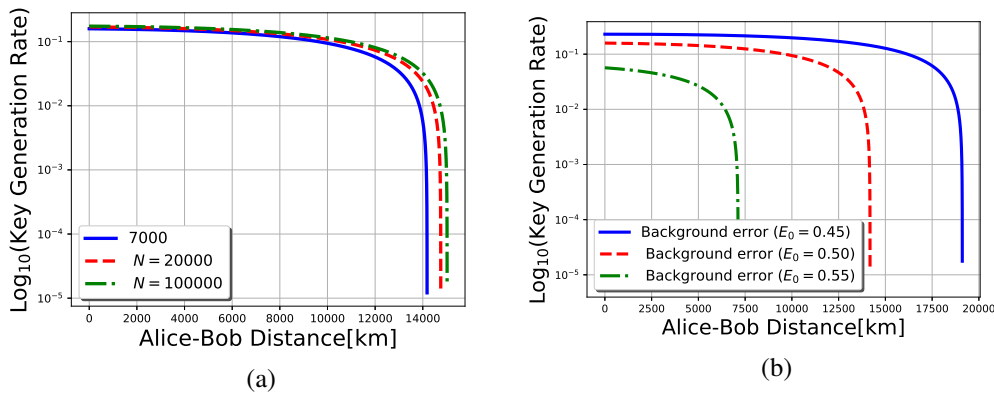


Figure 5: The secure key rate as function of  $N$ , the maximum photon block size (fig.5a) and the background error  $E_0$  due to atmosphere diffraction (fig.5b) both with respect to the communication distance ( $L$ ) separating Alice's and Bob's stations, considering the following parameters,  $E_d = 0.015$ ,  $\eta_A = \eta_B = 0.9$ ,  $\Upsilon_{0A} = \Upsilon_{0B} = 5.50 \times 10^{-5}$ , with a maximum tolerable atmospheric link loss of  $2 \times 10^{-4} \text{ dB/km}$ ,  $n = 4 \times 10^3$ ,  $\epsilon_{co} = \epsilon_{sec} = 10^{-14}$ .

$r_t = 10 \text{ mm}$ ,  $R_t = 20 \text{ mm}$ ,  $r_{re} = 0.01 \text{ mm}$ ,  $R_{re} = 2 \text{ m}$ , and  $\omega_0 = 2 \text{ mm}$ . For this reason, the photon gain mean (PGM) and the quantum bit error (QBE) are simulated with respect to the communication distance separating Alice's and Bob's stations on one hand and the results are depicted in fig.4.

It can be observed that the PGM decreases asymptotically and very fast with almost a similar speed as the QBE increases, confirming the predicted effects of noises and atmosphere diffraction on photon transfer. On the other hand, fig.5 and 6 plot the secure key generation rate with respect to the communication distance between Alice's and Bob's stations as function of the maximum photon block size (fig.5a), the background error due to atmosphere diffraction (fig.5b), the security parameter

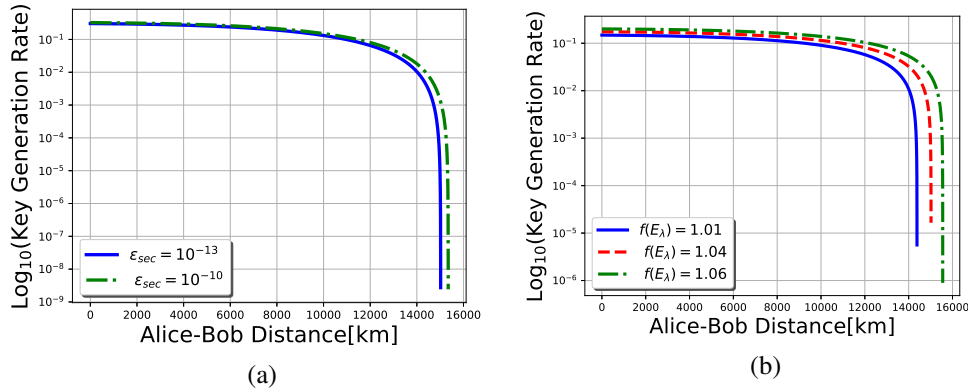


Figure 6: The secure key rate as function of ( $\epsilon_{sec}$ ), the security parameter (fig.6a) and the error cost function ( $f(E_\lambda)$ ) due to key authentication (fig.6b) both with respect to the communication distance ( $L$ ) separating Alice's and Bob's stations, considering the following parameters,  $E_0 = 0.5$ ,  $E_d = 0.015$ ,  $\eta_A = \eta_B = 0.9$ ,  $\Upsilon_{0A} = \Upsilon_{0B} = 5.50 \times 10^{-5}$ , under a maximum tolerable atmospheric link loss  $2 \times 10^{-4} dB/km$ , with  $N = 10^4$  and  $n = 4 \times 10^3$ ,  $\epsilon_{co} = 10^{-14}$ .

$\epsilon_{sec}$  (fig.6a) and the error cost function (fig.6b). The first observations lead to conclude that, with this protocol we could be able to achieve very long distance communication, since it is observed that the protocol can tolerate up to about 19000 km under lower atmosphere diffraction ( $E_0 = 0.45$ ) as the communication distance between Alice and Bob, while for high background error ( $E_0 = 0.55$ ), the maximum communication distance is not much significant (about 7400 km). However, most of protocols whose maximum communication distances are even less than 10000 km usually considered as background error  $E_0 = 0.5$  [53, 54], and with this value it is observed that we can reach more than 14000 km with our protocol. This achievement holds under an atmosphere rate lost of about  $10^{-4} dB/km$  compared to  $10^{-6} dB/km$  used in existing works and we also realize that the secure key rate remains very close to 1 for long distance before decreasing quickly. In addition, as far as the photon block size sent is high, the maximum communication distance increases showing that, the protocol is robust against noise if high amount of photon can be produced from the SPDC. Similar conclusion was provided by Chun-Hui *et al.* [55]. The latest point justify the efficiency of the combined type-I and type-II SPDC photon source compared to type-I or type-II photon source separately, since it help to improve the photon block size. Fig.5b shows that the communication distance significantly improves under noiseless down-link QKD conditions. Furthermore, fig.6b clearly explains the predicted effects of error correction on the key raw length as it consists of removing from the key those bits that do not coincide, thus reducing the length of the key. These results are very similar to those found by Mizutani *et al.* [56]. It turnout therefore that, our protocol provides efficient secure key since it can tolerate very long secure communication between legitimate users. Finally, the upper bound of the secure key rate remains very closer to 1 for very long distance inducing high secure key size compared to that of existing protocols.

## 6. Concluding remarks

The present research paper was aimed at providing new strategies to achieve long-distance and secure communication using satellite based QKD. For this reason, we proposed a new protocol, namely the pseudo-random bases entangled photons based QKD (PRB-EPQKD) protocol. The originality of the protocol is due to the use of the combined type-I and type-II SPDC-entangled photon pairs source, located in a LEO-type satellite instead of the type-I or type-II separately on one hand. On the second hand, the legitimate communication users prepared pseudo-random bases for entangled photon pairs polarization state measurement using the QLM as QPRNG. The steps for secure key generation have been provided

in detail, the QBER and the secure key rate were evaluated as well. Numerical simulations showed that, the protocol can provide high secure communication between legitimate users and the maximum communication distance has been improved significantly, since we can observe that the protocol can tolerate up to about 19000 km under lower atmosphere diffraction ( $E_0 = 0.45$ ) as the communication distance between Alice and Bob. However, most protocols whose maximum communication distances are even less than 10000 km usually considered as background error  $E_0 = 0.5$  [24, 54, 57], and with this value it is observed that we can reach more than 14000 km with our protocol, which is very high compared to a maximum of 1000 km in the case of optical link QKD. Furthermore, we realized that, with our protocol the secure key rate upper bound is strongly enhanced since public discussion that is usually performed in other protocols for key authentication is avoided, which induced the improvement of the secure key size.

## References

- [1] Časlav Brukner, Marek Żukowski, and Anton Zeilinger. Quantum communication complexity protocol with two entangled qutrits. *Phys. Rev. Lett.*, 89(19):197901, 2002.
- [2] Nicolai Friis, Marcus Huber, Ivette Fuentes, and David Edward Bruschi. Quantum gates and multipartite entanglement resonances realized by nonuniform cavity motion. *Phys. Rev. D*, 86(10):105003, 2012.
- [3] Kiyoshi Tamaki, Hoi-Kwong Lo, Akihiro Mizutani, Go Kato, Charles Ci Wen Lim, Koji Azuma, and Marcos Curty. Security of quantum key distribution with iterative sifting. *Quantum Science and Technology*, 3(1):014002, 2017.
- [4] Alexander V Sergienko. *Quantum communications and cryptography*. CRC press, 2018.
- [5] Monika Jacak, Janusz Jacak, Piotr Józwiak, and Ireneusz Józwiak. Quantum cryptography: Theoretical protocols for quantum key distribution and tests of selected commercial qkd systems in commercial fiber networks. *International Journal of Quantum Information*, 14(02):1630002, 2016.
- [6] Charles H Bennett and Gilles Brassard. Quantum cryptography: public key distribution and coin tossing. *Theor. Comput. Sci.*, 560(12):7–11, 2014.
- [7] Artur K Ekert. Quantum cryptography based on Bell's theorem. *Phys. Rev. Lett.*, 67(6):661, 1991.
- [8] Charles H Bennett, François Bessette, Gilles Brassard, Louis Salvail, and John Smolin. Experimental quantum cryptography. *J. Cryptol.*, 5(1):3–28, 1992.
- [9] Helle Bechmann-Pasquinucci and Nicolas Gisin. Incoherent and coherent eavesdropping in the six-state protocol of quantum cryptography. *Phys. Rev. A*, 59(6):4238, 1999.
- [10] Li Jun-Lin and Wang Chuan. Six-state quantum key distribution using photons with orbital angular momentum. *Chin. Phys. Lett.*, 27(11):110303, 2010.
- [11] Gan Gao, Chang-Cheng Wei, and Dong Wang. Cryptanalysis and improvement of dynamic quantum secret sharing protocol based on two-particle transform of Bell states. *Quantum Inf. Process.*, 18(6):186, 2019.
- [12] Sha-Sha Wang, Dong-Huan Jiang, Guang-Bao Xu, Yong-Hua Zhang, and Xiang-Qian Liang. Quantum key agreement with Bell states and Cluster states under collective noise channels. *Quantum Inf. Process.*, 18(6):190, 2019.
- [13] Martin Tchoffo and Alain Giresse Tene. Entanglement dynamics of a two-qubit xyz spin chain under both dzyaloshinskii-moriya interaction and time-dependent anisotropic magnetic field. *International Journal of Theoretical Physics*, pages 1–17, 2020.
- [14] Xiongfeng Ma. Quantum cryptography: theory and practice. *arXiv preprint arXiv:0808.1385*, 2008.
- [15] Qinyu Xue and Rongzhen Jiao. The performance of reference-frame-independent measurement-device-independent quantum key distribution. *Quantum Inf. Process.*, 18(10):313, 2019.
- [16] Robert Bedington, Juan Miguel Arrazola, and Alexander Ling. Progress in satellite quantum key distribution. *Npj Quantum Inf.*, 3(1):1–13, 2017.
- [17] Stefano Pirandola, Riccardo Laurenza, Carlo Ottaviani, and Leonardo Banchi. Fundamental limits of repeaterless quantum communications. *Nat. Commun.*, 8:15043, 2017.
- [18] Yoshiaki Tamura, Hirotaka Sakuma, Keisei Morita, et al. Lowest-ever 0.1419-dB/km loss optical fiber. In *Optical Fiber Communication Conference*, pages Th5D–1. Optical Society of America, 2017.
- [19] Wiley J Larson and James Richard Wertz. Space mission analysis and design. Technical report, Torrance, CA (United States); Microcosm, Inc., 1992.
- [20] Juan Yin, Yuan Cao, Yu-Huai Li, et al. Satellite-to-ground entanglement-based quantum key distribution. *Phys. Rev. Lett.*, 119(20):200501, 2017.
- [21] Vishal Sharma and Subhashish Banerjee. Analysis of atmospheric effects on satellite-based quantum communication: a comparative study. *Quantum Inf. Process.*, 18(3):67, 2019.
- [22] Giuseppe Vallone, Davide Bacco, Daniele Dequal, et al. Experimental satellite quantum communications. *Phys. Rev. Lett.*, 115(4):040502, 2015.
- [23] Nedasadat Hosseinidehaj, Zunaira Babar, Robert Malaney, Soon Xin Ng, and Lajos Hanzo. Satellite-based continuous-

- variable quantum communications: state-of-the-art and a predictive outlook. *IEEE Commun. Surv. Tut.*, 21(1):881–919, 2018.
- [24] Ahmed Ismael Khaleel and Shelan Khasro Tawfeeq. Key rate estimation of measurement-device-independent quantum key distribution protocol in satellite-earth and intersatellite links. *International Journal of Quantum Information*, 16(03):1850027, 2018.
- [25] Jian-Yu Wang, Bin Yang, Sheng-Kai Liao, et al. Direct and full-scale experimental verifications towards ground–satellite quantum key distribution. *Nat. Photonics*, 7(5):387, 2013.
- [26] Pan Jianwei. Quantum science satellite. *Chinese Journal of Space Science*, 34:547, 2014.
- [27] Juan Yin, Yuan Cao, Shu-Bin Liu, et al. Experimental quasi-single-photon transmission from satellite to earth. *Optics Express*, 21(17):20032–20040, 2013.
- [28] Sebastian Nauerth, Florian Moll, Markus Rau, et al. Air-to-ground quantum communication. *Nat. Photonics*, 7(5):382, 2013.
- [29] Hideki Takenaka, Alberto Carrasco-Casado, Mikio Fujiwara, et al. Satellite-to-ground quantum-limited communication using a 50-kg-class microsatellite. *Nat. Photonics*, 11(8):502, 2017.
- [30] Heasin Ko, Kap-Joong Kim, Joong-Seon Choe, et al. Experimental filtering effect on the daylight operation of a free-space quantum key distribution. *Scientific Reports*, 8(1):15315, 2018.
- [31] Sebastian Philipp Neumann, Siddarth Koduru Joshi, Matthias Fink, et al. Quantum communication uplink to a 3U CubeSat: Feasibility & design. *arXiv preprint arXiv:1711.03409*, 2017.
- [32] Yun-Hong Gong, Kui-Xing Yang, Hai-Lin Yong, et al. Free-space quantum key distribution in urban daylight with the SPGD algorithm control of a deformable mirror. *Optics Express*, 26(15):18897–18905, 2018.
- [33] Sheng-Kai Liao, Hai-Lin Yong, Chang Liu, et al. Long-distance free-space quantum key distribution in daylight towards inter-satellite communication. *Nat. Photonics*, 11(8):509, 2017.
- [34] Matthew P Peloso, Ilja Gerhardt, Caleb Ho, et al. Daylight operation of a free space, entanglement-based quantum key distribution system. *New J. Phys.*, 11(4):045007, 2009.
- [35] Erik Kerstel, Arnaud Gardelein, Mathieu Barthelemy, et al. Nanobob: a CubeSat mission concept for quantum communication experiments in an uplink configuration. *EPJ Quantum Technol.*, 5(1):6, 2018.
- [36] M Tchoffo and AG Tene. Privacy amplification of entanglement parametric-down conversion based quantum key distribution via quantum logistic map for photon bases choice. *Chaos, Solitons & Fractals*, 140:110110, 2020.
- [37] Alain Giresse Tene and Timoleon Crépin Kofane. Chaos generalized synchronization of coupled mathieu-van der pol and coupled duffing-van der pol systems using fractional order-derivative. *Chaos Soliton Fract.*, 98:88–100, 2017.
- [38] Alain Giresse Tene and Timoleon Crépin Kofane. Novel cryptography technique via chaos synchronization of fractional-order derivative systems. In *Advanced Synchronization Control and Bifurcation of Chaotic Fractional-Order Systems*, pages 404–437. IGI Global, 2018.
- [39] ME Goggin, B Sundaram, and PW Milonni. Quantum logistic map. *Phys. Rev. A*, 41(10):5705, 1990.
- [40] AS Trushechkin, PA Tregubov, EO Kiktenko, et al. Quantum-key-distribution protocol with pseudorandom bases. *Phys. Rev. A*, 97(1):012311, 2018.
- [41] Valerio Scarani, Antonio Acin, Grégoire Ribordy, and Nicolas Gisin. Quantum cryptography protocols robust against photon number splitting attacks for weak laser pulse implementations. *Phys. Rev. Lett.*, 92(5):057901, 2004.
- [42] Zhantong Qi, Cong Du, Xiaojuan Qin, Jindong Wang, Zhengjun Wei, and Zhiming Zhang. Improvement of the safe transmission distance via optimization of the photon number distribution for the faint optical pulse in practical quantum key distribution systems. *The European Physical Journal D*, 73(8):161, 2019.
- [43] Martin Tchoffo and Alain Giresse Tene. Security and communication distance improvement in decoy states based quantum key distribution using pseudo-random bases choice for photon polarization measurement. *Optical and Quantum Electronics*, 53(8):1–24, 2021.
- [44] A Akhshani, A Akhavan, A Mobaraki, et al. Pseudo random number generator based on quantum chaotic map. *Commun. Nonlinear Sci. Numer. Simul.*, 19(1):101–111, 2014.
- [45] Andrew Rukhin, Juan Soto, James Nechvatal, et al. A statistical test suite for random and pseudorandom number generators for cryptographic applications. Technical report, Booz-Allen and Hamilton Inc Mclean Va, 2001.
- [46] S Ali and MRB Wahiddin. Fiber and free-space practical decoy state QKD for both BB84 and SARG04 protocols. *Eur. Phys. J. D*, 60(2):405–410, 2010.
- [47] L Moli-Sanchez, A Rodriguez-Alonso, and Gonzalo Seco-Granados. Performance analysis of quantum cryptography protocols in optical earth-satellite and intersatellite links. *IEEE Journal on Selected Areas in Communications*, 27(9):1582–1590, 2009.
- [48] Gláucia Murta, Suzanne B van Dam, Jérémy Ribeiro, Ronald Hanson, and Stephanie Wehner. Towards a realization of device-independent quantum key distribution. *Quantum Science and Technology*, 4(3):035011, 2019.
- [49] Xiaorui Wang, Guo Lei, Liu Yejun, and Zhang Lincong. Analysis of atmosphere channel for space-to-ground optical communications. *Optics Communications*, (306):42–48, 2013.
- [50] Saikat Guha, Hari Krovi, Christopher A Fuchs, Zachary Dutton, Joshua A Slater, Christoph Simon, and Wolfgang Tittel. Rate-loss analysis of an efficient quantum repeater architecture. *Phys. Rev. A*, 92(2):022357, 2015.

- 
- [51] Pavel Penchev, Stefan Dimov, and Debajyoti Bhaduri. Experimental investigation of 3D scanheads for laser micro-processing. *Optics & Laser Technology*, 81:55–59, 2016.
- [52] Kyongchun Lim, Heasin Ko, Changho Suh, and June-Koo Kevin Rhee. Security analysis of quantum key distribution on passive optical networks. *Optics express*, 25(10):11894–11909, 2017.
- [53] Cristian Bonato, Andrea Tomaello, Vania Da Deppo, et al. Feasibility of satellite quantum key distribution. *New J. Phys.*, 11(4):045017, 2009.
- [54] Paul Jouguet, Sébastien Kunz-Jacques, Anthony Leverrier, Philippe Grangier, and Eleni Diamanti. Experimental demonstration of long-distance continuous-variable quantum key distribution. *Nature photonics*, 7(5):378, 2013.
- [55] Chun-Hui Zhang, Chun-Mei Zhang, and Qin Wang. Improving the performance of practical decoy-state measurement-device-independent quantum key distribution with biased basis choice. *Commun. Theor. Phys.*, 70(3):331, 2018.
- [56] Akihiro Mizutani, Marcos Curty, Charles Ci Wen Lim, et al. Finite-key security analysis of quantum key distribution with imperfect light sources. *New J. Phys.*, 17(9):093011, 2015.
- [57] Yi-Bo Zhao, Wan-Li Zhang, Dong Wang, Xiao-Tian Song, Liang-Jiang Zhou, and Chi-Biao Ding. Proof-of-principle experimental demonstration of quantum secure imaging based on quantum key distribution. *Chinese Physics B*, 28(10):104203, 2019.

# Direct-coupled photovoltaic water pumping system sizing using borehole hydraulic parameters

L. Masevhe<sup>1</sup> and N.E. Maluta<sup>1,2\*</sup>

<sup>1</sup>University of Venda, Department of Physics, Private Bag X5050, Thohoyandou, 0950, South Africa

<sup>2</sup>National Institute for Theoretical Physics (NITheP), Braamfontein, Johannesburg, 2000, South Africa

Email: [livhuw1m@gmail.com](mailto:livhuw1m@gmail.com)

**Abstract.** Photovoltaic water pumping systems (PVWPS) are a promising solution to improve water access in isolated rural areas in developing countries. Each system must be carefully sized to satisfy local demand while being as affordable as possible. In order to design a successful and sustainable system, the knowledge of solar radiation and groundwater resources availability is crucial. There are several steps that are followed to size and model a PVWPS. The current study used the borehole and solar radiation characteristics at Vuwani Science Resource Centre to determine the suitable pump and the size of the PV power system for a sustainable battery-less pumping of groundwater without depletion. The hydraulic characteristics, optimal flow-rate of 69.12 m<sup>3</sup> /day and total dynamic head of 53 m were used as inputs for the sizing of the pump. Grundfos on-line software was used to validate the sizing of a proper submersible water pump that can supply the water needs. With the electrical load of the system known, the Microsoft Excel program was used to design a complete system which is customised to the site and borehole characteristics. . The proposed system consists of a PV, a submersible pump and storage tank. A system controller was also designed and analysed successfully.

## 1. Introduction

A direct-coupled photovoltaic water pumping systems (PVWPS) is one of the simplest methods which connect the pump direct to the PV array power converter without using batteries. The battery-less PVWPS is preferred for the fast recovery of investment in order to reduce the total system costs. Because the proposed system in this study has no battery to store the energy for later use, it stores the energy in the form of water in the tank to be used when the sun is not shining. Figure 1 shows block-diagram of the system consists of solar array, controller, DC submersible pump and water tank. As compared to AC drive which can be recovered in 8 years, DC drive can be recovered in 2.5 years [1]. Direct-coupled system provides both technically and economically feasible solutions. Unlike grid-tied, the system in this study is beneficial in remote and rural areas with no or limited access to electricity. The system functions by utilising the DC power generated from the solar array.

A properly designed system requires the sizing of individual components and the performance by using computer simulation to check the effect of climatic conditions on the peak power. Over- and under-design of the system should be avoided at all costs because it becomes expensive over time [3]. One of the common PVWPS challenges is the unsustainable wells which dry-up quickly if proper assessment of the available groundwater is not conducted. Sustainability of the system can be achieved by groundwater recharge-discharge rate balance through a well testing. This balance is a key factor for the determination of the suitable optimal pumping rate leading to a long life-cycle of the system. The current study is conceptualized for a sustainable system which is informed by the location characteristics. The idea is to design a system customised to the project site's groundwater availability and the climatic parameters like the temperature and solar irradiation.

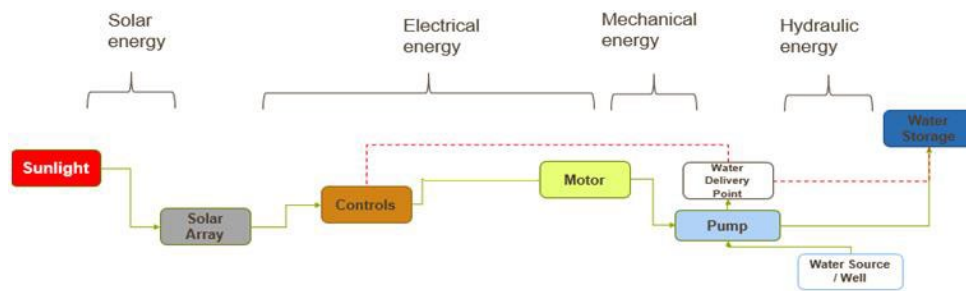


**Figure 1.** Block diagram of a direct-coupled PVWPS. [2]

The solar pumps available in the market can pump water from 5 m to over 200 m with outputs up to 250 m<sup>3</sup>/day, being used in boreholes of 15 to 50 m of depth [4]. Most of the PVWPS have a water reservoir. The capacity of water reservoir (system autonomy) is determined by the type of supply (domestic, animal, and irrigation) and the financial constraints of the investor [5]. In order to ensure that the water supply service is not impaired during periods of low or absent solar irradiance, the presence of a reservoir is of great importance, and require an analysis of the stochastic nature of the energy resource, flow and periods needs to meet the full demand [6]. However, the water source must recharge the reservoir faster than the water pumping rate, avoiding a reservoir drought as it could damage the pump. The purpose of this study was to size and analyse a solar water pumping system which is customised to the borehole characteristics and the local climatic conditions. This multi-stage method includes the well and aquifer losses in order to calculate the hydraulic head. Adding to the head and flow rate, the method combines the effect of temperature and solar radiation on the peak power to be generated based on these parameters

## 2. Methodology

### 2.1 System model

The sizing process of the system is to ensure that the groundwater in the well is sustainable and its exploitation matches the discharge-recharge rate [7]. This process is considered based on the parameters such as the pump power matching the site characteristics (depth of the wheel, hydraulic loop, and design flow rate), capacity of solar PV power, the running conditions and the reservoir dimensions [7]. The MATLAB simulations based on the design phase outputs are performed to evaluate the effects of climatic conditions and hydraulic parameters on the peak power of the system. The use of simulation programs allows solving problems of design and optimization of the PV systems [8]. The block diagram of the energy conversion model is presented in Figure 2. The model is the depiction of an automated system which has a control system that is responsible for the “start/stop” of the pump whenever the water level in the storage tank is either maximum or minimum. The blue line (arrows), red and purple represent the direction of the pumped water, power generated and communication lines, respectively. The pump runs when the water level in the tank reaches the lower pre-set value and stops when the water level reaches the highest pre-set value. Detailed methodology is presented to achieve an adequate design of the proposed PVWP system utilized for irrigation purposes.

### 2.2 Data collection

The proposed system is based on the local solar irradiation and groundwater characteristics at Vuwani location in the Limpopo Province, South Africa. Two sets of data were collected from the research and used as inputs to the sizing process and pump selection exercise. Figures 3 and 4 show the weather data collected from the study site and the well characteristics to be used for the sizing process. Figure 3 shows the graph of average temperature and solar irradiation data collected through USAid Venda (located at latitude: -23.13100052, longitude: 30.42399979 [9]), one of the South African Universities Radiometric Network (SAURAN) stations. The data was collected between 2018 and 2022, and shows that the lowest solar irradiation of 1231.63 Wh/day and the highest solar irradiation 1953.60 Wh/day were observed in June and February, respectively.

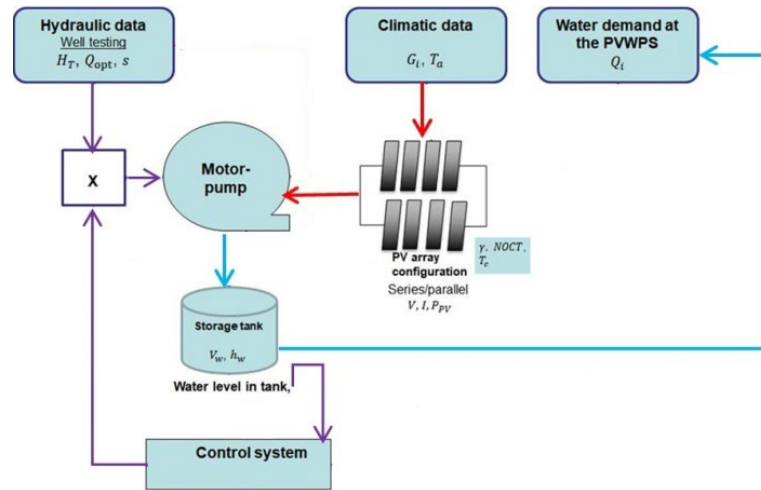


Figure 2. Operation model of the PV water pumping system.

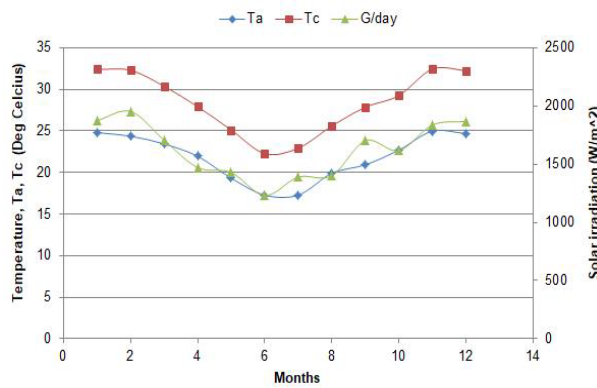


Figure 3. Four-years monthly average solar irradiation (green), ambient temperature (blue) and cell temperature (red) at Vuwani Science Resource Centre.

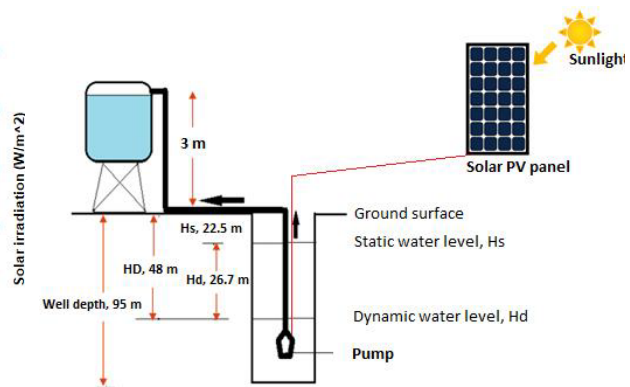


Figure 4. Adapted PV water pumping system with the hydraulic data from a well testing study.

The system was designed to meet the worst-case combination of solar radiation energy and water demand [10] which according to Figure 3 is in June. Figure 4 shows the well characteristics which was conducted to determine optimum pumping rate and total head through both the aquifer and the well losses. There are two fundamental hydraulic parameters that can be deduced from the information in the figure, i.e. total dynamic head and flow rate. The well characteristics show that the optimum flow-rate of 69.12 m<sup>3</sup>/day is required to determine the peak power of the pump which is placed at the total dynamic head of 53 m. The pump should be adjusted to pump the water at this optimum flow-rate to ensure that the well is sustained.

### 2.3 Sizing of the components of the system

A basic power calculation is provided below for the design of a solar DC pump for the required capacity. With an average discharge rate of 2880 m<sup>3</sup>/hour at the hydraulic head of 53 m in Figure 4, the pump's required hydraulic power ( $P_h$ ) is estimated and the electric power needed to run the pump ( $P_{MP}$ ) is expressed as equation 1 [11]:

$$P_{MP} = \frac{P_h}{\eta_{MP}} \tag{1}$$

where  $P_h$  is the hydraulic power ( $= \rho g Q H_T / 3600 = 2.72 Q H_T$ ),  $\rho$  is the water density ( $1000 \text{ kg/m}^3$ ),  $g$  is the acceleration due to gravity ( $9.8 \text{ m/s}^2$ ) and  $\eta_{MP}$ , efficiency of pump (60 %) is also taken into consideration [12]. Once the total dynamic head ( $H_T$ ) and the flow rate ( $Q$ ) of water and the borehole characteristics. The power required to run the given pump was produced from the solar panels with the total peak power ( $P_p$ ) based on the daily irradiance ( $G_{dm}$ ) and the performance ratio of the panels ( $\alpha$ ) dependent on the installation conditions is given by equation 2 [13]

$$P_p = \frac{P_{MP}}{\alpha \times G_{dm}}. \quad (2)$$

The value of  $P_p$  calculated in equation (2) is then used to determine the required total number and the unit power of the panels which vary depending on the voltage necessary for the operation of the pump. The number of panels multiplied by the unit power will give the total power supplied. The number of solar panels required to satisfy given estimated daily load is shown in equation (3) [14] as

$$N_{PV} = \frac{P_p}{P_{max}} \quad (3)$$

where  $P_{max}$  is the maximum power the solar panel can produce.

#### 2.4 Simulations with MATLAB

To calculate the power peak of the array, the output power of a photovoltaic generator under standard condition of measurements which are solar irradiance ( $G_{ref}=1000 \text{ W/m}^2$ ) and cell temperature ( $T_{ref} = 25^\circ\text{C}$ ) were used. The peak power ( $P_p$ ) that must be generated based on the water demand was calculated in equation (3) [12] below:

$$P_p = \frac{2.72}{f_m \times G_{dm} [1 - \gamma \times (T_c - T_{ref})] \times \eta_{PV}} \times Q \times H_T \quad (4)$$

where  $\eta_{PV}$  and  $f_m$  is the daily average efficiency of the generation in exploitation conditions and panel mismatch factor. The  $\gamma$  is the temperature coefficient of the cell, for monocrystalline module, it ranges from 0.004 to 0.005  $^\circ\text{C}$ . For polycrystalline silicon module, it ranges from 0.001 to 0.002  $^\circ\text{C}$  [12].  $G_T$  is the daily average irradiation on the module plane ( $\text{Wh/m}^2/\text{day}$ ) and  $T_c$  is the daily average cell temperature of the panel and expressed in equation (5)

$$T_c = T_a \left( \frac{NOCT - 20}{80} \right) \times G_T \quad (5)$$

### 3. Results and discussion

#### 3.1 Sizing

Based on the well characteristics as indicated in Figure 4, the optimal pumping rate of  $69.12 \text{ m}^3/\text{day}$  at the head of 53.00 m, the sizing of the sustainable system which fits these parameters is presented in Table 1. The calculated daily required electricity to power a pump which is capable of pumping the water at a given rate was used to select the right pump. The pump needs 6 solar panels with 255 W each to guarantee the desired flow. The results also indicated that the required capacity of the water tank is  $207.36 \text{ m}^3$ , which allows autonomy for three consecutive days.

Given the daily pumping rate at the given head, Figure 5 show the H-Q curve (pumping curve) was generated from the manufacturer, Grundfos online tool to select the pump [14]. A Grundfos SP3A-15 stainless-steel pump matched the sizing requirements of pumping the water from the well at a rate of  $2880 \text{ m}^3/\text{hour}$  at 53 m total dynamic head. The pump power peak of 1359.00 W was found to be very close to the calculated (sizing) peak power of 1348.45 W as indicated in Table 1. This pump is able to meet the desired pump rate of  $69.12 \text{ m}^3/\text{day}$  without depleting the groundwater in the well.

**Table 1: PVWPS sizing results**

Well characteristics		Pump sizing		PV panel sizing	
Parameter	value	Parameter	value	Parameter	value
$H_T$ (m):	53.00	Type:	*DC-Subm	Type:	Poly-Si
$H_h$ (m):	95.00	$P_{PM}$ (kWh/d):	16.95	$P_p$ (kW):	1.35
Drawdown (m):	26.70	$P_p$ (kW):	3.39	PV stand:	Fixed @ 45°
$Q$ (L/h):	2884	-	-	No. of panels:	5.6 ≈ 6 (in series series)

\* DC Sumersible pump.

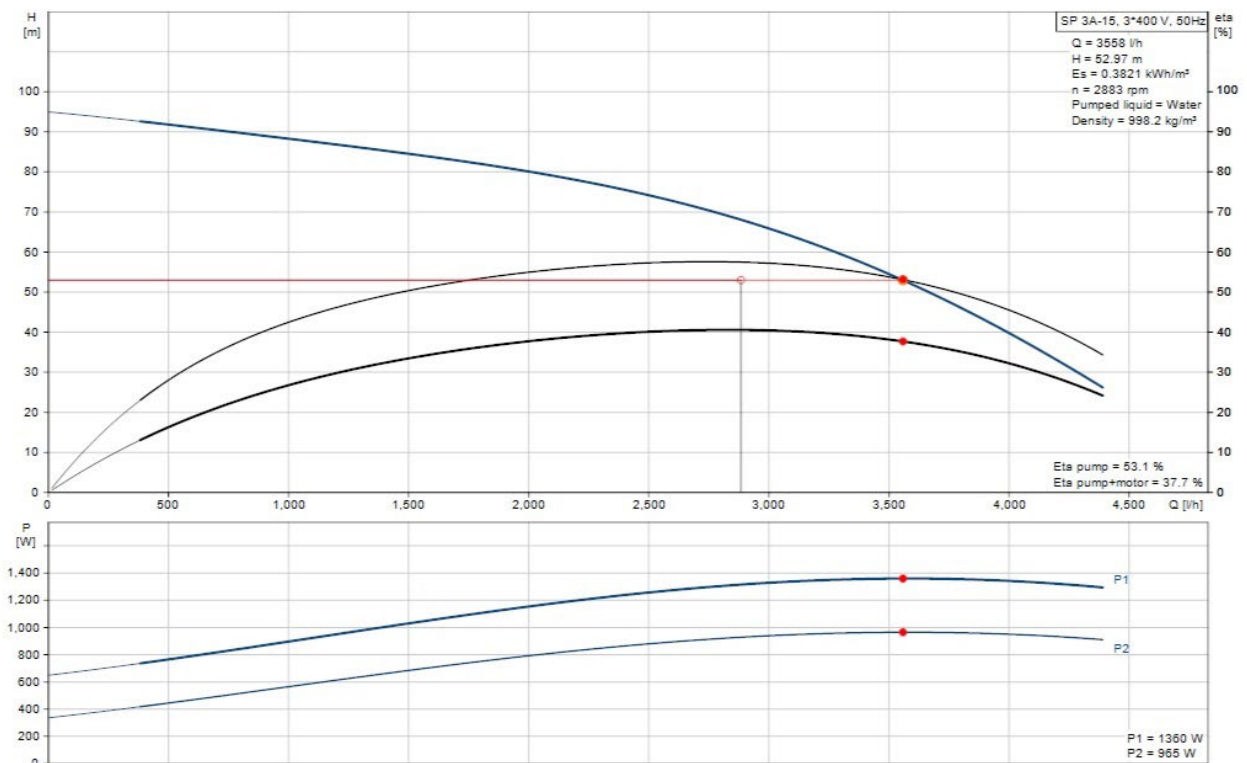


**Figure 5.** Illustration of pump curve of the pump operating point [15].

### 3.2 Effect of hydraulic parameters on peak power

The MATLAB simulations results in Figure 6 show the effects of the pump rate, solar irradiation and ambient temperature variations on the peak power of the system. Graphs in Figures 6 (a), (b) and (c) represent the relationship between the peak power required to pump the water from the well at varying head, but constant pumping rate, solar irradiation and ambient temperature, respectively. Figure 6(a) shows the effect of change of total dynamic head and the flow-rate on the peak power required to run the pump. The varying pumping rate (slopes) from 40 to 80 m<sup>3</sup>/day, increased proportionally with the peak power. Figures 6(b) and (c) represent the effect of two climatic conditions which are the solar irradiation and ambient temperature, respectively. An increase in solar irradiation shows that a lower power is required for the system to meet the hydraulic demands. On the other hand, the variation of temperature has negatively affected the PV panel power production. This shows that the peak power on site should be increased in order to compensate for any possible loss of production due the variation of temperature. Therefore, ignoring these variations may result in under-sized system.

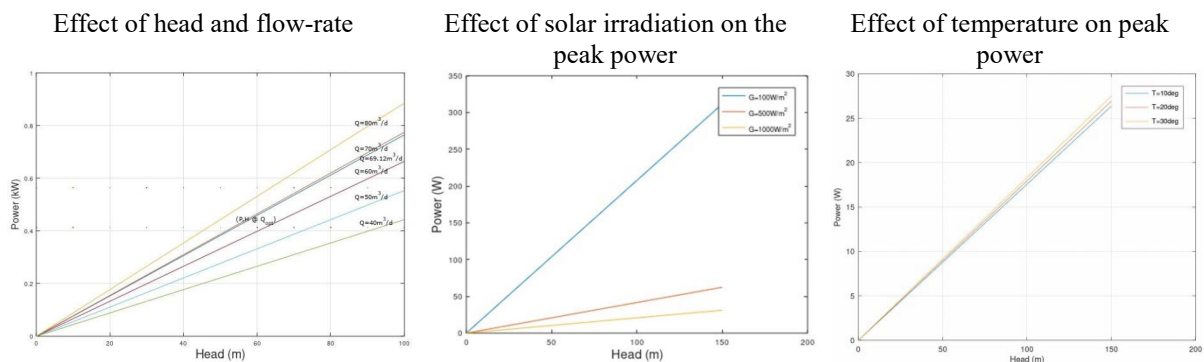


**Figure 6.** The effect of hydraulic parameters and climatic conditions on peak power; (a) flow rate, (b) solar irradiation and (c) temperature.

#### 4. Conclusion

The proposed analytical sizing method of PVWPS based on the available groundwater such that the discharge rate match the recharge rate and the local meteorological data was achieved in this study. The system was designed to supply a daily average of 69,120 liters/day at 54 m head in June with the lowest average solar irradiation. The P V array of 6 panels connected in series with the power unit of 255 W produced 1.35 kW under this winter condition which was enough to run a DC pump to pump the water from the well to the storage tank. Simulation results obtained with MATLAB shows the effect of variation temperature, solar irradiation and pumping rate on the peak power. The simulations were useful to avoid under-sizing or over-sizing of the system which always becomes very expensive. It was demonstrated that an increase in temperature do affect negatively the peak power generation while an increase of solar irradiation was proportional with the peak power. This method shows that well characteristics and local climate parameters are useful for a sustainable and reliable system to be designed.

#### References

- [1] Muralidhar K and Rajasekar N 2021 Solar Energy Research Cell (SERC), School of Electrical Engineering, VIT, Vellore, India
- [2] Chandela S S, Naika M N and Chandelb R 2015 Renewable and Sustainable Energy Reviews 49: 1084-1099
- [3] Knüppe K 2011 Water SA 37: 1 Pretoria
- [4] Lorenzo E. 1997 Progress in Photovoltaics: Research and Applications 5: 23-27
- [5] Rosa J. Chilundo, R J, Mahanjane U S and Neves D 2018 Journal of Power and Energy Engineering 6:32-63
- [6] Melendez T A F 2009 Master thesis, Universidade de sao Paulo, Sao Paulo
- [7] Alley W M, Reilly T E and Franke O L 1999 U.S. Geological Survey Circular 1186, Denver, Colorado
- [8] Omar M A and Mahmoud M M 2019 Hindawi, International Journal of Photoenergy ID 5216583 1-9
- [9] Zhang Q 2018 Advances in Meteorology 1 - 22
- [10] Argaw N, Foster R and Ellis A 2017 <http://www.osti.gov/bridge>
- [11] Nikzad A, Chahartaghi M, and Ahmadi M H 2019 J. Clean. Prod. 239: 118007
- [12] Acakpovi A, Xavier F F and Awuah-Baffour R 2012 ResearchGate: Conference Paper 65-69 \
- [13] Evain C and Lapegue J 2020 Action Against Hunger International
- [14] Mohamed A A, Cetin N S and Basaran K, Sizing and design of standalone PV water pumping system in Hargeisa/Somaliland: Case Study
- [15] Grundfos website (sizing) and pump curve. SP 3A-15 - 10001K15 | Grundfos.



DIVISION

G

THEORETICAL AND COMPUTATIONAL  
PHYSICS

# Black holes and nilmanifolds: quasinormal mode calculations

Anna Chrysostomou<sup>1,2</sup>, Alan S. Cornell<sup>1</sup>, Aldo Deandrea<sup>2</sup>, Étienne Ligout<sup>3</sup>, and Dimitrios Tsimpis<sup>2</sup>

<sup>1</sup> Department of Physics, University of Johannesburg, PO Box 524, Auckland Park 2006, South Africa

<sup>2</sup> Institut de Physique des Deux Infinis de Lyon, Université de Lyon, UCBL, UMR 5822 CNRS/IN2P3, 4 rue Enrico Fermi, 69622 Villeurbanne Cedex, France

<sup>3</sup> École Normale Supérieure de Lyon, Site Monod, 46 Allée d'Italie, 69364 Lyon Cedex 07, France

E-mail: achrysostomou@uj.ac.za, acornell@uj.ac.za, deandrea@ipnl.in2p3.fr, etienne.ligout-de-oliveiral@ens-lyon.fr, tsimpis@ipnl.in2p3.fr

**Abstract.** In the wake of a perturbation, a  $n$ -dimensional black hole emits complex and characteristic oscillations in spacetime known as “quasinormal modes” (QNMs). These black hole QNMs have been used to explore beyond the Standard Model (BSM) scenarios and quantum gravity conjectures. With the establishment of the LIGO-Virgo-KAGRA network of gravitational-wave (GW) detectors, we find ourselves presented with the unprecedented opportunity to compare computed QNMs against GW data from binary black hole merger events. Encouraged by this development, we investigate whether QNMs can be exploited in the search for signatures of extra dimensions. To address a gap in the BSM literature, we focus here on higher dimensions with negative Ricci curvature. As a first step, we consider a direct space formed from a 4D Schwarzschild black hole spacetime and a 3D nilmanifold (twisted torus); we model the black hole perturbations as a scalar test field. We find that the extra-dimensional geometry can be included in the QNM effective potential as a squared mass-like term  $\mu$ . We then calculate the corresponding QNM spectrum using three different numerical methods and determine a possible upper bound for a detectable  $\mu$ .

## 1. Introduction

Within the context of general relativity, Birkhoff’s theorem stipulates that the most general spherically-symmetric vacuum solution of the Einstein field equations is the Schwarzschild metric

$$ds_{BH}^2 = g_{\mu\nu}^{BH} dx^\mu dx^\nu = -f(r) dt^2 + f(r)^{-1} dr^2 + r^2(d\theta^2 + \sin^2 \theta d\phi^2), \quad (1)$$

where  $f(r) = 1 - r_H/r$  and  $r_H = 2M$  is the Schwarzschild event horizon. This metric describes an isolated, static, and neutral 4D black hole [1, 2] that is fully characterised by its mass  $M$  [3].

Astrophysically, black holes are perpetually in a perturbed state: even if somehow isolated from the fields and matter in their immediate vicinity, they interact with the surrounding vacuum through Hawking radiation. We may describe the perturbed black hole using the metric

$$g'_{\mu\nu} = g_{\mu\nu}^{BH} + \delta_{\mu\nu}, \quad (2)$$

where the unperturbed black hole metric  $g_{\mu\nu}^{\text{BH}}$  is referred to as the “background” and the “perturbations”  $\delta_{\mu\nu}$  are considered to be very small ( $\delta_{\mu\nu} \ll g_{\mu\nu}^{\text{BH}}$ ) at the lowest linear approximation [4]. In the wake of the perturbation, the black hole will emit gravitational radiation dominated by a discrete set of complex “quasinormal” frequencies (QNFs). The real part of these QNFs represent the physical oscillation frequency and the imaginary part is the inverse damping time. To model the perturbing field – known as the quasinormal mode (QNM) – we may consider a scalar test field evolving on a fixed background that contributes negligibly to the energy-density of the system.

Although dissipative systems are ubiquitous in nature, the black hole QNM boundary-value problem is of particular interest due to the physical origin of its damping and the characteristic black hole information that the QNFs convey.

The first of these features can be addressed by considering the black hole spacetime itself through the classical lens, where the presence of an event horizon  $r_H$  results in the irreversible loss of gravitational radiation to the black hole interior. Since gravitational radiation also cannot enter the system from beyond spatial infinity, we can then describe the QNM boundary conditions as purely ingoing at the horizon and purely outgoing at spatial infinity. The system is therefore not time-symmetric; the eigenvalue problem is non-Hermitian. In general, the corresponding eigenfunctions are then not normalisable and do not form a complete set (see reviews [4–6] for details).

The second feature, namely the relationship between QNMs and black hole characteristics, rests on the fact that black hole parameters like mass and spin can be accurately predicted from the QNF spectrum [7]. This has been a topic of interest within gravitational-wave (GW) research [8] and has been demonstrated successfully by the LIGO-Virgo-KAGRA collaboration [9–13].

Other more esoteric GW pursuits include searches for evidence of extra dimensions (see Ref. [14]), wherein which QNMs have recently been considered for a 5D braneworld case [15]. Here, we focus on an extra-dimensional setup in which a 4D Schwarzschild black hole is embedded into a 7D  $\mathcal{M}_4 \times \mathcal{N}_3$  manifold, where  $\mathcal{M}_4$  is the usual (3+1) flat spacetime and  $\mathcal{N}_3$  is a negatively-curved compact space. Specifically,  $\mathcal{N}_3$  here is a “nilmanifold” (twisted torus) fully characterised by the Heisenberg algebra, from which its geometric properties naturally follow (see section 2 for the nilmanifold’s construction, detailed further in Ref. [16]).

In this work, we determine an upper bound under which black hole QNMs may serve as an appropriate probe for extra dimensions. This is made possible by expressing the extra-dimensional components of our 7D Schwarzschild-nilmanifold setup as an effective mass-like term in the QNM potential, and then exploiting QNM techniques to solve the corresponding wave equation.

## 2. The potential of a Schwarzschild-nilmanifold setup

While the parameter space of flat and positively-curved extra dimensions has been probed and constrained [17], models involving higher-dimensional manifolds with negative Ricci curvature have remained under-explored. Phenomenologically, studies on compact negative spaces suggest that these models could be used to address the hierarchy problem [18] and cosmological observations [19, 20]. These motivate our interest in the manifold  $\mathcal{M}_4 \times \mathcal{N}_3$ .

To construct  $\mathcal{N}_3$ , recall that any Lie group  $G$  of dimension  $d$  can be understood as a  $d$ -dimensional differentiable manifold. To make  $G$  compact, we quotient by the lattice  $\Gamma$ . A group for which such a  $\Gamma$  always exists is called a “nilpotent group”. For  $d = 3$ , there is the trivial abelian algebra that leads to a three-torus, as well as three different solvable algebras. Of these, one is nilpotent: the Heisenberg algebra,

$$[Z_1, Z_2] = -f Z_3, \quad [Z_1, Z_3] = [Z_2, Z_3] = 0, \quad (3)$$

where the structure constant  $\mathbf{f} = -f^3_{12}$  is the “geometric flux” serving as the nilmanifold’s “twist parameter”. The corresponding geometric properties can be relayed through the Maurer-Cartan equation,

$$de^3 = \mathbf{f}e^1 \wedge e^2, \quad de^1 = 0, \quad de^2 = 0, \quad (4)$$

$$\Rightarrow e^1 = r^1 dy^1, \quad e^2 = r^2 dy^2, \quad e^3 = r^3(dy^3 + Nr^1 dy^2), \quad (5)$$

where  $N = r^1 r^2 \mathbf{f} / r^3$  with  $r^i$  representing constant radii [16]. In this way, the manifold is fully characterised and we can obtain the most general minimal left-invariant metric,

$$ds_{nil}^2 = \delta_{ab} e^a e^b = (r^1 dy^1)^2 + (r^2 dy^2)^2 + (r^3 dy^3 + Nr^1 r^3 dy^2)^2. \quad (6)$$

From eqs. (1) and (6), we can construct our extra-dimensional manifold  $ds_{7D}^2 = ds_{BH}^2 + ds_{nil}^2$ . Exploiting the spherically-symmetrical context, the 7D propagating scalar field can be expressed as

$$\Psi_{n\ell m}^s(\mathbf{z}) = \sum_{n=0}^{\infty} \sum_{\ell, m} \frac{\psi_{sn\ell}(r)}{r} Y_{m\ell}^s(\theta, \phi) Z(y^1, y^2, y^3) e^{-i\omega t}, \quad (7)$$

where spherical harmonics in  $(\theta, \phi)$  are denoted by  $(\ell, m)$ ,  $s$  represents the spin of the field, and  $n$  is the overtone number labelling the QNFs by increasing values of  $|\mathbb{I}m\{\omega\}|$ . To determine the QNM behaviour, we first apply the Laplacian. For this unusual spacetime, we can account for the higher dimensions by exploiting the separability of the metric. Recall that the Laplacian of a product space is the sum of its parts, such that

$$\nabla^2 \Psi(\mathbf{z}) = (\nabla_{BH}^2 + \nabla_{nil}^2) \Phi_{n\ell m}^s(\mathbf{x}) Z(\mathbf{y}). \quad (8)$$

However, if we choose to encode the higher-dimensional behaviour through an effective mass term representing a Kaluza-Klein tower of states, then we may describe the 7D scalar field evolution through a 4D “massive” Klein-Gordon equation,

$$\nabla_{nil}^2 Z(\mathbf{y}) = -\mu^2 Z(y^1, y^2, y^3) \quad \Rightarrow \quad \frac{1}{\sqrt{-g}} \partial_\mu (\sqrt{-g} g^{\mu\nu} \partial_\nu \Psi) - \mu^2 \Psi = 0. \quad (9)$$

Using the tortoise coordinate  $dr_* = dr/f(r)$ , we extract the radial component of the QNM to produce a characteristic wavelike equation containing the QNF and the effective scalar potential,

$$\frac{d^2 \psi}{dr_*^2} + (\omega^2 - V(r)) \psi = 0, \quad V(r) = \left(1 - \frac{2M}{r}\right) \left(\frac{\ell(\ell+1)}{r^2} + \frac{2M}{r^3} + \mu^2\right). \quad (10)$$

Within the QNM literature, a modified WKB approach informed by the QNM boundary conditions [21, 22] serves as a well-established numerical method for solving eq. (10). At lowest order [21], this WKB method yields

$$\omega^2(\ell, n) \approx V(r_0) - i(n+1/2)\sqrt{-2V''(r_0)}, \quad (11)$$

where derivatives with respect to  $r$  are denoted by primes and  $r_0$  represents the peak of the potential. For low values of  $n$ , eq. (11) demonstrates that the QNF can be closely determined by the height of its associated potential barrier, as well as its second derivative [23, 24]. As such, we may visualise the influence of the mass-like term on the QNF by studying the potential (see figure 1). We observe that  $\mu$  elevates the potential; as  $r_*$  increases, the potential no longer asymptotes to zero but instead approaches  $\mu^2$ . Beyond  $\mu \approx 0.6$ , the peak is smoothed out, suppressing the potential barrier.

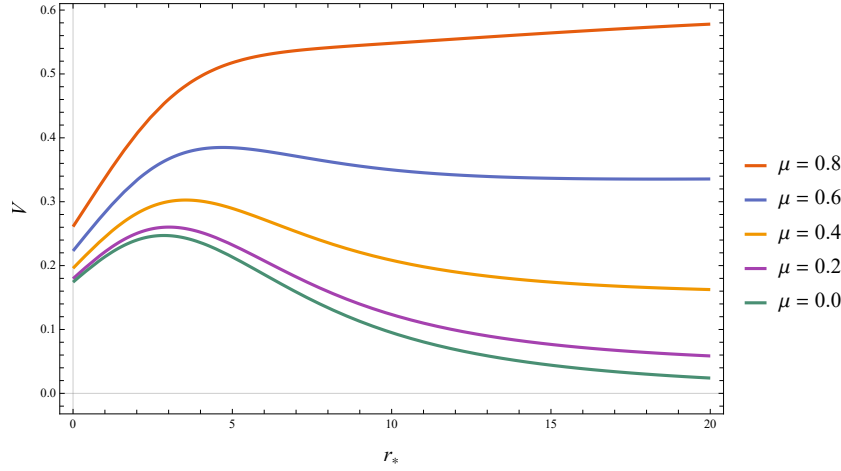


Figure 1: The  $n = 0$ ,  $\ell = 2$  mode of the scalar potential in eq. (10) for increasing values of  $\mu$ . Note that for  $\mu = 0$ ,  $V \rightarrow 0$  as  $r_* \rightarrow \infty$  and the effective potential has a distinct peak. For  $\mu \neq 0$ ,  $V \rightarrow \mu^2$  as  $r_* \rightarrow +\infty$ . However, when  $\mu^2 \gtrsim V(r_0)$ , the boundary condition at spatial infinity is more complicated; the peak is smoothed out and the potential barrier effectively becomes a potential step.

### 3. Computing the QNF spectrum for the Schwarzschild-nilmanifold setup

From eq. (11), we observe that the QNF value is strongly influenced by the potential; from figure 1, we observe that for some critical  $\mu$ , the QNM potential no longer retains its characteristic bell-like shape. To determine this  $\mu$ , we compute the QNF spectrum using a higher-order WKB approach [22] and an analytical method wherein which we calculate QNFs from the inverted Pöschl-Teller potential [25]. We also employ a technique put forth by Dolan and Ottewill that solves eq. (10) with a novel, physically-motivated ansatz to produce QNFs as a series expansion in inverse powers of  $L = \ell + 1/2$  [26]. The first two are well-known methods that rely on a barrier-shaped QNM potential to be effective [27]. We have studied the third extensively in the eikonal limit in Ref. [28]; here, we find that the QNF emerges as a function of both  $L$  and  $\mu$ :

$$\begin{aligned} \omega(L, \mu) = & \frac{1}{3}L - \frac{i}{6}L^0 + \left[ \frac{3\mu^2}{2} + \frac{7}{648} \right] L^{-1} + \left[ \frac{5i\mu^2}{4} - \frac{137i}{23328} \right] L^{-2} \\ & + \left[ \frac{9\mu^4}{8} - \frac{379\mu^2}{432} + \frac{2615}{3779136} \right] L^{-3} + \left[ \frac{27i\mu^4}{16} - \frac{2677i\mu^2}{5184} + \frac{590983i}{1088391168} \right] L^{-4} \\ & + \left[ \frac{63\mu^6}{16} - \frac{427\mu^4}{576} + \frac{362587\mu^2}{1259712} - \frac{42573661}{117546246144} \right] L^{-5} \\ & + \left[ \frac{333i\mu^6}{32} + \frac{6563i\mu^4}{6912} + \frac{100404965i\mu^2}{725594112} + \frac{11084613257i}{25389989167104} \right] L^{-6}. \end{aligned} \quad (12)$$

Our results are summarised in table 1, for which we set  $\ell = 2$  and  $n = 0$  to correspond to the least-damped/longest-lived “fundamental mode” that dominates the QNM signal [4, 6, 9]. We find that the sixth-order WKB and the Dolan-Ottewill methods are in close agreement. We can ascribe the deviations in the Pöschl-Teller results to the method’s stronger reliance on the potential shape, where the Pöschl-Teller potential is known to match closest to the inverted potential corresponding to a Schwarzschild black hole spacetime with a positive cosmological constant [29].

From table 1, we observe that  $\Re\{\omega\}$  increases steadily with  $\mu$  whereas  $\Im\{\omega\}$  decreases. As  $\mu$  approaches 0.7, there is a discernible change in the QNF behaviour: a large jump in both

Table 1: We calculate the QNFs at  $n = 0$  and  $\ell = 2$  for  $0.0 \leq \mu \leq 0.7$  using the WKB technique at  $\mathcal{O}(V^6)$ , the Pöschl-Teller (PT) method, and the Dolan-Ottewill (DO) expansion at  $\mathcal{O}(L^{-6})$ .

$\mu$	$\omega$ (WKB)	$\omega$ (PT)	$\omega$ (DO)
0.0	$0.4836 - 0.0968i$	$0.4874 - 0.0979i$	$0.4836 - 0.0968i$
0.1	$0.4868 - 0.0957i$	$0.4909 - 0.0968i$	$0.4868 - 0.0957i$
0.2	$0.4963 - 0.0924i$	$0.5015 - 0.0936i$	$0.4963 - 0.0924i$
0.3	$0.5123 - 0.0868i$	$0.5192 - 0.0881i$	$0.5124 - 0.0868i$
0.4	$0.5351 - 0.0787i$	$0.5443 - 0.0800i$	$0.5352 - 0.0787i$
0.5	$0.5649 - 0.0676i$	$0.5770 - 0.0690i$	$0.5653 - 0.0676i$
0.6	$0.6022 - 0.0528i$	$0.6181 - 0.0541i$	$0.6032 - 0.0532i$
0.7	$0.1396 + 0.2763i$	$0.6695 - 0.0312i$	$0.6500 - 0.0343i$

the real and imaginary parts is observed for all three methods, with a pronounced difference in the WKB result for  $\mu = 0.7$ : a sudden drop in  $\Re\{\omega\}$  and shift from negative to positive in  $\Im\{\omega\}$ . Mathematically, we can attribute this behaviour as evidence of a breakdown in the methodology: since the local maximum is eradicated after  $\mu = 0.6$  in fig. 1, it is impossible to carry out the WKB matching procedure beyond this  $\mu$  value. This justification is supported by the QNM literature for fields of large mass (see the WKB review by Konoplya [27]).

However, there is also the physical interpretation to consider. Massive QNMs for which  $\Re\{\omega^2\} > \mu^2$  are “propagative” and behave similarly to their massless counterparts, whereas QNMs for which  $\Re\{\omega^2\} < \mu^2$  are “evanescent” and contribute negligibly to the QNM spectrum for a perturbed black hole. This shift from propagative to evanescent is characterised by a change in sign in the imaginary part [24]. As  $\mu$  increases, the QNMs transition from propagative to evanescent; as the imaginary part goes to zero, the QNMs enter the “quasiresonance regime” [23, 30], where the QNMs are arbitrarily long-lived. In this regime, the ingoing wave amplitude at the event horizon of the black hole is considered much smaller than the amplitude far from the black hole; energy no longer “leaks” from the system at spatial infinity and the QNMs behave as standing waves [4].

In our extra-dimensional setup, the  $\mu$  parameter serves as a manifestation of the extra dimensions. The analysis of the QNM potential and corresponding QNF spectrum conducted here demonstrates that only the “propagative” QNMs can be used as a probe in extra-dimensional searches. This places an upper bound on  $\mu$ , such that  $\Re\{\omega^2\} > \mu^2$ . For a scalar test field in the Schwarzschild black hole spacetime, we require that  $\mu < 0.6$ .

#### 4. Conclusions

In this work, we have considered a novel extra-dimensional setup comprised of a Schwarzschild black hole embedded in a 7D product spacetime whose extra dimensions form a negative compact space – specifically, a nilmanifold built from Heisenberg algebra. We have pursued a strategy for an extra-dimensional search using QNMs. By positioning the extra-dimensional contribution as an effective mass-like  $\mu$  term in the QNM potential, we have demonstrated through a numerical study a possible upper bound on this  $\mu$ .

In an ongoing investigation based on the parametric deviation of GWs from the QNMs predicted by general relativity, we suggest that this bound may be further constrained. Our next immediate step is to subject the mass spectrum of the nilmanifold model studied in Ref. [16] to this constraint in order to extract tangible bounds on the radius of the nilmanifold extra dimensions herein constructed.

### Acknowledgments

ASC is supported in part by the National Research Foundation (NRF) of South Africa; AC is supported by the NRF and Department of Science and Innovation through the SA-CERN programme and a Campus France scholarship. EL is supported by the French Government through the École Normale Supérieure de Lyon.

### References

- [1] Misner C W, Thorne K S and Wheeler J A 1973 *Gravitation* (San Francisco: W. H. Freeman)
- [2] Chandrasekhar S 1983 *The Mathematical Theory of Black Holes* (New York: Oxford University Press)
- [3] Israel W 1967 *Phys. Rev.* **164**(5) 1776–9
- [4] Konoplya R A and Zhidenko A 2011 *Rev. Mod. Phys.* **83** 793–836
- [5] Nollert H P 1999 *Class. Quant. Grav.* **16** R159–R216
- [6] Berti E, Cardoso V and Starinets A O 2009 *Class. Quant. Grav.* **26** 163001
- [7] Echeverria F 1989 *Phys. Rev. D* **40**(10) 3194–203
- [8] Berti E, Cardoso V and Will C M 2006 *Phys. Rev. D* **73** 064030
- [9] Carullo G, Del Pozzo W and Veitch J 2019 *Phys. Rev. D* **99** 123029
- [10] Isi M, Giesler M, Farr W M, Scheel M A and Teukolsky S A 2019 *Phys. Rev. Lett.* **123** 111102
- [11] Abbott R *et al.* (LIGO Scientific, Virgo) 2021 *Phys. Rev. D* **103** 122002
- [12] Abbott R *et al.* (LIGO Scientific, VIRGO, KAGRA) 2021 (*Preprint* 2112.06861)
- [13] Ghosh A, Brito R and Buonanno A 2021 *Phys. Rev. D* **103** 124041
- [14] Yu H, Lin Z C and Liu Y X 2019 *Commun. Theor. Phys.* **71** 991–1006
- [15] Mishra A K, Ghosh A and Chakraborty S 2021 (*Preprint* 2106.05558)
- [16] Andriot D, Cacciapaglia G, Deandrea A, Deutschmann N and Tsimpis D 2016 *JHEP* **06** 169
- [17] Zyla P A *et al.* (Particle Data Group) 2020 *PTEP* **2020** 083C01
- [18] Orlando D and Park S C 2010 *JHEP* **08** 006
- [19] Starkman G D, Stojkovic D and Trodden M 2001 *Phys. Rev. Lett.* **87** 231303
- [20] Chen C M, Ho P M, Neupane I P, Ohta N and Wang J E 2003 *JHEP* **10** 058
- [21] Schutz B F and Will C M 1985 *Astrophys. J.* **291** L33
- [22] Konoplya R A 2003 *Phys. Rev. D* **68** 024018
- [23] Ohashi A and Sakagami M a 2004 *Class. Quant. Grav.* **21** 3973–84
- [24] Percival J and Dolan S R 2020 *Phys. Rev. D* **102** 104055
- [25] Ferrari V and Mashhoon B 1984 *Phys. Rev. D* **30** 295–304
- [26] Dolan S R and Ottewill A C 2009 *Class. Quant. Grav.* **26** 225003
- [27] Konoplya R A, Zhidenko A and Zinhailo A F 2019 *Class. Quant. Grav.* **36** 155002
- [28] Chen C H, Cho H T, Chrysostomou A and Cornell A S 2021 *Phys. Rev. D* **104**(2) 024009
- [29] Zhidenko A 2004 *Class. Quant. Grav.* **21** 273–80
- [30] Konoplya R A and Zhidenko A V 2005 *Phys. Lett. B* **609** 377–84

# The 5D MSSM at two loops

Howeida M. Esmail<sup>a</sup>, Aldo Deandrea<sup>b,c</sup>, Ammar Abdalgabar<sup>d,e</sup>,  
Mohammed Omer Khojali<sup>f</sup>, and Alan S. Cornell<sup>g</sup>

<sup>a</sup>Sudan University of Science and Technology, College of Graduate Studies, Department of physics, Khartoum 407, Sudan.

<sup>b</sup>Université de Lyon, Université Lyon 1, F-69622 Lyon, France

<sup>c</sup>Institut de Physique des 2 Infinis (IP2I), UMR5822 CNRS/IN2P3, F-69622 Villeurbanne Cedex, France.

<sup>d</sup>University of Hafr Al Batin, college of Science, department of physics, Hafr Al Batin 39524, Kingdom of Saudi Arabia.

<sup>e</sup> Department of Physics, Sudan University of Science and Technology, Khartoum 407, Sudan.

<sup>f</sup>Department of Physics, University of Khartoum, PO Box 321, Khartoum 11115, Sudan.

<sup>g</sup>Department of Physics, University of Johannesburg, PO Box 524, Auckland Park 2006, South Africa

E-mail: hwdmohamed@gmail.com, deandrea@ipnl.in2p3.fr, amari@uhb.edu.sa, khogali11@gmail.com, acornell@uj.ac.za

**Abstract.** Examining the evolution equations of the couplings and soft-terms derived from the two-loop renormalisation group equations in a five-dimensional minimal supersymmetric model compactified on an  $S_1/Z_2$  orbifold (which yields the standard four space-time dimensions), different possibilities can be discussed. In this work we shall consider the limiting case of superfields where the Standard Model matter fields are restricted to the brane. We will compare our two-loop results to the results found at one-loop level, where in this model the power law running in five dimensions and a compactification scale in the  $10 - 10^3$  TeV range has significant effects on the running. We also show that the gluino mass may drive a large enough  $A_t$  to reproduce the measured Higgs mass of 125 GeV and have a light stop superpartner below  $\sim 1$  TeV, as is preferred by the fine tuning argument for the Higgs mass.

## 1. Introduction

As one of the most successful results of the Large Hadron Collider (LHC) experiment, the discovery of the Higgs boson, with a mass of about 125 GeV [1, 2] has spawned many new models beyond the Standard Model (SM) as its properties are probed more and more [3]. Amongst these, R-parity violating supersymmetry (SUSY) scenarios can also lead to long-lived particles if the coupling is weak enough, giving a displaced decay of the metastable Lightest SUSY Particle (LSP). This interpretation was considered by a CMS analysis focussing on leptons with large impact parameters with respect to the beam line location, where the LSP is a stop which is pair-produced, giving an electron-muon pair in the displaced decay[4]. Different types of sparticles are searched for at the LHC, where strong production (squarks and gluinos) are the most favoured scenario, and ATLAS has set an exclusion limit on models considering the pair production of 3<sup>rd</sup> generation squarks. The lower limit on the top squark mass is about 1 TeV, see Ref. [5]. As such, amongst the researches into SUSY breaking models in the framework of the Minimal Supersymmetric SM (MSSM) recent results have been encouraging. However, the

origin of SUSY breaking remains the main unknown ingredient in supersymmetric theories [6, 7]. Another provocative extension to the SM is that of extra dimensional theories, where these may provide a new mechanisms by which to break SUSY and to solve the supersymmetric flavour problem [8]. The simplest amongst these are five dimensional (5D) theories, which when viewed as an effective four dimensional (4D) field theory with a cutoff are non-renormalisable, as many parameters such as gauge couplings, Yukawa couplings etc. are sensitive to this cutoff scale [9]. 5D MSSMs, with their power law running for a sufficiently low compactification radius  $R$ , generate at low energies a large enough trilinear soft breaking term  $A_t$  to explain the observed Higgs mass [9].

Using this 5D MSSM structure, one might be concerned that one-loop linear sensitivity to the cutoff, behaving as  $\Lambda R$ , does not result in terms of the form  $(\Lambda R)^2$  at two-loop. As such it is important to confirm the results and conclusions made at one loop, that are sensitive to this scale, are still consistent and under control at two loops [11]. This is the aim of this current proceeding, to begin the calculation and analysis of the two-loop contributions in such a model. Therefore, the structure of this paper is as follows: In section 2 we outline the five dimensional theory we will study here, in section 3 we explore the model, and in section 4 we present the the calculation of the two-loop renormalisation group equations (RGEs). In section 5 we conclude.

## 2. The Five Dimensional MSSM

We define the 5D MSSM to be the field theory in 4D space-time times an interval of length  $R$  in which the gauge fields and the Higgses ( $H_u, H_d$ ) propagate in the fifth dimension,  $y$ , whilst the matter fields in our model are restricted to the brane at  $y = 0$ . Therefore there are no contributions from Kaluza-Klein (KK) excited state of the fermions and sfermions on the brane. The compactification of bulk fields produces towers of new particle states in the 4D theory at  $Q > 1/R$ .

Even though gauge mediation is preferred for supersymmetry breaking (and some recent work on gauge mediated supersymmetry breaking (GMSB) in a five-dimensional context) can be found in Refs. [6], the universality of squark masses in GMSB ultimately means that even though the gaugino mediated limit [13] might allow for light squarks possibly below 500 GeV [12] (and 5D RGE evolution allows for a large  $A_t$  and the observed Higgs mass) [9]. We assume here that SUSY breaking occurs at the unification scale, which is found by determining the scale at which  $g_1 = g_2 = g_3$ , which is lower when compared to the 4D MSSM due to the effects of compactification, as seen in figure 1. As a result, we will be rather agnostic about the precise details of how SUSY is broken in this proceeding, and our conclusions will be quite general. We do, however, have some minimum requirements:

- i) We use the Yukawa and gauge couplings at the SUSY scale (1 TeV) as inputs.
- ii) We specify the value of the gluino mass,  $M_3$  at 1 TeV.
- iii) We take the trilinear soft breaking terms,  $A_{u/d/e}$ , to vanish at the unification scale (see figure 2).
- iv) We specified  $\mu$ ,  $B_\mu$  and the value of the sfermion masses at 1 TeV.

An interesting feature of the 5D MSSM is the approximate unification of gauge couplings [9, 14], which are here calculated to two-loop and presented in figure 1.

## 3. The Higgs mass at two-loop

To allow for the correct Higgs mass  $m_h = 125$  GeV, the electroweak parameters should be in the range

$$\tan \beta \in (5, 30), \quad \mu \leq 1\text{TeV}, \quad (3.1)$$

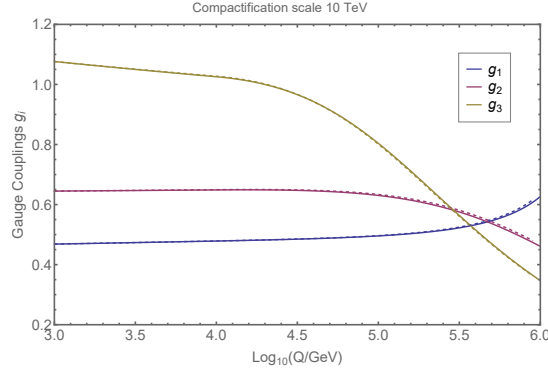


**Figure 1.** Running of the inverse fine structure constants  $\alpha_i^{-1}(Q)$ , for three different models with compactification scale 10 TeV as a function of  $\text{Log}_{10}(Q/\text{GeV})$ .

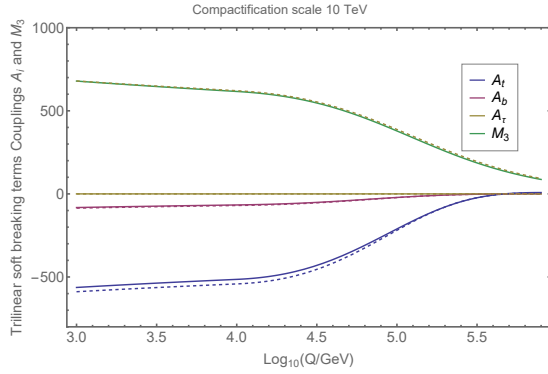


**Figure 2.** Running of the trilinear couplings  $A_i(Q)$ , for two different models with compactification scale 10 TeV, as a function of  $\text{Log}_{10}(Q/\text{GeV})$ .

as presented in figure 3. We do not expect  $\tan\beta$  to be much larger, due to  $B_s \rightarrow X_s\gamma$  flavour constraints [15] and  $\mu$  being bounded by naturalness considerations of the renormalisation group effects on the Higgs tadpole equations (minimisation of the scalar potential). As such, one may achieve the correct Higgs mass with a lower stop mass scale. Using the (MSSM) two-loop Higgs mass formula given in Ref. [16] figure 3 is generated.

#### 4. The two-loop RGEs

The calculation of  $M_h$  shows a significant hierarchy between the EW scale and the sfermion scale, as well as massive logarithms involving  $M_{SUSY}$  and other quantities, such as the top-quark mass. These can be resummed by integrating out the sfermions at  $M_{SUSY}$  and then evolving the couplings below  $M_{SUSY}$  using RGEs down to the electroweak scale at which the SM-like Higgs-boson mass is computed [10].

The dominant two-loop correction to the gauge couplings in our model are proportional to  $(2\mu/M_c)^2$ , and these exclusively come from two-point diagrams with heavy KK mode interchanges [11]. However, we have

$$P_H^H = P_{H'}^{H'} = 0, \text{ and } P_{\Sigma_B}^{\Sigma_A} = 2g^2[T(H) + C(\Sigma)]\delta_{AB} = g^2Q\delta_{AB}, \quad (4.1)$$

where  $r = \delta_{AA}$  is the dimension of the group,  $P_H^H$  and  $P_{H'}^{H'}$  are the Higgs self-energies and the

leading contribution to  $\beta_g^{(2)}$  vanishes. This cancellation reflects the fact that a model with  $N = 2$  SUSY has to be renormalised only at the one-loop level, i.e., the one-loop counter-terms render the theory finite at any order of perturbation.

The sub leading two-loop correction, proportional to  $2\mu/M_c$ , where this correction does not vanish because the underlying  $N = 2$  SUSY is broken by the interaction of the field in the loops, can be written as [11]:

$$\begin{aligned} \beta_g^{(2)} = & 2\tilde{g}^5 C(V) \{3[T(H) + T(H')] + T(f) + C(\Sigma) - 9C(V)\} \\ & - 2g^3 r^{-1} C(H) \left[ (4 - 6)g^2 C(H) d(H) + \frac{1}{2} y^{Hff'} y_{Hff'} + (H \leftrightarrow H') \right] \\ & - 2g^3 C(\Sigma) 2g^2 [2T(H) - C(\Sigma)] - 2g^3 r^{-1} C(f) \left[ \frac{1}{2} y^{fkl} y_{fkl} - 2g^2 C(f) d(f) \right], \end{aligned} \quad (4.2)$$

where  $d(\Phi)$  is the dimension of the  $\Phi$  representation and  $f$  stands for the chiral fermions. The terms in the first line in equation (4.3) come from the possible Feynman diagrams. Diagrams with exchanges of  $(H, V)$  and  $(H', V)$  and  $V$  fields have a factor of 3, since there are three different ways to distribute the momentum along the fifth dimension (i.e., the KK modes) among the fields in the internal loops. For diagrams with  $(f, V)$  and  $(\Sigma, V)$  in the loops, there is only one possible configuration, corresponding to the exchange of lower of  $V$  and  $\Sigma$  fields, respectively. The contribution in diagrams with a chiral fermion  $f$ , the generic expression in equation (4.2) becomes

$$\gamma_f^{(2)f} = -\tilde{h}_f^2 P_{fc}^f - 2g^2 C(f) P_f^f + 2g^4 C(f) \times [2T(H) + C(\Sigma) - 3C(V)]. \quad (4.3)$$

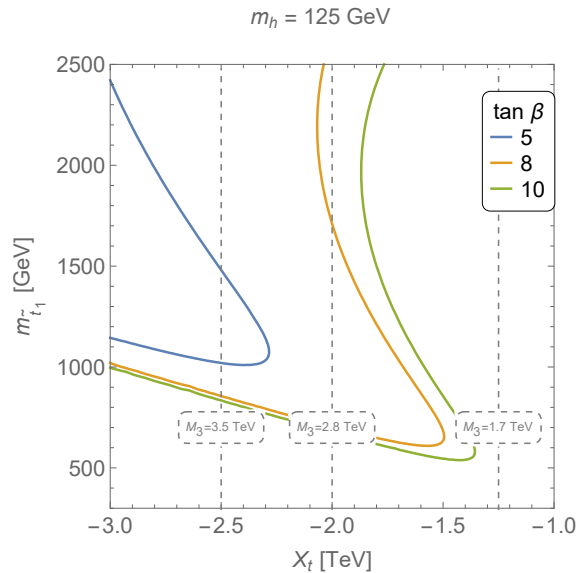


**Figure 3.** Contour plot of the Higgs mass at two-loops as a function of  $X_t$ .

The full set of gauge couplings in 5D at two-loop are given by:

$$\beta_{g_1}^{(2)} = g_1^3 \left( \frac{199}{25} g_1^2 + \frac{27}{5} g_2^2 + \frac{88}{5} g_3^2 - \frac{26}{5} Y_u^2 - \frac{14}{5} Y_d^2 - \frac{18}{5} Y_e^2 \right), \quad (4.4)$$

$$\beta_{g_2}^{(2)} = g_2^3 \left( \frac{3}{2} g_1^2 + g_2^2 + 24 g_3^2 - 6 Y_u^2 - 6 Y_d^2 - 2 Y_e^2 \right), \quad (4.5)$$

$$\beta_{g_3}^{(2)} = g_3^3 \left( \frac{11}{5} g_1^2 + 9 g_2^2 - 40 g_3^2 - 4 Y_u^2 - 4 Y_d^2 \right). \quad (4.6)$$

The gaugino mass Parameters in 5D at two-loop can be written as:

$$\begin{aligned} \beta_{M_1}^{(2)} = & 2g_1^2 \left( \frac{398}{25} g_1^2 M_1 + \frac{27}{5} g_2^2 M_1 + \frac{88}{5} g_3^2 M_1 + \frac{27}{5} g_2^2 M_2 + \frac{88}{5} g_3^2 M_3 - \frac{26}{5} Y_u (-A_u + M_1 Y_u) \right. \\ & \left. - \frac{14}{5} Y_d (-A_d + M_1 Y_d) - \frac{18}{5} Y_e (-A_e + M_1 Y_e) \right), \end{aligned} \quad (4.7)$$

$$\begin{aligned} \beta_{M_2}^{(2)} = & 2g_2^2 \left( \frac{3}{2} g_1^2 M_2 + 2g_2^2 M_2 + 24g_3^2 M_2 + \frac{3}{2} g_1^2 M_1 + 24g_3^2 M_3 - 6Y_u (-A_u + M_2 Y_u) \right. \\ & \left. - 6Y_d (-A_d + M_2 Y_d) - 2Y_e (-A_e + M_2 Y_e) \right), \end{aligned} \quad (4.8)$$

$$\begin{aligned} \beta_{M_3}^{(2)} = & 2g_3^2 \left( \frac{11}{5} g_1^2 M_3 + 9g_2^2 M_3 - 80g_3^2 M_3 + \frac{11}{5} g_1^2 M_1 + 9g_2^2 M_2 \right. \\ & \left. - 4Y_u (-A_u + M_3 Y_u) - 4Y_d (-A_d + M_3 Y_d) \right), \end{aligned} \quad (4.9)$$

$$\begin{aligned} \beta_{Y_d}^{(2)} = & Y_d \left( \frac{167}{900} g_1^4 - \frac{9}{4} g_2^4 - \frac{160}{9} g_3^4 + \frac{1}{10} g_1^2 g_2^2 + \frac{8}{9} g_1^2 g_3^2 + 8g_2^2 g_3^2 + \frac{1}{2} g_1^2 Y_d^\dagger Y_d - \frac{3}{2} g_2^2 Y_d^\dagger Y_d \right. \\ & \left. - 4Y_d^\dagger Y_d Y_d^\dagger Y_d - 2Y_u^\dagger Y_u Y_u^\dagger Y_u - \frac{1}{10} g_1^2 Y_d^\dagger Y_d + \frac{3}{2} g_2^2 Y_d^\dagger Y_d - 2Y_d^\dagger Y_d Y_u^\dagger Y_u \right), \end{aligned} \quad (4.10)$$

$$\begin{aligned} \beta_{Y_u}^{(2)} = & Y_u \left( \frac{767}{900} g_1^4 - \frac{9}{4} g_2^4 - \frac{160}{9} g_3^4 + \frac{1}{10} g_1^2 g_2^2 + \frac{136}{45} g_1^2 g_3^2 + 8g_2^2 g_3^2 - \frac{1}{2} g_1^2 Y_u^\dagger Y_u + \frac{3}{2} g_2^2 Y_u^\dagger Y_u \right. \\ & \left. - 4Y_u^\dagger Y_u Y_u^\dagger Y_u - 2Y_d^\dagger Y_d Y_d^\dagger Y_d + \frac{1}{10} g_1^2 Y_d^\dagger Y_d - \frac{3}{2} g_2^2 Y_d^\dagger Y_d - 2Y_d^\dagger Y_d Y_u^\dagger Y_u \right), \end{aligned} \quad (4.11)$$

$$\beta_{Y_e}^{(2)} = Y_e \left( \frac{303}{100} g_1^4 - \frac{9}{4} g_2^4 + \frac{9}{10} g_1^2 g_2^2 + \frac{9}{10} g_1^2 Y_e^\dagger Y_e + \frac{3}{2} g_2^2 Y_e^\dagger Y_e - 4Y_e^\dagger Y_e Y_e^\dagger Y_e \right) \quad (4.12)$$

and

$$\begin{aligned} \beta_{T_d}^{(2)} = & T_d \left( \frac{167}{900} g_1^4 - \frac{9}{4} g_2^4 - \frac{160}{9} g_3^4 + \frac{1}{10} g_1^2 g_2^2 + \frac{8}{9} g_1^2 g_3^2 + 8g_2^2 g_3^2 \right) \\ & - Y_d \left( \frac{334}{900} g_1^4 M_1 - \frac{18}{4} g_2^4 M_2 - \frac{320}{9} g_3^4 M_3 + \frac{1}{5} g_1^2 g_2^2 (M_1 + M_2) \right. \\ & \left. + \frac{16}{9} g_1^2 g_3^2 (M_1 + M_3) + 16g_2^2 g_3^2 (M_2 + M_3) \right) + \frac{1}{2} g_1^2 T_d Y_u^\dagger Y_u - \frac{1}{2} g_1^2 M_1 Y_d Y_u^\dagger Y_u \\ & - \frac{3}{2} g_2^2 T_d Y_u^\dagger Y_u + \frac{3}{2} g_2^2 M_2 Y_d Y_u^\dagger Y_u - \frac{3}{10} g_1^2 T_d Y_d^\dagger Y_d + g_1^2 Y_d T_u Y_u \\ & + \frac{1}{10} g_1^2 M_1 Y_d Y_d^\dagger Y_d + \frac{9}{2} g_2^2 T_d Y_d^\dagger Y_d - \frac{3}{2} g_2^2 M_2 Y_d Y_d^\dagger Y_d - 3g_2^2 Y_d T_d Y_d - 20T_d Y_d^\dagger Y_d Y_d^\dagger Y_d \\ & - 2T_d Y_u^\dagger Y_u Y_u^\dagger Y_u - 8Y_d T_u Y_u Y_u^\dagger Y_u - 6T_d Y_d^\dagger Y_d Y_u^\dagger Y_u - 4T_u Y_u Y_d Y_d^\dagger Y_d, \end{aligned} \quad (4.13)$$

$$\begin{aligned}
\beta_{T_u}^{(2)} = & T_u \left( \frac{767}{900} g_1^4 - \frac{9}{4} g_2^4 - \frac{160}{9} g_3^4 + \frac{1}{10} g_1^2 g_2^2 + \frac{136}{45} g_1^2 g_3^2 + 8 g_2^2 g_3^2 \right) - Y_u \left( \frac{1352}{900} g_1^4 M_1 \right. \\
& - \frac{18}{4} g_2^4 M_2 - \frac{320}{9} g_3^4 M_3 + \frac{1}{5} g_1^2 g_2^2 (M_1 + M_2) + \frac{272}{45} g_1^2 g_3^2 (M_1 + M_3) + 16 g_2^2 g_3^2 (M_2 + M_3) \Big) \\
& - \frac{3}{2} g_1^2 T_u Y_u^\dagger Y_u + \frac{1}{2} g_1^2 M_1 Y_u Y_u^\dagger Y_u + \frac{9}{2} g_2^2 T_u Y_u^\dagger Y_u - \frac{3}{2} g_2^2 M_2 Y_u Y_u^\dagger Y_u + \frac{1}{10} g_1^2 T_u Y_d^\dagger Y_d \\
& + \frac{1}{5} g_1^2 Y_u T_d Y_d - \frac{1}{10} g_1^2 M_1 Y_u Y_d^\dagger Y_d - \frac{3}{2} g_2^2 T_u Y_d^\dagger Y_d + \frac{3}{2} g_2^2 Y_u Y_d^\dagger Y_d - 3 g_2^2 Y_u T_d Y_d \\
& - 20 T_u Y_u^\dagger Y_u Y_u^\dagger Y_u - 2 T_u Y_d^\dagger Y_d Y_d^\dagger Y_d - 8 Y_u T_d Y_d Y_d^\dagger Y_d - 6 T_u Y_u^\dagger Y_u Y_d^\dagger Y_d - 4 T_d Y_d Y_u Y_u^\dagger Y_u,
\end{aligned} \tag{4.14}$$

$$\begin{aligned}
\beta_{T_e}^{(2)} = & T_e \left( \frac{303}{100} g_1^4 - \frac{9}{4} g_2^4 + \frac{9}{10} g_1^2 g_2^2 \right) - Y_e \left( \frac{606}{100} g_1^4 M_1 - \frac{18}{4} g_2^4 M_2 + \frac{18}{10} g_1^2 g_2^2 (M_1 + M_2) \right) \\
& + \frac{27}{10} g_1^2 T_e Y_e^\dagger Y_e - \frac{9}{10} g_1^2 M_1 Y_e Y_e^\dagger Y_e + \frac{9}{2} g_2^2 T_e Y_e^\dagger Y_e - \frac{3}{2} g_2^2 M_2 Y_e Y_e^\dagger Y_e - 20 T_e Y_e^\dagger Y_e Y_e^\dagger Y_e.
\end{aligned} \tag{4.15}$$

## 5. Conclusions

In this proceeding we have explored the 5D MSSM at two-loop. We computed the full two loop RGEs for all the supersymmetric and soft term parameters and compared these results to those found at one-loop level in Ref. [9]. In our plots we have confirmed that a large  $A_t$  may be generated at low energies from a UV boundary condition, where  $A_t$  is vanishing, through power-law running.

## References

- [1] Aad G *et al.* [ATLAS] 2012 *Phys. Lett. B* **716**, 1-29 (*Preprint* 1207.7214).
- [2] Chatrchyan S *et al.* [CMS] 2012 *Phys. Lett. B* **716**, 30-61 (*Preprint* 1207.7235).
- [3] G. Aad *et al.* [ATLAS and CMS], *Phys. Rev. Lett.* **114** (2015), 191803 doi:10.1103/PhysRevLett.114.191803 [arXiv:1503.07589 [hep-ex]].
- [4] V. Khachatryan *et al.* [CMS], *Phys. Rev. Lett.* **114** (2015) no.6, 061801 doi:10.1103/PhysRevLett.114.061801 [arXiv:1409.4789 [hep-ex]]. G. Aad *et al.* [ATLAS], *Eur. Phys. J. C* **81** (2021) no.11, 1023 doi:10.1140/epjc/s10052-021-09761-x [arXiv:2106.09609 [hep-ex]].
- [5] [ATLAS], ATL-PHYS-PUB-2018-046.
- [6] McGarrie M and Russo R 2010 *Phys. Rev. D* **82**, 035001 (*Preprint* 1004.3305; McGarrie M and Thompson D C 2010 *Phys. Rev. D* **82**, 125034 (*Preprint* 1009.4696); McGarrie M 2011 *Preprint* 1109.6245).
- [7] Kribs G D, Martin A and Menon A 2013 *Phys. Rev. D* **88** (2013), 035025 (*Preprint* 1305.1313).
- [8] Boussejra M A, Mahmoudi F and Uhrich G 2022 *Phys. Rev. D* **106** 1, 015018 (*Preprint* 2201.04659).
- [9] Abdalgabar A, Cornell A S, Deandrea A and McGarrie M 2014 *JHEP* **07**, 158 (*Preprint* 1405.1038); Abdalgabar A, Cornell A S, Deandrea A and McGarrie M 2016 *JHEP* **01**, 083 (*Preprint* 1504.07749).
- [10] H. Bahl, S. Liebler and T. Stefaniak, *Eur. Phys. J. C* **79** (2019) no.3, 279 doi:10.1140/epjc/s10052-019-6770-z [arXiv:1901.05933 [hep-ph]].
- [11] Masip M 2000 *Phys. Rev. D* **62**, 065011 (*Preprint* hep-ph/0001115).
- [12] G. Belanger, D. Ghosh, R. Godbole and S. Kulkarni, *JHEP* **09** (2015), 214 doi:10.1007/JHEP09(2015)214 [arXiv:1506.00665 [hep-ph]].
- [13] Mirabelli E A and Peskin M E 1998 *Phys. Rev. D* **58**, 065002 (*Preprint* hep-th/9712214); Chacko Z, Luty M A, Nelson A E and Ponton E 2000 *JHEP* **01**, 003 (*Preprint* hep-ph/9911323); Schmaltz M and Skiba W 2000 *Phys. Rev. D* **62**, 095005 (*Preprint* hep-ph/0001172); Schmaltz M and Skiba W 2000 *Phys. Rev. D* **62**, 095004 (*Preprint* hep-ph/0004210).
- [14] Dienes K R, Dudas E and Gherghetta T 1998 *Phys. Lett. B* **436**, 55-65 (*Preprint* hep-ph/9803466); Dienes K R, Dudas E and Gherghetta T 1999 *Nucl. Phys. B* **537**, 47-108 (*Preprint* hep-ph/9806292); Pomarol A 2000 *Phys. Rev. Lett.* **85**, 4004-4007 (*Preprint* hep-ph/0005293); Nomura Y and Poland D 2007 *Phys. Rev. D* **75**, 015005 (*Preprint* hep-ph/0608253).
- [15] J. L. Yang, T. F. Feng, S. M. Zhao, R. F. Zhu, X. Y. Yang and H. B. Zhang, *Eur. Phys. J. C* **78** (2018) no.9, 714 doi:10.1140/epjc/s10052-018-6174-5 [arXiv:1803.09904 [hep-ph]].
- [16] Espinosa J R and Zhang R J 2000 *Nucl. Phys. B* **586**, 3-38 (*Preprint* hep-ph/0003246).

# Matters of the $R_h = ct$ universe

**Amare Abebe**

Centre for Space Research, North-West University, Mahikeng 2745, South Africa  
National Institute for Theoretical and Computational Sciences (NITheCS), South Africa

E-mail: Amare.Abebe@nithecs.ac.za

**Abstract.** Decades of astronomical observations have shown that the standard model of cosmology based on General Relativity - the closest we have to a standard theory of gravitation - does not adequately describe our universe without the *ad hoc* introduction of dark matter, dark energy to late-time cosmology and inflation to early-universe cosmology. This certainly has created dilemmas in the cosmology and the wider astronomy community, and several alternative models of cosmology and gravitation are being considered at the moment. Here I will give a brief overview of the cosmological dynamics of the  $R_h = ct$  universe, a cosmological model with a vanishing active gravitational mass. We will show that the model presents, *inter alia*, a theoretical solution to the synchronicity problem in the framework of non-standard forms of matter and gravitation.

## 1. Introduction

Modern cosmology based on Einstein's General Relativity (GR) theory in a maximally symmetric spacetime, the Friedmann-Lemaître-Robertson-Walker (FLRW) metric [1, 2], describing a universe that is homogeneous (all regions of space look alike, no preferred positions) and isotropic (no preferred directions). The recent discovery of the accelerated rate of cosmic expansion has inspired a wave of new research into the nature of gravitational physics. Although it is not conclusively known what caused this recent cosmic acceleration, the prevailing argument is that dark energy caused it. Moreover, new alternatives to dark energy and/or generalisations to GR already abound [3, 4, 5], such as:

- Adding extra matter fields, e.g. scalar-tensor models, Modified Newtonian Dynamics [6].
- Adding extra dimensions, e.g., Kaluza-Klein [7], Gauss-Bonnet [8], braneworld models [9].
- Higher-order theories, e.g., Hořava-Lifshitz [10],  $f(R)$  gravity [11] theories.

Melia's  $R_h = ct$  spacetime model [12] is one such attempt to solve existing cosmological dilemmas that the concordance  $\Lambda$ -Cold-Dark-Matter ( $\Lambda$ CDM) cosmology has not resolved through a simple manipulation of the field equations in the existing GR framework. As we will show in the following section, this model requires the vanishing of the active gravitational mass (AGM). It is not possible to achieve a vanishing AGM in the standard description of GR if the universe is filled with standard forms of matter. This is because the energy density and the pressure of standard forms of matter are non-negative. Getting conditions for vanishing AGM in the standard framework are among the sticking points of the  $R_h = ct$  universe, and the main objective of this article is to provide a mechanism to achieve this in the framework of modified theories of gravitation.

### 1.1. Matters of gravity

Relativistic physics treats gravity as a manifestation of spacetime curvature. There are three different geometrical representations of spacetime curvature [13] as shown in Fig. (1) leading

to the three possible gravitational interpretations depicted in Fig. (2). In Fig. (1), we see the so-called geometric trinity: geometry manifesting itself as curvature - described by the Riemann tensor  $R^\alpha{}_{\beta\mu\nu}$ , as torsion - described by the torsion tensor  $T^\alpha{}_{\mu\nu}$ , or as non-metricity - described by the eponymous tensor  $Q^\alpha{}_{\mu\nu}$ . Fig. (2) shows the three possible broad avenues to formulate a theory of gravitation: GR and its extensions in the curvature interpretation, the Teleparallel Equivalent of GR (TEGR) and its extensions in the torsion interpretation, and the Symmetric TEGR (STTEGR) and its extensions in the non-metricity interpretation of geometry.

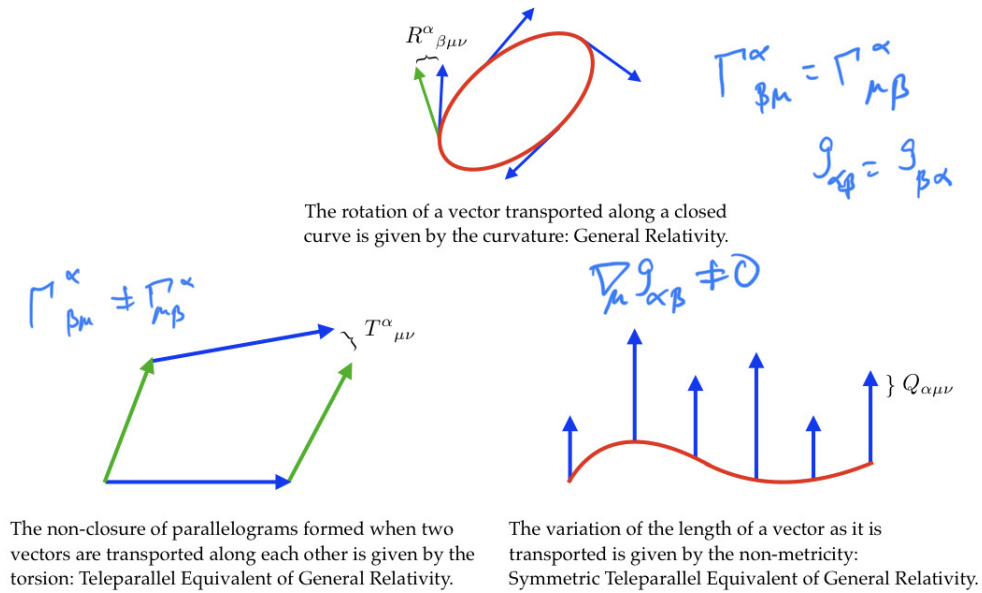


**Figure 1.** The geometrical meaning of curvature, torsion and non-metricity. Adapted from Beltran-Jimenez et al [13]. Here  $R^\alpha{}_{\beta\mu\nu}$  is the Riemann curvature tensor,  $\Gamma^\alpha{}_{\beta\mu}$  is the affine connection, and  $\nabla_\mu$  represents the covariant derivative operator. The failure of two parallel-transported vectors to form a parallelogram is given by the torsion tensor  $T^\alpha{}_{\mu\nu}$  whereas the failure of the connection to be metric is given by the non-metricity tensor  $Q^\alpha{}_{\mu\nu}$ .

1.2. Standard cosmology

The standard (or “concordance”) cosmological model is based on the GR description of gravitation the action of which is given by:

$$S_{GR} = \frac{c^4}{16\pi G} \int d^4x \sqrt{-g} [R + 2(L_m - \Lambda)] ,$$

where  $c$  and  $G$  are the speed of light and the Newtonian gravitational constant,  $g$  is the trace of the metric tensor  $g_{\mu\nu}$ ,  $R$  is the Ricci scalar. The corresponding Einstein’s field equations read <sup>1</sup>:

$$G_{\mu\nu} + \Lambda g_{\mu\nu} = T_{\mu\nu} , \tag{1}$$

with the first (geometric) term represented by the Einstein tensor, the right hand side of the equation representing the energy-momentum tensor of matter fluid forms, and  $\Lambda$  represents the cosmological constant. The other two descriptions of gravity, i.e., TEGR and STTEGR [13] describe similar background expansion history provided  $R = T = Q$  whereas their respective generalisations to  $f(R)$ ,  $f(T)$  and  $f(Q)$  do not necessarily do so [14].

<sup>1</sup> From here onwards, unless explicit use is necessary, we will assume  $8\pi G = 1 = c$ .

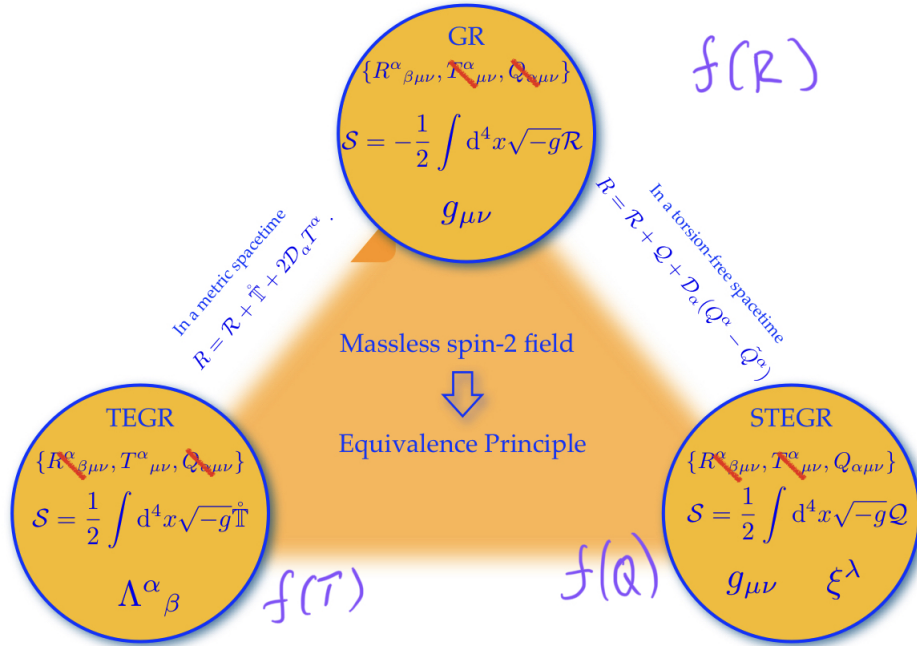


**Figure 2.** Three alternative gravitational descriptions defined in terms of the Ricci scalar  $R$ , torsion scalar  $T$  and non-metricity scalar  $Q$ , and their modified  $f(R)$ ,  $f(T)$  and  $f(Q)$  generalisations. Adapted from Beltran-Jimenez et al [13]. In the GR case, all but the curvature tensor vanish, in TEGR only the torsion survives whereas in STEGER, the non-metricity survives while the curvature and torsion both vanish. Due to the vanishing curvature, there is a pure gauge field  $\Lambda^\alpha_\beta$  associated with the connection in TEGR, and a tangent space coordinate  $\xi^\alpha$  associated with STEGR.

In the absence of the cosmological constant in the above field equations (1), the basic evolution equation for the scale factor  $a(t)$  of the universe is given by the Raychaudhuri equation

$$3\frac{\ddot{a}}{a} = -\frac{1}{2}(\rho + 3p) ,$$

where  $\rho$  and  $p$  are the matter energy density and isotropic pressure, respectively, and an overdot represents differentiating with respect to (w.r.t) the cosmic time  $t$ . For ordinary matter, the “active gravitational mass”

$$\rho + 3p > 0 .$$

This means that ordinary matter will tend to cause the universe to decelerate, *i.e.*,  $\ddot{a} < 0$ . But astronomical observations show that cosmic expansion is accelerating in recent epoch, *i.e.*,  $\ddot{a} > 0$ . A positive cosmological constant causes an accelerated expansion, so  $\Lambda$  could be a quick fix provided that it dominates in the right-hand side of the following equation:

$$3\frac{\ddot{a}}{a} = -\frac{1}{2}(\rho + 3p) + \Lambda .$$

Some serious problems associated with the cosmological constant, among them the eponymous *cosmological constant problem* [15] and the *coincidence problem* [16] challenge the choice of  $\Lambda$  as a dark energy candidate.

The Big Bang model is by far the most successful theory in predicting many cosmological features confirmed observationally expansion of space, origin of the cosmic microwave background, Big Bang nucleosynthesis, galactic evolution and distribution, and the formation

of large-scale structures [4]. However, there are still, broadly speaking, two serious puzzles that remain unanswered in the standard Big Bang-based cosmology [17]:

- Early-universe problems: horizon, flatness, structure/smoothness/homogeneity, and magnetic-monopole problems. The suggested solution here is cosmic inflation, an early-epoch cosmic acceleration.
- Late-time (large-scale) problems: rotational curves of galaxies plus large-scale structure formation, and late-time cosmic acceleration. This is usually where the dark stuff comes in. The former aspect is generally thought to be solved by introducing dark matter, and the latter by dark energy (and often with the cosmological constant as the candidate for the dark energy).

One other puzzling, but not as widely explored, problem is the  $R_h(t_0) = ct_0$  coincidence (often referred to as the synchronicity problem)<sup>2</sup>: the observed equality of our gravitational horizon  $R_h(t_0)$  with the distance  $ct_0$  light has travelled since the Big Bang in  $\Lambda$ CDM cosmology.

Some potential new frontiers to address the above shortcomings of the  $\Lambda$ CDM cosmology include:

- Inhomogeneous cosmological models, such as Lemaître-Tolman-Bondi (LTB) [18] and Szekeres [19] cosmologies.
- Anisotropic cosmological models, such as Bianchi cosmologies [20].
- Changing [fundamental] ‘constants’, such as evolving  $\Lambda$  and  $G$  cosmologies [21, 22, 23].
- Modification/generalization of GR, such as  $f(R)$ ,  $f(T)$  [24], and  $f(Q)$  [25, 26] models of gravitation, just to mention a few.

In addition, the  $R_h = ct$  model has recently joined the fray as a potential cosmological model to address, in particular, the synchronicity problem.

## 2. The $R_h = ct$ universe

First proposed by Melia, the controversial  $R_h = ct$  model has the following characteristics [12, 27, 28]:

$$R_h = \frac{c}{H} = ct, \quad a = t/t_0, \quad H = 1/t \Rightarrow Ht = 1 \quad \forall t. \quad (2)$$

Here  $R_h$  and  $H \equiv \frac{\dot{a}}{a}$  are, respectively, the gravitational [horizon] radius and the Hubble parameter. The term  $c/H$  corresponds to the Hubble radius, also known as the Hubble horizon, and sets the scale for physically relevant causal relationships. The first part of Eq. (2) shows that the event horizon due to purely gravitational processes equals the Hubble horizon due purely to the cosmological expansion. This model follows from the imposition of a vanishing total AGM,

$$\rho + 3p = 0, \quad (3)$$

in the gravitational theory. No cosmological constant  $\Lambda$  as the source of dark energy is needed in this model.

Among other things, this model resolves the so-called synchronicity problem: why is it true that today, the dimensionless age of the universe

$$H_0 t_0 \sim 1?$$

Here  $H_0$  is the Hubble constant (*i.e.*, present-day value of the Hubble parameter). Problem: for standard forms of matter,  $\rho + 3p > 0$ . So how can one get a vanishing AGM? This is where modified models of gravitation come in as they naturally provide the extra “curvature”, “torsion”, etc. . . fluid terms that contribute to the total AGM. We will therefore assume from now on that the total fluid density and pressure terms are composed of pure matter forms denoted by the subscript  $m$  and the terms coming from the modifications in the form of curvature, torsion or non-metricity.

<sup>2</sup> Here  $t_0$  denotes the age of the universe since the Big Bang.

### 2.1. Solutions from $f(R)$ gravity

$f(R)$  theories are a sub-class of *fourth-order* theories of gravitation [29, 3, 4, 30]:

$$S_{f(R)} = \frac{1}{2} \int d^4x \sqrt{-g} [f(R) + 2L_m] ,$$

with corresponding generalized Einstein field equations:

$$f' G_{\mu\nu} = T_{\mu\nu}^m + \frac{1}{2}(f - Rf')g_{\mu\nu} + \nabla_\nu \nabla_\mu f' - g_{\mu\nu} \nabla_\gamma \nabla^\gamma f' .$$

Here and in the following,  $f, f', \dots$  are shorthands for the arbitrary function  $f(R)$  of the Ricci scalar  $R$  and its first, etc. derivatives w.r.t  $R$ . The sub/superscripts  $m$  and  $R$  stand for the standard matter and curvature components, respectively. The background curvature- fluid thermodynamics (introducing the volume expansion parameter  $\Theta \equiv 3H$ ) can be represented as:

$$\begin{aligned} \rho_R &= \frac{1}{f'} \left[ \frac{1}{2}(Rf' - f) - \Theta f'' \dot{R} \right] , \\ p_R &= \frac{1}{f'} \left[ \frac{1}{2}(f - Rf') + f'' \dot{R} + f''' \dot{R}^2 + \frac{2}{3} \Theta f'' \dot{R} \right] , \end{aligned}$$

whereas the total energy density and pressure terms can be given by

$$\rho \equiv \frac{\rho_m}{f'} + \rho_R , \quad p \equiv \frac{p_m}{f'} + p_R .$$

Imposing the vanishing AGM condition in  $f(R)$  theories with energy and pressure terms as defined above, together with the flat-FLRW relation  $R = 6H^2$  and matter solution for the  $R_h = ct$  case:

$$\rho_m = \frac{\rho_{m0}}{a^{3(1+w)}} = 3H_0^2 \Omega_{m0} (t_0/t)^{3(1+w)} = \alpha R^{3(1+w)/2} ,$$

where  $\alpha \equiv 3t_0^{1+3w} \Omega_{m0} 6^{-3(1+w)/2}$  and  $w$  is the equation of state parameter such that  $p_m = w\rho_m$ , we get the following second-order ordinary differential equation (ode) in  $f$ :

$$2R^2 f'' - f + 2\alpha R^{3(1+w)/2} = 0 . \quad (4)$$

Here we have used the fact that  $\dot{R} = -\frac{2}{3}R\Theta = -\sqrt{\frac{2}{3}}R^{3/2}$ . Moreover, we have introduced the notations  $\rho_{m0}$  and  $\Omega_{m0} \equiv \frac{\rho_{m0}}{3H_0^2}$  as the present-day energy density of matter and its fractional value, respectively. Solving (4) gives

$$f(R) = c_1 R^{\frac{1+\sqrt{3}}{2}} + c_2 R^{\frac{1-\sqrt{3}}{2}} - \frac{4\alpha}{1+12w+9w^2} R^{\frac{3(1+w)}{2}} , \quad (5)$$

with  $c_1$  and  $c_2$  integration constants. This same solution was obtained in [31]. This exact  $f(R)$  solution was found [32] as a counter-example of the shear-free conjecture [33], i.e., describes a universe with simultaneous expansion and rotation. This then implies that the  $R_h = ct$  universe is a simultaneously expanding and rotating spacetime solution! If one compares this result with the GR general condition [34], the  $R_h = ct$  universe with  $\rho + 3p = 0 \Rightarrow p = -\frac{\rho}{3} \Rightarrow c_s^2 = -1/3$ , which is not an allowed solution for standard matter forms. This is an apparent contradiction and needs further investigation.

### 2.2. Solutions from $f(T)$ gravity

In the torsion (TEGR) interpretation of gravitation, the extended-TEGR action reads:

$$S_{f(T)} = \frac{1}{2} \int d^4x \sqrt{-g} [f(T) + 2L_m] ,$$

with corresponding modified field equations

$$f' G_{\mu\nu} = T_{\mu\nu}^m - \frac{1}{2} g_{\mu\nu} (f - f'T) + f'' S_{\mu\nu}{}^\gamma \nabla_\gamma T ,$$

where primes here denote differentiation w.r.t  $T$  and the last term denotes some “super-potential” related to the torsion. The background “torsion-fluid” and total thermodynamic quantities can be given by:

$$\begin{aligned} \rho_T &= \frac{1}{f'} \left[ \frac{1}{2} (Tf' - f) \right] , \\ p_T &= \frac{1}{f'} \left[ \frac{1}{2} (f - Tf') + 2Hf''\dot{T} \right] , \end{aligned}$$

$$\rho \equiv \frac{\rho_m}{f'} + \rho_T = \frac{\rho_m}{f'} + \frac{1}{2f'} (Tf' - f) , \quad p \equiv \frac{p_m}{f'} + p_T = \frac{p_m}{f'} + \frac{1}{2f'} (f - Tf') + \frac{2Hf''\dot{T}}{f'} .$$

The vanishing AGM condition leads to the o.d.e

$$2T^2 f'' - Tf' + f + (1 + 3w)\alpha(-T)^{\frac{3(1+w)}{2}} = 0 ,$$

the solution of which is given by

$$f(T) = c_3 T + c_4 \sqrt{T} - \frac{2\alpha}{2 + 3w} (-T)^{\frac{3(1+w)}{2}} , \quad (6)$$

where  $c_3$  and  $c_4$  are integration constants. Hence any normal-matter-filled universe described by the  $f(T)$ -gravity needs to have the form of  $f(T)$  Lagrangian density given by Eq. (6) if it is to satisfy Eq. (3) and thus describe the  $R_h = ct$  universe. It is worth noting that particular solutions of this result can be shown to be a subset of the more general paradigmatic models of the extended teleparallel gravity solutions reconstructed in [35].

### 2.3. Solutions from $f(Q)$ gravity

In the STEGR interpretation of gravitation:

$$S_{f(Q)} = \frac{1}{2} \int d^4x \sqrt{-g} [f(Q) + 2L_m] .$$

The background non-metric and total-fluid thermodynamics are given by

$$\begin{aligned} \rho_Q &= 3H^2 f' - f/2 = \frac{1}{2f'} (Qf' - f) , \\ p_Q &= f/2 - \left( 3H^2 + \frac{f'' H \dot{Q}}{f'} \right) f' = \frac{1}{f'} \left[ \frac{1}{2} (f - Qf') + 2Hf''\dot{Q} \right] , \\ \rho &\equiv \frac{\rho_m}{f'} + \rho_Q , \quad p \equiv \frac{p_m}{f'} + p_Q . \end{aligned}$$

The vanishing AGM condition leads to the ode

$$2Q^2 f'' - Qf' + f + (1 + 3w)\alpha Q^{\frac{3(1+w)}{2}} = 0 ,$$

the solution of which is given by

$$f(Q) = c_5 Q + c_6 \sqrt{Q} - \frac{2\alpha}{2 + 3w} Q^{\frac{3(1+w)}{2}}, \quad (7)$$

$c_5$  and  $c_6$  representing constants of integration, to be determined upon the imposition of initial conditions. This result shows that the background field equations describing a universe with normal matter and in which the underlying theory of  $f(Q)$  gravitation has the Lagrangian density given by Eq. (7) satisfies the condition (3) and hence is a solution of the  $R_h = ct$  universe.

### 3. Conclusion and outlook

The  $R_h = ct$  universe is a possible cosmological alternative to  $\Lambda$ CDM in explaining certain issues such as the synchronicity problem. However, there are no sources of normal matter that satisfy the vanishing AGM  $\rho + 3p = 0$  condition within the standard GR framework. We have demonstrated that this condition can be obtained from  $f(R)$ ,  $f(T)$  and  $f(Q)$  gravity models provided that the gravity Lagrangians are as given by Eqs. (5), (6) and (7). In particular, we have shown that the  $f(R)$  solution that satisfies vanishing AGM corresponds to the shear-free solution that allows a simultaneously expanding and rotating universe. This is a theoretical solution to the synchronicity problem in the framework of non-standard forms of matter and gravitation, and a lot needs to be done other cosmological aspects, such as perturbations, needs to further scrutinise these solutions for more cosmological viability.

### References

- [1] Carroll S M 2019 *Spacetime and geometry* (Cambridge University Press)
- [2] Hobson M P, Efstathiou G P and Lasenby A N 2006 *General relativity: an introduction for physicists* (Cambridge University Press)
- [3] Clifton T, Ferreira P G, Padilla A and Skordis C 2012 *Physics reports* **513** 1–189
- [4] Gidelew A A 2013 *Beyond concordance cosmology* Ph.D. thesis University of Cape Town
- [5] Saridakis E N, Lazkoz R, Salzano V, Moniz P V, Capozziello S, Jiménez J B, De Laurentis M and Olmo G J 2021 *Modified Gravity and Cosmology* (Springer)
- [6] Milgrom M 2014 *Canadian Journal of Physics* **93** 107–118
- [7] Overduin J M and Wesson P S 1997 *Physics reports* **283** 303–378
- [8] Li B, Barrow J D and Mota D F 2007 *Physical Review D* **76** 044027
- [9] Sahni V and Shtanov Y 2003 *Journal of Cosmology and Astroparticle Physics* **2003** 014
- [10] Kiritsis E and Kofinas G 2009 *Nuclear Physics B* **821** 467–480
- [11] De Felice A and Tsujikawa S 2010 *Living Reviews in Relativity* **13** 1–161
- [12] Melia F and Shevchuk A 2012 *Monthly Notices of the Royal Astronomical Society* **419** 2579–2586
- [13] Beltran Jimenez J, Heisenberg L and Koivisto T S 2019 *Universe* **5** 173
- [14] Capozziello S, De Falco V and Ferrara C 2022 *The European Physical Journal C* **82** 1–30
- [15] Weinberg S 1989 *Reviews of Modern Physics* **61** 1
- [16] Velten H E, Vom Marttens R and Zimdahl W 2014 *The European Physical Journal C* **74** 1–8
- [17] Debono I and Smoot G F 2016 *Universe* **2** 23
- [18] Dunsby P, Goheer N, Osano B and Uzan J P 2010 *Journal of Cosmology and Astroparticle Physics* **2010** 017
- [19] Peel A, Ishak M and Troxel M 2012 *Physical Review D* **86** 123508
- [20] Ellis G F and Elst H V 1999 *Cosmological models Theoretical and Observational Cosmology* (Springer) pp 1–116
- [21] Alfedeel A H and Abebe A 2022 *Open Astronomy* **31** 198–204
- [22] Alfedeel A H, Abebe A and Gubara H M 2018 *Universe* **4** 83
- [23] Tiwari R K, Alfedeel A H, Sofuoğlu D, Abebe A, Hassan E I and Shukla B 2022 *Frontiers in Astronomy and Space Sciences* **9** 965652
- [24] Cai Y F, Capozziello S, De Laurentis M and Saridakis E N 2016 *Reports on Progress in Physics* **79** 106901
- [25] Jiménez J B, Heisenberg L, Koivisto T and Pekar S 2020 *Physical Review D* **101** 103507
- [26] Ayuso I, Lazkoz R and Salzano V 2021 *Physical Review D* **103** 063505
- [27] Melia F 2013 *Astronomy & Astrophysics* **553** A76
- [28] Melia F 2015 *Monthly Notices of the Royal Astronomical Society* **446** 1191–1194
- [29] de la Cruz-Dombriz A 2010 *arXiv preprint arXiv:1004.5052*
- [30] Cruz-Dombriz Á d l 2021 A flavour on  $f(R)$  theories: Theory and observations *Modified Gravity and Cosmology* (Springer) pp 43–78

- 
- [31] Sultana J and Kazanas D 2017 *Monthly Notices of the Royal Astronomical Society* **472** 2583–2589
  - [32] Abebe A, Goswami R and Dunsby P K 2011 *Physical Review D* **84** 124027
  - [33] Ellis G R 1967 *Journal of Mathematical Physics* **8** 1171–1194
  - [34] Nzioki A M, Goswami R, Dunsby P K and Ellis G F 2011 *Physical Review D* **84** 124028
  - [35] De la Cruz-Dombriz Á, Farrugia G, Said J L and Gómez D S C 2017 *Classical and Quantum Gravity* **34** 235011

# The QCD Equation of State in Small Systems

**W. A. Horowitz**

Department of Physics, University of Cape Town, Private Bag X3, Rondebosch 7701, South Africa

E-mail: wa.horowitz@uct.ac.za

**Abstract.** Multiparticle correlations measurements in even the smallest collision systems are consistent with predictions from viscous relativistic hydrodynamics calculations. However, these hydrodynamics calculations use a continuum extrapolated—i.e. infinite volume—equation of state. For the modest temperature probed in these small collisions, the controlling dimensionless product of the temperature and system size  $T \times L \sim 400 \text{ MeV} \times 2 \text{ fm} / 197 \text{ MeV fm} \sim 4$  is not particularly large. One should therefore investigate the small system size corrections to the equilibrium QCD equation of state used in modern viscous hydrodynamics simulations.

We present first results on just such finite system size corrections for two model systems: 1) free, massless scalar theory and 2) quenched QCD with periodic boundary conditions (PBC). We further present work-in-progress results for quenched QCD with Dirichlet boundary conditions.

We show that free, massless scalar fields, which are maximally sensitive to the finite size box, deviate enormously from their infinite volume conformal limit. Quenched QCD with PBC show corrections of  $\sim 20\%$  for the trace anomaly near the phase transition. These corrections are more modest, but will have a meaningful, quantitative impact on the extracted bulk and shear viscosities in these small systems.

## 1. Introduction

In the theoretical and experimental study of heavy ion collisions, the interest is in understanding the non-trivial, emergent many-body dynamics of the strong nuclear force, quantum chromodynamics (QCD). What does that mean? The strong force is one of the four fundamental forces of nature: gravity, electromagnetism, the weak force, and the strong force. The particle physics of, e.g., the electromagnetic force is extremely well understood, with predictions of, e.g., the anomalous magnetic moment of the electron made out to the part per trillion level, in exact agreement with data [1]. However, when a large number of particles whose dynamics is given by the electromagnetic force interact, there are emergent properties. For example, and perhaps both most important and most famous, water is a substance whose properties are dictated by the electromagnetic force. A system with a large number of water molecules is no longer relevantly described by the position and momentum of the individual particles that make up the various water molecules. Rather, one uses quantities such as the temperature, pressure, entropy, heat capacity, conductivity, etc. to describe the system. We have a unique opportunity with the strong force to study both experimentally and theoretically the emergent many-body properties of a non-Abelian gauge theory.

Experimentally, in a heavy ion collision, a large nucleus such as  $^{197}\text{Au}$  or  $^{208}\text{Pb}$ , is collided with another large nucleus at nearly the speed of light. The centre-of-mass energy of a nucleon-nucleon pair in one of these collisions is  $\sim 200 \text{ GeV}$  at the Relativistic Heavy Ion Collider (RHIC)

at Brookhaven National Laboratory and  $\sim 5$  TeV at the Large Hadron Collider at CERN. These are macroscopically large energies; the total energy in a RHIC collision is about that of two mosquitoes colliding. Through Einstein's equation  $E = mc^2$ ,  $\mathcal{O}(10000)$  particles are generated in an LHC collision. These particles are measured in giant detectors such as PHENIX and STAR at RHIC and ALICE, ATLAS, and CMS at LHC.

## 2. Geometry and Flow

One of the crucial measurements made in heavy ion collisions at RHIC or LHC is the momentum distribution of “low” momentum particles. These are particles with momenta  $\lesssim 2$  GeV in the plane transverse to the axis defined by the collision direction of the nuclei. Experimentally, one may extract the Fourier decomposition of the momenta for these measured particles. The even moments of the decomposition dominate over the odd moments, and the second Fourier coefficient,  $v_2$ , dominates over all other moments [2].

One may interpret these Fourier coefficient data as follows. In a heavy ion collision, the nuclei will collide at some non-zero impact parameter. The geometrical anisotropy formed by this off-centre collision is then translated through collective motion into a momentum anisotropy. One naturally imagines that the collective motion is dictated by relativistic viscous hydrodynamics [2–5]; i.e. through energy-momentum conservation and an equation of state  $e(p)$ . The equation of state relates the energy density  $e$  to the pressure  $p$  of the system and is specific to the underlying theory. In a conformal (or scale-free) system in 3 spatial dimensions, the tracelessness of the energy-momentum tensor dictates that  $e = 3p$ . The deviation from this tracelessness for a classically conformal theory induced by quantum corrections is known as the trace anomaly. QCD is approximately conformal (the quark masses are very small), but quantum corrections lead to a non-trivial trace anomaly which has been computed using lattice QCD, see figure (1). Detailed comparisons between the measured Fourier coefficients as a function of momentum and predictions from relativistic viscous hydrodynamics with a realistic equation of state computed from lattice QCD are in very good agreement for large collision systems [2–4].

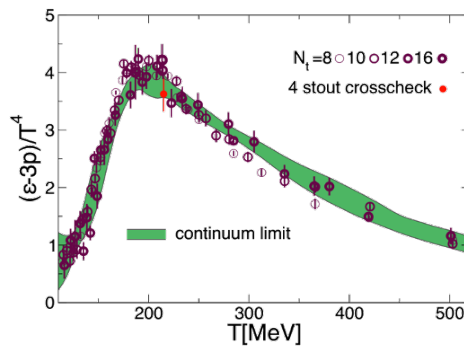


**Figure 1.** The trace anomaly  $\Delta$  from lattice QCD, which is used to determine the equation of state  $e(p)$  [6].

One can see in figure (2) that these hydrodynamics predictions describe data well not only for large nuclear collision systems but, shockingly, the predictions describe very well the measured collective motion even in the smallest collision systems in which protons are collided [4].

One then naturally is led to ask: what are the QCD predictions for the corrections to various thermodynamic quantities due to finite system sizes?

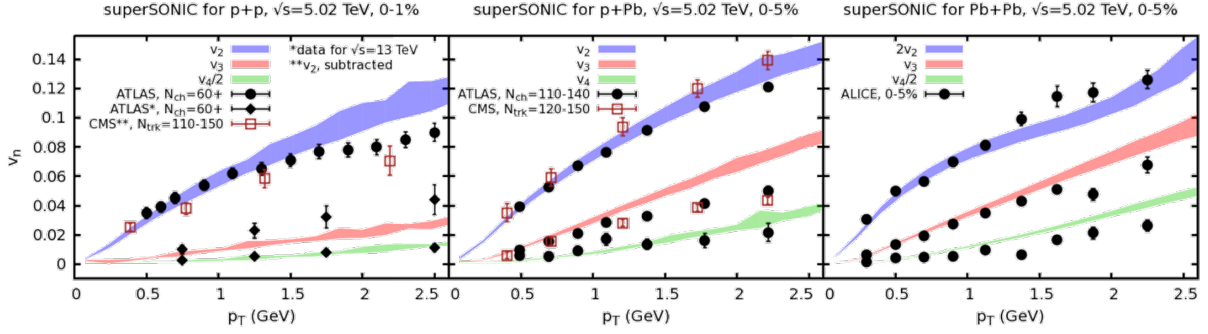


**Figure 2.** The measured Fourier coefficients  $v_n$  as a function of transverse momentum  $p_T$  compared to predictions from a viscous relativistic hydrodynamics calculation [4].

### 3. Finite System Size Corrections

Since QCD is a notoriously complicated theory, it's valuable to investigate the importance of finite system size corrections in simpler systems first. One may, for example, consider a massless scalar field theory that has certain dimensions constrained to lie between perfectly reflecting walls [7]. Interestingly, then, many of the thermodynamic variables as a function of system size appear to mimic the usual temperature dependence of the phase transition predicted by lattice QCD in infinite volume systems [6]; see figure (3). One may compare the analytic results derived using scalar field theory to a full lattice QCD calculation that tested the sensitivity to system asymmetry [8]. One sees in figure (4) that the full lattice simulations show a qualitatively similar behavior as that predicted by the scalar theory.

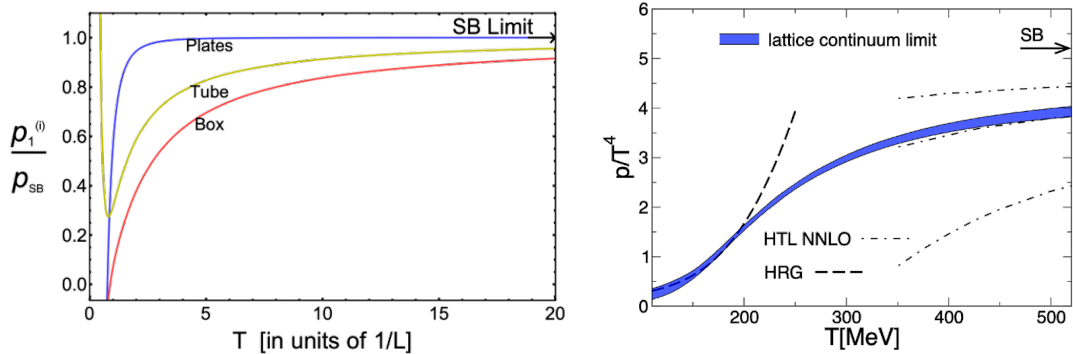


**Figure 3.** (Left) The pressure as a function of the dimensionless variable  $T \times L$  for a massless scalar field confined between two infinite parallel plates divided by the infinite volume pressure, inside a symmetric tube of infinite length, or a symmetric box [7]. (Right) The dimensionless pressure divided by temperature to the fourth power as a function of the temperature as computed in lattice QCD [6].

One may then attempt to determine the sensitivity to the trace anomaly, which is the driving quantity needed for the equation of state. It turns out that the trace of the energy momentum tensor for a massless scalar field is identically zero, even when conformal invariance is broken by the system's boundary conditions. Therefore, analytically, the finite system size corrections to the trace anomaly can only come from finite system size corrections to the running coupling. In [9], an estimate of the finite system size corrections to the thermodynamic properties derived using thermal field theory in QCD [10] was found using the lattice running coupling for a scalar

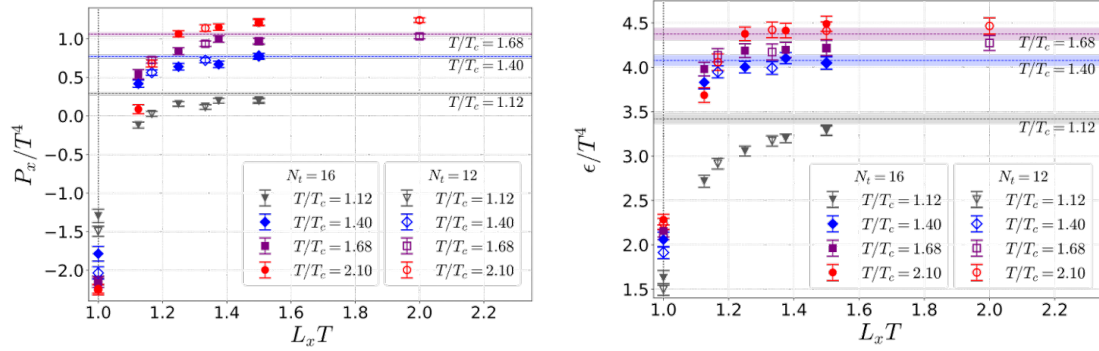


**Figure 4.** (Left) The pressure in the short direction divided by temperature to the fourth power as a function of the dimensionless variable  $T \times L$  for quenched lattice QCD [8]. (Right) The dimensionless pressure divided by temperature to the fourth power as a function of the dimensionless variable  $T \times L$  as computed in quenched lattice QCD [8].

field [11]. We show the result of making such an estimate in figure (5). One may see that the trace anomaly  $\Delta \equiv T^\mu_\mu$  decreases with system size. We may again compare the analytics to a full, quenched lattice QCD calculation [9]; we show a preliminary result of such a calculation in figure (5). The figure shows the non-normalized (and hence very preliminary) scaled trace anomaly  $\Delta/T^4$  as function of the temperature  $T$  in GeV for several values of the number of spatial lattice sites:  $N_x = 24$  (red), 16 (green), 8 (orange) and 4 (blue) at fixed coupling. One can see that the trace anomaly is largest for the largest system, and that the trace anomaly is the most well defined for this largest system size. As the system size decreases, one can see that the magnitude of the trace anomaly decreases and its width increases. Thus the full numerics agree with our expectations: the scaled trace anomaly  $\Delta/T^4$  decreases with system size, and, further, the phase transition is washed out by a decreasing system size.

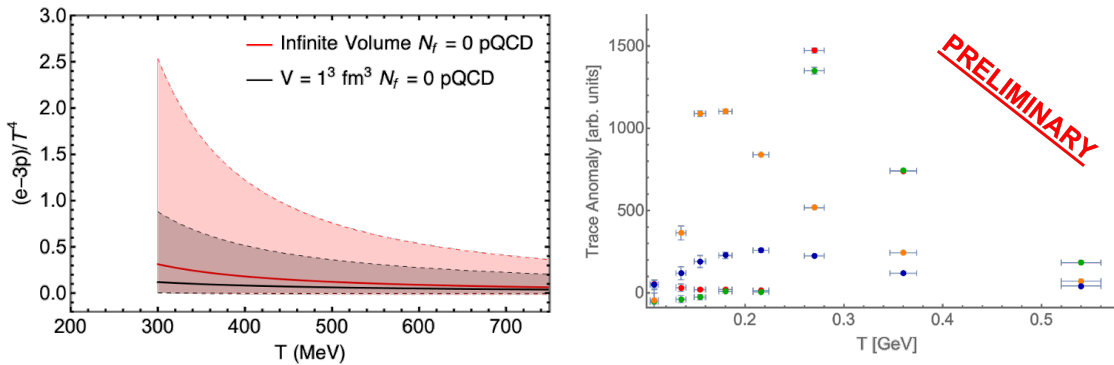


**Figure 5.** (Left) The trace anomaly from using a running coupling from lattice scalar field theory [11] in thermal QCD [9, 10]. (Right) The scaled trace anomaly  $\Delta/T^4 \equiv (\epsilon - 3p)/T^4$  as a function of temperature  $T$  (GeV) in quenched QCD with periodic boundary conditions with sides  $N_x = 24$  (red), 16 (green), 8 (orange) and 4 (blue) at fixed coupling [9].

#### 4. Conclusions

We are interested in the fundamental research in the emergent dynamics of QCD. We live in an especially interesting time for such research, as the community is able to simultaneously

investigate this physics theoretically and experimentally. Detailed comparison of data with viscous relativistic hydrodynamics predictions imply that there is near perfect fluidity in the aftermath of large nuclear collisions. Surprisingly, this near perfect fluidity is also seen in the smallest hadronic collision systems. Since  $T \times L$  is not small in these smallest systems, we must ask: what are the finite system size corrections to the inputs into the hydrodynamic simulations that are being compared to data?

We have shown in this proceedings that finite size effects can, in fact, be large for the thermodynamic properties of quantum field theories at sizes relevant for hadronic collisions at RHIC and LHC. In particular, there is likely a non-trivial impact on the extraction of the QCD equation of state from data and/or conclusions for the viscosity to entropy density ratio determined by comparing experimental measurements to relativistic hydrodynamics predictions.

In future work, we look forward to explicitly computing the finite size effects in the QCD running coupling, refining finite size lattice calculations with periodic boundary conditions, and implementing more realistic Dirichlet boundary conditions in lattice calculations. In all of these future works, maintaining gauge invariance will be a challenge. As a first step towards computing the finite size corrections to the running coupling, a calculation of the next-to-leading order contribution to  $2 \rightarrow 2$  scattering in  $\phi^4$  theory on an asymmetric torus has been carried out [12]. One cannot use the usual method of dimensional regularization on an asymmetric manifold; other regularization schemes had their own disadvantages. In order to derive the result in [12], a new regularization scheme was invented, denominator regularization. In denominator regularization, the power of the denominator is analytically continued. It was shown in [12] that this procedure gave a result that correctly asymptotically approached the known infinite volume result; it was further shown in [12] that the finite system size result satisfied unitarity. Denominator regularization was then shown in [13] that denominator regularization maintains gauge invariance in QED and QCD in infinite volume by checking that the one loop correction to the photon and gluon propagators is transverse and, further, that denominator regularization manifestly gives the correct axial anomaly. One then has good reason to believe that such a regularization scheme can be applied to QED and QCD on an asymmetric torus to determine the finite system size corrections to the running coupling in those theories. One will then have some analytic insight into the finite system size corrections to the trace anomaly for QED and QCD. In the higher momentum regime, parton energy loss provides another tool for investigating the properties of the quark-gluon plasma generated in heavy ion collisions [14]. Recent work computed the finite system size corrections to energy loss [15]; it will be interesting to see these finite system size effects propagated through to a full energy loss model.

### Acknowledgments

The author wishes to thank the South African National Research Foundation and the South Africa-CERN Collaboration for support. The author further gratefully acknowledges extensive valuable discussions with Alexander Rothkopf, Sylvain Mogliacci, and Isobel Kolbé.

### References

- [1] Hanneke D, Fogwell S and Gabrielse G 2008 *Phys. Rev. Lett.* **100** 120801 (*Preprint* 0801.1134)
- [2] Schenke B, Jeon S and Gale C 2011 *Phys. Rev. Lett.* **106** 042301 (*Preprint* 1009.3244)
- [3] Heinz U and Snellings R 2013 *Ann. Rev. Nucl. Part. Sci.* **63** 123–151 (*Preprint* 1301.2826)
- [4] Weller R D and Romatschke P 2017 *Phys. Lett. B* **774** 351–356 (*Preprint* 1701.07145)
- [5] McNelis M, Bazow D and Heinz U 2021 *Comput. Phys. Commun.* **267** 108077 (*Preprint* 2101.02827)

- [6] Borsanyi S, Fodor Z, Hoelbling C, Katz S D, Krieg S and Szabo K K 2014 *Phys. Lett. B* **730** 99–104 (*Preprint* 1309.5258)
- [7] Mogliacci S, Kolbé I and Horowitz W A 2020 *Phys. Rev. D* **102** 116017 (*Preprint* 1807.07871)
- [8] Kitazawa M, Mogliacci S, Kolbé I and Horowitz W A 2019 *Phys. Rev. D* **99** 094507 (*Preprint* 1904.00241)
- [9] Horowitz W and Rothkopf A 2022 *SciPost Phys. Proc.* **10** 025 (*Preprint* 2109.01422)
- [10] Andersen J O and Strickland M 2005 *Annals Phys.* **317** 281–353 (*Preprint* hep-ph/0404164)
- [11] Montvay I and Munster G 1997 *Quantum fields on a lattice* Cambridge Monographs on Mathematical Physics (Cambridge University Press) ISBN 978-0-521-59917-7, 978-0-511-87919-7
- [12] Horowitz W A and Plessis J F D 2022 *Phys. Rev. D* **105** L091901 (*Preprint* 2203.01259)
- [13] Horowitz W A 2022 (*Preprint* 2209.02820)
- [14] Majumder A and Van Leeuwen M 2011 *Prog. Part. Nucl. Phys.* **66** 41–92 (*Preprint* 1002.2206)
- [15] Kolbe I and Horowitz W A 2019 *Phys. Rev. C* **100** 024913 (*Preprint* 1511.09313)

# Energies of the Anharmonic Oscillator using the Metropolis Algorithm and Matrix Methods

**B A Ngwenya<sup>1</sup>, A K Rothkopf<sup>2</sup> and W A Horowitz<sup>1</sup>**

<sup>1</sup>Department of Physics, University of Cape Town, Rondebosch 7700, South Africa

<sup>2</sup>Department of Mathematics and Physics, University of Stavanger, PO Box 8600, 4036 Stavanger, Norway

E-mail: ngwble001@myuct.ac.za

**Abstract.** We present results of the energies and energy differences of the quantum harmonic oscillator as well as the quantum anharmonic oscillator at quartic coupling constants of different magnitudes. These observables are computed using the Markov Chain Monte Carlo approach (Metropolis Algorithm) and are compared to results obtained using matrix elements methods at various basis sizes. We illustrate the consistency in the two methods and show that for the anharmonic oscillator, a sufficiently large basis size is required with increasing energy in order for the matrix result to converge to the lattice result. We also show that large quartic coupling constants are more sensitive to the truncation of the basis size.

## 1. Introduction

In classical mechanics, the harmonic oscillator is a very popular example of a restoring force acting on an object about its equilibrium position, and has many applications. In a one dimensional case, one can consider a particle of mass,  $m$ , attached to a spring and experiencing a restoring force as described by Hooke's law [1],  $F = -kx$ . The corresponding potential energy is given by  $E = kx^2/2$ , has a parabolic shape and describes the continuous energies that the particle can attain during its oscillation. The quantum harmonic oscillator is the corresponding analogue of the harmonic oscillator in quantum mechanics and is characterized by the Schrödinger equation,

$$\hat{H}\psi = \left( -\frac{\hbar^2}{2m} \frac{d^2}{dx^2} + \frac{m\omega^2 x^2}{2} \right) \psi = E\psi \quad (1)$$

where the first term in the Hamiltonian ( $\hat{H}$ ) is the kinetic term and the second term is the same potential we saw in the classical analogue, with  $\omega = \sqrt{k/m}$  and describes the natural frequency of the oscillator. Various analytical methods have been formulated to solve the above equation for the energy eigenvalues, and they show that unlike in the classical case, the energies of the quantum harmonic oscillator are discrete, quantized and given by [2];

$$E_n = \left( n + \frac{1}{2} \right) \hbar\omega \quad (2)$$

where  $n = 0$  corresponds to the ground state. Note that this ground state energy is not equal to zero, a consequence of the uncertainty principle [3].

In general, molecular vibrations with arbitrary potentials can be approximated as harmonic potentials around a stable equilibrium through expanding the potential as a Taylor series. The harmonic oscillator describes such an expansion truncated at second order [4]. At higher order, the potential contains quartic terms and the motion becomes that of an anharmonic oscillator. The corresponding Hamiltonian with a quartic term, in one dimension is given by [5],

$$\hat{H} = -\frac{\hbar^2}{2m} \frac{d^2}{dx^2} + \frac{m\omega^2 x^2}{2} + \lambda x^4 \quad (3)$$

where  $\lambda$  is the coupling constant of the quartic (anharmonicity) term.

Unlike the harmonic oscillator which has exact analytic solutions, the anharmonic oscillator cannot be solved analytically and we need to resort to numerical methods. In this paper, we employ the Markov Chain Monte Carlo technique to compute the exact, as well as energy differences of the first few lowest energies of the one-dimensional anharmonic oscillator while varying the coupling constant of the quartic term. In doing this, we reproduce the results of [5] using our own calculations in order to learn techniques that are applicable to lattice QCD calculations as we are interested in lattice QCD as a tool for understanding how QCD behaves in small systems. We then compare these lattice solutions to corresponding results when using matrix elements at varying basis size to explore the effect of basis size truncation on the accuracy of the numerical result.

## 2. The Metropolis Algorithm and Matrix Elements

A starting point in formulating an approach to numerically solve the quantum anharmonic oscillator on the lattice is to build an understanding of how the state of a particle evolves with time. That is, given a particle at  $(x_0, t_0)$ , what is the probability of finding it at  $(x_f, t_f)$ , where  $t_f$  is some later time. Schrödinger and Heisenberg formulated solutions to this problem employing the eigenstates of the Hamiltonian. As an alternative, Feynman formulated the path integral approach to quantum mechanics [6], motivated by the work of Paul Dirac suggesting that a Lagrangian formulation is more fundamental than a Hamiltonian one.

The main idea behind the path integral formulation is the equivalence of the transition probability amplitude,  $\langle \psi(x_f, t_f) | \psi(x_0, t_0) \rangle$  between any two points and the exponential of the classical action,  $\exp\{iS[x(t)]\}$  of the trajectory. Given that a particle cannot take a well-defined path between any two points, Feynman showed that the total transition probability amplitude is given by the sum of the amplitudes of all the possible paths that the particle can take between the two points. We then define the imaginary time propagator (which fully describes the evolution of a system with time) between the two spacetime points as the probability transition amplitude between the wavefunction evaluated at those two points,

$$U(x_f, \tau_f; x_0, \tau_0) = \langle \psi(x_f, \tau_f) | \psi(x_0, \tau_0) \rangle \quad (4)$$

$$= \langle x_f | e^{-\hat{H}(\tau_f - \tau_0)/\hbar} | x_0 \rangle \quad (5)$$

$$= \int_{\text{all paths}} \exp \left[ -\frac{1}{\hbar} \int_{\tau_0}^{\tau_f} L[x(\tau)] d\tau \right] \quad (6)$$

where  $L$  is classical Euclidean Lagrangian, and we perform the integration over all possible trajectories between the two spacetime points. Notice also, the Wick rotation (change in the time parameter)  $t = -i\tau$ , where  $\tau = \hbar/k_B T$  is the ‘imaginary time’ and allows for a direct comparison to the partition function in statistical mechanics. A complete derivation of the above path integral can be found in Ref. [7].

We then use the Metropolis Hastings algorithm [8, 9] to generate the many different paths on the lattice, that can be used to compute the propagator. A discrete time lattice with  $N_\tau$

sites (lattice points in the time direction), employing periodic boundary conditions (to avoid rejecting paths affected by lattice site edges) is used. Euclidean time increments  $\delta\tau$  are used, such that the lattice points are given by  $x_i = i\delta\tau$ , with  $i = 1, \dots, N_\tau$ . In order to perform these calculations computationally, we start by expressing our equations in dimensionless form by setting  $\hbar = c = 1$  such that the discretised action for the anharmonic oscillator is given by [5],

$$\tilde{S}(\tilde{x}_i) = \sum_{i=1}^{N_\tau} \left[ \frac{\tilde{m}}{2} (\tilde{x}_{i+1} - \tilde{x}_i)^2 + \frac{\tilde{m}\tilde{\omega}^2 \tilde{x}_i^2}{2} + \tilde{\lambda} \tilde{m}^2 \tilde{\omega}^3 \tilde{x}_i^4 \right] \quad (7)$$

$$\tilde{x}_i = \frac{x_i}{\delta\tau}, \quad \tilde{m} = m\delta\tau, \quad \tilde{\omega} = \omega\delta\tau \quad (8)$$

where  $\tilde{x}_i$ ,  $\tilde{m}$ ,  $\tilde{\omega}$  and  $\tilde{\lambda}$  are dimensionless variables.

The Metropolis algorithm requires as an input an array with  $N_\tau$  entries containing the initial path between the two points. This initial path can be set to an array of zeros (a cold start), or an array of random numbers (a hot start). We also need to input a real number,  $h$  the target interval which determines the acceptance rate in the simulation (i.e. how many paths should be accepted/rejected on average), as well as the various parameters appearing in the action. Every time we traverse through the lattice (one sweep), we produce one trajectory with real coordinates  $(x_1, \dots, x_{N_\tau})$  in Euclidean time, and these coordinates have probability density  $\rho[\{x_i\}] \sim \exp\{-\tilde{S}(\tilde{x}_i)\}$  [10]. This procedure is repeated many times to create an ensemble of paths in Monte Carlo time, forming a Markov Chain and this ensemble of paths is then used for analysis.

Prior to taking any measurements that will be used for analysis, one has to discard the first ‘few’ paths that are generated before the system thermalises because these paths are not representative of the equilibrium distribution of the system. Given that once the random number generator used to produce these paths is seeded, the produced paths are correlated. To reduce the effect of these correlations in the measurements, one also needs to discard a certain number of paths between any two subsequent measurements used for analysis. These correlations lead to increased uncertainties in the measurements and can be quantified using the autocorrelation time [11].

We then make use of these measurements (ensembles of paths) to compute various quantities of interest. The ground state energy is computed from the correlation functions of the position operator  $\hat{x}$  [12],

$$E_0 = m\omega^2 \langle \hat{x}^2 \rangle + 3\lambda \langle \hat{x}^4 \rangle \quad (9)$$

while the energies are calculated as follows [13, 11];

$$E_1 - E_0 = -\hbar \lim_{\tau \rightarrow \infty} \left[ \frac{d \log[G_2(\tau)]}{d\tau} \right], \quad G_2(\tau) = \langle \hat{x}(\tau)\hat{x}(0) \rangle - \langle \hat{x}(\tau) \rangle \langle \hat{x}(0) \rangle \quad (10)$$

$$E_2 - E_0 = -\hbar \lim_{\tau \rightarrow \infty} \left[ \frac{d \log[G_4(\tau)]}{d\tau} \right], \quad G_4(\tau) = \langle \hat{x}(\tau)^2 \hat{x}(0)^2 \rangle - \langle \hat{x}(\tau)^2 \rangle \langle \hat{x}(0)^2 \rangle \quad (11)$$

where  $G_2(\tau)$  and  $G_4(\tau)$  are the connected two-point and four-point correlation functions respectively.

We now discuss the matrix elements method [14], which is another numerical method that can be used to solve the time-independent Schrödinger equation (TISE) for the eigenfunctions ( $\psi$ ) and energy eigenvalues. When using this method, one needs to express the eigenfunctions as a linear combination of a collection of simple orthonormal basis functions ( $\phi_n$ ),

$$\psi = \sum_{n=1}^{\infty} c_n \phi_n \quad (12)$$

and find the unknown coefficients  $c_n$ . Substituting this expression into the TISE and applying Fourier's trick, one obtains,

$$\sum_{n=1}^{\infty} \left( \int_{-\infty}^{\infty} \phi_m^* \hat{H} \phi_n dx \right) c_n = E c_m \quad (13)$$

where  $H_{nm}$  is the matrix element of the Hamiltonian which can be easily obtained computationally. The above equation can be expressed in matrix form and one finds the energies of the system (anharmonic oscillator in our case) as the eigenvalues of the Hamiltonian matrix.

### 3. Results

Our MCMC energy result is computed while varying the effective lattice spacing ( $a$ ), see ref. [5] for a detailed discussion on the procedure. Lattice calculations converge to the correct result in the continuum limit (i.e.  $a \rightarrow 0$ ), however it is unrealistic to gradually decrease the effective lattice spacing in simulations to its continuum value as this is limited by computational resources. Instead, one uses the results obtained from a few lattice spacings and extrapolates to the continuum limit.

In Figure 1, we show the energies of the ground state and first excited state of the quantum anharmonic oscillator respectively. These energies are computed using matrix elements with varying basis size, and using the correlation functions of the position operator in the lattice approach. On the lattice, the ground state energy is given by Eq. 9, while the first excited state is obtained from adding  $E_0$  to the two-point connected correlation function in Eq. 10 which gives  $E_0 - E_1$ . A graphical representation of this energy difference is shown in Figure 2, as well as the energy difference of the second excited state and ground state, which is obtained from the four-point connected correlation function in Eq. 11. In the case of the harmonic oscillator (i.e.  $\lambda = 0$ ), the Hamiltonian matrix is diagonal and we obtain the exact energy eigenvalues for  $E_0$ ,  $E_1$  etc. irrespective of the basis size (recall that the basis size just gives you the number of energy levels of interest). As we increase the quartic coupling,  $\lambda$ , to a non-zero value (where the Hamiltonian matrix is no longer diagonal) while keeping the basis size the same (i.e. as low as in the harmonic oscillator case), we obtain the correct result for lower energies but inaccurate results for higher energies which are more sensitive to the truncation of the basis size.

The effect of the basis size on the accuracy of the measured energies is also observed as one increases the quartic coupling. In general, the higher the quartic coupling, the more sensitive the energies of the corresponding oscillator are to the truncation of the basis. The reason for this sensitivity is that, the energy values of the various energy levels of the anharmonic oscillator increase with  $\lambda$  i.e.  $E_i(\lambda = 0) < E_i(\lambda = 1) < E_i(\lambda = 2)$  etc., where  $i$  corresponds to the energy levels. Thus increasing  $\lambda$  implies an increase in the energies, which are sensitive to the truncation of the basis size. Looking at Figure 1 and 2, the effect of the basis truncation is clear at large quartic coupling where the MCMC result is only consistent with the matrix result at a high basis size.

### 4. Conclusions

We have presented numerical results of the ground state and first two excited states energies of the one-dimensional quantum anharmonic oscillator at varying quartic coupling constants. These energies were computed on the lattice using the metropolis algorithm, which allows for computational solutions to the path integral formulation of quantum mechanics. We compare these lattice results to energy eigenvalues of the Hamiltonian obtained using the matrix elements method for varying basis size.

We showed that one obtains accurate energies for the harmonic oscillator using both the lattice approach and matrix elements even for a small basis size since the Hamiltonian is diagonal.

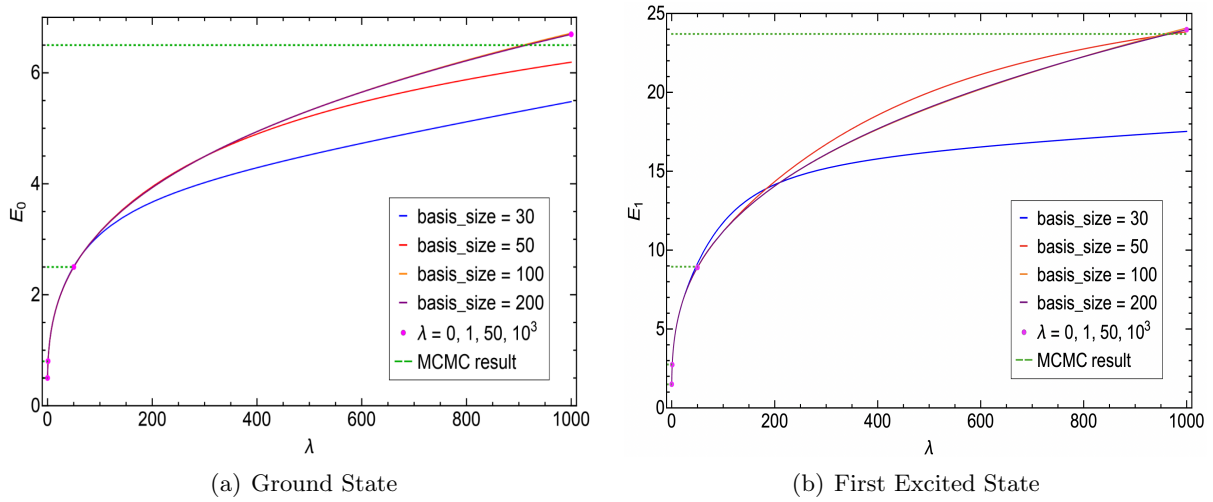


**Figure 1.** Comparison of the energies of the harmonic and anharmonic oscillator computed using lattice and matrix methods.

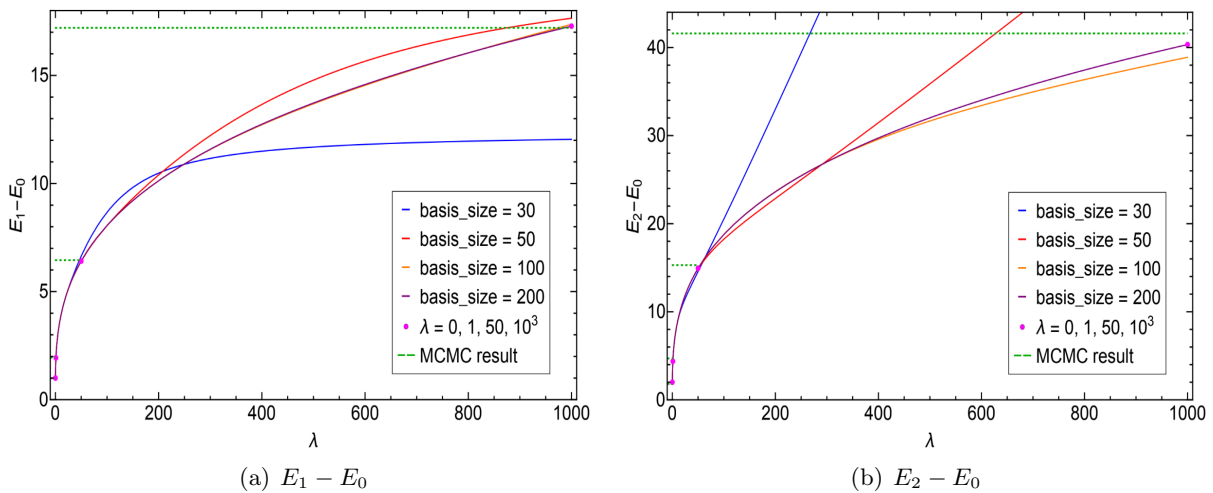


**Figure 2.** Harmonic and anharmonic oscillator energy differences computed using lattice and matrix methods.

However, for the anharmonic oscillator, higher energies (excited states) are very sensitive to the truncation of the basis size, thus one needs to increase the basis size to improve the accuracy of the numerical result for excited state energies. In addition, we also showed that the larger the quartic coupling constant ( $\lambda$ ), the more sensitive the energies are to the basis size truncation. This sensitivity with increasing  $\lambda$  is because the magnitude of the energies at various energy levels increases with increasing  $\lambda$ . At a sufficiently large basis size, we show that the matrix elements result converges to the results obtained on the lattice. While one can compute energies of even higher excited states using matrix elements with a large basis size (limited by computational resources), performing such a calculation on the lattice becomes increasingly difficult due to increasing statistical fluctuations.

### Acknowledgments

The authors would like to acknowledge the SA-CERN Collaboration and the South African National Research Foundation (NRF) for their generous financial contributions towards this work.

### References

- [1] Thompson J O *Science* **64** **1656** 298–9
- [2] Griffiths D J and Schroeter D F 2018 *Introduction to quantum mechanics* (Cambridge university press)
- [3] Heisenberg W 1927 *Z. Phys.* **43** 172–198
- [4] Blukis U and Howell J 1983 *Journal of Chemical Education* **60** 207
- [5] Mittal S, Westbroek M J E, King P R and Vvedensky D D 2020 *Eur. J. Phys.* **41** 055401 (*Preprint* 1811.04669)
- [6] Feynman R P 1948 *Rev. Mod. Phys.* **20**(2) 367–387
- [7] MacKenzie R 1999 Path integral methods and applications *6th Vietnam International School on Physics* (*Preprint* quant-ph/0004090)
- [8] Hastings W K 1970 *Biometrika* **57** 97–109 ISSN 0006-3444
- [9] Gubernatis J E 2005 *Physics of plasmas* **12** 057303
- [10] Morningstar C 2007 The Monte Carlo method in quantum field theory *21st Annual Hampton University Graduate Studies Program (HUGS 2006)* (*Preprint* hep-lat/0702020)
- [11] Joseph A 2020 *Markov Chain Monte Carlo Methods in Quantum Field Theories* (Springer International Publishing)
- [12] Binney J and Skinner D 2013 *The physics of quantum mechanics* (Oxford University Press)
- [13] Creutz M and Freedman B 1981 *Annals of Physics* **132** 427–462 ISSN 0003-4916
- [14] Schwartz C 1967 *Journal of Computational Physics* **2** 90–113 ISSN 0021-9991

# Quantum Network Coding on a Superconducting Processor

**H Rall, M S Tame**

Department of Physics, Stellenbosch University, Private Bag X1, Matieland, South Africa

E-mail: [hjalmar.rall1@gmail.com](mailto:hjalmar.rall1@gmail.com)

**Abstract.** An important consideration for quantum communication within the current noisy intermediate-scale quantum regime is the resource requirements of routing information within a complex network such as a quantum internet. Quantum network coding (QNC) reduces the resource requirements for simultaneous communication over a network by eliminating the problem of contention for network resources. In this work we implement measurement-based QNC (MQNC) on the latest generation IBM Q superconducting processor `ibm_cairo` by making use of an alternative to SWAP-based transpiling and demonstrate that improvements in processor hardware allow for greatly improved fidelity of the protocol compared to a prior work. Using these improved results we study noise within the code and identify a major contributor to noise in the final states.

## 1. Introduction

A major goal in the development of quantum computers and quantum communication is the creation of a quantum internet [1], which would allow the establishment of entanglement between multiple pairs of distant end nodes using a single common quantum communication network. By making use of a shared network, the resource cost of performing tasks such as quantum key distribution (QKD) and distributed quantum computing is greatly reduced compared to the scenario where each pair of end nodes must share a direct quantum communication channel. This holds also for the case of communication within a single processor.

Simple quantum networks are starting to become feasible with, for example, a 3-qubit solid-state network [2] and a large-scale QKD network with a satellite link [3] being demonstrated successfully. Furthermore, there is ongoing research into enabling optical communication between superconducting quantum processors [4, 5], which raises the possibility of using quantum processors to control more complex quantum networks in the near future. Thus the hardware for a quantum internet may be developed in the near future, but this hardware will still fall under the noisy intermediate scale quantum (NISQ) regime where the number of qubits is limited and gates increase the amount of noise in the system. Accordingly, steps must be taken to make efficient use of the available resources.

The major disadvantage of a shared network (whether classical or quantum) is that routing information along a path between end nodes means that channels along the path become unavailable for other messages if the channels do not have sufficient capacity. If such a clash between routes exists and no alternate routing is available, the situation is referred to as contention. If routing is to be used, the only resolution to this problem is time-multiplexing, where some of

the messages are delayed while the others are sent. This has the effect of reducing the bandwidth (information transfer per unit time) of the channel. This problem can be circumvented by making use of network coding, or the analogous quantum network coding (QNC) [6, 7], instead of routing.

Measurement-based quantum network coding (MQNC) [8] is a variation on QNC which offers greater simplicity and reduced gate count by making use of measurement-based computing. MQNC was recently performed on a previous-generation IBM superconducting processor by Pathumsoot et al. [9], but processor noise proved too high to obtain useful final states. By making use of a novel transpiling technique, we implemented MQNC on newer IBM hardware and show that the improvements in the hardware allow for greatly improved quality of the final states. We also investigate the role of depolarising noise in gates on the quality of the final state, and discuss the implications of our results.

## 2. Background

### 2.1. Graph States

MQNC falls within the category of measurement-based quantum algorithms. These make use of entangled states known as graph states which have the property that their qubits and entanglement correspond directly to the edges and vertices of an undirected graph. A graph  $G(V, E)$  with vertex set  $V$  and edge set  $E$  defines a graph state with a statevector given by

$$|G\rangle = \prod_{i < j; i, j \in G} CZ_{i, j}^{\Gamma_{i, j}} \bigotimes_{k=1}^n |+\rangle_k,$$

where  $\Gamma_{i, j}$  is the adjacency matrix of the underlying graph. There are a number of local operations and measurements which serve to transform one graph state into another [10], the two most useful of which are summarised below:

- **T1:** A Z-basis measurement on a qubit  $a$  removes the corresponding vertex and incident edges from the graph.
- **T2:** X-basis measurements on two adjacent qubits  $a$  and  $b$  removes them and complements the bipartite subgraph induced by  $N_a$  and  $N_b$ . i.e.  $G(V, E) \rightarrow G(V/\{a, b\}, E \Delta K)$  with  $K$  the complete bipartite subgraph induced by  $N_a \cup \{a\}$  and  $N_b \cup \{b\}$ . In other words, all the neighbours of  $a$  are connected to all the neighbours of  $b$  unless a connection already exists, in which case it is broken.

### 2.2. Network Coding

MQNC solves contention in the butterfly network, shown in Fig. 1 (a). The goal is to be able to manipulate the network to achieve either of the two final states shown on the right-hand sides of Fig. 1 (b) and (c). This is achieved by performing either two X-measurements (Rule T2) or two Z-measurements (Rule T1) on the central qubits as shown. The final 2-qubit graph states can subsequently be used for communicating quantum information by means of teleportation. By using measurements to redistribute the existing entanglement (communication channels), the network has been reconfigured so that the bottleneck no longer exists.

## 3. Experimental implementation

The current generation of IBM Q processors have the layout shown in Fig. 2. Unlike the prior experiment in Ref. [9] which made use of the grid-like layout of the older IBM Q 20 Tokyo processor, it is not possible to directly create the 6-qubit resource state necessary for MQNC on this new layout. It is possible to transpile quantum circuits to layouts on which they cannot be executed directly, but this ordinarily requires the use of noisy SWAP operations to move

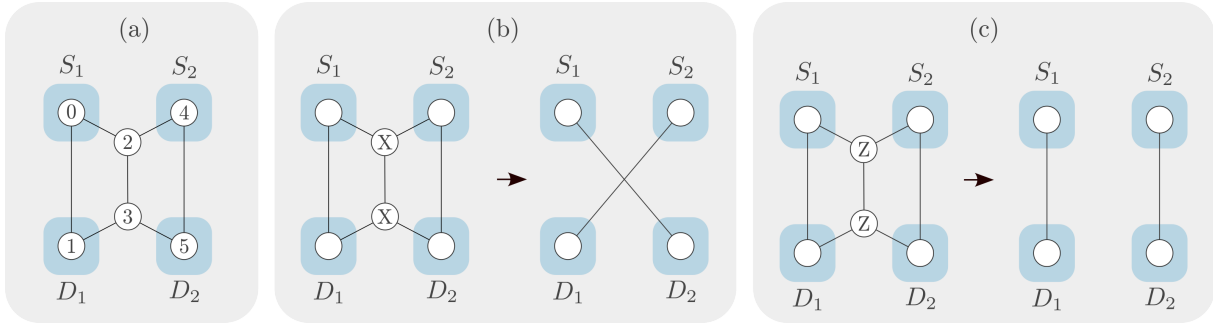


**Figure 1.** (a) The 6-qubit resource state for MQNC. (b) Creation of cross pairs via X-measurements. (c) Creation of straight pairs via Z-measurements. White circles represent qubits and lines represent entanglement, corresponding to the vertices and edges of a graph respectively. Blue squares represent end nodes in the network.

logical qubits to adjacent physical qubits before they can be entangled. In the case of graph states, however, there is an alternative. By making use of local complementation (LC) [10] it is possible to redistribute entanglement in a controlled manner using only single-qubit operations. Using LC, we were able to create the MQNC resource state on `ibm_cairo` using only seven 2-qubit gates as opposed to the much larger number required for SWAP-based transpiling.

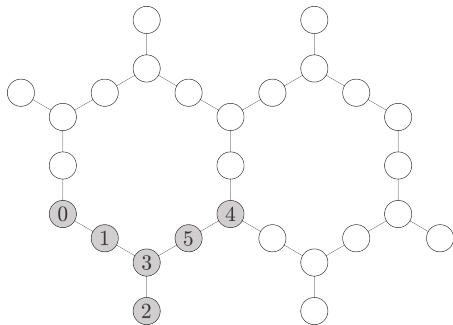


**Figure 2.** Layout of `ibm_cairo`. Edges indicate neighbouring qubits on which CNOT gates may be performed. Light grey qubits are used to create the 6-qubit resource state for the network code.

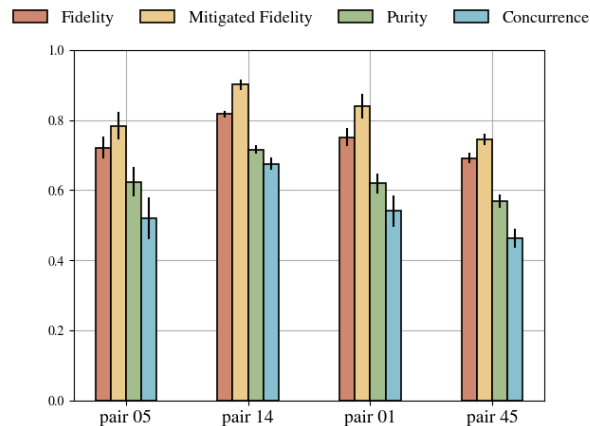


**Figure 3.** Results of full state tomography on the 2-qubit entangled states generated using the MQNC protocol on `ibm_cairo`. Fidelity is shown before and after application of readout error mitigation on the 2 qubits.

We performed MQNC as outlined in Fig. 1 on the IBM Q falcon superconducting processor `ibm_cairo` using LC instead of standard transpiling. This is a 27-qubit device with the layout shown in Fig. 2. The processor was accessed remotely through the IBMQ API and the QISKIT Python library.

A single run of the experiment constitutes calibration for readout error mitigation and state tomography of one of the 2-qubit graph states (pairs) generated using MQNC. This is repeated for each of the four pairs in turn, and the whole procedure is then repeated 30 times to account for variation in processor noise. The runs were spread out between 9PM 26 Apr 2022 and 5AM 27 Apr 2022 (UTC) due to use of the fair-share queuing system. The variation in processor noise is found to be sufficiently small over a time-scale of minutes that the delay between calibration

and experiment is not significant and results are not skewed by varying noise from one pair to the next. The measurements in the protocol result in probabilistic byproduct operations on the desired final state. The IBM processors do not support the feed-forward functionality necessary to undo these operations, so results must be post-selected based on measurement outcomes. The four possible outcomes of two measurements at the central qubits of the network code correspond to four possible byproducts (including the identity) on each of the final 2-qubit states, which occur with equal probability so that 1/4 of the results are kept.

In order to measure the quality of the state generated and to compare to the results of the previous study [9], we perform quantum state tomography [11] on each of the four pairs that can be generated using MQNC. Readout error mitigation is then applied to the results, and they are subsequently post-selected so as to correspond to the byproduct-free graph state. 4000 shots are used for each of the 9 tomography circuits so that approximately 1000 shots remain after post-selection. Density matrices are obtained from the tomography results, and the fidelity compared to the ideal state  $|G_2\rangle = \frac{1}{\sqrt{2}}(|0+\rangle + |1-\rangle)$ , as well as the purity and concurrence are calculated. The results are shown in Fig. 3 and are compared to those of the prior experiment in Table 1. Note that only values for the cross pairs are reported in Ref. [9]. As in the prior experiment, the fidelity is defined as

$$F(\rho_1, \rho_2) = \left( \text{Tr} \sqrt{\sqrt{\rho_1} \rho_2 \sqrt{\rho_1}} \right)^2.$$

Fidelity is a measure of the overlap between quantum states, having a value of 1 for identical states and 0 for orthogonal states. In addition to fidelity, we also consider the concurrence, an entanglement monotone defined according to

$$C(\rho) = \max\{0, \lambda_1 - \lambda_2 - \lambda_3 - \lambda_4\},$$

where the  $\lambda_i$  are the square roots of the eigenvalues of  $\tau = \rho(Y \otimes Y)\rho^*(Y \otimes Y)$  in descending order.

Despite the additional noise incurred by the transpiling process, `ibm_cairo` shows a significant improvement in both fidelity and concurrence over the results of Pathumsoot et al. [9]. Notably, the improvement in concurrence proves that a higher degree of entanglement has been established in the final state.

**Table 1.** Comparison of the new results on `ibm_cairo` with the prior experiment by Pathumsoot et al. on IBM Q 20 Tokyo.

	New Results	Pathumsoot et al. [9]
Fidelity cross pair 1	$0.75 \pm 0.05$	$0.57 \pm 0.01$
Fidelity cross pair 2	$0.83 \pm 0.03$	$0.58 \pm 0.01$
Concurrence cross pair 1	$0.5 \pm 0.10$	$0.25 \pm 0.02$
Concurrence cross pair 2	$0.61 \pm 0.06$	$0.36 \pm 0.02$

#### 4. Noise Modelling

While the results presented above demonstrate that recent improvements in superconducting processor technology have significantly improved the fidelity with which MQNC can be performed, the final states are still significantly affected by processor noise. It is therefore of interest to study how noise affects the protocol.

The three main sources of error in the IBMQ processors are gate infidelities, state-preparation and measurement errors, and thermal decoherence and dephasing [12]. All three contribute to

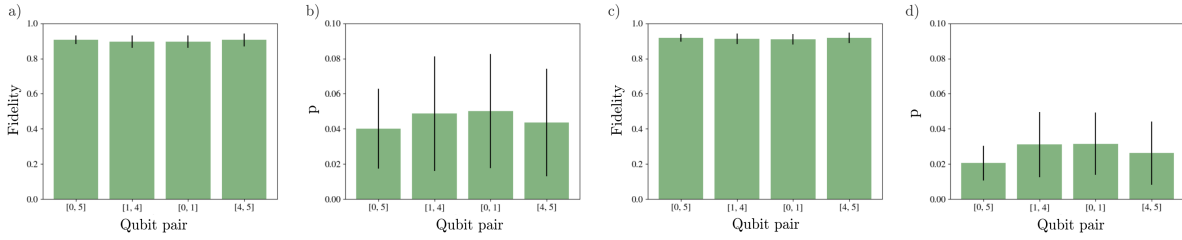


**Figure 4.** (a) Fidelity between experimental final state and model of final state with single-qubit depolarising noise applied. Results are shown separately for each of the four pairs generated using MQNC. Error bars indicate one standard deviation. (b) Value of the noise parameter  $p$  which maximises fidelity between model and experiment. (c), (d) The same plots for the model of single qubit depolarising noise applied before measurements.

the error in a final state, and a detailed error model meant to mimic an actual processor should ideally incorporate all of them. It turns out, however, that by studying only the gate error through a simple analytical model of depolarising noise, it is possible to gain a clear insight into a large portion of the noise within the protocol. Depolarising noise is given for a single qubit by the channel

$$\mathcal{E}(\rho) = p\frac{I}{2} + (1-p)\rho, \quad (1)$$

and models the worst-case gate error where the state of the qubit is replaced by the maximally mixed state with probability  $p$ . That is to say, it models the scenario where there is some probability of all information in the state being lost to the environment. Single-qubit depolarising noise has two shortcomings as a general noise model in that it assumes noise to be symmetrical and not coherent, and as such it can only provide an approximation of a true noise channel. Nevertheless, it does account for some fraction of the total noise and allows us to study this fraction of the noise. In the case of many gates being applied to a single qubit it may happen (though it is not guaranteed) that biased noise cancels out and that the overall noise becomes approximately symmetrical. It was found that the single-qubit depolarising noise channel models noise in MQNC on `ibm_cairo` with high fidelity. This is likely due to readout error mitigation and the short circuit depth of MQNC lessening the effect of non-gate errors.

#### 4.1. Noise acting on the final state

At first, we modelled noise as single-qubit depolarising noise acting on the final 2-qubit graph states  $|G_2\rangle = \frac{1}{\sqrt{2}}(|0+\rangle + |1-\rangle)$ . The single-qubit depolarising noise channel acting on each qubit of the 2-qubit graph state yields the final state

$$\frac{1}{4} \begin{pmatrix} 1 & (p-1)^2 & (p-1)^2 & -(p-1)^2 \\ (p-1)^2 & 1 & (p-1)^2 & -(p-1)^2 \\ (p-1)^2 & (p-1)^2 & 1 & -(p-1)^2 \\ -(p-1)^2 & -(p-1)^2 & -(p-1)^2 & 1 \end{pmatrix}.$$

in the case of equal depolarising noise on both qubits.

In Fig. 4 (a) the maximum fidelity between the experimental state and the ideal final state with equal amounts of depolarising noise applied to each qubit is shown for each pair of MQNC. By varying  $p$  and calculating the corresponding fidelity the value of  $p$  for which the fidelity is maximum can be determined. These are shown in Fig. 4 (b).

#### 4.2. Noise applied prior to MQNC measurements

More insight into noise in MQNC on IBM processors can be gained by modelling noise applied before the final  $ZZ$  or  $XX$  measurements. We begin by initialising the density matrix of the

circuit to that of the state  $|+\rangle^{\otimes 6}$ . Controlled phase gates are then applied to produce the 6-qubit resource state for MQNC and then the single-qubit depolarising channel is applied to each qubit in turn after which measurements are made. The 2-qubit final states are obtained by means of the partial trace operation. The states take the form

$$\frac{1}{4} \begin{pmatrix} 1 & -1(p-1)^3 & -1(p-1)^3 & -1(p-1)^4 \\ -1(p-1)^3 & 1 & 1(p-1)^4 & 1(p-1)^3 \\ -1(p-1)^3 & 1(p-1)^4 & 1 & 1(p-1)^3 \\ -1(p-1)^4 & 1(p-1)^3 & 1(p-1)^3 & 1 \end{pmatrix}.$$

Using this model of the noise and repeating the previous analysis we obtain the results shown in Fig. 4 (c) and (d). While there is little difference in the fidelity between model and experiment compared to the case of noise applied to the final 2-qubit states, the noise parameter  $p$  is significantly less for the new model. This is a result of the final state density matrices of the new model containing  $(1-p)^3$  and  $(1-p)^4$  terms instead of the  $(1-p)^2$  terms of the simple model. A greater value of  $p$  per qubit is required for noise applied after measurements to achieve the same fidelity between model and experiment as when the noise is applied prior to measurements. This leads to the physical interpretation that the amount of depolarising noise per qubit is greater in the final state than in the pre-measurement state, and hence the measurement has the effect of compounding the noise in the remaining qubits.

## 5. Conclusion

The purpose of this study was to investigate MQNC on superconducting technology which is available at this point in time. The main result was demonstrating that recent improvements in the hardware have made it possible to perform MQNC with final state fidelities upwards of 0.7 and as high as 0.9. Compared to the maximum cross-pair fidelity of 0.58 obtained just two years previously on the previous generation processor IBM Q 20 Tokyo, this represents a major improvement, and suggests that MQNC on superconducting hardware will likely become practical within the next few years. The improved results made it possible to study the noise experimentally in greater detail than before, and it was determined that the MQNC measurements have the effect of compounding single-qubit depolarising noise, so that the individual qubits in the final states have a higher amount of this noise than the individual qubits before measurement.

## Acknowledgements

We thank Stellenbosch University, the Department for Science and Innovation (DSI) and the National Research Foundation (NRF) of South Africa. We also thank the University of Witwatersrand for access to the IBM processors via the ARUA network.

## References

- [1] Kimble H J 2008 *Nature* **453** 1023–1030
- [2] Pompili M *et al.* 2021 *Science* **372** 259–264
- [3] Chen Y A *et al.* 2021 *Nature* **589** 214–219
- [4] Magnard P *et al.* 2020 *Phys. Rev. Lett.* **125**(26) 260502
- [5] Mirhosseini M, Sipahigil A, Kalaei M and Painter O 2020 *Nature* **588** 599–603
- [6] Hayashi M 2007 *Phys. Rev. A* **76**(4) 040301
- [7] Kobayashi H, Le Gall F, Nishimura H and Rötteler M 2009 *Automata, Languages and Programming* ed Albers S, Marchetti-Spaccamela A, Matias Y, Nikolettseas S *et al.* (Berlin, Heidelberg: Springer Berlin Heidelberg) pp 622–633 ISBN 978-3-642-02927-1
- [8] Matsuo T, Satoh T, Nagayama S and Van Meter R 2018 *Phys. Rev. A* **97**(6) 062328
- [9] Pathumsoot P *et al.* 2020 *Phys. Rev. A* **101**(5) 052301
- [10] Hein M, Eisert J and Briegel H J 2004 *Phys. Rev. A* **69**(6) 062311
- [11] James D F, Kwiat P G, Munro W J and White A G 2005 *Asymptotic Theory of Quantum Statistical Inference: Selected Papers* (World Scientific) pp 509–538
- [12] Georgopoulos K, Emary C and Zuliani P 2021 *Phys. Rev. A* **104** 062432

# Cavity QED based Open Quantum Walks

Ayanda Zungu<sup>1</sup>, Ilya Sinayskiy<sup>2,3</sup>, Francesco Petruccione<sup>2,3,4</sup>

<sup>1</sup>Centre for Space Research, North-West University, Mahikeng, 2745, South Africa

<sup>2</sup>Quantum Research Group, School of Chemistry and Physics, University of KwaZulu-Natal Durban, 4001, South Africa

<sup>3</sup>National Institute for Theoretical and Computational Sciences (NITheCS), South Africa

<sup>4</sup>School of Data Science and Computational Thinking, Stellenbosch University, Stellenbosch 7600, South Africa

E-mail: <sup>1</sup>arzngu@gmail.com

**Abstract.** In this work, we propose a possible experimental scheme for the implementation of open quantum walks (OQWs). The scheme is based on a model consisting of a weakly coupled atom-field system in the dispersive regime inside a high- $Q$  resonator ( $Q \sim 10^{12}$ ). This setup implements an OQW on the line with a two-level atom (driven by a laser) playing the role of the “walker” and the Fock states of the cavity mode as lattice sites of the OQW. The master equation for this system is solved analytically using generating functions for the zero temperature case. Furthermore, the dynamics of the observables are presented for various parameters and their behavior corresponds to the usual physical dynamics, which display collapses and revivals in the evolution of the system observables.

## 1. Introduction

Realistic quantum systems are open, and therefore any physical system describing their behavior must always include the unavoidable interaction with the environment [1]. The study of open quantum system (OQS) dynamics has recently become crucial, as quantum technologies are approaching regimes where decoherence and dissipation play an important role. For instance, physical systems may experience phase loss and energy exchange with the surroundings, because of this, the quantum effects are suppressed and the system evolves in a non-unitary fashion [1,2].

To address dissipation and decoherence in unitary quantum walks (UQWs) [3,4], which have been used as a basic tool for quantum algorithms, a new type of non-unitary QWs called open QWs was introduced with the aim of incorporating OQS [5]. OQWs are formulated as quantum Markov chain on lattices or graphs. Mathematically, they are described by completely positive trace-preserving (CPTP) maps [1,6] on graphs. The CPTP maps correspond to some dissipative processes which are driving the transition between the nodes of a graph. Unlike UQWs which uses quantum interference effects [3,4,7], in OQWs, the transitions between the nodes are strictly driven by the interaction with the environment. Thus, the effects of the environment play a crucial role in the time evolution of OQWs.

Furthermore, it has been suggested that OQWs are capable of performing dissipative quantum computation and to create complex quantum states [5,8]. The complete description of the framework of OQWs can be found in [5] and a recent article [9] reviews progress on this topic. More importantly, [10] suggested a quantum optics implementation of OQWs, and then derived an OQWs based on the microscopic system-environment model [11].

In this paper, we propose a cavity quantum electrodynamics (QED) based implementation of OQWs. The proposed scheme consist of a single two-level atom interacting with a single cavity mode in a non-resonant fashion driven by the external field. A similar model for the microscopic

maser was suggested in [12]. In the proposed cavity QED scheme, a two-level atom plays the role of the “walker” and the Fock states of the cavity mode correspond to the lattice sites of the OQW. We derive the master equation for this system and construct the analytic expressions for the populations using the generating functions for the zero temperature case.

This paper is organized as follows: In Sec. 2 we introduce the model and derive the effective master equation. Then, we apply a specific unitary operator to the effective master equation to include the classical laser driving. Sec. 3 contains the analytical solution for the generalized master equation and discussions; and in Sec. 4 we summarize the results of this paper.

## 2. Model

We consider the interaction between a two-level atom (qubit) and a quantized single mode field. The interaction Hamiltonian within the rotating wave approximation (RWA) of this system is given by ( $\hbar = 1$ ) [13],  $\hat{H}_{\text{int}} = \Delta \hat{a}^\dagger \hat{a} + g(\hat{a} \hat{\sigma}_+ + \hat{a}^\dagger \hat{\sigma}_-)$ , and the dynamics for the system under Born-Markov approximation are given by the Lindblad master equation (ME) [14],

$$\frac{d}{dt} \hat{\rho}(t) = -i[\hat{H}_{\text{int}}, \hat{\rho}] + \gamma(n_{\text{th}} + 1) \mathcal{L}[\hat{\sigma}_-, \hat{\sigma}_+] \hat{\rho} + \gamma n_{\text{th}} \mathcal{L}[\hat{\sigma}_+, \hat{\sigma}_-] \hat{\rho}, \quad (1)$$

where  $\Delta = \omega_f - \omega_a$  stands for the frequency detuning between the field and the qubit,  $g$  is the dipole interaction strength,  $\hat{\sigma}_\pm$  are the Pauli raising and the lowering operators for the qubit, satisfying the commutation relation  $[\hat{\sigma}_+, \hat{\sigma}_-] = \hat{\sigma}_z$ . The bosonic operators  $\hat{a}^\dagger$  and  $\hat{a}$  are the creation and annihilation operators for the cavity photons. In Eq. (1), the constant  $\gamma$  is the spontaneous emission rate,  $n_{\text{th}} = [\exp(\hbar\omega/k_B T) - 1]^{-1}$  is the mean number of thermal photons,  $k_B$  is the Boltzmann's constant,  $T$  is the temperature, and  $\omega$  is the frequency. The superoperator  $\mathcal{L}[\hat{x}, \hat{x}^\dagger] \hat{\rho} = \hat{x} \hat{\rho} \hat{x}^\dagger - (1/2)(\hat{x}^\dagger \hat{x} \hat{\rho} + \hat{\rho} \hat{x}^\dagger \hat{x})$  is the standard Gorini-Kossakowski-Sudarshan-Lindblad (GKSL) dissipator [14].

### 2.1. Effective Dynamics

To derive the effective dynamics, we consider a weakly coupled atom-field system in the dispersive limit, in which the qubit and the cavity are far detuned compared to the coupling strength ( $\lambda = \frac{g}{\Delta} \ll 1$ ). In this regime, the atom and the field do not exchange energy directly. To obtain the effective Hamiltonian and dissipator, we use the method of small unitary rotations [10, 15]. The following unitary operator  $\hat{U} = \exp[\lambda(\hat{a}^\dagger \hat{\sigma}_- - \hat{a} \hat{\sigma}_+)]$  is used to transform  $\hat{H}_{\text{int}} \rightarrow \hat{H}_{\text{eff}} = \hat{U} \hat{H}_{\text{int}} \hat{U}^\dagger$ . Using the standard expansion  $e^{\lambda A} B e^{-\lambda A} = B + \lambda[A, B] + \frac{\lambda^2}{2!}[A, [A, B]] + \dots$  and keeping terms up to second order in  $\lambda$ , it is easy to show that the effective system Hamiltonian has the form

$$\hat{H}_{\text{eff}} = \Delta \hat{a}^\dagger \hat{a} - \frac{g^2}{\Delta} \left( \hat{a}^\dagger \hat{a} \hat{\sigma}_z + \frac{\hat{\sigma}_z}{2} + \frac{1}{2} \right). \quad (2)$$

Following the same procedure, one can show that the effective ME is given by

$$\begin{aligned} \frac{d}{dt} \hat{\rho}_{\text{eff}}(t) = & -i[\hat{H}_{\text{eff}}, \hat{\rho}_{\text{eff}}] + \gamma(n_{\text{th}} + 1) \left[ \mathcal{L}[\hat{\sigma}_-, \hat{\sigma}_+] \hat{\rho}_{\text{eff}} + \frac{g}{\Delta} \mathcal{L}[\hat{a} \hat{\sigma}_z, \hat{\sigma}_+] \hat{\rho}_{\text{eff}} + \frac{g}{\Delta} \mathcal{L}[\hat{\sigma}_-, \hat{a}^\dagger \hat{\sigma}_z] \hat{\rho}_{\text{eff}} \right. \\ & + \frac{g^2}{\Delta^2} \mathcal{L}[\hat{a} \hat{\sigma}_z, \hat{a}^\dagger \hat{\sigma}_z] \hat{\rho}_{\text{eff}} - \frac{g^2}{\Delta^2} \mathcal{L}[\hat{\sigma}_-, (\hat{a}^\dagger \hat{a} + 1) \hat{\sigma}_+ + 2\hat{a}^{\dagger 2} \hat{\sigma}_-] \hat{\rho}_{\text{eff}} \\ & - \frac{g^2}{\Delta^2} \mathcal{L}[(\hat{a}^\dagger \hat{a} + 1) \hat{\sigma}_- + 2\hat{a}^2 \hat{\sigma}_+, \hat{\sigma}_+] \hat{\rho}_{\text{eff}} \left. + \gamma n_{\text{th}} \left[ \mathcal{L}[\hat{\sigma}_+, \hat{\sigma}_-] \hat{\rho}_{\text{eff}} - \frac{g}{\Delta} \mathcal{L}[\hat{\sigma}_+, \hat{a} \hat{\sigma}_z] \hat{\rho}_{\text{eff}} \right. \right. \\ & - \frac{g}{\Delta} \mathcal{L}[\hat{a}^\dagger \hat{\sigma}_z, \hat{\sigma}_-] \hat{\rho}_{\text{eff}} + \frac{g^2}{\Delta^2} \mathcal{L}[\hat{a}^\dagger \hat{\sigma}_z, \hat{a} \hat{\sigma}_z] \hat{\rho}_{\text{eff}} - \frac{g^2}{\Delta^2} \mathcal{L}[\hat{\sigma}_+, (\hat{a}^\dagger \hat{a} + 1) \hat{\sigma}_- + \hat{a}^2 \hat{\sigma}_+] \hat{\rho}_{\text{eff}} \\ & \left. - \frac{g^2}{\Delta^2} \mathcal{L}[(\hat{a}^\dagger \hat{a} + 1) \hat{\sigma}_+ + \hat{a}^{\dagger 2} \hat{\sigma}_-, \hat{\sigma}_-] \hat{\rho}_{\text{eff}} - \frac{g^2}{\Delta^2} \mathcal{L}[\hat{\sigma}_+, \hat{\sigma}_-] \hat{\rho}_{\text{eff}} \right]. \quad (3) \end{aligned}$$

In the next subsection, we transform the above equation to include classical laser driving.

### 2.2. External Driving

In order to include the effects of external driving in Eq. (3), we first define a unitary operator  $\hat{U}_1 = \hat{U}\hat{U}_0\hat{U}^\dagger$  where  $\hat{U}_0 = e^{-i\alpha\hat{\sigma}_x}$  and  $\alpha = \epsilon\tau_{\text{int}}$ . Here,  $\epsilon$  is the driving amplitude,  $\tau_{\text{int}}$  is the interaction time and  $\hat{\sigma}_x$  is the Pauli matrix. A transformation to the rotating frame of the laser driving is made with a unitary operator  $\hat{U}_1$ , applied to the density matrix  $\tilde{\rho} = \hat{U}_1\hat{\rho}_{\text{eff}}\hat{U}_1^\dagger$ . The next step is to omit the counter-rotating terms (RWA) and write the ME in the Fock space representation using  $\tilde{\rho} = \sum_k \tilde{\rho}_k \otimes |k\rangle\langle k|$ . After some algebra one can show that the ME takes the following form

$$\begin{aligned} \frac{d}{dt}\tilde{\rho}_k(t) &= i\frac{g^2}{\Delta}[\tilde{J}_k, \tilde{\rho}_k] + \gamma(n_{\text{th}} + 1)\frac{g^2}{\Delta^2}(k+1)(\hat{\alpha}_{zy} - \sin^2\alpha\mathbb{1})\tilde{\rho}_{k+1}(\hat{\alpha}_{zy} - \sin^2\alpha\mathbb{1}) \\ &+ \gamma n_{\text{th}}\frac{g^2}{\Delta^2}k(\hat{\alpha}_{zy} + \sin^2\alpha\mathbb{1})\tilde{\rho}_{k-1}(\hat{\alpha}_{zy} + \sin^2\alpha\mathbb{1}) + \gamma(k - n_{\text{th}})\frac{g^2}{\Delta^2}(\hat{A}\tilde{\rho}_k + \tilde{\rho}_k\hat{A}) \\ &+ \gamma n_{\text{th}}\frac{g^2}{\Delta^2}(k+1)\sin^4\alpha\tilde{\rho}_{k+1} + \gamma(n_{\text{th}} + 1)\frac{g^2}{\Delta^2}k\sin^4\alpha\tilde{\rho}_{k-1} - \gamma\frac{g^2}{\Delta^2}X'_k\tilde{\rho}_k. \end{aligned} \quad (4)$$

Here, the operator  $\hat{\alpha}_{zy}$  is given by  $\hat{\alpha}_{zy} = \cos 2\alpha\hat{\sigma}_z + \sin 2\alpha\hat{\sigma}_y$ , where  $\hat{\sigma}_z$  and  $\hat{\sigma}_y$  are Pauli matrices. Also the operator  $\hat{A}$  is given by  $\hat{A} = \sin^2\alpha\hat{\alpha}_{zy}$ ,  $X'_k = (2n_{\text{th}} + 1)\bar{X} + n_{\text{th}}\mathbb{1}$ , where  $\bar{X} = \sin^4\alpha(k+1)\mathbb{1} + \sin^4\alpha k\mathbb{1} + k\mathbb{1}$ ,  $\mathbb{1}$  is a 2 by 2 identity matrix and  $\tilde{J}_k = \frac{3}{2}\sin^2\alpha k\mathbb{1} + (k + \frac{1}{2})\hat{\alpha}_{zy} + \frac{1}{2}\mathbb{1}$ .

We are interested in the analytical expression of the observables. In order to achieve this, we transform Eq. (4) into a basis where its possible to solve it analytical using generating functions. By defining  $\hat{\sigma}'_z = \cos 2\alpha\hat{\sigma}_z + \sin 2\alpha\hat{\sigma}_y$ ,  $\hat{\sigma}'_x = \hat{\sigma}_x$  and  $\hat{\sigma}'_y = -\sin 2\alpha\hat{\sigma}_z + \cos 2\alpha\hat{\sigma}_y$ , it is straight forward to verify that  $[\hat{\sigma}'_x, \hat{\sigma}'_y] = 2i\hat{\sigma}'_z$ . Hence, one can derive the following transformation operator  $\hat{U}_2 = \begin{pmatrix} \cos\alpha & i\sin\alpha \\ i\sin\alpha & \cos\alpha \end{pmatrix}$ . Using the above operator  $\hat{U}_2$ , we can transform Eq. (4) to a new basis  $\hat{\rho}_k = \hat{U}_2^\dagger\tilde{\rho}_k\hat{U}_2$  and write the transformed ME as follow

$$\begin{aligned} \frac{d}{dt}\hat{\rho}_k(t) &= i\frac{g^2}{\Delta}[\hat{J}_k, \hat{\rho}_k] + \gamma(n_{\text{th}} + 1)\frac{g^2}{\Delta^2}(k+1)(\hat{\sigma}_z - \sin^2\alpha\mathbb{1})\hat{\rho}_{k+1}(\hat{\sigma}_z - \sin^2\alpha\mathbb{1}) \\ &+ \gamma n_{\text{th}}\frac{g^2}{\Delta^2}k(\hat{\sigma}_z + \sin^2\alpha\mathbb{1})\hat{\rho}_{k-1}(\hat{\sigma}_z + \sin^2\alpha\mathbb{1}) + \gamma n_{\text{th}}\frac{g^2}{\Delta^2}(k+1)\sin^4\alpha\hat{\rho}_{k+1} \\ &+ \gamma(n_{\text{th}} + 1)\frac{g^2}{\Delta^2}k\sin^4\alpha\hat{\rho}_{k-1} - \gamma\frac{g^2}{\Delta^2}X'_k\hat{\rho}_k + \gamma(k - n_{\text{th}})\frac{g^2}{\Delta^2}(\hat{\sigma}_z\hat{\rho}_k + \hat{\rho}_k\hat{\sigma}_z). \end{aligned} \quad (5)$$

The exact solution of the above equation (5) for the zero temperature case ( $n_{\text{th}} = 0$ ) will be outlined in the next section.

### 3. General Solution

In this section, we write Eq. (5) in the matrix elements form  $\rho_k^{(i,j)}(t)$  ( $i, j = 0, 1$ ) and solve each system analytically using the matrix generating function given by

$$\rho_s^{(i,j)}(x, t) = \sum_{k=0}^{\infty} x^k \rho_k^{(i,j)}(t), \quad (6)$$

where  $|x| \leq 1$ . If  $\rho_s^{(i,j)}$  is known, the transformed matrix elements can be found from

$$\rho_k^{(i,j)}(t) = \left. \frac{1}{k!} \frac{\partial^k}{\partial x^k} \rho_s^{(i,j)}(x, t) \right|_{x=0}. \quad (7)$$

The generating function system of equations are solved using the method of characteristics with some arbitrary initial conditions. If we assume that at  $t = 0$  the walker is localized at site  $p$  ( $p \in \mathbb{Z}$ ) with  $\hat{\rho}(0) = \begin{pmatrix} a & z \\ \bar{z} & b \end{pmatrix} \otimes |p\rangle\langle p|$ , where  $a + b = 1$ ,  $(a, b) \in \mathbb{R}_{\geq 0}$  and  $z \in \mathbb{C}$ , it is easy to show that  $\rho_s^{(0,0)}(x, 0) = ax^p$  and  $\rho_s^{(1,1)}(x, 0) = bx^p$ . Using the method of characteristics and the initial conditions, one can show that the analytic expression for the populations of the ground state and excited state (for  $n_{\text{th}} = 0$ ) are given by

$$\begin{aligned} \rho_k^{(0,0)}(t) &= \frac{1}{k!} \sum_{q=0}^k \binom{k}{q} a \cos 2\alpha (\sin^4 \alpha - \cos^4 \alpha e^{-\alpha' t \cos 2\alpha})^q (1 - a e^{-\alpha' t \cos 2\alpha})^{k+p-2q} (\sin^4 \alpha)^{k-q} \\ &\times (\cos^4 \alpha)^{p-q} \frac{(p+k-q)!}{(p-q)!} (-1)^{-q} (\cos^4 \alpha - \sin^4 \alpha e^{-\alpha' t \cos 2\alpha})^{-p-k+q-1} \theta(p-q), \end{aligned} \quad (8)$$

and

$$\begin{aligned} \rho_k^{(1,1)}(t) &= \frac{1}{k!} \sum_{q=0}^k \binom{k}{q} b (\cos 2\alpha - 2) (\sin^4 \alpha - (\sin^4 \alpha + 1)^2 e^{-\alpha'(2-\cos 2\alpha)t})^q (\sin^4 \alpha)^{k-q} \\ &\times (1 - a e^{-\alpha'(2-\cos 2\alpha)t})^{k-2q+p} \frac{(p+k-q)!}{(p-q)!} (\sin^2 \alpha + 1)^{2p-2q} (-1)^{p+k-2q} \\ &\times (\cos^4 \alpha - 2 - \sin^4 \alpha (1 - e^{-\alpha'(2-\cos 2\alpha)t}))^{-p-k+q-1} \theta(p-q), \end{aligned} \quad (9)$$

where  $\binom{k}{q}$  denotes the binomial coefficient,  $\alpha' = \frac{\gamma g^2}{\Delta^2}$  and  $\theta(l)$  is the Heaviside step function

$$\theta(l) = \begin{cases} 1, & l \geq 0 \\ 0, & l < 0. \end{cases}$$

Using Eqs. (8) and (9), we obtain the probability to find the walker at site  $k$ ,  $P_k(t) = \rho_k^{(0,0)} + \rho_k^{(1,1)}$ . After sufficiently long period of time,  $\sum_{k=0}^{\infty} \rho_k^{(0,0)}(t \rightarrow \infty) = a$ ,  $\sum_{k=0}^{\infty} \rho_k^{(1,1)}(t \rightarrow \infty) = b$ , assuming  $\alpha \geq 0$ , the system settles down into the initial condition,  $\sum_{k=0}^{\infty} P_k(t) = 1$ . The probability to find the walker at site  $k$  is shown in Fig. 1 for various parameters. The off-diagonal elements (the coherences) are complex conjugates of each other,  $\rho_k^{(1,0)} = (\rho_k^{(0,1)})^*$ . Following the same steps with initial condition  $\rho_s^{(0,1)}(x, 0) = zx^p$ , the solution for the off-diagonal element is given by

$$\begin{aligned} \rho_k^{(0,1)}(t) &= e^{-\gamma\tau} z \operatorname{cosec}(\tau) (\tan(\tau))^{-p} \left( \frac{\operatorname{cosec}^4 \alpha}{2\gamma} \right)^{p-k} \frac{1}{k!} \sum_{q=0}^k \binom{k}{q} \frac{(p+q)!}{(p-k+q)!} (\cot(\tau)\lambda - w)^{-p-1-q} \\ &\times \left( (w^2 + \lambda^2) \tan(\tau) \right)^{p-k+q} \left( \lambda + w \tan(\tau) \right)^{k-q} \theta(p-k+q). \end{aligned} \quad (10)$$

Here  $w = 2i\Delta - 1 - 2\gamma \sin^4 \alpha$ ,  $\lambda = \sqrt{4\gamma^2 \sin^4 \alpha (\sin^4 \alpha - 1) - w^2}$ ,  $\tau = \frac{1}{2} t \varepsilon \lambda$  where  $\varepsilon = \frac{g^2}{\Delta^2}$ , and  $z = x + iy$ . Eqs. (8), (9) and (10) provide a complete solution for the matrix elements of the density operator Eq. (5). Hence, it is straight forward to transform these expressions ((8), (9) and (10)) to the original basis and construct the observables of interest (see Figs. 2, 3) using  $W_k(t) = \operatorname{Tr}[\hat{\sigma}_W \tilde{\rho}_k(t)]$  i.e.,  $W_k \in (X_k, Y_k, Z_k)$  ( $\hat{\sigma}_W$  is the corresponding Pauli matrix).

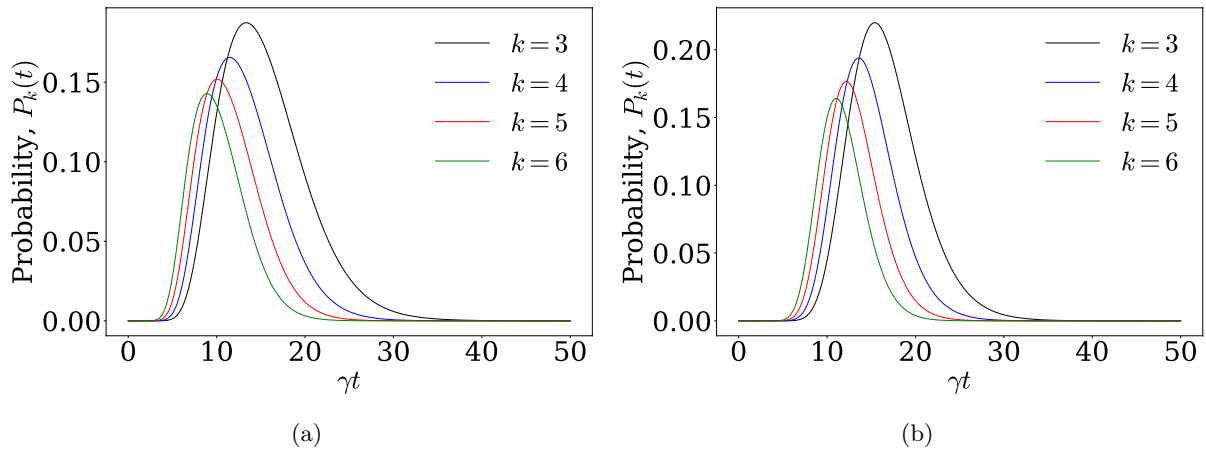


Figure 1: (Color online) The probability  $P_k(t)$  of finding a walker at site  $k$  as a function of dimensionless time  $\gamma t$  for different Fock states (stated in the legend). The initial sites are  $p = 25$  (a) and  $p = 35$  (b), with  $\alpha = 0.3, 0.2$ , respectively. Other parameters are set as  $\gamma = 0.1$ ,  $g = 0.4$  and  $\Delta = 1$ .

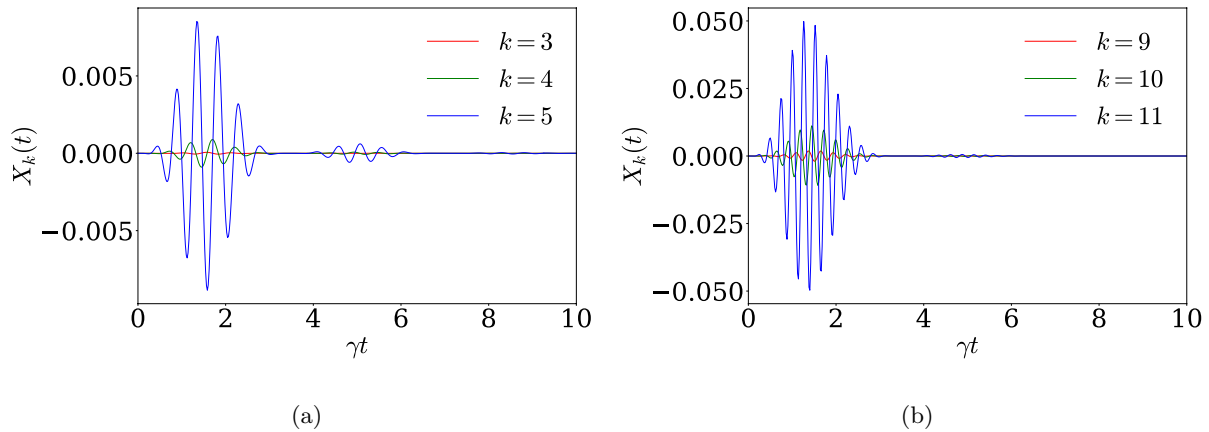


Figure 2: (Color online) The real part  $X_k(t)$  of the coherences are shown as a function of the dimensionless time  $\gamma t$  for different Fock states (stated in the legend). The initial sites are  $p = 9$  (a) and  $p = 15$  (b), with  $\alpha = 0.4, 0.2$ , respectively. Other parameters are  $\gamma = 0.1$ ,  $g = 0.3$  and  $\Delta = 1$ .

#### 4. Conclusion

In this contribution, we have proposed a scheme for implementing OQWs in a cavity QED setup. We derived the generalized master equation for this OQW from the effective master equation. Further, we solved the generalized master equation using generating functions and constructed the analytic expressions for the populations for the zero temperature case. In order to verify our results, the dynamics of the observables are presented for various parameters and their behavior corresponds to the usual physical dynamics, which display collapses and revivals in the evolution of the system observables. Future work will show how Eq. (4) implements an OQW on  $\mathbb{Z}^+$  at discrete driving time steps.

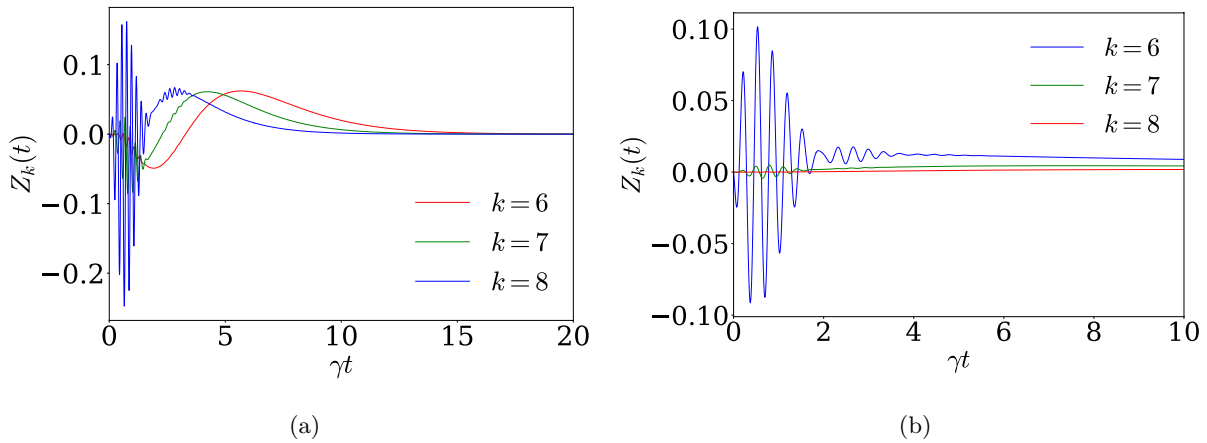


Figure 3: (Color online) The population inversion  $Z_k(t)$  is shown as a function of dimensionless time  $\gamma t$  for different sites  $k$  (stated in the legend). The initial sites are  $p = 10$  (a) and  $p = 5$  (b), with  $\alpha = 0.4, 0.7$ , respectively. Other parameters are  $\gamma = 0.1$ ,  $g = 0.4$  and  $\Delta = 1$ .

### Acknowledgements

This work is based upon research supported by the South African Research Chair Initiative, Grant No. 64812 of the Department of Science and Innovation and the National Research Foundation (NRF) of the Republic of South Africa. AZ acknowledge support in part by the NRF of South Africa (Grant No. 129457). The Grant-holder (AZ) acknowledges that opinions, findings and conclusions or recommendations expressed in any publication generated by the NRF supported research is that of the author(s), and that the NRF accepts no liability whatsoever in this regard.

### References

- [1] H.-P. Breuer and F. Petruccione, 2002 *The Theory of Open Quantum Systems* (Oxford University Press, Oxford).
- [2] C. W. Gardiner and H. Haken, 1991 *The Quantum Noise* (Springer, Berlin).
- [3] Y. Aharonov, L. Davidovich, and N. Zagury, 1993 *Phys. Rev. A* **48**, 1687.
- [4] J. Kempe, 2003 *Contemp. Phys.* **44**, 307.
- [5] Attal et al., 2012 *Phys. Lett. A* **376**, 1545; S. Attal et al., 2012 *J. Stat. Phys.* **147**, 832; I. Sinayskiy and F. Petruccione, 2012 *Phys. Scr.* **T 151**, 014077.
- [6] K. Kraus, 1983 *States, Effects and Operations: Fundamental Notions of Quantum Theory* (Springer-Verlag, Berlin).
- [7] S. E. Venegas-Andraca, 2012 *Quant. Inf. Proc.* **11**, 1015.
- [8] I. Sinayskiy and F. Petruccione, 2012 *Quant. Inf. Proc.* **11**, 1301.
- [9] I. Sinayskiy and F. Petruccione, 2019 *Eur. Phys. J. Spec. Top.* **227**, 1869-1883.
- [10] I. Sinayskiy and F. Petruccione, 2014 *Int. J. Quantum Inform.* **12**, 1461010.
- [11] I. Sinayskiy and F. Petruccione, 2015 *Phys. Rev. A* **92**, 0321205; I. Sinayskiy and F. Petruccione, 2013 *Open Syst. Inf. Dyn.* **20**, 1340007.
- [12] P. Filipowicz, J. Javanainen, and P. Meystre, 1986 *Phys. Rev. A* **34**, 3077.
- [13] E. T. Jaynes and F. W. Cummings, 1963 *Proc. IEEE.* **51**, 89.
- [14] G. Lindblad, 1976 *Commun. Math. Phys.* **48**, 119-130; V. Gorini, A. Kossakowski, and E. C. G. Sudarshan, 1976 *J. Math. Phys.* **17**, 821.
- [15] A. B. Klimov and S. M. Chumakov, 2009 *A Group-Theoretical Approach to Quantum Optics* (Wiley-VCH, Darmstadt); M. O. Scully and M. S. Zubairy, 1997 *Quantum Optics* (Cambridge University Press, Cambridge).

# Analytic Continuation of the Generalized Epstein zeta function for calculating finite system corrections in $\phi^4$ theory

JF Du Plessis<sup>1,\*</sup> and WA Horowitz<sup>2</sup>

<sup>1</sup> Department of Physics, Stellenbosch University, Matieland, 7602, South Africa

<sup>2</sup> Department of Physics, University of Cape Town, Rondebosch 7701, South Africa

E-mail: \*23787295@sun.ac.za

**Abstract.** Previously an equation of state for the relativistic hydrodynamics encountered in heavy-ion collisions at the LHC and RHIC has been calculated using the QCD trace anomaly obtained with lattice methods. This lattice calculation extrapolates the trace anomaly to an infinite system, which neglects the possible finite system size corrections that should be present in heavy-ion collisions. In order to check whether the corrections are indeed negligible at the scales encountered at these experiments, it is necessary to understand how these corrections arise in quantum field theories. We construct a massive  $\phi^4$  theory with periodic boundary conditions on  $n$  of the 3 spatial dimensions.  $2 \rightarrow 2$  NLO scattering is then computed, while analytically verifying unitarity remains intact. Due to needing to employ a novel regularization method dubbed denominator regularization, it was crucial to derive an analytic continuation to the Generalized Epstein zeta function, which is expected to have applications in further studying finite size corrections to field theories using denominator regularization.

## 1. Introduction

In heavy-ion Colliders such as at the LHC and RHIC, heavy-ions (such as Pb nuclei) are collided at nearly the speed of light ( $\gamma \gg 10$  Lorentz factor). In these heavy-ion collisions [1, 2] there is an apparent formation of Quark Gluon Plasma (QGP) [3], where the correlations between the outgoing low-momentum particles appear to be well described by nearly inviscid relativistic hydrodynamics. This calculation uses an Equation of State (EoS) provided by a lattice QCD calculation that is extrapolated to infinite system size [4].

It is currently unclear what happens in QCD just above the transition temperature  $T = 150$  MeV [5]. There is strong evidence of a second order phase transition, but the nature of the new phase is unknown. While for large temperatures asymptotic freedom requires that the phase is essentially an ideal gas, the more complicated behaviour discussed above is found at relatively small (and experimentally accessible) temperatures. It is therefore necessary to understand how reliably the behaviour found in the finite systems (such as heavy-ion or parton collisions) can be extrapolated to effectively infinite systems, such as the QGP found in the  $\sim 0.000001$  seconds after Big Bang. Understanding and modeling this phase is therefore not only of interest in high energy physics but also in cosmology, in particular in studies of the early universe.

The dependence of the low viscosity on the lattice QCD calculation of the EoS brings the underlying assumptions of the calculation under scrutiny. A possible erroneous assumption to be investigated is that heavy-ion collisions can be well approximated as infinite sized systems [6]. Indeed quenched lattice QCD calculations have shown significant possible corrections dependent on the size of the system [7]. An analytic derivation of the finite size effects on the equation of state (or equivalently the trace anomaly) is therefore sought. This work is a step in that direction, with the intention to develop and understand the mathematical techniques necessary for a full treatment necessary for finite temperature finite sized QCD.

## 2. Finite Sized $\phi^4$ Theory

Let us consider the  $\phi^4$  Lagrangian

$$\mathcal{L} = \frac{1}{2} \partial^\mu \phi \partial_\mu \phi - \frac{1}{2} m^2 \phi^2 - \frac{\lambda}{4!} \phi^4 \quad (1)$$

in a system with periodic boundary conditions. If we consider  $n$  compact spatial (and 1 infinite temporal) dimensions, with the  $i$ th dimension being parameterized by  $[-\pi L_i, \pi L_i]$  with periodic boundary conditions (or equivalently identifying the endpoints  $\pm\pi L_i$ ). This discretizes the possible spatial momenta to  $\vec{p} = (\frac{k_1}{L_1}, \frac{k_2}{L_2}, \dots, \frac{k_n}{L_n},)$  where  $\vec{k} \in \mathbb{Z}^n$ . In analogy with [8] we can

define  $(-i\lambda)^2 iV(p^2) \equiv \text{X}$  with  $p$  being the total incoming momentum. One then finds [9]

in  $n = 3$  spatial dimensions that up to NLO

$$V(p^2, \{L_i\}) = -\frac{1}{2} \int_0^1 dx \int \frac{d\ell_E^0}{2\pi} \sum_{\vec{k} \in \mathbb{Z}^3} \frac{1}{(2\pi)^3 L_1 L_2 L_3} \frac{1}{[\ell_E^2 + \Delta^2]^2} \quad (2)$$

where  $\Delta^2 \equiv -x(1-x)p^2 + m^2 - i\epsilon$  and  $\ell_E^\mu = (\ell_E^0, \frac{k^i}{L_i} + x p^i)^\mu$ . Using denominator regularization as introduced in [9] we can regularize 2 using some  $\epsilon > 0$  as follows:

$$V(p^2, \{L_i\}) = -\frac{1}{2} \int_0^1 dx \int \frac{d\ell_E^0}{2\pi} \sum_{\vec{k} \in \mathbb{Z}^3} \frac{1}{(2\pi)^3 L_1 L_2 L_3} \frac{\mu^\epsilon}{[\ell_E^2 + \Delta^2]^{2+\frac{\epsilon}{2}}}. \quad (3)$$

We now safely perform the  $\ell_E^0$  integral to get

$$V(p^2, \{L_i\}) = -\frac{1}{2} \int_0^1 dx \frac{1}{(2\pi)^4 L_1 L_2 L_3} \frac{\sqrt{\pi} \Gamma(\frac{3+\epsilon}{2})}{2\Gamma(\frac{4+\epsilon}{2})} \sum_{\vec{k} \in \mathbb{Z}^3} \frac{\mu^\epsilon}{[\sum_{i=1}^3 (\frac{k_i}{L_i} + x p^i)^2 + \Delta^2]^{\frac{3+\epsilon}{2}}}. \quad (4)$$

The sum at the end of Equation 4 can be related back to the generalized Epstein zeta function, so we will need to find some useful analytically continued form of it in order to regularize Equation 4 properly. It is noted that the use of denominator regularization and the generalized Epstein zeta function should not be confuse with zeta function regularization, which is a distinct regularization procedure.

## 3. Generalized Epstein zeta Function

We have seen above that we require an analytic continuation of the generalized Epstein zeta function [10], which would allow us to isolate the divergence in Equation 4. Let us then explicitly define

$$\zeta(\{a_i\}, \{b_i\}, c; s) \equiv \sum_{\vec{n} \in \mathbb{Z}^p} [a_i^2 n_i^2 + b_i n_i + c]^{-s}, \quad (5)$$

where repeated indices are implicitly summed over. We can now employ the Poisson Summation formula over an  $n$ -dimensional lattice  $\Lambda^n$  with lattice dual  $\Lambda^{*n}$ , which is given by

$$\sum_{\vec{m} \in \Lambda^n} f(\vec{m}) = \frac{1}{\sqrt{\det(\Lambda^n)}} \sum_{\vec{k} \in \Lambda^{*n}} F(\vec{k}), \quad (6)$$

where  $F$  is the Fourier transform given by  $F(\vec{k}) \equiv \int d^n m \exp(2\pi i \vec{k} \cdot \vec{m}) f(\vec{m})$ . Here we are interested in

$$f(\vec{m}) = [a_i^2 m_i^2 + b_i m_i + c - i\varepsilon]^{-s}, \quad (7)$$

with some  $\varepsilon > 0$  is introduced to ensure no poles are integrated over. We can then calculate (where all suppressed indices of sums and products runs from  $i = 1$  to  $i = n$ ):

$$F(\vec{k}) = \int d^n m \exp(2\pi i \vec{k} \cdot \vec{m}) [a_i^2 m_i^2 + b_i m_i + c - i\varepsilon]^{-s} \quad (8)$$

Now by shifting  $x_i = m_i + \frac{b_i}{2a_i^2}$  and  $c' = c - \sum_{i=1}^n \frac{b_i^2}{4a_i^2}$  we get

$$F(\vec{k}) = \exp\left(-2\pi i \sum \frac{k_i b_i}{2a_i^2}\right) \int d^n x \exp(2\pi i \vec{k} \cdot \vec{x}) [a_i^2 x_i^2 + c' - i\varepsilon]^{-s} \quad (9)$$

We can now see that that integral almost looks like the Fourier transform of some radial function over a lattice with lattice spacings  $a_i$ , so we can actually use the formula for a Fourier transform of a radial function[11] to get

$$F(\vec{k}) = \frac{\exp(-2\pi i \sum \frac{k_i b_i}{2a_i^2})}{\prod a_i} \frac{2\pi^{n/2}}{\Gamma(n/2)} \int_0^\infty dr r^{n-1} [r^2 + c' - i\varepsilon]^{-s} {}_0F_1\left(\begin{matrix} n \\ 2 \end{matrix}; -\pi^2 r^2 \sum \frac{k_i^2}{a_i^2}\right). \quad (10)$$

While this might look intimidating, this integral (with  ${}_0F_1$  being the generalized hypergeometric function) can be evaluated using software such as Mathematica to get (valid for  $\text{Re}(s) > \frac{n}{2}, n > 1, c' \in \mathbb{R}, \varepsilon > 0, \|\vec{k}\| \neq 0$ )

$$F(\vec{k}) = \frac{\exp(-2\pi i \sum \frac{k_i b_i}{2a_i^2})}{\prod a_i} \frac{2\pi^{\frac{n}{2}}}{\Gamma(\frac{n}{2})} \left(\frac{\pi \sum \frac{k_i^2}{a_i^2}}{c' - i\varepsilon}\right)^{\frac{s-2n}{4}} \frac{\Gamma(\frac{n}{2})}{\Gamma(s)} K_{\frac{n-2s}{2}}\left(2\pi \sqrt{\sum \frac{k_i^2}{a_i^2}} \sqrt{c' - i\varepsilon}\right) \quad (11)$$

$$F(\vec{k}) = \frac{2\pi^s}{\prod a_i \Gamma(s)} \exp\left(-2\pi i \sum \frac{k_i b_i}{2a_i^2}\right) \left(\frac{\sum \frac{k_i^2}{a_i^2}}{c' - i\varepsilon}\right)^{\frac{s-2n}{4}} K_{s-\frac{n}{2}}\left(2\pi \sqrt{(c' - i\varepsilon) \sum \frac{k_i^2}{a_i^2}}\right), \quad (12)$$

where  $K_\nu(z)$  is the modified Bessel function of the second kind. For the  $\vec{k} = \vec{0}$  case we can either very carefully take the limit, or redo the above calculation with  $\vec{k}$  identically  $\vec{0}$ . Both yield

$$F(\vec{0}) = \frac{\pi^{\frac{n}{2}}}{\prod a_i} \frac{\Gamma(s - \frac{n}{2})}{\Gamma(s)} (c' - i\varepsilon)^{\frac{n-2s}{2}} \quad (13)$$

Since we were careful with keeping track of the lattice spacings of the dual lattice, we can now plug our results straight into the Poisson summation formula to get (after expanding  $c' = c - \sum \frac{b_i^2}{4a_i^2}$ )

$$\sum_{\vec{m} \in \mathbb{Z}^n} [a_i^2 m_i^2 + b_i m_i + c - i\varepsilon]^{-s} = \frac{\pi^{\frac{n}{2}}}{\prod a_i} \frac{\Gamma(s - \frac{n}{2})}{\Gamma(s)} (c - \sum \frac{b_i^2}{4a_i^2} - i\varepsilon)^{\frac{n-2s}{2}} + \frac{2\pi^s}{\prod a_i \Gamma(s)} \times \quad (14)$$

$$\sum'_{\vec{k} \in \mathbb{Z}^n} \exp\left(-2\pi i \sum \frac{k_i b_i}{2a_i^2}\right) \left(\frac{\sum \frac{k_i^2}{a_i^2}}{c - \sum \frac{b_i^2}{4a_i^2} - i\varepsilon}\right)^{\frac{s-2n}{4}} K_{s-\frac{n}{2}}\left(2\pi \sqrt{(c - \sum \frac{b_i^2}{4a_i^2} - i\varepsilon) \sum \frac{k_i^2}{a_i^2}}\right),$$

which agrees with previous results [9]. Note that  $\sum'$  above denotes that it does no sum over  $\vec{0}$ .

#### 4. Amplitude and Unitarity

We can now substitute Equation 14 into Equation 4 which gives in  $n = 3$

$$V(p^2, \{L_i\}) = -\frac{1}{32\pi^2} \int dx \left[ \frac{2}{\epsilon} - 1 + \ln\left(\frac{\mu^2}{\Delta^2}\right) \right. \quad (15)$$

$$\left. + 2 \sum'_{\vec{k} \in \mathbb{Z}^3} \cos\left(2\pi x \sum k_i p^i L_i\right) K_0\left(2\pi \sqrt{\Delta^2 \sum (k_i L_i)^2}\right) \right].$$

Then using a modified  $\overline{\text{MS}}$  subtraction scheme, we can get the renormalized

$$\bar{V}(p^2, \{L_i\}) = -\frac{1}{32\pi^2} \int dx \left[ \ln\left(\frac{\mu^2}{\Delta^2}\right) \right. \quad (16)$$

$$\left. + 2 \sum'_{\vec{k} \in \mathbb{Z}^3} \cos\left(2\pi x \sum k_i p^i L_i\right) K_0\left(2\pi \sqrt{\Delta^2 \sum (k_i L_i)^2}\right) \right].$$

Here we can recognize the  $\ln$  term as corresponding to the standard result in infinite  $\phi^4$  systems [8]. As one would then expect the second term in the integral vanishes in the limit as all  $L_i \rightarrow \infty$  since  $\lim_{x \rightarrow \infty} K_0(x) = 0$ . We can also see that we can reduce the effective number of finite dimensions by quite simply taking the corresponding  $L_i \rightarrow \infty$ , since only terms in the sum with the corresponding  $k_i = 0$  will survive the limit. We can then find that, as in the infinite system case,

$$\mathcal{M} = \lambda [1 + \lambda (\bar{V}(s) + \bar{V}(t) + \bar{V}(u))] \quad (17)$$

up to NLO, with  $s, t$  and  $u$  being the Mandelstam variables. The optical theorem then requires that the total cross-section

$$\sigma_{\text{tot}} = 2 \text{Im}(\mathcal{M}), \quad (18)$$

where  $\text{Im}(\mathcal{M})$  is the imaginary part of the amplitude. By then setting  $L_i = L$  and introducing  $R = L\sqrt{\frac{s}{4} - m^2}$ , one can then find that

$$\sigma_{\text{tot}} = \frac{\lambda^2}{16\pi} \frac{\pi^{\frac{1-n}{2}}}{\Gamma(\frac{3-n}{2})} \frac{1}{L\sqrt{s}} \sum_{0 \leq l < R^2}^* \frac{r_n(l)}{\sqrt{R^2 - l}^{n-1}} \quad (19)$$

and

$$2 \text{Im}(\mathcal{M}) = \frac{\lambda^2}{16\pi} \frac{1}{L\sqrt{s}} \frac{1}{\pi^{\frac{n-1}{2}} \Gamma(\frac{3-n}{2})} \sum_{0 \leq l < R^2}^* \frac{r_n(l)}{\sqrt{R^2 - l}^{n-1}}, \quad (20)$$

showing that the amplitude respects the optical theorem, and equivalently our S-matrix is therefor unitary.

## 5. Conclusion

The analytic continuation of the generalized Epstein zeta function presented here was shown to give a self-consistent theory up to NLO in finite sized  $\phi^4$  theory. It is hugely valuable for regularizing and renormalizing in this finite system, and one can expect that it will be in other finite sized field theories as well. We have therefore shown a derivation of the formula, shown it leads to self-consistent results (and limits to the standard infinite system result) and shown how it is necessary in the above calculation.

## Acknowledgments

W.A.H. wishes to thank the South African National Research Foundation and the SA-CERN Collaboration for support and New Mexico State University for its hospitality, where part of the work was completed. The authors wish to thank Matt Sievert, Alexander Rothkopf, Bowen Xiao, Stan Brodsky, Andrea Shindler, Kevin Bassler and Herbert Weigel for valuable discussions.

## References

- [1] Aamodt K *et al.* (ALICE) 2008 *JINST* **3** S08002
- [2] Aamodt K *et al.* (ALICE) 2010 *Phys. Rev. Lett.* **105** 252302 (*Preprint* 1011.3914)
- [3] Weller R D and Romatschke P 2017 *Physics Letters B* **774** 351–356 ISSN 0370-2693 URL <https://www.sciencedirect.com/science/article/pii/S037026931730789X>
- [4] Bzdak A, Schenke B, Tribedy P and Venugopalan R 2013 *Phys. Rev. C* **87**(6) 064906 URL <https://link.aps.org/doi/10.1103/PhysRevC.87.064906>
- [5] Petreczky P 2012 *Journal of Physics G: Nuclear and Particle Physics* **39** 093002 URL <https://dx.doi.org/10.1088/0954-3899/39/9/093002>
- [6] Mogliacci S, Kolbé I and Horowitz W A 2020 *Phys. Rev. D* **102** 116017 (*Preprint* 1807.07871)
- [7] Kitazawa M, Mogliacci S, Kolbé I and Horowitz W A 2019 *Phys. Rev. D* **99** 094507 (*Preprint* 1904.00241)
- [8] Peskin M E and Schroeder D V 1995 *An Introduction to quantum field theory* (Reading, USA: Addison-Wesley) ISBN 978-0-201-50397-5
- [9] Horowitz W A and Du Plessis J F 2022 *Phys. Rev. D* **105** L091901 (*Preprint* 2203.01259)
- [10] Kirsten K 1994 *Journal of Mathematical Physics* **35** 459–470
- [11] Johnson-McDaniel N K 2012 *Journal of Fourier Analysis and Applications* **18** 367–385

# Structural, thermodynamics, mechanical and thermal properties of monazite-type $\text{LnPO}_4$ ( $\text{Ln}=\text{La}, \text{Ce}$ ): A first principles study

L Motsomone<sup>\*a</sup>, R G Diale<sup>b</sup>, P E Ngoepe<sup>a</sup>, R Koen<sup>c</sup> and H R Chauke<sup>a</sup>

<sup>a</sup>Materials Modelling Centre, University of Limpopo, Private Bag X 1106, Sovenga, 0727, South Africa

<sup>b</sup>Advanced Materials Division, MINTEK, Private bag X 3015, Randburg, 2125, South Africa

<sup>c</sup>The South African Nuclear Energy Corporation Ltd. (Necsa), P.O. Box 582, Pretoria, 0001, South Africa

E-mail: [lmotsomone@gmail.com](mailto:lmotsomone@gmail.com)\*

**Abstract.** Monazite is an ore mineral consisting of various rare earth elements (REEs), thorium (Th), and uranium (U). These components are utilized in numerous modern areas of technology, including metallurgy, catalysis, and magnetic fields. This monazite mineral has a notoriously stable structural conformation, making the conventional cracking process extremely inefficient. However, new innovative technologies (e.g. thermal cracking) have been proposed for improving the extraction of REEs (such as La, Ce, Nd), Th and U. In this study, we use the first principles calculation based on density functional theory to investigate vibrational and thermodynamic properties of monazite systems. It was found that the lattice parameters of  $\text{LaPO}_4$  and  $\text{CePO}_4$  monazite correlate well with experimental values to within 5% error. The heats of formation value for  $\text{LaPO}_4$  (-0.766 eV/atom) is more negative than for  $\text{CePO}_4$  (-0.729 eV/atom), suggesting the most stable structure. The phonon dispersion curves revealed that  $\text{LaPO}_4$  and  $\text{CePO}_4$  systems are vibrationally not stable. Furthermore, monazite systems were found to exhibit structural transitions at 500 K. The findings assisted in understanding the stability and thermodynamic structure of monazite as the temperature increases.

## 1. Introduction

Monazite is a radioactive phosphate mineral containing the light rare earth metals [Ce, La, Nd, Pr and Y], thorium and uranium [1]. The mineral is mined mainly for its rare elements and thorium content, which are critical to modern technology (such as the screen of a smartphone or computer) and nuclear power production [2]. Monazite is a mineral formed by a variety of rock types and conditions. The formation of these conformations occurs under a variety of pressure and temperature conditions in sedimentary, metamorphic, and igneous rocks [3]. Previously, monazite was reported to contain about 60 percent of rare-earth elements with cerium oxide (up to 32 %), thorium as  $\text{ThO}_2$  (up to 10 %) and uranium as ( $\text{U}_3\text{O}_8$ ) (up to 0.4 %) being the most industrially relevant constituents [4].

In contrast, conventional chemical processes have become highly complicated and costly to use for extracting REE, thorium, and uranium from monazite [5]. Hence, a new process (thermal plasma) is being developed to improve the extraction efficiency of monazite [1]. In that regard, a computational modelling is used, since it offers an opportunity to simulate labour intensive experiments in a more effective and less costly manner. We investigated the physical properties of  $\text{LaPO}_4$  and  $\text{CePO}_4$  using first-principle calculations based on density functional theory (DFT) to explore how the monazite molecules move when thermally cracked to gain insight into the best way to extract these REEs.

## 2. Methodology

All calculations were carried out using the first-principles method within the framework of density functional theory (DFT), as implemented in the Vienna ab initio simulation package (VASP) code [6]. The influence of the different k-point samplings and plane-wave cut-off energy was explored in a series of test calculations, leading to the calculations for the electronic properties being performed with  $12 \times 11 \times 13$  k-point sampling and a cut-off energy of 600 eV containing 24 atoms. The geometry optimization is accomplished by employing the generalized gradient approximation (GGA) [7] of the Perdew-Burke-Ernzerhof (PBE) [8]. The positions of atoms in the simulation cell, the lattice parameters, and the corresponding angles are fully optimized using the conjugate gradient method until the atomic force is smaller than  $0.01 \text{ eV/\AA}$ . A precision was set at "accurate" to make errors of the calculation into a reasonable scale. A strain value of 0.006 was chosen for the deformation of the lattice when calculating elastic properties. A PHONON code [9] was used to evaluate the vibrational stability from phonon dispersion curves with an interaction range of 7 ( $\text{\AA}$ ).

## 3. Structural properties

The structure of  $\text{LnPO}_4$  ( $\text{Ln} = \text{La, Ce}$ ) consists of  $\text{PO}_4$  tetrahedral sharing only corners with  $\text{LnO}_9$  polyhedral, as illustrated in figure 1. Monazite crystals comprise  $\text{LnPO}_4$  which has monoclinic symmetry ( $P2_1/n$  space group), containing four formula units. Each of the axes is unequal in length, while two are perpendicular to each other (angles are  $90^\circ$ ) and one is not (angle is  $103^\circ$ ). In addition, this forms a lopsided rectangular prism unit cell.

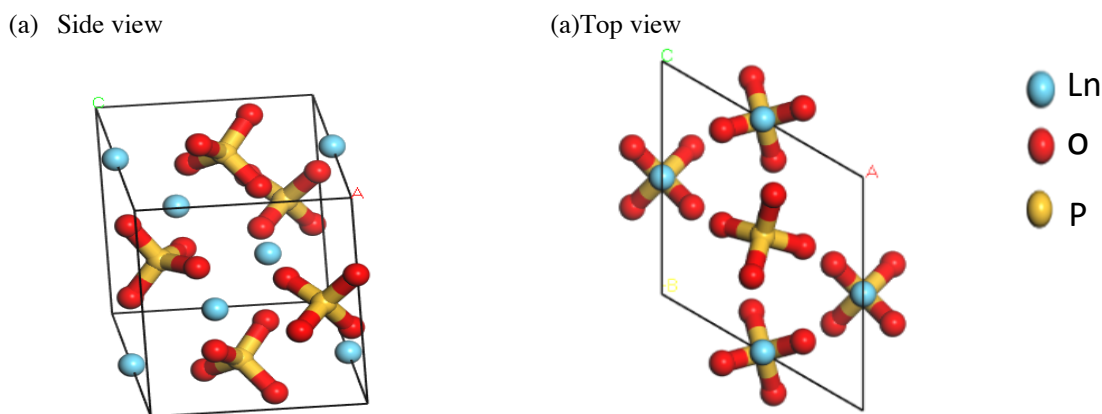


Figure 1: Optimized monoclinic  $\text{LaPO}_4$  and  $\text{CePO}_4$ . (a) represents the side-view, whereas (b) represents top-view. Blue, mustard, and red atoms represent Ln ( $\text{Ln} = \text{La or Ce}$ ), P, and O elements, respectively.

## 4. Results and Discussion

### 3.1. Structural and thermodynamic Properties

The experimental unit cell parameters for  $\text{LaPO}_4$  structure were found to be  $a=6.841 \text{ \AA}$ ,  $b=7.078 \text{ \AA}$  and  $c=6.515 \text{ \AA}$  [10], also for  $\text{CePO}_4$  experimental observed unit cell parameters are  $a=6.777 \text{ \AA}$ ,  $b=7.993 \text{ \AA}$ ,  $c=6.445 \text{ \AA}$  [11]. In addition, Table 1 lists the calculated and experimental lattice parameters, as well as the heats of formation for the optimised structures of various monazite systems. The thermodynamic stability of these systems can be deduced from the heats of formation ( $\Delta H_f$ ). For a structure to be confirmed as the most stable structure, the  $\Delta H_f$  must have the lowest possible value (generally  $\Delta H_f < 0$ ), whereas for  $\Delta H_f > 0$  implies thermodynamic instability of a structure. The following expression is used to estimate the heats of formation ( $\Delta H_f$ ):

$$\Delta H_f = E_c - \sum_i x_i E_i \quad (1)$$

where  $E_c$  is the calculated total energy of the compound,  $x_i$  is the number of atoms of each element in the compound and  $E_i$  is the calculated total energy of each element in the compound. The predicted  $\Delta H_f$  values of  $\text{LnPO}_4$  shows that the  $\text{LaPO}_4$  has the lowest heat of formation (-0.766 eV/atom), while  $\text{CePO}_4$  has the highest heat of formation (-0.729 eV/atom). These values suggest that  $\text{LaPO}_4$  is the most stable structure compared to  $\text{CePO}_4$  structure.

Table 1. The lattice parameters and the heats of formation ( $\Delta H_f$ ) for monazite type  $\text{LnPO}_4$  ( $\text{Ln} = \text{La}, \text{Ce}$ ).

Structure (P21/n)	Lattice parameters ( $\text{\AA}$ )			$\Delta H_f$ (eV/atom)	
	a	b	c		
$\text{LaPO}_4$	Cal.	6.841	7.078	6.515	-0.766
	Exp. [10]	6.841	7.078	6.513	
$\text{CePO}_4$	Cal.	6.770	6.990	6.450	-0.729
	Exp. [11]	6.777	7.993	6.445	

### 3.2. Elastic moduli

The calculated Bulk (B), Shear (G), Young 's modulus (E), Poisson ( $\sigma$ ) and the Pugh (B/G) ratios are determined and shown in Figure 2. The bulk modulus is a measure of resistance to volume change under pressure, it is used to measure the hardness/strength of the material. Shear modulus describes the resistance to shape change caused by shearing force, in this case it is used to check the material rigidity where the high value indicates that the material is highly rigid otherwise flexible. Young's modulus describes the relative stiffness of a material. Furthermore, we determined the ratio of bulk modulus to shear modulus (B/G) to investigate the extent of fracture range in these structures. Pugh proposed that materials are considered ductile if the value of Pugh's criterion (B/G) > 1.75 [12]. In addition to substantiate this even further, the Poisson ratio ( $\sigma$ ) was determined and considered as ductile if ( $\sigma$ ) > 0.26 [13]. The calculated Bulk, Shear and Young modulus, as well as Pugh and Poisson ratio, are shown in Figure 2. From the calculated results, it is indicated that  $\text{LaPO}_4$  structure has high value of Bulk, Shear and Young 's modulus suggesting that it is hard and has a high degree of free stiffness also not easily compressed than  $\text{CePO}_4$ . The Pugh and Poisson 's ratio is greater than 1.75 and 0.26, respectively for  $\text{LaPO}_4$  and  $\text{CePO}_4$  structures. The results suggest ductility behaviour in these systems at 0 K. In addition, the calculated moduli values are compared with the experimental values, which showed that they agree well with each other to within 10% for all moduli (see Table2).

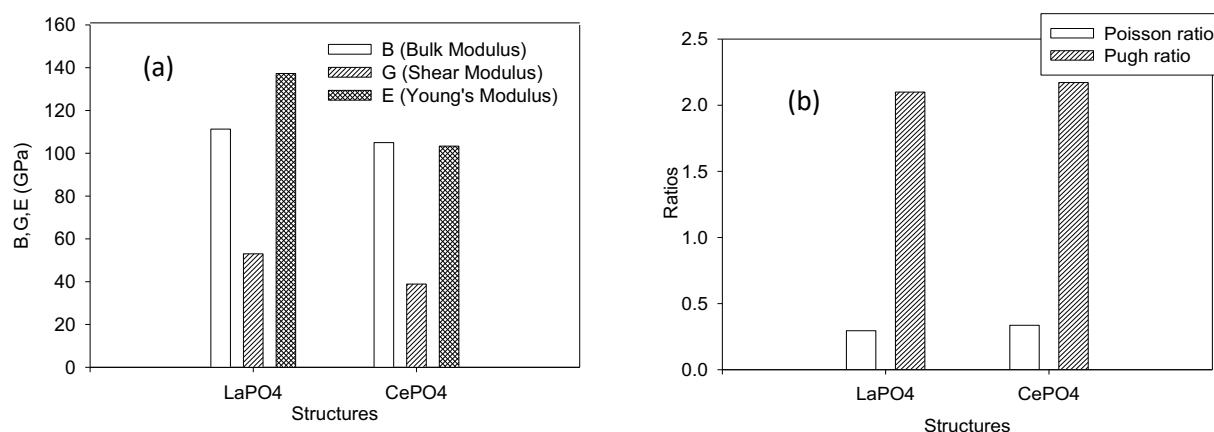


Figure 2: Calculated (a) bulk (B), shear (G) and Young's (E) moduli values as well as the (b) Poisson and Pugh ratios of  $\text{LaPO}_4$  and  $\text{CePO}_4$  at 0 K

Table 2: Calculated bulk (B), shear (G) and Young's (E) moduli values as well as the Poisson and Pugh ratios of  $\text{LaPO}_4$  and  $\text{CePO}_4$  at 0 K

Elastic modulus (GPa)	$\text{LaPO}_4$		$\text{CePO}_4$	
	Cal.	Exp. [14]	Cal.	Exp. [14]
B	111.28	117.00	105.00	121.00
G	53.01	51.00	38.86	58.00
E	137.24	133.00	103.35	150.00
B/G	0.295	0.310	0.336	0.293
$\sigma$	2.099	2.294	2.717	2.086

### 3.3. Phonon dispersion curves

Phonon dispersion curves are used to investigate the vibrational stability of the structures. The structure is considered stable if all the phonon frequencies are positive, however if some of the phonon frequencies are negative the system is considered unstable [15] Figure 3 shows the calculated phonon dispersion curves of monazite type  $\text{LnPO}_4$  at 0 GPa pressure along different symmetry directions. The dispersion curves show the presence of negative phonon frequencies on both structures that suggests that they are vibrationally unstable.

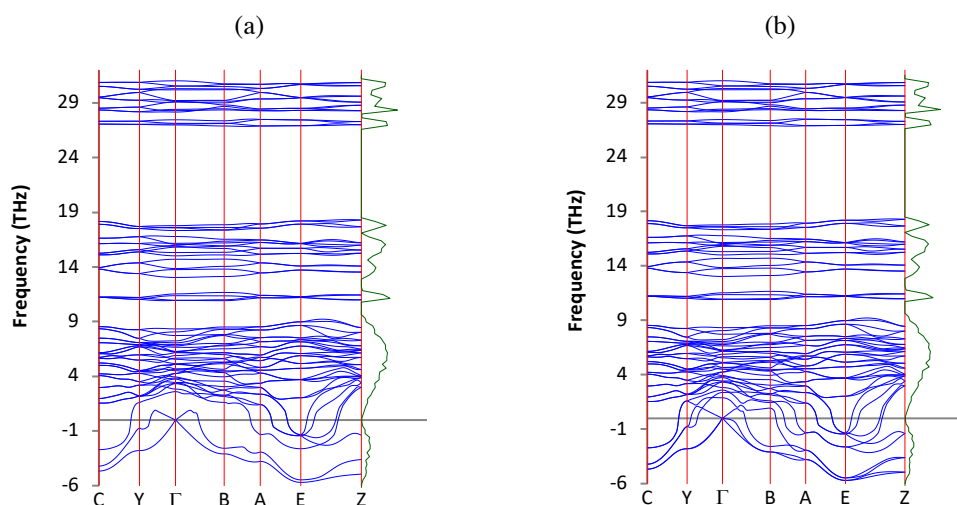


Figure 3. Phonon dispersion curves of (a)  $\text{LaPO}_4$  and (b)  $\text{CePO}_4$  monazite structures.

### 3.4. Thermal Properties

An understanding of thermodynamic properties of materials is of great importance to extend our knowledge about their specific behaviours when exposed to severe constraints such as high pressure and high temperature environments. Heat capacity ( $C_v$ ) gives information about lattice vibration, phase transition and motion of molecules. In figure 4, the specific heat capacity increases in the temperature range from 0 K to 500 K before it starts to be constant.

Our computed results of the specific heat capacity of the monazite systems indicate that  $C_v$  has obeyed the Dulong-Petit law at the high-temperature limit [16] which is reasonable to all solids at high temperatures. For all the studied materials, the  $C_v$  functions flatten out as the temperature increases above 500 K, thus suggesting that structural transition occurs at a very low temperature below 500 K for

all monazite systems. Furthermore, the results suggest that bonds between atoms become weak as temperature increases above 500 K. Debye's model of heat capacity predicts that in the limit of sufficiently low temperature ( $T$ ), the heat capacity due to vibrations of the crystal lattice must vary as  $T^3$ . The low- $T$  heat capacity is given by the expression:

$$Cv = \frac{12 R\pi^4}{5} \left(\frac{T}{\theta_D}\right)^3 \quad (2)$$

where  $R = Nk_B$ ,  $\theta_D$  Debye's temperature and  $T$  is absolute temperature. From the results at low temperature  $T^3$  behaviour matches Debye's model.

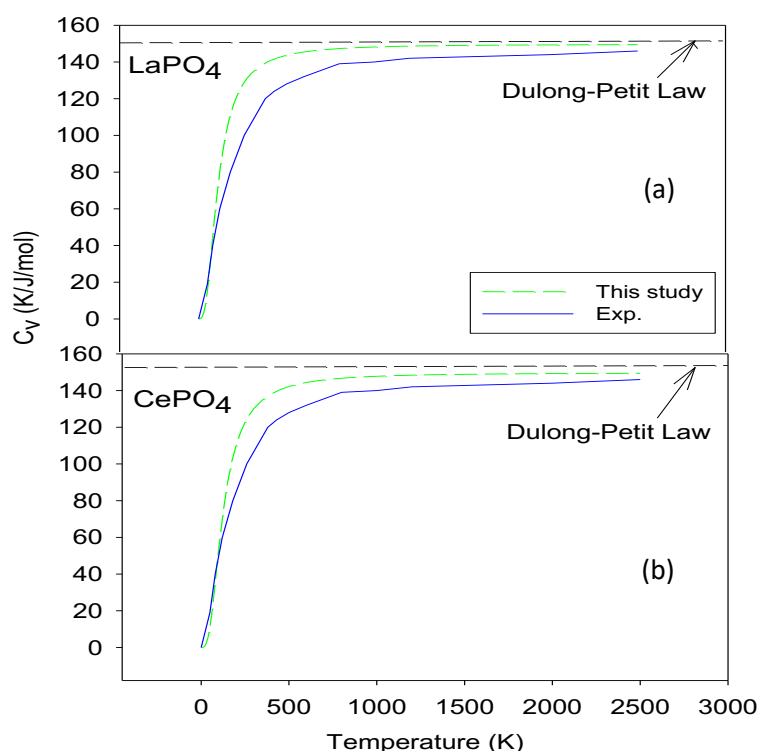


Figure 4. The heat capacity at the constant volume ( $Cv$ ) as a function of temperature for the monazite systems, the solid line (blue) represents the experimental results of Gavrichev et al. [17] and Popa et al. [18] for (a)  $\text{LaPO}_4$  and (b)  $\text{CePO}_4$  respectively.

## 5. Conclusion

The first-principle calculations were used to study the equilibrium lattice parameters, heats of formation, elastic properties and phonons of monazite systems. The results of lattice parameters were found to be in good agreement with the experimental values for both monazite-type structures (within 5%). From calculated heats of formation, it was found that  $\text{LaPO}_4$  is the most stable structure. Furthermore, Pugh and Poisson ratios of monazite systems were found to be greater than 1.75 and 0.26 respectively, which revealed ductility behaviour. The results also revealed that the monazite systems are vibrationally unstable. In addition, the structural transition happens below 500 K.

## 6. Acknowledgement

The work was carried at the Materials Modelling Centre, University of Limpopo. The authors would like to acknowledge the Centre of High Performance Computing (CHPC) and the financial support of the Department of Science and Innovation (DSI), through the Nuclear Materials Development Network

(at Necsa) of the Advanced Materials Initiative (AMI). The support of South African Research Chair initiative of Department of Science and Innovations is highly appreciated.

### References

- [1] Kemp D and Cilliers A C 2016 High-temperature thermal plasma treatment of monazite followed by aqueous digestion *J. S. A. Inst. of Mining and Met.* **10** 901-6
- [2] Catlos E J, Baker C B, Çemen I and Ozerdem C 2008 Whole rock major element influences on monazite growth: examples from igneous and metamorphic rocks in the Menderes Massif, western Turkey *Mineralogia* **39** 7-30
- [3] Hoshino M, Sanematsu K and Watanabe Y 2016 Chapter 279-REE mineralogy and resources *Handbook Phys. Chem. Rare Earth* **49** 129-291
- [4] Udayakumar S, Mohd-Noor A, Sheik A, Teuku A, Anderson G and Rama P 2020 Chemical and Mineralogical Characterization of Malaysian Monazite Concentrate *Min., Met. and Expl.* **37** 415-31
- [5] Hurst C 2010 China's Rare Earth Elements Industry: What Can the West Learn? *Institute for the Analysis of Global Security* (Potomac, MD)
- [6] Kresse G and Hafner J 1993 Ab initio molecular dynamics for liquid metals *Phys. Rev. B* **47** 558
- [7] Perdew J P and Yue W 1991 Correlation hole of the spin-polarized electron gas, with exact small wave-vector and high-density scaling *Phys. Rev. B* **24** 13298
- [8] Perdew J P, Burke K K and Ernzerhof M 1996 Generalized Gradient Approximation Made Simple *Phys. Rev. Lett.* **77** 3865
- [9] Parlinski K, Li Z Q and Kawazoe Y 1997 First-Principles Determination of the Soft Mode in Cubic ZrO<sub>2</sub> *Phys. Rev. Lett.* **78** 4063
- [10] Callejas G, Blanco M, Cabrera S, Prieto O, Luna I, Choque V and Crespo P 200 Simulation of the crystal structure of low temperature monazite LaPO<sub>4</sub> phase from x-ray diffraction diffraction pattern *Bol. Sci. J. Chem.* **17** 22-7
- [11] Keller G and Walter K 1965 Representation, lattice constants and chemical properties of some ternary oxides of plutonium, americium and curium of type MeIII<sub>2</sub>XVO<sub>4</sub> *J. Inorg. Nucl. Chem.* **27** 1253-60
- [12] Pugh S F 1954 XCII. Relations between the elastic moduli and the plastic properties of polycrystalline pure metals *London, Edinburgh, and Dublin Phil. Mag. and J. of Sci.* **367** 823-43
- [13] Greaves G N, Greer A L, Lakes R S and Rouxel T 2011 Poissons Ratio and Modern Material *Nat. Mat.* **10** 823-37
- [14] Du A, Wan C, Qu Z and Pan W 2009 Thermal Conductivity of Monazite-Type REPO<sub>4</sub> (RE= La, Ce, Nd, Sm, Eu, Gd) *J. of the Am. Cer. Soc.* **11** 2687-92
- [15] Togo A and Tanako I 2015 First principles phonon calculations in materials science *Scrip. Mat.* **108** 1-5
- [16] Hofmeister A M 2006 Thermal diffusivity of garnets at high temperature *Phys. Chem. Min.* **1** 45-62
- [17] Gavrichev K S, Ryumin M A, Tyurin A V, Gurevich V M and Komissarova L N 2008 Refined heat capacity of LaPO<sub>4</sub> in the temperature range 0-1600 K *Therm. Acta* **474** 47-51
- [18] Popa K, Sedmidubsky D, Benes O, Thiriet C and Konings P 2006 The high-temperature heat capacity of LnPO<sub>4</sub> (Ln = La, Ce, Gd) by drop calorimetry *J. Chem. Therm.* **38** 825-9

# Particle rapidity distributions in Pb+Pb and Au+Au high-energy collisions from the Ultra-relativistic Quantum Molecular Dynamics (UrQMD 3.3p2) model at $E_{elb} = 200$ AGeV.

**T.E Nemakhavhani**

Physics Department, University of Johannesburg, P.O.Box 524. Auckland Park 2006, Johannesburg, RSA.

E-mail: [tnemakhavhani@uj.ac.za](mailto:tnemakhavhani@uj.ac.za)

**Abstract.** The Ultra-relativistic Quantum Molecular Dynamic model (UrQMD 3.3p2) is a microscopic model based on a phase space description of nuclear reaction and it can now support the Large Hadron Collider energies (LHC) of up to a  $\sqrt{s_{nn}}= 14$  TeV. This model is used to simulate the ultra-relativistic heavy-ion collisions of finite matter between Pb+Pb and Au+Au collisions at an incident kinetic beam energy (lab frame) of  $E_{elb} = 200$  AGeV for the duration of  $t = 400$  fm/c. The simulated results are then used to calculate the rapidity distributions and particle ratios of both mesons ( $\pi$ ,  $\rho$ ,  $\eta$ , and  $K$ ) and baryons (p and  $\bar{p}$ ). The rapidity results show that at early time  $t$  the rapidity of all three light mesons is maximum at mid-rapidity and that of (p and  $\bar{p}$ ) are depicted at mid-rapidity for both Pb+Pb and Au+Au collisions. The time evolution of rapidity distributions for Au+Au and Pb+Pb collisions reaches saturation time at different time intervals. The particle ratios between different particle species are then compared between that of Pb+Pb collisions with that of Au+Au collisions. The results do not show big differences between both Pb+Pb and Au+Au systems and with the previous studies done in both experimental and theoretical studies.

## 1. Introduction

A large number of studies in heavy ion physics and high energy physics have been done using the results from the Relativistic Heavy Ion Collider (RHIC) but now with the restart of the Large Hadron Collider (LHC) physics programme, the field of high energy nuclear physics, and especially heavy ion physics, has gone into a new era [1, 2]. It is now possible to explore the properties of Quantum-Chromo-Dynamics (QCD) at unprecedented particle densities and temperatures, and at much higher energies than that produced at RHIC, from  $\sqrt{s} = 200$  GeV to  $\sqrt{s} = 14$  TeV at the LHC [3]. High energy heavy ion reactions are studied experimentally and theoretically to obtain information about the properties of nuclear matter under extreme conditions at high densities and temperatures, the phase transition of a new state of matter and the quark-gluon plasma (QGP) [4, 5].

This work reports on particle rapidity distributions in Pb+Pb and Au+Au high-energy collisions from the Ultra-relativistic Quantum Molecular Dynamics (UrQMD 3.3p2) model at  $E_{elb} = 200$  AGeV which corresponds to that of RHIC and widely previously used in different studies for a good comparison [6]. The study will focus on the comparison of the two systems of Pb+Pb and Au+Au collisions and determines if they are the same or different by studying the

rapidity distributions of hadronic particles at different time steps. The study of the distribution as a function of time will also give insights into whether the two systems do reach a phase transition at the same time, which has been poorly documented as many studies focus on energy distributions and comparing data simulated from models with experimental data, instead of the time evolution of heavy-ion collisions [7, 8]. The particle ratios will help us to understand the particle production between the two systems, which will help in the understanding of the effect of different degrees of freedom and phase transitions that lead to the final state of particle production [9]. The study will help in the continuous development and updating of the models such as the UrQMD model and as well as the future development of the high energy heavy ion experiments such as LHC and RHIC.

The rest of the paper is organized as follows: In section 2 we study the description of the UrQMD model. In section 3 we study the particle rapidity distributions in Pb+Pb and Au+Au high-energy collisions, concluding in section 4.

## 2. Brief description of the UrQMD model

The UrQMD is a microscopic model based on a phase space description of nuclear reactions. We use version 3.3p2 of the UrQMD model for this study as the latest version of UrQMD-3.4 is currently unstable while compiling [10, 11, 12]. The UrQMD 3.3p2 hybrid approach extends previous ansatzes to combine the hydrodynamic and the transport models for relativistic energies. The UrQMD model describes the phenomenology of hadronic interactions at low and intermediate energies from a few hundred MeV up to the new LHC energy of  $\sqrt{s} = 14$  TeV per nucleon in the center of mass system [13, 14]. The UrQMD collision term contains 55 different baryon species and 32 meson species, which are supplemented by their corresponding anti-particles and all the isospin-projected states [11, 13, 15]. The properties of the baryons and the baryon-resonances which can be populated in UrQMD can be found in [11, 15], together with their respective meson and the meson resonances. A collision between two hadrons will occur if

$$d_{trans} \leq \sqrt{\frac{\sigma_{tot}}{\pi}}, \quad \sigma_{tot} = \sigma(\sqrt{s}, type), \quad (1)$$

where  $d_{trans}$  and  $\sigma_{tot}$  are the impact parameter and the total cross-section of the two hadrons respectively [13, 15]. In the UrQMD model, the total cross-section  $\sigma_{tot}$  depends on the isospins of colliding particles, their flavour and the centre-of-mass (c.m) energy  $\sqrt{s}$ . More details about the UrQMD model are presented in Refs. [13, 14, 15].

## 3. Particle rapidity distributions

This section focuses on the different results of the particle rapidity distributions in Pb+Pb and Au+Au high-energy collisions. The results will be discussed as follows: in subsection 3.1 we look at the rapidity distributions results for meson particles, namely the pions  $\pi$ , the rhos  $\rho$ , the etas  $\eta$ , and the kaons  $K$ . In subsection 3.2: similar analysis is done as in subsections 3.1 but this time the focus is on baryon species, namely the proton(p) and the anti-proton( $\bar{p}$ ). The study then compares the particle rapidity distributions at a lower time of  $t = 2$  fm/c with that of a later time after the heavy-ion collisions at  $t = 198$  fm/c. In subsection 3.4 we then look at the time evolution of particle rapidity distributions in Au+Au and Pb+pb high-energy collisions for both mesons and baryon species and find the saturation times leading to phase transitions. Lastly, in subsection 3.5 the study compares the particle ratios for both Pb+Pb and Au+Au high-energy collisions.

### 3.1. Rapidity distributions of mesons: $\pi$ , $\rho$ , $\eta$ and $K$

Here we observe that in both figure 1 at  $t = 2$  fm/c and figure 2 at  $t = 198$  fm/c both the two systems of Au+Au and Pb+Pb high-energy collisions are comparable with each other. In both

systems, at  $t = 2$  fm/c we also observe that less particles are produced at mid-rapidity just below  $dN/dy \simeq 80$  for pions and just below  $dN/dy \simeq 20$  for rhos, etas and kaons when compared to a later time of  $t = 198$  fm/c and where a large number of particles are now produced above  $dN/dy \simeq 200$  for pions and  $dN/dy \simeq 48$  for kaons. At higher time  $t = 198$  fm/c it is observed that rhos and etas decay almost completely to form other particles. This is the reason a large number of pions and kaons are observed.

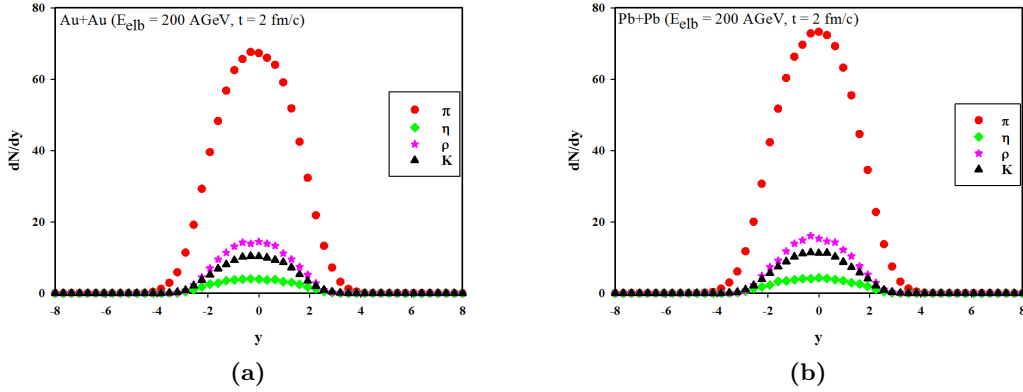


**Figure 1:** Particle rapidity distributions in Pb+Pb and Au+Au high-energy collisions for four different meson species: pion( $\pi$ ), rho( $\rho$ ), eta( $\eta$ ) and kaon( $K$ ) at  $t = 2$  fm/c.

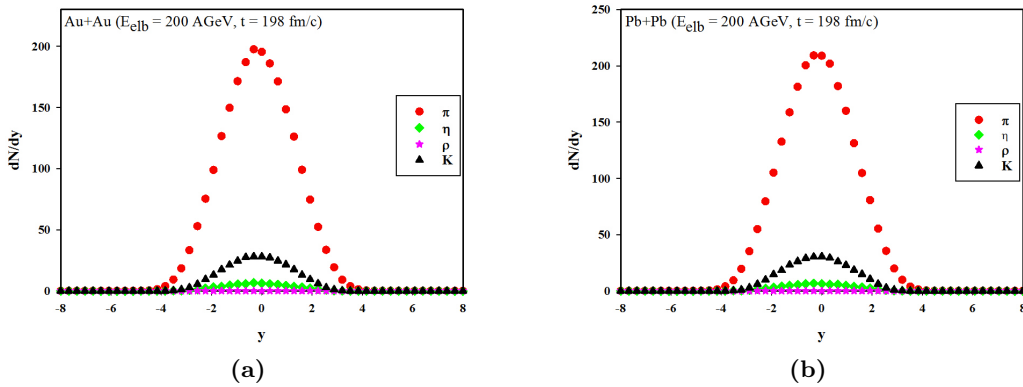


**Figure 2:** Particle rapidity distributions in Pb+Pb and Au+Au high-energy collisions for four different meson species: pion( $\pi$ ), rho( $\rho$ ), eta( $\eta$ ) and kaon( $K$ ) at  $t = 198$  fm/c.

### 3.2. Rapidity distributions of baryons: $p$ and $\bar{p}$

In this subsection it is observed that in both figure 3 at  $t = 2$  fm/c and figure 4 at  $t = 198$  fm/c both systems Au+Au and Pb+Pb, are comparable with each other. At  $t = 2$  fm/c we observe that less particles are produced at mid-rapidity, around  $dN/dy \simeq 5$  for both  $p$  and  $\bar{p}$  in both systems when compared to that of a later time of  $t = 198$  fm/c, where a large number of particles were produced just above  $dN/dy \simeq 14$  for both  $p$  and  $\bar{p}$  respectively. In figure 3 it is observed that particle rapidity distributions are depicted at mid-rapidity, and this is due to the mid-rapidity at an early time in the system still being very hot and dominated by mesons. Similarly,

at the later time of  $t = 198$  fm/c in figure 4 at mid-rapidity, the rapidity distribution for both baryon species behaves like a Gaussian curve. The reason behind this behaviour is because at a later time (after the collision) the systems have now cooled down and are dominated by baryon species. The inserts in both figures show dot-line plots for a clear behaviour of rapidity distributions in both systems.

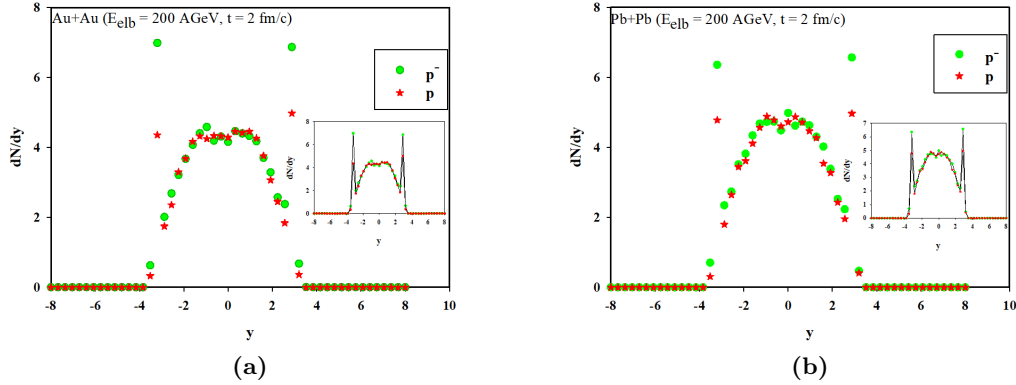


**Figure 3:** Particle rapidity distributions in Pb+Pb and Au+Au high-energy collisions for baryon particles proton( $p$ ) and anti-proton( $\bar{p}$ ) at  $t = 2$  fm/c.

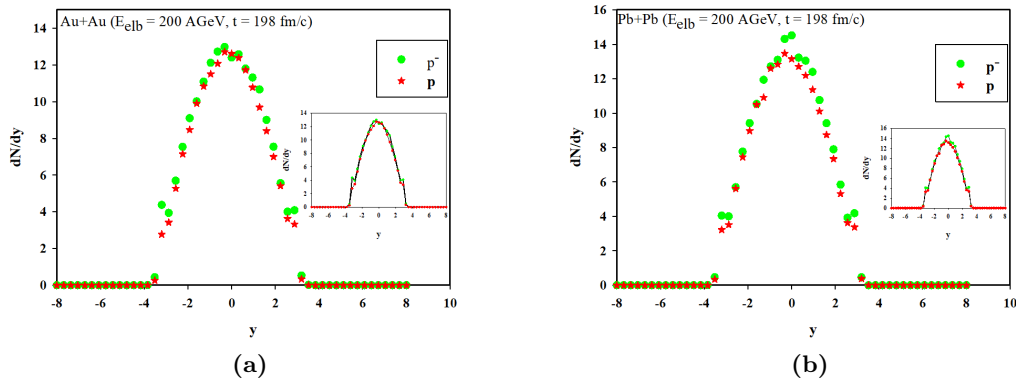


**Figure 4:** Particle rapidity distributions in Pb+Pb and Au+Au high-energy collisions for baryon particles proton( $p$ ) and anti-proton( $\bar{p}$ ) at  $t = 198$  fm/c.

### 3.3. Time evolution of rapidity distributions for mesons: $\pi$ , $\rho$ , $\eta$ and $K$

In this subsection, we now focus on the time evolution of rapidity distribution in Au+Au and Pb+Pb high-energy collisions for meson species. In figure 5 (a) and (b) we observe that particle rapidity distributions saturates with time for both systems. The saturation for (a) is around  $t \simeq 50$  fm/c and for (b) it is around  $t \simeq 60$  fm/c. The difference in saturation time is that (a) is a smaller system and (b) is a larger system.

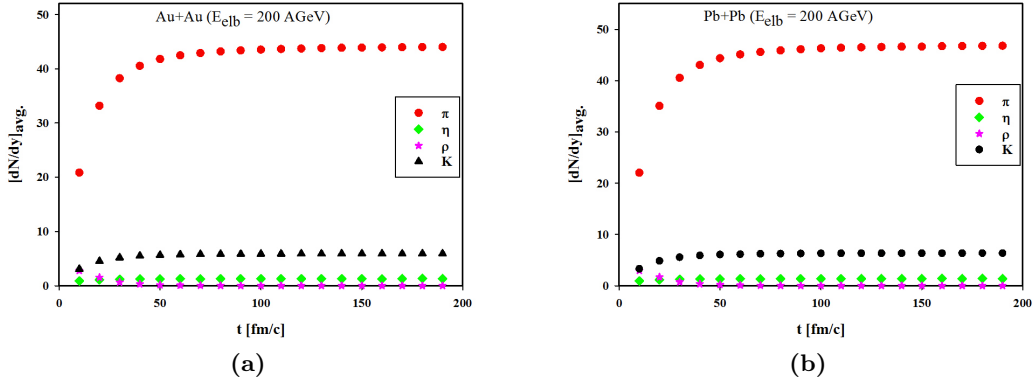


**Figure 5:** Time evolution of particle rapidity distributions in Pb+Pb and Au+Au high-energy collisions for four different meson species pion( $\pi$ ), rho( $\rho$ ), eta( $\eta$ ) and kaon( $K$ ).

### 3.4. Time evolution of rapidity distributions for baryon particles: $p$ and $\bar{p}$

As in subsection 3.3 we now focus on the baryon species. The same behaviour as in subsection 3.3 is observed but now the saturation time of the baryon species in both systems is higher. In figure 6 (a) and (b) it is observed that the particle rapidity distribution saturation for (a) is around  $t \simeq 70$  fm/c and for (b) is around  $t \simeq 80$  fm/c. The saturation times for both systems are higher than that of meson species because baryons are only formed and dominate the systems at a later time after the high-energy collisions.

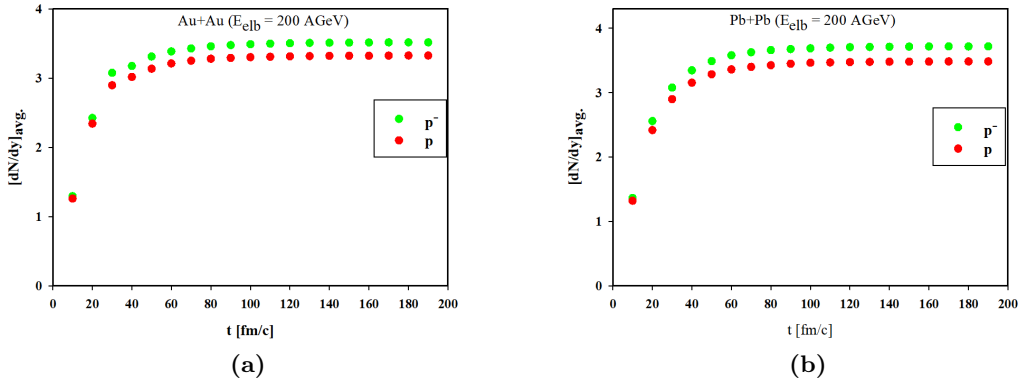


**Figure 6:** Time evolution of particle rapidity distributions in Pb+Pb and Au+Au high-energy collisions for baryon particles: proton( $p$ ) and anti-proton( $\bar{p}$ ).

### 3.5. Au+Au and Pb+Pb particle ratios.

This subsection discusses the particle ratios of both Pb+Pb and Au+Au high-energy collisions at different time intervals  $t = 2$  fm/c and  $t = 198$  fm/c. In both table 1 and 2 different behaviour of particle ratios between mesons to mesons and baryons to mesons with time are observed. In both tables  $p/\pi^+$  and  $K^+/\pi^+$  increase with time, and  $\bar{p}/\pi^-$  and  $K^-/\pi^-$  decrease with time. The results between the two systems are very much comparable regardless of the other system being heavier than the other.

**Table 1:** Au+Au high-energy collisions particle ratios.

time fm/c	$p/\pi^+$	$\bar{p}/\pi^-$	$K^-/\pi^-$	$K^+/\pi^+$
2	0.19	0.28	0.21	0.14
198	0.24	0.24	0.20	0.21

**Table 2:** Pb+Pb high-energy collisions particle ratios.

time fm/c	$p/\pi^+$	$\bar{p}/\pi^-$	$K^-/\pi^-$	$K^+/\pi^+$
2	0.19	0.27	0.22	0.14
198	0.23	0.24	0.20	0.21

#### 4. Conclusion

From the presented results, it is observed that particle rapidity distributions for both mesons and baryons are comparable to both larger systems (Pb+Pb) and smaller systems (Au+Au) collisions at  $t = 2$  fm/c and  $t = 198$  fm/c. At mid-rapidity, it is observed that the distributions increase with time for pions and kaons while decreasing with time for rhos and etas. This is due to these particles decaying to form extra pions and kaons. Similarly for baryons, at mid-rapidity at  $t = 2$  fm/c, a depiction of both protons and anti-protons is observed such that at the higher time  $t = 198$  fm/c they both behave like mesons, and this is because baryons only dominate the system at mid-rapidity at a very later time after the heavy ion collisions when both systems have cooled down. The time evolution of the rapidity distributions shows that both systems reach phase transitions at different times for mesons and baryons and lastly, the particle ratios for both systems are comparable with each other. As such, one can conclude that both systems are very much comparable with each other at lower and higher times at  $E_{elb} = 200$  AGeV. Both systems reach phase transitions at different times, which will help in understanding the different stages of nuclear collisions, phase transitions, and chemical freeze out formed at different times after collisions. The results are again comparable to the previous studies done, even though with different systems, energies, models, and experimental data [8, 9, 16].

#### 5. Acknowledgments

I would like to thank the financial support from UJ Department of Physics.

#### References

- [1] Reichert T and Bleicher M 2022 *arXiv preprint arXiv:2206.00410*
- [2] Xu J, Yu S, Liu F, Luo X *et al.* 2016 *Physical Review C* **94** 024901
- [3] Campbell J M, Ellis R K and Williams C 2011 *Journal of High Energy Physics* **2011** 1–36
- [4] Demir N and Wiranata A 2014 *Journal of Physics: Conference Series* vol 535 (IOP Publishing) p 012018
- [5] Chen Z, Greiner C, Xu Z and Zhuang P 2019 *Physical Review C* **100** 014906
- [6] Lin Z w, Pal S, Ko C M, Li B A and Zhang B 2001 *Physical Review C* **64** 011902
- [7] Gao L N, Liu F H, Sun Y, Sun Z and Lacey R A 2017 *The European Physical Journal A* **53** 1–11
- [8] Li Q, Wang Y, Wang X and Shen C 2016 *SCIENCE CHINA Physics, Mechanics & Astronomy* **59** 1–4
- [9] Kundu S K, Bailung Y, Rode S P, Bhaduri P P and Roy A 2021 *Physical Review C* **104** 024907
- [10] Hussain N and Bhattacharjee B 2017 *Physical Review C* **96** 024903
- [11] Collaboration U *et al.* The urqmd user guide (2014)
- [12] Vovchenko V Y, Anchishkin D and Gorenstein M 2015 *Nuclear Physics A* **936** 1–5
- [13] Bleicher M, Zabrodin E, Spieles C, Bass S A, Ernst C, Soff S, Bravina L, Belkacem M, Weber H, Stöcker H *et al.* 1999 *Journal of Physics G: Nuclear and Particle Physics* **25** 1859
- [14] collaboration P *et al.* 2005 *Technical Progress Report, GSI, Darmstadt*
- [15] Bass S A, Belkacem M, Bleicher M, Brandstetter M, Bravina L, Ernst C, Gerland L, Hofmann M, Hofmann S, Konopka J *et al.* 1998 *Progress in Particle and Nuclear Physics* **41** 255–369
- [16] Hoelck J and Wolschin G 2020 *Physical Review Research* **2** 033409

# Modeling the infectiousness of droplets when exposed to ultra-violet germicidal system: A computational fluid dynamics approach

Emmanuel Igumbor<sup>1</sup>, Mbolahasina Ralijaona<sup>1</sup>, Muaaz Bhamjee<sup>1</sup>, Kennedy Otwombe<sup>2,3</sup>, Firdaus Nabeemeeah<sup>2</sup>, Neil Martinson<sup>2</sup>, Pedro Mafa<sup>4</sup>, Lerothodi Leeuw<sup>5</sup> and Simon Connell<sup>1</sup>

<sup>1</sup> Department of Mechanical Science Engineering, University of Johannesburg, Auckland Park, Johannesburg, South Africa.

<sup>2</sup> Perinatal HIV Research Unit, Chris Hani Baragwanath Academic Hospital, Faculty of Health Sciences, University of the Witwatersrand South Africa.

<sup>3</sup> School of Public Health, Faculty of Health Sciences, University of the Witwatersrand South Africa.

<sup>4</sup> Department of mathematical Sciences and UNISA - ATLAS High Energy Physics Group, University of South Africa, Johannesburg, 1710, South Africa

<sup>5</sup> Department of Physics and Astronomy, University of the Western Cape, Bellville 7535, Cape Town, South Africa

E-mail: shconnell@uj.ac.za; elgumuk@gmail.com

**Abstract.** Coronaviruses rapidly spread in humans and vertebrates, and cause respiratory, enteric, hepatic, and neurological diseases. Due to the risk associated with coronaviruses, many studies have attempted to identify mitigation measures to reduce their infectiousness and understand their dynamics, evolution and control. Despite the progresses, there is limited modelling data that shows the decay process of the coronavirus infectiousness in a confined environment, when subjected to ultra-violet germicidal irradiation (UVGI) system. Hence, in this study we report the result of a mathematical model that predicts the infectiousness of coronavirus while dispersing using computational fluid dynamics. A UV system was constructed as a fluid domain filled with air. The droplets were modelled using the discrete phase approach under transient flow conditions. Droplets particles were injected from the inlet at  $5 \text{ ms}^{-1}$  to a fluid domain and allowed to move in the ambient flow, subject to illumination with UVGI in the regions of the fluid domain. The survival rate of the virus follows an exponential decay as the concentration reduces. The results of this study show that our modelling describes the viral concentration, and its reduction over time. The model after validation could be used to predict the infectiousness of droplets when subjected to a UVGI system in these different scenarios.

## 1. Introduction

Coronavirus disease 2019 (COVID-19) is an infectious disease that was declared a pandemic in 2020 [1] due to its high level of transmissibility and spread across different continents. COVID-19 is caused by a novel betacoronavirus, which is named severe acute respiratory syndrome coronavirus 2 (SARS-CoV-2). SARS-CoV-2 is present in small droplets aerosols which could be classified as one of the main sources of air pollutants in a confirmed environment [2]. Furthermore, the coronavirus as an infectious disease is mainly inhaled as droplets from carriers

and patients [3]. Studies focusing on finding solutions to mitigate the spread and dangers associated with viruses in human health have been carried out since the discovery of the COVID-19 disease [4]. Amongst those studies are reports that are generally based on experimental and theoretical methods [5]. The main transmission mode of COVID-19 is human to human via propagation in the form of droplets and close contact.

Computational Fluid Dynamics (CFD) accounts for the inherent complex fluid behaviour of real indoor airflows including the dispersion of droplets from a cough or sneeze [6]. Thus, it is appropriate and ideal for modelling of the airflow behaviour, droplet dispersion and the fluid droplet interaction. The effect of a specific spatial distribution of the UV irradiance field can be introduced to the CFD model, which is needed to understand how infectiousness of droplets is attenuated by a UVGI system [6]. CFD is an approach that can be used to model the physical behaviour and evolution of fluids and droplets [6] and the transmission of airborne infectious diseases. People in a confined place such as an aircraft, commuter buses and hospitals are likely to be highly susceptible to airborne contagious agents [7]. Reports suggesting a higher risk of infectious disease transmission in confined environments, in particular those environments with poor ventilation, have been reported [8]. The CFD method has been used to validate COVID-19 infection data in confined environments, for example, a train, as in [9]. The formation of droplets of saliva has been numerically modelled using the CFD. An example is the report on the droplets from the mouth and lips of an infected person during the sneezing process [10]. From this point on, the virus transport could be modelled as propagating droplets [10].

The ultra-violet germicidal irradiation (UVGI) system is a technique employed to deactivate viruses, and has been used to reduce the survival rates of infectiousness in an open place [11]. The combination of the CFD and the UVGI system is essential as the technicalities and inherent characteristics of the combined process could help to introduce an enhanced technology which could assist to understand and mitigate the survival rate, the propagation and evolution of droplets [11]. Despite the numerous studies that reported the spread and control of COVID-19, there is still more to be understood. For instance, the survival rate of SARS-CoV-2 when exposed to the UVGI system in confined environments such as ambulances, taxis and hospitals are not yet fully understood. It is imperative that the evolution and spread of the COVID-19 in confined environments should be well understood to mitigate the transmission of diseases and viruses.

In this study, we present a CFD model of the evolution of the infectiousness of a droplet in a confined environment when subjected to a UVGI system. The CFD as implemented in ANSYS Fluent (v2020R2) [12] was used to model the survival rate of droplets in a confined environment as the droplets moved through the UVGI system. Additional code, which was used to model the effect of the UVGI on the viruses within the droplets, was developed and added to the CFD model. We adopted the discrete phase model (DPM) with specific boundary conditions for the simulations. We show that the infectiousness of the droplets reduced as the droplets pass through the UVGI system. The results of this study is envisaged to be implemented for the study of the control and spread of infectious diseases such as coronaviruses and tuberculosis.

## 2. Methodology

Viruses spread in the air is assumed to flow in small droplets. The Navier-Stokes equation for viscous incompressible flow employed to describe the air flow as experienced by droplets during propagation. Generally, the CFD approach involves solving numerically the fluid momentum, energy, transport and turbulent kinetic energy equations (Navier-Stokes equation ) in a discrete number of cells defined across the fluid domain. The droplets tracked in this study have large turbulence effects. Hence, the general Navier-Stoke equation which deals with viscous flow and turbulence is used. The Navier-Stokes equations governing airflow is:

$$\frac{\partial u_i}{\partial x_i} = 0, \quad \frac{\partial u_i}{\partial t} + u_j \frac{\partial u_i}{\partial x_j} = -\frac{1}{\rho} \left( (v + \nu_T) \left[ \frac{\partial u_i}{\partial x_j} + \frac{\partial u_j}{\partial x_i} \right] \right), \quad (1)$$

where  $u$ ,  $\rho$ ,  $v$  and  $\nu_T$  are the velocity, density, kinematics viscosity and turbulence viscosity, respectively. The  $i, j = 1, 2, 3$  are the components of the velocity vector and the spatial coordinates. Turbulence is modelled using the standard  $k - \epsilon$  model.

The CFD approach as implemented in ANSYS Fluent (v2020R2) employing the discrete phase model (DPM) was used for the modelling of the infectiousness of droplets passing through a UVGI system. When using the DPM to model the flow of a droplet, the trajectories can be determined by integrating the force balance in the Lagrangian reference frame. The droplets inertial as well as the forces acting on the droplet should be equal to the force balance in the Lagrangian frame as:

$$m_p \frac{d\mathbf{u}_p}{dt} = m_p \frac{18\mu C_D Re}{\rho_p d_p^2} \frac{1}{24} (\mathbf{u} - \mathbf{u}_p) + m_p \frac{\mathbf{g}(\rho_p - \rho)}{\rho_p} + m_p \frac{\rho}{\rho_p} \mathbf{u}_p \nabla \mathbf{u} + \bar{F}_{other} \quad (2)$$

where the  $m_p$ ,  $Re$ ,  $C_D$ ,  $d$ ,  $\mu$ ,  $\mathbf{g}$ , are the mass of droplet, relative Reynold number, drag force coefficient, diameter of the droplet, dynamic viscosity of the air and acceleration due to gravity, respectively. A suitable UVGI test-system was constructed as a rectangular box with  $500 \times 160 \times 60$  mm dimension (note this is the simplest case, the dimension could be varied depending on the type of the UVGI), placed in a relatively confined room. The rectangular fluid domain is used to define the region of the computational domain, which in this case is filled with air. The meshing scheme of the rectangular box and room are shown in Figure 1. The enthalpy, incompressible flow, mass fraction of species and radiation were accounted for in the energy equation.

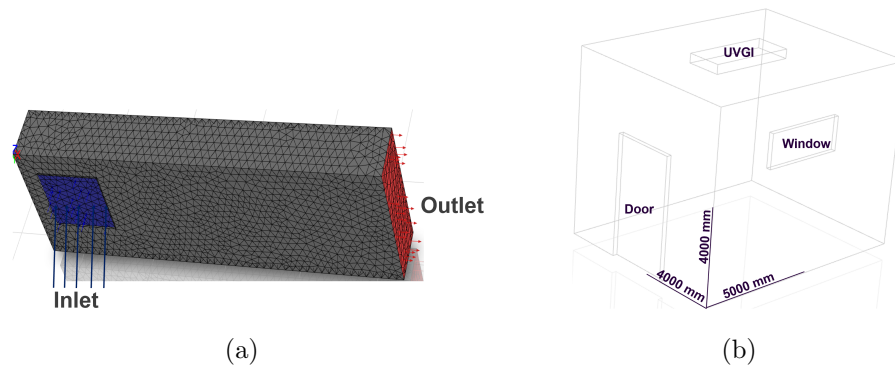


Figure 1: (a) A rectangular box with  $500 \times 160 \times 60$  mm dimension showing the inlet and outlet boundary conditions of the UVGI fluid domain, and (b) a confined room with the UVGI on the top.

Acceleration due to gravity ( $\mathbf{g}$ ) was set to  $9.82 \text{ ms}^{-2}$ . In the DPM, the integration with continuous phase was used to describe the droplet transition through the fluid domain. The droplets' concentrations were described by a scalar parameter. The scalar was updated via a user defined function (UDF) which described the survival rate. The Rorim-Ramler diameter distribution was used to describe the ensemble of droplet diameters. In the particular example, the droplets maximum (minimum) size and number of diameters were  $10^{-4}$  ( $10^{-6}$ ) m and 100, respectively. Droplets (water-liquid) were injected from the inlet using the face normal direction as shown in Figure 1a. The injection and inlet velocities were set to  $5 \text{ ms}^{-1}$  and the turbulence intensity and viscosity ratios for both the inlet and outlet were set to 5 and 10, respectively. A

total of 19526 droplets were injected from the inlet. The outlet pressure was set to zero. The discrete phase boundary conditions for the inlet and outlet were set to “escape“ whereas the stationary wall was set to ”trap“ with no slip condition allowing droplets to be trapped when they come in contact with the wall. The room temperature was set to 25 °C, the mass flowrate of the droplet is  $2.51 \times 10^{-7} \text{ kgm}^{-3}$ .

The simplest case of a droplet containing microorganisms is treated as simple object with parameters such as mass, momentum and energy. The UV dose  $D(r, t)$  is defined as the product of the irradiance  $I(r, t)$  and exposure time  $t$ . The irradiance  $I(r, t)$  ( $\text{Wm}^{-2}$ ) is a function of time and position  $r(x, y, z)$ , where  $x, y$ , and  $z$  are the position coordinates. The position of a droplet with respect to a point source is defined as  $r(x, y, z) = \sqrt{(x_1 - x_2)^2 + (y_1 - y_2)^2 + (z_1 - z_2)^2}$ , where subscript 1 and 2 are initial and final positions of droplet as it moves through a particular cell. The survival rate ( $S_R$ ) of microorganisms when exposed to UV radiation is used to evaluate the disinfection effect of UVGI-system [13]. The survival rate  $S_R$  of microorganisms passing through the UVGI system is defined as

$$S_R = \frac{C_t}{C_0} \exp^{-KIt} \quad (3)$$

where  $C_t$ ,  $C_0$  and  $K$ , are the microorganism concentration level after exposure for  $t$  seconds, the initial concentration of the microorganism from the inlet and the UV sterilization coefficient ( $\text{m}^2 \text{J}^{-1}$ ), respectively. While the concentration  $C(r, t)$  is a function of space and time, the  $K$  is a characteristics of the sensitivity of each microorganisms to the UV. The sterilization effect of the UVGI system is predominantly determined by  $K$ ,  $I$  and  $t$ . Equation 3 can be written in its differential form as

$$\frac{\partial C}{\partial t} = -KIC, \quad (4)$$

where  $C$  is the concentration of microorganisms per unit volume within the droplet. Equation 4 enables us to calculate the concentration evolution of airborne microorganisms as a function of time, by a UVGI system. For this study, the value of  $K$  is assumed to be unity. The infectiousness of a droplet is operationally defined as proportional to the viral load carried by the droplet. Initially, this is the product of the viral concentration and volume of droplet. In this simple initial model, a droplet is infectious if it has a certain viral load (above a threshold) and no longer infectious when the load is insufficient to cause infection. Refinements and the point where the above scenario maintains will form the focus of future studies.

### 3. Results and Discussion

In this study, we have considered the droplets UVGI scenarios at four different conditions (case I, case II, case III and case IV) as the droplets passed through the fluid domain (see Fig 2).

For the first simplest condition (case I) the initial concentration ( $C_0$ ) of viruses within the droplets and the irradiance ( $I$ ) are fixed and the same for all points as the droplets move from one cell to the other. The plot of the resulting droplet’s infectiousness is shown in Figure 2a. All droplets started from the same initial concentration with a decreasing exponential decay with the same slope (due to the same irradiance). The above shows in the first simple context that the scalar tracking the droplet infectiousness was reduced as expected when subjected to the UVGI system. The log-linear plot shown in Figure 2a for the time-dependent droplets’ infectiousness lie in the same straight line with the survival rate obeying an exponential decay as expected from the assumptions. The result of the simplest case I is in agreement with the decreasing viral concentrations resulting from initial expiration of droplets where the droplet viral load is attenuated due to the far-UVC irradiation in a room. The viral concentrations follow an exponential decay [11].

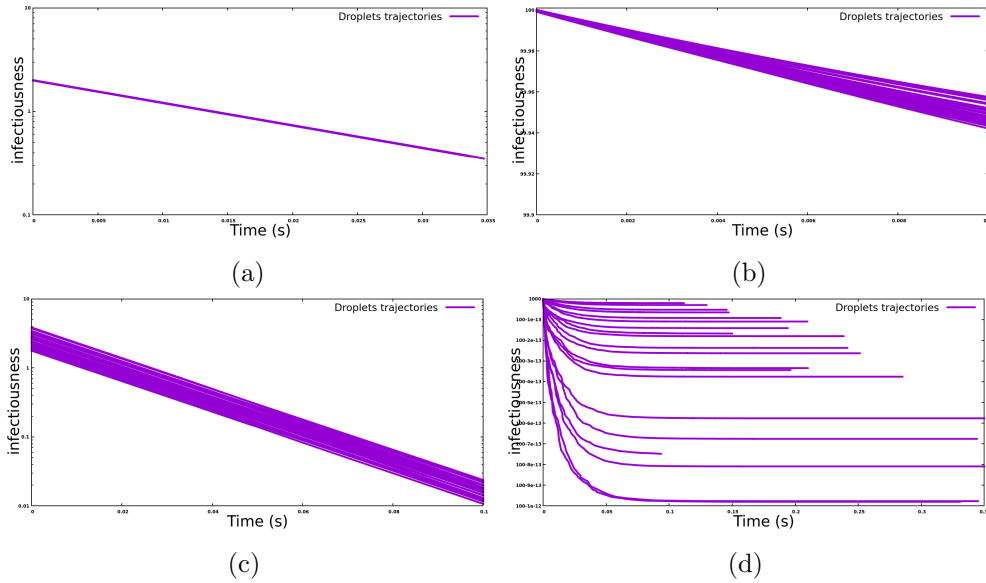


Figure 2: The plots of the survival rate of droplets for (a) uniform fixed irradiance and uniform initial concentration (b) irradiance is proportional to the inverse square of the droplet-point source distance (c) initial droplets concentration varied with the initial position of the droplets in the UVGI system and (d) the irradiance is a function of the position of the droplets as in (b) and the droplets move through the UVGI system, sampling a larger variation of irradiance values. Note each line represents a droplet.

For the second condition the initial concentrations of droplets were still assumed to be constant. That is all the droplets have the same viral concentrations at the inlet, however, the irradiance is not constant but is inversely proportional to the square of the distance apart of the droplets from the irradiation (point) source ( $I \propto 1/r^2$ ). Hence, the irradiance term in Equation 4 could be expressed as  $I = \kappa/r^2$ ; where  $\kappa$  is the constant of proportionality. At this stage, the value of  $\kappa$  and the functional form of the  $I(r,t)$  is arbitrary, but it can later be determined from measurement or modelling. For case II, the Equation 4 can now be written as

$$\frac{\partial C}{\partial t} = -KC \frac{\kappa}{r^2}. \quad (5)$$

The droplets' infectiousness behavior with respect to Equation 5 is shown in Figure. 2b. The results confirm that the droplet viral concentrations obeys approximate exponential decay with a range of similar slopes due to the variation of the irradiance.

In case III, the droplets were assumed to experience once again, uniform irradiance. However, the initial infectiousness of the droplets which is proportional to the initial droplet volume ( $C \propto V_{\vartheta}$ ) changes. The initial volume ( $V_{\vartheta}$ ) is defined as  $m/\rho_{\nu}$ , where  $m$  is the mass of the droplet and  $\rho_{\nu}$  is the initial density of a droplet. Hence, for the case III, the initial concentration at  $t = 0$  is mathematically equivalent to  $C_0 = C\eta \times (m/\rho_{\nu})$ , where  $\eta$  is the constant of proportionality. Therefore, applying the the assumption of case III for Equation 4 has the same equation but each droplet has a different initial infectiousness. The plot of the survival rate per droplet in response to the concentration and irradiance is shown in Figure 2c. The droplets have different viral concentrations at the inlet, however, they all are exposed to the same irradiance throughout their life span in the UVGI system. For case III, the droplets maintained the same slope in the log-linear plot as expected all through the UVGI system.

Finally, for the case IV, the droplets are considered to have the same initial concentration

as described for case III. However, they experience non-uniform irradiance which also evolves with time as they travel through the fluid domain. This is because the irradiance in the domain varies with position, and the droplets move through the domain and experience a time varying irradiance. In the case IV category, Equation. 4 is represented as

$$\frac{\partial C}{\partial t} = -KC \frac{\kappa}{r^2}. \quad (6)$$

As shown in Figure 2d, the infectiousness of droplets exhibit different and changing slopes. This is due to the different irradiance.

In the general case, the droplets should be modeled to experience different irradiance as a function of position, different initial volumes and finally, when coupled to the evaporation model, with time dependent volume. The model shows the approximate exponential decay of the survival rate of viruses infectiousness with a time varying rate, depending on the irradiance as it evolves with droplets changing position in its flow trajectory. This study is an introduction of the effect of UVGI system for deactivating transported microorganisms.

#### 4. Summary

Using the CFD approach, the behavior of the droplets in the UVGI system as subjected to four different conditions were ascertained. The survival rate of droplets and their concentrations exhibit an approximate exponential decay behaviour. The droplets' concentration reduced as they passed through the UVGI system. Four conditions were selected to exhibit separately different simple exponential behaviours (except case IV which behaves approximate exponential) as the droplets are transported in the UVGI system as expected in these simple cases. The effect of the UVGI can be accommodated within the CFD simulation by the method of additional code deployed as a User Defined Function to describe the scalar property of time dependent infectiousness for each droplet. In addition, the evaporation model of the companion paper will be accommodated in the same CFD model in the future.

#### Acknowledgments

This study is supported by the research grant of the University of Johannesburg. The authors thank the PHRU and its staff for access to utilise their AVGU equipment. The Centre for High Performance Computing is acknowledged for providing computational resources.

#### Reference

- [1] Di Gennaro F, Pizzol D, Marotta C, Antunes M, Racalbutto V, Veronese N and Smith L 2020 *International journal of environmental research and public health* **17** 2690
- [2] He Q, Niu J, Gao N, Zhu T and Wu J 2011 *Building and Environment* **46** 397–408
- [3] Ai Z, Mak C M, Gao N and Niu J 2020 *Building Simulation* vol 13 (Springer) pp 489–496
- [4] Ashby M P 2020 *Crime Science* **9** 1–16
- [5] Khan S, Siddique R, Ali A, Xue M and Nabi G 2020 *Journal of Hospital Infection* **104** 449–450
- [6] Messa G V, Yang Q, Adedeji O E, Chára Z, Duarte C A R, Matoušek V, Rasteiro M G, Sanders R S, Silva R C and de Souza F J 2021 *Processes* **9** 1566
- [7] Sodiq A, Khan M A, Naas M and Amhamed A 2021 *Environmental Research* **199** 111329
- [8] Dbouk T and Drikakis D 2021 *Physics of Fluids* **33** 011905
- [9] Wang Z, Galea E R, Grandison A, Ewer J and Jia F 2022 *Safety science* **147** 105572
- [10] Mesgarpour M, Abad J M N, Alizadeh R, Wongwiset S, Doranehgard M H, Ghaderi S and Karimi N 2021 *Journal of Hazardous Materials* **413** 125358
- [11] Buchan A G, Yang L and Atkinson K D 2020 *Scientific reports* **10** 1–7
- [12] ANSYS "Release 2020 R2" *Fluent Theory Guide*
- [13] Luo H and Zhong L 2021 *Building and environment* **197** 107852

# An Introduction to Statistical Thermal Models for Particle Production in Heavy-Ion Collisions

R.I. Maphoto<sup>a</sup>, B.L. Sekori<sup>b</sup>, K.E. Sithole<sup>c</sup>, V. Masilela<sup>d</sup>, and T. Khumalo<sup>e</sup>

<sup>a</sup>University of Limpopo, Private Bag X1106, Sovenga, 0727, South Africa

<sup>b</sup>Sol-Plaatje University, Private Bag X5008, Kimberley, 8300, South Africa

<sup>c</sup>University of the Western Cape, Private Bag X17, Bellville, 7535, South Africa

<sup>d</sup>University of Johannesburg, PO Box 524, Auckland Park, 2006, South Africa

<sup>e</sup>University of the Witwatersrand, Private Bag 3, P O Wits, 2050, South Africa

Email: [thuthukilekhumalo87@gmail.com](mailto:thuthukilekhumalo87@gmail.com)

**Abstract:** The number of various particles reported in relativistic heavy-ion collision research is consistent with the notion that they attain thermal equilibrium at temperatures substantially higher than those at which they kinetically freeze-out, which is a remarkable conclusion. This study attempts to explain this phenomenon by using a statistical thermal model based on statistical mechanics principles to simulate the behaviour, properties, and distribution of matter at extreme temperatures of microscopic matter. Additionally, the focus of the study is to apply statistical thermal models to determine how particle ratios and density are influenced by temperature for particles produced in heavy-ion collisions. Statistical thermodynamics models are applied in the last stage of heavy-ion collision, which is hypothesized to be in thermal equilibrium. The reason for this is that, as the temperature rises beyond 200 MeV, the quark-gluon plasma begins to form and after the quark-gluon plasma forms, hadronization occurs, resulting in the production of elementary particles. The study obtained the particle ratios such as  $\bar{p}/p$  and  $K/\pi$  and were found to be in good agreement with the experimental results obtained from other studies.

## 1. Introduction

The Big-Bang theory, which explains particle pair-production in heavy-ion collisions, is utilized to describe matter at all scales (from quarks to cosmos) [1]. There is currently more matter than antimatter in the universe because of the temperature change [2]. Since the beginning of the universe, the temperature has dropped, which has led to a decrease of antimatter [3]. Finding out what happens to antimatter and why there is an asymmetry between matter and antimatter is one of the challenging questions in physics [4].

The theory of quantum chromodynamics (QCD) is the main theory that explains the interaction of matter under extreme conditions. The QCD phase diagram can be studied to understand the properties of the different phases of matter by studying the systems formed in relativistic heavy-ion collisions [5]. QCD predicts that under extreme conditions, such as high temperature or high baryonic density, a new phase of matter known as quark-gluon plasma (QGP) will form, in which degrees of freedom can be observed in a volume larger than the size of a single hadron [6,7].

The lattice QCD calculations [8,9] predict a phase transition to a quark-gluon plasma at around  $T = 170$  MeV, which is equivalent to  $10^{12}$  K. This extreme condition is like the early stages of the evolution of the Universe following the Big Bang. Thus, studying the QGP's characteristics and how it evolves will allow us to probe the various stages of expansion of the Universe [10]. Statistical mechanics offers a more suitable theoretical framework for working with matter, producing many particles [11,12]. Moreover, it provides a convenient way to relate macroscopic and microscopic worlds through

computer simulations. The properties of strongly interacting nuclear matter under extreme conditions are important for understanding the early universe, when it was just atoms right after the big bang.

This study implements a statistical thermal model based on statistical mechanics and thermodynamics principles [13,14] for application in systems in thermal equilibrium. Since we are only going to evaluate particle numbers and particle ratios produced in heavy-ion collisions, we derive the expression of particle number density. The Fermi-Dirac and Bose-Einstein statistical distribution equations are derived to perform detailed statistical thermal model calculations on matter and antimatter to evaluate particle production under extreme conditions in heavy-ion collisions and to further understand the thermodynamic properties of macroscopic particles through the microscopic world [15,16]. The statistical thermal models together with statistical distributions are applied in the freeze-out stage of heavy-ion collisions.

## 2. Methodology

To evaluate the properties of particles produced under extreme conditions in relativistic heavy-ion collisions, this study implements a statistical thermal model based on statistical mechanics principles. In order to describe Fermi particles and bosons, we derived particle distribution expression using Fermi-Dirac and Bose-Einstein statistics.

The particle distribution of the Fermi or Bose gas is given by:

$$dN = \frac{g d\tau}{e^{(\epsilon-\mu)/T} \mp 1}, \quad (1)$$

where  $g$  is the degeneracy of the particle, which is  $g = 2s + 1$ ,  $s$  is the spin,  $\mu$  is the baryon chemical potential,  $T$  is the temperature, and  $\epsilon$  is the energy.

Integration is carried out over the phase space, so

$$d\tau = \frac{dV}{(2\pi\hbar)^3} dp_x dp_y dp_z. \quad (2)$$

To evaluate this integral, it is best to convert it to spherical coordinates and obtain the momentum particle density.

$$dN_p = \frac{1}{(2\pi\hbar)^3} \int_0^{2\pi} \int_0^{2\pi} \frac{gV}{e^{(\epsilon-\mu)/T} \mp 1} \sin\theta d\theta d\phi dp \quad (3)$$

$$= \frac{4\pi gV}{(2\pi\hbar)^3} \frac{p^2}{e^{(\epsilon-\mu)/T} \mp 1} dp \quad (4)$$

$$= \frac{1}{2\pi^2 \hbar^3} \frac{gV p^2}{e^{(\epsilon-\mu)/T} \mp 1} dp. \quad (5)$$

For this, we only need to substitute the appropriate expression for the energy and integrate over all possible energy values. In the relativistic case we should use:

$$E^2 = p^2 c^2 + m^2 c^4. \quad (6)$$

The expression becomes

$$dN_\epsilon = \frac{gV}{2\pi^2 (\hbar c)^3} \frac{\sqrt{\epsilon^2 + c^4 m^2}}{e^{(\epsilon-\mu)/T} \mp 1} d\epsilon. \quad (7)$$

Finally, to obtain the particle density, we integrate equation (7), noting that we must start integrating from the rest mass energy, since the energy was gained during its acceleration, and this maintains the kinetic energy unless the speed changes.

$$\frac{N}{V} = \frac{g}{2\pi^2 (\hbar c)^3} \int_{mc^2}^{\infty} \frac{\sqrt{\epsilon^2 + c^4 m^2}}{e^{(\epsilon-\mu)/T} \mp 1} d\epsilon. \quad (8)$$

To assess the particle density of massless up-quarks and massless gluons, we further simplified the particle density expression of relativistic particles into a dimensionless form (which are ultra-relativistic particles). According to the Fermi-Dirac, the particle density of ultra-relativistic (dimensionless) particles is expressed as:

$$\frac{N}{V} = 1.808 \frac{gT^3}{\pi^2(\hbar c)^3}. \quad (9)$$

For Bose-Einstein, the expression for the particle density of ultra-relativistic (dimensionless) particles is

$$\frac{N}{V} = 0.244 \frac{gT^3}{\pi^2(\hbar c)^3}. \quad (10)$$

Considering that the derived expressions are not always analytically solvable, we used a computational approach using Python as the programming language since it is good for prototyping and has a quick implementation code.

### 3. Results and Discussions

#### 3.1 Particle ratio calculations

The quantity of various particles reported in relativistic heavy-ion collision research is consistent with the notion that they attain thermal equilibrium at temperatures substantially higher than those at which they kinetically freeze out, which is a remarkable conclusion. Particle production analysis in heavy-ion collisions is used to understand everything from the microstructure of nature to its macrostructure, including how the universe was created. Table 1 shows the calculated particle ratios of matter and antimatter at a temperature  $T = 174$  MeV and the baryon chemical potential  $\mu = 46$  MeV [17,18]. We chose a temperature of 174 MeV because the quark-gluon plasma is believed to start forming at 170 MeV. The particle ratios are calculated with the respective mass of each particle. The antiproton and the proton have the same mass of 938.27 MeV, the pion negative has the same mass as the pion positive of 139.57 MeV, and the kaon negative and the kaon positive have the same mass of 493.68 MeV. The ratio of  $\bar{p}/p$  obeys the Pauli principle, and they have a half integer spin, which implies that they are fermions. Thus, the particle ratio of  $\bar{p}/p$  was calculated using the Fermi-Dirac distribution function. The ratios of  $\bar{p}/\pi^-$ ,  $K^-/\pi^-$ , and  $K^+/\pi^+$  use the Bose-Einstein distribution function since the particles do not obey Pauli principle, they are bosons with integer spin.

Since kaon and pion are light particles, Table 1 below shows that the  $\bar{p}/p$  particle ratio is larger than that of  $K/\pi$ . This is because the transverse flow parameter values of lighter particles are typically found to be less than those of heavier particles (proton and antiproton). The pions are the lightest mesons and hadrons, unlike the kaon mesons, and they create the smallest particle ratio when colliding with the antiproton. According to the measured  $K/\pi$  ratios, particle production is enhanced by about a factor of two when compared to collisions at comparable energy. With an increase in temperature and strangeness, the  $K/\pi$  ratio rises quickly. The slight variation in the  $\bar{p}/\pi$  particle ratio results when compared to the theoretical results of this study and with the experimental results of other studies could be attributed to the methodology adopted, as some parameters like volume were ignored. Results from this study show a greater  $K^-/\pi^-$  particle ratio than those from other investigations. This suggests that heavier mesons are produced more frequently at higher energy, and as a result, one must consider the strangeness in other meson-meson collisions.

In the universe today there is more matter than antimatter; this is due to the change in temperature. Figure 1 shows the particle ratio of  $\bar{p}/p$ , which takes us back to the early universe when antimatter and matter existed in equal quantities. From the plots, it is observed that the  $\bar{p}/p$  particle production increases with an increase in temperature. This is because protons and antiprotons usually produce other particles when they annihilate at rest; however, their total kinetic and rest mass energies add up to twice the proton's rest mass energy. The plot of the  $\bar{p}/p$  particle ratio shows high production compared to the  $\bar{p}/\pi^-$ . This is because the pions are light mesons, and when in collision with heavy baryons like the antiproton it produces the smallest particle ratio.

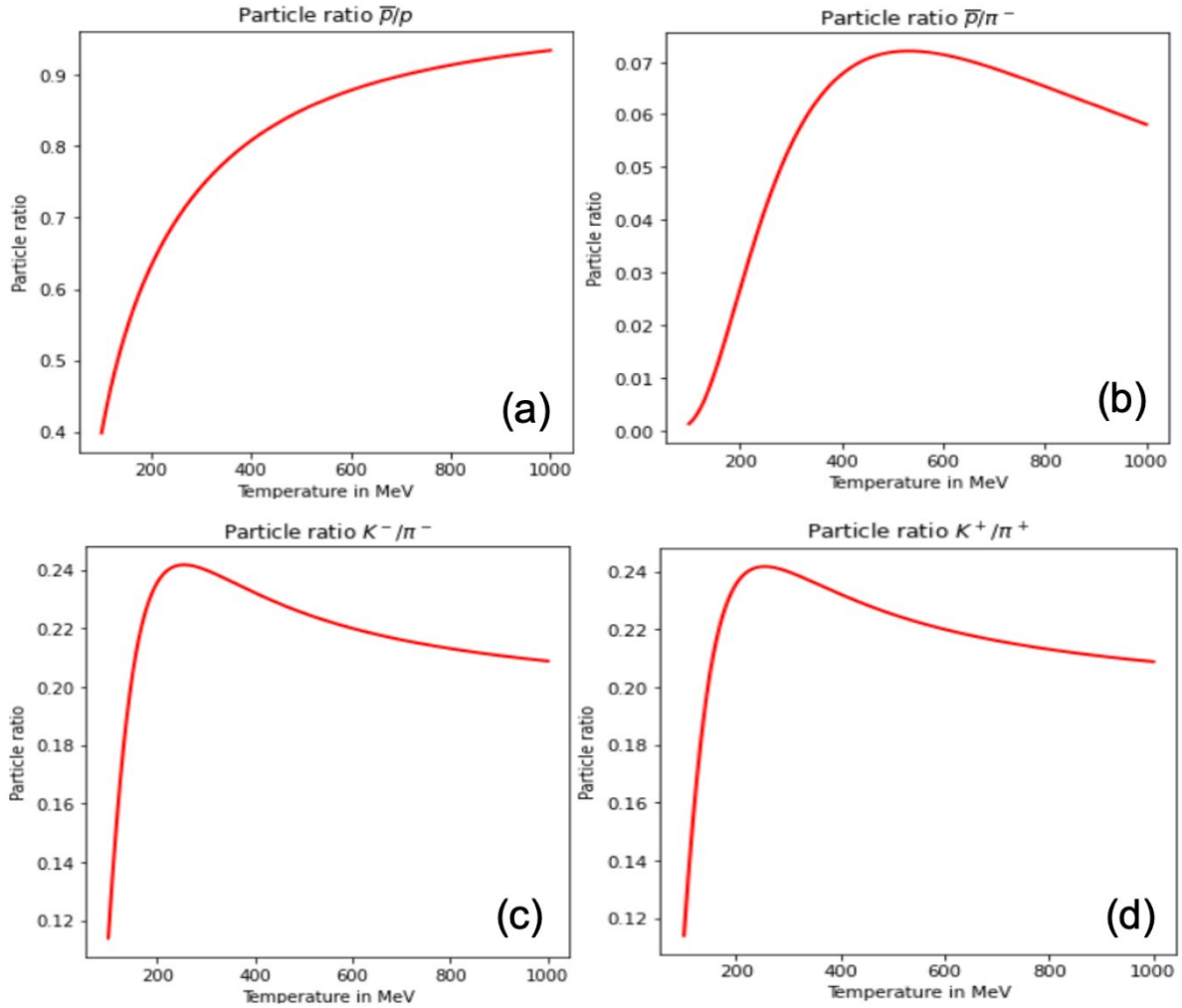


**Figure 1.** The particle ratio of (a)  $\bar{p}/p$ , (b)  $\bar{p}/\pi^-$ , (c)  $K^-/\pi^-$  and (d)  $K^+/\pi^+$  as a function of temperature.

**Table 1.** The calculated particle ratios at  $T = 174$  MeV and  $\mu_B = 46$  MeV.

Particle ratio	Theoretical data	Experimental [13]
$\bar{p}/p$	0.59	$0.65 \pm 0.07$
$\bar{p}/\pi^-$	0.09	$0.08 \pm 0.01$
$\pi^-/\pi^+$	1.00	$1.0 \pm 0.02$
$K^-/K^+$	1.00	$0.88 \pm 0.05$
$K^-/\pi^-$ [1]	0.23	$0.149 \pm 0.02$

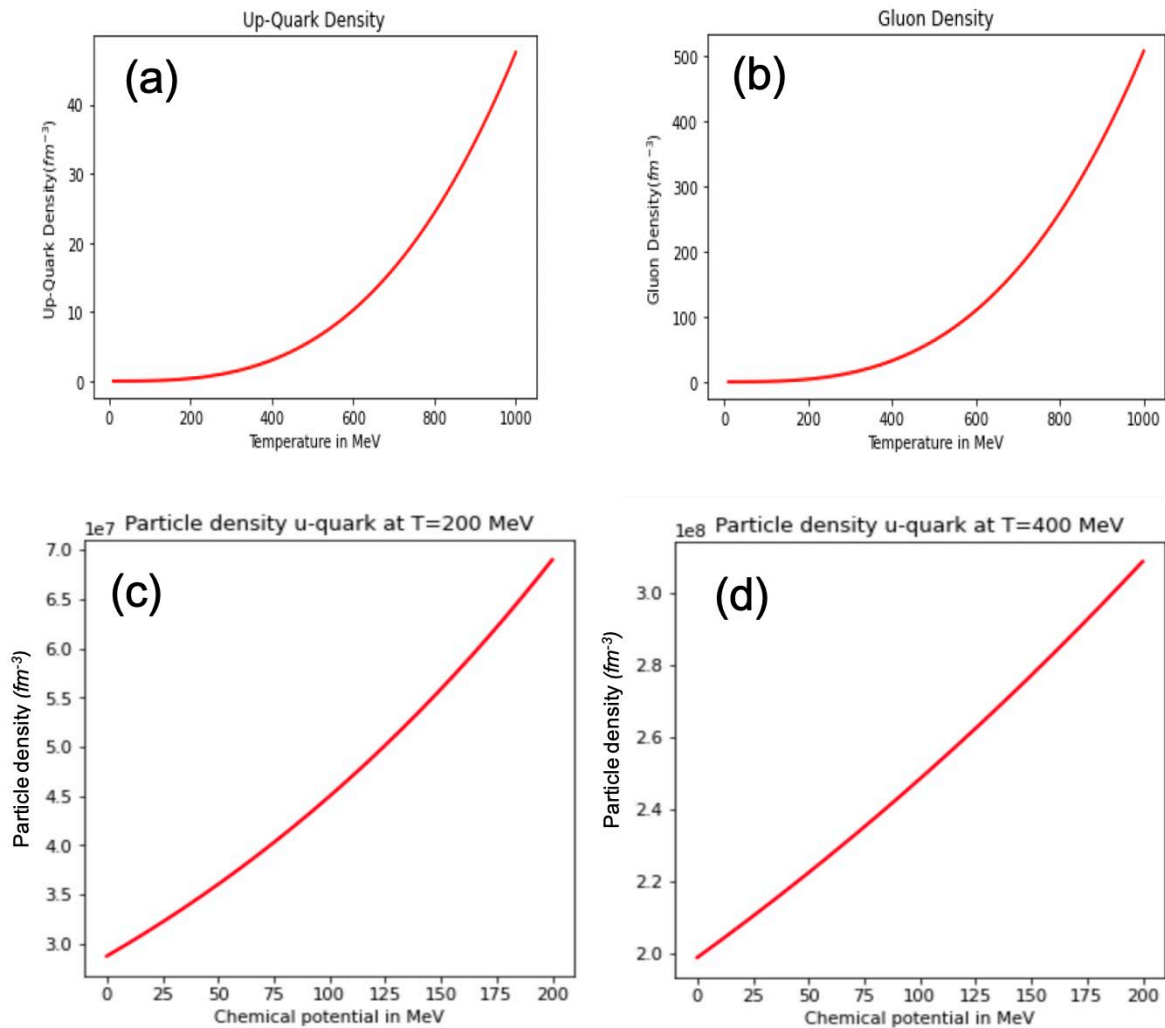


**Figure 2.** The particle density of (a) up-quark, (b) gluon as a function of temperature (c) and (d) up-quark particle density as a function of the chemical potentials at  $T = 200$  MeV and  $T = 400$  MeV.

To evaluate the strangeness production, the particle ratio of kaons and pions was calculated. The particle ratio plots of (c)  $K^-/\pi^-$  and (d)  $K^+/\pi^+$ , show similar behaviour, this is because the kaons and pions are fermions, which implies that the particles are distributed similarly using Fermi-Dirac statistics. The plots show a production of horn-like strangeness with an increase in temperature, which is consistent with the results obtained from other studies [19].

To determine the particle production of the QGP, we calculated the particle density of the up quark and the gluon as a function of temperature. In the plots, the dotted lines indicate the early stage of production when the quarks have not yet formed when it was just kaon and proton in the gluon particle density plot. Hence, the density is very small in both plots. It is observed that the quark-gluon plasma starts to form as the temperature rises above 200 MeV, whereby hadronization occurs and elementary particles like protons and neutrons are formed.

### 3.2 Particle density calculations

This section discusses the particle density of quark and antiquark particles as a function of the baryon chemical potential at temperatures  $T = 200$  MeV and  $T = 400$  MeV. Figure 2 shows the plot of the particle density of the antiquark and quark particles. From the plots, it is observed that the particle density values at  $T = 400$  MeV are much higher than at  $T = 200$  MeV. This happens because when the temperature increases, the average velocity of the particles increases. The average kinetic energy of these particles is also increased. The result is that the particles will collide more frequently because the particles move around faster and will encounter more reactant particles.

### 4. Summary and Conclusion

In the present study, we have performed detailed statistical thermal model calculations of matter and antimatter particles to evaluate the properties of the particles produced under extreme conditions in heavy-ion collisions. The statistical distributions were derived and applied to matter and antimatter particles using thermal and statistical model. The  $K/\pi$  ratios are often used to study the enhancement of strangeness production. For heavy-ion collisions, both the  $K^+/\pi^+$  and  $K^-/\pi^-$  ratios are found to increase steadily with the collision energy. This behaviour is consistent with the increasing pair-production rate as the collision energy increases. The  $K/\pi$  ratio measured  $K/\pi$  ratios in RHIC show a two-factor enhancement in particle production during collisions. The calculations of  $K^+/\pi^+$  and  $\bar{p}/p$  were found to be in good agreement with the experimental results of other studies. The quark-gluon plasma formed as the temperature rose above 200 MeV, and hadronization occurred, which resulted in the production of elementary particles. The particle density of the antiquark quark particle was determined at temperatures  $T = 200$  MeV and  $T = 400$  MeV, as a function of the baryon chemical potential. The findings provide a solid foundation for further evaluation of the particle density of antimatter and matter using more parameters, such as volume and pressure, for a better understanding of the effect of temperature on the system as a function of chemical potential.

### Acknowledgement

We thank Professor Azwinndini Muronga for hosting the internship and providing mentorship. Financial support from the National Institute of Theoretical and Computational Sciences (NITheCS) is acknowledged.

### References

- [1] Rubakov V A and Gorbunov D S 2017 *Introduction to the Theory of the Early Universe* (Singapore:World Scientific)
- [2] Manousakis E 2022 *Phys. Lett. B* **829** 137049
- [3] di Bari P 2022 *Prog. Part. Nucl. Phys.* **122** 103913
- [4] Xu J and Ko C M 2017 *Phys. Lett. B* **772** 290–3
- [5] Senger P 2004 *Prog. Part. Nucl. Phys.* **53** 1–23
- [6] Rischke D H 2004 *Prog. Part. Nucl. Phys.* **52** 197–296
- [7] Shuryak E V 1980 *Phys. Rep.* **61** 71–158
- [8] Karsch F, Redlich K and Tawfik A 2003 *Phys. Lett. B* **571** 67–74
- [9] Karsch F 2001 *Nucl. Phys. A* **698** 199–208
- [10] Stephanov M, Rajagopal K and Shuryak E 1998 *Phys. Rev. Lett.* **81** 4816
- [11] le Roux C, Navarra F S and Abreu L M 2021 *Phys. Lett. B* **817** 136284
- [12] Shuryak E 2009 *Prog. Part. Nucl. Phys.* **62** 48–101
- [13] Landau L D and Lifshitz E M 2013 *Statistical Physics* vol 5
- [14] Cleymans J, Kraus I, Oeschler H, Redlich K and Wheaton S 2006 *Phys. Rev. C* **74** 1–6
- [15] Bastian N U F, Blaschke D, Fischer T and Röpke G 2018 *Universe* **4** 67
- [16] Tiwari S K and Singh C P 2013 *Adv. High En. Phys.* 805413
- [17] Magestro D 2002 *J. Phys. G* **28** 1745–52
- [18] Braun-Munzinger P and Stachel J 2002 *J. Phys. G* **28** 1971–6
- [19] Tawfik A N, Elyazeed E R A and Yassin H 2021 *Preprint arXiv:2108.10320* [hep-ph]